PhD work

„Improving print mottle of coated papers"

Erich Zeyringer

Sappi Gratkorn

INDEX of CONTENTS

Chapter 5: Penetration by capillary pressure

5.1 Definition and measurement of contact angle

5.2 Calculating capillary pressure from Lucas Washburn equation for substrates with known pore radius

5.3 Calculating capillary pressure from Lucas Washburn equation for coating layers

5.4 Calculating capillary pressure from Lucas Washburn equation for substrates with unknown pore radius – theory and principal measurements

5.5 Calculating capillary pressure from Darcy equation for substrates with unknown pore radius – detailed measurements and calculations

5.6 Calculation of precoating holdout

5.7 Comparing porosity of paper substrates with absorbed liquid volume

5.8 Determination of capillary sorption pressure of coating layer and base paper

5.9 Capillary sorption of different base papers and coated papers

5.10 Influence of test liquid on capillary sorption

5.11 Calculation of base paper capillary sorption from mass balance of coating circuit

5.12 Reduce capillary sorption of base papers / precoated papers

Chapter 6: Pressure penetration

6.1 Darcy's law and Carman Kozeny equation

6.2 Calculating permeability from Bendtsen air porosity measurements

6.3 Calculating permeability by pressuring liquids through porous coating layers

6.4 Development of a new pressure penetration test at the Prüfbau lab printing machine

6.5 Calculation of the Darcy coefficient of coating layers

6.6 Prüfbau pressure penetration test with different liquids

6.7 Changing the application conditions for the Prüfbau pressure penetration test

6.8 Measurement of surface permeability of base papers

6.9 Measurements with OMYA's pressure penetration cell

6.10 Two-sidedness of PM11 papers

Chapter 7: Blade and film press coaters

7.1 Introduction – The four stages of penetration in blade coating

7.2 Application of coating colour (Phase A)

7.3 Free draw between application and blade (Phase B)

Chapter 12: Executive summary and outlook

Equations

Figures

Chapter 1: Summary

Mottling can be defined as uneven print density in printed screen areas caused by local differences in ink penetration depth. The deeper the ink penetrates or the more ink is transferred, the higher the local ink density. These differences may be derived from either pressure penetration of the ink in the application nip or from capillary sorption of coating layer after the application nip. As the ink is pulled of in the following printing nips ("back trapping") local differences in ink anchorage will cause local differences in ink density.

Pressure penetration of ink can be described by Darcy's law $\frac{dV}{dt} = Q = \frac{K * A * \Delta p}{\eta * L}$.

Local ink density will depend mainly on penetration depth of ink which is a function of local pressure Δp, local permeability of coating layer K and viscosity of ink η.

Capillary sorption pressure Δp_c will depend mainly on pore radius r, contact angle θ and surface tension γ of ink according to Lucas Washburn equation

$$\Delta p_c = \frac{2 * \gamma * \cos \theta}{r}.$$

Two kinds of mottling are investigated in this work: Formation mottling and drying mottling.

Formation stands for basis weight differences in base paper. Cutting out dark and light areas in base paper (which corresponds to flocs and voids) and measuring their basis weight showed differences up to 25% of mean basis weight which will cause in consequence local pressure differences in printing nips and coating stations.

As more fines and soluble substances from precoatings are pressed into the base paper at flocs where local pressure is higher, permeability of coating layer raises. Higher local pressure combined with higher local permeability of coating layer leads to higher ink penetration depth and higher ink density at flocs.

Drying induced motting has a total different pattern than formation induced mottling. Latex, which is pressed together with liquid phase into the substrate, migrates during drying with vapour to the surface. Vapour will search for the easiest path to the

surface and latex content will therefore be locally higher at spots with low vapour permeability. Higher latex content at the surface causes reduced local permeability and less capillary sorption when film formed.

A second mechanism of drying mottle is uneven latex film forming. When drying rate is low, latex is not properly film formed. Local differences in latex film forming cause differences in capillary sorption of ink. Non-film-formed latex stays in its original sphere shape. Capillary radius between non-film-formed latex particles is low and capillary pressure is much higher than at spots with totally film formed latex where the pores are closed. These local differences in capillary sorption pressure cause drying induced back trap mottling.

As pressure penetration of ink into the coating layer follows Darcy's law it is linearly depending on local pressure, permeability of coating layer (Darcy coefficient) and inversely on liquid viscosity.

To improve formation mottling the following counter measures are described:

1. Reduce local differences in pressure by improving base paper formation
2. Reduce local differences in coating layer permeability
3. Increase liquid phase viscosity

Ad 1) Formation:

Local basis weight variations are measured by Ambertec Beta formation. As compression of flocs is more pronounced in press and drying section their compressibility is lower. Higher basis weight and lower compressibility of flocs result in higher local pressure at flocs compared to voids next to them.

Solutions to improve formation:

- Lower the gradient of basis weight between flocs and voids – create bigger but "softer flocs"
- Reduce crowding number by lowering fibre length and consistency in headbox
- Increase shear in headbox and D-bar section of former
- Reduce consistency in headbox and D-bar section of former to relieve transformation of shear energy into formation improvement
- Reduce bridge flocculation of fibres by retention chemicals

Reduction of local compressibility can be achieved by:
- Lower wet pressing (stays in contradiction to press solids and runablity)
- Increase elasticity of fibre network by lowering the beating energy, less entanglement by rotational turbulence in the headbox feed flow or ionic bridging by retention chemicals
- W'fr furnish instead of w'c fibres
- Increasing the elasticity of the flocs

Realization at PM11:
- Formation of gap former PM11 was improved by switching to a new three component retention system with less bridge flocculation of fibres.
- The sheets in the headbox were shortened in length to reduce rotational swirls which led to fibre entanglement and small but stable flocs. Floc size increased with this measure but fibres from these flocs could be easier moved in the D-bar section of the former to voids. Formation was therefore "softer" and formation mottling dropped.
- New wire types were developed with a higher fibre support index and lower permeability. Primary dewatering was reduced and consistency in the blade part of the forming section dropped resulting in improved formation.
- These measures improved formation to a minor degree. Further development in headbox and former design is necessary to improve formation in w'fr. gap formers to a bigger extend.

Ad 2) Permeability of coating layer:
Lab trials, pilot trials and mill trials showed that reducing the permeability of precoating layers resulted in more homogeneous holdout of top coat latex as pressure penetration of liquid phase was reduced. Fine particles like latices will travel with liquid front into the precoating layer.

Lowering the permeability of precoating layers can be achieved by:

- Replacing latex by starch as liquids have better barrier properties than dispersion and starch increases shrinkage of high solids coating layers during drying
- Increasing the binder content by either adding more binder or improve the water retention of the precoating – higher water retention stands for less fine particles and soluble binders travelling with liquid phase into the base
- Replacing partly coarse pigments by finer types (flat PSD instead of steep PSD)
- Reducing application pressure of precoating. Filmpress coater are lower in application pressure than blade coaters and show therefore more uniform coating layer permeability at similar in-plane coat weight distribution. Curtain coaters apply the coating colour pressure-less and are superior in uniformity of coating layer permeability.

At PM11/OMC11 mottling was improved by:
- Changing pigment mixture of pre- and middle coating from 100% coarse Hydrocarb 60 to 35% fine Hydrocarb 90 + coarse 65% Hydrocarb 60.
- Replacing latex in precoating by starch. It was totally new for most coating experts, that starch can improve mottling in all coatings but a long list of mill trials prooved the lab experiments. Lowering the permeability of the precoating and adding barrier properties to that coating improved significantly mottling.
- Increasing the amount of film press precoating and lowering blade middle coating.

Ad 3) Liquid phase viscosity:
The lower the water retention of the coating colour, the more water penetrates into the base paper under the pressure of application or equalisation.
Coating colours with low water retention are more sensitive to non-uniform loss of water which will contain soluble binders and small binder or pigment particles, resulting in more pronounced in-plane permeability differences of dry coating layer and in consequence worse mottling. This was proven in pilot and machine trials. Thickeners like starch, CMC or synthetic types are used in coatings to improve water retention. A method was developed to describe separately the liquid phase viscosity

of the two phase coating colour and compare it with the rheology of the complete coating.

Mottling can be significantly improved when thickeners are used which raise the liquid phase viscosity and are low in interaction with the solid phase of the coating colour.

Drying induced mottling improves when water retention of the coating colour is increased as the amount of latex which penetrates the substrate and the penetration depth of the fine latex particles is reduced. Uneven migration to the surface together with vapour during drying will be less pronounced.

Drying energy demand drops with higher water retention of coating colour as diffusion length of vapour to the surface is lowered.

Unfortunately most of the water retention measurements which are currently in use are not capable to describe the fast pressure penetration process under the blade. The new KCL-Clara system allows measurements within parts of seconds and correlated well with liquid phase viscosity.

Chapter 2: Mottling in offset printing

2.1 Ink transfer in offset printing

In offset printing three colours are printed: Cyan, magenta and yellow.

Pict. 2.1.1: Subtractive mixing of colours cyan, magenta and yellow

In pict. 2.1.2 it is shown how mixing these inks leads to every possible colour. Black colour is often added as the forth printing ink to improve the printing result.
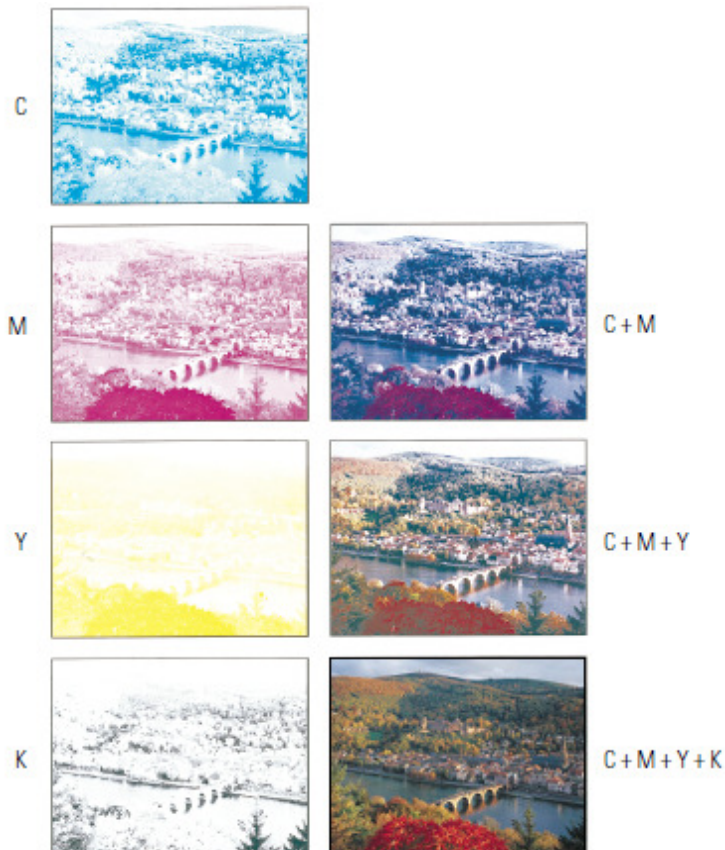
Pict. 2.1.2: Four colour offset printing – combining cyan, magenta, yellow and black to achieve any possible colour

The colour of a printed area is determined by the ratio of print dots of each colour while dot density is defined by the colour density.

Pict. 2.1.3 shows a typical screen print with all four colours cyan, magenta, yellow and black.

In full tone areas the whole paper surface is covered with ink.
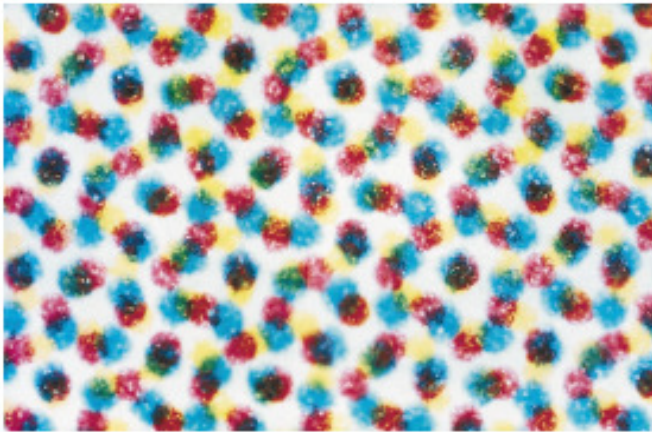
Pict. 2.1.3: Ink dots of cyan, magenta and yellow in screen area

Some printing machines (Pict. 2.1.4) have additional printing stations to add certain colours which are extensively used in the printed image. Printing quality improves when this colour is printed separately, especially in full tone areas.
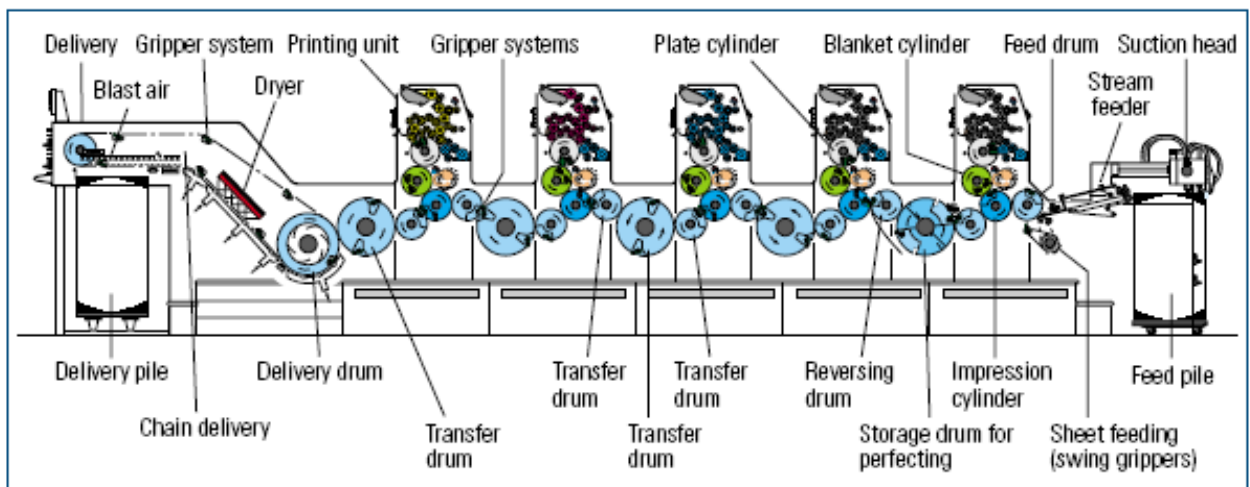
Pict. 2.1.4: Five colour sheet offset printing machine
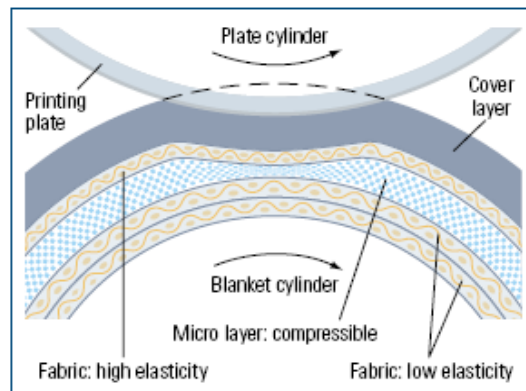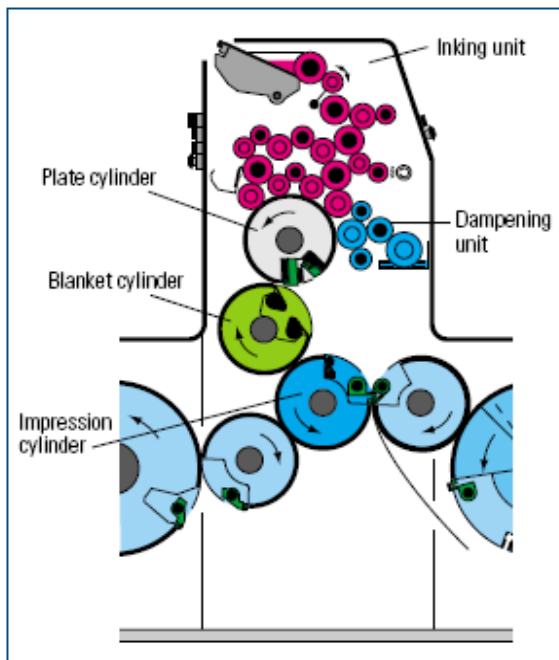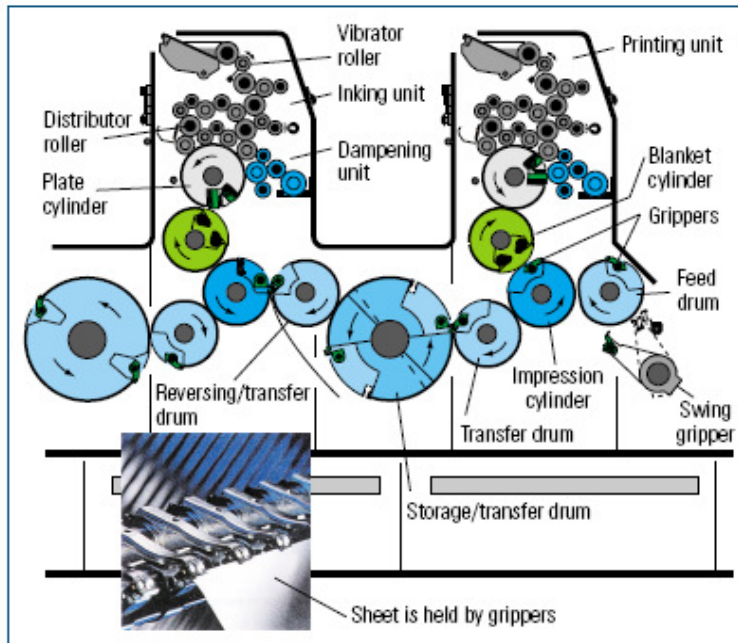
Pict. 2.1.5: Offset printing station

Offest printing is an indirect process to transfer ink to the substrate (eg. paper). Pict. 2.1.5 shows the ink application and the transfer to the paper.

Ink and water are applied on a plate cylinder, covered with a photo-sensitive film. Both media are transferred to a blanket cylinder. This cylinder is pressed with a defined pressure to the print substrate (eg. paper) and transmits thereby the ink and the water.

This indirect process is needed to provide dot transfer on rough paper surfaces e.g. uncoated paper qualities. The high compressibility of the blanket compensates surface defects of the substrate.

The ink is first applied together with fountain water on an aluminium plate. Unprinted areas are covered at the aluminium plate with fountain water while printed areas are covered with ink.

To separate printed and unprinted areas at the aluminium plate is coated with a photo sensitive film which is developed by illumination including the printed image (pict. 2.1.6, 2.1.7 and 2.1.8): At unprinted area the film is removed and the hydrophilic surface of the aluminium plate will be wetted by fountain water. The remaining area on the plate which is covered with film will is hydrophobic and will be wetted solely by ink.
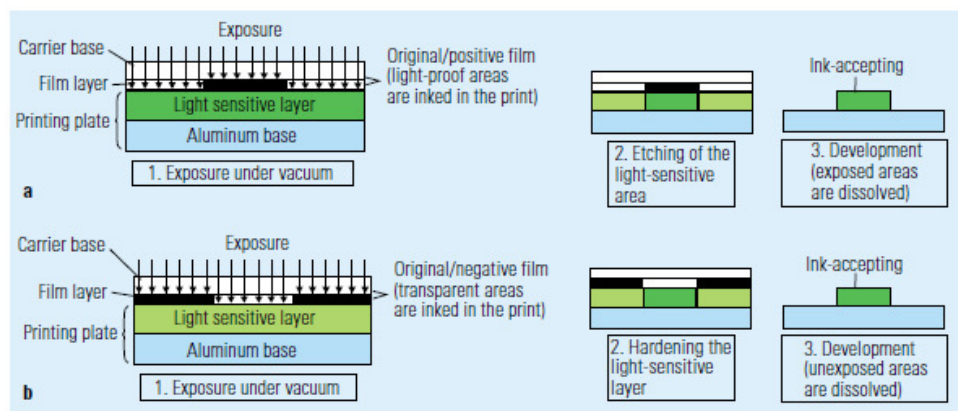
Pict. 2.1.6: Plate making process (a: Using a positive image, b: Negative image) (Heidelberger)
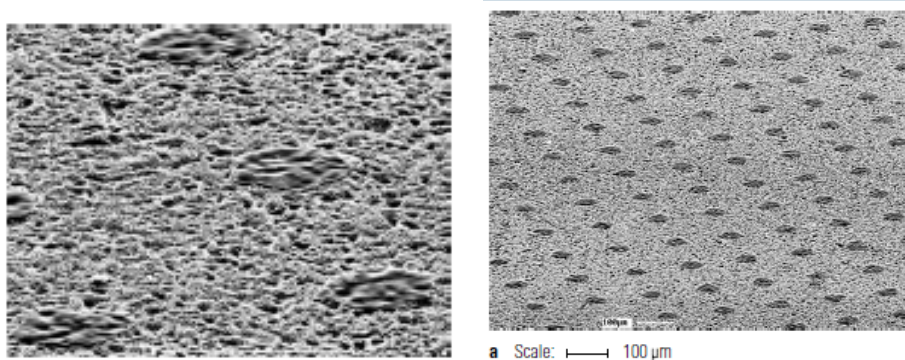
Pict. 2.1.7: Dots of on aluminium plate after removal of photo sensitve film at unprinted areas (dots: Oleophilic coating has remained on plate)
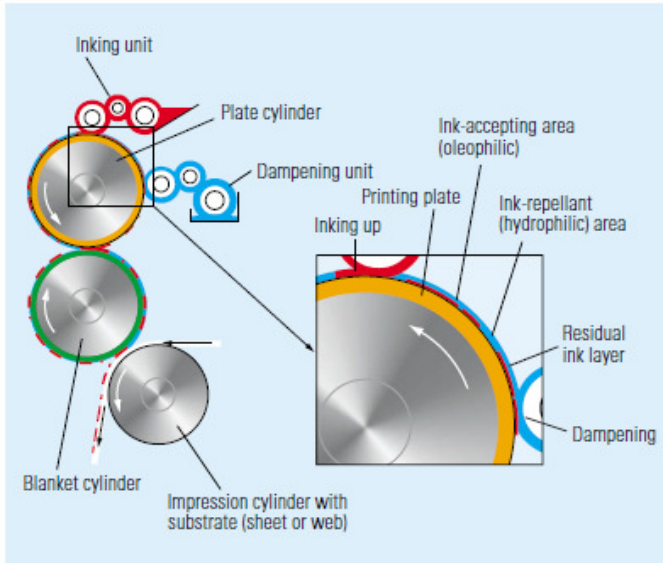
Pict. 2.1.8: Transfer of ink and fountain water to plate

At full tone areas the photo sensitive film at the aluminium plate remains in its original thickness.

The transfer of ink and fountain water to the paper is done by pressure penetration in the printing nip. At the nip exit a film split of the ink happens.
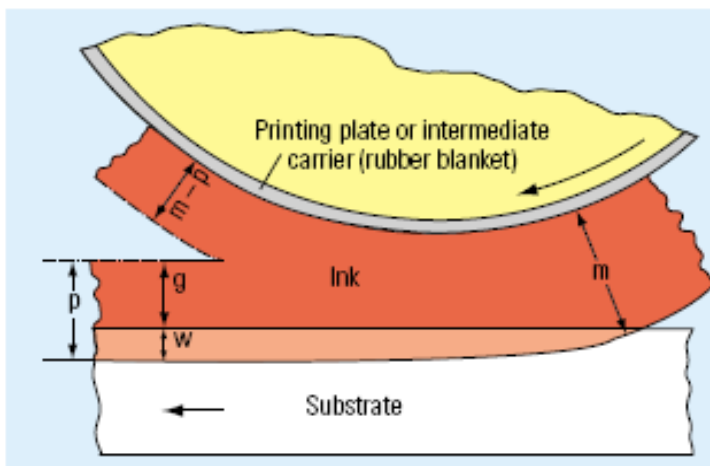
Pict. 2.1.9: Transfer of ink to the substrate

2.2 Definition of mottling

Mottling is defined as an uneven printing and occurs mainly in screen areas. The pictures 2.2.1 and 2.2.2 show the difference: The image of the blue sky in pict. 2.2.1 appears "cloudy", it shows the pattern of the base paper formation, while pict. 2.2.2 shows an even print image in all areas. Papers with bad formation or drying induced mottling show this mottling commonly in areas with 50 – 75% ink density and three colour images like violet or blue.

Pict. 2.2.1: Bad back trap mottle (cloudy structure of PM11 formation)

Pict. 2.2.2: Good back trap mottle

Three kinds of mottle are defined in literature:

    a) Screen mottling

    b) Back trap mottling

    c) Water interference mottling

All kinds of mottling are caused by local differences in ink and/or fountain water absorption.

Screen mottling (a)

One colour is printed with a screen pattern of defined dot density in the first print station and no back trapping is done in the following print stations (the screen area is cut out in the following rubber blankets). Sometimes the screen is printed in the last printing station where no back trapping can occur. Mottling is defined as local differences in ink density which are caused by non-uniformities of the substrate and not by the printing process. Screen mottling is influenced only by local differences in ink penetration depth at the application nip. The deeper the ink is pressed into the

paper the higher the local ink density. No influence of paper pre-wetting or capillary sorption after application can occur.

Back trap mottling (BTM) (b)

When a single colour is printed in a printing station and this colour is partly pulled off in the following printing nips back trap mottling can occur by local differences in ink density caused by non-uniformities of the substrate.

A common example is a cloudy structure in images of blue heaven or grey background which is caused by the same pattern of coating layer non-uniformity in the substrate.

The worse the anchorage of the dots in the application nip due to low penetration depth, the more colour is pulled off in the following back trapping stations and the lower the local colour density will be at the end of the printing machine.

Back trap mottling is very common in black areas where black ink is printed in the first station and back-trapping happens in all following printing stations (3 – 5 nips). It occurs also often in purple tones where cyan and magenta are printed in the 2nd and 3rd station and back-trapping is done 1 – 3 times in the following printing nips.

BTM gets always worse when printers switch from 4 colour to 6 colour printing machines as the number of back-trapping units increase.

Water interference mottling (c)

In the first printing station no ink, only fountain water is locally applied. Example: Purple image where no black should be printed which is commonly printed in the first printing station.

In the next printing stations colour dots are printed on this pre-wetted surface. Irregularities in water absorption in the first nip lead to differences in print dot penetration in the following nips. When fountain water is not absorbed properly the ink cannot penetrate the substrate in the following printing station as polarity is the opposite.

Fountain water has a lower viscosity than printing inks but a higher contact angle and therefore the wetting of a coated surface is worse. Printers add IPA to the fountain water to lower the contact angle and to reduce the surface tension, which improves

the wetting ability of the fountain water and increases capillary sorption after the application.

Both **screen and back trap mottle** are mainly determined by local irregularities in pressure penetration of the ink. In **water interference mottle** differences in water penetration are leading to mottling.
Back trap mottle can be a combination of screen mottling and water interference mottling when in the first nip only fountain water is applied, inks are printed in the next stations and back trapped in the following printing nips.

Why does mottling mainly occur in screen areas and not in full tone areas? The answer is relatively simple: The in-plane ink adhesion within the ink film (in X-Y direction) is much lower at screen areas. There it is disturbed by fountain water between the dots. Additionally fountain water is emulsified into the ink, ink viscosity drops and contact angle increases. Inks containing emulsified water can be pulled off easier in screen areas.

In full tone areas mottling can be seen as glossy spots, mainly in black: At areas with pour ink absorption, where less ink is remaining at the surface after back trapping, print gloss is lower.

Like in coating process the penetration depth of ink / water into coated papers is higher when coating porosity is high – exactly spoken when the Darcy coefficient of the coating layer is high (see chapter "floc analysis").
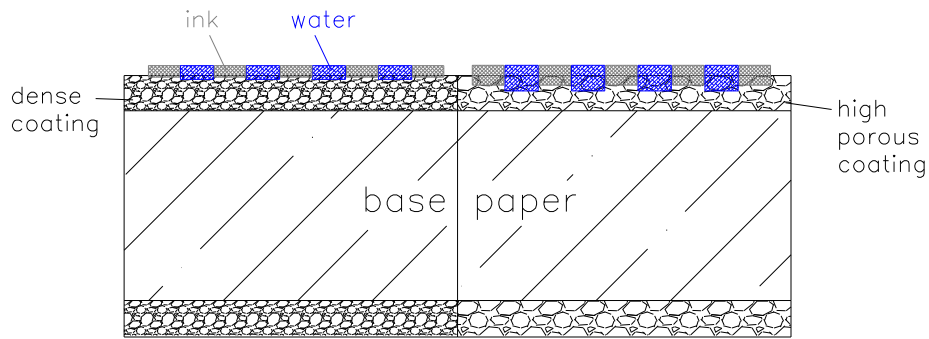
Pict. 2.2.3: Difference of ink absorption without pre-wetting on porous / dense coating surface (screen mottling and back trap mottling)
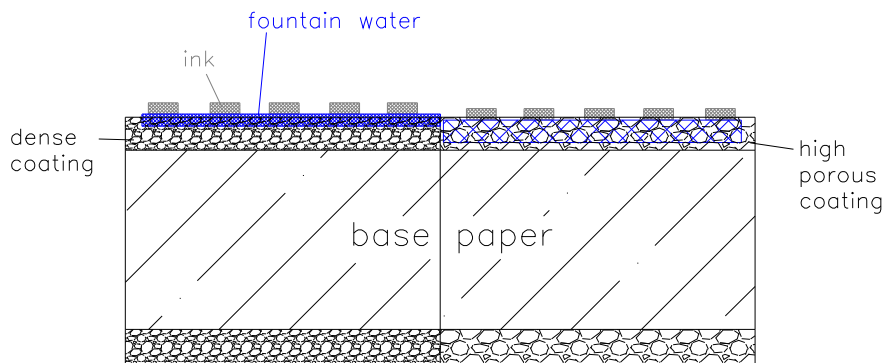
Pict. 2.2.4: Difference of ink absorption with pre-wetting on porous / dense coating surface

Most often back trap mottling is more severe than screen mottling due to the fact that back trapping multiplies the local differences in ink penetration depth (=ink density). Pict. 2.2.3 and 2.2.4 show that the lower the penetration depth of the ink, the easier the ink will be pulled off in the following printing stations and local ink density will drop again.

2.3 Explaining screen mottling (a)

The main difference between screen mottling and back trap mottling is the physics of ink penetration: While screen mottling is ruled only by Darcy's law for pressure penetration, back trap mottling is influenced additionally by capillary sorption of the ink and fountain solution between the printing stations. Capillary sorption is described by the Lucas Washburn equation $\Delta P_c = \dfrac{2 * \gamma * \cos \theta}{r}$.

Screen mottling is dominated by differences in local ink penetration depth caused by non-uniformities in surface permeability of substrate (e.g. the coating layer). Ink is transferred by pressure penetration in the application nip. If local differences in capillary sorption of the ink would occur after the nip (e.g. due to local differences in coating layer pore radius) the local ink density would remain unchanged.

Pict. 2.3.1 – 2.3.3 show results from the self developed Prüfbau penetration test which is explained in detail in chapter 6 (pressure penetration). Different substrates (single, double and triple coated paper) were tested. No difference in pressure penetration between oil and water when viscosity was detected although contact angle of oil and water is totally different (see pict. 2.3.4). This proves the assumption, that the transfer of fountain solution or ink into paper in a single printing station which is ruled by pressure penetration can be described solely by Darcy's law where viscosity is included but contact angle is left out.
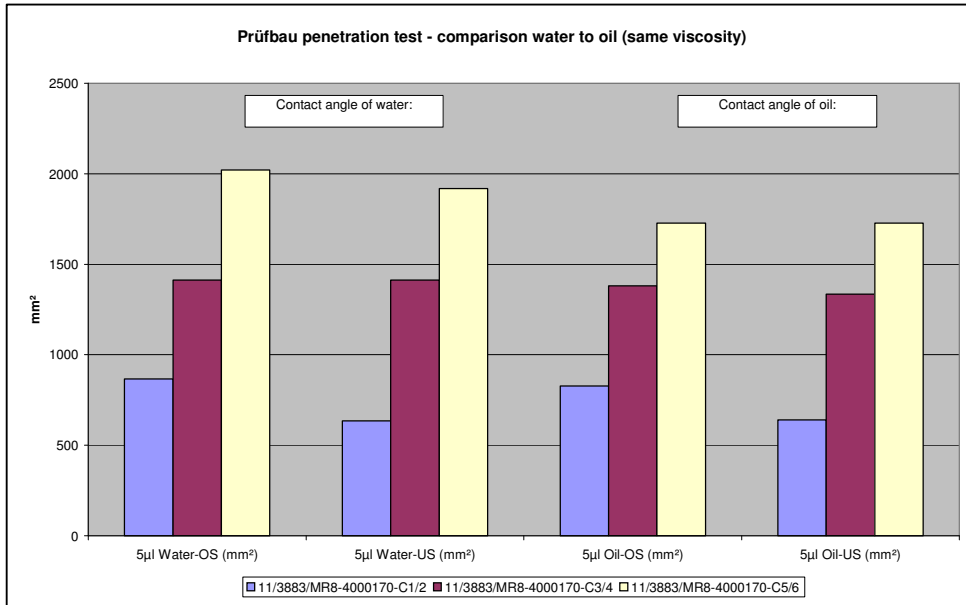
Pict. 2.3.1: Prüfbau pressure penetration test with water + oil at (C1/2 = precoated, C3/4 = middle coated, C5/6 = top coated)
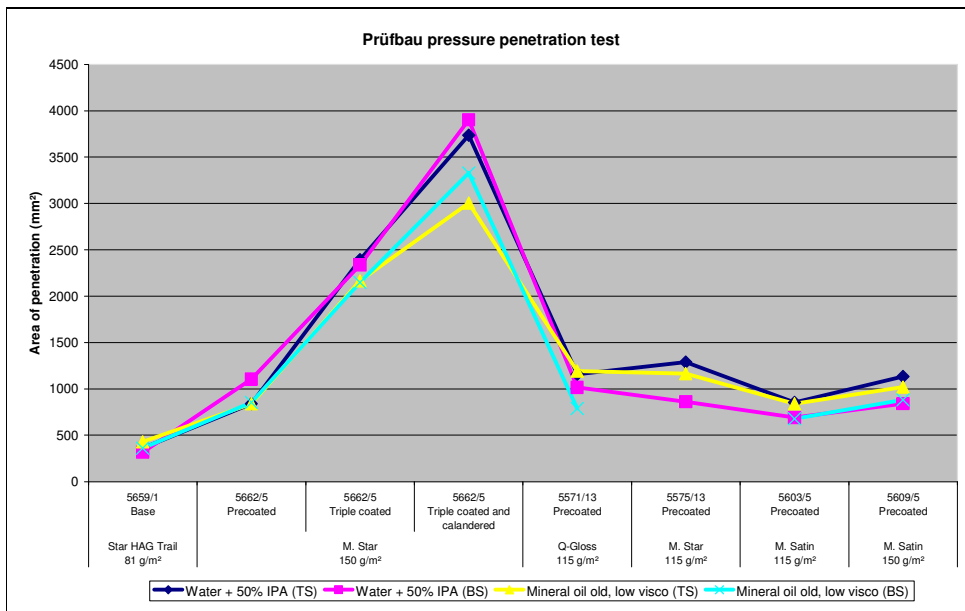
Pict. 2.3.2: Prüfbau pressure penetration test with water + oil for different papers
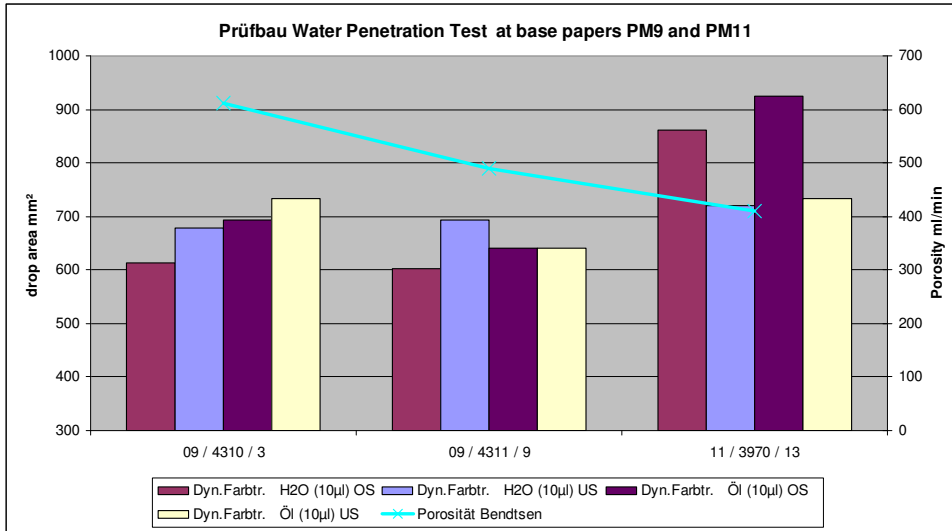
Pict. 2.3.3: Prüfbau water + oil penetration test at base papers

sappi GK/PQ	Comparison of different liquids for pressure and capillary penetration tests				
	Surface tension	Contact angle after 0,04 s		Viscosity	
		On precoated paper	On base paper	Spindel 2 / 100 rpm	Spindel 2 / 20 rpm
	mN/m	cp	cp	cp	cp
Water	71,5	92	81	26	15
Water + IPA (20%)	43,1	78	72	38	15
Waster + IPA (50%)	26,7			19	8
CMC solution 1,1 %	70,1			90	40
CMC solution 2 %					
Oil (Flint)	29,4	42	33	24	13

Pict. 2.3.4: Liquids for penetration tests

Applying Darcy's law the local penetration of the printing ink under pressure and in consequence screen mottling will be influenced by:

- Local differences in coating layer permeability (described by the Darcy coefficient K).
- Local thickness and compressibility differences of the whole substrate: The higher the local thickness of the paper and/or the lower the local compressibility, the higher the local pressure in the printing nip will be.

- The <u>viscosity of the ink</u>: The thinner the printing ink, the deeper the ink will penetrate in average and the lower the local differences in ink density will be. High viscous black ink is therefore most critical in screen mottling.

Screen mottling is mainly detected at single or double coated papers with low coat weight due to high differences in local pressure and in local Darcy coefficient of coating layer (see chapter 3 "floc analysis").

As the base paper of light weight coated papers is dominating in mass against coat weight, formation of base paper is ruling screen mottling as local basis weight differences lead to local pressure differences in the printing nip.

2.4 Explaining BTM - back trap mottling (b)

The ink penetration in the application nip will be ruled by Darcy's law as described above.
During the dwell time between the application nip and the following back trapping printing stations the ink penetration and anchorage will be extended by capillary penetration, described by Lucas Washburn: $\Delta P_c = \dfrac{2 * \gamma * \cos\theta}{r}$.
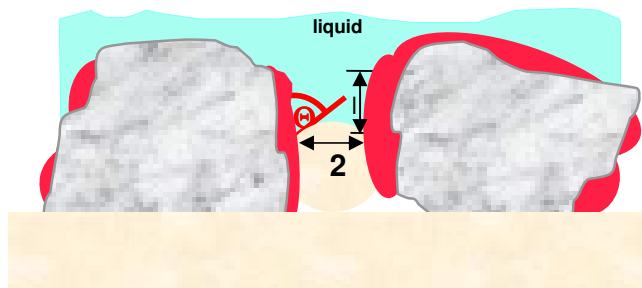
Pict. 2.4.1: Capillary sorption in pores of coating (blue = pentrating liquid, white = coating pigment, red = hydration layer of dispersant on pigment surface, changing the wetting abilities of the pigment)

According to Lucas Washburn capillary pressure increases with higher surface tension γ of liquid, lower contact angle θ (better wetting) and lower capillary radius. The higher the local capillary pressure, the deeper the liquid component of the ink (oil components) will penetrate after the application nip, the more ink particles will be immobilized on the paper surface, the bigger the distance of film split in the ink from the paper surface and the higher the local ink density after back-trapping will be.

As surface tension of ink is constant over the whole printed area the capillary sorption is influenced by three parameters:
  I. Local differences in pore radius of the coating layer
  II. Local differences in penetration depth at the application nip
  III. Local differences in contact angle

When two or three of the listed local differences are identical in structure, the risk of back trap mottle is high.
Example: The structure of coating layer porosity is identical with in-plane basis weight distribution.

Ad I: Differences in <u>pore radius</u> of the coating layer can be caused by:
  - Differences in fine particles content in the coating layer due to penetration differences under the blade. Fines are latex or pigment particles. They reduce the local pore radius. Solubles like starch or PVOH can also influence the measured pore radius.
  - Differences in latex content caused by latex migration before and during drying of the coating colour.
  - Differences in latex film forming: Un-film formed latex remains in sphere shape, creating fine pores with high capillary sorption while film formed latex closes the pores of the pigment matrix.
  - Calandering: The higher the local pressure, the lower the local porosity and pore radius (see mercury porosity) will be.

Ad II: Differences in <u>ink penetration depth</u> at the application nip:
  - The lower the local Darcy coefficient, the deeper the ink will be pressed into the coating

- The same happens with local pressure which is mainly a function of local base paper basis weight (see chapter "floc analysis").
- The deeper the ink penetration, the less ink will be pulled off in the following back trapping stations and the higher the local ink density
- The deeper the ink is pressed into the coating layer, the more pores are wetted by pressure penetration and the faster capillary sorption starts – more ink will be immobilized until back trapping happens in the next nip and less ink will therefore be pulled off by back trapping.

Facts from mill trials – improvement of BTM was achieved by:

- Top coatings based on coarse latices (most often acrylics) are generally better in BTM than SB based coatings due to a high amount of micropores with low pore radius which enhances capillary penetration of liquid ink components after application of the ink and reduces thereby backtrap mottling.
- Matt coated papers show less mottle than glossy papers due to the same reason.
- Silica based coatings are superior in mottling due to ultra-fast ink immobilization after application (high capillary force by high amount of ultra-fine pores).

Ad III: Local differences in <u>contact angle</u>:

- In the chapter 11 "drying induced mottling" the impact of latex content at the surface of the coating layer on contact angle is described. The contact angle of ink and fountain water on film formed latex is totally different from pigment.
- Back trap mottle is very often caused by latex migration during drying of the coating colour leading to local differences in contact angle.

The higher the ink tack the more ink is pulled of by back trapping and the bigger the risk for back trap mottling. Therefore BTM is more pronounced for the high viscous black and cyan inks than for the low viscous magenta and yellow,

2.5 Water interference mottling (c)

Similar to back trap mottling, water interference mottling is caused by a combination of pressure penetration and capillary penetration.

Fibro-DAT droplet penetration tests show, that the time between two printing stations is too low to start capillary sorption of fountain water on a coated surface (see capillary sorption).

But the pressure penetration of fountain water in the application nip forces the water into the pores of the substrate and therefore wetting is much faster when the application is done under pressure.

At areas with low coating porosity the water is not transferred properly into the coating layer and the ink of the following printing stations is therefore repelled. Ink absorption is pour and the ink dots are pulled off in the following back trap printing stations.

Water interference mottling occurred in the past when high amounts of latices were used in the top coatings. Differences in latex content at the surface led to differences in capillary penetration of fountain water and ink. Additionally the coating layer porosity was low due to the high latex content and pressure penetration depth of the fountain water in the first nip was low. The water was kept at the surface.

The Prüfbau test for water interference mottling simulates capillary sorption between the printing stations. A drop of fountain water is put without external pressure on the paper surface. The droplet spreads wets the paper surface capillaries and capillary penetration lasts for a few second. Afterwards the remaining water in the droplet is rolled by an aluminium roll, covered with ink, into the paper. The higher the ink density differences between wetted area and un-wetted area the worse water absorption is.

Chapter 3: Formation induced mottling - Floc analysis

The assumption that local pressure will be higher at flocs was investigated in this chapter.

3.1 Origin of flocs

According to Bo Norman from STFI (L7.10), fibre flocculation is mainly caused by:

- Crowding number (describing the mechanical collision of fibres in a suspension)
- Fibre flexibility
- Fibre – fibre – friction
- Chemical forces e.g. from retention aids
- Fluid rheology (viscosity, non-Newtonian effects)

The **Crowding factor N** is the number of fibres divided by the volume swept out by the length of fibre (the volume one fibre needs for rotation without collision with other fibres).

$$N = \frac{Number}{Volume} = c_V * \frac{4}{\pi * D^2 * L} * (\frac{\pi}{6} * L^3)$$

Eq. 3-1-1: $N = \frac{2}{3} * c_V * \left(\frac{L}{D}\right)^2$ .... [ ]

With c_V the volume concentration of fibres in the suspension, L the mean length of fibres and D the mean fibre diameter

Using fibre coarseness the equation can be transformed to use mass concentration which is more common in use:

$$\omega * dx = \rho_{fibre} * \frac{\pi * D^2}{4} * dx \;\rightarrow\; D^2 = \frac{\omega * 4}{\rho_f * \pi}$$

With dx a part of the length L and ω the fibre coarseness = fibre mass divided by the fibre length L.

Inserting the fibre coarseness gives the Crowding factor N:

Eq. 3-1-2: $N = \frac{2}{3} * \frac{c_m}{\rho_f} * \frac{L^2 * \rho_f * \pi}{\omega * 4} \approx \frac{1}{2} * \frac{c_m * L^2}{\omega} \approx \frac{5 * c_m * L^2}{\omega}$

Calculation of the Crowding factor for PM11: The concentration of fibres and fillers is in average 1%. Removing 20% ash in the suspension leads to a fibre concentration $c_m = 0,8\%$.

Assuming an ideal fibre furnish of 100% Eucalyptus the fibre coarseness is $\omega = 0,06$. The average fibre length of eucalyptus is $L = 0,7$ mm. The Crowding factor is calculated with:

$$N = \frac{5*8*(0,7*10^{-3})}{0,6*10^{-6}} = 40$$

When long fibres from spruce pulp with a mean fibre length of 2 mm are replacing eucalyptus fibres, like e.g. in the long fibre dominated furnish of PM11, the Crowding Number triples:

$$N = \frac{5*8*(2*10^{-3})}{0,6*10^{-6}} = 114$$

According to Bo Norman the gel crowding number N_{gel} is 16. In their experiments they found in out that at $N < 16$ no fibre flocculation and network formation occurred due to fibre collision.

At $N > 16$ formation got exponentially worse with increasing crowding number.

Norman et al. (L7.10) showed that flocculation occurs when Crowding number exceeds 16 only when fibres are moved together e.g. by stirring a fibre suspension.

In conventional head boxes the Crowding Number is with $20 < N < 115$ unfortunately always above the threshold of $N = 16$. Fibre flocculation will take place when fibres are moved together by rotational turbulence in the tube bank and at wall boundary layers.

As crowding number increases with fibre length, base papers containing long fibres show significantly worse formation compared to base papers formed solely with short fibres (pict. 3.1.1). Normalized Ambertec formation is $0,4 - 0,6$ $\sqrt{g/m^2}$ for 60 g/m²

base papers of PM9 / PM11, containing a high amount of integrated long fibres from spruce, and 0,3 - 0,35 $\sqrt{g/m^2}$ for Asian base papers based on 100% Eucalyptus.
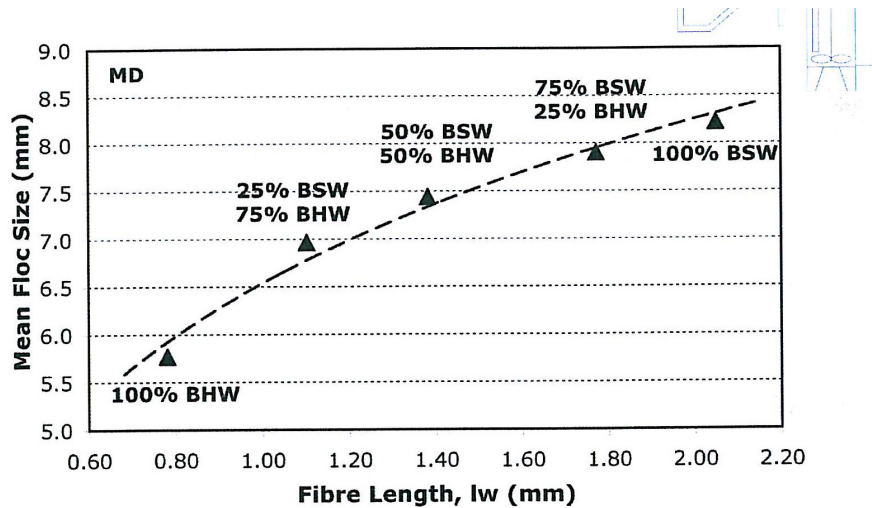
BSW — Bleached softwood pulp   BHW — Bleached hardwood pulp
Fibre concentration: 5 g/l   Flow velocity: 8 m/s

Pict. 3.1.1: STFI flocculation circuit – floc size versus fibre length

The map of in-plane basis weight distribution is measured by Ambertec instrument using beta radiation transmission.

Normalized Ambertec formation is commonly used to describe base paper formation. It is calculated from:

$$F_{norm} = \frac{\sigma}{w_{avg}} * \sqrt{\frac{w_{avg}}{w_n}}$$ with σ the standard deviation of basis weight, w_{avg} the mean value of basis weight and w_n a reference basis weight.

Flocs which are formed in the feed flow to the headbox by mechanical collision when N is greater than 16 or by ionic charged retention aids are partly destroyed in the headbox.
Fluid studies in plastic glass flow channels with high speed cameras at STFI (L7.10) showed that turbulence caused by **rotational swirls** (e.g. in the diffuser at the tube bank exit) reduce floc size temporarily but re-flocculation happens quickly when turbulence energy decays (pict. 3.1.2).
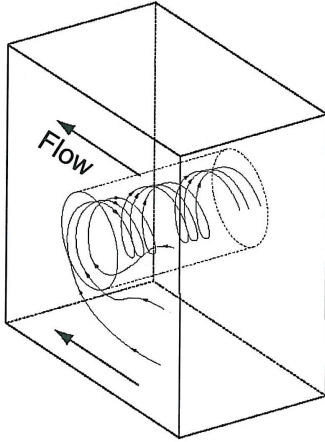
Pict. 3.1.2: Rotational turbulence in the tube bank

Pict. 3.1.3 shows the same kind of rotational swirls, created at the boundary areas in the headbox nozzle and at the surface of headbox vanes.
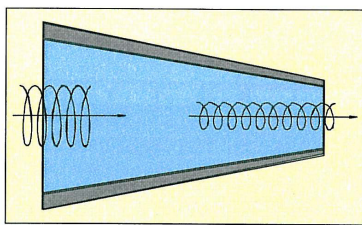
Vortex stretching
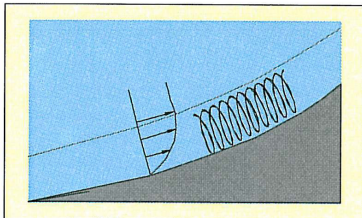
Centrifugal instability
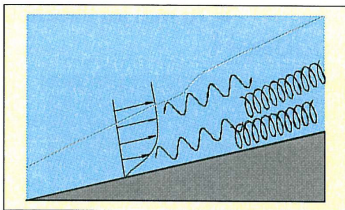
Boundary layer transition
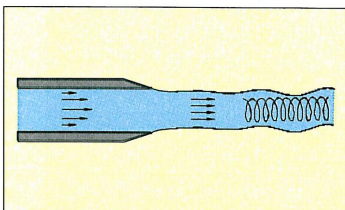
Wave break-down

Pict. 3.1.3: Boundary swirls

Streaks of rotational swirls are extremely dangerous – they create streaks with basis weight and fibre orientation differences in the base paper.

Pict. 3.1.4 shows the plastic glass headbox unit used for the flocculation studies of Bo Norman et al (L7.10).

They proved that a persistent break down of flocs can only be achieved by mechanical stretching forces in headbox or in forming section.
This longitudinal stretch reduces the specific weight of flocs by moving fibres from flocs to the surrounding void area and reducing therefore the basis weight difference between flocs and voids.

Flow direction

**Maximum flow rate:
300 liters/min**

**Maximum flow velocity:
16 m/s (960 m/min)**

Headbox

← **Step diffuser** →

← **Nozzle contraction** →

← **Extended nozzle** →
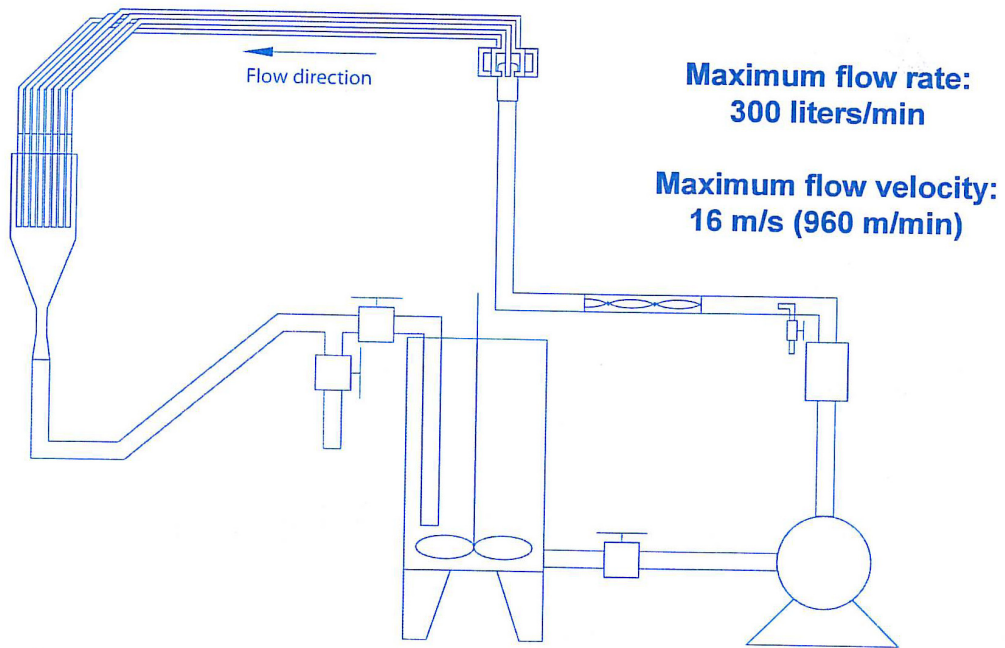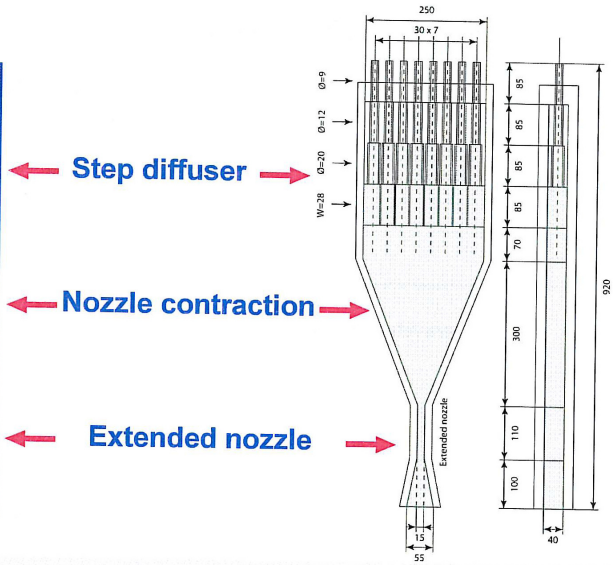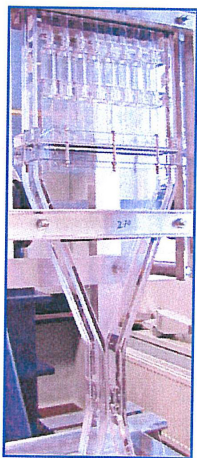
Yan 2004

Pict. 3.1.4: STFI plastic glass headbox

Unfortunately reflocculation happens immediately when these stretching forces are removed and Crowding number is above 16.
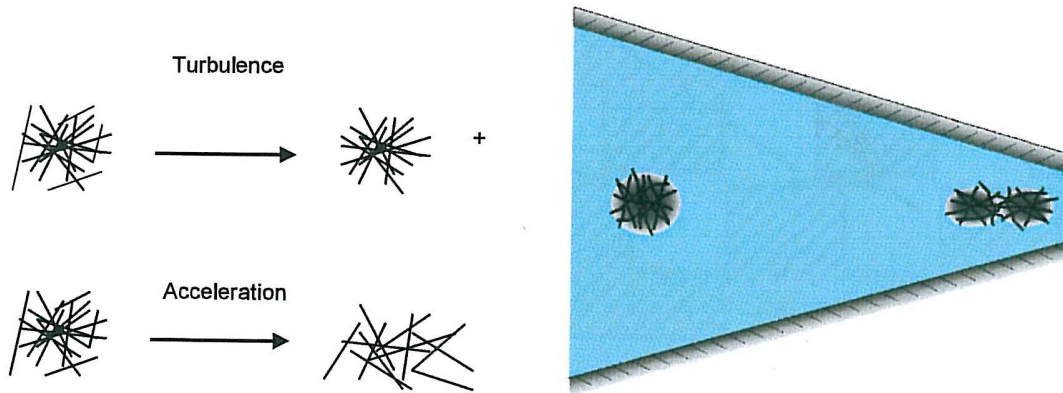
Pict. 3.1.5: Forming and destroying of flocs in headbox

Pict. 3.1.5 shows the stretching forces in the headbox noozle.
Headboxes with high contraction and high acceleration of flow show therefore better formation.

The same effect of floc stretching happens when the jet from headbox is landing at the wire and jet to wire ratio is under 1. Flocs are stretched by the wire, which is moving faster than the feed flow. Therefore formation is worst for the lowest possible MD/CD ratio (pict. 3.1.6). As the stretching forces in the headbox noozle and the landing area of the jet are immediately followed by dewatering of the fibre mat, their impact on formation improvement cannot by destroyed by reflocculation. Therefore they are most often successfully used to improve formation.
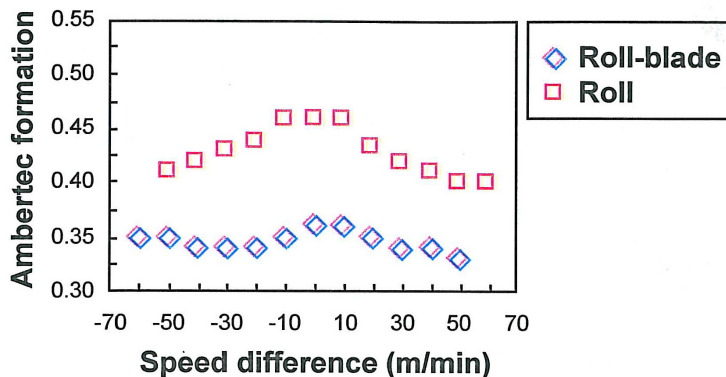
Pict. 3.1.6: Formation versus MD/CD ratio (Nordström 2003)

Modern hybrid formers or gap formers have a blade section after pre-dewatering on a fourdrinier where flocs are stretched between the wires and fibres are mechanically

moved from flocs to voids next to them (pict. 3.1.7). Consistency has to be below a certain threshold of appr. 4,5% to allow fibre movement.

Loadable blade
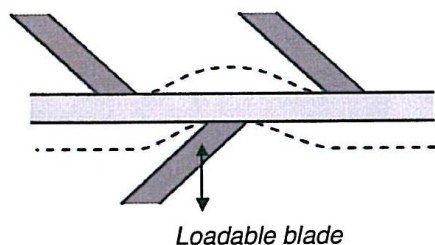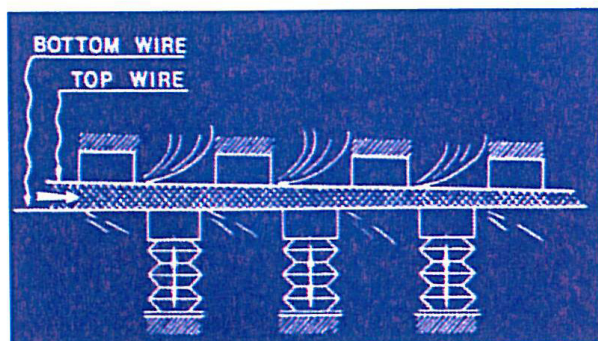
Pict. 3.1.7: Floc break down in twin wire blade section

Gap formers are commonly worse in formation than hybrid formers especially when they are operated with high speed, low basis weight and furnish is fast in dewatering which is unfortunately the case for w'fr base papers of PM11 (pict. 3.1.8 – 3.1.10). The reason for this disadvantage of gap formers is the short length of the primary dewatering area. Dewatering has to be therefore very fast and is driven by the pressure p = T/R with T the wire tension and R the radius of the forming roll where the primary dewatering mainly takes place within a forming length of appr. 1 m.

Hybrid formers have a much longer primary dewatering area of 8 – 14 m length before the top former at the fourdrinier. Pressure pulses at the entrance tip of the foils lead to the "self-healing effect" where fines are moved from flocs to voids next to them and formation improves. Shaking units at the breast roll amplify additionally this self healing effect.
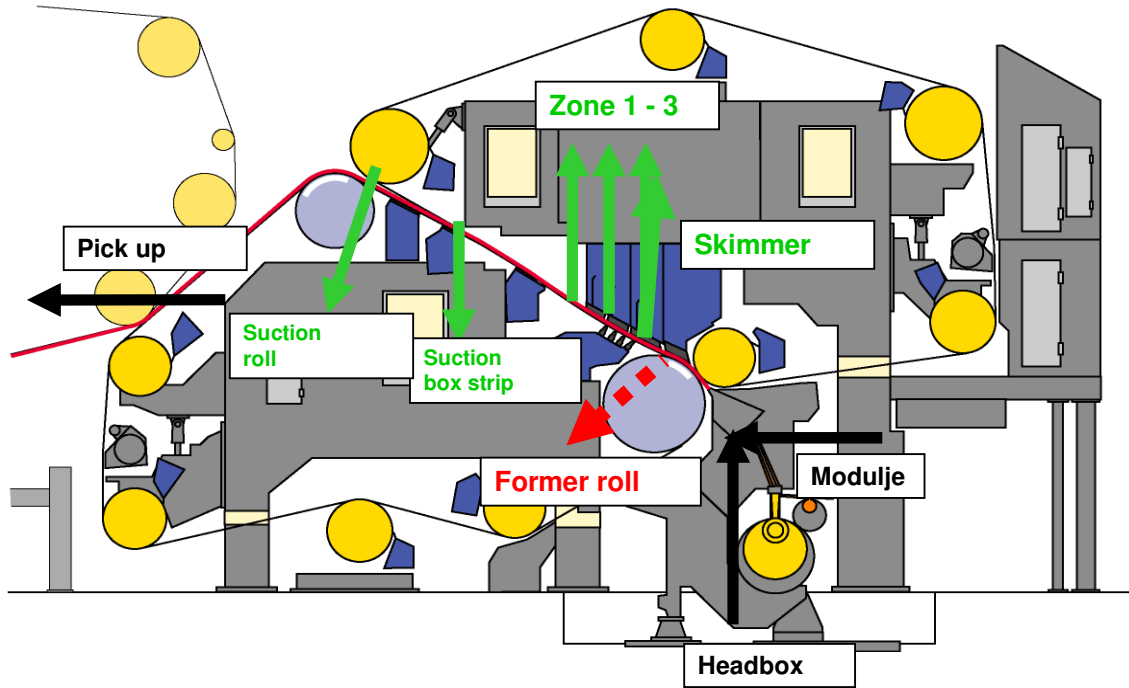
Pict. 3.1.8: Gap former of PM11 (Voith TQm)
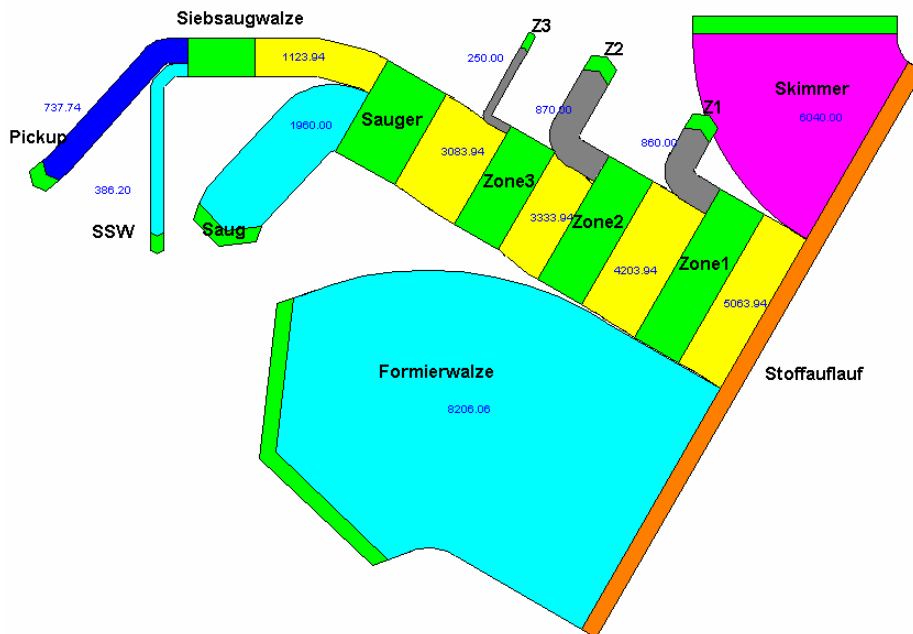
Pict. 3.1.9: Volume balance of Gap former PM11 for 60 g/m² by S-Draw software
(flow rate in l/min)

| Roll Dewatering | Blade Dewatering, D-Bar section |
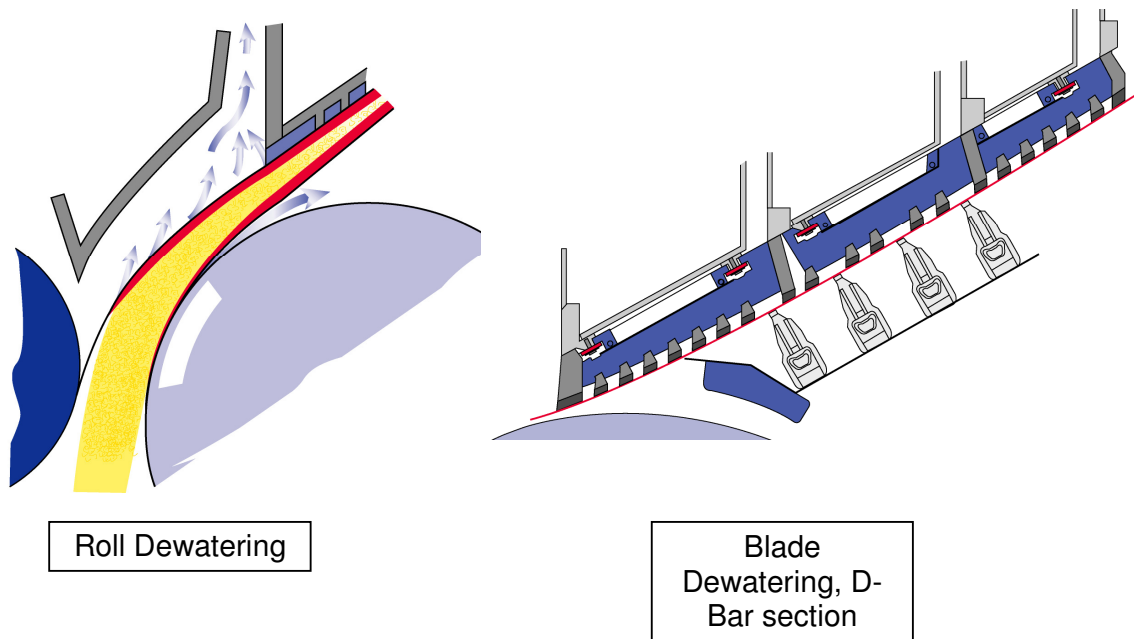
Pict. 3.1.10: Primary (roll) and secondary (blade) dewatering section of PM11

The consistency between the wires was calculated with S-Draw software (pict. 3.1.9 and 3.1.11) using the measured flow rates of the wire dewatering flows and measuring its consistency additionally.

Σ **supplied feed** **=** Σ **removed feed**
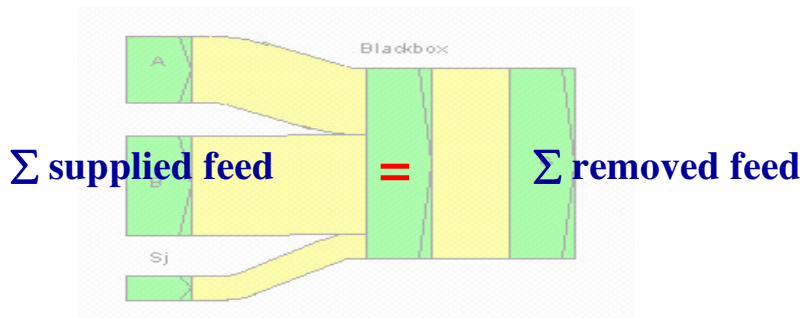
Σ Sj + A + B = G   ... pulp balance
Σ (Sj* x kj) + A x kA + B x kB = G*kG   ... atro balance

1)   A = G – B - Σ Sj
2)   B = (G*kG - Σ (Sj* x kj) - (G - Σ Sj) x kA)/ (kB – kA)

Sj   ... known feed
A,B ... unknown feed
G   ... total feed

Pict. 3.1.11: Balancing forming section of PM11 with S-Draw

Thickness and consistency of the fibre mat in the D-bar section, where bars are pressed into the wires to reform the sheet and improve formation, is of utmost importance for formation of base paper. The lower the consistency in the D-bar section, the easier the fibres can be moved and the bigger the formation improvement.
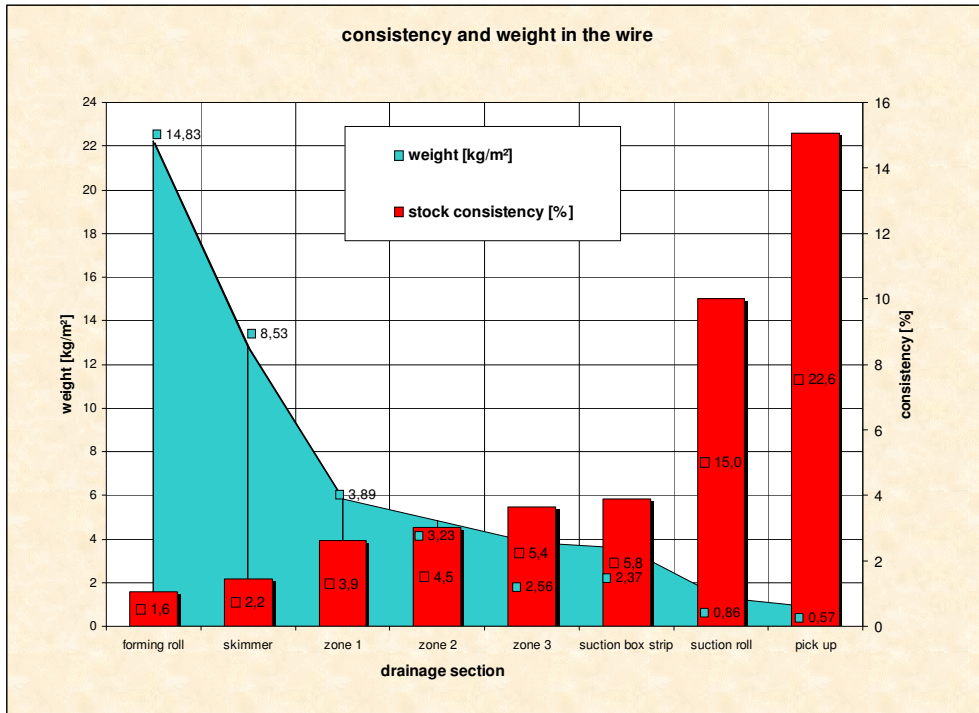
Pict. 3.1.12: Typical weight and consistency of fibre mat at PM11 gap former measured gamma gauge
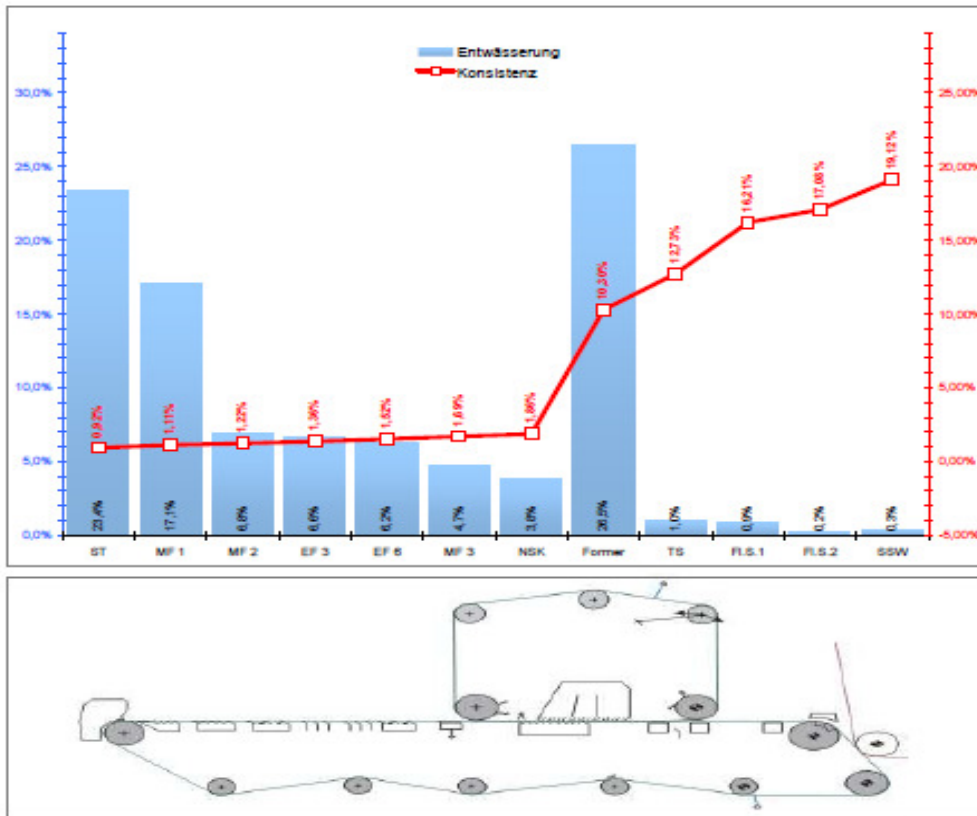
Pict. 3.1.13: Consistency at wire for hybrid former PM9

Consistency at the entrance of D-bar section at gap former PM11 (pict. 3.1.12) is with 2,2 - 3% much higher than at hybrid former PM9 (pict. 3.1.13) where it is 1,6 – 1,9%. Therefore free volume for fibre movement in the fibre mat is much smaller in blade section of gap formers and formation improvement is lower than for hybrid formers.

Measured Ambertec formation of PM11 was with $0,50 - 0,55 \sqrt{g/m^2}$ always higher than formation of PM9 with Ambertec of $0,35 - 0,45 \sqrt{g/m^2}$ at comparable furnish mixture and head box consistency.

3.2 Mottling analysis of printed samples from PM11 at STFI / Sweden:

To identify base paper formation as root cause for mottling the structure of printed pattern has to be compared with the structure of formation. A wave length analysis was used for this purpose. The printed image was digitized by scanning at STFI at a high resolution scanner. Alternatively digital photos can be taken from a camera under special illumination. The structure of the image was analysed by band pass filtering.
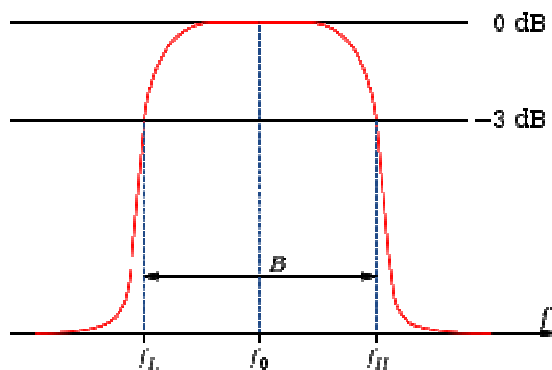
Pict. 3.2.1: Bandpass filter with lower frequency f_L, upper frequency f_H and bandwidth B

A bandpass filter is a filter where frequencies within a certain range can pass. Theoretically all frequencies outside this range are rejected. All practical filters have a region just outside the intended passband where frequencies are attenuated, but not rejected. This is known as the filter roll-off, and it is usually expressed in dB of attenuation per octave or decade of frequency.

The bandwidth of the filter is simply the difference between the upper and lower cutoff frequencies. The shape factor is the ratio of bandwidths measured.

To determine certain structures in digital images of Ambertec formation or print motte the band pass filter eliminates all structures which are lower or bigger in size than the investigated size of structure (e.g. range 4 – 8 mm in size). All structures with size within bandwidth B are counted. The more structures of this size per investigated

area are found the more dominating this structure will be in the sum of all detected structures.

Example: Classes of size from bandpass filtering of STFI mottle analysis:

Black 80%									
File	a	Comment	Mottle 1-8 mm	Mottle 4-16 mm	0.25-0.50	0.5-1.0	1-2	2-4	4-8	8-16
b449_os		B449_OS, 80% K	2,1871	1,0435	9,8997	2,8063	1,6954	1,1126	0,8186	0,6465
b449_us		B449_US, 80% K	3,285	1,4876	10,538	4,0987	2,6111	1,6685	1,086	1,0158
d314_os		D314_OS, 80% K	2,3699	1,3327	10,372	2,9919	1,8038	1,1814	0,97733	0,90564
d315_us		D315_US, 80% K	2,8707	1,8439	10,5	3,1435	2,0144	1,5163	1,372	1,2295

Two pairs of printed samples were compared with the scanner and mottling evaluation software at STFI in Sweden.

One pair (Star 170 g/m²) was produced at PM11 with a big difference in formation and the other pair (Quatrogloss 115 g/m²) was dryed at OMC11 with a totally different drying strategies.

- Pair 1: Star 170 g/m² with good and bad backtrap mottle in purple. The bad mottle was caused by bad formation – the structure of the **bad base paper formation** was visible after triple coating.
- Pair 2: Quatrogloss 115 g/m² with good and bad backtrap mottle in purple. The bad mottle derived from **low drying temperatures** in the top coaters of OMC11 and non-uniform binder film forming in consequence.

The difference in mottling pattern could be easily detected by the human eye: The structure of drying mottling was significantly bigger in size of print non-uniformity than that of formation induced mottling.

Additionally the visual structure of formation mottling corresponded well with typical visual formation structure of base paper PM11.

Image size 5 x 5 cm
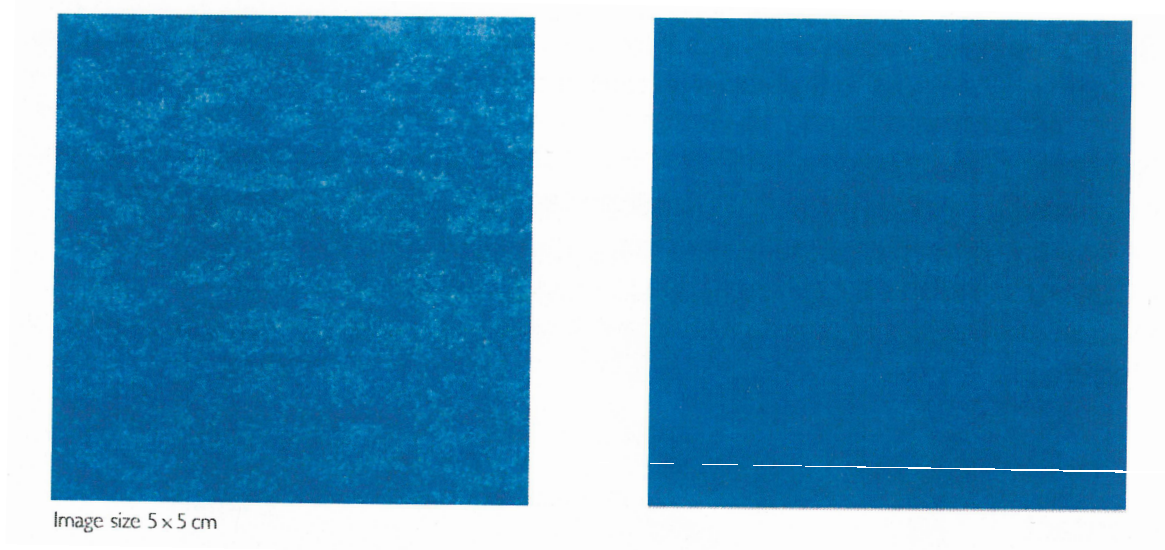
Pict. 3.2.2: Image of STFI Mottle analysis of back trap mottle (left bad mottling) before software wave let analysis

STFI uses a flat bed scanner to digitize the printed image and data is calibrated to reflectance using a calibration set.

With frequency analysis small and big scale variations are eliminated and the range of 1 – 8 mm is further analysed (pict. 3.2.2).
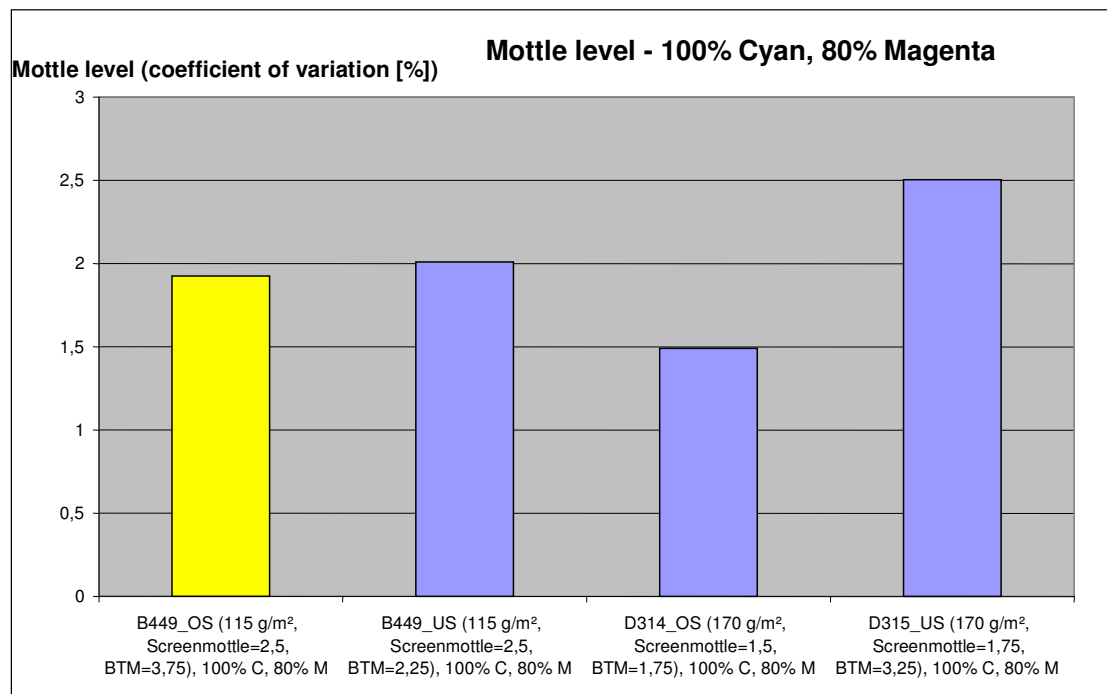
Pict. 3.2.3: Mottling index (variation coefficient) of STFI for BTM in purple screen area (100% cyan + 80% magenta)

The visual ranking of the BTM fitted well to the STFI mottling index for the all samples except B449-OS where the visual impression was much worse than the STFI index (pict. 3.2.3).
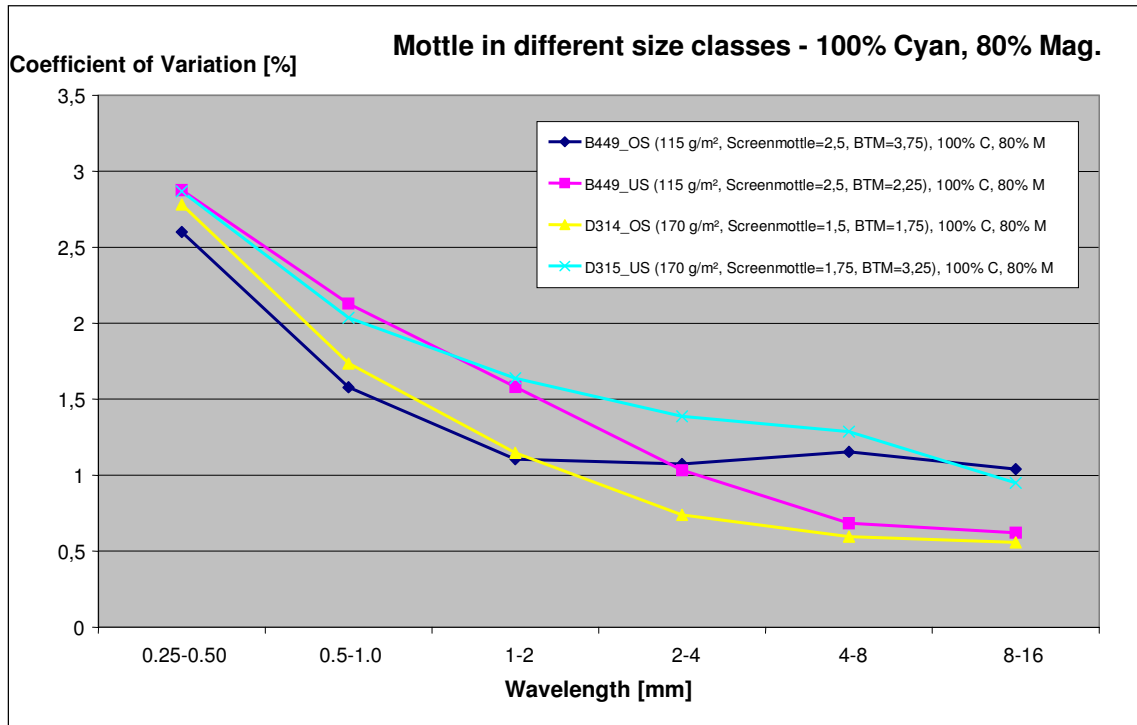
Pict. 3.2.4: Wave let analysis of backtrap mottling for all samples

Pict. 3.2.4 shows that the STFI method cannot fully remove the small scale variation of printed image screen pattern – which is a common problem for all kinds of print pattern analysis tools. The variation coefficient in the wavelength range of < 1 mm is relatively high, caused by printing screen pattern. Although this regular pattern of printed screen image is filtered out by the software of the wave let analysis, a certain part of it remains in statistics.
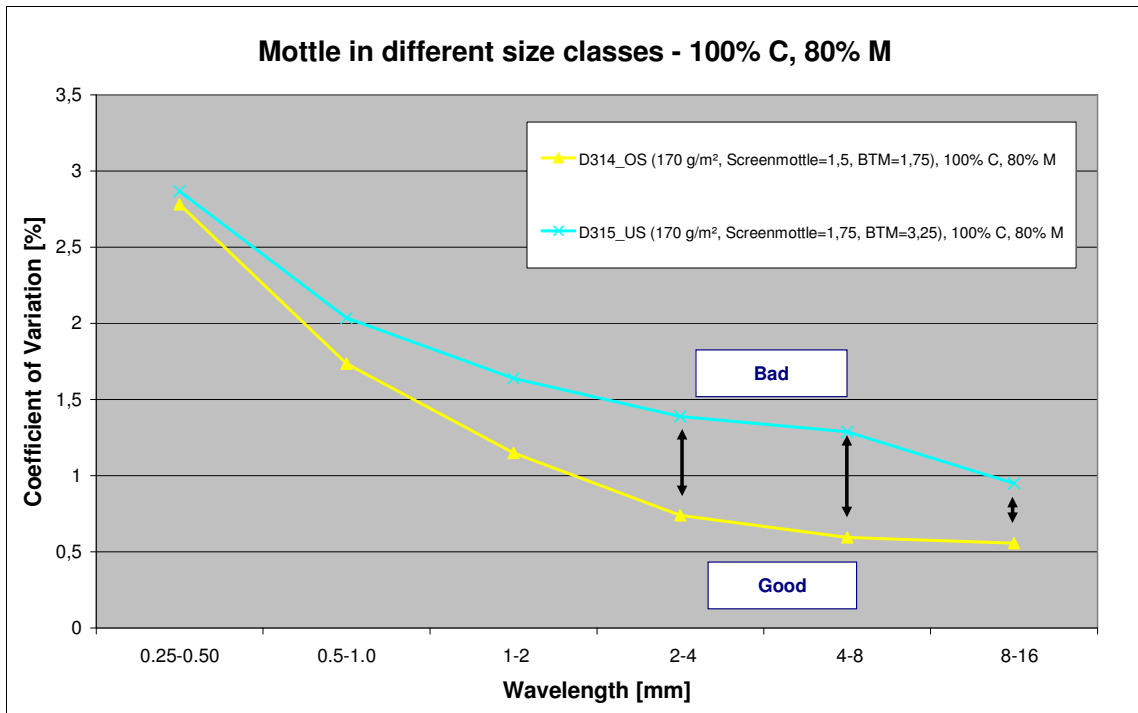
Pict. 3.2.5: Wave let analysis of backtrap mottling for 170 g/m² (formation mottle)
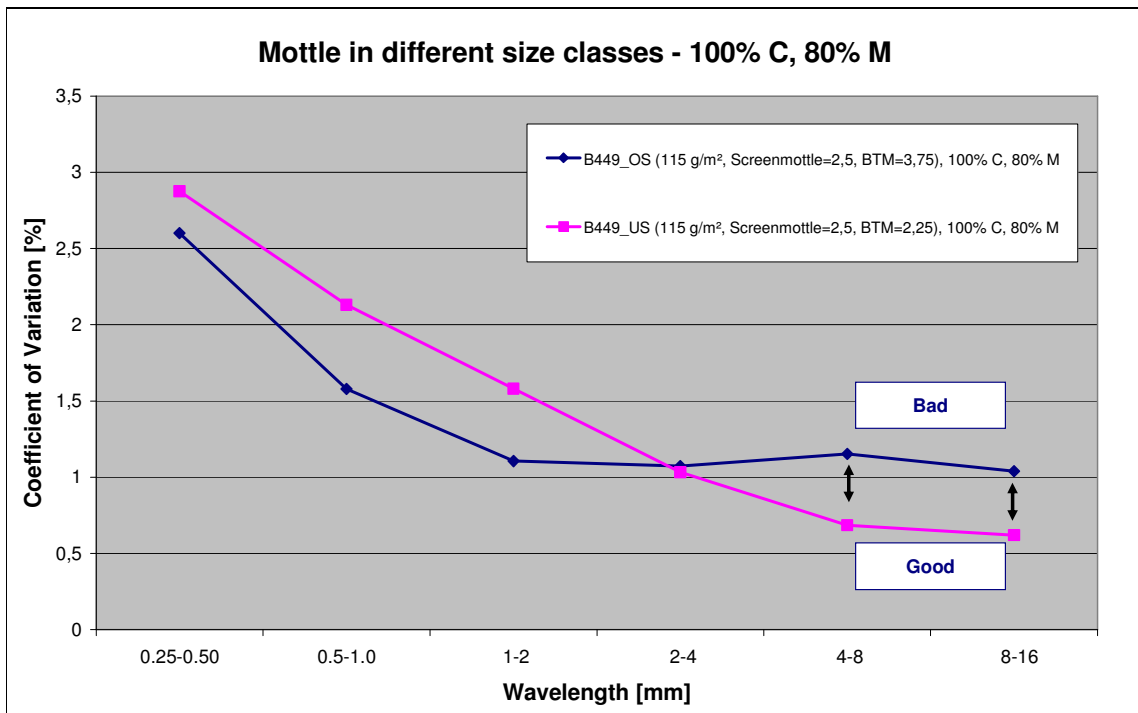
Pict. 3.2.6: Wave let analysis of backtrap mottling for 115 g/m² (drying mottle)

The difference in back trap mottling structure between formation and drying induced mottling could be well described by the wave-let analysis.

Pict. 3.2.5 shows a big difference in mottling variation coefficient in the size class of 2 – 8 mm which corresponds to floc size from Ambertec wave let analysis (pict. 3.2.8) while drying mottling led to bigger irregularities in the classes of 4 – 16 mm (pict. 3.2.6).

These results were typical for drying mottle of OMC11, caused by low drying energy in the 1st part of the IR-drying section, leading to non-uniform latex film forming and big differences in capillary sorption of the top coating layer (see chapter "drying induced mottling")

Mottle in diffent size classes - 80% screens
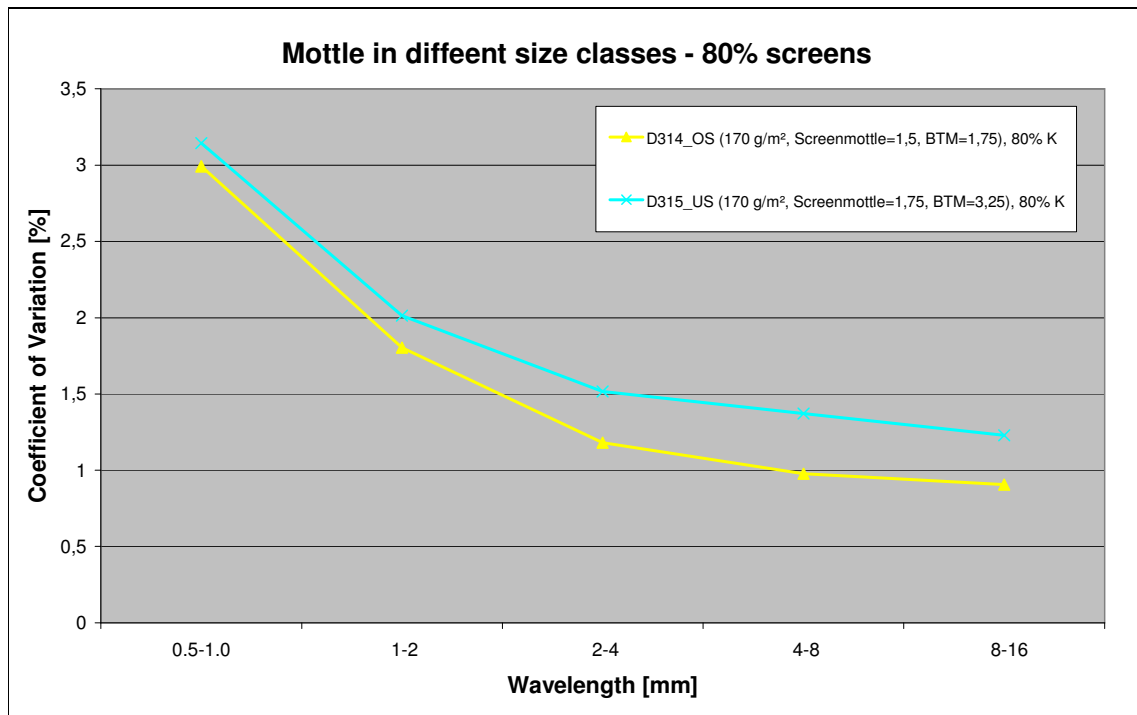
Pict. 3.2.7: Wave let analysis of screen mottle (without back-trapping) of 170 g/m²

When formation is the root cause for back trap mottling the formation structure is most often also visible in screen mottling. The 170 g/m² sample with bad back trap mottling, caused by bad formation showed also the worst visual screen mottling and in the highest STFI screen mottle index.

The samples of 115 g/m², where mottling was caused by drying, showed no difference in visual and measured screen mottle.
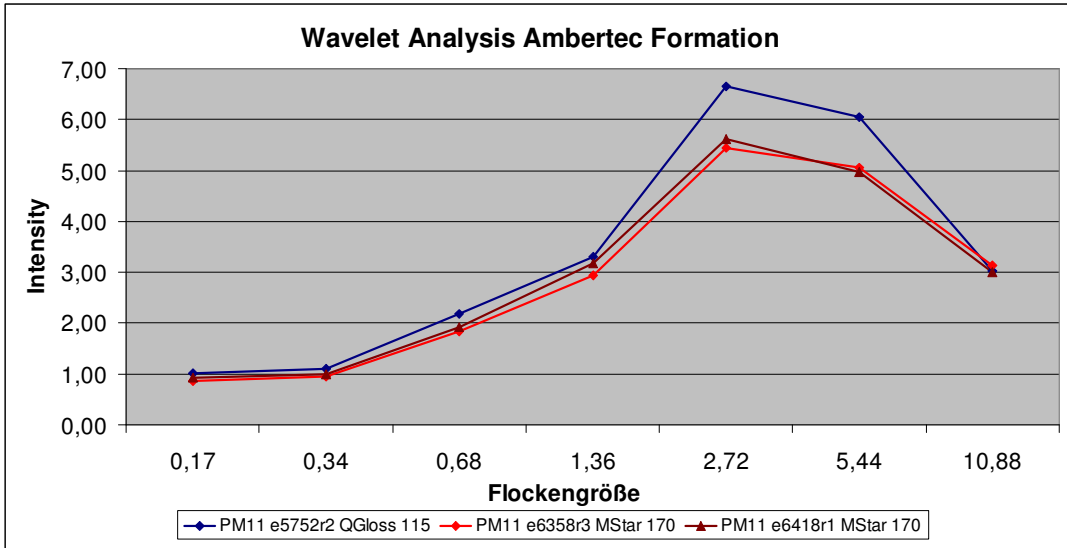
Pict. 3.2.8: Wave length analysis of PM11 base paper formation
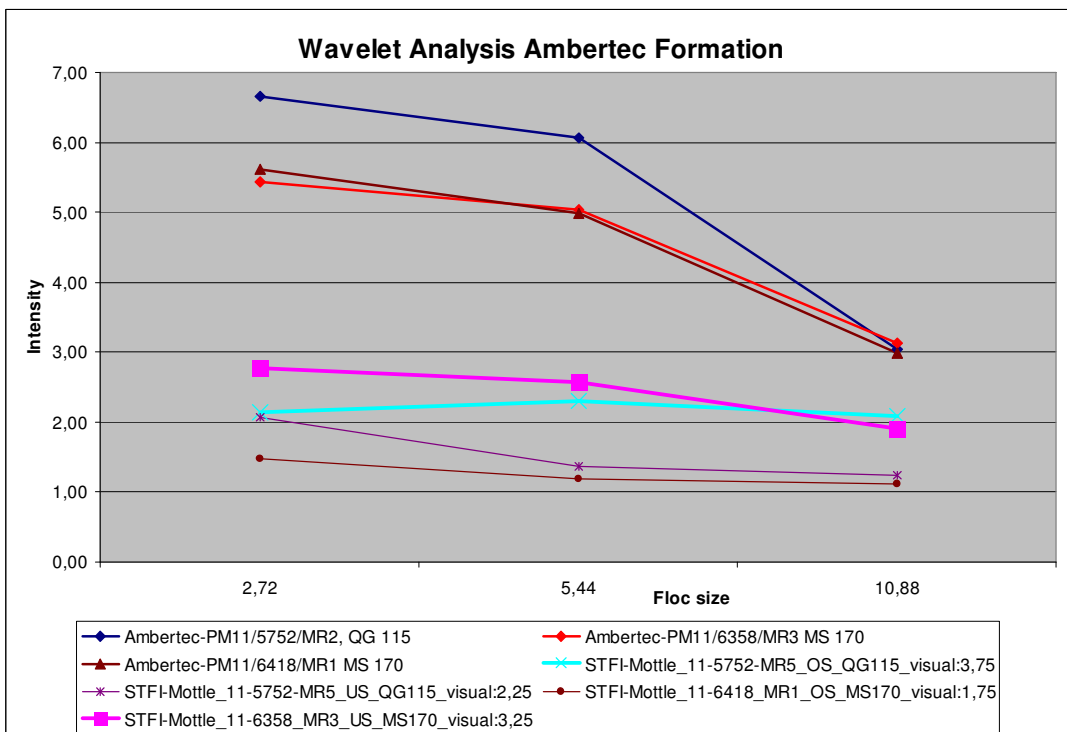
Pict. 3.2.9: Comparison of wave length analysis of Ambertec formation and purple mottle in the range of 2 – 15 mm floc size
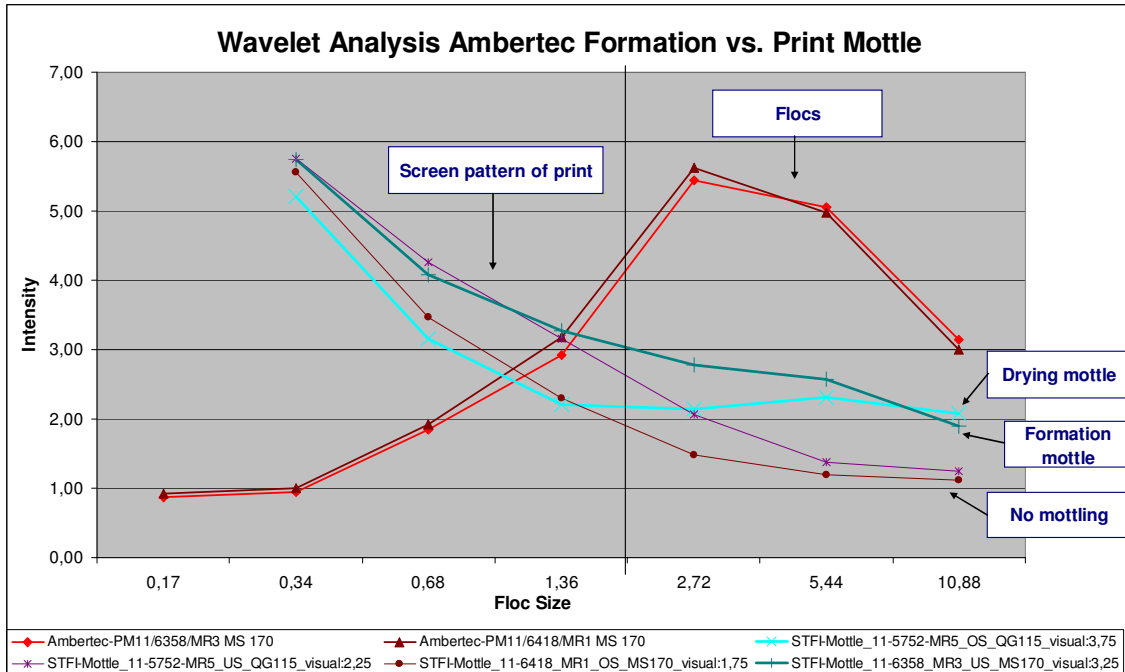
Pict. 3.2.10.: Comparison of wave length analysis of base paper formation with print mottle

When the wave length analysis of backtrap mottle in purple printed area is compared to the wave length analysis of Ambertec formation of the corresponding base papers formation induced mottling can be proven as the root cause (pict. 3.2.8 – 3.2.10): The sample 11-6358-MR3-US (170 g/m²) with formation induced mottling showed of similar shape of the curves in the range of 2 – 15 mm floc size while the sample 11-5752-MR2-OS with drying induced mottling showed a different behaviour: Ambertec formation showed a maximum at 2 – 8 mm floc size but the size of mottling unevenness was in the range of 2 – 15 mm.

3.3 Floc analysis in basis weight, thickness and density

Base paper of gap fomer PM11 at sappi Gratkorn was analysed. Approximately 50 flocs and 50 voids were cut out with a special die cutter. The resulting spot samples had a diameter of 3 – 4 mm and were analysed separately in the paper lab.
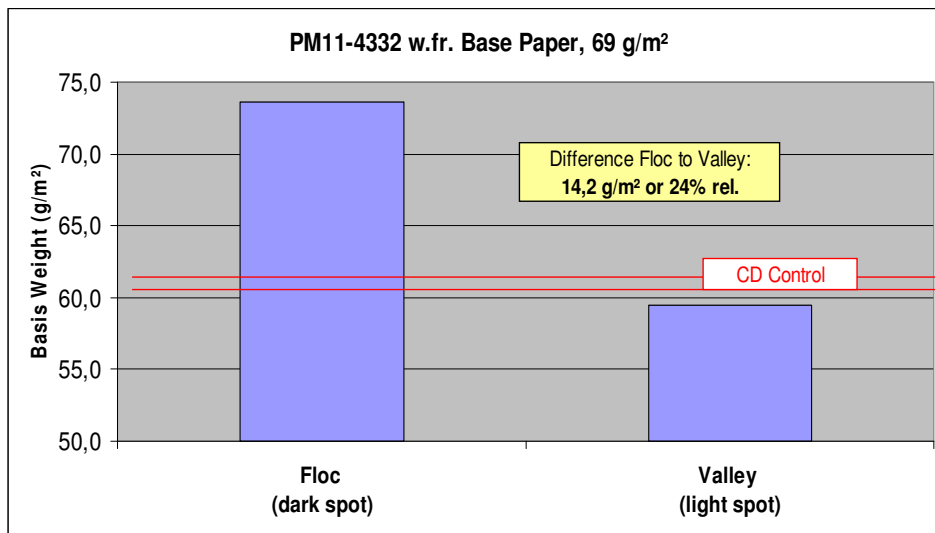
Pict. 3.3.1: Basis weight difference between flocs and valleys

A difference of 15 – 25% in average of basis weight was detected between the stamped out flocs and voids (pict. 3.3.1)

When this local micro scale differences in basis weight are compared with macro scale differences of a typical base paper CD-profile the conclusion can be drawn that the micro scale differences are one magnitude higher than the macro scale differences.
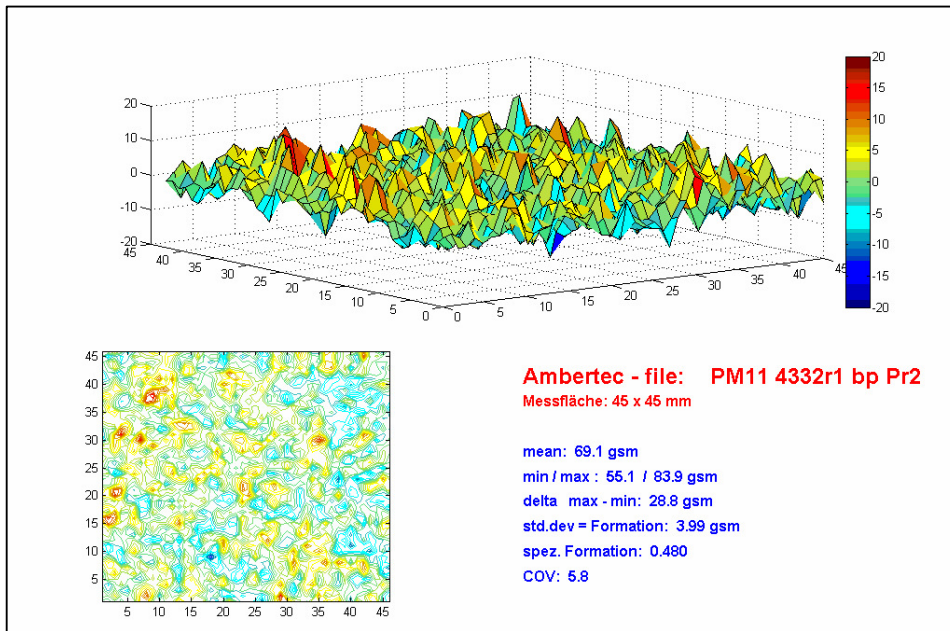
Pict. 3.3.2: Ambertec basis weight distribution of PM11 base paper, 45 x 45 mm spot

Ambertec 3D-picture of base paper PM11 in pict. 3.3.2 showed the same variation in basis weight as the weight analysis of cut out flocs and voids: 4σ of Ambertec was 16 g/m² while the mean difference between cut out flocs and voids was with 14 g/m² in a comparable range.

In the next part the impact of local basis weight differences on base paper surface was investigated.

When the surface of base paper PM11 is compared to its local basis weight variations, the conclusion can be drawn, that surface looks much more even than the corresponding basis weight distribution (pict. 3.3.3 and 3.3.4) which leads to the assumption that the in-plane specific volume is also non-uniform.
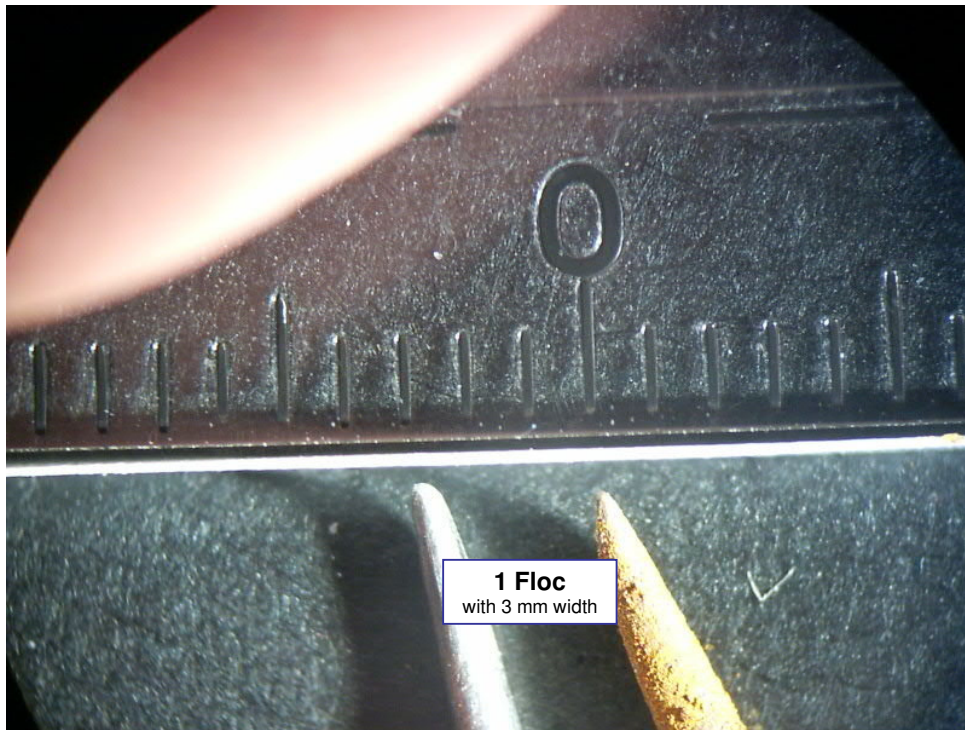
Pict. 3.3.3: Base paper thickness variation at a floc in cross section under the microscope

UBM laser is used to analyse the surface of media like paper. A laser is moved in X- and Y-direction to scan the distance to a reference area. The sample is kept flat by vacuum on the bottom side. The result is an image of paper surface roughness.

UBM surface topography confirmed the visual impression of base paper surface: The flocs of base paper PM11 could not be detected anymore in the UBM map although basis weight variations were relatively high (pict. 3.3.4).
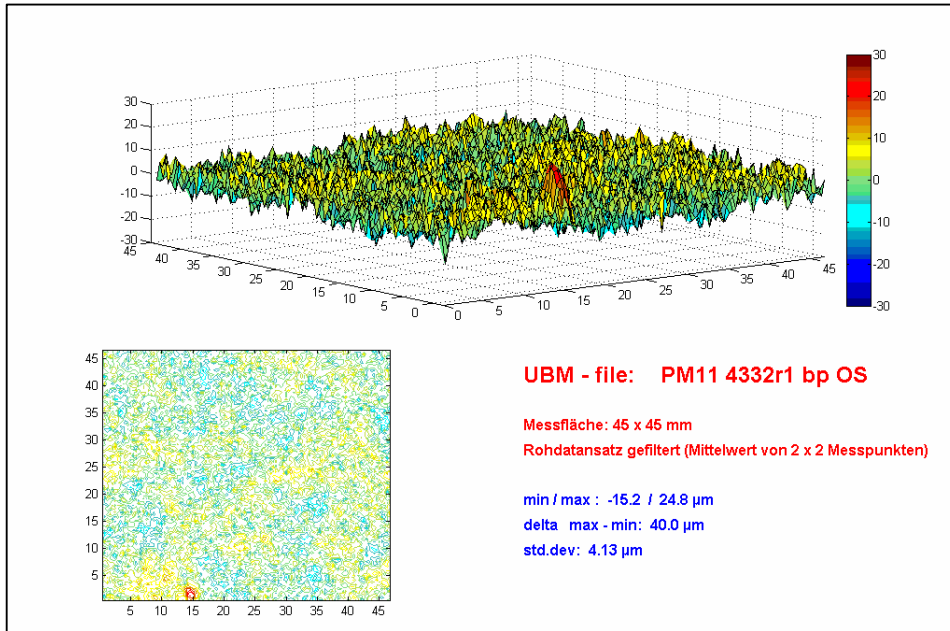
Pict. 3.3.4: UBM laser surface topography of PM11 base paper, 45 x 45 mm spot

As a comparison to the UBM-laser topography measurements the local thickness was determined by cutting out flocs and voids and measuring their thickness by the standard thickness instrument. Results are shown in pict. 3.3.5.
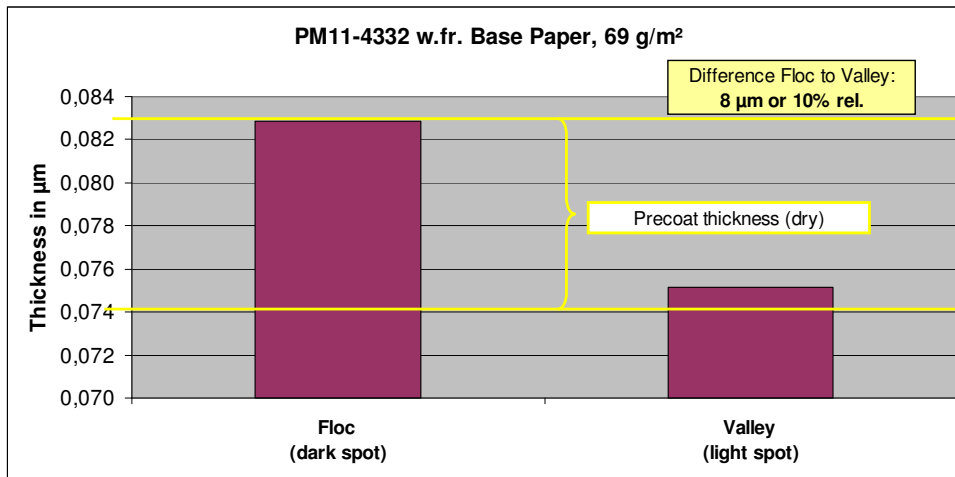
Pict. 3.3.5: Thickness of flocs and valleys at base paper PM11
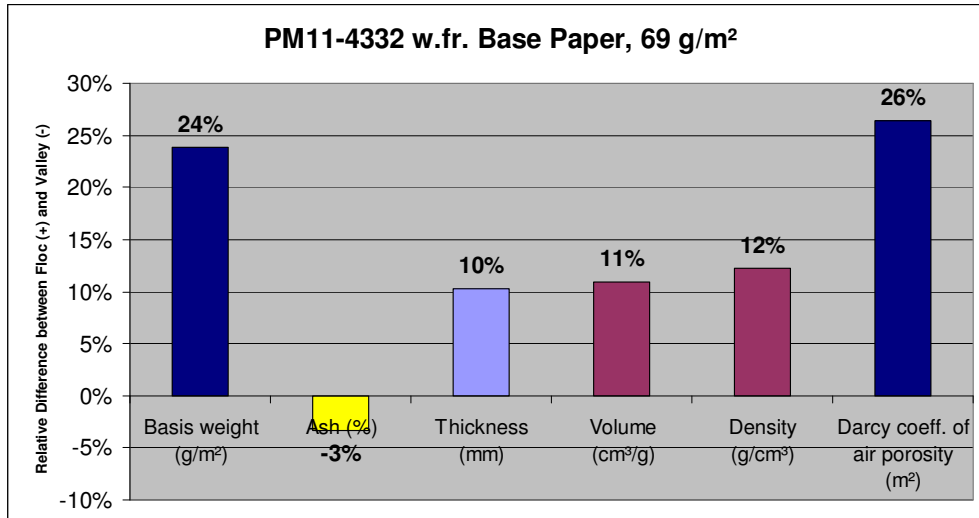
Pict. 3.3.6: Floc analysis of PM11 base paper

Pict. 3.3.6 compares the relative differences of the paper properties of the stamped out flocs and voids. The difference in thickness between flocs and voids was lower than the corresponding basis weight difference. Therefore **density was higher at flocs**, indicating a higher compression of the flocs in press and drying section. Local thickness difference between flocs and voids of base paper PM11 was with 8 μm in the range of the thickness of a single dry coating layer (6 - 10 μm).

The higher density of flocs was detected also in a lower Darcy coefficient, measured by air permeability. As shown in chapter "pressure penetration" air porosity can be used for samples with high porosity to calculate Darcy coefficient. It is not applicable for coated samples.
A new measuring head with 3 mm diameter was manufactured for the Bendtsen porosity instrument to measure local spot porosity. Air pressure was adjusted in the range 0 – 8 bar to achieve reproducible results. For coated paper samples pressure was raised to 8 bars while for base papers it could be kept at a lower level of 2 bars. Remark: The standard pressure for Bendtsen air porosity is 1 bar.
The influence of thickness differences between flocs and voids was eliminated when permeability was calculated as thickness of penetrated sample is included in the

Darcy equation $\frac{dV}{dt} = Q = \frac{K * A * \Delta p}{\eta * L}$.

At flocs the calculated air permeability coefficient was 25% lower than at voids showing the higher density of fibre/filler matrix at flocs.

To find the cause for local density differences of base paper PM11, **lab sheets** were formed as comparison by using the same furnish of PM11. In contradiction to PM11 no pressing was applied at the wet sheets before they were dried.

Lab Sheet (100 g/m², 32% ash, w.fr. stock)

A bar chart titled "Lab Sheet (100 g/m², 32% ash, w.fr. stock)" with y-axis "Relative Differencies" ranging from 0% to 60%. Bars: Basis weight (g/m²) 24%, Ash (%) 3%, Thickness (mm) 22%, Density (g/cm³) 1%, Darcy of air porosity 3%.
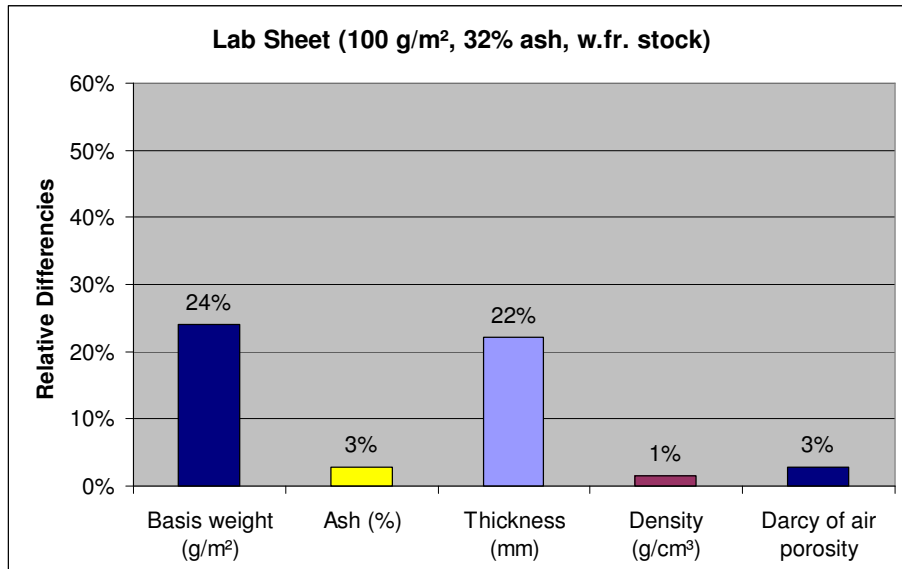
Pict. 3.3.7: Floc analysis of lab sheet from head box stock PM11

Pict. 3.3.7 shows that in contrast to PM11 base paper the flocs and valleys of the lab sheet showed no difference in density, bulk and Darcy coefficient as they were compacted to the same extend.

For all measured base papers base ash was similar at flocs and voids, indicating no difference in ash retention. Fibre analysis shown in pict. 3.3.8 proved that fibre dimensions and amount of fines was identical in flocs and voids which stays in contradiction to the assumption that only fines and short fibres are moved in the wire section from flocs to voids.
This fibre analysis indicates that retention of fines in the wire section is similar at flocs and voids which is surprising as flocs have more mass per volume to retain fines.

Length, lw

Width
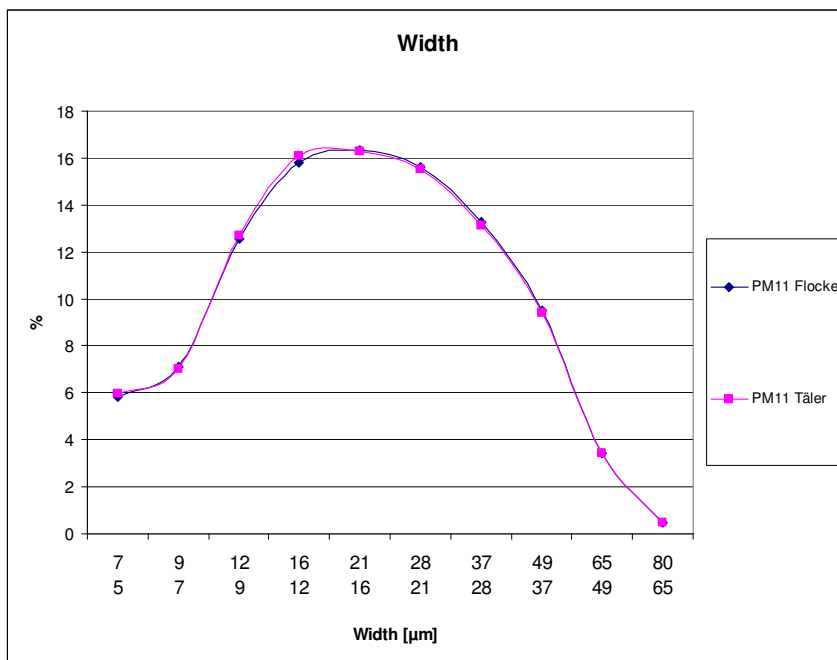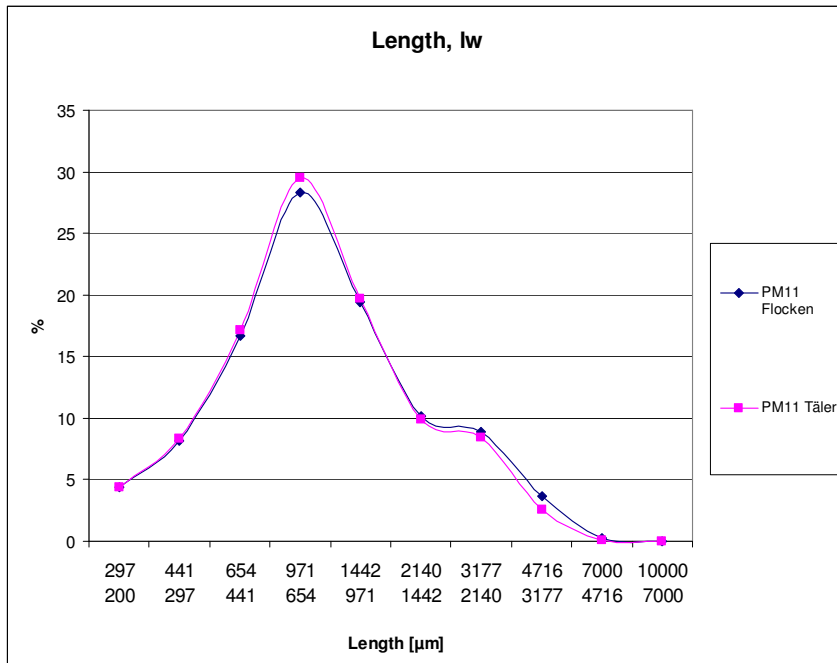
Pict. 3.3.8: Morfi fibre length distribution and fines analysis of flocs and voids

Local basis weight differences correlated well with Ambertec formation index. At a base paper with normalized Ambertec index of 0,55 a relative basis weight difference between flocs and valleys was measured with 25%, when Ambertec index was 0,45 the difference was 15% and for Ambertec index of 0,35 it was 7-8%.

PM11 Base Paper, 2660, w.fr. 68 g/m², 11% ash
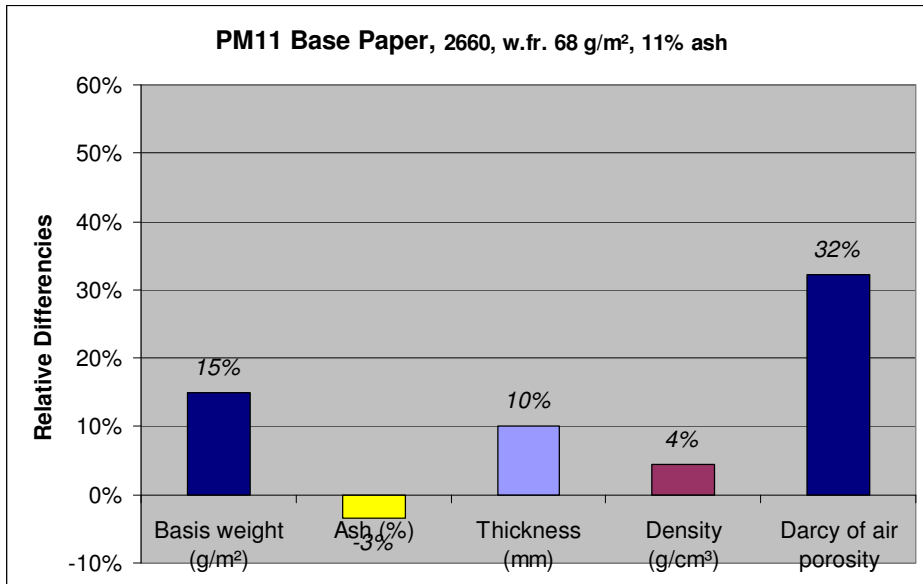
Pict. 3.3.9: Floc analysis of second PM11 base paper

3.4 Match analysis

Another method to correlate local base paper properties like basis weight with thickness is match analysis, which was developed together with Peter Fuchs at RD-Gratkorn.

The procedure is shown in pict. 3.4.1 – 3.4.3. In the first step the area which is measured by different methods has to be marked. Two edge lines are made with an angle of 90° in between.

In the second step the measurements are done at the marked areas and digital images are produced where the edge line must be visible.

In the third step each image must be rotated some degrees to be parallel to the edge lines and cut to the edge lines.
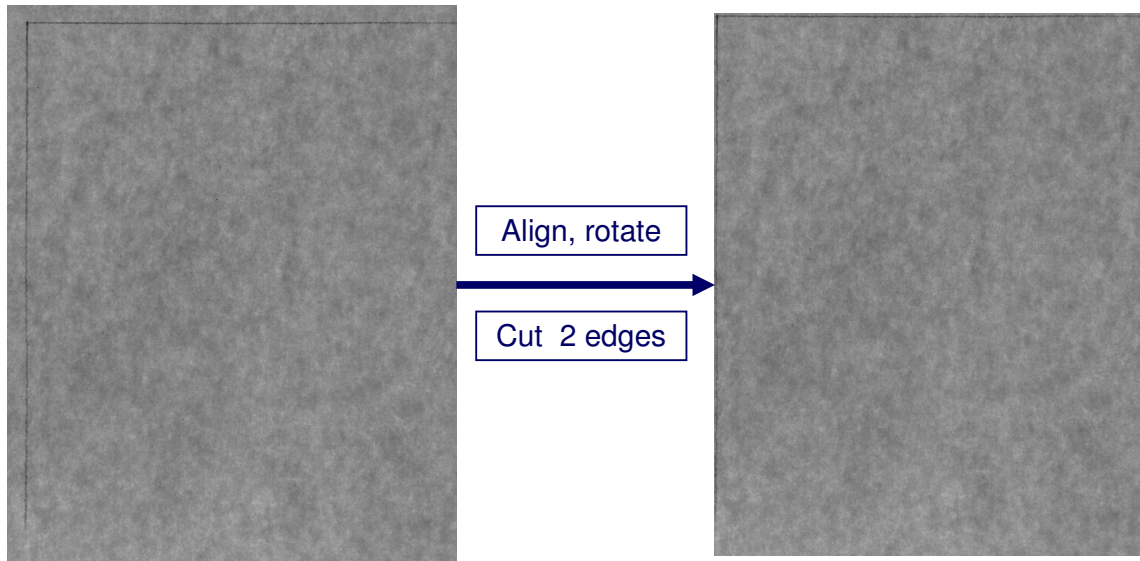
Pict. 3.4.1: Aligning, rotating and cutting the images for match analysis

In the forth step the images, which are compared must be cut to the same size. In pair comparisons the smallest image determines the size of all images.

In the fifth step all images are band pass filtered and smoothened. Smoothening is necessary when the resolution of the images is different. For instance Ambertec has a resolution of 45 dpi and UBM surface profile has a resolution of 300 dpi.

In the sixth step the FFT match factor and mottle matches are calculated.
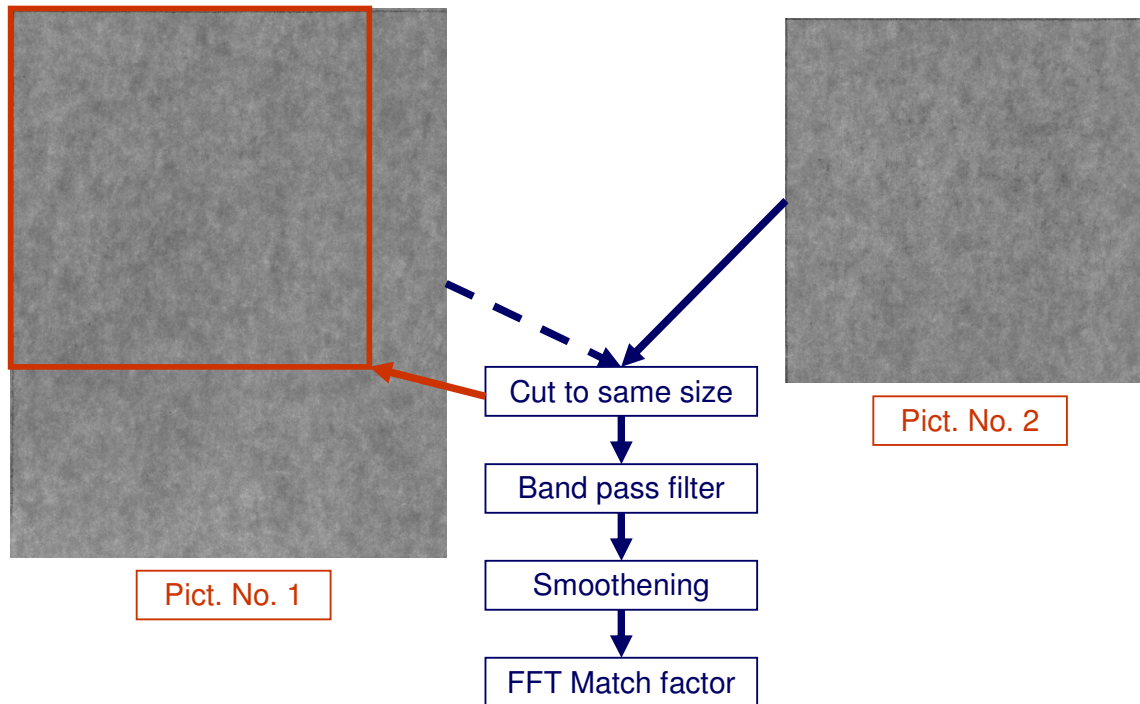
Pict. 3.4.2: Fit sizes and filtering of images for software analysis

For images with different resolution a match factor of 70% is perfect, for same resolution the match factor for good correlation should be >90%.

dataset
raw data

build 8bit image 150 dpi
- bilinear (nearest or bicubic)
- range: 0.....1

image-1　　　image-2

image processing
- rotate +/- 90°
- flipp raws and colls
- invert (white <--> black)

image-1
image-2

save image to hard disc

cut image-1 and image-2 to the same size

find best match position
1.) band pass filter: 1..15 mm
2.) increase contrast [gain: f(std.dev)]
3.) 2D correlation in the frequency domain
　　--> I, J position of highest correlation
4.) cut image-1 and image-2 (max. 50 pixel)

image-1
image-2

Wiener filter (smooth images)
variable (0, 0.5, 1.0, 1.5, 2.0 mm)

image-1
image-2

calculate fft-matchfactor
1.) compare and set contrast and brightness to the same level
　　(image-1a and image-2a)
2.) 2-D correlation in the frequency domain

image-1a　　　image-2a

image-1a　　　image-2a

Band Pass Filter: 1...15mm
increase contrast [gain: f(std.dev)]

image-

image-

calculate BP-filtered mottle image
(Code by University Maastricht)

calculate binary mottle images
top mottles:　　　> 0.75
bottom mottles:　< 0.25

top mottles　　botom mottles

compare mottle images (pixel by pixel)
mottle image-1 <--> mottle image-2
mottle image-2 <--> mottle image-1

Match factor for top- and bottom-matchimages

Export Match figures to Hard Disc as *.jpg files

Export Match factors to excel

Pict. 3.4.3: Principle of match analysis

Page 61

Pict. 3.4.4: Match analysis of Ambertec basis weight and UBM topography of lab sheet

Pict. 3.4.5: Match analysis of Ambertec and UBM topography of PM11 base paper

Match analysis of surface topography and basis weight from Ambertec beta radiogram showed a perfect correlation for the un-pressed lab sheet where thickness differences were in the same range as basis weight differences. For mill produced base paper the correlation was worse due to the higher density of the flocs, created mainly in the press section.

3.5 Zwick compressibility measurements

To prove the theory of higher floc compaction the **compressibility** was measured by the **Zwick thickness instrument**. Flocs and voids were pressed by Zwick instrument by using a stamp of 7 mm diameter. Thickness was measured with increasing pressure in a load and a relief period (pict. 3.5.1).
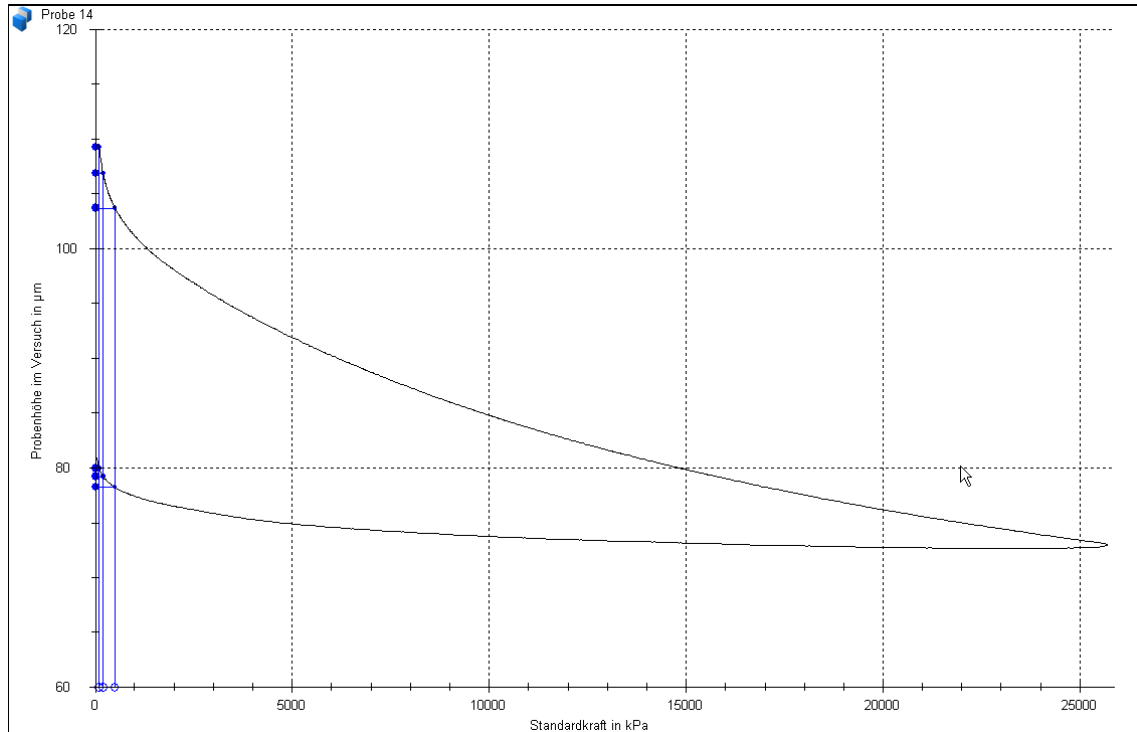
Pict. 3.5.1: Zwick thickness (Y axis) vs. load (X-axis): Upper black curve: load, lower curve: relief – remaining thickness difference on Y-axis = plastic deformation of paper
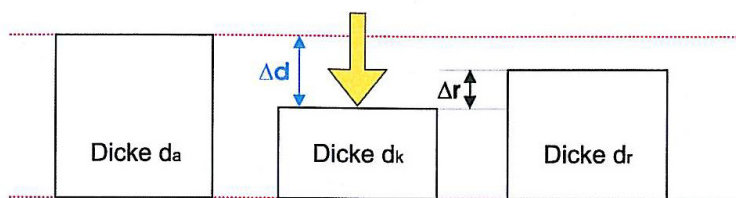
Pict. 3.5.2: Definition of compressibility according to Brecht and Schädler (1961): Original sample thickness d_a is compressed to d_k in the load period. After relief of load thickness increases to d_r
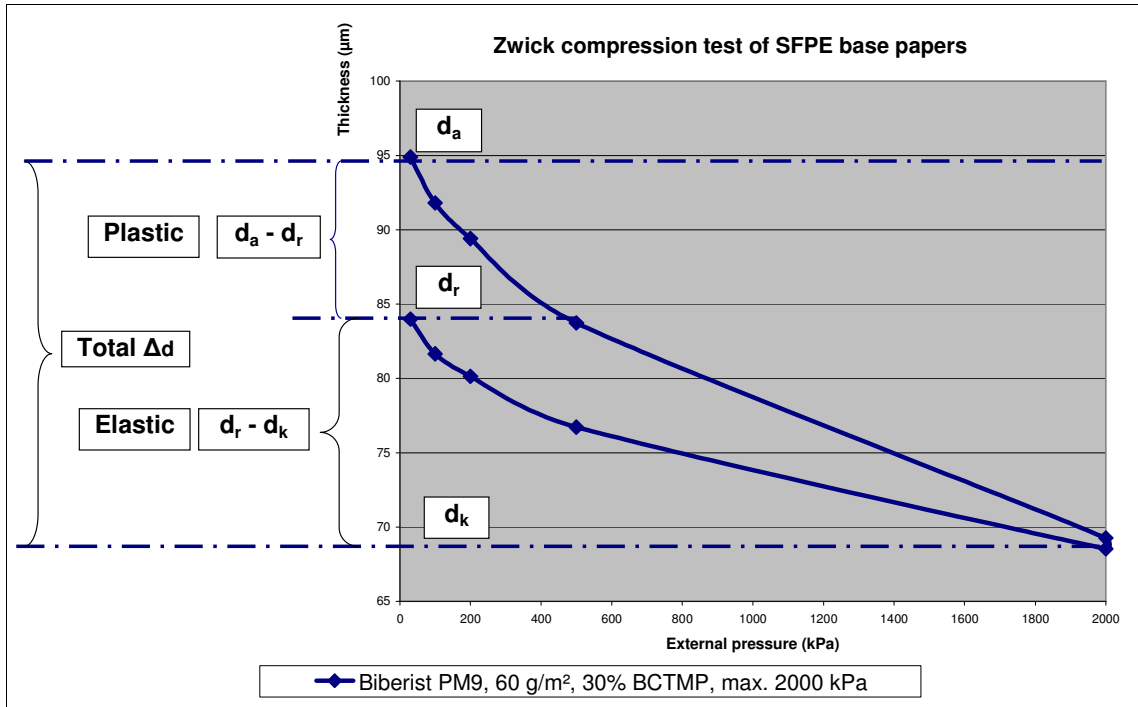
Pict. 3.5.3: Deformation of base paper – components of compression

Definition of compressibility according to Brecht and Schädler (pict. 3.5.2 – 3.5.3) and Markus Lechthaler (L7.11):

Absolute compressibility [µm]: $\Delta d = d_a - d_k$

Relative compressibility [%]: $K_{rel} = \dfrac{d_a - d_k}{d_a} * 100$

Absolute back swelling during relief of load [µm]: $\Delta r = d_r - d_k$

Relative back swelling during relief of load [%]: $R_{rel} = \dfrac{\Delta r}{\Delta d} = \dfrac{d_r - d_k}{d_a - d_k} * 100$

When the deformation ε of the paper is compared with the applied tension σ (correspond to vertical force F) the elasticity modulus can be calculated by Hooke's law $\sigma = E * \varepsilon$. The gradient of the linear correlation of ε with σ is defined as the E-modulus (pict. 3.5.4 – 3.5.5).
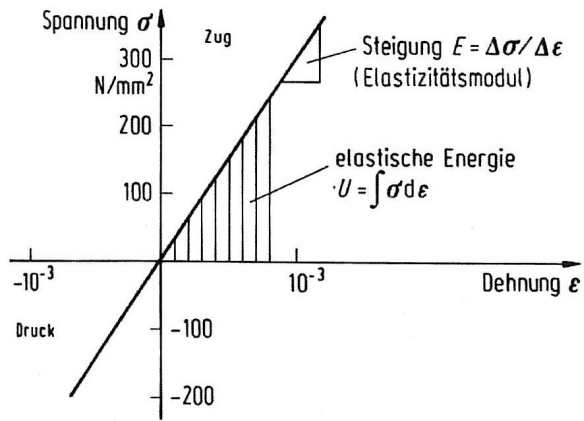
Pict. 3.5.4: Definition of elasticity modulus E according to Kluge (1996)

Hooke's law is valid for linear correlation of ε with σ. This is detected for paper only at low level of load.
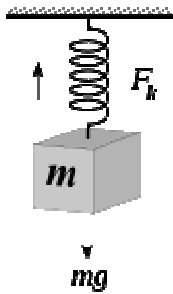
Pict. 3.5.5: Hooke's law: Spring stretches by vertical force F = m*g
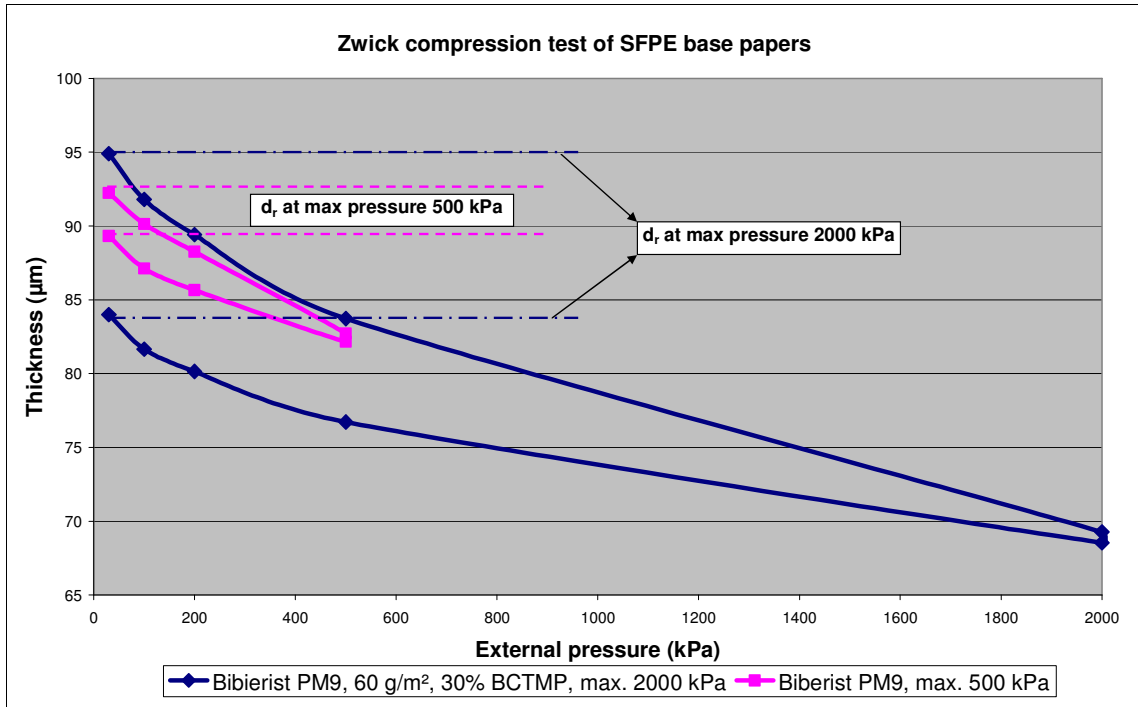
Pict. 3.5.6: Deformation $\varepsilon = \Delta L$ vs load σ (corresponds to vertical force F) for base paper PM9 from Biberist ($d_r - d_k$ = elastic deformation, $d_a - d_r$ = plastic deformation)

For all tested base papers a plastic deformation of approximately 5% was detected at low pressure level of 0,5 bar which increased to 10% when an external pressure similar to blade load (25 bars = 2500 kPa) was applied by the Zwick instrument.

Time of load was with 5 sec relatively long in the Zwick instrument, when compared to mill coaters (some milli seconds). As deformation of paper is depending on time (Jokio 1998 and Markus Lechtaler L7.11), elastic and plastic deformation will be much lower at blade coaters than at the Zwick instrument.
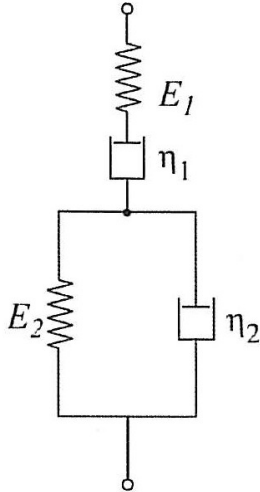
Pict. 3.5.7: Burgers model for deformation of paper: Spring for elastic part and attenuator for plastic compression (Jokio 1998)

Jokio 1998: $\varepsilon(t) = \dfrac{\sigma}{E_1} + \dfrac{\sigma}{E_2} * (1 - e^{\frac{-t*E_2}{\eta_2}}) + t * \dfrac{\sigma}{\eta_1}$

..with E_1, E_2, η_1 and η_2 the elasticity and viscosity coefficients of corresponding springs and attenuators.

For small change in applied external pressure **Hooke's law** can be used to calculate compressibility of paper:

Equ. 3-5-1: $F = -D * \Delta L$, with D the spring constant (N/m=kg/s²)

Equ. 3-5-2: $D = \dfrac{E * A}{L_0}$, with E the E-modulus.

When spring constant D or E-modulus E is low, the spring is "soft"; the load F leads to a high compression distance ΔL in the spring.

Pict. 3.5.7 shows the Burgers model for elastic and plastic deformation which is in accordance with the Zwick measurements, shown in 3.5.6. Under compression paper behaves elastic until a certain threshold is reached. Above this threshold which is depending on furnish or pre-pressing, plastic deformation takes place.
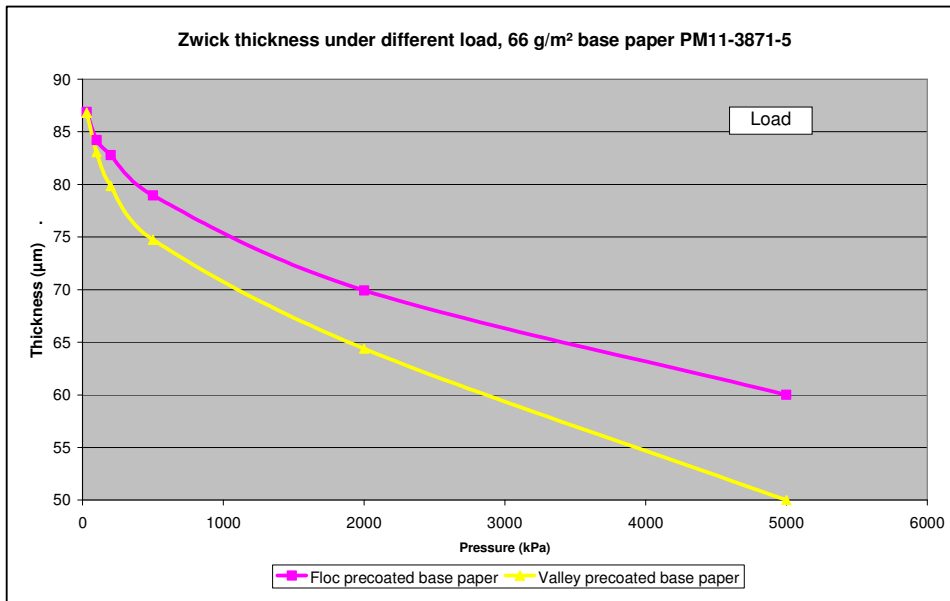
Pict. 3.5.8: Thickness vs. External pressure at Zwick
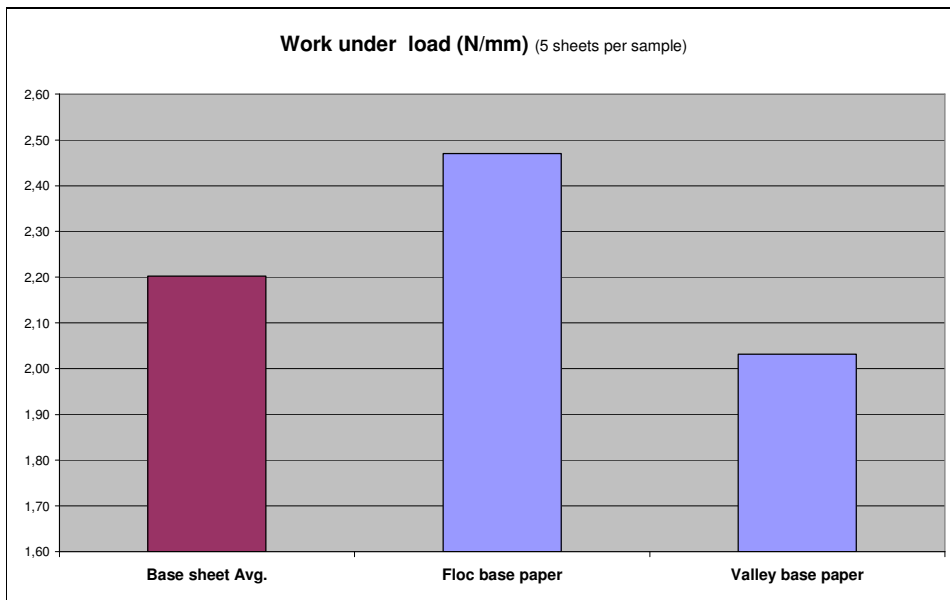
Pict. 3.5.9: Work under load (integration of thickness vs. pressure) for base paper

For small changes in load a linear relationship between F and ΔL was measured in the Zwick instrument (it has to be checked for every medium to apply Hooke's law). The difference in compression between flocs and voids is shown in pict. 3.5.8. Multiplying the reduction in thickness with the applied load the work under load can be determined (pict. 3.5.9). Applying Hooke's law the spring constant D is calculated from the Zwick measurements (pict. 3.5.10 – 3.5.11).
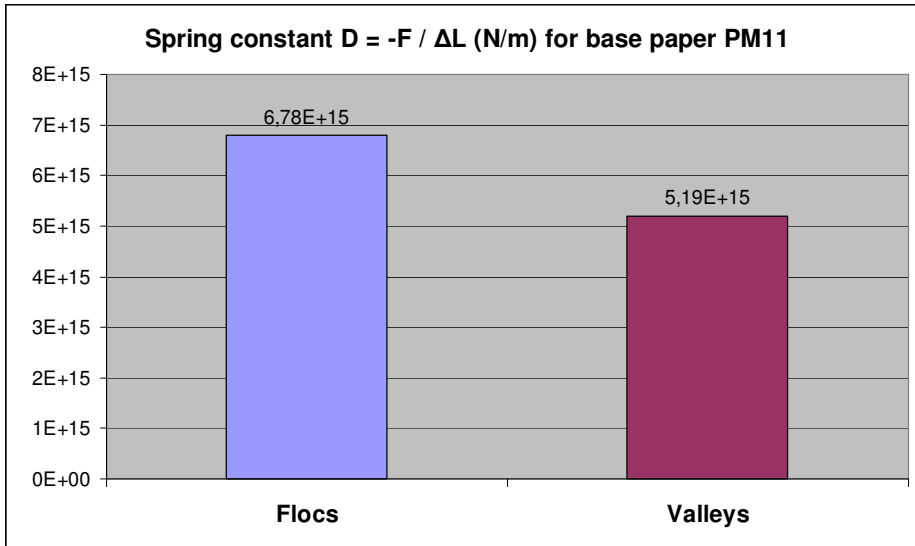
Pict. 3.5.10: Spring constant D and E-modulus under compression for base paper PM11 (100 – 500 kPa)

Due to their higher density flocs are "harder" springs with higher E-modulus. They are less compressed under external pressure than valleys.
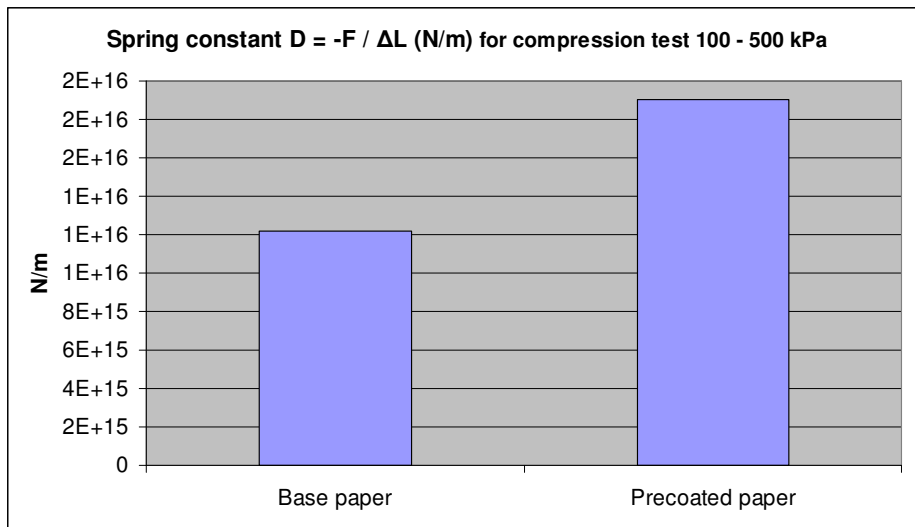
Pict. 3.5.11: Comparison of spring constants for base paper and precoated paper

Coatings add compressibility stiffness to the base paper. Therefore thickness differences can be easier levelled out by calendering when papers are coated.

3.6 Lab press experiments

The higher thickness and density of flocs must lead to a higher pressure when an external pressure is applied on the surface by a printing nip or a blade in a coater. This can be proven by lab press experiments where the local pressure is detected by a pressure sensitive film.

Isabel Endres (L7.12) was the first who showed the pictures of local pressure distribution by using the LCSA device at STFI.
Pict. 3.6.1 shows this instrument. Isabel Endres used a pressure sensitive photo film to detect local pressure. A small piece of paper was pressed under external pressure in contact with the photo film. Results are shown in pict. 3.6.2.
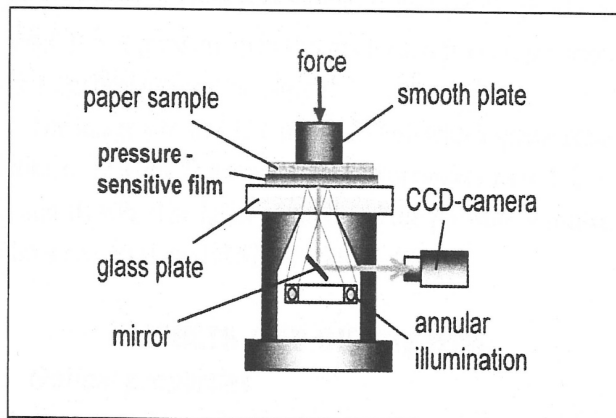
Pict. 3.6.1: LCSA at STFI for compression measurements
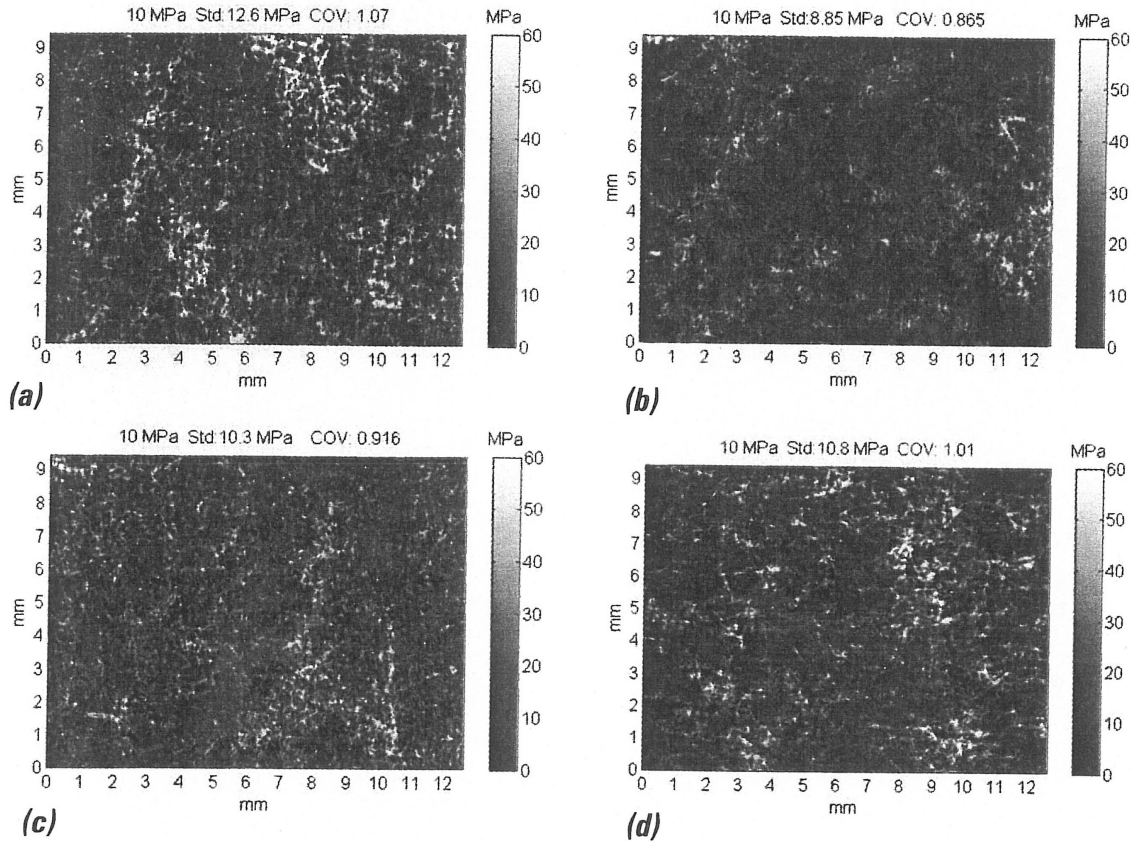
Pict. 3.6.2: Pressure image map at 10 MPa of a) uncoated base, b) blade coated, c) film-coated d) curtain coated

The only disadvantage of the LCSA device is the small measurement area of 2 x 2 mm. With this method it is difficult to detect local pressure differences between flocs and voids as they are of bigger size than measured area.

To confirm the theory of higher local pressure at flocs due to higher thickness and higher density, different base papers and coated papers from PM11 and other paper mills were pressed in a new lab press device. The method of Isabel Endres (L7.12) was further developed to measure a bigger area of 100 x 100 mm.

The lab press device is shown in pict. 3.6.3.
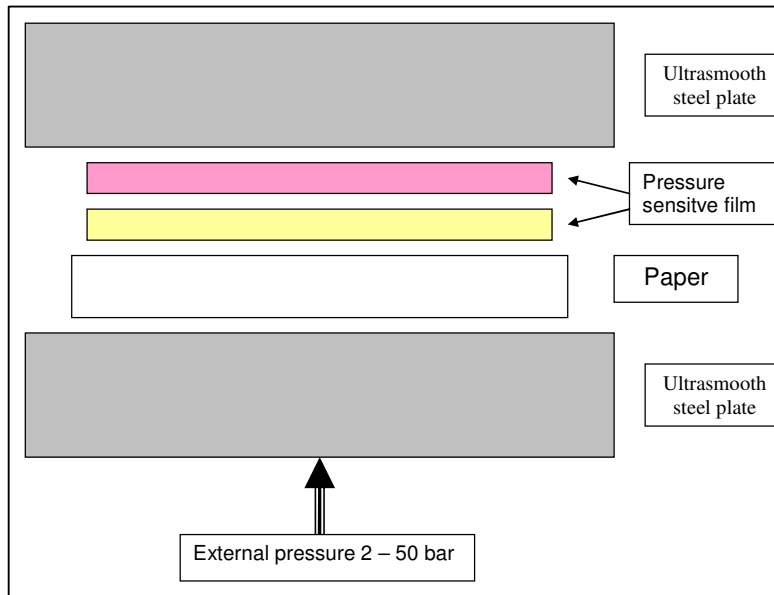
Pict. 3.6.3: Lab press with pressure sensitive film

Two steel plates were made with ultra smooth surface and exact constant inplane thickness.

The tested substrate was put together with a pressure sensitive Fuji film between the plates. The Fuji film consisted of two separate films. One carried the colours particles and one was developing them. The higher the local pressure, the deeper the red dot of the Fuji film. By comparing the local colour with a red scale standard the local pressure was determined in absolute figures. A digital pressure map of the investigated surface was the result.

The sandwich of test substrate plus Fuji films was put with into a conventional lab press which was used for lab sheet press dewatering. The pressure level had to be adjusted to the Fuji film in use. In these trials a film for 5 – 100 bars pressure range was used and an external pressure of 50 bars, similar to blade coaters, was applied by the lab press.

Two result of these press experiments is shown in pict. 3.6.4 for a base paper of PM11 (bad formation) and an asian base paper (good formation due to low fibre length and hybrid former).
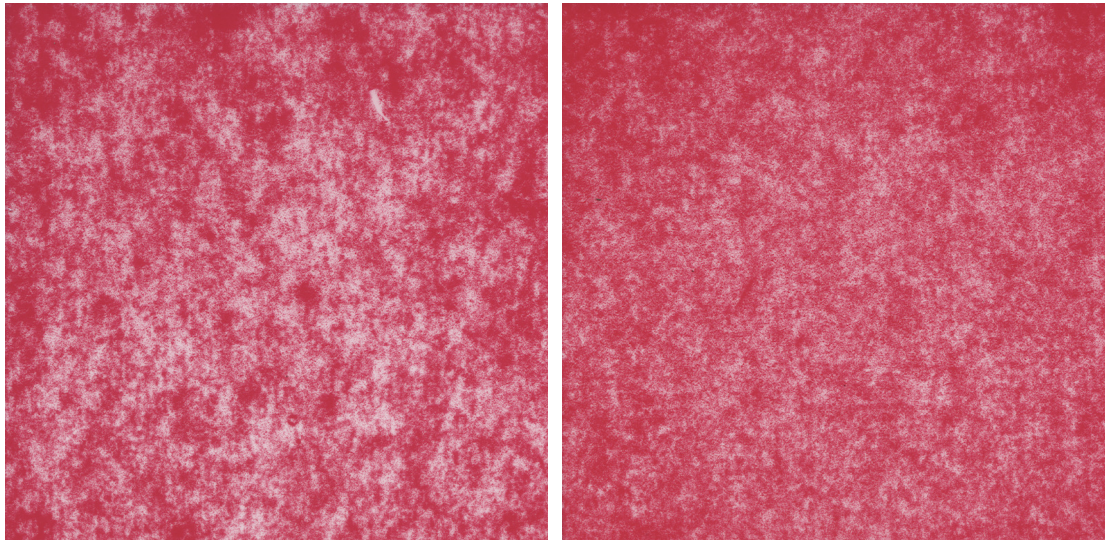
Pict. 3.6.4: Fuji pressure sensitive film image of base paper with Ambertec = 0,5 (left) and base paper with Ambertec = 0,3 (right) – deeper red = higher pressure

Again the match analysis was used to correlate local pressure from Fuji film image with local basis weight from Ambertec image (pict. 3.6.5).
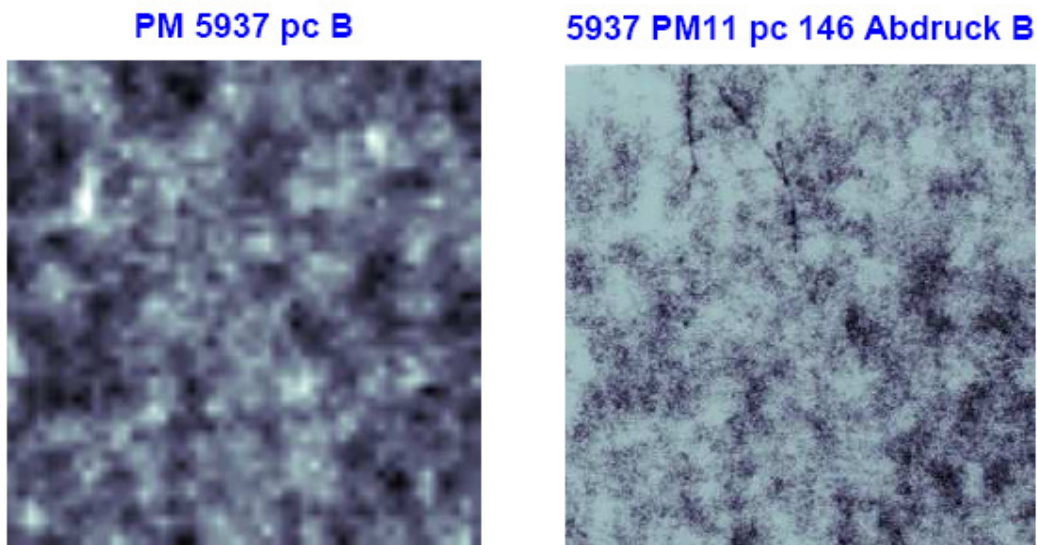
Pict. 3.6.5: Comparison of Ambertec image (left) with Fuji film scan ("Abdruck") of same area of base paper PM11 (dark = high pressure)

PM 5937 pc B   BandPass 1..15mm   Mottles of BP 1..15mm

5937 PM11 pc 146 Abdruck B

FFT-matchfactor: 64.2 %
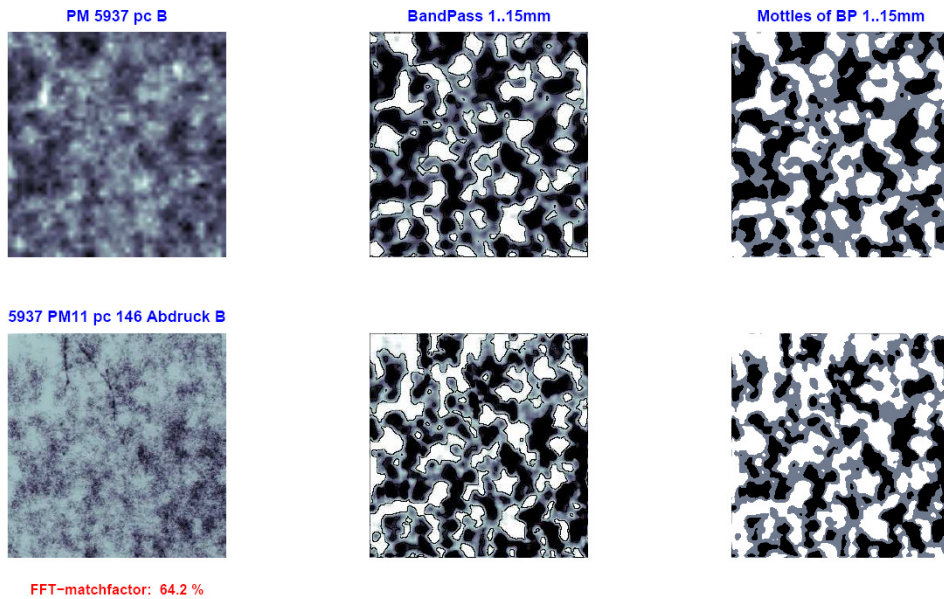
Pict. 3.6.6: Match analysis of Ambertec basis weight and Fuji film colour ("Abdruck")

The correlation between local basis weight and local pressure was perfect. The higher the local basis weight or density of the paper, the higher the local pressure was. For images with different in resolution a match factor of 60 – 75% can be regarded as perfect match, which was shown in pict. 3.4.4.

TR 5937 PM11 pc 146 B   BandPass 1..15mm   Mottles of BP 1..15mm

5937 PM11 pc 146 Abdruck B

FFT-matchfactor: 64.3 %
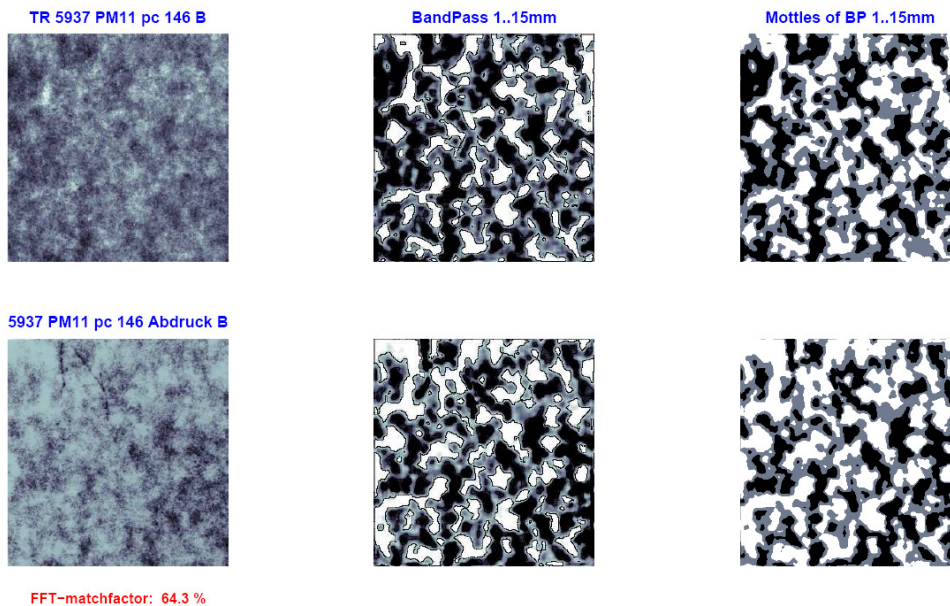
Pict. 3.6.7: Match analysis of Transmission light formation ("TR") and Fuji film colour ("Abdruck")

Formation was checked additionally by transmission light scanning (pict. 3.6.7). The match results with lab press experiments didn't differ from Ambertec formation measurement.

The duration of pressing is not of importance as Fuji pictures with different press times and lab press experiments with different time and pressure show in pict. 3.6.8:
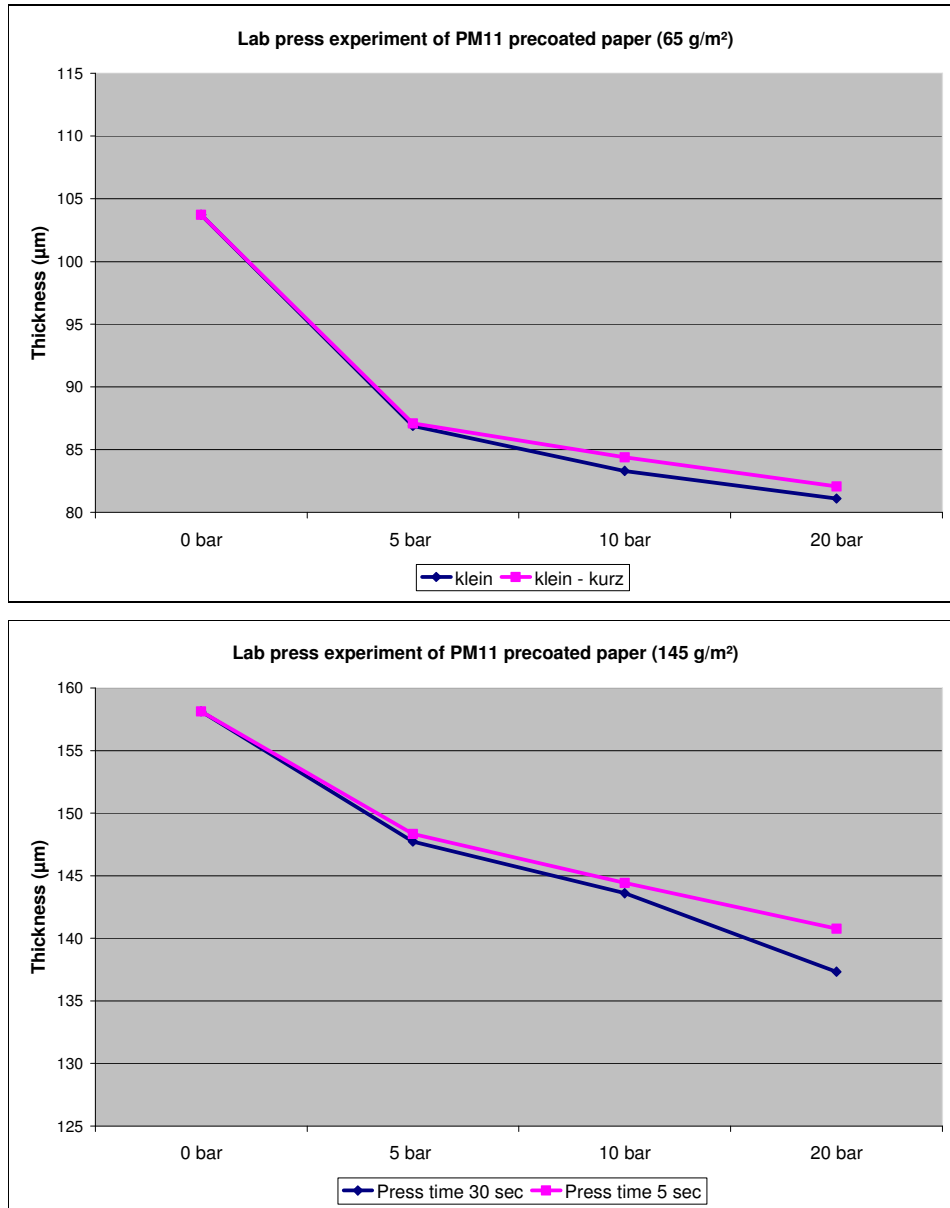
Pict. 3.6.8: Thickness of PM11 precoated papers at different press time and pressure

3.7 Coating layer analysis

What will happen to the coating layer on top of flocs and voids, when local pressure under the blade or in the film press nip is higher at flocs and lower at valleys? Pict. 3.7.1 shows the thickness measurements of stamped out flocs and voids.
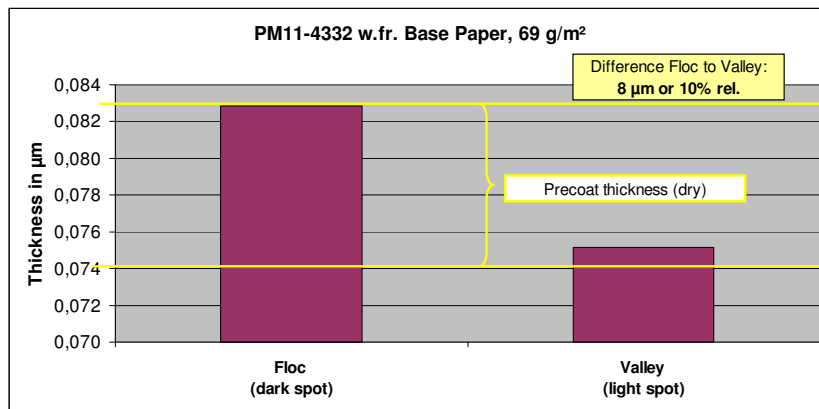
Pict. 3.7.1: Thickness variations in base paper

If the blade trails over the surface under low pressure, the voids will be filled with coatings and surface of flocs will remain uncoated. Many REM pictures from microtome cuttings prove this theory in literature. But reality is totally different. Fig. 3.7.2 shows of single coated paper where thickness of the coating layer is either zero or double of the mean value.
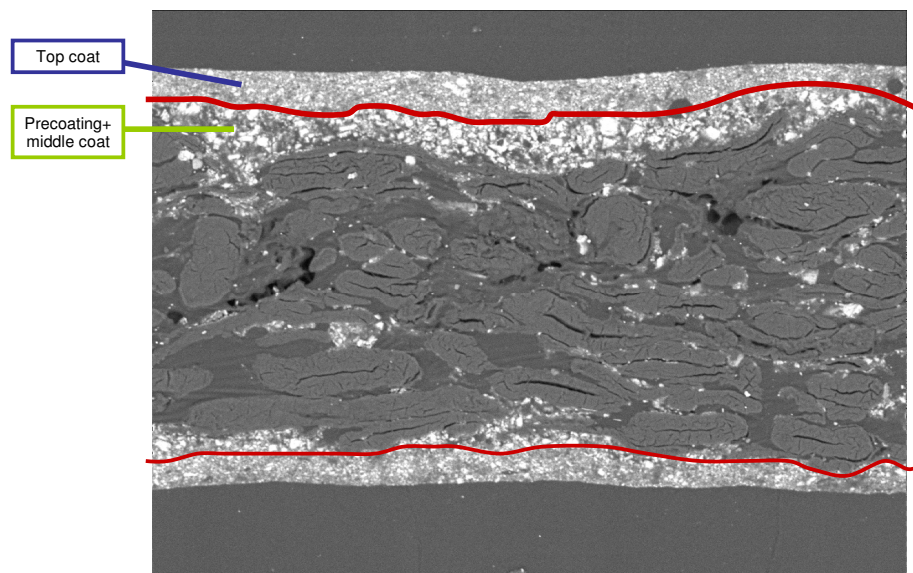
Pict. 3.7.2: REM picture of cross cuttings in CD from triple coated paper PM11– length of cutting is 160 µm (comparison: paper thickness is 85 µm)

When a single REM photo of cross cutting is regarded, the differences in coat weight have an in plane size in CD or MD of 10 – 20 µm. But this size is much too small to explain mottling as mottled spots in printed image have a mean size of 2000 – 5000 µm!

Therefore a cutting length of 4 – 8 mm has to be investigated by microtome cuttings to get an impression of the coating layer thickness variations over flocs and valleys. This means 50 REM-pictures have to be added next to each other.

These long microtome cuttings are done at the technical university of Graz.
Coating layer thickness on top of flocs and valleys of film press (MSP precoated paper PM11) was analysed at TUG.
Comparison with curtain coatings will be done in the future.
50 microtome cuttings were made in CD with a cutting length of 3,5 mm in MD. The investigated areas were marked before measurement and consisted of two typical flocs and two valleys.
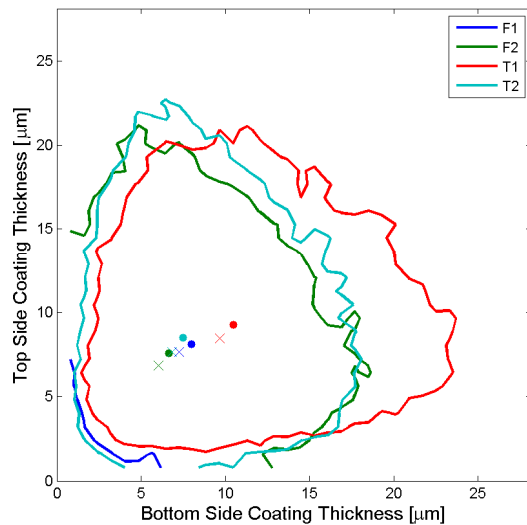
Pict. 3.7.3: Coating layer thickness on top side and bottom side upon flocs (F1,2) and valleys (T1,2) of MSP precoated paper PM11 (90 g/m² with 12 g/m² precoat per side)

PM11 MSP precoated paper, 90 g/m² - microtom cutting TUG

Legend: Mean coating layer thickness (µm) - Top Side ■ Mean coating layer thickness (µm) - Bottom Side
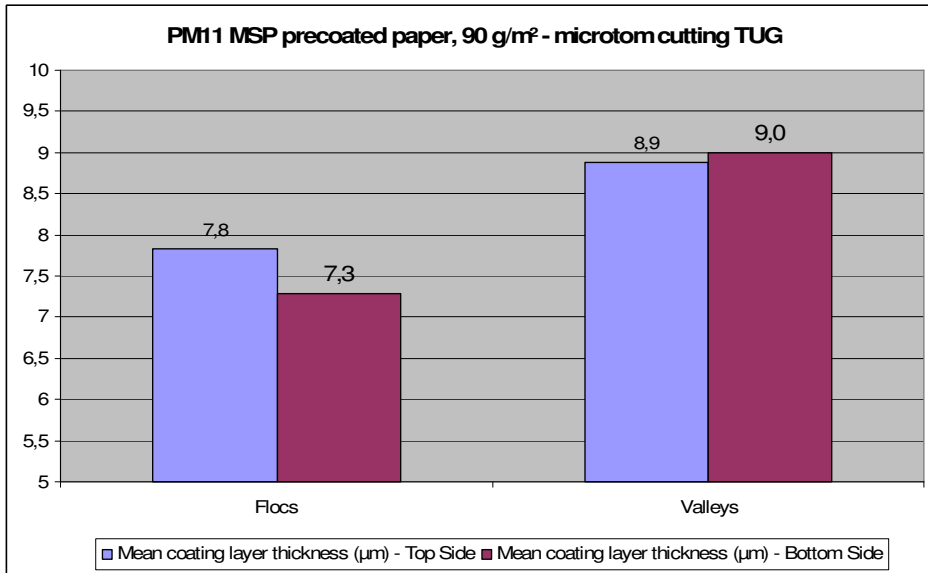
Pict. 3.7.4: Mean coating layer thickness on top side and bottom side of flocs and valleys

The measurement of coating layer thickness of the MSP precoated paper from PM11 by microtome cuttings at TUG showed in pict. 3.7.3 and 3.7.4 a 10 – 15% higher coating layer thickness on top of voids. Earlier microtome cuttings at PTS proved this result (pict. 3.7.5):

	Mean Value of Thickness				Variance in thickness			
	Coated Paper	Base Paper	Coating TS	Coating BS	Coated Paper	Base Paper	Coating TS	Coating BS
Valley	107,57	77,61	16,93	13,04	1,42	4,91	3,84	3,14
Floc	111,97	90,01	10,36	11,60	2,00	6,15	3,41	2,91
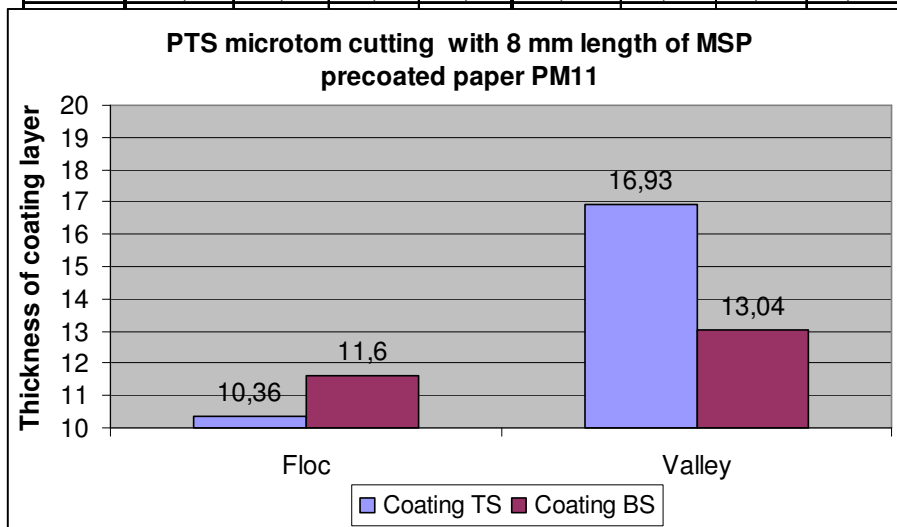
Pict. 3.7.5: REM analysis of 8 mm long microtome cutting at PTS in 2003 (PM11 MSP precoating)

Voids were 12 µm lower in base paper thickness than flocs (10% relative difference). This difference was partly levelled out by a 6,5 µm thicker coating at the top side (65%)and 1,4 µm thicker coating on the bottom side (15%).

To check this result flocs and valleys of coated paper were cut out with the special die (3-4 mm diameter) and analysed. By measuring the local basis weight of the coated paper and assuming constant base ash, the coat weight on top of flocs and voids can be calculated from ratio basis weight to overall ash.

Calculated coat weight of MSP precoated papers PM11
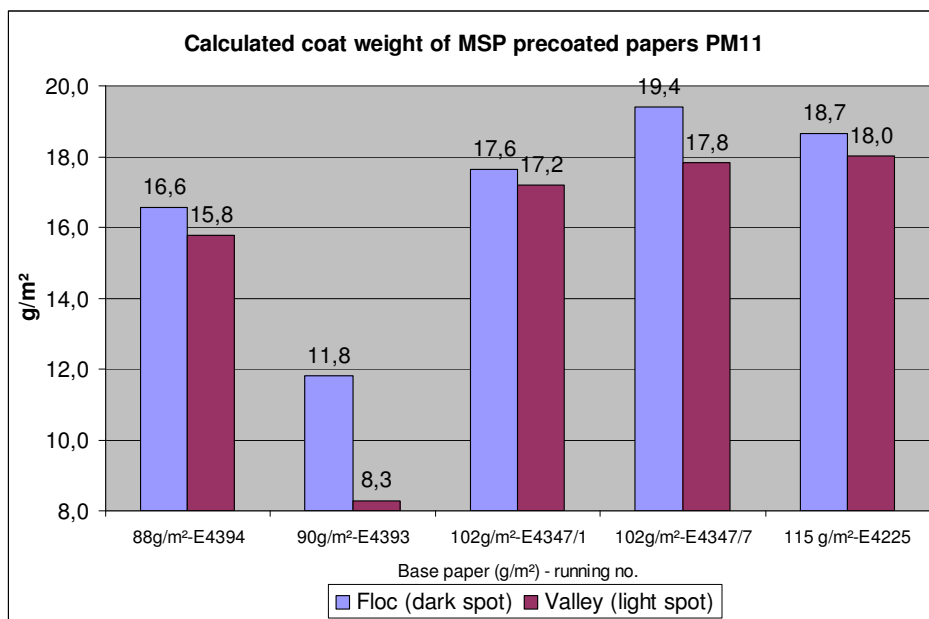
Pict. 3.7.6: Calculated coat weight at flocs and valleys (film coating)

The basis weight and ash analysis of flocs and voids (pict. 3.7.6) showed the total opposite to coat weigth analysis by REM pictures:
When the whole cross section of coated sample was analysed by basis weight analysis, coat weight was higher at flocs.
Taking into account that REM photos clearly showed lower coating thickness at the surface of flocs, the conclusion can be drawn, that more coating colour is pressed at flocs into the base paper (due to higher local pressure) and less coating remains at the surface.

3.8 Lab coating experiments

To verify the theory of constant coating layer thickness upon flocs and valleys, a lab coating trial was done by using the **Heliocoater** of CIBA RD in France. Heliocoaters have the advantage of blade loads which are close to mill practice as the speed is in the range of 1000 – 2000 m/min. As blade pressure is significantly higher than at other lab coaters, realistic coating colour penetration under the blade and realistic coat weight distributions are achieced by Heliocoater, similar to mill coaters. This can be easily checked by UV inspection or lab mottle tests.

Six areas of 45 x 45 mm were marked in a base paper PM11 and analysed by Ambertec basis weight and UBM-surface topography before and after the coating. 12 g/m² coat weight of a standard top coat was applied with the Heliocoater at 1200 m/min. Results are shown in pict. 3.8.1 – 3.8.2.

Local coat weight was calculated by match analysis (pict. 3.8.3 – 3.8.4). Ambertec basis weight maps of same area of coated and uncoated paper were put over each other. The difference is the coat weight.
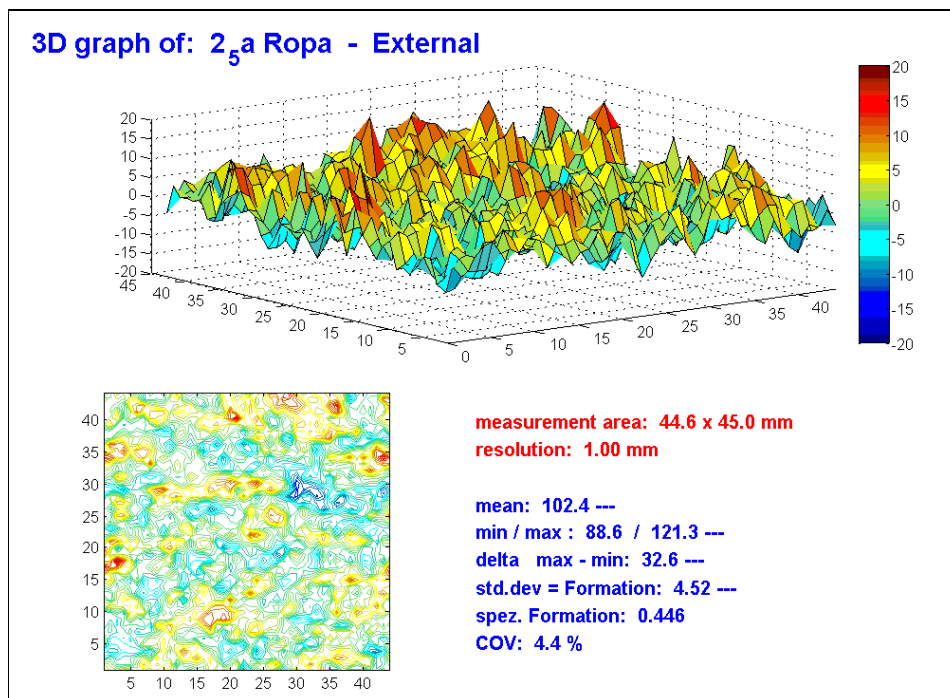
Pict. 3.8.1: 3D-diagramm of base paper basis weight by Ambertec and Anbertec variation data's
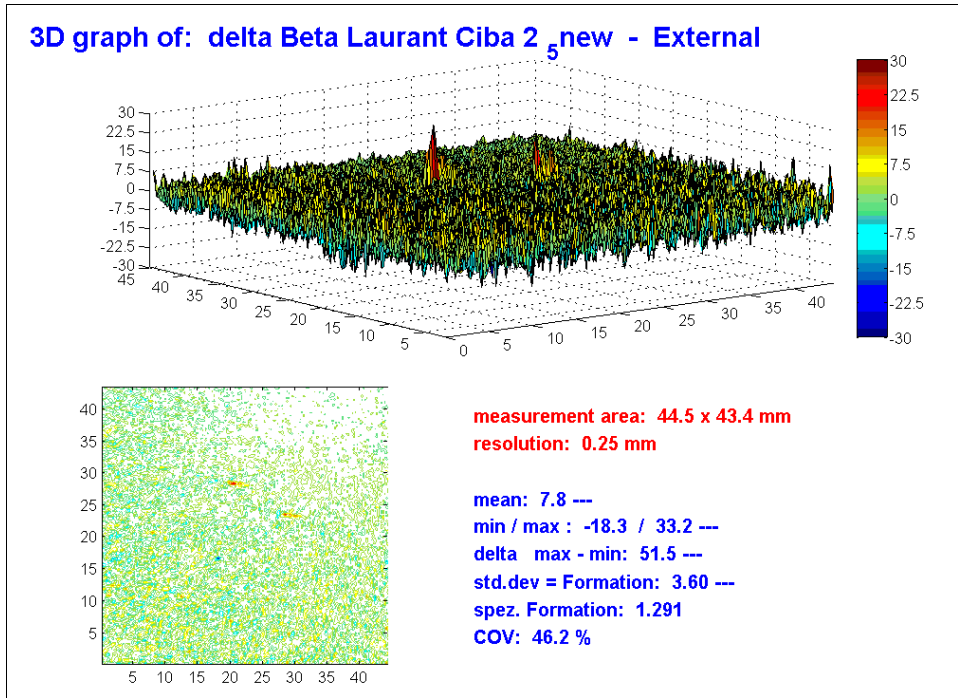
Pict. 3.8.2: 3D-diagramm of calculated coat weight
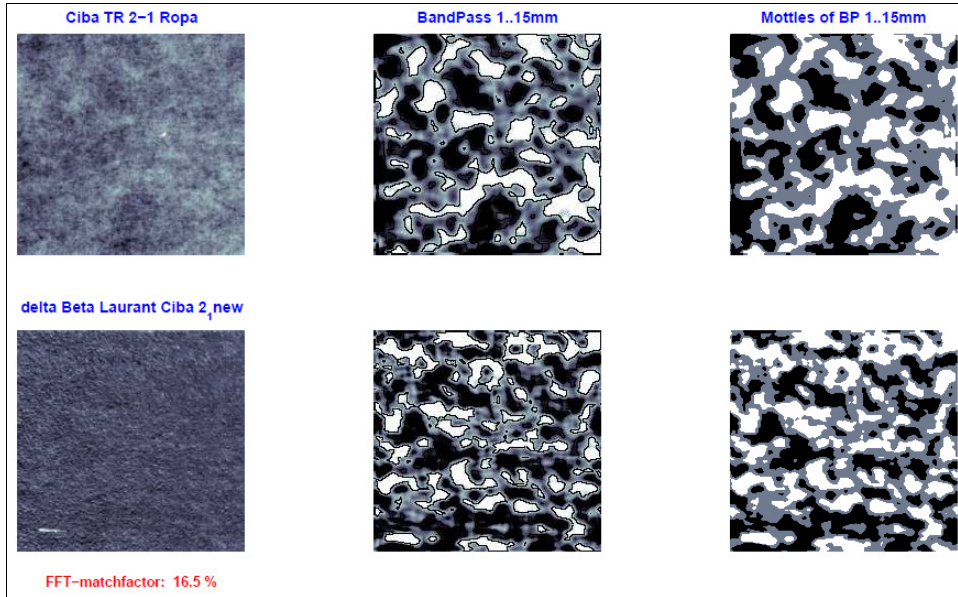
Pict. 3.8.3: Match analysis for base paper basis weight and coat weight
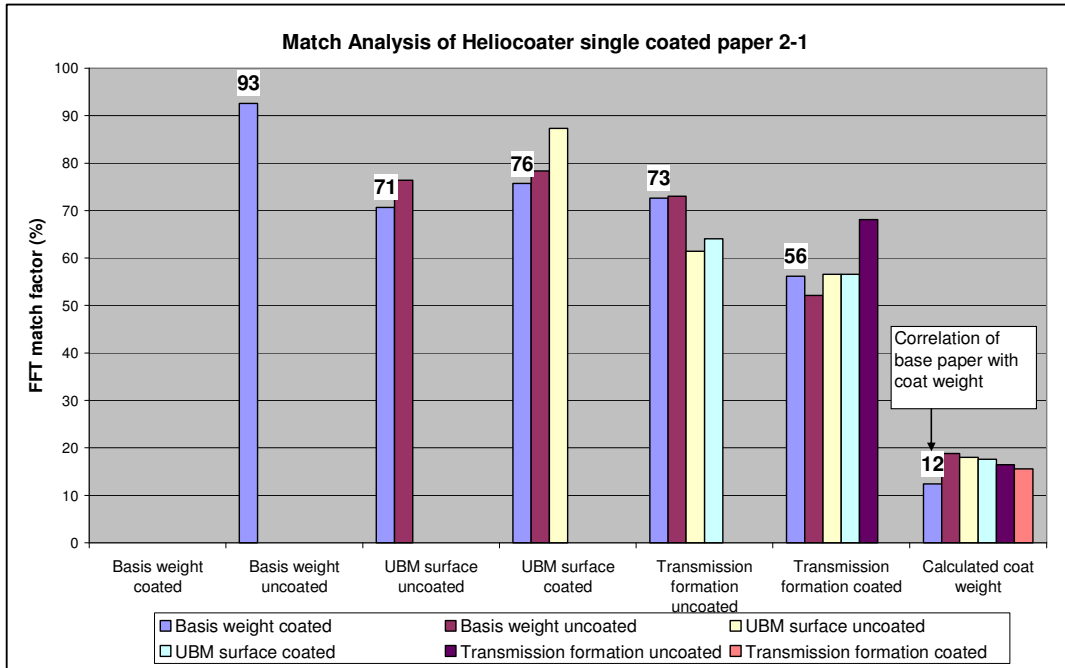
Pict. 3.8.4: Match factors for Heliocoater samples (mean of six areas)

Match analysis gave a poor correlation of 15 – 20% between in-plane basis weight distribution of base paper and coat weight. In-plane coat weight distribution showed uniform coat weight like microtome cross cuttings and cut out flocs and voids. **Coat weight at the Heliocoater did not correlate with basis weight distribution of base paper.**

3.9 Ash distribution of base papers and coated papers from X-Ray analysis

Another method to determine coat weight distribution is to make Gamma Radiograms in an X-Ray scanner. This was done first for a base paper of PM11, proving a homogeneous in-plane base ash distribution. In a second investigation precoated samples were analysed (pict. 3.9.1).
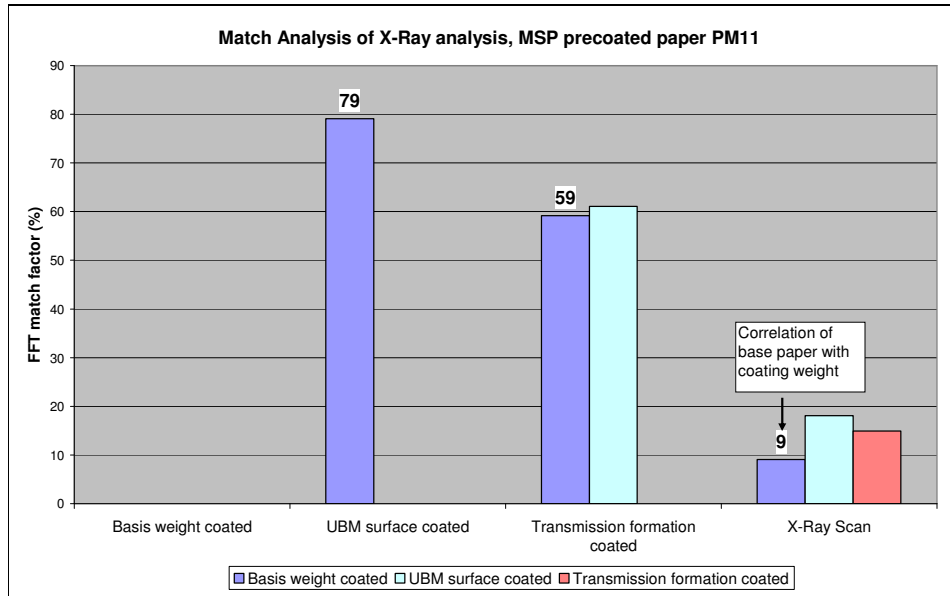
Pict. 3.9.1: Gamma radiogram of coated paper

Again no correlation was found between coat weight and basis weight distribution, confirming the theory that coat weight differences cannot be responsible for formation induced mottling.

3.10 Compaction of the base paper under the blade

To find an explanation for the relatively low variations in local coat weight the total blade coating process was analyzed. In the chapter "blade coating" the **normal pressure under the blade** was calculated.

A volume of fluid method for non Newtonian media was used to calculate the resulting forces at the blade tip. Different blade geometries were simulated. The viscosity of the different coating colours was measured with ACAV capillary and SLIT geometry. The detailed results are shown in the chapter 7 "blade coating".
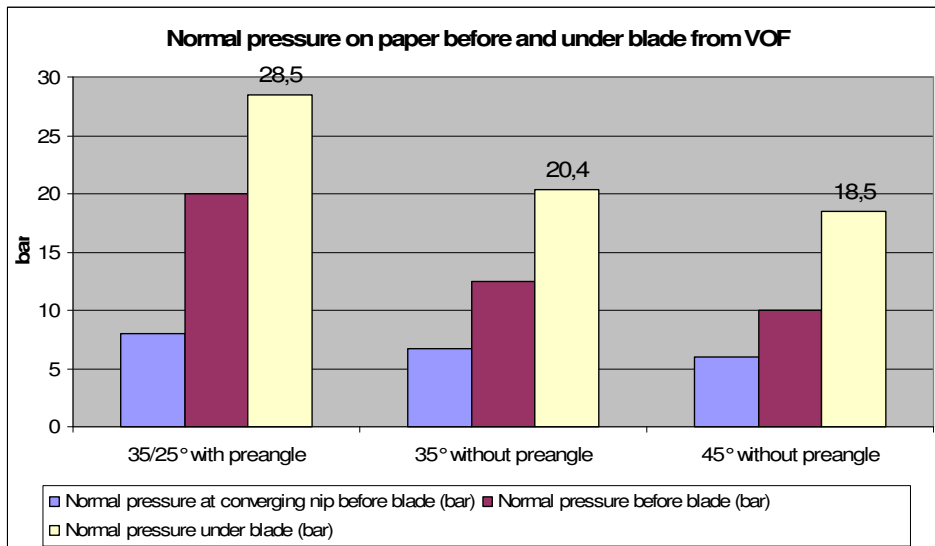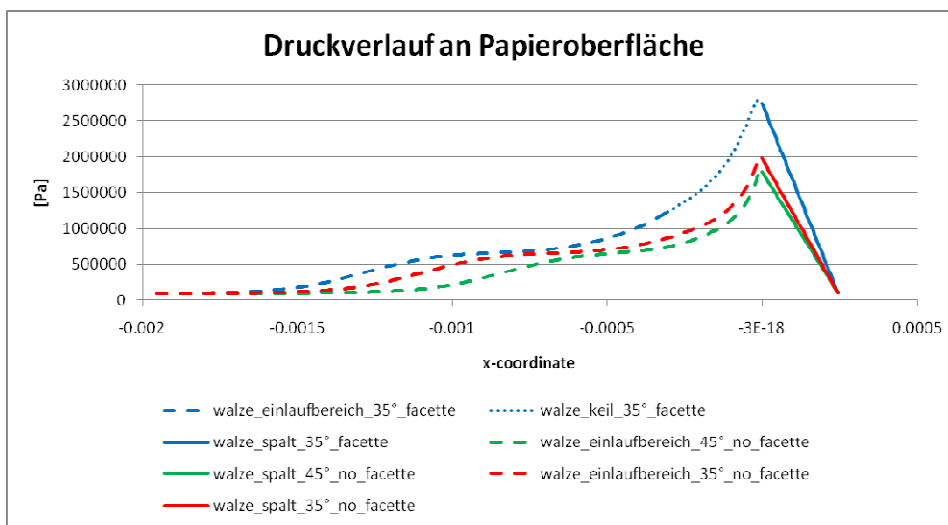
Pict. 3.10.1: Pressure distribution before and under the blade for different facet geometries

From the VOF simulation of different blade geometries a peak pressure of 20 – 30 bars under the blade can be taken for calculating the deformation of the base paper under the blade.

If VOF methods are not available the blade pressure can be approximated by adding the impulse force $F = p * A$ with $p = \rho/2 * v^2$ and the shear force $F_{shear} = \tau * A$ with $\tau = \eta * \gamma$ to get the sum of forces F_2 in coating direction (pict. 3.10.2). With the blade angle α the resulting normal force can be calculated with $F_{normal} = F_2 * \tan(90-\alpha)$ (see also chapter 7 "blade pressure calculation").

Normal forces on paper under blade (N)

	35° with preangle 25°	35° without preangle	45° without preangle

Resultant impulse force, normal to coating direction ■ Resultant shear force normal to coating direction
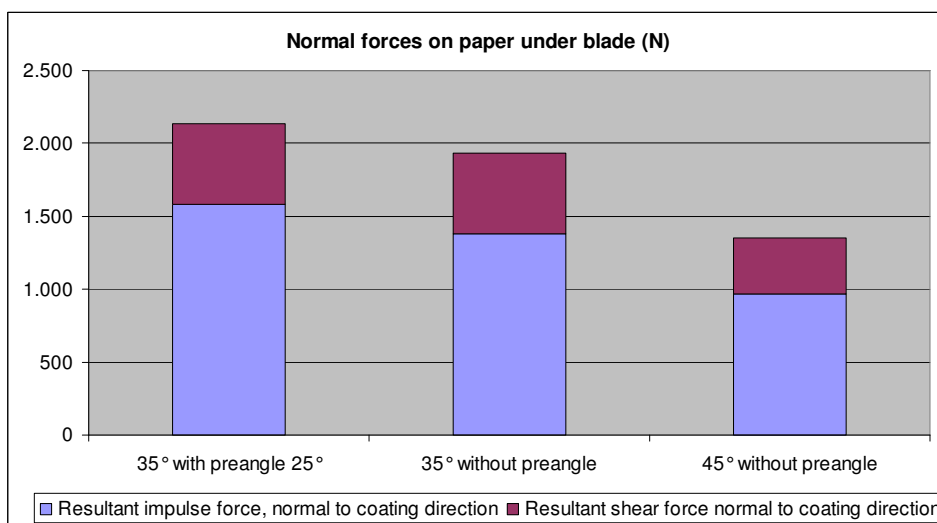
Pict. 3.10.2: Calculated normal pressure with Bernoulli and capillary shear measurements

The calculation shows, that the normal blade pressure is dominated by the tangential impulse force of the coating colour. It is a function of colour density (solid content) and coater speed. Both factors are of limited influence for the operator.
The shear force is a function of high shear viscosity and can be influenced by the coating colour formulation and the shear length. In modern high speed blade coaters blades with short facet are used to reduce shear forces (see chapter "blade coating").

The lab press experiments, described in 3.6 showed that normal pressure of the blade will be mainly applied at flocs.

Inserting the calculated mean pressure under the blade from VOF into the relationship of base paper thickness versus external compression pressure from Zwick compression experiments, the local thickness of the paper under the blade can be calculated. Results are shown in pict. 3.10.3.
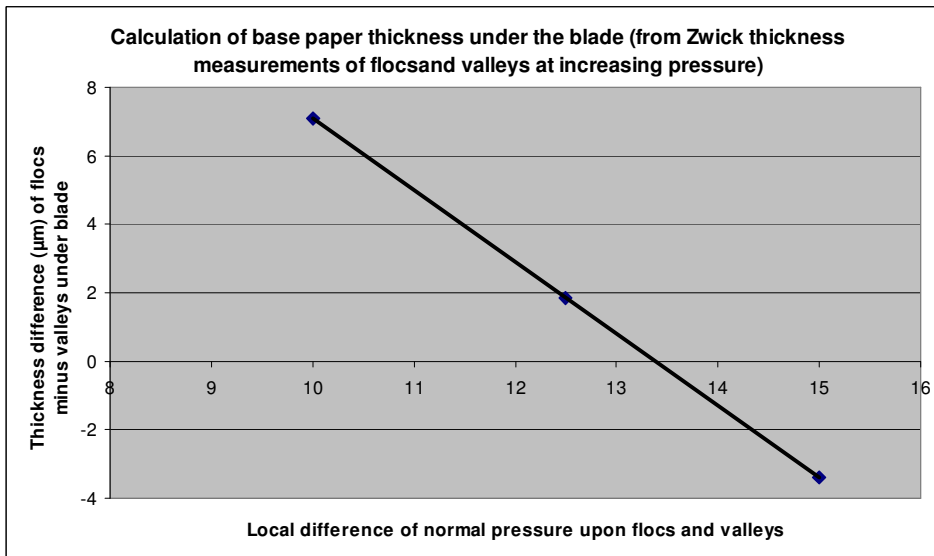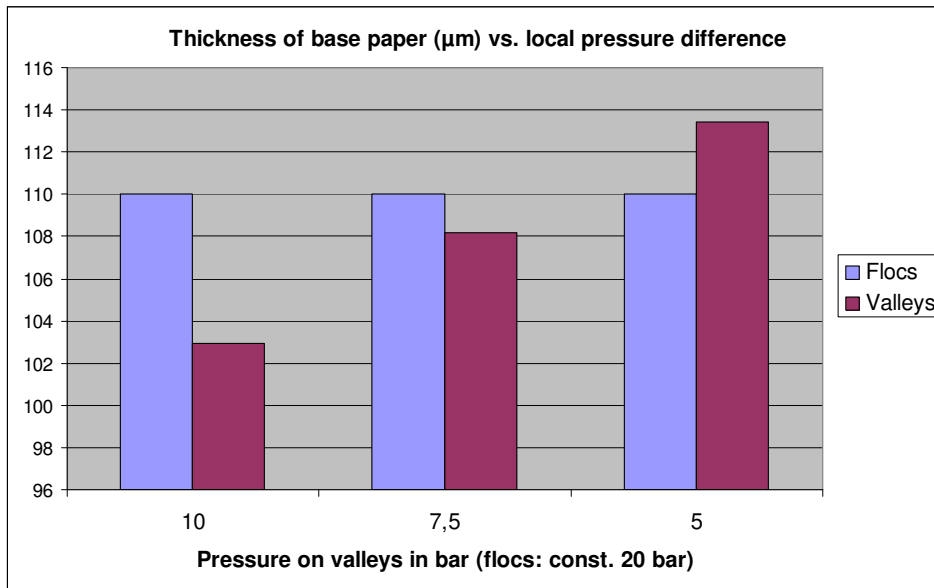
Thickness of base paper (µm) vs. local pressure difference

Calculation of base paper thickness under the blade (from Zwick thickness measurements of flocsand valleys at increasing pressure)

Pict. 3.10.3: Base paper thickness difference between flocs and valleys as a function of local pressure difference

The calculation shows, that base paper is totally even under the blade, when local pressure difference between flocs and valleys reaches a level of 13 bars.

The experiments with pressure sensitive Fuji film on base papers showed, that this local pressure difference is reality at a mean pressure level similar to that at blade coaters. Pict. 3.10.3 shows that when a pressure level of 32 bars is assumed at flocs and a pressure of 19 bars at voids, the base paper of PM11 would be totally even under the blade. For this calculation the compression behaviour of the PM11 base paper was taken form the Zwick compression measurements.

In the chapter "blade pressure penetration" the application pressure of a **film press coater** is calculated by the Hertz equation. It is with 2 – 4,5 bars much lower than the blade pressure which is the cause for improved mottling of film press precoated papers in comparison to blade precoated papers.

3.11 Impact of formation and compressibility on screen mottling

The influence of formation on screen mottling was observed by measuring Ambertec formation of different base papers and comparing it with the visual printing result of double coated grades of PM11 (pict. 3.11.2). Screen mottling is dominated by formation and in consequence by local pressure differences leading to local differences in ink density which are judged by the human eye as mottling. They are caused by differences in ink penetration depth. The deeper the ink penetrates locally the higher the local ink density is.
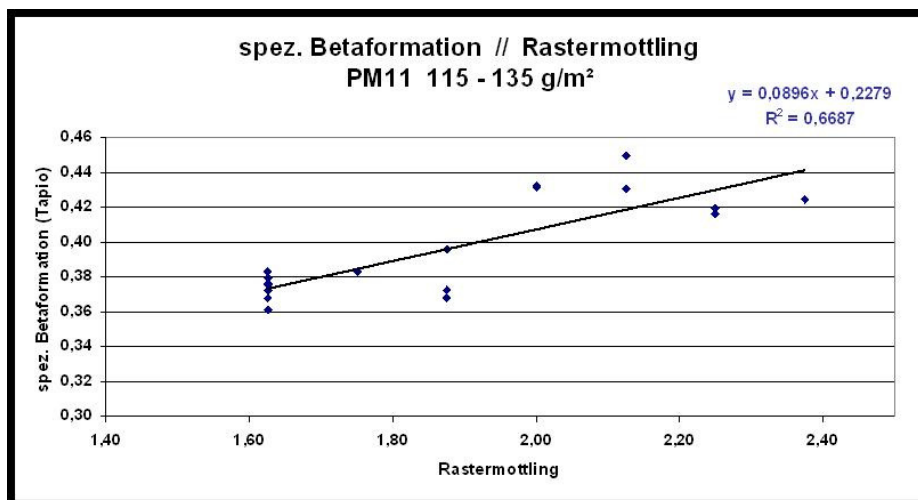
Pict. 3.11.1: Beta formation of PM11 base paper vs. screen mottling of coated paper

The correlation between screen mottling and formation of different base papers from PM11 was good. Many fourdriniers like e.g. M-Real Zanders PM3 were successfully rebuilt to modern hybrid formers with blades in the D-bar section to improve beta formation and in consequence screen mottling.

Another tool to qualify the base paper formation is the wave let analysis. It can be used for optical formation and for beta radiograms.
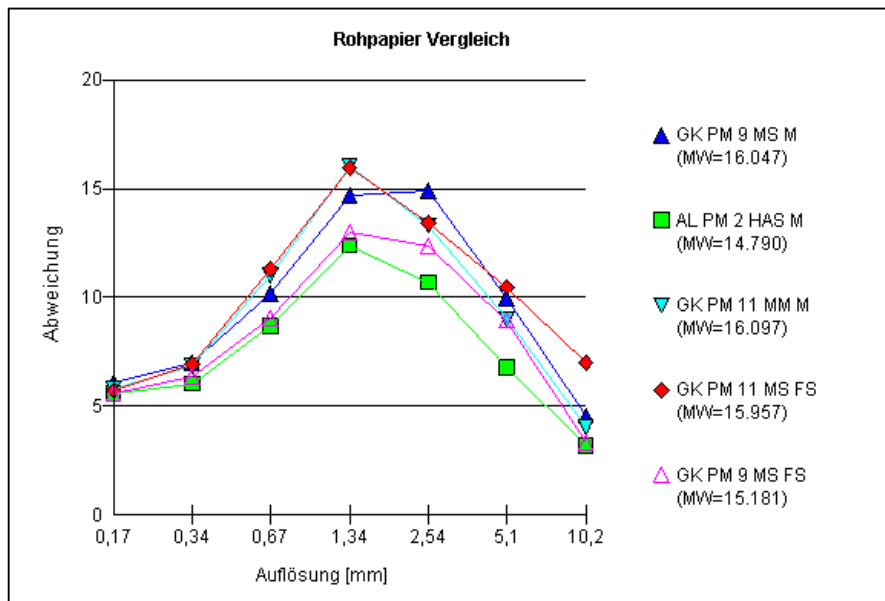
Pict. 3.11.2: Floc size distribution by wave let analysis of different base papers from PM9 / 11 measured with Ambertec (measured area: 45x45 mm)

Pict. 3.11.2 shows that the typical floc diameter of all investigated base papers was in the range of 1 – 5 mm with a maximum at 2 - 3 mm floc diameter.

Base papers from hybrid former machines like PM9 in Gratkorn and PM2 in Alfeld showed lower intensity in basis weight in the range of 2 – 3 mm floc size than base paper from gap former PM11 and have better Ambertec formation index:

Gapformer PM11: 0,45 – 0,58 $\sqrt{g/m²}$ (70 g/m² base sheet)

Hybrid formers PM9-GK and PM2-Al: 0,38 – 0,42 $\sqrt{g/m²}$

In a pilot coating trial at <u>Vestra</u> different base papers with big differences in formation were double coated under identical conditions (formulations, coat weight, speed, drying,…), super-calendered and printed. Results are shown in pict. 3.11.3 – 3.11.4.

Characteristics of the used base paper rolls:

PM11-Gratkorn: Gap former, long fibre dominated furnish

PM7-Husum: Gap former, short fibre

PM9-Gratkorn, PM2-Alfeld, PM6-Ehingen: Hybrid former, long fibre

PM1-Celpav: Hybrid former, 100% eucalyptus short fibre, best formation
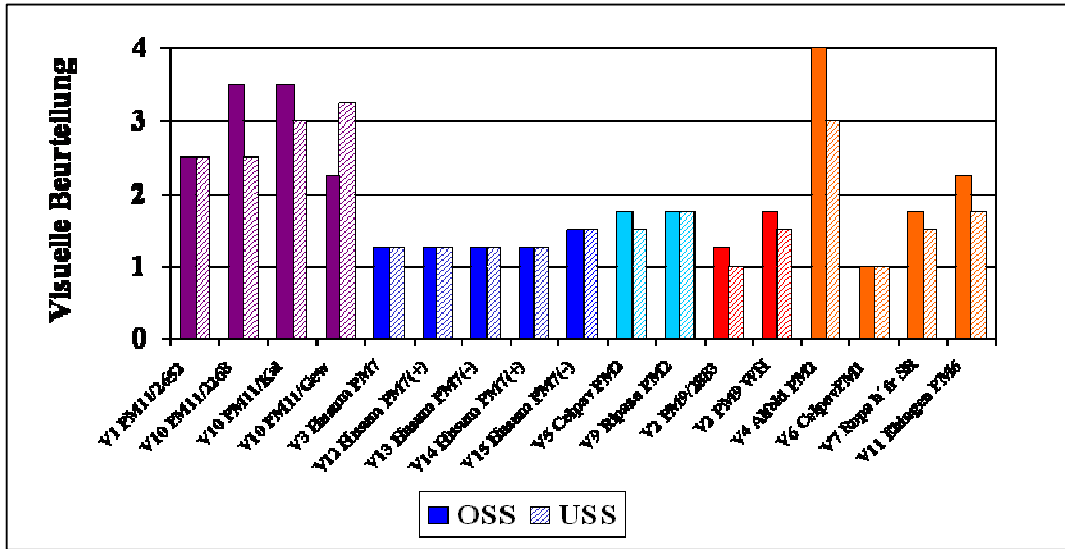
Pict. 3.11.3: Screen mottling (visual) of different base papers, coated and calendered
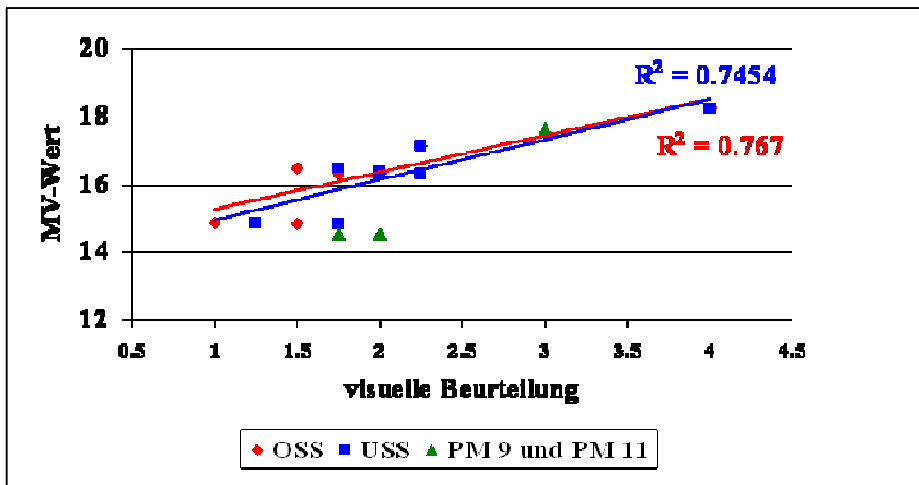
Pict. 3.11.4: Screen mottling (visual) vs. Ambertec mottle viewer formation index

Ambertec formation of the different base papers and screen mottling after coating, calendering and printing correlated well, which confirms the assumption that more ink transfer is different at flocs and voids due to local pressure differences in the printing nip and local permeability differences in the coating layer.

In a second pilot coating trial at Vestra different base papers from <u>Voith pilot paper machine</u> equipped with gap former "TQE" were double coated with blade, calendered and printed. Base papers from PM9 with surface sizing (m. OL) and without surface sizing (o. OL) and PM11 with surface sizing were added.

Pict. 3.11.5 shows that again Formation and screen mottling correlated well.
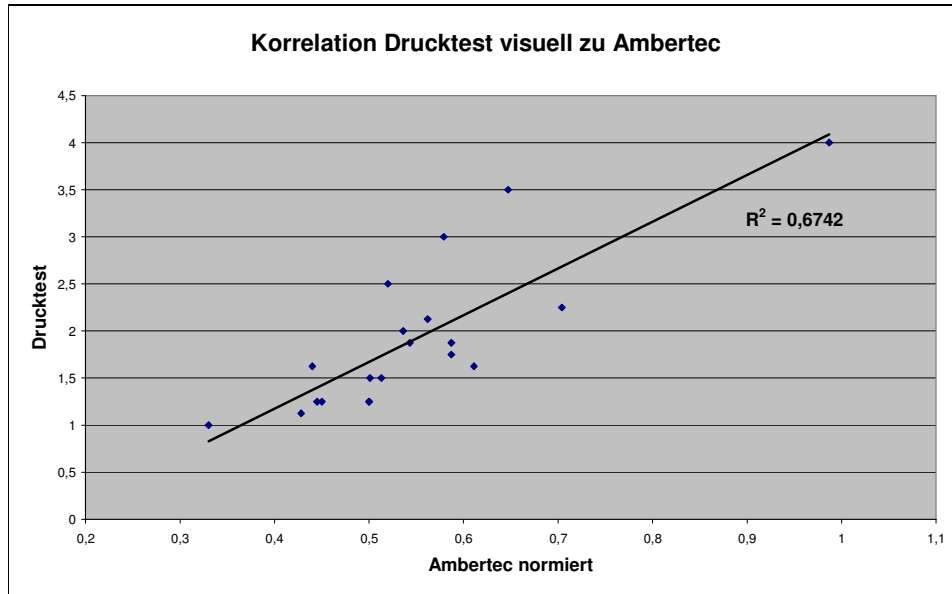
Korrelation Drucktest visuell zu Ambertec

$R^2 = 0,6742$

Drucktest

Ambertec normiert

Pict. 3.11.5: Formation vs. screen mottling
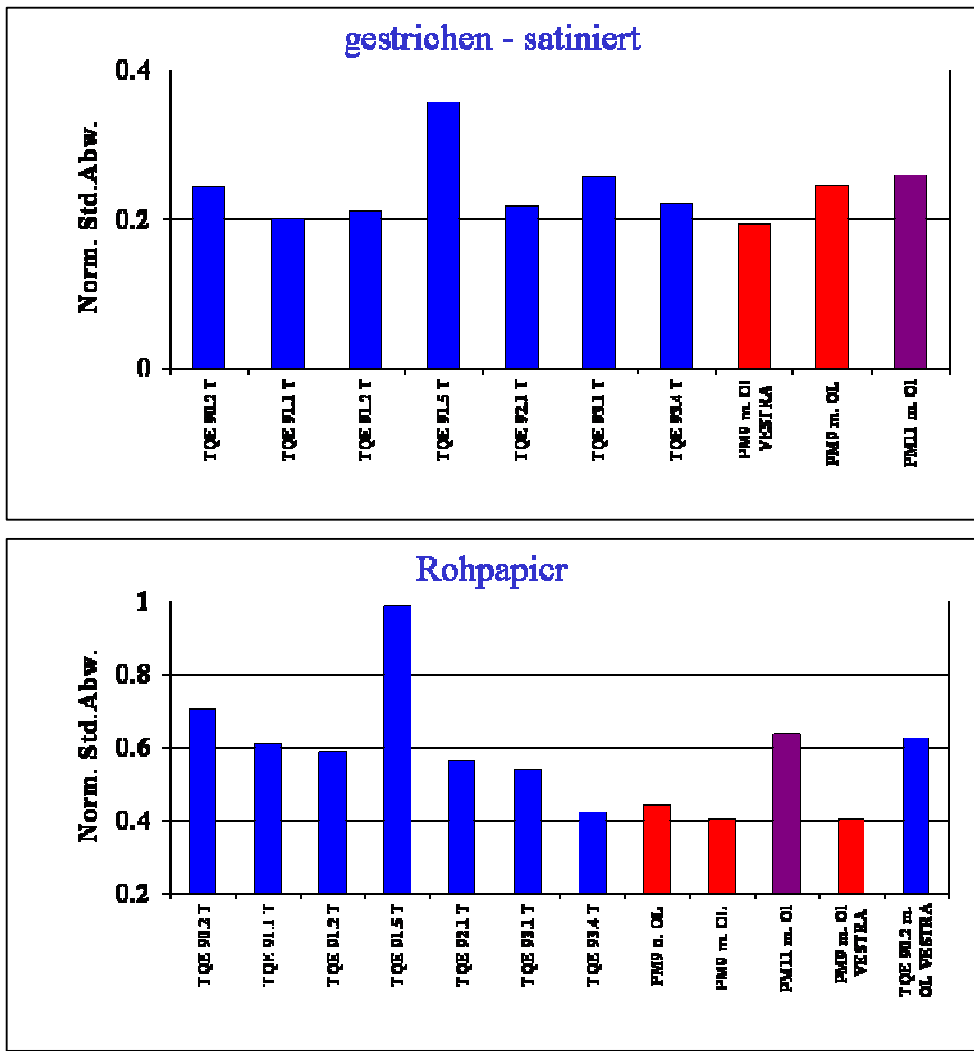
Pict. 3.11.6: Comparison of Ambertec of base paper and coated sheet

A distinctive correlation between Ambertec of base paper and Ambertec of coated and calendered paper was found in this study, proving the theory of an even coating layer on an uneven base paper (pict. 3.11.5 – 3.11.6).

Remarkable is the increase in difference of normalized Ambertec from base paper to calendered paper of PM11. The difference is much lower for PM9 paper samples. This can be explained by the lower compressibility of PM11 base paper caused by the shoe press of PM11 in the third nip. The less compressible the base paper, the bigger the pressure differences under the blade between flocs and valley will be and the bigger the differences in local penetration.
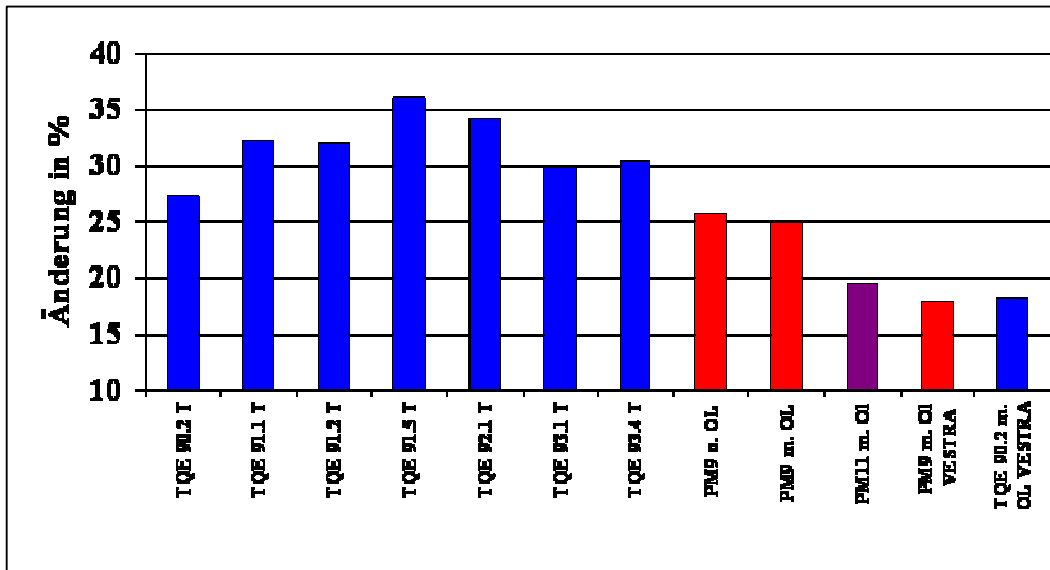
Pict. 3.11.7: Thickness change of base paper by 5-nip-lab calendering
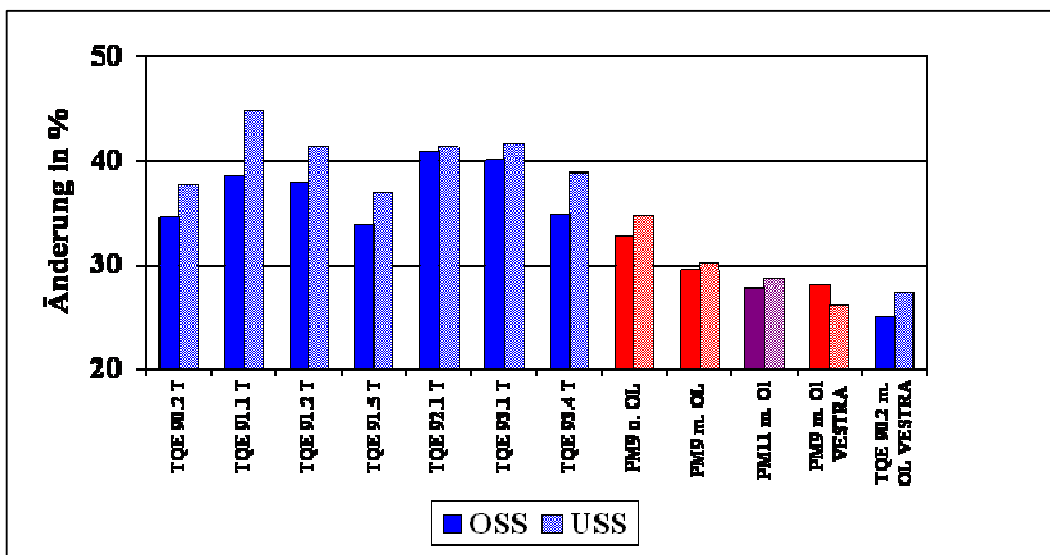
Pict. 3.11.8: Change in Ra value of base paper by 5-nip-lab calendering

Pict. 3.11.7 – 3.11.8 show that base papers from the pilot machine showed higher compressibility than mill papers due to less pre-compression in the press section and missing machine calender.

3.12 Impact of formation upon coating layer porosity

As coating layer thickness couldn't be identified as the root cause for mottling the porosity of the coating layer on top of flocs and voids was analyzed by Mercury porosity. From the whole spectrum of Mercury porosity as shown in pict. 3.12.1 the pore size range of 0,04 – 0,7 µm was taken as it describes the coating layer (see Resch P. et al, L1.78).
In the range of pores above 0,7 µm diameter base paper porosity is measured.
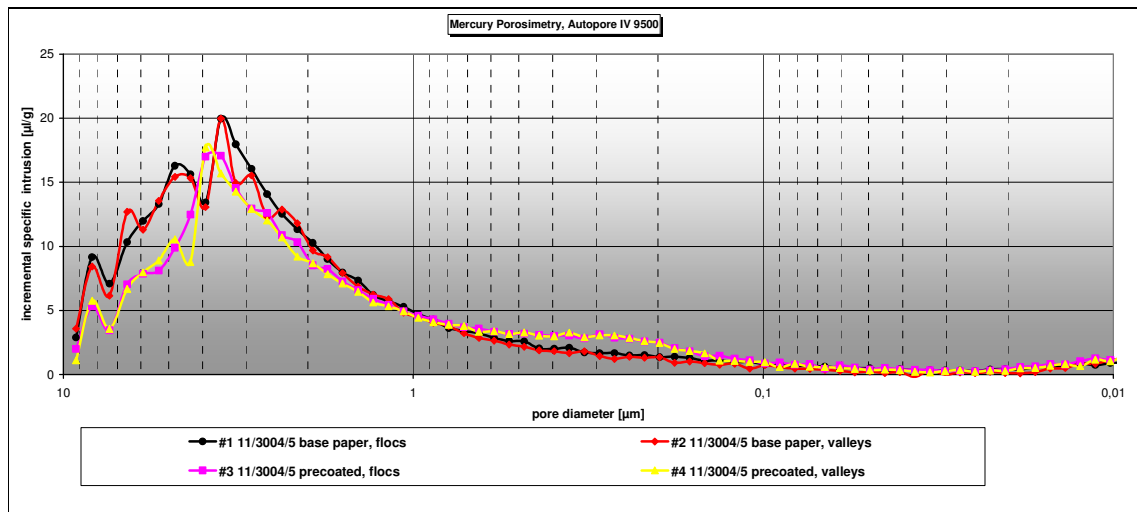
Pict. 3.12.1: Mercury porosity of base paper and precoated paper
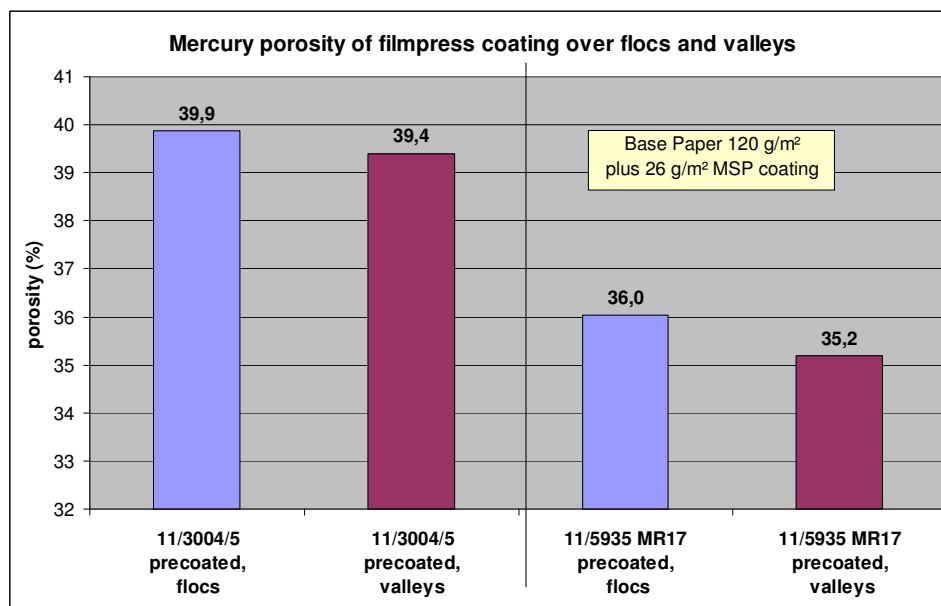
Pict. 3.12.2: Mercury porosity of coating layer on top of flocs and valleys of MSP single coated paper (0,04 – 0,7 µm pores)

Pict. 3.12.2 shows higher porosity of coating layer on top of flocs. At flocs the liquid phase is pressed with pigment / binder fines and soluble binders like starch deeper into the base paper due to higher local external pressure. More fines and soluble substances get lost from coating colour into the base paper. Therefore local coating porosity is lower on top of flocs.

Pict. 3.12.3 shows that curtain coating would be the only successful answer to avoid coating layer local porosity differences. Various pilot trials with curtain coaters prove their advantage in mottling against blade coaters which can be explained by the measurements shown in pict. 3.12.3.

Mercury porosity (%) of coating layer upon flocs/valleys, single precoated paper, 80 g/m² base + 24 g/m² coating (0,04 - 0,7 µm pores)

Flocs Curtain PM11	Valleys Curtain PM11	Flocs MSP PM11/5935	Valleys MSP PM11/5935	Flocs Blade PM11/3871	Valleys Blade PM11/3871
32,3	33,2	31,7	30,9	31,4	29,5
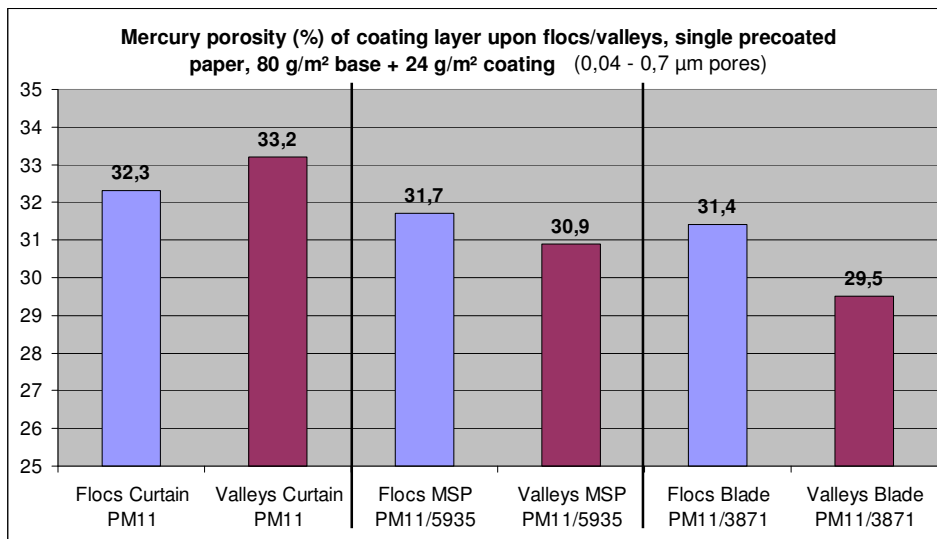
Pict. 3.12.3: Comparison of Mercury porosity of coating layer upon flocs and valleys

Pict. 3.12.3 shows also that coating layer porosity differences were slightly higher for high pressure blade coatings than for film press coatings.
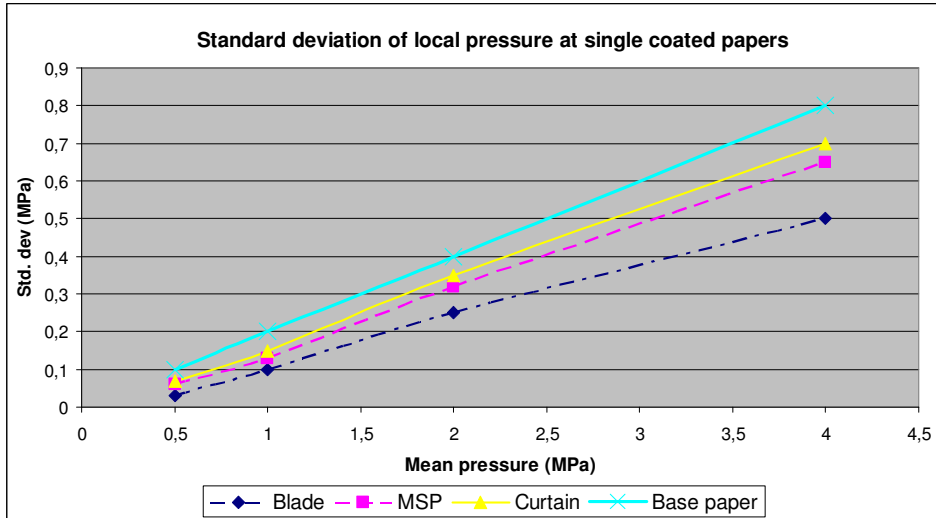
Pict. 3.12.4: Standard deviation of local pressure experiments on single coated papers

The lab press experiments showed that local pressure differences increase with increasing mean pressure level (pict. 3.12.4). Therefore penetration will be more uniform in film press coaters due to much lower pressure level (5 bars) compared to blade coaters (10 – 50 bar).

To evaluate the consequence of the porosity differences in the dry coating layer on flocs and valleys the penetration differences in the following coating station or printing nip can be calculated by Darcy's law which describes the pressure penetration through porous Medias:

Eq. 3-12-1: $\dfrac{dV}{dt} = Q = \dfrac{K * A * \Delta p}{\eta * L}$ [m³/s]

with A the area of penetration, L the penetration depth, η the viscosity of the liquid phase, Δp the pressure loss during penetration and K the Darcy coefficient (m²).

Kozeny defined the Darcy coefficient as a function of the porosity of the porous media:

Eq. 3-12-2: $K_1 = \dfrac{\varepsilon^3}{K * S_0{}^2 * (1-\varepsilon)^2}$ with ε the porosity in %, S_0 the specific surface area in m²/m³ and K a constant of 5.

Inserting the porosity of the coating layer upon flocs and valleys into the Kozeny equation leads to the difference in penetration resistance or Darcy coefficient of the coating layer for following penetration operations:

MSP precoated paper PM11 / 5935

Porosity at flocs	31,7	%
Porosity at valleys	30,9	%
Spec. Surface from BET	23797241	m²/m³
Kozeny coeff. at flocs	2,412E-17	m²
Kozeny coeff. at valleys	2,182E-17	m²
Relative difference	10,5	%

A difference of 1% in the coating layer porosity will lead to 10% difference in penetration depth of applied ink or liquid phase.

The combination of higher local pressure and lower local Darcy coefficient of the coating layer on top of flocs will lead to deeper penetration of the printing ink and higher local ink density at flocs.
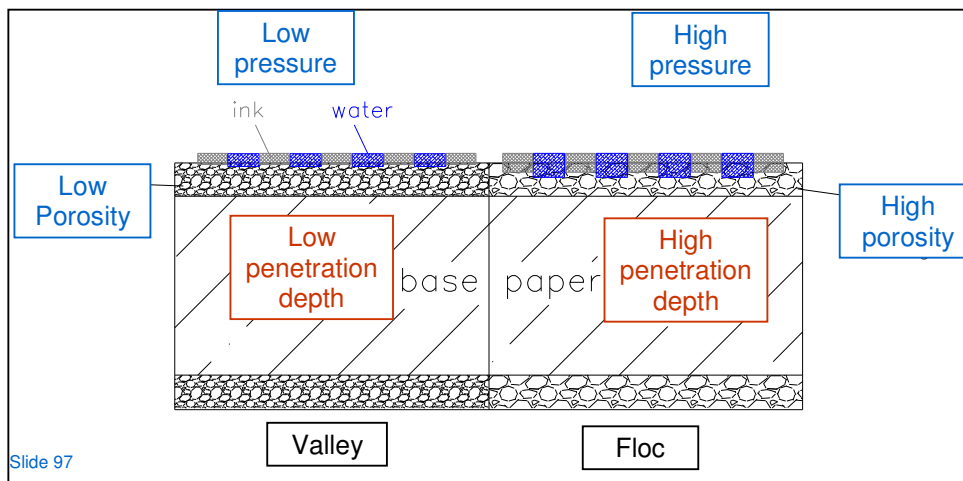
Pict. 3.12.5: Difference of ink absorption in screen areas on porous / dense coating surface (left: valley, right: floc)

3.13 Coating layer analysis of middle and top coating

In the following part the impact of local porosity differences in precoating layer and the local density differences in base paper on following coating layers (middle + top coat) was investigated.

The loss of base paper volume by external blade pressure can be calculated when pore volume of the dry coating is known from Mercury porosity. The calculation is shown in pict. 3.13.1. The only pre-assumption for this calculation is a perfect coating holdout. REM pictures from microtome cuttings of coated PM11 papers showed that this assumption is wrong for the 1st precoat but valid for the 2nd coating layer.
For this calculation paper samples before and after the investigated coating station were needed. Thickness and basis weight had to be measured accurately.
By knowing the coating colour formulation and the density of the dry components the pore volume of the coating layer could be calculated.
This theoretical coating layer thickness was added to the measured base paper thickness and the result can be compared to the measured paper thickness of the coated samples. The difference is the remaining compression of the base paper under the blade after the whole coating and drying process.
As thickness measurements are done at a pressure of 1 bar and blade pressure is much higher, this calculation is reliable.

sappi GK/PQ	TITEL ZIEL	Strichauftragsüberprüfung an der SM 11 (ES-Mitte)		
INT.U-NR.	Sorte-g/m²	MSatin, 115 g/m²		
	Erz. / MR	11/3871/5		
PM11 - 35/2007		**Pope PM = Base**	**Coater 3 - 4**	**Coater 3 - 6**
Basis weight	g/m²	66,2	90,1	112,6
Thickess	mm	0,082	0,088	0,096
Volume	cm³/g	1,24	0,98	0,85
					= Input
Coat weight (basis weight difference)	g/m²		14,0	10,4
Sum of coat weight	g/m²		23,9	46,4
Area of investigation	m²		1	1	1
Coat weight	g/m²		23,9	46,4	22,5
Density of binder	g/cm³		1,2	1,2	1,2
Density of pigment	g/cm³		2,6984	2,6984	2,6984
Binder content in coating colour	%		12	10	10	Pigment = 100%
Binder content	%		13,44	11	11	Pigment + Binder = 100%
Pigment content	%		86,56	89	89	Pigment + Binder = 100%
Volume of dry coating without air	cm³/g		0,433	0,421	0,421	Base paper: 1,257 cm³/g
Density of dry coating without air	g/cm³		2,311	2,373	2,373
Porosity of coating layer	cm³/g coating		0,115	0,15	0,18	From Mercury porosimetrie
Volume of dry coating with air	cm³/g		0,548	0,571	0,601	Base paper: 1,257 cm³/g
Density of dry coating with air	g/cm³		1,826	1,750	1,663
Binder	g/m²		3,21	5,10	2,48
Pigment	g/m²		20,69	41,30	20,03
Spec. Volume of binder	cm³/m²		2,677	4,253	2,063
Spec. Volume of pigment	cm³/m²		7,667	15,304	7,421
Spec. Volume of air	cm³/m²		2,749	6,960	4,050
Spec. Volume of coating	cm³/m²		13,092	26,517	13,534
Thickness of coating layer	µm		13,092	26,517	13,534	At 100% coating holdout
Base paper basis weight	g/m²		66,2	66,2	90,1
Base paper thickness	mm		0,082	0,082	0,088
Base paper + coating basis weight	g/m²		90,1	112,6	112,6	Base + coat weight
Base paper + coating thickness (calc.)	mm		**0,095**	**0,109**	**0,102**	Base + coating thickness
Spec. Volume of coated paper (theor.)	cm³/g		1,055	0,964	0,902
Measured compression of base paper under blade = (Thickness of precoated paper + calc. Coating thickness) -measured thickness of coated paper	µm		**7,092**	**12,517**	**5,534**	= Compression
Compression of base paper under blade	%		8,06	13,04	6,75	refering to base paper thickness
Remaining compression of base paper per bar	µm/bar		0,77	0,77	0,77	from Zwick (only load, no relief)
Blade pressure	bar		20,00	20,00	20,00
Compression of base paper under blade (theor.)	µm		15,40	15,40	15,40
Compression of base paper per bar	µm/bar		0,26	0,26	0,26	from Zwick (only load, no relief)
Blade pressure	bar		20,00	20,00	20,00
Calculated compression of base paper under blade (from	µm		5,29	5,29	**5,29**
			C3 - 4	C3 - 6	C5 - 6

Pict. 3.13.1: Calculation of base paper compression under blade
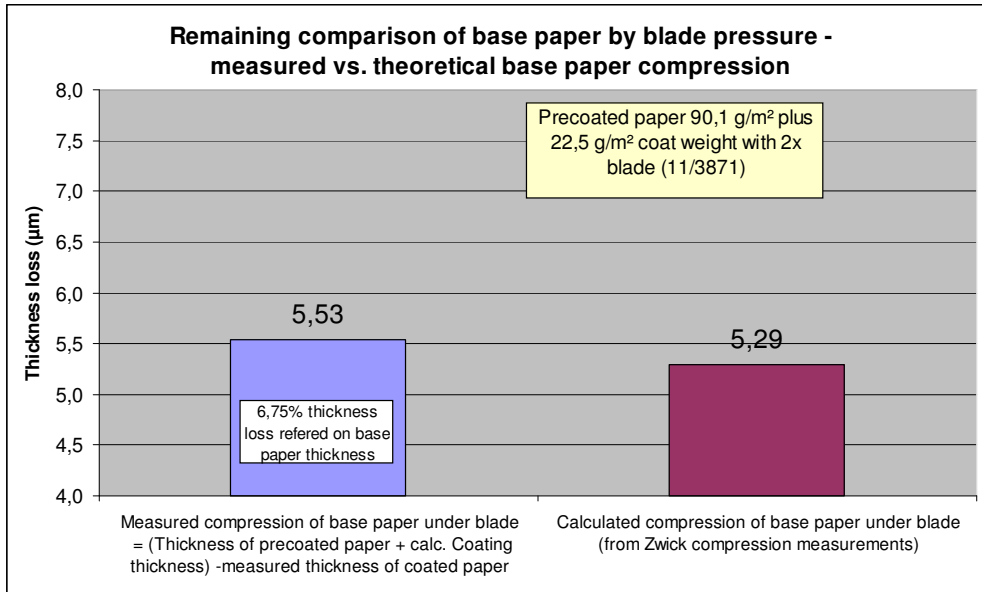
Pict. 3.13.2: Calculation of base paper compression under blade

The calculated base paper compression under the blade of as shown in pict. 3.13.2 can be compared with the measured base paper compression at the Zwick instrument at blade load (25 bar). Both gave similar results of **7% plastic base paper compression under the blade** (refered on base paper) which remains after blade coating. The same result was found in chapter 4.2.

These measurements are mean values for flocs and voids. As local pressure is higher at flocs, elastic and plastic compression will be also higher. **Therefore paper should get more even in thickness by the external pressure of a blade.**

Comparing the floc analysis by using the special die cutter for MSP and blade precoated papers with the corresponding base papers led to the totally opposite result. This is shown in the next chapter 3.14.

3.14 Change of base paper structure by coating

Floc analysis of base paper and MSP precoated paper, PM11/5080/MR2

Coating on flocs: 21,7 g/m²
Coating on valleys: 21,7 g/m²
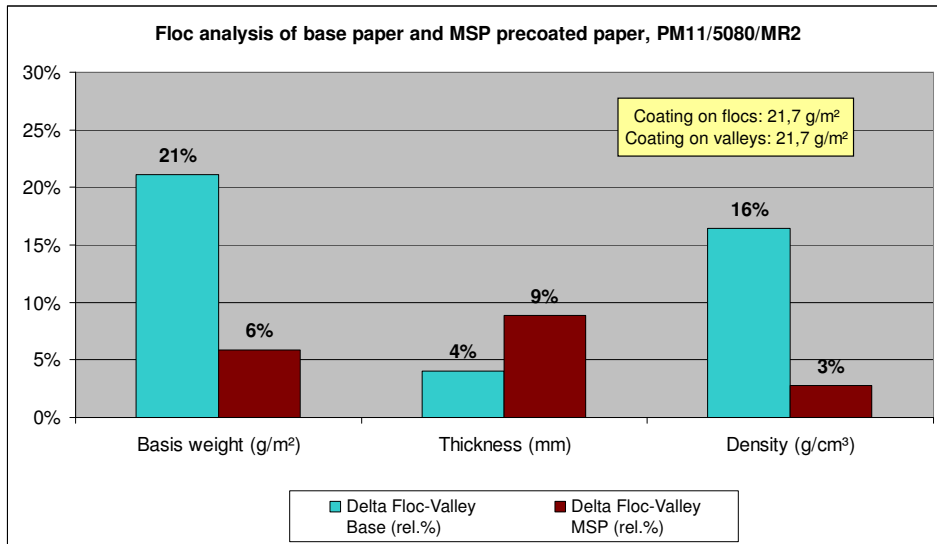
Pict. 3.14.1: Comparison of relative differences between 60 g/m² base and corresponding MSP precoated paper

Floc analysis of base paper and blade precoated paper, PM11/3871/MR5 (115 g/m²)

Coating on flocs: 20,2 g/m²
Coating on valleys: 21,3 g/m²
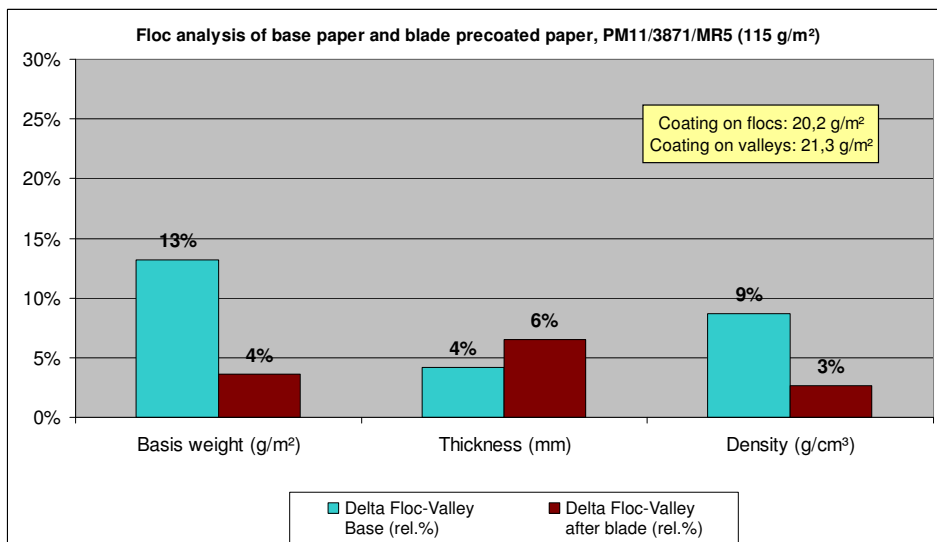
Pict. 3.14.2: Comparison of relative differences between 60 g/m² base and corresponding blade precoated paper

The calculated coat weight on top of flocs and voids is shown in pict. 3.14.1 for a filmpress precoated paper and in pict. 3.14.2 for a blade precoated paper. For both precoated papers the thickness differences between flocs and voids increased with the application of the coating and density differences decreased.

Page 101

The precoated paper looks more uneven than the base paper although flocs are more severely compressed under the blade. This indicates an **expansion of the flocs** after the pressure impulse of coating application caused **by wetting** during pressure application or by capillary forces after coating.

It is well described in literature (L1.69) that base papers expand after external pressure when they are wetted. As local pressure is higher, more liquid phase will be pressed into flocs and expansion will be more pronounced there than at valleys.

Compressibility experiments of these paper samples were made with the Zwick thickness instrument to verify these results (pict. 3.14.3 − 3.14.6).
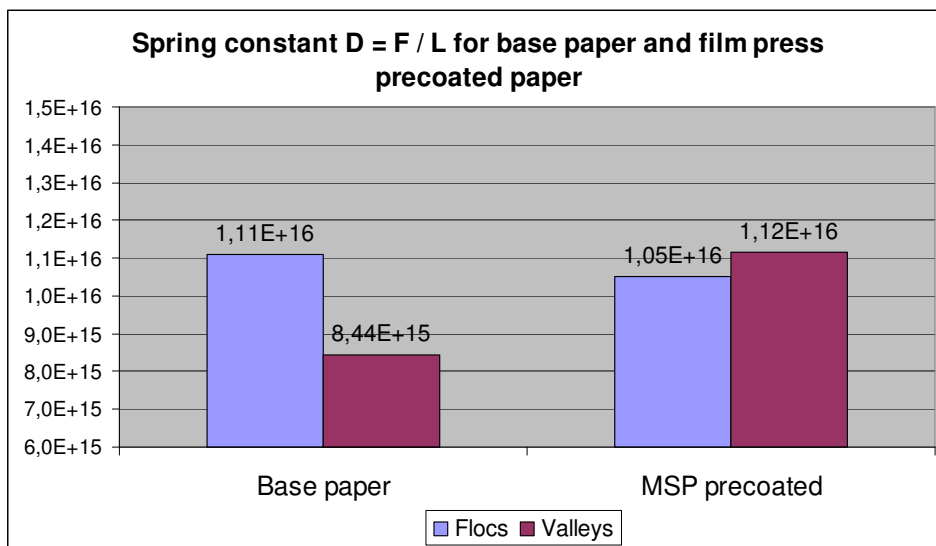
Pict. 3.14.3: Flocs expansion by film press precoating
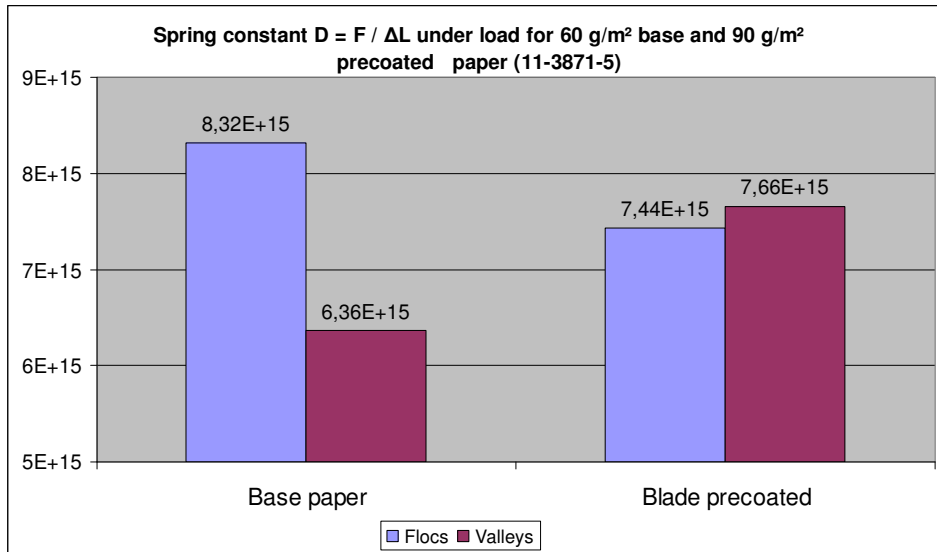
Pict. 3.14.4: Expansion of flocs by wetting under / after single blade coating

Both MSP and blade precoaters removed the compressibility difference between flocs and valleys.

Conclusion: Mean thickness of base papers gets lower by blade and MSP coaters due to external pressure but density differences between flocs and valleys decrease due to wetting. Surface of the sheet gets more uneven but uniformity of compressibility improves.

Consequence for the following coating layers:

As the density differences between flocs and valleys decrease with 1st precoat, the local pressure distribution should get more uniform for the following coating layers although the thickness differences will be responsible for a certain in-plane standard deviation in local pressure under the blade of the next coating station. This can be easily verified by using the lab press experiment with pressure sensitive film:
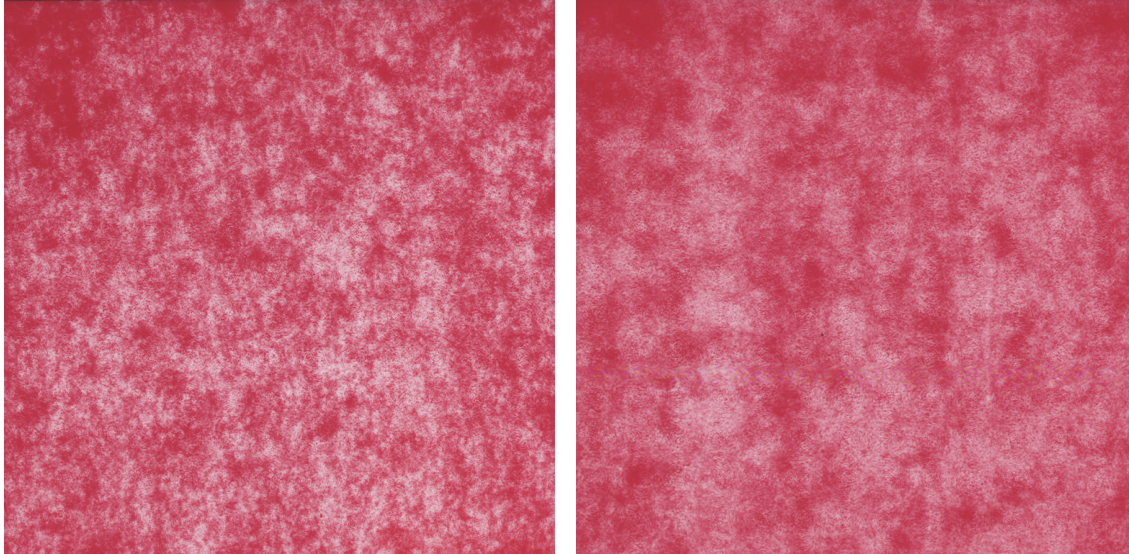
Pict. 3.14.5: Local pressure with pressure sensitive film at base paper (left) corresponding double blade coated paper (right), 115 g/m²
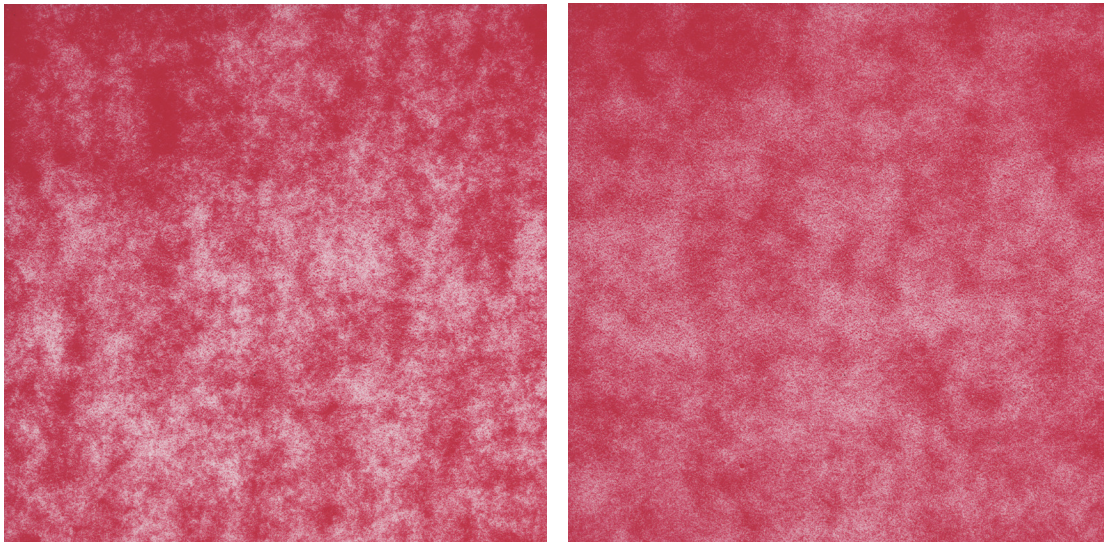
Pict. 3.14.6: Local pressure with pressure sensitive film at MSP precoated paper (left) and triple coated paper (right), 200 g/m²

Std. Dev. of local pressure (bar) in lab press experiment with pressure sensitve film
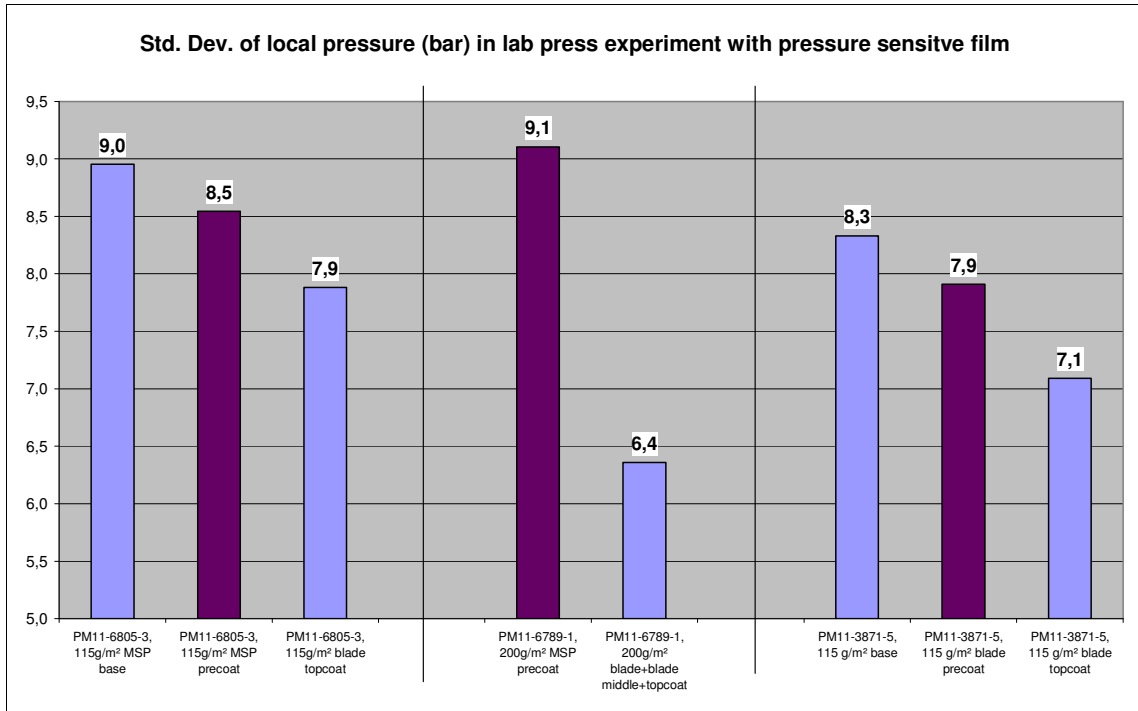
Pict. 3.14.7: Std. dev. of local pressure for base, precoated and top coated paper

Match factor of local pressure at pressure sensitve film and Ambertec formation
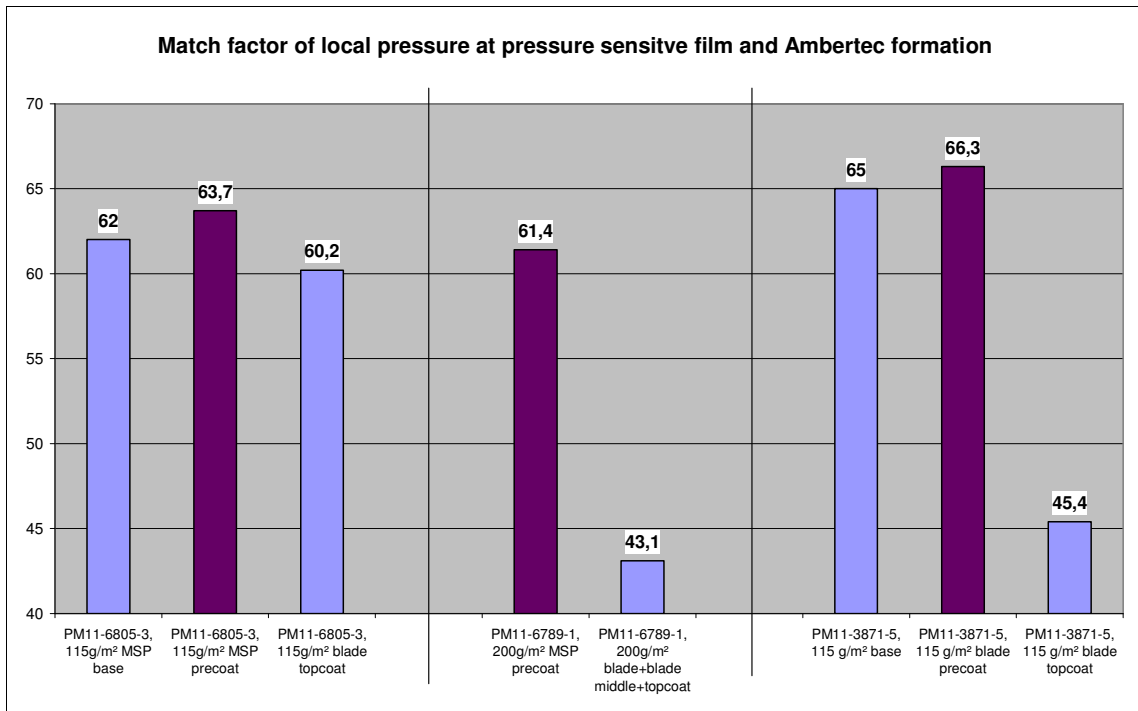
Pict. 3.14.8: Match factor of formation with transmission scan and local pressure

Pict. 3.14.7 and 3.14.8 show that the comparison of match factors and standard deviations of precoated and top coated samples proved this theory. The standard

deviation gets lower with every coating layer and matching the local pressure with formation (which is dominated in coated papers by the base paper) gives worse results for double or triple coated papers than for single precoated papers. Comparing the thickness of the coating layer upon flocs and voids at triple coated papers, no difference can be found. The small differences after the 1st precoat are totally levelled out by the 2nd and 3rd blade coating.

These findings explain the finding that formation induced screen mottle diminishes with the number of coating layers applied: The lower the density differences in base paper and the higher water and fines retention in coating layers, the more uniform the coating layer porosity of middle and top coat will be.

The pattern of formation diminishes in print mottle with every coating layer.
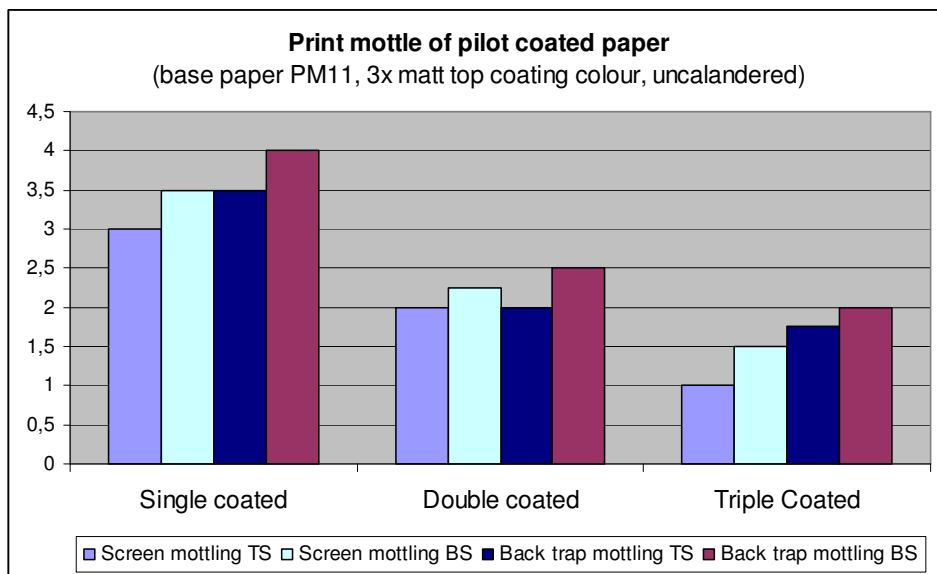
Pict. 3.14.9: Mottling of single, double and triple coated paper (pilot trial with same coating colour in all coating applications)

Chapter 4: Solution 1 for formation mottle: Improve base paper structure

4.1 Improving formation of PM11

A small step to improve the formation of base paper PM11 was made by lowering the permeability of the wires. Dewatering was delayed thereby and consistency of fibre mat between the wires dropped before the D-bar section. The current SSB wire design was taken from rotogravure SC paper machines where ultrafine wires must be used to retain the high amount of filler (up to 36%) at low basis weight of the fibre lat.
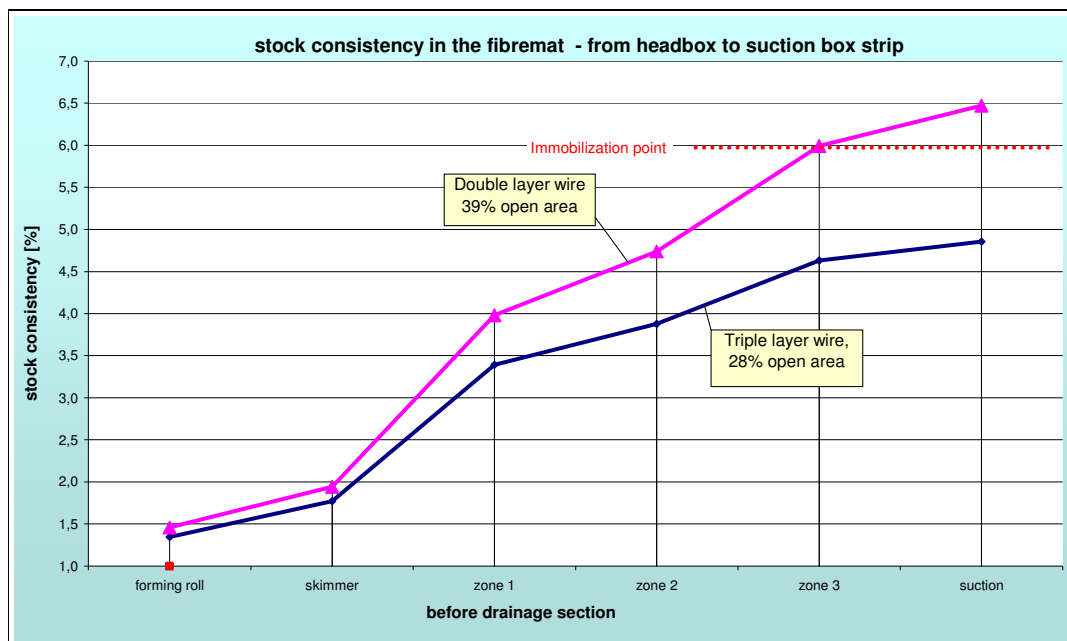
Pict. 4.1: Lowering the consistency in the fibre mat between the wires in the D-part by new top and bottom wire design with less open area

A second step in formation improvement was made when the retention system was changed from two component system using cationic polyacrylaminde (CPAM) and bentonite to a three component system which used additionally an anionic organic micro particle to reduce the amount of CPAM.
CPAM's create bridge flocculation in fibre networks as they have a relatively high molecular weight and their cationic chain ends react with the anionic fibre surface.

4.2 Reduction of compressibility differences in base paper

G. Engström, V. Morin and Song Lin Bi (L1.29) analysed the porosity distribution in coating layers by using the burnout test followed by image analysis. The higher the coating layer porosity, the lower the print density. They showed that when pre-calendering is used for base papers which are coated in a filmpress coater, mottle got worse. They explained their finding with increased compressibility differences between flocs and voids when a base paper is pre-calendered.

J. Skowronski and P. Lepoutre (L1.69) studied the influence of base paper roughness and pre-calendering on coating holdout using a lab puddle type coater. Pre-calendering had surprisingly no major impact on coating hold out.
Wetting of base paper surface resulted in an increase of paper roughness mainly for wood containing grades (pict. 4.2.1).
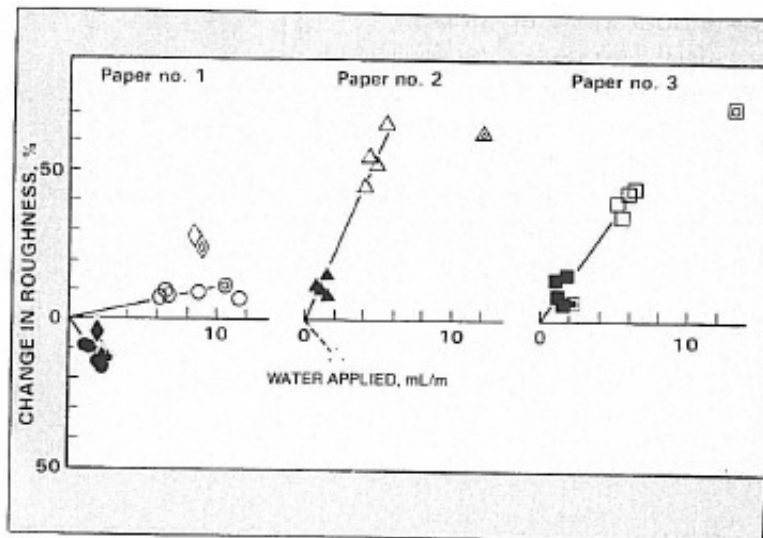
Pict. 4.2.1: Change in paper roughness (PPS) by water treatment (paper No. 1 = woodfree, paper No. 2+3: wood containing base papers)

When elastic and plastic deformation in Z-direction has to be measured, thickness loss under external pressure can be used for calculating base paper compressibility. The external pressure can be applied by a lab calender.
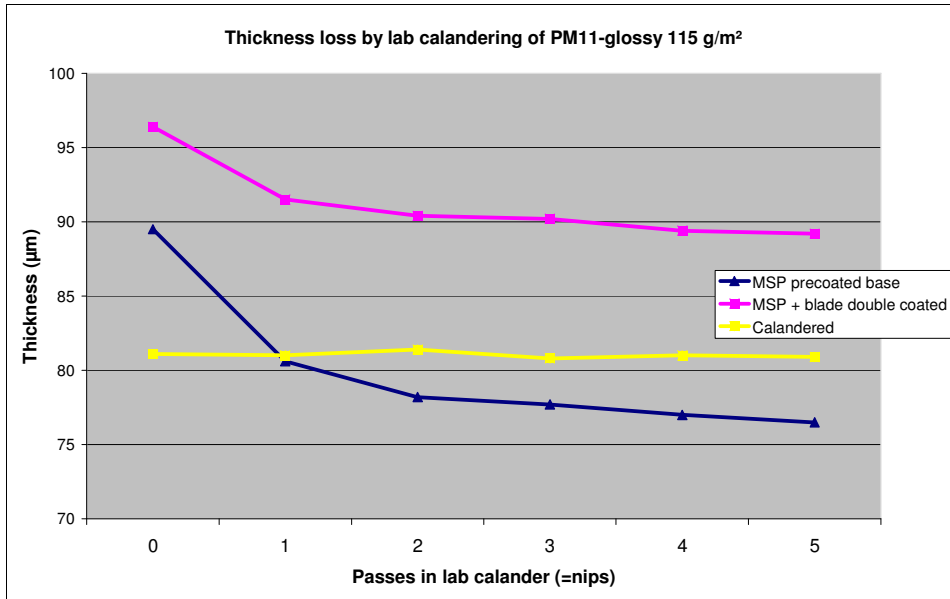
Pict. 4.2.2: Lab calendering of mill coated papers

Pict. 4.2.2 shows that triple coated papers (MSP precoat + double blade middle and top coat) are less compressible than single coated papers (MSP precoated).
The conclusion can be drawn that due to the rigid structure of coatings stiffness is added in Z-direction with every coating layer, depending on the binders in use and the coat weight. Stiff latices and brittle starch add more stiffness than soft latices.
Pict. 4.2.2 shows also that calendered papers are almost incompressible due to the collages of the fibre network during the calendering process.
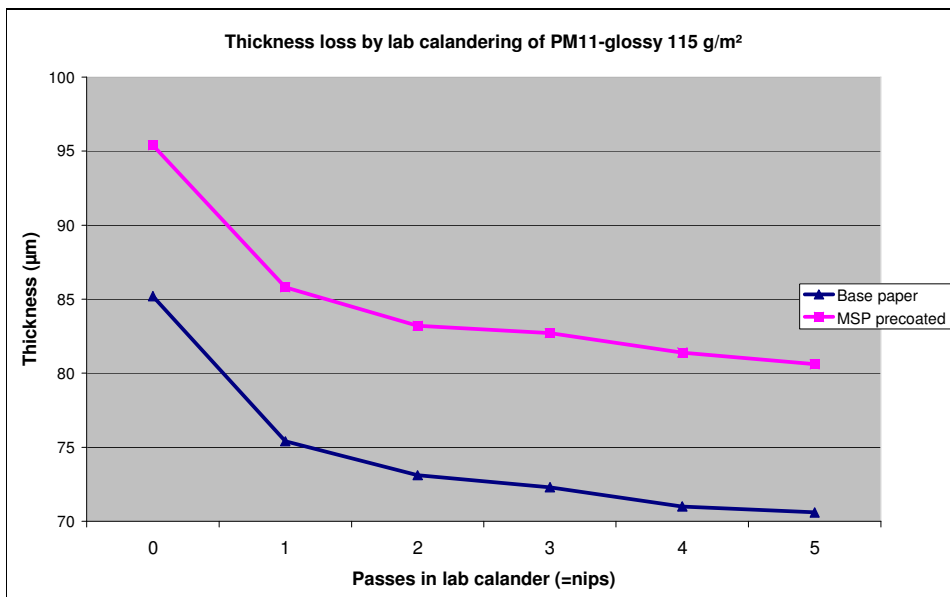
Pict. 4.2.3: Lab calendering of mill base paper and film press coated paper

Page 109

Pict. 4.2.3 shows that the compressibility doesn't change by film press coating. This stays in contradiction to the fact that blade precoated papers are less compressible than their corresponding base paper.

Filmpress coaters compress the sheet in the application nip and expand it by filmsplit forces at the nip exit. Therefore compressibility doesn't change by MSP coating.

Another method to show the expansion of the base paper after MSP or blade coating is thickness measurement with standard L&W instrument. At a single spot 30 consecutive measurements were made at a PM11 base paper and the corresponding film press precoated paper. The local pressure is 1 bar at this instrument.

The higher the compressibility, the higher the thickness loss at these sequential measurements will be.
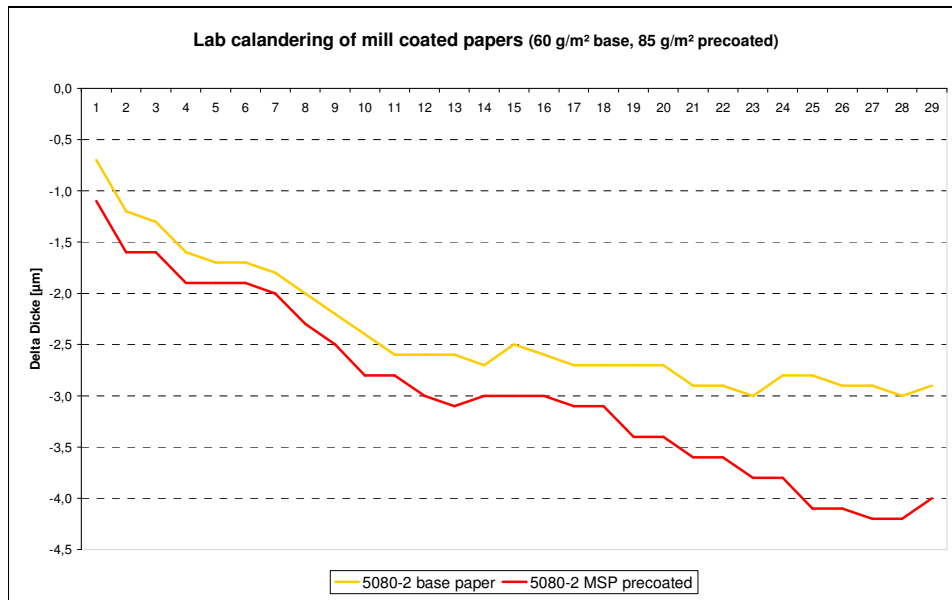
Pict. 4.2.4: Compressibility of base paper PM11 vs. MSP precoated paper

Lab calandering of mill coated papers (60 g/m² base, 85 g/m² precoated, 115 g/m² double coated)

Legend: 6879-1 MSP precoated — 6879-1 MSP+blade — 6879-1 calandered
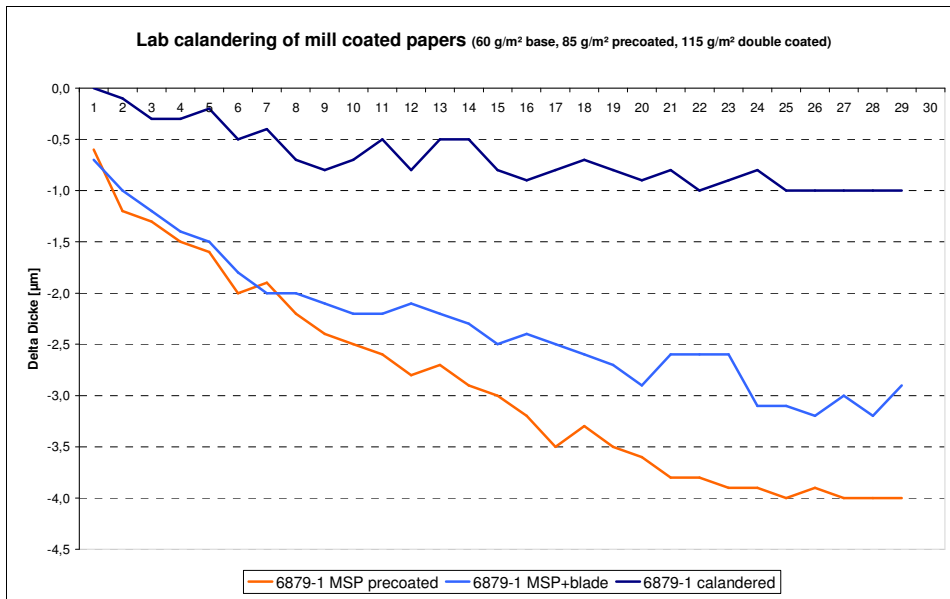
Pict. 4.2.5: Compressibility of precoated paper PM11 vs. double coated and calendered paper (X-axis: number of passes in calender, Y-axis: Loss in thickness)

Pict. 4.2.4 shows that paper gets more elastic in Z-direction by filmpress coating as more thickness is lost by external compression for the precoated paper than for the corresponding base paper. The compression of the fibre network in press and drying section is partially removed by the filmpress coating and spring constant of base paper decreases – paper gets more elastic.

Pict. 4.2.5 shows that in the following blade coating stations compressibility is again reduced by normal pressure under the blade – paper gets more plastic.

The biggest loss in compressibility is achieved by calendering of the coated paper as pressure is much higher than in coating stations.

The release of internal tension by wet compression in press and drying section can be shown also by wetting of base papers with water.
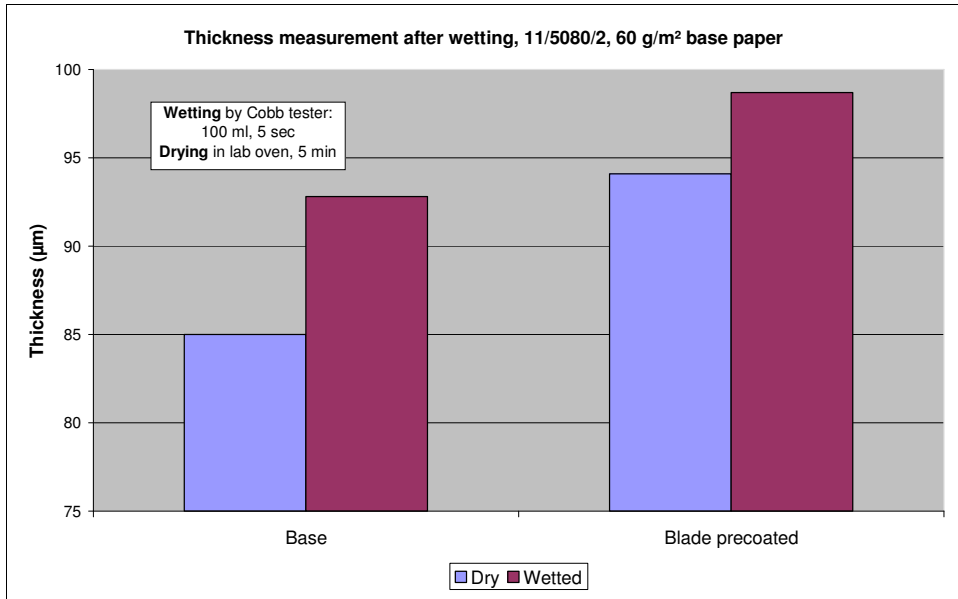
Pict. 4.2.6: Increase in thickness by wetting of base paper and blade precoated paper
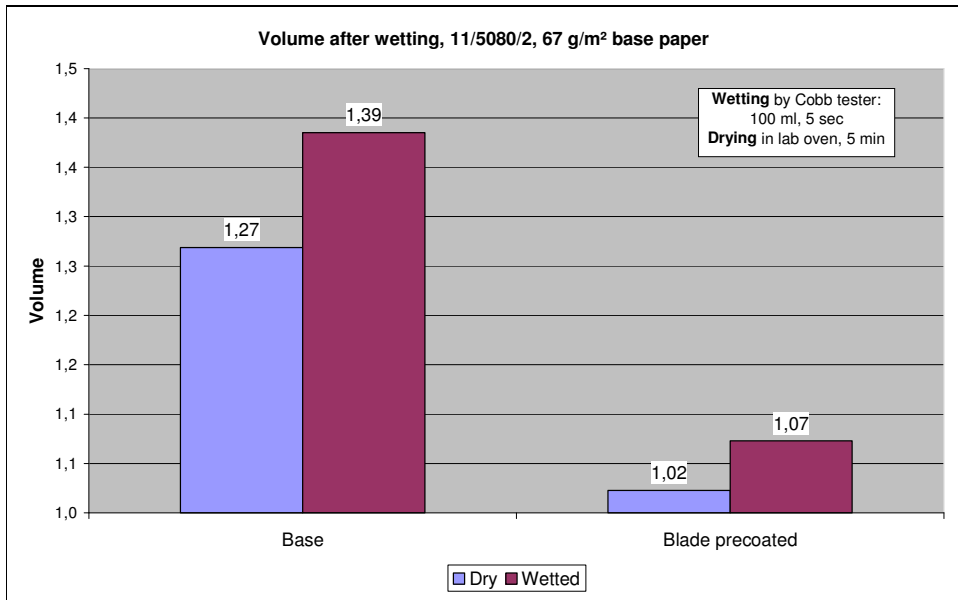
Pict. 4.2.7: Increase in volume by wetting of base paper and blade precoated paper

Thickness measurement after wetting, 135 g/m² finished paper

Wetting by Cobb tester: 100 ml, 5 sec
Drying in lab oven, 3 min
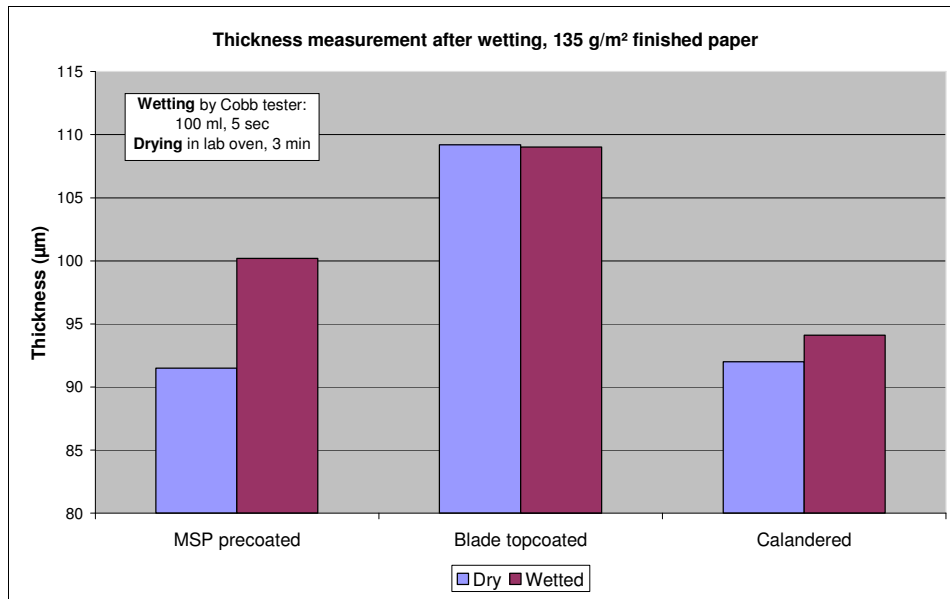
Pict. 4.2.8: Increase in thickness by wetting of precoated, topcoated and calendered paper

Pict. 4.2.6 and 4.2.7 show that base papers and precoated papers showed a huge increase in thickness by wetting. Part of the fibre network collapse in press and drying section is removed.

A base paper volume of 1,4 is reached after short time wetting in the Cobb tester which corresponds to a lab sheet produced with pressure-less drying.

This was found also by G. Engström (L3.3) who showed that supercalendered base papers regain their volume when wetted at blade coaters.

When formation induced mottling has to be improved, the local differences in compressibility eg. at flocs and voids have to be reduced to a minimum.

In the 1st lab work the compressibility of different fibre types was compared by forming Rapid Köthen hand sheets and lab calendering.
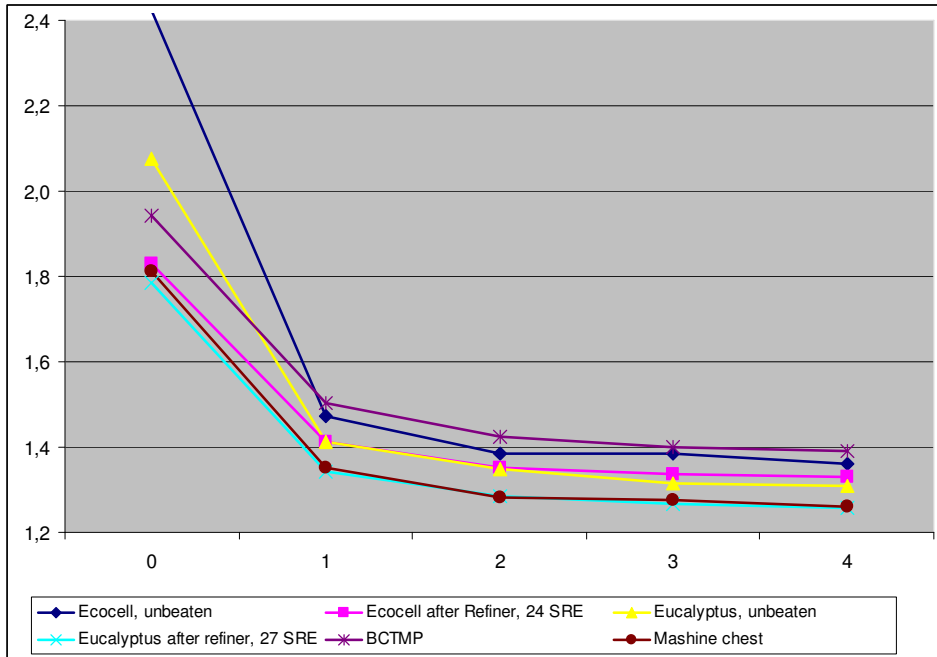
Pict. 4.2.9: Lab calendering of lab sheets (X-axis: passes in lab calender, Y-axis: thickness)
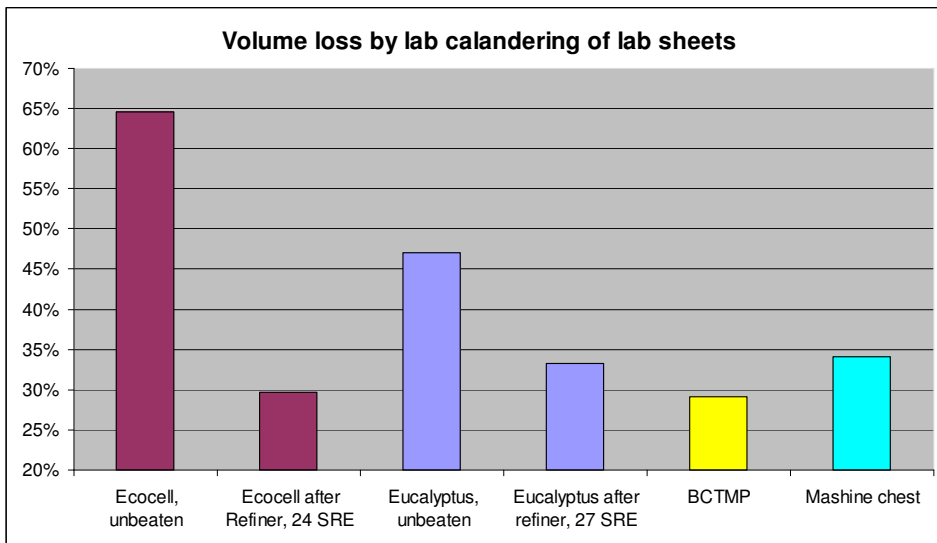
Pict. 4.2.10: Lab calendering of lab sheets, relative volume loss after 1st nip (elastic deformation)

Pict. 4.2.9 and 4.2.10 show that paper compressibility dropped with refining of pulps especially for long fibre sulfite pulp "Ecocell" as number of binding points increase and structure of fibre mat gets more rigid. CTMP fibres were less compressible than eucalyptus fibres due to the higher stiffness of the fibre walls.

A second method to compare the compressibility of different fibres is the Zwick instrument with compression unit.
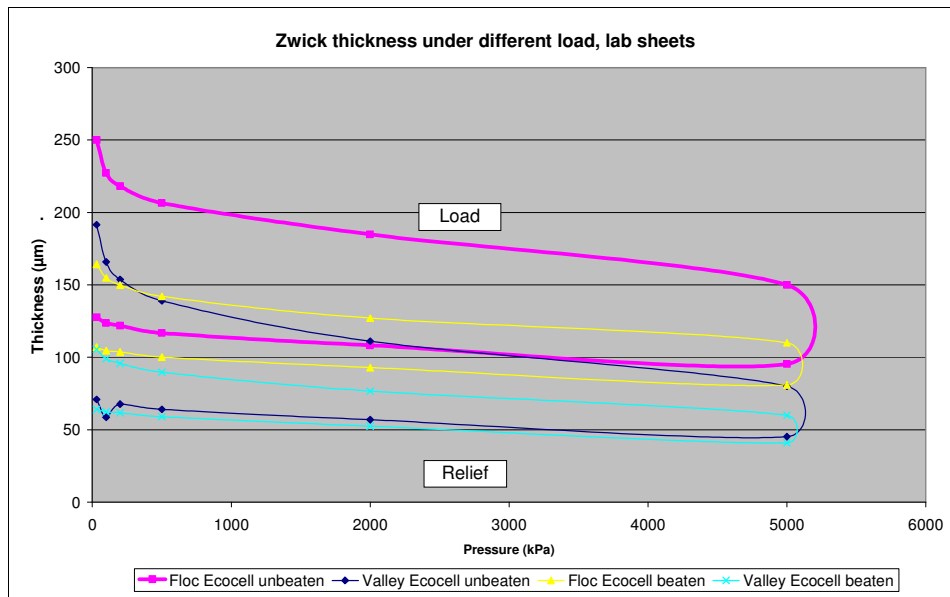
Pict. 4.2.11: Zwick compression test of Ecocell lab sheets (upper part of curve: compression, lower part: relief)
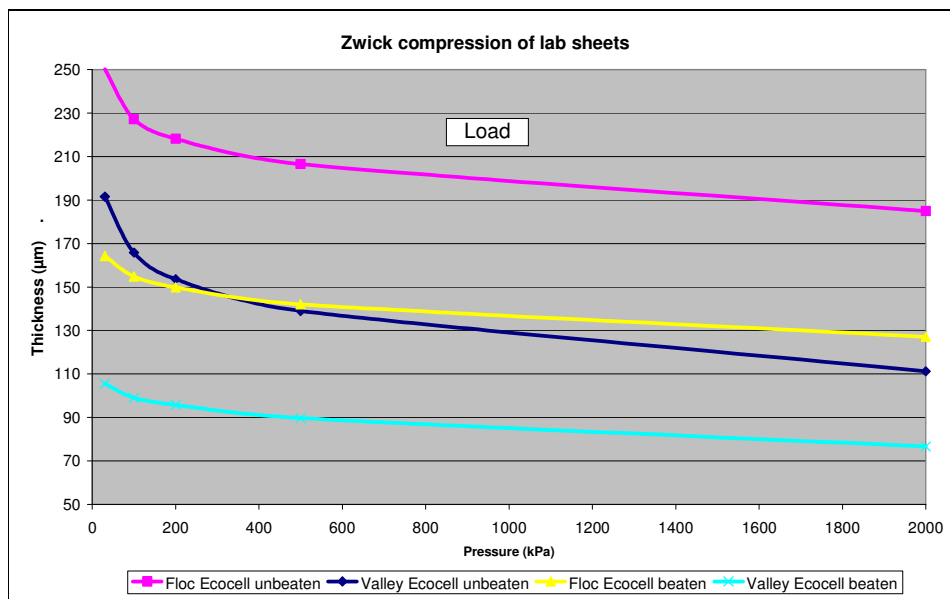
Pict. 4.2.12: Zwick compression test of Ecocell lab sheets, load phase

From pict. 4.2.11 and 4.2.12 the spring constant D was calculated. It is shown in pict. 4.2.13 and 4.2.14. The spring constant D (N/m) from $F = -D * \Delta L$ describes the elasticity against compression. The lower the spring constant D, the more

compressible the paper is; a defined load F leads to a higher compression length ΔL in the spring.

The pressure of 200 kPa in the Zwick instrument corresponds to a MSP pressure of 2 bars and a Zwick pressure of 2000 kPa to a blade pressure of 20 bars.

Relative spring constant D (N/m) at 200 kPa external pressure for lab sheets
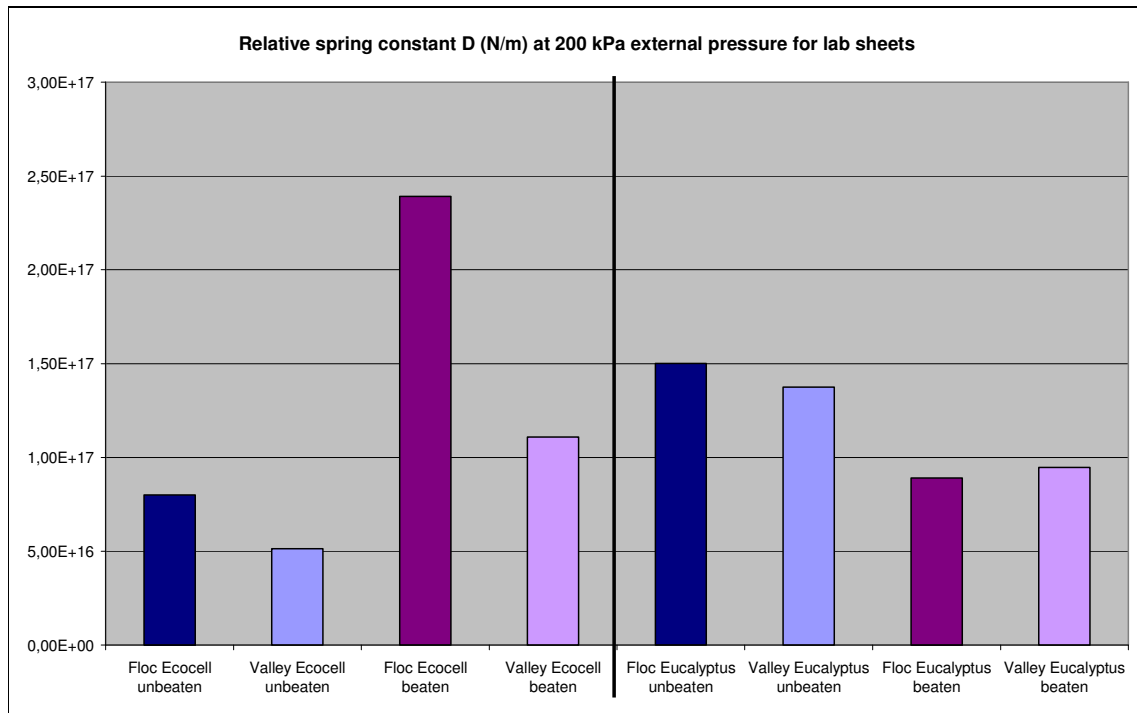
Pict. 4.2.13: Spring constant of unbeaten and beaten (24 SRE) Ecocell long fibre sulfite, compared with unbeaten and beaten (27 SRE) Eucalyptus short fibre sulfate lab sheets (at an external pressure level of a filmpress coater)
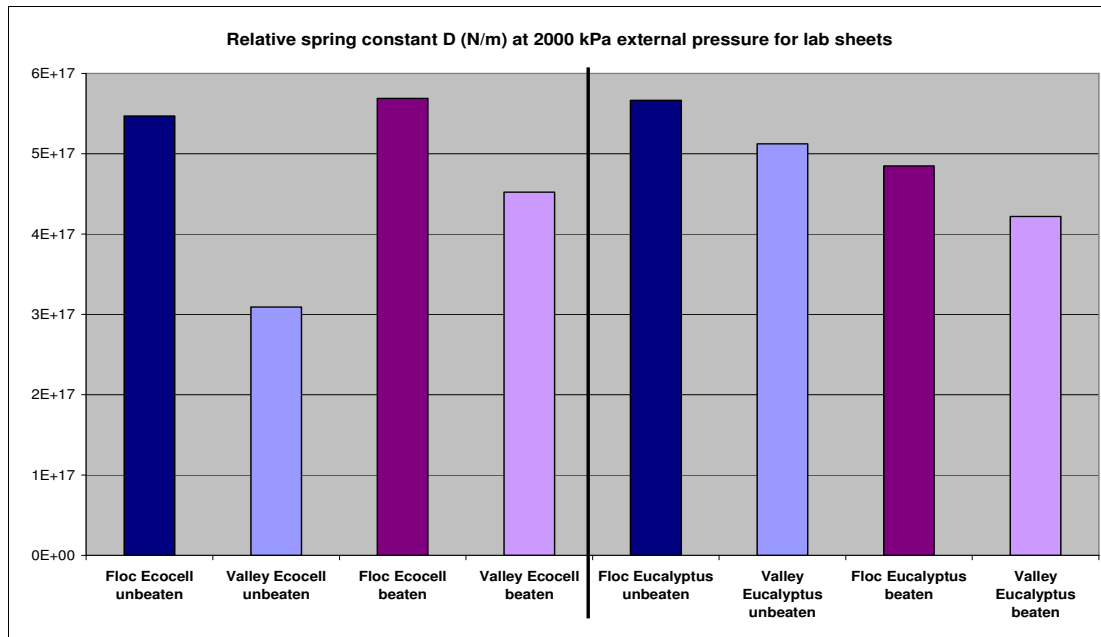
Pict. 4.2.14: Spring constant of Ecocell long fibre sulfite and Eucalyptus short fibre sulfate lab sheets (blade pressure)

Lab sheets with different furnishes were wet pressed in a lab press under mill conditions before drying. Therefore the differences in spring constant between flocs and voids were similar to mill base papers: **Flocs were less compressible** and showed in all investigations a higher spring constant than voids, especially at the higher pressure of blade coaters.

Looking at an average of Zwick results with 2 and with 20 bars the following conclusions can be drawn:

- A huge difference in fibre network structure was found between long fibre sulfite Ecocell and short fibre eucalyptus sulphate pulp
- The compressibility stays constant with increased refining for the stiff eucalyptus fibres while for Ecocell it is reduced by beating. The removal of fibrils from the fibre wall reduces fibre wall thickness and increases therefore fibre flexiblility. Fibre bonding area increases and denser fibre packing is promoted by increased fibre flexibility and generation of fines by refining.
- **The differences in compressibility between flocs and voids increases with raising beating energy for Ecocell sulfite pulp** but stays constant for eucalyptus. Therefore beating creates more formation mottling for Ecocell based papers than for Eucalyptus based papers.

Page 117

Summing up **formation induced mottling can be improved by**:

- Less beating of w'fr long fibres

- Replace w'c. CTMP fibres by w'fr short fibres

- Short fibre pulp instead of long fibre w'fr pulp

The next figures show comparisons of flocs and voids from different base papers within sappi fine paper Europe. The Zwick compression tester was used to measure the compressibility of voids and flocs cut out from these base papers.

The external pressure was increased from a minimum pressure of 30 kPa to a certain max pressure and reduced afterwards again to 30 kPa.

The applied max pressure level was 500, 2000, 5000 and 26.000 kPa.

The remaining thickness difference after press impulse and relief describes the plastic deformation of the paper sample as a function of max pressure.
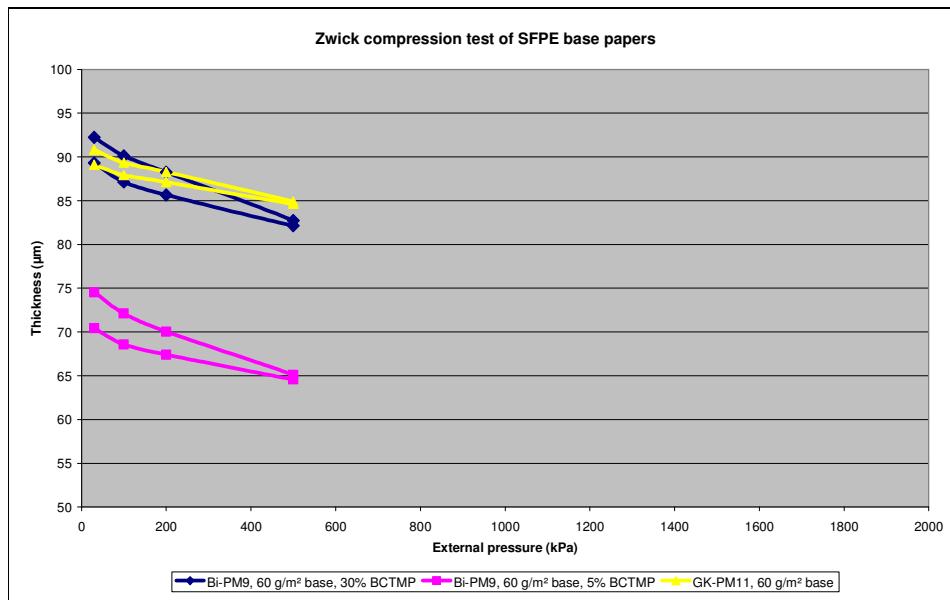
Pict. 4.2.15: Compression of base papers from PM11-GK and PM9-Biberist at 500 kPa max pressure
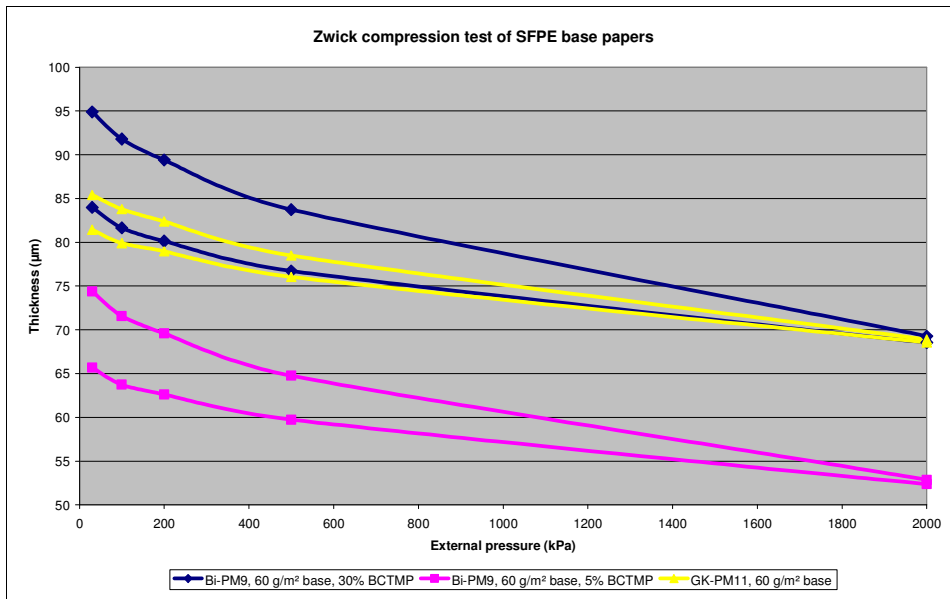
Pict. 4.2.16: Compression of base papers from PM11-GK and PM9-Biberist at 2.000 kPa max pressure
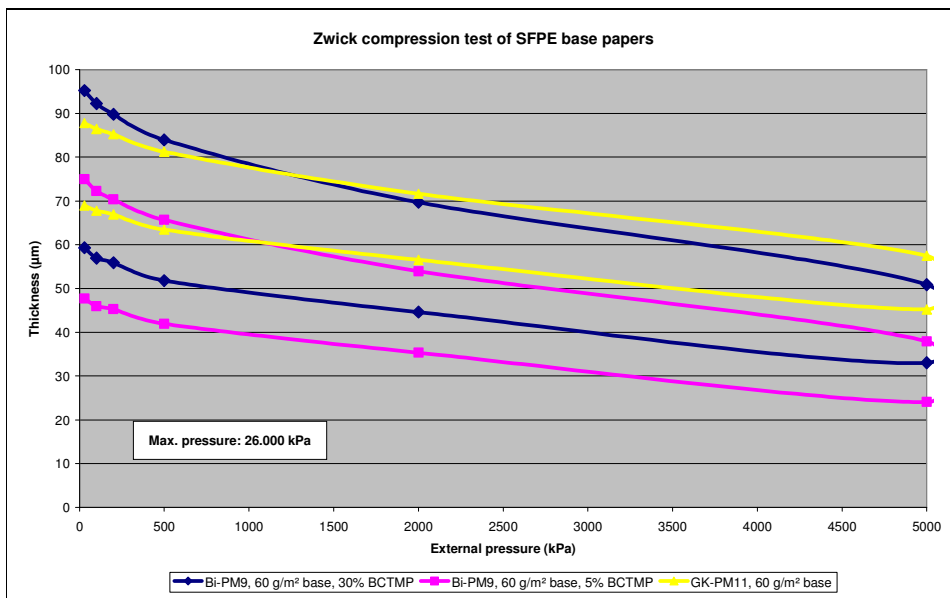
Pict. 4.2.17: Compression of base papers from PM11-GK and PM9-Biberist at 26.000 kPa max pressure
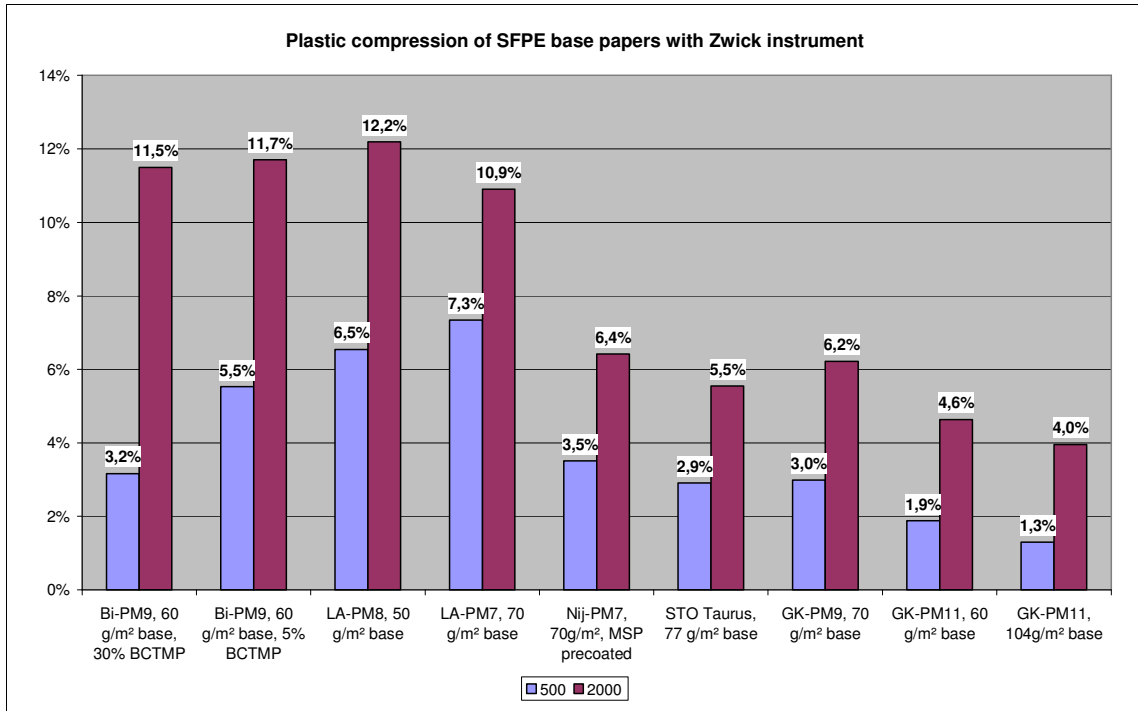
Pict. 4.2.18: Plastic compression of SFPE base papers at 500 and 2000 kPa max pressure
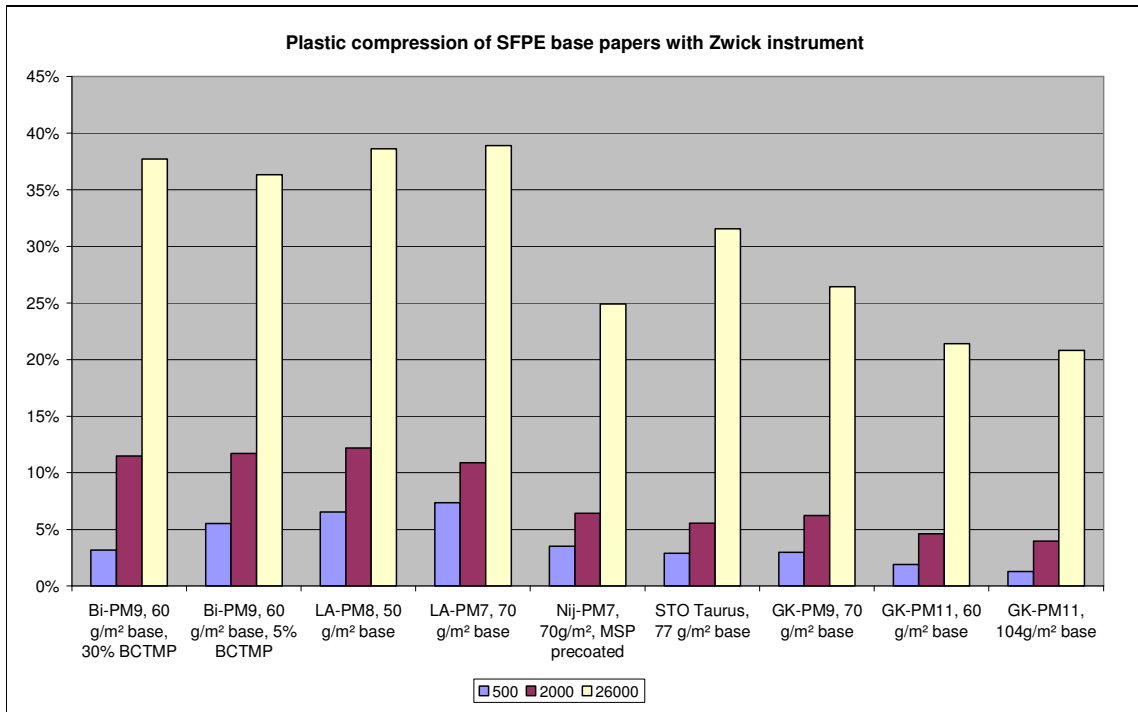
Pict. 4.2.19: Plastic compression of SFPE base papers at 500, 2000 and 26.000 kPa max pressure

Plastic deformation by compression of tested base papers starts at relative low pressure of 100 – 500 kPa. Compare: The application pressure in a film press coater is appr. 5 bar = 500 kPa and in a blade coater 25 bar = 2500 kPa.

Therefore a plastic deformation in Z-direction is taking place in every film press and every blade coater, as shown in earlier thickness measurements of MSP and blade coated papers compared with the theoretical thickness without external pressure from coaters. In film press coaters this deformation in the application nip is removed by film split forces at the nip exit.
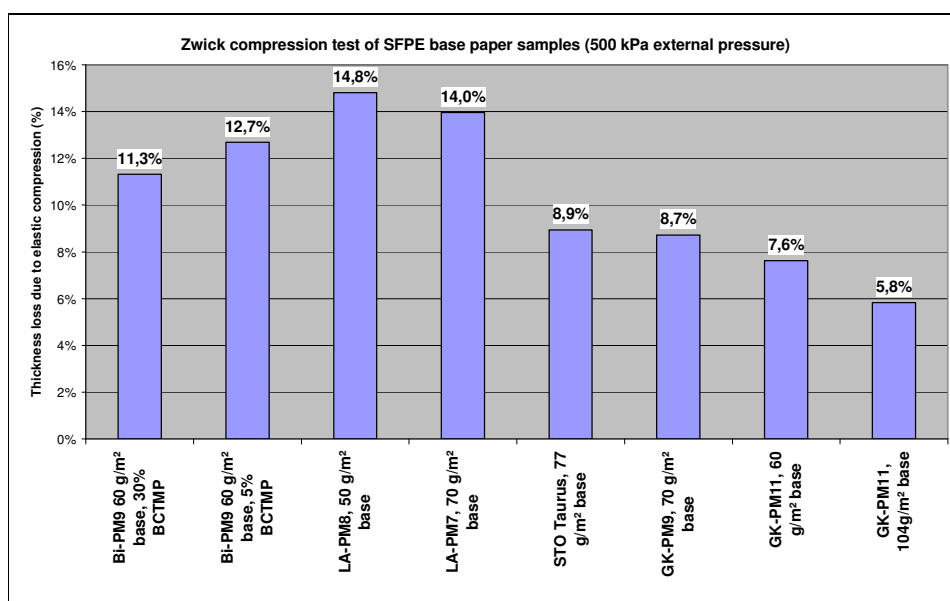
Pict. 4.2.20: Compression of different SFPE base papers at 500 kPa

Pict. 4.2.15 – 4.2.20 show that in accordance with the results of compression tests of different fibre types, the Biberist base paper with higher BCTMP content had a lower compressibility than the corresponding base paper of the same paper machine with low BCTMP content.

Base papers of PM11-Gratkorn were much lower in compressibility than the other w'fr base papers from PM9-Gratkorn, PM2-Stockstadt and PM9-Biberist due to much higher compression in press section, mainly by shoe press in the 3rd nip.
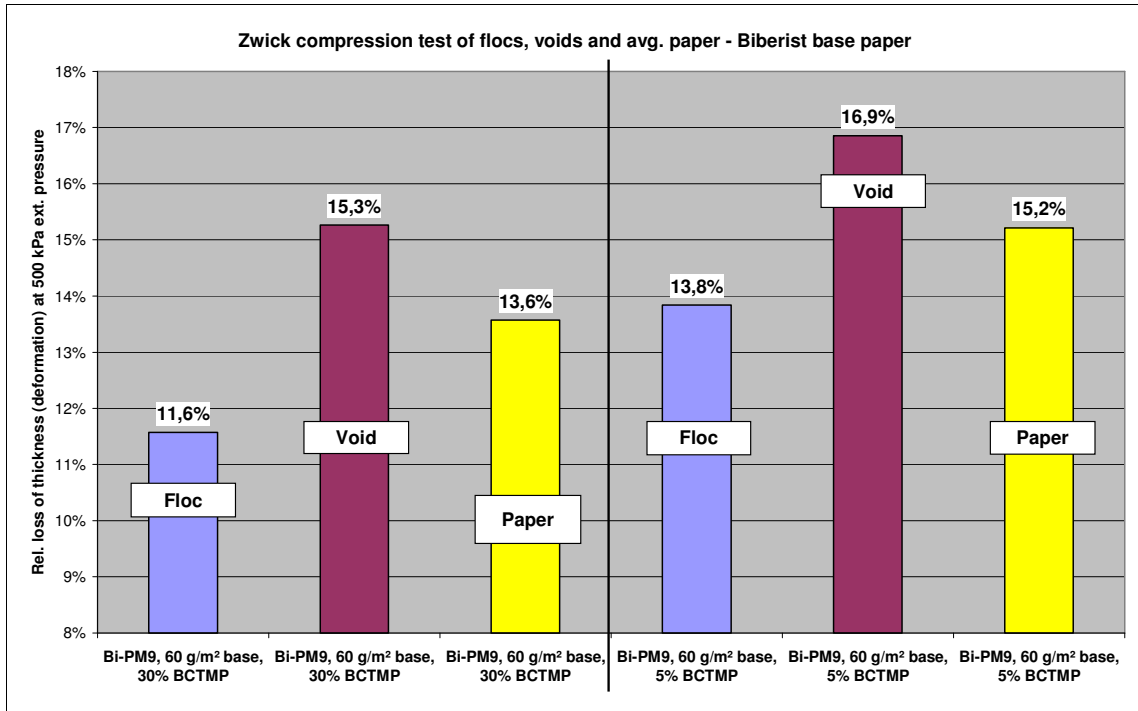
Pict. 4.2.21: Elastic + plastic compression of Biberist base papers at 500 kPa
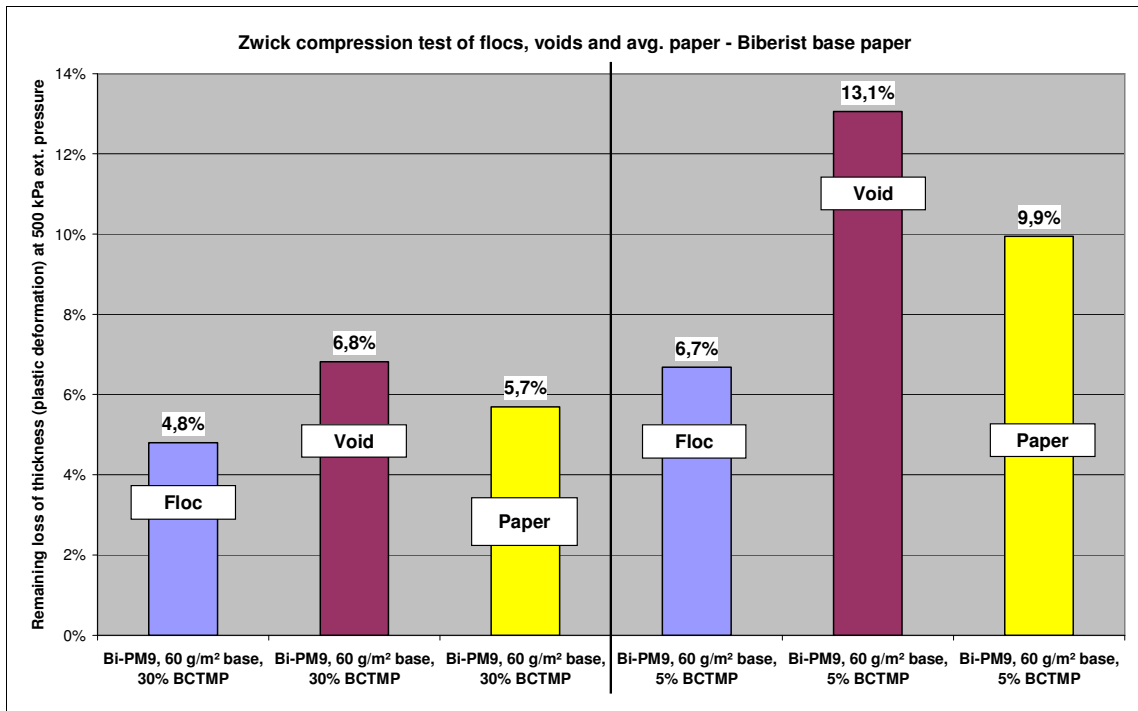
Pict. 4.2.22: Plastic compression of Biberist base papers at 500 kPa

The lower compressibility of Biberist base paper with higher BCTMP content was also visible for the average of thickness after compression of flocs and voids (pict.

4.2.21 – 4.2.22). Similar to the results of GK-PM11 base paper the flocs of the Biberist base paper were also less compressible (higher spring constant) than the voids.

Compressibility difference of flocs and voids increased with higher BCTMP content as stiffer fibres contributed to compressibility differences between flocs and voids.
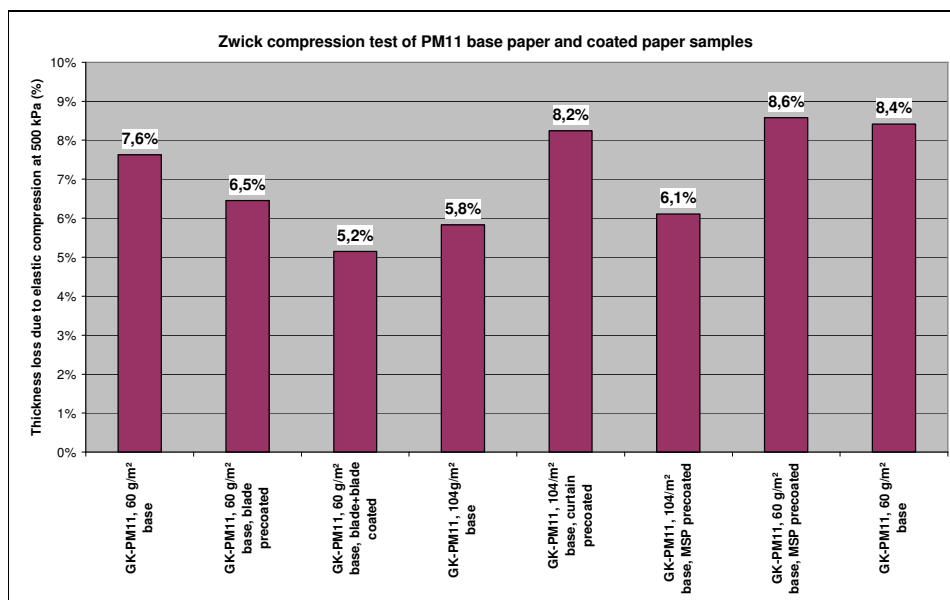
Pict. 4.2.23: Comparison of compression deformation of base papers and coated papers from PM11 at 500 kPa (left and right columm: Two different base papers of PM11 with 60 g/m² B.W.)

Blade coated papers were less compressible than their corresponding base papers as coatings added compressibility stiffness to the paper. This was investigated by Charles S. Kan, L.H. Kim, Do I. Lee and R. v. Gildern (L3.14) from DOW who studied the viscoelastic properties of coatings. They measured the storage modulus of coatings with different types of latices. Storage modulus of the latex is with $10^8 - 10^9$ four magnitudes lower than the pigment (10^5) and therefore dominating the elastic/plastic properties of dry coatings when based mainly on latex and pigment. Increasing the storage modulus by using latices with higher Tg increased paper stiffness. When latices with low Tg were used in top coatings gloss was lower as calendering energy could not be dissipated in the coating layer due to high elasticity of the latex.

The authors showed that mechanical properties of coatings depend also strongly on pore volume. Higher pore volume led to lower gloss.

After MSP coating the paper compressibility remains unchanged due to the balance of plastic compression in the application nip and plastic expansion at the nip exit.

Curtain coaters increase the compressibility due to wetting of the base paper and releasing the internal tension in Z-direction from the press and drying section.

Conclusions of floc analysis

- Formation should be improved (local basis weight differences should be reduced) by less flocculation in the headbox (rotational swirls in tube bank and at sheets) and better reforming of the sheet in the blade section. Formation is the most important tool to improve mottling as local differences create local pressure differences.

- The best way to measure formation is the Ambertec index or Ambertec 2 sigma. Correlation to screen mottle and formation induced backtrap mottle is perfect.

- Compressibility differences between flocs and fibres should be reduced by less fibre bonding and using elastic w'fr fibres instead of stiff w'c fibres.

- Ash content at the base paper surface should be increased. It acts like a filler coating, improves holdout of the 1st precoat and reduces penetration differences into flocs and voids.

- The pressure under the blade should be kept as low as possible. Film press or curtain coaters give better mottling due to lower pressure at application.

- The coating holdout should be improved by increasing the retention of small binder particles and soluble components in the coating colour (see chapter 10, "water retention of coating colours").

- Smoothing the base paper surface by press nips, drying cylinders or machine calenders doesn't necessarily lead to better print mottle. The opposite can happen as local compressibility differences increase.

Chapter 5: Penetration by capillary pressure

5.1 Definition and measurement of contact angle

The wetting of a liquid on a solid surface is defined by the Young equation (pict. 5.1.1):
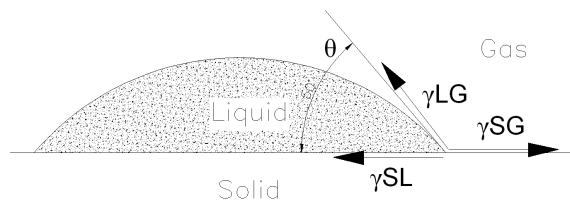
Pict. 5.1.1: Definition of contact angle

With the three contacting media: Liquid = L,   Solid = S,   Gas/Vapour = V.

γ_{SV} ....the solid-vapor interfacial energy (or surface energy)

γ_{SL} ....the solid-liquid interfacial energy

$\gamma = \gamma_{LV}$ ...the liquid-vapor energy (i.e. the surface tension)

Surface tension is caused by the lack of neighbouring molecules at the liquid – air – boundary. Liquids are held together by intermolecular forces of attraction between neighbouring molecules. At the surface this lack results in a net attraction of the molecules into the bulk of the liquid.

λ_{SV} = Surface tension at the solid – air – interface, when saturated with coating vapour

λ_{LV} = Surface tension at the liquid coating – air – interface

λ_{SL} = Interfacial tension at the liquid coating -solid interface

Work of Adhesion $W_A = \lambda_{SV} + \lambda_{LV} + \lambda_{SL}$

Work of cohesion $W_C = 2 \lambda_{LV}$

Spreading coefficient $S_{L/S} = W_A - W_C = \lambda_{SV} - \lambda_{LV} - \lambda_{SL}$

The difference between work of adhesion and work of cohesion will determine whether or not spontaneous spreading (= good wetting) or retraction of the liquid on the solid substrate will occur.

If adhesion forces are bigger than cohesion forces, spontaneous spreading will occur. If cohesion exceeds adhesion, retraction will happen.

To prevent retraction both the equilibrium and dynamic surface tension for λ_{SL} and λ_{LA} must be low.

Eq. 5-1-1: Young equation $0 = \gamma_{SV} - \gamma_{SL} - \gamma * \cos\theta_C$ … equilibrium between the chemical potential of all three phases

The lower the contact angle θ, the better the liquid will wet the solid surface as the droplet spreads fast on the substrate.

From Fibro-DAT-measurements, shown in pict. 5.1.2 typical contact angles for the liquid phases used in coating and printing applied on different paper substrates can be defined:

Uncoated paper: $\theta_{oil} = 55°$, $\theta_{water + CMC} = 60 - 70°$, $\theta_{water+20\%IPA} = 40 - 60°$.
Coated paper: $\theta_{oil} = 50 - 55°$, $\theta_{water + CMC} = 70 - 80°$, $\theta_{water+20\%IPA} = 40 - 60°$.

Wetting of paper surface (coated and uncoated) improves with:
CMC + water < water < water + IPA < oil
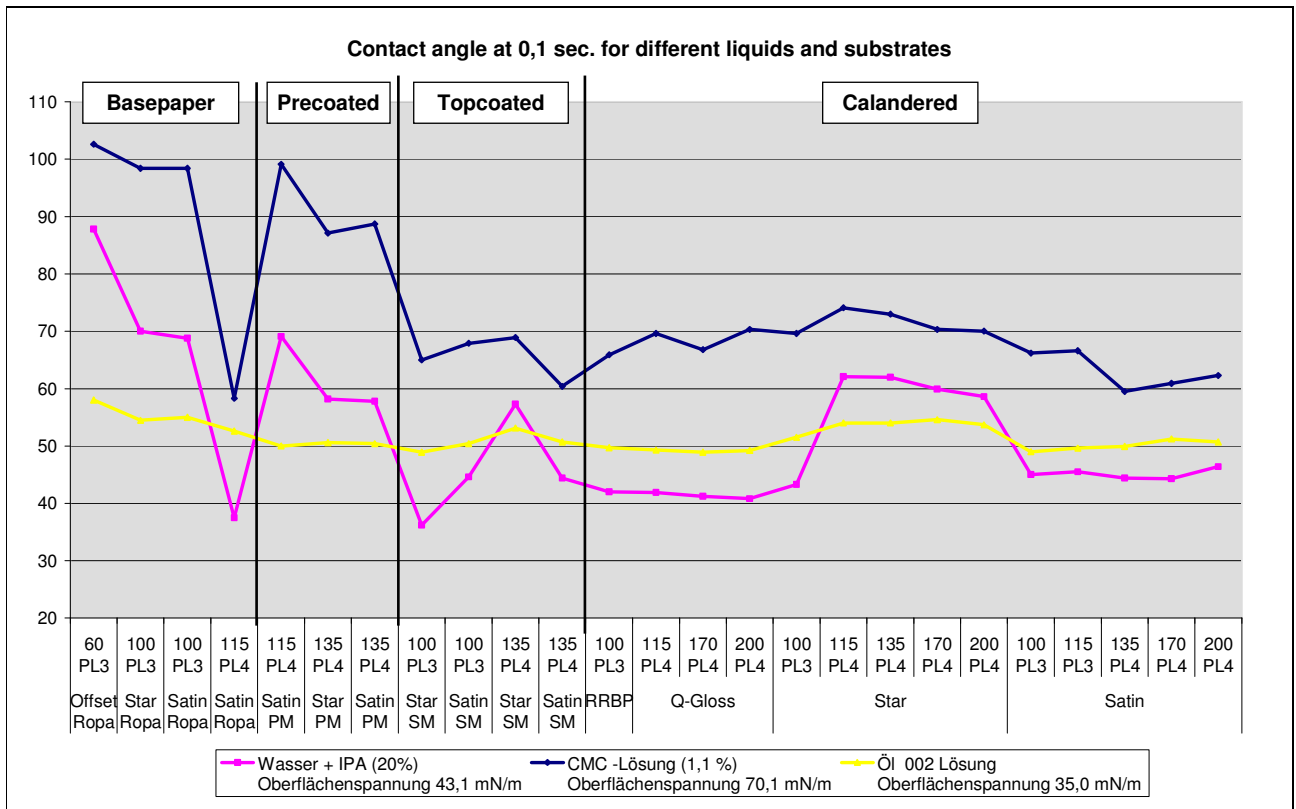
Pict. 5.1.2: Contact angle of different liquids on different substrates ("Ropa" = base paper, "PM" = precoated, "SM" = triple coated (2x pre + 1x top), "Star" and "Q-Gloss" = triple coated + glossy calendaring, "Satin" = triple coated + matt caladering)

5.2 Calculating capillary pressure from Lucas Washburn equation for substrates with known pore radius

Capillary pressure in capillaries shown in pict. 2.4.1 can be calculated with Washburn equation:

Eq. 5-2-1: Lucas Washburn $\Delta P_c = \dfrac{2 * \gamma * \cos\theta}{r}$

γ …..surface tension

θ……contact angle

r…….pore radius

Lucas Washburn equation is valid for:

- Tube shaped capillaries with constant radius over the length of the tube
- Laminar flow in the capillary
- Endless reservoir in the pores (no limit in pick up of liquid by dead end pores)

The Fibro-DAT instrument is used to determine the surface tension, the contact angle of liquids on different substrate and to determine the speed of penetration. A small droplet is put on the paper surface and simultaneously the contact angle, the drop diameter and the drop height is measured with a high speed camera. The movement of liquid front into the substrate (the penetration depth x) corresponds to dV/dA and the penetration speed v to dV/dt. The measurement principle is explained in pict. 5.2.1.
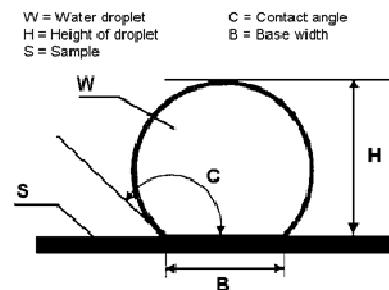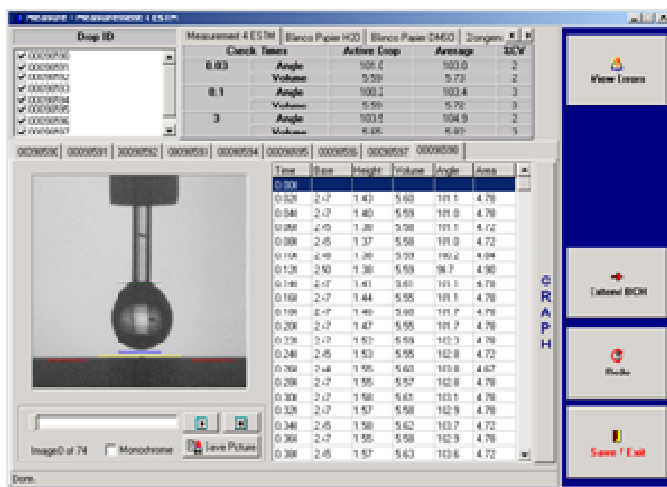
Pict. 5.2.1: Principle of Fibro-DAT capillary sorption measurement
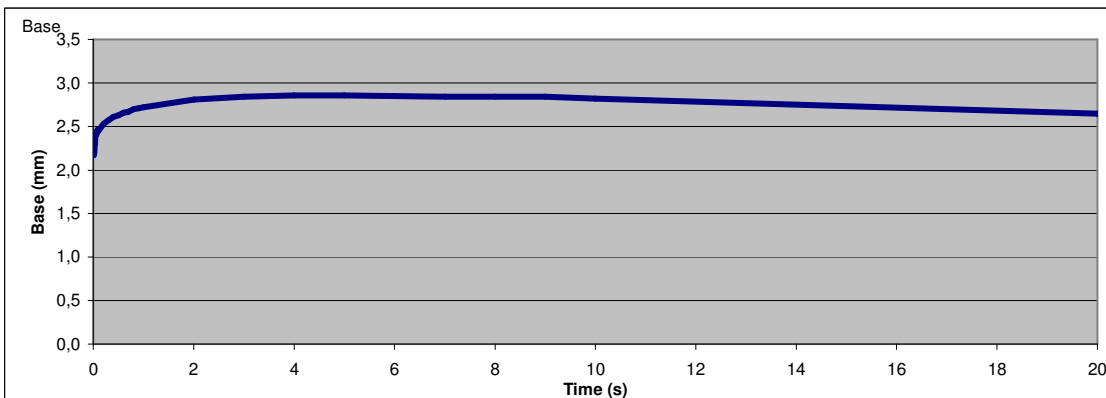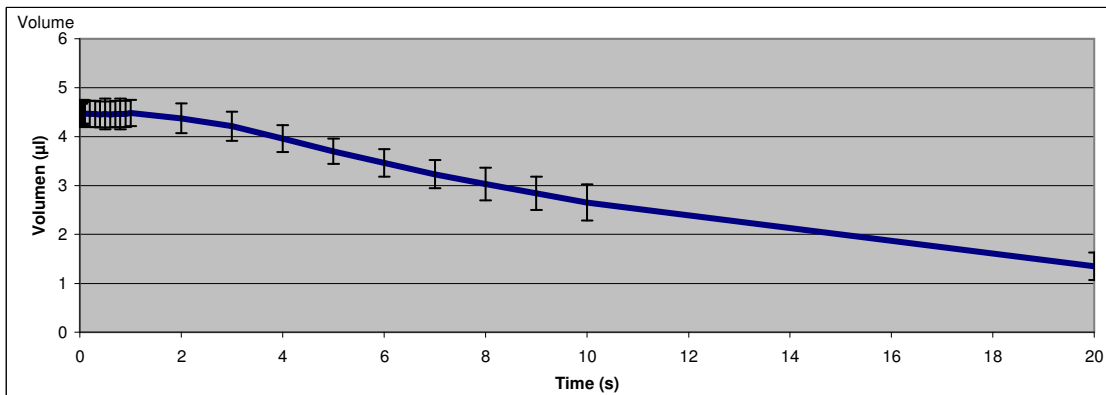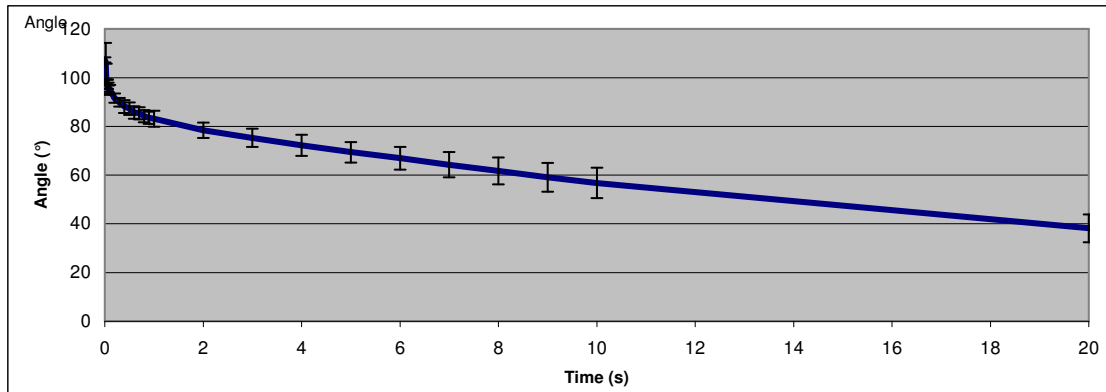
Pict. 5.2.2: Fibro-DAT measurement with water droplet on base paper PM11 (3408-MR3)

From the three typical penetration curves of the Fibro-DAT instrument, shown in pict. 5.2.2 (contact angle, volume and droplet diameter = base diameter) the most important curve for the following calculations is the graph volume V vs. time t, as dV/dt corresponds to the speed of penetration by capillary sorption.
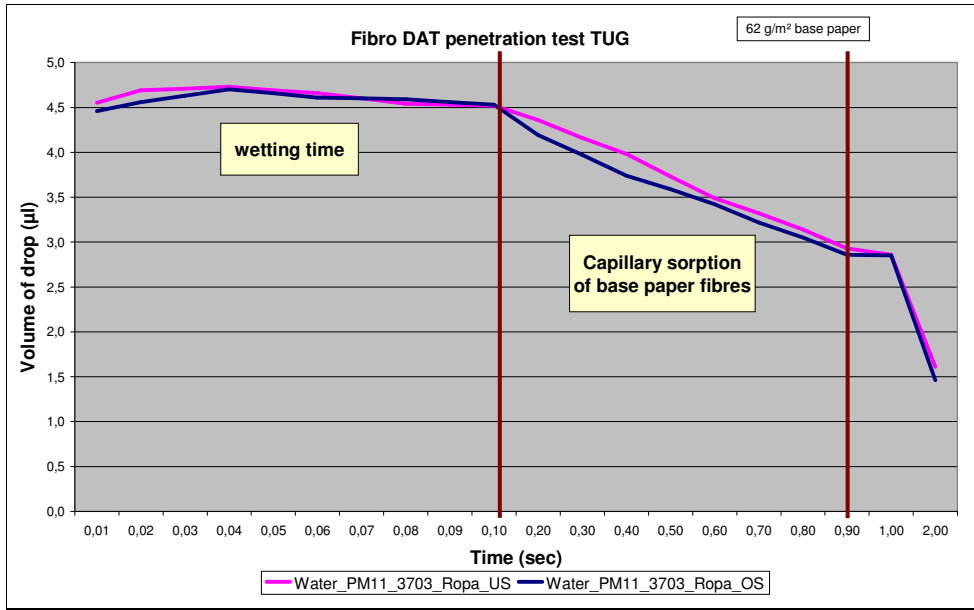
Pict. 5.2.3: Fibro DAT volume of drop vs. time for base paper (liquid: water)
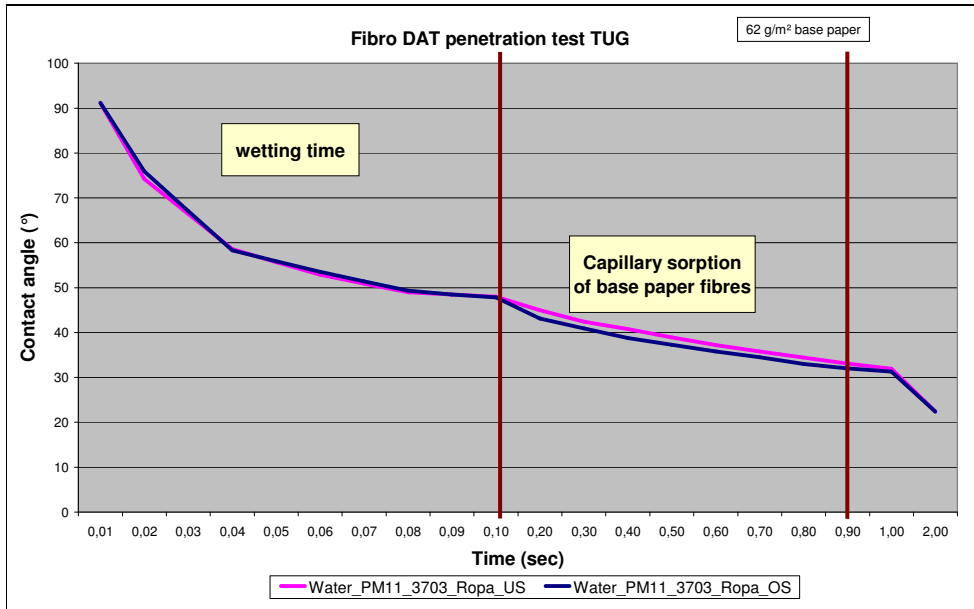
Pict. 5.2.4: Fibro DAT contact angle vs. time for base paper (liquid: water)

Fibro-DAT sorption starts with a short time period where contact angle drops fast while no loss of drop volume is observed (pict. 5.2.3 and 5.2.4). This period is called the wetting time where the surface of the substrate and the walls of the surface capillaries are wetted by the test liquid. During this period the droplet spreads on the substrate and contact angle drops exponentially. The volume of the liquid stays constant – no penetration can be observed during the wetting period.

The duration of wetting time depends on contact angle (substrate – liquid – interaction) and on surface tension of the liquid. Typical data's for wetting time were 0,1 ms for base papers, 5 s for precoated papers and 10 s for double precoated papers (pict. 5.2.5).

The capillary sorption starts after this wetting time and capillary pressure can be calculated from dV/dt (see later).
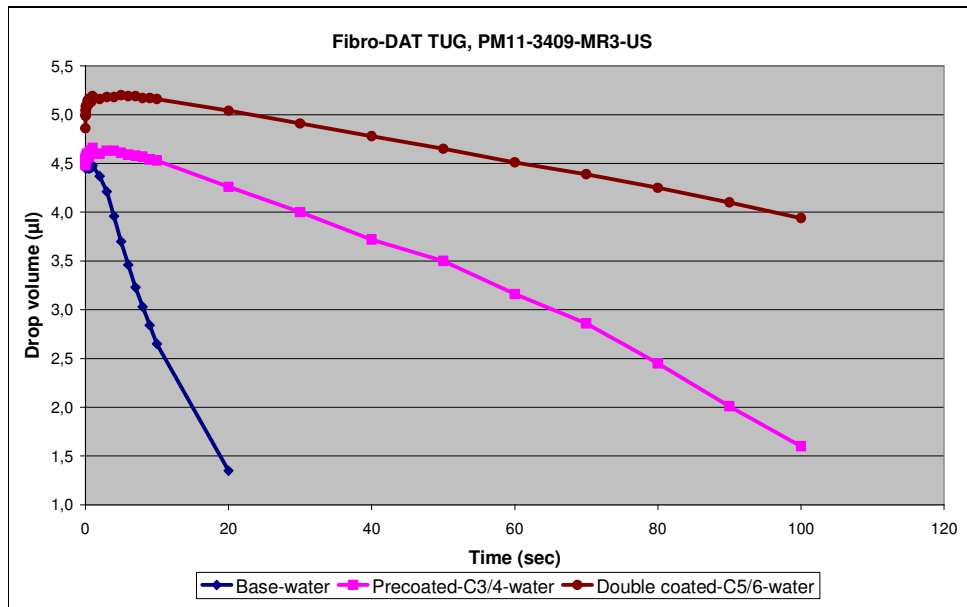
Pict. 5.2.5: Fibro DAT volume of drop vs. time for base, pre- and middle coated paper (liquid: water)

To calculate sorption pressure p_c the surface tension of the liquid has to be measured either by Fibro-DAT of with Ring dipping method. Data's are shown in pict. 5.2.6.

sappi GK/PQ	TITEL					
	ZIEL	Surface tensiond and viscosity of liquids used for Fibro-DAT capillary sorption and Prüfbau pressure penetration test				
INT.U-NR.		Surface tension	Viscosity of pure liquid		Viscosity of coloured liquid	
PM 11 53/2008			Spindel 2 / 100 rpm	Spindel 2 / 20 rpm	Spindel 2 / 100 rpm	Spindel 2 / 20 rpm
		mN/m	cp	cp	cp	cp
Wasser		71,5	11,0	4,0	26,0	15,0
Wasser + IPA (20%)		43,1			38,0	15,0
Wasser + IPA (50%)		26,7			19,0	8,0
CMC Lösung 1,1 %		70,1			90,0	40,0
CMC Lösung 2 %			67,0	30,0		
Öl (Drucköl 002)		35,0	84,4	54,9	89,2	58,0
Öl (Flint)		29,4	22,0	10,0	24,0	13,0

Pict. 5.2.6: Surface tension and viscosity of test liquids for Fibro DAT experiments

The contact angle (the wetting) of the capillary pore wall is difficult to determine. The measured contact angle of the droplet on the substrate can be used as a substitute for the unknown wall wetting where no measurement method exists.

If the mean pore radius of the substrate is known, capillary pressure can be calculated by Lucas-Washburn equation when tube shaped capillaries of unlimited reservoir are penetrated.

For coatings the mean pore radius can be determined by Mercury porosity but it can't be used for capillary pressure calculation with Lucas Washburn equation because coatings have a sponge like structure with many dead end pores.

For fibres the mean network pore radius of the inter fibre pores can be determined by Mercury porosity but it is far too big to cause capillary sorption. The hygroscopic nature of fibres is originated by the intra-fibre pores, the space between the fibrils.

Sixta et al measured an average of 0,1 μm for these intra-fibre pore diameter.

Pekka Salminen et al calculated the capillary pressure of base papers for pure water with 0,2 – 1 bar, depending on type of fibre and degree of internal sizing (pict. 5.4.4 – 5.4.5).

Taking the Fibro-DAT measurements of water droplets on a base paper of PM11, shown in pict. 5.1.2 into the Lucas Washburn equation and assuming a mean radius in the fibre walls of 0,1 µm, the capillary pressure of fibres can be calculated with 0,25 bars which fits perfectly to the measurements of Pekka Salminen:

Lucas Washburn for substrate: Base paper PM11 (unsized w'fr.), Liquid: Water			
Viscosity	η	0,001	Pa s	
Surface tension	γ	0,073	N/m	
Contact angle	Θ	89	Grad	From Fibro-DAT
Contact angle	Θ	1,553	rad	
Porosity	ε	43	%	from Hg-porosimetrie
Mean pore radius	**r**	**0,1**	**µm**	Fibro pores from Literature
capillary pressure	Δp_c	$\Delta p_c = (2 * \gamma * \cos \theta) / r$		**Lucas Washburn**
	Δp_c	25481	N/m²	Pa = N/m²
	Δp_c	**0,25**	**bar**	

5.3 Calculating capillary pressure from Lucas Washburn equation for coating layers

Assuming the coating layer to be a matrix with cylindrical shaped pores, Hagen Poiseuille and Lucas Washburn can be applied:

Hagen Poiseuille for cylindrical pores:

Eq. 5-3-1: $\dfrac{dl}{dt} = \dfrac{r^2 * \Delta p}{8\mu * l}$

l.......penetration depth (m)

t.......time for penetration (sec)

r......radius of cylindrical capillary (m)

Δp...pressure drop across the capillary (Pa)

μ......viscosity of liquid medium (Pa s)

Total pressure drop in capillary (Lucas Washburn equation):

$\Delta p = \dfrac{2 * \gamma * \cos\theta}{r}$

γ......surface tension (N/m)

θ......contact angle

Lucas Washburn + Hagen Poiseuille :

$\dfrac{dl}{dt} = \dfrac{r * \gamma * \cos\theta}{4\eta * l}$

$l^2 = \dfrac{r \times \gamma \times \cos\theta}{4\eta \times l} \times t$ without external pressure = before and after blade

$l^2 = \dfrac{r \times \gamma \times \cos\theta \times t}{4\eta \times l} + \dfrac{r^2 \times t \times \Delta p}{4\eta}$ with external pressure (under jet and blade)

From Mercury porosity measurements shown in pict. 5.3.1 and 5.3.2 the mean radius of the pores was taken into the Lucas Washburn equation to calculate the theoretical capillary pressure of coatings assuming the pore to be of cylindrical shape with endless length and constant radius over the whole pore length.
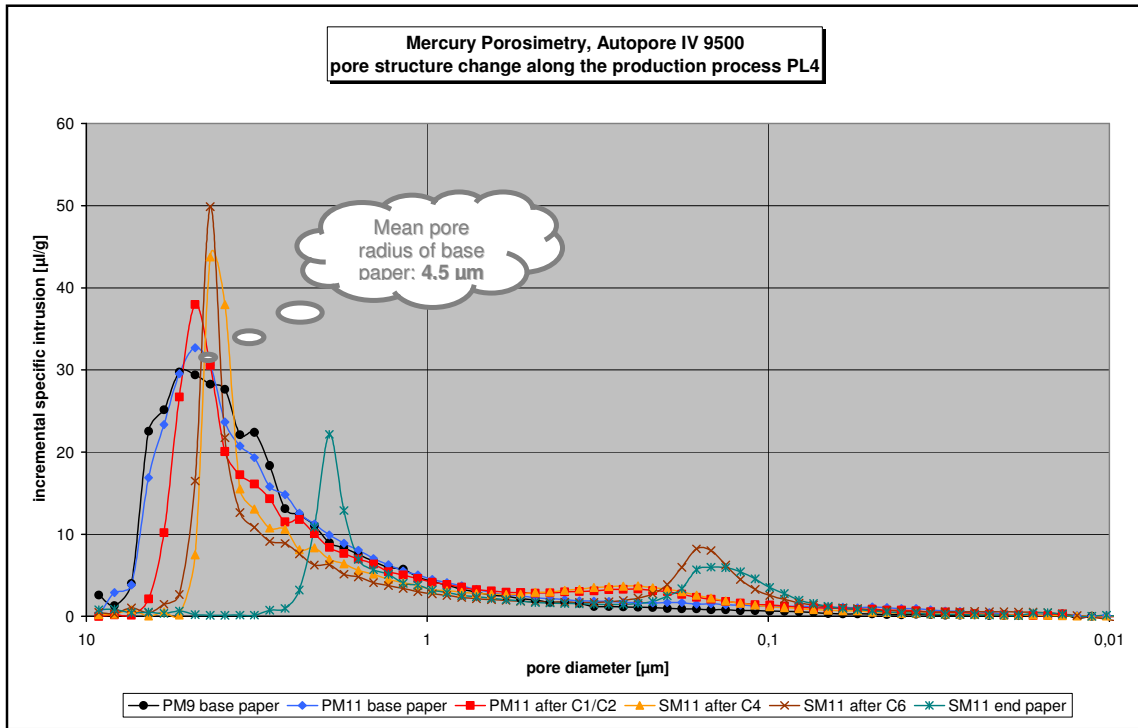
Pict. 5.3.1: Mean pore radius of base paper from Mercury porosity of base papers,
pre-, middle- and topcoated papers from PM11

Pict. 5.3.2: Mean pore radius of coating layer from Mercury porosity of base papers,
pre-, middle- and topcoated papers from PM11

Page 136
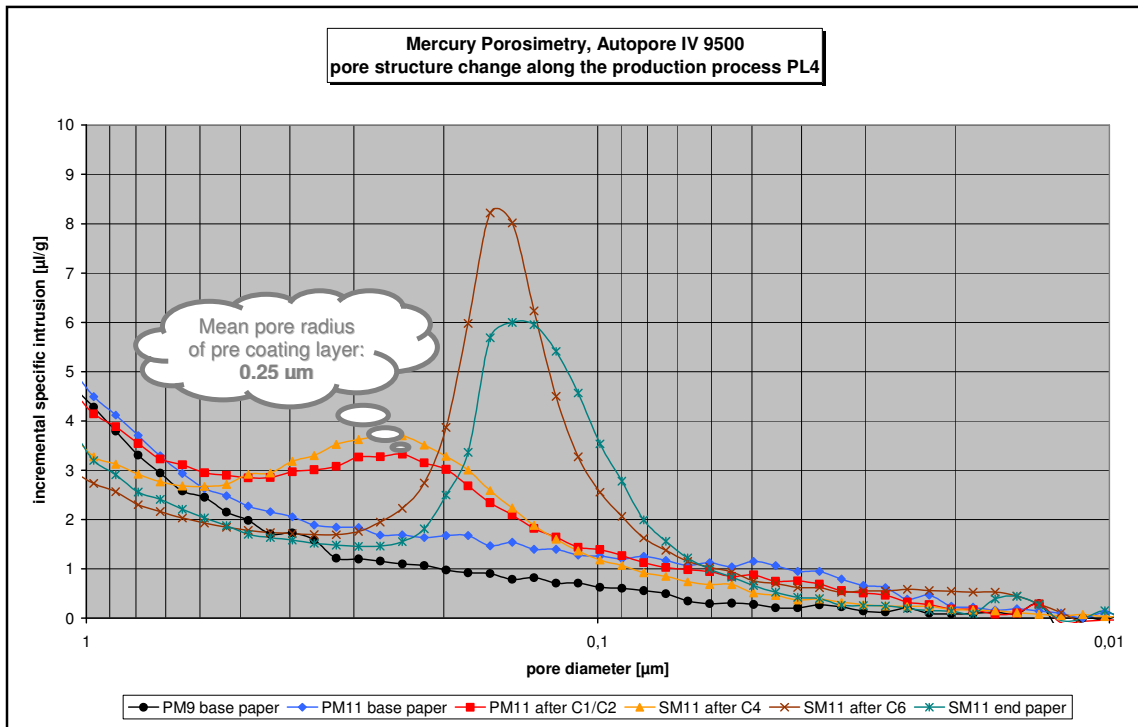
The mean radius of the base paper pore was measured with 4,5 µm while the pores of the precoating layer had a mean radius of 0,25 µm.

Inserting the surface tension and the contact angle of Fibro DAT test liquid components into Lucas Washburn equation gave the theoretical sorption pressure of base paper and coatings:

<div>

Capillary force for water sorption of coating colour between application and blade:

Precoat on base paper:

density	ρ	1600	kg/m³	
surface tension	γ	0,057	N/m	
contact angle	Θ	60	Grad	
contact angle	Θ	1,047	rad	
mean pore radius	r	4,5	µm	

height of movement in capillary	h	$h = (2 \times \gamma \times \cos \theta) / (\rho \times g \times r)$		
	h	**0,81**	**m**	Much too high!

capillary pressure	Δp_c	$\Delta p_c = (2 * \gamma * \cos \theta) / r$		Lucas Washburn
	Δp_c	12667	N/m²	Pa = N/m²
	Δp_c	**0,13**	**bar**	

topcoat on two times precoated paper

density	ρ	1600	kg/m³	
surface tension	γ	0,057	N/m	
contact angle	Θ	80	Grad	
contact angle	Θ	1,396	rad	
mean pore radius	r	0,25	µm	

height of movement in capillary	h	$h = (2 \times \gamma \times \cos \theta) / (\rho \times g \times r)$		
	h	**14,5**	**m**	Means: 18 times of base paper!!

capillary pressure	Δp_c	$\Delta p_c = (2 * \gamma * \cos \theta) / r$		Lucas Washburn
	Δp_c	79184	N/m²	Pa = N/m²
	Δp_c	**0,79**	**bar**	

</div>

Pict. 5.3.3: Calculation of capillary pressure of base papers

The calculation of capillary pressure in pict. 5.3.3 shows that water sorption from coating colours should be higher for coated papers than for uncoated base papers. Fibro DAT measurements showed the opposite.

The reason is the wrong assumption that coating pores are tube shaped with open ends where Hagen-Poiseulle' law and the Lucas Washburn equation can be applied.

Coating colours have a sponge like structure with a network of capillaries, connected by tubes with much smaller capillary radius or totally blocked conjunctions. Therefore

the real capillary sorption pressure of a coating layer is much lower than that of a tube with the same mean pore radius. This difference is called tortuosity.

For base papers the opposite result was achieved: The calculation of sorption pressure of fibre networks by taking the mean pore diameter of the inter fibre network (4,5 µm) from Mercury porosity gave a much lower calculated pressure than measured by Fibro DAT instrument.

Capillary sorption of fibre networks is a combination of intra fibre network pores which are rather big in diameter (2 – 10 µm) and low in sorption pressure and of the inter fibre surface pores, which are much lower in diameter (10 – 100 nm) and therefore much higher in sorption pressure.

5.4 Calculating capillary pressure from Lucas Washburn equation for substrates with unknown pore radius – theory and principal measurements

For base papers and coating layers the pore radius is most often unknown. In that case capillary pressure can be calculated from Fibro-DAT measurements by using dV/dt-readings.

Assuming fibre pores to be of cylindrical shape, Hagen Poiseuille's law can be combined with Lucas Washburn to:

$$\frac{dl}{dt} = \frac{r^2 * \Delta p}{8\mu * l} \quad \text{and} \quad \Delta p_c = \frac{2 * \gamma * \cos\theta}{r} \quad \text{leads to}$$

$$x^2 = \frac{r * t * \gamma * \cos\theta}{2 * \eta} \quad \text{or} \quad V_p = n_p * \pi * r^2 * \sqrt{\frac{r * \gamma * \cos\theta * t}{2 * \eta}} \quad \text{with x = l = dV/dA the}$$

penetration depth or the distance travelled by the liquid front in the time t, η the fluid viscosity, r the pore radius of the cylindrical pore, n_p the number of pores, γ the surface tension of the liquid, cosθ the contact angle of the liquid at the pore surface.

According to this modified Lucas Washburn equation capillary sorption volume should increase with raising pore radius and **square root of time**.

Lucas Washburn's law is only valid when straight capillaries with constant radius are filled with laminar flow and sufficient void volume is provided by the capillary reservoir.

When water is soaked into the capillary pores of the fibre wall, most of these conditions are fulfilled. The only exception is the pore radius which increases with time due to swelling of fibre wall.

In contradiction to fibre wall pore the pores in coatings do not fulfil these preconditions as their pore radius is changing and void volume is limited.

Due to missing term of inertia the Lucas Washburn equation was replaced later by the Bosanquet relation:

$$F_i + F_{vd} = F_p + F_w$$

F_i...inertial force = $d(m * \dfrac{dx}{dt}) / dt$ with $m = \pi * r^2 * \rho * x$ the mass in the capillary and

$m * \dfrac{dx}{dt}$ the momentum or inertia of the fluid

F_{vd}...viscous drag force according to Poiseuille's law

F_p.... external pressure force

F_w....wetting force

Bosanquet relation in its dynamic form:

$$\frac{d}{dt} * (\pi * r^2 * \rho * x * \frac{d}{dt}) + 8 * \pi * \eta * x * \frac{d}{dt} = pe * \pi * r^2 + 2 * \pi * r * \cos\theta$$

With η the fluid viscosity, r the pore radius of the cylindrical pore, p_e the external pressure, γ the surface tension of the liquid, cosθ the contact angle of the liquid at the pore surface.

Assuming external pressure to be negligible, the distance of the liquid front travelled in the pore can be calculated by:

Eq. 5-4-1: $x^2 = \dfrac{2 * \gamma * \cos\theta * t^2}{r * \rho}$ for a*t<<1 and p_e=0 (Bosanquet)

Or

Eq. 5-4-2: $V_p = n_p * \pi * r^2 * \sqrt{\dfrac{2 * \gamma * \cos\theta}{r * \rho}} * t$ (Bosanquet)

According to **Bosanquet** equation **capillary sorption volume should be proportional to time of sorption.**

Lucas Washburn came to the conclusion that penetration depth should be proportional to the square root of time:

Equ. 5-4-3: $x^2 = \dfrac{r * t * \gamma * \cos\theta}{2 * \eta}$

P. Resch proved in his PhD thesis as well as J. Preston that the Bosanquet equation can be applied for ink absorption into coating layers by capillary pressure. Penetrated volume was depending on the square root of time.

Dan Eklund (L1.10) was the first to start investigations of penetration. He presented in 1986 the water absorption instrument of Abo Academy shown in pict. 5.4.1.
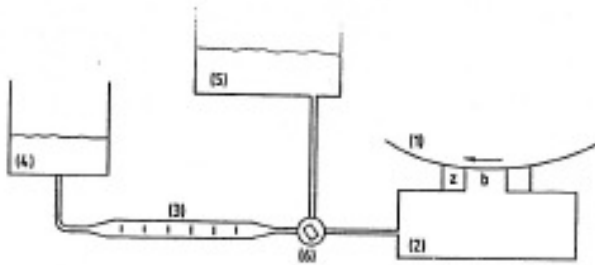
Pict. 5.4.1: Water transfer unit invented by Dan Eklund / Abo Akademi

Water was transferred via a pressure chamber on a running web in a lab coating unit. Short term penetration could be measured with this liquid application instrument under external pressure and without external pressure.
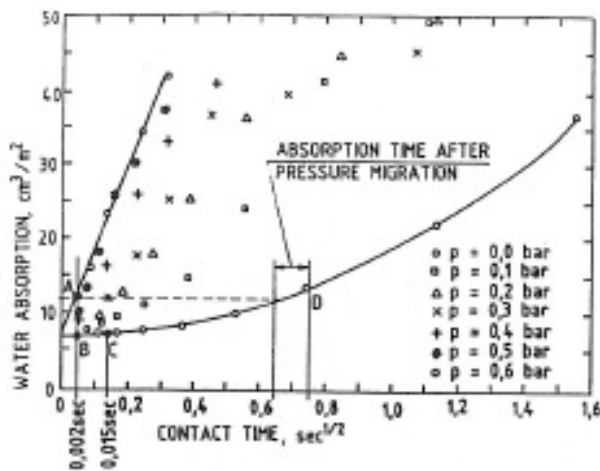
Pict. 5.4.2: Absorbed water vs. square root of time for different application pressure levels

Pict. 5.4.2 show that pressure penetration was described by linear dependency of V^2 on t while for pressure less capillary sorption a linear relationship of V on t was investigated (according to Lucas Washburn equation).

Pressure penetration increased with rising external pressure according to Darcy's law (see chapter 6 "pressure penetration").

Transferring the measurements of the Abo roll applicator into practice and assuming application of pure water Dan Eklund came to the following conclusion: At a SDTA short dwell applicator almost no water is absorbed by the base paper in the dwell time of 0,002 sec between application and blade while at jet applicators with a dwell

Page 141

time of 0,015 sec 1 – 3 g/m² water will be absorbed by the base paper. This calculation shows advantage of SDTA coaters in avoiding capillary penetration before the blade by shortening the contact time.

Pekka Salminen (L1.11) continued the work of Dan Eklund at Abo Academy with the roll applicator. For application of water under pressure again a linear correlation was found between the amount of penetrated water V^2 and t the time of contact according to Darcy's law.
Pressure-less penetration was described by linear relation of V and t (pict. 5.4.3).
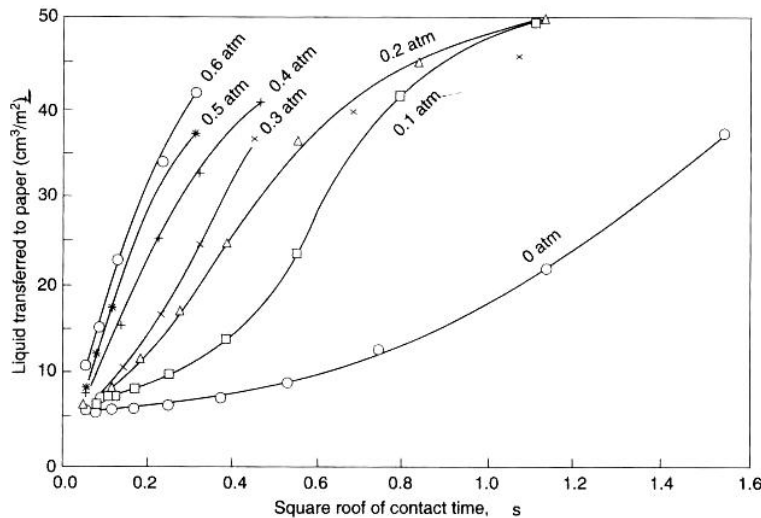
Pict. 5.4.3: Water penetration vs square root of time for different pressure levels (P. Salminen)

The linear influence of the viscosity on pressure penetration according to Darcy's law was proven by adding a thickener into the water (pict. 5.4.4).
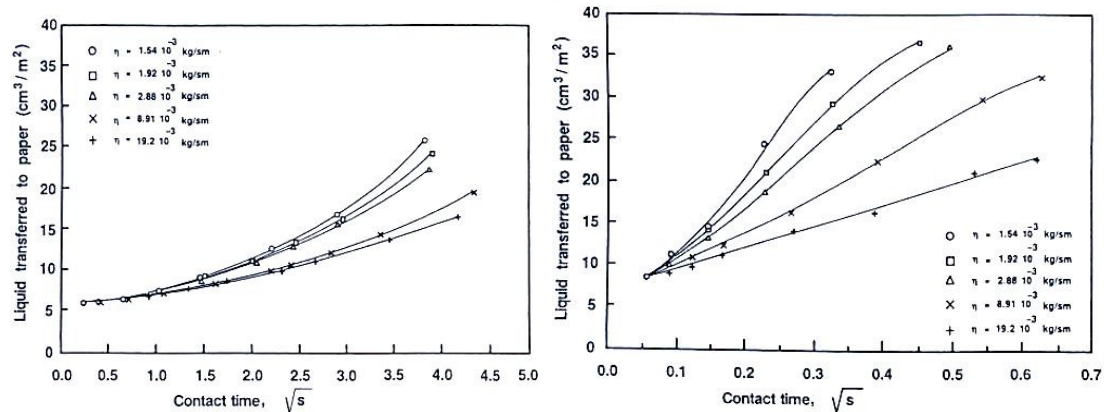
Pict. 5.4.4: Influence on water viscosity on penetration: Left: 0 kPa, right: 50 kPa application pressure (P. Salminen)

For pressure-less application driven by capillary pressure of the substrate the transferred liquid was a function of time and not square root of time according to the Lucas Washburn equation.

The capillary penetration could be reduced by internal rosin sizing (pict. 5.4.5).
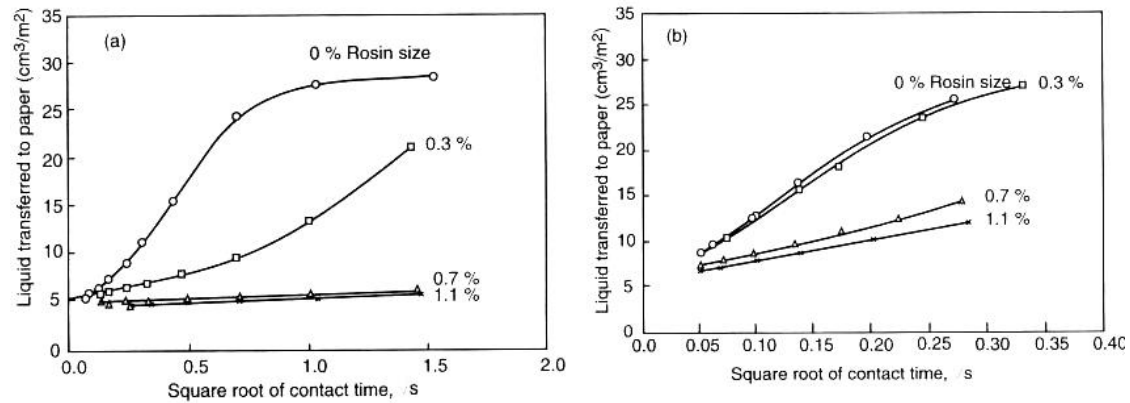
Pict. 5.4.5: Influence of rosin sizing on capillary penetration (left) and pressure penetration with 50 kPa (right) for water as test liquid (P. Salminen)

Pekka Salminen proved that speed of capillary penetration can be increased by wetting more fibres at the start e.g. by a short pressure impulse during wetting of the substrate.
To reduce the capillary penetration of coating colour between the application and blade Salminen suggested to reduce the temperature of coating colour by cooling units, to increase coating colour viscosity by using appropriate thickeners or by increasing the contact angle of the coating colour on the base paper.
Using a machine calander for the base paper had no influence on capillary sorption but reduced pressure penetration as the pore radius of base paper was reduced.

S. Ramaswamy, B.V. Ramarao, A. Goel, G. Lee, D. Choi and S. Lavrykov (L1.31) compared in their experiments liquid penetration into porous base paper with theoretical calculations. They used a modified Liquid Air Displacement Device (LADA) and calculated pressure-less capillary penetration with the Lucas Washburn equation.
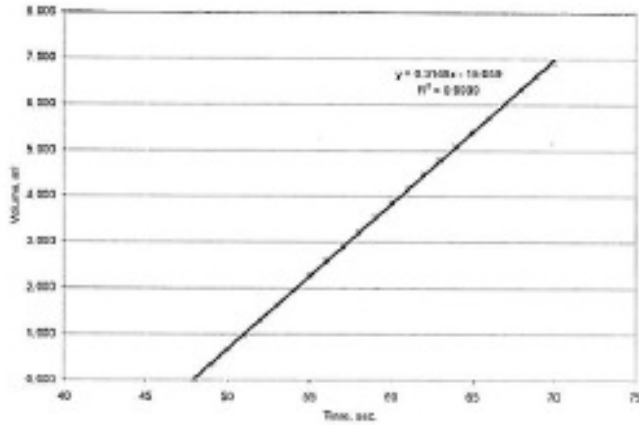
In-plane permeability results (V² vs t)
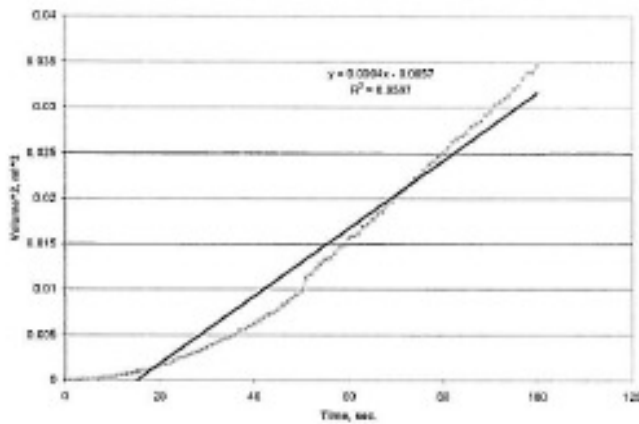
Transverse "saturated" permeability results (V vs t)

Pict. 5.4.6: Experimental results of pressure-less penetration (Y-axis: Penetrated volume of liquid V, X-axis: time t) for liquid packaging board with varying structure and sizing level (S. Ramaswamy)

When the wetting time of capillaries at the beginning of the measurements was removed, a linear correlation of penetrated liquid volume V and penetration time t was achieved.

Dganit Danino and A. Marmur (L1.24) studied capillary penetration into porous filter paper by using un-polar liquids. They calculated the dependency of penetrated liquid from time with the equation $(\dfrac{R}{V^{1/3}}) = K_1 * (\dfrac{\sigma * (r * \cos\theta)_{eff}}{\mu} * t)^n$,

which is a combination of the Lucas Washburn equation $p_c = \dfrac{2 * \sigma * \cos\theta}{r}$ and the

Kissa equation $R^2 = K * (\dfrac{\sigma}{\mu})^u * V^m * t^n$. (u=0,3, m=0,7, n=0,3). They found a linear

dependency of $R^2/V^{2/3}$ with time t (pict. 5.4.7).
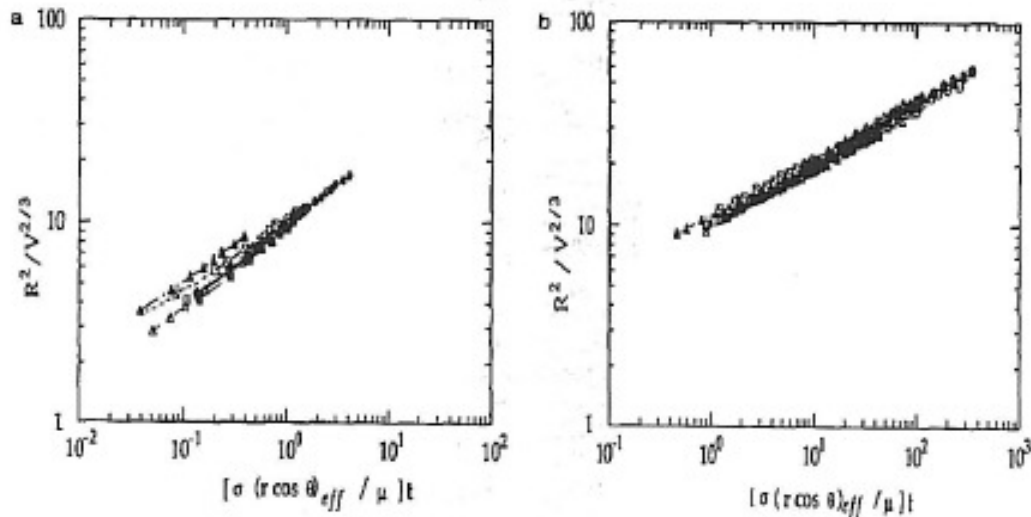
Pict. 5.4.7: Kinetics of penetration: a) drop in the capillary, b) drop out of the capillary
(D. Danino)

J.E. Elftonson, G. Strom (L1.42) studied capillary penetration of different liquids into a
porous aluminium oxide powder. They found a linear correlation between penetrated
liquid volume and time (pict. 5.4.8).
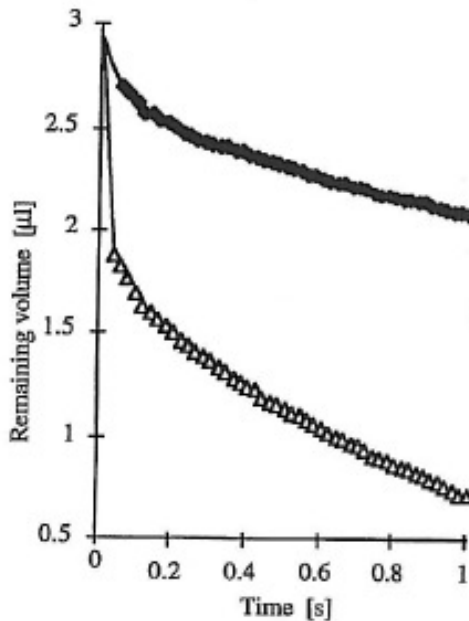
Pict. 5.4.8: Penetration of surfactant drops (upper line) and isopropanol (below) (G. Strom)

T. Karppinen, I. Kassamakov and E. Haeggström (L7.9) measured the paper wetting process by laser transmission. A rapid measurement method was developed to describe the sorption process. Wetting was done by spray and fibre sorption was measured by ultrasonic pulse reflection. The transmission of laser light through the tested paper samples was measured during penetration. When air in the inter fibre and intra fibre pores is replaced by liquid, the transmission changes.

From 0 to 0,1 sec the samples were wetted. Air is removed by the liquid. Afterwards the light transmission increased linearly with time by capillary wetting according to the classical Lucas Washburn equation. This process lasted between 0,25 and 0,65 sec.

Lucas Washburn: $l = \sqrt{\dfrac{2 * r * \gamma * \cos\theta}{4 * \eta}} * \sqrt{t}$

A higher lignin content and degree of AKD-sizing increased the contact angle between water and fibre capillary surface and delayed the penetration.

After 0,65 sec water entered the intra-fibre pores, the fibre walls were swollen and fibre-fibre plus fibre-water reflection was replaced by fibre-air reflection - the light transmission decreased.

Unlike water, isopropanol didn't swell the fibre walls or break the fibre-fibre-bonds. Light intensity remained constant after 0,6 sec.

When Fibro-DAT measurements in pict. 5.4.9 and 5.4.10 are compared for different papers the conclusion can be drawn that **the amount of penetrated liquid V by capillary sorption is proportional to time t and not to the square root of time** $\sqrt{t}$.

The same conclusion was drawn by Pekka Salminen and Dan Eklund (see pict. 5.4.1 – 5.4.5).
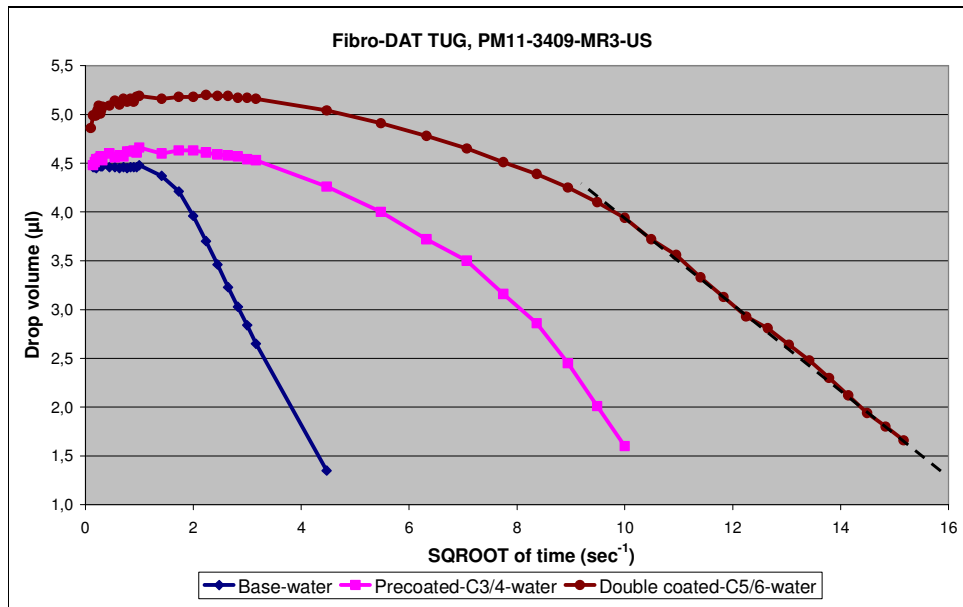
Pict. 5.4.9: Fibro DAT of different stages of paper production at PM11 / OMC11 – penetrated volume vs. **SQROOT of time** for water + 20% IPA (A = constant)
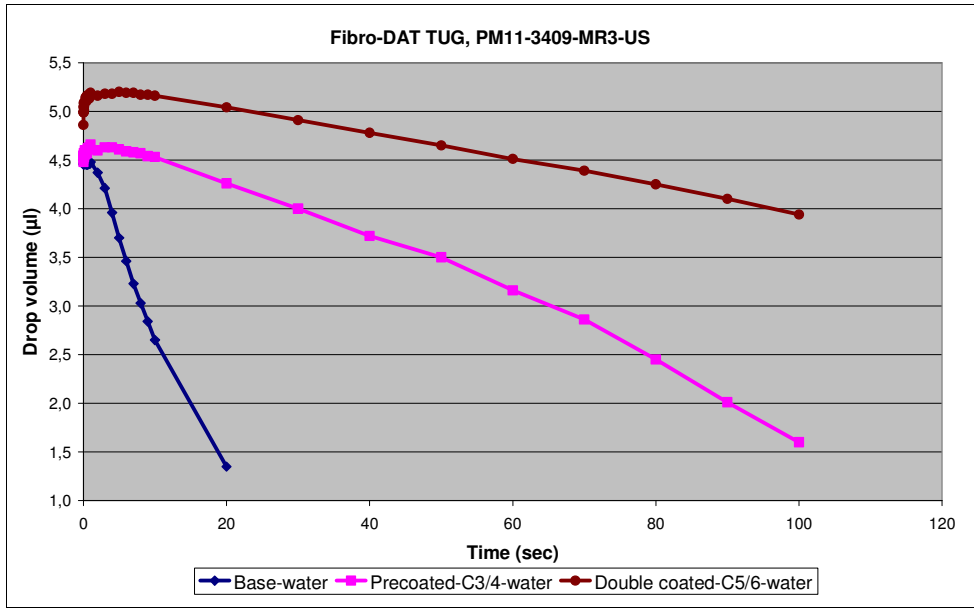
Pict. 5.4.10: Fibro DAT of different stages of paper production at PM11 / OMC11 – penetrated volume vs **time** for water + 20% IPA (A = constant)

In mill coaters this wetting time is of minor importance as the coating colour is applied always be external pressure at jet, roll or MSP applicators.

A. Marmur and R.C. Cohen (L1.22) tried to characterize capillary penetration into media by the kinetics of liquid penetration. They compared their results with the Lucas-Washburn equation.

They tried to calculate the term $r*\cos\theta$ from the slope of the curve x^2 versus t but they recognized that from this curve r and θ cannot be determined separately.

Therefore they transformed the equation of Lucas Washburn (for a vertical capillary, containing a fluid of negligible viscosity) using the two parameters A and B:

$$A*t = -B*h - \ln'*(1 - B*h)$$

$$A = \frac{\rho^2 * g^2 * r^3}{16 * \sigma * \mu * \cos\theta} \quad \text{and} \quad B = \frac{\rho * g * r}{2 * \sigma * \cos\theta}$$

The authors concluded that a cylindrical capillary model does not fit to measurements in porous media like sand or coatings as contact angle is not constant within the porous medium.

5.5 Calculating capillary pressure from Darcy equation for substrates with unknown pore radius – detailed measurements and calculations

Darcy's law is a better alternative to Hagen Poiseuille to calculate capillary sorption pressure of a sponge like substrate of unknown pore radius.

Darcy: $Q = \dfrac{dV}{dt} = \dfrac{K * A * \Delta p}{\eta * L}$

When a membrane of known permeability K and known thickness L is put on top of a base paper capillary sorption of base paper can be measured with Fibro-DAT instrument by putting a droplet of water on the membrane and measuring dV//dt. The higher the capillary sorption pressure p_c of the base, the faster the droplet will be penetrating through the membrane into the base paper and the the higher dV/dt will be.

Coated papers are ideal media for determining capillary pressure of base paper by Fibro-DAT instrument as the coating layer can be used as membrane layer. The permeability of the coating layer must be measured separately by the Prüfbau pressure penetration test (see chapter 6 "pressure penetration") and the thickness is easy to measure as it is the difference of between base paper and coated paper thickness.
Liquid flow through this coating membrane of known permeability must be measured. This can be done by the Fibro-DAT instrument where the loss of drop volume dV/dt is measured over time by a high speed camera. The drop area A is also measured by Fibro-DAT.

Alternatively a conventional laser drilled plastic foil of known pore diameter, thickness and permeability (e.g. the membranes used for Abo-GWR measurements) can be used as membrane layer.

Assuming that capillary sorption pressure of the coating layer is negligible against the sorption of fibres underneath (which is proven later), the capillary pressure of fibres in base paper can be calculated by Darcy's law:

Darcy: $Q = \dfrac{K * A * \Delta p}{\eta * L}$ integrated and rearranged leads to:

$$\left[\dfrac{m_f}{A}\right]^2 = (K * \varepsilon) * \dfrac{\rho_f{}^2}{\eta} * \Delta p * \Delta t \quad \text{or} \quad (m_f / A) = \sqrt{C * A * \Delta p * \Delta t}$$

And with $\Delta P_c = \dfrac{2 * \gamma * \cos\theta}{r}$ the capillary pressure and without external pressure →

$$(m_f / A) = \sqrt{C * A * \Delta p_c * \Delta t} \quad \rightarrow \quad \boxed{(m_f / A) = \sqrt{\overline{C} * \overline{A} * \Delta t}}$$

with $\boxed{\overline{C} = \dfrac{K * \varepsilon}{r}}$ the <u>material constant of the substrate</u> (K = permeability coefficient of

coating layer, ε = porosity of substrate, r = pore radius of substrate)

and $\boxed{\overline{A} = \dfrac{\rho_f{}^2 * \gamma * \cos\theta}{\eta}}$ the <u>material constant of the liquid</u> (ρ = density, γ = surface

tension, η = viscosity of liquid, θ = contact angle).

Combining Lucas Washburn with Darcy's law, capillary sorption dV/dA or m_f/A should be proportional to the square root of time, surface tension, contact angle and 1/r.

Literature (pict. 5.5.1) and lab measurements with Fibro-DAT at different stages of coating application (pict. 5.5.3 – 5.5.8) show the validity of this equation:
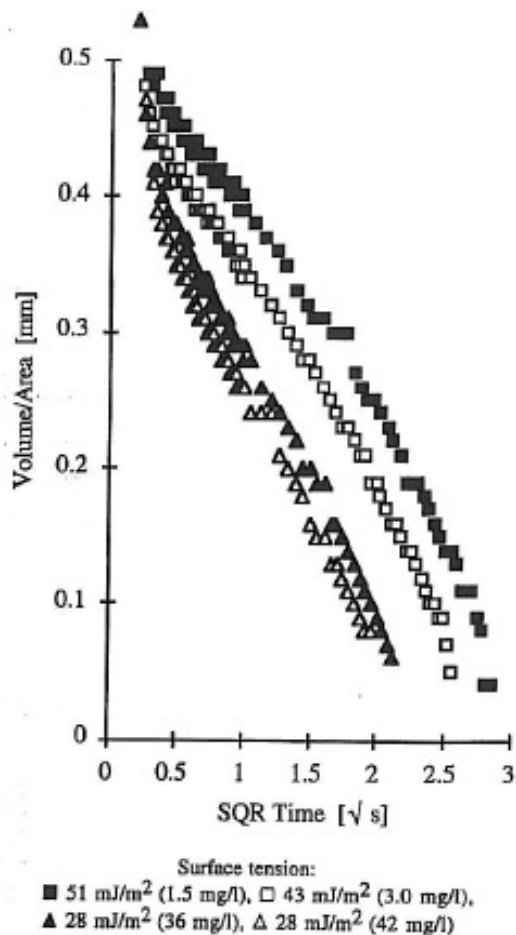
Surface tension:
■ 51 mJ/m^2 (1.5 mg/l), □ 43 mJ/m^2 (3.0 mg/l),
▲ 28 mJ/m^2 (36 mg/l), △ 28 mJ/m^2 (42 mg/l)

Pict. 5.5.1: J.E. Elftonson, G. Strom (L1.42) : Penetration of aqueous solutions into models for coating layers - V/A vs. SQROOT of time t for surfactants

To calculate capillary sorption of base paper intra-fibre-pores a precoated paper of PM11 and CMC-solutions of different concentrations were used for Fibro-DAT experiments.

A similar process happens when coatings are applied in the middle coaters of OMC11 on precoated paper of PM11: The liquid phase of the coating colour is soaked through the precoating membrane into the base paper in the area between coating application and blade.

A solution of 3% medium viscous CMC Niclacell CH90 has the same viscosity as the liquid phase in middle coatings of OMC11 and similar surface tension / contact angle. In film press coaters of PM11 the Brookefield viscosity is with 500 cp at 20 RpM much lower than at blade middle coater of OMC wher BF viscosity is with 5000 cp a

magnitude higher. A higher amount of thickeners is used in middle coatings and liquid phase is therefore 5 – 10 times higher.

To simulate liquid phase sorption of low viscous film press precoatings, a 1,1% CMC solution was added to the Fibro-DAT measurements.

The precoated paper of PM11 had a high amount of coating and good coverage of the base paper.

Pict. 5.5.2 shows similar contact angle for all tested solutions with 1 – 3% concentration of CMC in contact with a precoated paper of PM11. Generally wetting of this precoated surface by CMC-solutions was much worse than for water (contact angle was lower) and therefore capillary sorption on base papers is slower for CMC-solutions.
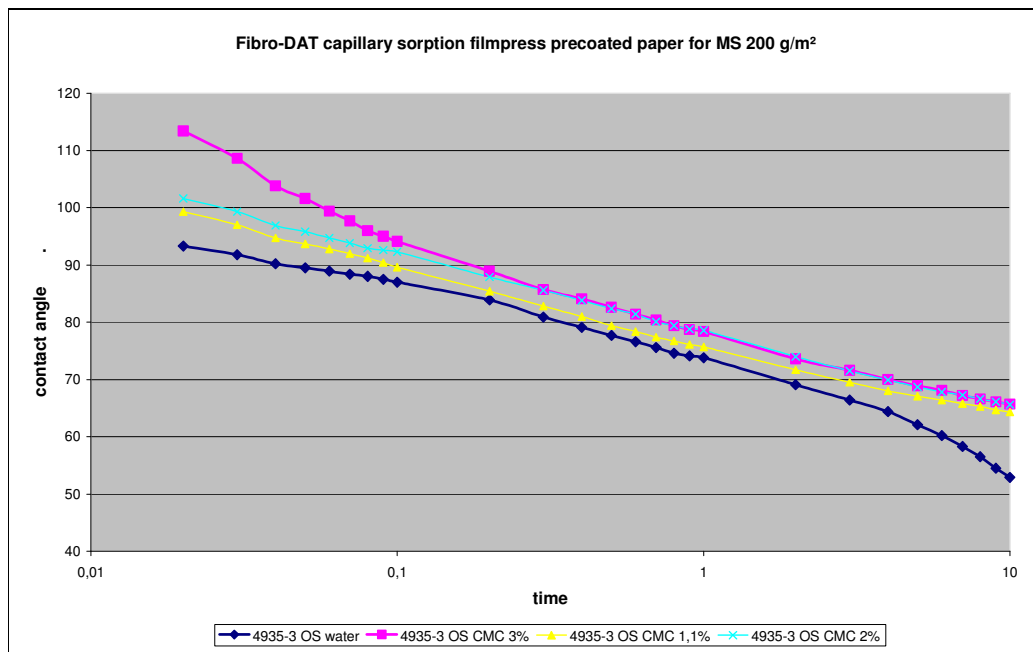
Pict. 5.5.2: Contact angle comparison of CMC solution with water
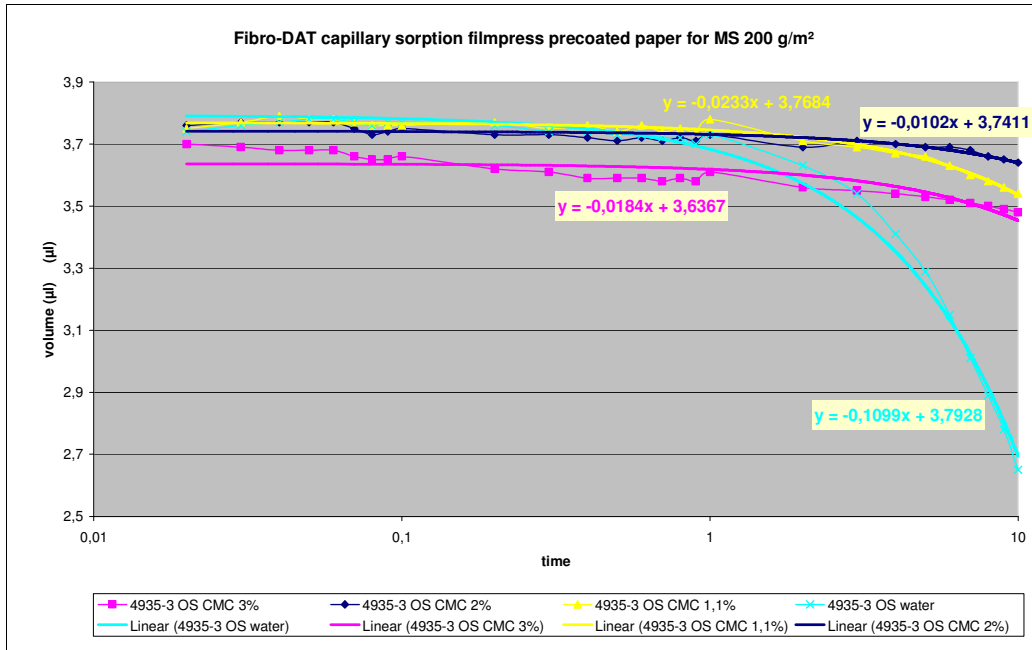
Pict. 5.5.3: Fibro-DAT of different liquids, top side of precoated paper PM11; 0,01 – 10 s; volume vs. log t
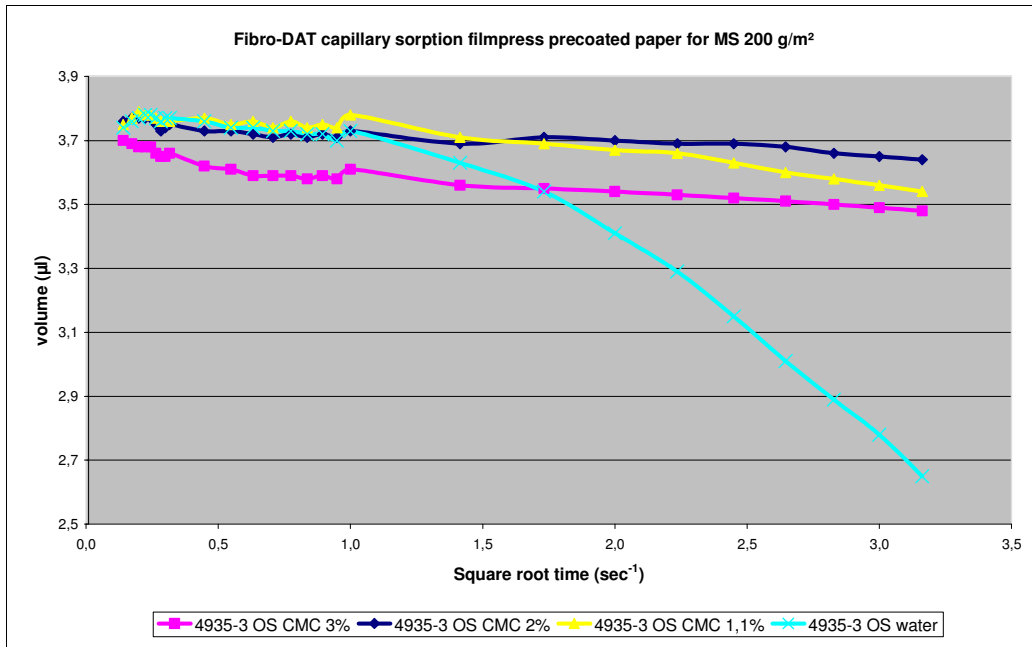
Pict. 5.5.4: Fibro-DAT of different liquids, top side of precoated paper PM11; 0,01 – 3s; volume vs. log t

Pict. 5.5.3 shows the drop of droplet volume due to capillary sorption of the substrate. A "wetting time" of approximately 1 sec was measured for all tested liquids on the

precoated paper. This period of time is needed to wet the capillaries of the substrate when a droplet of water based liquid is put pressure-less on the surface.

Pict. 5.5.4 – 5.5.6 show that after this wetting time a linear correlation between penetrated specific volume V/A and the square root of penetration time was measured when the test liquid was soaked through the pores of the precoating layer into the pores of the base paper fibres.
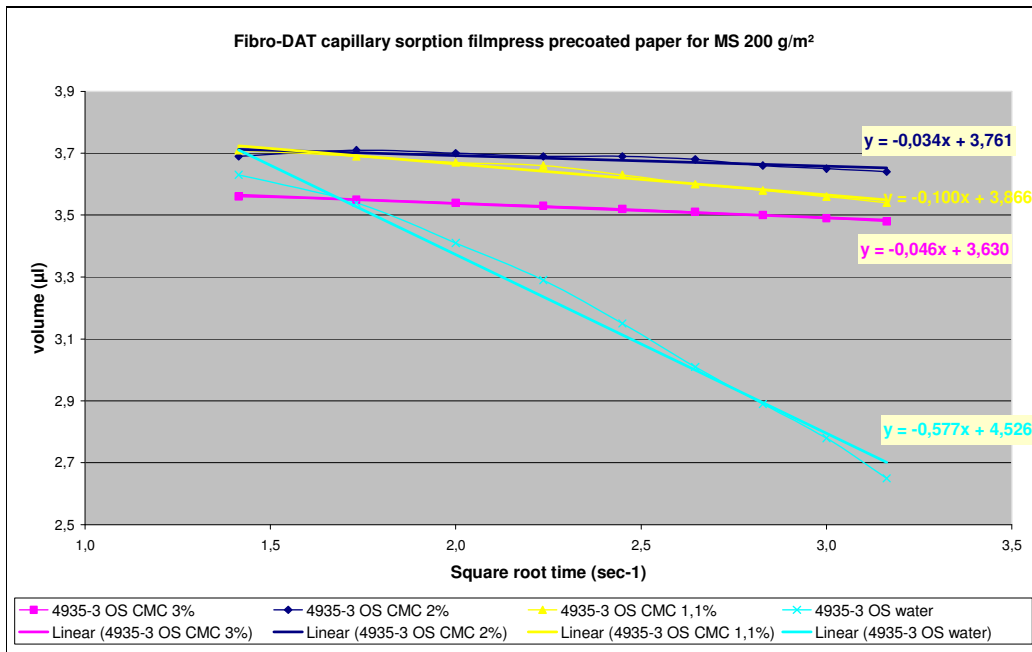
Pict. 5.5.5: Fibro-DAT 1 – 10 sec, top side of precoated paper PM11
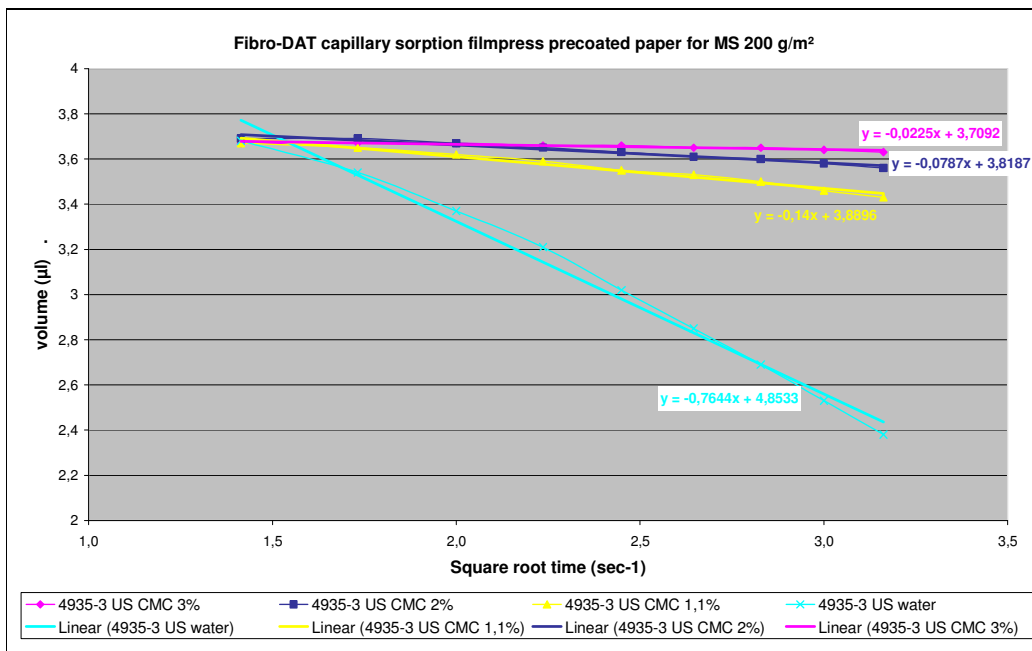
Pict. 5.5.6: Fibro-DAT 1 – 10 sec, bottom side of precoated paper PM11

The capillary sorption of top and bottom side of base paper PM11 was compared with the 3% CMC solution which corresponds to the liquid phase of the middle coating colour (pict. 5.5.7 – 5.5.10).
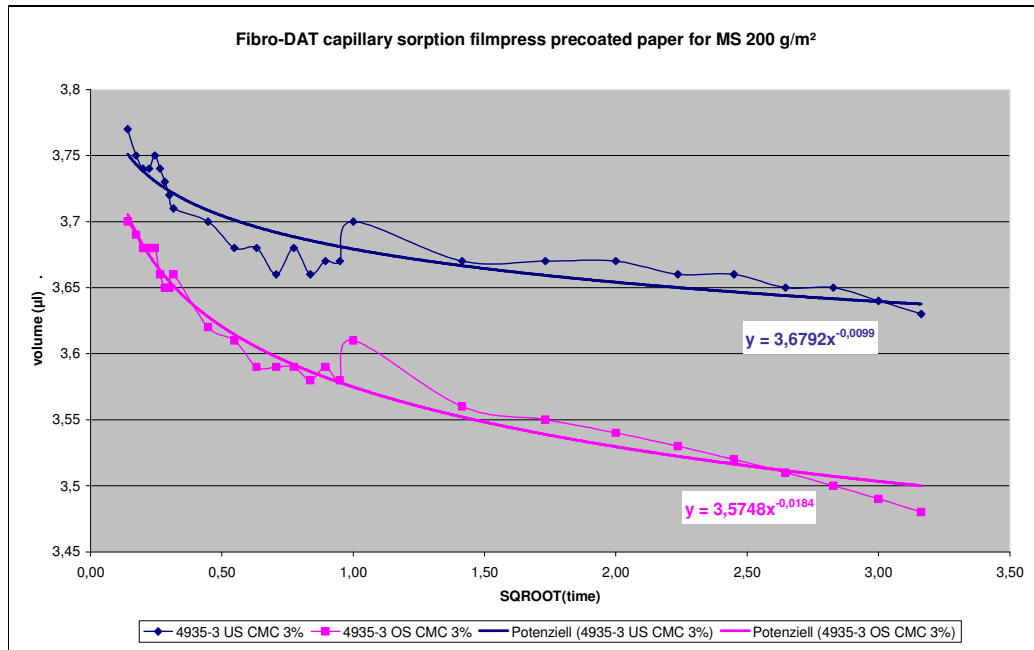
Pict. 5.5.7: Fibro-DAT V/A vs. square root of time for top side + bottom side, 0 – 10 s
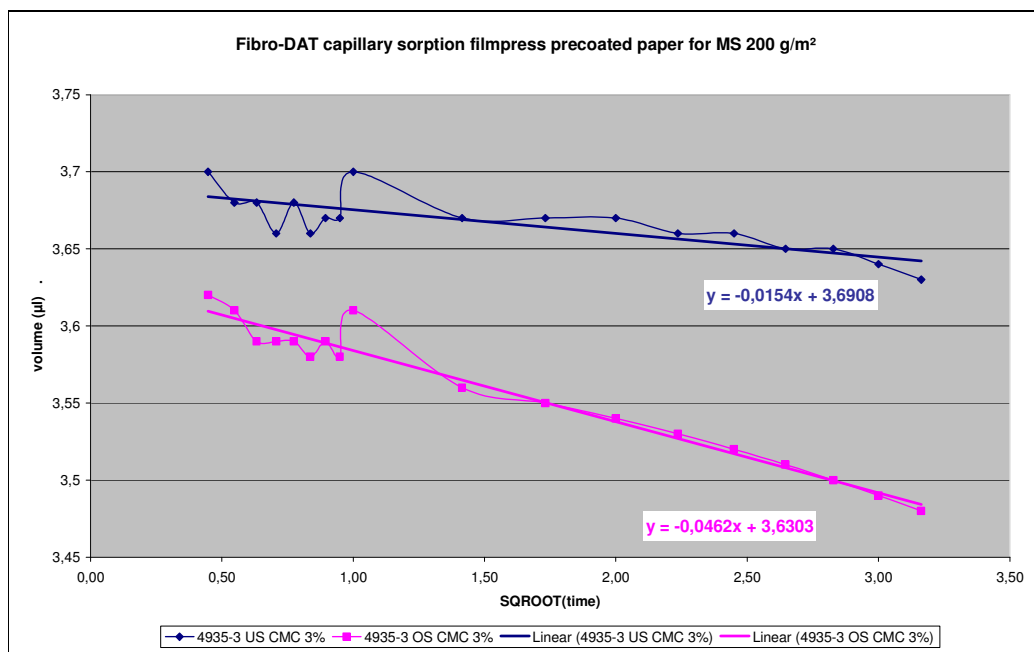
Pict. 5.5.8: Fibro-DAT V/A vs square root of time for TS and BS, 0,2 – 10 sec
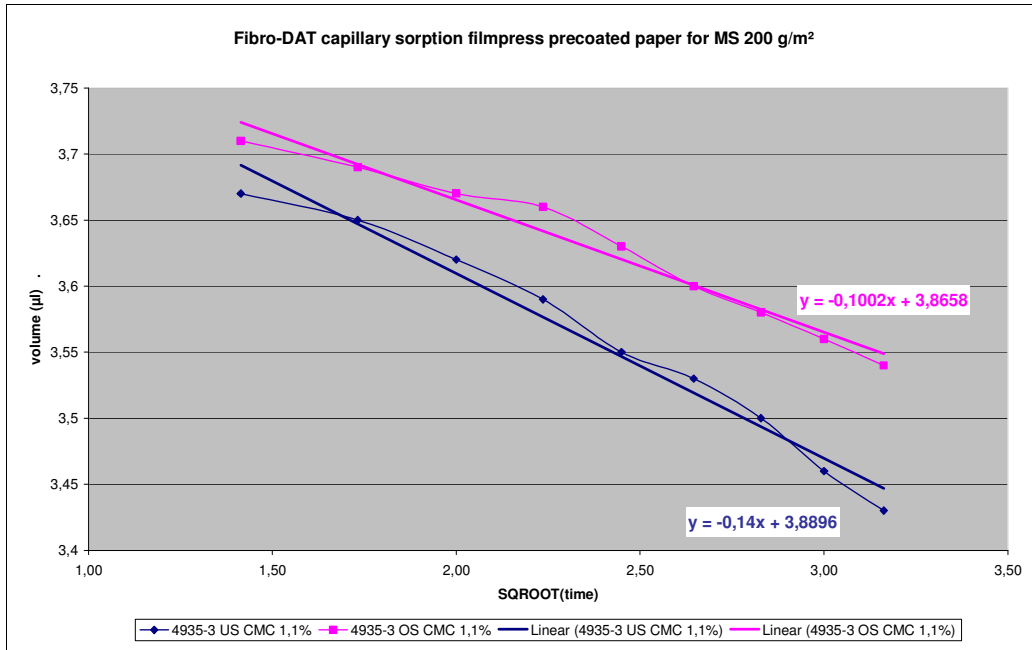
Pict. 5.5.9: Fibro-DAT V/A vs. square root of time for top side + bottom side, 0,2 – 10 sec, 1,1% CMC solution

PM11 precoated paper (11-4935-MR3) for 200 g/m²

	Fibro-DAT penetration flow rate (µl/sec)	
	Top Side	Bottom Side
Water	0,1253	0,1373
CMC 1%	0,0218	0,0277
CMC 2%	0,0078	0,0119
CMC 3%	0,01	0,0088
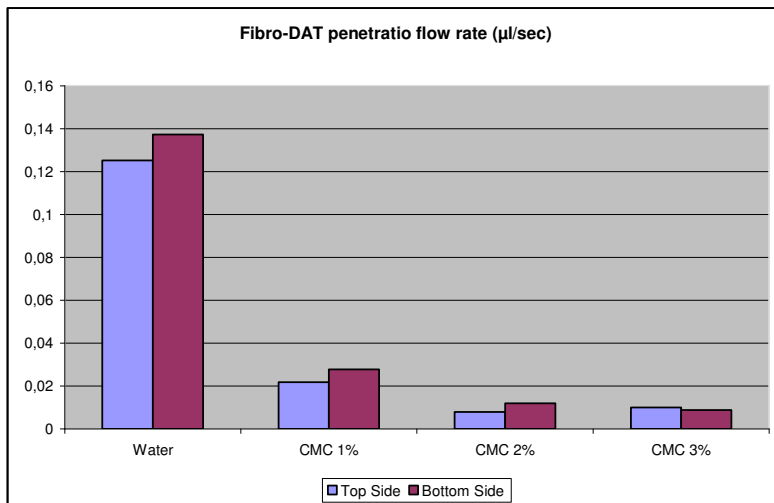
Pict. 5.5.10: Comparison of capillary penetration pressure of top and bottom side of precoated paper PM11

When top side of PM11 precoated paper was compared with bottom side, a lower penetration speed through the coating layer was detected for the top side although the coating layer is thinner on the top side (14 g/m² coat weight for BS, 11 g/m² for TS).

The reason is the higher base ash on the top side of the base paper which reduces the permeability of base paper surface at the top side and leads to better holdout if fines in the precoating layer, again reducing permeability of this coating layer.

Pict. 5.5.11 shows the ash distribution of a 100 g/m² PM11 base paper measured by sheet split into 8 layers.
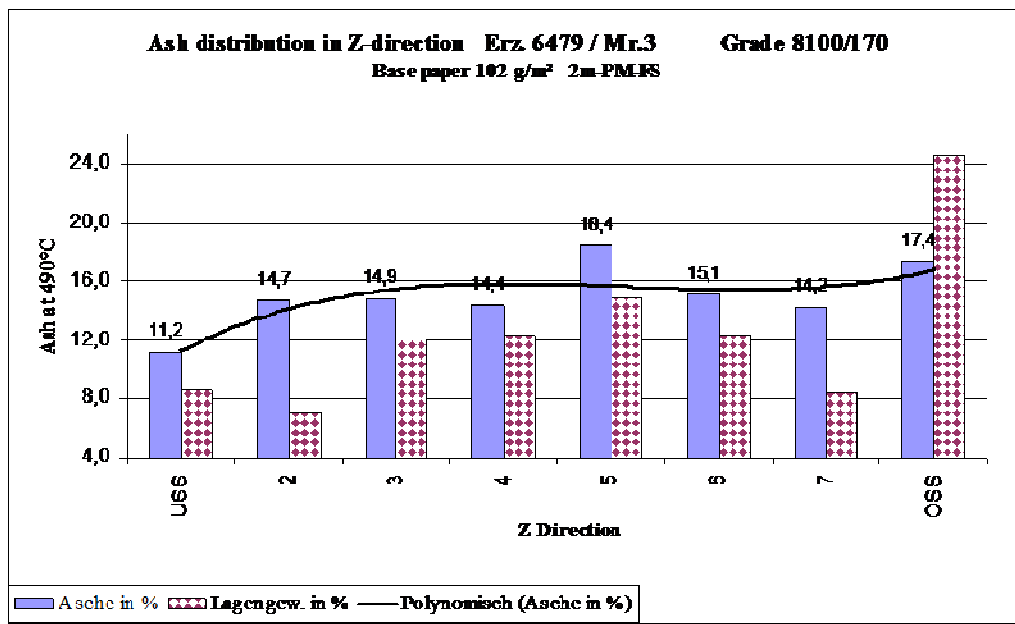
Pict. 5.5.11: Base ash two-sidedness PM11

Pict. 5.5.12 shows the calculation of capillary pressure for the four different liquids (water + CMC-solutions), which were applied on the precoated paper 11/4935-MR3 (120 g/m²):

Top side with 11 g/m² coat weight		Water	1,1% CMC	2% CMC	3% CMC	
Fibro DAT capillary sorption	Q=dV/dt	0,1253	0,0218	0,0078		µl/s
Fibro-DAT penetration area	A	3,73	3,74	3,73		mm²
Viscosity of Fibro-DAT liquid	η	0,001	0,005	0,012		Pas
Darcy coefficient of coating layer	K	6,0E-18	6,0E-18	6,0E-18		m/s
Avg. thickness of coating layer (per side)	L	6,20	6,20	6,20		µm
Darcy:	**dV/dt = (K x A x Δp) / (η x L)**					
Calculated sorption pressure	$p_{capillary}$	34712,2	30115,9	25930,3		Pa
--"--	**$p_{capillary}$**	**0,3**	**0,3**	**0,3**		**bar**

Bottom side with 14 g/m² coat weight		Water	1,1% CMC	2% CMC	3% CMC	
Fibro DAT capillary sorption	Q=dV/dt	0,1373	0,0278	0,0119	0,0088	µl/s
Fibro-DAT penetration area	A	3,73	3,74	3,73	3,61	mm²
Viscosity of Fibro-DAT liquid	η	0,001	0,005	0,012	0,018	Pas
Darcy coefficient of coating layer	K	6,0E-18	6,0E-18	6,0E-18	6,0E-18	m/s
Avg. thickness of coating layer (per side)	L	6,76	6,76	6,76	6,76	µm
Darcy:	**dV/dt = (K x A x Δp) / (η x L)**					
Calculated sorption pressure	$p_{capillary}$	41494,5	41850,8	43156,7	49462,6	Pa
--"--	**$p_{capillary}$**	**0,4**	**0,4**	**0,4**	**0,5**	**bar**

Pict. 5.5.12: Calculation of base paper sorption pressure from Fibro-DAT with Darcy equation for hydrophilic liquids with different viscosity

From this calculation the following conclusions can be drawn:
- Calculated capillary sorption pressure was similar for all tested liquids. Penetration speed falls with rising viscosity of the liquid according to Darcy's law.
- The bottom side of MSP precoated paper of PM11 showed higher capillary pressure due to worse holdout of precoating and less base ash at the base paper surface. To reduce the two sidedness of capillary sorption, coat weight of precoat is higher at bottom side than on top side.
- A weak point in this calculation is the fact, that the thickness of 1st precoating layer is not constant. REM pictures show many spots, where fibres are hitting the surface and coating layer thickness is zero. At these spots, fibres can absorb water unhindered by an insolating coating layer on top of them.

5.6 Calculation of precoating holdout

The theoretical bulk of a coated paper can be calculated by adding to base paper bulk the bulk of coating layer calculated by adding to the volume of the components the porosity measured by Mercury intrusion.

When this theoretical bulk is compared to the measured bulk of precoated papers at film press of PM11 the conclusion can be drawn, that app. 30% of the coating volume is lost into the base paper by pressure penetration (pict. 5.6.1).

Theoretical volume of coating layer:			
Density of pigment	ρ_{Pigm}	2650	kg/m³
Density of binder	ρ_{Binder}	1200	kg/m³
Density of air	ρ_{Air}	1	kg/m³
Coat weight		10	g/m²
Pigment content	c_{Pigm}	90	Mass-%
Binder content	c_{Binder}	10	Mass-%
Pigment weight on 1m²	M_{Pigm}	9	g/m²
Binder weight on 1m²	M_{Binder}	1	g/m²
Pigment volume on 1m²	V_{Pigm}	3,396E-06	m³/m²
Pigment volume on 1m²	V_{Binder}	8,333E-07	m³/m²
Sum volume pigment + binder on 1m²	V_{solid}	4,230E-06	m³/m²
Air content in coating layer (from Hg-poros.)	cv_{air}	35	Vol-%
Solid content	cv_{solid}	65	Vol-%
Air volume on 1m²	V_{air}	2,277E-06	m³/m²
Sum coating volume (air + pigment + binder) on 1m²	V_{total}	6,507E-06	m³/m²
--"--	V_{total}	6507	µl per m²
Fibro-DAT area of drop penetration	A_{drop}	2,2	mm²
Coating volume under Fibro-DAT drop	$V_{coating}$	**0,0143**	**µl**

Coating layer of MSP precoating PM11 with penetration into base:			
Thickness of coating layer (measured)	L	**4,2**	µm
Porosity of coating layer	ε	35	%
Area of Fibro-DAT drop	A_{drop}	2,2	mm²
Volume of coating layer under area A_{drop}	V_{max}	9,240E-12	m³
--"--	V_{max}	**0,0092**	µl

Coating layer of MSP precoating PM11 with ideal coating holdout:			
Thickness of coating layer (theoretical)	L	**6,5**	µm
Porosity of coating layer	ε	35	%
Area of Fibro-DAT drop	A	2,2	mm²
Volume of coating layer under area A_{drop}	V_{max}	1,430E-11	m³
--"--	V_{max}	**0,0143**	µl

Pict. 5.6.1: Calculating the theoretical thickness of coated paper

5.7 Comparing porosity of paper substrates with absorbed liquid volume

An important precondition for the shown calculations of capillary pressure is an unlimited reservoir in the capillaries of the substrate. The calculations in pict. 5.7.1 from the previously illustrated Fibro-DAT measurements show that the absorbed volume of the different tested liquids was significantly higher than the void volume of the precoating layer:

Coating layer of MSP precoating PM11 with penetration into base:			
Thickness of coating layer (measured)	L	4,2	µm
Porosity of coating layer	ε	35	%
Area of Fibro-DAT drop	A_{drop}	2,2	mm²
Volume of coating layer under area A_{drop}	V_{max}	9,240E-12	m³
--"--	V_{max}	0,0092	µl
Air volume in coating layer under area A_{drop}	V_{max}	3,234E-12	m³
--"--	V_{max}	0,0032	µl
Comparison: Drop volume of Fibro-DAT	V_{drop}	4	µl
Penetrated volume after 10 sec - water	V_{pen}	1,1	µl
Penetrated volume after 10 sec - CMC 1,1%	V_{pen}	0,2	µl
Penetrated volume after 10 sec - CMC 3%	V_{pen}	0,1	µl

Lab coating layer with 250 µm slot coater			
Thickness of base paper	L	200	µm
Porosity of base paper	?	35	%
Area of Fibro-DAT drop	A	2,2	mm²
Void volume base under area A_{drop}	V_{max}	1,540E-10	m³
--"--	V_{max}	0,1540	µl
Comparison: Drop volume of Fibro-DAT	V_{drop}	4	µl
Penetrated vol. after 10 sec - water on precoated paper	V_{pen}	1,1	µl
Penetrated vol. after 10 sec - CMC 1,1% on precoated paper	V_{pen}	0,2	µl
Penetrated vol. after 10 sec - CMC 3% on precoated paper	V_{pen}	0,1	µl

Pict. 5.7.1: Calculation of pore volume of base paper

Comparing the base paper void volume with the amount of liquid which had penetrated at the Fibro-DAT experiments, one can conclude, that void volume of base paper was much too small to pick up the Fibro-DAT liquid. The fibres must have swollen when they absorbed the liquid in the micro-pores of the fibre walls.

Theoretical volume of coating layer:			
Density of filler pigment	ρ_{Pigm}	2650	kg/m³
Density of fibre	ρ_{Fibre}	1200	kg/m³
Density of air	ρ_{Air}	1	kg/m³
Basis weight		120	g/m²
Pigment content	c_{Pigm}	20	Mass-%
Binder content	c_{Fibre}	80	Mass-%
Pigment weight on 1m²	M_{Pigm}	24	g/m²
Fibre weight on 1m²	M_{Fibre}	96	g/m²
Pigment volume on 1m²	V_{Pigm}	9,057E-06	m³/m²
Pigment volume on 1m²	V_{fibre}	8,000E-05	m³/m²
Sum volume pigment + binder on 1m²	V_{solid}	8,906E-05	m³/m²
Air content in coating layer (from Hg-poros.)	cv_{air}	43	Vol-%
Solid content	cv_{solid}	57	Vol-%
Air volume on 1m²	V_{air}	6,718E-05	m³/m²
Sum coating volume (air + pigment + binder) on 1m²	V_{total}	1,562E-04	m³/m²
--"--	V_{total}	156240	µl per m²
Fibro-DAT area of drop penetration	A_{drop}	2,2	mm²
Coating volume under Fibro-DAT drop	**$V_{coating}$**	**0,3437**	**µl**

Base paper:			
Thickness (measured)	**L**	**148**	**µm**
Porosity of coating layer	ε	43	%
Area of Fibro-DAT drop	A_{drop}	2,2	mm²
Volume of coating layer under area A_{drop}	V_{max}	3,256E-10	m³
--"--	**V_{max}**	**0,3256**	**µl**
Void volume in coating layer under area A_{drop}	V_{max}	1,40E-10	m³
--"--	**V_{max}**	**0,140**	**µl**
Comparison: Drop volume of Fibro-DAT	V_{drop}	4	µl
Penetrated volume after 10 sec - water	V_{pen}	1,1	µl
Penetrated volume after 10 sec - CMC 1,1%	V_{pen}	0,2	µl
Penetrated volume after 10 sec - CMC 3%	V_{pen}	0,1	µl

Pict. 5.7.2: Base paper pore volume vs. absorbed water at middle coaters OMC11

Comparing the Fibro-DAT results with capillary sorption of middle coating colour between jet application and blade at OMC11 (pict. 5.7.2) the major difference lays in the sorption time which is with 0,044 sec much shorter at OMC11 than at Fibro-DAT (10 sec.).

```
Fibro DAT (water):
Base paper                                    1,5      µl/s
Precoated with MSP                            0,18     µl/s
Double precoated wih MSP+blade                0,025    µl/s

Drop area A                                   3,35     mm²
Drop diameter D                               2,066    mm

Penetration time t between jet and blade      44,3     msec
--"--                                         0,044    sec

Penetrated water in t with Fibro DAT:
Base paper                                    0,066    µl
Precoated with MSP                            0,008    µl
Double precoated wih MSP+blade                0,001    µl

Penetrated water per m² in t with Fibro-DAT:
Base paper                                    19,8     g/m² = ml/m²
Precoated with MSP                            2,4      g/m²
Double precoated wih MSP+blade                0,3      g/m²

Penetrated water volume per m² with Fibro DAT:
Base paper                                    448      ml/(s x m²)
Precoated with MSP                            54       ml/(s x m²)
Double precoated wih MSP+blade                7        ml/(s x m²)

Pore volume:
Base paper                                    43       %
Precoated with MSP                            38       %
Double precoated wih MSP+blade                35       %

Pore volume:
Base paper                                    32       ml/m²
Precoated with MSP                            3,9      ml/m²
Double precoated wih MSP+blade                4,5      ml/m²
```

Pict. 5.7.3: Comparison of pore volumes and penetrated liquid volume at coater

Taking the Fibro-DAT sorption measurements on precoated paper and the sorption time between jet application and blade, the amount of liquid phase which penetrates the substrate at middle coaters of OMC11 can be calculated. The results shown in pict. 5.7.3 illustrate that the penetrated volume of liquid phase in MSP or blade coating process is smaller than the void volume of the precoating layer and much smaller than the pore volume in the base paper between the fibres.

The assumption can be made that the liquid from coating colour is sorbed by capillary forces into the pore of the precoating layer which are with a mean pore radius of 0,25 µm relatively small and create therefore a high capillary pressure. This assumption was checked in the next paragraph.

5.8 Determination of capillary sorption pressure of coating layer and base paper

To verify this theory the capillary pressure of the precoating layer has to be determined separately. In pict. 5.8.1 the capillary sorption of coating colours is compared with the sorption of the same colour applied on a base paper. Two coatings were testet: Rez. 87 is a precoating colour and Rez. 94 is a top coating colour. 100 µm of coating colour were applied on a plastic foil and capillary sorption was measured by Fibro-DAT. The result was compared to the corresponding Fibro-DAT measurements of precoated paper ("labgestr.") with the same coating.
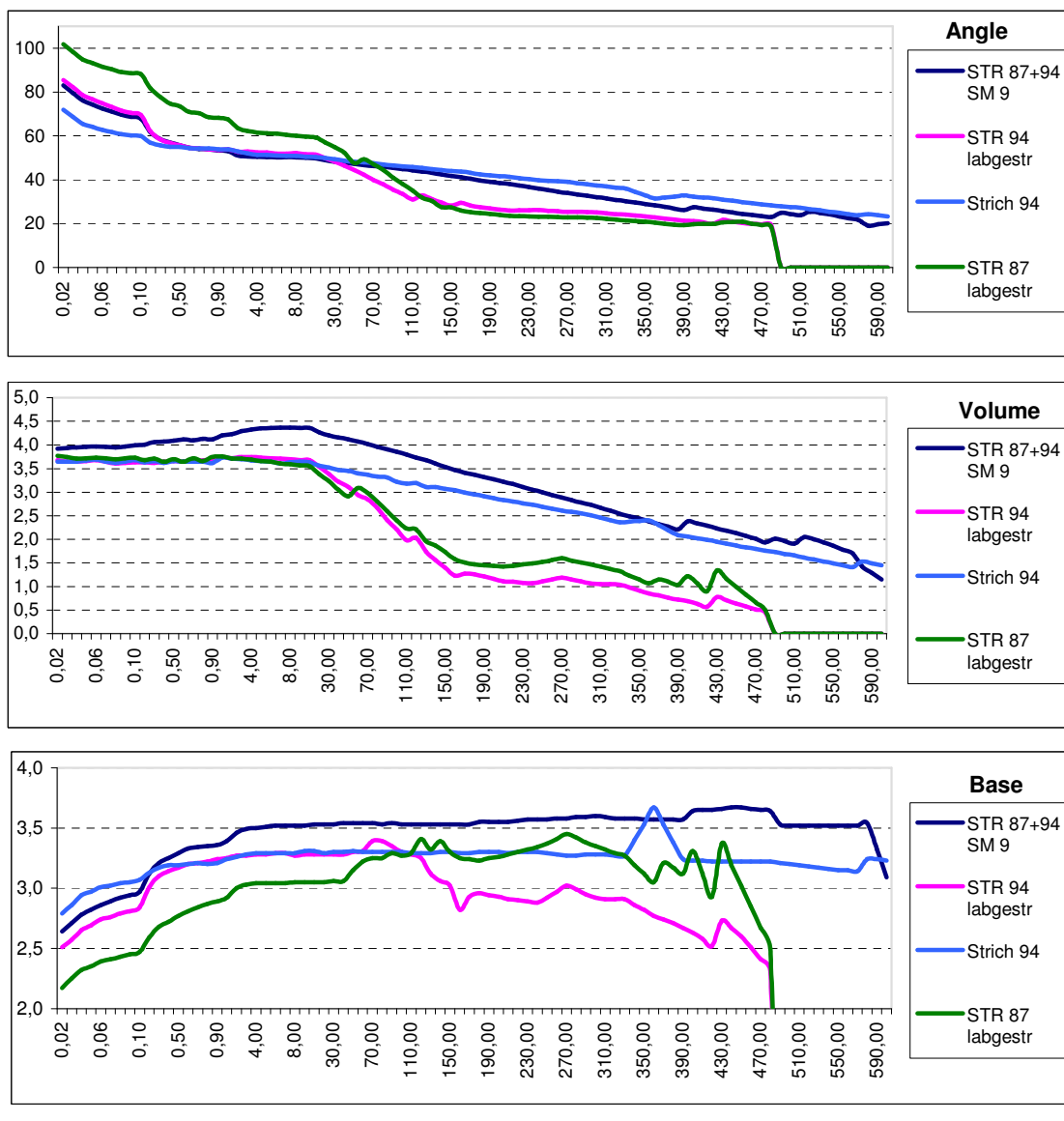
Pict. 5.8.1: Capillary sorption of coating layer

Fibro-DAT capillary penetration dV/dt of lab coatings

Rez. 87: starch based precoating
Rez. 94: Latex based top coating

Evaporation of liquid corrected
Penetration time: 150 - 300 sec
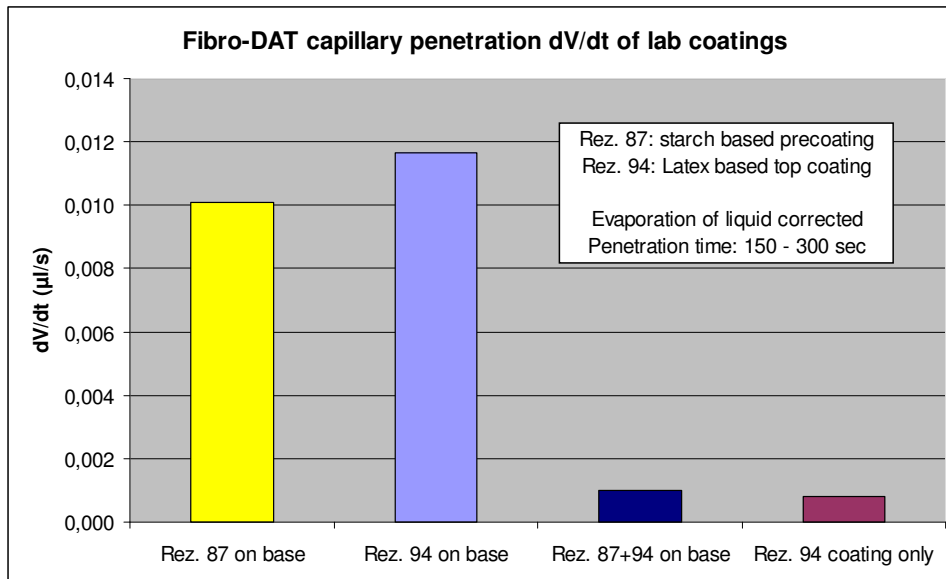
Pict. 5.8.2: Capillary sorption of lab coated papers, compared to coating films. Liquid for Fibro-DAT: Distilled Water (04-2009)

The pure coating colour no. 94 (glossy top coat) which was applied by a lab slot coater on a plastic foil showed almost no capillary sorption when compared to the precoated paper of PM11 with the same formulation.

The assumption in 5.7 that the whole liquid is absorbed by the capillaries of the precoating is therefore wrong. Coatings have a sponge like coating structure with many dead end pores and in consequence a relative low capillary pressure when compared with base papers where the pores in the surface of fibres are lower in diameter and tube shaped with endless reservoir.

Double coated base paper (with coating no. 87+94) was much lower in capillary sorption than the single precoated paper as highly absorbent fibres were effectively covered with a dense coating layer.

Assuming the precoating layer to act as an isolating layer which hinders water to penetrate into the base paper and by knowing its Darcy coefficient (see Prüfbau pressure penetration test), the capillary pressure of the base paper can be calculated by:

Darcy: $\dfrac{dV}{dt} = \dfrac{K * A * \Delta p}{\eta * L} \rightarrow \Delta p_c = \dfrac{dV}{dt} * \dfrac{\eta * L}{K * A}$

Page 164

Knowing the surface tension of the liquid and its contact angle, Lucas Washburn equation can be used to calculate fibre pore radius.

The calculated capillary pressure Δp_c from the Darcy equation has to be inserted into the Lucas Washburn equation:

$$\Delta p_c = \frac{2 * \gamma * \cos\theta}{r} \rightarrow r = \frac{2 * \gamma * \cos\theta}{\Delta p_c}$$

	Unit	Rez. 87 on base	Rez. 94 on base	Rez. 87+94 on base	Rez. 94 coating only
contact angle θ	°	60,50	52,06	50,24	50,97
--"--	rad	1,056	0,909	0,877	0,890
cos θ		0,492	0,615	0,640	0,630
dV	µl	2,01	2,25	1,20	1,14
dt	s	149,97	149,97	299,97	299,97
dA	mm²	2,92	3,14	3,40	3,23
dV evaporated in dt	µl	0,50	0,50	0,90	0,90
viscosity η	mPas	15	15	15	15
surface tension σ	mN/m	43	43	43	43
coating layer thickness	µm	10	10	20	
Darcy coefficient of coating	m²	1E-18	1E-18	2E-19	
dV/dt	**µl/s**	**0,0101**	**0,0117**	**0,0010**	**0,0008**
capillary pressure of fibres	Pa	517182,5	557836,1	441126,2	
--"--	bar	51,72	55,78	44,11	
capillary radius of fibres r	µm	0,17	0,15	0,19	

Pict. 5.8.3: Calculation of fibre wall pore radius from Fibro-DAT measurements

The result shown in pict. 5.8.3 fit well into the pore data's from literature (Sixta et al).

5.9 Comparing the capillary sorption of different base papers and coated papers

With the Fibro-DAT instrument the capillary sorption of different steps of paper production from base paper to top coated paper was measured (pict. 5.9.1).
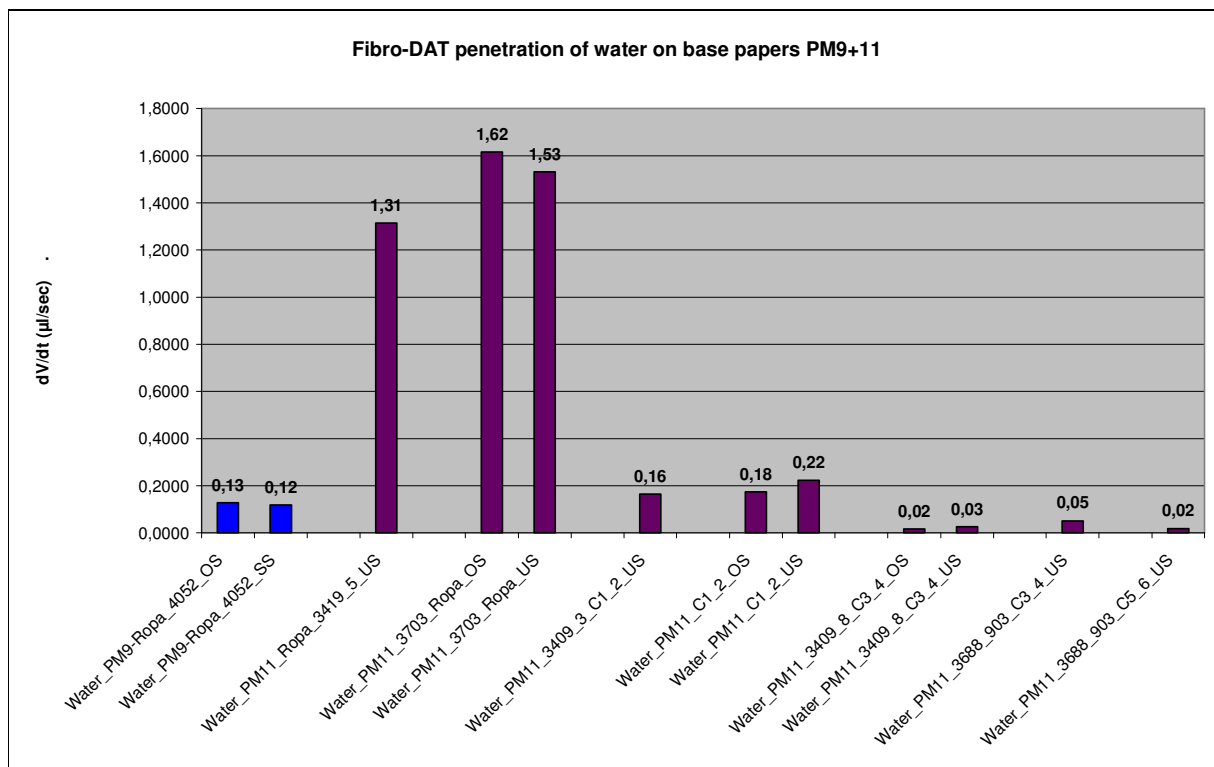
Pict. 5.9.1: Fibro-DAT water penetration dV/dt into different papers (C1/2 = precoated, C3/4 = middle coated, C5/6 = top coated)

Capillary sorption of un-sized base paper PM11 is a magnitude higher than that of AKD sized base paper of PM9.

A precoated paper sample of PM11 reaches the same level of capillary sorption pressure as the base paper PM9. Therefore coating colours thickening between application and blade at middle coaters of OMC11 is always as critical as for precoaters at OMC9.

Middle coating reduces capillary sorption again by a magnitude. In consequence no coating colour thickening was observed at top coaters of OMC11.

5.10 Influence of test liquid on capillary sorption
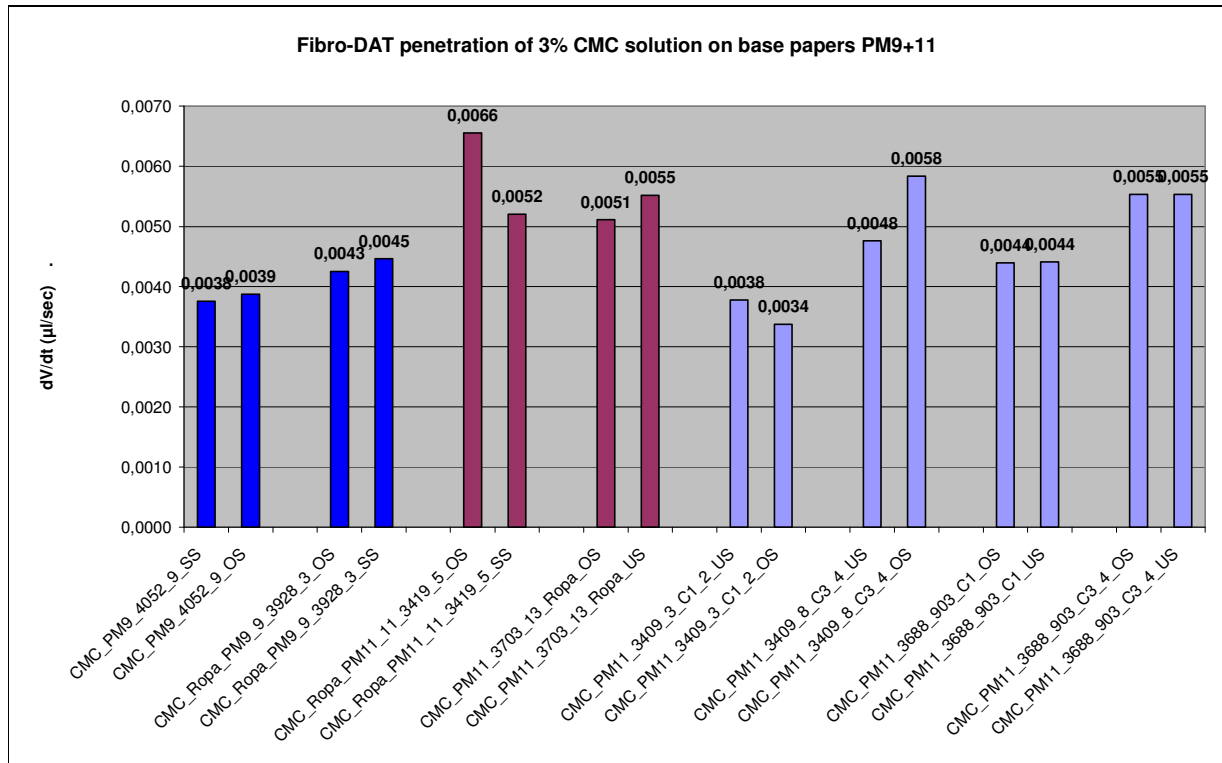
Pict. 5.10.1: Fibro-DAT penetration dV/dt of 3% CMC solution into different papers
(C1/2 = precoated, C3/4 = middle coated, C5/6 = top coated)

When a 3% CMC solution was used instead of water capillary sorption was reduced
by factor 300 and differences between the substrates were also reduced (pict.
5.10.1).
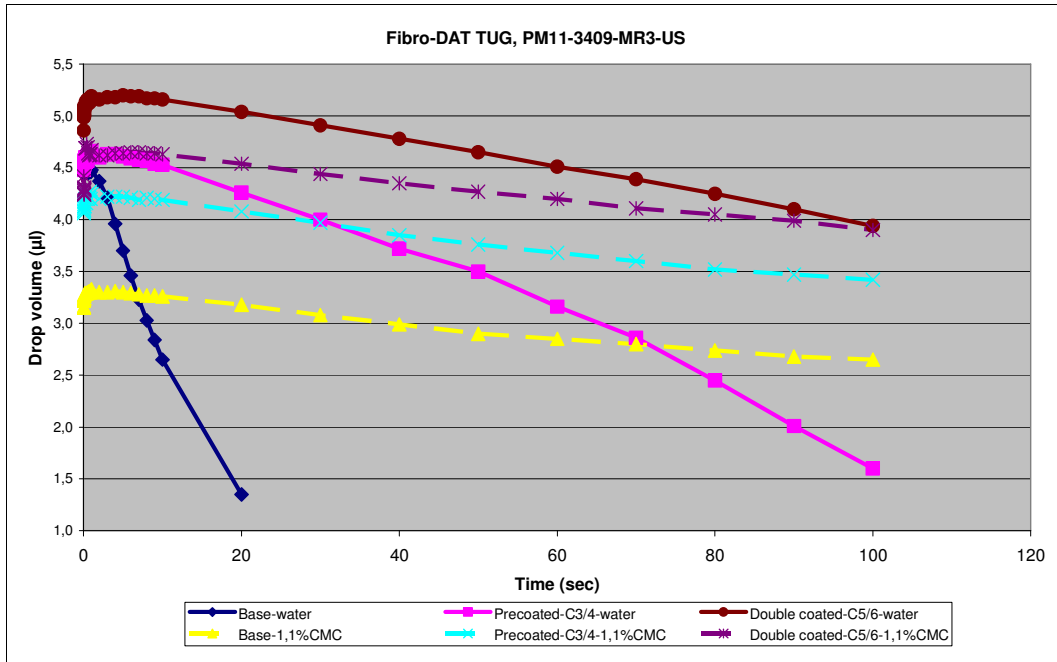
Pict. 5.10.2 : Fibro-DAT capillary penetration at base paper, precoated and double coated paper (0-100 sec)
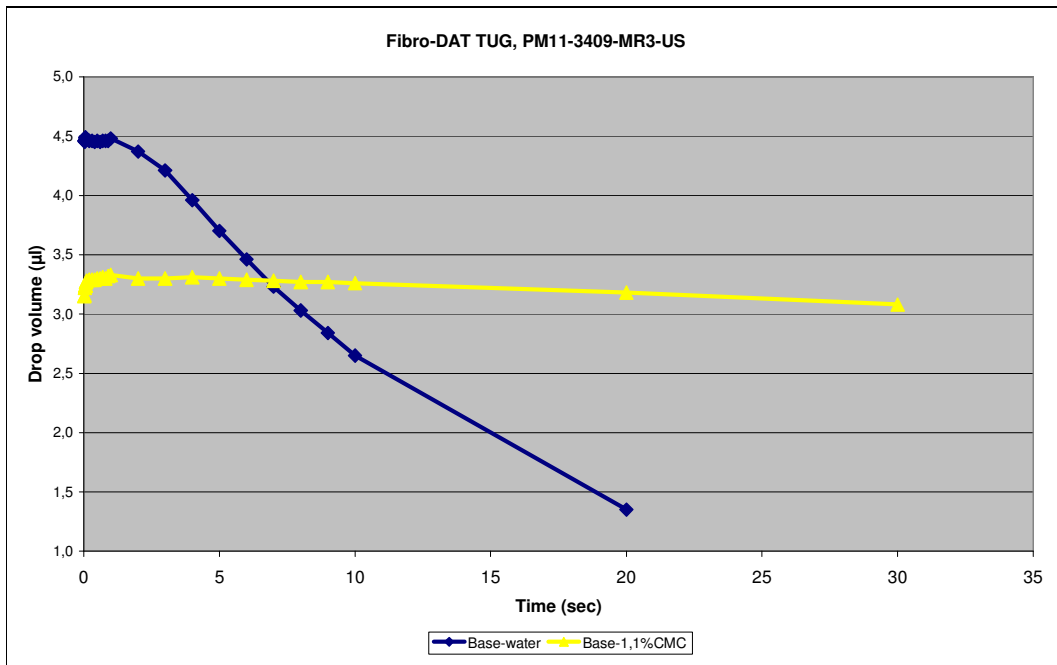
Pict. 5.10.3: Fibro-DAT capillary penetration at base paper with water and CMC solution

Wetting time is much higher for the CMC solution (10 sec) than for pure water (0,5 sec) because of higher contact angle for CMC (pict. 5.10.2 and 5.10.3).

This is of minor importance for mill coaters as wetting time is reduced by pressure application of the coating colour.

Contact angle at 0,1 sec. for different liquids and substrates

| | Basepaper | | | | Precoated | | | Topcoated | | | | Calandered | | | | | | | | | | | | | | | |

| 60 PL3 | 100 PL3 | 100 PL3 | 115 PL4 | 115 PL4 | 135 PL4 | 135 PL4 | 100 PL3 | 100 PL3 | 135 PL4 | 135 PL4 | 100 PL3 | 115 PL4 | 170 PL4 | 200 PL4 | 100 PL3 | 115 PL4 | 135 PL4 | 170 PL4 | 200 PL4 | 100 PL3 | 115 PL3 | 135 PL4 | 170 PL4 | 200 PL4 |

Offset Ropa, Star Ropa, Satin Ropa, Satin Ropa, Satin PM, Star PM, Satin PM, Star SM, Satin SM, Star SM, Satin SM, RRBP, Q-Gloss, Star, Satin

Wasser + IPA (20%) Oberflächenspannung 43,1 mN/m — CMC -Lösung (1,1 %) Oberflächenspannung 70,1 mN/m — Öl 002 Lösung Oberflächenspannung 35,0 mN/m

Pict. 5.10.4: Contact angle of water and CMC solution

An increase in contact angle from 60 to 89° by replacing water with a CMC solution (see pict. 5.10.4) leads to a 30 times lower cos θ (and in consequence lower capillary pressure Δp_c)!

This reduction in sorption pressure by using a CMC solution instead of water leads to a reduction of sorption speed into base paper in the same magnitude:
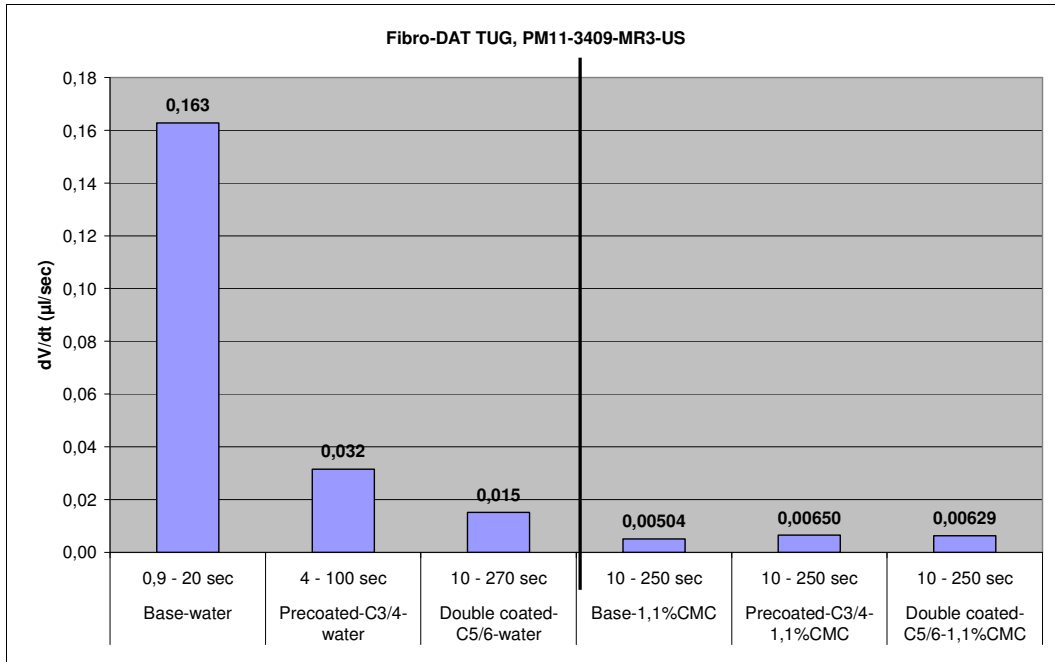
Pict. 5.10.5: Penetration speed from Fibro-DAT experiments

Capillary penetration of water is reduced when a coating layer is applied on the base paper. For the CMC solution the difference was lower (pict. 5.10.5).

The presented Fibro-DAT experiments with water at base papers were compared with the penetration tests of Pekka Salminen at the roll coater of Abo Akademi (pict. 5.10.6):
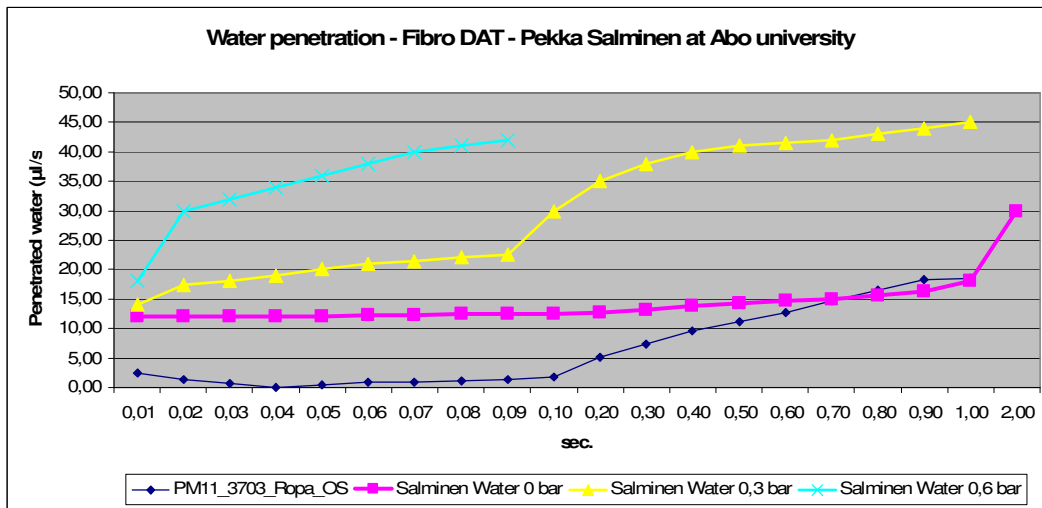
Pict. 5.10.6: Comparison of water penetration with Fibro-DAT and capillary penetration experiments of Pekka Salminen at Abo university

From these Fibro-DAT measurements with water on different coated substrates the capillary pressure was also calculated by the Darcy equation:

		Pre-coated	Pre- + Middle Coated	
Fibro DAT capillary sorption with water	Q=dV/dt	0,18	0,025	µl/s
Fibro-DAT penetration area	A	3,35	3,35	mm²
Viscosity of Fibro-DAT liquid (water)	η	0,001	0,001	Pas
Darcy coefficient of coating layer	K	6,0E-18	6,5E-19	m/s
Thickness of coating layer (per side)	L	4,274	8,500	µm
Darcy:	**dV/dt = (K x A x Δp) / (η x L)**			
Calculated sorption pressure	$p_{capillary}$	38274,6	97110,9	Pa
	$p_{capillary}$	**0,4**	**1,0**	**bar**

Pict. 5.10.7: Calculation of base paper sorption pressure from Fibro-DAT with Darcy equation for pre- and middle coated paper

The results shown in pict. 5.10.7 indicate a capillary pressure of un-sized fibres in the base paper PM11 of 0,4 bar, which is close to the results in literature. Pekka Salminen determined a capillary sorption pressure of 0,5 - 1bar for these kind of base papers.

When the Fibro-DAT measurements of double precoated paper are taken for this calculation, theoretical sorption pressure of base paper is much higher, which leads to the conclusion, that the middle coating layer adds capillary sorption pressure.

5.11 Calculation of base paper capillary sorption from mass balance of coating circuit

Another way to calculate the base paper sorption pressure is to take the results from the water sorption calculation between jet application and blade at the middle coaters of OMC11 into the same equation.

Parameter		Value	Unit	Comment
Speed of coating mashine		1600	m/min	
--"--		26,7	m/s	
Free draw between jet and blade		750	mm	
Area of free draw	A	6,375	m²	
Time between jet and blade	t	0,02813	sec	
Coated width	B	8,5	m	
Speed of coater		1600	m/min	
coated width of web		8,44	m	
coat weight dry		10	g/m²	
coat weight wet		13,89	g/m²	
measured solids in the working tank = feed to blade		**72,00**	**%**	
water in coating colour after blade		3,89	g/m²	
wet coating colour after blade		3,126	kg/s	
		8,42	ml/m²	Target: 10 - 15 ml/m²
volume flow to jet application		150	m³/h	
density of coating colour in working tank		1650	kg/m³	
wet mass flow to jet application		68,75	kg/s	
		185,1	ml/m²	Target: appr. 200 ml/m²
Ratio mass flow of feed to blade		*22,0*	*o.k.*	
coating colour at jet application		305,5	g/m²	
water at jet application		85,5	g/m²	
solids at jet application		219,9	g/m²	
Measured solids in the return flow from blade		72,20	%	From mass balance:
Mass flow before blade		68,8	kg/s	Coating kitchen 68%
coating colour before blade		305,5	g/m²	Working tank: 72%
water before blade		84,9	g/m²	
solids before blade		220,5	g/m²	
Calc. water penetration between jet and blade		**0,611**	**g/m²**	
Penetrated mass of liquid per m²	dM/dA	0,611	g/m²	from mass balance of working tank
Density of liquid phase in coating colour		1,1	g/cm³	from lab measurement
Penetrated volume of liquid per m²	dV/dA	0,672	ml/m²	
Time between jet application and blade	dt	0,02813	sec	
Darcy coefficient of precoated layer	K	6E-18	m/s	from Prüfbau pressure pen. test
Viscosity of liquid phase in coating colour	η = µ	0,005	Pa s	from lab meas. at delta solids 4%
Thickness of coating layer (per side)	L	4,274	µm	from thickness measurement
Darcy:	**dV/dt = (K x A x Δp) / (η x L)**			
Calculated sorption pressure	$p_{capillary}$	85099	Pa	
	$p_{capillary}$	**0,9**	**bar**	

Pict. 5.11.1: Calculation of base paper capillary sorption from mass balance around the working tank of middle coating station OMC11

The result shown in pict. 5.11.1 indicates again a similar capillary pressure of base paper fibres when compared with Pekka Salminen's experiments.

5.12 Reduce capillary sorption of base papers / precoated papers

To check the impact of capillary sorption on mottling droplets of water wer put on top of flocs and voids which were marked in a base paper of PM11. With the Fibro-DAT instrument the drop in water droplet volume was measured over time.
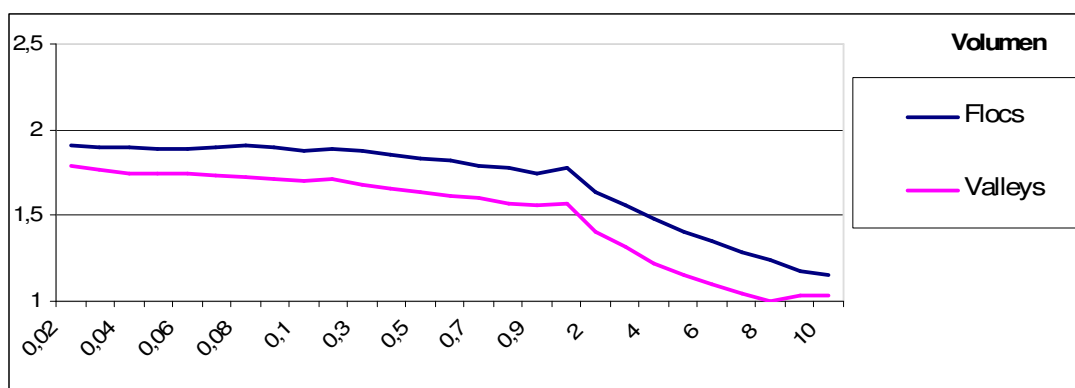
Pict. 8.8.1: Fibro-DAT capillary water sorption of flocs/valleys of base paper PM11 (Y-axis: droplet volume V, X-axis: time t)

The results shown in pict. 8.8.1 indicate no difference in capillary sorption between flocs and voids.
As shown later in the chapter "blade coating" an immobilized coating layer before the blade, created by capillary sorption of base paper fibres, lowers the penetration of liquid phase from coating colour into the base and improves thereby the runability of the coating colour.

To lower capillary sorption of base paper would improve therefore mainly the runability of a coating colour as solids under the blade drops.

W. Windle and K.M. Beazley (L1.3) stated that liquid penetration without external pressure depends on:
- Ability of the liquid to wet the paper surface
- Viscosity of the liquid
- Pore size of the paper

- Pore size of the filter cake
- Interaction of water with latex and pigment
- Amount of free water in the coating colour

The authors showed that under pressure latex and water migrate together into the base paper with the exception when pigment affine latices were used.
Pressure migration was independent on surface tension but a function of viscosity.

K.M. Beazley (L1.4) continued the work with a modified Warren tester. Conductivity was measured on the reverse side of the tested base papers to detect liquid penetration depth with increasing time. The results showed increased capillary penetration of water for base papers with higher base ash. According to Lucas Washburn capillary penetration increases with falling pore radius of substrate. This occurs with increasing filler content of base papers.

Milton Voelker from Consolidated paper (L1.5) studied the coating penetration into lab base sheets with a lab blade coater.
The higher the beating energy, the lower the base paper porosity was and the better the coating holdout.
Internal sizing and wet end starch had no influence on coating penetration. The absorption of liquid water phase of coating colour by the base paper led to an expansion (increase in thickness and porosity).

E. Bohmer and J. Lute from Billerud RD (L1.6) used a modified SD-Warren water retention tester to investigate liquid phase penetration by capillary pressure of coating colours into base papers. The positive impact of natural and synthetic thickeners on water retention could be enhanced when more latex was used. All thickeners and latices which increase contact angle were slower in capillary penetration of the corresponding coating colour according to Lucas Washburn equation.

Doeung Choi, Shri Ramaswarmy analysed pressure and capillary penetration into base papers (L1.8). They sucked water into a paper edge and measured V versus t. Darcy's law could be proved: V^2 and t showed linear correlation. Pressure-less

penetration gave a capillary pressure of 0,3 – 0,4 bar which fits well to later studies by Salminen et al. AKD internal sizing reduced capillary sorption of the fibres remarkable. Wet strength resins had no impact on initial sorption but reduced fibre swelling avoiding an increase in capillary sorption with time.

To reduce capillary sorption the following solutions can be suggested from the illustrated Fibro-DAT measurements:

a) Contact angle of the coating colour on fibres should be increased by using the right additives in the coating colour (e.g. CMC)

b) Surface tension of the liquid phase should be increased (avoid tensides)

c) Viscosity of the liquid phase should be increased without raising the high shear viscosity too much (see chapter 10 "water retention")

d) Darcy coefficient of the precoating layer should be lowered (see chapter 9 "dense precoatings")

e) Thickness of the isolating precoating layer on the base paper should be increased (This effect can be clearly seen at OMC11: Grades with higher basis weight show less thickening of coating colour before the blade due to higher precoat weight)

f) Fibre sorption should be reduced e.g. by sizing or beating or predrying of the fibres in the pulp mill (see paragraph 5.12)

Ad f) – Reduce fibre sorption by internal sizing:

Y. Jiang and T. Amari (L1.66) studied capillary sorption of water based inks into internal sized base papers.
Ink penetration was noticeable reduced with increasing degree of internal sizing although no difference in Mercury porosity was measured between the tested base paper samples.
Therefore the reduction in ink penetration by internal sizing is mainly caused by covering the fibre surface with hydrophobic substances closing the intra-fibre pores.

To detect the difference between internal sized and un-sized papers the base papers of PM9 (hard internal sizing with Cobb60 = 20 g/m²) and PM11 (un-sized) can be compared with Fibro-DAT (pict. 5.12.1 and 5.12.2).
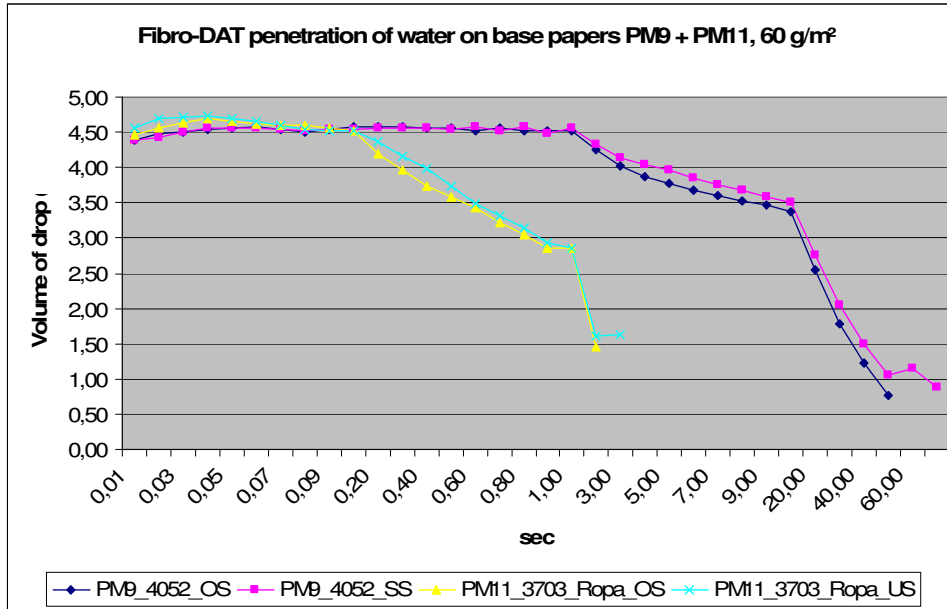
Pict. 5.12.1: Fibro-DAT water penetration into sized base paper PM9 and unsized PM11
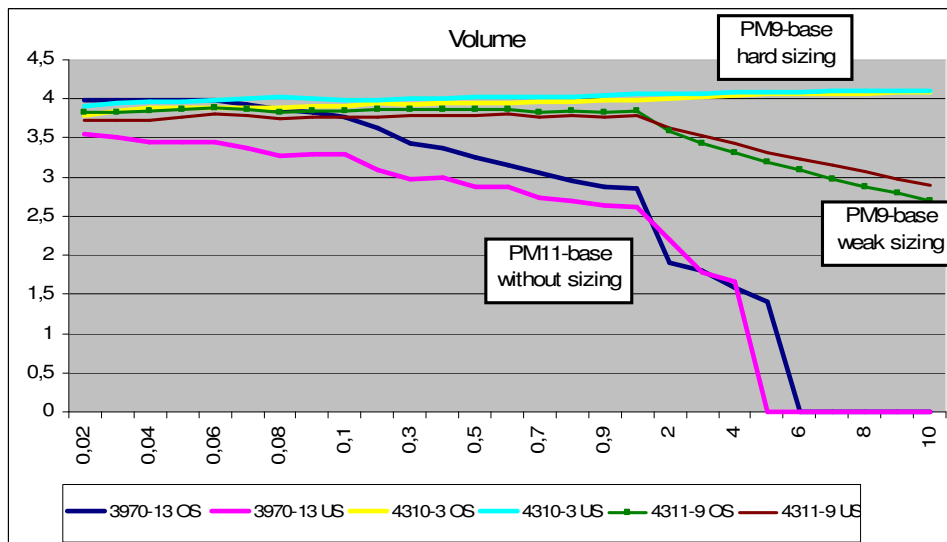
Pict. 5.12.2: Effect of AKD sizing on capillary sorption of water

Prüfbau Water Penetration Test
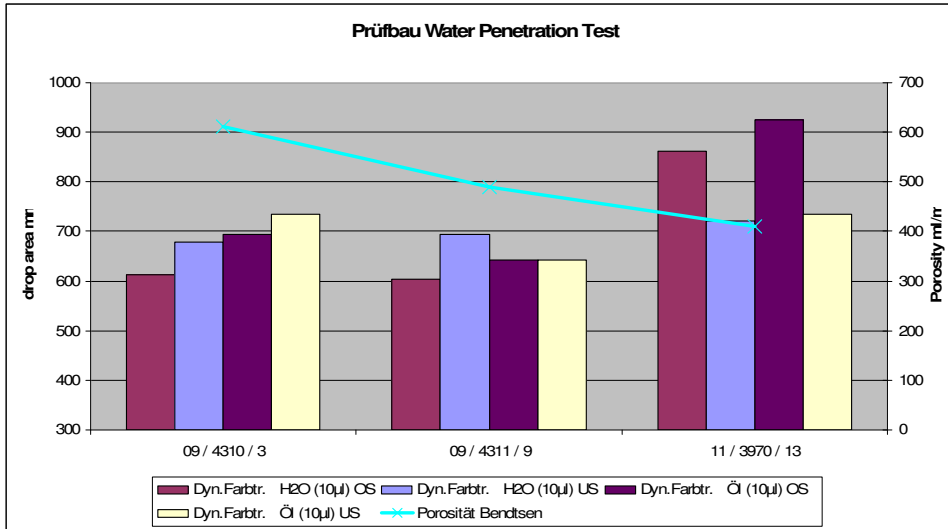
Pict. 5.12.3: Prüfbau pressure penetration test of different base papers

The comparison of the penetrated liquid volume in pict. 5.12.3 shows the independency of the pressure penetration and capillary sorption. The dense base paper of PM11 with lower air porosity has a higher pressure penetration resistance compared to the open PM9 base papers (same basis weight). Capillary sorption was the opposite: It was much lower at the hard sized PM9 base paper than for the un-sized PM11 base paper. Lower amount of AKD at PM9 leads to higher fibre water sorption.

AKD sizing clearly reduces fibre sorption when it is fully developed. Unfortunately this happens rarely in practice as time interval between paper production and online or offline coating is too short. That's the cause for thickening of pre-coating colours at OMC9, even at high amounts of AKD. ASA sizing is advantageous as it delivers instant sizing and could therefore reduce runability problems at pre-coaters with too high solids under the blade.

Okubayashi and Griesser (L7.3) studied the water uptake of Lyocell and viscose fibres.

The increase in amorphous fibre fraction, in pore volume, in surface area and additional sorption sites heightened the total extend of moisture sorption. Covering the fibres with spinning agents or drying them at high temperatures reduced sorption. Viscose fibre showed higher water uptake at 60% RH and higher moisture regain than Lyocel fibre due to lower crystallinity.

Water retention measurements with a centrifuge correlated well with water uptake of the fibres at 60% RH.

Ad f) – Reduce fibre sorption by refining of fibres:

A cheap way to reduce base paper sorption is beating in LC or HC refiners.

Cross cuttings analysed by microscope of lab sheets with beaten and unbeaten fibres at TUG showed that fibre wall thickness is reduced by 10 – 30% by refining, depending on the beating degree. This removal of fibrils leads simply to less capillary pores in the fibre wall and therefore to reduced capillary sorption.

Additionally the surface capillaries, the pits, are "smeared" or blocked by mechanical friction between fibre surface and refiner plates.

T. Bither and J. Waterhous (L7.7) showed the reduction of intra-fibre pores in fibre walls by refining. Water sorption of fibres is reduced by beating due to closing the fibre wall surface with mechanical energy. Fibre wall thickness is reduced by rubbing off fibrils. With falling thickness of the fibre wall the number of intra-fibre pores between the fibrils is reduced in the same extend.

Additionally the fines, which were created by beating, close the inter-fibre pores in the fibre network.

L. Paavilainen from RD Jakko Pöyry (L7.8) tried to find the optimal strength properties of reinforcement pulps were.

To increase strength wet fibres should collapse easy and should be as flexible as possible to increase bonding area during sheet forming and pressing. This is achieved by fibre beating where the cell wall thickness is reduced and fibres get therefore more flexible.

Stiff fibres with high cell wall thickness show low collapsibility and flexibility but the potential to delaminate the fibre wall by refining is bigger than for elastic fibres – the amount of generated fines by refining increased with rising stiffness of fibre wall.

Unfortunately only 5 – 10% of the fibres are treated in conventional refiners. Increasing the cutting length by new plate designs and increasing the number of refiners in series can successfully reduce capillary sorption.

Different types of fibres were beaten by Valley-Beater and capillary sorption of corresponding lab sheets was measured by Fibro-DAT instrument. Results are sown in pict. 5.12.4 and can be compared with other paper paramters shown in pict. 5.12.5 – 5.12.7).
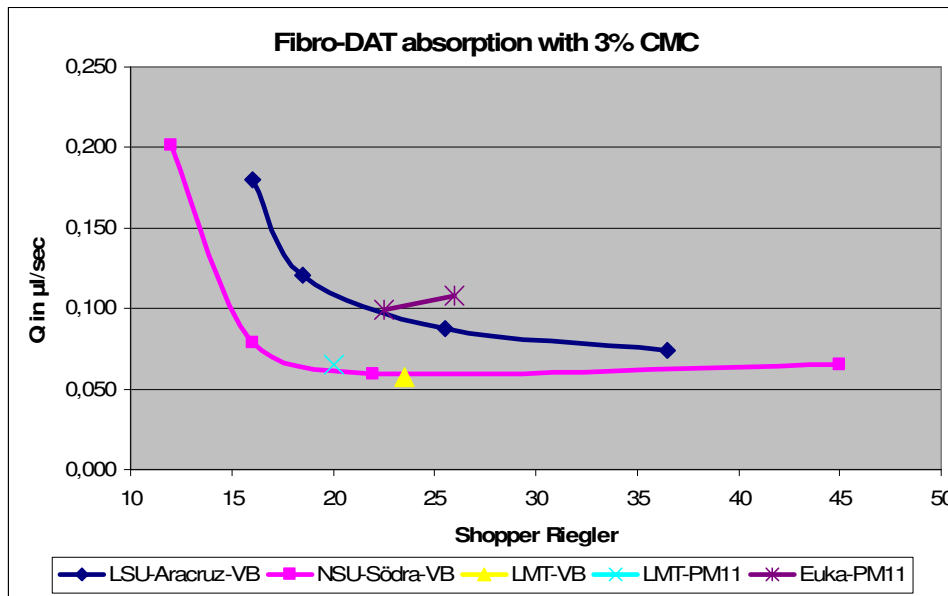

Pict. 5.12.4: Reduction of water sorption with beating of fibres (Fibro-DAT)

Pict. 5.12.4 shows that unbeaten fibres are extremely absorbent. With beating of the fibres the capillary sorption drops exponentially and levels out at a threshold of 20
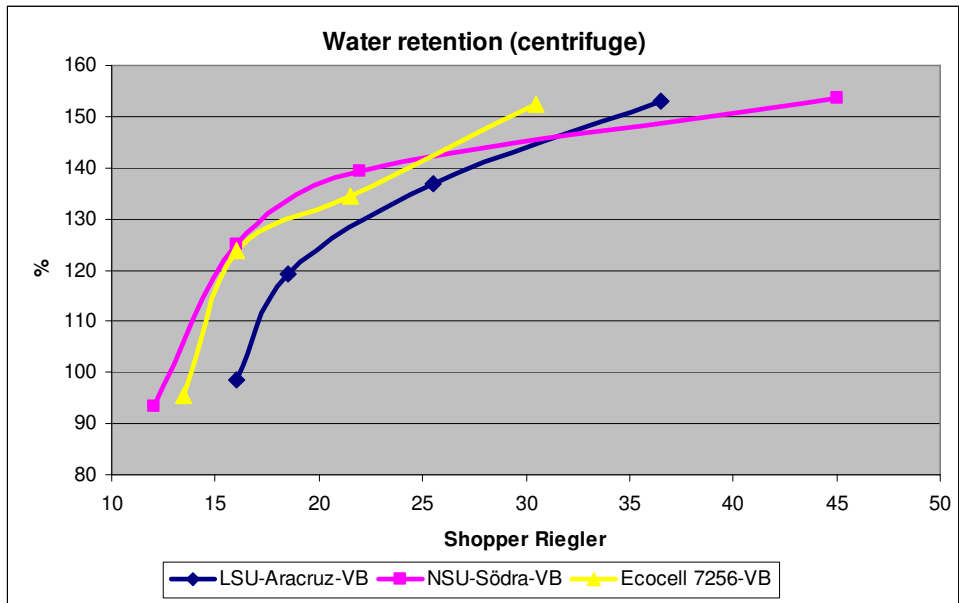
SRE for long fibre pulps and 35 SRE for short fibre pulps. Eucalyptus short fibre is more absorbent that long fibre pulp (NSU = NBSK, LM = Ecocell).
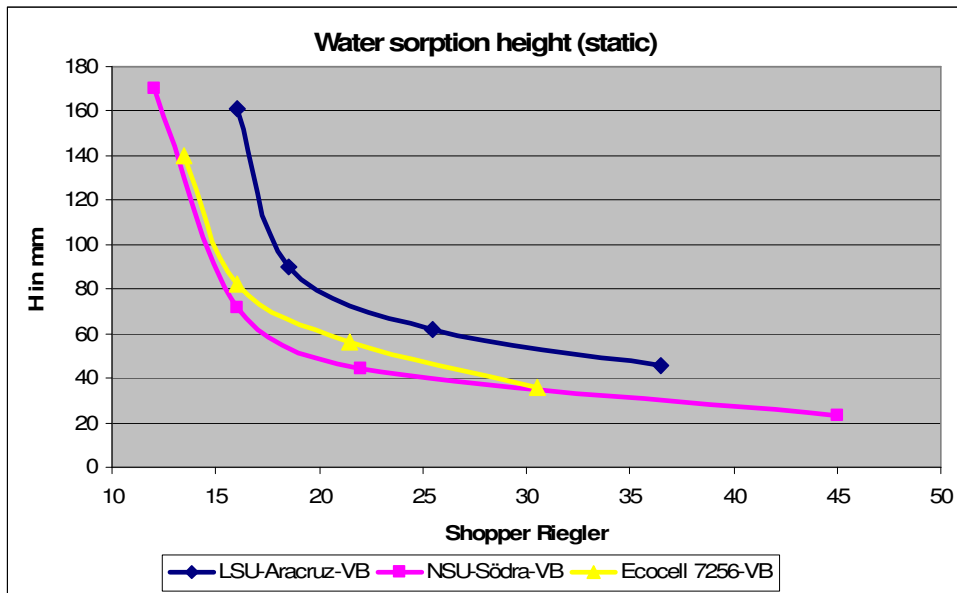
Pict. 5.12.5: Reduction of water sorption with beating of fibres (Suction height)
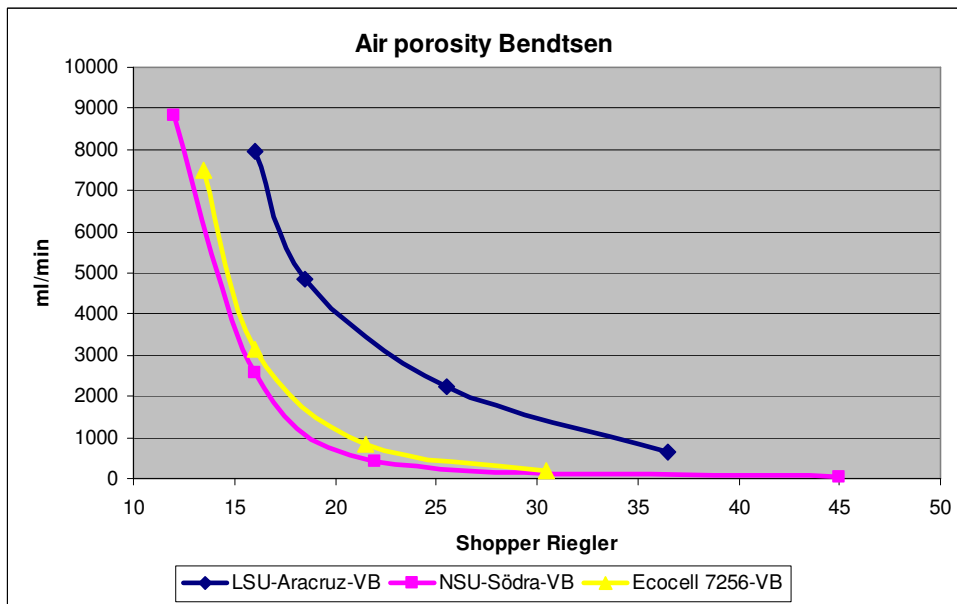
Pict. 5.12.6: Bendtsen porosity of lab sheets with different beating degree

Pict. 5.12.7: Water retention of fibres with different beating degree

In many mills air porosity of base paper is measured and limits are setup to avoid extensive water sorption from coating colour at the first precoating stations. The assumption is made that the lower the base paper air porosity, the less water will be absorbed.

Trials at PM11 showed that this assumption is wrong. Water penetration before the blade was independent on base paper porosity, when changed by refining energy:

	Unit	15.10.06 - 5.4.07	15.4.06 - 15.10.06
Avg. porosity base paper	ml/min	**575**	**400**
FGH-VB 200	%	67,9	67,74
FGH-AB-C3	%	68,9	69,5
FGH-AB-C4	%	69,7	70,4
Delta FGH AB-C3 to VB	%	**1,0**	**1,8**
Delta FGH AB-C4 to VB	%	**1,8**	**2,7**
Binder VB 200	%	11,7	12,11
Binder AB-C3	%	10,4	10,6
Binder AB-C4	%	10,2	10,3
Binder loss in AB-C3	%	**-1,3**	**-1,5**
Binder loss in AB-C4	%	**-1,5**	**-1,8**
Brookfield Viscosity AB-C3	cp at 20Rpm	3860	4075
Brookfield Viscosity AB-C4	cp at 20Rpm	4060	4378

Pict. 5.12.8: Comparison of coating colour thickening before the blade for base papers with low and high porosity

Bendtsen porosity can be used as an indication to control the absorbtivity of a base sheet but it doesn't correlate totally with paper sorption (pict. 5.12.8).

Ad f) – Reduce fibre sorption by drying of fibres in pulp mill:

In an integrated paper mill never dried pulp is often used with higher capillary sorption of fibre wall.
Drying of fibres to solids over the fibre saturation point leads to a hornification of the fibre wall surface and pores are closed.

Erik Baggrud and Stig Stenström (L7.4) established a model of moisture gradients for convective drying of industrial pulp sheets.
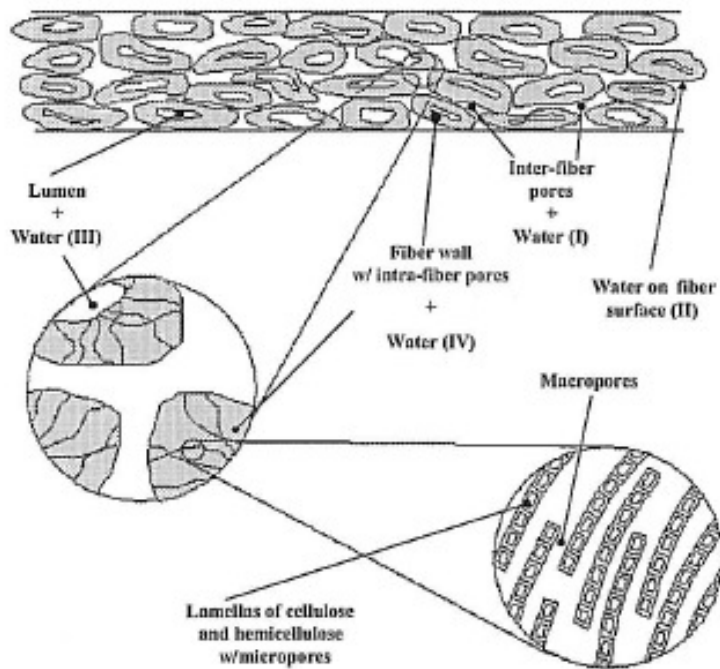
Pict. 5.12.9: Fibre wall structure

Three kinds of pores in fibre networks can be distinguished into the following groups as shown in pict. 5.12.9:

 a) Lumen in each fibre.
 b) Inter-fibre pores: Space between the single fibres or in the fibre network.
 c) Intra-fibre pores: Situated in the fibre wall. Diameter is less than 0,1 µm.

With the solute exclusion method one can measure the pore size of the cell wall and the fibre saturation point (FSP), which gives the amount of water in the fibre wall.

Pure wood has a FSP of 0,4 g H_2O / g dry wood.
Pulps have a FSP of 1 – 2 g H_2O / g dry

Another method to measure the FSP is the WRV with a centrifuge. The results are the same.

Differential scanning calorimetry (DSC) is used to characterize the three types of water in paper:

  a) NFW – non freezing water
  b) FBW – freezing bound water, which freezes below free water
  c) BW – bulk water with freezing point equal to water

NFW and FBW are located in the micro pores (25 A). Chemical binding and physical capillary pressure depress the freezing point.

BW is located in the macro-pores. BW increases with lower yield in pulping, increased refining energy and corresponds with an increased FSP.

Dried and rewetted pulps have a lower FSP than never dried pulps as macro-pores close irreversible.

At 0,5 – 0,8 g H_2O / g dry fibre all BW is removed and at 0,24 – 0,28 g H_2O / g dry fibre only NFW is left in the fibre wall.

In a modern press section a dry content of 40 – 50% is reached, which corresponds to 1,5 – 1,0 g H_2O / g dry fibre. It is in the same range as the FSP. Therefore most of the water will be situated within the fibre wall after the press section.
Removing further water in the drying section closes the macro-pores and reduces capillary sorption.

For highly swollen sheet water is transported during drying from fibre to fibre through fibre bonds. When the fibres collapse, the drying rate drops dramatically.

G.V. Laivins and A.M. Scallan from P&P RD Quebec (L7.6) measured the fibre saturation point (FSP) by using a dextrane liquid which didn't penetrate into the intra-fibre-capillaries in the fibre wall due to higher particle diameter (regulated by the molecular weight) than pore diameter. The dextrane molecules could be detected by during the dewatering experiments due to high optical rotation. At the FSP all inter-fibre water containing dextrane molecules was pressed out. When pressing was continued only pure water from intra-fibre-pores was detected in the filtrate. The ratio

of inter-fibre-water and intra-fibre-water removal could be determined with this method.

Nylon fibres contained a high amount of inter-fibre water, which dropped fast during pressing. No intra-fibre water could be determined.

Craft pulp fibres show a similar behaviour for removing the inter-fibre water at the start of the pressing process but a certain amount of intra-fibre water remains, which is extremely difficult to remove. When kappa number was lowered in cooking and pulp yield dropped to 65% a large increase of intra-fibre water was measured as the pore volume in the fibre walls was increased.

M.C. Asensio, J. Seyed-Yagoobi and C.C. Tijerina (L7.1) used water retention measurements with the standard centrifuge to determination the capillary pressure of different fibres. This method describes the amount of free moisture, which is held in the fibre structure. It is a good approximation of the fibre saturation point. Typical water retention values are in the range of 2 kg water per kg dry fibre.

The general capillary pressure function of all experiments was:

$P_c = 4,03 * S^{-5,86}$ with S the wetting phase saturation (volume of liquid per volume of voids).

Danny G. Eagleton and Jorge A. Marcondes (L7.2) measured the difference between water sorption and desorption of packaging papers which is called hysteresis. Typically the moisture content will be greater during desorption than during adsorption.

Water activity is defined as the ratio of water-vapour pressure of the material to the water-vapour pressure of pure water at the same temperature: $a_w = \dfrac{p}{p_0}$

Temperature has to be included using the Clausius-Clapeyron equation:

$$\frac{d \ln(a_w)}{d(1/T)} = \frac{-\Delta H}{R} \quad \text{or} \quad \ln \frac{a_{w2}}{a_{w1}} = \frac{\Delta H}{R} * (\frac{1}{T_1} - \frac{1}{T_2})$$

With a_{wi} = water activity at T_i and ΔH = isotherm net heat of sorption (J/mol).

Therefore ln a_w vs. 1/T must be a linear correlation. Water activity increases with temperature at any given moisture content, according to the Clausius-Clapeyron equation.

The <u>BET isotherm</u> (Brunauer-Emmett-Teller) is used for calculation of isotherms from measured moisture content:

$$\frac{m}{m_0} = \frac{C * a_W}{[(1 - a_w) * (1 - a_w + C * a_w)]}$$

With C = constant, m = equilibrium moisture at water activity a_w and m_0 = moisture content of the monolayer

The <u>GAB isotherm</u> (Guggenheim-Anderson-de Boer) is considered as an extension of the BET model.

$$\frac{m}{m_0} = \frac{C * k * a_W}{[(1 - k * a_w) * (1 - k * a_w + C * k * a_w)]}$$

With k = factor for correcting the multilayer properties with respect to bulk liquid

BET and GAB are identical up to a_W = 0,45. For 0,45 < a_W < 0,9 the GAB model is used.

For the measured experimental data's, the BET model could not be used but the GAB model fitted very well.

E.K.O. Hellén, J.A. Ketoja, K.J. Niskannen and M.J. Alava from KCL (L7.5) measured the diffusion of liquids through fibre networks. Their experiments showed that the one-dimensional diffusion theory (Fick's law) which uses the diffusion equation

$\frac{\partial C(z,t)}{\partial t} = D_g * \frac{\partial^2 C(z,t)}{\partial z^2}$ is not valid for lower basis weigths. A random walk simulation

was developed in the KCL-PAKKA project.

Ad a) and b) – Reduce surface tension and increase contact angle:

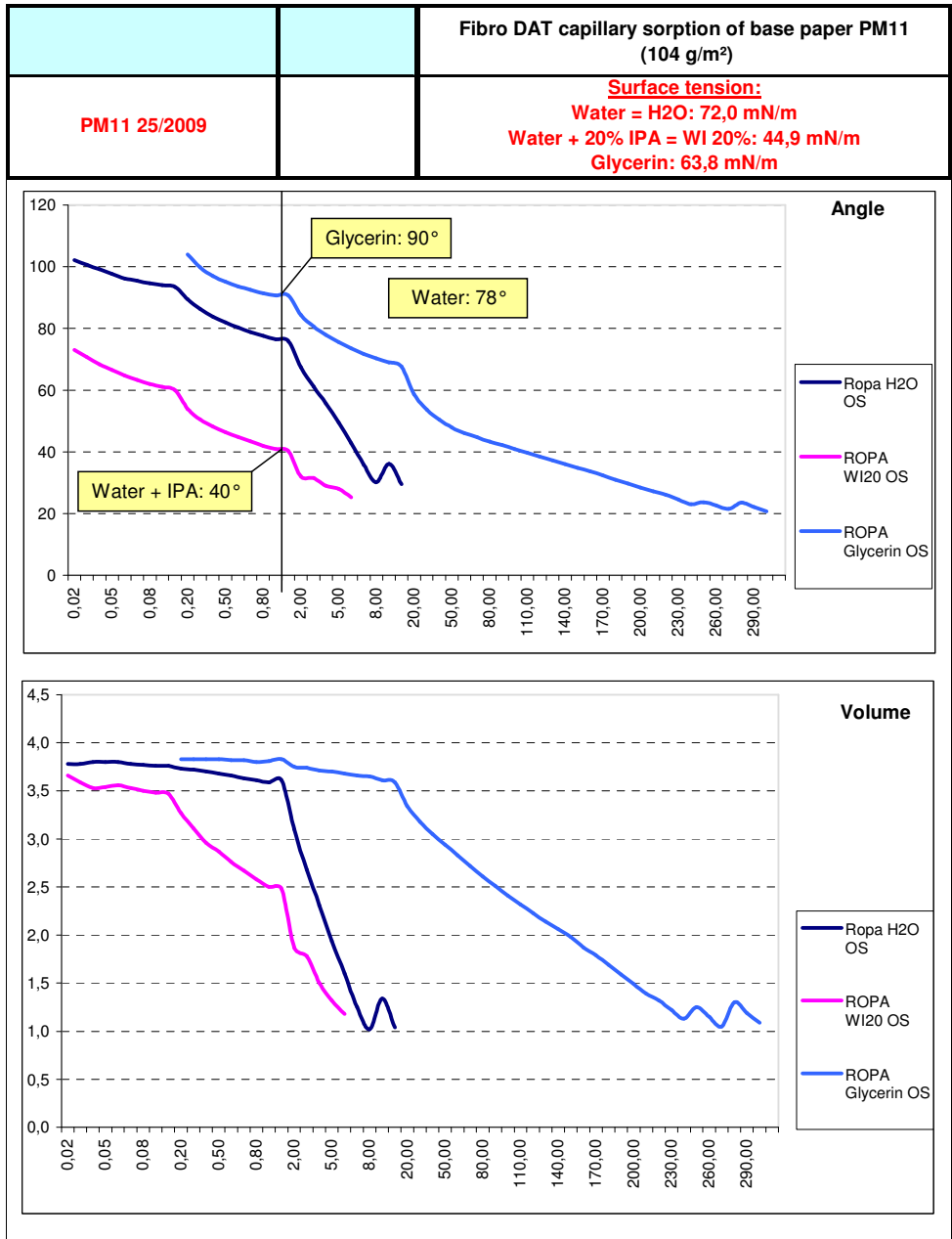The influence of liquids with big differences in contact angle and surface tension was investigated by the Fibro DAT instrument. According to the Lucas Washburn equation $\Delta P_c = \dfrac{2 * \gamma * \cos\theta}{r}$ the capillary pressure should be reduced by lower surface tension of the liquid and higher contact angle.

Isopropanol was added to water to reduce the contact angle and the surface tension. Glycerin was used instead of water to increase the contact angle at a comparable level of surface tension (pict. 5.12.10).
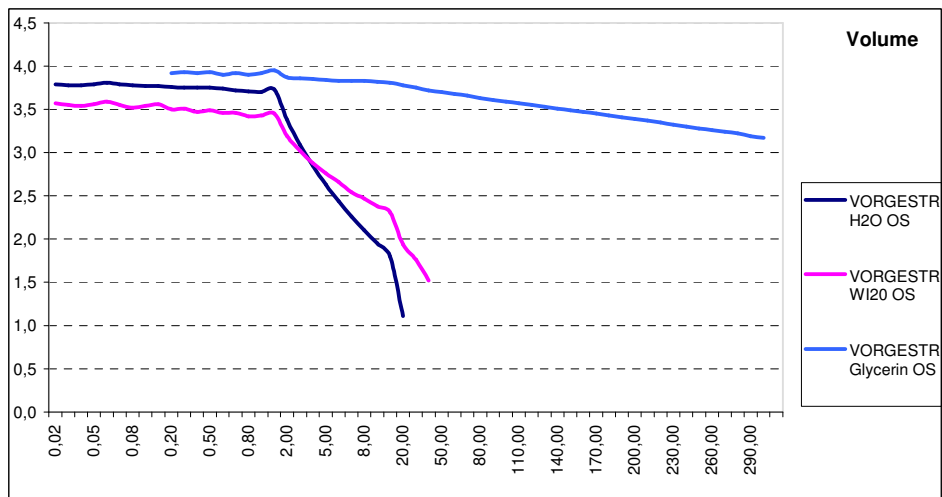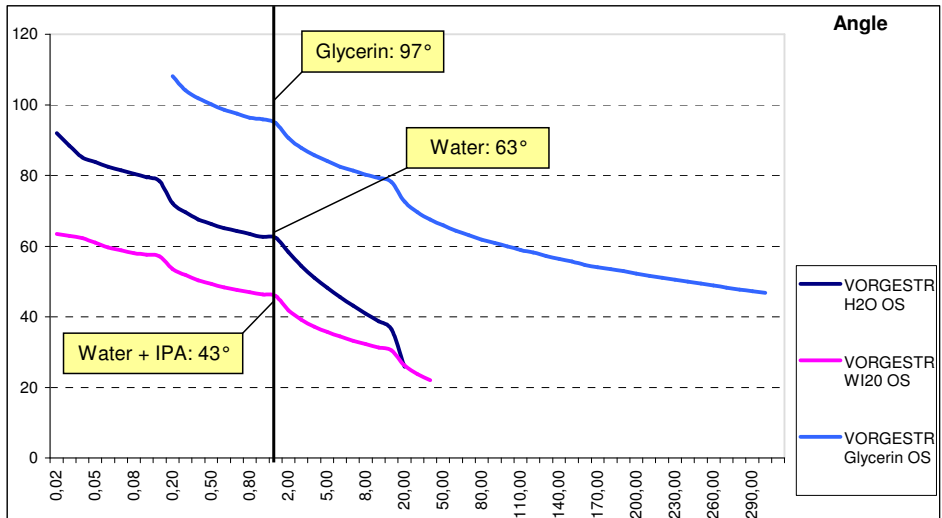
INT.U-NR.	Surface tension	Viscosity		
PM 11 53/2008	by Fibro DAT	Spindel 4 / 100 rpm	Spindel 4 / 50 rpm	Spindel 4 / 20 rpm
	mN/m	cp	cp	cp
Water	71,5	6,0	0,0	0,0
Water + IPA (20%)	43,1	4,0	0,0	0,0
Water + IPA (50%)	26,7	8,0	0,0	0,0
CMC solution 1,1 %	70,1	13,0	8,0	0,0
CMC solution 2 %		38,0	30,0	20,0
Print oil 002	35,0			
Flint oil	29,4	14,0	8,0	0,0
Glycerin	63,9	126,0	112,0	100,0

Pict. 5.12.10: Surface tension and viscosity of tested liquids

		Fibro DAT capillary sorption of base paper PM11 (104 g/m²)
PM11 25/2009		**Surface tension:** **Water = H2O: 72,0 mN/m** **Water + 20% IPA = WI 20%: 44,9 mN/m** **Glycerin: 63,8 mN/m**

Angle

Glycerin: 90°

Water: 78°

Water + IPA: 40°

— Ropa H2O OS

— ROPA WI20 OS

— ROPA Glycerin OS

Volume

— Ropa H2O OS

— ROPA WI20 OS

— ROPA Glycerin OS

Pict. 5.12.11: Capillary penetration of different liquids into base paper PM11

		Fibro DAT capillary sorption of precoated paper PM11 (97 g/m²) - 11/6622/MR3
PM11 25/2009		**Surface tension:** **Water = H2O: 72,0 mN/m** **Water + 20% IPA = WI 20%: 44,9 mN/m** **Glycerin: 63,8 mN/m**

Angle

Glycerin: 97°

Water: 63°

Water + IPA: 43°

- VORGESTR H2O OS
- VORGESTR WI20 OS
- VORGESTR Glycerin OS

Volume

- VORGESTR H2O OS
- VORGESTR WI20 OS
- VORGESTR Glycerin OS

Pict. 5.12.12: Capillary penetration of different liquids into precoated paper PM11

	Unit	Base paper, water	Base paper, water + 20% IPA	Base Paper, Glycerin	Precoated paper, water	Precoated paper, water + 20% IPA	Precoated Paper, Glycerin
contact angle θ	°	52,29	96,17	55,15	47,93	36,15	70,27
--"--	rad	0,913	1,679	0,963	0,837	0,631	1,226
cos θ		0,612	-0,108	0,571	0,670	0,807	0,338
dV/dt	µl/s	0,37	0,26	0,01	0,21	0,13	0,0028
dA	mm²	2,68	2,31	3,04	3,02	3,44	2,85
dV/dt, evaporated	µl/s	0,0033	0,0003	0,0000	0,0003	0,0033	0,0000
viscosity η	mPas	1	1	115	1	1	115
surface tension σ	mN/m	72	44,9	63,8	72	44,9	63,8
dV/dt effective	**µl/s**	**0,37**	**0,26**	**0,0144**	**0,21**	**0,12**	**0,0028**

Page 189

Fibro-DAt capillary penetration of different liquids on different substrates
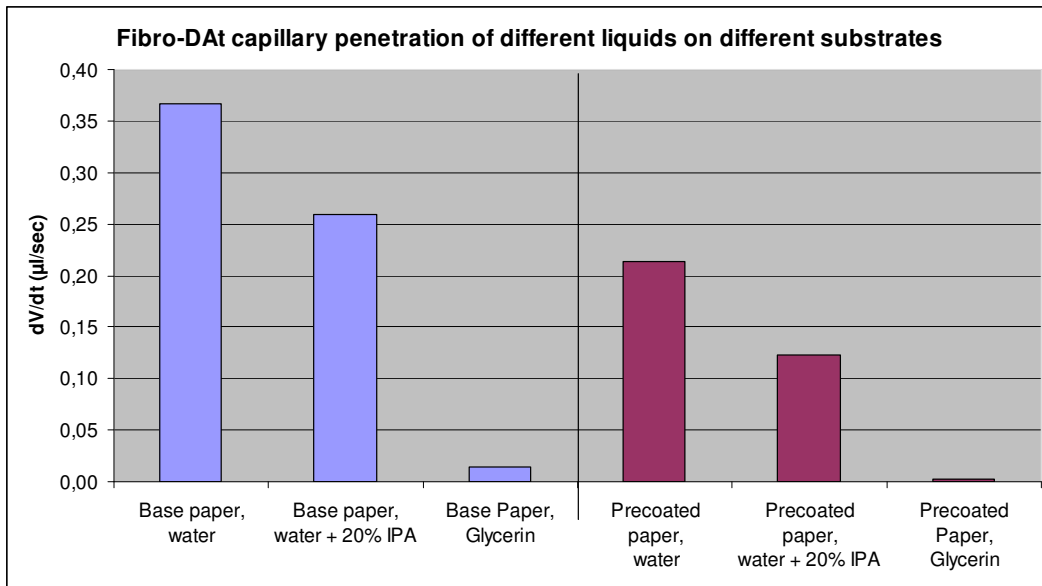
Pict. 5.12.13: Comparison of capillary penetration

Pict. 5.12.11 – 5.12.13 show again that capillary sorption of the precoated paper was much lower than that of the uncoated base paper (both from PM11).

Replacing water by Glycerin as the liquid phase of a coating colour reduces the capillary sorption by the factor 30 due to much higher contact angle, similar to the effect which was achieved by adding CMC into water.

Adding Glycerin to the water phase of coating colours will therefore reduce thickening of the coating colours before the blade and is relatively easy to implement as the product is cheap, highly hydrophilic and compatible with all coating colour components.

When isopropanol IPA is added to water, sorption is reduced to a smaller extent. IPA is lower in surface tension which increases the capillary pressure but also lower in contact angle which reduces the sorption. In sum the capillary sorption is reduced.

Chapter 6: Pressure penetration

6.1 Darcy's law and Carman Kozeny equation

All existing coaters except the curtain coater transfer the coating colour by a pressure impulse to the paper. After this pressure application the liquid phase of the coating colour is sucked deeper into the paper by capillary pressure of the fibre and coating pores.

The transfer of ink and fountain water to different substrates in offset printing is also done under pressure in the application station. Until the ink gets dry capillary sorption will occur by the coating and fibre capillaries.

For calculating the pressure penetration Darcy's law is used.

Eq. 3-12-1: $Q = \dfrac{K * A * \Delta p}{\eta * L}$

Q......Vol. flow (m³/s)

K......Darcy's permeability coefficient (m²)

L.......Length of penetration

A.......cross sectional area (m²)

Δp.....pressure differential (Pa)

η ......viscosity of liquid (Pa s)

Carman and Kozeny calculated the permeability coefficient K in their Carman-Kozeny equation:

$$K = \frac{(1 - \Phi)^3}{k_0 * T^2 * \Phi^2 * A_s{}^2}$$

τ......tortuosity

A_s....spec. surface area of porous medium (m²/m³)

K_o....shape factor (between 2 and 3)

Φ.....porosity (%)

Precondition is a sufficiently slow, steady unidirectional flow through the porous medium. The Reynolds number has to be < 0,1. The penetrated medium has to be incompressible.

Darcy established this law for flow of liquids through porous beds like sand. The unknown variable of the penetrated bed is the "Darcy's coefficient". In Lab experiments the liquid is pressed under controlled conditions (Δp, A, L, η) through the porous medium and flow of liquid through the bed (m³/s) is measured. From this readings the Darcy coefficient K can be calculated.

By integrating Darcy's equation one can see, that penetration speed is always a function of square root of pressure and time with two multiplying constants, describing the porous medium and the liquid:

Rearranged Darcy law:

$$\frac{dV_f}{dt} = \frac{K * A * \Delta p}{\eta * L},$$ with V_f the Volume of penetrated liquid with viscosity η in an area

A through a porous medium with thickness L at an applied external pressure of Δp.

Integrated Darcy law: $V_f = \frac{K * A}{\eta * L} * \Delta p * \Delta t$

With $V = A * L$ (V the volume of the penetrated section of the substrate) or $L = \frac{V}{A}$ $\rightarrow$

$$V_f = \frac{K * A^2}{\eta * V} * \Delta p * \Delta t$$

with ε, the porosity of the substrate with $\varepsilon = \frac{V_f}{V}$ or $V = \frac{V_f}{\varepsilon}$ $\rightarrow$

$$V_f = \frac{K * A^2 * \varepsilon}{\eta * V_f} * \Delta p * \Delta t \rightarrow V_f{}^2 = \frac{K * A^2 * \varepsilon}{\eta} * \Delta p * \Delta t \rightarrow \left[\frac{V_f}{A}\right]^2 = (K * \varepsilon) * \frac{1}{\eta} * \Delta p * \Delta t$$

with $m_f = V_f * \rho_f$ the penetrated mass $\rightarrow$

$$\left[\frac{m_f}{A * \rho_f}\right]^2 = (K * \varepsilon) * \frac{1}{\eta} * \Delta p * \Delta t \rightarrow \left[\frac{m_f}{A}\right]^2 = (K * \varepsilon) * \frac{\rho_f{}^2}{\eta} * \Delta p * \Delta t$$

$\rightarrow (m_f / A) = \sqrt{C * A * \Delta p * \Delta t}$, with m_f/A in g/m², the penetrated liquid in Δt and C the substrate constant including porosity and Darcy coefficient and A the liquid constant.

Literature (pict. 6.1.1) and lab tests show, that the amount of penetrated water per area during pressure penetration is always a function of $\sqrt{\Delta p * \Delta t}$:
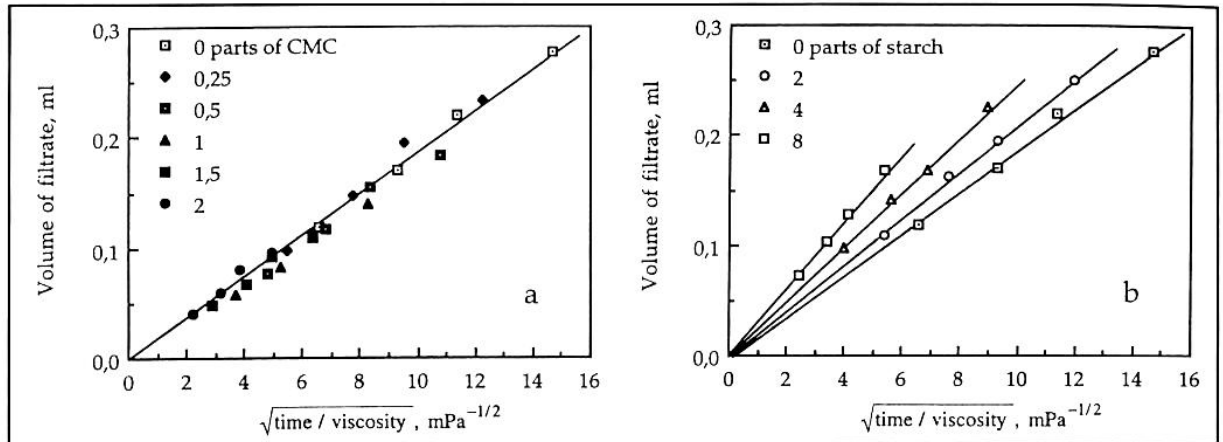
Pict. 6.1.1: Ericson & Rigdahl (L1.49, L1.56): Pressure penetration of liquids with increasing viscosity


Windle and Beazley (L1.1) from Imerys designed in 1969 an apparatus to measure capillary and pressure penetration by reflectance and Kubelka Munk calculation. The conditions were realistic like under a blade of a high speed coater (68 bar, 0,01 msec). They proved Darcy's law – penetration speed was depending upon the square root of time.

Pressure penetration was reduced by higher ash content in the base or precoating layers.

Capillary penetration was reduced by beating of the fibres, internal sizing or surface sizing.

The authors stated that latex and soluble binders penetrate the base paper mainly under pressure penetration. Capillary pressure is negligible.

In a second paper (L1.1b) the same authors used an optical device to measure penetration with short term time intervals (msec). Pressure was with 68 bars over the range of blade coaters. The amount of liquid pressed into the sheet under external pressure was of one magnitude higher than for capillary penetration. Pressure penetration was independent on surface tension (which is not included in Darcy's law) but according to Darcy linearly depending on the square root of time (pict. 6.1.2).
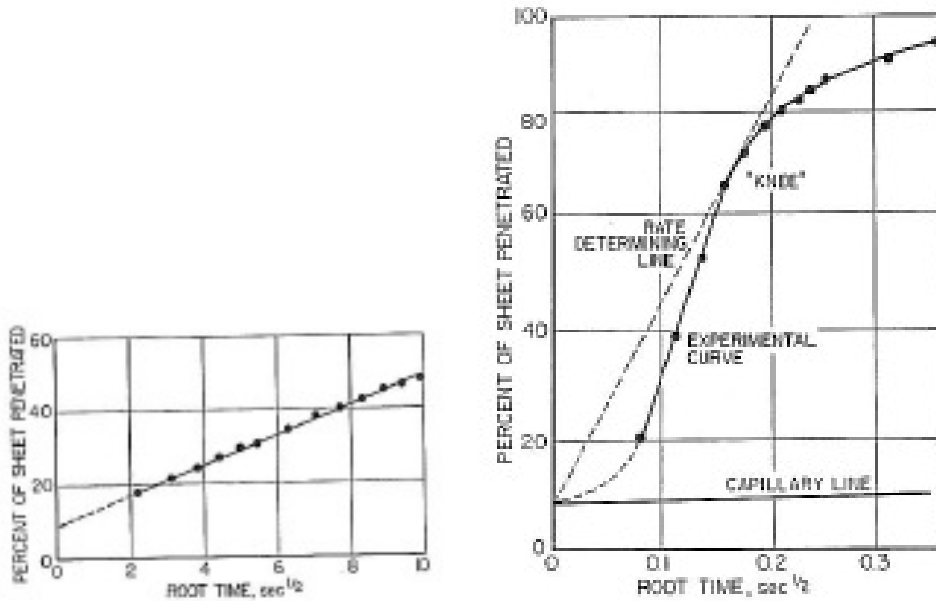
Pict. 6.1.2: Penetrated volume vs square root of time (Windle and Beazley)

Increasing liquid phase viscosity by raising the starch concentration led to lower amounts of penetrated liquid according to Darcy's law (pict. 6.1.3).
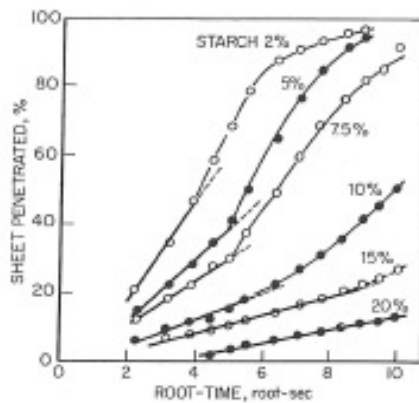
Pict. 6.1.3: Penetrated liquid as a function of viscosity (Windle and Beazley)

1967 Bristow constructed the so called Bristow-wheel, described in L1.2. On a rotating wheel a droplet is transferred to a paper and penetration time/length if measured. The measurements fitted into the Lucas Washburn equation for capillary

penetration $\dfrac{V}{L*B} = K_r + K'_a * \sqrt{\dfrac{\gamma * \cos\theta * t}{\eta}}$. The absorbed amount of water was a

function of the square root of time. For water based liquid a short wetting time of 0,2

sec was measured which had to be overcome to wet enough fibre surface to start penetration.

S. Ramaswamy, B.V Ramaro and A. Goel (L1.21) proved with pressure penetration experiments into porous media that penetrated volume is proportional to the square root of time according to Darcy and Lucas Washburn.

P.A. Bodurtha, G.P. Matthews and J.P. Kettle (L1.70) studied the influence of structural anisotropy on fluid permeation in clay/carbonate based coatings.

Penetration was calculated by combining Darcy's law with the Poiseuille equation:

Darcy: $\dfrac{dV}{dt} = -\dfrac{k*A*\partial P}{\mu*l}$

Poiseuille for cylindrical tubes: $\dfrac{dV}{dt} = -\dfrac{\pi*r^4*\partial P}{8*\mu*l} = -\dfrac{\pi*F*\partial P}{8*\mu}$

with $F = \dfrac{r4}{l}$ the volume flow capacity.

Poiseuille for ellipsoidal tubes: $\dfrac{dV}{dt} = -\dfrac{\pi*r_a{}^3*r_b{}^3*\partial P}{4*\mu**h*(r_a{}^2+r_b{}^2)}$

Poiseuille for square tube: $\dfrac{dV}{dt} = -\dfrac{\partial P}{\mu}*\dfrac{4*L^3}{57}$ with L the width of the pore

The flow rate through the arc for cylindrical throats and cubic pores is:

$\dfrac{dV}{dt}_{arc} = -\dfrac{\partial P}{\mu} * \left[\dfrac{1}{\dfrac{57}{4*L_1{}^3}+\dfrac{8*h}{\pi*r^4}+\dfrac{57}{4*L_2{}^3}}\right]$ with L_1 and L_2 the width of the pores and h the

length of the connecting throat.

Inserting the Poiseulle equation $\dfrac{dV}{dt} = -\dfrac{\pi*r^4*\partial P}{8*\mu*l} = -\dfrac{\pi*F*\partial P}{8*\mu}$ gives:

$F_{arc} = -\dfrac{8}{\pi}*\dfrac{dV}{dt_{arc}}*\dfrac{\mu}{\partial P} = -\dfrac{8}{\pi}*\left[\dfrac{1}{\dfrac{57}{4*L_1{}^3}+\dfrac{8*h}{\pi*r^4}+\dfrac{57}{4*L_2{}^3}}\right]$

For flow through a pore with rectangular cross section (slit-like or rod-like pores) a new equation was set up by O'Neil (Viscous and compressible fluid dynamics 1989):

$$\frac{dV}{dt} = -\frac{\partial P}{\mu} * \frac{L_b * L_a{}^3}{6*L_c} * \left[1 - \frac{192*L_a}{\pi*L_b} * \sum_{i=1,3,5,...}^{\alpha} \frac{\tanh(i*\pi*L_b/2*L_a)}{i^5} \right]$$

with $L_a > L_b$ the two widths of the pore normal to flow and L_c the width in flow direction.

Resulting in: $\quad F_{arc} = -\frac{8}{\pi} * \left[\dfrac{1}{\dfrac{1}{A} + \dfrac{1}{B} + \dfrac{1}{C}} \right]$ with

$$A = \frac{L_{1,b} * L_{1,a}{}^3}{6*L_{1,c}} * \left[1 - \frac{192*L_{1,a}}{\pi*L_{1,b}} * \sum_{i=1,3,5,...}^{\alpha} \frac{\tanh(i*\pi*L_{1,b}/2*L_{1,a})}{i^5} \right]$$

$$B = \frac{\pi * r_a{}^3 * r_b{}^3}{4**h*(r_a{}^2 + r_b{}^2)}$$

$$C = \frac{L_{2,b} * L_{2,a}{}^3}{6*L_{2,c}} * \left[1 - \frac{192*L_{2,a}}{\pi*L_{2,b}} * \sum_{i=1,3,5,...}^{\alpha} \frac{\tanh(i*\pi*L_{2,b}/2*L_{2,a})}{i^5} \right]$$

They compared the calculated permeability data's with ink penetration from ISIT tests.
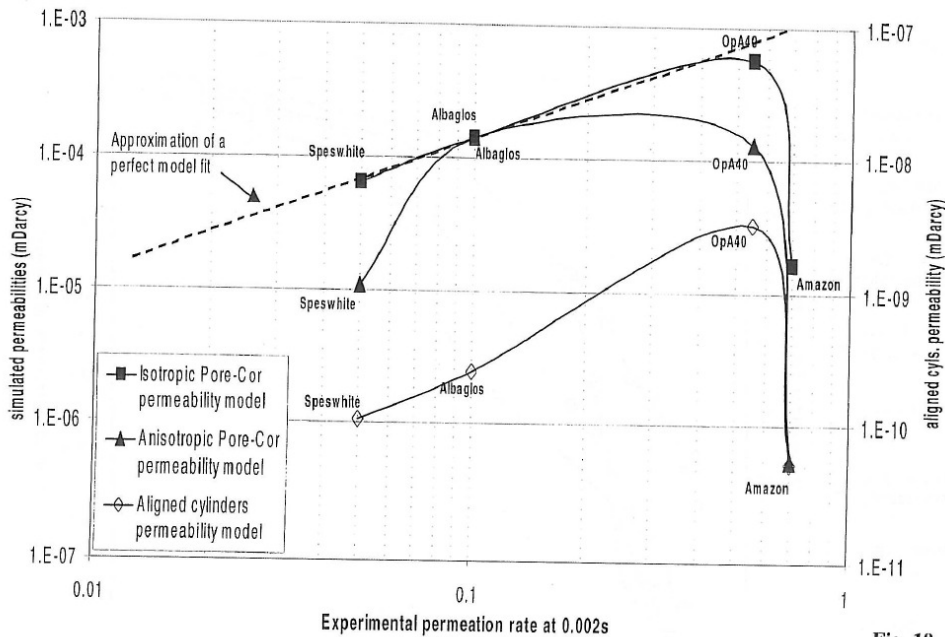
Fig. 19

Pict. 6.1.4: ISIT ink transfer at 0,002 sec versus simulated permeability

For fine amazone clay none of the permeability models fitted (pict. 6.1.4). For the other pigments the isotropic model would be good enough for simulations. The anisotropic model didn't improve the correlation to ISIT ink transfer measurements further.

Darcy's law is guilty for laminar flow in the penetrated pores of the substrate (Re < 10^3). This was checked for the top coat of OMC11, where under the blade an increase in solid content was measured from 68% to 71% (measured by scraping off the coating colour from the surface after the blade).

Parameter of top coat		Value	Unit	
Speed of coater		1600	m/min	
Coated width of web		8,44	m	
Coat weight dry of top coat on double precoated paper		10	g/m²	
Measured solids of coating colour after blade		71,0	%	
Wet coat weight after blade		14,08	g/m²	
Water in coating colour after blade		4,08	g/m²	
Measured solids of coating colour before blade		68,0	%	
Wet coat weight before blade		14,71	g/m²	
Water in coating colour before blade		4,71	g/m²	
Density of coating colour in working tank		1650	kg/m³	
Calculation: penetrated water under blade	Q/A	0,62	g/m² = ml/m²	
Corrected volume of penetration at free area	Q/A	1,17	g/m²	Water can penetrated only into free pore vol.
Pore volume of double precoated layer		4,5	ml/m²	per side (from Hg porosimetrie)
Thickness of double precoated layer		8,5	µm	per side (from thickness meas.)
Volume of coating layer		8,5	ml/m²	
Pore volume		53%		
Penetration depth of liquid phase in top coat	L	1,17	µm	
Viscosity of liquid phase	η	20	mPa s	1 Pa = 1 kg / (m*s²)
Density of liquid phase	ρ	1050	kg/m³	
Kinematic viscosity of liquid phase	v = η / ρ	0,000019	m²/s	
Penetration time before and under the blade	t	0,056	msec	
Penetration speed of liquid phase	w	0,021	m/s	w = (Q/A) / t with Q/A at free pore vol.
Reynolds number	Re	1,29E-03		Re = (w * L) / v

Pict.6.1.5: Calculation of Reynolds number for penetration of liquid phase under the blade for normal solids increase

Parameter of top coat		Value	Unit	
Speed of coater		1600	m/min	
Coated width of web		8,44	m	
Coat weight dry of top coat on double precoated paper		10	g/m²	
Measured solids of coating colour after blade		**75,0**	**%**	
Wet coat weight after blade		13,33	g/m²	
Water in coating colour after blade		**3,33**	**g/m²**	
Measured solids of coating colour before blade		68,0	%	
Wet coat weight before blade		14,71	g/m²	
Water in coating colour before blade		**4,71**	**g/m²**	
Density of coating colour in working tank		1811	kg/m³	
Calculation: penetrated water under blade	**Q/A**	**1,37**	**g/m²** = ml/m²	
				Water can penetrated only
Corrected volume of penetration at free area	Q/A	3,92	g/m²	into free pore vol.
Thickness of double precoated layer		8,5	μm	per side (from thickness meas.)
Pore volume of double precoated layer	ε	35	%	from Mercury porosity
avg. Pore radius	r	0,25	μm	$d_H = r/2$
Penetration depth of liquid phase in top coat	**L**	**2,59**	**μm**	
Viscosity of liquid phase	**η**	10	mPa s	1 Pa = 1 kg / (m*s²)
Density of liquid phase	**ρ**	1050	kg/m³	
Kinematic viscosity of liquid phase	**v = η / ρ**	0,000010	m²/s	
Length of penetration before and under blade	**x**	2,135	mm	from VOF
Penetration time before and under the blade	**t**	**0,080**	**msec**	t = x / v
Penetration speed of liquid phase	**w**	**0,047**	**m/s**	w = (Q/A) / t
Reynolds number 1	**Re₁**	**1,3E-02**		Re = (w * L) / v
Reynolds number 2	**Re₂**	**6,1E-04**		Re = (w * d_H) / v

Pict. 6.1.6: Calculation of Reynolds number for penetration of liquid phase under blade for extreme solids increase (Re_1 for penetration length L and Re_2 for hydraulic pore diameter d_H)

The calculations in pict. 6.1.5 and 6.1.6 proove that even when an extremely long time of penetration and high amount of penetrated water is assumed, Reynolds number stays low and penetration flow will be laminar.

6.2 Calculating permeability from Bendtsen air porosity measurements

Standard measurements in paper industry are air porosity measurements by Gurley or Bendtsen but the results cannot be used for calculation of the Darcy coefficient as Darcy's law is invalid for compressible mediums, pressed through porous beds.

Therefore air porosity can be used only with restrictions for base papers, where porosity is high and pressure difference and compression of air is low.
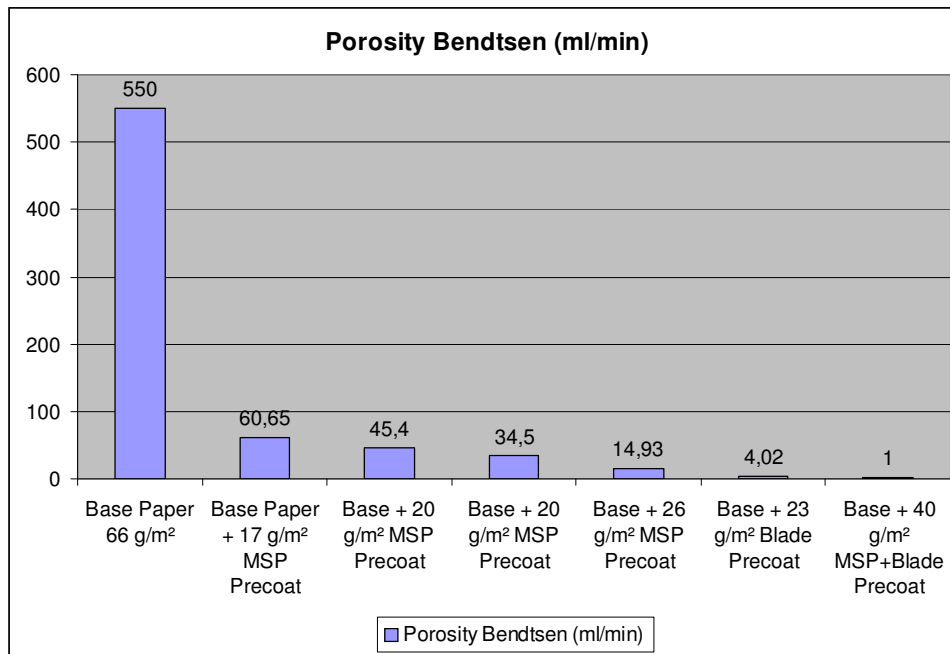
Pict. 6.2.1: Air porosity of different coated papers

Measurements and calculations shown in pict. 6.2.1 – 6.2.3 show that the higher the coat weight and the lower the coating layer porosity (high amount of fine particles) the lower the air permeability.

Base paper:			
Paper data:			
mean pore radius	r	4,5	µm
Thickness	L	0,124	mm
Void fraction	ε	43	%
Calculation of Darcy's coefficient from Bendtsen porosity readings:			
Bendtsen Porosity	Q_{Air}	470	ml/min
Area of Bendtsen poros. Measurement	$A_{Bendtsen}$	10	cm²
Air pressure at porosity measurement	p_{Air}	20000	Pa = N/m²
Air viscosity at 23℃	μ_{Air}	1,80075E-05	Pa s = Ns/m²
formula:	$Q = (K \times \Delta p \times A) / (\mu \times \Delta L)$		
	$K = (Q \times \mu \times \Delta L) / (\Delta p \times A)$		
Darcy coefficient for air	K_{Air}	8,74564E-16	m²

Double precoated paper:			
Paper data:			
mean pore radius	r	0,25	µm
Thickness	L	0,02	mm
Void fraction	ε	35	%
Calculation of Darcy's coefficient from Bendtsen porosity readings:			
Bendtsen Porosity	Q_{Air}	1,01	ml/min
Area of Bendtsen poros. Measurement	$A_{Bendtsen}$	10	cm²
Air pressure at porosity measurement	p_{Air}	20000	Pa = N/m²
Air viscosity at 23°C	$µ_{Air}$	1,80075E-05	Pa s = Ns/m²
Darcy coefficient for air	K_{Air}	**3,03126E-19**	**m²**

Pict. 6.2.2: Darcy coefficient, calculated from Bendtsen porosity measurements

Air permeability is used mainly to compare the permeability of base papers as pressure drop is low for this medium and compressibility influence gets lower.

R.C. Hamlen, and L.E. Scriven (L1.7) from U Minnesota calculated three-dimensional flow through a base paper network using three-dimensional Darcy equation. The calculated normal permeability coefficient was in the range of 10^{-14} to 10^{-12} which fits quite well to Bendtsen air permeability measurements of base papers in this work. In-plane penetration is reduced with lower fibre aspect ration (length to width ratio) which is in the range of 0,1 – 0,3 for commercial pulp fibres and is also reduced by compression of the base sheet e.g. by a machine calander.

PPS air porosity was already used by Lokendra Pal, Margaret K. Joyce and Paul Fleming (L1.58) to determine the permeability of single coated papers. Clay based coatings were applied by blade and MSP on a 70 and a 226 g/m² base papers.
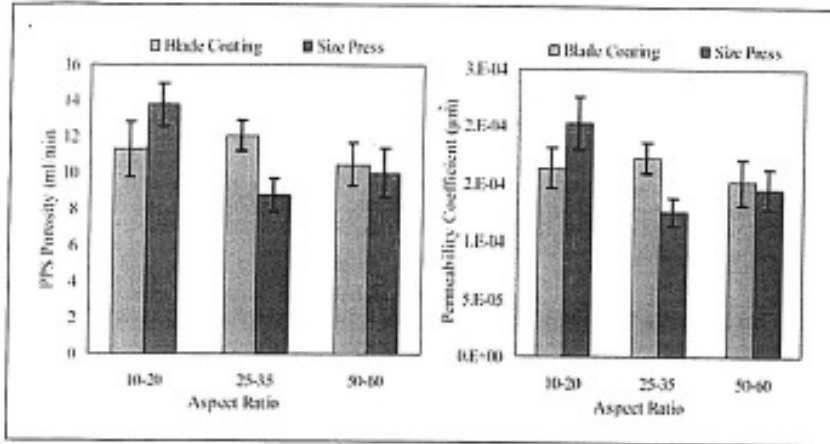
Pict. 6.2.3: Influence of pigment aspect ratio on porosity (70 g/m² base) (Fleming et al)

Porosity decreased with higher aspect ratio of clay, especially for size press application (pict. 6.2.3).

On a 70 g/m² base paper, size press gave lower porosity showing the improved holdout of these engineered pigments.

Pict. 6.2.4 shows that coating of thickboard instead of thin paper led to totally different results. Blade coating gave denser packing than size press coating.
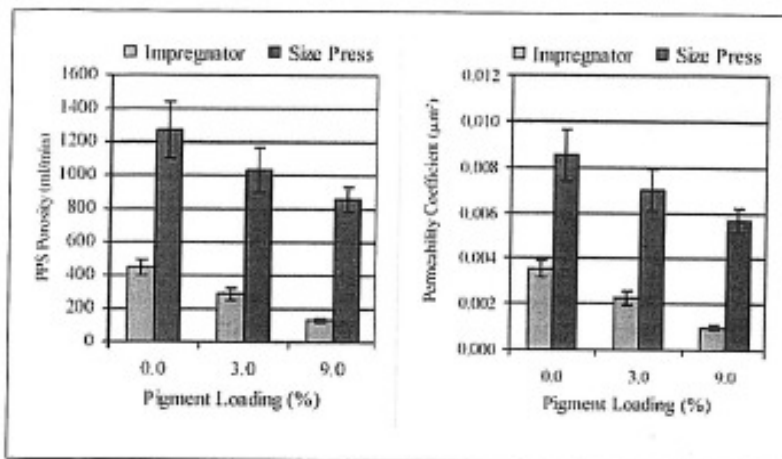
Pict. 6.2.4: Influence of pigment loading on porosity (216 g/m2 base) (Fleming et al)

6.3 Calculating permeability by pressuring liquids through porous coating layers

J. Schoelkopf, P.A.C. Gane and C.J. Ridgeway (L1.64) tried to correlate Mercury porosity of pigment tablets with permeability of the same tablets to prove Darcy's law and the Carman-Kozeny equation.

Darcy: $q = K * \dfrac{A * \Delta p}{\eta * l}$

Carman-Kozeny: $K = \xi * \dfrac{\rho * g}{\eta} * \dfrac{\Phi^3}{\tau^2 * (1 - \Phi^2) * s^2}$ with $\tau = \dfrac{l_e}{l}$, the tortuosity term,

comparing l_e the effective path length through the sample with l the thickness of the sample and Φ the porosity.

They used a pressed tablet from HC60 powder and pressed an un-polar oil through this tablet with OMYA's pressure penetration cell. No correlation was found when the pressure was slowly raised as the entrapped air dominated the measurements. Correlation got linear when air was removed first by high pressure and pressure was released afterwards (pict. 6.3.1).
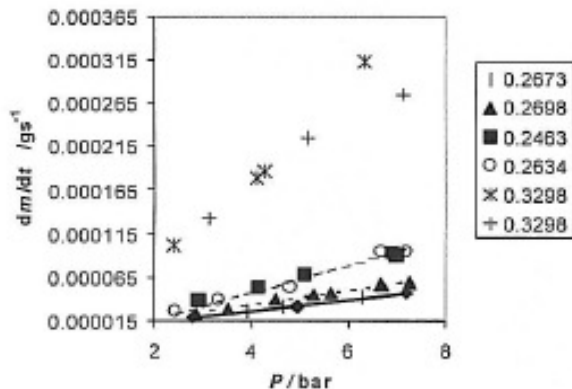
Pict. 6.3.1: Permeation gradients (legend: mercury porosity) (Schölkopf)

When the pigment tablet is regarded as a membrane with a series of tube shaped capillaries, Hagen Poiseuille's law could be applied: $q = \dfrac{r^2 * A * \Delta p}{8 * \eta * l} = K * \dfrac{A * \Delta p}{\eta * l}$

with $r_h = \dfrac{\Phi}{s * (1 - \Phi)}$ the "hydraulic" radius.
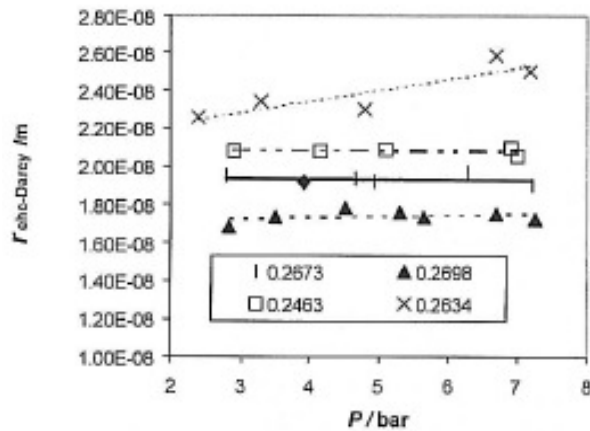
Pict. 6.3.2: Hydraulic radii vs. porosity (legend: Hg porosity) (Schölkopf)

Pict. 6.3.2 shows that no correlation was found for this assumption which leads to the conclusion that dry coating layers have more likely a structure of a sponge than cylindrical channels. In the dead end capillaries air is entrapped which makes the Darcy equation un-valid.

When air porosity measurements are applied to determine permeability of coating layers, air gets entrapped in dead end pores and is compressed. This will distort the permeability measurements.

The same finding was detected by S. Moser (L1.65) who tried to correlate air porosity measurements of different silicone base papers with the holdout of silicone oil on these substrates (pict. 6.3.3). Silicone oil is applied under pressure e.g. by gravure rolls and therefore no influence of liquid surface tension or contact angle was found similar to the pressure penetration experiments in this work. The holdout was determined by colouring the silicone oil and the measuring brightness of the paper surface.
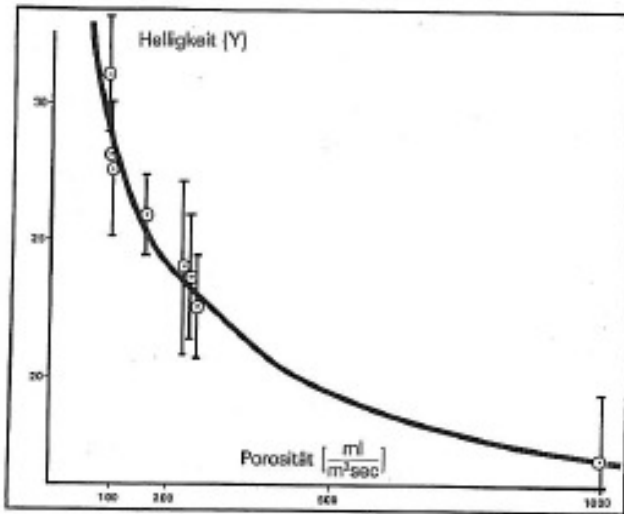
Pict. 6.3.3: Silicone coating with solvent (S. Moser)

To determine the permeability of a coating layer a **liquid** must pressed through the investigated coating layer.
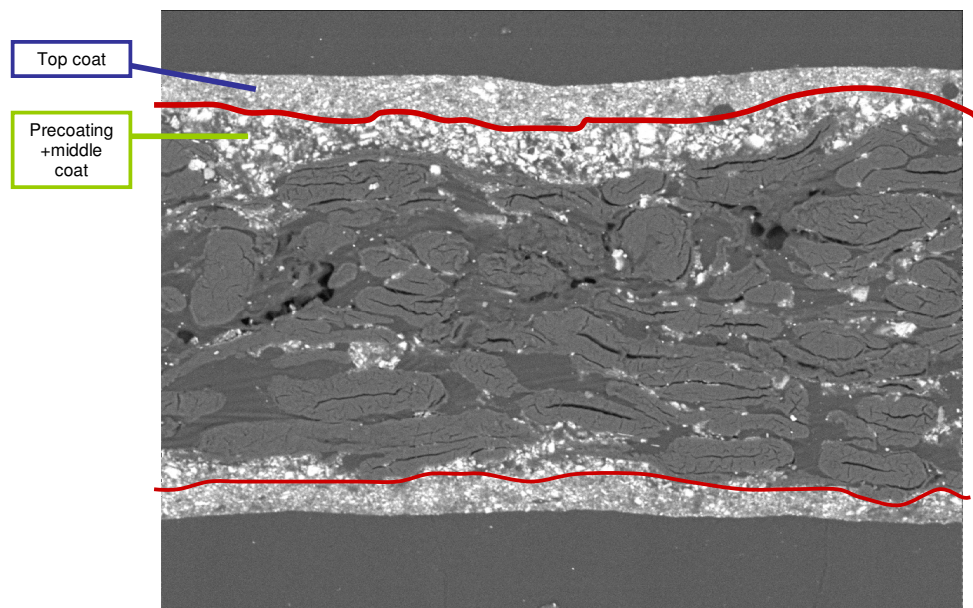
Pict. 6.3.4: REM picture of triple coated paper (pictured area: L = 200 µm, H = 100 µm)

When a coating layer is applied on a base paper its uniformity in in-plane thickness will always be far from perfect. REM pictures like pict. 6.3.4 show areas without any precoat and area with double the amount of precoat compared to mean value. The

calculated coating layer permeability will be an approximation when a liquid is pressed through this non-uniform layer.

U. Höke and E. Daub (L1.48) were pioneers in developing a new pressure penetration test. They adapted the IGT tester to apply a droplet under pressure on different paper samples (pict. 6.3.5).
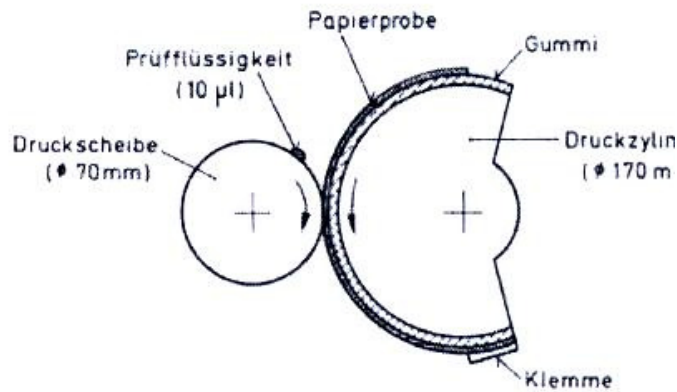
Pict. 6.3.5: IGT pressure penetration test (Höke and Daub)
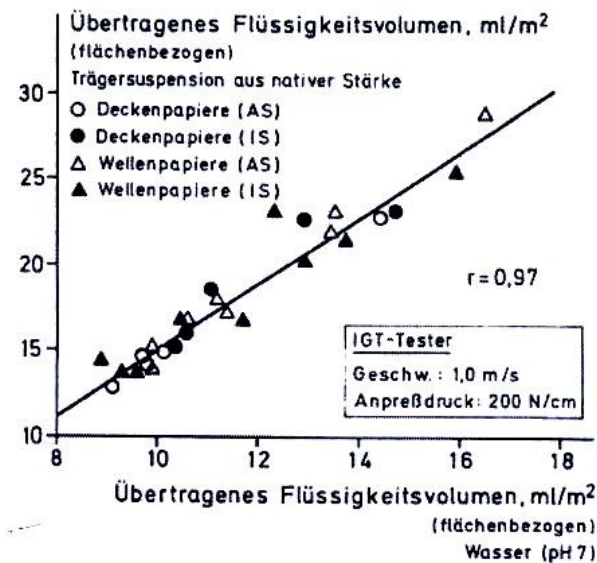
Pict. 6.3.6: Comparison of water and starch at IGT penetration tests (Höke and Daub)

Höke and Daub found a linear correlation between penetrated liquid volume and liquid viscosity / permeability of substrate according to Darcy's law (pict. 6.3.6).

For pressure-less capillary penetration experiment they developed a special short term application tester, shown in pict. 6.3.7.

Behälter

L_B

Prüfflüssigkeit (40 µl)

Papierprobe

v_p

rotierende Scheibe

Kontaktzeit $t = \dfrac{L_B}{v_p}$ in s

Übertragenes Flüssigkeitsvolumen = $\dfrac{\text{Prüfflüssigkeits - Volumen}}{\text{Meßflecklänge} \times \text{Meßfleckbreite}}$ in ml/m² (flächenbezogen)

v_p = Geschwindigkeit der Papierprobe in mm/s

L_B = Abstand der Behälterinnenwände in Laufrichtung (1mm)
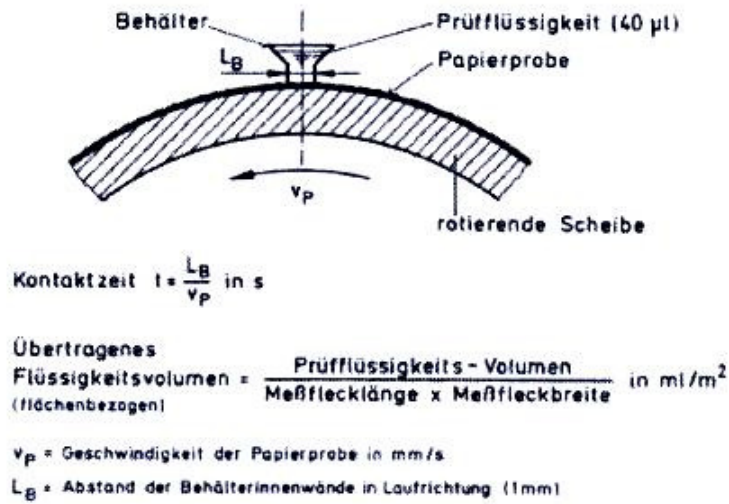
Pict. 6.3.7: Short term absorption tester (Höke and Daub)

A paper sample is mounted on a rotating disc. 40µl of liquid are filled in a small container on top of the sample. When the container touches the paper, sorption starts. The contact time is changed by the speed of the disc.

Übertragenes Flüssigkeitsvolumen, ml/m² (flächenbezogen)

t_w = Benetzungszeit
K_r = Rauhigkeitskoeffizient
K_a = Absorptionskoeffizient

$K_a = \dfrac{z_2 - z_1}{\sqrt{t_2 - t_w} - \sqrt{t_1 - t_w}}$ in ml/m² $\sqrt{s}$

Benetzungszeit

Kontaktzeit, s
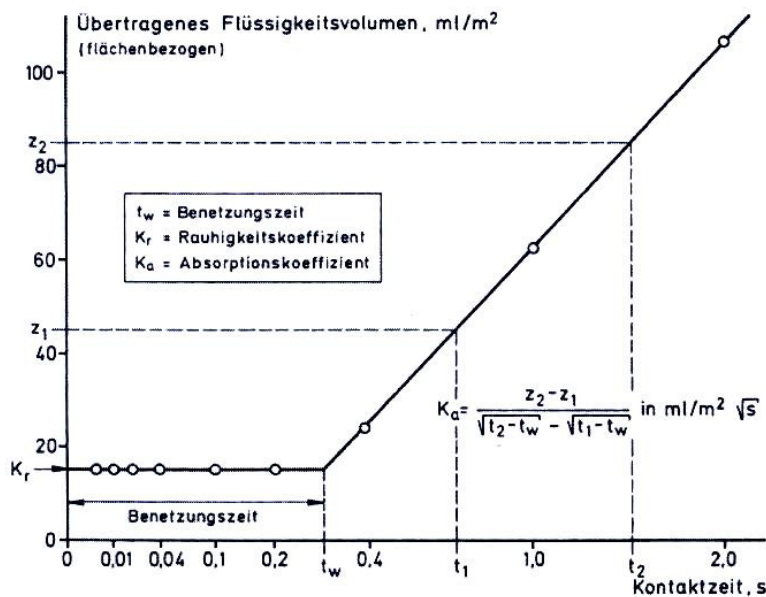
Pict. 6.3.8: Wetting time and absorption time of **water** from short term absorption tester (Höke and Daub)

Höke and Daub found almost exactly the same wetting time of 0,3 sec (pict. 6.3.8), which can alse be seen in the Fibro-DAT measurements shown in chapter 5.

For starch this wetting time was set to zero, which can be explained by higher contact angle θ.

6.4 Development of a new pressure penetration test at the Prüfbau lab printing machine

To determine the Darcy coefficient of coating layers and base papers a new Prüfbau tests was developed by the author similar to the apparatus of Höke and Daub, as shown in pict. 6.3.5.

A small volume of coloured liquid is pressed in the printing nip of the Prüfbau apparatus into the paper surface.

The area of penetration is measured.

The denser the paper surface, the lower the penetration depth and the bigger the coloured area of penetration.

All kinds of liquids can be used – water, IPA, printing oils,…

A paper sample of 46 x 230 mm size is put on the 30 cm long sample holder with a fixed blanket underneath (pict. 6.4.1 – 6.4.3).

Pict. 6.4.1: Sample holder, coloured ink, aluminium roll, pipette

Pict. 6.4.2: Standard Prüfbau lab printing apparatus
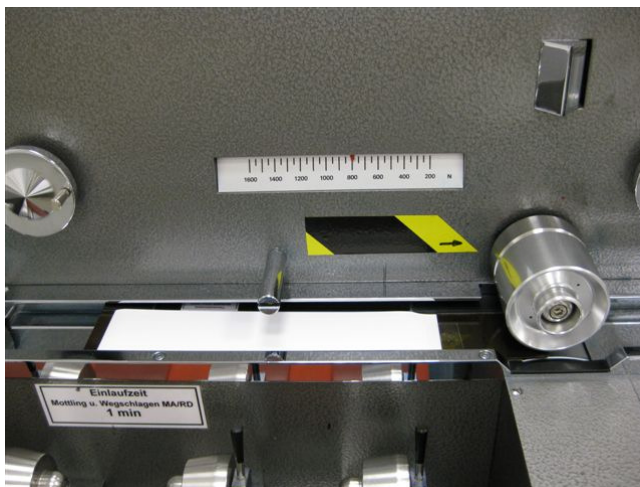
Pict. 6.4.3: Sample on the sample holder

The ink drop is put with a micro pipette on top of a clean aluminium printing roll (pict. 6.4.4 – 6.4.5).

The droplet volume must be adapted to the paper surface porosity. For base papers 5 – 10 µl are used, for precoated papers 5 µl and for coated and calandered papers 3 – 5 µl.

The surface tension of the liquid must be high enough and the wetting of the aluminium roll must be sufficient to prevent lift-off of droplet from aluminium roll during the following printing process.

Water based liquids are coloured with Cartaren Violett BLNF and oil based liquids with Sudangreen 985 to detect the penetration area at the printed substrate.
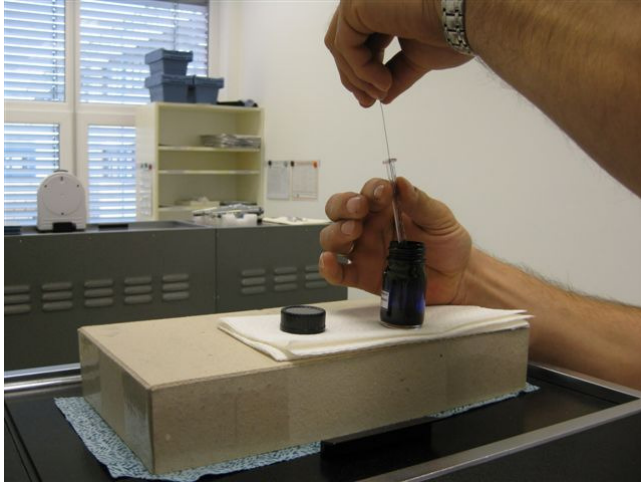
Pict. 6.4.4: Ink in the pipette

Pict. 6.4.5: Ink on the aluminium roll

Printing conditions: 800 N pressure, 50 cm/sec speed (pict. 6.4.6 – 6.4.8).

Pict. 6.4.6: Starting the printing process
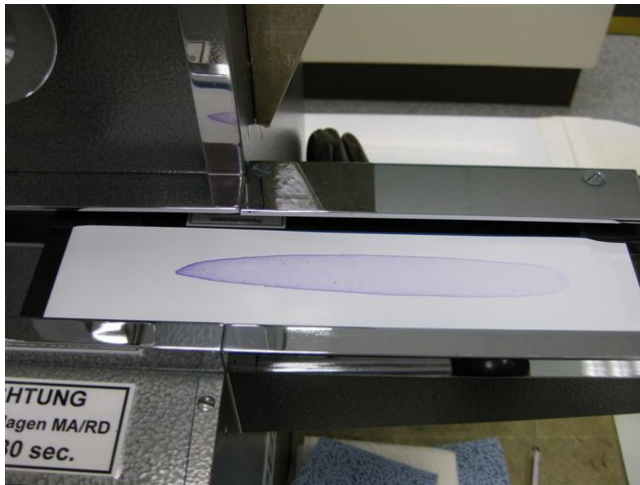
Pict. 6.4.7: Ink rolled into the paper surface
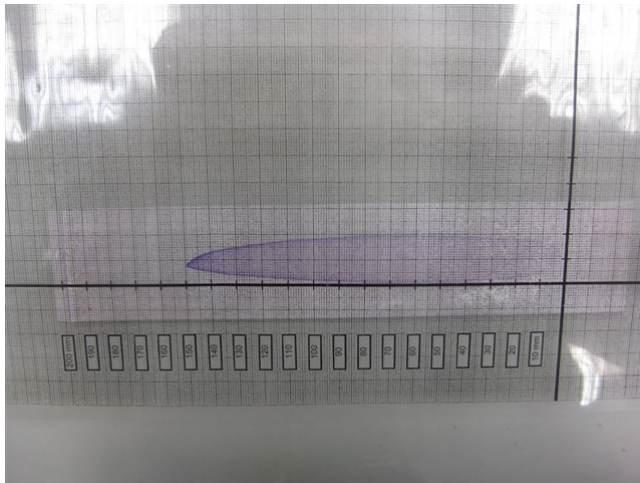
Pict. 6.4.8: Measuring the size of the penetrated area

The elliptical area of penetration is calculated with: $A = \dfrac{B*L*\pi}{4}$

Pict. 6.4.9 shows the calculation of the Darcy coefficient of the surface layer from penetration area by using Darcy's law $\dfrac{dV}{dt} = Q = \dfrac{K*A*\Delta p}{\eta*L}$.

The pressure in the Prüfbau nip can be measured, the viscosity of the ink must be determined separately and dV/dt is calculated from penetrated area A.

The most difficult parameter is the penetrated length L. It can be calculated when the porosity of the coating layer is known from Mercury porosity.

Paper: Double precoated base (11/3688/MR5, 4000170, Avg of OS/US):

				Comment
				Comment
basis weight		102,2	g/m²	
thickness, total		9,6	µm	from thickness measurements of paper samples
pore volume in precoating layer		9	ml/m²	topside + bottom side from Hg-poros.
avg. Pore radius	r	0,25	µm	from Hg-porosimetry
max. penetration volume	$V_{p, max}$	4,5	ml/m²	total pore volume / 2
Porosity from mercury		35,0	%	from Hg-porosimetry
Coating layer thickness (MSP+blade), both sides		0,0171	mm	from thickness measurements of paper samples
-- " --	$H_{coating}$	8,5476	µm per side	
Liquid: Coloured dest. Water				
contact angle	θ	45	°	after wetting (1 sec)
	θ	0,7854	rad	
	cos θ	0,707		
surface tension	γ	73	mN/m	
viscosity	η = µ	0,001	Pa s = kg/ms	
density	ρ	1000	kg/m³	
Prüfbau:				
speed of test	v	0,5	m/s	
pressure at nip	Δp	800	N	1 N = 1 kg m / s², Pa = N/m²
formula No.2:		dV/dt = (K x A x Δp) / (η x L)		
		K = ((dV/dt) x η x L) / (A x Δp)	(Δp in Pa)	
Measures at double precoated paper (11/3688/MR5, 4000170, Avg of OS/US):				
drop volume	V_{drop}	5	µl	known
drop lenght	B_{drop}	87,5	mm	mesured
drop width	L_{drop}	19,5	mm	mesured
drop area	A_{drop}	1339,4	mm²	$A_{drop}=B_{drop}*L_{drop}*3,14/4$
time for drop penetration	t_{drop}	0,2	sec	$t_{drop}=L_{drop}/v_{Prüfbau}$
mean width of penetrated drop	b	15,3	mm	
appr. lenght of pressure under Prüfbau roll at Δp	l	5,0	mm	measured by pressure sensitve film
area of pressure under Prüfbau roll at Δp	A	76,5	mm²	
penetrated water under prüfbau roll	$V_{p,spez}$	0,004	µl/mm²	$V_{p,spez}=V_{drop}/A_{drop}$
-- " --	$V_{p,spez}$	3,73	ml/m²	-- " --
comparison: Pore volume of coating layer	$V_{p, max}$	4,5	ml/m²	from Hg measurement
penetrated water under prüfbau roll	V_p	0,3	µl	$V_p=V_{p,spez}*A$
-- " --	V_p	0,00029	ml	-- " --
theor. penetration depth	L_{th}	3,73	µm	at 100% free volume
true penetration depth from porosity ε	**L**	**7,09**	**µm**	$L = (V_{Drop}/V_{paper})$ x $H_{coating}$
comparison: maximum penetration depth	L_{max}	8,55	µm	$H_{coating}$
penetration time under prüfbau roll	t	0,010	sec	
spec. Pressure	Δp	10452393	Pa = N/m²	
	Δp	105	bar	
	Δp	1056,2	m WS	Δp in m WS = (Δp in N) / ($ρ_w$ x 9,81 x A)
Darcy's coefficient with formula No. 2:	**K**	**2,5324E-19**	**m²**	

Pict. 6.4.9: Calculating the Darcy coefficient from Prüfbau pressure penetration test

If coating layer porosity is unknown, the area of penetration (mm²) or the amount of penetrated ink per area (ml/m²) can be used as a simplification to describe the surface permeability of the coating layer.

Pressure level at the Prüfbau pressure penetration test is higher than blade pressure (113 bar at Prüfbau vs. 20 - 30 bar at blade) and penetration time is with 5 ms close to dwell time under the blade (0,1 ms).

Pict. 6.4.10 and 6.4.11 proove the assumption that penetration resistance increases with coat weight.
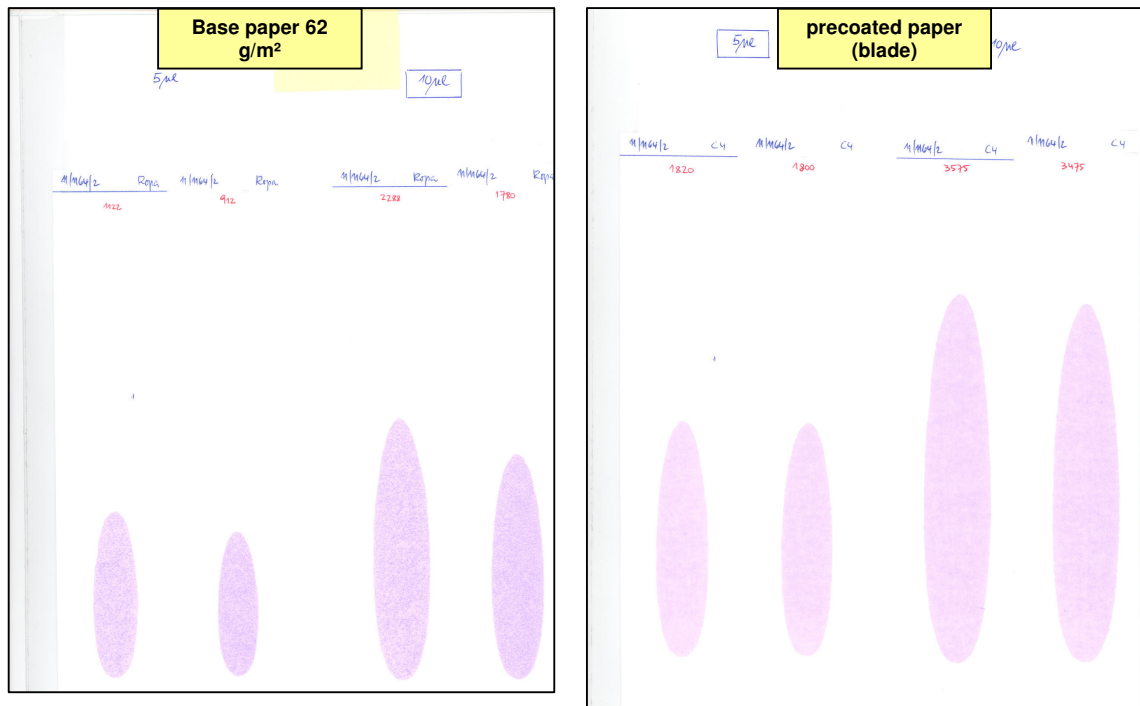
Pict. 6.4.10: Prüfbau water penetration test – comparison base paper (10 µl) to pre-coated paper (only 5 µl) – area of penetration

The area of penetration (mm²) was much bigger for the precaoted paper. Penetration depth L was lower at the precaoted paper as surface permeability was also lower. As droplet volume V is kept constant the area of penetration A increases with falling penetration depth (at comparable surface pore volume).
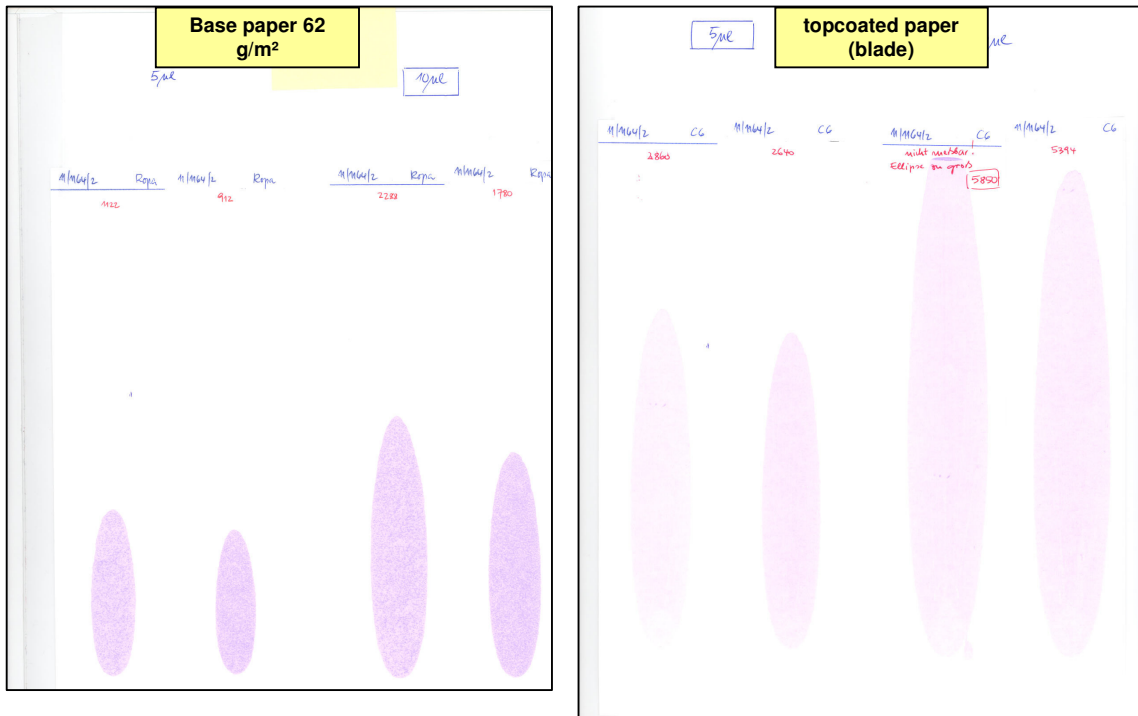
Pict. 6.4.11: Prüfbau water penetration test – comparison base paper (10 µl) to top coated paper (5 µl)

When permeability of a coating layer is low, penetration depth of the coloured liquid is low and the measured area of droplet penetration gets larger (pict. 6.4.12).
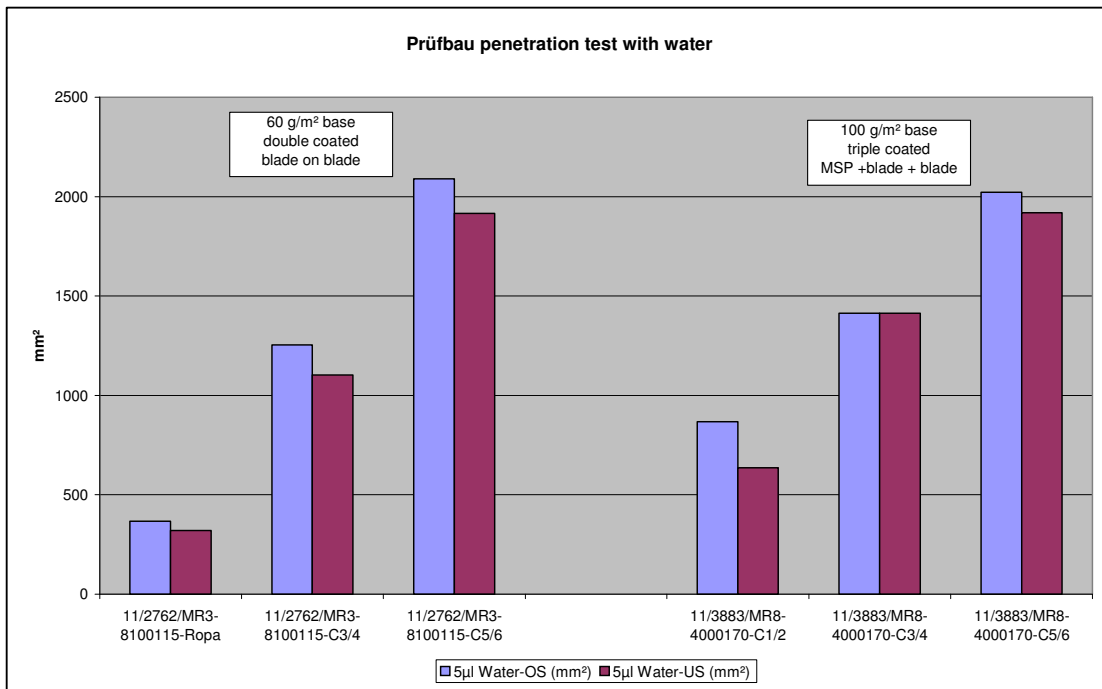
Pict. 6.4.12: Prüfbau water penetration test for all stages of coating of PM11 papers (area of ink penetration)

As coating holdout and base paper coverage improve with every coating layer, permeability drops with every coating layer. This can be detected by comparing the Prüfbau droplet pressure penetration of the middle coating layer with that of the precoating layer (pict. 6.4.13 and 6.4.14).
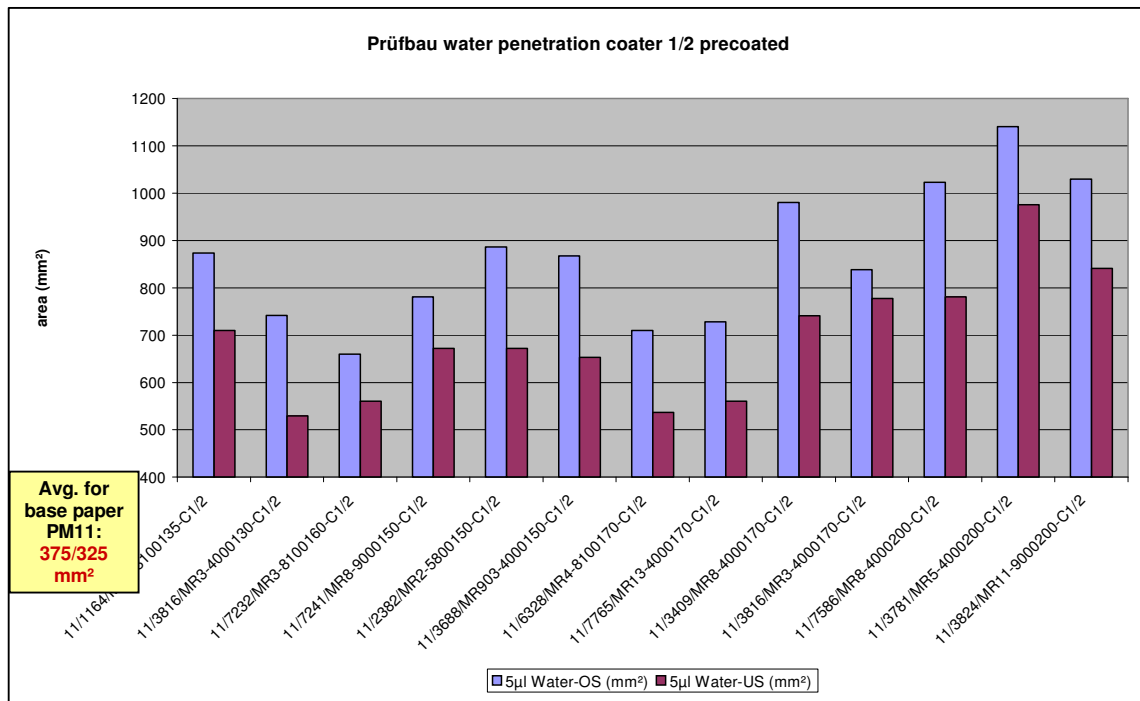
Pict. 6.4.13: Prüfbau water penetration test for precoated samples PM11 (film press precoating)
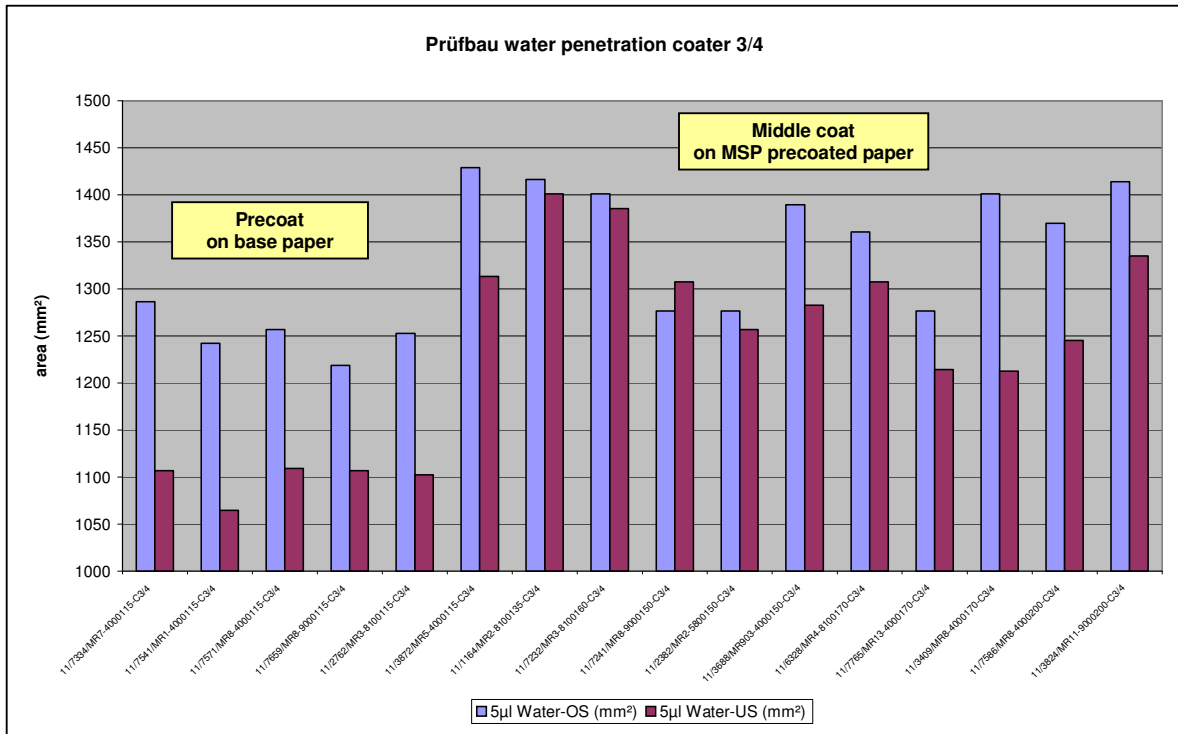
Pict. 6.4.14: Prüfbau water penetration test for middle coated samples PM11 (MSP + blade)

Permeability of coating layer can be reduced by improving the holdout of its fine particles. The dominating factor for coating holdout will be the pore size and the permeability of the substrate.

The calculation in pict. 6.5.2 shows that coating layer permeability was
- 5×10^{-18} for precoating layer
- 5×10^{-19} for middle coating layer (comparable formulation to precoating)
- (10^{-17} for base paper)

Permeability dropped with improved holdout of fines in the coating layer.

The consequence of two sidedness of ash distribution in Z-direction in the base paper of PM11 (see end of chapter) is a big difference in permeability of top and bottom side coating layer. The higher base ash of the top side leads to improved holdout of fines in top side precoating. The permeability of this coating layer, measured with the new Prüfbau pressure penetration test, is clearly lower than for bottom side coating layer. The difference in permeability of top and bottom side coating layer can be detected even at the middle coated papers!

Page 216

J. Grön (L1.36, L1.5.1) came to the same conclusion when he applied LWC coating by metering size press (MSP) on base papers with different base ash content. He measured the holdout ESEM-BSSE of burnout tests and the latex surface concentration by LIPS. Pict. 6.4.15 – 6.4.16 show his results. Coating holdout of base paper improved with higher ash content at the surface especially when coating colour viscosity was low (which is often the case for filmpress coaters).
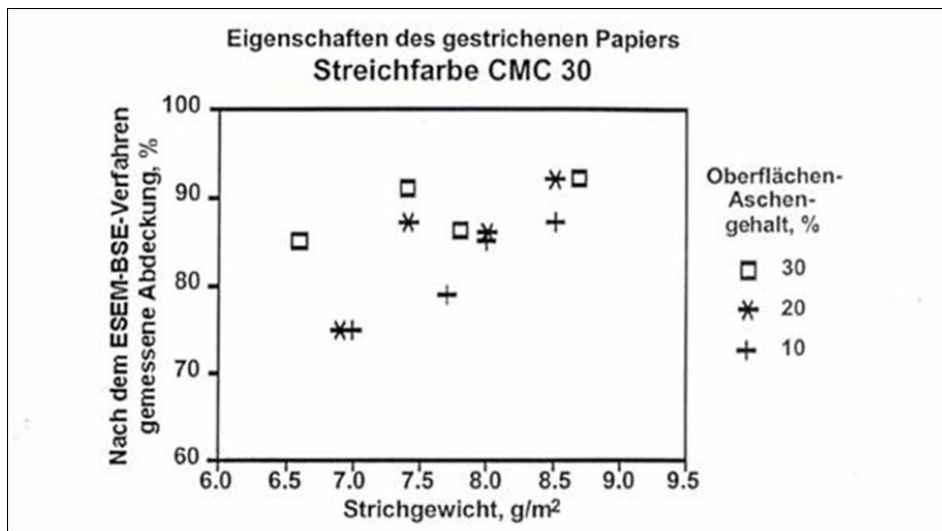
Pict. 6.4.15: J. Grön: Coating holdout in MSP as a function of base ash
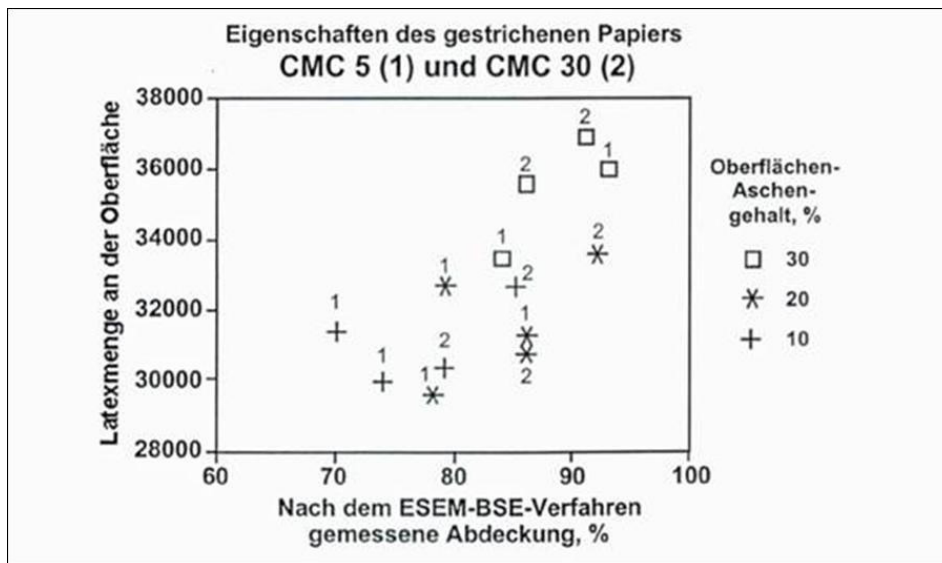
Pict. 6.4.16: J. Grön: Latex holdout as a function of base ash
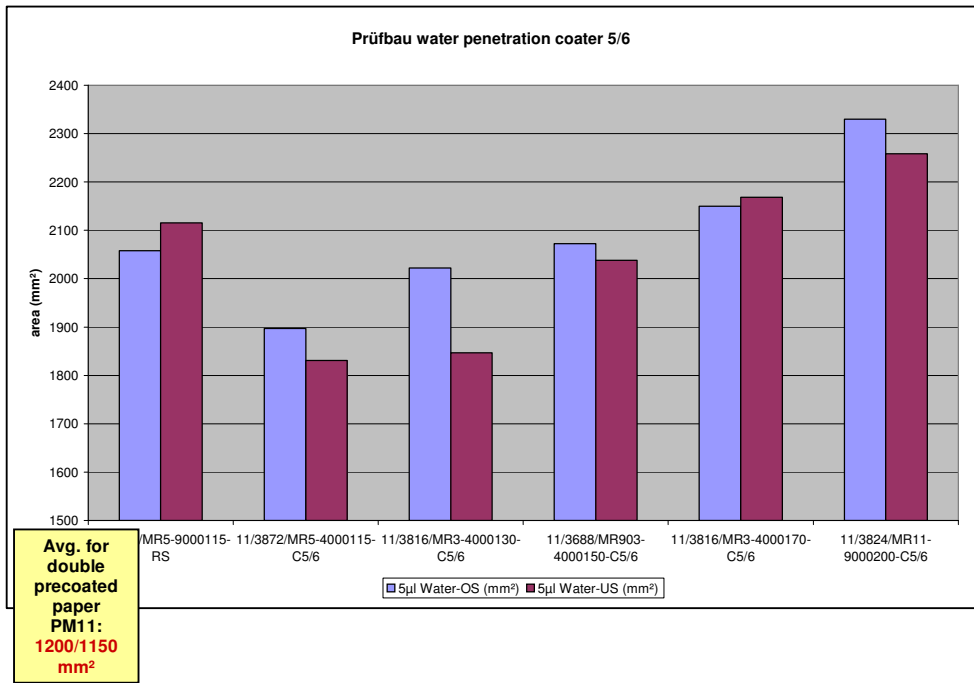
Pict. 6.4.17: Prüfbau water penetration test for top coated samples PM11 (MSP+blade+blade)

6.5 Calculation of the Darcy coefficient of coating layers

From Prüfbau penetration test the Darcy coefficient (the permeability) of the three coating layers of triple coated paper of PM11 was calculated in same way as it was done for the Bendtsen air porosity measurements:

Measures at base paper (11/3419/MR5, 9000115, OS):				
drop volume	V_p	10	µl	
drop lenght		56,0	mm	mesured
drop width		18,0	mm	mesured
drop area	A_{drop}	791,3	mm²	
time for drop penetration	t_{drop}	0,1	sec	
mean width of penetrated drop	b	14,1	mm	
appr. lenght of pressure under Prüfbau roll at Δp	l	5,0	mm	measured in lab (not exactly possible)
area of pressure under Prüfbau roll at Δp	A	70,7	mm²	
penetrated water under prüfbau roll	$V_{p,spez}$	0,013	µl/mm²	calculated on A_{drop}
-- " --	**$V_{p,spez}$**	**12,64**	**ml/m²**	-- " --
Pore volume of paper	**$V_{p,max}$**	27,0	ml/m²	from Hg-Porometrie
theor. penetration depth	L_{th}	12,64	µm	with 100% free volume
true penetration depth	**L**	**50,93**	**µm**	$L = V_{Drop}/V_{Paper}$ x Thickness of paper
maximum penetration depth	L_{max}	54,40	µm	
penetration time under prüfbau roll	t	0,005	sec	
spec. Pressure	Δp	11323425	Pa = N/m²	
	Δp	113	bar	
	Δp	1144,2	m WS	Δp in m WS = (Δp in N) / (ρ_w x 9,81 x A)
formula No.2:	dV/dt = (K x A x Δp) / (η x L)			
	K = ((dV/dt) x η x L) / (A x Δp)		(Δp in Pa)	
Darcy's coefficient with formula No. 2:	**K**	**1,13673E-17**	**m²**	area under the prüfbau roll, o.k.

Pict. 6.5.1: Calc. Darcy coefficient from Prüfbau pressure penetration test at base paper (water as test liquid)

Measures at double precoated paper (11/3688/MR5, 4000170, Avg of OS/US):				
drop volume	V_p	5	µl	
drop lenght		87,5	mm	mesured
drop width		19,5	mm	mesured
drop area	A_{drop}	1339,4	mm²	
time for drop penetration	t_{drop}	0,1	sec	
mean width of penetrated drop	b	15,3	mm	
appr. lenght of pressure under Prüfbau roll at Δp	l	5,0	mm	measured in lab (not exactly possible)
area of pressure under Prüfbau roll at Δp	A	76,5	mm²	
penetrated water under prüfbau roll	$V_{p,spez}$	0,004	µl/mm²	calculated on A_{drop}
-- " --	**$V_{p,spez}$**	**3,73**	**ml/m²**	-- " --
Pore volume of coating layer	$V_{p,max}$	4,5	ml/m²	from Hg measurement
theor. penetration depth	L_{th}	3,73	µm	at 100% free volume
true penetration depth from porosity ε	**L**	**7,09**	**µm**	from free volume of coating layer
maximum penetration depth	L_{max}	8,55	µm	
penetration time under prüfbau roll	t	0,005	sec	
spec. Pressure	Δp	10452393	Pa = N/m²	
	Δp	105	bar	
	Δp	1056,2	m WS	Δp in m WS = (Δp in N) / (ρ_w x 9,81 x A)
formula No.3:	dV/dt = (K x Δp) / (η x L)		p in Pa, A=1m²	
	K = ((dV/dt) x η x L) / (Δp)		(Δp in Pa)	
Darcy's coefficient with formula No. 3:	**K**	**5,0648E-19**	**m²**	

Pict. 6.5.2: Calc. Darcy coeff. from Prüfbau pressure penetration test at double precoated paper (water as test liquid)

The calculated Darcy coefficients from air porosity measurement and from Prüfbau droplet pressure penetration test (pict. 6.5.1 and 6.5.2) were on a comparable level:

<u>Air:</u>
- Base paper: $K = 8 \times 10^{-16}$
- Double precoated paper: $K = 3 \times 10^{-19}$

<u>Water:</u>
- Base paper: $K = 1 \times 10^{-17}$
- Double precoated paper: $K = 5 \times 10^{-19}$

In principle the new Prüfbau pressure penetration test measures the permeability of the coating layer at the surface, not of the whole substrate. This is a difference to the experiments of Darcy, who pressed liquids through the whole porous bed. To apply Darcy's law for Prüfbau pressure penetration tests, the penetration depth L has to be calculated and inserted. This can be easily done when the porosity is known from separate Mercury porosity measurement (see previous calculation).

In principle this additional step of measurement and calculation is a disadvantage of the new Prüfbau pressure penetration test against the much simpler permeability measurements with conventional permeability cell (e.g. at OMYA) where the whole cross section of the substrate is penetrated. But the disadvantage of the Prüfbau droplet pressure penetration test of being a surface permeability test is in the same moment an advantage. When the pressure penetration depth of a top coating layer into the precoated substrate must be determined, the surface permeability is of greater importance than the permeability of the whole paper.

6.6 Prüfbau pressure penetration test with different liquids

To prove the validity of Darcy's law, different liquids were used for the Prüfbau pressure penetration test.

According to Darcy's law $\frac{dV}{dt} = \frac{K * A * \Delta p}{\eta * L}$ pressure penetration is independent from

liquid surface tension and from contact angle but linearly depending on the inverse of liquid viscosity.

Oil and coloured water with the same viscosity but totally different contact angle and surface tension were used for the new Prüfbau test.

Oil wets the paper surface much better. Its contact angle is half of that of water (pict. 6.6.1).

sappi GK/PQ	Comparison of different liquids for pressure and capillary penetration tests				
	Surface tension	Contact angle after 0,04 s		Viscosity	
		On precoated paper	On base paper	Spindel 2 / 100 rpm	Spindel 2 / 20 rpm
	mN/m	cp	cp	cp	cp
Water	71,5	92	81	26	15
Water + IPA (20%)	43,1	78	72	38	15
Waster + IPA (50%)	26,7			19	8
CMC solution 1,1 %	70,1			90	40
CMC solution 2 %					
Oil (Flint)	29,4	42	33	24	13

Pict. 6.6.1: Physical properties of test liquids
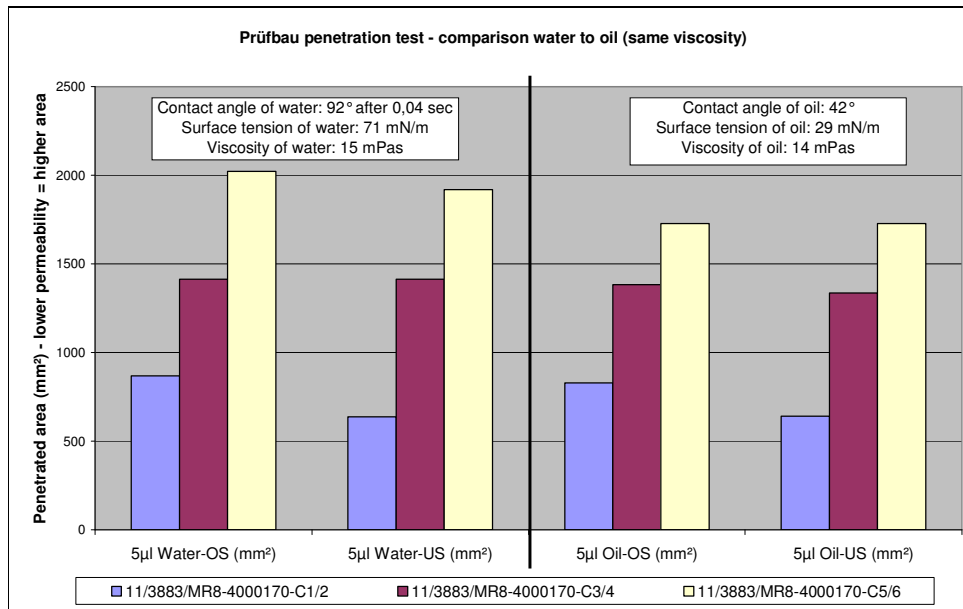
Pict. 6.6.2: Prüfbau water + oil penetration test: C1/2 = precoated, C3/4 = middle coated, C5/6 = top coated

The results shown in pict. 6.6.2 prooved Darcy's law:

Pressure penetration depth was independent from contact angle and surface tension.

This is important for all kinds of pressure application like coaters or printing nips. Transfer of applied liquids (ink or water) will be depending on liquid viscosity and not on contact angle and surface tension of liquid.

Contact angle and surface tension of liquids will be dominating when capillary sorption starts in pores of the substrate <u>after</u> pressure application of the coating colour or the ink.

The contact angle at the surface of the substrate (which is easy to measure by Fibro-DAT) will be of minor importance once the liquid is pressed into the pores. The contact angle of the liquid at the pore walls, the pore radius and the liquid surface tension will dominate capillary sorption.

Pict. 6.6.3 shows that this finding was proven for all kinds of paper substrates.
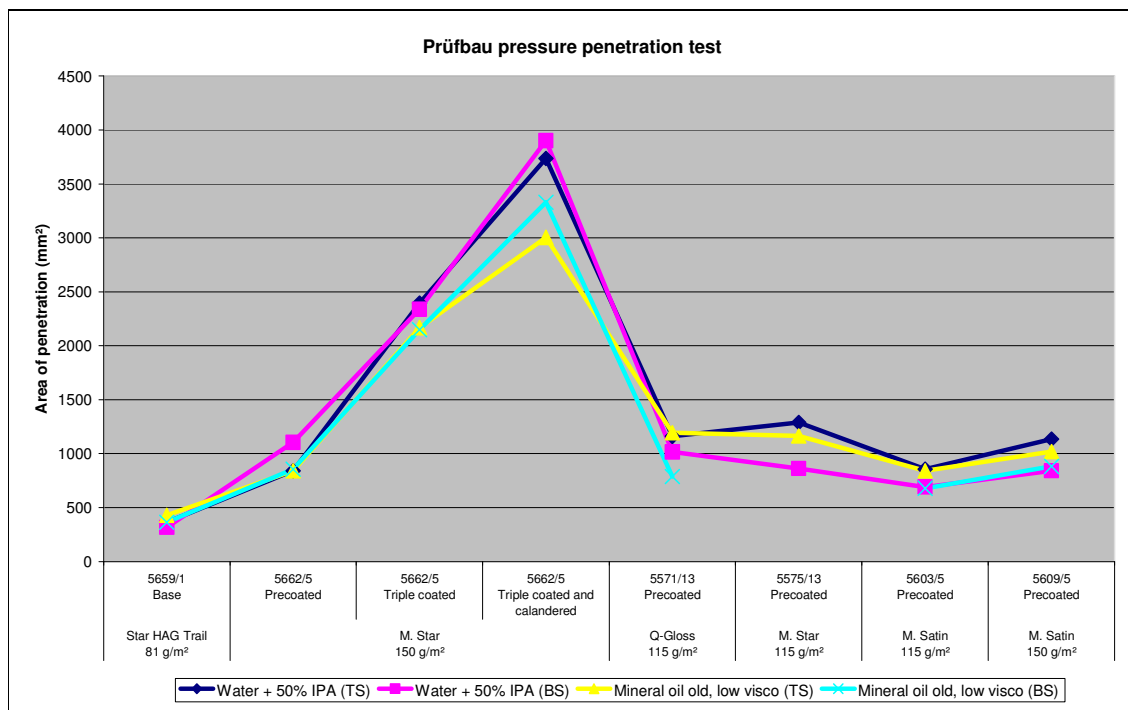
Pict. 6.6.3: Correlation of Prüfbau pressure penetration test on different substrates for oil and water with same viscosity

To evaluate the influence of liquid viscosity on pressure penetration, CMC was added to the test water and viscosity increased.

Vergleich der Druckpenetrationen mit verschiedenen Benetzungsflüssigkeiten

60 PL3	100 PL3	100 PL3	115 PL4	115 PL4	135 PL4	135 PL4	100 PL3	100 PL3	135 PL4	135 PL4	100 PL3	115 PL4	170 PL4	200 PL4	100 PL3	115 PL4	135 PL4	170 PL4	200 PL4	100 PL3	115 PL3	135 PL4	170 PL4	200 PL4
Offset Ropa	Star Ropa	Satin Ropa	Satin Ropa	Satin PM	Star PM	Satin PM	Star SM	Satin SM	Star SM	Satin SM	RRBP RS	Q-Gloss RS			Star RS					Satin RS				

Legend:
- Wasser + IPA (20%) Oberflächenspannung 43,1 mN/m
- CMC -Lösung (1,1 %) Oberflächenspannung 70,1 mN/m
- Öl 002 Lösung Oberflächenspannung 35,0 mN/m
- Öl Flint Lösung Oberflächenspannung 29,4 mN/m

Pict. 6.6.4: Prüfbau pressure penetration test with different liquids on different substrates (Ropa = base paper, PM = precoated, SM = topcoated, RS = calandered)

Comparing the pressure penetration results of CMC solution with pure water (pict. 6.6.4) proves Darcy's law: Less liquid was pressed into all tested substrates when liquid viscosity was increased with CMC.

Water and oil of same viscosity were on a comparable level, proving again that pressure penetration under a blade or in a printing nip is ruled by Darcy's law.

6.7 Changing the application conditions for the Prüfbau pressure penetration test

The new Prüfbau pressure penetration test was repeated on a single substrate with different application conditions to verify the calculation of the Darcy coefficient. The speed of the test and the application pressure were varied.

Prüfbau "Drop penetration test"		M-Star,200 middle coated Water + 20% IPA Standard 800 N - 0,5m/sec.	M-Star,200 middle coated Water + 20% IPA Versuch 800 N - 1,0m/sec.	M-Star,200 middle coated Water + 20% IPA Versuch 400N - 0,5m/sec.	M-Star,200 middle coated 1,1% CMC solution Standard 800 N - 0,5m/sec.		
Paper: Double precoated base (11/3824/MR5, OS):							Comment
basis weight		120	120	120	120	g/m²	
thickness, total		9,6	9,6	9,6	9,6	µm	from thickness measurements of paper samples
pore volume in precoating layer		9	9	9	9	ml/m²	topside + bottom side from Hg-poros.
avg. Pore radius	r	0,25	0,25	0,25	0,25	µm	from Hg-porosimetry
max. penetration volume	$V_{p, max}$	4,5	4,5	4,5	4,5	ml/m²	total pore volume / 2
Porosity from mercury		35,0	35,0	35,0	35,0	%	from Hg-porosimetry
Coating layer thickness (MSP+blade), both sides		0,0171	0,0171	0,0171	0,0171	mm	from thickness measurements of paper samples
-- " --	$H_{coating}$	8,5476	8,5476	8,5476	8,5476	µm per side	
Liquid: Coloured dest. Water							
contact angle	θ	78	78	78	85	°	after wetting (0,04 sec)
	θ	1,3614	1,3614	1,3614	1,4835	rad	
	cos θ	0,208	0,208	0,208	0,087		
surface tension	γ	43	43	43	70,1	mN/m	
viscosity	η = µ	0,015	0,015	0,015	0,040	Pa s = kg/ms	
density	ρ	1000	1000	1000	1000	kg/m³	
Prüfbau:							
speed of test	v	0,5	1,0	0,5	0,5	m/s	
pressure at nip	Δp	800	800	400	800	N	1 N = 1 kg m / s², Pa = N/m²
Measures at double precoated paper (11/3688/MR5, 4000170, Avg of OS/US):							
drop volume	V_{drop}	5	5	5	5	µl	known
drop lenght	B_{drop}	70,0	83,3	83,0	92,0	mm	mesured
drop width	L_{drop}	15,0	18,5	18,5	20,4	mm	mesured
drop area	A_{drop}	824	1210	1205	1473	mm²	$A_{drop}=B_{drop}*L_{drop}*3,14/4$
time for drop penetration	t_{drop}	0,140	0,083	0,166	0,184	sec	$t_{drop}=L_{drop}/v_{Prüfbau}$
penetrated water under prüfbau roll	$V_{p,spez}$	0,006	0,004	0,004	0,003	µl/mm²	$V_{p,spez}=V_{drop}/A_{drop}$
-- " --	$V_{p,spez}$	6,07	4,13	4,15	3,39	ml/m²	-- " --
comparison: Pore volume of coating layer	$V_{p, max}$	4,5	4,5	4,5	4,5	ml/m²	from Hg measurement
mean width of penetrated drop	b	11,8	14,5	14,5	16,0	mm	
appr. lenght of pressure under Prüfbau roll at Δp	l	5,0	5,0	5,0	5,0	mm	measured by pressure sensitve film
area of pressure under Prüfbau roll at Δp	A	58,9	72,6	72,6	80,1	mm²	
penetrated water under prüfbau roll	V_p	0,357	0,300	0,301	0,272	µl	$V_p=V_{p,spez}*A$
-- " --	V_p	0,00036	0,00030	0,00030	0,00027	ml	-- " --
theor. penetration depth	L_{th}	6,07	4,13	4,15	3,39	µm	at 100% free volume
true penetration depth from porosity ε	**L**	**11,52**	**7,85**	**7,88**	**6,45**	**µm**	L = (V_{Drop}/V_{paper}) x $H_{coating}$
comparison: maximum penetration depth	L_{max}	8,55	8,55	8,55	8,55	µm	$H_{coating}$
penetration time under prüfbau roll	t	0,010	0,005	0,010	0,010	sec	
spec. Pressure	Δp	13588110	11017387	5508693	9991258	Pa = N/m²	
	Δp	136	110	55	100	bar	
	Δp	1373,0	1113,2	556,6	1009,6	m WS	Δp in m WS = (Δp in N) / (ρ_w x 9,81 x A)
formula No.2:		dV/dt = (K x A x Δp) / (η x L)					
		K = ((dV/dt) x η x L) / (A x Δp)	(Δp in Pa)				
Darcy's coefficient with formula No. 2:	**K**	**7,72E-18**	**8,84E-18**	**8,90E-18**	**8,76E-18**	**m²**	
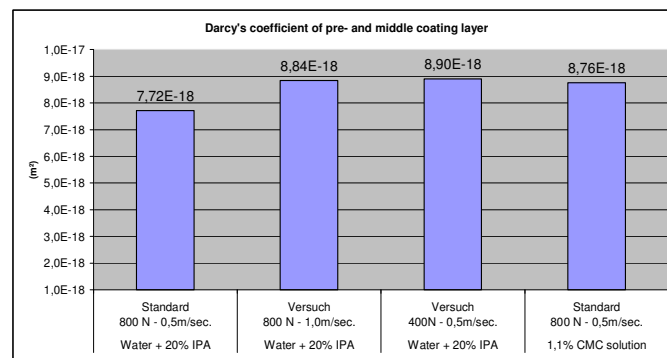
Pict. 6.7.1: Prüfbau pressure penetration test with different conditions of application

The calculation shown in pict. 6.7.1 shows that calculated Darcy coefficient remained constant for different application pressure, application time and viscosity of the liquid.

6.8 Measurement of surface permeability of base papers

The Prüfbau pressure penetration test is currently not only used to describe the permeability of a coating layer - it is also used to specify the surface permeability of a base paper or in other words its coating holdout. The larger the drop area, the lower is the surface permeability and the better the coating holdout will be.

The 62 g/m² base paper of PM11 of double coated 115 g/m² was developed in 2006 – 2007 to improve the coating holdout. Base ash was increased to lower the surface porosity, ash retention and fibre beating was raised.
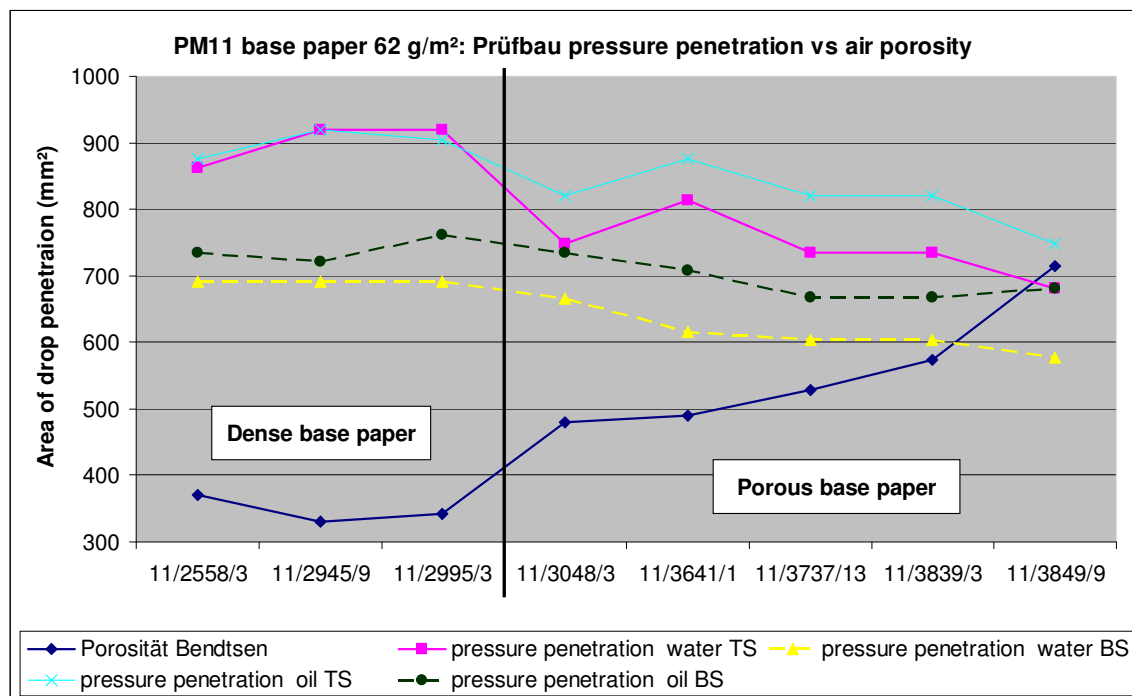
Pict. 6.8.1: Prüfbau pressure penetration test versus Bendtsen air porosity for base different papers PM11

Pict. 6.8.1 shows that the correlation of air porosity and Prüfbau pressure penetration test with water and oil was quite good for the tested base papers. Higher air permeability corresponded to lower drop area or higher permeability of the base

paper. The assumption was proven that Bendtsen air permeability can be used for base papers but not for coated papers where air is compressed to a greater extend.

The Prüfbau pressure penetration tests on base papers showed again that the results of oil and water with same viscosity correlated well.

6.9 Measurements with OMYA's pressure penetration cell

To control the measurements with the new Prüfbau pressure penetration test a third method was used, a pressure penetration cell at OMYA / Oftringen. The test unit is shown in pict. 6.9.1. It is the standard procedure to determine the permeability of a solid material.

A dry tablet of the tested coating colour was prepared under pressure. The size fitted exactly to the pressure cell. The thickness of the tablet was measured seperately.
In the pressure cell an un-polar liquid was pressed under a certain pressure through the dry coating tablet. The amount of liquid per unit of time was measured with a scale under the permeability cell. Darcy coefficient was calculated from:

$$K = \frac{dV}{dt} * \frac{\eta * L}{A * \Delta p}$$
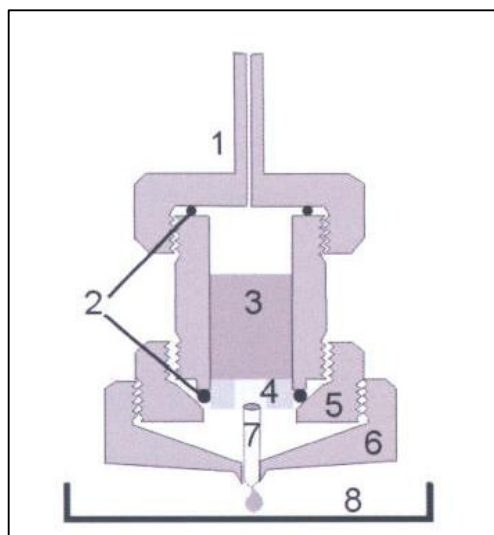
1....pressure inlet
2....sealing
3....liquid cell
4....tablet (sample)
5....fixing ring for O-ring
6...security shroud and drop collector
7....drop captor
8....dish on micro balance

Pict. 6.9.1: Pressure cell for calculation of Darcy coefficient at OMYA
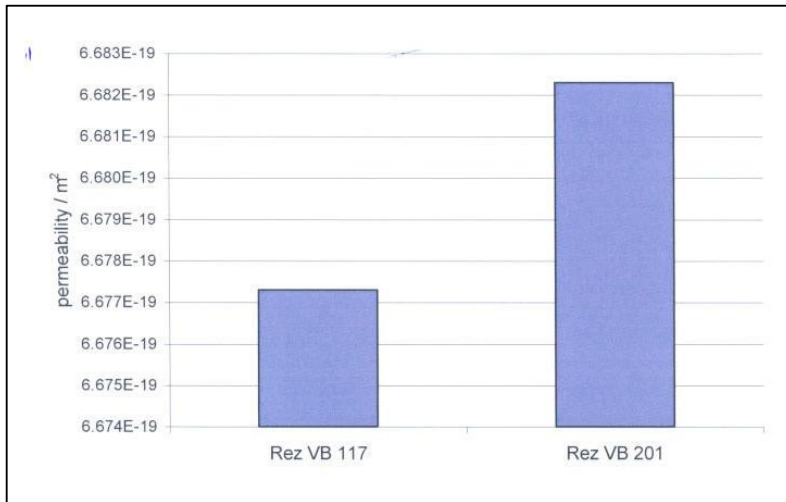
Pict. 6.9.2: Darcy coefficient with OMYA pressure cell of precoat (Rez. 117) and middle coat (Rez. 201)

Pict. 6.9.2 shows that the Darcy coefficient of pre and middle coating tablets, calculated from measurements with OMYA pressure cell (avg. K = 6,8 x 10^{-19}) were comparable with those from Prüfbau droplet pressure penetration tests at double pre-coated papers (K = 5 x 10^{-19}).

The disadvantage of OMYA's pressure penetration cell is that when coatings are measured alone they have to be prepared as thick tablets. Porosity of these tablets is influenced by drying conditions and thickness of tablet. Therefore permeability of coating tablets made at OMYA may differ from mill coatings where thickness is much lower, drying is faster and application is done under pressure on a porous substrate (loss of fines).

When coated papers are measured in OMYA's penetration cell, the Darcy coefficient is a sum of base paper and coating layer permeability.

The Prüfbau pressure penetration test detects the surface permeability which is the coating layer permeability when coated papers are measured. This surface permeability is more important for the following coating application or print nip than the whole permeability of the paper – coating – composite.

Remark: Precoated papers show most often big differences in in-plane coating layer thickness.

REM picture like 6.9.3 show spots with almost no coating on the fibres. At these areas the permeability will be dominated by the base paper which is of two magnitudes lower than that of the coating layer
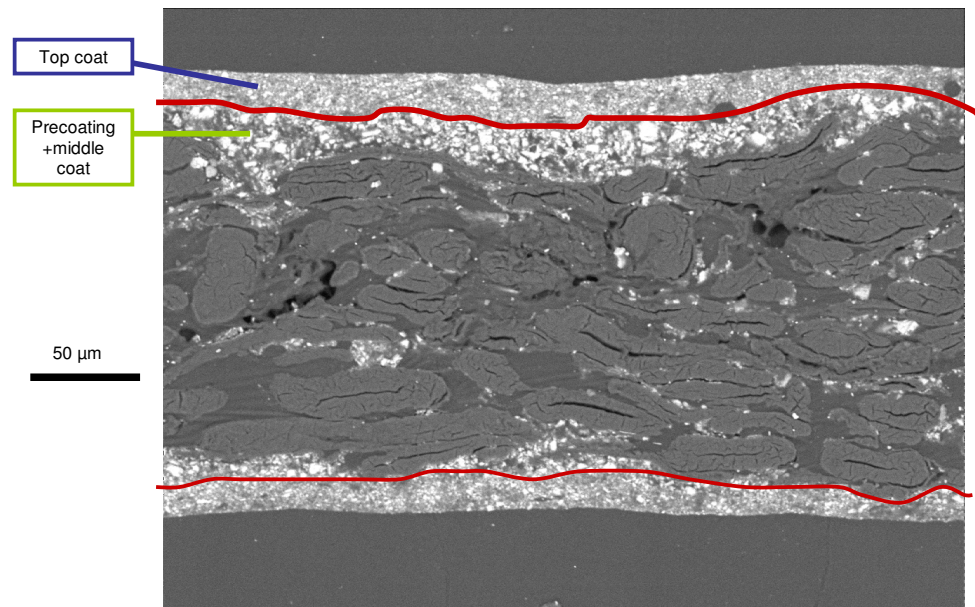
Pict. 6.9.3: Coating layer thickness from REM

The measured permeability of the Prüfbau test is a mean value for all these non-uniformities in coating layer thickness.

Darcy coefficient of a pre-coating layer is determined by the colour formulation and its holdout.

To reduce permeability of PM11 precoating layer the pigment mixture was changed from 100% HC60 to 50% coarse HC60 and 50% fine HC90 (pict. 6.9.4)

Calculated Darcy Coefficient versus Coat weight
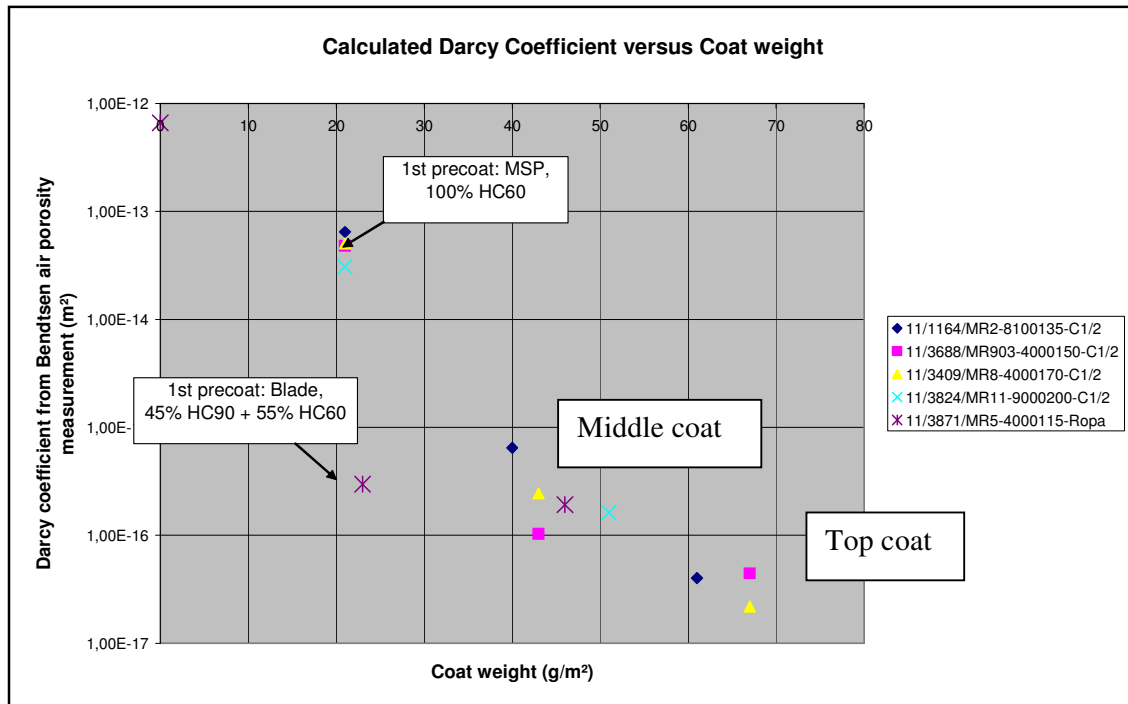
Pict. 6.9.4: Darcy coefficient of different coating layers PM11

Precoating formulation 1:

- 100% HC60, 5% dextrine starch, 7% latex, 10+12 g/m²
- Bendtsen porosity of precoated paper: 40 ml/min
- Pre-coated paper: **K = 7 x 10^{-17}**

Precoating formulation 2:

- 50% HC90, 50% HC60, 8% dextrine starch, 4% latex, 10+12 g/m²
- Bendtsten porosity of precoated paper: 5 ml/min
- Pre-coated paper: **K = 9 x 10^{-18}**

Permeability could be remarkably reduced by the new formulation and reached the level of middle coatings which are always lower in permeability than precoating due to better holdout of fines.

The improvement of coating colour holdout with increasing number of pre coating layers can be also seen in the thickness of the coating layers. If holdout is bad,

coating colour penetration depth is high and increase in thickness (drop in volume) by coating is low:

Loss of paper volume by applying coating colour with different meetring systems at PM11/CM11

- Precoat MSP (17g/m²): **0,19** loss in volume
- Blade after MSP (20 g/m²): **0,10** loss in volume !!!
- Topcoat blade (20 g/m²): **0,12** loss in volume
- Precoat blade (23 g/m²): **0,23** loss in volume
- Topcoat blade (22 g/m²): **0,16** loss in volume
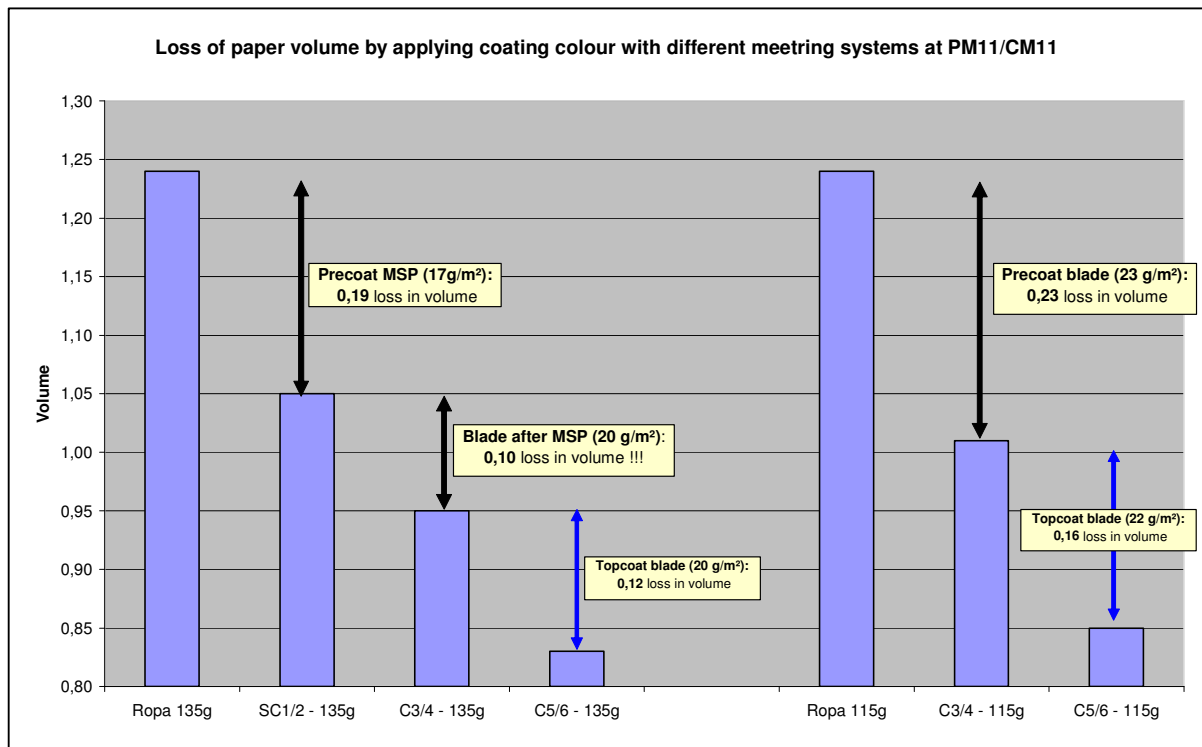
Pict. 6.9.5: Loss in volume as a function of coating holdout (Ropa = base paper, SC1/2 = precoated, C3/4 = middle coated, C5/6 = topcoated)

Pict. 6.9.5 shows that when the coating holdout of a film press coater (MSP) is compared with a blade coater the holdout is better for film press coater as the drop in volume of precoated paper by MSP is lower.

Blade top coatings showed also better coating holdout than blade precoatings as their drop in volume was also much lower.

The pressure penetration cell is also used at OMYA to compare the permeability data's of pigment and coating tablets with Mercury porosity. Besides the calculation from Darcy's law $K = \frac{dV}{dt} * \frac{\eta * L}{A * \Delta p}$ permeability can be calculated from Mercury porosity measurements according to

Equ. 6-9-1: Carman Kozeny equation: $K = \frac{(1 - \Phi)^3}{k_0 * T^2 * \Phi^2 * A_s{}^2}$

τ......tortuosity

A_s....spec. surface area of porous medium (m²/m³)

K_0....shape factor (between 2 and 3)

Φ.....porosity (%)

Results are shown in pict. 6.9.6.
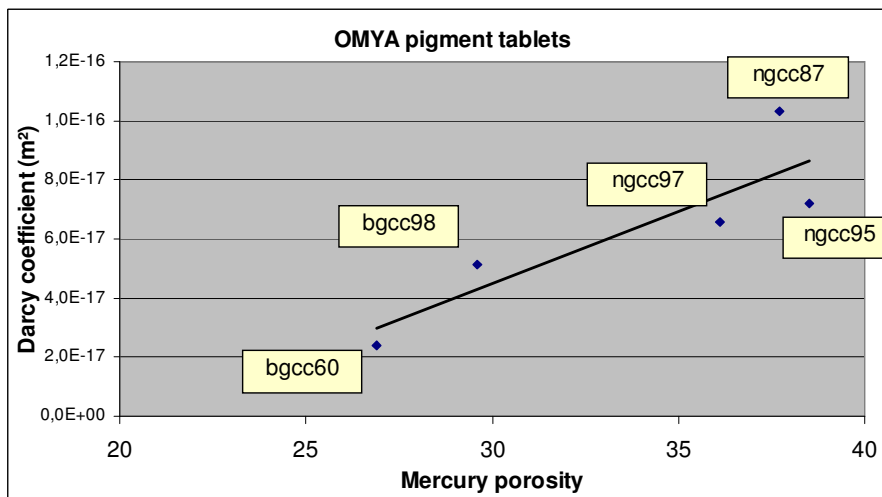
Pict. 6.9.6: Comparison of measured mercury porosity with measured permeability (OMYA pressure penetration cell)

Calculating the permeability from Mercury porosity by applying Carman-Kozeny (pict. 6.9.7):
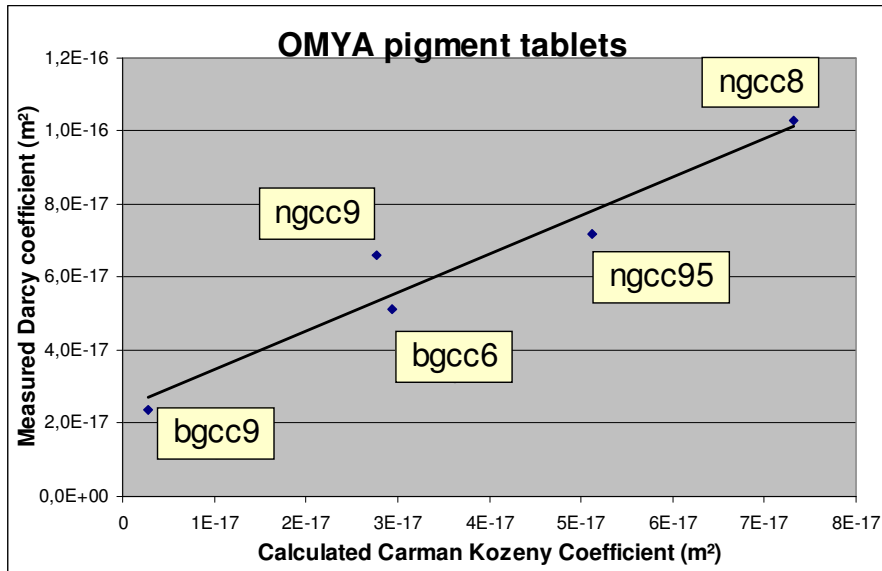
Pict. 6.9.7: Correlation of calculated permeability (from mercury porosity) with measured permeability

Calculated permeability from Mercury porosity correlated quite well with the measured permeability in the OMYA pressure penetration cell without including different levels of tortuosity in this calculation. The cell can be used to calculate the tortuosity of a pigment / coating tablet by comparing the permeability data's with Mercury porosity. When monosized particles are used the permeability depends on porosity according to the Carman Kozeny equation with т the tortuosity = 1.

When pigments with broad particle size distribution are used the channels in the porous tablet are partly blocked by fine material and tortuosity increases. T can be calculated from the Carman Kozeny equation when the permeability, the porosity and the specific surface area of the particles in the tablet have been measured. Tortuosity plays an important role for ink drying. In principle the pores of the top coating layer shouldn't be blocked by fine particles as ink drying will be prolonged. Therefore the right choice of pigment and latex mixture is important for fast ink drying.

6.10 Two-sidedness of PM11 papers

PM11 top coated papers show always a higher gloss on the topside when symmetrically lab calandered, although the coat weight of the precoating is higher on the bottom side. Two-sidedness increases with basis weight (pict. 6.10.1).
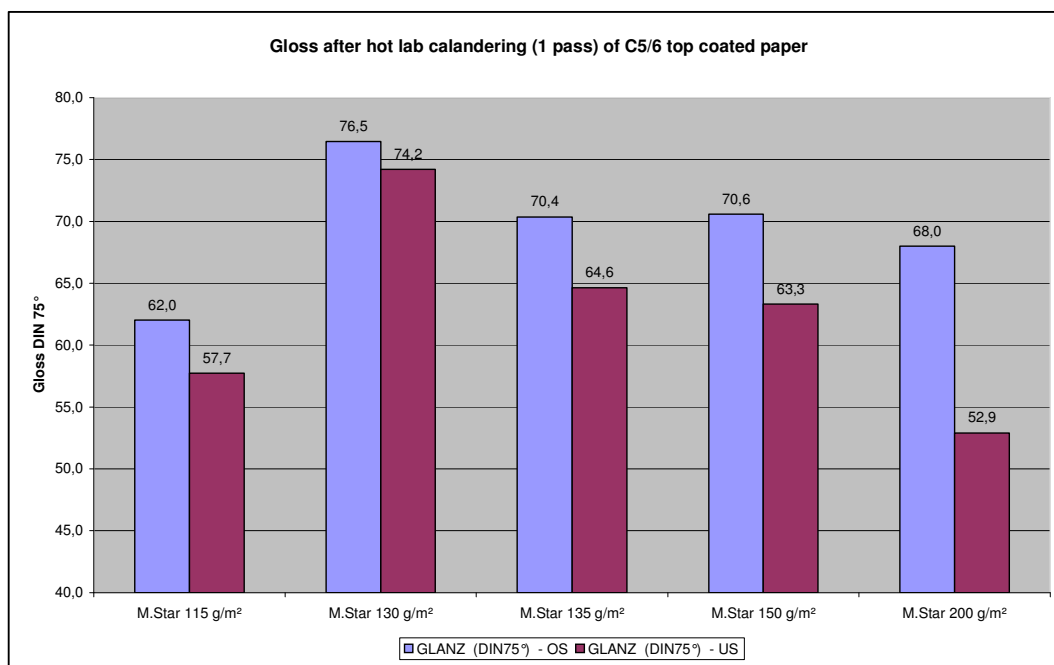
Gloss after hot lab calandering (1 pass) of C5/6 top coated paper

	M.Star 115 g/m²	M.Star 130 g/m²	M.Star 135 g/m²	M.Star 150 g/m²	M.Star 200 g/m²
GLANZ (DIN75°) - OS	62,0	76,5	70,4	70,6	68,0
GLANZ (DIN75°) - US	57,7	74,2	64,6	63,3	52,9

Gloss DIN 75°

Pict. 6.10.1: Gloss two sidedness PM11 double and triple coated papers, increasing with basis weight

There are two possible causes for the worse gloss of PM11 bottom side:
a) Two sidedness of base ash distribution in the base paper (pict. 6.10.3 and 6.10.4 show results from sheet split measurements where the top side is 2 – 8% higher in ash content at the surface).
b) Two sidedness in smoothness, as shown in pict. 6.10.2 (the bottom side is the last side, touching a felt and thus rougher than the topside).
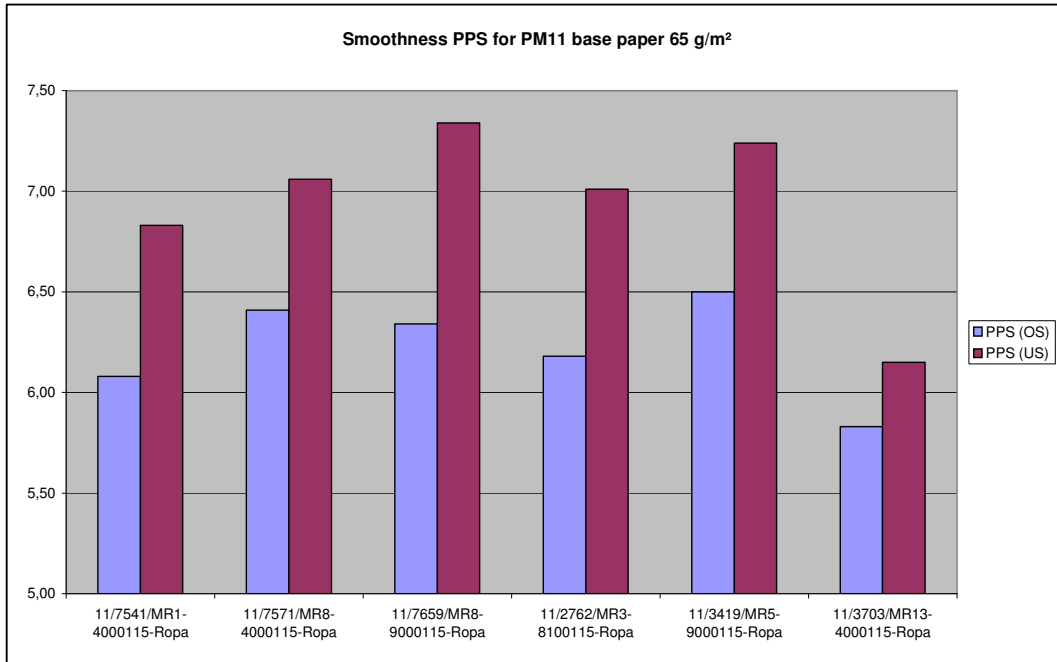
Pict. 6.10.2: Smoothness two sidedness of base paper PM11 due to 4th press felt on bottom side
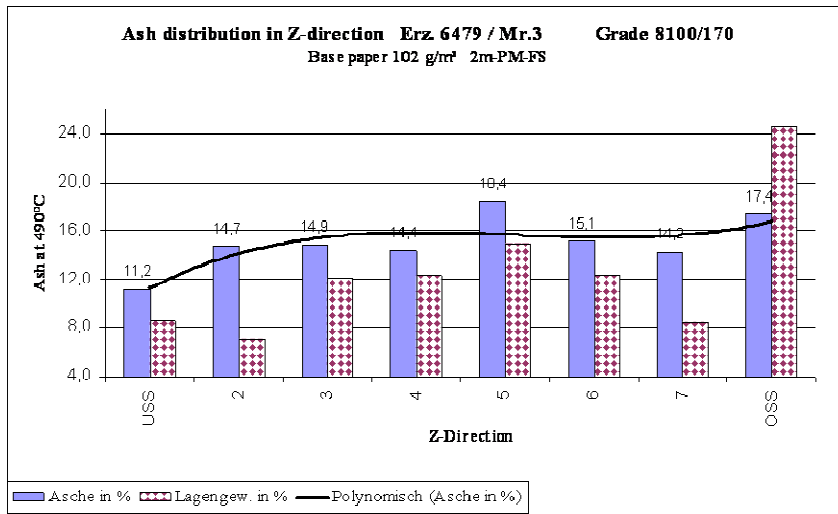
Pict. 6.10.3: Base ash two-sidedness at heavy basis weight of PM11 (100 gm² base)
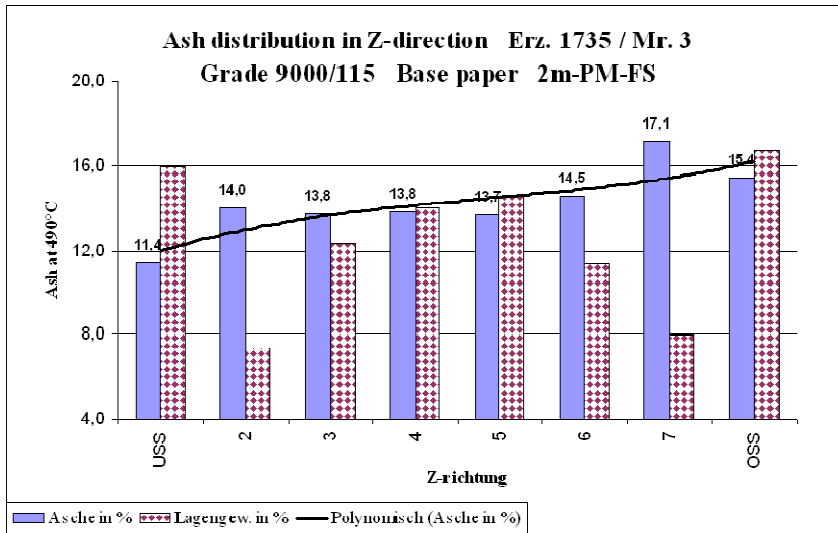
Pict. 6.10.4: Base ash two-sidedness at low basis weight of PM11 (60 gm² base)

Pict. 6.10.3 and 6.10.4 proove that the two-sidedness in base ash at the surface increases for PM11 with basis weight. The Prüfbau pressure penetration tests shown in pict. 6.10.5 show that coating holdout is much better at the top side of PM11 base paper as pressure penetration resistance is higher.

As a consequence the gloss of top side is always higher than that of bottom side.
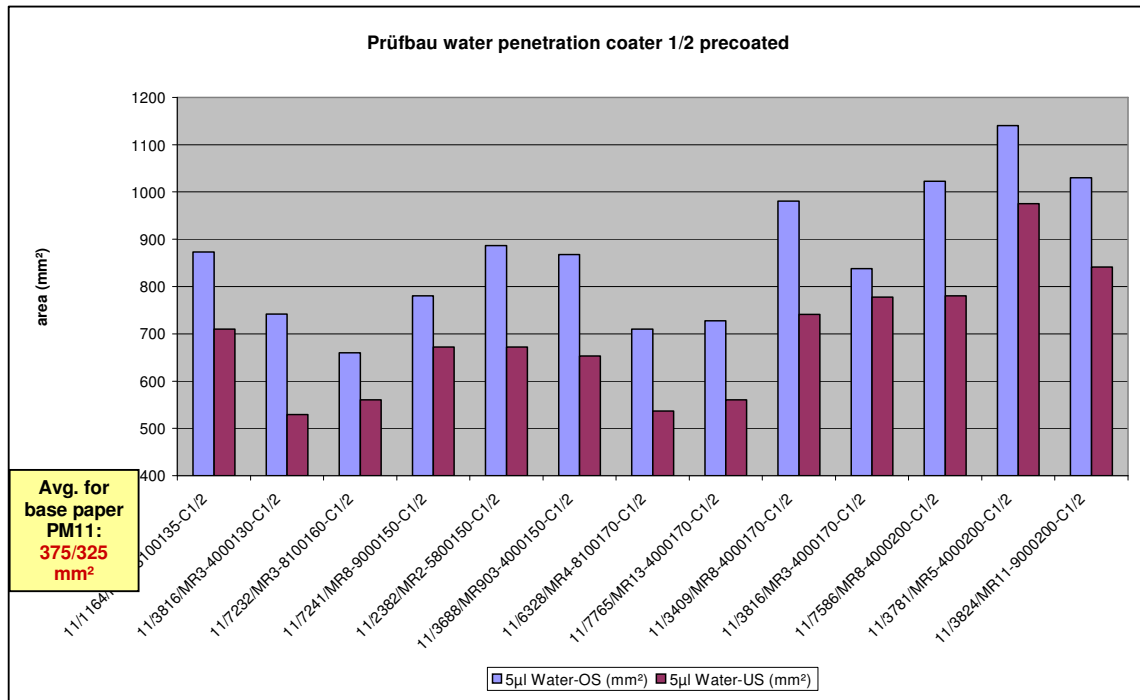
Pict. 6.10.5: Prüfbau water penetration test for precoated samples PM11 (MSP coater)

The cause of base ash two-sidedness is the layout of gap former PM11 as shown in pict. 6.10.6:
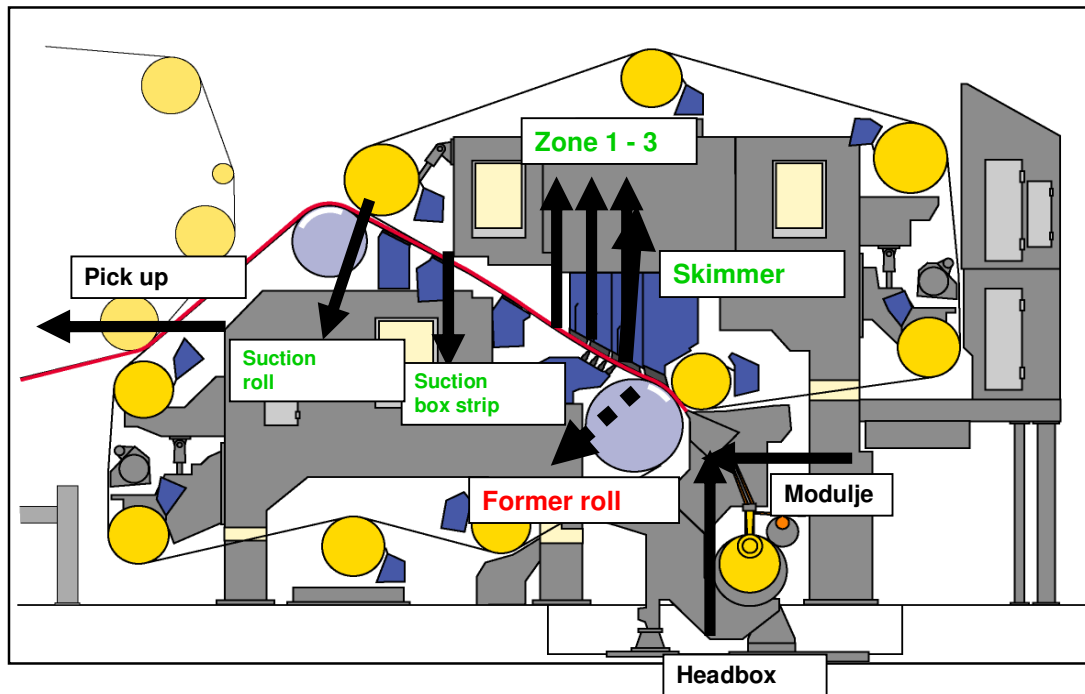
Pict. 6.10.6: Gap former layout of PM11

In a diploma thesis the mass balance of the wire section of PM11 was measured and calculated with the S-Draw balancing programme.
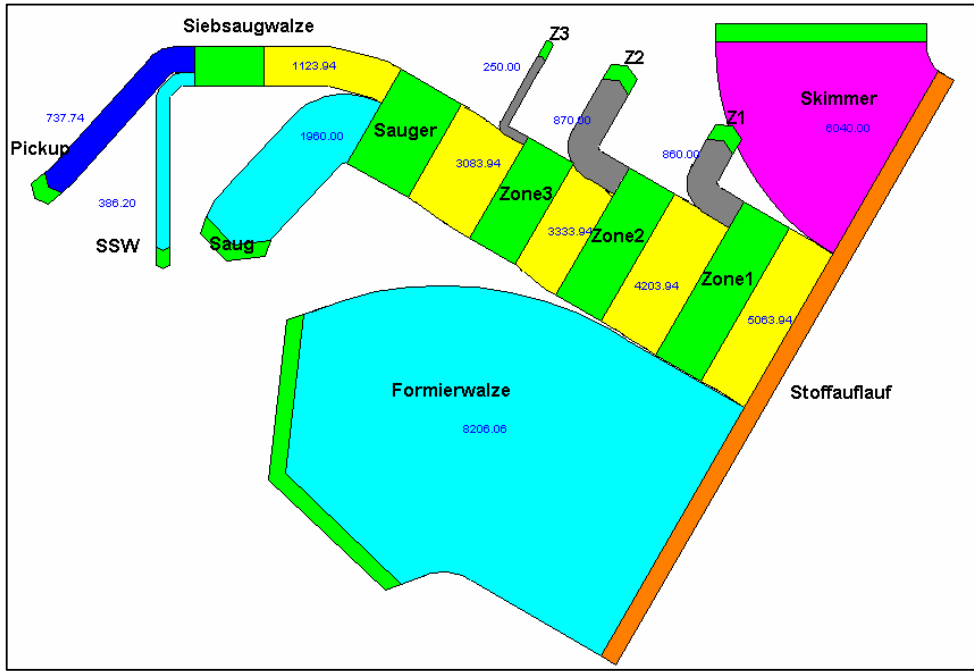
Pict. 6.10.7: Mass balance of wire section PM11for a 100 g/m² base (mass flow of fibres and pigments in g/s)
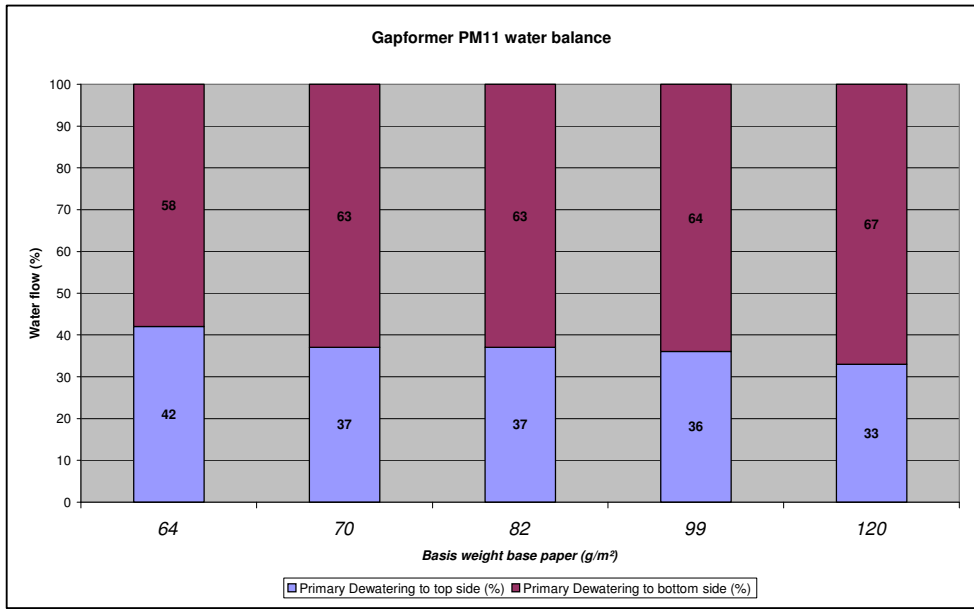
Pict. 6.10.8: Calculated two sidedness of dewatering in primary dewatering section of PM11

The results show a two sidedness in the primary dewatering zone, which increases with basis weight (pict. 6.10.8). More water is removed to the bottom side and fine

ash particles get lost through the wire pores. This two-sidedness can be adjusted by wire design or wire porosity of top wire and bottom wire.

The two-sidedness in base ash, which is created in the primary dewatering section of PM11 is increased in the D-Bar section (pict. 6.10.9). Here the web is reformed by the impact of ceramic covered D-bars, which hit the bottom wire:
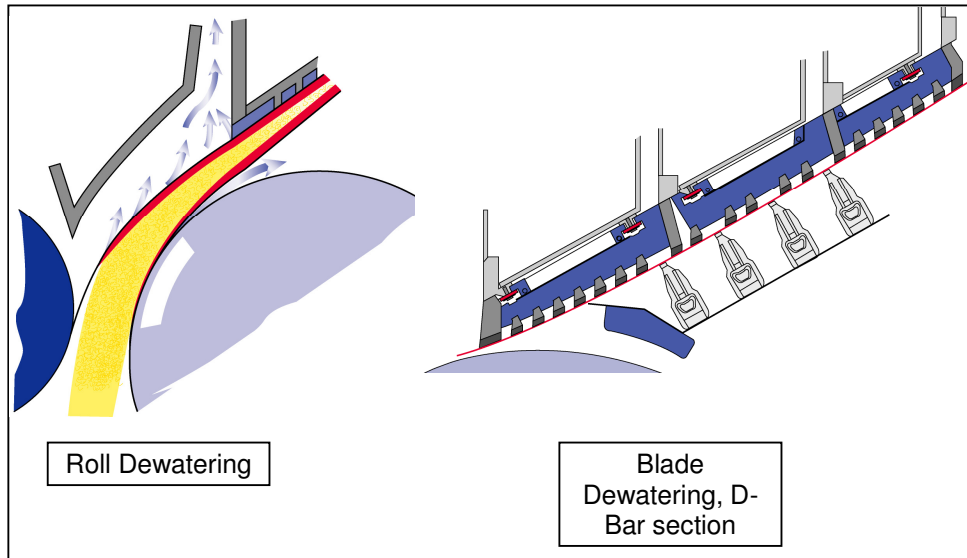
Pict. 6.10.9: Primary and secondary dewatering section of PM11

The gap former of PM11 has a 45° design. Therefore water has to be removed by vacuum in the D-bar section. Small filler particles follow the water flow through the wet sheet to the top side in this section and ash content increase at the topside.

At vertical gap formers the wire water is removed symmetrically.

In the last part of the forming section of PM11 wire water is transported by suction box and suction roll vacuum solely to the bottom side. This leads to compensation of the wire water dewatering two-sidedness, created in the wire section. Pict. 6.10.10 shows that the overall water removal in the wire section of PM11 is symmetrical:
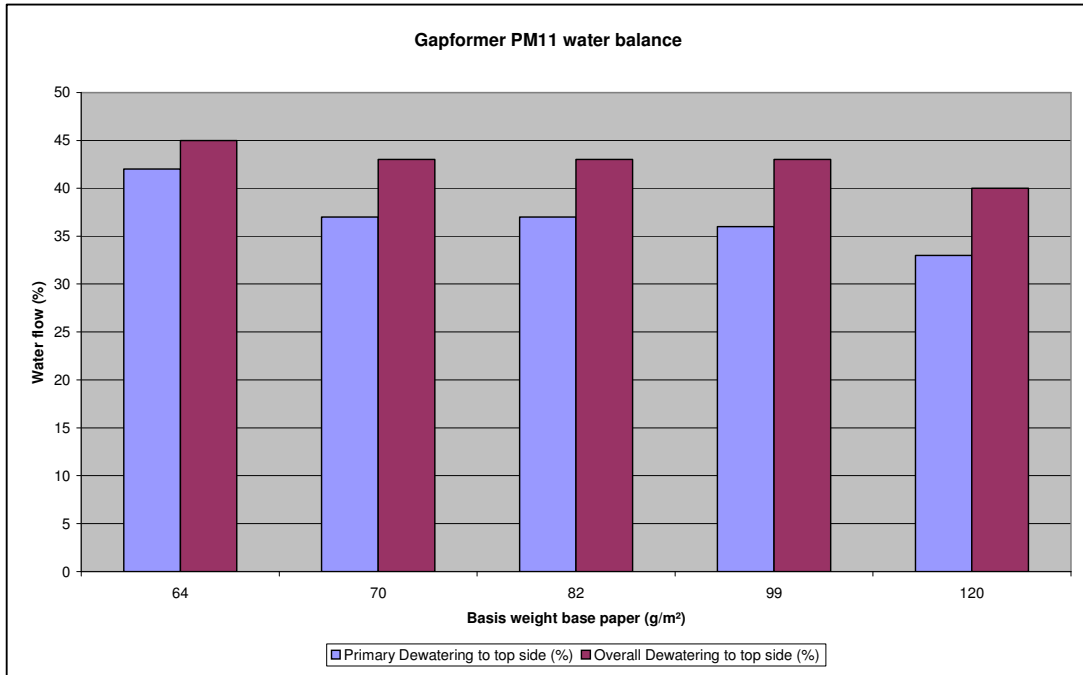
Pict. 6.10.10: Comparison of primary and secondary dewatering two-sidedness PM11

The two-sidedness in filler content cannot be compensated anymore by the flow of wire water into to the wire side in the last part of PM11 wire section because the dry content of the fibre/filler mat is already too high and fines can no more move in the wet sheet.

Pict. 6.10.11 shows the impact of base ash on print mottle of the triple coated sheet: The higher base ash at the top side leads to improved back trap mottling of the top side as the permeability of the pre and middle coat is lower (see chapter "dense precoatings").
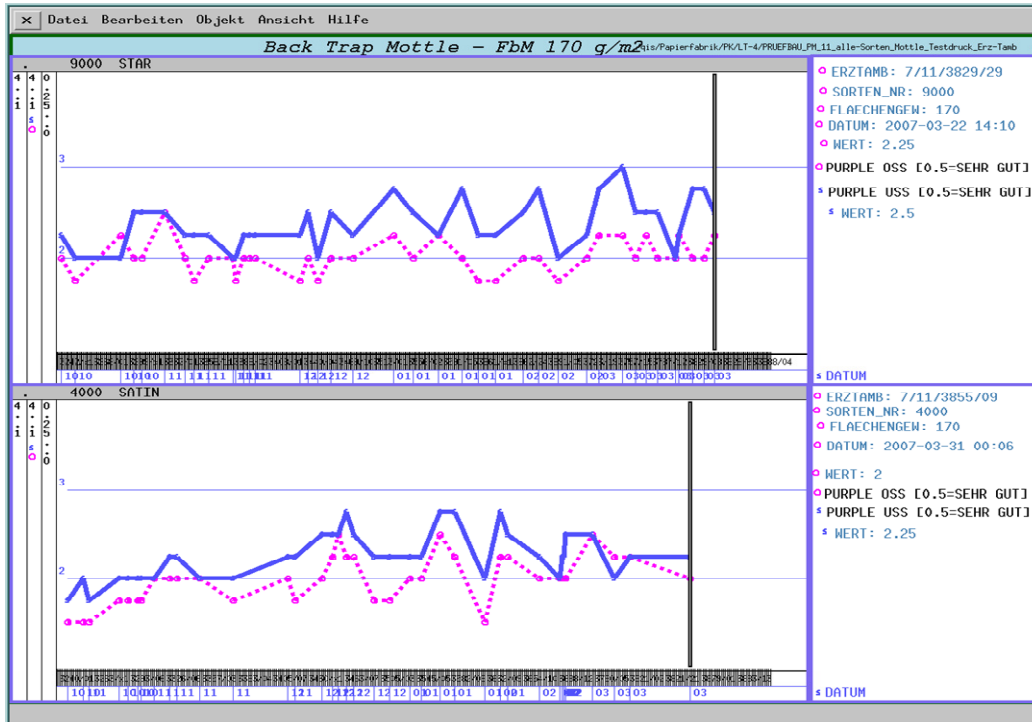
Pict. 6.10.11: Two-sidedness in back trap mottle PM11 (visual ranking of back trap mottling in purple printed areas: 0,5 = very good, 4 = bad – blue = bottom side, magenta = top side)

Sometimes the two-sidedness in mottle is caused by an asymmetric drying in the coating machine. To eliminate this route cause a reel was turned before the coating machine 11. The sides were marked after the coating machine according to the side marking in the paper machine (the wire marking).

Turning of a tambour before the coating mashine
Marking of sides: According to paper mashine!

	Standard, Erz. 3566/MR1+9	Trial 3566/MR11
Screen mottling OS	2	1,75
Screen mottling US	2	2
BTM solids 100% OS	1,9	1,75
BTM solids 100% US	2,4	2,25
BTM Purple OS	2,5	2,25
BTM Purple US	3	2,75

Pict. 6.10.12: Mottle two-sidedness PM11: Standard = Bottom side coated first in OMC11; Trial = Top side coated first

The trial showed that the worse mottle of bottom side was created by the dewatering two-sidedness in the paper machine (pict. 6.10.12). The trials to improve mottling were mainly concentrated on bottom side of PM11.

Another way to improve coating holdout is to increase the nip pressure in the machine calander.

H. Koyamoto (L1.46) investigated the effect of a pre-calender on coating holdout of LWC coating. Surface porosity dropped and coating holdout improved (SEM pictures of burn out test). Bulk of end paper could be kept constant as post-calendering could be reduced to half of the original pressure.

Mill trials at PM11 showed that surface porosity decreases when pressure in the machine calander is increased but unfortunately mainly at the dense top side where ash content is higher and higher loads in the machine calender could be transformed more effeiciently in reducing surface permeability. Therefore mottling improved mainly at the top side when machine calender load was increased.

Chapter 7: Blade and film press coating:

7.1 Introduction – The four stages of penetration in blade coating

The penetration of the coating colour at blade coaters can be split into four phases (pict. 7.1.1):

   A) Pressure penetration at the application point (jet or LDTA)
   B) Capillary penetration between application and blade
   C) Pressure penetration under the blade
   D) Capillary penetration in the drying section between blade and FCC (first critical immobilisation solids)

A....Pressure penetration at jet application point: **10-20 kPa**
B....Capillary penetration between jet and blade: Lit. **20-50 kPa**
C....Pressure penetration under blade: **2500 kPa**
D....Capillary penetration until drying: **20-30 kPa**

2.....Water penetration in free draw before blade
3.....Water penetration under blade
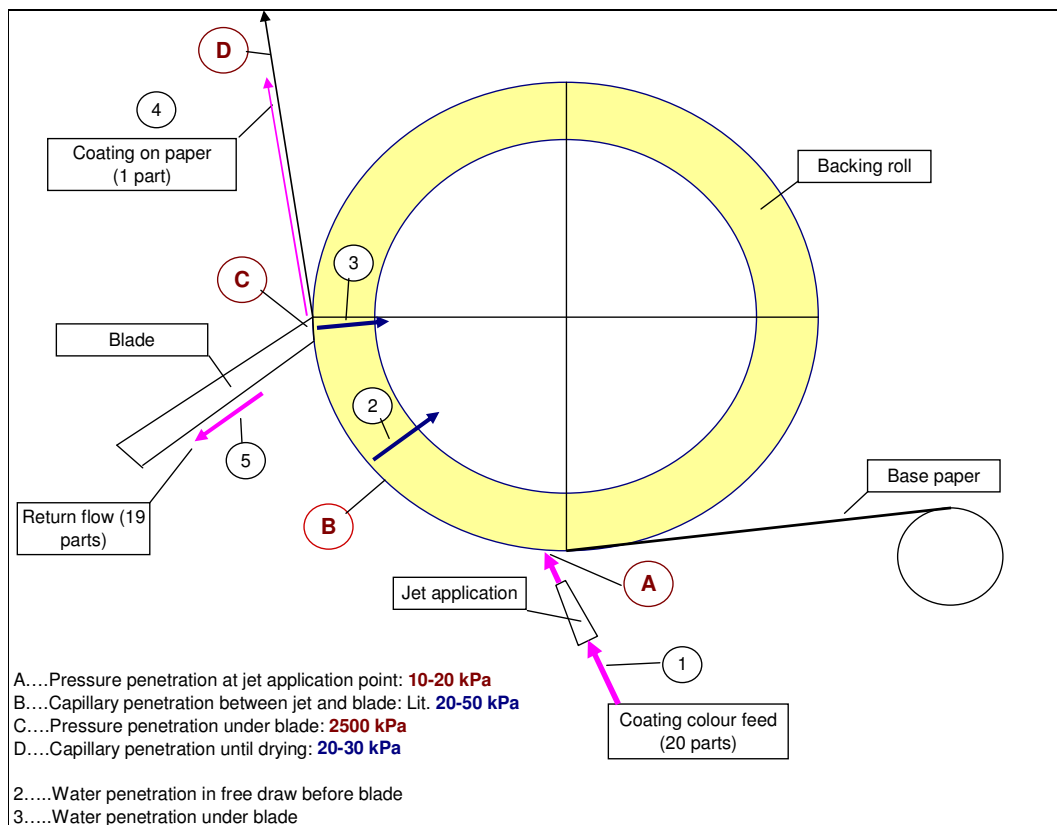
Pict. 7.1.1: Areas of coating colour penetration at a blade coater

In pict. 7.1.2 and 7.1.3 the pressure levels and the dwell time of the four stages in blade coating are compared. The highest pressure level is achieved under the blade while the longest penetration time occurs in the free draw after the blade where the

coating colour is immobilized by external drying energy. The immobilization point is called FCC (first critical concentration).
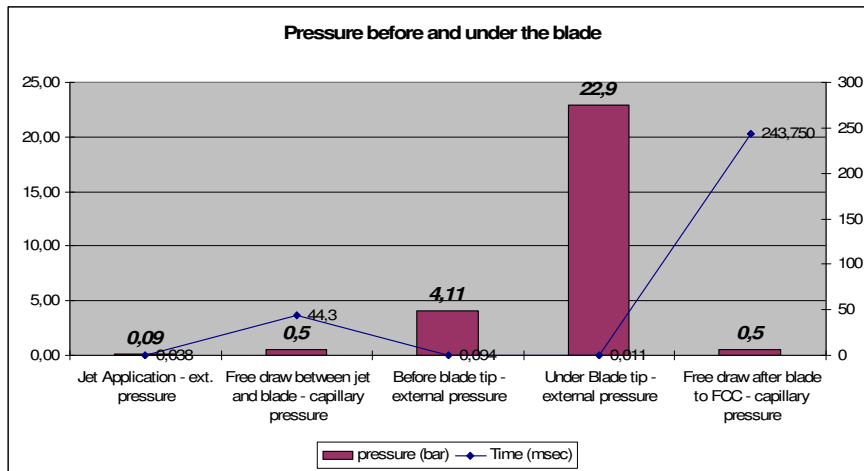
Pict. 7.1.2: Pressure and time of penetration in the blade coating process
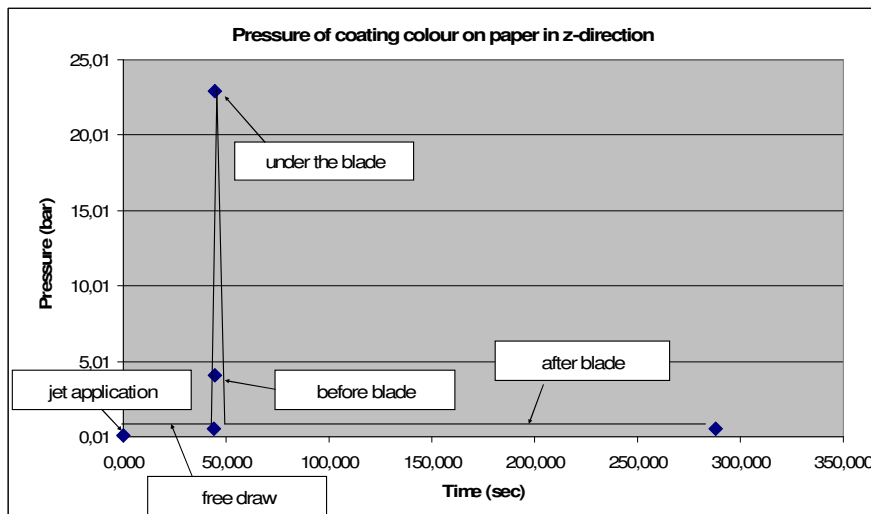
Pict. 7.1.3: Pressure development from application to blade

Pressure-less penetration of liquid phase from coating into the base paper or the precoating layer of the substrate is determined by (see also chapter 5 "capillary penetration"):

- Contact angle of liquid and solid substrate (depending on polarity of the substrate)
- Surface tension of the liquid phase
- Time of penetration

- Pore size (pore radius) of the substrate
- Darcy coefficient of the filter cake and viscosity of the liquid phase which penetrates through the filter cake
- Water retention of the coating colour – Interaction of water with latex and pigment surface
- Amount of free water for penetration which corresponds to solid content of coating colour

Calculation is made with the Lucas Washburn equation for capillary penetration:

Equ. 7-1-1: $\dfrac{dl}{dt} = \dfrac{r * \gamma * \cos\theta}{4\eta * l}$

Pressure penetration through porous medias is calculated with Darcy's law:

Eq. 3-12-1: $Q = \dfrac{K * A * \Delta p}{\eta * L}$

Darcy, re-arranged

$\dfrac{dV}{dt} = \dfrac{K * A * \Delta p}{\eta * L}$

$dV = A * \Delta L$

$\dfrac{A * L}{\Delta t} = \dfrac{K * A * \Delta P}{\eta * L}$

$K = \dfrac{L^2 * \eta}{\Delta p * \Delta t}$

Darcy, re-arranged:

$\dfrac{dV}{dt} = \dfrac{\rho * g * K * A^2 * \Delta p}{\eta * V}$

Pressure penetration of the liquid phase into the base paper is determined by:
- Viscosity of the liquid phase
- Pressure level (can be external pressure or fibre sorption pressure)
- Time of pressure pulse

- Darcy coefficient of the paper as a function of pore size and pore volume of the paper and the thickness + Darcy coefficient of the immobilized filter cake of coating colour

Darcy, integrated:

$$\frac{V^2}{t} = \frac{2 * g * \rho * K * A^2 * \Delta p}{\eta}$$

Equ. 7-1-2: $V = \sqrt{C} * \sqrt{A} * \sqrt{\Delta p} * \sqrt{t}$ ..the amount of penetrated liquid in time t (C, A = constants)

Integrating Darcy's equation leads to the conclusion that the penetrated volume of liquid phase is proportional to the square root of penetration time and pressure.

In pict. 7.1.4 the calculated penetration coefficient $\sqrt{\Delta p} * \sqrt{t}$ is compared for the four stages before the blade and the drying stage after the blade. It should correlate with the amount of liquid phase from coating colour penetrating the base paper. For these calculation the following assumptions were made, based on detailed calculations in this chapter:

- External pressure of 0,14 bar at jet application
- Capillary sorption pressure of 0,5 bar
- Blade pressure of 23 bar.
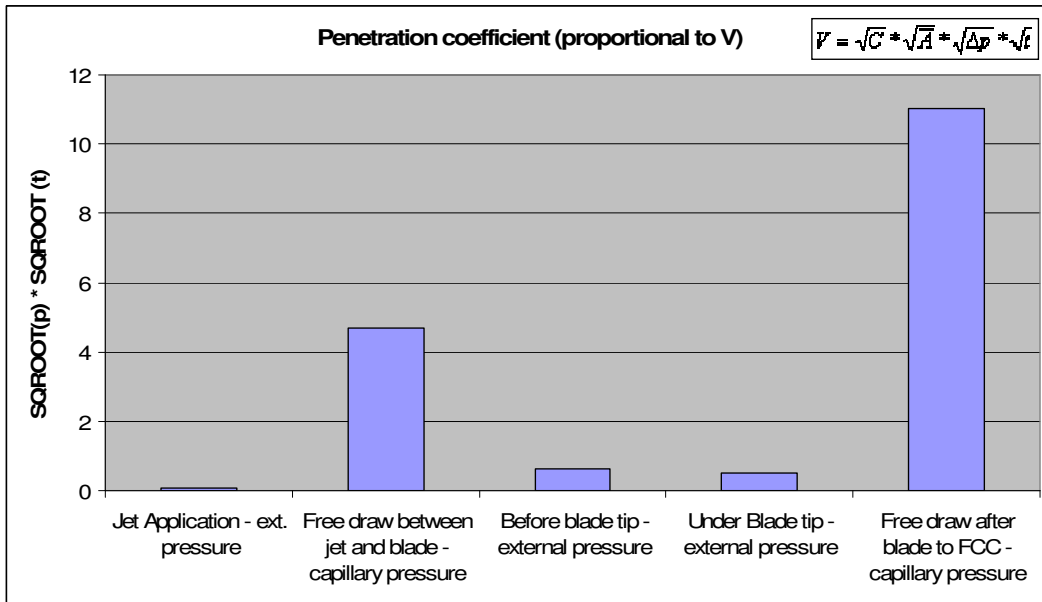
Pict. 7.1.4: Penetrated liquid in blade coating phases (FCC = First critical concentration)

When $\sqrt{\Delta p} * \sqrt{t}$ is compared for all parts of penetration in blade coating process, most of the liquid should penetrate in the areas of capillary sorption after application and during drying.

The built up of a filter cake which will slow down penetration was left out in this rough estimation of penetration coefficient $V = \sqrt{C} * \sqrt{A} * \sqrt{\Delta p} * \sqrt{t}$.

7.2 Application of coating colour (phase A)

At the application point the coating colour is fixed at the base paper by a relatively low pressure of the application unit.

Pict. 7.2.1 shows the two main application systems which are currently used in paper industry: Jet application and roll application (also defined as LDTA – long dwelling time application).
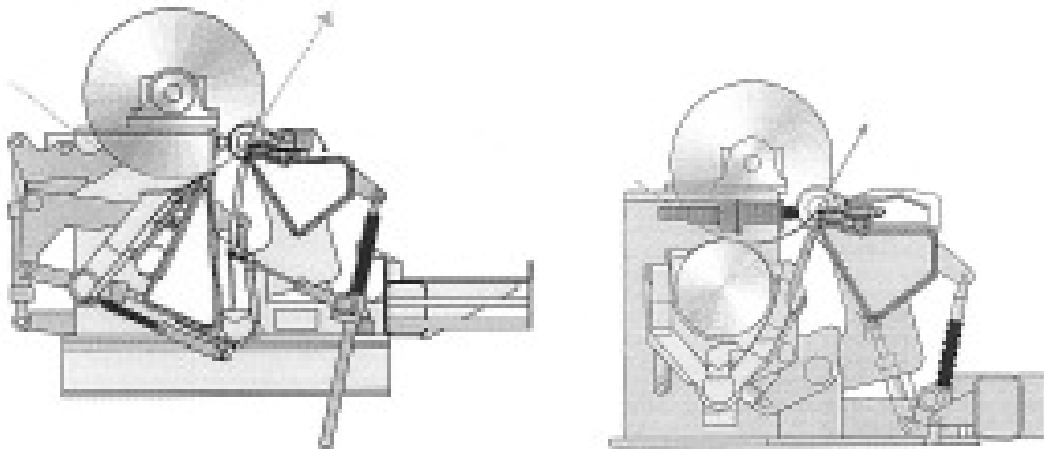
Pict. 7.2.1: Jet application (left) and LDTA roll application (right)

Blade coating in paper industry is done since decades with an excess of coating colour in the feed flow to the blade. This flow rate to the blade is 10 – 20 times higher than the amount of coating colour which is left on the paper after the blade. Therefore 9 – 19 parts are scrapped off by the blade and return to the working tank.

There are different coating colour application systems on the market. Most common is the LDTA system with an applicator roll and the jet applicator.

One advantages of jet application is the low application pressure leading to low penetration depth. The second advantage is the adjustable amount of applied coating colour by changing the nozzle opening area.

To reduce blade pressure the height of coating colour before the blade should be as low as possible or in other words the excess flow should be minimized to the point where quality problems occur (stripes, scratches,..).

At high speed coaters with LDTA applicators the excess flow can be lowered only by closing the gap between applicator roll and paper to a height of 0,1 mm. This leads to a higher application pressure and very often to web breaks when paper defects are caught by the applicator roll. Therefore most of the LDTA applicators have been removed in high speed coaters since the 90's by jet application systems.

For jet applications the hydrodynamic pressure can be calculated with: $p = \rho/2 * v^2$:

CM11, jet application:			
Flow rate through jet nozzle	Q	150	m³/h
Working width	B	8,4	m
Open width of nozzle	d	0,8	mm
Speed of jet v = Q/(B*d)	**v**	**6,20**	**m/s**
Density of coating colour	ρ	1650	kg/m³
Impuls p = ρ/2 * v²	p	31717	Pa
--"--	p	0,32	bar
Angle between jet and paper	α	27	°
Pressure on paper in vertical direction $p_z = p * \sin \alpha$			
--"--	**p_z**	**0,14**	**bar**
Speed of coating mashine	v_{CM}	1600	m/min
--"--	**v_{CM}**	**26,7**	**m/s**
Contact lenght of jet	l_1	1,2	mm
Contact time at jet	t_1	0,000045	sec
--"--	**t_1**	**0,045**	**msec**
Lenght between jet and blade	l_2	1,18	m
Contact time between jet and blade	t_2	0,0443	sec
	t_2	**44,25**	**msec**
Contact lenght under blade	l_3	0,5	mm
Contact time under blade	t_3	0,0000	sec
--"--	**t_3**	**0,019**	**msec**

Contact time is very short at jet applications: **0,045 ms** (1650 m/min at OMC11) and pressure is with **0,15 bar** also low. Therefore the product of the square root of time and pressure is lowest for blade coating part A, the jet application.

According to Darcy's law for pressure penetration the penetration depth of the liquid phase is depending on the permeability coefficient of the base paper surface, the viscosity of the coating colour, the pressure time and the pressure level.

Mill experience from blade coater rebuilds at OMC9 in Gratkorn and PM8 in Lanaken proved, that after a rebuilt from roll application to jet application, the solid increase between jet and blade decreased. Roll applicators show higher penetration depth due to longer dwell time plus higher pressure. In chapter "capillary sorption" was shown that the more fibres are wetted by the coating colour at the application point, the faster capillary sorption of the fibres will start and the more water will be absorbed by fibres in the next penetration part B, the free draw between application and blade.

Pilot trials with dense paper surfaces, achieved by applying barrier liquids, showed that the low pressure and short contact time of a jet applicator is high enough to fix the coating colour even on dense barrier coatings. When a small amount of coating colour has penetrated the base paper by the external jet pressure and has wetted the fibre wall capillaries, the water from coating colour is soaked into the base paper by capillary force of the fibres.

Tangential speed of coating colour after jet application is lower than the speed of the web. Due to anchorage of the coating colour boundary layer at the paper surface by capillary sorption and due to viscous forces in the coating colour, it is accelerated and stretched by the web. For instance at OMC11 the coating colour is accelerated from 6,2 m/s at the application point to 26,7 m/s before the blade (factor 4 in speed difference).

The operating window of a jet applicator is limited:
- If the pressure impulse is too low, <u>back flow</u> will occur.
- If the coating colour viscosity is too low, elongation forces in the coating colour, which stretch the coating colour, exceed cohesion forces within the coating colour and thickness differences in MD will occur, called "<u>baring</u>".

7.3 Free draw between application and blade (Phase B)

Water sorption starts as most fibres are a hydrophilic medium. Pekka Salminen measured the sorption pressure of different base papers. It is in the range of 0,2 – 0,8 bar, depending on sizing rate, fibre type, beating degree, chemicals added in wet end,…
A good approximation for an un-sized base paper is a sorption pressure of 0,5 bar.

Capillary sorption is described by Lucas Washburn equation: $\Delta P_c = \frac{2 * \gamma * \cos\theta}{r}$

The better the pores of the substrate are wetted by the liquid (high cos θ), the more pores are wetted, the lower the surface tension of the liquid γ the smaller the pore radius, the higher the sorption pressure Δp_c will be.

Penetration part B is the second longest (20 - 50 ms for high speed coater OMC11) compared to all other phases (only part D after the blade is longer).
In almost all blade coaters dewatering of coating colour into the base paper is measured in penetration part B. Especially at board coaters with low speed (long dwell time) and low viscous colours this dewatering effect is highly pronounced.

When solid content of coating colour at the application is close to its immobilisation solids an immobilized filter cake is formed at the boundary layer between coating colour and base paper.

The thickness of this immobilized layer rises continuously from the application point to the blade.
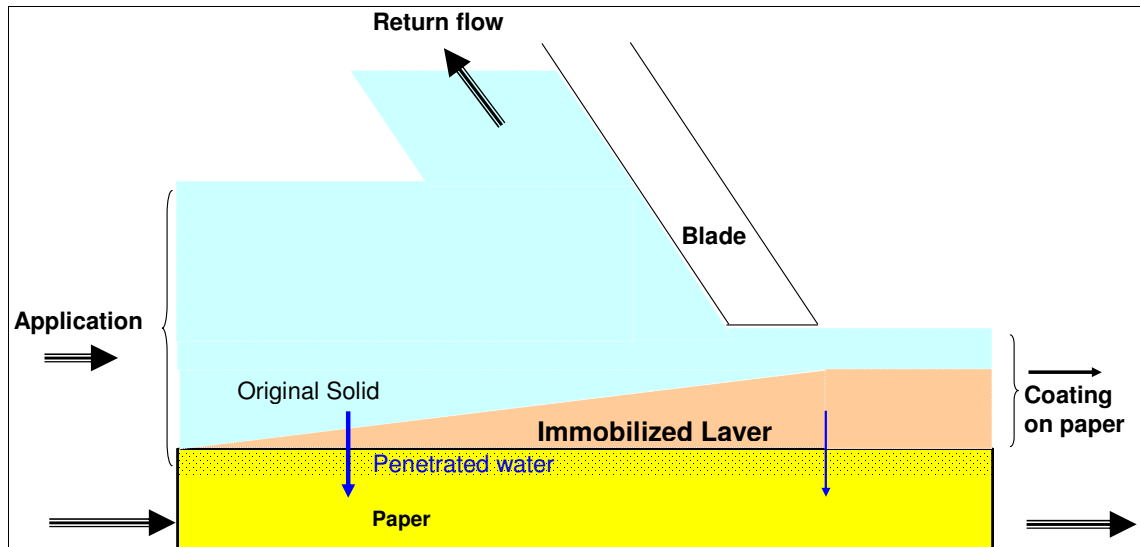
Pict. 7.3.1: Built-up of filter cake from coating colour before the blade tip

Thickness of immobilization layer will increase when:

- dwell time is long - distance between application and blade is high and speed is low
- fibre sorption pressure is high
- permeability of surface is high
- water retention of the coating colour is low
- gap between applied solids content and immobilization solids is low

If time of penetration would be long enough, all coating colour would be immobilized before the blade and severe runability problems would occur as the blade should not touch the immobilized layer.

The dewatering levels with time because the filtration resistance of base paper is added by the filtration resistance of the immobilized filter cake at the boundary to the substrate. The thicker this filter cake is, the lower the overall permeability h/K will be.

Equ. 7-3-1: $v = \dfrac{d(V/A)}{dt} = \dfrac{\Delta p_f + \Delta p_s}{\eta * \left[\dfrac{h_f}{K_f} + \dfrac{h_s}{K_s} \right]}$

$$\Delta p = \Delta p_f + \Delta p_M$$

K_f.....Darcy coefficient of filter cake

H_f.....Thickness of filter cake at time t

K_s....Darcy coeff. of the penetrated substrate, here the penetrated pre-coating layer

H_s.....Thickness of the pre-coating layer

The Darcy coefficient of the filter cake can be measured by static water retention measurements. For coatings the Abo-GWR instrument is commonly used. Data's are shown in the chapter "water retention of coating colours".
To reduce the Darcy coefficient of the immobilized layer the PSD of the particles should be broad with a high amount of fines and the viscosity should by low (low flocculation of filter cake).

The amount of penetrated water can be either measured by the described mass balance around the working tank or by static water retention measurements with the Abo-GWR instrument. Data's are shown in the next part.

G. Engström (L3.3) compared LDTA with SDTA application for coatings. With SDTA application no immobilized layer is formed before the blade and blade pressure is lower than for LDTA application due to lower solids before the blade.

He substituted a 0,508 mm thick stiff blade by two blades with 0,254 mm thickness where only one blade was touching the paper. Blade pressure declined as the facet length got shorter and tangential high shear force was reduced.

Philippe Letzelter and D. Eklund from Abo Akademi (L1.37) calculated coating colour dewatering before the blade from measurements with the Abo-GWR water retention instrument. He compared LDTA application with SDTA. At SDTA coaters the coating colour is applied by a chamber which is directly situated before the blade. The blade is integrated in this chamber.

The thickness of the immobilized layer before the blade was calculated with the Darcy equation:

$$\dot{m} = \frac{f * b * dp}{\mu_f * \mu_l * L} \quad .....\text{from Darcy:} \quad Q = \frac{K * A * \Delta p}{\eta * L}$$

m......mass flow

f........filtration amount

b.......flow coefficient $= \dfrac{d^2}{32 * \gamma}$ for laminar flow

γ.......kinematic viscosity

μ_f......pore coefficient = proportional $1/\varepsilon$,

μ_l......path coefficient = flow determined, depending on the form, size and distribution of the pigment used.

Leading to $m = \int \dot{m} * dt = f * C * \dfrac{dp}{L} * t$ or $m = \sqrt{f^2 * C * A * dp * t}$

C......structure coefficient

dp the pressure difference of liquid flow through the filter cake must be constant over the penetration time

The pore coefficient μ_f is indirect proportional to the porosity: $\mu_f = f\,(1/\varepsilon)$
The porosity can be measured. The path coefficient μ_l must be determined experimentally.

Application pressure at LDTA was assumed by Ph. Letzelter with 2,5 bar, sorption pressure of fibres with 0,1 bar and blade pressure with 12 bar.
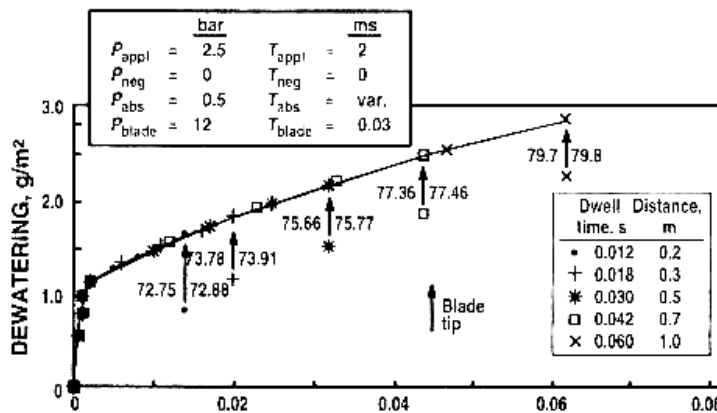
Pict. 7.3.2: Dewatering at LDTA application – X-Axis: Time t (Ph. Letzelter)
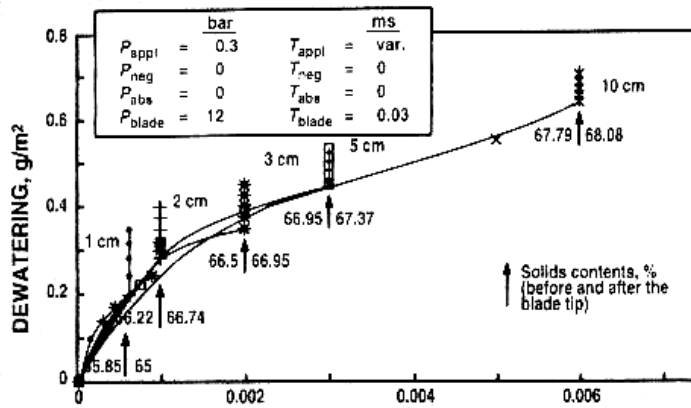
Pict. 7.3.3: Dewatering with SDTA application – X-Axis: Time t (Ph. Letzelter)

The increase of solid content before the blade is much higher for the LDTA application than for SDTA (pict. 7.3.2 and 7.3.3). As thickness of immobilized coating layer before the blade is much higher for LDTA coaters the increase in solid content by the external blade pressure is much lower.(pict. 7.3.4).
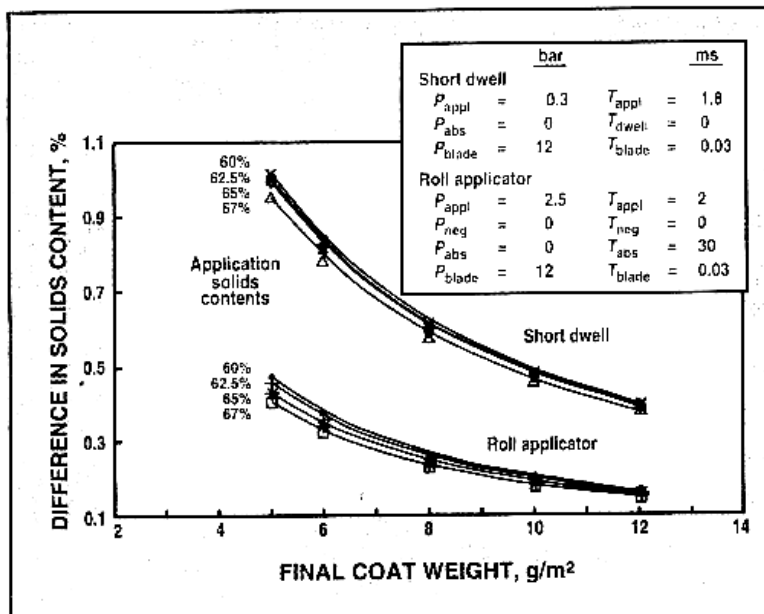
Pict. 7.3.4: Difference in penetration under the blade for LDTA vs. SDTA application (Ph. Letzelter)

For SDTA coaters some attempts to increase the thickness of the immobilized layer before the blade have been made by increasing the chamber volume to increase

penetration time. Unfortunately this is limited by flow instabilities and deposits at the walls. Therefore no more SDTA coaters were built in the last years.

Another way to increase thickness of the immobilized layer before the blade is a highly absorbent base paper.
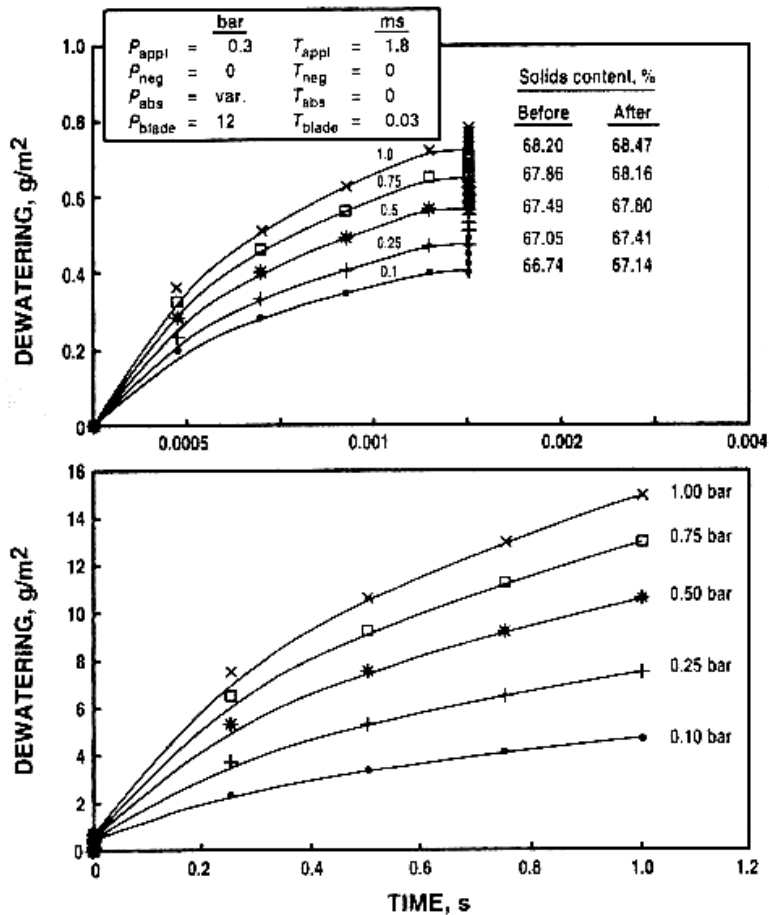
Pict. 7.3.5: Dewatering between application and blade for different paper sorption pressure levels (Ph. Letzelter)

Pict. 7.3.5 shows that raising fibre sorption pressure level leads to higher solids before the blade and lower solids increase under the blade. But the risk of running into problems with scratches increases as the solid content under the blade is much higher.

Another way to increase immobilized layer thickness would be a higher solid content at the application to reduce the gap between c.c. solids and immobilized solids.
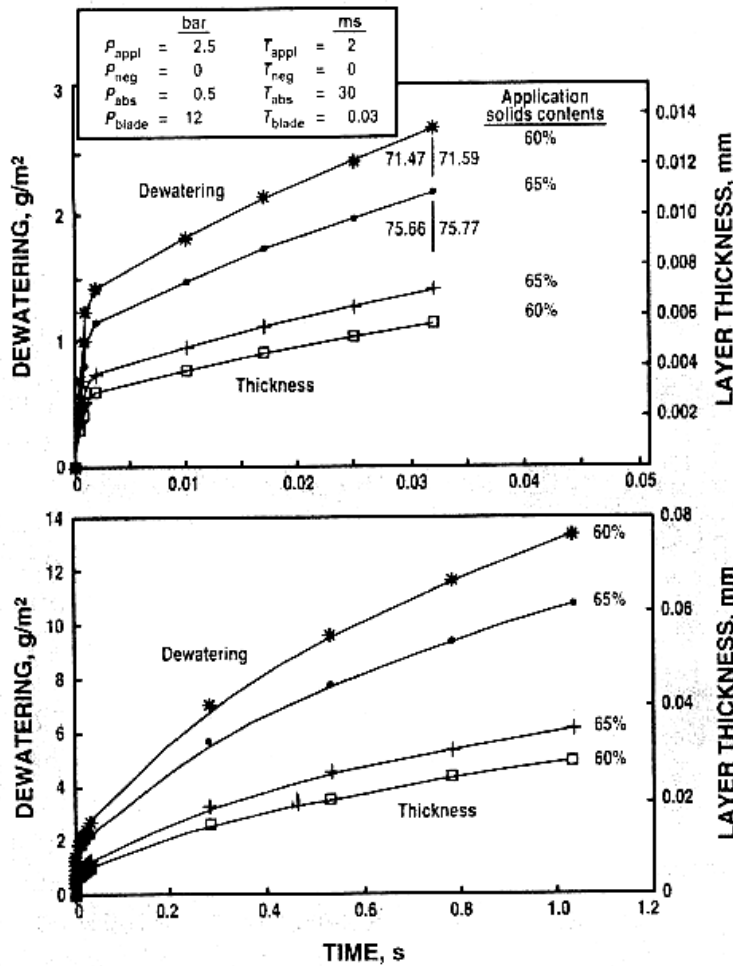
Pict. 7.3.6: Dewatering before the blade for roll application as a function of application solids (Ph. Letzelter)

Pict. 7.3.6 shows that a higher application solids leads to a thicker immobilized layer before the blade and less dewatering under the blade but again the absolute solids under the blade is higher and therefore the risk for runability problems.

The risk of immobilizing the whole coating colour before the blade increases with higher solids at the application, high base paper sorption, long dwell time, low water retention of the coating colour and low coat weight (=small gap).

The lower thickness of immobilized layer before the blade for jet applicators (pict. 7.3.8) compared to LDTA led to the development of Opticoat Duo (pict. 7.3.9) where the distance between application and blade was elongated by using separate rolls for application and blade. Stefan Kuni and Matti Lares presented at Tappi Coating

Conference 2002 this new jet coating technology which was developed especially for coated board grades. The compared three different application systems at the Valmet/Metso pilot coater in Järvenpää.

a) LDTA roll applicator
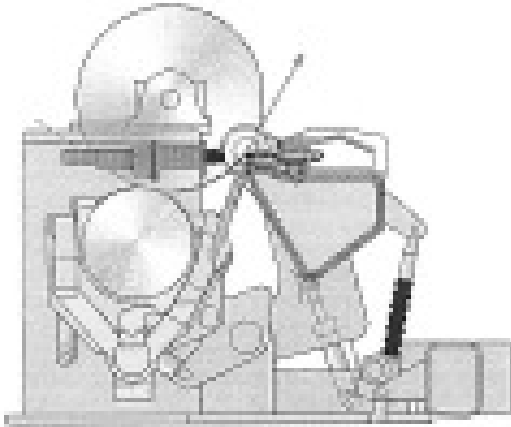
Pict. 7.3.7: Roll applicator

In a LDTA roll applicator (pict. 7.3.7) the speed of the applicator roll is 10 – 20% of the web speed. The gap between paper and applicator roll is 0,5 – 1mm. The distance to the blade is appr. 500 mm.

Critical points are:
- Breaks at very low gap width between paper and applicator roll
- Deposits at the edges
- Thickening of the coating colour in the colour pan and deposits
- Skip coating due to low viscosity of the coating colour

b) Jet applicator
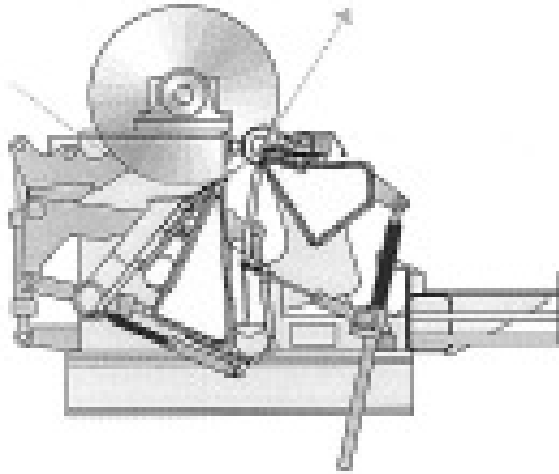
Pict. 7.3.8: Jet applicator

The nozzle of a modern jet coater (pict. 7.3.8) has a slit width of 0,5 – 1mm, the distance of the nozzle to the paper is 10 – 20 mm. The jet speed is 2 – 3 times lower than the web speed. The distance to the blade is approximately 500 mm.
Points of attention are:
- Efficient air removal from the coating colour to avoid skip coating
- Minimum elongation viscosity for the coating colour stretch
- Plugging of the nozzle by deposits

c) Opticoat Duo with Jet (pict. 7.3.9):
With OptiCoat Duo the distance between jet and blade is increased to about 1,6 m and can be adjusted by the distance of the application unit and the backing roll / blade unit.
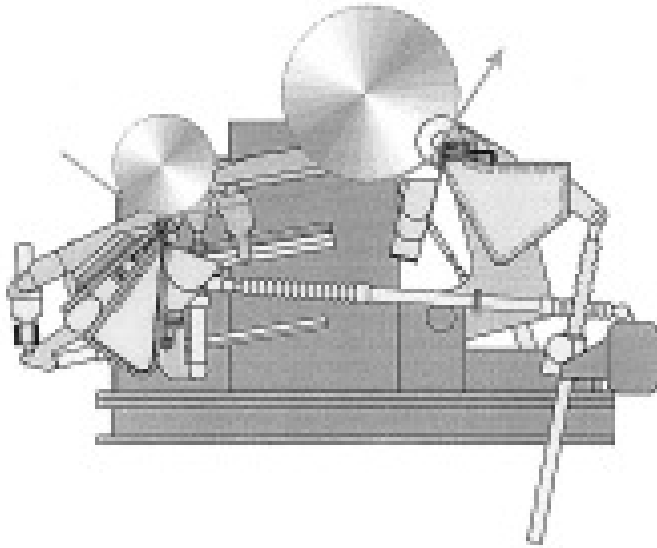
Pict. 7.3.9: OptiCoat Duo – jet with long dwell time application

This application method was developed to improve coverage of board grades. Roll applicators showed better coverage than jet coaters because a thicker immobilized layer is formed by the pressure impulse of the applicator roll. The pressure in a roll applicator is approximately 1 bar while the pressure in a jet applicator is 0,1 – 0,2 bar and therefore more liquid phase is pressed into the base board.

With OptiCoat Duo Jet this effect is achieved with low application pressure but increased dwell time between application and blade (pict. 7.3.10). The base paper sorption is prolonged. As capillary dewatering is proportional to the square root of time a thicker immobilized layer is built up before the blade compared to conventional jet applicators where the distance to the blade tip is in the range of 0,5 – 0,75 m.
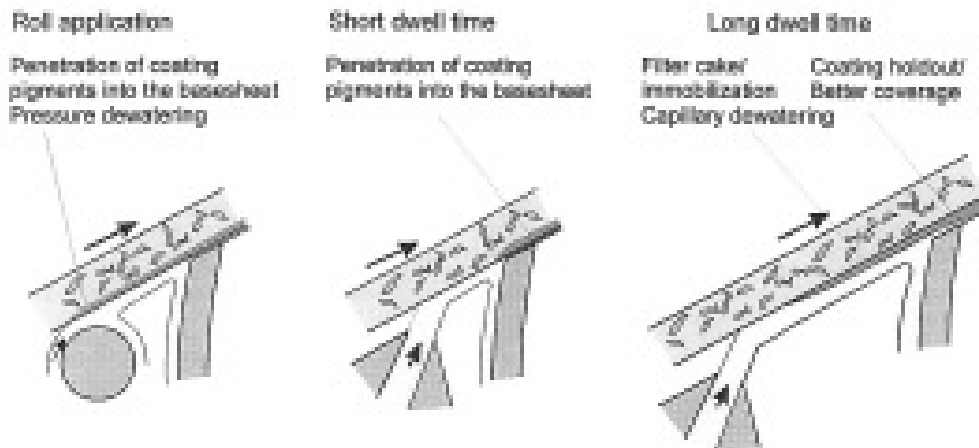
Pict. 7.3.10: Comparing the dewatering of different application systems

The pilot trials showed clearly that fibre coverage improved with increased filter cake thickness but when solids under the blade got closer to the immobilization point of the coating colour, scratches, stripes, severe blade wear and bleeding occurred (pict. 7.3.11 and 7.3.12).

At un-calendered board grades the roughening in the coating process should be as low, as possible.
When LWC machines switched from LDTA to SDTA application in the 1980's, a rougher surface had to be accepted.
The cause for rougher surface after coating was fibre swelling and fibre lifting before the blade. With LDTA more pronounced fibre swelling took place before the blade as more fibres were wetted by pressure impulse at the application and longer dwell time between application and blade. Fibres were lifted before the blade due to swelling and the blade cut off the lifted fibres. A smoother surface was the consequence for LDTA coatings. The more fibres were swollen before the blade the less swelling happened after the blade. With SDTA all fibre swelling happened after the blade where no egalization of the surface is possible anymore.

With OptiCoat Duo the effect of LDTA was expanded: A longer dwell time led to more pronounced fibre swelling before the blade but less swelling after the blade.

Coating Concept		Surface structure	PPS-s10	Hunter-gloss
pre-coating	top-coating			
Duo	Jet	9	0.74	51.0
Jet	Jet	8	0.77	52.0
Jet	Roll	7	0.79	51.0
Roll	Roll	5	0.85	49.0

Pict. 7.3.11: Pilot coater study of different pre- and topcoat application systems on a 220 g/m² three ply base board with MG cylinder and hard nip calander for base
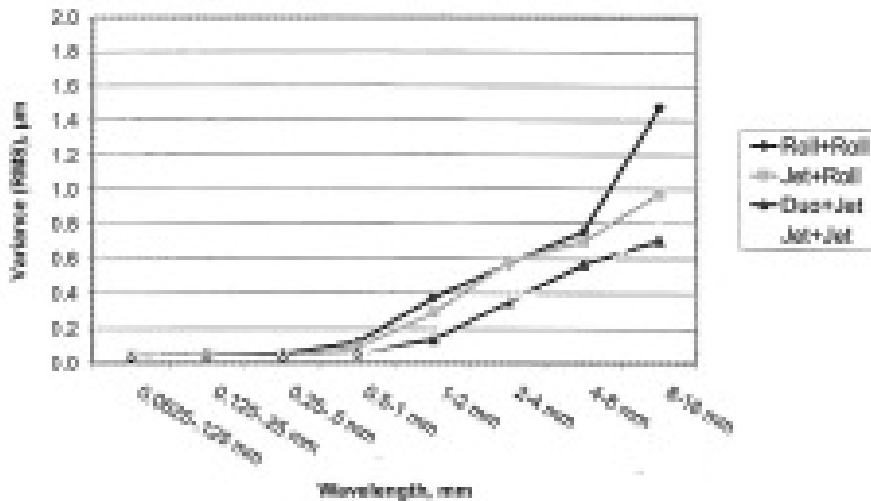
Pict. 7.3.12: Topography of different double coated samples (higher variance = rougher surface)

With roll applicators in pre- and topcoating a higher roughness variance and a higher PPS value could be observed. The cause was the pressure penetration of water in the applicator nip through the hydrophobized top ply into the un-sized middle ply.

Compared to a normal jet applicator OptiCoat Duo improved smoothness. Coating holdout, measured by burn out test, improved with jet instead of roll application and with OptiCoat Duo instead of jet.

Hideku Fujiwara (L4.1) studied the effect of water penetration during blade coating on offset mottling.
Dry solids of scraped coating colour after the blade and after the dryer was measured for a single stiff blade coating applied on a 63 g/m² wood free base sheet. The coating colour consisted of 50% clay, 40% fine carbonate, 10% coarse carbonate, 10% latex, 5% starch. Pilot coater speed was 1000 m/min.
No differences in solid content directly after the blade were found between LDTA (roll application) and VDTA (jet application). LDTA showed less water penetration of the coating colour into the base paper in the drying section due to filter cake barrier at boundary to the base paper, formed at the application.
Higher latex surface concentrations were found for VDTA applications especially when the distance between jet and blade was shortened.

Local differences in PSD of the pigment mixture caused local differences in gloss. Mottling correlated well with these gloss variations.

As blade coating is a process with an excess flow of coating colour – 20 parts of colour are applied – only 1 part remains on the paper after the blade – the return flow of coating colour has a higher solid content than the feed flow when dewatering between application and blade happens (data's see next part).
The consequence is a constant increase of solids in the working tank when the coater is started with fresh coating colour.

Pict. 7.3.13 shows the online density measurement of coating colour in the working tank of OMC 11 middle coater C4. Density correlates linearly with solid content (pict. 7.3.14). The increase in solid increase in the instationary period after start up of the coater can be seen.
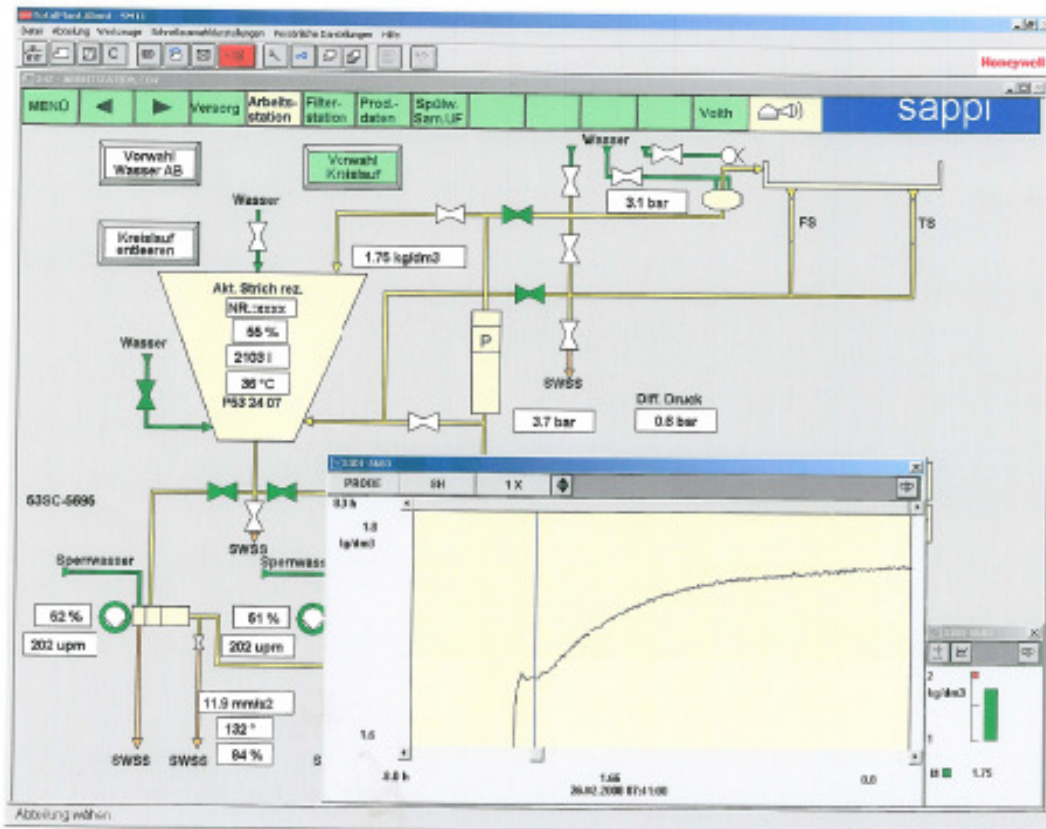
Pict. 7.3.13: Density increase of coating colour in the working tank of Coater 4 over 6 hours after coater start up

The density increased at Coater 4 from 1,66 g/cm³ at the start up to 1,76 g/cm³ after 6 hours of operation (Delta density = 0,1 g/cm³). To correlate density with solids content the coating colour of the working tank was taken and diluted stepwise. Solids and density were measured simultaneously.
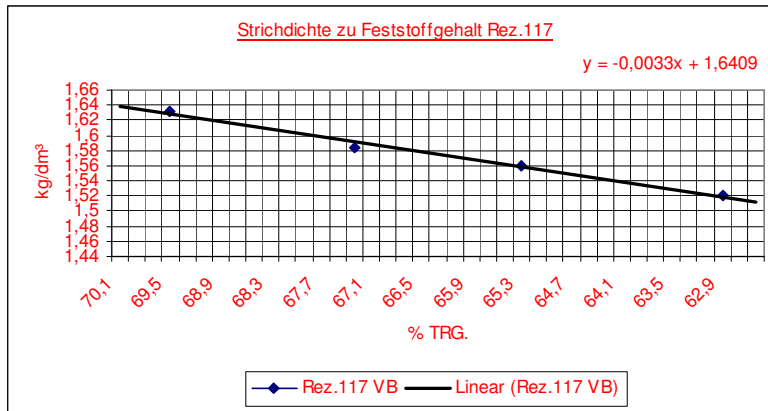
Pict. 7.3.14: Density vs. solid content of precoating colour

The correlation between density and solids was measured with:

$\Delta\rho$ = 0,1 g/cm³ density difference corresponds to Δc = 5,9% delta in solids content.

Therefore an increase in solids of 6% was measured during the start up of middle coater 4 at OMC11. According to offline lab measurements the solid content increased from 65% to 71%.
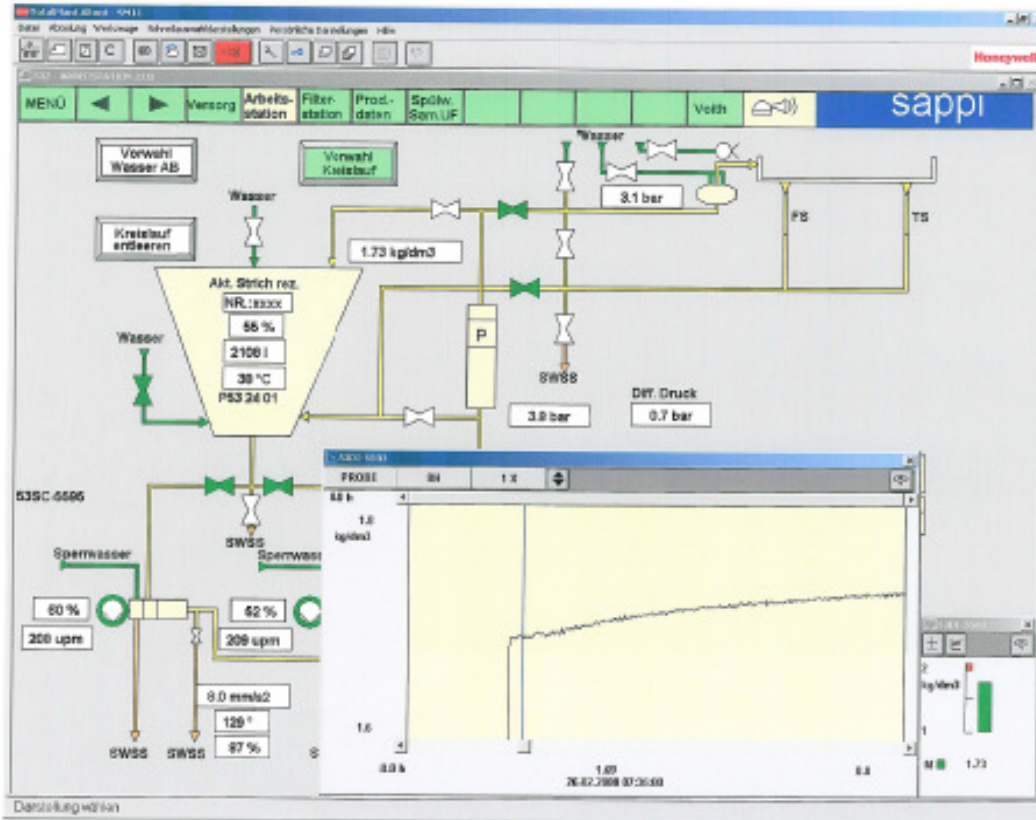
Pict. 7.3.15: Density increase of coating colour in the working tank of Coater 3 over 6 hours after coater start up

At Coater 3 density increased from 1,69 to 1,74 kg/m³, which corresponds to a solid increase of 3% from 65,5 to 68,5% (pict. 7.3.15).

Drainage of liquid phase is always lower at Coater 3, compared to coater 4.
This can be seen in a slower rise of solids after start up (instationary period) and in a generally lower solid content in the working tank of Coater 3 (stationary period) – see pict. 7.3.14 and 7.3.15.
The reason is the higher precoat weight at the bottom side, which is middle coated at C3. Higher amount of dense precoating leads to a lower surface permeability (see chapter "dense precoatings").

Pict. 7.3.16 shows the increase in solids at the precoaters of OMC9 where precoating is applied by blade coaters directly on base paper. Coating samples were taken every hour after start up.

OMC9 startup precoater 1

Solid content (%) / Brookfield viscosity 20 RpM (cp)

	VB85 - 7:00	MR2 - 09:10	MR1 - 10:05	MR3 - 11:00	MR4 - 11:50	MR5 - 12:40	MR10 - 15:50 Strich "85"
	W1	W3	W4	W7	W9	W11	W13

Legend: Solid content — Brookfield Viscosity 20 1/min

OMC9 startup precoater 1

Solid content (%) / ACAV high shear viscosity at 600.000 1/sec (cp)

	VB85 - 7:00	MR2 - 09:10	MR1 - 10:05	MR3 - 11:00	MR4 - 11:50	MR5 - 12:40	MR10 - 15:50 Strich "85"
	W1	W3	W4	W7	W9	W11	W13

Legend: Solid content — ACAV - viscosity

Page 264

Pict. 7.3.16: Solid increase in working tank at startup of of coater 1 at OMC9

This increase in solids at precoaters of OMC9 is instationary over 2 – 4 hours. Afterwards a stationary balance is reached and delta solids between coating tank and fresh colour feed from coating kitchen stays constant. For blade pre-coaters of OMC9 and OMC11 this solid difference is in the range of 2 - 8% depending on speed, water retention of coating colour and base paper sorption.

When starch containing colours are used, starch content in the working tank drops with running time as coating starches are relatively low in molecular weight and penetrate therefore with water into the base paper. This can be detected by falling viscosity, falling water retention and reduced picking strength with running time (see pict. 7.3.16 - OMC9). Increasing solids lead to improvement in water retention and the reduction starch content in working tank is levelled out.

As the solids in the working tank increases, the solid content at the application increases and the thickness of the immobilized layer or the solid content before the blade increases in the same magnitude.

When thickness of immobilized layer before the blade reaches the dimension of the gap between blade and paper, the whole coating colour is immobilized under the blade. Severe runability problems of the coating colour like dry bleeding or streaks are the consequence.

For coating machine 11 the solids content was measured at stable conditions in the middle coating station C3/4 and the top coating stations C5/6 (pict. 7.3.17 and 7.3.18).
The solid content after the blade was determined by using a small blade to scrap off the coating colour from the paper surface.
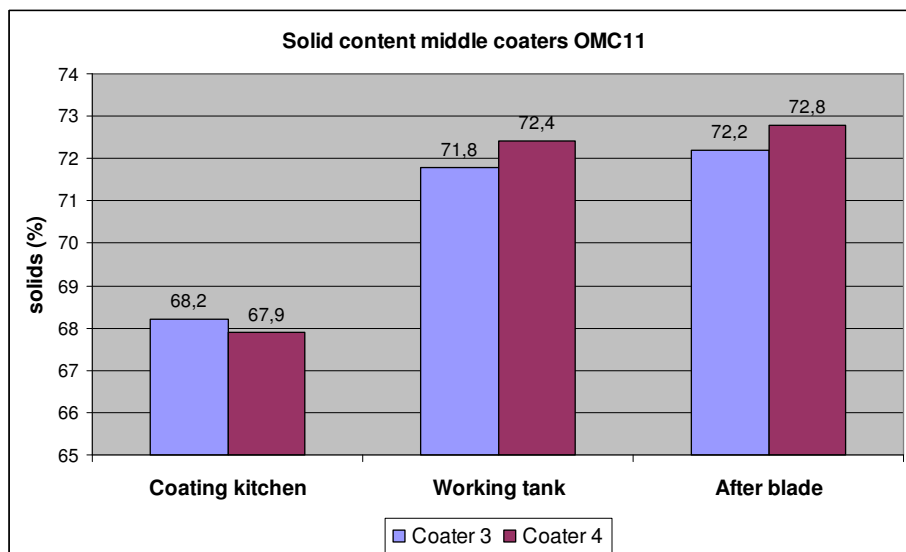
Fig. 7.3.17: Solid content of fresh coating colour, in working tank and after blade C3/4
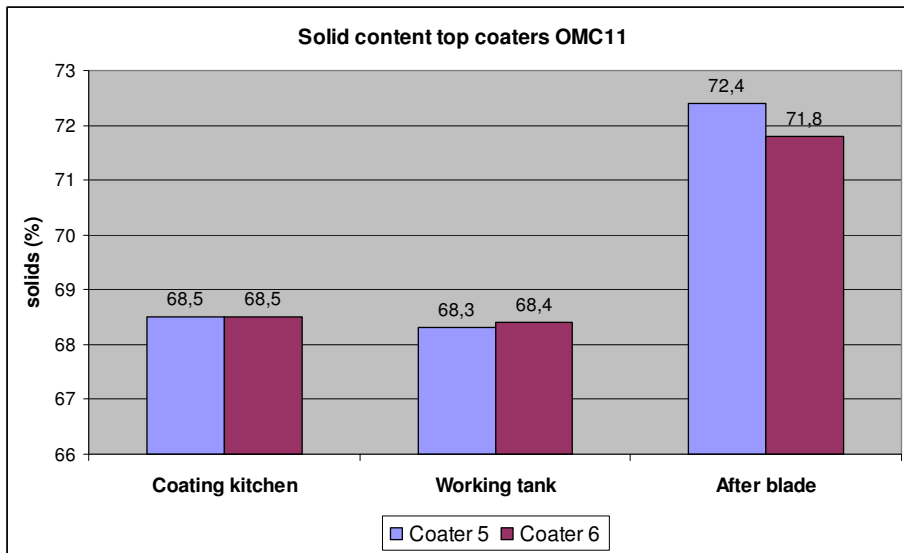
Fig. 7.3.18: Solid content of fresh coating colour, in working tank and after blade C5/6

Measurements of coating solids at the triple coating machine OMC11 show that for top coatings applied on a middle coating layer, which covers perfectly the base paper fibres, no capillary sorption after the application takes place and the isolating immobilized layer is missed for reducing the penetration of the top coating colour under the blade. The consequence is a higher penetration rate under the top coating blades compared to middle coaters although water retention of top coating colours is much higher due to use of fine pigments.

The increase of solids between application and blade is accompanied by a loss of soluble binders and fines like latex particles into the base paper.
Coating colours with low water retention and base papers with high capillary sorption lead to an enhanced binder demand in pre-coating colours.

In the drying sections (part D) the latex and starch are transported together with the evaporating water through the dense immobilized pre-coating layer. The more latex has penetrated before part D, the more pronounced the mottling problem will be.

Mass balances were established for coating machine 11. The solid content in all flows and the thickness of the immobilized layer before the blade was calculated:

1....Pressure penetration at jet application point
2....Capillary penetration between jet and blade
3....Pressure penetration under blade
4....Capillary penetration until drying

Coating on paper (1 part)

Balance room 3

Backing roll

Balance room 2

Blade

Return flow (19 parts)

Jet application

Base paper

Coating colour feed (20 parts)

Balance room 1

Working tank
4,5 m³
(including pipes)

Fresh coating colour from coating kitchen (1 part)

Balance room 1:

Overall mass balance:	$(V_1 \times \rho_1) = (V_8 \times \rho_8) + (V_5 \times \rho_5)$
Solid mass balance	$(V_1 \times \rho_1 \times k_1/100) = (V_8 \times \rho_8 \times k_8/100) + (V_5 \times \rho_5 \times k_5/100)$

Balance room 2:

Overall mass balance:	$(V_8 \times \rho_8) = (V_6 \times \rho_6) + (V_3 \times \rho_3)$	$\rho_3 = 1000$ kg/m³
Solid mass balance	$(V_8 \times \rho_8 \times k_8/100) = (V_6 \times \rho_6 \times k_6/100)$	

Balance room 3:

Overall mass balance:	$(V_6 \times \rho_6) = (V_3 \times \rho_3) + (V_4 \times \rho_4)$	$\rho_3 = 1000$ kg/m³
Solid mass balance	$(V_6 \times \rho_6 \times k_6/100) = (V_4 \times \rho_4 \times k_4/100)$	

Balance room 1:
Known: V_1 (from pump datas), V_5 (19/20 of V_1), V_8 (1/20 of V_1)
k_1 (measured in working tank), k_8 (measured in coating kitchen)
ρ_1, ρ_8 as a function of k_1, k_8 - correlation measured in lab

Calculated: k_5, ρ_5

Balance room 2:
Known: V_8 (1/20 of V_1)
k_8 (measured in coating kitchen), $k_6 = k_4$ (measured for pre-/middle coat) or $k_6 = k_8$ (measured for top coat)
ρ_8, ρ_6 as a function of k_8, k_6 ; $\rho_3 = 1000$ kg/m³

Calculated: V_6 (calculation point), V_2 (penetrated water into base between jet and blade)

Balance room 3:
Known: V_6 (from balance room 3)
k_4 (measured by scrapp off method), $k_6 = k_4$ (measured for pre-/middle coat) or $k_6 = k_8$ (measured for top coat)
ρ_4, ρ_6 as a function of k_8, k_6 ; $\rho_3 = 1000$ kg/m³

Calculated: V_4 , V_3 (penetrated water into base under blade)

Page 268
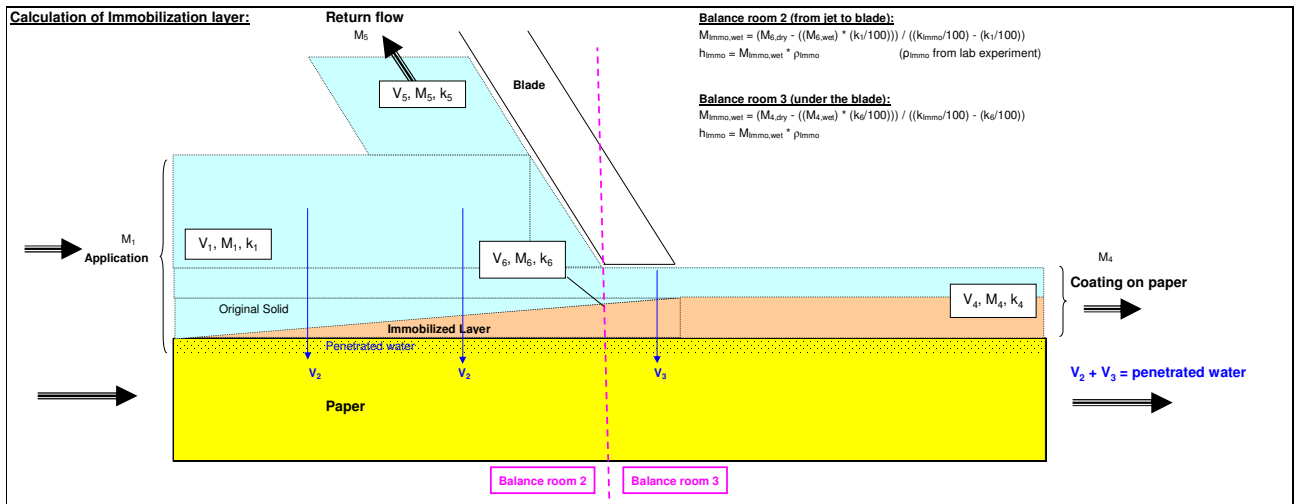
Pict. 7.3.19: Development of the immobilized layer before/under the blade

To calculate the thickness of the immobilized layer the solid content of the immobilized layer has to be determined by a separate experiment. This was done for different mill coating colours at OMYA with the Anton Paar Rheometer MCR300 and the immobilization cell of BASF (7.3.20).

Pict. 7.3.20: Anton Paar MCA300 with BASF immobilization unit

The distance between plate and paper was 0,5 mm. The plate diameter was 5 cm. Base paper from grade sappi Magnostar 58 g/m² was used as substrate to absorb water from the tested coating colours.

1,8 ml of a coating colour / pigment slurry was put on the paper.

The Rheometer was started and ran with constant shear rate. Viscosity was measured continuously. The base paper picked up water from the coating colour and solid content between paper and the turning plate increased.

When the measured viscosity increased exponentially, the immobilization point was reached. The Rheometer was stopped and the solid content of the coating colour at the boundary layer to the paper was measured. The time until the immobilization solids is reached is called the immobilization time.
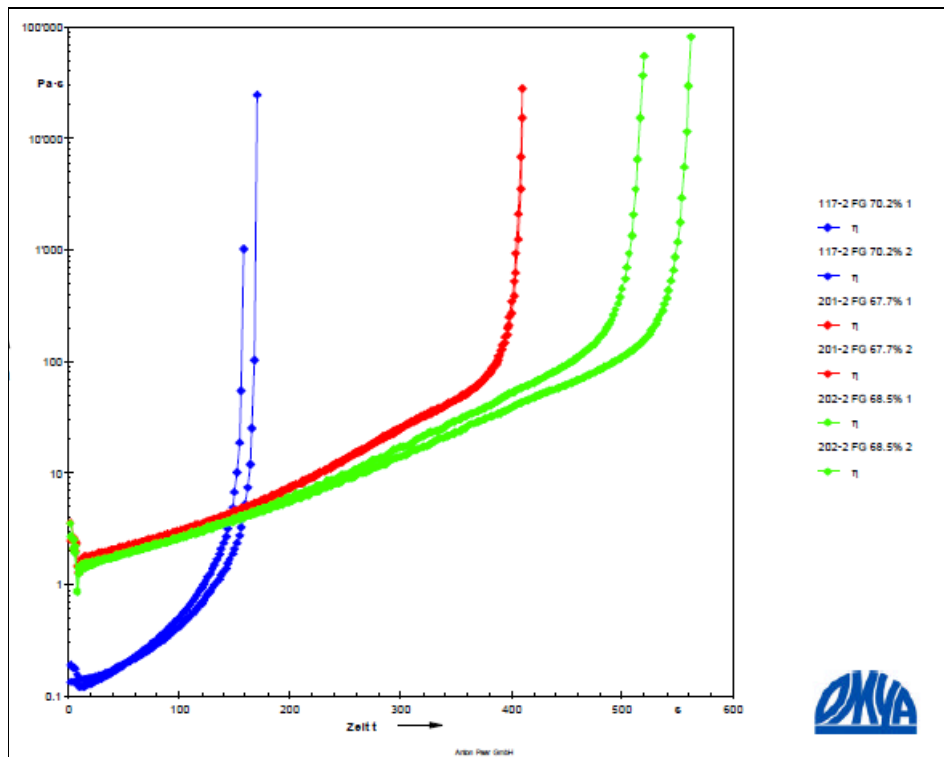
Pict. 7.3.21: Paar Physica viscosimeter with BASF immobilized cell –precoatings OMC11
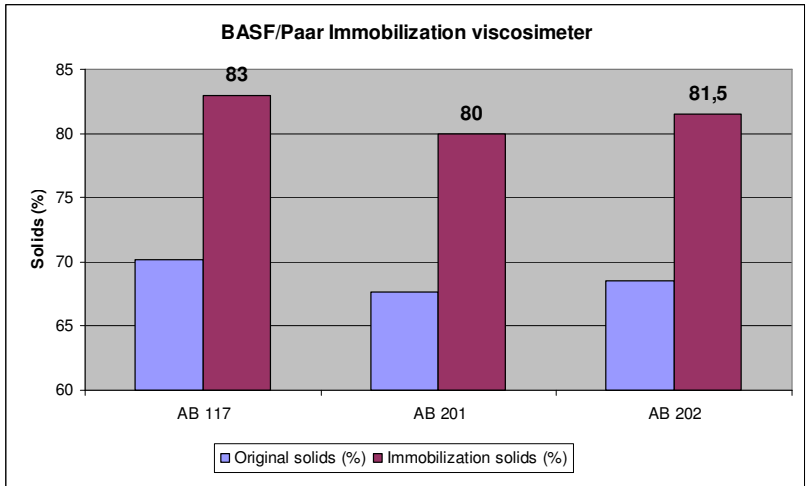
Pict. 7.3.22: Immobilization solids of mill coating colours (carbonate based precoatings with 2 – 6% starch) – samples from fresh colour from coating kitchen

For coating colour 117 with lower starch content a somewhat higher immobilized solid was measured as the increase in viscosity is less pronounced with higher solids (pict. 7.3.22 and 7.3.23). Generally the immobilized solids is higher when viscosity of coating colour is low as the exponential rise in viscosity with increasing solids starts earlier for high viscous coatings (compare pict. 7.3.22 with 7.2.23 and 7.3.24 with 7.3.25).
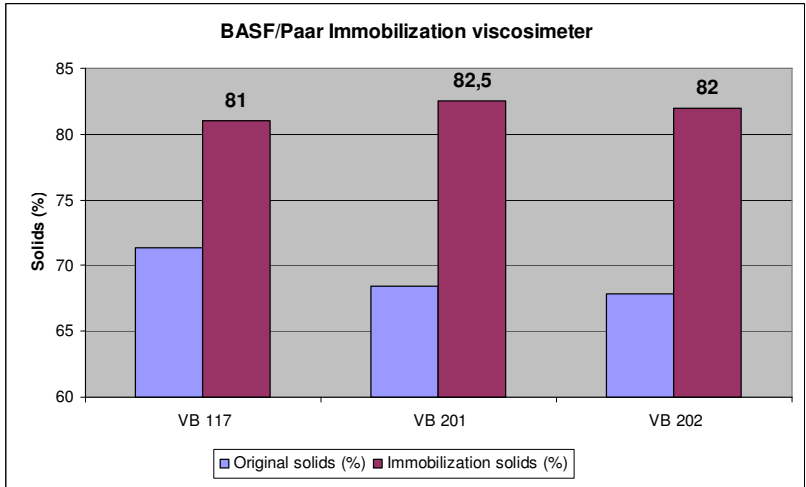
Pict. 7.3.23: Immobilization solids of same mill coating colours from working tank
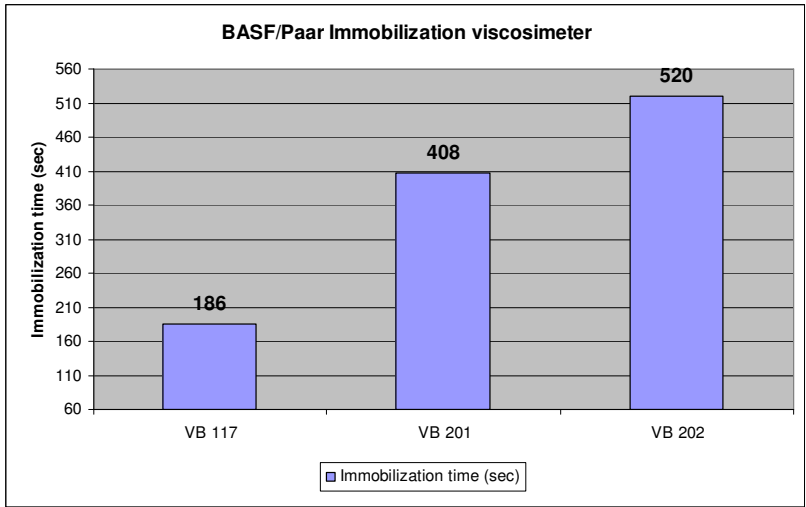
Pict. 7.3.24: Immobilization time of fresh mill coating colours from coating kitchen
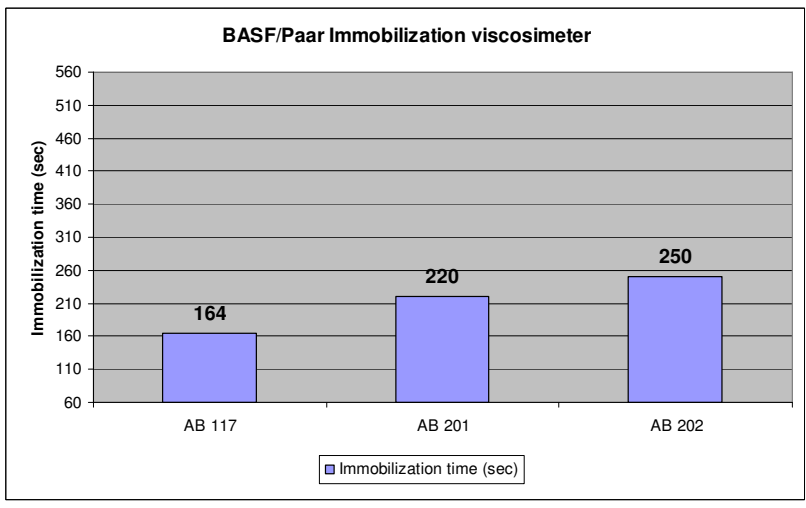
Pict. 7.3.25: Immobilization time of mill coating colours from working tank

In pict. 7.3.26 and 7.3.27 the results of a second immobilization study using the BASF immobilization cell at OMYA are shown.
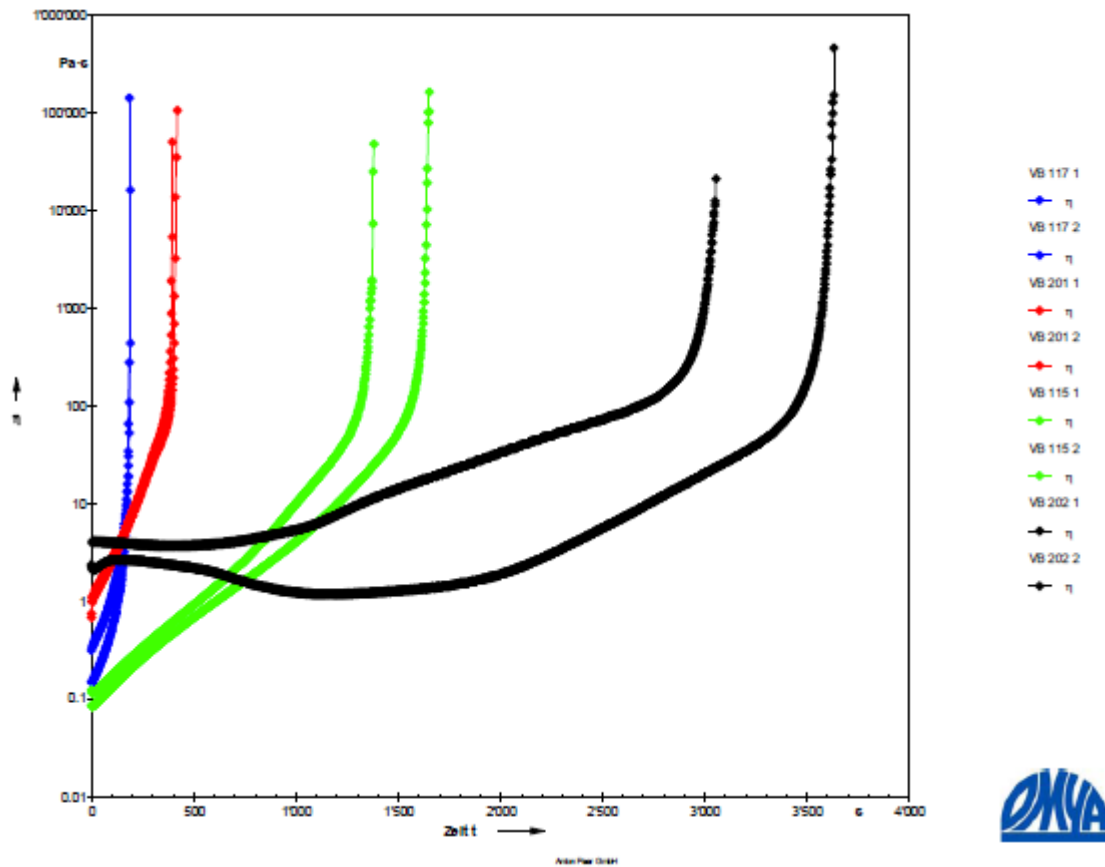
Pict. 7.3.26: Immobilization time of different precoatings

Coating Colours	Solid content %	Immobilization time s	Solid content at Immo. time %
VB 117 1	71.4	182	80
VB 117 2	71.3	190	82
VB 201 1	68.4	398	82
VB 201 2	68.4	414	83
VB 115 1	66.6	1380	80
VB 115 2	67.2	1650	81
VB 202 1	67.9	3052	82
VB 202 2	68.0	3632	82

Pict. 7.3.27: Immobilization solids of precoatings

Precoatings with high starch content (Rez. 115 and 201: 6% starch) have longer immobilization time than coatings with low starch content (Rez. 117: 2% starch and Rez. 201: 3% starch).

Adding viscosity by CMC increases immobilization time: Middle coating Rez. 202 with BF20 viscosity of 6400 cp has an immobilization time of 3000 sec while precoating Rez. 117 with BF20 viscosity of 790 cp has an immobilized time of 200 sec.

Another method to determine the immobilization solids is to carefully evaporate the free water of the coating colour on a heating plate under stirring. Viscosity increases exponentially when the immobilization solids is reached. The immobilized sample "Ende" was taken when no more movement of coating colour could be achieved by external mixing.

Results of the coating colours which were investigated in the previous pictures are shown in pict. 7.3.28.

Immo solids of precoatings PM11

117 VB	21.08.2007	Start: Ende:	67,72% 79,39%	+ 11,67%
117 VB	12.09.2007	Start: Ende:	66,75% 79,78%	+ 13,03%
115 VB - 1	27.08.2007	Start: Ende:	73,93% 81,17%	+ 7,24%
115 VB - 2	03.09.2007	Start: Ende:	68,02% 81,18%	+ 13,16%
115 VB - 3	11.09.2007	Start: Ende:	66,76% 80,71%	+ 13,95%
201 VB - 1	22.08.2007	Start: Ende:	73,84% 81,44%	+ 7,60%
201 VB - 2	11.09.2007	Start: Ende:	66,82% 80,47%	+ 13,65%

Pict. 7.3.28: Immobilization solids by evaporation method

When the thickness of the immobilized layer before the blade has to be determined the mass balance of working tank including the blade from pict. 7.3.19 can be applied. This was done in pict. 7.3.29 for middle coaters of OMC11. For this calculation the solid contents of fresh coating colour, of colour from working tank and at immobilization point have to be measured in lab.

MASS BALANCE CM11, Middle coat, coater 3/4

Date:			Date:				
Speed	**1600**	m/min	Solids feed	**68**	%		Input
	26,67	m/s					
Width	**8,5**	m	Solids working tank	**72**	%		Output
Pump speed	**150**	m³/h	Solids after blade	**72,22**	%		

Immo solid	Immo density	
% solids	kg/m³	Formula for density as a function of solid content at CM11 (lab measurement):
81,1	1933	**Pre-/Middlecoating:** Density (kg/m³) = 0,01697 x solids + 0,4526
		Topcoating: Density (kg/m³) = 0,02182 x solids + 0,1520

Balance room 1: Mass balance around working tank (middle coat C3/4):

V_8 = feed from kitchen	k_8	ρ_8	$M_{8,dry}$	M_8	$M_{8,wet}$	W_8	
m³/s	% solids	kg/m³	kg/s (dry)	g/m² (dry)	g/m² (wet)	g/m² water	
0,00208	**68**	1607	2,276	**10,04**	14,77	4,73	

| | | | | 10 | Control: Measured coat weight (Measurex) | | |

	Measured in working tank		$M_1 = V_1 \cdot \rho_1 \cdot k_1$	$M1=M_1/(v \cdot AB)$	$M_{1,wet}=M_1/k_1$	$W_1=M_{1,wet} - M_1$	
V_1=feed to coater	k_1	ρ_1	$M_{1,dry}$	$M_{1,dry}$	$M_{1,wet}$	W_1	h_1
m³/s	% solids	kg/m³	kg/s (dry)	g/m² (dry)	g/m² (wet)	g/m² water	µm (wet)
0,0417	**72**	1674	50,23	221,62	307,80	86,18	183,82

$V_5 = 19/20 \cdot V_1$	$k_5 = (M_1-M_8) \cdot 100 /(V_5 \cdot \rho_5)$						
V_5=return from coater	**k_5 = calc.**	**ρ_5 = calc.**	$M_{5,dry}$	$M_{5,dry}$	$M_{5,wet}$	W_5	
m³/s	% solids	kg/m³	kg/s (dry)	g/m² (dry)	g/m² (wet)	g/m² water	
0,03958	**72,20**	1678	47,96	211,58	293,04	81,46	

| | 1678 | Density control from f(k) | | | | | |

Balance room 2: From coating kitchen to blade (calc. Point 6 before blade):

V_8	k_8	ρ_8	M_8	M_8	M_8	W_8	
m³/s	% solids	kg/m³	kg/s (dry)	g/m² (dry)	g/m² (wet)	g/m² water	
0,00208	68	1607	2,276	10,04	14,77	4,73	

$V_6=(M_8)/(\rho_6 \cdot k_6)$	$k_6=k_5$ for middle coat						
V_6 = calc.	k_6	ρ_6	$M_{6,dry}$	$M_{6,dry}$	$M_{6,wet}$	W_6	h_6
m³/s	% solids	kg/m³	kg/s (dry)	g/m² (dry)	g/m² (wet)	g/m² water	µm (wet)
0,00188	72,20	1678	2,28	10,04	13,91	3,87	8,29

$V_2=(V_8 \cdot \rho_8-V_6 \cdot \rho_6)/\rho_2$	**Penetrated water from jet to blade**		$M_{Ret, atro}=M_{6,dry}$	$M_{Ret,wet}=M_{6,wet}$			
V_2 = calc.		ρ_2	M_2	$M_{Ret, atro}$	$M_{Ret,wet}$	$M_{Immo,wet}$	$h_{Immo,2}$
m³/s		kg/m³	g/m² (water)	g/m² (dry)	g/m² (wet)	g/m² (wet)	µm (wet)
0,00019		1000	**0,86**	10,04	13,91	**0,31**	0,16

Balance room 3: Mass balance at blade tip (from point 6 to free draw after blade)

V_6	k_6	ρ_6	M_6	M_6	M_6	W_6	
m³/s	% solids	kg/m³	kg/s (dry)	g/m² (dry)	g/m² (wet)	g/m² water	
0,00188	72,20	1678	2,276	10,04	13,91	3,87	

$V_4=(M_6)/(\rho_4 \cdot k_4)$	$k_6=k_5$ for middle coat						
V_4 = calc.	k_4	ρ_4	$M_{4,dry}$	$M_{4,dry}$	$M_{4,wet}$	W_4	h_4
m³/s	% solids	kg/m³	kg/s (dry)	g/m² (dry)	g/m² (wet)	g/m² water	µm (wet)
0,001878	**72,22**	1678	2,28	10,04	13,90	3,86	8,28

$V_3=(V_6 \cdot \rho_6-V_4 \cdot \rho_4)/\rho_3$	**Penetrated water under blade**		$M_{Ret, atro}=M_{4,dry}$	$M_{Ret,wet}=M_{4,wet}$			
V_3 = calc.		ρ_3	M_3	$M_{Ret, atro}$	$M_{Ret,wet}$	$M_{Immo,wet}$	$h_{Immo,3}$
m³/s		kg/m³	g/m² (water)	g/m² (dry)	g/m² (wet)	g/m² (wet)	µm (wet)
0,0000008		1000	**0,00**	10,04	13,90	**0,03**	0,01

Pict. 7.3.29: Mass balances for middle coaters OMC11
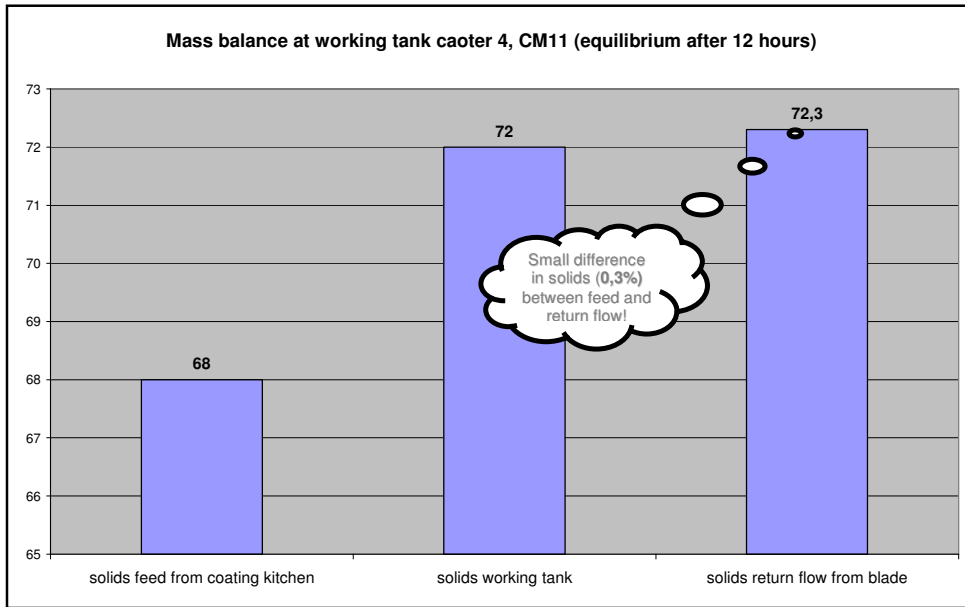
Pict. 7.3.30: Mass balance of working circuit in middle coat CM11 at stationary conditions

The mass balance in pict. 7.3.29 and 7.3.20 **shows that solid content increases only by 0,2% from application to blade when a stationary difference in solids between coating kitchen and working tank of 4% is reached.**
This is due to the fact that the flow at the jet application is 20 times higher than the feed from the coating kitchen.

The thickness of the immobilized layer was calculated by:

$$M_{Im\,mo} = \frac{M_{atro} - M_{Start} * c_{Start}}{c_{Im\,mo} - c_{Start}} \;\ldots M \text{ in g/m}^2, \; c \text{ as solid content} / 100$$

$$h_f = h_{Im\,mo} = \frac{M_{Im\,mo}}{\rho_{Im\,mo}} \;\ldots \text{Thickness of immobilized layer}$$

When solid content increases from 72 to 72,2% between jet and blade, an **immobilized layer is formed with a thickness of 0,16 μm**.
An immobilized layer thickness of 0,16 μm seems to be very thin when compared to 8 – 10 μm gap between blade and paper (corresponds to the wet coating film thickness after the blade).

Comparison of penetration at mddle coaters OMC11 with and without immobilized lyer before blade:

Delta solids between working tank and fresh coating colour: 4%

Coater at OMC11	Applied coating	Penetrates through:	Penetration depth into coating layer h_s (µm)	Darcy coeff. of dry precoating layer K_s (m²)	Thickness of immo layer before blade h_f (µm)	Darcy coeff. of immo layer K_f (m²)	SUM of h/K	Penetrated Liquid V ( )
C3/4	Middle coat	precoating layer + immo layer before blade	0,652	5,0E-18	**0,16**	1,3E-16	1,32E+11	100%
C3/4	Middle coat	precoating layer	0,652	5,0E-18			1,30E+11	**101%**
			from mercury porosity and mass balance	from Prüfbau pressure penetration test	from mass balance	from Abo-GWR measurements		

Coater at OMC11	Applied coating	Penetrates through:	Penetration depth into coating layer h_s (µm)	Darcy coeff. of dry precoating layer K_s (m²)	Thickness of immo layer before blade h_f (µm)	Darcy coeff. of immo layer K_f (m²)	SUM of h/K	Penetrated Liquid V ( )
C5/6	Top coat	middle coating layer	0,652	5,0E-18			1,30E+11	100%
C5/6	Top coat	middle coating layer + assumed immo layer before blade	0,652	5,0E-18	**0,16**	1,3E-16	1,32E+11	**99%**
			from mercury porosity and mass balance	from Prüfbau pressure pen. Test	from mass balance	from Abo-GWR measurements		

$$v = \frac{d(V/A)}{dt} = \frac{\Delta p_f + \Delta p_s}{\eta * \left[\frac{h_f}{K_f} + \frac{h_s}{K_s}\right]}$$

Pict. 7.3.31: Reduction of penetration under blade with an immobilized layer of 0,16 µm thickness

Inserting an immobilized layer of 0,16 µm thickness into Darcy's law leads to a reduction of water penetration of only 1% (pict. 7.3.31).

When a higher increase in solids in the working tank is assumed, thickness of immobilized layer will also increase. Various measurements of solid content in the working tanks of OMC9 and OMC11 showed a max solids of 75% (pict. 7.3.32).

Date: 14.5., 16:30				Grade:	4013/MR2, 9800200
	After blade	Working tank	Coating kitchen	Diff. AB - VB	Diff. blade - tank
Coater 3	75,2	73,8	69,5	**4,3**	1,4
Coater 4	74,8	73,3	69,5	**3,8**	1,5
Coater 5	**75,6**	68,3	68,5	-0,2	**7,3**
Coater 6	**74,1**	68,4	68,5	-0,1	**5,7**

Pict. 7.3.32: Extreme high solids after the blade, caused in the middle coating by fibre sorption and in the top coating by pressure penetration

MASS BALANCE CM11, Middle coat, coater 3/4

Date:			Date:				Input
Speed	**1600**	m/min	Solids feed	**68**	%		
	26,67	m/s					Output
Width	**8,5**	m	Solids working tank	**75**	%		
Pump speed	**150**	m³/h	Solids after blade	**75,34**	%		

Immo solid	Immo density
% solids	kg/m³
81,1	1933

Formula for density as a function of solid content at CM11 (lab measurement):

Pre-/Middlecoating: Density (kg/m³) = 0,01697 x solids + 0,4526

Topcoating: Density (kg/m³) = 0,02182 x solids + 0,1520

Balance room 1: Mass balance around working tank (middle coat C3/4):

V_8 = feed from kitchen	k_8	ρ_8	$M_{8,dry}$	M_8	$M_{8,wet}$	W_8	
m³/s	% solids	kg/m³	kg/s (dry)	g/m² (dry)	g/m² (wet)	g/m² water	
0,00208	**68**	1607	2,276	**10,04**	14,77	4,73	

				10	Control: Measured coat weight (Measurex)		

	Measured in working tank		$M_1 = V_1 \cdot \rho_1 \cdot k_1$	$M1 = M_1/(v \cdot AB)$	$M_{1,wet} = M_1/k_1$	$W_1 = M_{1,wet} - M_1$	
V_1 = feed to coater	k_1	ρ_1	$M_{1,dry}$	$M_{1,wet}$	$M_{1,wet}$	W_1	h_1
m³/s	% solids	kg/m³	kg/s (dry)	g/m² (dry)	g/m² (wet)	g/m² water	µm (wet)
0,0417	**75**	1725	53,92	237,87	317,16	79,29	183,82

$V_5 = 19/20 \cdot V_1$	$k_5 = (M_1-M_8) \cdot 100 /(V_5 \cdot \rho_5)$						
V_5 = return from coater	k_5 = calc.	ρ_5 = calc.	$M_{5,dry}$	$M_{5,dry}$	$M_{5,wet}$	W_5	
m³/s	% solids	kg/m³	kg/s (dry)	g/m² (dry)	g/m² (wet)	g/m² water	
0,03958	**75,34**	1732	51,64	227,83	302,39	74,56	

	1731	Density control from f(k)					

Balance room 2: From coating kitchen to blade (calc. Point 6 before blade):

V_8	k_8	ρ_8	M_8	M_8	M_8	W_8	
m³/s	% solids	kg/m³	kg/s (dry)	g/m² (dry)	g/m² (wet)	g/m² water	
0,00208	68	1607	2,276	10,04	14,77	4,73	

$V_6=(M_8)/(\rho_6 \cdot k_6)$	$k_6=k_5$ for middle coat						
V_6 = calc.	k_6	ρ_6	$M_{6,dry}$	$M_{6,dry}$	$M_{6,wet}$	W_6	h_6
m³/s	% solids	kg/m³	kg/s (dry)	g/m² (dry)	g/m² (wet)	g/m² water	µm (wet)
0,00174	75,34	1732	2,28	10,04	13,33	3,29	7,70

$V_2=(V_8 \cdot \rho_8-V_6 \cdot \rho_6)/\rho_2$	**Penetrated water from jet to blade**		$M_{Ret, atro}=M_{6,dry}$	$M_{Ret,wet}=M_{6,wet}$			
V_2 = calc.		ρ_2	M_2	$M_{Ret, atro}$	$M_{Ret,wet}$	$M_{Immo,wet}$	$h_{Immo,2}$
m³/s		kg/m³	g/m² (water)	g/m² (dry)	g/m² (wet)	g/m² (wet)	µm (wet)
0,00033		1000	**1,44**	10,04	13,33	**0,75**	0,39

Balance room 3: Mass balance at blade tip (from point 6 to free draw after blade)

V_6	k_6	ρ_6	M_6	M_6	M_6	W_6	
m³/s	% solids	kg/m³	kg/s (dry)	g/m² (dry)	g/m² (wet)	g/m² water	
0,00174	75,34	1732	2,276	10,04	13,33	3,29	

$V_4=(M_6)/(\rho_4 \cdot k_4)$	$k_6=k_5$ for middle coat						
V_4 = calc.	k_4	ρ_4	$M_{4,dry}$	$M_{4,dry}$	$M_{4,wet}$	W_4	h_4
m³/s	% solids	kg/m³	kg/s (dry)	g/m² (dry)	g/m² (wet)	g/m² water	µm (wet)
0,001745	75,34	1731	2,28	10,04	13,33	3,29	7,70

$V_3=(V_6 \cdot \rho_6-V_4 \cdot \rho_4)/\rho_3$	**Penetrated water under blade**		$M_{Ret, atro}=M_{4,dry}$	$M_{Ret,wet}=M_{4,wet}$			
V_3 = calc.		ρ_3	M_3	$M_{Ret, atro}$	$M_{Ret,wet}$	$M_{Immo,wet}$	$h_{Immo,3}$
m³/s		kg/m³	g/m² (water)	g/m² (dry)	g/m² (wet)	g/m² (wet)	µm (wet)
-0,0000001		1000	**0,00**	10,04	13,33	**0,00**	0,00

Pict. 7.3.33: Mass balance for higher solid increase between application and blade

Comparison of penetration resistance coefficient between middle- and top coat OMC11

Delta solids between working tank and fresh coating colour: 7% (68 --> 75%)

Coater at OMC11	Applied coating	Penetrates through:	Penetration depth into coating layer h_s (μm)	Darcy coeff. of dry precoating layer K_s (m²)	Thickness of immo layer before blade h_f (μm)	Darcy coeff. of immo layer K_f (m²)	SUM of h/K	Penetrated Liquid V ( )
C3/4	Middle coat **with** immo layer	precoating layer	0,652	5,0E-18	**0,39**	1,3E-16	1,33E+11	100%
C5/6	Middle coat **without** immo layer	precoating layer	0,652	5,0E-18			1,30E+11	**102%**
			from mercury porosity and mass balance	from Prüfbau pressure pen. Test	from mass balance	from Abo-GWR measurements		

Pict. 7.3.34: Reduction of penetration under blade with an immobilized layer of 3 μm thickness

Inserting this max solids of 75% in working tank into the mass balance around the whole blade coating unit leads to a thickness of the immobilized layer of 0,39 μm but again the influence upon penetration under the blade is low. These calculation stands in contradiction to the findings of Ph. Letzelter (pict. 7.3.6) who showed that the immobilized layer of a roll applicator slowed down dewatering under the blade.

The calculation conflicts also with measured solids after the blade, shown in pict. 7.3.17, 7.3.18 and 7.3.32: For top coaters of OMC11 a severe increase in solids under the blade was measured but for middle coaters this increase under the blade was much lower which can be caused only by the added permeability of the immobilized layer under the blade as all other properties like coating colour water retention and permeability of substrate are disadvantageous for the middle coaters.

The explanation for this contradiction lies in the wrong assumption of the coating colour thickness or flow rate before the blade.

In the previous calculations the assumption was made that the coating colour which is applied by the jet applicator is transferred totally to the blade tip.
At high speed coaters one can see that parts of the coating colour are sprayed from the paper surface before the blade is reached by centrifugal force. Therefore the calculation of immobilized layer thickness is repeated in pict. 7.3.35 for lower application flow rate (and therefore lower transfer rate):

MASS BALANCE CM11, Middle coat, coater 3/4

Date:				Date:				**Input**
Speed	**1600**	m/min		Solids feed	**68**	%		**Output**
	26,67	m/s						
Width	**8,5**	m		Solids working tank	**72**	%		
Pump speed	**25**	m³/h		Solids after blade	**73,51**	%		
		Flow rate before/after blade						
Excess rate	3,5							

Immo solid	Immo density
% solids	kg/m³
81,1	**1933**

Formula for density as a function of solid content at CM11 (lab measurement):

Pre-/Middlecoating: Density (kg/m³) = 0,01697 x solids + 0,4526

Topcoating: Density (kg/m³) = 0,02182 x solids + 0,1520

Balance room 1: Mass balance around working tank (middle coat C3/4):

V_8 = feed from kitchen	k_8	ρ_8	$M_{8,dry}$	M_8	$M_{8,wet}$	W_8	
m³/s	% solids	kg/m³	kg/s (dry)	g/m² (dry)	g/m² (wet)	g/m² water	
0,00198	**68**	1607	2,168	**9,56**	14,06	4,50	

10   Control: Measured coat weight (Measurex)

	Measured in working tank		$M_1 = V_1{}^*\rho_1{}^*k_1$	$M1 = M_1/(v{}^*AB)$	$M_{1,wet} = M_1/k_1$	$W_1 = M_{1,wet} - M_1$	
V_1 = feed to coater	k_1	ρ_1	$M_{1,dry}$	$M_{1,dry}$	$M_{1,wet}$	W_1	h_1
m³/s	% solids	kg/m³	kg/s (dry)	g/m² (dry)	g/m² (wet)	g/m² water	µm (wet)
0,0069	**72**	1674	8,37	36,94	51,30	14,36	30,64

$V_5 = 19/20{}^*V_1$	$k_5 = (M_1-M_8){}^*100 /(V_5{}^*\rho_5)$						
V_5 = return from coater	k_5 = calc.	ρ_5 = calc.	$M_{5,dry}$	$M_{5,dry}$	$M_{5,wet}$	W_5	
m³/s	% solids	kg/m³	kg/s (dry)	g/m² (dry)	g/m² (wet)	g/m² water	
0,00496	**73,51**	1702	6,20	27,37	37,24	9,86	

1700   Density control from f(k)

Balance room 2: From coating kitchen to blade (calc. Point 6 before blade):

V_8	k_8	ρ_8	M_8	M_8	M_8	W_8	
m³/s	% solids	kg/m³	kg/s (dry)	g/m² (dry)	g/m² (wet)	g/m² water	
0,00198	68	1607	2,168	9,56	14,06	4,50	

$V_6=(M_8)/(\rho_6{}^*k_6)$	$k_6=k_5$ for middle coat						
V_6 = calc.	k_6	ρ_6	$M_{6,dry}$	$M_{6,dry}$	$M_{6,wet}$	W_6	h_6
m³/s	% solids	kg/m³	kg/s (dry)	g/m² (dry)	g/m² (wet)	g/m² water	µm (wet)
0,00173	73,51	1702	2,17	9,56	13,01	3,45	**7,65**

$V_2=(V_8{}^*\rho_8-V_6{}^*\rho_6)/\rho_2$	Penetrated water from jet to blade		$M_{Ret, atro}=M_{6,dry}$	$M_{Ret,wet}=M_{6,wet}$			
V_2 = calc.		ρ_2	M_2	$M_{Ret, atro}$	$M_{Ret,wet}$	$M_{Immo,wet}$	$h_{Immo,2}$
m³/s		kg/m³	g/m² (water)	g/m² (dry)	g/m² (wet)	g/m² (wet)	µm (wet)
0,00024		1000	**1,05**	9,56	13,01	**2,16**	1,12

Balance room 3: Mass balance at blade tip (from point 6 to free draw after blade)

V_6	k_6	ρ_6	M_6	M_6	M_6	W_6	
m³/s	% solids	kg/m³	kg/s (dry)	g/m² (dry)	g/m² (wet)	g/m² water	
0,00173	73,51	1702	2,168	9,56	13,01	3,45	

$V_4=(M_6)/(\rho_4{}^*k_4)$	$k_6=k_5$ for middle coat						
V_4 = calc.	k_4	ρ_4	$M_{4,dry}$	$M_{4,dry}$	$M_{4,wet}$	W_4	h_4
m³/s	% solids	kg/m³	kg/s (dry)	g/m² (dry)	g/m² (wet)	g/m² water	µm (wet)
0,001734	**73,51**	1700	2,17	9,56	13,01	3,45	**7,65**

$V_3=(V_6{}^*\rho_6-V_4{}^*\rho_4)/\rho_3$	Penetrated water under blade		$M_{Ret, atro}=M_{4,dry}$	$M_{Ret,wet}=M_{4,wet}$			
V_3 = calc.		ρ_3	M_3	$M_{Ret, atro}$	$M_{Ret,wet}$	$M_{Immo,wet}$	$h_{Immo,3}$
m³/s		kg/m³	g/m² (water)	g/m² (dry)	g/m² (wet)	g/m² (wet)	µm (wet)
0,0000000		1000	**0,00**	9,56	13,01	**0,00**	0,00

Pict. 7.3.35: Calculation of immobilized layer thickness with lower application flow rate

The corrected calculation shows that when the flow rate of the coating colour before the blade is severely reduced from 150 to 25 m³/h the solid content of the coating colour before the blade rises from 72,2 to 73,5% and the thickness of the immobilized layer raises from 0,16 to **1,12 µm**.

In pict. 7.3.36 the mass balance was repeated for extreme conditions of max solids 75% in working tank and flow rate of 25 m³/h coating colour reaching the blade (= 1/6 of application).

MASS BALANCE CM11, Middle coat, coater 3/4

Date:			Date:			Input
Speed	**1600**	m/min	Solids feed	**68**	%	
	26,67	m/s				Output
Width	**8,5**	m	Solids working tank	**75**	%	
Pump speed	**25**	m³/h	Solids after blade	**77,54**	%	
		Flow rate before/after blade				
Excess rate	3,5					

Immo solid	Immo density
% solids	kg/m³
81,1	**1933**

Formula for density as a function of solid content at CM11 (lab measurement):

Pre-/Middlecoating: Density (kg/m³) = 0,01697 x solids + 0,4526

Topcoating: Density (kg/m³) = 0,02182 x solids + 0,1520

Balance room 1: Mass balance around working tank (middle coat C3/4):

V_8 = feed from kitchen	k_8	ρ_8	$M_{8,dry}$	M_8	$M_{8,wet}$	W_8	
m³/s	% solids	kg/m³	kg/s (dry)	g/m² (dry)	g/m² (wet)	g/m² water	
0,00198	**68**	1607	2,168	9,56	14,06	4,50	

| | | | | 10 | Control: Measured coat weight (Measurex) | | |

		Measured in working tank	$M_1 = V_1 \cdot \rho_1 \cdot k_1$	$M1=M_1/(v \cdot AB)$	$M_{1,wet}=M_1/k_1$	$W_1=M_{1,wet} - M_1$	
V_1=feed to coater	k_1	ρ_1	$M_{1,dry}$	$M_{1,dry}$	$M_{1,wet}$	W_1	h_1
m³/s	% solids	kg/m³	kg/s (dry)	g/m² (dry)	g/m² (wet)	g/m² water	µm (wet)
0,0069	**75**	1725	8,99	39,64	52,86	13,21	30,64

$V_5 = 19/20 \cdot V_1$	$k_5 = (M_1-M_8) \cdot 100 /(V_5 \cdot \rho_5)$						
V_5=return from coater	k_5 = calc.	ρ_5 = calc.	$M_{5,dry}$	$M_{5,dry}$	$M_{5,wet}$	W_5	
m³/s	% solids	kg/m³	kg/s (dry)	g/m² (dry)	g/m² (wet)	g/m² water	
0,00496	**77,54**	1773	6,82	30,08	38,80	8,71	

| | | 1768 | Density control from f(k) | | | | |

Balance room 2: From coating kitchen to blade (calc. Point 6 before blade):

V_8	k_8	ρ_8	M_8	M_8	M_8	W_8	
m³/s	% solids	kg/m³	kg/s (dry)	g/m² (dry)	g/m² (wet)	g/m² water	
0,00198	68	1607	2,168	9,56	14,06	4,50	

$V_6=(M_8)/(\rho_6 \cdot k_6)$	$k_6=k_5$ for middle coat						
V_6 = calc.	k_6	ρ_6	$M_{6,dry}$	$M_{6,dry}$	$M_{6,wet}$	W_6	h_6
m³/s	% solids	kg/m³	kg/s (dry)	g/m² (dry)	g/m² (wet)	g/m² water	µm (wet)
0,00158	77,54	1773	2,17	9,56	12,33	2,77	6,96

$V_2=(V_8 \cdot \rho_8-V_6 \cdot \rho_6)/\rho_2$	**Penetrated water from jet to blade**		$M_{Ret, atro}=M_{6,dry}$	$M_{Ret,wet}=M_{6,wet}$			
V_2 = calc.		ρ_2	M_2	$M_{Ret, atro}$	$M_{Ret,wet}$	$M_{Immo,wet}$	$h_{Immo,2}$
m³/s		kg/m³	g/m² (water)	g/m² (dry)	g/m² (wet)	g/m² (wet)	µm (wet)
0,00039		1000	**1,73**	9,56	12,33	**5,13**	2,65

Balance room 3: Mass balance at blade tip (from point 6 to free draw after blade)

V_6	k_6	ρ_6	M_6	M_6	M_6	W_6	
m³/s	% solids	kg/m³	kg/s (dry)	g/m² (dry)	g/m² (wet)	g/m² water	
0,00158	77,54	1773	2,168	9,56	12,33	2,77	

$V_4=(M_6)/(\rho_4 \cdot k_4)$	$k_6=k_5$ for middle coat						
V_4 = calc.	k_4	ρ_4	$M_{4,dry}$	$M_{4,dry}$	$M_{4,wet}$	W_4	h_4
m³/s	% solids	kg/m³	kg/s (dry)	g/m² (dry)	g/m² (wet)	g/m² water	µm (wet)
0,001581	77,54	1768	2,17	9,56	12,33	2,77	6,97

$V_3=(V_6 \cdot \rho_6-V_4 \cdot \rho_4)/\rho_3$	**Penetrated water under blade**		$M_{Ret, atro}=M_{4,dry}$	$M_{Ret,wet}=M_{4,wet}$			
V_3 = calc.		ρ_3	M_3	$M_{Ret, atro}$	$M_{Ret,wet}$	$M_{Immo,wet}$	$h_{Immo,3}$
m³/s		kg/m³	g/m² (water)	g/m² (dry)	g/m² (wet)	g/m² (wet)	µm (wet)
0,0000001		1000	**0,00**	9,56	12,33	**0,01**	0,00

Pict. 7.3.36: Calculation of immobilized layer thickness with lower application flow rate

When a lower flow rate before the blade and a higher solid content in the working tank (75%) is assumed the immobilized layer thickness increases up to **2,65 µm**.

Comparison of penetration resistance coefficient between middle- and top coat OMC11
Delta solids between working tank and fresh coating colour: 7% (68 --> 75%),   higher immo layer thickness

Coater at OMC11	Applied coating	Penetrates through:	Penetration depth into coating layer h_s (µm)	Darcy coeff. of dry precoating layer K_s (m²)	Thickness of immo layer before blade h_f (µm)	Darcy coeff. of immo layer K_f (m²)	SUM of h/K	Penetrated Liquid V ( )
C3/4	Middle coat **with** immo layer	precoating layer	0,652	5,0E-18	**2,65**	1,3E-16	1,50E+11	100%
C5/6	Middle coat **without** immo layer	precoating layer	0,652	5,0E-18			1,30E+11	**115%**
			from mercury porosity and mass balance	from Prüfbau pressure pen. Test	from mass balance	from Abo-GWR measurements		

This immobilized layer with 2,65 µm thickness reduces the penetration under the blade noticeable.

The previous calculations were based on the assumption that the coating forms an immobilized layer at the boundary layer to the paper and the rest of the coating on top of that remains in the original solid.

In reality the solid content of the coating layer at the paper surface will be a gradient between immobilized solids and original solids. This theory is confirmed by the fact of higher coating colour solids in the return flow to the working tank which can occur only if the blade pulls off parts of the coating colour with higher solids than in the original coating colour.

The disadvantage of a higher thickness of immobilized layer is the **risk of severe runability problems**.

Lab measurements of coating colour rheology shown in pict. 7.3.37 – 7.3.40 indicate that the higher the solid content is, the higher the high and low shear viscosity of the coating colour will be.
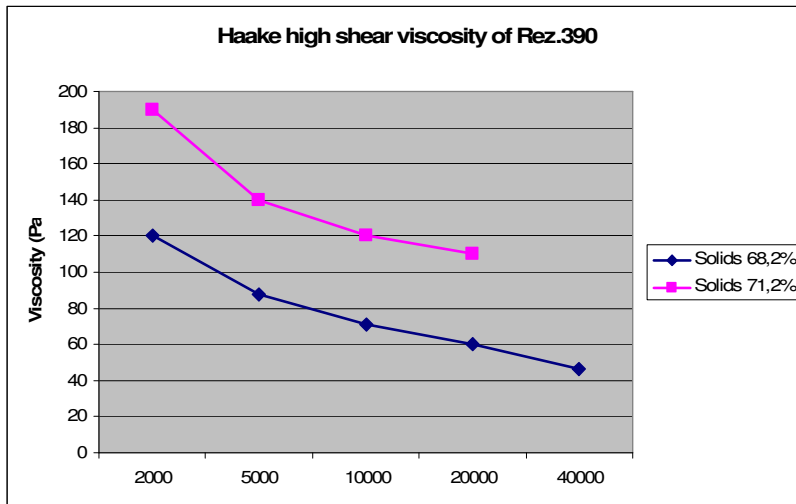
Pict. 7.3.37: Viscosity versus shear rate as a function of solid content
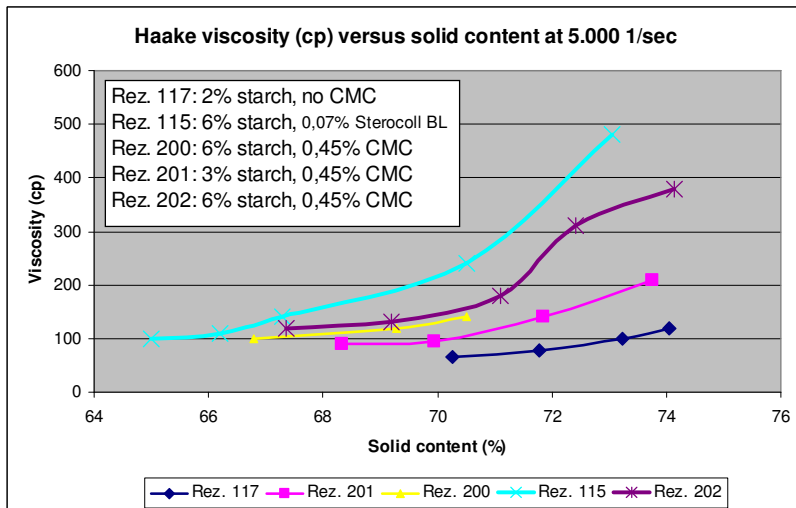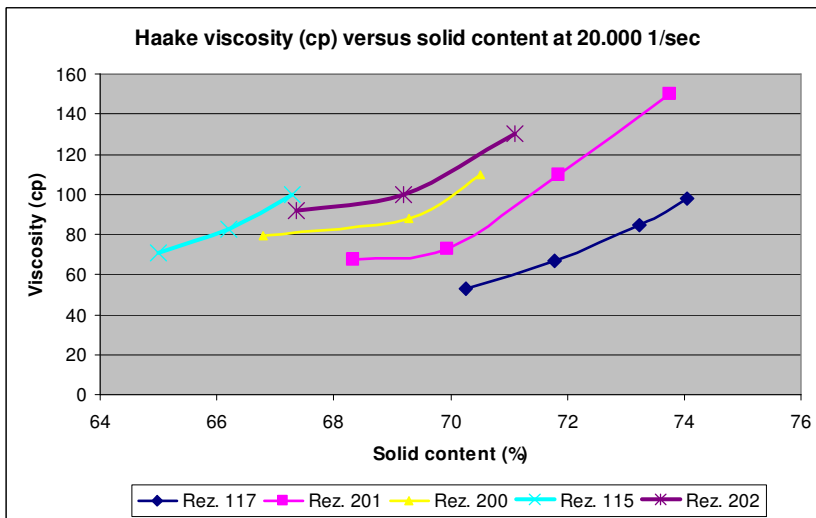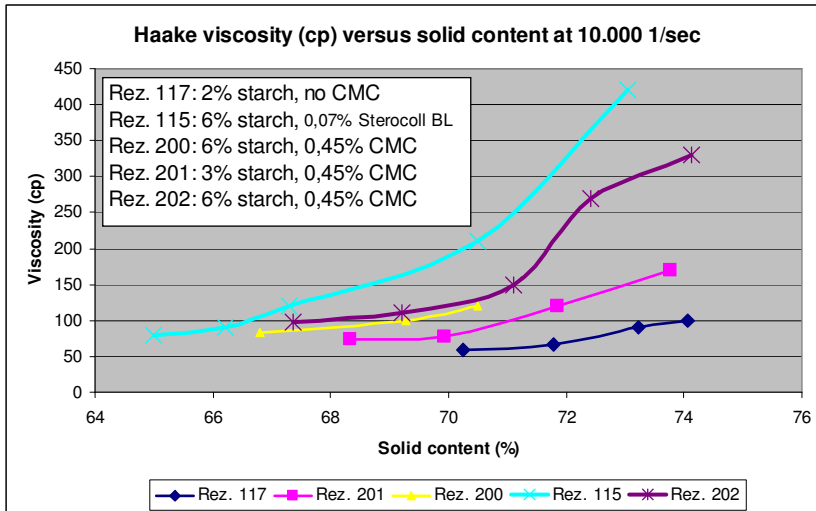
Pict. 7.3.38: Haake low and high shear viscosity versus solid content of mill coatings
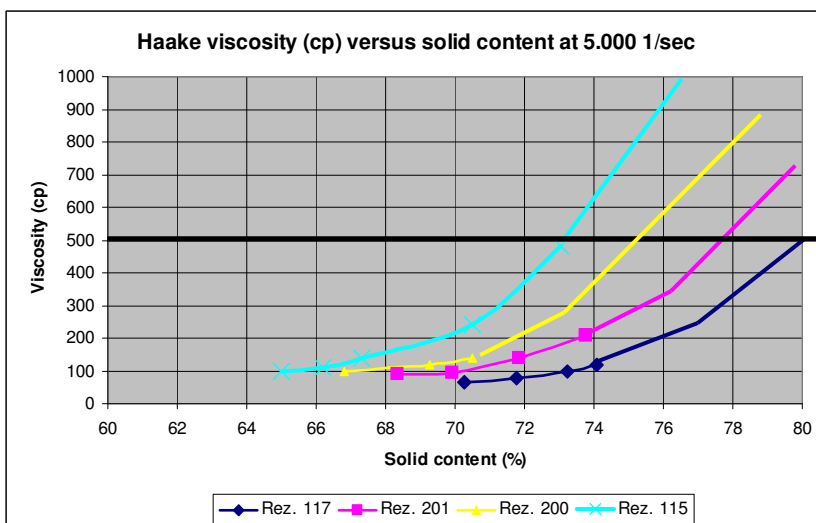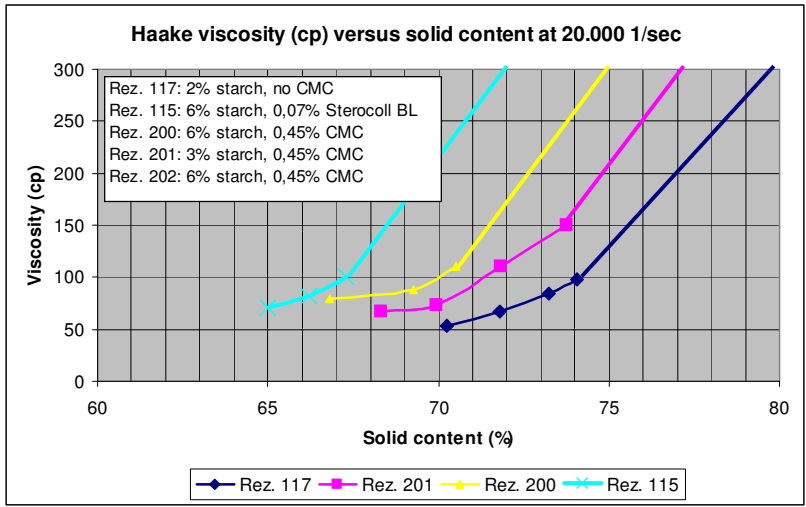
Pict. 7.3.39: Interpolated low and high shear viscosity versus solid content of mill coatings
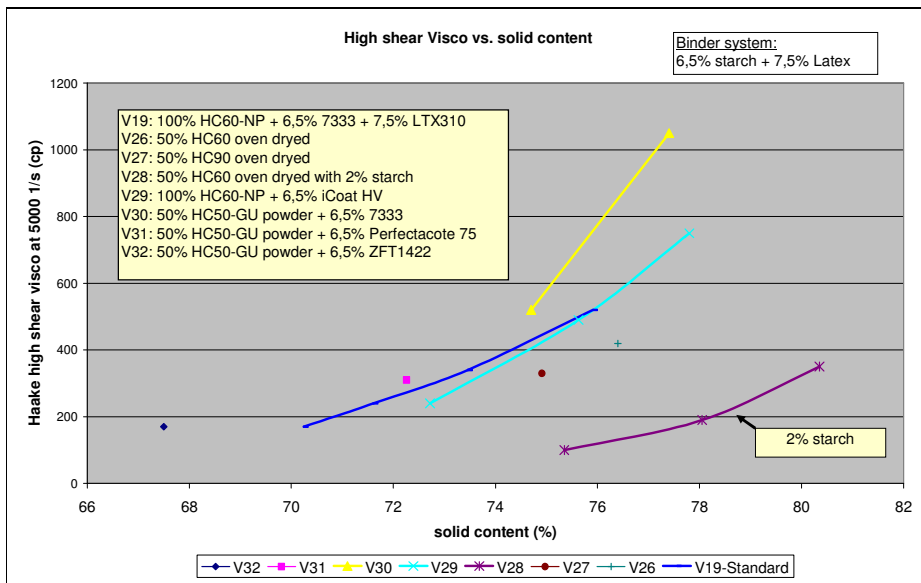
Pict. 7.3.40: High shear viscosity vs. solid content of lab coatings

When the viscosity of the liquid phase is increased by soluble thickeners like starch, CMC or synthetic thickeners the low and high shear viscosity increases faster with raising solids.

Therefore coatings with high amounts of thickeners with high molecular weight are more critical in runability when the solid content gets close to the immobilization point under the blade.

Due to paper surface roughness the gap between blade and paper can be locally lower than average (6 - 10 µm) and the blade hits the immobilized layer (up to 3 µm thick).

Common runability problems with solids close to immobilization under the blade are:
- Wet bleeding = immobilized coating colour on the back side on the blade after the tip exit
- Local wearing of the blade due to higher shear forces leading to glossy stripes at the wet mirror after blade and to locally higher coat weight ending in flatness problems of the end product
- Rheology scratches

D. Bousfield from U Maine (L1.20): developed a calculation model to predict the built-up of the coating colour filter cake before the blade. He tried to predict the maximum speed to run without runability problems including blade forces, coat weight, roughness and porosity of base paper in his model.
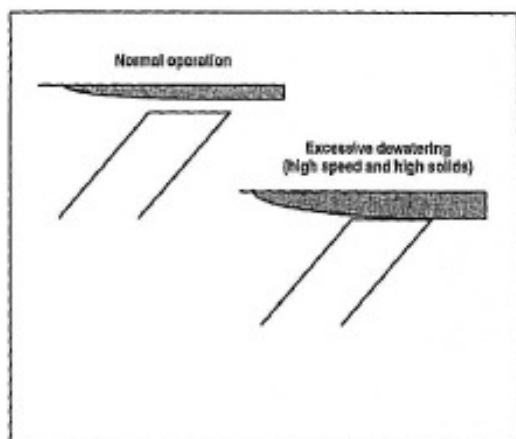
Pict. 7.3.41: Low/high thickness if immobilized layer (D. Bousfield)

At low coat weights the immobilized layer is touched earlier by the blade and scratches, streaks or deposits like weeps, spits, whiskers or stalagmites occur (pict. 7.3.41).

R. Knappich, P. Burri and G. Lohmüller from OMYA and DOW (L 1.52) compared the wet and dry coating structure of calcium carbonate pigments with broad and narrow particle size distributions.

Immobilization solids was measured by BASF-Paar-Immobilization cell and found to be 5% lower for the narrow PSD carbonate.
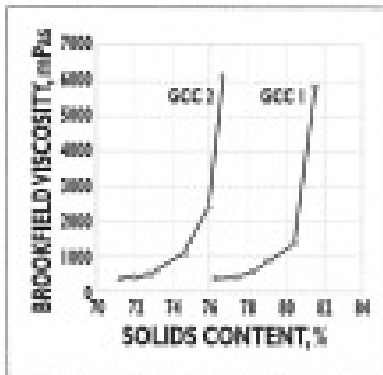
Pict. 7.3.42: Immobilized solids of GCC1 (broad) and GCC2 (steep) (R. Knappich)

Therefore steep carbonates are critical in runability at fast blade coaters. Latex with lower particles size was developed by DOW which gave the same solids when mixed with steep carbonate compared to broad carbonate plus standard latex. High shear viscosity could be reduced by 50%. Pilot trials confirmed the lab trials: Speed was the same with this mixture of special latex and steep PSD carbonate as for broad carbonate.

M. Johnson (L4.3) investigated the exit flow from a bevelled blade coater. Dry weeping occurs when a filter cake of high thickness is formed before the blade. Cavitation of water can lead to wet weeping at the blade tip exit when speed of the coater is high.

J. Weigl and H. Grossmann (L4.7) recapitulated the most important factors impeding the runability of high speed blade coaters.

Increasing the solid content before the blade by base paper sorption led to faster blade wear, scratches, streaks, bleeding, stalagmites and skip coating due to increased high shear viscosity of coating colour. The higher the base ash, the higher the micro porosity (remark: the lower the pore radius and the higher the capillary

sorption pressure), the more water was penetrating before the blade. More stalagmites occurred.

Bleeding was caused by excessive local dewatering and reaching the immobilization solids locally under the blade. With higher base ash the risk of bleeding was raised. Lowering high shear viscosity of coating colour was suggested as a measure against bleeding.

Loosely bound fines can also create scratches or stalagmites. Microscopic analysis showed that stalagmites always contained fibres. Surface sizing and machine calendering of base paper reduces stalagmite forming by either binding fibre fines into the base paper surface or rubbing them off from the surface.

Gunnar Engström (L 4.9) compared SDTA (short dwell) with LDTA (roll) applicators. At 1000 m/min he estimated a line pressure of 1 -2 kN/m in the nip of the applicator roll of a LDTA.

Blade pressure was higher with an LDTA unit due to water penetration and increased thickness of immobilized layer before the blade. The coating layer was more even and the print mottle got better than for SDTA application.

Increasing the speed of the coater led to higher blade pressure. Higher blade pressure caused intensified compression of base paper and in consequence coating layer was more uniform in thickness and porosity. Print mottle also got better.

Pressure release after the blade was regarded by the authors to be responsible for paper roughness, especially for wood containing base papers. The higher the blade pressure, the bigger the pressure release, the rougher the coated paper was.

G. Engström showed that standard deviation of latex content in the coating layer increased when the LWC-base paper was internally sized. The reason might be an uneven distribution of size in the base paper flocs and voids.

Fibro-DAT measurements were made to compare capillary penetration in the lab with calculated amount of penetrated liquid between jet and blade at OMC11 (see chapter 5 "capillary penetration"). The drop in droplet volume with penetration time as shown for base paper of PM11 in pict. 7.3.43 can be used to calculate the gradient of penetrated volume vs. time (dV/dt). Using this experimentally determined dV/dt the amount of water from coating colour absorbed by the base paper before the blade can be calculated.

Fibro-DAT measurements were made under room temperature. At OMC11 coaters the temperature is with 35°C somewhat higher and base paper sorption will be elevated.
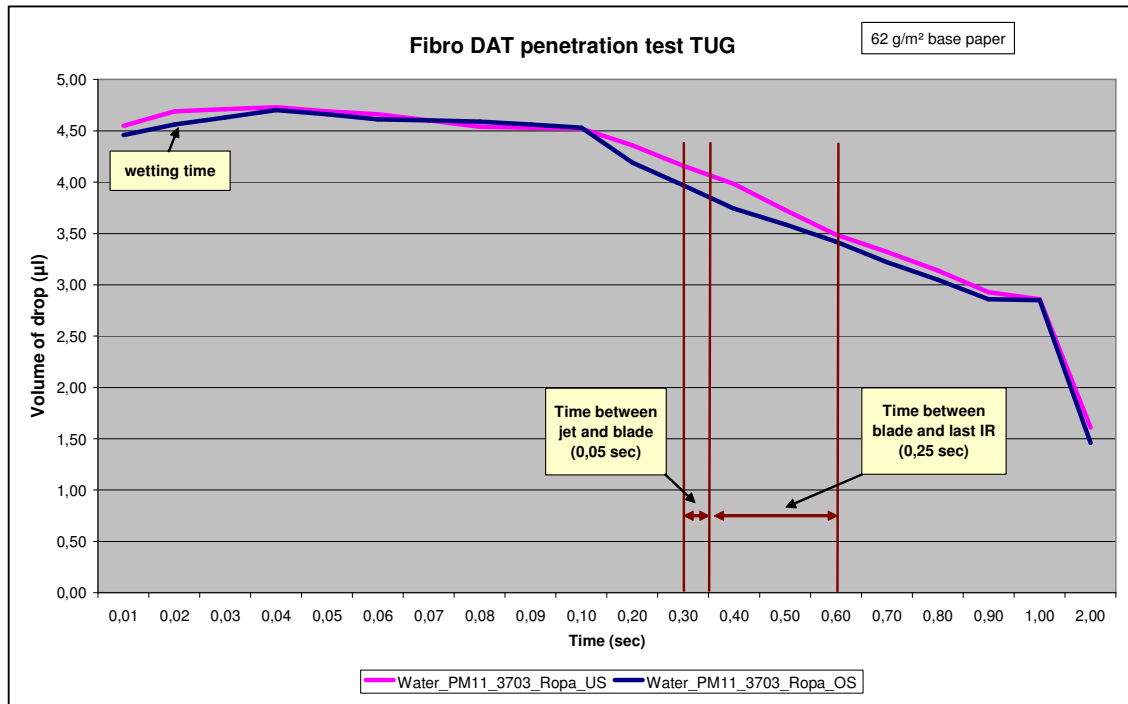
Pict. 7.3.43: Fibro-DAT penetration of water + 20% IPA on base paper PM11
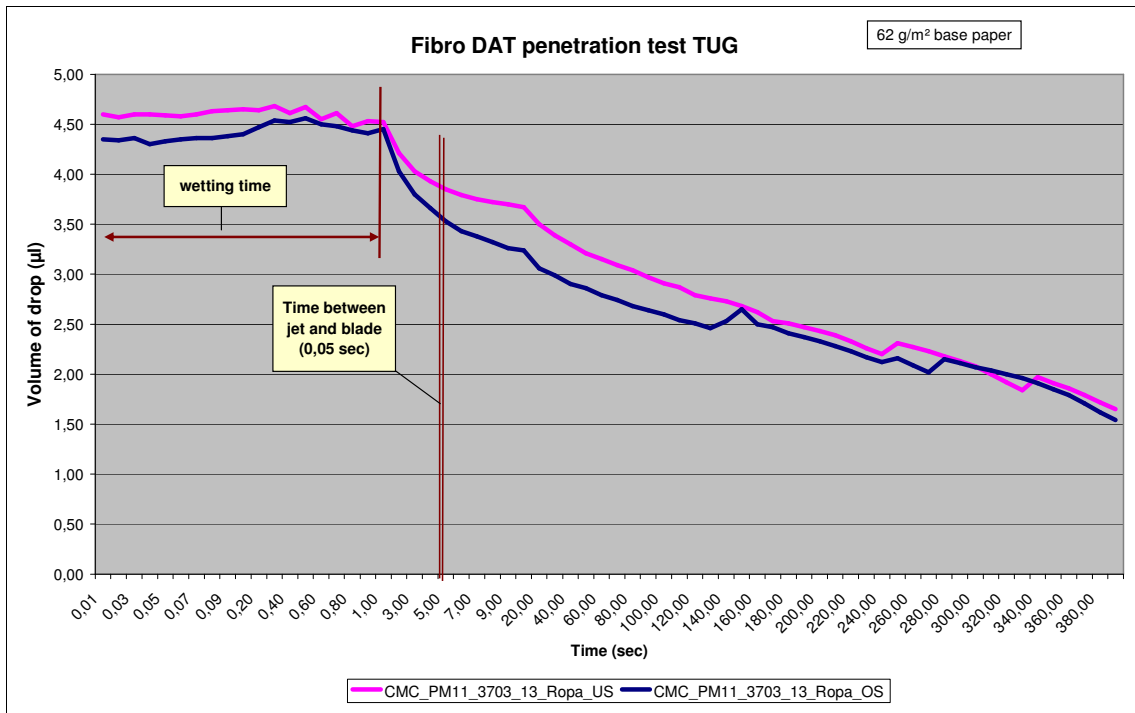
Pict. 7.3.44: Fibro-DAT penetration of 3% CMC solution into unsized base paper
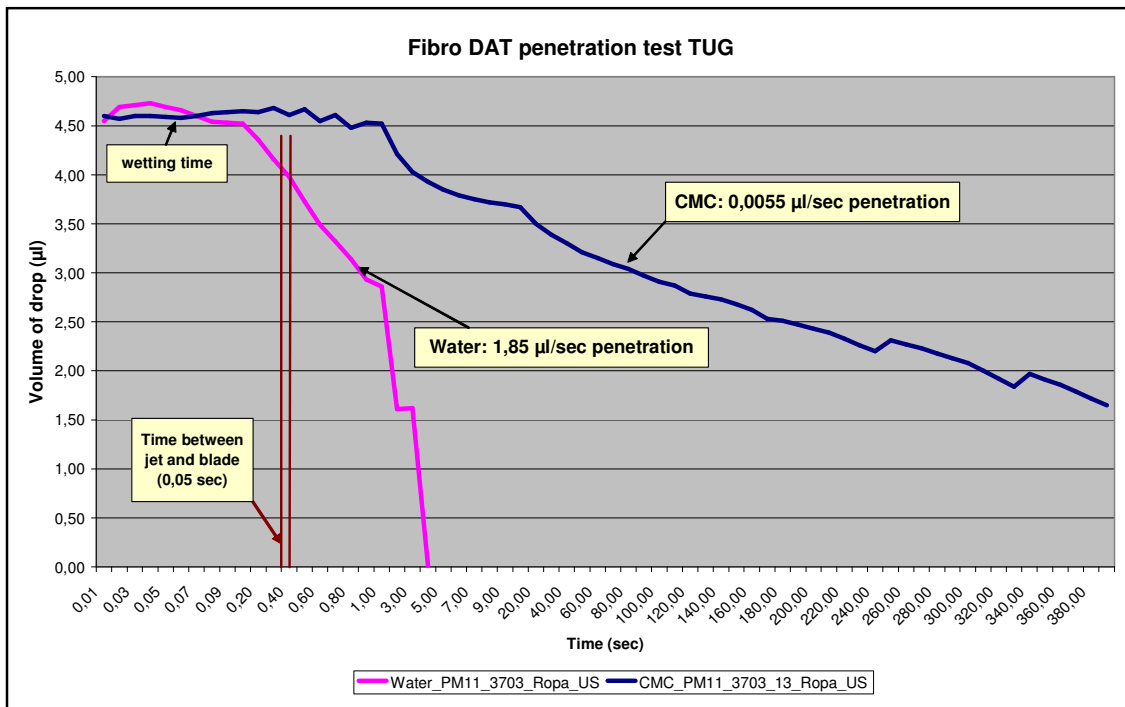
Pict. 7.3.45: Fibro-DAT penetration into base paper PM11, comparison of distilled water with a 3% CMC solution which has the same viscosity as the liquid phase in a coating colour

When droplets are applied by Fibro-DAT instrument, penetration of water and similar liquids is delayed due to necessary wetting time of capillaries. Air has to be removed from the fibre capillaries until capillary sorption starts.

Capillary sorption is delayed for CMC solution and sorption speed is much slower than that of pure water as surface tension of CMC solution is with 70 mN/m much higher than that of water + 20% IPA (43 mN/m) and contact angle is also higher (90 – 100° instead of 60 – 70°).

Lucas Washburn: $\Delta P_c = \dfrac{2 * \gamma * \cos\theta}{r}$

Comparing the amount of penetrated water per unit of time between the Fibro-DAT readings and the calculation of the middle coat thickening before the blade from mass balance one can see comparable results in pict. 7.3.46:

Calculation of water penetration into base paper at coater 3/4, CM11:

Parameter	Value	Unit	Comment
Speed of coater	1600	m/min	
coated width of web	8,44	m	
coat weight dry	10	g/m²	
coat weight wet	13,89	g/m²	
measured solids of coating colour after blade	72,00	%	
water in coating colour after blade	**3,89**	**g/m²**	
wet coating colour after blade	3,126	kg/s	
	8,42	ml/m²	Target: 10 - 15 ml/m²
volume flow to jet application	150	m³/h	
density of coating colour in working tank	1650	kg/m³	
wet mass flow to jet application	68,75	kg/s	
	185,1	ml/m²	Target: appr. 200 ml/m²
Ratio mass flow of feed to blade	*22,0*	*o.k.*	
coating colour at jet application	0,3	kg/m²	
water at jet application	85,5	g/m²	
solids feed from coating kitchen	68	%	
solids working tank	72	%	
solids jet application	72	%	
solids return flow from blade	72,2	%	from mass balance
wet mass flow to jet application	68,75	kg/s	
dry mass flow to jet application	49,50	kg/s	
water mass in flow to jet	19,25	kg/s=l/s	
wet mass flow before blade	68,75	kg/s	
dry mass flow before blade	49,64	kg/s	
water flow to blade	19,11	kg/s=l/s	
water penetration before blade	0,138	kg/s=l/s	
-- " --	**0,611**	**g/m²**	
wet coating colour after blade	3,126	kg/s	
solid content after blade	72,00	%	measured with scratch
dry coating colour after blade	2,251	kg/s	
water in coating colour after blade	0,875	kg/s	
	3,889	**g/m²**	
plus water, penetrated into base	1,013	kg/s	
	4,500	g/m²	
calculated solid after blade	**69,0**	**%**	
Control 1: Fibro Penetration of water into base	0,15	µl/s	pure dest. Water
Area of Fibro drop	3,35	mm²	
Fibro penetration of water into base	44,776	g/m² per sec	
time between jet and blade (t1)	0,044	sec	
Fibro penetration of pure water into base at t1			Delta to pressed water into
(time between jet and blade)	**1,970**	**g/m²**	base is pressure impuls at jet
Control 2: Fibro Penetration of CMC+water into base	0,0035	µl/s	3% CMC solution
Area of Fibro drop	3,35	mm²	
Fibro penetration of CMC+water into base	1,045	g/m² per sec	
time between jet and blade (t1)	0,044	sec	
Fibro penetration of CMC+water into base at t1			Delta to pressed water into
(time between jet and blade)	**0,04597**	**g/m²**	base is pressure impuls at jet
Base paper:			
basis weight	66,2	g/m²	
thickness	0,082	mm	
volume	1,24		
porosity ε	42,9	%	
void volume	**28,4**	**g/m²**	??? Ml/m² is right!
water penetration before blade	0,611	g/m²	
depth of water penetration before blade	0,00176397	mm	
-- " --	**1,76**	**µm**	
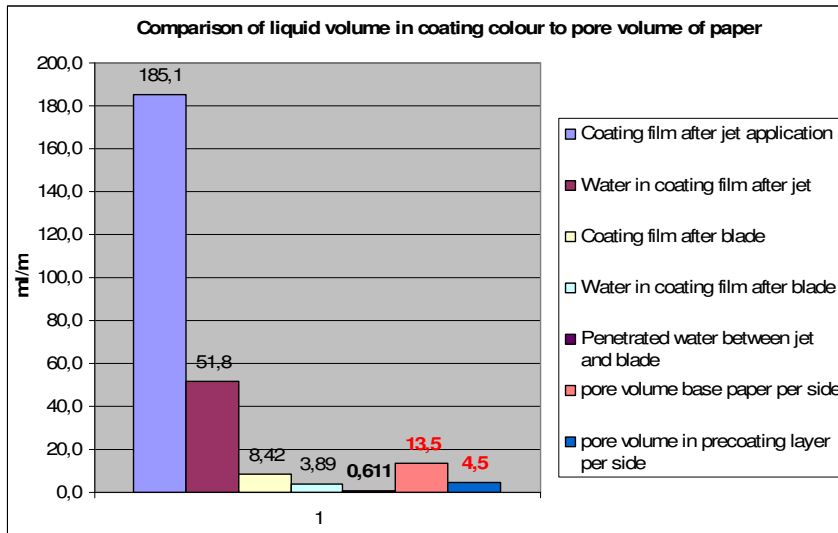
Pict. 7.3.46: Comparison of calculated liquid volumes from mass balance of middle coaters OMC11 (Y-axis: Penetrated volume of water from c.c. in ml/m²)

Comparing the penetrated volume of water between application and blade with the pore volume of the base paper or the pore volume in the precoating layer one can see that enough free pore volume exists for both cases to pick up the penetrated water between application and blade. When solids increase from 68% to 72% between fresh coating from coating kitchen and working tank, which corresponds to a solid increase in the wet coating layer between application and blade from 72 to 72,2%, 0,611 ml/m² of liquid has penetrated the base paper which has a pore volume of 13,5 ml/m². But water is mainly absorbed in the pores of the fibre walls, a pore volume which is not measured by Mercury porosity.

When coating is applied on a precoated paper the free pore volume of this substrate is also high enough to pickup the liquid from capillary sorption. The pre-coating layer has a pore volume of 4,5 ml/m².

Compared to total amount of water, applied by jet or LDTA (51,8 ml/min), the penetrated volume of water between jet and blade is with 0,6 ml/m² relatively small.

As the excess rate between application flow and coating flow under blade is with 20:1 very high, the small difference of solids between application and blade of 0,2 – 0,3% leads to a solids difference of 4% between coating colour feed and working tank.

This difference in solids is influenced by dwell time, water retention of coating colour, immobilized layer at the boundary and paper sorption pressure.

As the solid content in the working tank increases with time in the instationary phase the delta between application solids and immobilization solids gets smaller with time.

The formation of an immobilized coating layer before the blade is leading always to a balance between the positive effect of reduced penetration under the blade and the negative effect of runability problems like scratches, bleeding and blade wearing.

Therefore the immobilized layer should be as thin as possible but low in permeability.

High water retention of middle coating colour reduces thickening in the working circuit and before the blade. Delta solids between applied coating colour and immobilization point increases and runability gets better. The improvement in water retention should be done without increasing high shear viscosity of coating colour as this would again worsen the runability of coating colour (see chapter "water retention").

In pict. 7.3.47 Fibro-DAT sorption measurements on base paper PM11 with CMC solutions of varying CMC content are compared to calculation of water sorption into base paper before the blade from mass balance calculations.

Calculation of water penetration into base paper at coater 4, CM11

Solids feed from coating kitchen: 68%
Solids working tank: 72%
Solids return flow from blade: 72,3%

- 3,889 — water in coating colour after blade
- 0,611 — water penetration before blade
- 1,970 — Fibro penetration of pure water into base at t1 (time between jet and blade)
- 0,04597 — Fibro penetration of CMC+water into base at t1 (time between jet and blade)

Pict. 7.3.47: Comparison of penetrated water between jet and blade to void volume

Comparison of the absorbed volume of liquid:

a) Calculated amount of penetrated water at middle coaters OMC11 between jet and blade from mass balance: 0,611 g/m²

b) Fibro-DAT: Water sorption into precoated paper in 28 ms: 1,97 g/m²

c) Fibro-DAT: Sorption of 1,1% CMC solution in 28 ms: 0,078 g/m²

d) Fibro-DAT: Sorption of 3% CMC solution in 28 ms: 0,046 g/m²

The lab sorption with Fibro-DAT of a 2% CMC solution would give the same amount of penetrated liquid in the time span between application and blade (0,028 s) than the calculated amount of absorbed liquid from mass balance.

To check the calculation of the immobilized layer between jet and blade lab experiments were made with the Abo-GWR pressure dewatering cell.

Rearranging Darcy's law leads to an often used equation in membrane filtration technique:

$Q = C * A * \sqrt{\Delta p * \Delta t}$ (see Equ. 7-1-2)

Q in g/m² (Volume/Area)

C, A = constant parameters, depending on filtrated medium

Using this equation different filtration experiments in the lab can be compared to mill practice when the same coating colour is used (pict. 7.3.48).

Pressure penetration middlecoat CM11

Abo-GWR water retention measurement at 5 μm membrane, middle coat formulation 201, 72% solids:

Membrane diameter	**5**	**μm**	
Pressure	**0,5**	**bar**	Fibro Sorption pressure (ass.)
Time for pressure penetration	**10**	**sec**	
Amount of penetrated water	**0,0113**	**g**	
	17,11	g/m²	
Carman Kozeny + Darcy: Q = C x A x SQROOT(Δp x Δt)…..Q in g/m²			INPUT-DATAS (measured)
From Abo-GWR measurement: Constant (C x A) =	**0,0242**	for Q in g/m²	

Calulated penetration of water at jet application:

Pressure lenght under jet	1,34	mm	0,8 mm jet nozzle width
Pressure at jet application	0,15	bar	
Speed of coating mashine	1600	m/min	
	26,7	m/s	
Time under jet application	0,00005	sec	
Calculated penetrated water at jet application	**0,02**	**g/m²**	Q = C x A x SQROOT(Δp x Δt)
Calc. increse in solids under jet	**0,01**	**%**	

Calulated penetration of water between jet and blade from Abo-GWR measurements:

Water sorption pressure of double precoated base paper	**0,32**	**bar**	from Fibro-DAT measurements
Speed of coating mashine	1600	m/min	
	26,7	m/s	
Time before+under blade	0,04400	sec	
Calculated penetrated water between jet and blade	**0,91**	**g/m²**	Q = C x A x SQROOT(Δp x Δt)
Measured water penetration between jet and blade	0,9	g/m²	From Abo-GWR
water before blade	84,6	g/m²	
coating colour before blade	305,5	g/m²	
solids before blade	220,8	g/m²	
Calc. solids before blade	**72,30**	**%**	
Calc. increse in solids between jet and blade	**0,30**	**%**	From mass balance: 0,2% solid increase!

Calculation of water penetration between jet application and blade (mass balance):

Parameter	Value	Unit	Comment
Speed of coater	1600	m/min	
coated width of web	8,44	m	
coat weight dry	10	g/m²	
coat weight wet	13,89	g/m²	
measured solids in the working tank = feed to blade	72,00	%	
water in coating colour after blade	**3,89**	**g/m²**	
wet coating colour after blade	3,126	kg/s	
	8,42	ml/m²	Target: 10 - 15 ml/m²
volume flow to jet application	150	m³/h	
density of coating colour in working tank	1650	kg/m³	
wet mass flow to jet application	68,75	kg/s	
	185,1	ml/m²	Target: appr. 200 ml/m²
Ratio mass flow of feed to blade	*22,0*	*o.k.*	
coating colour at jet application	305,5	g/m²	
water at jet application	85,5	g/m²	
solids at jet application	219,9	g/m²	
Measured solids in the return flow from blade	72,20	%	
Mass flow before blade	68,8	kg/s	
coating colour before blade	305,5	g/m²	
water before blade	84,9	g/m²	
solids before blade	220,5	g/m²	
Calc. water penetration between jet and blade	**0,611**	**g/m²**	

Pict. 7.3.48 : Calculation of water penetration between jet and blade and comparison to Abo-GWR readings and mass balance for a middle coater CM11

Abo-GWR lab readings of this middle coating colour were taken from 5 µm membrane and 0,5 bar pressure to simulate base paper sorption. From this lab dewatering experiment with middle coating colour of OMC11 the coefficient C * A was calculated with 0,0242.

This coefficient C * A from Abo-GWR was inserted with a fibre sorption pressure Δp_c of 0,32 bar and the dwelling time t between jet and blade of 44 ms into the Darcy equation and led to an amount of penetrated water between jet and blade Q = 0,91 g/m² (compare: Calculated amount of penetrated water between application and blade by mass balance; 0,611 g/m²).

Salminen showed that a linear relationship between Q and $\sqrt{t}$ is valid for pressure applications but not for pressure less experiments proving the independency of both penetration mechanisms.

He proved with his application machine that wetting time is reduced and capillary sorption is enhanced when liquid is applied under pressure. Pict. 7.3.49 shows that similar results were achieved when the Abo pressure penetration tester was used.
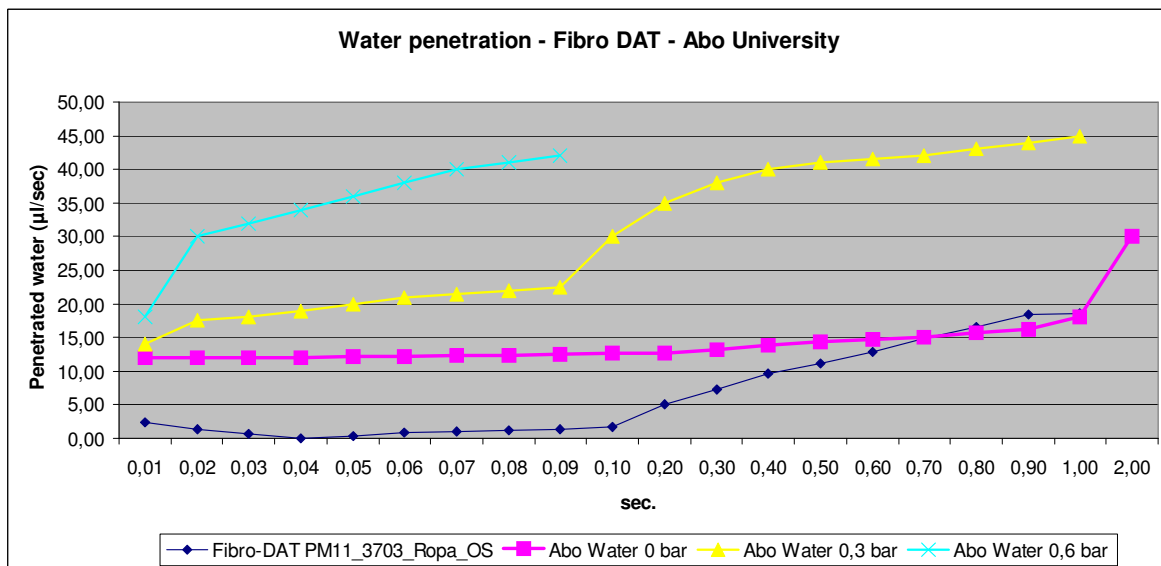
Pict. 7.3.49: Comparison of Fibro-DAT penetration experiments in Gratkorn with pressure less/pressure penetration results from Abo university (P. Salminen) – all measurements done with water as liquid phase

7.4 Blade (Phase C)

Under the blade the dwell time is the shortest (0,009 - 0,02 ms) but pressure is the highest of all penetration phases (15 – 25 bar, see pict. 7.4.65 – 7.4.67).

Dewatering of the coating colour follows Darcy's law:

Eq. 3-12-1: $\dfrac{dV}{dt} = \dfrac{K * A * \Delta p}{\eta * L}$

Water and fine particles like latex have to pass two layers:
1) The immobilized layer of coating colour, which is formed in phase B) between application and blade
2) The dry precoating layer underneath.

Equ. 7-3-1: Darcy including filter cake: $v = \dfrac{d(V/A)}{dt} = \dfrac{\Delta p_f + \Delta p_s}{\eta * \left[\dfrac{h_f}{K_f} + \dfrac{h_s}{K_s} \right]}$

$\Delta p = \Delta p_f + \Delta p_M$

K_f.....Darcy coefficient of filter cake

h_f.....Thickness of filter cake at time t

K_s....Darcy coefficient of the penetrated substrate, here the penetrated precoating layer

h_s.....Thickness of the pre-coating layer
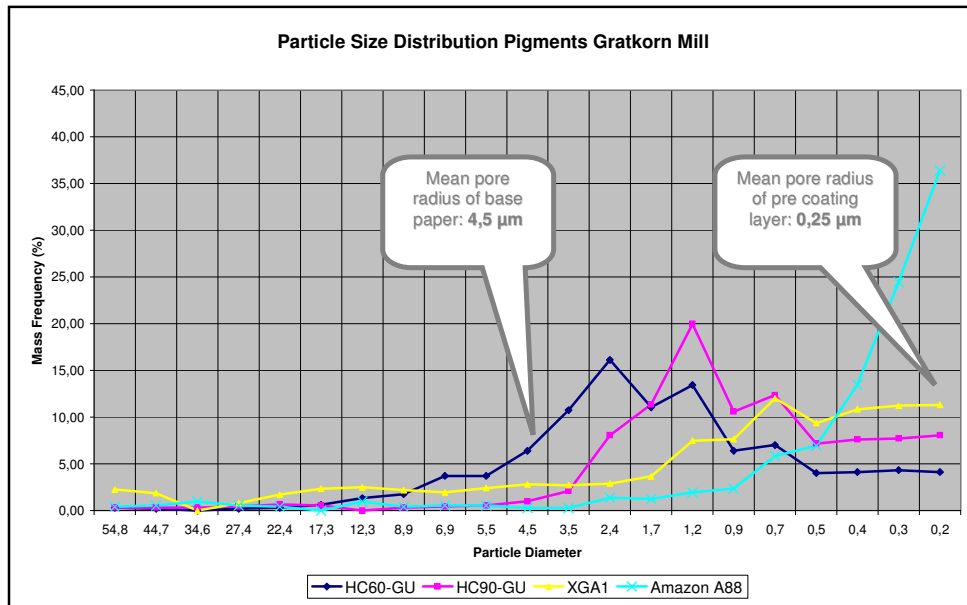
Pict. 7.4.1: Particle size distribution of different pigments vs. pore radius of base and pre coating layer (particle size of latex: 0,1 – 0,15 µm)

Carbonates: HC60: 60% of particles < 2 µm; HC90: 90% of particles < 2 µm; XGA1: 96% of particles < 2 µm

Brazilian fine clay Amazon 88: 98% of particles < 2 µm

Pict. 7.4.1 shows a comparison of substrate pore sizes with the size of particles used in coating colours:

1) Substrates:
- Base Paper: 4,5 µm mean pore diameter
- Double pre-coated paper: 0,25 µm mean pore diameter

2) Coating colour components:
- Pigments:
  – HC60: 0,5 – 7 µm (mean: 2 µm)
  – XGA1: 0,01 – 1,5 µm (mean: 0,3 µm)
  – Amazone: 0,01 – 0,7 µm (mean: 0,15 µm)
- Latex: 0,1 – 0,15 µm particle diameter

Base paper pores are much bigger in size than the coarsest particles in the coating colour while the pores of double precoated paper are in the size of the small latex particles. Therefore holdout of fines, especially latex particles improves with every coating layer. Soluble substances like starch or PVOH will penetrate on all substrates to a greater extend than latex particles.

According to **Darcy's law** the amount of penetrated water (plus latex and starch) under the blade depends upon:
- Pressure level
- Dwell time before and under the blade (a function of facet length and blade angle)
- Coating colour water retention (exactly: liquid phase viscosity)
- Filtration resistance of the substrate (Darcy coefficient of precoating layer)
- Thickness and permeability of the immobilized filter cake, which is formed between application and blade.

For reducing the penetration of water and latex the following counter measures should be taken:
- **Minimize pressure**: Curtain coater > film press >> blade (especially at high speed!)
- **High water retention of coating colour**: Mainly the liquid phase viscosity must be increased according to Darcy's law
- **Low permeability of substrate** (e.g. precoating layer)
- **High thickness of immobilized layer before pressure impulse**: Stays in contradiction with runability of the coating colour at the blade (see previous chapter).

P.A.C. Gane, N. Gerteiser and C.J. Ridgeway (L1.74) measured pore structure of curtain coated samples to find out why curtain coaters always show better mottling than blade coaters.
Single curtain coating was compared to single blade coating. Double coating was done with blade + blade and MSP + blade in a pilot coater under commercial coating conditions.
A starch/latex based GCC formulation was used for all trials.

Mercury porosity was applied for the single coated samples. No difference was found in pore volume between MSP, blade and curtain coated samples which disproves the theory of improved mottle by curtain coating due to higher porosity of the coating layer.

As application pressure is much lower at curtain coaters the packing of coating should be less dense than for blade coaters. The experiments show that at the application solids no packing by external pressure is possible; water between particles circumvents packing.

Therefore the biggest influence on dry coating layer porosity, beside the formulation, is the way how the coating is dried. Shrinkage forces and latex film forming are the dominating parameters.

For dry curtain coatings a lower pore radius was found due to the fact that no synthetic thickener was used which flocculated fine particles in blade coatings and lowered gloss (pict. 7.4.2).
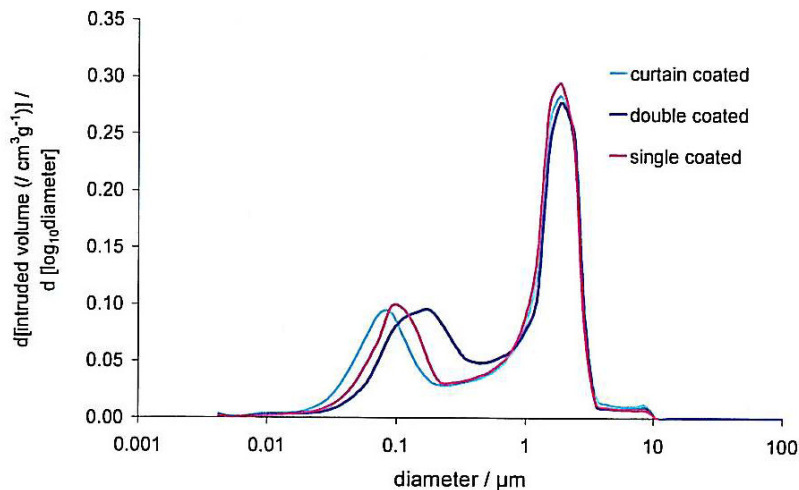
Pict. 7.4.2: Mercury porosity of dry coated samples (P.A.C. Gane)
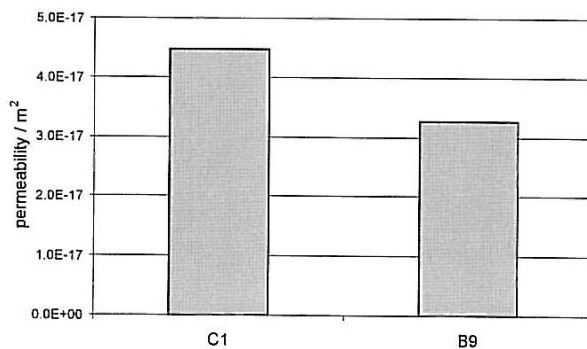
Pict. 7.4.3: Permeability of single coated papers (C1 = curtain, B9 = blade) (P.A.C. Gane)

Pict. 7.4.3 shows that single blade coated paper had a somewhat lower permeability than curtain coated paper although mean pore diameter of coating layer was somewhat higher. The explanation of the authors was a filling of base paper pores by pigments from coating due to blade pressure.

Therefore <u>curtain coaters</u> have besides their huge advantage of homogeneous in-plane coating layer porosity also two small disadvantages when used as precoater:
- Higher permeability of the coating layer (see chapter 9: Disadvantage for precoatings to improve mottling but advantage for top coatings)
- Lower pore radius which leads to higher capillary forces and more pronounced thickening of next coating colour before blade (again a disadvantage for precoatings but advantage for top coating).

Dewatering of middle and top coating colours under the blade was measured at OMC11 by scraping off the wet coating colour directly after the blade with a plastic blade. The plastic blade pressure had to be high enough to get the partially immobilized layer at the boundary layer to the paper and a good average of complete wet coating layer.

Pict. 7.4.4 shows measurements at top coaters C5/6 at OMC11. A solid increase under the blade from 68% to 70 – 76% was detected.

Date: 23.02.2007 Grade: 9800130

	After blade	Working tank	Coating kitchen	Diff. AB - VB	Diff. blade - tank
Coater 3	68,9	69,1	68	1,1	-0,2
Coater 4	69,9	69,8	68	1,8	0,1
Coater 5	71,5	68,3	68	0,3	3,2
Coater 6	71,6	68	68	0	3,6

Date: 17.4., 9:00 Grade: 9000135

	After blade	Working tank	Coating kitchen	Diff. AB - VB	Diff. blade - tank
Coater 3	69,8	69,4	68	1,4	0,4
Coater 4	70,1	69,9	68	1,9	0,2
Coater 5	72,5	67,7	68,2	-0,5	4,8
Coater 6	71,2	67,5	68,2	-0,7	3,7

Date: 14.5., 16:30 Grade: 4013/MR2, 9800200

	After blade	Working tank	Coating kitchen	Diff. AB - VB	Diff. blade - tank
Coater 3	68,8	69,6	67,5	2,1	-0,8
Coater 4	69,65	69,8	67,5	2,3	-0,15
Coater 5	75,6	68,3	68,5	-0,2	7,3
Coater 6	74,1	68,4	68,5	-0,1	5,7

Pict. 7.4.4: Solid content of coating colour at coaters 3 – 6, OMC11

Due to low permeability of double precoated substrate and almost perfect coverage of base paper fibres, capillary sorption is negligible at top coaters of OMC11 (C5(6) between application and blade. In contradiction to the middle coaters C3/4 (see also chapter 7.3) no raise in solids was measured at the top coater working tanks.

The lack of an immobilized layer before the blade leads to a much higher increase of solid content under the blade of C5/6, compared to middle coaters C3/4 although the Darcy coefficient of double precoated paper is lower than for the single pre-coated paper.

When double coated grades are produced at OMC11 the top coating colour is applied on a single pre-coated layer. Water penetration under the top coater blades is much lower for this grade than for triple coated papers as an immobilized layer is formed before the blade (pict. 7.4.5).

Date: 26.3., 9:00   Grade: 3838/MR14, 9000115

	After blade	Working tank	Coating kitchen	Diff. AB - VB	Diff. blade - tank
Coater 3	69,5	68,3	67,5	0,8	1,2
Coater 4	70,65	69,1	67,5	1,6	1,55
Coater 5	68	67,8	67,5	0,3	0,2
Coater 6	68,4	67,8	67,5	0,3	0,6

Date: 26.02.2007   SM9: 4199/MR2, MMC 115 g/m2

	After blade	Working tank	Coating kitchen	Diff. AB - VB	Diff. blade - tank
Coater 1	70,1	71,5	68,5	3,0	-1,4
Coater 2					
Coater 3	71,1	70,3	69	1,3	0,8
Coater 4					

Pict. 7.4.5: Solid increase under the blade of top coaters – comparison of OMC11 double coated grades (above) with OMC9 double coated grades (below)

To compare liquid phase penetration with and without filter cake before blade the filter cake equation of Darcy is used:

$$v = \frac{d(V/A)}{dt} = \frac{\Delta p_f + \Delta p_s}{\eta * \left[\dfrac{h_f}{K_f} + \dfrac{h_s}{K_s} \right]}$$

$$\Delta p = \Delta p_f + \Delta p_M$$

K_f.....Darcy coefficient of filter cake

h_f.....Thickness of filter cake at time t

K_s.....Darcy coefficient of the penetrated substrate, here the penetrated pre-coating layer

h_s.....Thickness of the pre-coating layer

The higher the sum of h_i/K_i is, the less water will penetrate under the external blade pressure into the substrate.

When external blade pressure, viscosity of liquid phase in coating colour and time of penetration are given by speed and blade geometry, the penetrated volume of liquid phase will depend linearly on the sum of h_i/K_i.

Comparing the penetrated volume of liquid under the middle coater blades of C3/4 showed that this volume can be reduced up to 15% when a dense immobilized layer is formed before the blade.

A similar reduction was calculated for the top coaters C5/6:

Coater at OMC11	Applied coating	Penetrates through:	Penetration depth into coating layer h_s (µm)	Darcy coeff. of dry precoating layer K_s (m²)	Thickness of immo layer before blade h_f (µm)	Darcy coeff. of immo layer K_f (m²)	SUM of h/K	Penetrated Liquid V ( )
C5/6	Top coat	middle coating layer	1,540	6,68E-19			2,31E+12	100%
C5/6	Top coat	middle coating layer + assumed immo layer before blade	1,540	6,68E-19	**2,65**	8,3E-18	2,62E+12	**88%**
			from mercury porosity and mass balance	from Prüfbau pressure pen. Test	from mass balance	from Abo-GWR measurements		

Unfortunately this filter cake doesn't exist before the top coaters of OMC11 and therefore penetration of liquid phase depends on vertical pressure, permeability of the middle coating layer, time interval and viscosity of the liquid phase.Thickness of immobilized layer under blade was calculated by mass balance at C5/6 (pict. 7.4.6).

MASS BALANCE CM11, Top coat, coater 5/6

Date:				Date:		
Speed	**1600**	m/min		Solids feed	**68**	%
	26,67	m/s				
Width	**8,5**	m		Solids working tank	**68,2**	%
Pump speed	**150**	m³/h		Solids after blade	**72**	%

Input
Output

Immo solid	Immo density
% solids	kg/m³
81,1	1939

Formula for density as a function of solid content at CM11 (lab measurement):

Pre-/Middlecoating: Density (kg/m³) = 0,01697 x solids + 0,4526

Topcoating: Density (kg/m³) = 0,02182 x solids + 0,1520

Balance room 1: Mass balance around working tank (middle coat C3/4):

V_8 = feed from kitchen	k_8	ρ_8	$M_{8,dry}$	M_8	$M_{8,wet}$	W_8
m³/s	% solids	kg/m³	kg/s (dry)	g/m² (dry)	g/m² (wet)	g/m² water
0,00208	**68**	1636	2,317	**10,22**	15,03	4,81

10   Control: Measured coat weight (Measurex)

	Measured in working tank		$M_1 = V_1 \cdot \rho_1 \cdot k_1$	$M1 = M_1/(v \cdot AB)$	$M_{1,wet} = M_1/k_1$	$W_1 = M_{1,wet} - M_1$	
V_1=feed to coater	k_1	ρ_1	$M_{1,dry}$	$M_{1,dry}$	$M_{1,wet}$	W_1	h_1
m³/s	% solids	kg/m³	kg/s (dry)	g/m² (dry)	g/m² (wet)	g/m² water	µm (wet)
0,0417	**68,2**	1640	46,61	205,62	301,49	95,87	183,82

$V_5 = 19/20 \cdot V_1$	$k_5 = (M_1-M_8) \cdot 100 /(V_5 \cdot \rho_5)$					
V_5=return from coater	**k_5 = calc.**	**ρ_5 = calc.**	$M_{5,dry}$	$M_{5,dry}$	$M_{5,wet}$	W_5
m³/s	% solids	kg/m³	kg/s (dry)	g/m² (dry)	g/m² (wet)	g/m² water
0,03958	**68,21**	1640	44,29	195,39	286,46	91,06

1640   Density control from f(k)

Balance room 2: From coating kitchen to blade (calc. Point 6 before blade):

V_8	k_8	ρ_8	M_8	M_8	M_8	W_8
m³/s	% solids	kg/m³	kg/s (dry)	g/m² (dry)	g/m² (wet)	g/m² water
0,00208	68	1636	2,317	10,22	15,03	4,81

$V_6 = (M_8)/(\rho_6 \cdot k_6)$	$k_6 = k_5$ for middle coat					
V_6 = calc.	k_6	ρ_6	$M_{6,dry}$	$M_{6,dry}$	$M_{6,wet}$	W_6	h_6
m³/s	% solids	kg/m³	kg/s (dry)	g/m² (dry)	g/m² (wet)	g/m² water	µm (wet)
0,00207	68,21	1640	2,32	10,22	14,99	4,76	9,14

$V_2 = (V_8 \cdot \rho_8 - V_6 \cdot \rho_6)/\rho_2$	**Penetrated water from jet to blade**		$M_{Ret, atro} = M_{6,dry}$	$M_{Ret,wet} = M_{6,wet}$		
V_2 = calc.		ρ_2	**M_2**	$M_{Ret, atro}$	$M_{Ret,wet}$	**$M_{Immo,wet}$**	$h_{Immo,2}$
m³/s		kg/m³	g/m² (water)	g/m² (dry)	g/m² (wet)	g/m² (wet)	µm (wet)
0,00001		1000	**0,05**	10,22	14,99	**0,01**	0,01

Balance room 3: Mass balance at blade tip (from point 6 to free draw after blade)

V_6	k_6	ρ_6	M_6	M_6	M_6	W_6
m³/s	% solids	kg/m³	kg/s (dry)	g/m² (dry)	g/m² (wet)	g/m² water
0,00207	68,21	1640	2,317	10,22	14,99	4,76

$V_4 = (M_6)/(\rho_4 \cdot k_4)$	$k_6 = k_5$ for middle coat					
V_4 = calc.	k_4	ρ_4	$M_{4,dry}$	$M_{4,dry}$	$M_{4,wet}$	W_4	h_4
m³/s	% solids	kg/m³	kg/s (dry)	g/m² (dry)	g/m² (wet)	g/m² water	µm (wet)
0,001868	**72,00**	1723	2,32	10,22	14,20	3,98	8,24

$V_3 = (V_6 \cdot \rho_6 - V_4 \cdot \rho_4)/\rho_3$	**Penetrated water under blade**		$M_{Ret, atro} = M_{4,dry}$	$M_{Ret,wet} = M_{4,wet}$		
V_3 = calc.		ρ_3	**M_3**	$M_{Ret, atro}$	$M_{Ret,wet}$	**$M_{Immo,wet}$**	$h_{Immo,3}$
m³/s		kg/m³	g/m² (water)	g/m² (dry)	g/m² (wet)	g/m² (wet)	µm (wet)
0,0001788		1000	**0,79**	10,22	14,20	**4,17**	2,15

Pict. 7.4.6: Mass balance of top coat OMC11 for solid increase under blade from 68 to **72%**

A solid increase of 4% under the blade corresponds to an amount of penetrated water of 0,79 g/m² - almost the same amount, which penetrates at the middle coat between jet and blade by fibre sorption: 0,86 g/m².

Between jet and blade the wet coating layer has a specific volume of 185 ml/m². This layer contains 51,8 ml/m² water. Compared to this high amount of applied water volume the liquid of 9 ml/m² which is pressed by the blade into the paper is relatively low.
Mass balance gives a thickness of the immobilized layer under the blade of **2,1 µm** when the coating solids rises from 68 to 72% under the blade.

But when the solid content increases under the top coater blades to 75% (which was detected at OMC11) the thickness of the immobilized layer raises to **3,7 µm** (pict. 7.4.7). Taking into account that the gap between blade and paper can get locally lower than the calculated average of 10 µm, the blade will touch the immobilized layer at these areas and runability problems like bleeding, scratches and blade wearing will occur.

MASS BALANCE CM11, Top coat, coater 5/6

Date:				Date:				Input
Speed	**1600**	m/min		Solids feed	**68**	%		
	26,67	m/s						Output
Width	**8,5**	m		Solids working tank	**68,2**	%		
Pump speed	**150**	m³/h		Solids after blade	**75**	%		

Immo solid	Immo density
% solids	kg/m³
81,1	1939

Formula for density as a function of solid content at CM11 (lab measurement):

Pre-/Middlecoating: Density (kg/m³) = 0,01697 x solids + 0,4526

Topcoating: Density (kg/m³) = 0,02182 x solids + 0,1520

Balance room 1: Mass balance around working tank (middle coat C3/4):

V_8 = feed from kitchen	k_8	ρ_8	$M_{8,dry}$	M_8	$M_{8,wet}$	W_8
m³/s	% solids	kg/m³	kg/s (dry)	g/m² (dry)	g/m² (wet)	g/m² water
0,00208	**68**	1636	2,317	**10,22**	15,03	4,81

				10	Control: Measured coat weight (Measurex)

	Measured in working tank		$M_1 = V_1 \ast \rho_1 \ast k_1$	$M1=M_1/(v \ast AB)$	$M_{1,wet}=M_1/k_1$	$W_1=M_{1,wet} - M_1$	
V_1=feed to coater	k_1	ρ_1	$M_{1,dry}$	$M_{1,dry}$	$M_{1,wet}$	W_1	h_1
m³/s	% solids	kg/m³	kg/s (dry)	g/m² (dry)	g/m² (wet)	g/m² water	µm (wet)
0,0417	**68,2**	1640	46,61	205,62	301,49	95,87	183,82

$V_5 = 19/20 \ast V_1$	$k_5 = (M_1-M_8) \ast 100 /(V_5 \ast \rho_5)$					
V_5=return from coater	k_5 = calc.	ρ_5 = calc.	$M_{5,dry}$	$M_{5,dry}$	$M_{5,wet}$	W_5
m³/s	% solids	kg/m³	kg/s (dry)	g/m² (dry)	g/m² (wet)	g/m² water
0,03958	**68,21**	1640	44,29	195,39	286,46	91,06

	1640	Density control from f(k)

Balance room 2: From coating kitchen to blade (calc. Point 6 before blade):

V_8	k_8	ρ_8	M_8	M_8	M_8	W_8
m³/s	% solids	kg/m³	kg/s (dry)	g/m² (dry)	g/m² (wet)	g/m² water
0,00208	68	1636	2,317	10,22	15,03	4,81

$V_6=(M_8)/(\rho_6 \ast k_6)$	$k_6=k_5$ for middle coat					
V_6 = calc.	k_6	ρ_6	$M_{6,dry}$	$M_{6,dry}$	$M_{6,wet}$	W_6	h_6
m³/s	% solids	kg/m³	kg/s (dry)	g/m² (dry)	g/m² (wet)	g/m² water	µm (wet)
0,00207	68,21	1640	2,32	10,22	14,99	4,76	9,14

$V_2=(V_8 \ast \rho_8-V_6 \ast \rho_6)/\rho_2$	**Penetrated water from jet to blade**		$M_{Ret, atro}=M_{6,dry}$	$M_{Ret,wet}=M_{6,wet}$		
V_2 = calc.		ρ_2	M_2	$M_{Ret, atro}$	$M_{Ret,wet}$	$M_{Immo,wet}$	$h_{Immo,2}$
m³/s		kg/m³	g/m² (water)	g/m² (dry)	g/m² (wet)	g/m² (wet)	µm (wet)
0,00001		1000	**0,05**	10,22	14,99	**0,01**	0,01

Balance room 3: Mass balance at blade tip (from point 6 to free draw after blade)

V_6	k_6	ρ_6	M_6	M_6	M_6	W_6
m³/s	% solids	kg/m³	kg/s (dry)	g/m² (dry)	g/m² (wet)	g/m² water
0,00207	68,21	1640	2,317	10,22	14,99	4,76

$V_4=(M_6)/(\rho_4 \ast k_4)$	$k_6=k_5$ for middle coat					
V_4 = calc.	k_4	ρ_4	$M_{4,dry}$	$M_{4,dry}$	$M_{4,wet}$	W_4	h_4
m³/s	% solids	kg/m³	kg/s (dry)	g/m² (dry)	g/m² (wet)	g/m² water	µm (wet)
0,001728	**75,00**	1789	2,32	10,22	13,63	3,41	7,62

$V_3=(V_6 \ast \rho_6-V_4 \ast \rho_4)/\rho_3$	**Penetrated water under blade**		$M_{Ret, atro}=M_{4,dry}$	$M_{Ret,wet}=M_{4,wet}$		
V_3 = calc.		ρ_3	M_3	$M_{Ret, atro}$	$M_{Ret,wet}$	$M_{Immo,wet}$	$h_{Immo,3}$
m³/s		kg/m³	g/m² (water)	g/m² (dry)	g/m² (wet)	g/m² (wet)	µm (wet)
0,0003075		1000	**1,36**	10,22	13,63	**7,18**	3,70

Pict. 7.4.7: Mass balance of top coat OMC11 for solid increase under blade of 68 to **75%**

Forming an immobilized coating layer before the blade increases the risk of runability problems in the same way as when a layer of the same thickness is built up under by the high external pressure under the blade.

When these two effects are combined the risk is further increased.

The top coating colours of CM11 were also tested with the Abo-GWR pressure dewatering cell. The results were taken into the same calculation for the penetrated water like in the middle coater.

This time the penetrated water under the blade was calculated with:

$$Q = C * A * \sqrt{\Delta p * \Delta t}$$

Q in g/m² (Volume/Area)

C, A = constant parameters, depending on filtrated medium

Pressure penetration topcoat CM11

Abo-GWR water retention measurement at 5 µm membrane, top coat formulation 390, 68% solids:

Membrane diameter	**5**	**µm**
Pressure	**2**	**bar**
Time for pressure penetration	**10**	**sec**
Amount of penetrated water	**0,034**	**g**
	51,48	g/m²

Carman Kozeny + Darcy: Q = C x A x SQROOT(Δp x Δt)…..Q in g/m²

From Abo-GWR measurement: Constant (C x A) =	**0,0364**	for Q in g/m²

Calulated penetration of water at jet application:

Pressure lenght under jet	1,34	mm	0,8 mm jet nozzle width
Pressure at jet application	0,15	bar	
Speed of coating mashine	1600	m/min	
	26,7	m/s	
Time under jet application	0,00005	sec	
Calculated penetrated water at jet application	**0,03**	**g/m²**	Q = C x A x SQROOT(Δp x Δt)
Calculated increse in solids under jet	0,01	%	

Calculation of coating colour penetration under the blade:

Speed of coating mashine	1600	m/min	
	26,7	m/s	
Pressure before blade	4	bar	
Pressure lenght before blade	2	mm	
Time before blade	0,00008	sec	
Calculated penetrated water before blade	**0,20**	**g/m²**	Q = C x A x SQROOT(Δp x Δt)
Pressure under blade	19	bar	
Pressure lenght under blade	0,87	mm	
Time under blade	0,00003	sec	
Calculated penetrated water under blade	**0,29**	**g/m²**	Q = C x A x SQROOT(Δp x Δt)
Calculated penetrated water before+under the blade	**0,49**	**g/m²**	
measured water penetration under blade	0,49	g/m²	
water in coating colour after the blade	4,22	g/m²	
wet coat weight after blade	14,22	g/m²	
calculation: solid content after blade	**70,3**	**%**	
Control: Calculated solid increase under blade	**2,3**	**%**	measured at CM1: 3-4% solid increase

Calculation of water penetration under blade from mill measurements at CM1:

Parameter of top coat	Value	Unit
Speed of coater	1600	m/min
coated width of web	8,44	m
coat weight dry of top coat on double precoated paper	10	g/m²
measured solids of coating colour after blade	**72,0**	**%**
wet coat weight after blade	13,89	g/m²
water in coating colour after blade	**3,89**	**g/m²**
measured solids of coating colour before blade	68,0	%
wet coat weight before blade	14,71	g/m²
water in coating colour before blade	**4,71**	**g/m²**
density of coating colour in working tank	1650	kg/m³
calculation: penetrated water under blade	**0,82**	**g/m²** = ml/m²

Pict. 7.4.8: Calculation of water penetration between jet and blade with Abo-GWR readings and mass balance for a top coater CM11

Comparing Abo-GWR readings with mass balance data's in pict. 7.4.8 shows similar but somewhat lower dewatering for the Abo-GWR experiments. This is caused by

much longer dewatering time in Abo-GWR instrument leading to a thicker immobilized layer.

The Prüfbau pressure penetration test was used as 2nd comparison. To compare results, a liquid of similar viscosity to coating colour liquid phase had to be used. A CMC solution with 1,1% solids was chosen for the Prüfbau pressure penetration tests.

Penetration of liquid phase was calculated by taking the measured solids into the mass balance under the blade. Approximately 0,8 g/m² of liquid will penetrate the middle coating layer.
When permeability of the substrate, penetration depth, pressure under the blade and liquid properties are known, the amount of penetrated liquid can be calculated from the Prüfbau penetration test results by Darcy's law. Similar results were found compared to the mass balance in pict. 7.4.9:

Pressure penetration topcoat CM11

Prüfbau pressure penetration for 3% CMC:				
basis weight		102,2	g/m²	
thickness, total		9,6	µm	from thickness measurements of paper samples
pore volume in precoating layer		9	ml/m²	topside + bottom side, from Hg-porometrie
avg. Pore radius	r	0,25	µm	from Hg-porometrie
max. penetration volume	$V_{p, max}$	**4,5**	ml/m²	total pore volume / 2
calc. Porosity in Hg	ε	35,0	%	from Hg-porometrie
coating layer thickness (MSP+blade), both sides		0,0171	mm	from thickness measurements of paper samples
coated layer thickness		**8,5476**	**µm**	for double precoated layer, per side
Control: Pore volume from ε		0,00000299	m³/m²	
-- " --		**2,99**	**ml/m²**	

Parameter of top coat		Value	Unit	
Speed of coater	v	1600	m/min	
Coated width of web	AB	8,44	m	
Coat weight dry of top coat on double precoated paper		10	g/m²	
Measured solids of coating colour after blade		**72,0**	**%**	
Wet coat weight after blade		13,89	g/m²	
Water in coating colour after blade		**3,89**	**g/m²**	
Measured solids of coating colour before blade		**68,0**	%	
Wet coat weight before blade		14,71	g/m²	
Water in coating colour before blade		**4,71**	**g/m²**	
Density of coating colour in working tank	ρ	1650	kg/m³	
From mass balance:				
penetrated water under blade	Q/A	**0,82**	**g/m²** = ml/m²	
Pore volume of double precoated layer	$ε_{vol}$	4,5	ml/m²	per side (from Mercury porosimetrie)
Thickness of double precoated layer	L_{max}	8,5	µm	per side (from thickness meas.)
Penetration depth of				
liquid phase into substrate	L	**1,54**	**µm**	

Darcy coefficient of middle coating		9,1E-17	m²	from OMYA pressure pen. cell (Rez. 201)
Viscosity of liquid phase	η	8	mPa s	1 Pa = 1 kg / (m*s²)
Density of liquid phase	ρ	1050	kg/m³	
Kinematic viscosity of liquid phase	v = η / ρ	0,000008	m²/s	

		Converging nip	Before blade	Under Blade		
Distance to blade		0	0,0004	0,00125	mm	from VOF
Lenght of penetration area	x	0,85	0,4	0,244	mm	from VOF
Normal pressure	p	8	20	28,5	bar	from VOF
Dwell time at converging nip before blade	dt	0,0319	0,0150	0,0092	msec	t = x / v
Sum of penetration time before and under the blade	dt	**0,056**			**msec**	
Penetration speed of liquid phase	w	**0,015**			**m/s**	w = (Q/A) / t
						dV/dt = (K x A x Δp) / (η x L)
Calculation of penetrated volume with Darcy		1,88E-07	2,21E-07	1,92E-07	m³/m²	dV/dA = (K x dt x Δp) / (η x L)
-- " --		0,188	0,221	0,192	g/m² = ml/m²	
Sum of penetrated volume from Darcy		**0,60**			**g/m²**	

Pict. 7.4.9: Comparing the calculated volume of penetrated liquid under the blade
from mass balance with Darcy equation

The more liquid is pressed into the middle coating, the more latex will penetrate with the liquid as latex particles are most often lower in size hydrophobic than the pores of the substrate (0,1 – 1 µm). In water - latex dispersions the particles are stabilized by hydrophobic particle surface given by emulsifiers. This hydrophobic particle surface increases the mobility of latex particles in water based coating colours – affinity to hydrophilic components like pigment dispersants or starch molecules is low.

Pilot coater studies showed that the more pronounced the latex penetration, the bigger the risk of drying induced mottling is as latex particles will travel with water vapour to surface and differences in local concentration of latex at the surface will be the consequence.

As local pressure is a function of base paper basis weight (see chapter "floc analysis") more latex will be pressed into the middle coating at flocs. Local differences in contact angle, pore size and porosity of the top coating layer will be the consequence, leading to formation induced back trap mottling.

Therefore measures were identified to reduce latex and liquid penetration under the top coater blades. According to Darcy this can be implemented by:
- Increasing the liquid phase viscosity (see chapter "water retention")
- Lowering the permeability of the precoating layers (see chapter "dense precoatings")
- Reducing pressure and time at the blade (see following paragraphs)

Calculation of blade pressure

Ilkka Kartovaara (L 4.13) used a quite simple but clever method to calculate lateral force (tangential friction force or shear force) from torque of backing roll.
Lateral force decreased steeply with increasing wet layer thickness under and after the blade. Surface void volume of used base paper was measured with 6,9 g/m² water volume. Lateral force approached zero at a coating thickness corresponding to the roughness volume (pict. 7.4.10).
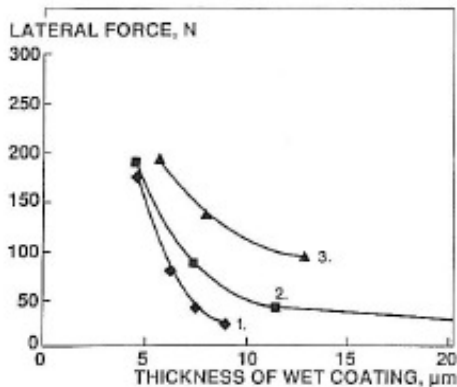
Pict. 7.4.10: Lateral force as a function of machine speed (1 = 300 m/min, 2 = 600 m/min, 3 = 1000 m/min) for a CMC solution (Ilkka Kartovaara)

From these curves viscosity was calculated by equation $\eta = \dfrac{\tau}{D}$ with т the shear stress and D the shear rate.

Rearranged: $\eta = \tau * \dfrac{d}{v}$ with d the thickness of the sheared layer and v the velocity of the moving boundary.

Modelling the lateral force T with the equation $T = \dfrac{v * b * \eta_1}{2 * (d - r)} + v * \eta_2$ (T = lateral force, b = bevel width, d = thickness of wet coating layer, r = roughness volume of paper, η_1 = viscosity of colour under blade, η_2 = entrance viscosity) led to a correlation coefficient of r² = 0,93.

The biggest influence on lateral force in Kartovaara's experiments was besides coating speed the shape factor of the clay particles in use.

P. Isakson, M. Rigdahl, P. Flink and S. Forsberg (L4.14) measured and calculated the coating colour flow field in a converging channel.

Under the blade the coating suspension is subjected not only to shear but also to an elongation flow field.

The corresponding lab method is the extensional viscosity, based on forcing the suspension through a converging channel. The shape of the experimental fluid channel is chosen to constantly increase Reynolds number and strain (pict. 7.4.11).

20 mm
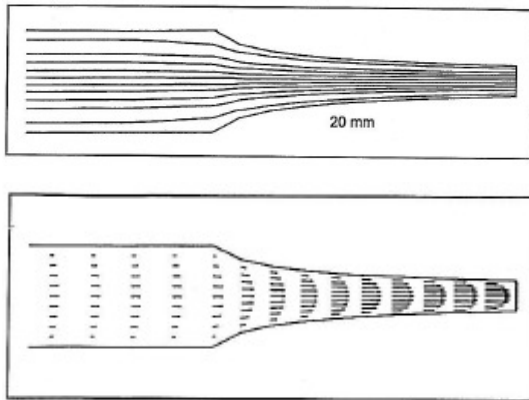
Pict. 7.4.11: Schematic picture of converging channel (P. Isakson)

While at the wall boundary the shear forces (expressed by Bohlin viscosity measurements $\eta = K * \dot{\gamma}^{n-1}$) are of major importance, in the centre of the fluid field the extensional forces are dominating.

The authors expressed the extensional viscosity is $\eta_E = (\tau_{zz} - \tau_{rr})/\dot{\varepsilon}$, with ε the extension in flow direction z at a channel radius R and the stress difference

$\tau_{zz} - \tau_{rr} = \Delta p_{in} - \Delta p_{el} - \int_0^R \frac{N^2}{r} dr$. The measured pressure drop is Δp_{el} and the calculated pressure drop for a corresponding inelastic fluid is Δp_{in}.

An increase in CMC content led to an increase in extensional viscosity at a given strain rate. All colours showed shear thinning behaviour: the extensional viscosity decreased with increasing strain rate.

Surprising was the fact, that extensional viscosity was much higher than shear viscosity.

When capillary high shear viscosimeters are used the extensional forces are included in the measurements.

In MSP coating operations misting might correlate well with the extensional viscosity of a coating colour.

P.A.C. Gane and L. Coggon (L4.15) measured coat weight as a function of blade pressure using a Heliocoater and a SPS-clay based coating.
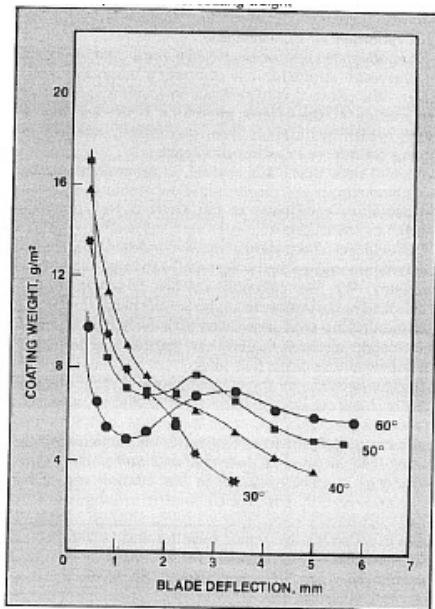
Pict. 7.4.12: Coat weight as a function of blade pressure at different blade angles (P.A.C. Gane)

They found out that a certain minimum coat weight cannot be under run (pict. 7.4.12). This coat weight corresponds to the surface roughness of the base paper.
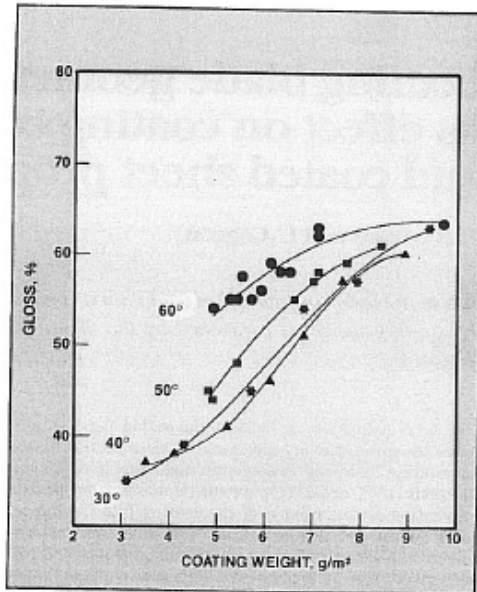
Pict. 7.4.13: Gloss as a function of blade geometry and coat weight at 62% solids (P.A.C. Gane)

The authors measured increased calendered gloss (pict. 7.4.13) when higher blade angles were used for clay based coating colours at comparable coat weights. The authors guessed that platy particles may collide at the heel of the blade, prior to the coating nip. Turbulence will be created. The higher the blade angle, the smaller the area of turbulence (see VOF pictures 7.4.55 – 7.4.62) and the more clay particles will be orientated in flow direction at the tip entrance point. When shear forces are applied under the blade many clay particles will be re-orientated and realigned. Wet bleeding at the blade exit will be the consequence.
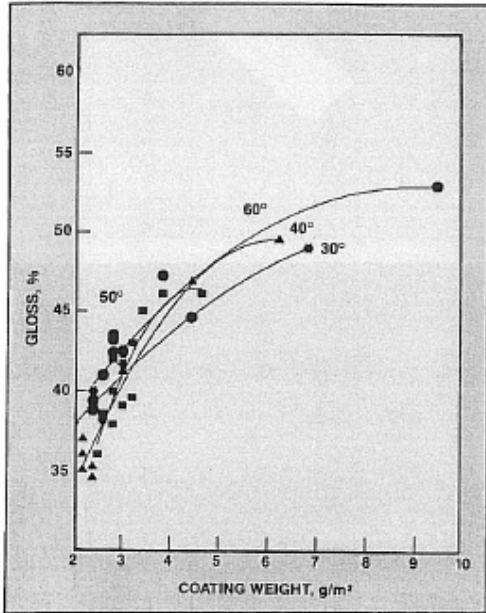
Pict. 7.4.14: Gloss vs. coat weight for CaCO$_3$ coating (HC90) (P.A.C. Gane)

For carbonate coatings no gloss increase with higher blade angle was measured as particles show no alignment in flow lines upstream (pict. 7.4.14).

Nick Triantafillopoulos and N. Altug (L4.10) found out by pilot coater trials that the minimum coat weight was 3 g/m² which they could achieve at low speed with clay based single coating on a w'fr base. The hydrodynamic force dominated the blade pressure while viscous forces and hydrodynamic lift of the blade were of minor importance at low speed.

P.A.C. Gane, Ph. McGenity and Ph. Watters (4.16) tested the runability of different clay based coating colours at a Heliocoater. Common runability problems of clay based coating colours at high speed and high solids are: Scratches, skips, streaks, spits, beards, bleeding and stalagmites. They found that CMC improved runability at low speed as water retention improves and less coating colour was immobilized before the blade. At high speed CMC worsened runability as high shear viscosity increased.

Gane, McGenity and Watters tested different blade geometries (pict. 7.4.15) to improve runability and found out that long blade facets worsen runability as shear forces increase with blade tip length.
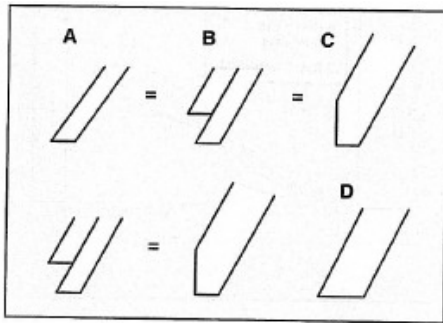
Pict. 7.4.15: Investigated blade geometries (Gane)

Non delaminated, coarse SPS clay with high shape factor was worse in runability than fine U.S. Alpha plate clay due to the fact that the coarsest clay particles in the SPS slurry are in the size of the gap between blade and base paper.

D. Eklund, T.O. Granvist, R. Salahetetdin from U.Abo (L4.17) studied the influence of viscosity and water retention on the blade forces. Blade pressure was determined by high shear viscosity of the coating colour. Viscosity increased with solid content. Worse water retention of coating colour and High sorption of base paper led to an increase in solids before or under the blade and thus to a higher blade pressure.

W.J. Follette and R.W. Fowells (L4.18) measured coat weight of clay based coatings at a trailing blade pilot coater.
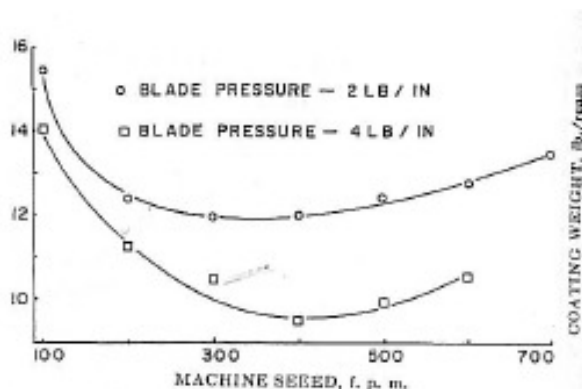
Pict. 7.4.16: Coating speed vs. coat weight at two different blade pressures (66%, 200 cp, 20° blade angle) (W.J. Follette)

They found that coat weight increases with increasing speed as the hydrodynamic

pressure $p = \dfrac{u * s}{h^2} * G$ (according to Fuller) increases.

At lower speeds the coat weight decreased with speed as water retention got dominant. The lower the speed, the more coating colour was immobilized before the blade and the higher the coat weight was at a fixed blade pressure.

The authors found a logarithmic correlation $\log W = \log B - A * \log P$ or $W = \dfrac{B}{P^A}$

between blade pressure P and coat weight W (pict. 7.4.17)
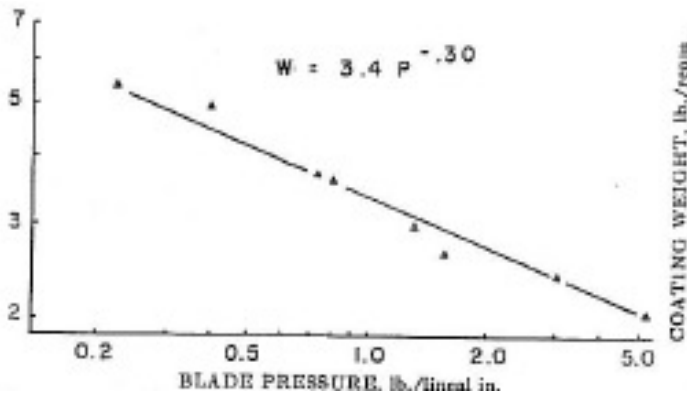
Pict. 7.4.17: Blade pressure vs. coat weight (66% solids, 170 cp, 600 f.p.m.) (W.J. Follette)

D. Eklund, S.J. Kahila and D. Obetko (L4.12) studied the influence of big changes in blade angle on coat weight. Increasing blade angle by 2 – 3 ° led to 3 – 4 g/m² increase in coat weight. The reason was the increasing hydrodynamic pressure in the contracting area under the blade. With thicker blades the maximum is reached with lower delta angle.

Lowering the blade angle leads to lower coat weight. Contact area under the blade is smaller and the specific pressure increases as blade pressure is kept constant.

D. Eklund, T.O. Granvist and R. Salahetetdin from Abo University (L4.6) studied the impact of small blade angle changes on coat weight by using a mathematical blade pressure simulation (pict. 7.4.18 – 19).
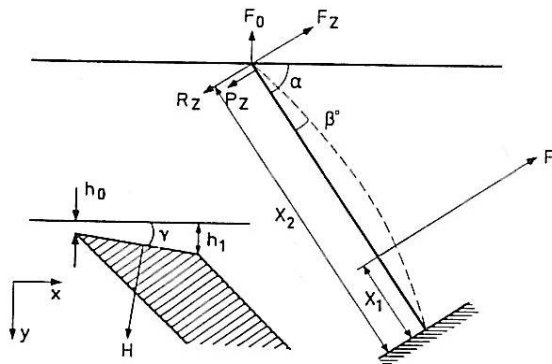
Pict. 7.4.18: Forces at blade tip (R. Salahetetdin)

$$F_z = F * \left[1 + \frac{1}{2} * (\frac{x_1}{x_2})^3 - \frac{3*x_1}{2*x_2} \right] + \frac{3*D*W}{x_2{}^2} \quad \text{with} \quad D = \frac{E*d^3}{12*(1-v)^3}$$

W...bending of the blade

D....stiffness modulus of the blade

v....material constant, 0,3 for steel

U_1...machine speed

d_1 (mm)	D, Nm
0,305	0,550
0,381	1,064
0,450	1,767
0,508	2,543
0,680	6,100

Pict. 7.4.19: Stiffness modulus D (R. Salahetetdin)

$R_z = m * U_1 * (1 + \cos\alpha) * \sin\alpha$

$P_z = m * U_1 * f(h_0, h_2, \alpha)$

$$H = \frac{6*\eta*U_1}{\tan^2\gamma} * \left[\ln(1+m) - \frac{2*m}{2+m} \right] \quad \text{with} \quad m = \frac{h_1}{h_0} - 1 = \frac{d*\sin\gamma}{h_0*\sin\alpha} \quad \text{and} \quad H_z = H*\cos\alpha$$

$F_0 = (F_z - R_z - P_z)\cos\alpha$

If γ > 0 an additional hydrodynamic pressure H is formed at the tip, which can be calculated from the geometry. The additional force H_z increases the coat weight (7.4.20).
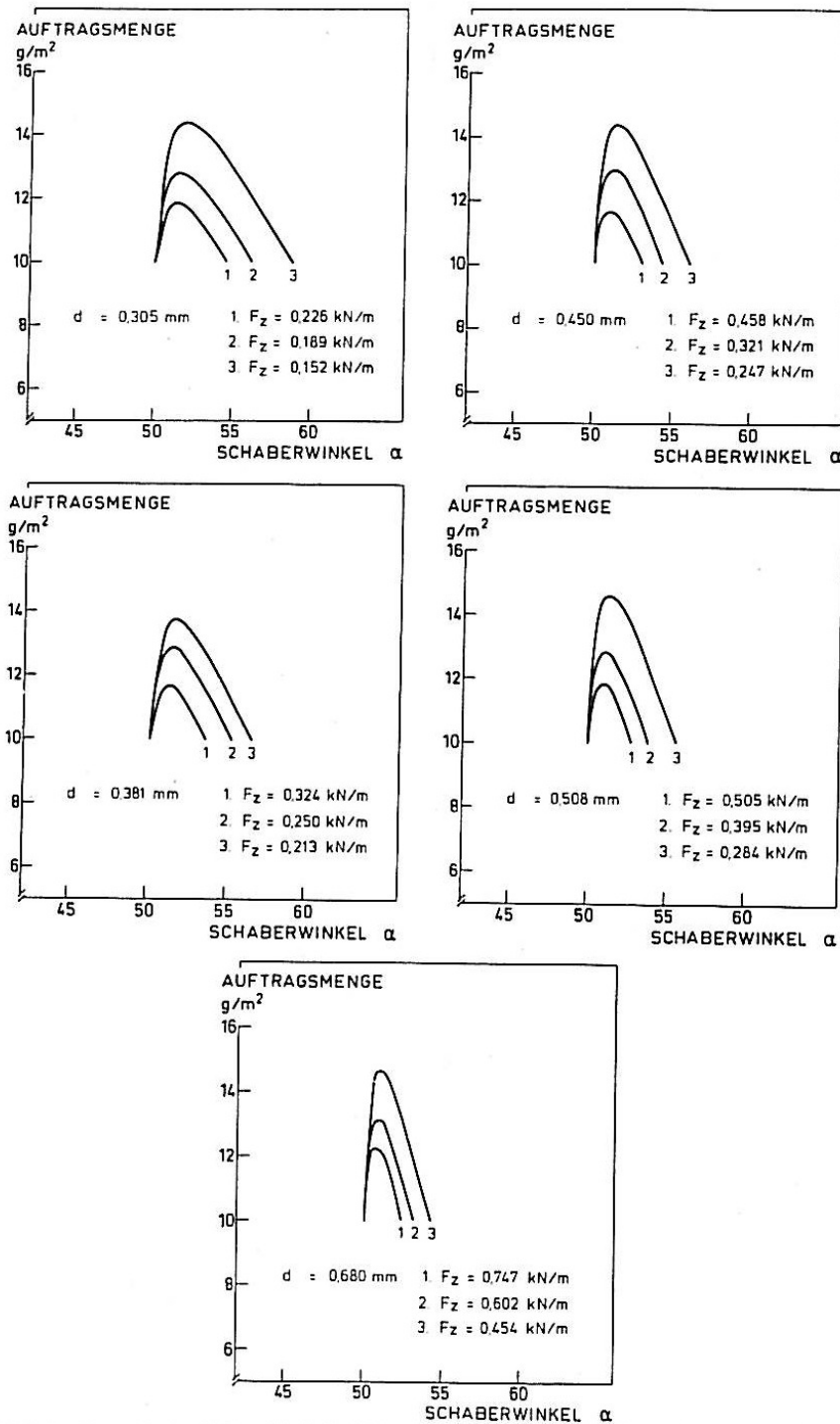
Pict. 7.4.20: Coat weight as a function of a small blade angle variation (R. Salahetetdin)

Maximum coat weight was achieved, when the blade angle was increased 1 – 2°. Blade pressure is determined by high shear viscosity of coating colour. Worse water retention of the coating colour and high sorption of base paper leads to an increase of solids before the blade and thus to a higher blade pressure.

In the following paragraph an example of blade force calculation for a **35° stiff blade** is shown.

<u>Simplification</u>: No bending of the blade at the bar contact point (F1)

<u>Forces</u>:

F_{Ax}, F_{Ay} = forces at the blade holder

F_1 = vertical force of the pressure bar which is used for adjustment of coat weight

F_2 = sum of impulse force and shear force at the blade tip
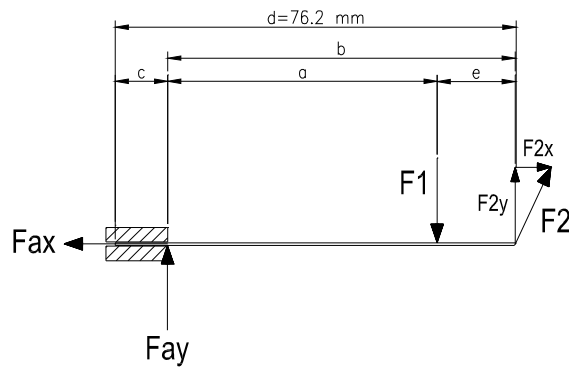
<u>Measured geometry</u>:

d = 76,2 mm (blade height)

e = 15 mm (free length of blade from coater geometry)

b = 55 mm (measured)

<u>Calculated</u>:

a = b – e = 40 mm

c = d – b = 21,2 mm

$$\sin\alpha = \frac{F_{2y}}{F_2}; \quad \cos\alpha = \frac{F_{2x}}{F_2}$$

I) $\Sigma F_{ix} = 0$: $F_{Ax} - F_{2x} = 0$ or $F_{Ax} - \cos\alpha * F_2 = 0$

II) $\Sigma F_{iy} = 0$: $F_{Ay} - F_1 + F_{2y} = 0$ or $F_{Ay} - F_1 + \sin\alpha * F_2 = 0$

III) $\Sigma M_{iA} = 0$: $-F_1 * a + F_{2y} * b = 0$ or $-F_1 * a + \sin\alpha * F_2 * b = 0$

II) $F_1 = F_{Ay_1} + \sin\alpha * F_2 = 0$

II) in III) : $-a * (F_{Ay} + \sin\alpha * F_2) = -\sin\alpha * F_2 * b$

$$F_{Ay} = F_2 * \sin\alpha * (\frac{b-a}{a})$$

In II) $F_1 = F_2 * \sin\alpha * (\frac{b-a}{a}) + \sin\alpha * F_2$

$$F_1 = \frac{b}{a} * \sin\alpha * F_2$$

F_2 is the sum of the impulse force in coating direction and shear force under the blade.

F_1 can be directly calculated from F_2, blade angle α and the blade geometry.

Remark: sin α is increasing with α. **Therefore a higher bar pressure p_1 is needed, if the blade angle α is increased** to stop the impulse force of the incoming coating flow at the blade tip. In other words: F_{2y} increases with α and therefore F_1 must increase with α.

Example:

Calculation of blade bar force F_1

Blade angle α	35	50	°
	0,611	0,873	rad
sin α	0,574	0,766	
Impulse + shear force F_2	1352	1352	N
b	55	55	mm
a	40	40	mm
F_1=b/a*sinα*F_2	**1066**	**1424**	**N**
Increase in blade load to 35°		34	%
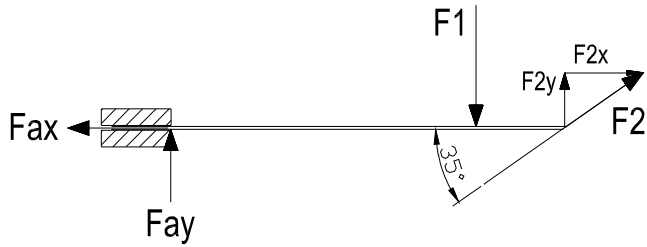
Pict. 7.4.21: Blade forces for 35° blade angle
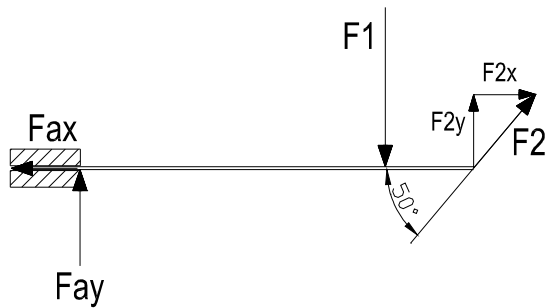
Pict. 7.4.22: Blade forces for 50° blade angle
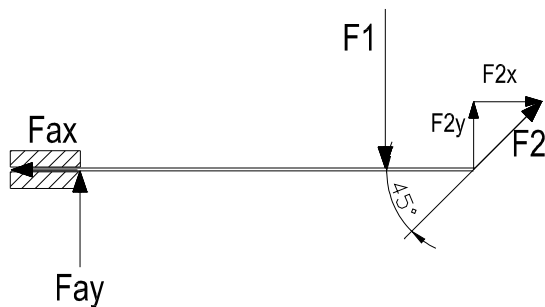
Pict. 7.4.23: Blade forces for 45° blade angle

With lower blade angle the tear force F_{ax} in the blade holder is increasing (risk of blade slip out of the blade holder) but the resulting force on the pressure bar is reduced (pict. 7.4.21 – 7.4.23).

In the following calculation the **impulse force** was calculated with $\bm{\rho/2*v^2}$, assuming a constant blade angle of 35° before the blade tip.

The **shear stress τ = η * γ** (product of viscosity and shear rate) was taken from ACAV high shear capillary viscosimeter measurements where the shear rate is in the range of the shear under the blade (pict. 7.4.24).
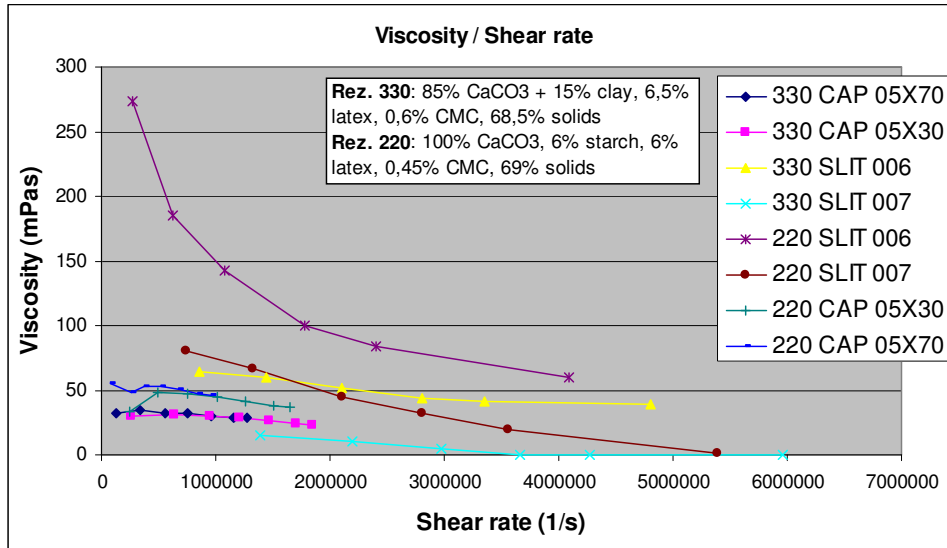
Pict. 7.4.24: High shear viscosity of topcoat 330 and middle coat 220 measured by ACAV capillary (CAP) and SLIT geometry
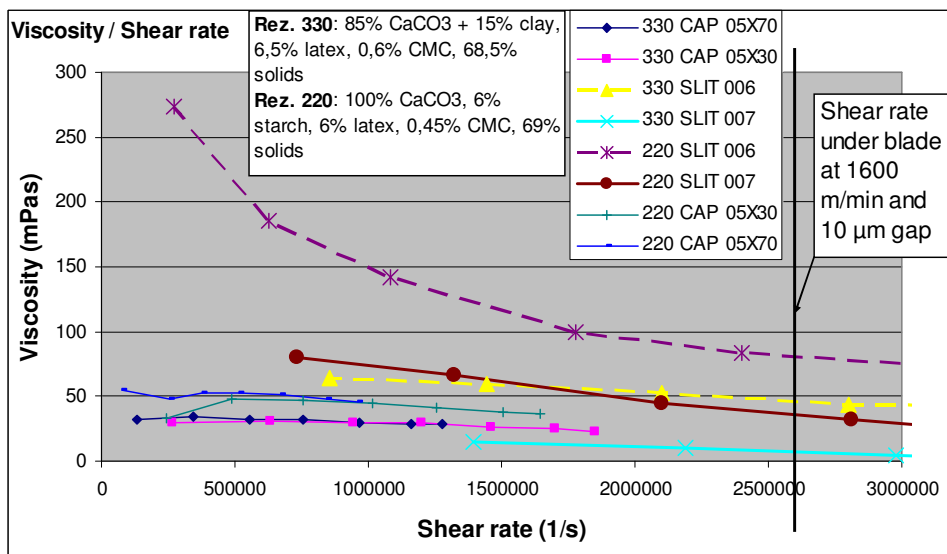
Pict. 7.4.25: Viscosity vs shear rate under blade (2,66 Mio 1/s)

High shear viscosity of the coatings measured by capillary geometry by ACAV is approximately 30 mPas at a shear rate of 2,66 Mio 1/s.

With SLIT geometry the measured viscosities were higher depending on geometry.

As coating colours are non-Newtonian fluids, the shear force under the blade is increased by the energy dissipation at the blade tip and at the exit of the blade – paper nip which can be evaluated by the Bagley correction. This energy dissipation happens is different for every blade geometry and is simulated by the SLIT geometry.

Calculation of hydrodynamic impulse pressure of coating colour on blade:

Speed of coater	1.600	m/min	
--"--	26,67	m/s	v
Width of coater	8,5	m	B
Density of coating colour	1.680	kg/m³	ρ
Height of coating colour under blade	10	µm	
Excess factor of application	20		
Height of coating colour before blade	190	µm	h_z
Blade angle	**35**	°	
Blade angle	0,611	rad	
Impulse of colour on blade p	597.333	Pa	$p = \rho/2 * v^2$
Cross section area of incoming coating layer	0,00162	m²	$A = h_z * B$
Resulting force in coating direction	**965**	**N**	F_{hydr}

Calculation of shear force under blade:

Rez. 340, 20.8.2008			
Brookefield 20 UpM = 5120 cp, Abo WRV = 60,6 g/m²			
Height of coating colour under blade	10	µm	h_z
Speed of coater	26,67	m/s	v
Shear rate γ	2.666.667	1/s	$\gamma = v / h_z$
Viscosity η	0,070	Pas	from ACAV
Shear stress τ	186.667	Pa = N/m²	$\tau = \eta * \gamma$
Coated width	8,5	m	
Contact lenght l	244	µm	
Area of shear A	0,0021	m²	A_{shear}
Shear force in coating direction	**387**	**N**	$F_{shear} = \tau * A$

Calculation of blade pressure under blade:

Speed of coater	1.600	m/min	
--"--	26,67	m/s	
Width of coater	8,5	m	
Sum of forces in coating direction	**1.352**	**N**	
Blade angle	35	°	
--"--	0,611	rad	
Inverse blade angle	0,960	rad	90 - α
Resulting force on paper, normal to coating directio	**1.931**	**N**	$F_{normal} = F * \tan(90-\alpha)$
Resulting pressure on paper	**9,31**	**bar**	$p_{norm} = F_{norm} / A_{shear}$
Distance blade holder to tip	66	mm	b
Free length	15	mm	e
Blade force on bar	**1.433,06**	**N**	$F_1 = b/(b-e) * \sin\alpha * F_2$

Pict. 7.4.26: Blade force and pressure upon paper in Z-direction of 35° blade with short facet length (0,508 mm thick)

With increasing speed stiffer blades with higher thickness must be used to resist the increasing impulse forces (F=f(v²)!).

If standard blades are used, facet length increases with lower blade angle and with rising thickness of blade (pict. 7.5.27). Therefore switching to thicker blades or lowering the blade angle doesn't contribute to reduction of blade pressure because shear force increases due to higher facet length when standard blades are used.

50°   663

35°   885
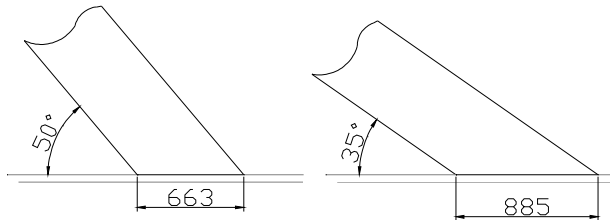
Pict. 7.5.27: Facet length in µm of 50° and 35° standard blades with 0,508 mm thickness

Calculation of increase in shear force by higher facet length when thicker blades are used (pict. 7.5.28):

Comparison of facette lenghts (blade thickness 0,508 mm)

Calculation of shear force under blade:

Blade angle	35°	50°	35°		
Facette manufacturing	Standard	Standard	cut at the exit		
Height of coating colour under blade	10	10	10	µm	h_z
Speed of coater	26,67	26,67	26,67	m/s	v
Shear rate γ	2.666.667	2.666.667	2.666.667	1/s	$\gamma = v / h_z$
Viscosity η	0,070	0,070	0,070	Pas	from ACAV
Shear stress τ	186.667	186.667	186.667	Pa = N/m²	$\tau = \eta * \gamma$
Coated width	8,5	8,5	8,5	m	
Contact lenght l	885	663	244	µm	
Area of shear A	0,0075	0,0056	0,0021	m²	A_{shear}
Shear force in coating direction	**1.404**	**1.052**	**387**	**N**	$F_{shear} = \tau * A$

Increase of shear force to 244 µm facette lenght: 263   172   %

Pict. 7.5.28: Calculation of shear force increase by lower blade angle

Therefore blades were developed for high speed coaters, which are cut at the exit or at the entrance of the blade tip to reduce the facet length and the blade load (pict. 7.4.29 and 7.4.30).
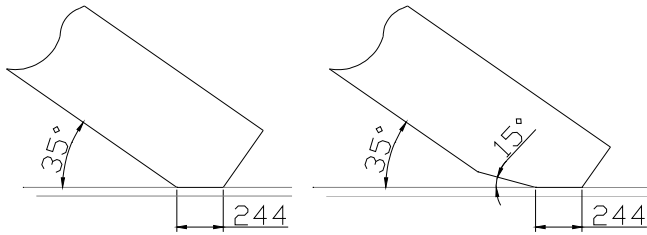
Pict. 7.4.29: New 35° blades with shorter facet length (µm)
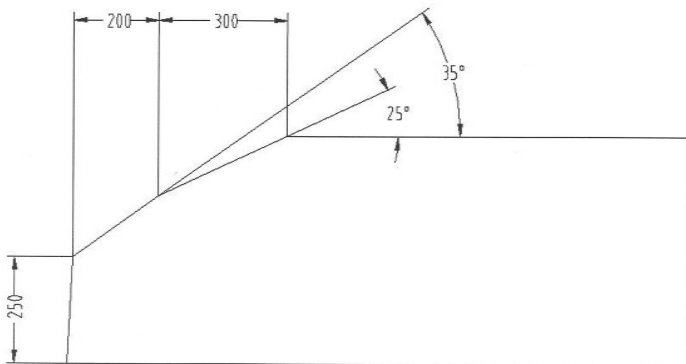
Pict. 7.4.30: OMC11 standard blade since 2007 (35° stiff blade with shorter facet length (µm))

Calculation of resulting blade pressure from shear force under blade:
35° blade, 0,509 mm thick, 0,877 mm facet length

Rez. 340, 20.8.2008			
Brookefield 20 UpM = 5120 cp, Abo WRV = 60,6 g/m²			
Shear rate γ	3.000.000	1/s	equ. 1750 m/min, 10 µm gap
Viscosity η	0,030	Pas	from ACAV
Shear stress τ	90.000	Pa = N/m²	τ = η * γ
Speed of coater	1.600	m/min	
Coated width	8,5	m	
Contact lenght l	887	µm	
Area of shear A	0,0075	m²	
Shear force F_x	**679**	**N**	$F_x = τ * A$
Blade angle	35	°	
--"--	0,611	rad	
Resulting vertical F_z	970	N	$F_z = F_x * \tan α$
Resulting vertical pressure p_z	128.533	Pa = N/m²	$p_z = F_z / A$
Vertical pressure p_z	**1,29**	**bar**	
Time of shear	0,000033	sec	
SQROOT (time*pressure)	**2,07**	**Pa^{-1}s^{-1}**	

Blade angle	35	°
--"--	0,611	rad
Blade thickness	0,509	mm
Max. facet length	0,89	mm

Pict. 7.4.31: Shear force and penetration factor $\sqrt{p} * \sqrt{t}$ of standard blade with long facet

Calculation of resulting blade pressure from shear force under blade:

35° blade, 0,509 mm thick, cut at the tip entrance and exti, 0,244 mm facet length

Rez. 340, 20.8.2008			
Brookefield 20 UpM = 5120 cp, Abo WRV = 60,6 g/m²			
Shear rate γ	3.000.000	1/s	equ. 1750 m/min, 10 µm gap
Viscosity η	0,030	Pas	from ACAV
Shear stress τ	90.000	Pa = N/m²	τ = η * γ
Speed of coater	1.600	m/min	
Coated width	8,5	m	
Contact lenght l	244	µm	
Area of shear A	0,0021	m²	
Shear force F_x	**187**	**N**	$F_x = τ * A$
Blade angle	35	°	
--"--	0,611	rad	
Resulting vertical F_z	267	N	$F_z = F_x * \tan α$
Resulting vertical pressure p_z	128.533	Pa = N/m²	$p_z = F_z / A$
Vertical pressure p_z	**1,29**	**bar**	
Time of shear	0,000009	sec	
SQROOT (time*pressure)	**1,08**	**$Pa^{-1}s^{-1}$**	

Pict. 7.4.32: Shear force and penetration factor $\sqrt{p} * \sqrt{t}$ of new blade with short facet

Shear force under the blade in coating direction is 3 times higher for the blade with the original long facet of 0,887 mm (pict. 7.4.31). When the facet length is reduced to 0,244 µm the penetration factor $\sqrt{p} * \sqrt{t}$ can be reduced by 50% (pict. 7.4.32).

Three blade geometries for high speed coater were compared in the following by a simple excel calculation and by a **Volume-of-fluid (VOF) simulation**:

   a) 35° blade with pre-angle of 25° and cut at the exit, facet length 244 µm
   b) 35° blade without pre-angle, cut at the exit for a short facet length of 244 µm
   c) 45° blade without pre-angle, cut at the exit, same facet length of 244 µm
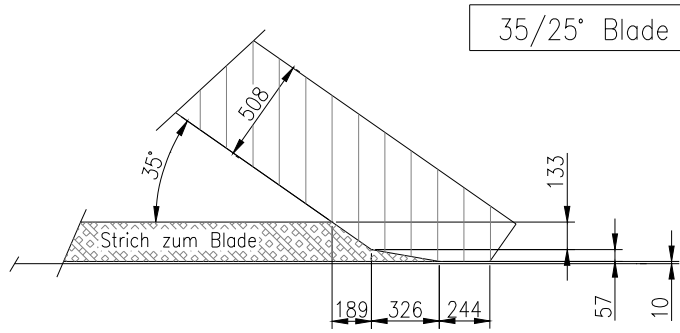
Pict. 7.4.33: 35/25° Blade with pre-angle and shorter facet length (µm)
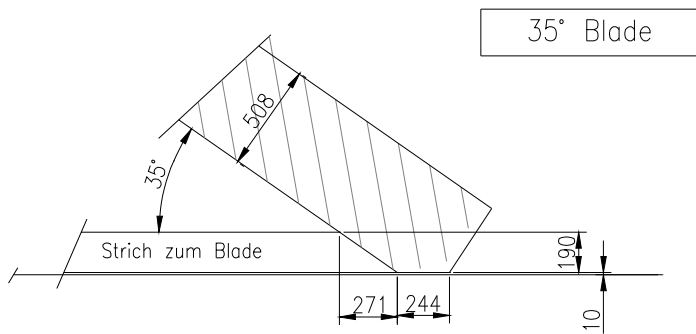
Pict. 7.4.34: 35° Blade without pre-angle and shorter facet length (µm)
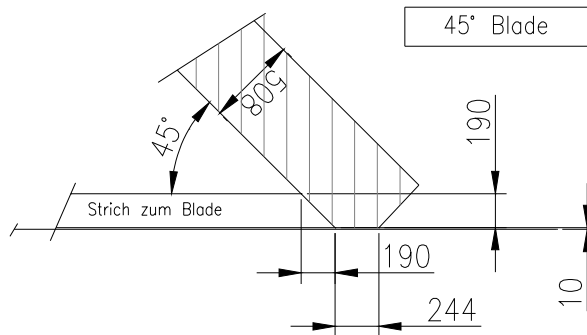
Pict. 7.4.35: 45° Blade without pre-angle and shorter facet length (µm)
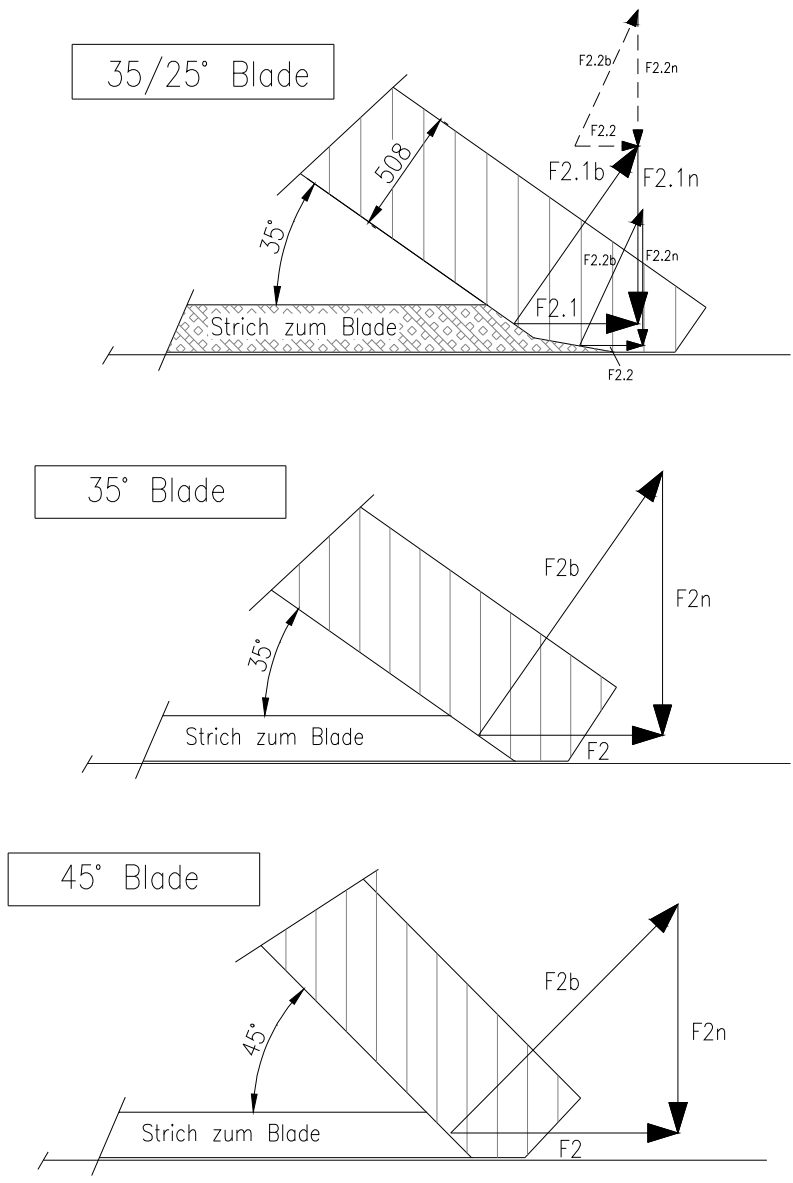
Pict. 7.4.36: Comparison of forces on blade and paper in Z-direction of 3 blade geometries

	35° with preangle 25°	35° without preangle	45° without preangle		
Speed of coater	1.600	1.600	1.600	m/min	
--"--	26,67	26,67	26,67	m/s	v
Width of coater	8,5	8,5	8,5	m	B
Density of coating colour	1.685	1.685	1.685	kg/m³	ρ
Height of coating colour under blade	18	18	18	µm	
Excess factor of application	25	25	25		
Area before preangle:					
Blade angle	**35**	**35**	**45**	°	**Angle before tip**
Blade angle	0,611	0,611	0,785	rad	α
Inverse blade angle	0,960	0,960	0,785	rad	90 - α
Height of coating colour before blade	133	432	432	µm	h_z
Impulse of colour on blade p	599.111	599.111	599.111	Pa	$p = \rho/2 * v^2$
Cross section area of incoming coating layer	0,00113	0,00367	0,00367	m²	$A = h_z * B$
Resulting force in coating direction	**677**	**2.200**	**2.200**	N	$F_{hydr} = F_{2.1}$
Resulting force on paper	**967**	**3.142**	**2.200**	N	$F_{normal} = F_2 * \tan(90-\alpha)$
Facette lenght	244	244	244	µm	l_{x1}
Area of coating colour pressure on paper	0,0021	0,0021	0,0021	m²	A_1
Resulting pressure on paper	**4,66**	**15,15**	**10,61**	bar	$p_{norm} = F_{norm} / A_{shear}$
Area before blade tip (preangle):					
Blade preangle	**25**			°	**Angle at tip**
Blade preangle	0,436			rad	$α_2$
Inverse blade angle	1,134			rad	$90 - α_2$
Height of coating colour before blade	299			µm	$h_{z.2}$
Impulse of colour on blade p	599.111			Pa	$p = \rho/2 * v^2$
Cross section area of incoming coating layer	0,00254			m²	$A = h_z * B$
Resulting force in coating direction	**1.523**			N	$F_{hydr} = F_{2.2}$
Resulting force on paper	**3.265**			N	$F_{normal} = F_2 * \tan(90-\alpha)$
Facette lenght	244			µm	l_{x1}
Area under blade	0,0021			m²	A_1
Resulting pressure on paper	**15,74**			bar	$p_{norm} = F_{norm} / A_{shear}$
Resultant normal force from impulse	**4.233**	**3.142**	**2.200**	N	F_{normal}
Normal pressure from impulse force on paper in Z-di	**20,4**	**15,1**	**10,6**	bar	p_{norm}
Calculation of shear force under blade:					
Rez. 340, 20.8.2008					
Brookefield 20 UpM = 5120 cp, Abo WRV = 60,6 g/m²					
Height of coating colour under blade	18	18	18	µm	h_z
Speed of coater	26,67	26,67	26,67	m/s	v
Shear rate γ	1.481.481	1.481.481	1.481.481	1/s	$\gamma = v / h_z$
Viscosity η	0,121	0,121	0,121	Pas	from ACAV
Shear stress τ	179.259	179.259	179.259	Pa = N/m²	$\tau = \eta * \gamma$
Coated width	8,5	8,5	8,5	m	
Contact lenght l	244	244	244	µm	
Area of shear A	0,0021	0,0021	0,0021	m²	A_{shear}
Shear force in coating direction	**372**	**372**	**372**	N	$F_{shear} = \tau * A$
Resultant normal force from shear	**531**	**531**	**372**	N	$F_{normal} = F_2 * \tan(90-\alpha)$
Calculation of blade pressure under blade:					
					m/min
Sum of forces in coating direction	**2.572**	**2.572**	**2.572**	N	F_2
Sum of blade forces, normal to coating direction	**4.764**	**3.673**	**2.572**	N	$F_{normal} = F_2 * \tan(90-\alpha)$
Resulting normal pressure on paper	**22,97**	**17,71**	**12,40**	bar	$p_{norm} = F_{norm} / A_{shear}$
Distance blade holder to tip	66	66	66	mm	b
Free length	15	15	15	mm	e
Blade force on bar	**1.909**	**1.909**	**2.353**	N	$F_1 = b/(b-e) * \sin\alpha * F_2$

Pict. 7.4.37: Comparison of blade force and pressure upon paper in Z-direction of three different blade geometries (0,508 mm thick blade)
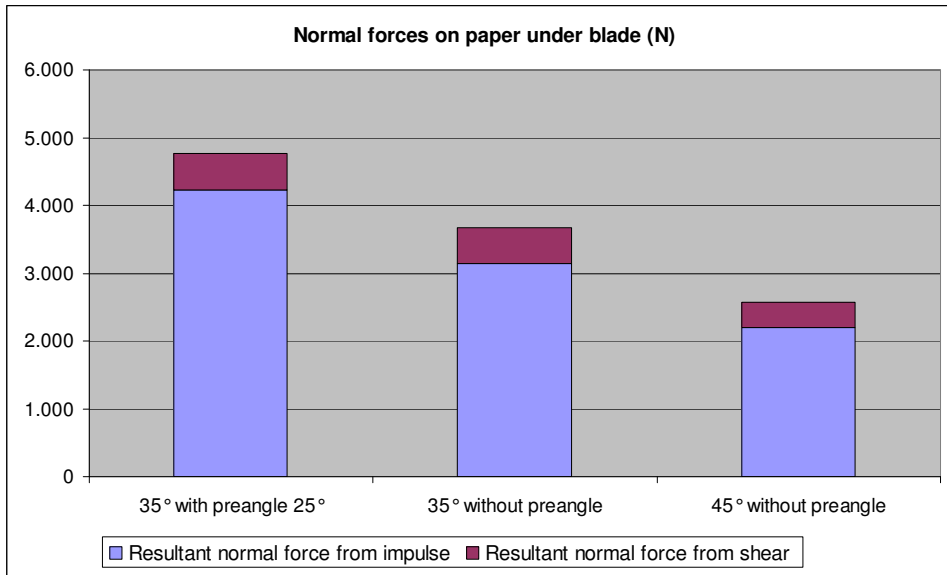
Pict. 7.4.38: Resulting normal force on paper from impulse and shear force
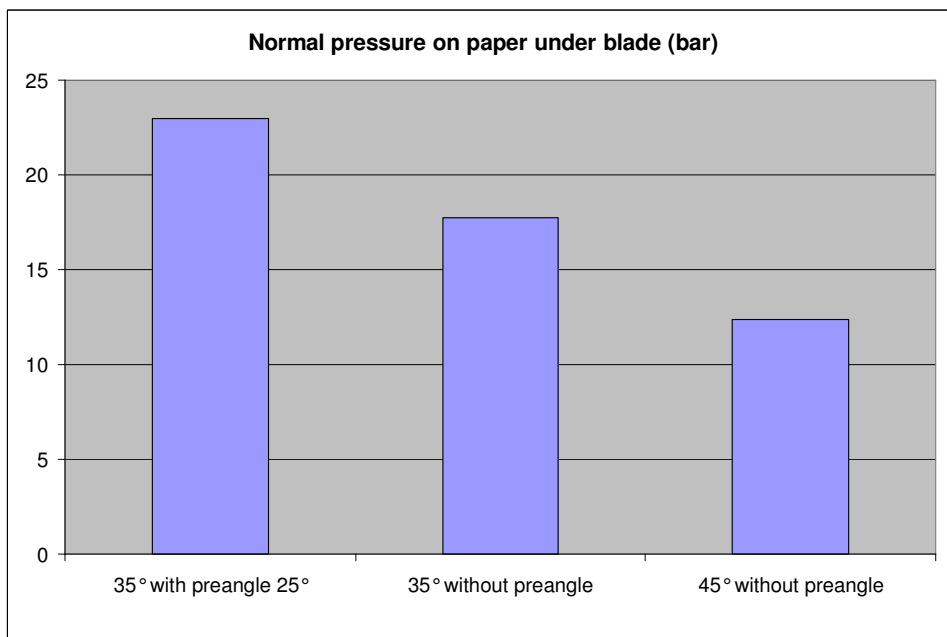
Pict. 7.4.39: Resulting normal peak pressure under blade from impulse and shear force

Switching from the standard 35°-blades at OMC11 with pre-angle to a blade with 45° angle and no pre-angle would reduce the peak pressure under the blade by approximately 40% (pict. 7.4.36 – 7.4.39).

VOF simulation

To verify this simplified method for blade pressure calculation a VOF simulation was made for the three different blade geometries.

Continuity equation:

Equ. 7-4-1: $\dfrac{\partial}{\partial t}(\alpha_q) + \dfrac{\partial}{\partial x_i}(u_j * \alpha_q) = \dfrac{S_{\alpha q}}{\rho_q} + \dfrac{\sum\limits_{p=1}^{n}(\dot{m}_{pq} - \dot{m}_{qp})}{\rho_q}$

With $\mu = \alpha_{coater} * \mu_{coater} + (1-\alpha) * \mu_{Luft}$ and $\rho = \alpha_{coater} * \rho_{coater} + (1-\alpha) * \rho_{Luft}$

Navier Stokes equation:

Equ. 7-4-2: $\dfrac{\partial}{\partial t}(\rho * \vec{v}) + \nabla * (\rho * \vec{v} * \vec{v}) = -\nabla p + \nabla\left[\mu * (\nabla\vec{v} + \nabla\vec{v}^{T})\right] + \rho * g + \vec{F}$

With F the additional forces like the surface tension at the walls.

The dependence of the viscosity on the shear rate was modelled by the equation

$\eta(\dot{\gamma}) = a + b * \dot{\gamma} + c * \dot{\gamma}^{n}$

To calculate shear forces high shear viscosity measurements of top coating PM11 where made by ACAV with capillary geometry (see pict. 7.4.24).

Natalia Egorova (L4.2) compared in her PhD work the blade pressure at a Helio coater with high shear viscosity measurements using different geometries (pict. 7.4.41). She compared tube capillaries of different diameter with slit geometries.
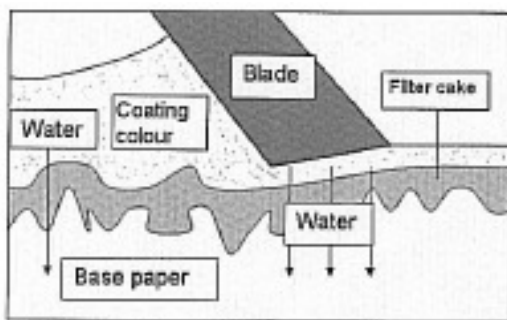
Pict. 7.4.40: Dewatering process under the blade
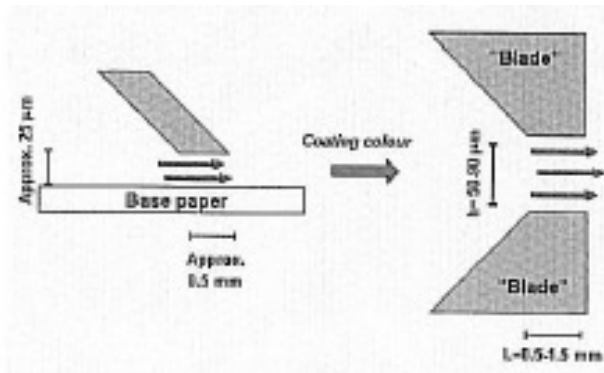
Pict. 7.4.41: SLIT rheometer (Natalia Egorova)

In a capillary viscosimter the measured pressure drop is.

$p_{meas} = p_{kin} + p_{Nent} + p_{visc} + p_{elast} + p_{exit}$
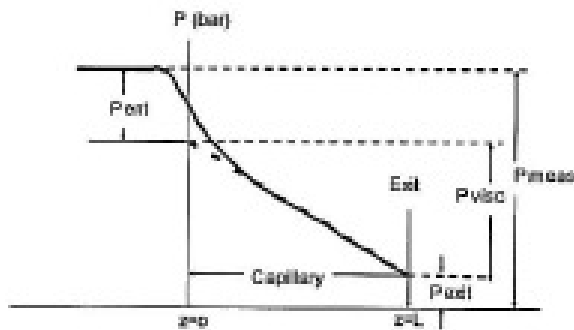
Pict. 7.4.42: Pressure distribution before and in the capillary (non-Newtonian fluid), with $p_{ent} = p_{kin} + p_{Nent} + P_{elast}$ (Natalia Egorova)

The parameter which we search for is p_{visc} but unfortunately it is impossible to measure it directly. A number of corrections have to be made:

Kinetic energy corrections: The pressure to accelerate the fluid ($p_{kin} = m*\rho*v^2$) has to be subtracted from p_{meas}.

Bagley corrections (pict. 7.4.43): For described entrance and end effects the viscous and elastic pressures p_{elast} and p_{exit} are removed from p_{meas}. This correction is depending on capillary geometry.
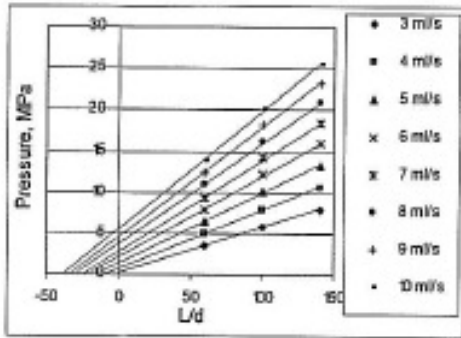
Pict. 7.4.43: Typical Bagley plot for $CaCO_3$ based coating colour (Natalia Egorova)

In SLIT rheometers the measuring principle is similar to capillary viscosimeters: Coating colour is pressed through a channel. Geometry is similar to a blade nip. Entrance angle of SLIT geometry at ACAV company is 45° and length of orifice is 0,5 mm. Shear rates up to $3*10^6$ s^{-1} are possible.

Shear rate is: $\dot{\gamma}_{wall} = \dfrac{6*Q}{w*h^2}$ (Q = flow rate, h = height, w = width of SLIT)

Shear stress is: $\tau_{wall} = \dfrac{p*h}{2*L}$ (p = extrusion pressure, L = SLIT length)

Viscosity is: $\eta = \dfrac{\tau}{\dot{\gamma}}$

A Couette correction must be made for the dissipation of the applied pressure into developing a constant flow profile.

For capillary viscosimeters this is not necessary because the length of the capillary is much bigger than its diameter.

An effective length L' = L + n has to be introduced, where n is the height of the SLIT.

Shear stress is corrected with: $\tau = \dfrac{p_{meas} - p_{kin}}{2*L}$

When coating colour has to change its direction at the blade tip entrance, a certain loss in pressure occurs which is not measured in capillary viscosimeters. Therefore no correlation was found between blade pressure at Heliocoater and high shear viscosity measured by capillary viscosimeter. Correlation with high shear viscosity measured by SLIT geometry was perfect.

A. Roshanzamir and C. Gooch (L4.4) used a volume of fluid method (VOF) to calculate the hydrodynamic pressure generated by doctor blades in gap formers. They used a simplified Navier Stokes equation.

Continuity equation: $u_j * \dfrac{\partial \varepsilon_k}{\partial x_i} = 0$

Navier Stokes: $\dfrac{\partial}{\partial x_i} * \rho * u_i * u_j = -\dfrac{\partial p}{\partial x_j} + \dfrac{\partial}{\partial x_i} * \mu * (\dfrac{\partial u_i}{\partial x_j} + \dfrac{\partial u_j}{\partial x_i})$

Assumptions:

- Newtonian behaviour of the pulp suspension
- Darcy's law for flow through the wire
- Constant permeability of the fibre mat
- Retention 100%, no drainage of fibres and fines
- No stiffness of the wire
- Same speed of water layer and wire upstream

The result of the VOF model is a pressure profile along the stream lines (pict. 7.4.44).
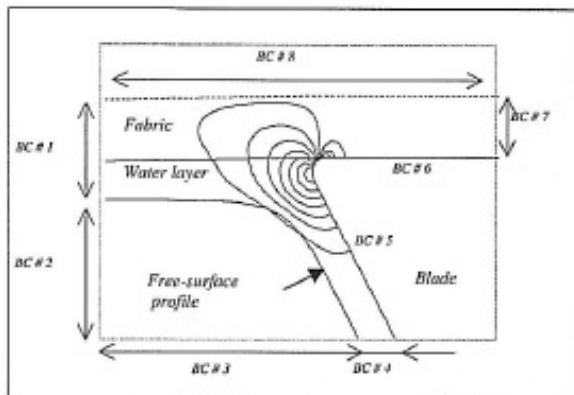
Pict. 7.4.44: Pressure contours from VOF model at the blade tip – coating colour flow from left to right; return flow to the working tank downwards (A. Roshanzamir)
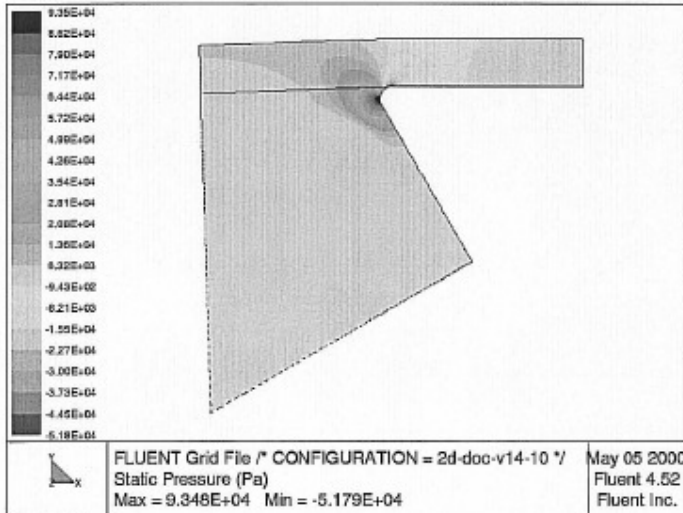
Pict. 7.4.45: Pressure contour lines from VOF model at the blade tip, blade 2:
Max pressure = 40 kPa (A. Roshanzamir)

A. Roshanzamir and C. Gooch compared different blade geometries with their VOF
model and discovered that with increasing nose radius the peak pressure in the gap
is also increased and shifted from the tip to the upstream direction (pict. 7.4.45 – 47).
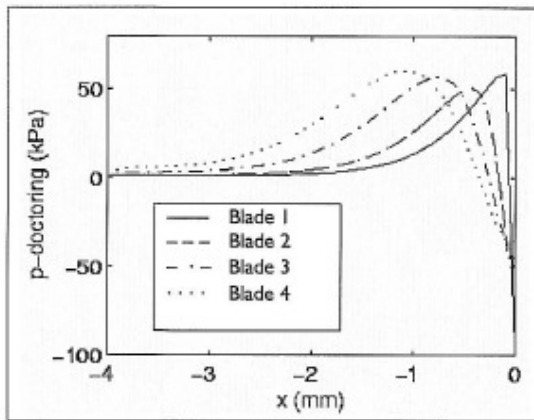
Pict. 7.4.46: Doctoring pressure as a function of blade geometry (A. Roshanzamir)
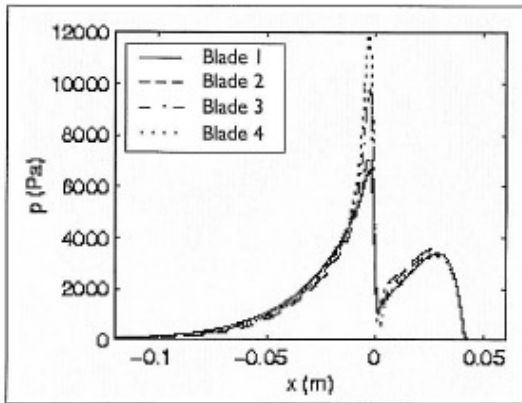
Pict. 7.4.47: Pressure pulses in the middle of the gap (A. Roshanzamir)

F.R. Prankh and L.E. Scriven (L4.5) used Navier Stokes equation for calculating the coat weight for stiff blade coaters either running on the heel of blade tip or at the toe. The calculation resulted in the conclusion that coat weight increases when blade is run at the toe due to a new converging nip at the blade tip and decreases when it is run at the heel.

Results from VOF simulations with 3 blade geometries for blade coaters at OMC11:

VOF (Volume of Fluid) methods are capable of describing the flow of two phase systems. The simulation was calculated by a 2D model.

Euler-Euler model can be used alternatively but interaction of components in a two phase system is left out.

With VOF a certain area of flow is observed. For blade coating this are was defined before the blade tip and under the blade (pict. 7.4.48).
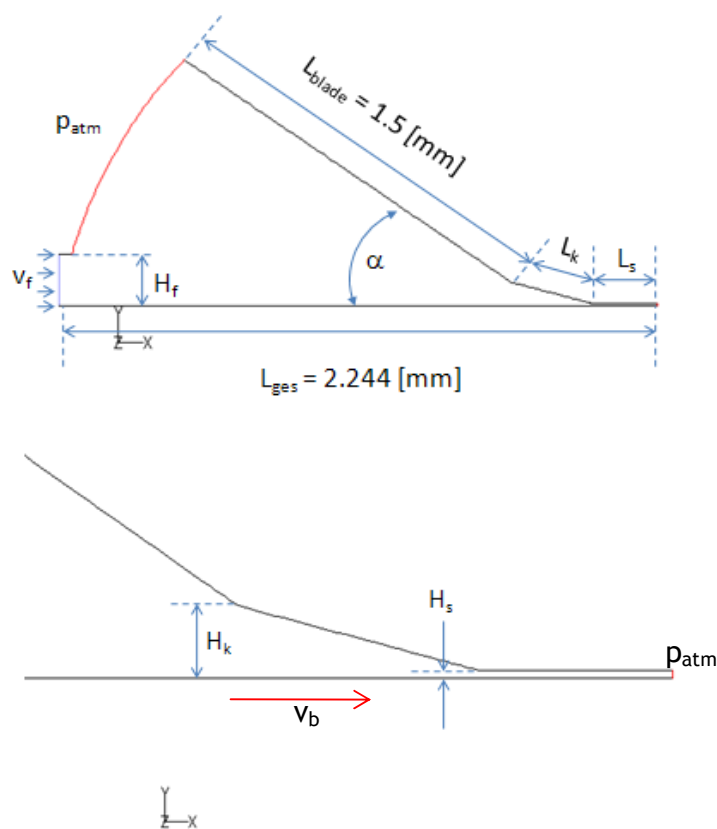
Pict. 7.4.48: Detailed blade geometry for 35/25° TC blade with pre-angle at tip

Size of elements for VOF of blade coating at OMC11 was 5 x 2 µm (pict. 7.4.49).
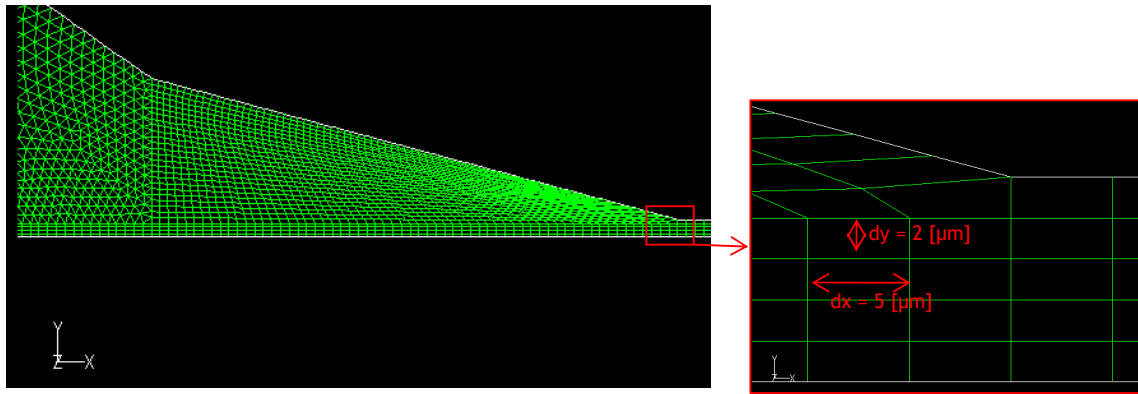
Pict. 7.4.49: Hybride grid of calculation (hexahedron & tetrahedron) with17904 elements of 5 x 2 µm size for OMC11 blade VOF.

At boundary the elements contain partly air and partly fluid (pict. 7.4.50). Volume fraction α is defined by: $\alpha = \dfrac{V_l}{V}$ with V_l the liquid volume and V the total volume of the element. α = 0: 100% air; α = 1 : 100% coating
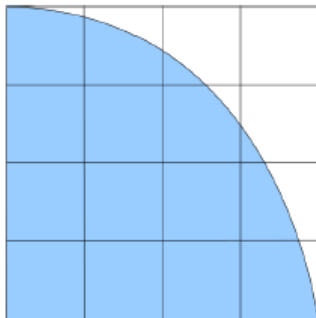
0,9	0,6	0,2	0
1	1	0,8	0,2
1	1	1	0,6
1	1	1	0,9

Pict. 7.4.50: Modelling of two phase systems by volume fraction α (blue = liquid, white = air)

The material constants dynamic viscosity µ and density ρ are defined as:

$$\mu = \alpha_{coater} * \mu_{coater} + (1 + \alpha) * \mu_{air}$$

$$\rho = \alpha_{coater} * \rho_{coater} + (1 + \alpha) * \rho_{air}$$

Page 343

The boundary conditions were taken from "real life" of off-coater 11 (pict. 7.4.51 and 7.4.52):

Geometrie	
Spalthöhe H_s:	10 µm
Spaltlänge L_s:	244 µm
Länge Einlaufkeil L_k:	305 µm
Eintrittshöhe Keil H_k:	90 µm
Farbfilmhöhe am Zulauf H_f:	200 µm
Neigung Klinge a:	35°

Pict. 7.4.51: Blade geometry data's for 35/25° TC blade with pre-angle at tip

Randbedingungen	
Bandgeschwindigkeit v_b:	26.67 m/s
Filmgeschwindigkeit am Zulauf v_f:	26.67 m/s konstant
Luftdruck p_{atm}:	Normaldruck = 1 bar
Schwerkraftvektor (x,y,z)	(0, 9.81,0)

Pict. 7.4.52: Parameters of OMC11 for 2D VOF simulation process parameters (speed 1600 m/min, coat weight 12 g/m², solids 68%, excess factor 1:20)

Viscosity was determined by ACAV high shear viscometer. A typical top coating colour of OMC11 was measured.
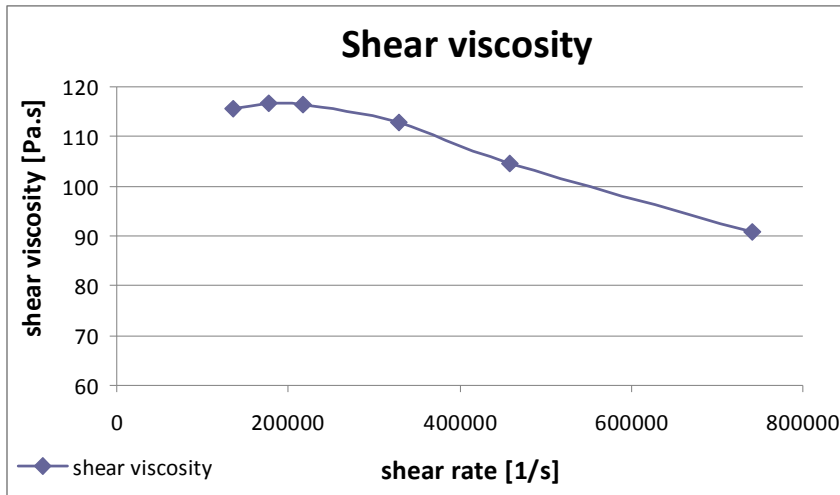
Pict. 7.4.53: ACAV high shear viscosity of top coating formulation No. 340

CFD and VOF model use Navier Stokes equation and continuity equation to determine the flow field of an in stationary flow.

Navier Stokes equation for incompressible media:

$$\rho * (\frac{\partial v}{\partial t} + v * \nabla v) = -\nabla p + \mu * \nabla^2 v + F$$

$\dfrac{\partial v}{\partial t}$ ....unsteady acceleration

$v * \nabla v$ ....convective acceleration

$-\nabla p$ ....pressure gradient

$\mu * \nabla^2 v$ ...shear stress (viscosity term)

F ...other body forces like gravity or surface tension

2D Cartesian coordinates:

$$\rho * (\frac{\partial u}{\partial t} + u * \frac{\partial u}{\partial x} + v * \frac{\partial u}{\partial y}) = -\frac{\partial p}{\partial x} + \mu * (\frac{\partial^2 u}{\partial x^2} + \frac{\partial^2 u}{\partial y^2}) + F_x$$

$$\rho * (\frac{\partial v}{\partial t} + u * \frac{\partial v}{\partial x} + v * \frac{\partial v}{\partial y}) = -\frac{\partial p}{\partial y} + \mu * (\frac{\partial^2 v}{\partial x^2} + \frac{\partial^2 v}{\partial y^2}) + F_y$$

Navier Stokes equation for VOF:

$$\frac{\partial}{\partial t}(\rho * \vec{v}) + \nabla * (\rho * \vec{v} * \vec{v}) = -\nabla p + \nabla * [\mu * (\nabla \vec{v} + \nabla \vec{v}^T)] + \rho * \vec{g} + \vec{F}$$

$\frac{\partial}{\partial t}(\rho * \vec{v})$ ...unsteady acceleration

$\nabla * (\rho * \vec{v} * \vec{v})$ ...convective acceleration

∇p ...pressure gradient

$\nabla * [\mu * (\nabla \vec{v} + \nabla \vec{v}^T)]$ ...stress tensor (shear stress) – general: $\mu * \nabla^2 v$

$$\frac{\partial}{\partial t}(\rho * \vec{v}) + \nabla * (\rho * \vec{v} * \vec{v}) = -\nabla p + \nabla * [\mu * (\nabla \vec{v} + \nabla \vec{v}^T)] + \rho * \vec{g} + \vec{F}$$

ρ*g....gravity

F......external force, e.g. surface tension

Continuity equation:

$$\frac{\partial \rho}{\partial t} + \nabla * (\rho * v) = 0 \ \rightarrow \text{ for incompressible media: } \nabla * v = 0$$

$$\frac{\partial \rho}{\partial t} + \frac{\partial(\rho * u)}{\partial x} + \frac{\partial(\rho * v)}{\partial y} = 0 \ \rightarrow \text{ for incompressible media: } \frac{\partial(u)}{\partial x} + \frac{\partial(v)}{\partial y} = 0$$

VOF simulation with 5 µm small elements where the mass in a single element is

$$m_{cv} = \alpha_{coate} r * \rho_{coate} r * V_{cv} \text{ with:}$$

α ...volume fraction: α = 0: Air; α = 1 : Coating

µ, α...material constants (dyn. Viscosity, density)

$$\mu = \alpha_{coater} * \mu_{coater} + (1 + \alpha) * \mu_{air}$$

$$\rho = \alpha_{coater} * \rho_{coater} + (1 + \alpha) * \rho_{air}$$

Continuity for a single element in VOF model:

$$\frac{\partial}{\partial t} * (\alpha_q) + \frac{\partial}{\partial x_j} * (u_j * \alpha_q) = \frac{S_\alpha}{\rho_q} + \frac{\sum_{p=1}^{n}(\dot{m}_{pq} - \dot{m}_{qp})}{\rho_q}$$

By putting α into a two-dimensional form the transport equation gets

$$\frac{\partial \vec{\alpha}}{\partial t} + \nabla * (\alpha * \vec{u}) = 0$$

The normal vector for flow (pict. 7.4.54) from one element into the other of to

boundaries is calculated from $\vec{n} = \dfrac{\nabla \vec{f}}{|\nabla f|}$

f=0	0	0	0
0,7	0,2	0 n	0
1	0,85	0,6	0,1
1	1	1	0,8
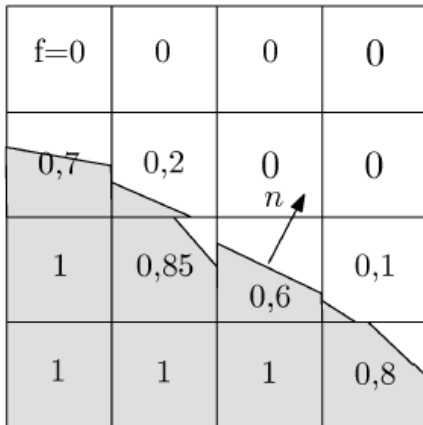
Pict. 7.4.54: Normal vector of flow

Legend to the following pictures 7.4.55 – 7.4.64 of VOF simulation for stationary flow:

Top picture: 35/25° blade,   mid picture: 35° blade,   bottom picture: 45° blade

Pict. 7.4.55: Velocity profile in flow of coating colour to the blade plus return flow and exit under the blade

Pict. 7.4.56: Velocity profile of flow before the blade tip

Pict. 7.4.57: Velocity profile of flow at the blade tip (35/25° blade with pre-angle only)

Pict. 7.4.58: Velocity profile of flow at the blade tip

Pict. 7.4.59: Dwelling time of coating colour before blade

Legend values (top to bottom):
```
4.16e-05
2.75e-05
1.81e-05
1.19e-05
7.86e-06
5.18e-06
3.42e-06
2.25e-06
1.49e-06
9.79e-07
6.45e-07
4.25e-07
2.80e-07
1.85e-07
1.22e-07
8.03e-08
5.30e-08
3.49e-08
2.30e-08
1.52e-08
1.00e-08
```

```
Blade Coating - base model
Contours of verweilzeit_in_zelle (coating-paint)  (Time=1.0000e-02)
```

Pict. 7.4.60: Dwelling time of coating colour at the blade tip (35/25° blade only)

Pict. 7.4.61: Strain rate (1/s) in the coating colour flow to the blade

Pict. 7.4.62: Strain rate (1/s) in the coating colour flow at the tip and under the blade
(35/25° blade only)

Pict. 7.4.63: Absolute pressure in the coating flow to the blade

Pict. 7.4.64: Absolute pressure at the blade tip

Pict. 7.4.65: Comparison of pressure on paper in Z-direction before and under the blade

zone name	35° facette			35° no_facette			45° no_facette		
	pressure force	viscous force	total force	pressure force	viscous force	total force	pressure force	viscous force	total force
	[N]	[N]	[N]	[N]	[N]	[N]	[N]	[N]	[N]
blade_einlaufbereich	4325.4	345.9	4671.3	5766.7	418.3	6185.0	3650.6	505.5	4156.2
blade_facette	4481.6	37.6	4519.2	0.0	0.0	0.0	0.0	0.0	0.0
blade_spalt	2737.6	0.0	2736.6	1946.2	0.0	1944.6	1751.6	0.0	1750.0
Σ blade	11544.6	383.6	11927.1	7712.8	418.3	8129.7	5402.2	505.5	5906.1
walze_einlaufbereich	-5521.9	0.0	-5520.0	-6982.4	0.0	-6979.3	-5126.5	0.0	-5122.9
walze_facette	-4517.7	0.0	-4516.6	0.0	0.0	0.0	0.0	0.0	0.0
walze_spalt	-2737.6	0.0	-2737.9	-1945.6	0.0	-1946.1	-1750.9	-0.5	-1751.4
Σ walze	-12777.2	0.0	-12774.5	-8928.1	0.0	-8925.4	-6877.4	0.0	-6874.3

Pict. 7.4.66: Comparison of pressure on paper in Z-direction before and under the blade
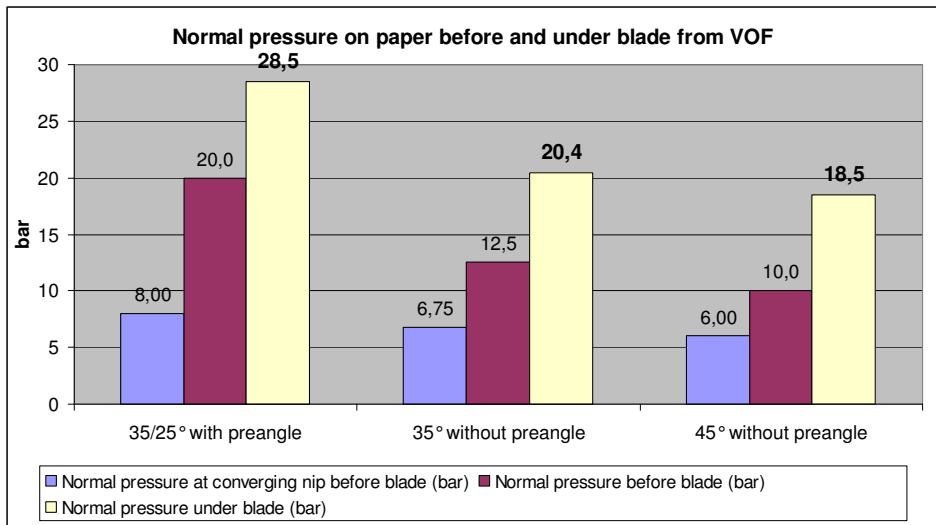
Pict. 7.4.67: Normal pressure before and under the blade from VOF simulation

A normal peak pressure of approximately 25 bars was calculated from VOF simulation for OMC11 blade coaters (pict. 7.4.65 – 7.4.67).

This peak pressure was comparable to the simplified Excel calculation. VOF simulation gives additional information about the pressure profile in the converging nip before the blade tip where a rising normal pressure of 6 – 20 bars occurs over a period of 0,03 ms (pict. 7.4.67 and 7.4.68).
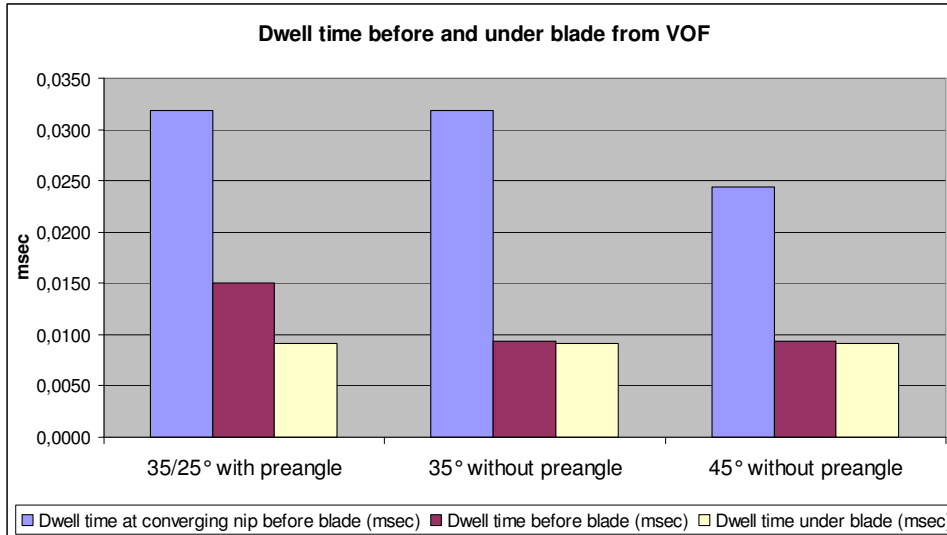
Pict. 7.4.68: Dwell time before and under the blade from VOF simulation

Dwell time is relatively short for the peak pressure while it is 7 times longer in the converging channel at the blade tip where a normal pressure of 6 – 8 bar starts to press liquid phase into the substrate.

7.5 Solution 2 for formation and drying mottle - Reduce blade pressure

Lowering the blade pressure leads to less penetration of the liquid phase in coatings including soluble substances, cobinders and latex particles into the base paper.
At high speed blade coaters blade pressure increases exponentially with speed due to quadratic dependence of coating colour impulse force $F = p * A$ by hydrodynamic pressure $p = \rho/2 * v^2$ on speed.
Therefore the risk of mottling increases with speed if no counter actions are taken.

As the VOF simulations of the 3 different blade geometries showed the right choice of blade tip is a key parameter to reduce the normal pressure under the blade.

To reduce amount of penetrated liquid (+latex and solubles) the penetration coefficient $\sqrt{p} * \sqrt{t}$ must be reduced.

Darcy: $\dfrac{dV}{dt} = \dfrac{K * A * \Delta p}{\eta * L}$; integrated: $V^2 = \dfrac{K * \overline{C} * A^2 * \Delta p}{\eta * \varepsilon} * t$ leads to:

$V = A * \sqrt{\dfrac{K * \overline{C}}{\eta * \varepsilon} * \Delta p * t}$ (see also Carman Kozeny: $\dfrac{m}{f} = \sqrt{C * A * \Delta p * t}$)

In pict. 7.5.1 four blade geometries are compared in penetration coefficient $\sqrt{p} * \sqrt{t}$, calculated by VOF:

Penetration coefficient under blade SQROOT(t)*SQROOT(p)

Blade geometry	Value
Blade 35° no preangle, long facet	180
Blade 35° with preangle, short facet	148
Blade 35° no preangle, short facet	131
Blade 45° no preangle, short facet	117
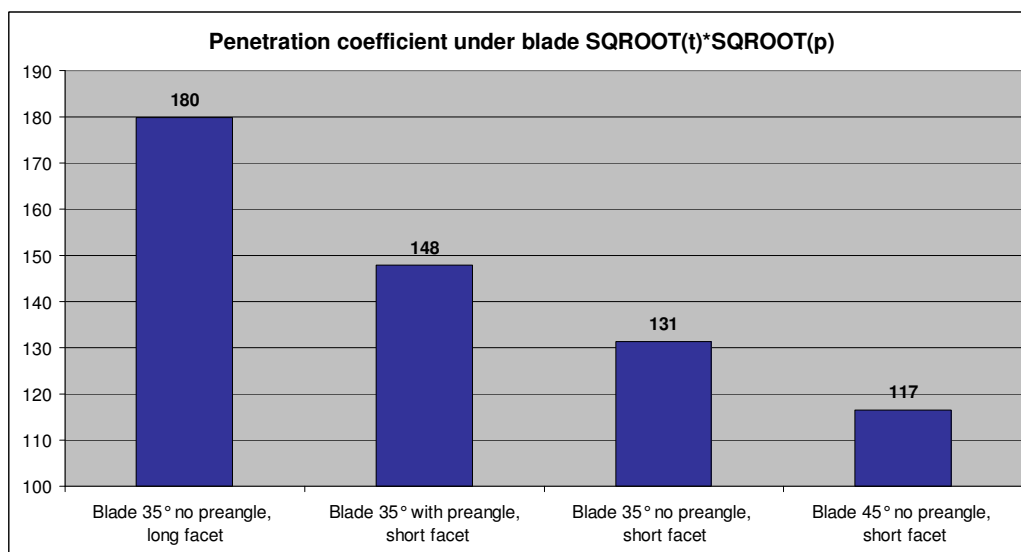
Pict. 7.5.1: Blade penetration coefficient for 4 different blade geometries

As the pressure starts to rise approximately 0,9 mm before the blade tip, the penetration factor $\sqrt{p} * \sqrt{t}$ is not only influenced by the peak pressure but also by the area before the blade.

The comparison of VOF simulation of different blade geometries showed a potential of **reduction of the penetration factor** $\sqrt{p} * \sqrt{t}$ **of 30%** when the current 35/25° blade would be changed to a 45° blade with same short facet length.

7.6 Curtain coater

The ideal coater to avoid pressure induced mottling is a **curtain coater**. Application is done without external pressure. Pilot trials of many paper companies show the advantage in mottling for this coater against applicators based on pressure penetration like blade or filmpress coaters.

The first mill installations at GD board machines have proven this experience. GD board is relatively critical for print mottle due to high in-plane basis weight and compressibility differences derived by high press load in the press section and paper compaction during drying at the Yankee cylinder.

One of the disadvantages of curtain coaters is the low degree of coating colour anchorage in the substrate due to the missing pressure impulse at the application.

7.7 Film press coaters (MSP coater)

Film press coaters (pict. 7.7.1 and 7.7.2) are well known for improved mottling when compared to blade coaters. The reason is again the lower pressure in the application nip (pict. 7.7.3).
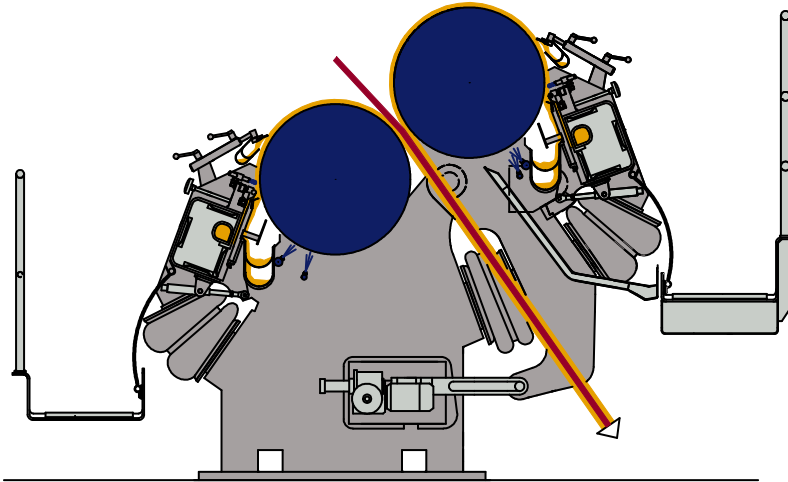
Pict. 7.7.1: Voith filmpress coater with double sided application
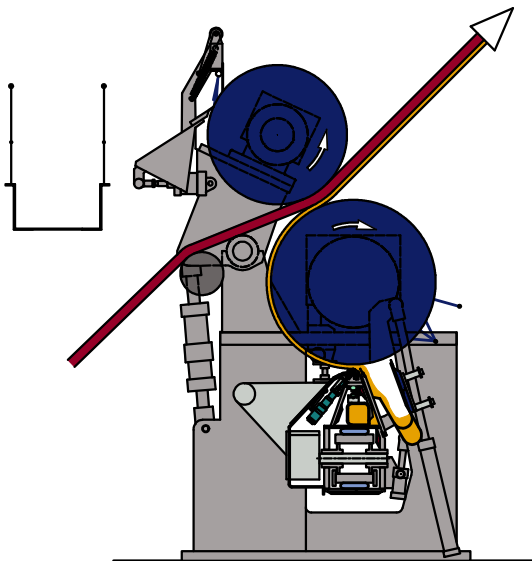
Pict. 7.7.2: Voith filmpress coater with single sided application

The application pressure of a film press coater can be calculated by the Hertz equation.
Hertz assumed linear deformation, no friction, isotropic and homogenous bodies.

Pressure is transferred in z-direction. The pressure curve is elliptical, with no pressure at the edges.

In reality roll covers show visco-elastic behaviour and energy is dissipated by increase of temperature. Therefore the practical nip width will be lower as theoretically calculated for a pure elastic cover.

The E-Modulus is a function of temperature and is taken at the nip temperature.

Equ. 7-1-1: $b = 2 * \sqrt{\dfrac{8 * q * r}{\Pi * E^*}}$

b….width of nip (mm)

Equ. 7-1-2: $r = \dfrac{R_1 * R_2}{R_1 + R_2}$

r…..radius for comparison (mm)

R_1…radius of applicator roll (mm)

R_2…radius of backing roll (mm)

Equ. 7-1-3: $E^* = \dfrac{2 * E_1 * E_2}{\left[(1 - \mu^2{}_1) * E_2 + (1 - \mu^2{}_2) * E_1 \right]}$

E*…..elastic modulus for comparison (N/mm²)

E_1…..E-Module of applicator roll (N/mm²)

E_2…..E-Modulus of backing roll (N/mm²)

μ_1…..Poisson number of the applicator roll (contraction number)

μ_2….. Poisson number of the backing roll (contraction number)

Equ. 7-1-4: $s_m = \dfrac{q}{b}$

s_m…mean pressure in Nip (N/mm²)

q…..nip load (N/mm)

Equ. 7-1-5: $s_{max} = \dfrac{4 * q}{\Pi * b}$

S_{max}…max. pressure in nip (N/mm²)

R_1	647	mm	Radius applicator roll
R_2	550	mm	Radius backing roll
r	297,3	mm	Radius for comparison
E_1	12	N/mm²	E-Modulus applicator roll
E_2	210	N/mm²	E-Modulus backing roll (steel)
μ_1	0,44		Poisson Number (contraction)
μ_2	0,3		Poisson Number (contraction)
E^*	28,0	N/mm²	Modulus for comparison
q	14	N/mm²	Nip load
b	**38,9**	**mm**	**Nip width**
s_m	**0,36**	N/mm² = MPa	**Mean pressure in nip**
s_m	**3,6**	**bar**	
s_{max}	**0,46**	N/mm² = MPa	**Max. pressure in nip**
s_{max}	**4,6**	**bar**	

Pict. 7.7.3: Calculation of film press nip pressure

The application pressure of a single sided film press coater with steel backing roll is with 4,6 bar much lower than the pressure under the blade for high speed blade coaters (20 – 30 bar).

A two sided film press coater with two opposite soft roll covers has even lower application pressure.

The advantage of lower application pressure against blade coaters was transferred to PM11/OMC11 by changing the precoating of double coated grades (115 g/m² end basis weight) from blade to filmpress coating. Pict. 7.7.4 shows that mottling improved when coating strategy was changed from blade on blade to blade on filmpress although viscosity and water retention of film press precoating was always much worse than that of the corresponding blade precoatings.
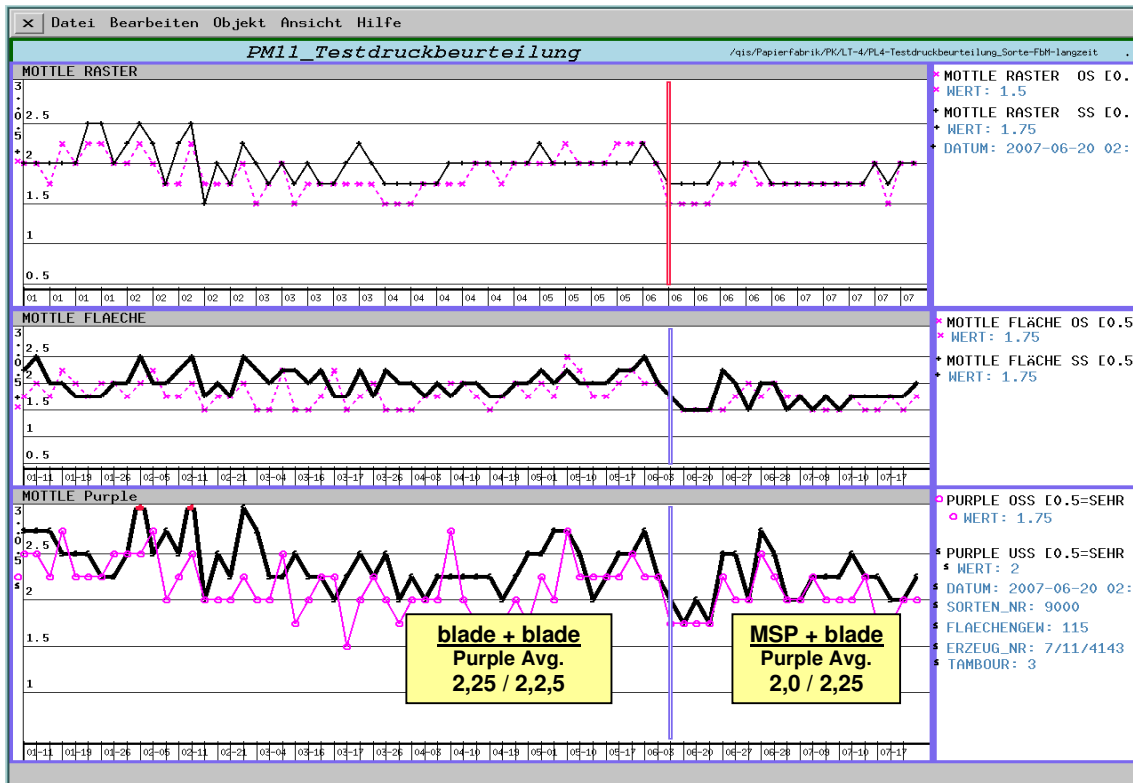
Pict. 7.7.4: Mottling of double coated glossy 115 g/m² - left side: blade on blade, right side: blade on film press ("Raster" = screen, "Fläche" = solid and purple mottling – see chapter 2, print mottling)

U. Firestorm and J. Grön (L1.36) studied the coating holdout on different base papers. A precoating was applied by a filmpress. Topcoating was done by blade. The higher base ash at the top side of the fourdrinier base paper led to an improvement of precoating holdout by 5% (pict. 7.7.5) measured by scanning electron microscope in the backscatter mode (BSE).
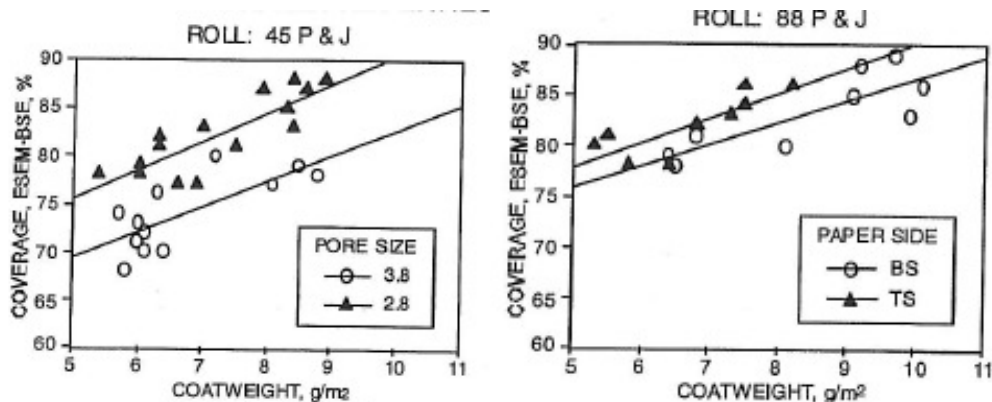
Pict. 7.7.5: Coating coverage as a function of base paper porosity and roll cover hardness (J. Grön)

Base paper surface chemistry, measured by contact angle didn't influence the coating holdout.

Improved precoating holdout led to a higher surface porosity as coatings have higher porosity than base papers (pict. 7.7.6).
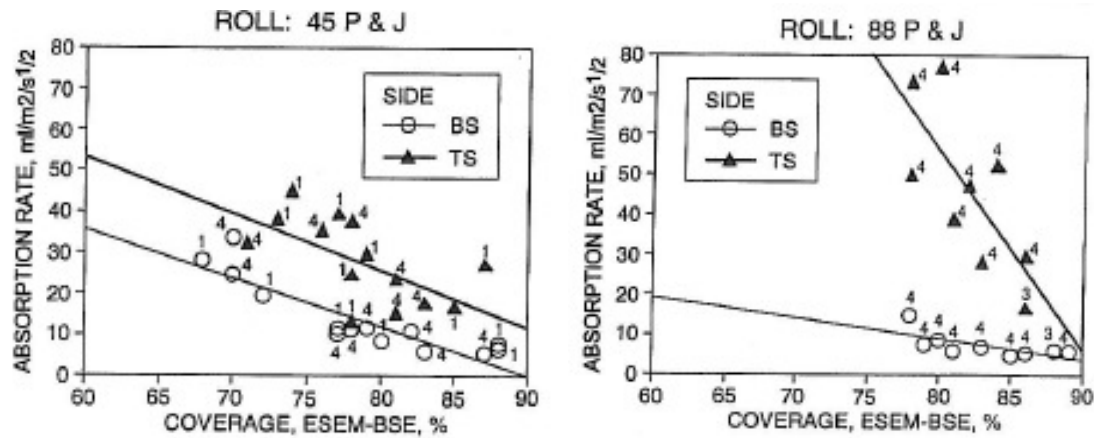
Pict. 7.7.6: Pre-coated paper surface porosity, measured by oil absorption rate (J. Grön)

Softer MSP application rolls lead to better uniformity of the coating layer and to a higher porosity.
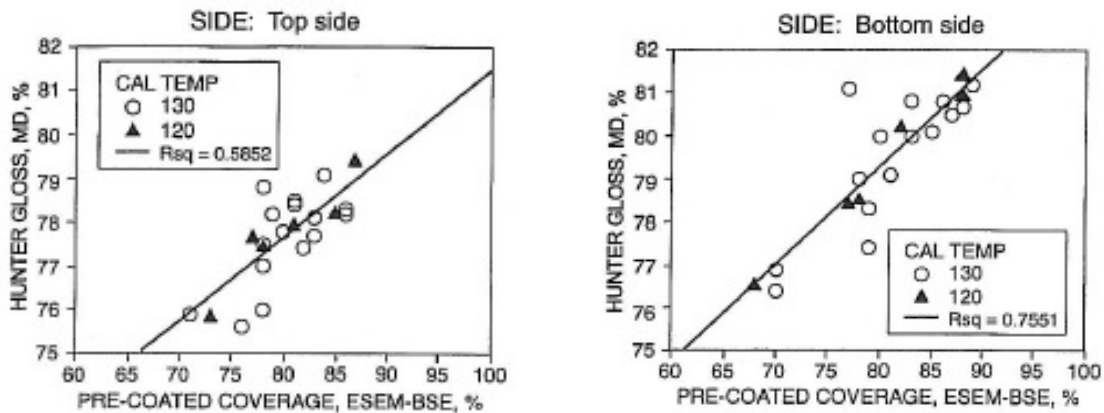
Pict. 7.7.7: Gloss of calendered papers vs. coverage of MSP precoating (J. Grön)

Improved holdout of precoating had a significant positive impact on top coated and calendered gloss (pict. 7.7.7).

Philipp Letzelter and Dan Eklund from Abo University (L5.2) developed a simulation model for dewatering of coating colours in filmpress nips including lab measurements with the Abo Web Peel meter and the Abo AA-GWR water retention instrument. When solid content of the coating colour is high, water retention is low, nip pressure is high, nip width is high (soft covers + high diameter) and speed is low an immobilized layer is formed in the MSP application nip (pict. 7.7.8).
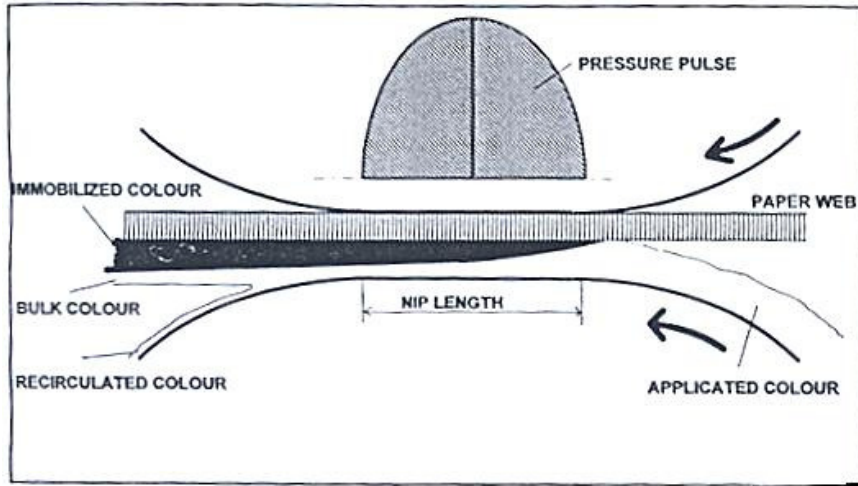
Pict. 7.7.8: Built up of immobilized layer in filmpress nips (MSP coater) (P. Letzelter)

Dewatering through this immobilized layer is depending on the density of packing of the pigment/latex particles - the Darcy coefficient of the immobilized layer.
Film splitting at the nip exit occurs at the layer with the lowest cohesion force. This point will be located in the layer with the lowest solid content.

Philipp Letzelter showed with his model that dewatering in the application nip can be reduced by 50% when:

- Liquid phase viscosity is increased 5 times (corresponds to adding 0,2% CMC)
- Pigment particle diameter is reduced to one third
- Random pigment particles are used instead of mono-sphere sized pigments

X Zou, D. Vidal (L5.3) showed surface roughness measurements of MSP and blade coated samples from previous studies of O. Suontausta (M-Real). They used SEM cross-section image analysis at Paprican.

MSP coated papers had a significant higher roughness in the in-plane area scale of 80 – 1280 µm, which is also responsible for the higher PPS values of MSP coated papers.
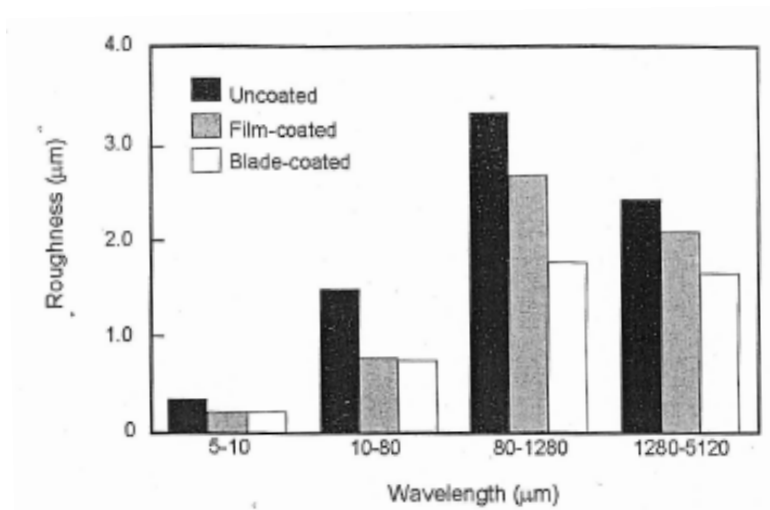
Pict. 7.7.9: Surface roughness at different wave lengths (X Zou)
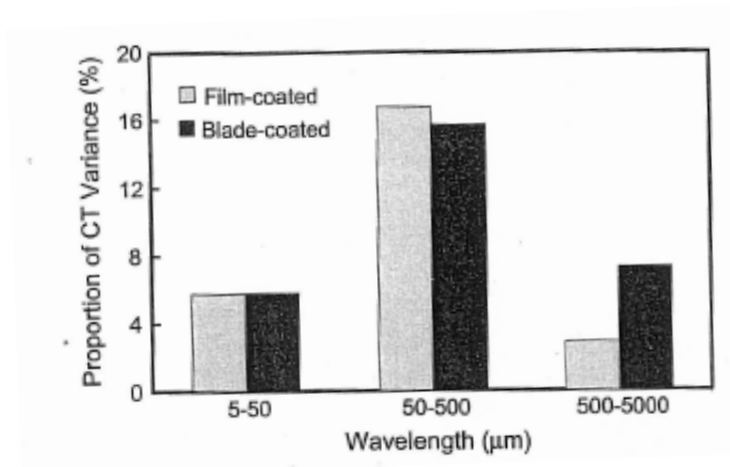
Pict. 7.7.10: Wavelength analysis of coating thickness (X Zou)

The higher micro roughness of MSP coaters is caused by the orange peel effect of film split pattern and leads to a higher PPS roughness after calendering at same Tappi Gloss (pict. 7.7.9 and 7.7.10).

Print mottle of single coated LWC and ULWC papers in heat set offset was always better for the MSP coated papers, compared with the blade coated papers.

To reduce the surface roughness of MSP coated papers, precalandering with high temperature and low load and a fibre furnish with less coarse and thinner walled fibres was suggested.

U. Forsström (L5.4) tested the coating holdout of MSP coatings on different pilot base papers.
Increasing the refining energy of hardwood and softwood furnish for a w'fr. base reduced the base paper pore diameter and porosity. Coating coverage and coating uniformity with MSP got better, especially at low coat weights.

The coating coverage of the MSP coater was relatively independent on formation or softwood/hardwood ratio.

A shadow marking of the suction roll of the pilot paper machine wire section caused large scale coating colour penetration differences at the top side of the paper. The marking was more pronounced at lower porosity of the base paper.
This indicated that a local difference in fines content had a strong impact on coating holdout.

The lower pressure in the film press nip can also be seen in a lower loss of paper volume after the coater (pict. 7.7.11).
Compression of base paper during coating can be described by the thickness difference or the difference in bulk before and after coating. Knowing the specific weight of the base paper (from measurement of thickness and basis weight) and the of the coating layer (by adding the specific weight of all dry components including air in the free pore volume measured by Mercury porosity) the theoretical volume of a coated paper can be calculated assuming ideal coating holdout. The more coating colour is pressed into the base paper the lower the volume of the coated paper will be and the higher the difference to the calculated theoretical volume (pict. 7.7.13)
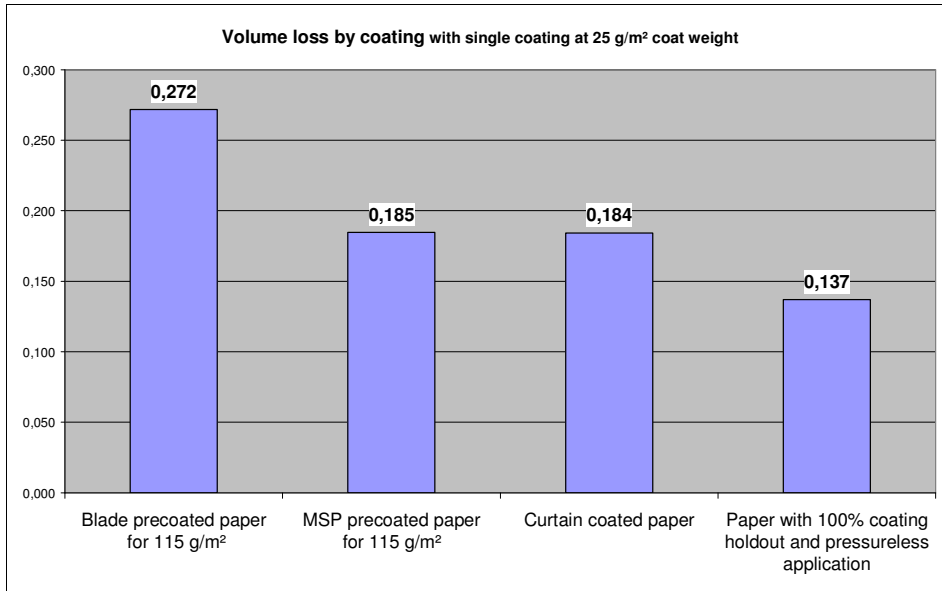
Pict. 7.711: Volume loss by coating: Y-axis: Difference in volume of base paper and coated paper – see pict. 7.7.13

Curtain coaters reduce paper volume to the same extend as film press coaters which is some kind of strange as they apply the coating colour pressure-less.

The explanation lies in the film press coating process: At the application nip the base paper is compressed and coating colour is partly forced into the base paper pores. Both mechanisms lead to loss of coated paper volume. At the nip exit film splitting of the coating colour leads to an increase of base paper volume which compensates partly the loss at the application (pict. 7.7.12 – 7.7.14). Therefore volume loss of MSP coaters is comparable with curtain coaters where the film split effect at the nip exit is missing.
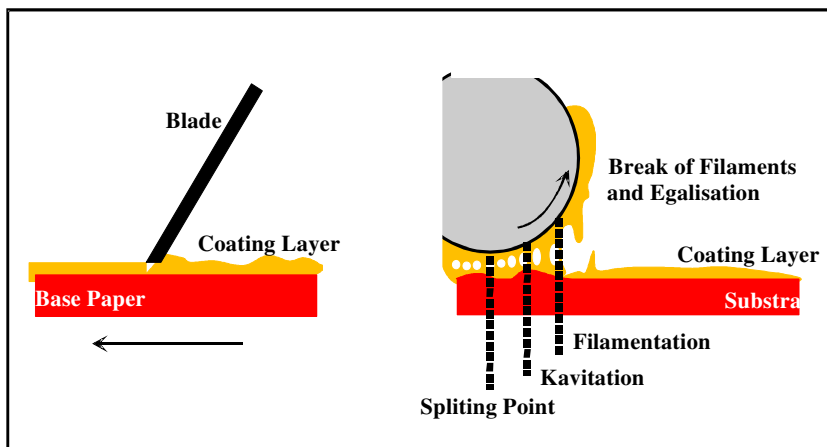
Pict. 7.7.12: Film equalisation under blade with improved smoothness and film split at nip exit of MSP coaters with increased coating roughness

	Basis weight (g/m²)	Thickness (mm)	Volume (cm³/g)	Delta volume (cm³/g)	Coat weight (g/m²)
Base paper for 115 g/m² (blade)	68,2	0,086	1,267		
Blade precoated paper for 115 g/m²	94,7	0,094	0,996	**0,272**	*26,3*
	(Datas from coat weight control PM11)				
Base paper for 115 g/m² (MSP)	62	0,0786	1,267		
MSP precoated paper for 115 g/m²	85,7	0,093	1,082	**0,185**	*25*
(from 11-65-2007)	(Datas from coat weight control PM11)				
Base paper for curtain coating	101,9	0,1281	1,257		
Curtain coated paper	116,8	0,134	1,147	0,110	*14,9*
(single sided at Vestra Lab)				**0,184**	25
Paper with 100% coating holdout and pressureless application			1,12	**0,137**	

from Mercury porosity and theor. Calculation

Pict. 7.7.13: Calculation of volume loss in 1st precoat from paper measurements

Area of investigation	m²	1	
Coat weight	g/m²	25	
Density of binder	g/cm³	1,2	
Density of pigment	g/cm³	2,6	
Binder content in coating colour	%	12	Pigment = 100%
Binder content	%	13,44	Pigment + Binder = 100%
Pigment content	%	86,56	Pigment + Binder = 100%
Volume of dry coating without air	cm³/g	0,445	Base paper: 1,257 cm³/g
Density of dry coating without air	g/cm³	2,248	
Porosity of coating layer	cm³/g	0,115	From Mercury porosimetrie
Volume of dry coating with air	cm³/g	0,560	Base paper: 1,257 cm³/g
Density of dry coating with air	g/cm³	1,786	
Binder	g/m²	3,36	
Pigment	g/m²	21,64	
Spec. Volume of binder	cm³/m²	2,800	
Spec. Volume of pigment	cm³/m²	8,323	
Spec. Volume of air	cm³/m²	2,875	
Spec. Volume of coating	cm³/m²	13,998	
Thickness of coating layer	µm	13,998	At 100% coating holdout
Base paper basis weight	g/m²	101,9	Base paper for curtain coating
Base paper thickness	mm	0,128	
Base paper + coating basis weight	g/m²	126,9	Base + coat weight
Base paper + coating thickness (calc.)	mm	0,142	Base + coating thickness
Spec. Volume of coated paper (theor.)	cm³/g	1,120	

Pict. 7.7.14: Calculation of theoretical coating volume and coated paper volume

G. Engström and V. Morin (L 4.11) studied base paper compression by blade forces and its impact on surface roughness of w'fr and w'c base papers.

Increasing blade pressure led to a more pronounced base paper surface compression. The compression was substantially.
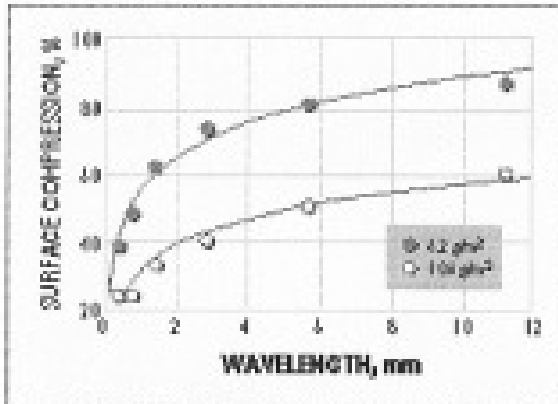
Pict. 7.7.15: Surface compression of the base paper at 6,2 and 10,6 g/m² (G. Engström)

Pict. 7.7.15 shows that compression was more effective for high wave lengths (bigger floc size). The roughening after the blade was more pronounced at low wave lengths of base paper floc size and for higher coat weights due to a higher amount of drained water. It increased to 25% of the initial roughness.

7.8 Solution against mottling: Increase thickness of precoating layer

As the calculations in 7.3 have shown, liquid phase penetration under the blade can be reduced by forming an immobilized layer before the blade.
Capillary sorption of the substrate must be high enough and/or coating colour water retention must be adjusted. Longer dwell time like in board machines lead most often to an immobilized layer before the blade

Fibro-DAT measurements showed that capillary sorption is the same at flocs and voids (pict. 7.8.1). Therefore thickness of immobilized layer will also be the same.
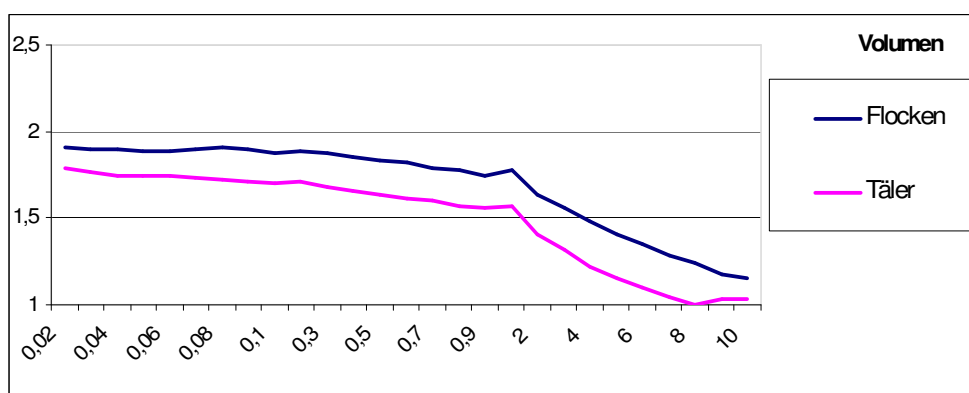
Pict. 7.8.1: Fibro DAT capillary penetration of water into base paper measured by loss of drop volume (µl) with time (s)

This finding is only valid when application of coating colour is done at lowest possible pressure (jet applicator). If more fibres are wetted at flocs (due to higher local pressure) capillary sorption will be more pronounced at flocs.

Increasing thickness of immobilized layer before the blade by reducing the water retention of the coating colour or by increasing the porosity of the middle coating layer would be detrimental for mottling as penetration of liquid phase under the blade would be increased by this measure due to lower liquid phase viscosity.

A successful measure to increase thickness of immobilized layer before blade is the increase in length of free draw before blade. Valmet/Metso did this by inventing the Opticoat Duo where dwell time between application and blade could be adjusted by the distance between application unit (separate backing roll) and blade unit.

Summary dewatering before and under the blade:

- Capillary pressure of base paper fibres dewaters the coating colour before and after the blade. Capillary sorption of coating layer is much lower than for base papers as most of the pores are plugged with fine particles.

- Latex particles and soluble binders like starch penetrate with the liquid phase of the coating colour during capillary sorption. Higher amounts of binder penetration increase the risk of drying induced back trap mottling. Therefore smooth drying conditions should be applied when high amount of binders are sucked into the base paper like in precoating stations where capillary sorption is high.

- Capillary sorption is reduced with every coating layer. When the coverage of the base paper fibres is perfect after middle coating no sorption is detected anymore.

- An immobilized layer before the blade reduces the pressure penetration up to 15% and has therefore a positive impact on mottling. This layer is formed at pre and middle coaters but no more at top coaters. Thickness of immobilized layer is limited by runability at the blade.

- In-plane permeability and thickness of immobilized layer should be uniform as no difference was found in capillary sorption of flocs and voids.

- Therefore pressure penetration is the main cause for mottling in phase A – C.

- The lack of an immobilized layer before top coater blades increases the risk of formation induced mottling as local pressure is higher at flocs and more latex is pressed into the precoatings.

- Coating holdout (exactly spoken: fine particles, solubles and liquid holdout) improves with lower permeability of the substrate. Permeability of coating layers can be reduced by the formulation and the holdout of fines (see chapter "dense precoatings"). Holdout improves with the number of coating layers.

- The denser the surface of the substrate, the lower the penetration differences of the following coating layer will be and the better the print mottle will be.

7.9 Drying (Phase D)

Capillary sorption rules this last part of coating process, similar to the penetration (phase B), between application and blade.

According to Carman Kozeny the penetrated amount of liquid phase from coating colour m_f/A is proportional to the square root of penetration time multiplied with square root of pressure $\sqrt{p} * \sqrt{t}$. Comparing this factor it is obvious that most of the water from coating colour including soluble binders and cobinders is absorbed in phase D (pict. 7.9.1). Therefore the risk of drying induced mottling is high in this phase.
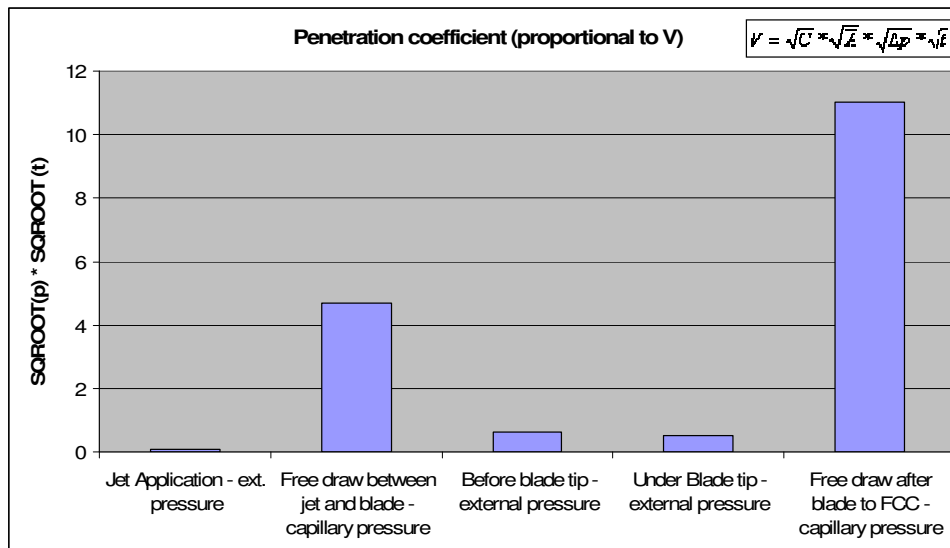
Pict. 7.9.1: Penetrated liquid in blade coating phases

To reduce the risk of drying induced mottling the penetration time for the liquid phase after the blade should be kept as low as possible. Drying must start fast and high specific energy input and evaporation rate is necessary to avoid excessive latex penetration into the base paper.
Coaters with delayed drying provoke mottling by local differences in latex surface concentration as a high amount of binder and cobinder penetrates the substrate by capillary sorption with the liquid phase into the base paper and will be moved later with water to the surface during drying. Evaporation will take place where coating

layer permeability is locally low and more binder particles, soluble binders like starch and cobinders like CMC will be transported to these spots.

As the structure of drying induced mottling doesn't correspond to base paper floc structure it can be assumed that drying induced mottling pattern is a kind of random structure.

To reduce latex penetration in phase D the following measures can be applied besides start drying as fast as possible:
- Increase thickness of the immobilized layer after blade, e.g. by lower delta solids between application and immobilization solids
- Reduce permeability of immobilized layer
- Increase viscosity of liquid phase in coating colour by synthetic thickeners
- Reduce blade pressure to reduce penetration depth, wet less fibres and delay capillary sorption

Pict. 7.9.2 shows that drying induced mottling was more pronounced for single coated papers than for triple coated papers:
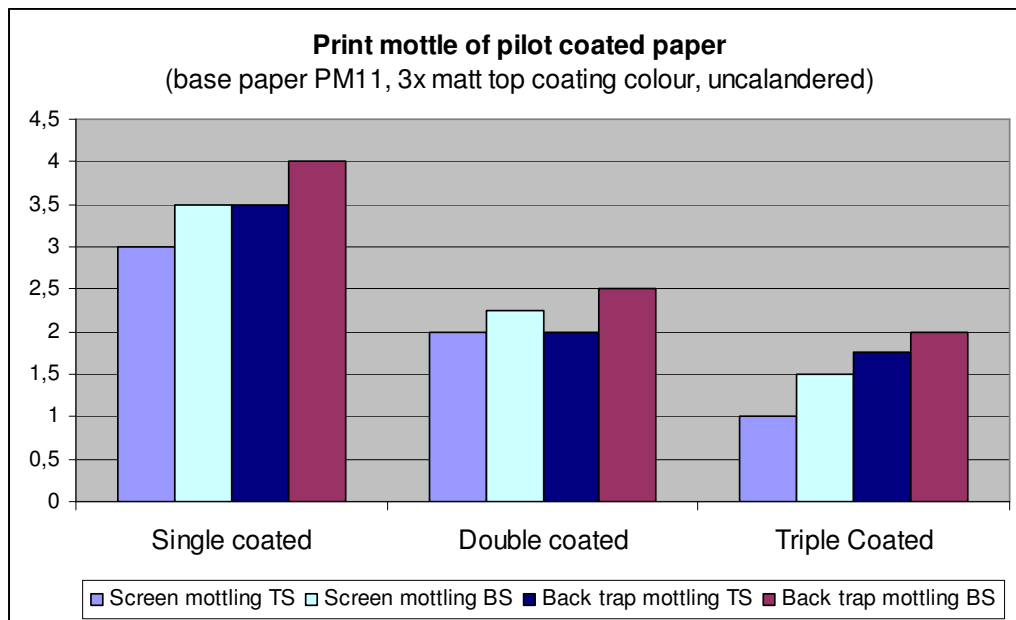
Pict. 7.9.2: Mottling of single, double and triple coated paper (pilot trial with same coating colour)

Capillary sorption pressure, shown in chapter "capillary sorption", is much higher for base papers than for double precoated papers. Therefore the risk of drying induced mottling increases as more water is soaked into the base after application and more drying energy is needed for evaporation (see chapter "drying induced mottling").

Top coatings applied on double precoated paper have a disadvantage which raises the risk of latex penetration in phase D: They contain low amounts of latex as coating holdout is usually excellent. Therefore the permeability of the immobilized coating layer is much lower than for top coatings applied on base papers.

G. Engström (L3.3 and L3.7) found for single coated papers that high drying rates before the FCC led to better mottling as the latex couldn't penetrate by capillary forces into the base paper between blade and FCC.

Binder migration increased as distance between blade and 1st dryer was increased. Engström measured the standard deviation of latex surface concentration in the top layer he scrapped off from the coated surface. He found the 2σ of latex surface concentration was reduced by higher initial drying rates.

Internal sizing of base paper did not improve latex holdout and increase the level of latex surface concentration (pict. 7.9.3). However standard deviation of latex surface concentration was highest for the sized paper. For a single base paper grade the standard deviation of latex surface concentration.
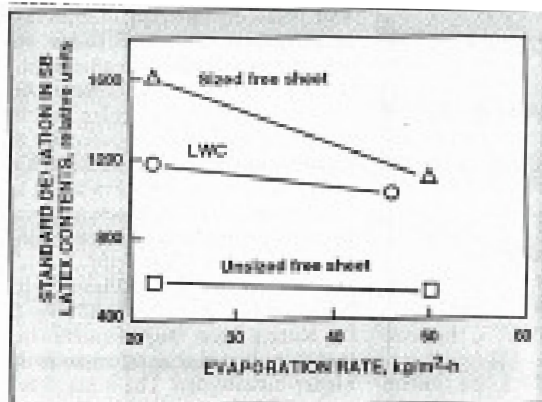
Pict. 7.9.3: Standard deviation of latex surface concentration (G. Engström)

R. Groves and A. Lanham (L3.15) showed that pore volume of dry coatings (measured by K&N ink absorption) was higher when drying was done at room temperature than for IR drying as shrinkage of coating layer was lower. When coat weight was low, pore volume was high as the particles in the coating colour had less time to move into the ideal packing structure during drying.
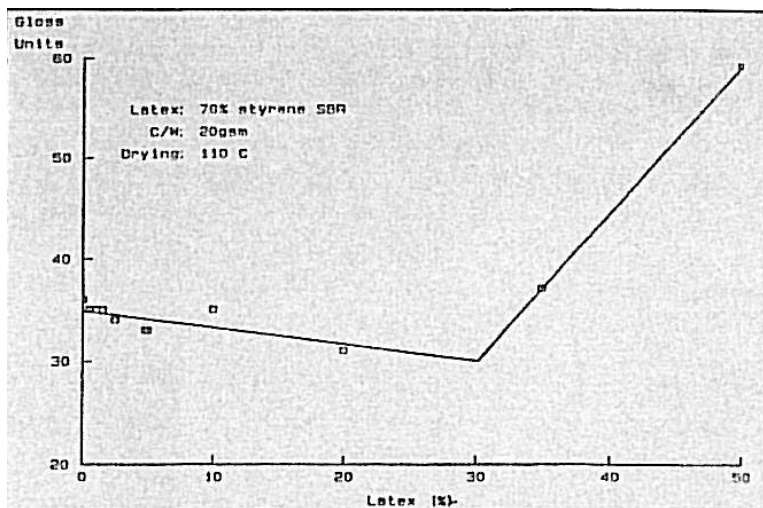
Pict. 7.9.4: Gloss vs. latex level (high coat weight) (G. Engström)

Gloss decreased with latex level but above 30% it increased sharply as the CPVC was exceeded and no voids were left in the coating (pict. 7.9.4). Therefore no shrinkage of coating layer during drying was possible over the CPVC.

At modern coaters IR dryers have replaced drying cylinders or air foils in the first part of the drying section. With IR the highest amount of specific energy can be put into the wet sheet and therefore drying starts faster than with drying cylinders or airfoils. The only exception is the use of modern airfoils with high air speed (> 90 m/s) and high temperature (> 350 °C) like Powerdry unit from Metso. But airfoils have a big disadvantage against IR-dryers: They dry mainly the top surface coating layer. SCC is reached fast at the surface and surface porosity drops fast with evaporation. The removal of water, which has penetrated into the base sheet before evaporation has been started, gets more difficult. The main advantage of IR is the faster rise in temperature across the whole sheet instead of surface sealing by immediate evaporation of the surface water.

Water, which is heated up inside the web needs less transport energy to the surface as the surface layer is kept wet by slow evaporation and diffusion speed increases with temperature of water.

Water inside the base paper is transported to the surface without "sidesteps" in XY direction due to spots which reach the FCC faster than spots next to them.

Measurements of OMYA showed that porosity of coating drops by 50% between FCC and total dry. Thus water evaporation through dense coating layers at the surface, which have exceed the SCC, requires high drying energy rates and leads to mottling as water (+latex) takes the easiest way to the surface through spots of the top coating colour with the lowest porosity. At these spots latex surface concentration will be higher leading to lower local coating layer porosity and lower ink absorption in printing = more back trapping of ink.

Lower solids in coatings lead to more pronounced mottling as more water will be soaked into the base paper after the blade. Local pressure under the blade will be higher at base paper flocs (see lab press experiments). Therefore liquid phase of the coating colour will be pressed deeper into the base paper at flocs. Capillary sorption will be locally higher as more fibres are wetted. Coating layer will reach the FCC faster. In consequence the coating layer porosity will be lower at flocs and latex will migrate to the surrounding area and will be enriched there at the surface.

Helmut Graab (L6.1) from Zanders applied different drying conditions in the 2nd drying part an off-coater to study the influence on mottling. In the 2nd drying part surface moisture so low, that vapour pressure under the surface is lower than the saturation pressure. Evaporation speed drops exponentially and web temperature increases. Vapour is transported to the surface only by diffusion. In the off-coater of Zanders the 2nd drying part could be adjusted by air speed and temperature of airfoils.

When air temperature was increases at the airfoils to lower end moisture, severe mottling occurred. The same result was achieved when coat weight was increased and the FCC (where the 2nd drying part starts) was shifted from IR-section into the airfoil section.

R. Aust (L6.3) from IR supplier Krieger set up a calculation for evaporation curve in the whole drying process (part 1 – 3). From various mill rebuilds where IR dryers replaced airfoils he found out that mottling improves when drying rate is high in the 1st drying part. The focus of Krieger was to maximized energy output of IR-dryers to improve mottling by fast evaporation in the 1st drying stage and avoiding penetration of liquid phase into base paper.

Three different IR dryers are commonly used in paper industry:

Metal Emitter
(KRIEGER standard)

Ceramic Emitter
(with screen)

Fibre Emitter
(w/o screen)
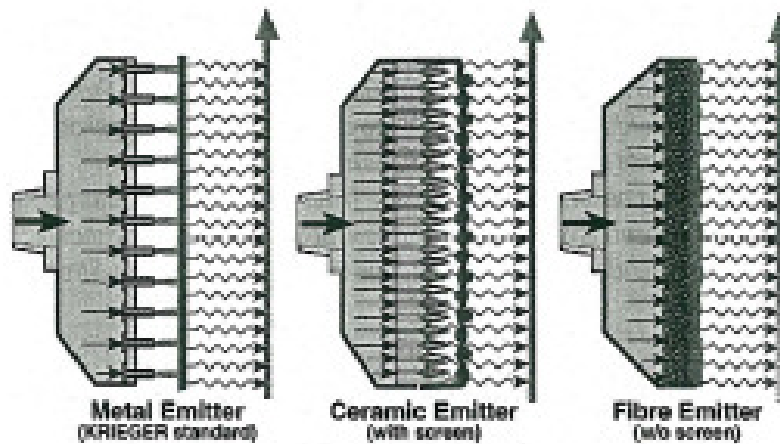
Pict. 7.9.5: IR dryers with metal, ceramic and fibre emitter (R.Aust – L6.3)

In all versions the flame hits the back side of the emitter and increases it's temperature by convective transmission. The flame itself has no energy in the IR wavelet range. Power output increases with temperature of emitter.

$$\eta = \frac{\varepsilon A \sigma (T_s^4 - T_p^4)}{V_g H_u}$$

$$P = V_g H_u / A = V_A \Delta H_A / A + \varepsilon \sigma (T_s^4 - T_p^4)$$

Spec. Power Input = Energy Flow of Exhaust Gas + Radiant Power
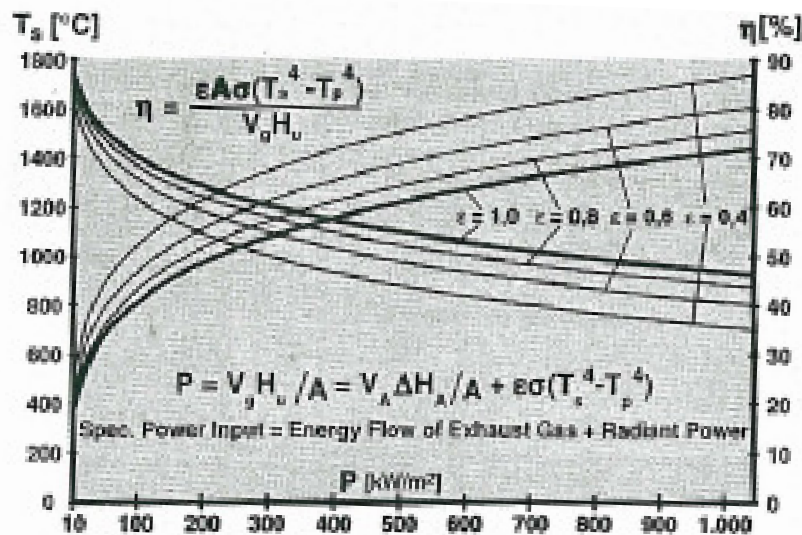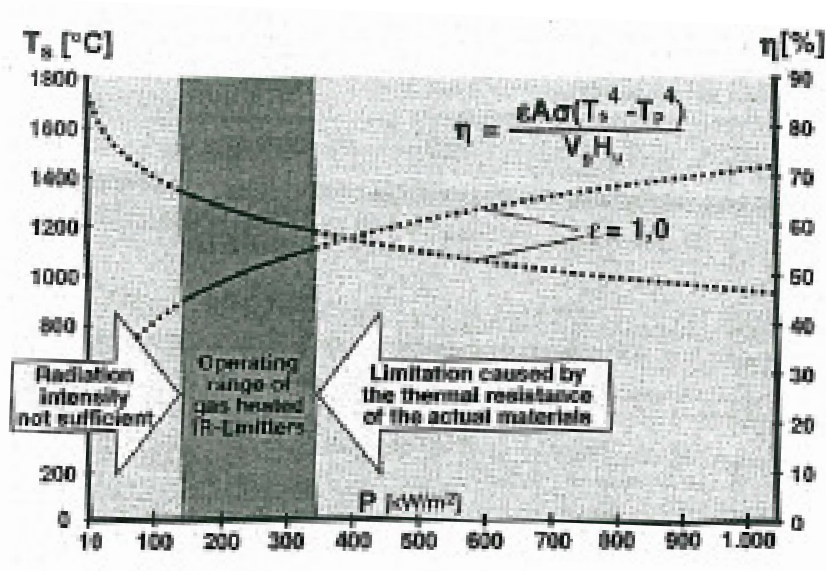
Pict. 7.9.6: Specific power of IR dryers as a function of flame temperature (R.Aust – L6.3)

The operating window of IR's is in the range of 140 – 340 kW/m². It's limited by thermal resistance of materials in use. For metal emitters input power is typically 220 kW/m², the corresponding emitter temperature is 1100 °C. Output power is 115 kW/m when efficiency is 52% (pict. 7.9.6 – 7.9.7).
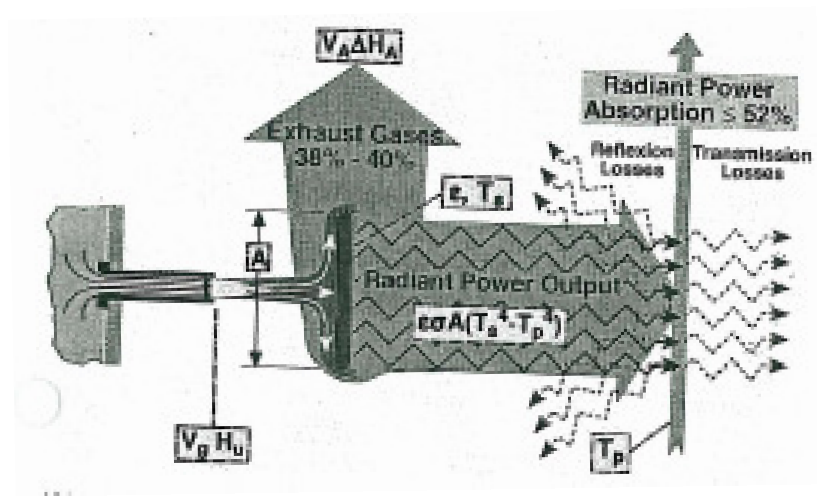
Pict. 7.9.7: Efficiency of metal emitter (R.Aust – L6.3)

IR dryers are low in efficiency. Less than 50% of the gas energy input is transferred into radiation energy.

To define the efficiency of an emitter it is compared to a black emitter which emits 100% of the energy input.

Metal Emitter: 52% - max. power 4,2 kW per module 150x200 mm

Ceramic Emitter: 46% - max. power 3,5 kW/module

Ceramic Fibre: 40% - max. power 2,7 kW/module
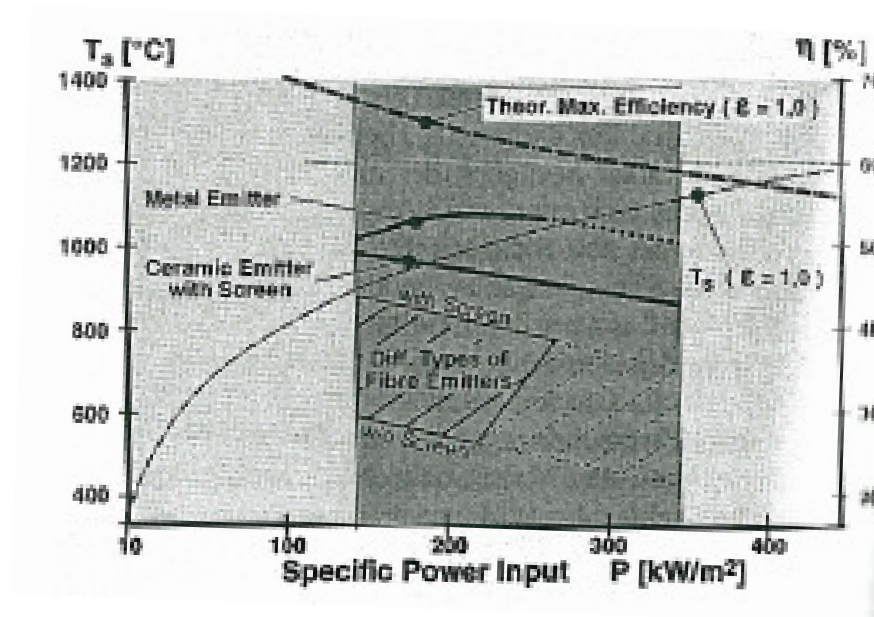
Pict. 7.9.8: Efficiency of different emitter materials (R.Aust – L6.3)

Efficiency drops with operating time as coating colour is deposited at the emitter surface during breaks of the web. Therefore the distance between IR dryer and web has to be increased. Absorbed energy drops with the forth power of distance,

Modern IR dryers are equipped with ceramic emitters where less coating colour is absorbed at the emitter surface during breaks than at metal or fibre emitters. Therefore the distance to the web can be reduced when ceramic IR-dryers are in use.

OMC11 was equipped with fibre emitters which could be operated theoretically at higher emitter temperatures. As many of them exploded when coated at the surface with coating colour the temperature had to be lowered to the same level of conventional IR dryers.
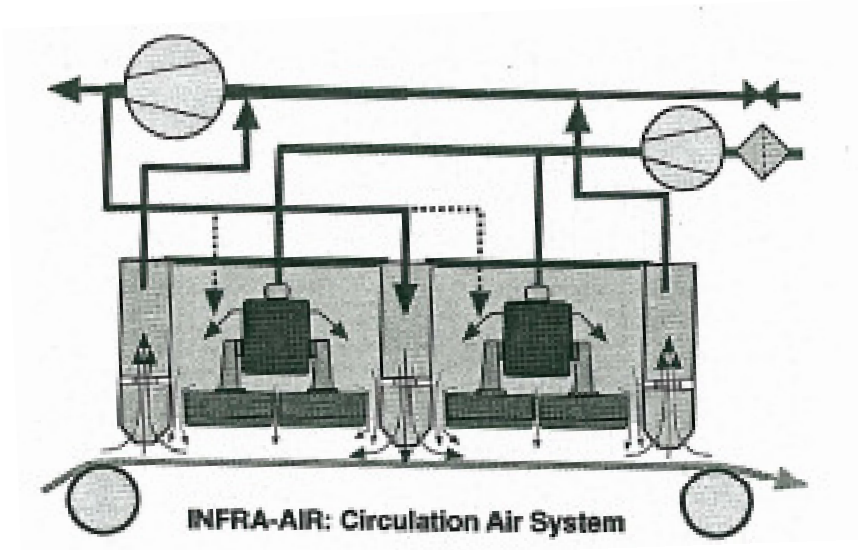
Pict. 7.9.9: Air circulation at IR-dryers (R.Aust)

Modern IR's have an air circulation system (pict. 7.9.9). The air from the circulation is blown on the coated surface, heated up by the IR and is soaked from the web at the end of the IR-unit. According to R. Aust drying energy efficiency improves by 3% (e.g. from 52 to 55%) when convective energy of the air circulation is used additionally to IR radiation.

Air speed is limited by ignition of the IR rows: When high air velocity is too high the ignition flame is blown out when the IR is started.

Modern concepts like integrated IR dryers or Infrafloat provide the highest possible energy input and drying rates (pict. 7.9.10):
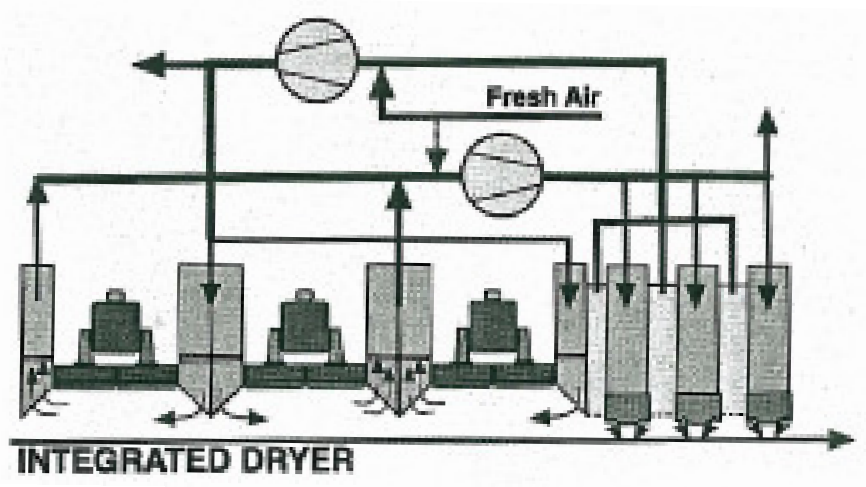
Pict. 7.9.10: Combining IR radiation energy with airfoil (R.Aust)

The INTEGRAL dryer of Krieger uses the heat of the IR rows in the following air dryer. Efficiency increases to 60% and up to 150 kW/m² output power can be transmitted to the paper (pict. 7.9.11).
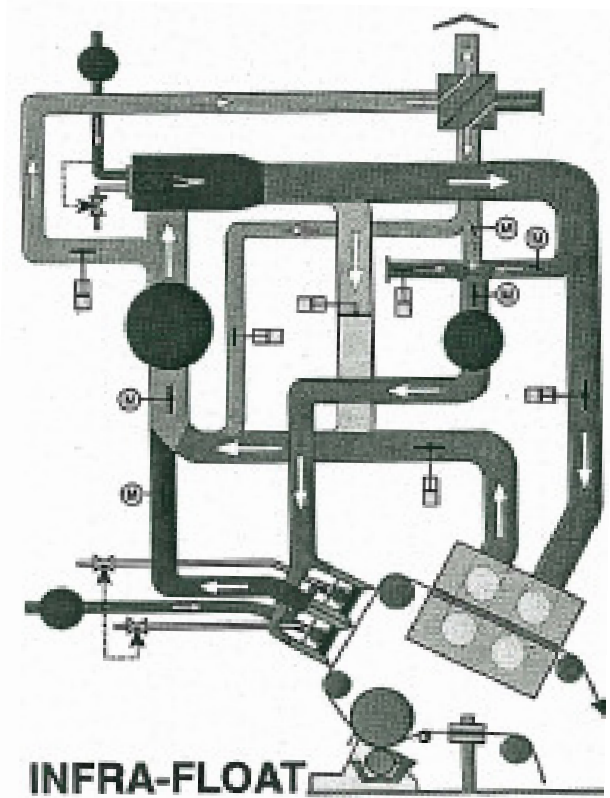
Pict. 7.9.11: Krieger Infra-Float integrated IR/airfoil system (R.Aust)

A similar concept is the INFRA-FLOAT system: The hot air from the IR rows is recirculated into the following air dryers. The overall efficiency is raised.
This system was realized at all coaters of CM11.

A comparison of the efficiency of IR dryers installed in pilot coaters with the data's of R. Aust is show in the chapter "drying induced mottling".

V. Traudt (L 6.14) calculated evaporation rate of conventional IR-dryers with metal emitters. 4 IR rows led to 30 kg/m h, 8 rows to 90 kg/m h and 16 rows to 270 kg/m h of water evaporation. The optimum in mottle was found when web temperature of an

LWC top coating was increased to 80 – 90 °C and web cooled down in the following air dryers to 70 °C by temperature loss with evaporation under moderate operation of air dryers (pict. 7.9.12).
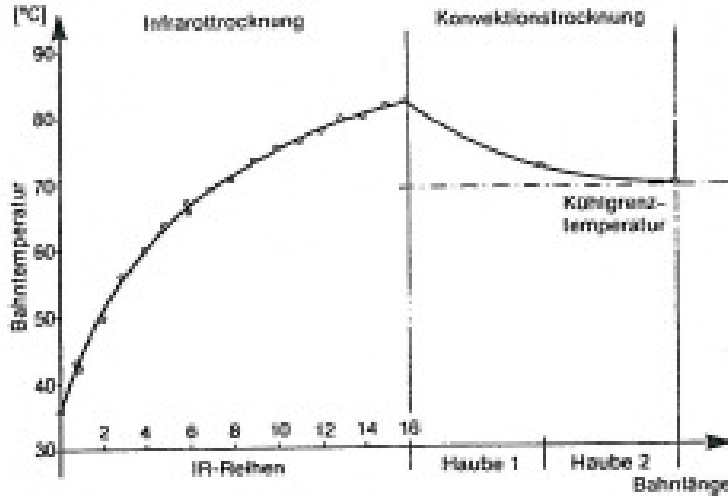
Pict. 7.9.12: Web temperature in a LWC coater (V. Traudt)

Ph. Norddahl (L6.6) studied the effect of drying conditions on single coated LWC print quality. He used low solids coatings based on clay (pict. 7.9.13 – 7.9.14).
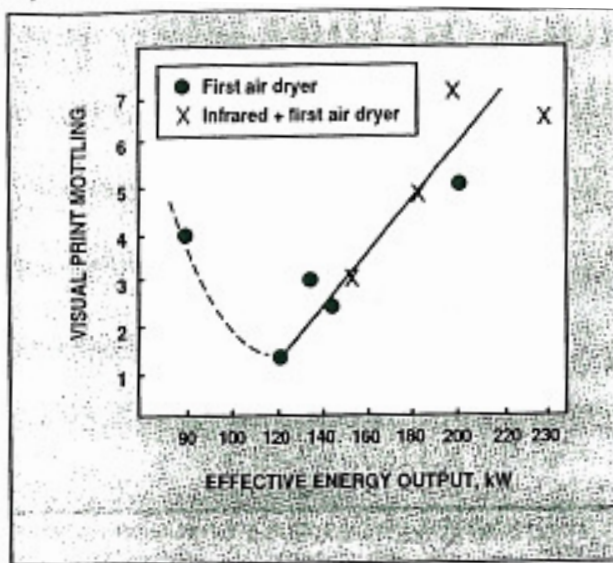
Pict. 7.9.13: Print mottle as a function of initial drying energy (P. Norddahl)
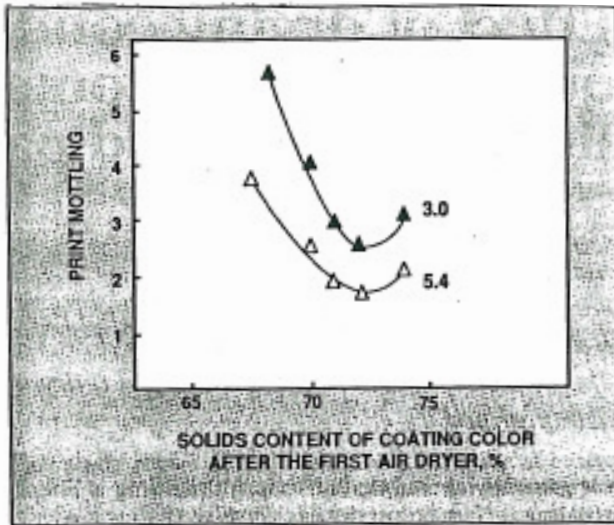
Pict. 7.9.14: Effect of the solid content after the initial drying on print mottling (P. Norddahl)

He showed that mottling worsens with lower energy input in the 1st drying stage (pict. 7.9.15) and in consequence lower solids after the first drying unit. He found a linear correlation between mottling and solids of partly immobilized coating colour before the intensive air drying zone.
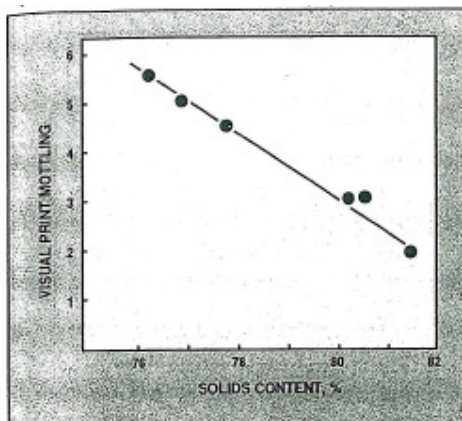
Pict. 7.9.15: Print mottling as a function of coating layer solids before high drying rate zone (P. Norddahl)
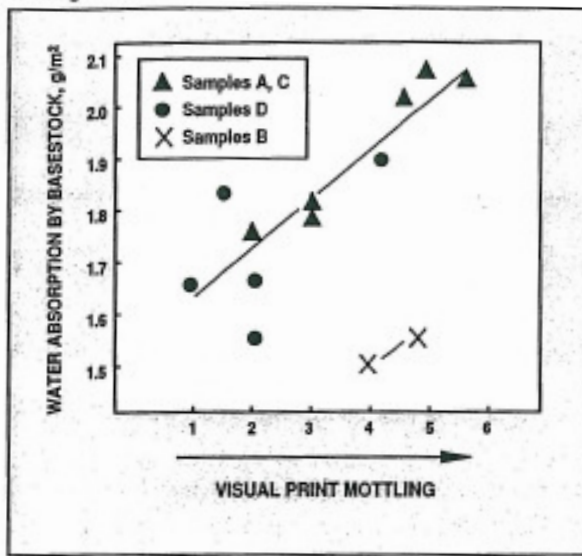
Pict. 7.9.16: Influence of base paper water absorption on print mottling (P. Norddahl)

Mottling got worse with rising water absorption of base paper (pict. 7.9.16) and drying energy in the 2nd drying part. P. Norddahl concluded that when coatings are applied on a hot base stock with high water absorption, drying has to start sooner to avoid water penetration into the base paper. P. Norddahl found no difference in mottling between IR or airfoil as an initial drying units.

P. Rajala (L6.7) made a statistical investigation of drying effect on offset paper quality. At three different pilot coaters 107 pilot trials were made on a 40 g/m² LWC base paper. Variations were made in coating formulations (100% clay, 50/50% clay / $CaCO_3$, starch/latex), speed (1000 – 1800 m/min), applicators (LDTA, SDTA, jet) and drying strategies. Solid content in the coating layer was calculated and measured at different positions during drying.
Increasing web temperatures in the initial drying period lead to more pronounced roughening of the surface due to faster drying or the coating and higher shrinkage forces.
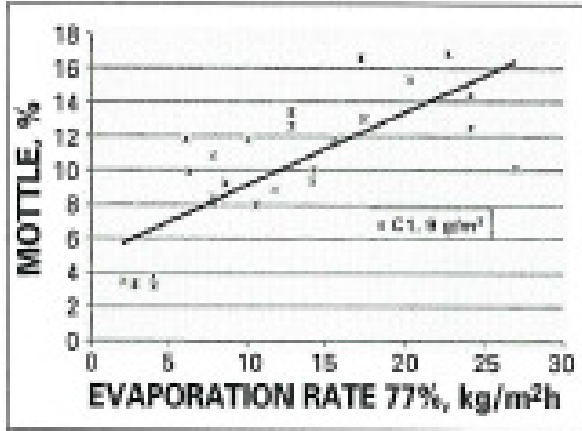
Pict. 7.9.17: Mottle vs. Evaporation rate at 77% solids (6% starch / 6% latex, delay to air drying 340 ms) (P. Rajala)

Mottle got worse when evaporation rate was high after FCC at 77% solids, when high amounts of starch were used in the coating colour formulation (pict. 7.9.17). For latex based coatings the correlation was not that significant.

Carbonate based coating were generally better than clay based coatings as their solid content was higher, less water was absorbed by the base paper in the 1st drying stage and FCC was reached faster.

J. Paaso (L6.8) equipped the KCL pilot coater with a series of new measuring instruments in 8 positions distributed over the drying zone, which measured simultaneously surface gloss and diffuse reflection with multiple geometries (pict. 7.9.18). These totally new instruments were designed by VTT Electronics in Oulo.
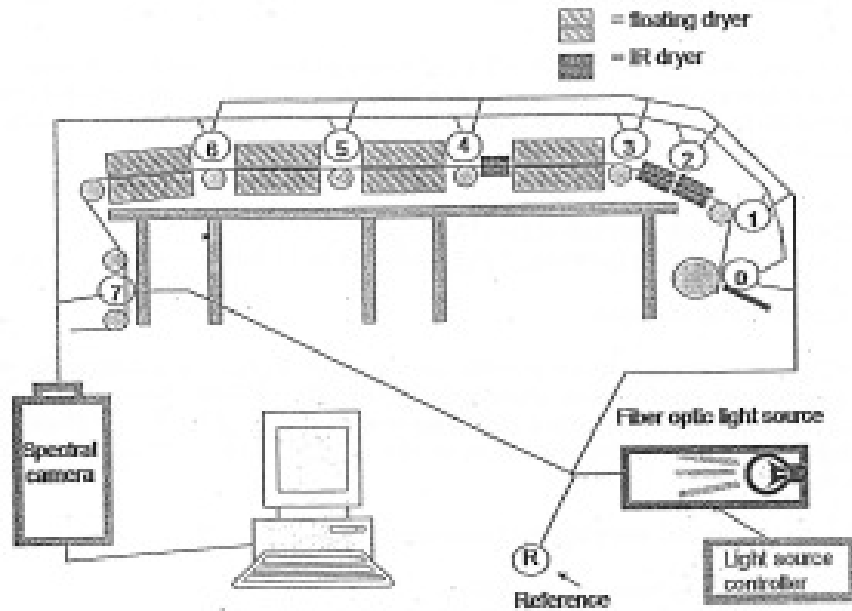
Pict. 7.9.18: KCL pilot coater

At the FCC the surface gloss drops exponentially. At the SCC diffuse reflectance (scattering) rises sharply.

The moisture was measured by IR at the coated surface and at the bottom side to determine the amount of water which has been absorbed by the base paper.

The instruments were positioned on top of the paper and on the bottom side.

10 g/m² coating was applied on uncoated base paper.
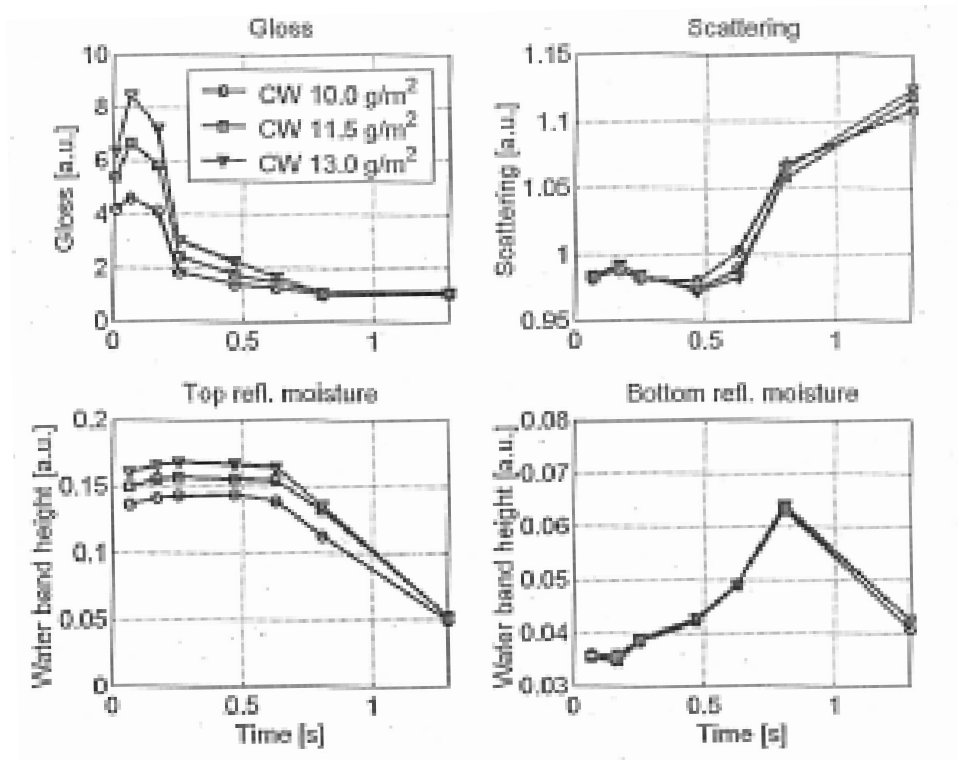
Pict. 7.9.19: VTT measurements for different coat weights (low-low-high drying strategy) (J. Paaso)

When drying was delayed by low energy in the 1st drying stage, FCC was reached after 0,25 sec and SCC after 0,75 sec (pict. 7.9.19). A significant increase in base paper moisture was detected until the SCC was reached. It increased with drying time which indicates that more water is absorbed by the base paper when temperature in liquid phase increases during drying. To avoid this sorption process the SCC has to be reached as fast as possible.

When coat weight was increased position of FCC remained unchanged.
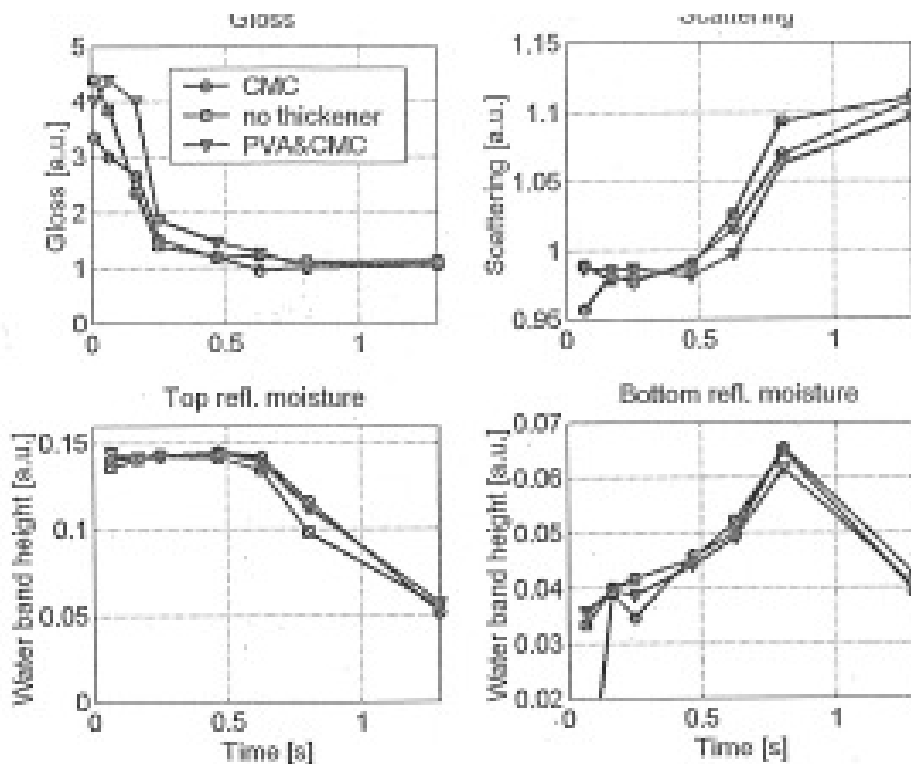
Pict. 7.9.20: Influence of thickeners (10 g/m², low-low-high drying) (J. Paaso)

Thickeners delayed the FCC and the SCC (pict. 7.9.20).

K.G. Hagen (L6.9) calculated the space for the latex particles to move during drying. 10 g/m² of coating have a wet thickness of 10,6 µm. With clay as a coating pigment this coating layer will have 21 layers of clay plates. Each wet layer has a thickness of 0,31 µm. Latex particles with 0,15 µm diameter will have enough space to move.

At the immobilization solids each layer has a thickness of 0,05 – 0,12 µm. Latex particles will have no more space to move. Latex migration will be stopped.

K.G. Hagen proposed to use electrical heated IR to increase energy input in the 1st drying part and reach immobilization solids as fast as possible. The highest drying energy is needed when water from fibre walls is evaporated through a dense precoating layer as capillary forces in the narrow fibre pores have to be overcome and permeability of precoating layer will hinder water vapour to pass.

The tungsten coil produces 2150 °C and a theoretical black body emission of 1950 kW/m². As the emitter area is limited to appr. 1/3, the energy density will be 585 kW/m². The glass cover of the electrical IR which is necessary to protect it against coating colour reduces the output to 375 kW/m², which is 3 - 4 times higher than with gas fired IR's.

But unfortunately paper absorbs IR energy mainly above a threshold of 2 µm wave length. Electric IR's have a peak of emission at 1,2 µm, gas fired IR's at 2 – 3 µm.

The lower the emitter temperature, the higher the mean wavelength and the higher the efficiency according to the equation:

$$Q = q_{max} * \int \alpha * \varepsilon * d\lambda$$

Q_{max}...peak emitted energy flux

α. ....paper absorptivity

ε ....relative emitter output

λ ....wavelength

K. Yamazaki (L6.11) developed a unique lab coater to apply coatings with an application speed of 45 m/min and drying them immediately after application (pict. 7.9.21).
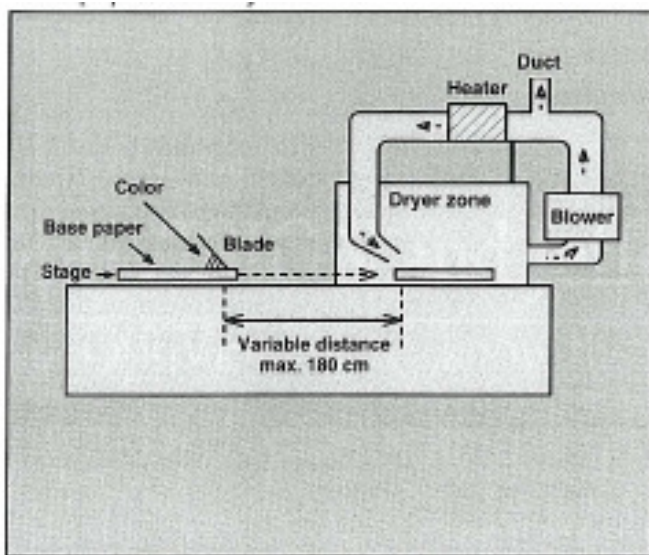
Pict. 7.9.21: Lab coater of K. Yamazaki
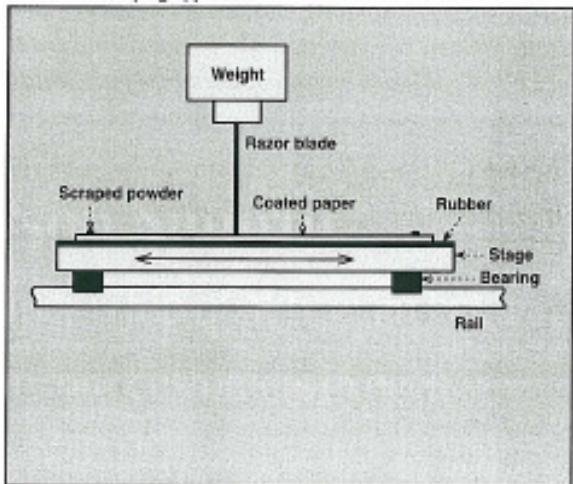
Pict. 7.9.22: Surface scraping apparatus (K. Yamazaki)

Latex surface concentration was measured by scrapping of the dry coating and measuring it by ECSA (pict. 7.9.22).
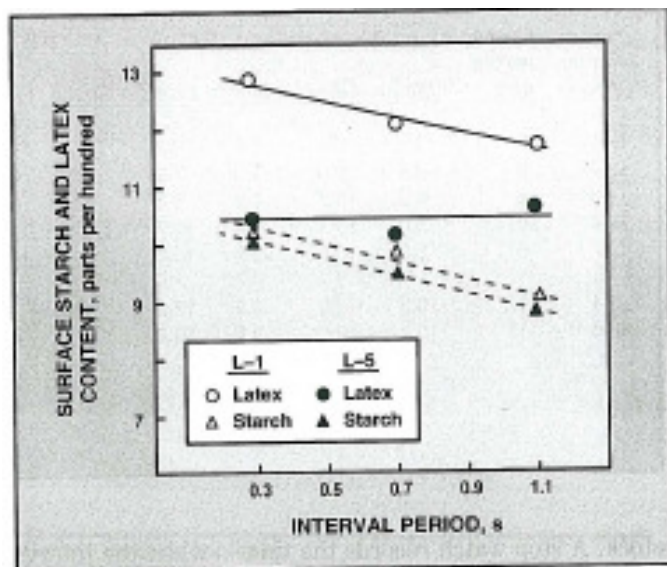
Pict. 7.9.23: Grooved rod coating (17g/m²) – influence of interval time between blade and dryer (K. Yamazaki)

Starch was soaked with water to a greater extend into the base paper than latex. Surface concentration of latex was higher for all trials (pict. 7.9.23). When Latex L-5 was used no migration to base was detected due to interaction with clay particles. The lab trials were confirmed by pilot trials where surface concentration of latex and starch was always lower than in the original coating due to base paper sorption.

E.J. Heisser and D.W. Cullen (L6.12) studied latex migration at a pilot coater for clay based coatings applied on a base paper.

A mechanical abrader was used to section the coating layer. A steel wool was moved over the surface on a reproducible path. The coarseness of the wool and the number of movements over the surface determined the depth of the cut. Latex was isolated by washing the cut with nitric acid.
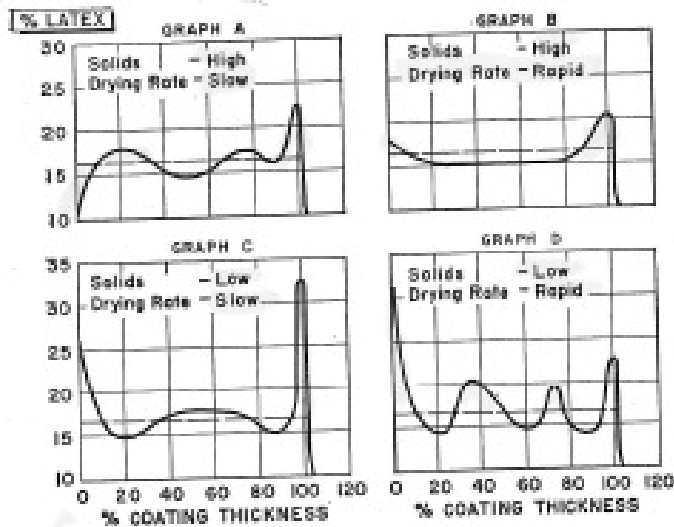
Pict. 7.9.24: Coatings on paper (zero percent = coating surface) (K. Yamazaki)

Low solids led to a severe migration of latex into base paper and to the surface during drying. Latex surface concentration was twice as high, as in the coating colour (pict. 7.9.24).

When solid content was high, latex concentration increased in the immobilized layer at the boundary to base paper.

With high drying rates latex was moved from the boundary to the surface. Rising latex surface concentrations lowered surface porosity and reduced ink and water absorption.

L. Kima and M. Pollock from DOW (L6.13) tested three different latices in clays/carbonate based coatings under different drying conditions. FCC was determined by online surface gloss measurement at the pilot coater.

Mottle was worst for all latices when drying energy was high between FCC and SCC

FCC was determined with 74% and SCC with 82% for the partly clay based coatings. Between FCC and SCC the sheet temperature raised significantly as water evaporation dropped exponentially and drying energy was transferred into increase of web temperature.

The authors suggested measuring the web temperature curve over the whole drying section to locate the critical area, where temperature raises. In this part, drying energy should be reduced.

Matti Toivakka, Dan Eklund and Douglas W. Bousfield (L6.15) calculated the package of spherical particles during drying using the electrostatic repulsive force theory of Brady and Bossis
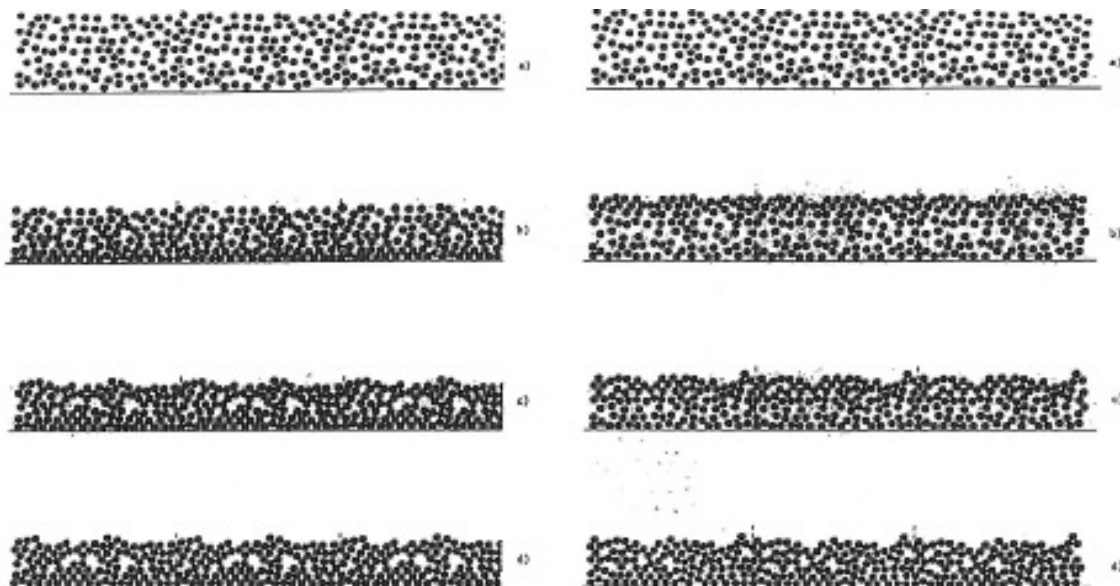
Pict. 7.9.25: Calculated pigment package; left slow drying, right: fast drying.   a) to d): increasing drying time (M. Toivakka)

M. Toivakka found out, that high drying rates produce "fluffy" coating structures with high porosity (pict. 7.9.25). The particles form fast mechanical interactions, hindering these particles to find their best packing structure.

At the surface the particles structure is very dense at high drying rates and this structure "falls" onto the lower layers during progressing drying.

High initial solids and high repulsive forces (good dispersion) produce compact structures. The hydrodynamic force pushes the spheres into a given free volume. The lower the repulsive forces, the easier the particles can move.

Pigment movement in horizontal direction during drying was calculated. The result was astonishing: Horizontal movement is almost impossible.
In Z-direction pigments move due to drainage flow and hydrodynamic repulsion as the particles move together during water evaporation at the surface.

High drying rates hinder the particles at the surface do move downwards, pigments are "locked" in their horizontal position. The "fluffy" coating structure with high porosity leads to a smoother coating surface.
Smoothness of coating layer increased also with higher solids of the coating colour.

Low drying rates resulted in a dense coating layer as particles had more time to move.
Pigment packing during drying is mainly determined by the shrinkage of the coating layer due to evaporation of water.

The models of M. Toivakka in this stage did not include the compaction of the coating layer by calendering.

Chapter 8: Solution 4 for formation and drying mottle: Thin barrier layer

8.1 Principle target

Depth of latex penetration at blade and film press coaters will be driven by surface permeability of the substrate e.g. the Darcy coefficient its precoating layer. Lowering the Darcy coefficient of the precoating layer would reduce the amount of penetrated top coating latex and additionally lead to a more even latex distribution in the top coating layer as local differences will be levelled out when level of penetration would be generally lower. Hold out of all solubles in the top coat like optical brightener, PVOH or starch and hold out of fine pigments or latices would also improve – the costs of the top coating formulation could be reduced significantly when applied on a dense precoating layer.

Two possibilities exist to reduce permeability of the precoated substrate: Either reduce the Darcy coefficient of the precoating layer by changing its formulation or apply a dense barrier layer on top of it.

In this chapter the solution of applying a barrier layer is described. When papers are triple coated, this barrier layer could be applied either on base paper or on precoated or on middle coated paper.
For double coated papers it can be applied on base or on precoating.

The later the barrier layer is applied, the better the holdout of this barrier layer will be and the more pronounced the positive effect on mottling.
On the other hand, the closer the barrier layer is applied to the top coat, the worse ink drying will be as pore volume and capillary sorption of the whole coating layer is reduced. For barrier applications close to the surface the barrier layer must have a high micro porosity at low permeability which was achieved with some of the tested substances.
A good compromise for triple coated papers is the application of the barrier after the 1st precoat. Microtome cuttings show a sufficient coverage of base paper when the 1st precoat is applied by a film press coater under low pressure.

Applying the barrier on the base paper has the disadvantage of bad hold of barrier layer on top of the uneven base paper (mean pore size 5 µm) as the barrier is in most cases a liquid or a dispersions with ultrafine particles. Costs will increase as much of the barrier material will get lost into the base.

When curtain coating is used for coating application the barrier could be applied in one step as the base layer in a multi layer coating. Pict. 8.1.1 shows the possibilities of curtain coating applications for barrier layers.
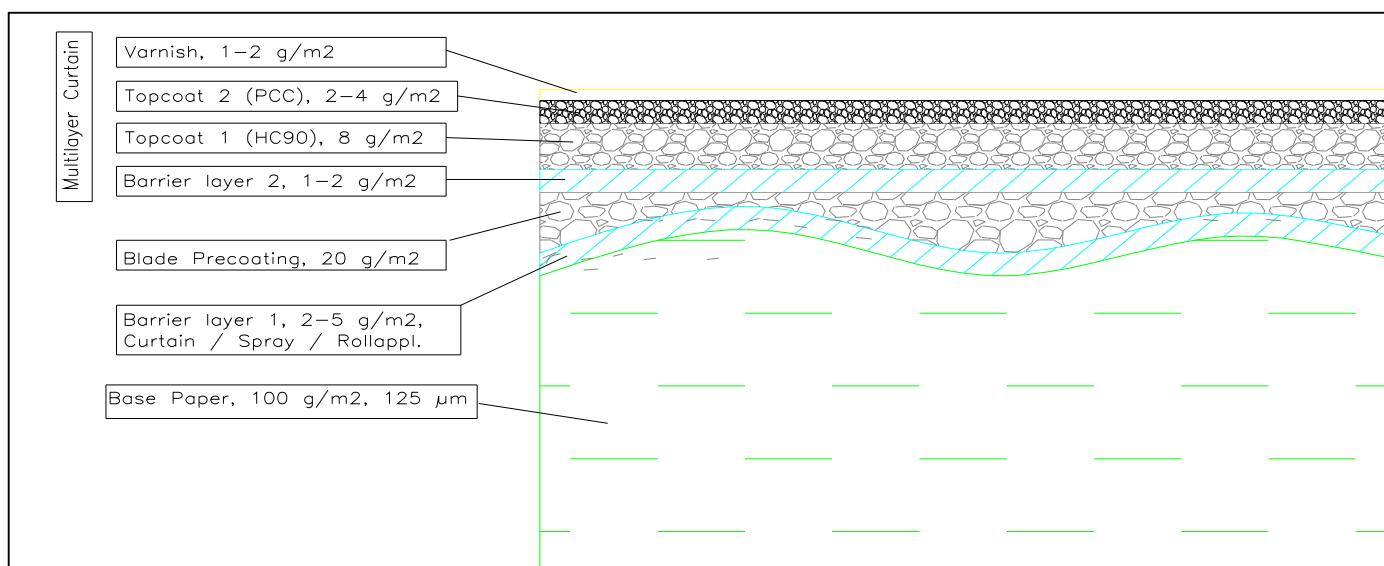
Pict. 8.1.1: Possible positions of barrier layers in multi layer coating

Possible formulations for thin dense barrier coatings:
  a) 100% liquid binder like e.g. starch or PVOH.
  b) A mixture of pigment plus liquid binder with the PVC (pigment volume concentration) under the CPVC (critical pigment volume concentration) where all interstices between the pigment particles are filled with liquid after drying.
  c) Binder dispersions with very fine particles
  d) Barrier pigments like bentonites or barrier clays (patented by Imerys) with low content of binder.

8.2 Influence of size press on mottling

Two mill trials at PM11 proved the positive effect of a simple barrier layer on mottling: Leaving out the size press, which applied a dense starch layer on the base paper, clearly worsened mottling, especially at the bottom side (lower surface ash content) of double coated grades. Both trials were made at 115 g/m² double blade coated paper (pict. 8.2.1).

Trial 1

	Standard Erz. 3608/MR3,9,903 with size press, 0,7 g/m²	Trial Erz. 3604 / MR902, without size press
Screen mottling OS	2,15	2
Screen mottling US	2,15	2,25
BTM solids 100% OS	2,25	2,25
BTM solids 100% US	2	2,75
BTM Purple OS	2,5	2,5
BTM Purple US	2,75	3,25
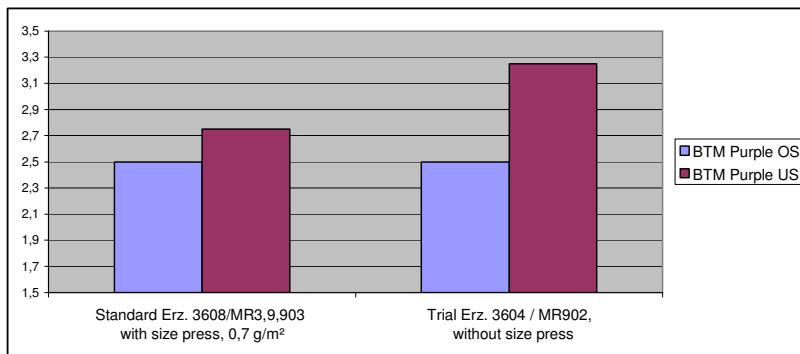
Trial 2

	Standard Erz. 3673 / MR9,17 with size press, 0,7 g/m²	Trial Erz. 3673 / MR 902,903 without size press
Screen mottling OS	2	2,25
Screen mottling US	2,15	2,5
BTM solids 100% OS	1,9	2
BTM solids 100% US	2	2,5
BTM Purple OS	2,5	2,5
BTM Purple US	2,4	3,25
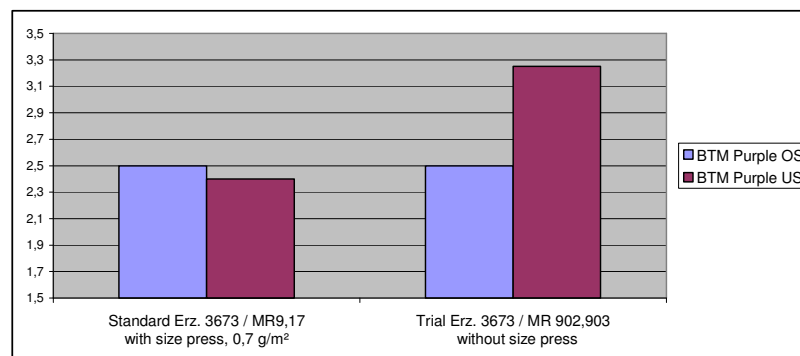
Pict. 8.2.1: Comparison of print mottle for double coated gloss 115 g/m² at PM11 with and without size press

For triple coated grades the difference in mottling with or without size press was not so much pronounced. As PM11 mainly produces triple coated grades, where starch clearly worsens cracking at the fold at heavier basis weights, the size press was left out generally in 2003.

8.3 Lab experiments with barrier layers

Different barrier formulations / substances were applied by a lab rod coater, which operates at low application pressure. The tests were performed on PM11 base paper and on double precoated = middle coated paper of OMC11 where holdout of barrier was expected to be much better. The target was to reduce permeability at lowest thickness of barrier layer. The higher the amount of applied barrier layer, the higher the costs will be as barrier liquids are very expensive substances.

Tested liquids:
- Primer varnishes with ultra fine latex particles as used in printing industry
- Starches
- CMC solutions
- Nano-pigments (Nanotop from Top Chim Ltd.)
- Acrylate dispersions
- Resin dispersions
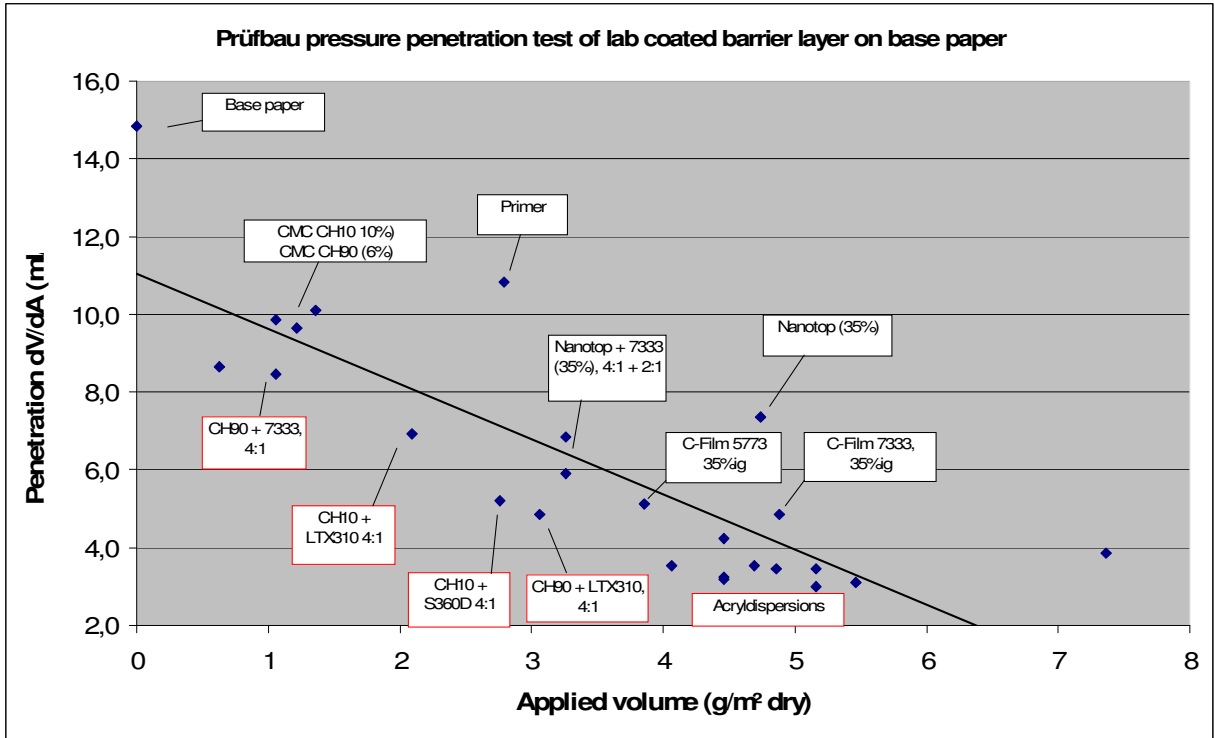
Pict. 8.3.1: Barrier effect of tested barrier substances on base paper depending on application weight (Prüfbau water pressure penetration test dV/dA in ml/m²)
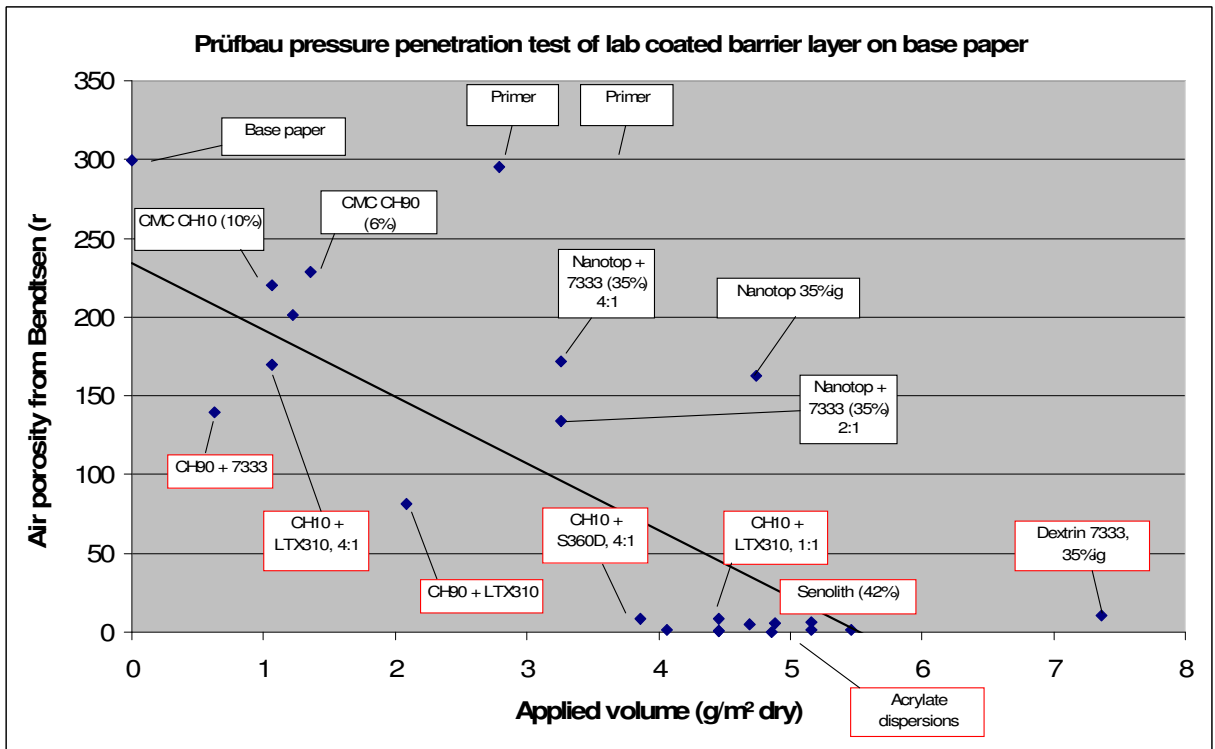
Pict. 8.3.2: Barrier layer on base paper (air porosity in ml/min)
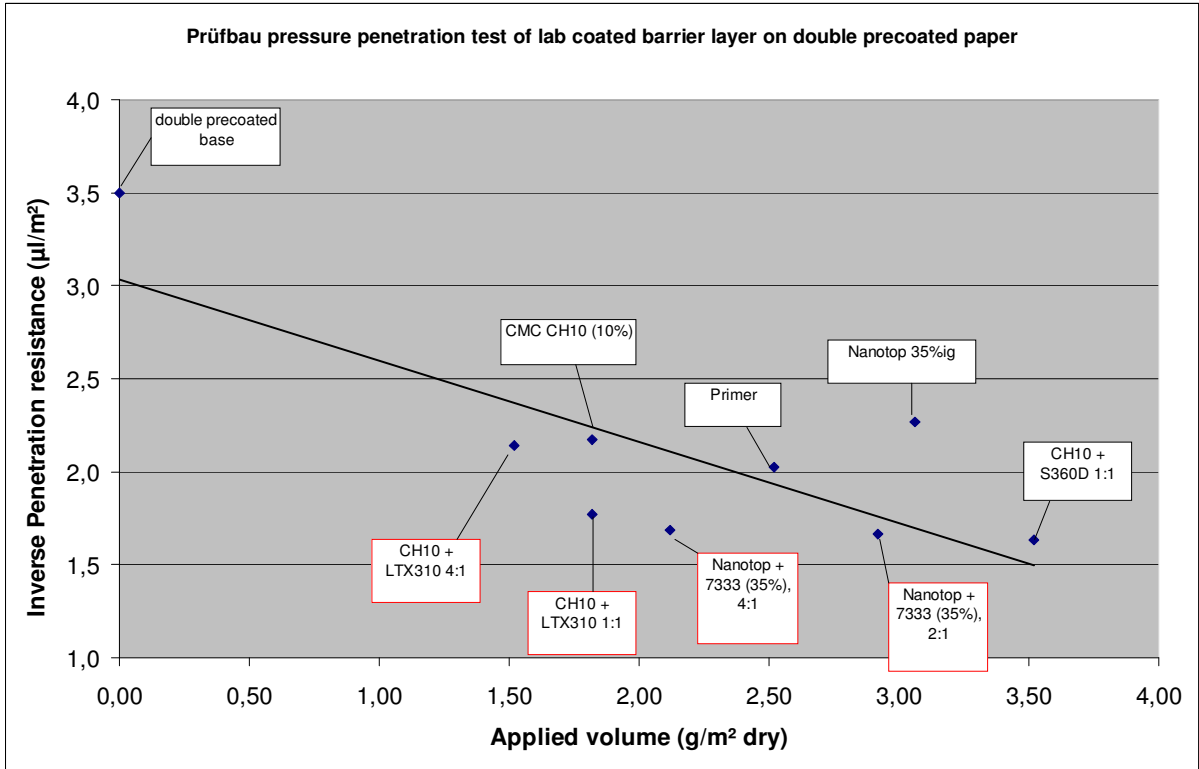
Pict. 8.3.3: Barrier layers with liquids on double precoated papers
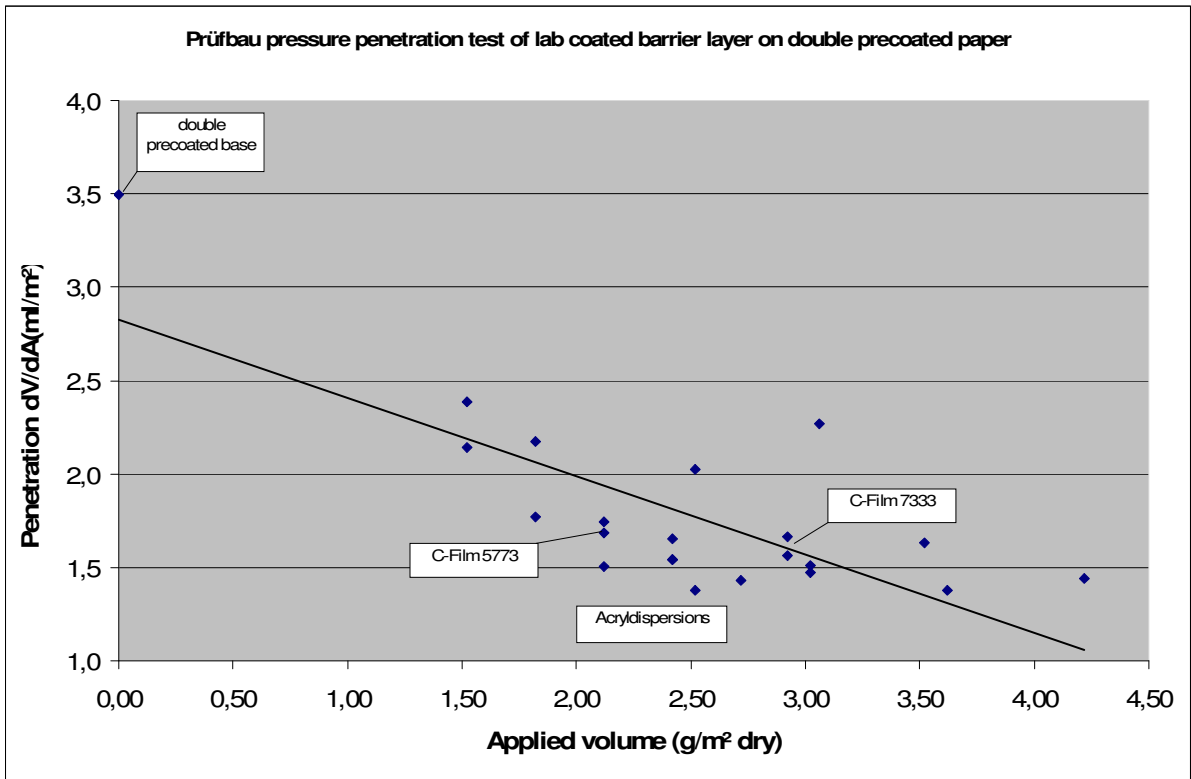
Pict. 8.3.4: Barrier layers with liquids on double precoated papers
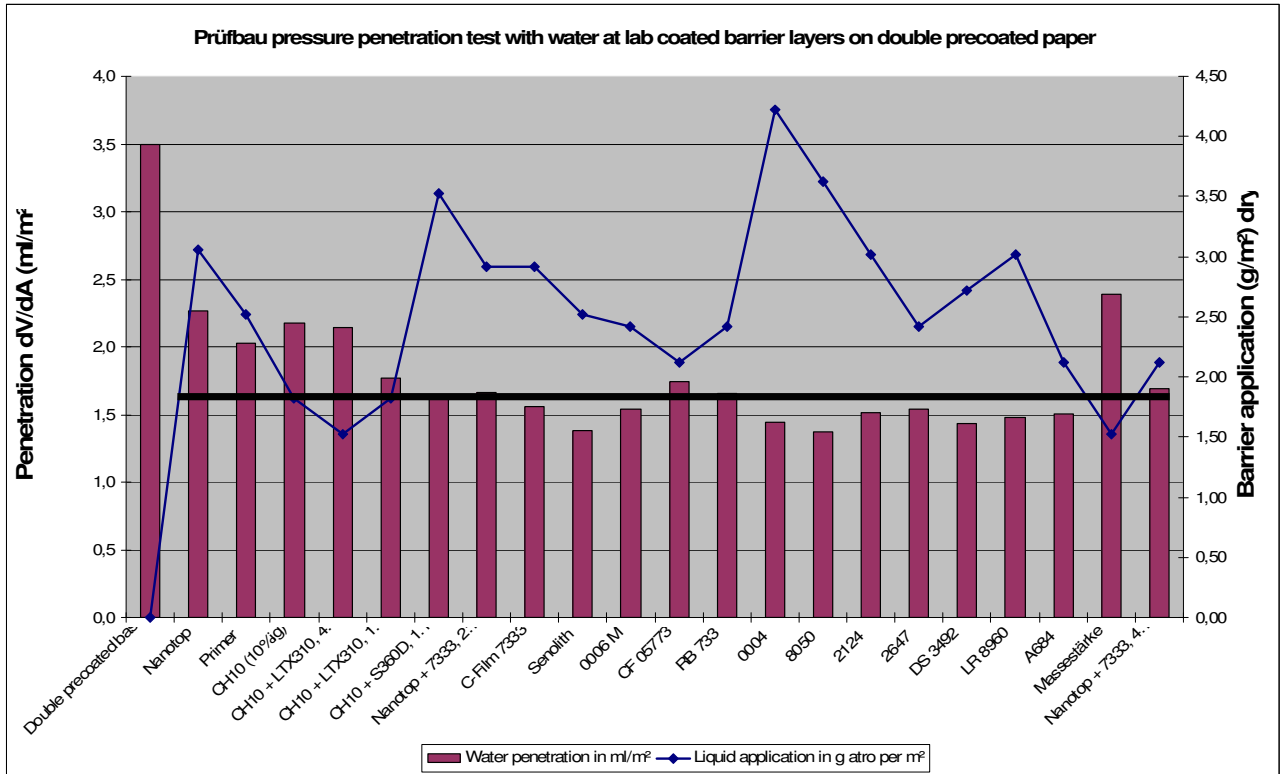
Pict. 8.3.5: Barrier layers with liquids on double precoated papers
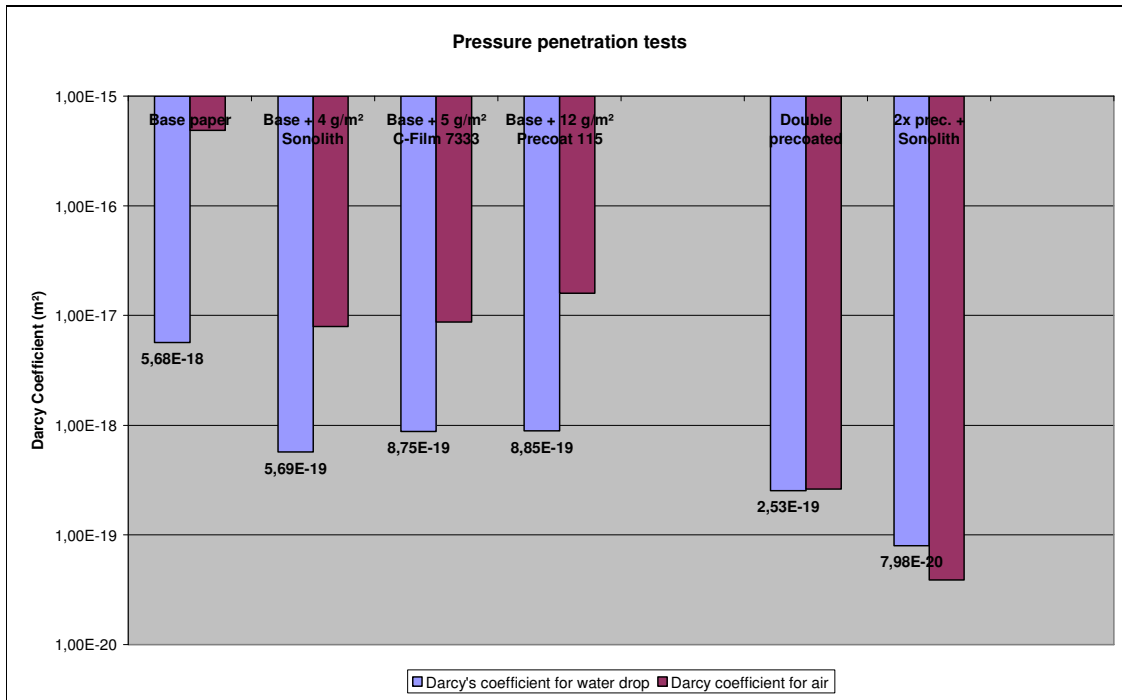
Pict. 8.3.6: Darcy coefficient of barrier layers, compared to coating layers

In pict. 8.3.1 – 8.3.6 the barrier effect of the tested barrier substances is shown by drawing the amount of applied liquid against the Prüfbau pressure penetration test (dV/dA penetrated volume of liquid per unit of area). Applying a barrier layer of 3 – 4 g/m² on base paper reduced the Darcy coefficient by one magnitude (10^{-1}). The same drop in permeability is achieved when a precoating layer of 10 – 12 g/m² is applied on base paper.

When the barrier layer is applied on double precoated paper the reduction of Darcy coefficient by one magnitude can be achieved by a much thinner barrier film of 2 – 3 g/m² as holdout of barrier layer improves on this dense and smooth substrate. Reduction in permeability was 3 times higher when the same amount of barrier layer was applied on double precoated paper compared to barrier application on base paper.

The best cost to barrier ratio was evaluated for the fine SB dispersion BASF Styrofan 3492 and for all tested starches. Liquids like starches form a dense film while dispersions have pores between the particles. When latices are film formed these pores are closed depending on the film forming abilities of the latex (see chapter "drying induced mottling". Styrofan DS3492 is a SB dispersion with low particle diameter of 130 nm and good film forming properties (Tg = 0 ℃).

Prüfbau pressure penetration test with water on pigmented barrier precoatings
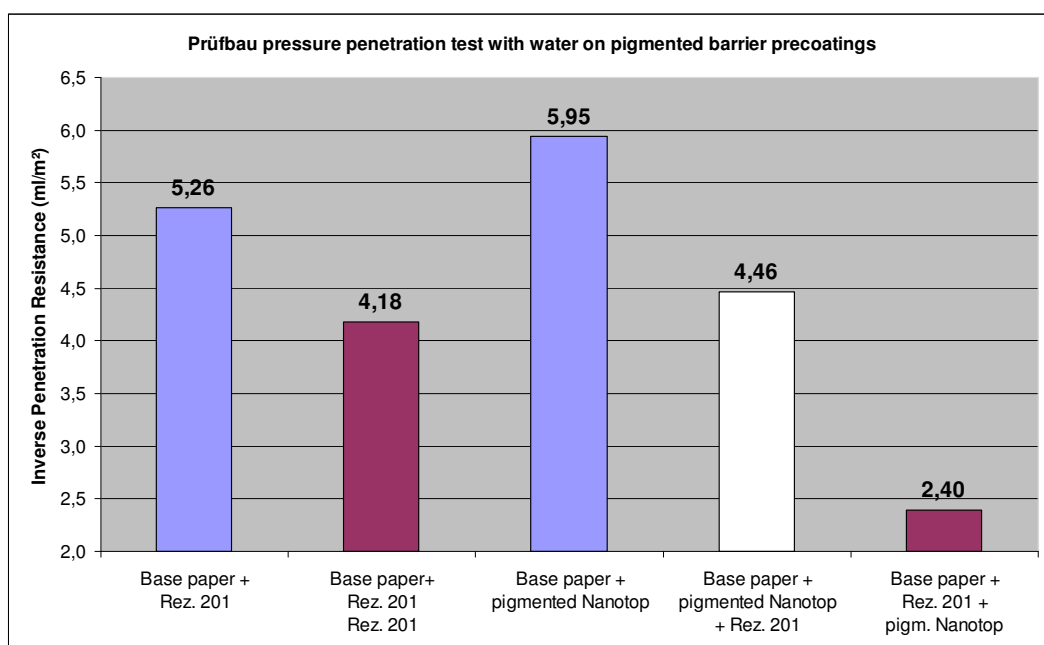
Pict. 8.3.7: Nano particles as barrier layer (left to right: Base + PC / Base + PC + PC / Base + Nanotop / Base + Nanotop + PC / Base + PC + Nanotop)

Applying nano particles as barrier coatings led to the same conclusion as for starch and acrylic dispersions/solution (pict. 8.3.7): The holdout of these ultrafine particles is insufficient when applied on base papers. Applications of 2 – 4 g/m² on precoated paper led to the same drop in permeability as a single coating layer with 10 – 12 g/m² basis weight.

In the following scale up process pilot coating trials were performed with these two liquids.

8.4 Pilot trials at Hueck

In a small pilot coating unit at Hueck, a coating and laminating company in Austria, selected liquids were applied. The width of the pilot coater at Hueck is 300 mm and the speed was 300 m/min at the trial. From different available application systems the reverse gravure application was chosen. A gravure roll with a fine pattern of holes at the surface transports the barrier liquid from a pan to the application nip. It rotates against the web run direction to improve the uniformity of the applied layer. The nip pressure, the rotation speed of the applicator roll, the viscosity and the solid content can be varied. All these parameters determine the coat weight. Application pressure is relatively low for this kind of wide spread application unit. It increases with speed.

A standard precoating (2% starch, 10% latex, 65% HC60, 35% HC90) was compared with starch and Styrofan DS3492 as barrier layers.
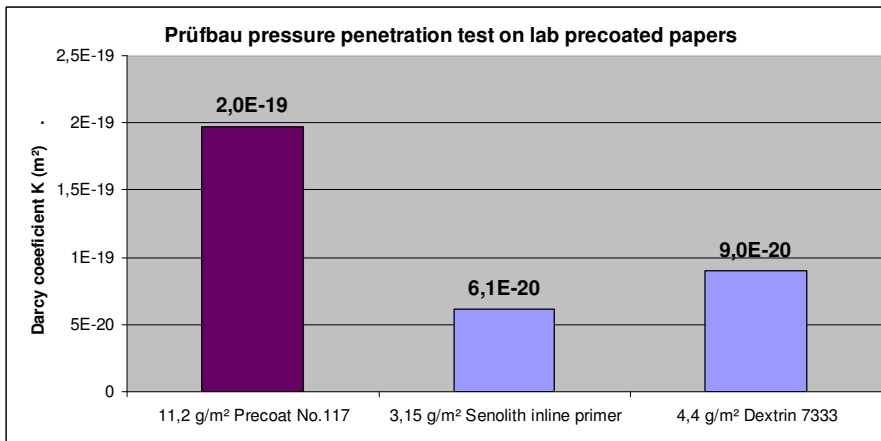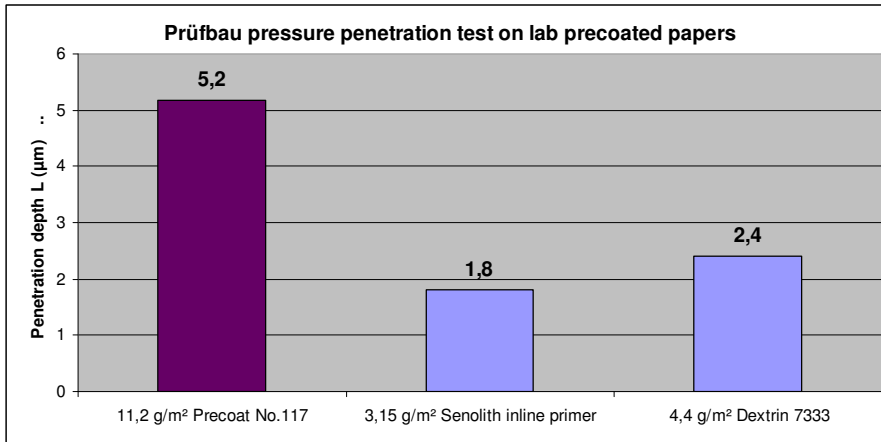
Pict. 8.4.1: Comparing permeability of a standard precoating with barrier layers on base paper of PM11, applied at Hueck

Pict. 8.4.1 shows the results of the pilot trial at Hueck which confirmed the previous lab trials: Permeability described as depth of water penetration on barrier layer or Darcy coefficient of barrier layer (pict. 8.4.2) was lower for the barrier layers than for a single precoat with much higher coat weight.

		11,2 g/m² Precoat No.117	3,15 g/m² Senolith inline primer	4,4 g/m² Dextrin 7333		Comment
basis weight		108,1	92	94,5	g/m²	
Coat weight per side		**11,2**	**3,15**	**4,4**	g/m²	base weight difference
thickness, total					µm	from thickness measurements of paper samples
pore volume in precoating layer		9	7	8	ml/m²	both sides from Hg-poros.
avg. Pore radius	r	0,25	0,1	0,1	µm	from Hg-porosimetry
max. penetration volume per side = air volume in coat	$V_{p, max}$	4,5	3,5	4	ml/m²	total pore volume / 2
Porosity from mercury measurement		35,0	35,0	35,0	%	from Hg-porosimetry
Coating layer thickness (MSP+blade), both sides		0,0120	0,0040	0,0050	mm	from thickness measurements of paper samples
-- " --	$H_{coating}$	**6,00**	**2,00**	**2,50**	µm per side	
air volume in coating	V_p	2,10	0,70	0,88	ml/m²	from porosity in % and thickness coating
Liquid: Coloured dest. Water + 50% IPA						
contact angle	θ	45	45	45	°	after wetting (1 sec)
	θ	0,7854	0,7854	0,7854	rad	
	cos θ	0,707	0,707	0,707		
surface tension	γ	73	73	73	mN/m	
viscosity	η = µ	0,001	0,001	0,001	Pa s = kg/ms	
density	ρ	1000	1000	1000	kg/m³	
Prüfbau:						
speed of test	v	0,5	0,5	0,5	m/s	
pressure at nip	Δp	800	800	800	N	1 N = 1 kg m / s², Pa = N/m²
Measures at double precoated paper (11/3688/MR5, 4000170, Avg of OS/US):						
drop volume	V_{drop}	5	5	5	µl	known
drop lenght	B_{drop}	82,0	92,0	83,0	mm	mesured
drop width	L_{drop}	20,0	22,0	20,0	mm	mesured
drop area	A_{drop}	1287,4	1588,8	1303,1	mm²	$A_{drop}=B_{drop}*L_{drop}*3,14/4$
time for drop penetration	t_{drop}	0,2	0,2	0,2	sec	$t_{drop}=L_{drop}/v_{Prüfbau}$
penetrated water under prüfbau roll	$V_{p,spez}$	0,004	0,003	0,004	µl/mm²	$V_{p,spez}=V_{drop}/A_{drop}$
-- " --	$V_{p,spez}$	**3,88**	**3,15**	**3,84**	ml/m²	-- " --
comparison: Pore volume of coating layer	$V_{p, max}$	**4,5**	**3,5**	**4,0**	ml/m²	from Hg measurement
mean width of penetrated drop	b	15,7	17,3	15,7	mm	
appr. lenght of pressure under Prüfbau roll at Δp	l	5,0	5,0	5,0	mm	measured by pressure sensitve film
area of pressure under Prüfbau roll at Δp	A	78,5	86,4	78,5	mm²	
penetrated water under prüfbau roll	V_p	0,305	0,272	0,301	µl	$V_p=V_{p,spez}*A$
-- " --	V_p	0,00030	0,00027	0,00030	ml	-- " --
theor. penetration depth	L_{th}	3,88	3,15	3,84	µm	at 100% free volume
true penetration depth from porosity in ml/m²	**L**	**5,18**	**1,80**	**2,40**	**µm**	L = (V_{Drop}/V_{paper}) x $H_{coating}$
true penetration depth from porosity ε	L	11,10	8,99	10,96	µm	L = L_{th} * ε
comparison: maximum penetration depth	L_{max}	6,00	2,00	2,50	µm	$H_{coating}$
penetration time under prüfbau roll	t	0,010	0,010	0,010	sec	
spec. Pressure	Δp	10191083	9264621	10191083	Pa = N/m²	
	Δp	102	93	102	bar	
	Δp	1029,8	936,1	1029,8	m WS	Δp in m WS = (Δp in N) / ($ρ_w$ x 9,81 x A)
formula No.2:		dV/dt = (K x A x Δp) / (η x L)				
		K = ((dV/dt) x η x L) / (A x Δp)	(Δp in Pa)			
Darcy's coefficient with formula No. 2:	**K**	**1,97347E-19**	**6,10821E-20**	**9,02909E-20**	**m²**	
	dV/dt	**0,0305**	**0,0272**	**0,0301**	**ml/sec**	

Pict. 8.4.2: Calculating the permeability coefficient of barrier layers applied on base paper PM11 at Hueck – comparison of permeability with precoated paper of PM11

8.5 Pilot trial at BASF

The positive results of the Hueck coating trials led to the next step in the scale up process, in which the barrier liquids and the following coatings were applied at a pilot coater with commercial speed (1000 – 1500 m/min). Base paper, precoated paper and middle coated paper of PM11 were used as substrates.
Fine SB based dispersion Styrofan DS3492 was applied at the BASF Pagendarm pilot coater which is normally used for coatings on plastic films. Reverse gravure coating was chosen for application. Application weight of Styrofan dispersion was 4,5 g/m² bone dry for the base paper and 3 g/m² for the precoated and middle coated papers of PM11.

Starch was applied later at CTC pilot plant by film press coater.

At the same CTC pilot the following standard pre-, middle- and top-coatings were applied on top of the CTC- and BASF-barrier layers.

Prüfbau pressure penetration test of BASF coated samples

Legend: Penetration 1,1% CMC, TS (ml/m²) — Penetration 1,1% CMC, WS (ml/m²)
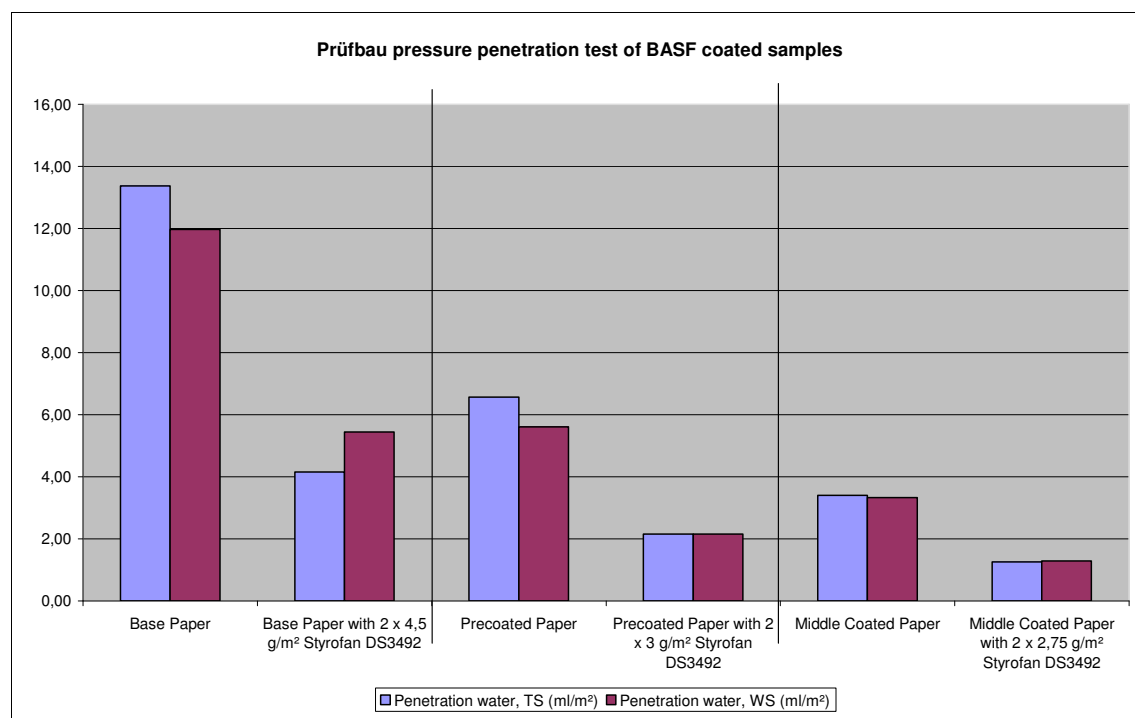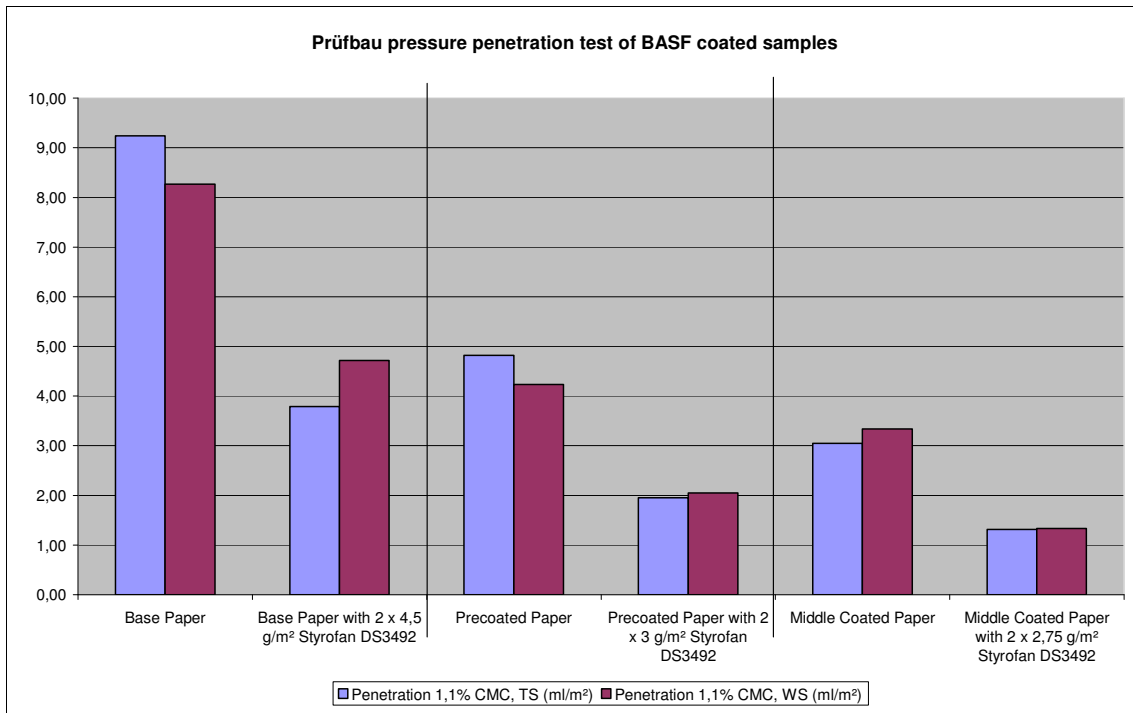
Pict. 8.5.1: Lowering the penetrated volume dV/dA, measured with Prüfbau pressure penetration test by Styrofan DS3492 barrier layer on different substrates

Pict. 8.5.1 shows the permeability measurements of the pilot trial at BASF which gave similar results as the pilot trial at Hueck.

Applying 4,5 g/m² of Styrofan DS3492 on base paper of PM11 instead of 12 g/m² conventional precoating (HC60/HC90/latex/starch) led to the same drop in permeability.

When 3 g/m² of Styrofan DS3492 was applied on PM11 precoated paper permeability was lower than that of a double precoated (middle coated) paper. Again the holdout of fine dispersions was much better on a precoated paper with a mean pore diameter of 0,25 µm compared to a base paper with a mean pore diameter of 5 µm.

Pict. 8.5.2 shows the paper quality parameters of the barrier coatings with Styrofan DS3492:

		Base Paper	Base Paper with 2 x 4,5 g/m² Styrofan DS3492	Precoated Paper	Precoated Paper with 2 x 3 g/m² Styrofan DS3492	Middle Coated Paper	Middle Coated Paper with 2 x 2,75 g/m² Styrofan DS3492
Coating Layer Styrofan (g/m²)			9,0		5,8		5,5
Air porosity Bendtsen (ml/min)		363	2,5	30,7	0,65	0,68	0,26
Brightness without UV, TS		84,1	81,3	84,9	82,7	84,1	80,4
Brightness without UV, BS		83,7	81,6	84,8	82,2	84,2	80,8
Brightness with UV, TS		89,4	87,4	92,3	90,2	92,7	89,9
Brightness with UV, BS		89,1	87,8	92,1	90,0	93,4	90,7
Opacity (%)		84,0	79,0	93,3	92,9	94,8	94,5
Smoothness Bendtsen, TS (ml/min)		306	181	236	102	70	43
Smoothness Bendtsen, BS (ml/min)		206	326	151	160	85	111
Gloss Tappi 75°, TS (%)		4,6	12,5	5,8	27,4	6,1	45,2
Gloss Tappi 75°, BS (%)		5,3	8,8	5,5	27,7	5,7	44,8
Scott Bond (mJ)		277	726	169	183	199	209
Stiffness MD (mNmm)		252	236	599	592	924	899
Stiffness MD (mNmm)		89	86	235	263	523	508
Set off test Prüfbau at 30 sec, TS		0,13	0,10	0,11	0,12	0,15	0,16
Set off test Prüfbau at 30 sec, BS		0,13	0,12	0,09	0,08	0,17	0,23

Pict. 8.5.2: BASF coating trial with Styrofan DS3492

The paper data's confirmed the results of the Prüfbau pressure penetration tests: When liquids or fine dispersions were used as barrier substances, the optimal position is on top of first precoating: Barrier liquids close the pores of the substrate and eliminate thereby light scattering of these pores. The negative impact on opacity is much lower when the barrier is applied on top of a precoated paper than when applied on base paper. For lower basis weights this would be of high importance. This drop in opacity with application of a barrier layer on base paper was not found for the lab coating trials where the barrier layer was applied with a rod coater under low pressure as base paper voids were not filled by the barrier liquid. This leads to the conclusion that when barrier coatings are applied without external pressure (e.g. by a curtain coater) the drop in opacity will be low.

Smoothness and gloss increased with Styrofan while stiffness stays constant.

The measured drop in liquid permeability, which was measured for the Styrofan barrier layer with the Prüfbau pressure penetration test, was also measured by Bendtsen air permeability. It dropped for barriers on base paper from 360 to 2,5 ml/min and for barriers on precoated paper from 30 to 0,65 ml/min!

The advantage of a barrier coating with fine latex particles against starch based barrier layers is the high micro porosity of the barrier after drying – it can be detected in the unchanged set off test and ink drying test. This is important, when the thin layer is applied close to the topcoat e.g. after the middle coat and ink drying should remain unchanged. Latex particles which are not totally film formed provide a barrier with micro porosity between the particles. Therefore barrier properties like oxygen or vapour permeability are worse than for liquid based films like starch. For improving mottling by barrier layer under top coatings latex based films are advantageous as micro porosity provides better ink drying.

Barrier layer on base paper

Barrier layers should have a positive effect on holdout of the following coating layer. Capillary sorption of hydrophilic base paper substrate before the blade should be reduced. This was measured by Fibro-DAT experiments as shown in pict. 8.5.3:
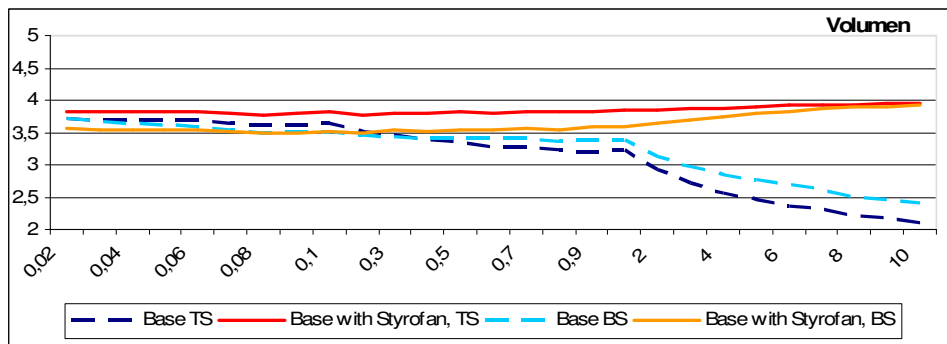
Pict. 8.5.3: Fibro-DAT capillary sorption of PM11 base paper (drop volume of 1%CMC)
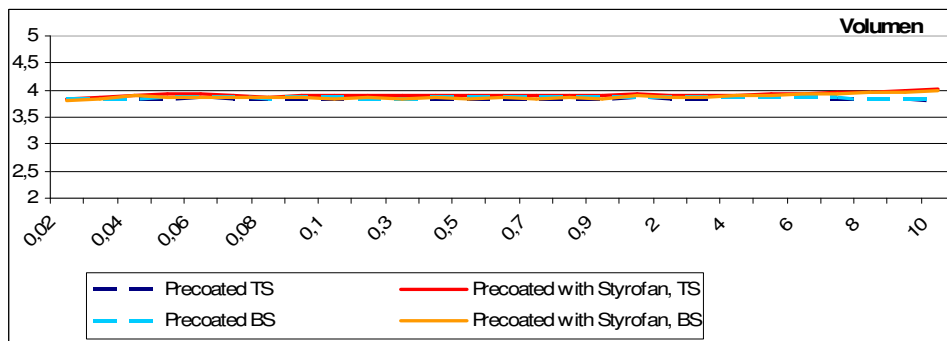
Pict. 8.5.3: Fibro-DAT capillary sorption of PM11 precoated paper (change in drop volume of 1% CMC solution)

Capillary sorption of fibre walls of un-sized PM11 base paper was totally eliminated when a barrier layer was applied either on base paper or on precoated paper.

Therefore thickening of following middle or topcoatings would be reduced when applied on barrier layers. Runability at these blade coaters would improve.

8.6 CTC blade coatings on top of barrier layers, applied on precoated paper

The barrier coated papers of chapter 8.5 were further coated at the CTC pilot coater using standard a blade coater and middle / top coating formulations of OMC11. Results of permeability after standard precoating, precoating with starch barrier, precoating with latex barrier and pre- + middle coating are shown in pict, 8.6.1 (from left to right):

Prüfbau pressure penetration test with water
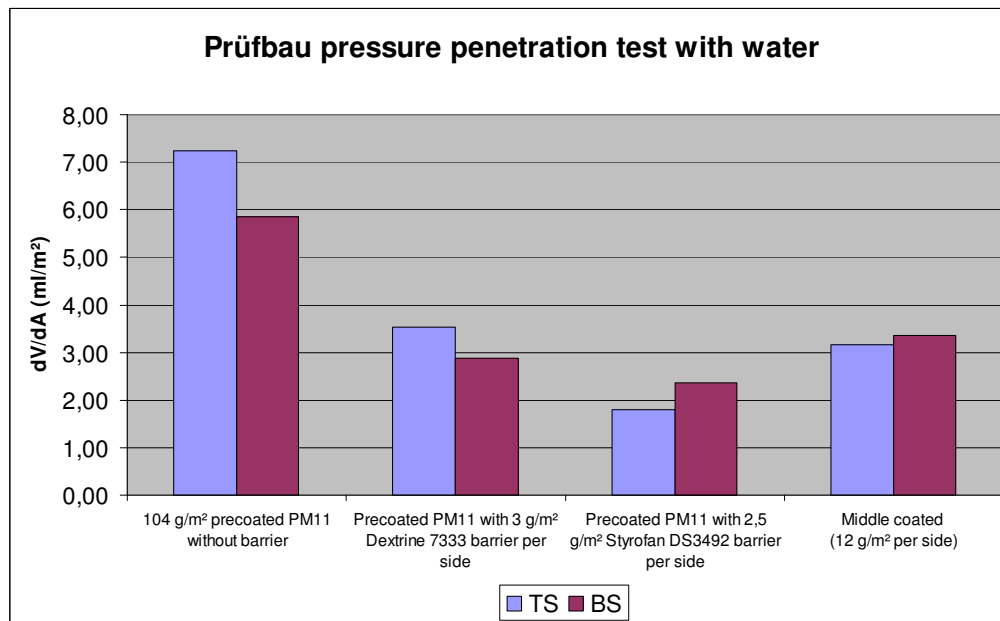
Pict. 8.6.1: Effect of barrier layer on precoated paper

Applying a 2 – 3 g/m² latex or liquid based barrier layer on a precoated paper reduced permeability to a greater extend than 10 – 12 g/m² middle coating layer on the same substrate.

			104 g/m² precoated PM11 without barrier	Precoated PM11 with 3 g/m² Dextrine 7333 barrier per side	Precoated PM11 with 2,5 g/m² Styrofan DS3492 barrier per side		Middle coated (12 g/m² per side)
Brightness with UV	%	TS	92,52	90,61	89,22		95,97
	%	BS	92,26	90,31	90,30		96,02
Opacity	%		**93,40**	**92,66**	**92,18**		**95,30**
Gloss Tappi	%	TS	5,2	17,8	34,8		8,4
	%	BS	5,9	24,0	25,7		9,5
PPS smoothness	µm	TS	5,65	5,65	3,97		3,54
	µm	BS	5,23	5,54	5,17		4,06
Bendtsen porosity	ml/min		**53,12**	**0,99**	**0,33**		**1,89**
Stiffness	mN/m	MD	0,641	0,815	0,580		1,130
	mN/m	CD	0,295	0,462	0,231		0,624
Internal bond	mJ		145	145	195		156
Set off 30 sec		TS	0,17	0,47	0,28		0,48
		BS	0,19	0,50	0,47		0,47
Droplet test		TS	74	14	6		28
		BS	63	9	9		27
Offset suitability wet (passes to fail)		TS	12	12	9		11
		BS	12	12	8		10
Offset suitability dry (passes to fail)			12	12	9		12
			12	12	8		11
IGT		TS	**205**	**230**	**230**		170
		BS	**175**	**230**	**230**		215
Lab mottle		TS	2,75	2,25	2		1,25
		BS	2,5	1,75	2,25		2,5

Pict. 8.6.2: Paper quality data's of barrier layers on precoated paper

The effect of the barrier layers can also be seen in lower Bendtsen air porosity, worse droplet test and in slower ink set off of the barrier coated papers.

Pict. 8.6.3 shows the results of paper quality tests from middle coated paper where standard middle coating colour was applied on the barrier layers by blade application.

			Middle coated without barrier	Middle coated with 3 g/m² Dextrine 7333 barrier per side after precoat	Middle coated with 2,5 g/m² Styrofan DS3492 barrier per side after precoat
Brightness with UV	%	TS	85,43	83,03	84,14
		BS	85,42	83,29	83,97
Opacity	%		**95,30**	**94,12**	**94,80**
Gloss Tappi	%	TS	8,4	**24,8**	10,2
		BS	9,5	**22,7**	11,4
PPS smoothness	µm	TS	3,54	3,54	3,37
	µm	BS	4,06	3,37	3,57
Stiffness	mN/m	MD	1,130	**1,367**	0,944
	mN/m	CD	0,624	**0,741**	0,942
Internal bond	mJ		156	160	187
Set off 30 sec		TS	0,48	**0,89**	**0,66**
		BS	0,47	**0,84**	**0,64**
Droplet test		TS	28	3	7
		BS	27	5	8
Offset suitability wet (passes to fail)		TS	11,0	12,0	12,0
		BS	10,0	12,0	12,0
Offset suitability dry (passes to fail)			12,0	12,0	12,0
			11,0	12,0	12,0
IGT		TS	170,0	**230,0**	**230,0**
		BS	215,0	**230,0**	**230,0**
Lab mottle		TS	1,25	1,25	**1,25**
		BS	2,5	3	**1,25**

Pict. 8.6.3: Paper quality data's of middle coated papers after barrier application on precoated paper

The positive effect of both barrier layers on top of precoated paper upon latex holdout of the following middle coating layer is shown in the slower set off and increased picking resistance of the middle coated papers. Therefore costs of these coatings could be reduced by lowering their latex content to compensate the additional costs of the barrier layer.

Starch based barriers were lower in permeability than Styrofan barriers as liquids applied on dense and smooth surfaces have better barrier properties than dispersions with fine particles.
On the other hand the opacity of starch barrier was lower as the liquid filled the pores of coatings and base papers easier than dispersions.

Styrofan barrier clearly improved lab mottle of triple coated papers. The floc structure in the mottling test of the worse bottom side of PM11 disappeared after middle coating. Opacity remained almost in the same level as the barrier had a good holdout

and the pores of the precoating layer were less filled than for the starch based barrier (a function of viscosity and application pressure).

8.7 Barrier layers applied on middle coated paper

Pict. 8.7.1 shows that similar results compared to barriers on precoatings (pict. 8.6.1) were achieved when the barrier was applied on middle coated paper of OMC11.

Prüfbau pressure penetration test with water

dV/dA /ml/m²

3,80
3,60
3,40
3,20
3,00
2,80
2,60
2,40
2,20
2,00

128 g/m² middle coated | Middle coated + 3 g/m² barrier per side with Dextrin 7333 | Middle coated + 2,3 g/m² barrier per side with Styrofan DS3492 | Top coated (12 g/m²)

☐ TS ☐ BS
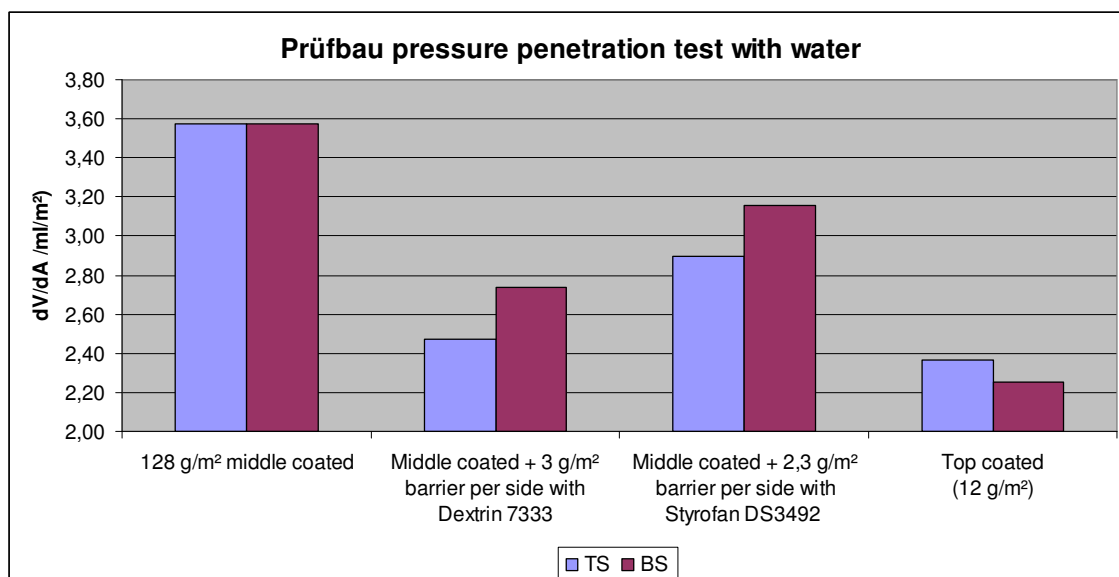
Pict. 8.7.1: Effect of a barrier layer applied on middle coated paper

The drop in permeability was comparable to barriers on precoated paper. Starch based barrier showed again a better performance than SB based barrier.
For comparison: A 12 g/m² glossy top coating layer with ultrafine pigments has a similar permeability than a 2 – 3 g/m² starch barrier layer on a middle coated paper.

The coated barrier samples were compared in Mercury porosity to correlate their permeability with the porosity of the barrier layer (pict. 8.7.2).
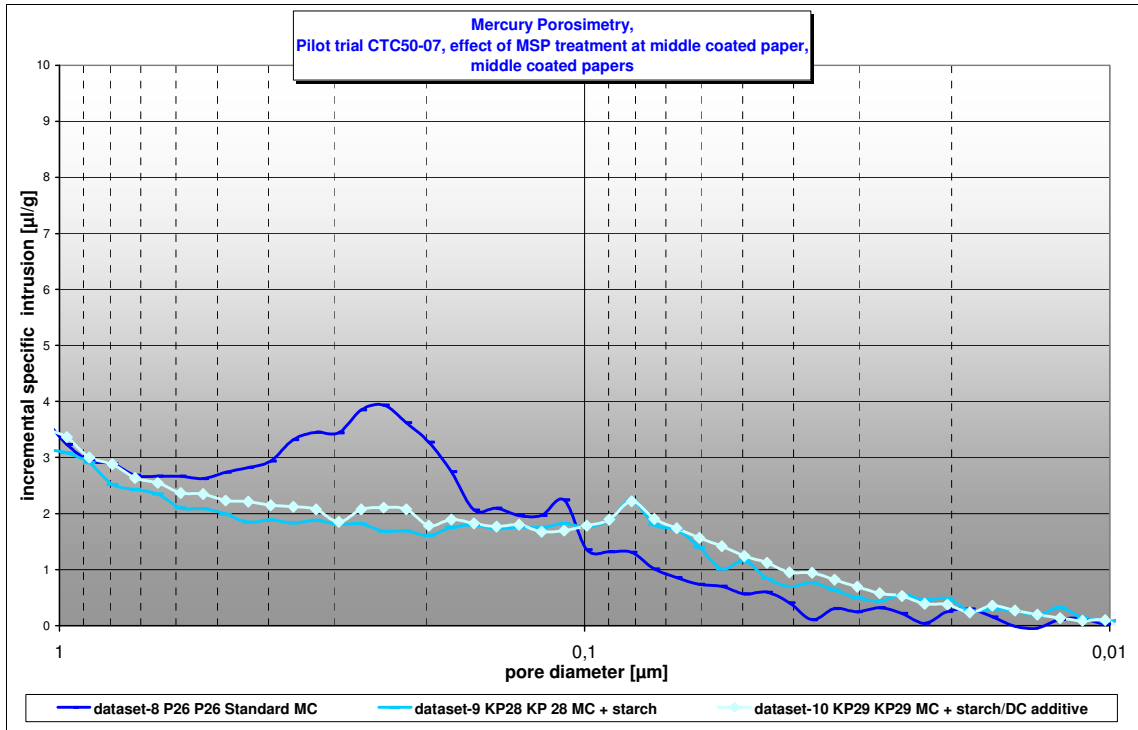
Pict. 8.7.2: Mercury porosity of middle coated paper and with applied starch barrier layer
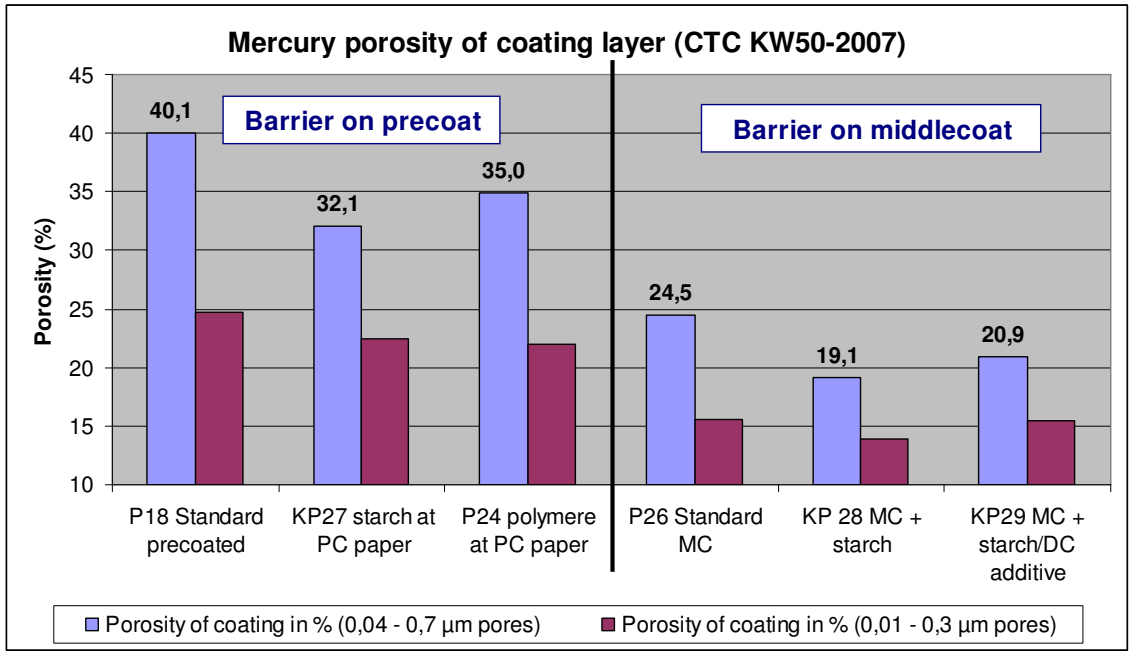
Pict. 8.7.3: Mercury porosity of coating layer – barrier layers on precoatings: KP27 = starch, P24 = Styrofan DS3492 – barrier layers on middle coatings: KP28 = starch

Pict. 8.7.3 shows that a clearly lower porosity of coating plus barrier layer was found for all barrier coated samples.

In the next pictures the results are shown for **top coated papers** from the CTC pilot plant.

dV/dA (ml/m²), water			Top coated (no barrier on middle coat)	Top coated + 3 g/m² per side Dextrin 7333 barrier on middle coat	Top coated with 2,3 g/m² per side Styrofan DS3492 barrier on middle coat	Top coated (no barrier on precoat)	Top coated with 3 g/m² Dextrine 7333 barrier on precoat	Top coated with 2,5 g/m² per side Styrofan DS3492 barrier on precoat
Gloss Tappi	%	TS	41,0	41,6	29,1	41,8	51,0	46,5
	%	BS	41,9	42,5	4,1	43,0	52,0	47,6
Gloss DIN75°	%	TS	12,3	11,8	10,4	14,0	17,9	16,2
	%	BS	12,5	11,8	0,8	13,4	17,6	16,3
Stiffness	mN/m	MD	1,353	1,691	1,268	1,428	1,632	1,306
	mN/m	CD	0,860	1,078	0,754	0,975	1,167	0,881
Mottle solids commercial prinitng (c+m)		TS	1,75	1,75	1,75	1,75	2	2
		BS	1,5	1,75	-	1,5	1,5	-

Pict. 8.7.4: Quality data's after top coating

dV/dA (ml/m²), water			Top coated+calandered (no barrier on middle coat)	Top coated +calandered with 3 g/m² per side Dextrin 7333 barrier on middle coat	Top coated + calandered with 2,3 g/m² per side Styrofan DS3492 barrier on middle coat	Top coated + calandered (no barrier on precoat)	Top coated + calanderdd with 3 g/m² Dextrine 7333 barrier on precoat	Top coated + calandered with 2,5 g/m² per side Styrofan DS3492 barrier on precoat
Brightness with UV	%	TS	97,70	96,50	99,00	99,70	97,90	98,90
		BS	97,40	96,40		99,60	98,10	98,90
Opacity	%		**96,19**	**94,60**	**96,10**	**96,29**	**95,20**	**95,54**
Gloss Tappi	%	TS	69,8	69,0	29,7	70,6	74,1	69,5
	%	BS	66,2	65,4		68,1	69,9	67,4
Gloss DIN75°	%	TS	45,0	43,5	10,9	50,0	**55,0**	43,8
	%	BS	40,3	36,5		45,2	**47,0**	41,9
PPS smoothness	µm	TS	0,94	1,14	2,11	0,93	**0,69**	0,76
	µm	BS	0,78	1,09		0,80	**0,71**	0,67
Stiffness	mN/m	MD	1,005	**1,131**	1,089	1,047	**1,173**	0,838
	mN/m	CD	0,544	**0,754**	0,670	0,754	**0,879**	0,503
Set off 30 sec		TS	0,62	**0,83**	0,55	0,60	**0,86**	**0,75**
		BS	0,67	**0,83**	0,00	0,70	**0,92**	**0,79**
Droplet test		TS	48	21	53	53	24	44
		BS	50	17		51	20	47
Offset suitability wet (passes to fail)		TS	6,5	**11,0**	7,5	3,5	**4,5**	6,5
		BS	5,5	**10,0**		3,5	**4,5**	6,5
Offset suitability dry (passes to fail)		TS	5,0	**11,5**	00	3,0	**4,5**	1,0
		BS	4,5	**9,5**		3,0	**4,0**	1,0
Multi colour ink setting, 6 min		TS	0,13	**1,03**	0,26	0,06	0,76	0,17
		BS	0,15	**0,93**		0,08	0,76	0,17
Mottle solids commercial prinitng (c+m)		TS	**1,25**	1,5	2,5	1,25	1,5	1,75
		BS	**1,5**	1,5	2	1,25	1,75	1,75

Pict. 8.7.5: Quality data's after top coating and calendaring

Applying the dense starch barrier on the precoated paper of PM11 led to a huge improvement in middle coating holdout as shown before (pict. 8.7.4 – 8.7.5). After top coating Tappi gloss improved by 10% abs as the holdout of fine pigments in the top coat improved. After calendaring gloss was increased by 5%, set off got 30% slower

and the picking resistance increased significantly which shows how much top coat latex is pressed into the substrate under the blade under normal conditions where these barrier layers are missing. This proves the assumption that much cheaper middle and top coating formulation can be used when a barrier layer is applied on precoated paper.

A big draw back is the much worse ink drying after top coating when a starch barrier layer is applied either on a precoated or on a middle coated paper. Pore volume of the whole coating sandwich got lost by barrier layers and capillary sorption of ink was limited. Part of that can be compensated by reducing the latex content in the middle and top coat formulation.
Applying the SB dispersion Styrofan DS3492 on a middle coated paper improved ink drying due to the micro capillarity of this layer which creates capillary sorption pressure.
Stiffness dropped with soft SB-latex Styrofan and increased with brittle starch.

In contrast to starch barriers, cracking on the fold improved with Styrofan barrier layer (pict. 8.7.6). A crack free paper can be produced when soft latices are applied as barriers on precoated paper!
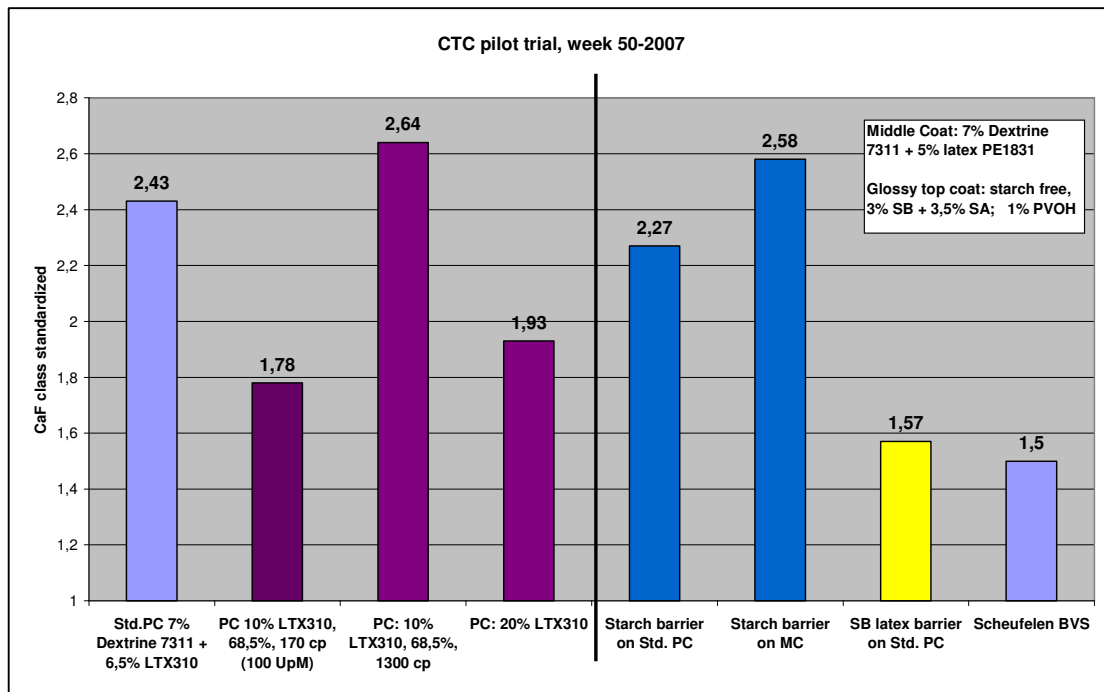
Pict. 8.7.6: Cracking on the fold of triple coated papers with starch or Styrofan barrier on precoat and middle coat (yellow: Barrier on precoat)

When starch is used as a barrier layer a humidifier should be added to improve cracking on the fold. This combination would be a cheap and effective barrier layer.

8.8 Conclusions

The best location to apply barrier layers in triple coating process is on top of the precoated paper.

The surprising result of CTC pilot trials was the fact that mottling in commercial printing test couldn't be improved by the described barrier layers.
One reason might be the exceptional good level of the standard samples without barrier layer which didn't show the typical formation mottle of PM11.
The second reason is the fact that all barrier layers were applied under pressure. As barrier liquids are low in viscosity to keep the applied amount as low as possible, their penetration depth and holdout will be highly dependent upon local pressure. At flocs, where local pressure is much higher, more barrier liquid will be pressed into the base and less barrier liquid will be kept on the surface compared to voids next to them. If the barrier layer "follows" the structure of formation, mottling can be even worse. The base paper floc structure would be multiplied by the barrier layer.

Therefore a necessary precondition for a barrier layer to improve mottling is application under the lowest possible pressure which is currently achieved solely by curtain coaters.
When curtain coaters are used for barrier applications multi layering is the ideal choice where the coating is applied on top of the barrier liquid in one step.

To improve holdout of barrier layer, viscosity and solid content of barrier dispersion should be as high as possible and drying should be as fast as possible after application.
To avoid loss of barrier liquid into base paper by capillary sorption of hydrophilic fibres, barrier liquid should be slightly hydrophobic.

Ideal application units:
- Curtain coater
- Multi layer curtain coater (cascade) where the first layer is a barrier layer
- Spray coater

Curtain coaters have the advantage of a much higher solid content at a given application weight against spray coaters. The disadvantage of curtain coaters is the high demand for space and the high investment costs.

Pilot trials with spray coaters at TU-Graz showed that droplet spreading of barrier liquids was not sufficient and barrier properties were therefore much worse than for curtain coating application.

As the capillary sorption between flocs and valleys in the base paper of PM11 is same, the holdout of a pressure-less barrier application should be uniform over the whole paper surface (pict. 8.8.1).
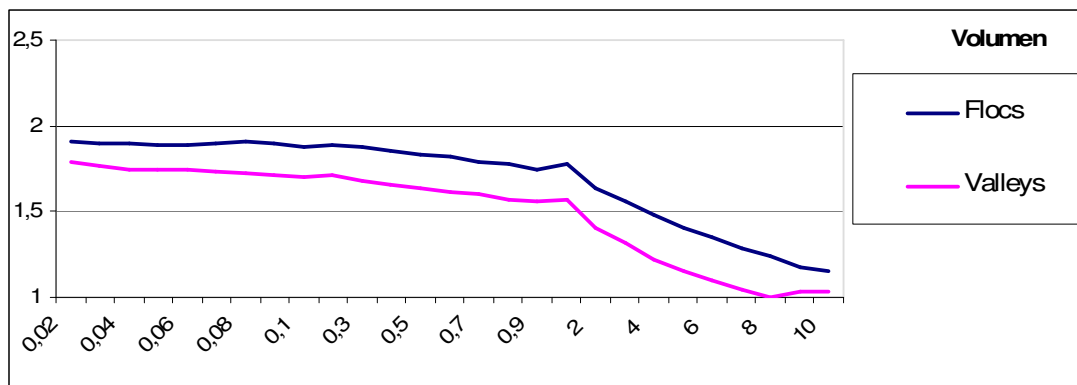
Pict. 8.8.1: Fibro-DAT capillary water sorption of flocs/valleys of base paper PM11 measured by droplet volume loss (µl) with time (s)

Second best choice of application (low pressure):
- Film press application (MSP coater)
- Gravure roll application (reverse or in running direction)

As all barrier coatings are very expensive costs should be compensated by the lower binder demand in the following coating layers. A cost calculation was made for OMC11:

Standard	Price (€/TA)	Pre-coat %	Barrier layer %	Middle-coat %	Top-coat %	SUM coat weight g/m²	Price of all coating layers €/TA
HC60	100	100		70			
HC90	130			30			
HC95	180				70		
Clay	200				30		
Latex	1500	8		7	9		
Starch	500	5		4			
Synth. Thickener	1500			0,4	0,5		
Price of coating (€/TA)		216,8		215,4	300,0		
Coat weight dry per side (g/m²)		12	0	12	12	**36**	**244,1**

Acrylate barrier on precoating	Price (€/TA)	Pre-coat %	**Barrier layer** %	Middle-coat %	Top-coat %	SUM coat weight g/m²	Price of all coating layers €/TA
HC60	100	100		70			
HC90	130			30			
HC95	180				70		
Clay	200				30		
Latex	1500	8		**3**	**7,5**		
Starch	500	5		4			
Acrylate barrier	1500		100				
Synth. Thickener	1500			**0,3**	0,5		
Price of coating (€/TA)		216,8	1500,0	166,4	283,3		
Coat weight dry per side (g/m²)		12	**3**	10	11	**36**	**330,1**

Starch barrier on precoating	Price (€/TA)	Pre-coat %	**Barrier layer** %	Middle-coat %	Top-coat %	SUM coat weight g/m²	Price of all coating layers €/TA
HC60	100	100		70			
HC90	130			30			
HC95	180				70		
Clay	200				30		
Latex	1500	8		**3**	**7,5**		
Starch	500	5	100	4			
Acrylate barrier	1500						
Synth. Thickener	1500			**0,3**	0,5		
Price of coating (€/TA)		216,8	500,0	166,4	283,3		
Coat weight dry per side (g/m²)		12	**3**	10	11	**36**	**246,7**

Acrylate barrier on base paper	Price (€/TA)	**Barrier layer** %	Pre-coat %	Middle-coat %	Top-coat %	SUM coat weight g/m²	Price of all coating layers €/TA
HC60	100		100	70			
HC90	130			30			
HC95	180				70		
Clay	200				30		
Latex	1500		**0**	**3**	**7,5**		
Starch	500		**8**	4			
Acrylate barrier	1500	100					
Synth. Thickener	1500			**0,3**	0,5		
Price of coating (€/TA)		1500,0	129,6	166,4	283,3		
Coat weight dry per side (g/m²)		**3**	12	10	11	**36**	**301,0**

Starch barrier on base paper	Price (€/TA)	**Barrier layer** %	Pre-coat %	Middle-coat %	Top-coat %	SUM coat weight g/m²	Price of all coating layers €/TA
HC60	100		100	70			
HC90	130			30			
HC95	180				70		
Clay	200				30		
Latex	1500		**4**	**3**	**7,5**		
Starch	500	100	**4**	4			
Acrylate barrier	1500						
Synth. Thickener	1500			**0,3**	0,5		
Price of coating (€/TA)		500,0	166,7	166,4	283,3		
Coat weight dry per side (g/m²)		**3**	12	10	11	**36**	**230,0**

Pict. 8.8.2: Cost comparison of barrier coating concept with conventional concept

The comparison of cost in pict. 8.8.2 shows comparable costs for thin layer barrier concept when cheap substances like starches are used as a barrier after the 1st precoating. The expensive latex based barrier coatings clearly increase paper costs. The exact potential of binder reduction by barrier layers was estimated in this calculation and must be more deeply investigated in future pilot trials.

An additional advantage of a barrier layer is the lower drying energy demand of the following coating layers.

Comparing the top coating with the middle coating at OMC11, a 30% higher drying demand can be observed for the middle coaters due to the higher penetration depth of the liquid phase at application and between coater and drying which is caused by the lower Darcy coefficient and higher capillary sorption of the substrate. This difference would be removed by a barrier layer on the precoated paper.

The advantage of lower drying costs of the following coating would be overcompensated by the additional drying costs for the low solids barrier layer.

Blade runability would improve at middle coater of OMC11 when the built up of an immobilized layer would be hindered by a barrier layer which reduces the fibre sorption.

A cheaper way to improve latex holdout of middle and top coating and reduce mottling compared to barrier layers would be to reduce the Darcy coefficient of the precoating layer – to make it dense. This is described in the chapter 9 "dense precoatings".

Chapter 9:

Solution 5 for formation mottle: Reduce permeability of precoatings

9.1 Introduction

A cheaper way to reduce latex penetration differences in top coating compared to barrier layers described in the previous chapter is the reduction of precoating layer permeability.

This can be done principally by two ways:
- Higher coat weight
- Lower permeability of precoating

Lowering permeability can be done in several ways:
- Finer pigments
- Liquid binders like starch instead of solid latex particles – liquids fill the pigment pores to a higher extend than latex particles do
- Higher amount of binder in general
- Increase the holdout of binder particles or soluble binders / cobinders
- Finer latex particles
- Higher degree of latex film forming by using a lower Tg latex or adding film forming additives
- Higher shrinkage of coating layer e.g. by using soluble latices instead of latex dispersions

9.2 Lab experiments part 1

In the 1st lab study the permeability and porosity of a single precoating layer was studied using different pigment mixtures, latices and starches.
Pict. 9.2.1 shows the lab rod coater of process lab at PM11 (PT4) which was used for coating application. Rod pressure is very low for these type of coaters when compared to mill blade coaters which gives better coating holdout. Drying was done by IR which was situated over the coated surface and which was started immediately after coating application.
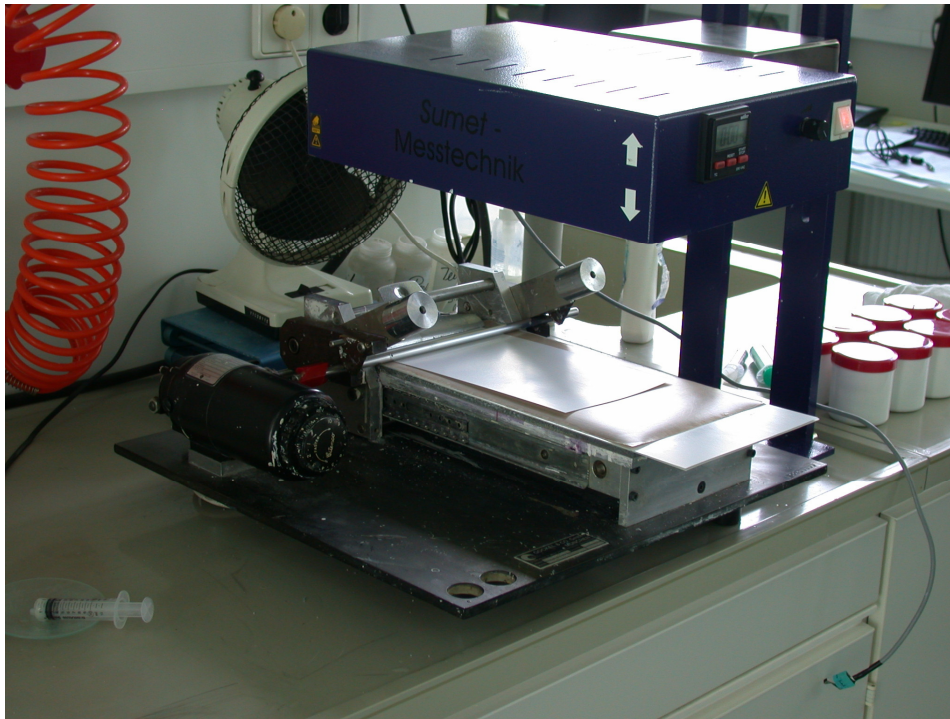
Pict. 9.2.1: Lab rod coater PT4

Permeability was measured by Bendtsen air porosity dV/dt (ml/min) and by Prüfbau pressure penetration test dV/dA (ml/m²) with water and oil as test liquids.

Lowering the permeability of the precoating layer should lead to:
- Higher the resistance against pressure penetration of the liquid phase in the following middle or top coating layer
- Less penetration of soluble binders and fine latex particles together with the liquid phase
- Lower the local differences in latex / soluble binder penetration

According to the Carman Kozeny equation the permeability (the Darcy coefficient K) is reduced with lower porosity of the coating layer:

$$u = \frac{1}{A} * \frac{dV}{dt} = K_1 * \frac{\Delta p}{\eta * L} \ \text{(Darcy)}$$

$$K_1 = \frac{\varepsilon^3}{K * S_0{}^2 * (1-\varepsilon)^2} \ \text{(Carman Kozeny with K = 5)}$$

The influence of latex type and amount was tested in the first part of this lab study.
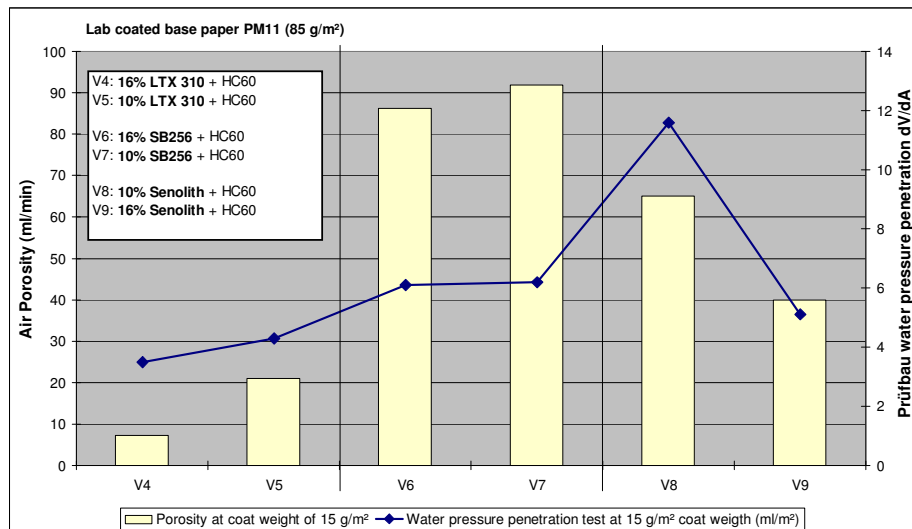
Pict. 9.2.2: Influence of latex type and amount on air permeability of dry coating layer

	100% HC60 10%LTX310	100% HC60 16%LTX310	100%HC60 10% SB256	100%HC60 16% SB256
Dmax [µm]	0,24	0,23	0,26	0,28
total pore volume [µl/g]	139	**105**	148	**118**
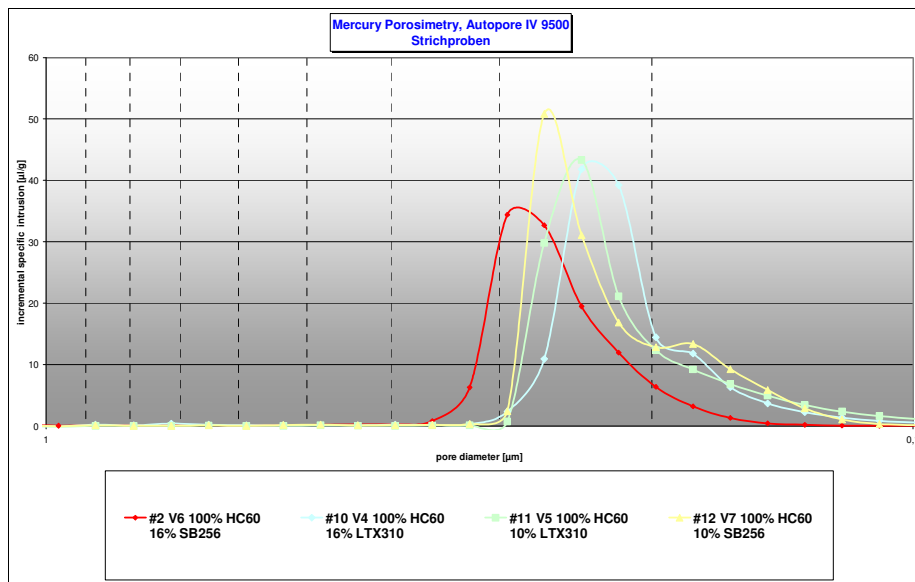
Pict. 9.2.3: Mercury porosity of coating tablets with different latex types

Pict. 9.2.2 shows that the higher the latex content, the lower the air permeability and the mercury porosity of the dry coating layer (pict. 9.2.3) was. Fine latex particles (0,15 µm) fill the pores of the pigment matrix (1 – 2 µm diameter in precoatings). This positive effect on mottling was later proven in a pilot trial at CTC.

Stiff web offset SB-latex SB 256 with a mean particle diameter of 180 nm, a Tg of 25°C and a gel content of 30% gave more porous coatings than soft sheet offset SB-latex LTX310 with a particle diameter of 135 nm, a Tg of 0°C and a gel content of 80%. The finer the latex and the higher the cross linking (the gel content) the lower the permeability of the coating layer as more pores are blocked by fine latex particles.

In pict. 9.2.4 and 9.2.5 results of replacing standard latex in precoating by Senolith, a latex based varnish, are shown
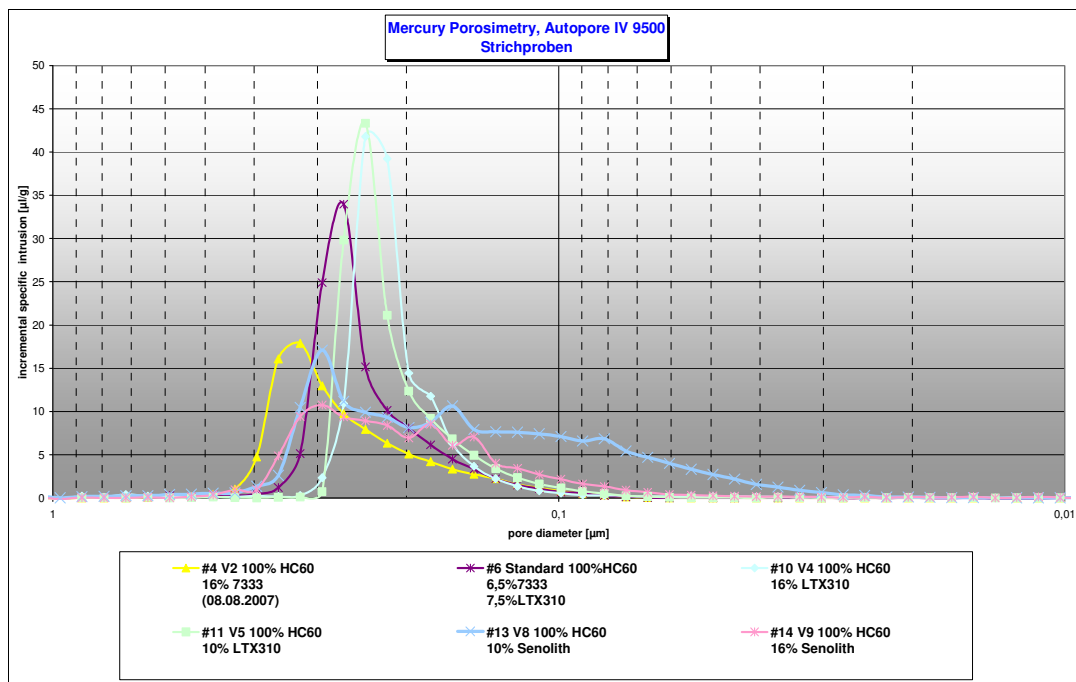
Pict. 9.2.4: Mercury porosity of standard latex LTX310 compared to Senolith varnish
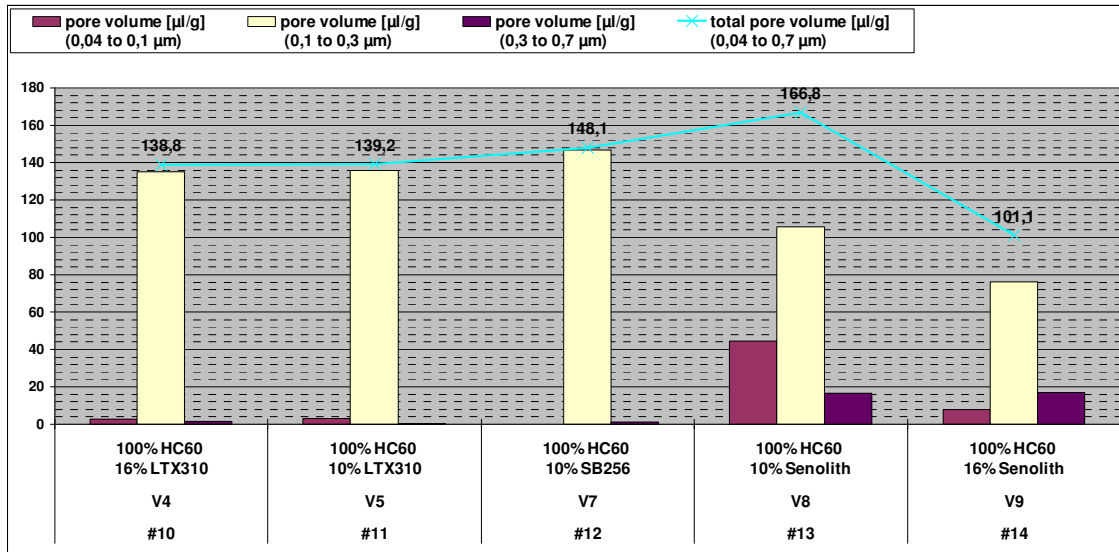
Pict. 9.2.5: Mercury porosity of Senolith inline primer varnish based coatings

Senolith is an ultra fine acrylate based inline primer varnish, which showed a good water retention of corresponding precoating colours when it replaced standard latices in the coating colour (see part "water retention"). It's a mixture of coarse and fine acrylic resins and contains much finer particles than conventional latices. It improved water retention of the coating colour as its fine particles blocked the path way of liquids in the immobilized layer.

Air permeability and the permeability against liquids (pict. 9.2.2) of Senolith based coatings on base paper was higher than that of standard SB-latex based precoatings due to more pronounced loss of fine Senolith resin particles into the base paper. Base paper pores are typically 1 – 10 µm in diameter and ultrafine latex particles with diameter of 50 – 100 nm will not be retained. Therefore these fine dispersions should be applied on dense middle coated paper where holdout is much better.

Mika Väha-Nissi, Antti Savolainen, Martti Talja, Raja Mörö (L1.61) studied the holdout of dispersion barrier coatings on high-density base. Speciality papers with barrier properties are normally produced by applying high refining energy and coating barrier coatings on a dense base paper. Pict. 9.2.6 shows that pre-calendering reduced base paper porosity and mean pore diameter of voids.
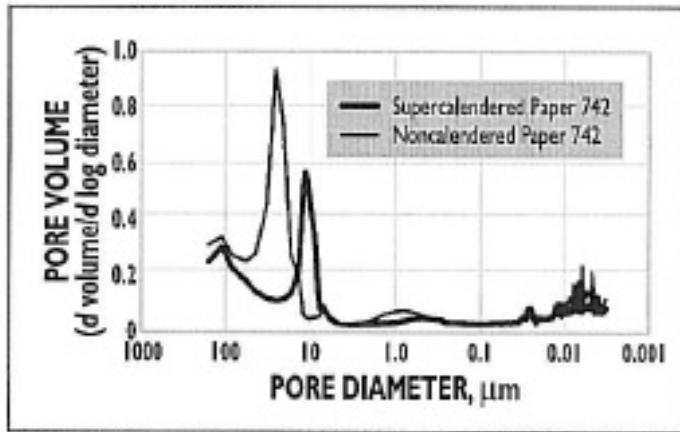
Pict. 9.2.6: Pore size distribution – effect of pre-calendering

Mika Väha-Nissi showed that the higher the smoothness of the base paper and the lower the pore size of the surface pores, the better the holdout of the barrier coating, based on fine resin dispersions, was.

Comparing the pore size of PM11 base paper (pict. 9.2.7) with particles in coating formulations (pict. 9.2.8) leads to the same conclusion: Inter fibre base paper pores are a magnitude higher than the size of the coarsest particles in coatings which leads to the well known problems in coating holdout of precoatings. Fine particles like latices will get lost into the base depending upon coating colour viscosity and base paper density.
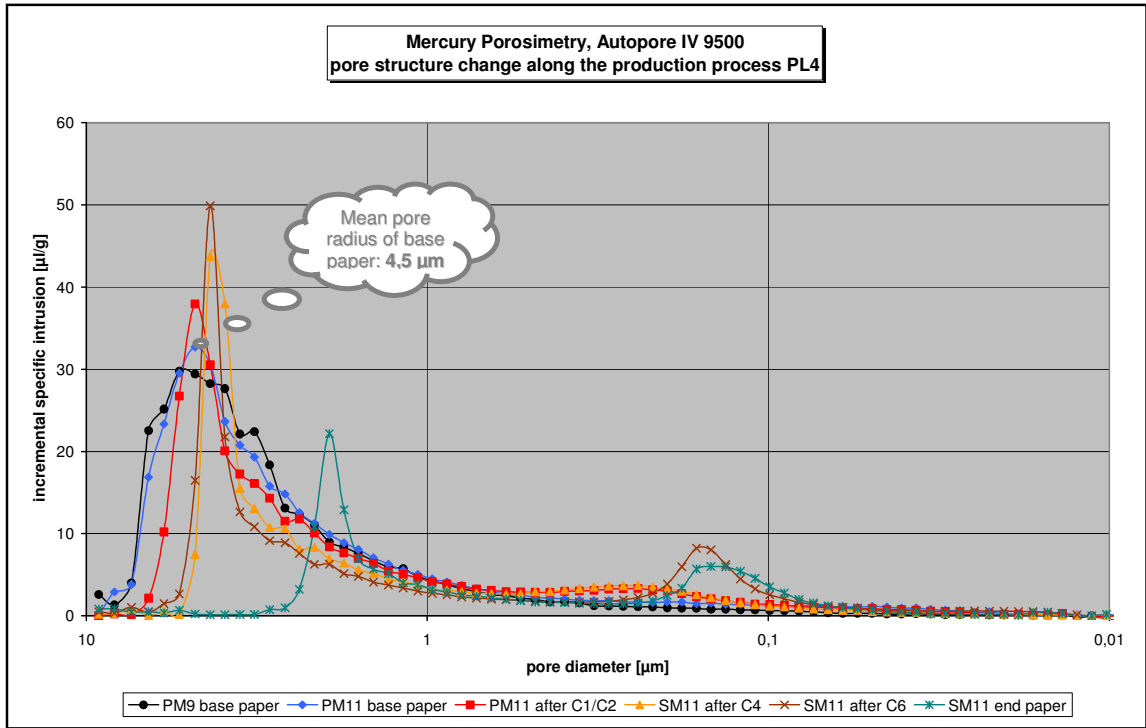
Pict. 9.2.7: Pore size distribution of base papers and coated / uncalendered papers
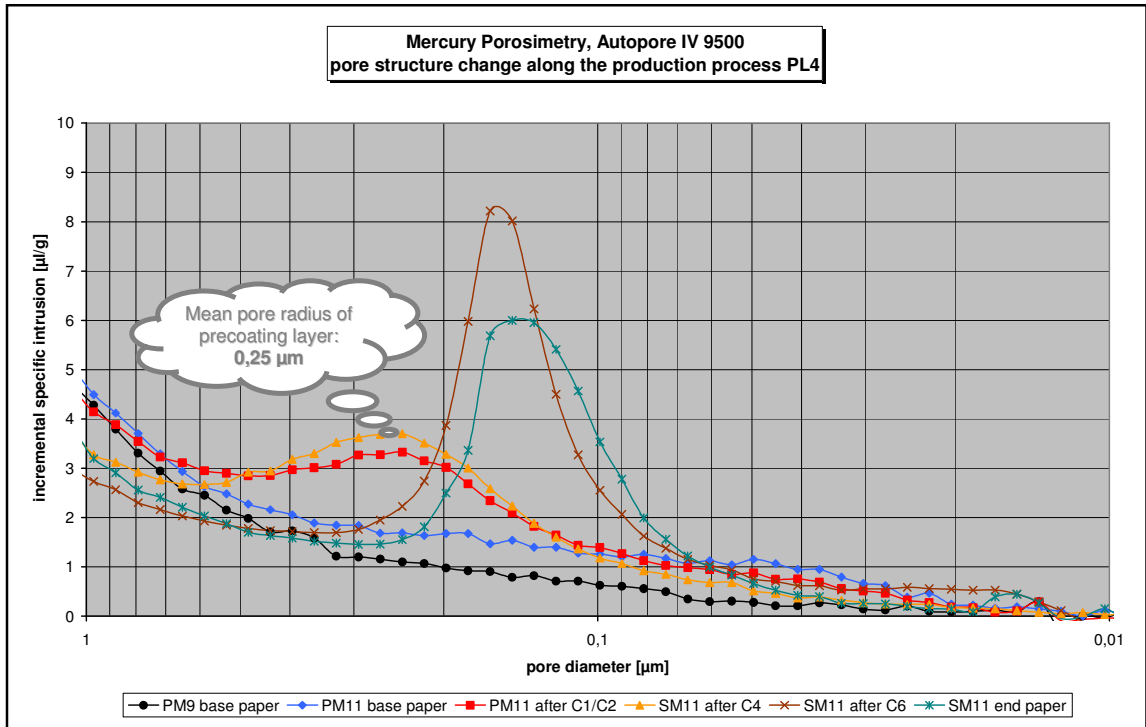
Pict. 9.2.8: Pore size distribution of coating layers without calendering

In the next part **starch** was compared with latex as a binder in precoating formulations.
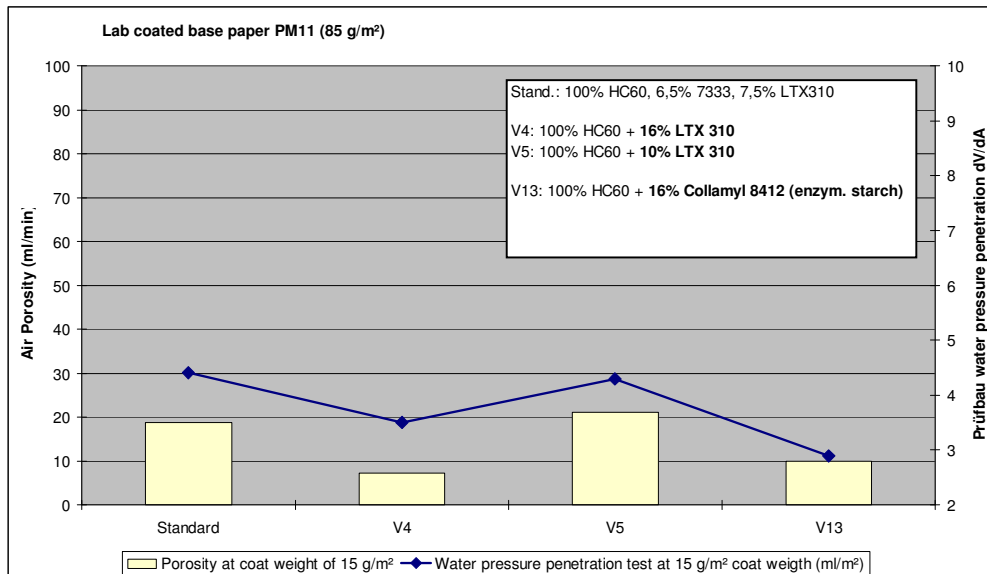
Pict. 9.2.9: Comparison of permeability of latex based coatings with starch based coatings
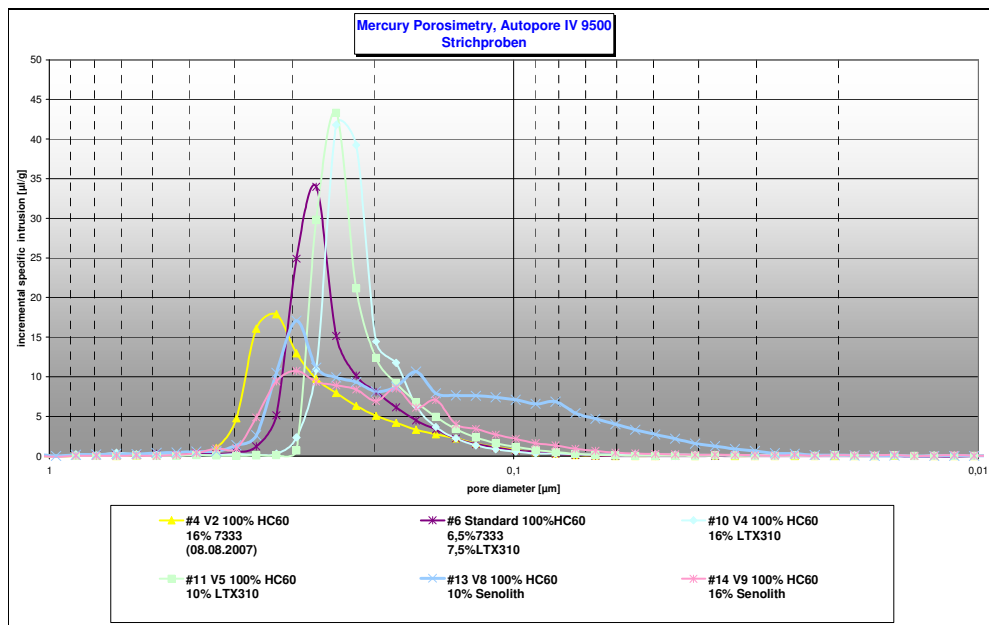
Pict. 9.2.10: Hg-porosity of starch and latex based precoatings
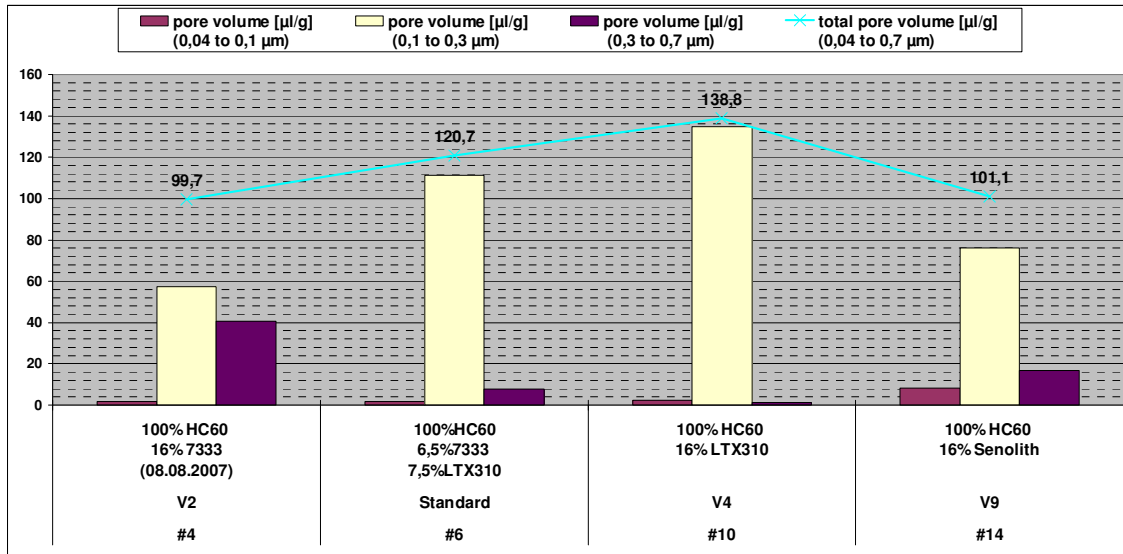
Pict. 9.2.11: Mercury porosity of starch based coatings

Starch based coatings showed lower permeability than latex based coatings at comparable binder levels (pict. 9.2.9 – 9.2.11). Starch is a liquid binder and can therefore fill the pores of the pigment matrix more effectively than latex particles.

Francis Aloi and Dr. Eric Weisser from National Starch (L1.53) studied the film-formation mechanisms of starch in size press applications to improve paper surface properties.

They compared hydrophobic starch esters which are well known for their film forming characteristics with standard starches and increased Gurley porosity data's by 30 – 100% (which stands for lower air porosity).

Starches with high elasticity gave the lowest sheet porosities. A high amylose content and addition of hydrophobic sodium alginate (film former) led to the best barrier properties which is necessary for the holdout of silicone on surface sized silicone base papers.

Additionally the **shrinkage** of the pigment matrix during drying of the coating is more pronounced for starch based coatings which was proven by Gane et al. (pict. 9.4.8)

The permeability of coating layers with **different types of carbonates** was compared in the next part. Pict. 9.2.12 – 9.2.13 shows results from a pre-study with standard carbonates.
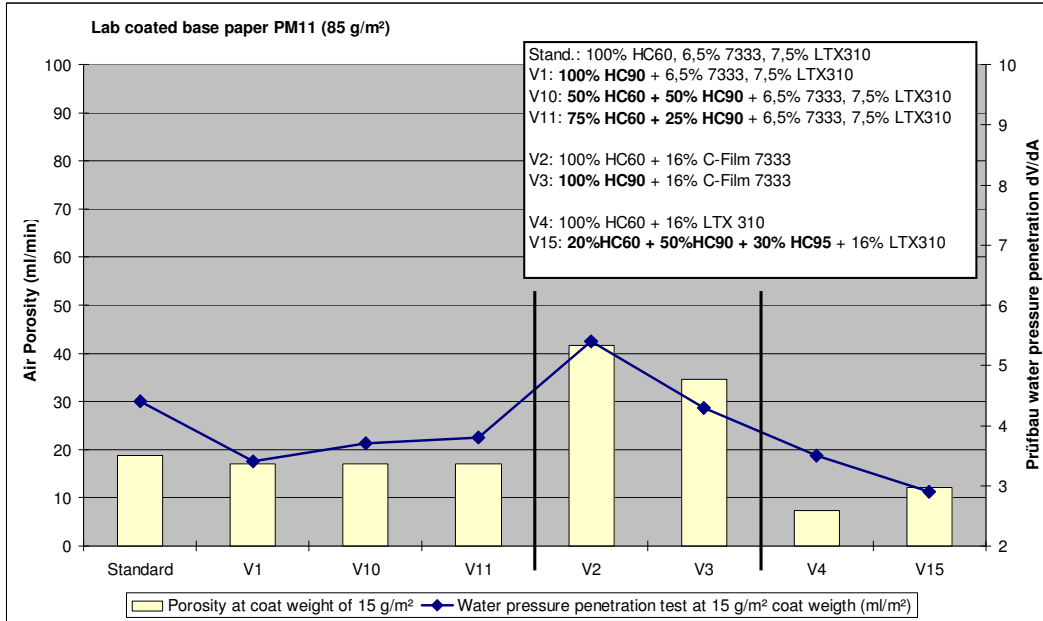
Pict. 9.2.12: Comparing different carbonates in precoating permeability

Pict. 9.2.13: Mercury porosity of precoating colours with coarse HC60 and fine HC90
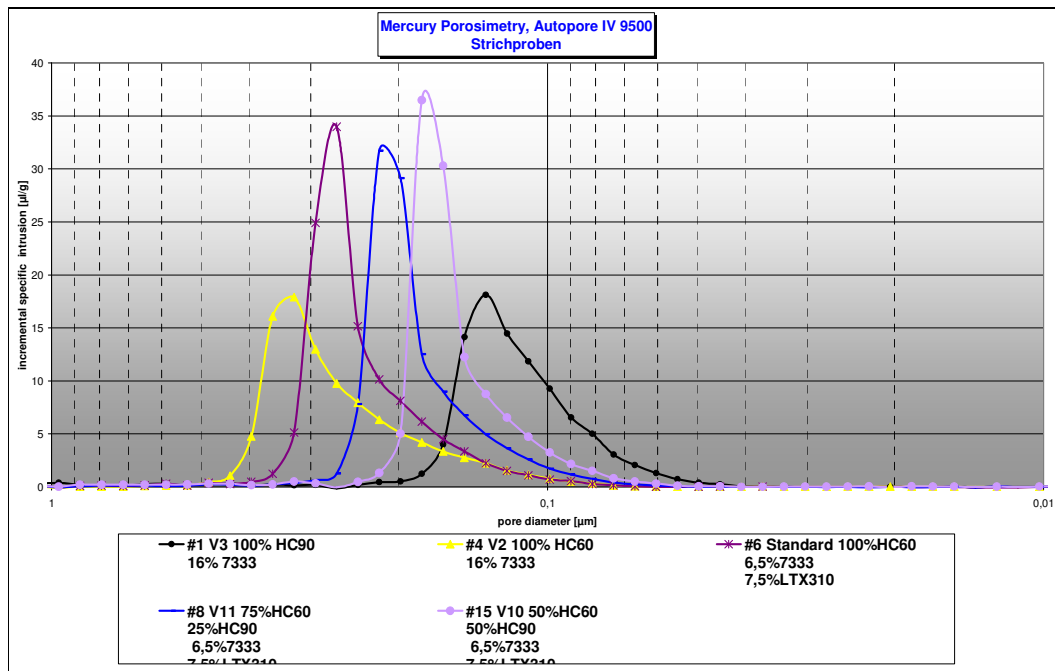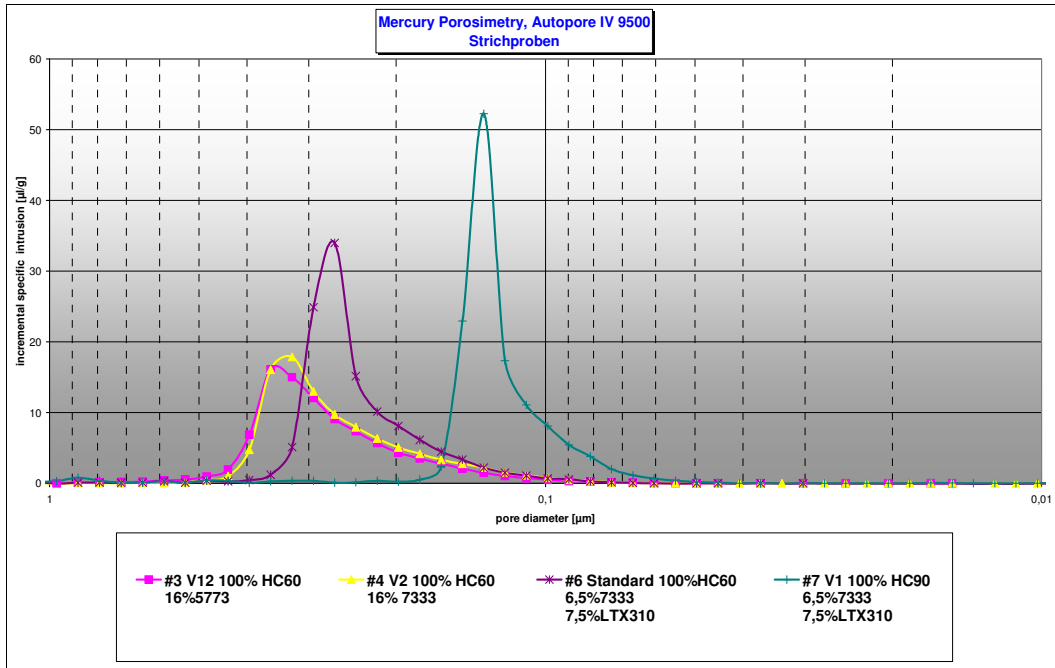
	100% HC60	100% HC60	100%HC60	100%HC90	100%HC90
		6,5% Dextrin	16% Dextrin	6,5% Dextrin	16% Dextrin
	10% LTX310	7,5%LTX310		7,5%LTX310	
Dmax [µm]	0,24	0,27	0,33	0,13	0,13
total pore volume [µl/g]	139	121	**100**	131	**95**

When finer carbonate HC90 was used instead of coarse HC60 the mean pore diameter, measured by Mercury porosity, was lower. Permeability of coating layer was reduced.

Pict. 9.2.14 shows the summary of lab experiments, part 1:
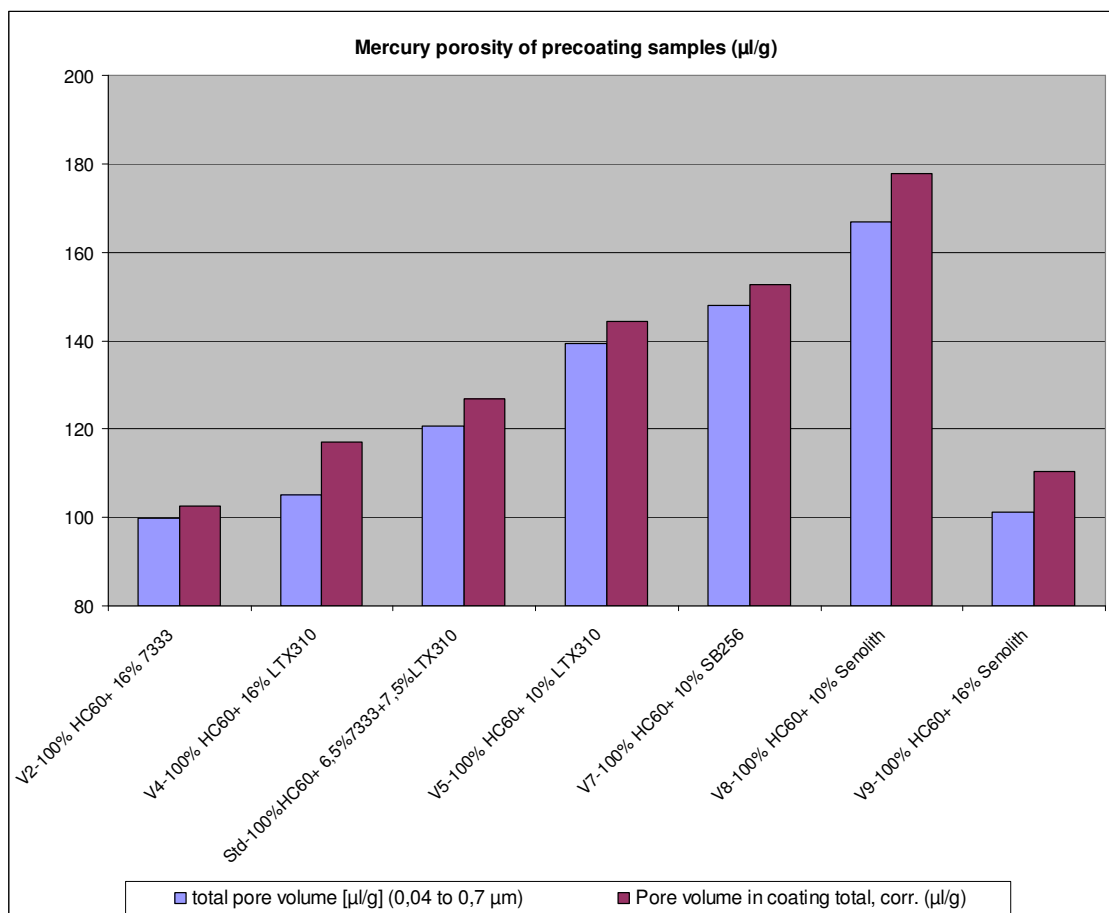
Mercury porosity of precoating samples (µl/g)

Legend:
- total pore volume [µl/g] (0,04 to 0,7 µm)
- Pore volume in coating total, corr. (µl/g)

Categories (x-axis):
- V2-100% HC60+ 16% 7333
- V4-100% HC60+ 16% LTX310
- Std-100%HC60+ 6,5%7333+7,5%LTX310
- V5-100% HC60+ 10% LTX310
- V7-100% HC60+ 10% SB256
- V8-100% HC60+ 10% Senolith
- V9-100% HC60+ 16% Senolith

Pict. 9.2.14: Porosity of coating tablets (no loss of fines and solubles into base paper) – comparison of different precoating formulations

Porosity of precoatings can be reduced by:

- Replacing latex by starch (or generally particle based binders by liquid binders)
- Increasing the amount of binder (liquid or solid) up to the CVC (critical volume concentration)
- Lower the diameter of latex particles (more particles will be used)
- Lower the Tg of latex – improve its film forming

9.3 Lab experiments part 2

Precoatings with different types of **pigments** (pict. 9.3.1) were compared in Darcy coefficient.

Muster	V46	V47	V48	V49	V50	V51	V52	V53	V54	V55	V56	V57
HC60-NW NP	100				100			70	30	50	75	50
HC90		100				100		30	70	30		25
HG40			100							20		
CC75				100			100				25	25
Dextrin VS2-Jetstärke	16	16	16	16				16	16	16	16	16
Latexia PE1844					16	16	16					

Pict. 9.3.1: Tested lab coatings

- HC60: Carbonate with broad particle size distribution and 60% of particles < 2 µm

- HC90: Carbonate with with broad particle size distribution and 90% < 2 µm

- HG40: Carbonate with with broad particle size distribution and 96% < 2 µm

- CC75: Carbonate with with steep particle size distribution and 75% < 2 µm

- Dextrin VS2-Jetstärke: Dextrine starch with low mean molecular weight

- Latexia PE1844: Styrene Butadiene based latex with Tg = 10°C and 150 µm PS

The coatings were again applied by a lab rod coater (pict. 9.2.1) and dried immediately after application by IR. In comparison to mill coaters the application pressure at the lab rod coater is much lower leading to a better holdout of fines. Permeability of lab coatings is therefore lower when compared to mill coatings and the influence of coating colour water retention on coating layer permeability is left out in this experiment.

The Darcy coefficient was calculated from Prüfbau pressure penetration test data's by using Darcy's law $\dfrac{dV_f}{dt} = \dfrac{K * A * \Delta p}{\eta * L}$ and compared to Mercury porosity measurements at OMYA.
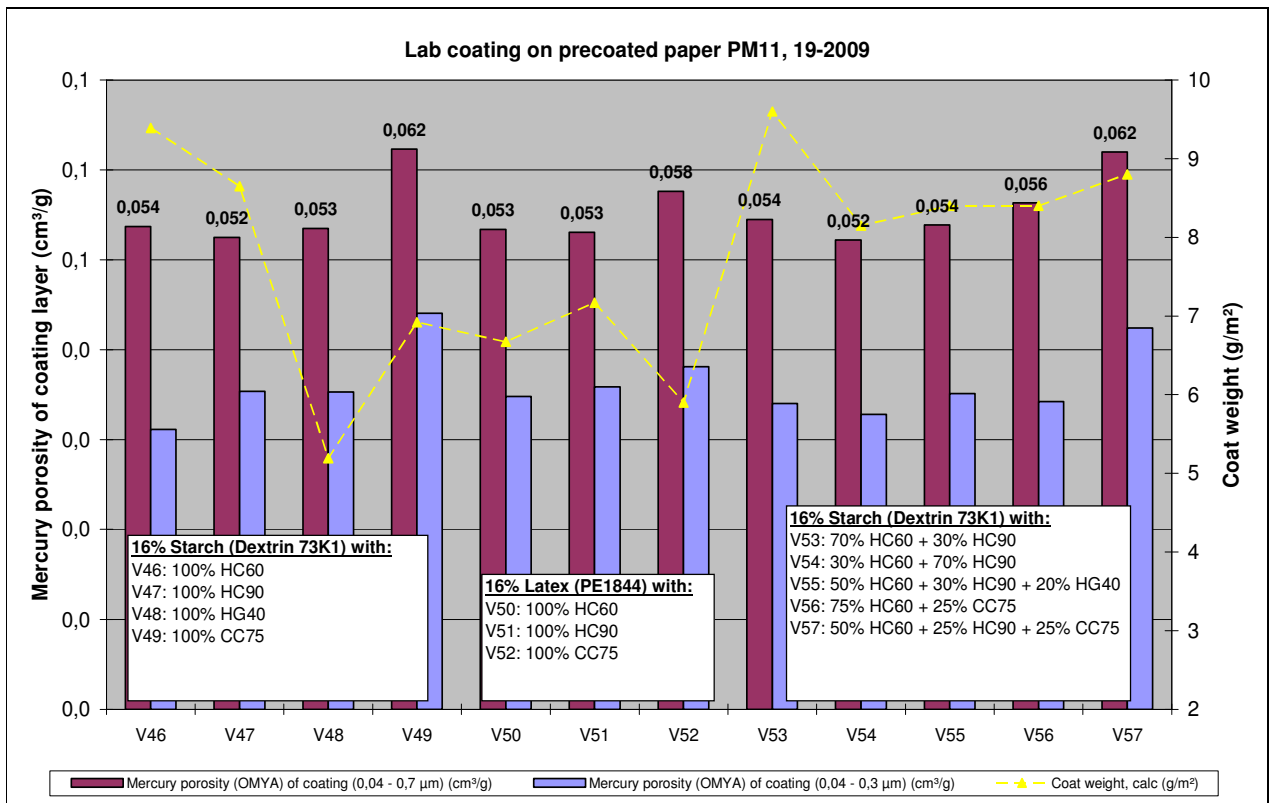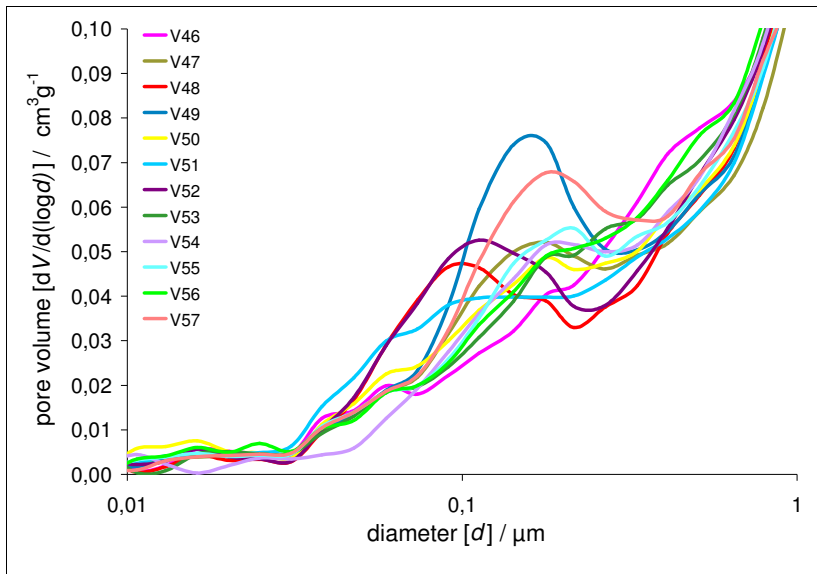
Pict. 9.3.2: Mercury porosity of the lab precoating layer
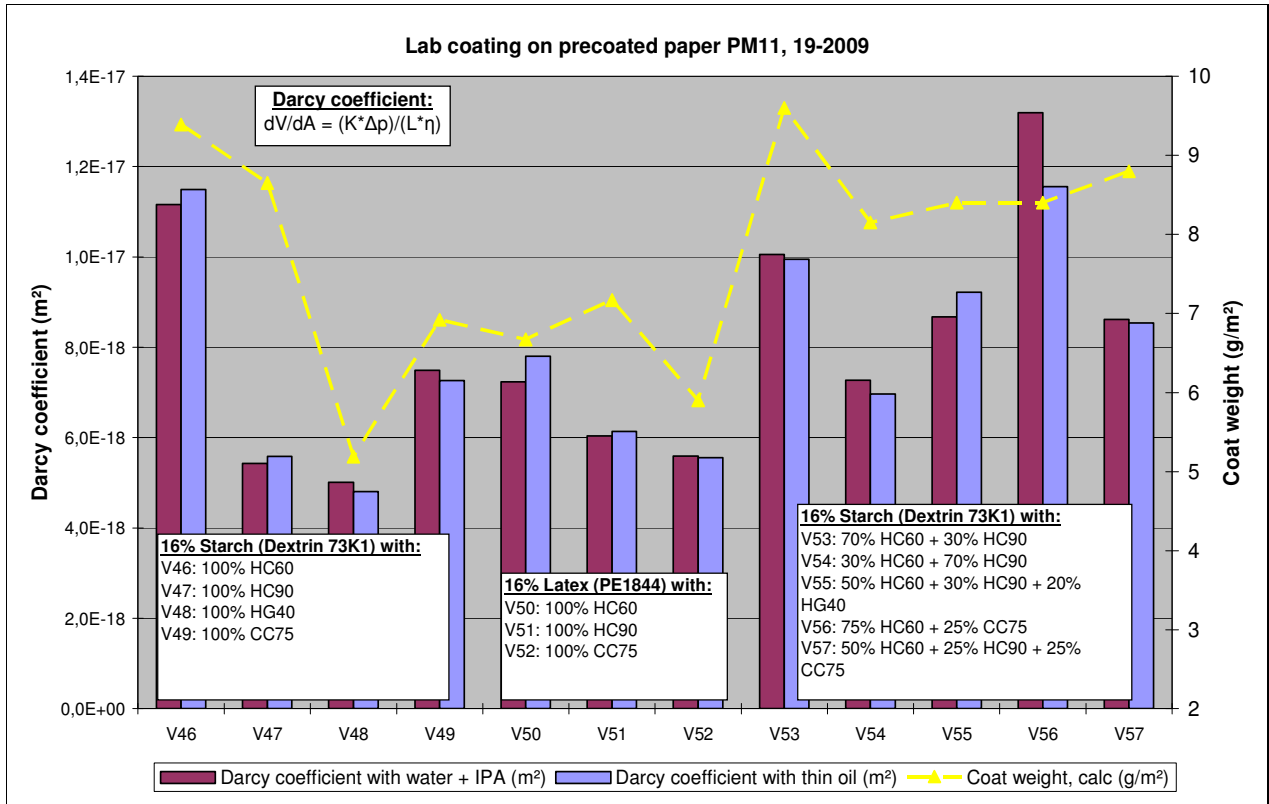
Pict. 9.3.3: Calculated Darcy coefficient of lab precoating layer from Prüfbau pressure penetration test

Pict. 9.3.3 shows that fine pigments (like HC90 or HG40) gave lower permeability than coarse HC60, both for latex and starch based coatings, as they created more dead end pores where fine pigment particles block the pathway of the liquid pressed through the coating layer. Unfortunately costs increase when finer carbonates are used but this solution is much cheaper than the previously shown increase in latex content.

Covercarb 75 with steep PSD increased permeability when compared to HC90 due to the higher porosity of the coating layer and less fine particles to block the pathway.

A good compromise between lower permeability and raising costs is a mixture of HC60 with HC90 which leads to an ideal packing of the pigment matrix. The more HC90 is used, the denser the layer gets.

Covercarb is clearly the wrong choice to reduce permeability except when fine Covercarb grades replace coarse GCC like done in mill trial BV12a-2007 (pict. 9.3.4).
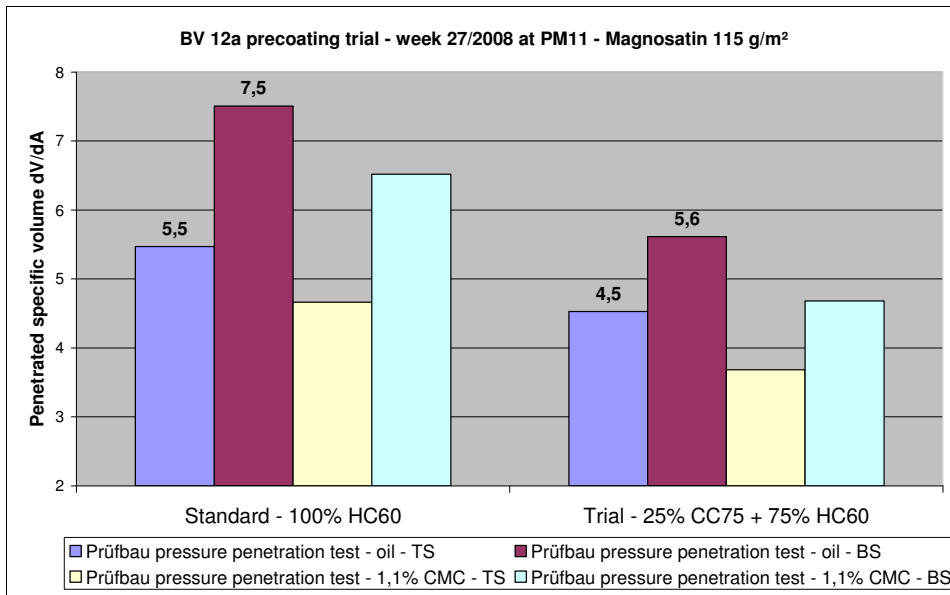
Pict. 9.3.4: Reducing precoating layer permeability by shifting from HC60 to Covercarb 75

As price of Covercarb is almost the double of HC60, this is no reasonable solution to improve mottling.

The same conclusion was drawn by G. Blouvol, M. Käßberger and F. Reichart from OMYA at the PTS coating symposium 2009 who tried to lower the permeability of precoating layers by the right choice of pigment mixture.

Mass and volume concentration of pigment slurries can be calculated with:

$C_{mass} = m_{solids}/(m_{solids} + m_{water})$

$c_{vol} = V_{solids}/(V_{solids} + V_{water})$ for a single solid component or

$c_{vol, A} = V_{solids\ of\ component\ A}/(\Sigma V_{solids} + V_{water})$ for a component A in multiphase systems

Examples:

GCC with density 2,7 g/cm³ and with c_m = 78%: c_V = 0,57%

GCC with density 2,7 g/cm³ and with c_m = 72%: c_V = 0,49%

Clay with density 2,6 g/cm³ and with c_m = 72%: c_V = 0,50%

TiO_2 with density 4,2 g/cm³ and with c_m = 78%: c_V = 0,46%

Latex with density 1,03 g/cm³ and with c_m = 50%: c_V = 0,49%

Theoretically an ultrafine GCC has the same volume fraction c_V (0,57 at 78% solids) than an ultra coarse GCC due to same solid density but a much higher amount of particles in the slurry.

But as the pigment particles are covered with a thin anionic polyelectrolyte layer to provide electrostatic stabilization and to prevent flocculation. According to OMYA this layer has a thickness of 20 nm.

The diameter of an HC60 particle is thereby increased from 1,52 µm to 1,54 µm (+8%) whereas it rises from 0,55 to 0,57 (+23%) for a ultrafine HC95 particle.

1,23 / 1,08 leads to 14% higher occupied volume of the ultrafine GCC.

Therefore the probability of flocculation by overlapping hydration layers increases with raising solids faster for ultrafine pigments.

OMYA entitles this increase of occupied volume by the hydration layer the "occupancy factor". It can be calculated from: $O_f = 1 + \dfrac{0,04}{d_{50}}$.

The effective volume fractions increase for GCC's (pict. 9.3.5):

HC60: 0,57 → 0,61
HC90: 0,57 → 0,66
HC95: 0,57 → 0,70

This increase in volume fraction is the reason for the improved water retention of fine pigment slurries as pigment packing is higher.

Literature indicates a maximum volume fraction $c_V = 0,74$ for uniform spheres but much higher volume fraction can be achieved when multiform particles are mixed:
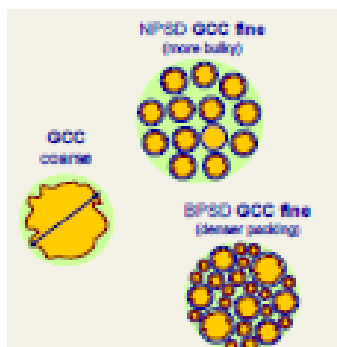
Pict. 9.3.5: Mono sphere vs. multi sphere particle packing (OMYA)

OMYA uses a pressure penetration cell (pict. 9.3.9) to measure the permeability coefficient. Pict. 9.3.6 shows comparisons of these permeability measurements with mercury porosity of different pigment tablets.
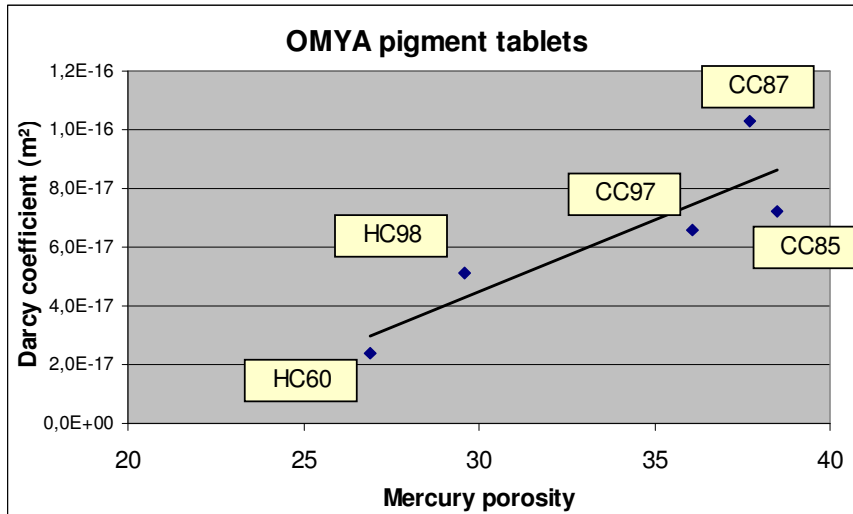
Pict. 9.3.6: Correlation between mercury porosity of coating layer and Darcy coefficient for different carbonates (data's from OMYA)

Pigments with lower Mercury porosity had a lower permeability according to Carman Kozeny equation. Broad GCC's lead therefore to lower permeability in precoatings than steep CC's or PCC's especially when they contain a significant amount of fine particles in the size of latex particles to block their path way through dry precoating layers.

Latex based coatings, applied by PT4 lab rod coater, gave lower permeability in the lab than starch based coatings while in mill trials this was always the other way round due to the superior water retention of starch based coatings.
This can also be seen in the opacity of the precoatings: There was no difference between latex and starch based lab coatings while mill coatings always show lower opacity for starch based coatings as more starch is retained and the pores between pigment particles are filled with starch instead of air which contributes to scattering.
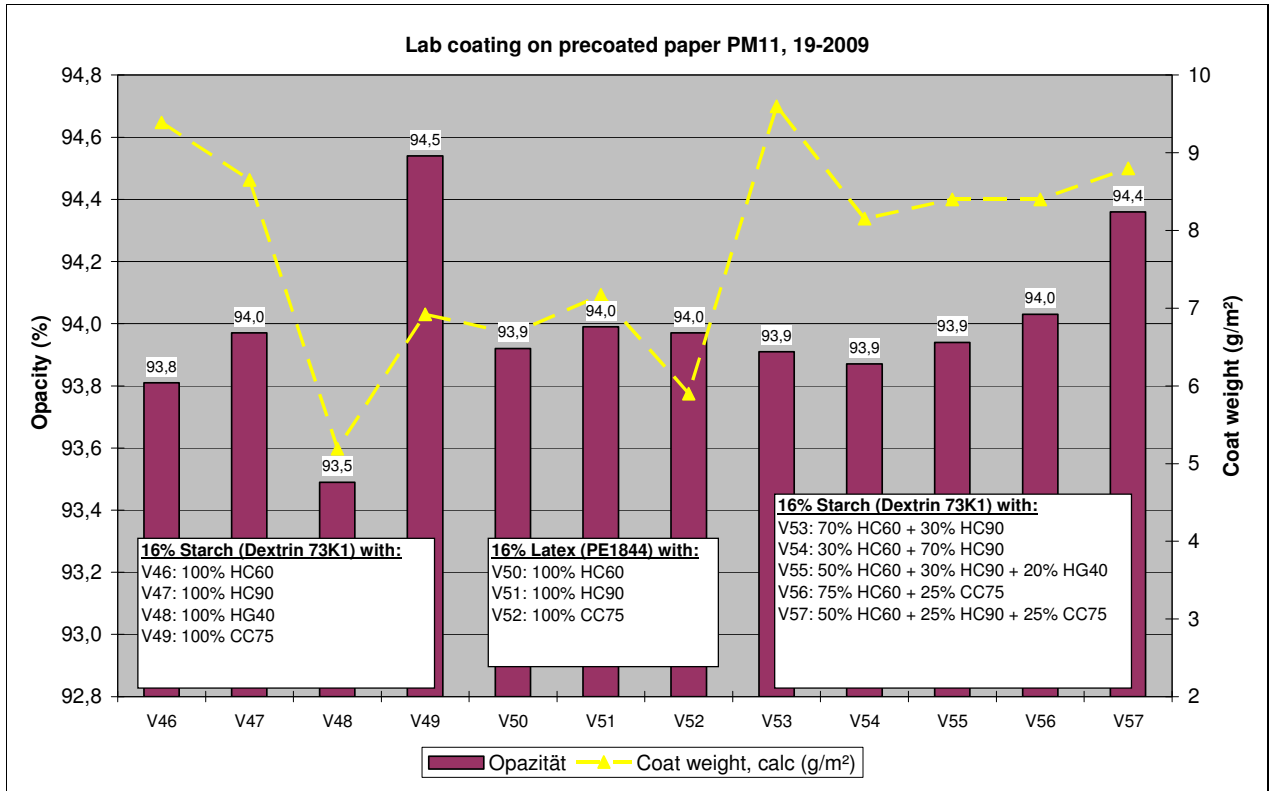
Pict. 9.3.7: Opacity of lab coatings

Steep PSD pigment Covercarb 75 led to higher opacity due to higher porosity of the coating layer (pict. 9.3.7).

Set off gets clearly faster when Covercarb (CC) is used instead of standard HC60 or HC90 as amount of fine pores is increased and less dead end pores are created with this type of pigment (pict. 9.3.8)
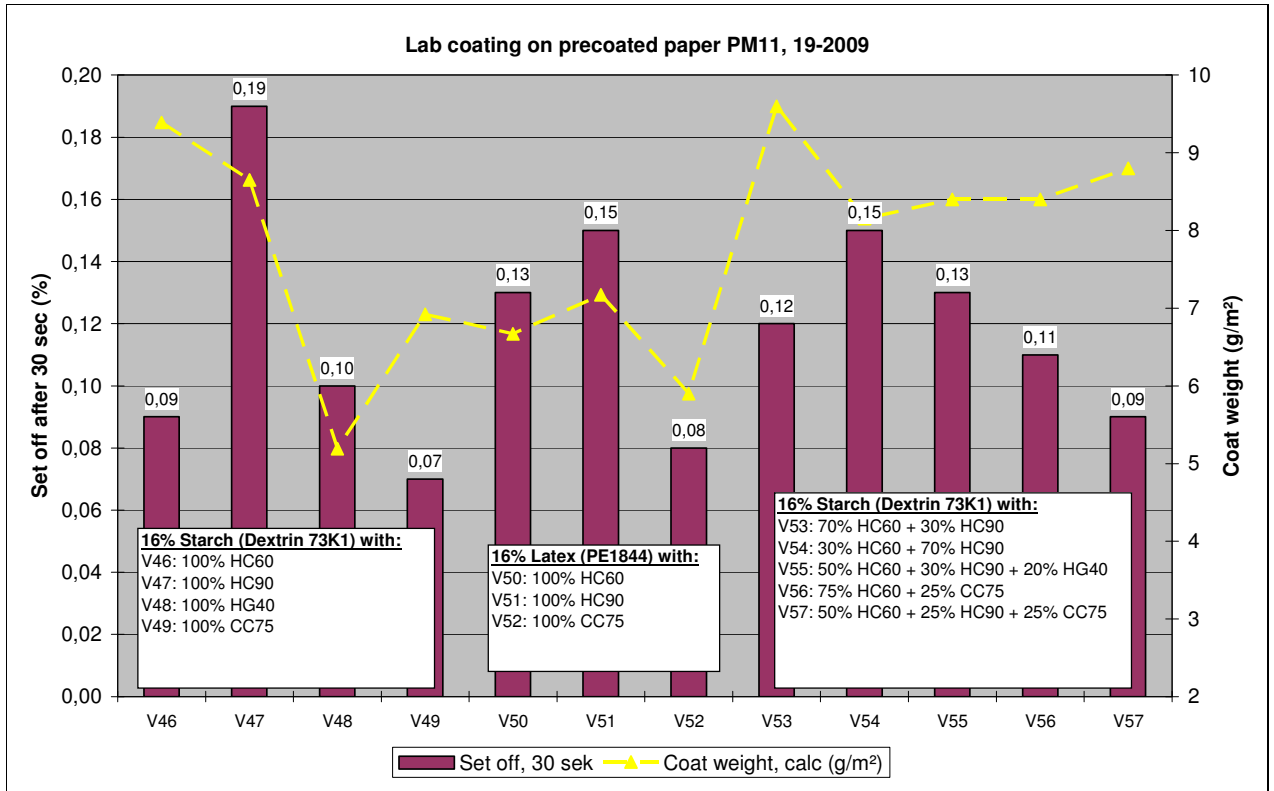
Pict. 9.3.8: Set off of lab precoatings

The precoated samples were sent to OMYA-Oftringen where their permeability was measured by the pressure penetration cell of OMYA (pict. 9.3.9).
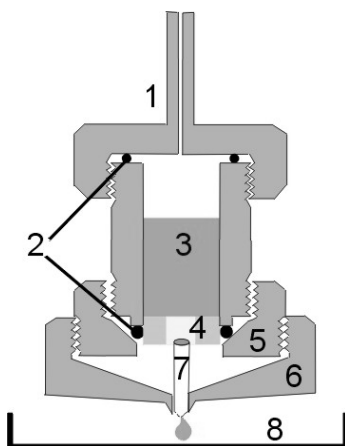
Pict. 9.3.9: OMYA permeability measurement cell : 1) lid with pressure inlet, 2) sealing O-rings, 3) liquid cell; outer diameter = 40 mm, 4) porous sample embedded in resin disc of diameter = 30 mm, 5) fixing ring compresses the O-ring which seals the resin disc, 6) security shroud and drop collector, 7) drop captor (Teflon tubelet), 8) dish on micro-balance

The samples were cut into small pieces (125 pieces cut to 1.5 x 1.5 cm^2 sheets) and put as a stack into the cell. A hydrophobic liquid with known viscosity (hexadecane with density, ρ = 773 kgm^{-3} and viscosity, η = 0.0034 kgm^{-1}s^{-1}) was pressed through the stack of paper samples.
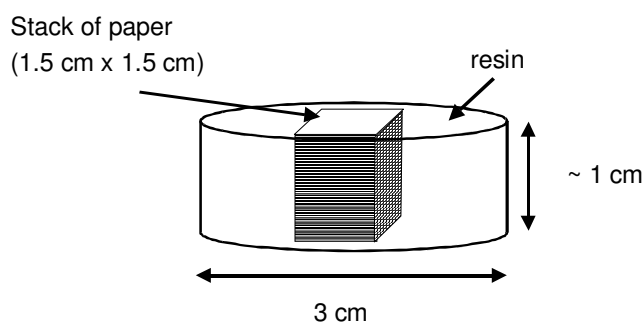
Pict. 9.3.10: Preparation of paper stack for permeability measurement.

By measuring the penetrated liquid on a scale over a certain period of time the Darcy coefficient of the complete coated paper can be calculated with $\dfrac{\mathrm{d}V(t)}{\mathrm{d}t} = \dfrac{-kA\Delta P}{\eta\, l}$
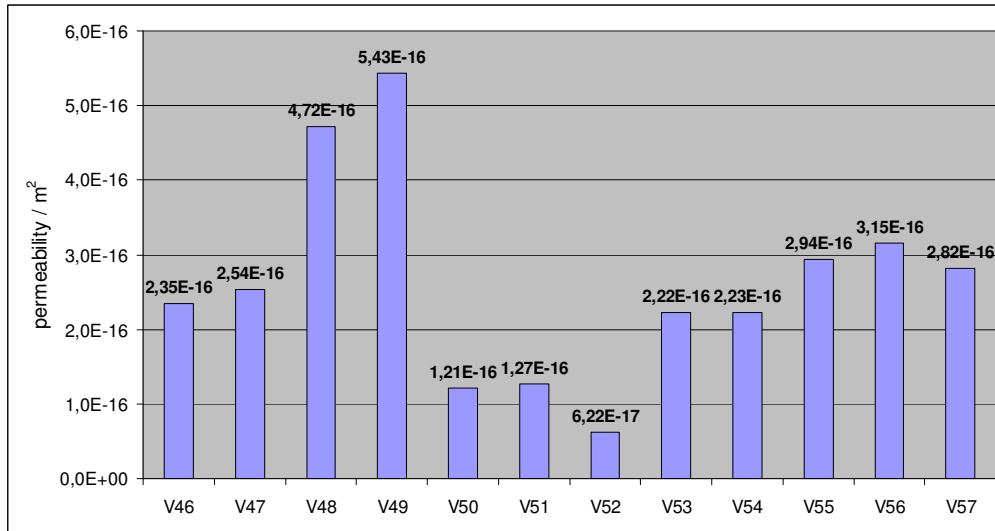
Pict. 9.3.11: OMYA pressure penetration data's of lab precoated papers (whole paper)

To split the permeability coefficient into the base paper part and the coating part the extended form of the Darcy equation for double layers has to be used:

$$v = \frac{d(V/A)}{dt} = \frac{\Delta p_f + \Delta p_M}{\eta * \left[\dfrac{h_f}{K_f} + \dfrac{h_M}{K_M} \right]} \quad \text{and} \quad \left[\frac{h_f}{K_f} + \frac{h_M}{K_M} \right] = \frac{\Delta p}{\eta * \dfrac{d(V/A)}{dt}} \quad \text{and}$$

$$K_f = \frac{h_f}{\dfrac{\Delta p}{\eta * \dfrac{d(V/A)}{dt}} - \dfrac{h_M}{K_M}}$$

With h_f the thickness of the coating layer and h_M the thickness of the base paper, measured by lab thickness instrument.

The Darcy coefficient of the base paper K_M has to be determined in a separate experiment (e.g. by Bendtsen air permeability or by OMYA permeability cell).
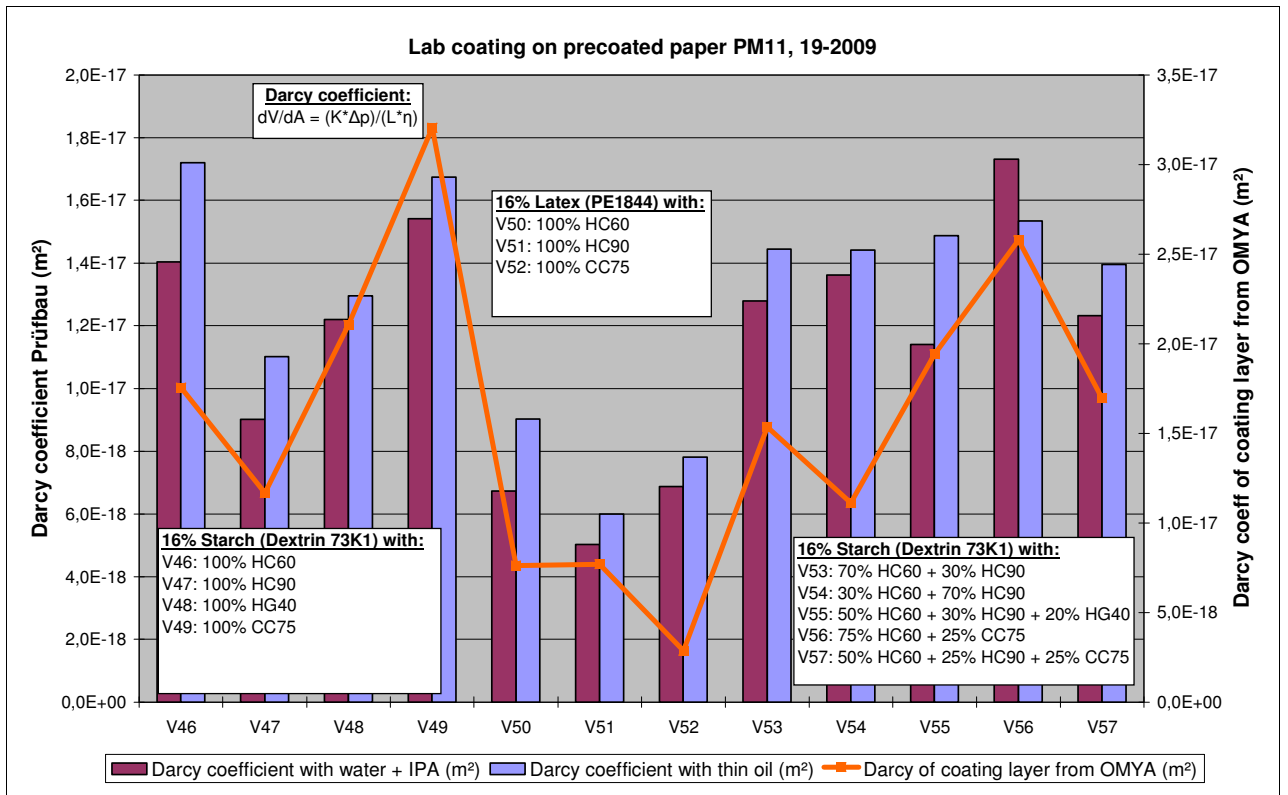
Pict. 9.3.12: Comparison of calculated coating layer Darcy K_f coefficient from Prüfbau and OMYA pressure penetration test
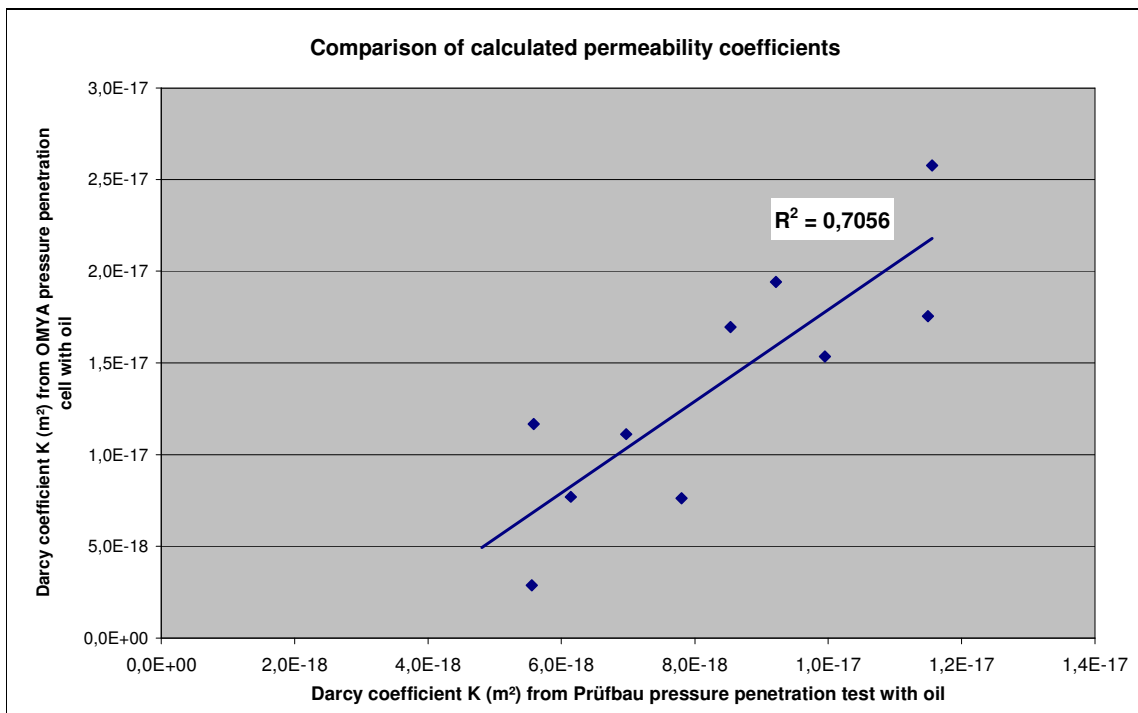
Pict. 9.3.13: Correlation of calculated Darcy coefficient from Prüfbau pressure penetration test and OMYA's pressure cell

The correlation of OMYA pressure penetration tests and Prüfbau pressure penetration test with thin oil as shown in pict. 9.3.12 and 9.3.13 was quite good, proving the practical usability of the Prüfbau test, which is much easier to operate.

Lab coating on precoated paper PM11, 19-2009

16% Latex (PE1844) with:
V50: 100% HC60
V51: 100% HC90
V52: 100% CC75

16% Starch (Dextrin 73K1) with:
V46: 100% HC60
V47: 100% HC90
V48: 100% HG40
V49: 100% CC75

16% Starch (Dextrin 73K1) with:
V53: 70% HC60 + 30% HC90
V54: 30% HC60 + 70% HC90
V55: 50% HC60 + 30% HC90 + 20% HG40
V56: 75% HC60 + 25% CC75
V57: 50% HC60 + 25% HC90 + 25% CC75

Porosity Bendtsen — Darcy coefficient of hole paper from OMYA (m²)

Pict. 9.3.14: Comparison of Bendtsen porosity of lab precoated papers with Darcy coefficient from OMYA pressure penetration cell

Pict. 9.3.14 shows that Bendtsen air porosity correlated also quite well with permeability of finished paper, measured by the OMYA pressure penetration cell with a hydrophobic liquid. As air is a compressible medium, Darcy's law is not applicable. Air porosity can be used as a rough and fast estimation when coatings are compared on constant base paper. Bendtsen measurements are possible at single coated papers, at double or triple coated papers the readings are too low. Gurley porosity has to be used for these kind of papers.

The precoated papers V46 – V57 were also analysed at OMYA by Mercury porosity (pict. 9.3.15).
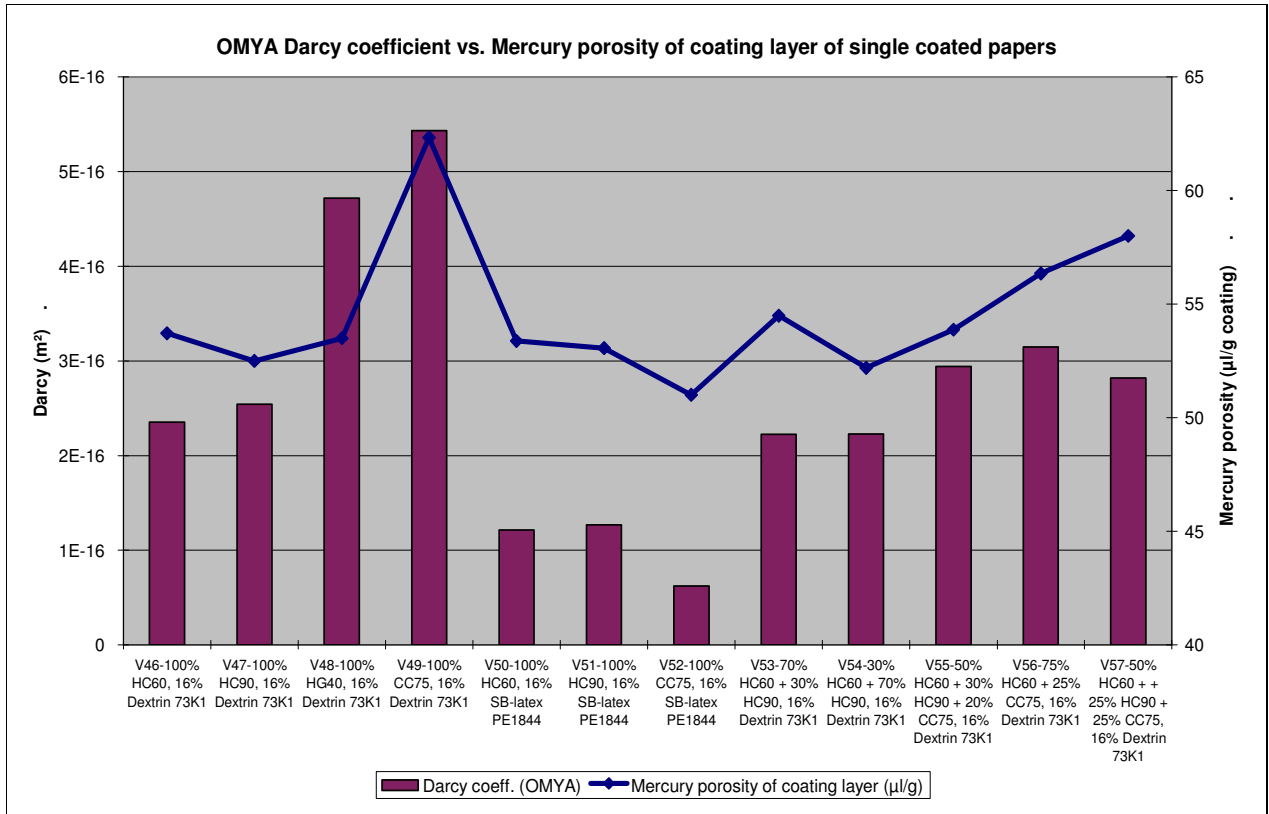
Pict. 9.3.15: OMYA Mercury porosity of coating layer (0,04 – 0,7 µm) vs. Darcy coefficient of whole precoated paper

The higher the porosity of the precoating layer, the higher the Darcy coefficient according to the Carman Kozeny equation. Precoatings containing Covercarb or PCC (HG40) with steep PSD have higher Darcy coefficients than broad PSD carbonates HC60/90. They cannot isolate the base paper properly against pressure penetration of the following coating layer.

Adding fine HC90 to coarse HC60 lowered the Darcy coefficient.

Latex based lab coatings had lower porosity of the coating layer which stood again in contradiction to mill trials where the latex retention in the coating was much worse due to much higher application pressure.

Latex holdout in the coating has a big impact on permeability of the coating layer. In a lab coating experiment the latex holdout of a top coating was compared for applications on either an uncoated base or a double precoated paper. Results are shown in pict. 9.3.16.

sappi GK/PQ	TITEL		Lab coated samples with glossy topcoat Rez. 390	
			on base paper	on double precoated paper
Gloss (Tapp 75°)	%	OS	**20,92**	**35,57**
Gloss (DIN75°)	%	OS	3,43	8,95
PPS smoothness	mikrons	OS	6,382	3,102
Porosity Bendtsen	ml/min		25,40	1,21
Set off test, 30 sec		OS	**0,04**	**0,20**
			5µl	5µl
Prüfbau pressure penetration test with water	mm²	OS	1451	2677
-- " --	ml/m²		**3,45**	**1,87**

Pict. 9.3.16: Comparison of latex holdout on two different substrates

Permeability of dry top coating layer was reduced by 50% when it was applied on dense double precoated paper compared to coating it on porous base paper due to improved holdout of latex and pigment fines.

This was also detected in a much higher gloss of the top coated sample which was applied on the double precoated paper.

This experiment was done under almost pressure-less conditions of the lab rod coater. In mill coaters the difference is even higher due to much higher application pressure.

Results of the 1st and 2nd lab study – measures to reduce permeability of precoatings:

- Use pigments with broad PSD instead of Covercarb or PCC with steep PSD.
- Using a pigment mixture with fine and coarse pigments leads to the densest possible packing.
- Use starch, PVOH or other liquid binders instead of latex.
- Increase the amount of binder (starch or latex) – expensive!
- Avoid web offset latices which create high coating porosity. Use soft latices with high cross linking.
- Use latex with broad PSD or mix fine and coarse latices to achieve broad PSD
- Use fine latices only in middle and top coatings not in the 1st precoat to avoid latex penetration into the substrate.

9.4 Pilot trials with dense precoatings

At CTC a pilot trial was performed in week 50-2007 to implement the strategy of increasing the latex content in the 1st precoating.
In the reference precoat 5% starch and 7% latex was used, in the starch free test precoating the latex content was 10.

The best barrier effect was expected for the precoat with 20% of soft SB latex.
It was compared with the thin layer barrier coatings, described in the previous chapter.

Prüfbau pressure penetration test with water
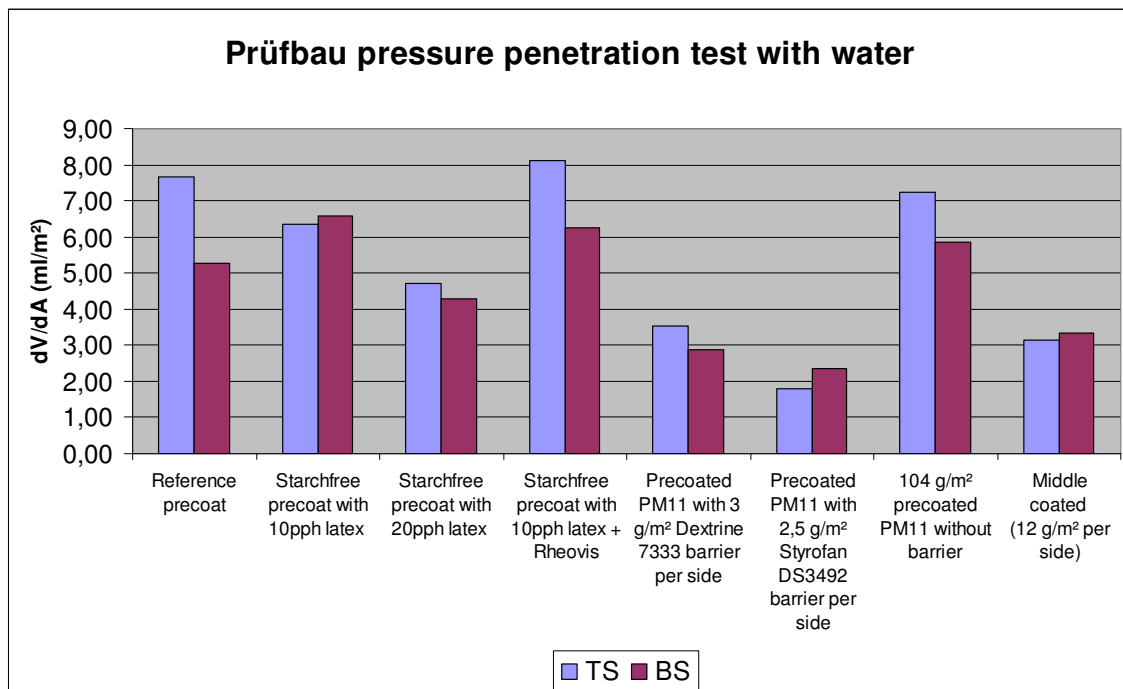
Pict. 9.4.1: Pressure penetration resistance after precoating + barrier layer – comparison barrier layer with dense precoating

Pict. 9.4.1 shows that permeability of the thin layer barrier layers was lower than that of precoating containing 20% latex. To achieve the same permeability the CPVC (critical pigment volume concentration) would have to be reached for the precoating which would have been the case for 30% latex.

L. Abrahams, C. Favorite, P. Caprano and R. Johnson (L1.23) used mercury porosity to characterize coating pore structure and it's relation to coating optical performance.

The pigment volume concentration (PVC) is the volume occupied by the pigment particles as a percentage of total volume. During drying the void volume between the pigment particles is reduced. At the critical pigment volume concentration (CPVC) all interstices are filled with pigment or binder particles.

Commercial paper coatings stay during drying under the CPVC – therefore dry coatings contain a significant volume of air filled voids.

Cathy Ridgeway and P.A.C. Gane (L1.59) measured the effect of latex and pigment volume concentration on suspension and consolidation packing. The viscosity of carbonate slurries was measured by adding increasing latex amounts and increasing solids in the way.
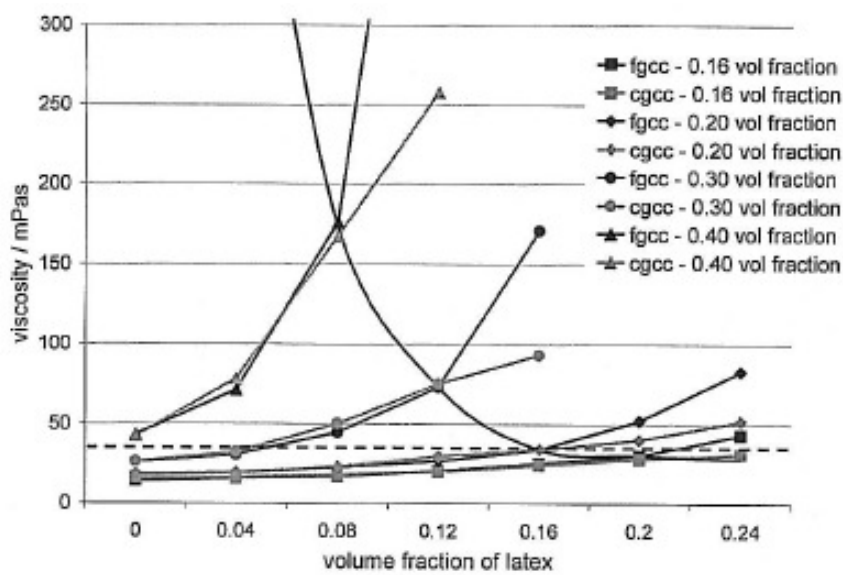
Pict. 9.4.2: Viscosity vs. latex content (C.Ridgeway)

Viscosity increased with latex content and solids, especially when finer carbonates were used (pict. 9.4.2).

When volume fraction of latex is raised at constant volume solids of pigment, the space between the host material particles (GCC) decreases logarithmically, as the total volume fraction decreases also logarithmically.

This effect can be used to form high viscous immobilized coating layers at the boundary to the base paper which prevent liquid phase penetration under the blade.

C. Ridgeway measured mercury porosity of pigment slurries with increasing latex content.
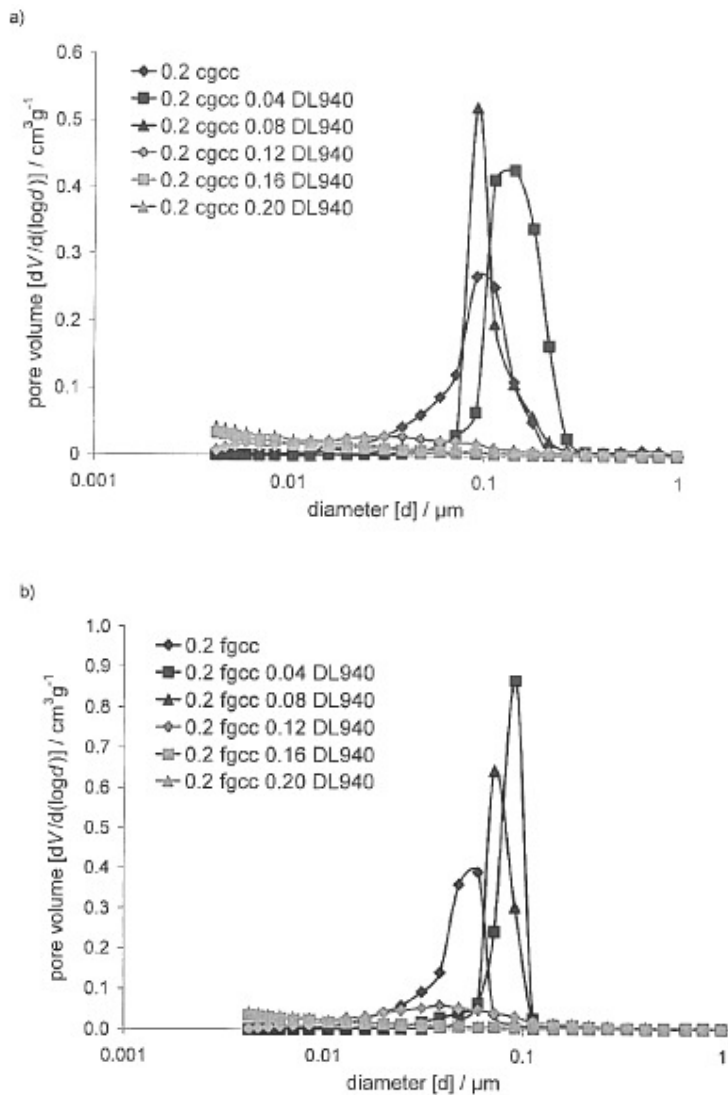
Pict. 9.4.3: Mercury pore size distribution of a) coarse GCC (HC60 and b) fine GCC (HC90) with increasing volume fraction of latex (C.Ridgeway)

Adding a small quantity of latex increases the pore volume. Further latex addition reduces the pore volume and the pore size. Adding a volume fraction of 0,2 of latex filled all the pores between the pigment particles (pict. 9.4.3).

The measurements of Cathy Ridgeway are important for the formation of a filter cake before the blade which should reduce pressure penetration of liquid phase and latex under the blade: The calculated porosities of filter cake in chapter "water retention" show that when synthetic thickeners or starches are used to improve the water retention of coating colours the viscosity and thus the porosity of the filter cake

increases. The positive effect of the improved water retention by using higher amounts of thickeners is partly compensated by the higher permeability of the filter cake before the blade.

Increasing the amount of fine particles in pre- and middle coatings lowers the permeability of the filter cake without any side effects.

Viscosity of coating colour and the way how the colour is dried are also important parameters which determine the dry porosity of the coating layer. Fast drying and high colour viscosity will increase porosity.

Alexandra Wallström and Lars Järnström (L1.60) studied the influence of thickeners on coating surface structure. They measured Mercury porosity of coatings with increasing amount of thickeners. Spherical polystyrene particles (250 nm) were used as pigment to avoid interaction of thickener ions with the hydration layer of carbonates or clays.
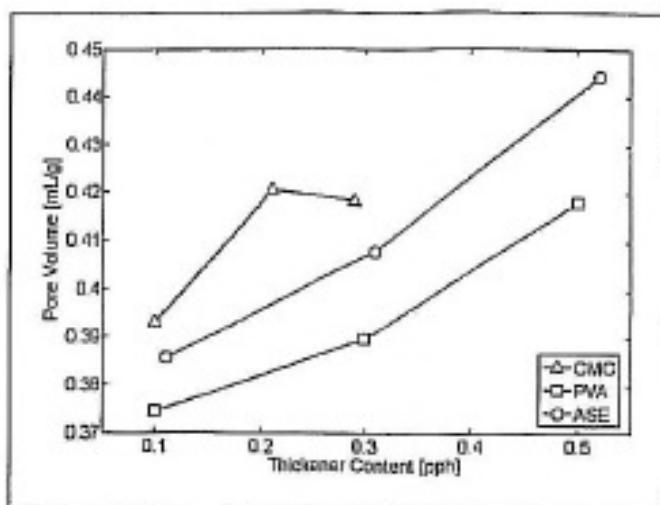
Pict. 9.4.4: Pore volume of coatings vs. thickener content (A. Wallström)

Pore volume increased with thickener content as the pigment particles could no more move into the optimum packing structure during coating and consolidation (pict. 9.4.4).

G.M. Laudone, G.P. Matthews and P.A.C. Gane (L1.73) modelled the shrinkage in pigmented coatings during drying and developed a stick-slip mechanism for the movement of particles together during drying.

Using the Pore-Cor model the capillary shrinkage forces during drying were calculated and compared to experimental measured forces.
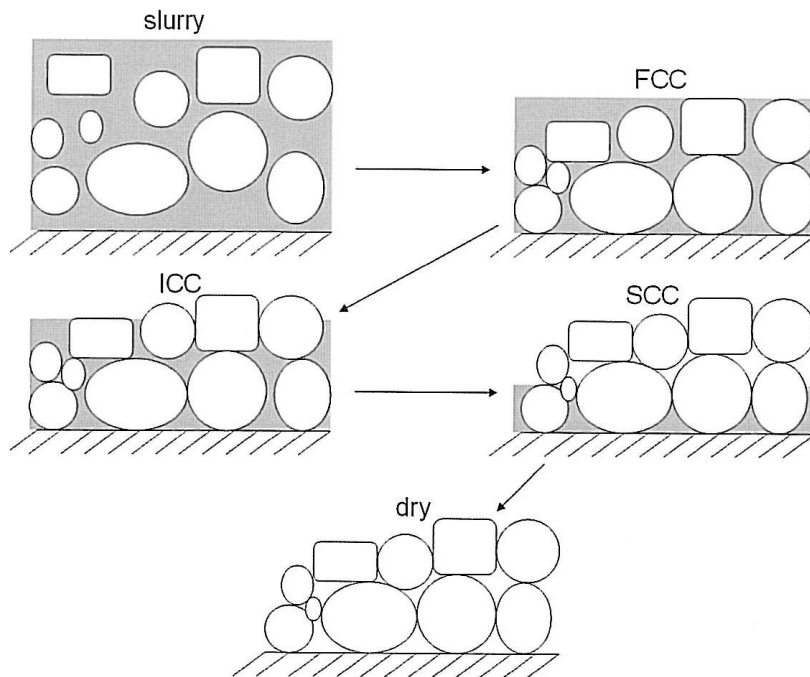
Pict. 9.4.5: Drying process, described by Watanabe and Lepoutre

When the first critical concentration (FCC) is reached during drying, a three-dimensional fluid-filled network is formed. Particle motion is restricted (pict. 9.4.5).

After the FCC the pores form capillaries and shrinkage of the coating layer starts. The structure gets distorted and collapses.

The process of collapsing is not continuous. It was described as a stick-slip process by the authors. When the capillary force overcomes the particle interaction forces, the particles will move stepwise together and coating layer porosity will drop.

At the second critical concentration (SCC) liquid is replaced by air. Particles touch each other. The position of the particles is locked. Migration of particles is not possible any more.

Sample :	Acrylic high T_g latex	SB low T_g latex
GCC60	19.8	14.2
GCC90	37.7	15.5

Pict. 9.4.6: Mercury porosity of dry samples (G.M. Laudone)

As non film formed latex particles remain in their original sphere form the porosity of the corresponding coating layer was higher than for totally film formed latex.

Sample / Drying stage	Immediately after FCC	ICC	SCC
GCC90 + 25 w/w% of acrylic high T_g latex	67	52.4	37.7
GCC60 + 25 w/w% of acrylic high T_g latex	53.1	36.4	19.8
GCC90 + 25 w/w% of SB low T_g latex	46.9	31.2	15.5
GCC60 + 25 w/w% of SB low T_g latex	63.2	38.7	14.2

Pict. 9.4.7: Porosity at FCC, ICC and SCC (G.M. Laudone)

The development of the mercury porosity of GCC90 + 25 w/w% S320D-latex is: **67% at the FCC**, **37,7 % at the SCC**, which is the same for the **dry sample**.

With a scale and a camera as shown in pict. 9.4.8 G.M. Laudone measured the shrinkage of a thick coating layer on a thin foil during drying (by air) and calculated the stress in the coating layer during drying.
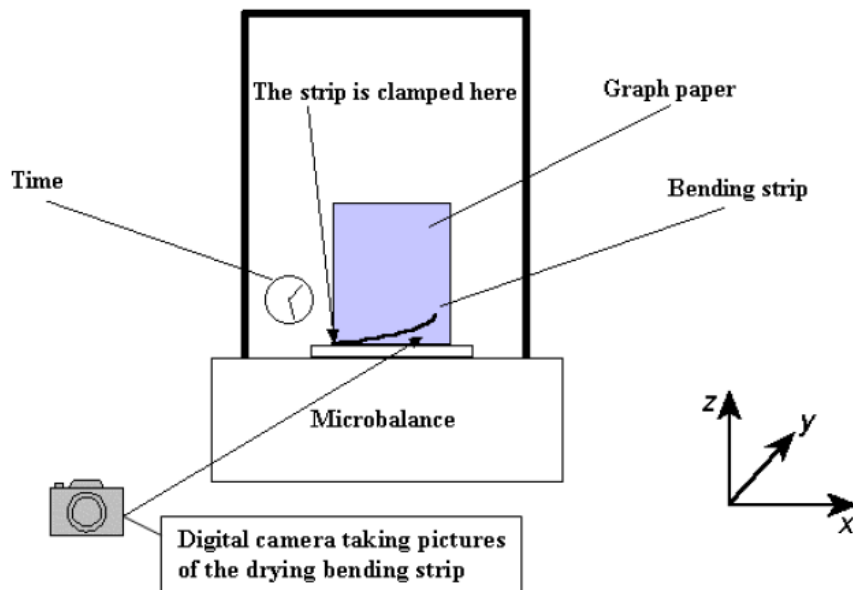
Pict. 9.4.8: Apparatus for measuring the shrinkage forces (OMYA)

Sample :	GCC60+acrylic high T_g latex	GCC90+acrylic high T_g latex	GCC60+SB low T_g latex	GCC90+SB low T_g latex
Maximum measured stress	45	11	121	55
Retained stress	11	0	101	41

Pict. 9.4.9: Max stress and retained stress during shrinkage of coating layer (G.M. Laudone)

The high Tg SA latex did not film form and the structure did not hold the shrinkage stress applied during drying (pict. 9.4.9). The soft SB retained the stress.

The higher shrinkage of GCC60 samples was explained by a more effective packing of the latex particles in the GCC60 matrix during drying.
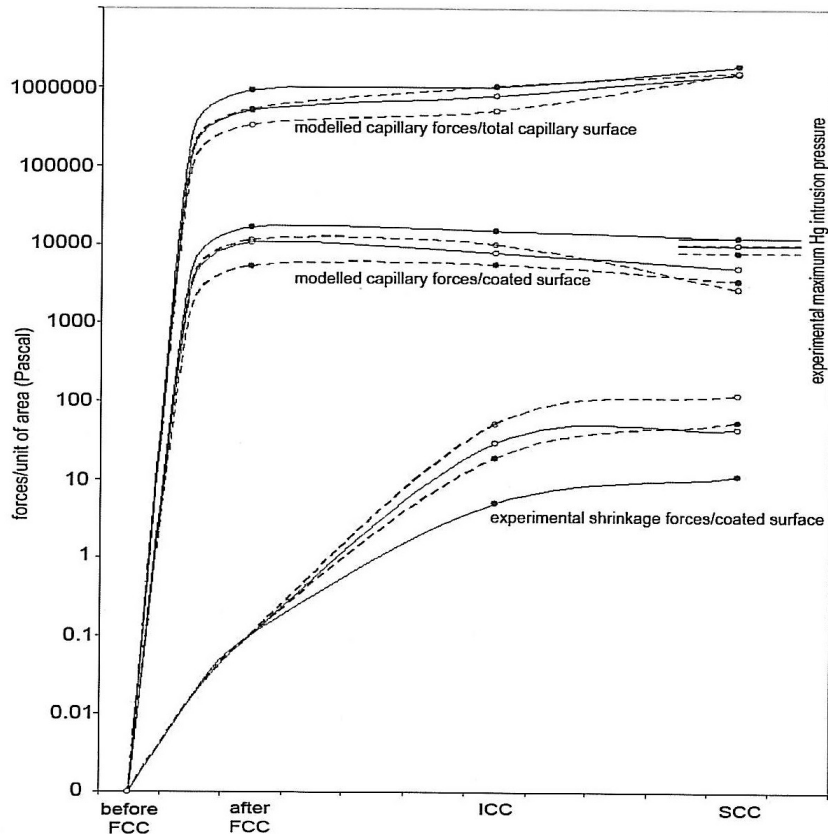
Pict. 9.4.10: Calculated and measured capillary forces (G.M. Laudone)

The shrinkage forces which were determined on the scale increased linearly until the ICC (intermediate point between FCC and SCC) was reached (pict. 9.4.10).

Cathy Ridgeway and P.A.C. Gane (L1.72) studied the effect of coating layer shrinkage on Mercury porosity.

A thin coating layer was applied on an aluminium foil and dried either at room temperature or at in a lab oven at 150°C.
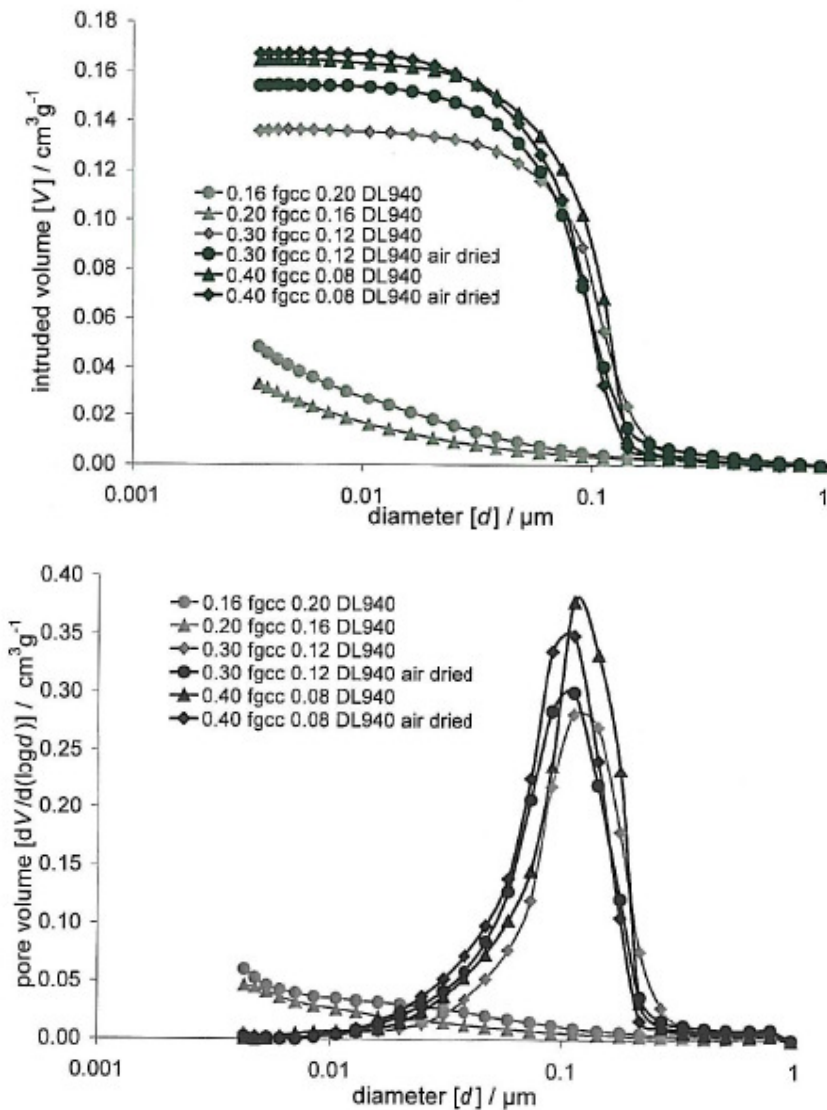
Pict. 9.4.11: Mercury intrusion curves for foil coated thin layer samples (C. Ridgeway)

The air dried samples had a higher pore volume than the oven dried samples (pict. 9.4.11). Pore size was similar. The coatings which were dried in the lab oven were expelled to higher shrinkage forces as water was evaporated faster. Due to the stick – slip – process more particles were reorganized. Free air volume dropped faster when external drying energy was applied.

Again at a volume fraction of 0,16% of latex the CPVC (critical pigment volume concentration) was exceeded and the complete pore volume of the pigment matrix was filled by latex particles.
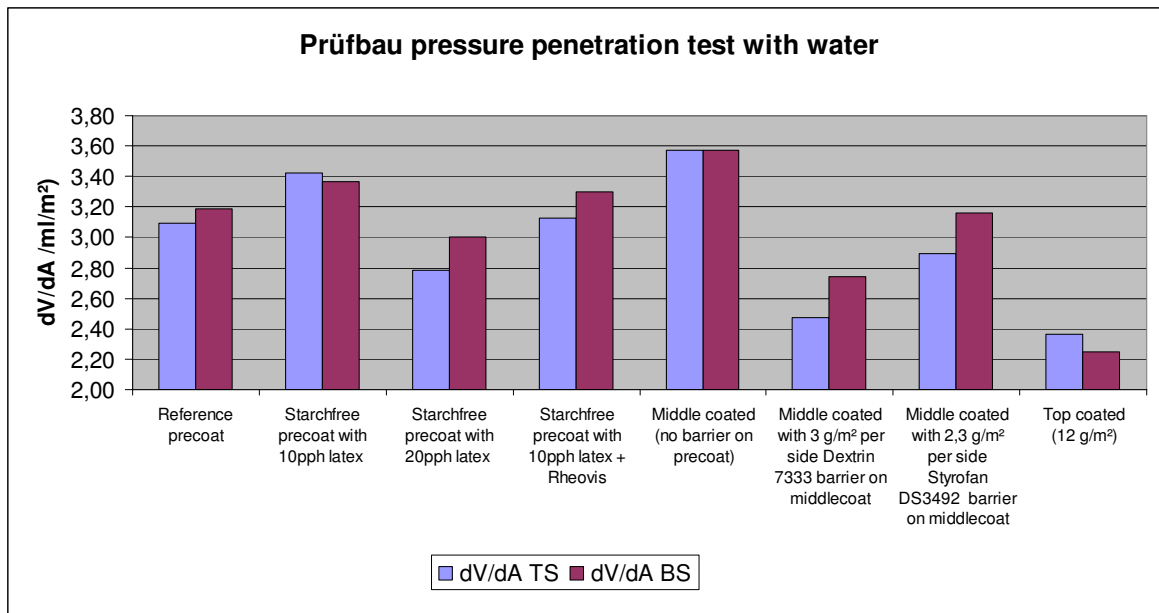
Pict. 9.4.12: Permeability explained by spec. pressure penetration dV/dA from Prüfbau test after middle coating – comparison of barrier layer with dense precoating

			Reference precoat	Starchfree precoat with 10pph latex	Starchfree precoat with 20pph latex	Starchfree precoat with 10pph latex + Rheovis	104 g/m² precoated PM11 without barrier	Precoated PM11 with 3 g/m² Dextrine 7333 barrier per side	Precoated PM11 with 2,5 g/m² Styrofan DS3492 barrier per side
Brightness with UV	%	TS	91,47	91,68	91,41	91,68	92,52	90,61	89,22
	%	BS	91,37	91,41	91,15	91,61	92,26	90,31	90,30
Opacity	%		**92,92**	**93,16**	**92,44**	**93,20**	**93,40**	**92,66**	**92,18**
Gloss Tappi	%	TS	5,5	6,6	5,2	4,3	5,2	17,8	34,8
	%	BS	6,5	7,7	6,5	5,5	5,9	24,0	25,7
PPS smoothness	µm	TS	6,37	6,67	6,32	6,60	5,65	5,65	3,97
	µm	BS	5,71	5,93	5,53	5,35	5,23	5,54	5,17
Bendtsen porosity	ml/min		**29,12**	**50,45**	**14,60**	**62,80**	**53,12**	**0,99**	**0,33**
Stiffness	mN/m	MD	0,586	0,471	0,497	0,497	0,641	0,815	0,580
	mN/m	CD	0,300	0,177	0,209	0,220	0,295	0,462	0,231
Internal bond	mJ		205	220	194	214	145	145	195
Set off 30 sec		TS	0,16	0,22	0,37	0,24	0,17	0,47	0,28
		BS	0,21	0,25	0,40	0,26	0,19	0,50	0,47
Droplet test		TS	63	77	48	48	74	14	6
		BS	44	60	45	29	63	9	9
Offset suitability wet (passes to fail)		TS	12	12	12	6	12	12	9
		BS	12	12	11	5	12	12	8
Offset suitability dry (passes to fail)			12	12	12	7	12	12	9
			12	12	10	6	12	12	8
IGT		TS	**185**	**225**	**230**	**230**	**205**	**230**	**230**
		BS	**185**	**185**	**230**	**190**	**175**	**230**	**230**
Lab mottle		TS	3	3	2,5	2,75	2,75	2,25	2
		BS	2,5	2,5	2	2,5	2,5	1,75	2,25

Pict. 9.4.13: Quality data's of precoated papers

Liquid and air permeability was lower for the barrier coated paper than for the precoating layer with 20% latex in the formulation (pict. 9.4.12 and 13).

dV/dA (ml/m²), water			Reference precoat	Starchfree precoat with 10pph latex	Starchfree precoat with 20pph latex	Starchfree precoat with 10pph latex + Rheovis	Middle coated without barrier	Middle coated with 3 g/m² Dextrine 7333 barrier per side after precoat	Middle coated with 2,5 g/m² Styrofan DS3492 barrier per side after precoat
Brightness with UV	%	TS	85,13	85,67	84,82	85,68	85,43	83,03	84,14
		BS	85,58	85,80	84,85	85,78	85,42	83,29	83,97
Opacity	%		**95,35**	**95,00**	**94,38**	**95,22**	**95,30**	**94,12**	**94,80**
Gloss Tappi	%	TS	8,8	8,5	8,6	7,9	8,4	**24,8**	10,2
		BS	8,9	9,7	9,9	8,4	9,5	**22,7**	11,4
PPS smoothness	µm	TS	3,78	3,77	3,65	3,41	3,54	3,54	3,37
	µm	BS	4,07	4,21	3,97	4,28	4,06	3,37	3,57
Stiffness	mN/m	MD	1,040	0,885	0,834	0,937	1,130	**1,367**	0,944
	mN/m	CD	0,619	0,459	0,474	0,522	0,624	**0,741**	0,942
Internal bond	mJ		195	232	193	212	156	160	187
Set off 30 sec		TS	0,48	0,51	0,55	0,52	0,48	**0,89**	**0,66**
		BS	0,49	0,51	0,54	0,48	0,47	**0,84**	**0,64**
Droplet test		TS	23	24	13	20	28	3	7
		BS	26	30	13	20	27	5	8
Offset suitability wet (passes to fail)		TS	12,0	12,0	12,0	12,0	11,0	12,0	12,0
		BS	12,0	11,0	12,0	12,0	10,0	12,0	12,0
Offset suitability dry (passes to fail)			12,0	11,0	12,0	12,0	12,0	12,0	12,0
			12,0	10,0	11,0	12,0	11,0	12,0	12,0
IGT		TS	195,0	185,0	230,0	195,0	170,0	**230,0**	**230,0**
		BS	230,0	230,0	230,0	230,0	215,0	**230,0**	**230,0**
Lab mottle		TS	2	2	**1,25**	1,75	1,25	1,25	**1,25**
		BS	3	3	**1,25**	3	2,5	3	**1,25**

Pict. 9.4.14: Quality data's after middle coating

Pict. 9.4.14 shows that holdout of binders in the middle coating colour was supreme for the starch barrier on precoated paper leading to a slow set off, high picking resistance and a high uncalendered gloss.

For the barrier precoat with 20% latex the same increase in set off and picking resistance was achieved .Lab mottling improved remarkable with increasing amount of latex in the precoat.

dV/dA (ml/m²), water			reference PC	starchfree 10pph latex	starchfree 20pph latex	starchfree 10pph latex + Rheovis	Top coated + calandered (no barrier on precoat)	Top coated + calanderdd with 3 g/m² Dextrine 7333 barrier on precoat	Top coated + calandered with 2,5 g/m² per side Styrofan DS3492 barrier on precoat
Brightness with UV	%	TS	99,60	99,60	99,10	99,50	99,70	97,90	98,90
		BS	99,70	99,60	99,20		99,60	98,10	98,90
Opacity	%		**95,94**	**95,83**	**95,46**	**95,93**	**96,29**	**95,20**	**95,54**
Gloss Tappi	%	TS	74,2	74,3	72,7	72,9	70,6	74,1	69,5
	%	BS	69,9	70,1	69,4		68,1	69,9	67,4
Gloss DIN75°	%	TS	53,5	56,8	50,2	54,3	50,0	**55,0**	43,8
	%	BS	48,2	50,5	46,5		45,2	**47,0**	41,9
PPS smoothness	µm	TS	0,73	0,65	0,78	0,63	0,93	**0,69**	0,76
	µm	BS	0,75	0,60	0,72		0,80	**0,71**	0,67
Stiffness	mN/m	MD	1,005	0,879	0,838	0,838	1,047	**1,173**	0,838
	mN/m	CD	0,712	0,544	0,544	0,503	0,754	**0,879**	0,503
Set off 30 sec		TS	0,67	0,66	0,69	0,64	0,60	**0,86**	**0,75**
		BS	0,67	0,70	0,69	0,67	0,70	**0,92**	**0,79**
Droplet test		TS	53	54	51	52	53	24	44
		BS	56	52	52		51	20	47
Offset suitability wet (passes to fail)		TS	4,0	3,5	**6,5**	4,0	3,5	**4,5**	**6,5**
		BS	4,0	4,0	**6,5**		3,5	**4,5**	**6,5**
Offset suitability dry (passes to fail)		TS	3,0	3,0	**5,5**	3,0	3,0	**4,5**	1,0
		BS	3,0	3,0	**5,5**		3,0	**4,0**	1,0
Multi colour ink setting, 6 min		TS	0,11	0,07	0,13	0,09	0,06	0,76	0,17
		BS	0,08	0,06	0,12		0,08	0,76	0,17
Mottle solids commercial prinitng (c+m)		TS	1,25	1,5	**1,25**	1,5	**1,25**	1,5	**1,75**
		BS	1,75	1,5	**1,5**	2	**1,25**	1,75	**1,75**

Pict. 9.4.15: Quality data's after top coating and calendering

After top coating and calendering the advantage of the precoating with 20% latex against the barrier liquids starch and Styrofan was visible (pict. 9.4.15): Due to the much better water retention of this coating colour, compared with low viscous barrier liquids, the uniformity of in-plane penetration of this coating into the base paper substrate was much better.

In consequence the variation of local permeability was lower for the barrier coating than for barrier liquids.

Mottling of the precoating with 20% latex after middle coating, top coating and calendering was clearly better than for the barrier liquids.
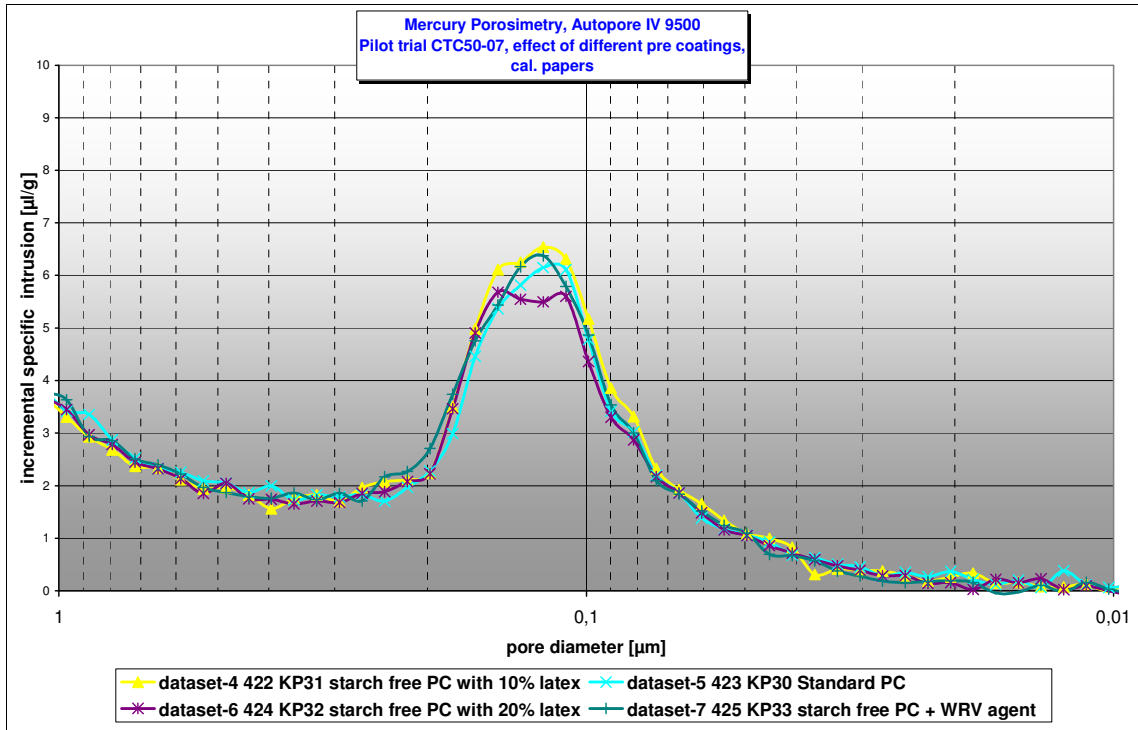
Pict. 9.4.16: Mercury porosity of CTC precoatings
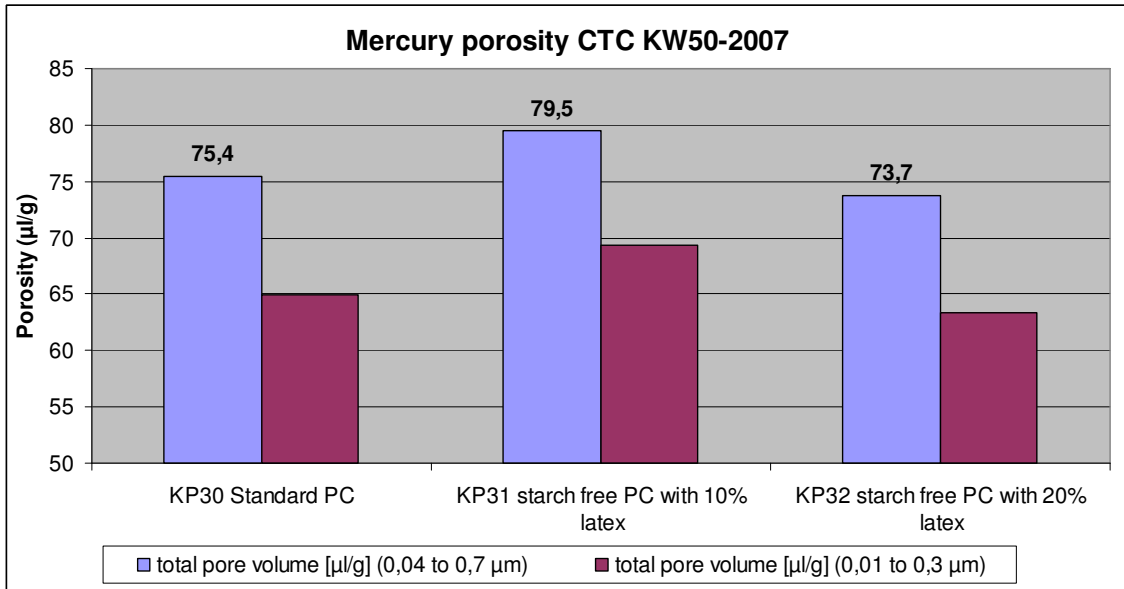
Pict. 9.4.17: Mercury porosity of coating layer – CTC precoated samples

The coating layer porosity (pict. 9.4.16 - 17) was increased when the standard precoating formulation (5% starch + 7% latex) was changed to a starch free precoating with 10% latex and mottling got worse. Increasing the latex content to 16% lowered the porosity of the coating layer to a level under the standard

Page 462

formulation and improved in this way mottling of the triple coated paper against the standard formulation. Unfortunately the costs of this formulation are much higher.

The loss in pore volume was measured after pre- and middle coating, after the top coating no difference in ink drying was observed if one includes the potential for latex saving in the top coating due to higher picking resistance.

9.5 Mill trials

In the first mill trials the cheapest solution to improve mottling was taken: Replace latex by starch in the precoatings to reduce permeability of the precoating layer.

In mill trial BV2a (pict. 9.5.1) 2 parts of latex were replaced by 2 parts of starch in the precoating of PM11. Permeability of precoating dropped and mottling improved while cracking on the fold worsened due to brittleness of starch.

Trial BV2a

	Standard Erz. 3701, 6% starch	Trial Erz. 3737, 8% starch
Screen mottling OS	1,9	1,75
Screen mottling US	2,1	1,75
BTM solids 100% OS	1,9	1,75
BTM solids 100% US	2,2	1,75
BTM Purple OS	**2,3**	**2**
BTM Purple US	**2,6**	**2,25**
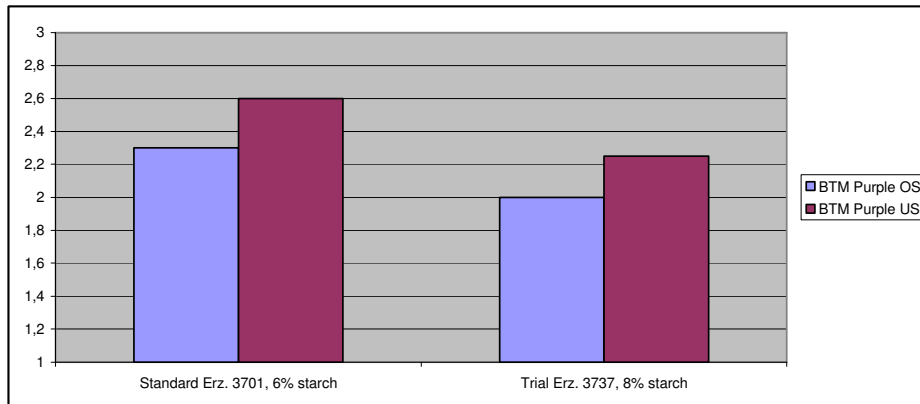
Pict. 9.5.1: Improvement of back trap mottling by increasing starch in pre- and middle coat from 6 to 8%.

In mill trial BV13a-2007 (pict. 9.5.2) the opposite strategy was implemented: Starch was replaced totally by latex in the precoating of PM11 to improve cracking on the fold. Back trap mottling worsened significantly, due to an increase of permeability in the precoating layer (pict. 9.5.3):
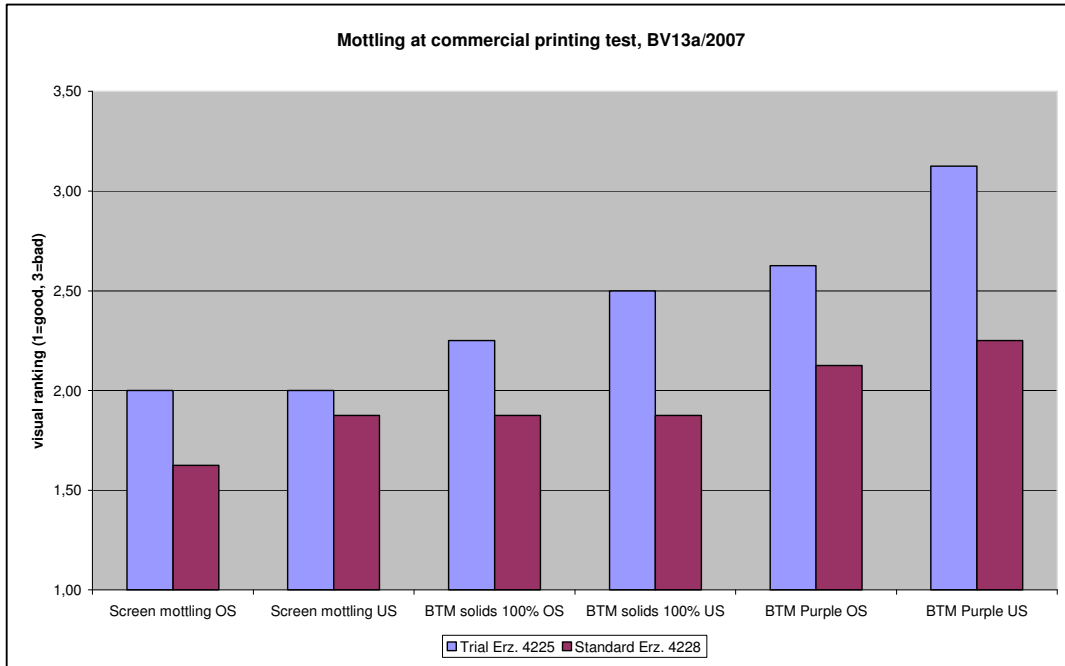
Pict. 9.5.2: Replace 7% starch plus 6,5% latex with 9,5% latex in $1^{st}+2^{nd}$ precoating – influence on back trap mottling (BTM)
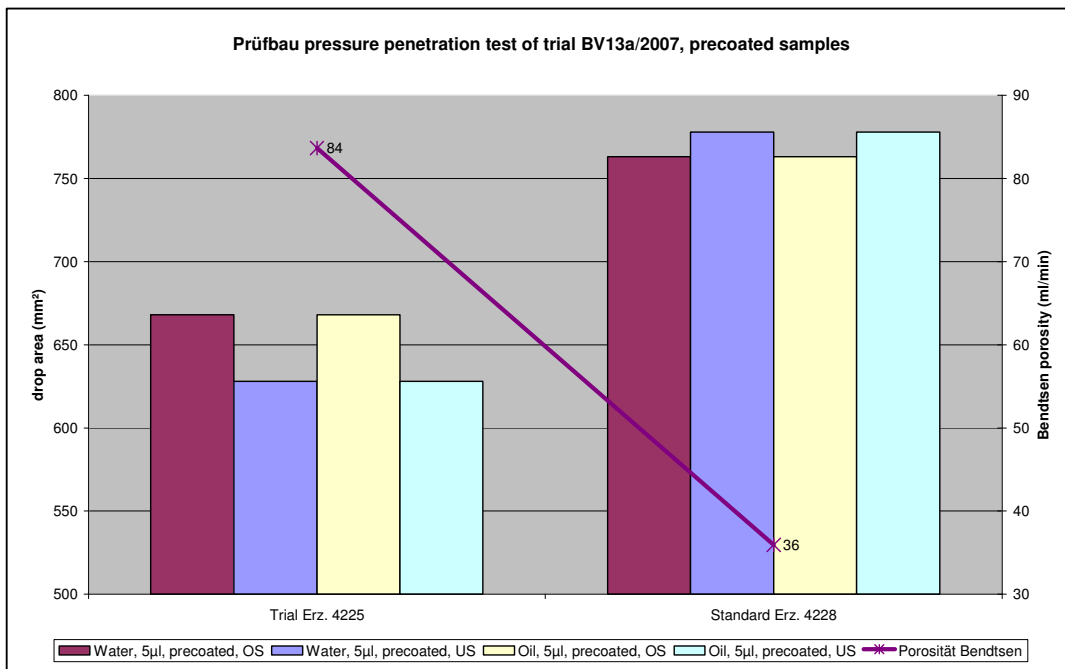
Pict. 9.5.3: Higher permeability of latex based precoatings, compared to starch based precoatings
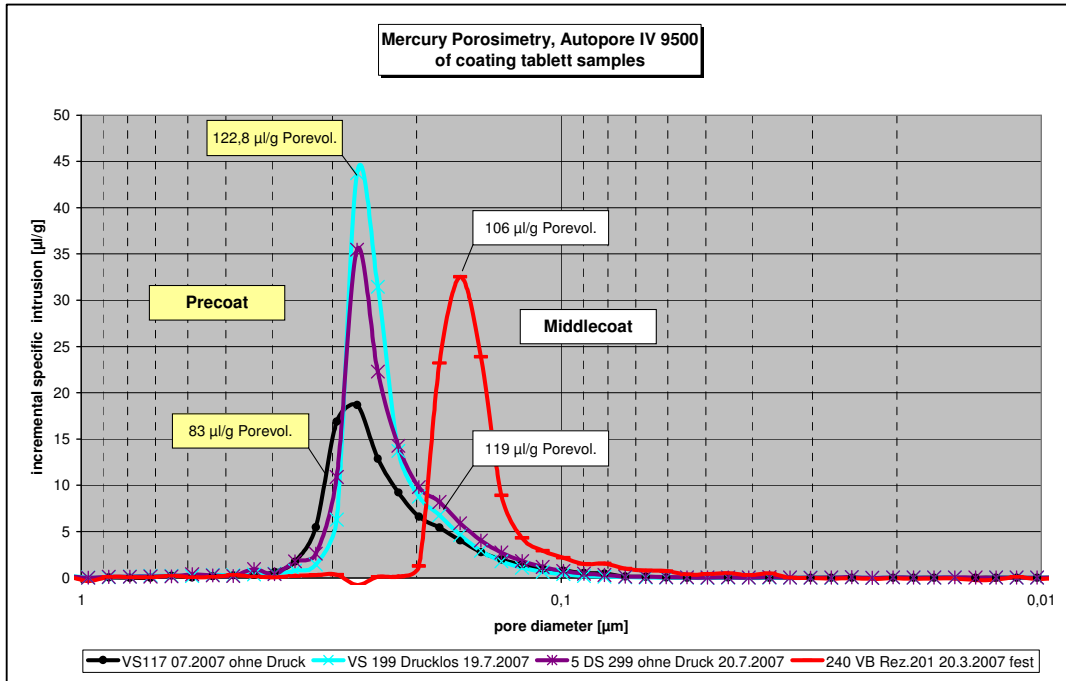
Pict. 9.5.4: Mercury porosity of coating colours: Formulation199+299: only latex, Formulation. 117+201: Latex + starch

In **mill trial BV2f-2007** an almost **latex free precoating** formulation was tested at PM11. Starch was increased from 7 to 13 parts and only 2 parts of latex were left in the precoating. As expected the permeability of precoated paper dropped (pict. 9.5.5 – 9.5.6) and mottling of the triple coated and calendered paper improved significantly mainly on the worse back side (pict. 9.5.7).
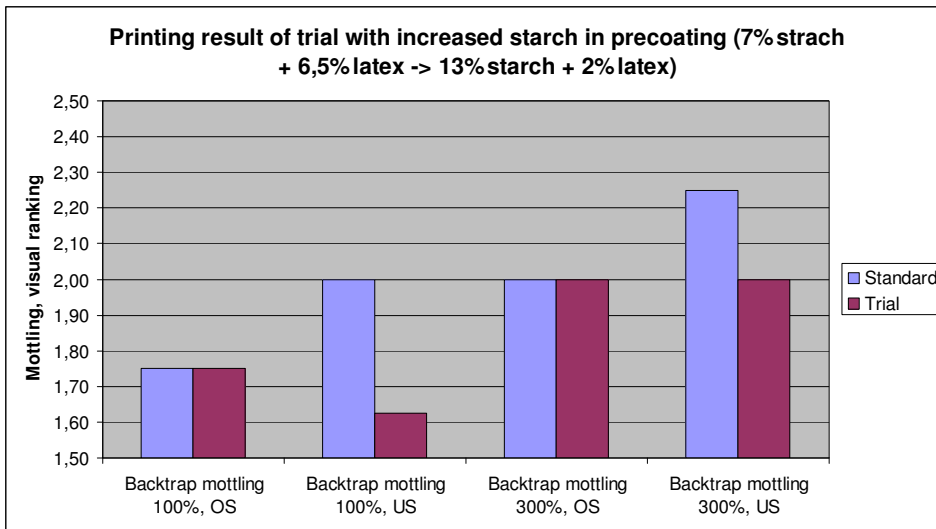
Pict. 9.5.5: Mill trial BV2f -2007 with increased starch content in film press precoating
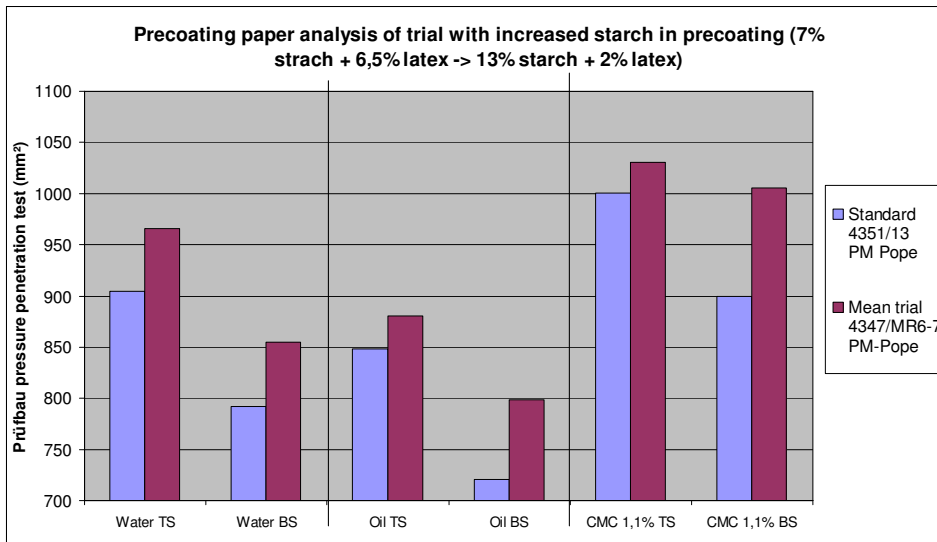
Pict. 9.5.6: Prüfbau pressure penetration test on precoated paper of trial

sappi GK/PQ	TITEL	Increase of starch in precoat from 7 to 13%				
	ZIEL	Improve mottling				
		Quatro Gloss, 150 g/m²				
PM11-73/2007 BV 2f KW 33/2007		**Standard**		**Trial**		
	Erz. / MR	4347/1 RS 112	Mean	4347/ 6 RS 111	4347/ 7 RS 112	Mean
Basis weight	g/m²	147,1	**147,1**	147,9	148,5	**148,2**
Ash	%	47,7	**47,7**	47,5	47,8	**47,7**
Opacity	%	96,3	**96,3**	96,7	96,6	**96,6**
Gloss Tappi 75°	% OS	67,7	**67,7**	65,8	67,0	**66,4**
	% SS	63,5	**63,5**	64,9	63,6	**64,3**
Gloss Din 75°	% OS	53,9	**53,9**	51,4	53,9	**52,7**
	% SS	50,7	**50,7**	51,9	50,7	**51,3**
Stiffness	mNmm L	923	**923**	966	995	**981**
	mNmm Q	650	**650**	749	770	**760**
Set off 30 sec	OS	0,65	**0,65**	0,68	0,72	**0,70**
	SS	0,65	**0,65**	0,65	0,66	**0,66**
Prüfbau mottle test	OS	3,00	**3,00**	2,25	1,75	**2,00**
	SS	3,25	**3,25**	2,50	2,25	**2,38**
Droplet test	% OS	53	**53**	50	43	**47**
	% SS	44	**44**	49	41	**45**
Offset suitabilty dry with parafin	OS	4,5	**4,5**	5,0	5,0	**5,0**
	SS	5,0	**5,0**	5,5	5,0	**5,3**
Offset suitabilty wet with parafin	OS	4,0	**4,0**	4,0	4,0	**4,0**
	SS	4,5	**4,5**	5,0	4,5	**4,8**
MCI-test ink drying	6 min. OS	0,11	**0,11**	0,19	0,17	**0,18**
	SS	0,11	**0,11**	0,23	0,22	**0,23**
Cracking on the fold, inner side		2,00	**2,00**	2,25	2,50	**2,38**
Cracking on the fold, outer side		2,75	**2,75**	3,00	3,00	**3,00**
Testdr./ Mottling Screen	OS	1,75	**1,75**	2,00	1,75	**1,88**
	SS	2,00	**2,00**	2,00	2,00	**2,00**
Backtrap mottling 100%, OS	OS	1,75	**1,75**	1,75	1,75	**1,75**
Backtrap mottling 100%, US	SS	2,00	**2,00**	1,50	1,75	**1,63**
Backtrap mottling 300%, OS	OS	2,00	**2,00**	2,00	2,00	**2,00**
Backtrap mottling 300%, US	SS	2,25	**2,25**	2,00	2,00	**2,00**

Pict. 9.5.7: Mill trial with increased starch content in film press precoating PM11
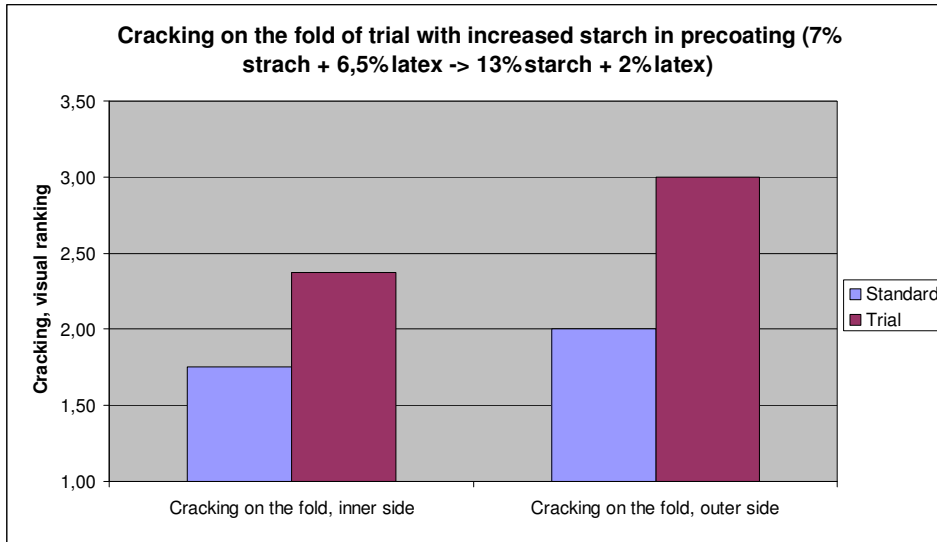
Pict. 9.5.8: Mill trial with increased starch content in film press precoating PM11

Stiffness improved by 10% in the triple coated and calendered paper due to higher starch content in the precoating and picking resistance got better due to the improved latex holdout in the middle and top coat (pict. 9.5.7).

As higher level of starch in precoatings worsened cracking at the fold (pict. 9.5.8), a switch to almost latex free formulation was not possible.

Therefore permeability of precoatings was lowered by raising the starch content from 2% to 5-6% and switching the pigment from 100% HC60 to a mixture of 65% HC60 + 35% HC90. As permeability dropped with these two measures, formation induced mottling improved.

Permeability of mill trials with different precoating formulations:

Formulation No.	115	117	114
HC60	65	65	100
HC90	35	35	
Starch	6,0	2,0	7,0
Latex LTX310	7,0	10,0	5,0
Coat weight TS (g/m²)	10,5	10,5	10,5
Coat weight BS (g/m²)	12,5	13,0	12,5
	23,0	23,5	23,0

Permeability of PM11 precoated papers

Correlation of permeability tests at precoated papers PM11
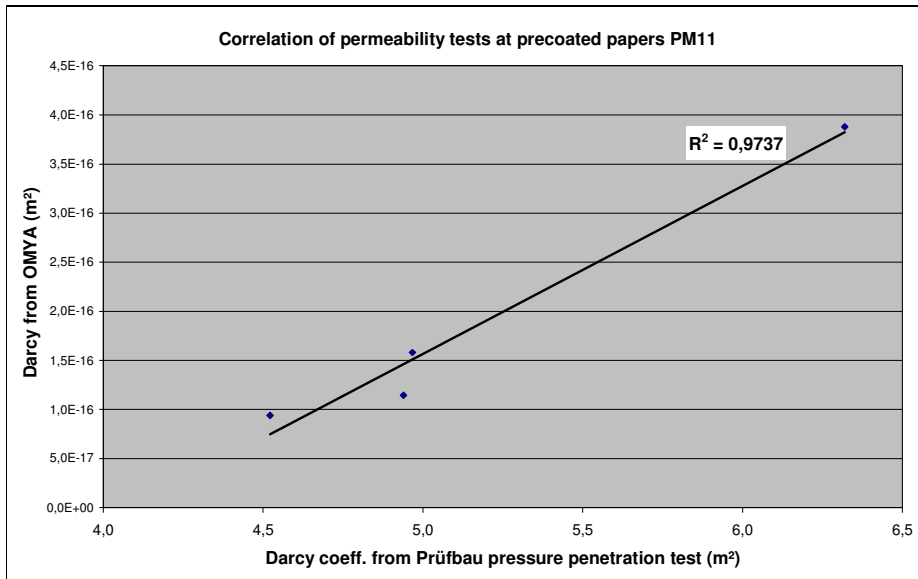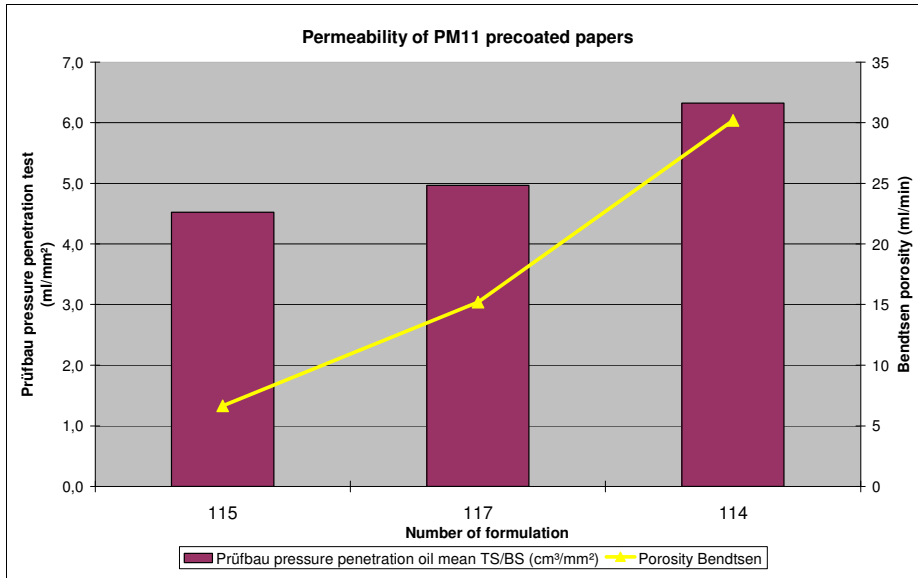
Pict. 9.5.9: Comparison of Prüfbau penetration test with OMYA pressure penetration cell

Permeability measurements from mill precoated papers proved the lab results (pict. 9.5.8):

Exchanging coarse HC60 by fine HC90 led to a reduction in permeability. Latex based coating had higher permeability than starch based coatings.
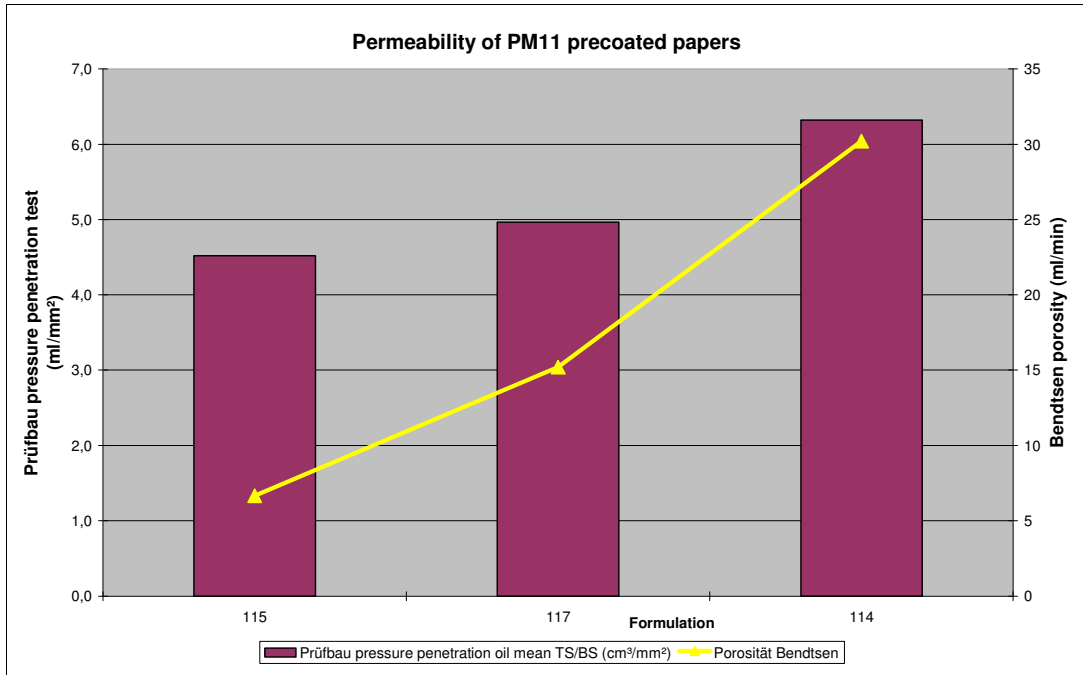
Pict. 9.5.10: Comparison of Bendtsen air porosity with Prüfbau pressure penetration test

Bendtsen air porosity correlated quite well with Prüfbau liquid penetration test (pict. 9.5.10). Therefore Bendtsen porosity was installed as a standard test for PM11 precoated papers. As the precoating layer is much lower in permeability than the base paper, it dominates the Bendtsen porosity.

As a side effect of the mottling study we observed an improvement of **paper flatness**, when trials with denser precoatings were run.

To implement this measure without extensive costs and without worsening of CAF, the pigment mixture in the precoating was changed from 100% HC60 to 65% HC60 + 35% HC90 in 2007 and kept in the following years to improve mottling and paper flatness.

Pict. 9.5.11: Reduction of porosity of precoated paper by changing from 100% HC60 to 65% HC60 + 35% HC90

The flatness of PM11 glossy papers got significantly worse in 2007 with the introduction of wolfram carbide (WC) blades at the middle coaters of OMC11. The reason was a higher amount of water penetration under the blade due to small facet length and worse coating profiles due to resistance of the blade tip to wear. The 1st quality rate dropped to 30 – 50%, compared to a stable level of >90% before changing to WC-blades.

The amount of water, which penetrates into the base paper, causes swelling of the fibres, especially at un-sized base papers, like PM11. In the drying part after the blade, the water is removed, the fibre network shrinks but the applied coating colour refuses the shrinkage, it behaves like a glued concrete on the paper surface. An internal tension is produced in CD, leading to over-stretched areas, especially at zones with less penetration resistance at the precoated paper surface.

To improve flatness, the porosity of precoated paper before OMC11 was reduced by using finer pigments and replacing latex by cooked starch.

Bendtsen porosity dropped by 70% (pict. 9.5.11) and coating layer permeability was 30% lower (pict. 9.5.12 - 13) measured by the Prüfbau droplet test. All liquids showed a much better hold out at the new precoating formulation.
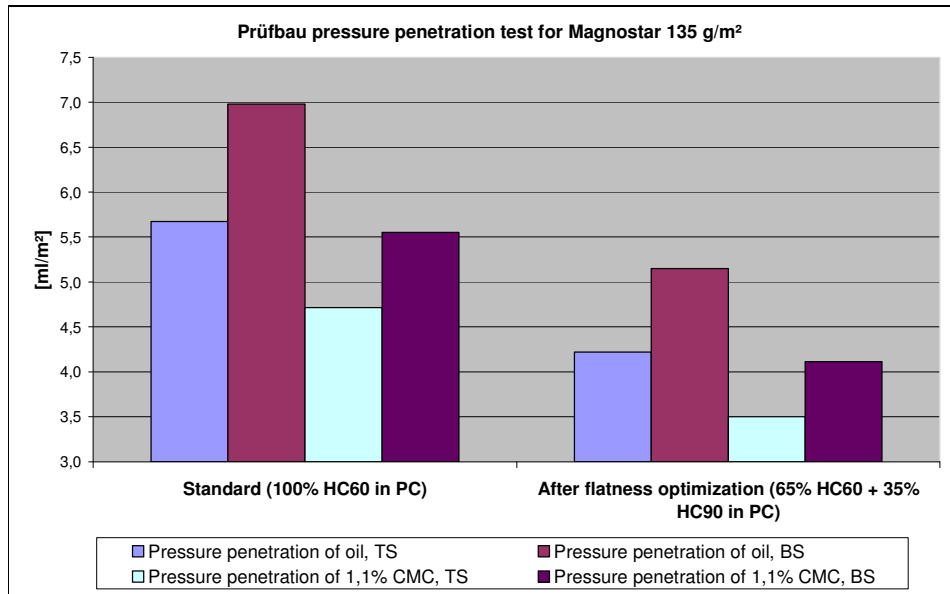
Pict. 9.5.12: Prüfbau pressure penetration test of flatness trials PM11 for Star 135 g/m²
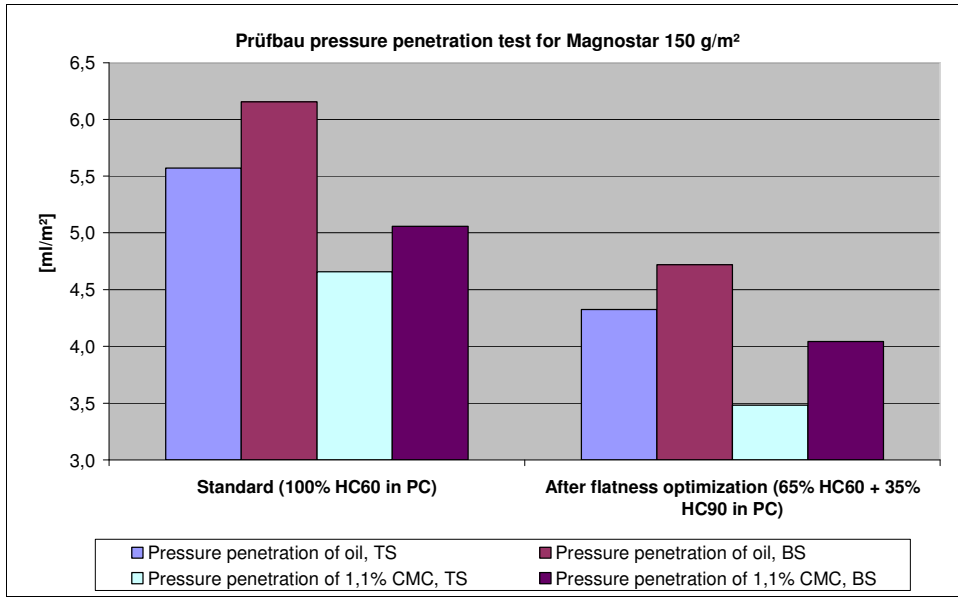
Pict. 9.5.13: Prüfbau pressure penetration test of flatness trials PM11 for Star 150 g/m²

The new precoating formulation with 35% HC90 + 65% HC60 became standard in Nov. 2007 and since then flatness problems were removed as 1st quality quote was again 90% in average (pict. 9.5.14).
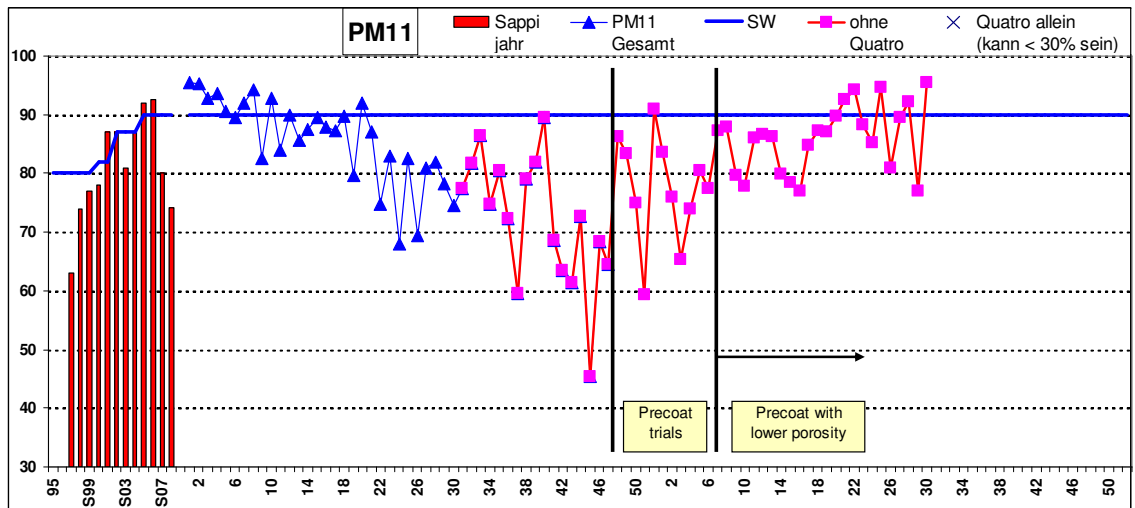
Pict. 9.5.14: Q1-Quality of PM11 – influence of flatness optimization by dense precoat

To compensate the higher costs of HC90 against HC60 parts of the precoat latex were replaced by starch.

Chapter 10: Solution 6 for formation and drying mottle: Improve water retention of coating colour

10.1 Introduction

Formation analysis showed that local pressure will be higher at flocs and local porosity of the dry coating layer will increase when more fines and soluble substances will be pressed into the substrate at flocs. These differences in coating layer porosity cause mottling in offset printing.

The demonstrated trials with dense precoatings or barrier layers in the previous chapters showed that lowering the permeability of the precoating layers led to improved holdout of top coat latex, more uniform holdout of top coat fines and better mottling.

The trials demonstrated also that a significant amount of fine latex particles get currently lost into the base when coatings are applied under external pressure.

To improve the water retention and thereby the retention of fine latex particles and soluble binders is a cheap solution to lower the permeability of the precoating layer and to improve its uniformity.
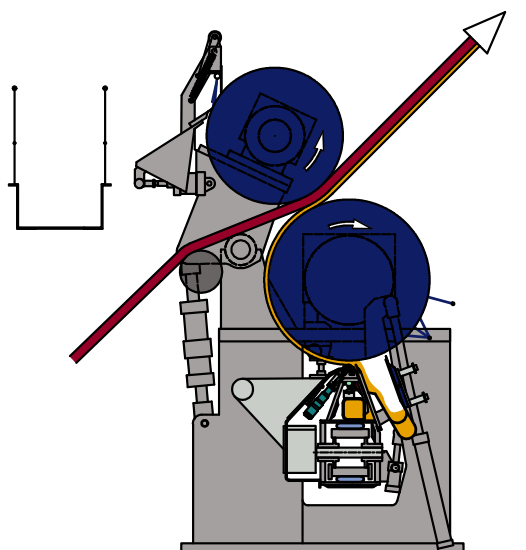
Pict. 10.1.1: Pressure penetration in application nip of a film press coater
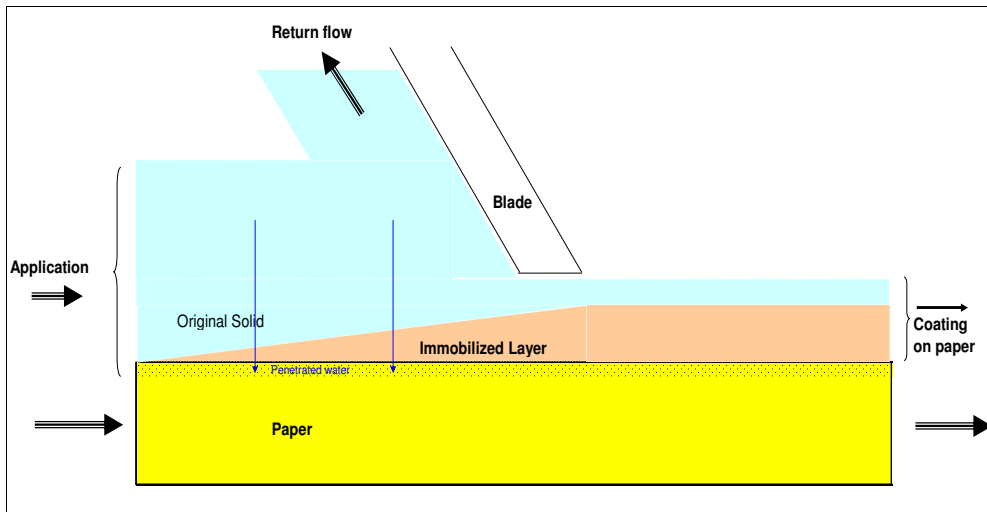
Pict. 10.1.2: Pressure penetration under the blade

During capillary and pressure penetration at any commercial coater a filter cake is formed at the boundary between coating colour and base paper (pict. 10.1.2). Water retention of coating will be mainly influenced by the permeability of this filter cake. Permeability is described by the Darcy coefficient K.

10.2 Calculation of filter cake permeability

Darcy's law is a simplification of the Navier-Stokes-Equation.

Navier-Stokes-Equation:

Equ. 10-2-1: $\rho * \dfrac{\partial v}{\partial t} + \rho * (v * \nabla) * v = -\nabla p + \eta * \Delta v + (\lambda + \eta)\nabla(\nabla * v) + f$

∇ …..Nabla operator (x,y,z)

λ, η….Lame´constants for viscosity

f….. volume force (gravity, coriolis)

For incompressible medias: $\nabla * v = 0$

Navier-Stokes-Equation for liquid flow in porous media with uni-dimensional flow in z-direction, incompressible media and no volume forces:

Equ. 10-2-2: $\frac{\partial}{\partial t} * \rho * v = -\frac{\partial}{\partial z} * \rho * v^2 + \eta * \frac{\partial^2 v}{\partial z} - \frac{\partial p}{\partial z}$

The viscous force can be approximated by the product of viscosity and velocity $\frac{1}{K} * \eta * v$ with K the permeability constant.

Navier-Stokes-Equation, transformed:

Equ. 10-2-3: $\frac{\partial}{\partial t} * \rho * v = -\frac{\partial}{\partial z} * \rho * v^2 - \frac{1}{K} * \eta * v - \frac{\partial p}{\partial z}$

Taking the equation of continuity $div\vec{v} = 0$ and assuming stationary flow with $\frac{\partial v}{\partial t} = 0$,

the first two terms can be neglected and the Navier-Stokes-Equation is transformed into **Darcy's law**:

Equ. 10-2-4: $v = -\frac{K}{\eta} * \frac{\partial p}{\partial z}$ or $Q = \frac{K * A * \Delta p}{\eta * L}$

Q.....dV/dt, flow rate of the liquid through the porous substrate

A.....Area of penetration

L.....Thickness of the substrate

Δp.....pressure drop (pressure at entrance minus pressure at exit)

K......permeability coefficient of the porous medium, which is penetrated by the liquid (structure coefficient) with K = K_{paper} + $K_{filtration\ layer\ of\ coating\ colour}$

η.......viscosity of penetrating liquid

To determine Darcy coefficients pressure penetration cells have been constructed where a liquid is pressed through a porous substrate. The area A and the length L are given by geometry of the cell. Pressure at the entrance is kept constant. Exit pressure is most often atmospheric. Viscosity of the liquid is measured separately before the experiment. The flow rate Q is determined at the pressure penetration cell by a scale at the exit and plotted versus time.

Darcy' law is valid for Re = $\frac{\rho * v * d}{\mu}$ < 10   (laminar flow through pores)

Darcy published his theory first in 1856 in "The permeability of Granular Beds" as a general equation of Poiseuilles law (1840 – 1842):

Darcy: $\dfrac{dV}{dt * A} = u = K * \dfrac{\Delta p}{L}$

Poiseuille: $u = \dfrac{d_{capillary}{}^{2}}{32 * \eta} * \dfrac{\Delta p * g}{L}$

Later Darcy included viscosity in his equation as he recognized that the original constant K is proportional to the inverse of viscosity (and to the square of "diameter of an equivalent capillary channel").

$u = K_1 * \dfrac{\Delta p}{\eta * L}$ …..with K_1 as the permeability coefficient (m²), a function of porosity ε.

In a bed with uniform spheres, porosity is independent of size.

Porosity was calculated by Hooke, Graton, Fraser. Typical figures are:
- Rhombohedra, each sphere touches 12 others: ε = 0,26
- Tetragonal, each sphere touches 10 others: ε = 0,302
- Orthorhombic, each sphere touches 8 others: ε = 0,395
- Cubic, each sphere touches 6 others: ε = 0,476

These figures could only be used for theoretical calculations; a uniform sphere distribution was rarely seen in practice. Thus Lee, Coulson, Westman and Hugill calculated porosity of granular beds with:
- Coarse sand: ε = 0,4
- Medium sand: ε = 0,41 – 0,48
- Fine sand: ε = 0,44 – 0,49
- Fine sandy loam: ε = 0,50 – 0,54

Penetration was calculated with:

$u = K_2 * \dfrac{d_m{}^{2}}{\eta} * \dfrac{\Delta p}{L}$ …with K_2=0,585 for sand beds with ε = 0,367

Actually K_2 varied from 1,15 for uniform grains to 0,46 for sands with a wide particle size distribution.

In 1927 Kozeny pointed out, that the term surface per unit volume of pore space

$\dfrac{S}{\varepsilon} = \dfrac{S_0(1-\varepsilon)}{\varepsilon}$ should be included in Darcy equation since it corresponds to the mean

hydraulic radius of a pipe with non circular radius.

$S_o = \dfrac{6}{d}$ …spec. surface or particles

Kozeny postulated that there should be no major difference between flow through a pipe with changing shape but constant cross sectional area and flow through a granular bed. Kozeny transferred Darcy's law into:

$u = \dfrac{\varepsilon^3}{k*S^2} * \dfrac{\Delta p * g}{\eta * L} = \dfrac{\varepsilon^3}{(1-\varepsilon)^2} * \dfrac{1}{K*\eta*S_o{}^2} * \dfrac{\Delta p * g}{L}$ ….valid for mod. $\mathrm{Re} = \dfrac{\rho * u}{\eta * S} < 2{,}0$

In 1938 **Carman** (L2.8) used Darcy's law for calculating rigid filter cakes.

In most industrial filtrations a liquid is pressed through a cloth. Soon a filter cake is formed. Carman stated, that the total loss of pressure arises from a) the pressure drop across the filter cake and b) the pressure drop across the cloth (initial resistance). If b) is neglected, Darcy's law is:

$u = \dfrac{1}{A} * \dfrac{dV}{dt} = K_1 * \dfrac{\Delta p}{\eta * L}$

From Kozeny's equation:

$K_1 = \dfrac{\varepsilon^3}{K*S_0{}^2*(1-\varepsilon)^2}$ …with K = 5 but depending on porosity, particle shape,…

Darcy + Kozeny lead to:

Equ. 10-2-5: $\dfrac{dV}{dt} = \dfrac{A*\Delta p}{r*\eta*L}$

with $r = \dfrac{K*S_0{}^2*(1-\varepsilon)^2}{\varepsilon^3}$ the specific filtration resistance of filter cake

As filtration continues, L, the thickness of the immobilized layer, increases. If the porosity of the increasing filter cake is constant, r will be constant and the same volume of cake will be deposited by each volume of filtrate (volume balance), leading to:

$L = \dfrac{v * V}{A}$ ....with v as volume of cake, deposited per volume of filtrate

and $\dfrac{dV}{dt} = \dfrac{\Delta p * A^2}{\eta * r * v * V}$

leads to: $V^2 = \dfrac{2 * \Delta p * A^2}{\eta * r * v} * t$ or $V = \sqrt{\dfrac{2 * A^2}{r * v} * \dfrac{\Delta p * t}{\eta}}$

A linear relationship between V and $\sqrt{t / \eta}$ should be seen for every filtration with constant pressure, independent structure of the filter cake from viscosity of the aqueous phase and low Reynolds numbers.

With $K' = \sqrt{\dfrac{2}{r * v}}$ the specific filter cake penetration resistance:

$V = K' * A * \sqrt{\dfrac{\Delta p * t}{\eta}}$ and $r = \dfrac{K * S_0^2 * (1 - \varepsilon)^2}{\varepsilon^3}$ ....from Kozeny's equation

If the filter resistance R of the filter cloth or membrane has to be integrated, Carman extended his equation to:

$\dfrac{dV}{dt} = \dfrac{\Delta p * A^2}{\eta * (r * v * V + R * A)}$

Integrated at constant pressure:

$t = \dfrac{\eta * r * v}{2 * \Delta p * A^2} * V^2 + \dfrac{\eta * R}{\Delta p * A} * V$ or: $\dfrac{t}{V} = \dfrac{\eta * r * v}{2 * \Delta p * A^2} * V + \dfrac{\eta * R}{\Delta p * A}$

Plotting $\dfrac{t}{V}$ against V leads to a linear correlation with a gradient $b = \dfrac{\eta * r * v}{2 * P * A^2}$ and r

can be calculated by: $r = \dfrac{2 * b * \Delta p * A^2}{\eta * v}$

In most industrial filtration processes, the filter cake porosity is a function of pressure. As pressure increases, filter cake porosity is reduced.

Darcy's law is no more valid, if pressure is changed during filtration.

Carman and Kozeny extended their coefficient K later to:

Equ. 10-2-6: $K = \dfrac{\varepsilon^3 * d^2{}_{eff}}{35 * (1-\varepsilon)^2 * \kappa} = \dfrac{(1-\phi)^3}{k_0 * \tau^2 * \phi^2 * A^2{}_s}$

D_{eff}.....mean diameter of particles (from sedigraph)

ε.........porosity

Φ........volume fraction of particles $= 1 - \varepsilon$ (from Hg-porosity)

K........Kozeny constant

T........Tortuosity

A_s......specific surface (from BET)

A common diagram for filtration is the dimensionless permeability $K/d^2{}_{eff}$ versus the volume fraction Φ or porosity ε for pigment slurries, coating colours, fibre mats,...
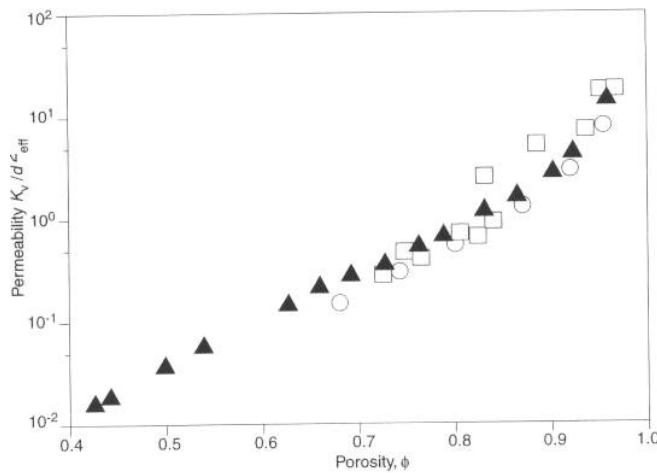
Pict. 10.2.1: Dim. Less permeability K_v/d_{eff}^2 vs. porosity Φ for fibre filters

Example: Double pre-coated paper of PM11:

D_{eff} = 1,84 µm ...mean particle diameter

ε=0,23

Mean pore diameter: 0,15 µm from Hg of tablets and 0,25 µm from paper samples

K/d^2eff = 0,8 x 10^{-2}

$\rightarrow$ K = 2,7 x 10^{-20}

D. Vidal and C. Ridgeway (L1.77) tried to verify the Carman – Kozeny relationship between porosity of a coating layer and its permeability coefficient.

$$k = \frac{1}{c_K} \frac{1}{S_0^2} \frac{\varepsilon^3}{(1-\varepsilon)^2}$$

With the Kozeny constant

$$c_K = c_0 \tau^2 = c_0 \left(\frac{L_{eff}}{L}\right)^2$$

And with the specific surface area for a spherical pigment (PSD discretization)

$$S_0 = \frac{\int_0^\infty D^2 p(D)\, dD}{\frac{1}{6} \int_0^\infty D^3 p(D)\, dD} = \frac{6}{D_{eff}}$$

HC60, Setacarb and Covercarb tablets were measured by Mercury porosity and OMYA's permeability cell.
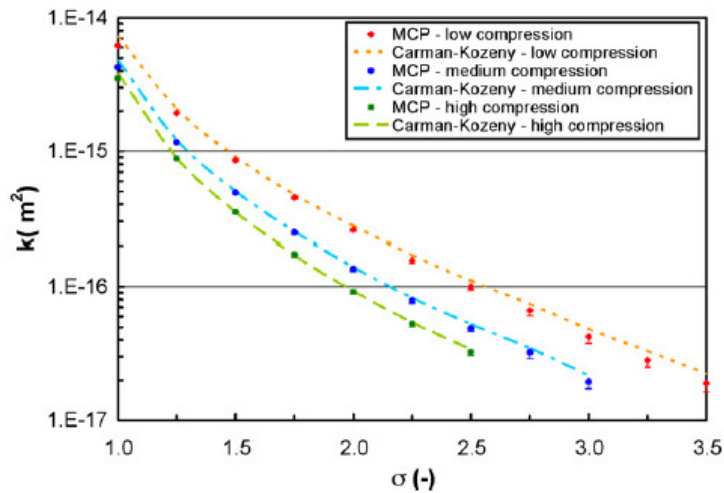
Pict. 10.2.2: Permeability coefficient as a function of poly-dispersity σ and compression (D. Vidal)

Permeability as shown in pict. 10.2.2 and 10.2.3 was highly depending on pre-compression of tablets which corresponds to shrinkage forces during drying of coatings.
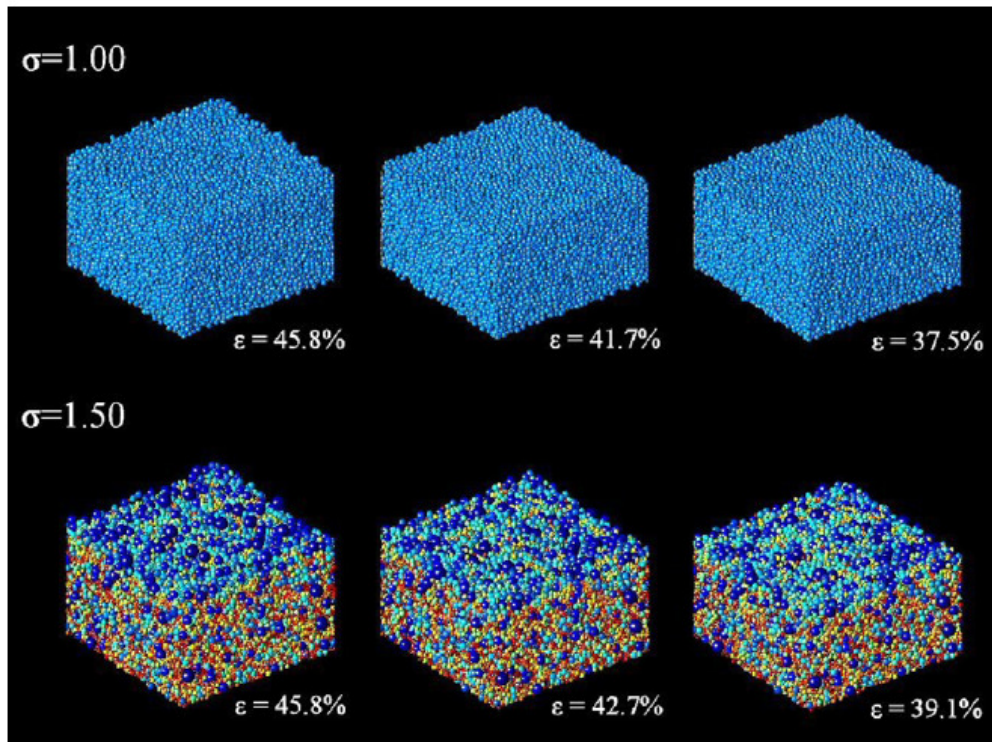
Pict. 10.2.3: Computer modelling of different pigment packings ε with different poly-dispersity σ and porosity (D. Vidal) – colours: particle size classes
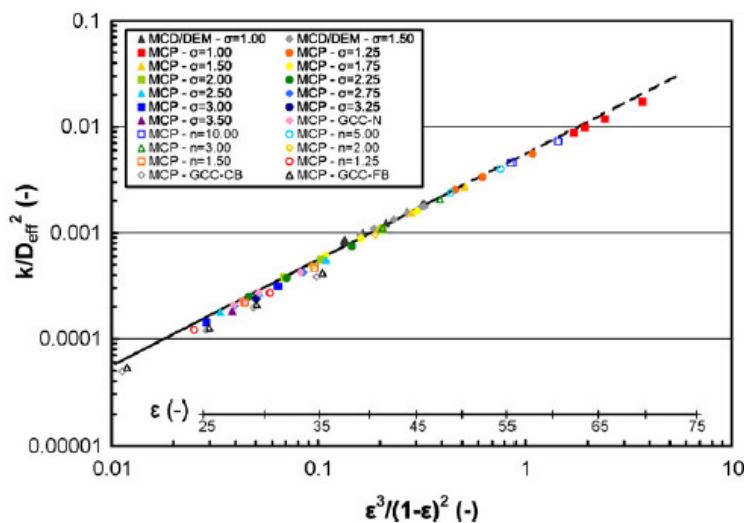
Pict. 10.2.4: Normalized permeability as a function of porosity ε with $c_k = 5$ (D. Vidal)

The experiments confirmed the Carman Kozeny equation: From pressure penetration experiments with OMYA cell the Darcy coefficient k was calculated. Mercury porosity gave ε (pict. 10.2.4). With BET the specific surface S_0 was measured and the

"representative" pore diameter D_{eff} was calculated. The comparison of k/D_{eff}^2 with the porosity ε led to a linear relationship as Carman Kozeny postulated.

Filter cake theory is applied in paper making not only for coating processes but also for dewatering of fibre suspensions in the **wire section of paper machines**.
M. Paradis, J. Genco and D. W. Bousfield (L.19) studied dewatering of fibre suspensions in a Britt Jar where a filter cake is formed on a wire under external shear of the suspension like in commercial paper machines. In principle the set up of Britt Jar dewatering experiment is similar as coating colour water retention measurements e.g. by the Abo-GWR instrument. A liquid suspension is pressed through a filter and an immobilized filter cake with increasing thickness. The only difference is the shear of the suspension during dewatering which is missing in Abo-GWR experiments which are therefore regarded to be "static".
The authors showed that dewatering was reduced by a compressing of fibre filter cake on the wire and by increasing the amount of fines in the suspension leading to a denser filter cake. They calculated a drainage resistance coefficient from Darcy's law
$\frac{\Delta p}{L} = a * v$ with a the coefficient of drainage resistance, L the thickness of the mat, v the drainage velocity.

The drainage velocity was calculated from: $v = \frac{1}{A} * \frac{dV}{dt}$.

The thickness of the mat L from: $L(t) = \frac{(C_0 * \rho_S *) * r * V(t)}{A * (1 - \varepsilon_m) * \rho_P}$

with r the retention coefficient, A the drainage area, C_0 and ρ_S the original consistency and density of the sample, ε_m the void fraction and ρ_P the density of the particles. Drainage coefficient a(t) can be calculated by

$$a(t) = \frac{\Delta P_t(t) - \Delta P_W(t)}{\left[\frac{R * \rho_S * c_0}{A^2 * (1 - \varepsilon_m) * \rho_P}\right] * V(t) * \frac{dV(t)}{dt}}$$

Softwood pulp shows much lower drainage resistance than TMP, ground wood or the headbox sample (with fines from the wire water).
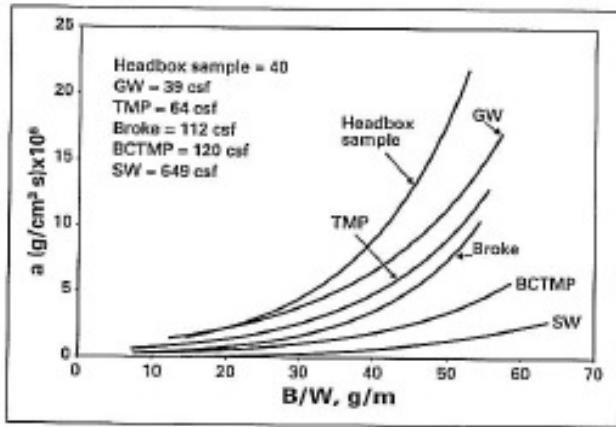
Pict. 10.2.5: Drainage resistance of all components in the LWC furnish (M. Paradis)

The bond grade with 355 ml CSF showed a faster drainage than the LWC furnish
which had a CSF of 40 ml and the highly filled opaque paper with 103 ml CSF (pict.
10.2.5). The calculated drainage resistance coefficient (a) was much lower for the
bond grade (pict. 10.2.6).
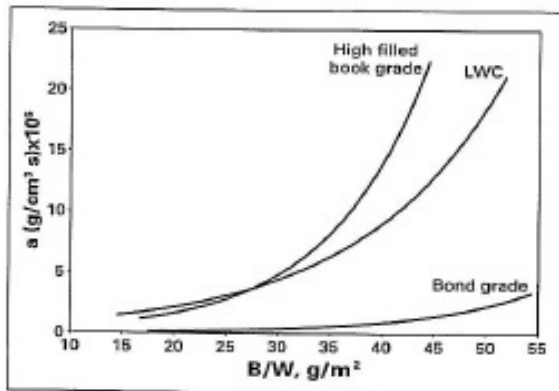
Pict. 10.2.6: Calculated drainage resistance coefficient (M. Paradis)

V. Wildfong and J.M. Genco (L1.38) calculated the dewatering of two different hybrid
top wire former configurations for newsprint production.
Dewatering in the paper machine forming section is quite nicely comparable to
dewatering under the blade. External pressure is applied by wire tension, the medium
consists of a solid and a liquid phase and a filter cake is formed during dewatering.

Darcy's law is applied for pressure penetration in wire sections by:

Equ. 10-2-7: $v = \dfrac{1}{A} * \dfrac{dV}{dt} = \dfrac{(\Delta p)_t}{L * a_m + a_w}$

a_m....drainage resistance of the fibre mat

a_w....drainage resistance of the wire

L.....thickness of the filtration mat

Total pressure drop $\Delta p_t = \Delta p_m + \Delta p_w$

The drainage resistance coefficients can be determined by drainage experiments at the Britt Jar Tester. This instruments works in a similar way than the Abo-GWR water retention tester for coating colours. The main difference is the introduction of shear forces in the dewatering zone which makes this test more dynamic than the Abo-GWR method.
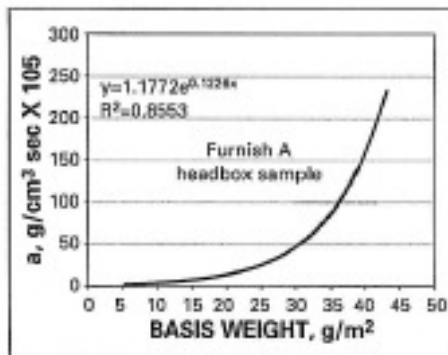
Pict. 10.2.7: Viscous resistance coefficient (a) for furnish A (V. Wildfong)

The thickness of the filter cake L can be calculated by: $L = \dfrac{W/A}{(1-\varepsilon)*\rho_p}$

W/A...filter mat mass per unit area

ε.......void volume fraction in the mat

ρ_p.......particle density

The basis weight of the wet web W/A can be calculated from the measured filtrate volume V(t):

$\dfrac{W}{A} = \dfrac{c_s * V * R_0}{A}$

c_s.....mass of solids per unit volume of filtrate

R_0.....overall retention coefficient

Darcy reformed: $v = \dfrac{1}{A} * \dfrac{dV}{dt} = \dfrac{(\Delta p)_t}{(\dfrac{W/A}{(1-\varepsilon)*\rho_p}) * a_m + a_w}$

External pressure between the two wires is calculated by: $P_T = \dfrac{T}{R}$ with T = wire

tension of the outside wire and R = Roll radius of the formation roll (1st roll).

Inserting the external pressure into Darcy's law leads to: $v = \dfrac{P_T - P_0}{L * a_m} \approx \dfrac{P_T}{L * a_m} = \dfrac{T/R}{L * a_m}$

where a_w the resistance of the wire is neglected.

The drainage at the forming roll was calculated with P_T = 15.600 Pa and a_m = 8 x 10^8 kg/m³sec. The roll radius R was assumed with 0,45 m and the wire tension with 7 kN/m.
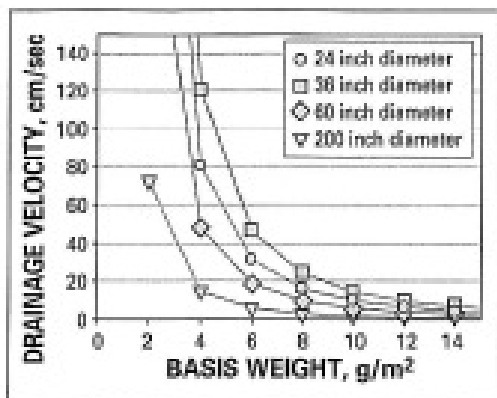
Pict. 10.2.8: Influence of forming roll diameter on drainage velocity (V. Wildfong)

Lowering the dewatering pressure by increasing the forming roll diameter (pict. 10.2.8) led to lower drainage velocity and higher retention.

A. Erk, W. Stahl (L2.1) and Ali Akar, Mehmet Polat (L2.5) studied the influence of the zeta potential on filtration behaviour of carbonate and clay slurries.

The van der Waals force between two identical spherical particles of a radius a is:

$$F_A = \frac{-a*A}{12*H^2}$$ with A the Hamaker constant and H the distance between the particles.

The repulsive force between charged particles due to overlap of the electric double

layers is: $$F_R = \frac{2*\pi*a*\varepsilon_0*\varepsilon*\kappa*\zeta^2*e^{-\kappa H}}{1+e^{-\kappa H}}$$

With ε= the permittivity of the vacuum, ε the dielectric constant of the medium, e the electronic charge, k the Boltzmann constant, T the temperature, ς the potential and κ the reciprocal value of the so called Debye length, which stays for the double layer thickness.

$$\kappa^{-1} = \left(\frac{\varepsilon_0*\varepsilon*k*T}{e^2*\sum n_i*z_i^2}\right)^{1/2}$$ with n_i as the number and z_i as the valence of the ion i.
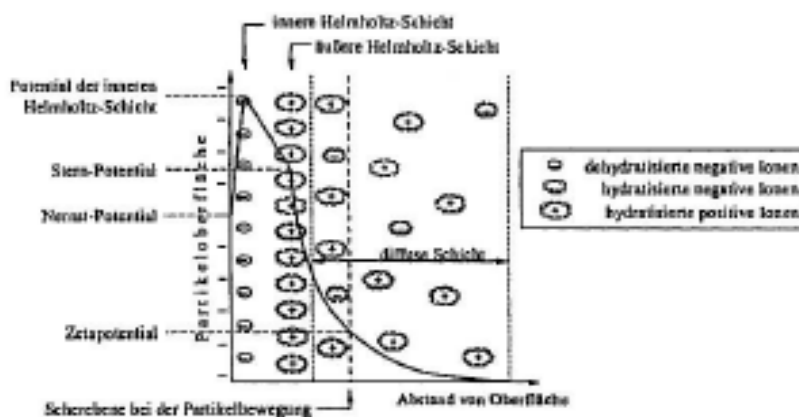
Pict. 10.2.9: Surface potential around a particle with negative charge (A. Erk, W. Stahl)

At the pigment surface anionic ions are fixed in the inner Helmholtz-layer (monolayer with linear change in charge) as shown in pict. 10.2.9.
On top of this layer the outer Helmholz-layer is fixed, which contains counter ions with positive charge.
The next layer, which represents the surface of the particle, contains both anionic and cationic ions, which can easily move within this layer.

The zeta potential is the potential at the area of shear, which is formed during particle movement relative to the liquid.

Whereas van der Waals forces cannot be changed for a given system, electrostatic forces can easily be manipulated by changing the pH, the ionic strength or by additives. This was done for the pigment slurries as shown in pict. 10.2.10.
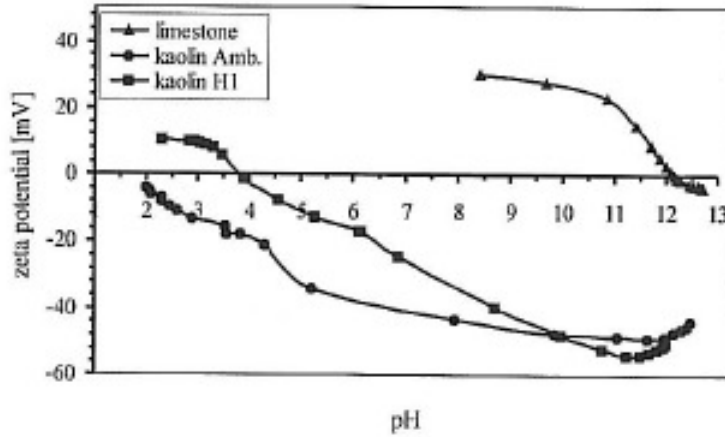
Pict. 10.2.10: Zeta potential vs. pH (A. Erk, W. Stahl)

The iso-electric point (IEP) of kaolin was at pH 3,8 and pH 1,5 respectively. The IPE of Limestone was at pH 12,1.

In filtration experiments the immobilized layer is characterized by a higher level of solids which leads to an exponential rise in viscosity. The solid content when the viscosity starts to rise is called the critical volume fraction or the first critical concentration (FCC) as shown in pict. 10.2.11.
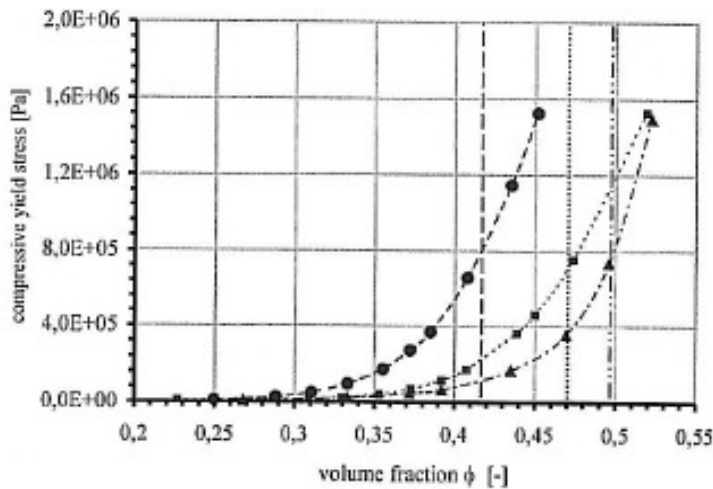
Pict. 10.2.11: Compressive yield stress vs. volume fraction at original pH (A. Erk)

The critical volume fraction Φ_{max} (=FCC) was measured with 0,5 for limestone and 0,47 / 0,42 for kaolin.
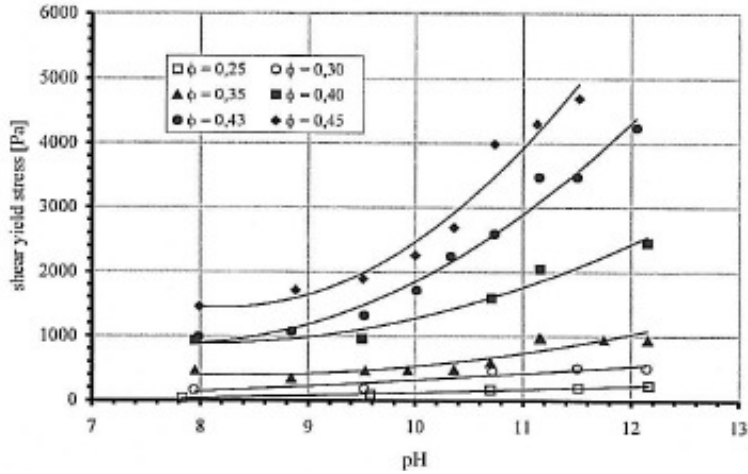
Pict. 10.2.12: Shear yield stress of limestone as a function of volume fraction and pH (A. Erk, W. Stahl)
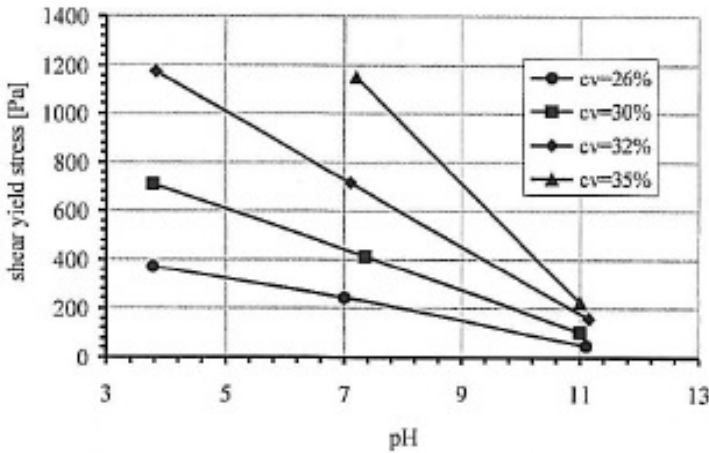
Pict. 10.2.13: Shear yield stress of kaolin H1 (A. Erk, W. Stahl)

Close to the iso-electrical point the suspension dewaters faster, solid content increases and shear yield stress rises (pict. 10.2.11 and 10.2.12). For carbonate slurries this was detected when the IPE at pH = 12 was exceed and for kaolin this effect took place when pH was lower than the IPE at pH = 4 (pict. 10.2.13).

Carina Maria Alles and Harald Anlauf (L2.2, L2.4) from U Karlsruhe studied the filter cake behaviour of different pigments. In ultra filtration units filter cake permeability should be as high as possible which stays in contradiction to the request for the filter cake of coatings before blade. U. Karlsruhe is specialized on filtration experiments and developed a permeability cell as shown in pict. 10.2.14.
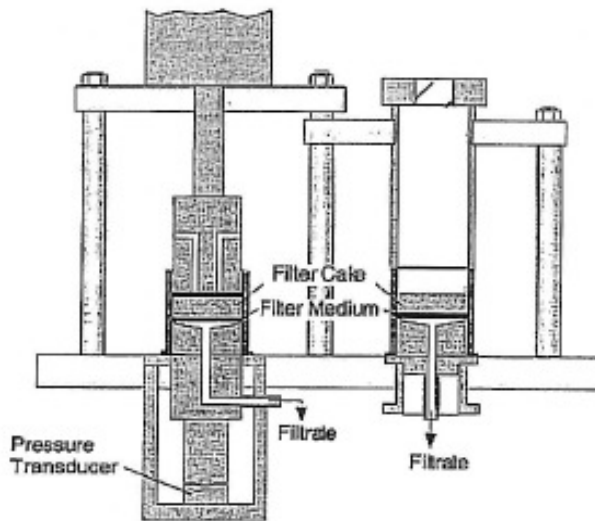
Pict. 10.2.14: Compression cell of TU-Karlsruhe (C.A. Alles)
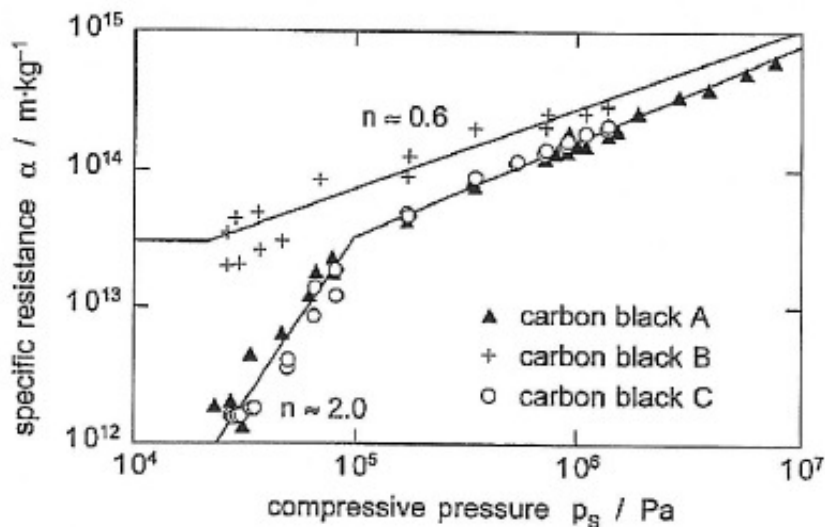
Pict.10.2.15: Permeability data of carbon black with different pre-treatment (C.A. Alles)

Carbon black A + C were pre-treated and aggregated. They showed a lower filtration resistance at low pressures (appr. 1bar) but at higher pressures the aggregation

Page 490

effect got lost (pict. 10.2.15). Therefore in many filtration processes dewatering is performed in two steps: One unit with low pressure, followed by a unit with high pressure to achieve lower investment costs. This is very important when extreme fine particles are filtrated as they built a highly compressible filter cake structure which is extremely difficult to dewater. The higher the compressibility, the more sensitive filtration is to mechanical stress.

G. Metreveli and J. Heuser (L2.3) compared the filtration resistance of different pigment slurries (SiO_2, clay, carbonate) by C-P-F-Cell of U Karlsruhe.

Laminar flow through a filter cake can be described by Darcy's law 1938 (L2.8):

$$\frac{dV}{dt} = \frac{A * \Delta p}{\eta * (r_e * h_K + R_M)}$$

Where η is the dynamic viscosity, r_e is the length depending filter cake resistance, h_K is the filter cake height and R_M is the filter medium resistance.

A specific filter cake resistance α is often used for all kind of filtration experiments:

$$R_C = r_e * h_K = \alpha * (1 - \varepsilon) * \rho_S * h_K$$

$$\alpha = \frac{A * \Delta p * dt}{\eta * \rho_S * h_K * dV * (1 - \varepsilon)}$$

Knowing α, a representative mean pore diameter can be calculated by using the Hagen-Poiseulle equation:

$$\frac{\Delta p}{h_K} = \frac{32 * U_m * \eta}{d_p{}^2}$$ with U_m the mean liquid velocity and d_p the mean pore diameter.

$$d_P = \sqrt{\frac{32}{\alpha * \varepsilon * \rho_S * (1 - \varepsilon)}}$$

Adding salt to pigment slurries changed the Helmholz layer and the zeta potential. In consequence the filtration resistance α was lowered.

M. Beiser (L2.6) studied the influence of additives on the sedimentation behaviour of fine grained solids in the centrifugal field.
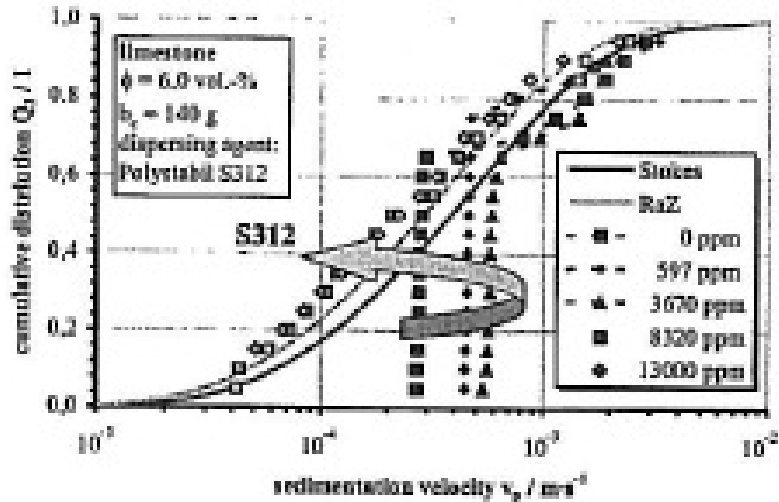
Pict. 10.2.16: Influence of anionic dispersing agent on sedimentation of limestone (M. Beiser)

Adding a polymer dispersant (anionic polyacrylate) to limestone led to a shift in the zeta potential from +20 mV to the iso-electric point (pict. 10.2.16). Sedimentation velocity increased due to coagulation and filtration resistance drops.

Conclusion for coating colours:
Close to the iso-electric point dewatering is fastest as flocculation of coating colour leads to increased filter cake porosity.
 Salts from CMC or other agents destabilize pigment slurries and water retention drops. Depletion flocculation of pigment particles by reaction of ionic components in the coating like PVOH or acidic ions from latex serum with hydration layer of pigment (see 10.7) leads also to worse water retention.

Thus a coating colour without any flocculant or salt should have the highest water retention. When water retention additives are used they should not contain salt or flock pigment slurries.

Carina Maria Alles and Harald Anlauf (L2.10) compared the results from filtration experiments with the CP-F cell of U Karlsruhe with calculated filtration resistance

from the Carman Kozeny equation. They used soot powder slurries which were partly aggregated (soot 1 + 3) by shifting the zeta potential to the IEP.
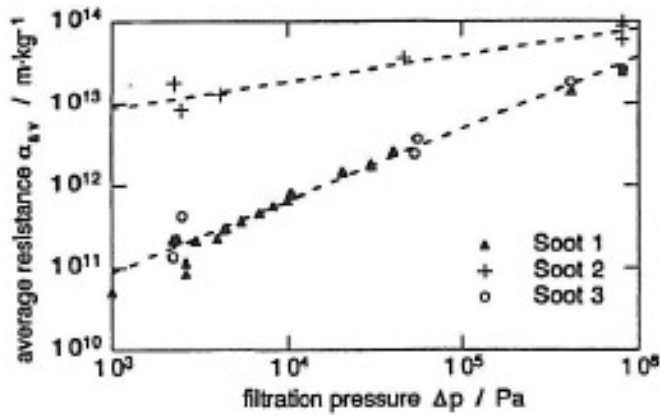
Pict. 10.2.17: Cake formation: filter resistance vs. filter pressure (C.A. Alles)

Filtration resistance was lowered by aggregating the soot particles (pict. 10.2.17).
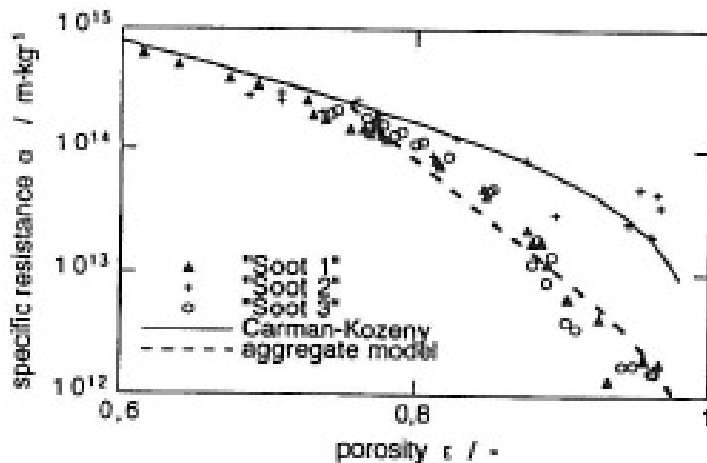
Pict. 10.2.18: Compression cell data: specific resistance vs. porosity (C.A. Alles)

For the aggregated powders the Carman-Kozeny equation couldn't be applied as permeability measurements didn't fit to calculated permeability from porosity ε. Therefore an additional porosity inside the aggregates ε_{in} was introduced to explain the filtration results (pict. 10.2.18).

Both porosities, inside the aggregates and outside contribute to total porosity ε:

$$1 - \varepsilon = (1 - \varepsilon_{in}) * (1 - \varepsilon_{out})$$

Total original filter resistance $\alpha = \dfrac{1}{(1-\varepsilon) * \rho_s * k}$ was extended with:

$$\alpha = \frac{1}{(1-\varepsilon) * \rho_s * (k_{in} + k_{out})} = \frac{36 * K}{(1-\varepsilon) * \rho_s} * \left[\frac{\varepsilon_{in}{}^3 * d_{Part}{}^2}{(1-\varepsilon_{in})^2} + \frac{\varepsilon_{out}{}^3 * d_{Agg}{}^2}{(1-\varepsilon_{out})^2} \right]^{-1}$$

to calculate the permeability coefficient k from the Carman Kozeny equation

$k = \dfrac{1}{K} * \dfrac{\varepsilon^3}{(1-\varepsilon)^2} * \dfrac{d}{36}$. This aggregate model fitted well to the experimental results.

10.3 Lab trials with pigment slurries

In the process lab of PM11 (PT4) different pigment slurries and coating colours were compared in their filter cake permeability. For these experiments the Abo-GWR water retention instrument was used (pict. 10.3.1).
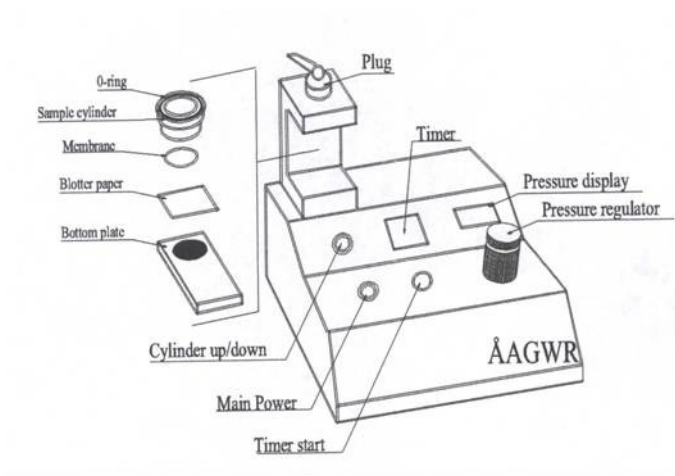
Pict. 10.3.1: Abo-GWR water retention instrument

The Abo GWR water retention instrument dewaters coating colours by external pressure through a membrane of defined pore size.
The drained water is captured at the back side of the membrane by a highly absorbent glass fibre pad which is weighted before and after the experiment.

The standard method with this instrument is done with a 5 μm membrane at 0,5 bar and 90 sec pressure time.
The 5 μm membrane corresponds to the pore size of base papers (pict. 10.3.2).
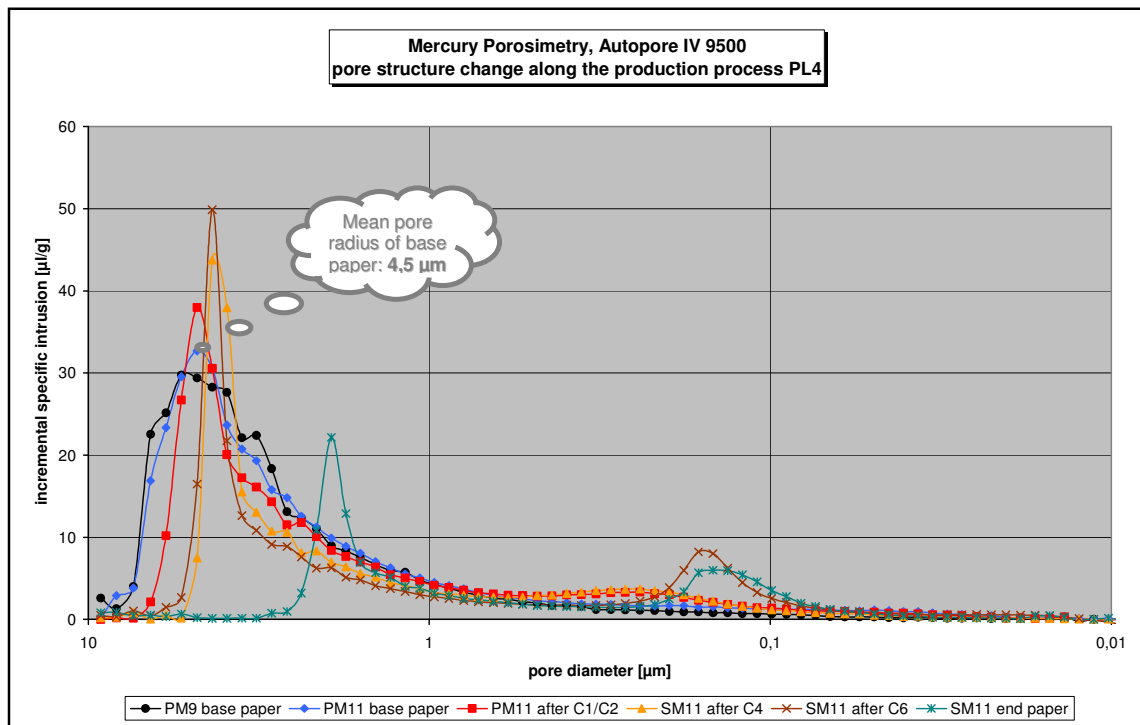
Pict. 10.3.2: Mercury porosity of base papers, pre-coated (C1/2), middle coated (C3/4) and top coated (C6) – hole measuring range

Pressure level of 0,5 bar corresponds to capillary sorption pressure of fibres (see chapter "capillary penetration"). This test procedure simulates capillary sorption of liquid phase from coating colour between application and blade. Time of penetration is with 90 sec relatively long to get low variance in results.

When coating colours are applied on pre- or middle coated papers where pore size is in the range of 0,25 μm (pict. 10.3.3) a much finer membrane has to be used in the Abo- GWR experiments to simulate coating colour dewatering on this layer.
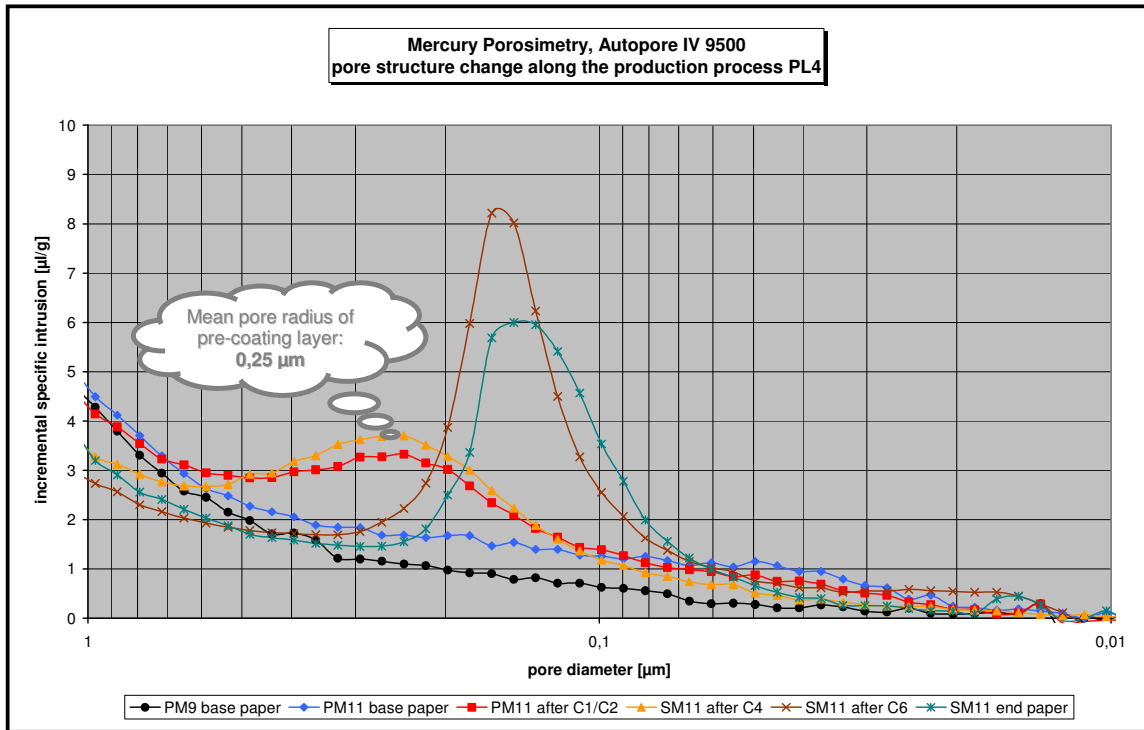
Pict. 10.3.3: Mercury porosity of base papers, pre-coated (C1/2), middle coated (C3/4) and top coated (C6) – pore range of coating colours

To simulate the penetration of top coatings into middle coated papers the experiments were extended by using a membrane with 0,1 µm pore diameter.

Standard procedure with Abo-GWR instrument is with 90 sec relatively long compared to penetration process at blade coaters which last milli seconds.
To improve correlation to mill data's the time of penetration was extended with 5, 10, 30 and 90 sec.

An additional pressure level of 2 bar was used for the experiments to get closer to blade pressure.

Abo-GWR experiments are regarded as "static" as shear is missing before the experiment starts. At blade coaters this shear is present under the blade when coating colour is dewatered by blade pressure. After the blade capillary sorption of base paper starts similar to Abo-GWR experiments with external pressure of 0,5 bar but again dewatering behaviour of coating colour will be different at commercial blade

coaters as it was sheared under the blade immediately before capillary sorption starts.

Pekka Salminen, John Roper, Mark Pollock and Yohannes Chonde from DOW (L1.57) came to the same conclusion when they tried to find a method to describe the "dynamic water retention" of a coating colour. The trigger for this study was the fact that long term static water retention measurements done with the Abo-GWR instrument and the SD-Warren tester didn't fit to runability problems in the mill. The authors used a fast CLC lab coater for runability simulations and scraped off the coating colour directly after the blade.

Salminen expected water retention to get worse when coating colour was sheared under the blade. Instead of static water retention measurements like Abo-GWR he regarded the solid content after the blade as a parameter describing the dynamic water retention of a coating colour where coating colour is sheared first under high shear forces and liquid phase penetrates afterwards into base paper due to external pressure and capillary sorption of the fibres.

The increase in solids under the blade which was detected by Salminen, was rather low for clay coatings with high static water retention. When drying was switched off, a remarkable solid increase was measured in the free draw after the blade. Therefore he suggested starting drying as fast as possible to avoid binder penetration into the base which might lead to non-uniform migration in the drying section.

In the drying part the static water retention ability of the coating colour is regained again but not immediately. Shear stress relaxation measurements show differences between different thickeners: The structure is faster recovered by associative thickeners, compared to cellulosic thickeners (CMC, HEC).

Therefore the solid increase in the free draw after the blade was lower with associative thickeners. This can be advantageous for mottling when drying starts late due to restrictions in machinery or energy.

Starch was found as the best water retention agent but what P. Salminen overlooked was the fact that in mill coaters the starch content drops in the working tank with running time as starch is relatively low in molecular weight. Water retention drops

with running time too. Salminen used fresh coatings where water retention of starch based colours is always high.

Static water retention measurements (e.g. by Abo-GWR) can be used to describe coating colour thickening between application and blade where it isn't pre-sheared to a high extend.
For liquid phase penetration after the blade these measurements cannot be used at high speed coaters as stress relaxation in the coating colour is too slow. The "dynamic" water retention (retention after shear) will dominate capillary sorption after the blade.

Data's from the drainage experiment and the corresponding calculation are shown in the following paragraph for a relative coarse carbonate Hydrocarb 60 (HC60) with 60% < 2 µm:

HC 60 NP   Rezeptur von 03. Juli 2007

Feststoffgehalt:	78,28 %		**Bindemittelgehalt:**	AW Ti+EW		g	
Low shear Visco:	105 mPa*s			Tiegel		g	
High shear Visco:	210 mPa*s	10000		Einwaage		g	
	- mPa*s	20000		Auswaage		g	
	- mPa*s	40000		**TG**	78,280 %		
pH:	9,33						
Temperatur:	40 ℃			Bmittel AW		g	
Bindemittelgehalt:	- %			Auswaage		g	
				Faktor			
Filtergewicht lutro bei 95,5 % TG --> 4,5 % Feuchte				**Bindemittel**	0,000 %		

Zeit [s]	Druck [bar]	Membrane [µm]	Filtergewicht lutro [g]	Filtergewicht atro [g]	lutro nach Abo [g]	atro nach Abo [g]	Wasser-retention [g]	W+P- Ret [g/m²]	**Wasserreten-tion [g/m²]**	Pigment [g] verascht	Pigment [g/m²]
5	0,5	5	1,394	1,331	1,447	1,333	0,053	80,295	77,265	0,0020	3,030
10	0,5	5	1,371	1,309	1,438	1,311	0,067	101,505	98,323	0,0021	3,182
30	0,5	5	1,410	1,347	1,523	1,347	0,113	171,195	167,711	0,0023	3,485
90	0,5	5	1,333	1,273	1,529	1,273	0,196	296,940	293,153	0,0025	3,788
1200	0,5	5	1,386	1,324	2,005	1,327	0,619	937,785	931,877	0,0039	5,909

0,5 bar / 5 µm

Zeit [s]	Druck [bar]	Membrane [µm]	Filtergewicht lutro [g]	Filtergewicht atro [g]	lutro nach Abo [g]	atro nach Abo [g]	Wasser-retention [g]	W+P- Ret [g/m²]	Wasserreten-tion [g/m²]	Pigment [g] verascht	Pigment [g/m²]
5	2	5	1,405	1,342	1,489	1,344	0,084	127,260	124,230	0,0020	3,030
10	2	5	1,395	1,332	1,512	1,334	0,117	177,255	173,922	0,0022	3,333
30	2	5	1,426	1,362	1,631	1,363	0,205	310,575	306,939	0,0024	3,636
90	2	5	1,416	1,352	1,765	1,353	0,349	528,735	524,493	0,0028	4,242
1200	2	5	1,373	1,311	2,496	1,317	1,123	1701,345	1695,437	0,0039	5,909

2 bar / 5 µm

Zeit [s]	Druck [bar]	Membrane [µm]	Filtergewicht lutro [g]	Filtergewicht atro [g]	lutro nach Abo [g]	atro nach Abo [g]	Wasser-retention [g]	W+P- Ret [g/m²]	Wasserreten-tion [g/m²]	Pigment [g] verascht	Pigment [g/m²]
5	0,5	0,1	1,368	1,306	1,407	1,308	0,039	59,085	58,327	0,0005	0,758
10	0,5	0,1	1,395	1,332	1,458	1,333	0,063	95,445	94,384	0,0007	1,061
30	0,5	0,1	1,425	1,361	1,530	1,361	0,105	159,075	157,712	0,0009	1,364
90	0,5	0,1	1,432	1,368	1,621	1,368	0,189	286,335	284,517	0,0012	1,818
1200	0,5	0,1	1,399	1,336	2,025	1,337	0,626	948,390	945,057	0,0022	3,333

0,5 bar / 0,1 µm

Zeit [s]	Druck [bar]	Membrane [µm]	Filtergewicht lutro [g]	Filtergewicht atro [g]	lutro nach Abo [g]	atro nach Abo [g]	Wasser-retention [g]	W+P- Ret [g/m²]	Wasserreten-tion [g/m²]	Pigment [g] verascht	Pigment [g/m²]
5	2	0,1	1,403	1,340	1,482	1,341	0,079	119,685	118,776	0,0006	0,909
10	2	0,1	1,388	1,326	1,516	1,327	0,128	193,920	192,557	0,0009	1,364
30	2	0,1	1,367	1,305	1,570	1,307	0,203	307,545	305,879	0,0011	1,667
90	2	0,1	1,417	1,353	1,767	1,354	0,350	530,250	528,129	0,0014	2,121
1200	2	0,1	1,372	1,310	2,496	1,313	1,124	1702,860	1698,012	0,0032	4,848

2 bar / 0,1 µm

Pict.10.3.4: Abo-GWR water retention measurement of HC60 with different membranes and pressure levels
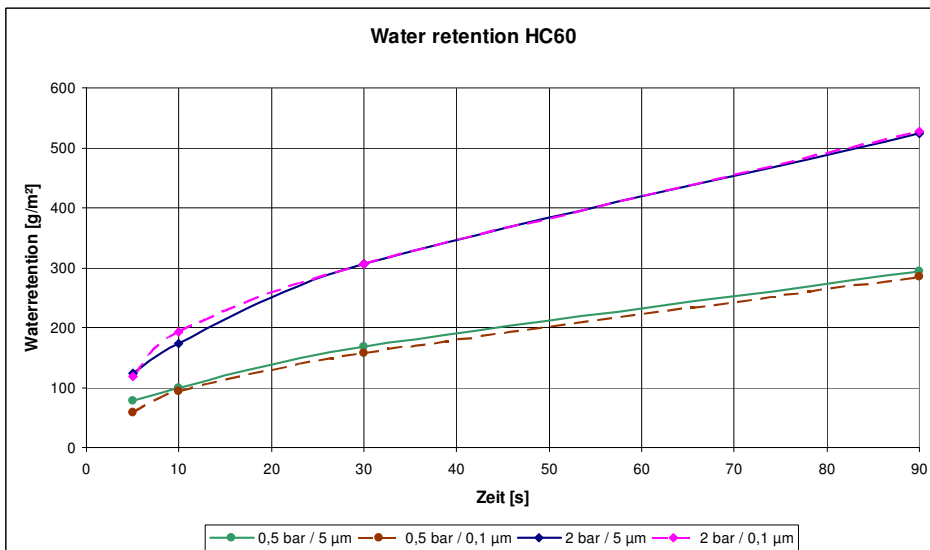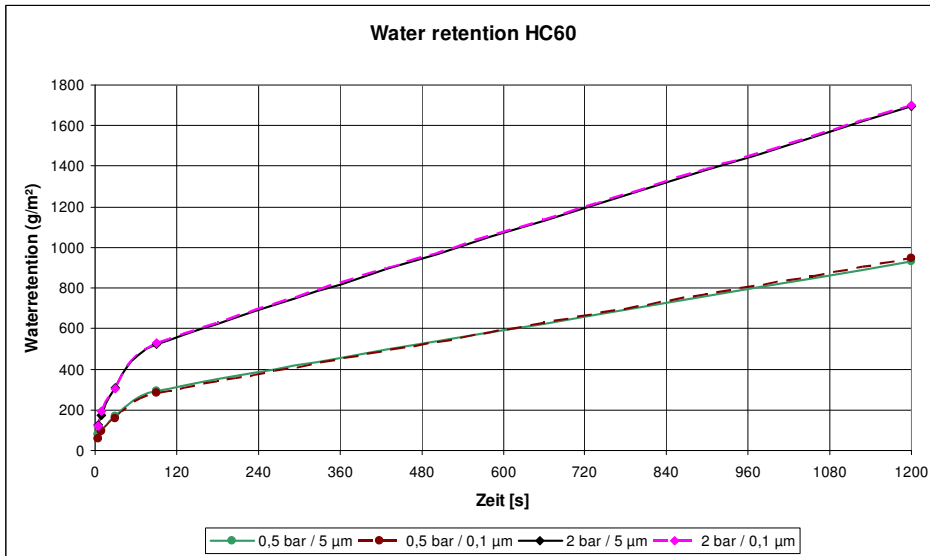
Pict. 10.3.5: Abo-GWR water retention measurement of Hydrocarb 60 slurry, 78% solids

Measured water retention of HC60 slurry was mainly influenced by pressure level (pict. 10.3.5).

Integrating Darcy's law leads to Carman-Kozeny equation which is commonly used for every filtration process:

$$\frac{dV}{dt} = \frac{K * A * \Delta p}{\eta * L}$$

$$dV = \int_0^t \frac{K * A * \Delta p}{\eta * L} * dt$$

$$V = \frac{K * A * \Delta p}{\eta * L} * t \text{ and with } dV = A * dL * \frac{100}{\varepsilon} \quad \varepsilon\text{....Porosity of penetrated medium}$$

$$V^2 = \frac{K * 100 * A^2 * \Delta p}{\eta * \varepsilon} * t$$

$$V = A * \sqrt{\frac{K * 100}{\eta * \varepsilon} * \Delta p * t}$$

or in general:

Carman-Kozeny: $\quad \dfrac{m}{f} = \sqrt{C * A * \Delta p * t}$

m/f in g/m²

C = f(Viscosity, packing density)

A = f(start solids, immobilisation solids).

Solid content of the material retained on the filter membrane was calculated for every measured period of time:
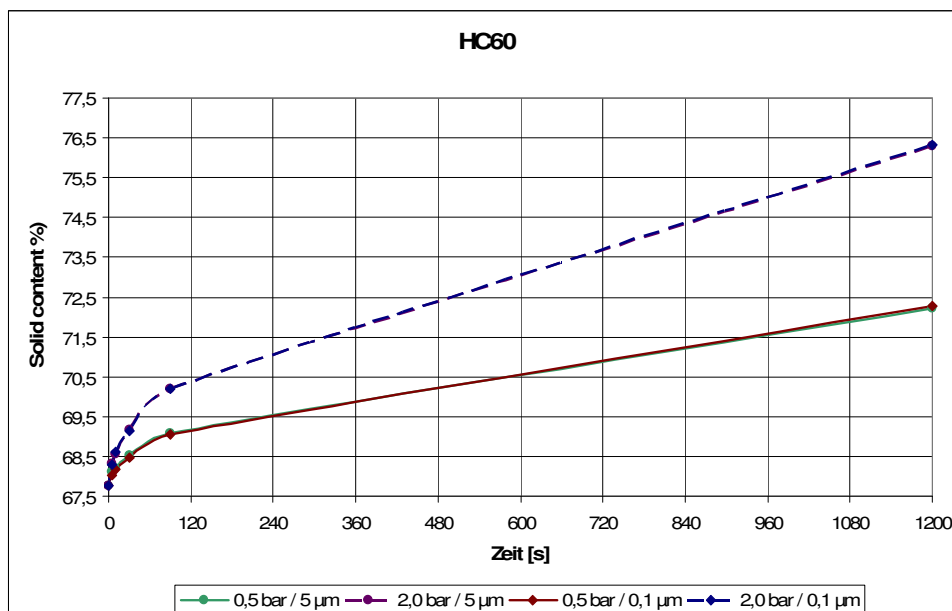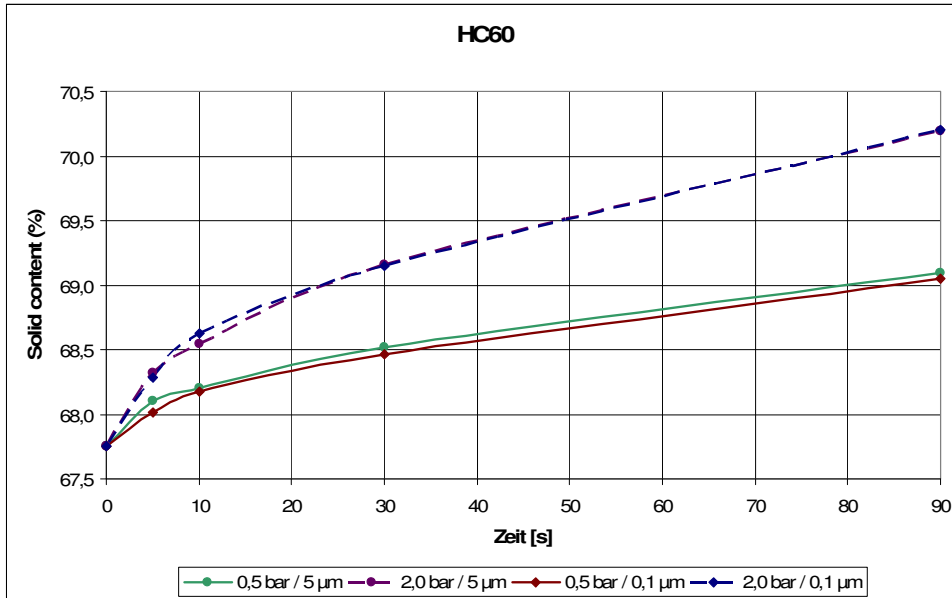
Pict. 10.3.6: Mean solid content in the retained material on the filter

This calculated solid content on the membrane as shown in pict. 10.3.6 is only of theoretical importance. Coating colours form immediately an immobilized filter cake on the membrane which hinders the rest of the coating colour to be dewatered. The solid content of the immobilized layer will be higher than that of the coating layer on top if it. Wet coating layer on top of the membrane was divided in later calculations into an immobilized layer at the boundary and a layer with original solids on top of it.

S. Lohmander, M. Martinez, L. Lason, M. Rigdahl (L1.71) showed the existence of the filter cake at the membrane surface by similar dewatering experiments, as shown in this study with Abo-GWR.

They used mono sized spherical polystyrene particles to apply Darcy's law. Integrated form of Darcy's law and Carman-Kozeny equation are only valid for nearly spherical particles and incompressible filter cakes. Previous experiments of Engström showed a concentration gradient over the height of the filter cake, which is an indication of compressibility.

The dewatering experiment is considered as a cylindrical vessel with a cross-sectional area A and a pressure Δp, creating a liquid flow of velocity q.

$$\phi_0 * H_0 = \phi_0 * [h(t) - \lambda(t)] + \int_0^{\lambda(t)} \phi(z,t)dz$$

with Φ_0 the initial solidity of the particle dispersion, H_0 the initial height of the dispersion, λ the filter cake thickness and h the distance of the surface of the fluid to the bottom of the vessel.

For an incompressible filter cake $\Phi(z,t)$ the rate of growth of the filter cake is:

$$\frac{d\lambda(t)}{dt} = -\left[\frac{\phi_0}{\phi - \phi_0}\right] * \frac{dh}{dt}$$ with Φ the average solidity of the filter cake, considered as constant.

Inserting Darcy's law and $q = -\dfrac{dh}{dt}$ leads to:

$$\lambda(t) = \sqrt{\frac{2\phi_o}{\phi - \phi_0} * \frac{k(\phi) * \Delta P}{\eta} * t}$$

With the boundary conditions $\lambda(0)=0$ and $h(0)=H_0$:

$$h(t) = H_0 - \sqrt{\frac{2*(\phi - \phi_o)}{\phi_0} * \frac{k(\phi) * \Delta P}{\eta} * t}$$

In dewatering experiments the flow of liquid $V_l(t)$ is measured:

$$V_l(t) = A((H_0 - h(t)) = A * \sqrt{\frac{2*(\phi - \phi_o)}{\phi_0} * \frac{k(\phi) * \Delta P}{\eta} * t}$$ with $k(\phi) = \frac{(1-\phi)^3}{K'' * S^2 * \phi^2}$

Where K'' is the Kozeny constant, which is K''=5 for spheres and S is the specific surface area, which is S=6/d for spheres (d is the sphere diameter).

In a compressible filter cake the function $\Phi(z,t)$ is unknown. Langman proposed 1991 that the solidity is governed by diffusion equation:

$$\frac{\partial \phi}{\partial t} = \frac{\partial}{\partial z} * \left(\frac{k(\phi) * f'(\phi) * \phi}{\eta} * \frac{\partial \phi}{\partial z}\right) - \frac{dh(t)}{dt} * \frac{\partial \phi}{\partial z}$$

with $f(\Phi)$ the compressibility function of the filter cake represented by a power-law relationship $f(\Phi)=m*\Phi^n$ (m,n empirical constants).

Compressibility of the filter cake depends upon colloidal forces in the system. When particle size is below 10 µm (which is the case for almost every coating colour) these forces dominate and compressibility will be high.

Furthermore compressibility will depend on pigment packing at different applied pressures. For mono disperse system there are six packing systems ranging from cubic particles with a solidity of 52% to rhombohedral particles with a solidity of 74% (densest packing). Practical systems will have a solidity of appr. 64%.

With the boundary conditions $\Phi(z,0)=\Phi_0$, $f(\Phi(0,t))=\Delta P$, $\Phi(\lambda(t),t)=\Phi0$, $d\Phi/dz(z=0)=\eta/(k(\Phi)*f'(\Phi)*\Phi)*dh(t)/dt$ and $d\Phi/dz(z)\lambda(t))=0$
Langman resulted in:

$$V_2(t) = A * \sqrt{\frac{2*\alpha*(\phi-\phi_o)}{\phi_0} * \frac{k(\phi(0,t))*\Delta P}{\eta} *t}$$ with α a constant between 0 and 1.

Both equations show a linear relationship between V(t) and $\sqrt{t}$.

Lohmander placed a magnetic device around the dewatering cell. Walls were made of plastic to let the magnetic radiation pass. MnCl$_2$ was dropped into the dispersions, decreasing the nuclear magnetic resonance (NMR).
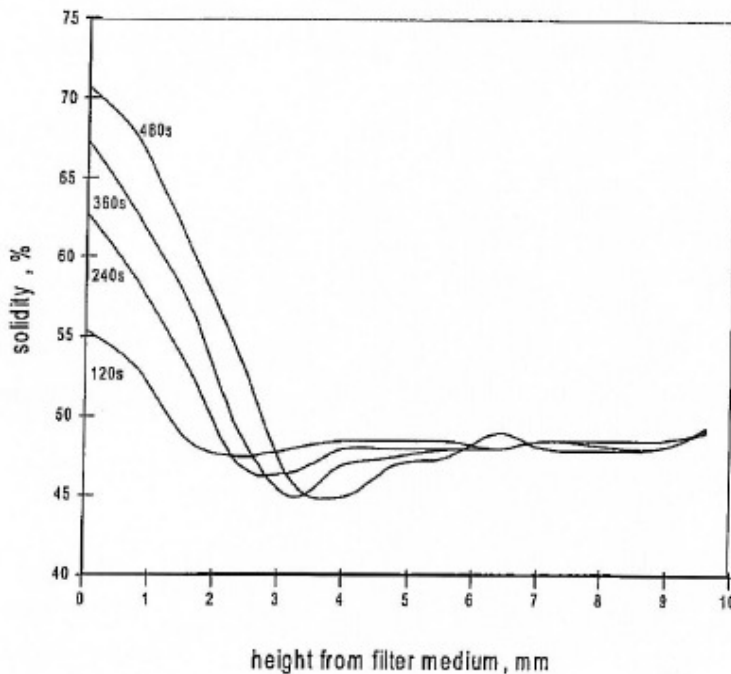
Pict. 10.3.7: Solid content profile in Z-direction for pure polystyrene dispersion – 0 mm height corresponds to membrane surface (Lohmander)

The increase of solid content at the membrane was measured according to the filter cake theory. Pict. 10.3.7 shows that the higher the dewatering time, the thicker the immobilized layer on top of the membrane was.

Adding CMC led to a thinner but higher viscous immobilized layer (pict. 10.3.8).
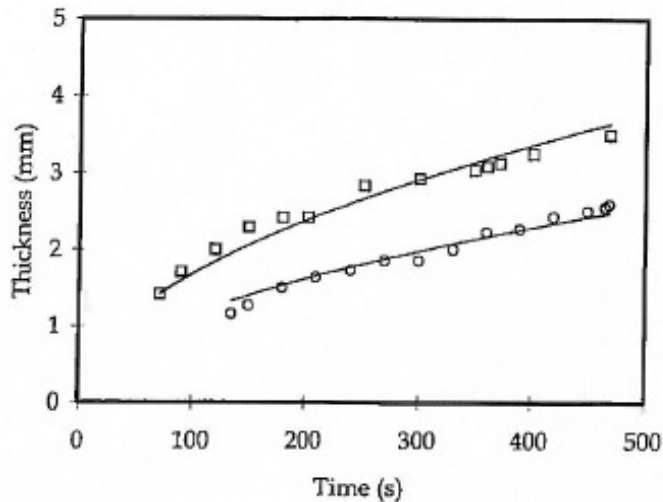
Pict. 10.3.8: Filter cake thickness vs. tie for polystyrene dispersion only (squares) and plus 0,8% CMC FF5 (circles) (Lohmander)

According to Darcy's law $q = -\dfrac{k(\phi)}{\eta} * \nabla P$ the product of q x η = η x V_{exp} should be constant for a certain time of flow. This was true for all polymer dispersions except with PAM where abnormal viscosity effects occurred (pict. 10.3.9).

Polymer	Added amount, mg	η_s, mPas	V_{exp}, ml	η_s x V_{exp}, kgm^2/s^2 x 10^6
None		0.89	6.2	5.5
CMC FF5	20	1.39	4.7	6.5
CMC FF5	40	1.72	3.8	6.5
CMC FF150	10	2.39	2.8	6.7
PAM	5	3.40	0.4	1.4

Pict. 10.3.9: Flow of polymer solution at 10 kPa, 60 sec (Lohmander)

When coating colour is pressed through a 5 µm membrane, fines will pass the membrane. This loss in solid fraction must be measured in the filtrate separately (pict. 10.3.10) for calculation of filter cake thickness by mass balance, especially when membranes with diameters bigger than the mean diameter of pigments in coating colours are used.
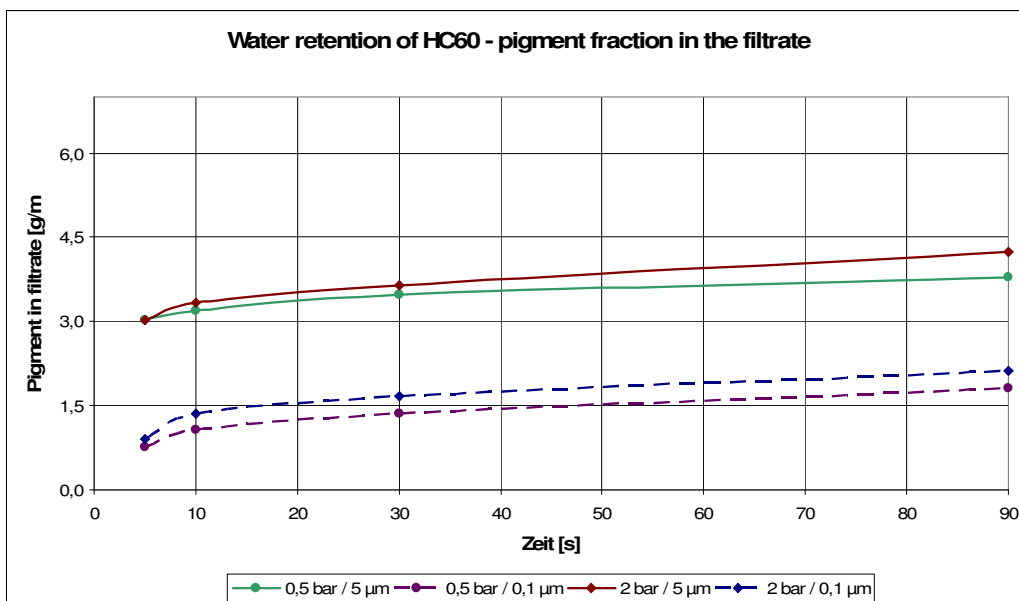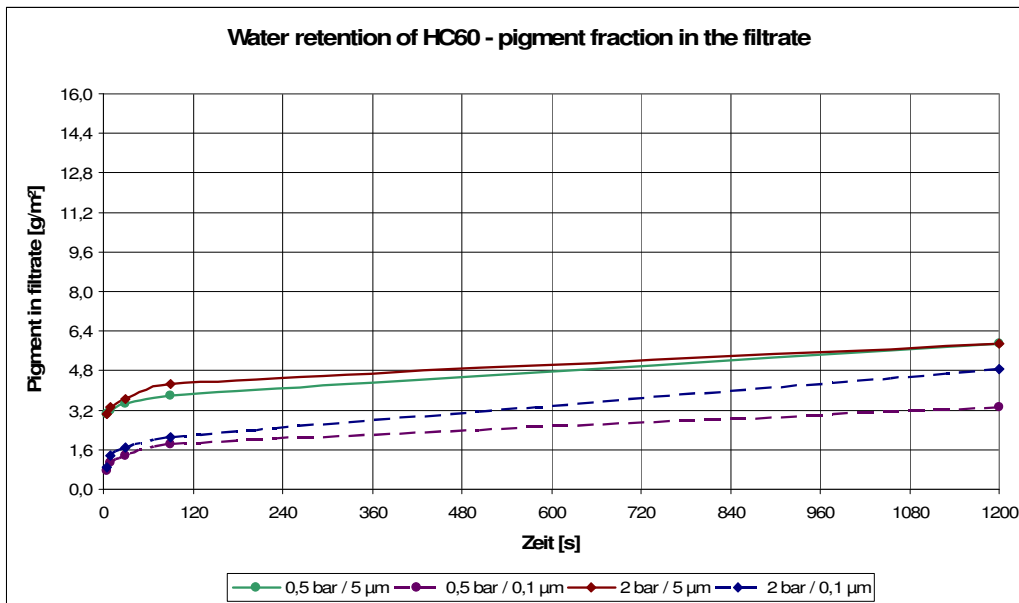
Pict. 10.3.10: Measured pigment content in the filtrate

In the next step the thickness of the immobilized layer is calculated. Therefore the solid content and the density of the immobilized layer must be known from separate experiments.

Different methods exist to measure immobilization solids. It's defined as the solids where particle packing is so dense that no movement of particles is possible. Viscosity increases exponentially when immobilization solids is reached.

Seongnam Ahn and Douglas W. Bousfield from U. Maine developed a laser gloss meter to measure the immobilization point of the coating colour (L1.12).

Different coating colours were applied by a lab rod coater. Drying was done under room temperature. The laser gloss meter was positioned over the coated surface and measured the gloss of the wet coating colour during solid increase by capillary sorption of the base paper (pict. 10.3.11).
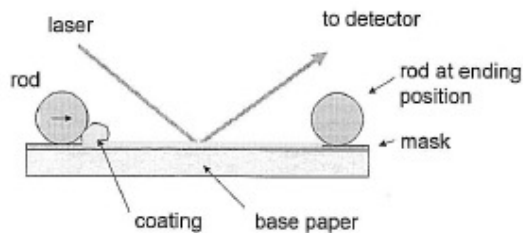
Pict. 10.3.11: Laser device for measuring FCC and SCC (S. Ahn)

At the first critical concentration (FCC) the gloss dropped and at the second critical concentration (SCC) it levelled out (pict. 10.3.12). The FCC corresponds to the immobilization point.
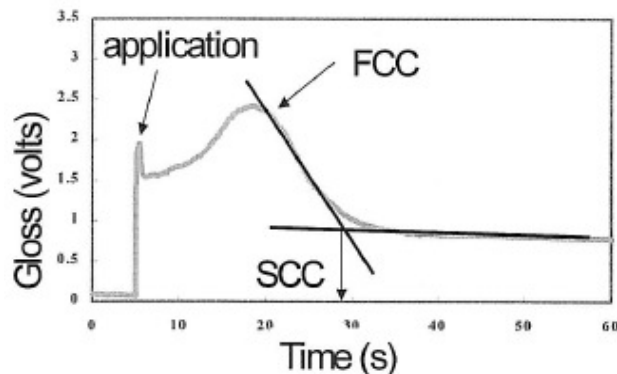
Pict. 10.3.12: Laser response during consolidation process (S. Ahn)

Clay based coatings reached the FCC faster than carbonate coatings. Adding water retention agents into carbonate coatings increased the immobilization time additionally.

Alkali swell-able latices had shorter immobilization times than standard SB latices. Internal sized base papers showed better coating holdout and longer immobilization time than un-sized papers (pict. 10.3.13).
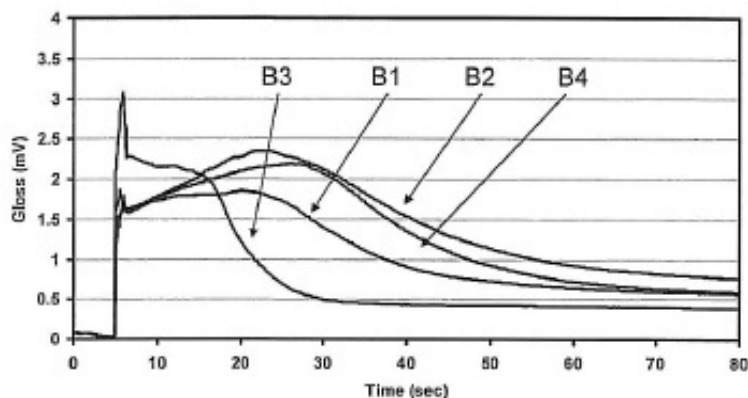
Pict. 10.3.13: Laser response – immobilization time for different base papers (S. Ahn)

Teng Shau Young studied penetration under dynamic conditions (L1.15). He used a Heliocoater which could be run up to 2000 m/min for his experiments. Immobilization point was determined by gloss measurement of the wet coated surface at different positions after the blade. To translate gloss measurements into solid content data's, a porous plate was used in a separate experiment where the coating colour was applied and the drop in gloss was measured. At the immobilization point (FCC) the coating colour was pulled off from the porous plate and the solid content was determined. Seven coating colours and 4 base papers were compared.

Young compared different cellulosic thickeners for a clay based rotogravure LWC formulation. He found that thickeners which built hydrogen bonds with clay particles and caused depletion flocculation delayed the capillary penetration after the blade. The immobilization time increased. Thickeners with no interaction with pigment particles reached FCC faster, increased gloss of coated paper and reduced the amount of missing dots.

Clay containing coatings reached the FCC earlier than colours with GCC (pict. 10.3.14) although the water retention value from Abo-GWR instrument was lower (=better) for the clay coatings – they dewatered slower and had a lower Darcy coefficient.

Colour No.	Clay (%)	CaCO3 (%)	Solid at appl. (%)	Immo solid (%)	Delta solids (%)	time to FCC (sec)	Abo-GWR WRV (g/m²)
2	75	25	60,3	75,5	15,2	38	394
4	25	75	60,2	83	22,8	48	450
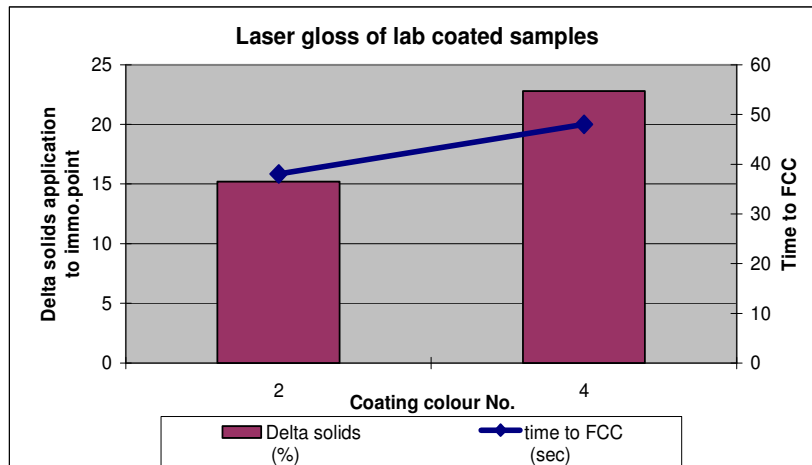
Pict. 10.3.14: Immobilization solids (S. Ahn)

The reason for this surprising result is the lower immobilization solids for clay containing coating colours, compared to GCC.

Seongnam Ahn compared different base papers with substantial differences in degree of sizing, air permeability and basis weight.

The FCC was reached much faster at an un-sized base paper. Differences in porosity and base weight didn't influence the penetration that much.

Ahn concluded that the Darcy coefficient should be calculated from Abo-GWR readings to compare different coating colours or pigments – a result, which was executed in this work.

A second method to measure the immobilization solids is to heat up the coating colour and evaporate water carefully with low ΔT. When immobilization solids is reached viscosity increases exponentially (data's see chapter "blade coating").

The third and easiest method to determine immobilization solids is the BASF immobilization cell, combined with Paar-Physica rheometer. Under shear the coating

colour is dewatered into a defined base paper. When viscosity increases exponentially the experiment is stopped and the immobilized coating colour is pulled off from the paper surface. Results of these measurements of pigments are shown in pict. 10.3.15.

Immobilization measurements at OMYA-Oftringen, 19.3.2008
Method: Rheometer MCR300 (Anton Paar) with immobilization cell of BASF

	Original solids (%)	Immobilisation time (sec)	Solids at immobilization (%)
XGA1, Jun.2006	71,9	562	80,4
HC60-GU	77,5	95	85,3
Amazon 88	72,8	450	78,5
HC90-GU	78	492	85,5
HC95-GU	78,2	685	83,5
HC60-NP	77,7	290	86,4
XGA1, Nov.2007	72,4	1690	81,4
CC60-GU, März2008	71,3	92	82,2

Pict. 10.3.15: Immobilization solids of standard coating pigments (pigments see pict. 9.3.1)

Thickness of immobilized layer is calculated according to the following mass balance:

Mass Balance for calculation of immobilized layer at Abo-GWR water retention measurements:

Start:

	Volume (ml)	Density	Mass wet (g/m²)	Solid content (%)	Mass dry (g/m²)
Coating colour with original solids	V_{Start} (10 ml at Abo) *Measured*	ρ_{Start} *Measured*	$M_{wet,Start}=V_{Start} * \rho_{Start} / A$	$c_{Start}=Solid_{Start}/100$ *Measured*	$M_{dry,Start} = M_{wet,Start} * c_{Start}$

Memrane (corresponds to coating layer)

Dewatering = Zero

Area A (m²)

Dewatering:

Coating colour with original solids

Immobilized filtercake
Membrane (corresponds to coating layer)

Filtrate: Water + pigment

Filtercake + coating colour together:

Mass wet (g/m²)	Solid content (%)	Mass dry (g/m²)
$M_{wet,t}=M_{wet,Start} - M_{wet,filtrate,P+W}$		$M_{dry,t} = M_{dry,Start} - M_{wet,filtrate,Pigment}$
$M_{wet,t,filtrate,P+W}$ *Measured*		$M_{wet,t,filtrate,Pigment}$ *Measured*

Dewatering:

Coating colour with original solids

Immobilized filtercake
Membrane (corresponds to coating layer)

Filtrate: Water + pigment

Filtercake + coating colour seperate:

Mass wet (g/m²)	Solid content (%)	Mass dry (g/m²)
$M_{wet,t,coating}$ *Equ. 2*	c_{Start}	$M_{dry,t,coating} = c_{Start} * M_{wet,t,coating}$
$M_{wet,t,filtercake}$ *Equ. 1*	c_{Immo} *Measured*	$M_{dry,t,filtercake} = c_{Immo} + M_{wet,t,filtercake}$

Equ. 1:
$$M_{wet,t,filtercake} = \frac{M_{dry,t} - M_{wet,t} * c_{Start}}{c_{Im\,mo} - c_{Start}}$$

Equ. 2:
$$M_{wett,coating} = M_{wett} - M_{wett,filtercak}$$

$$M_{Im\,mo} = \frac{M_{Pigment} - M_{Start} * c_{Start}}{c_{Im\,mo} - c_{Start}}$$

$$h_f = h_{Im\,mo} = \frac{M_{Im\,mo}}{\rho_{Im\,mo}}$$

For the calculation of the immobilized layer thickness, the solid content and the density of the immobilized layer must be known from separate lab experiments.

$$M_{Im\,mo} = \frac{M_{Pigment} - M_{Start} * c_{Start}}{c_{Im\,mo} - c_{Start}}$$ …M in g/m², c as solid content / 100

$$h_f = h_{Im\,mo} = \frac{M_{Im\,mo}}{\rho_{Im\,mo}}$$ …Thickness of immobilized layer

or: $$h_f = \frac{V}{A} * \frac{\phi}{\phi_f * (1-\phi)}$$

Page 512

$$\phi = \frac{V_s}{V_{ges}} \quad .....\text{Pigment volume fraction in coating colour}$$

ϕ_f ....Pigment volume fraction in immobilized layer

Calculation of Φ:

$$\phi = \frac{V_s}{V_{ges}} = \frac{\dfrac{1000 * c_s}{\rho_s}}{\dfrac{1000 * c_s}{\rho_s} + \dfrac{1000(1 - c_s)}{\rho_{H2O}}}$$

Knowing all data's of the immobilized layer the material which remains on top of the membrane can be divided into the immobilized layer and the coating colour with the original solid content (pict. 10.3.16). The height of the immobilized layer is important for calculating the penetration resistance to describe the water retention of a coating colour.

Thickness of immo layer hf of HC60

Thickness of membrane: 11 µm
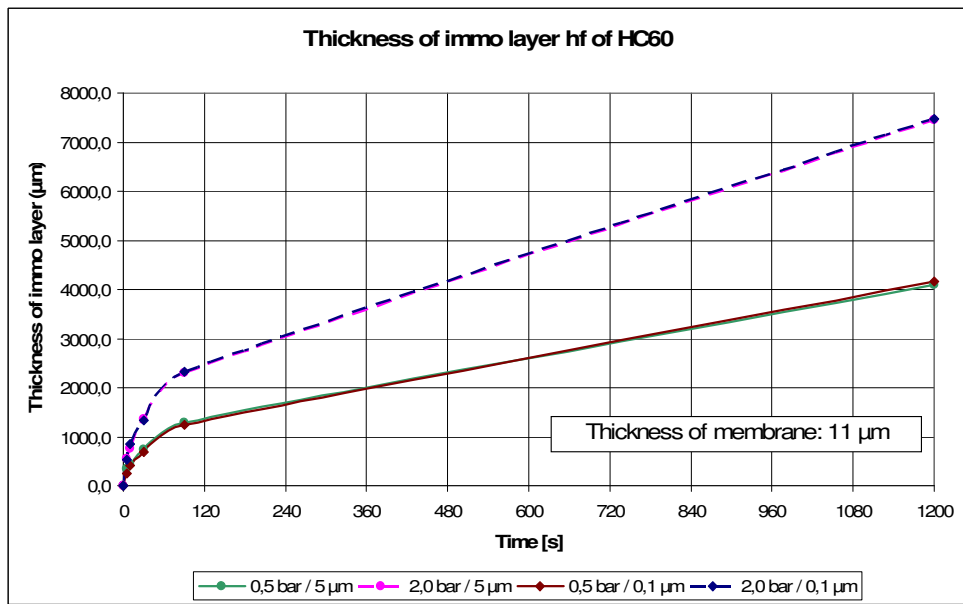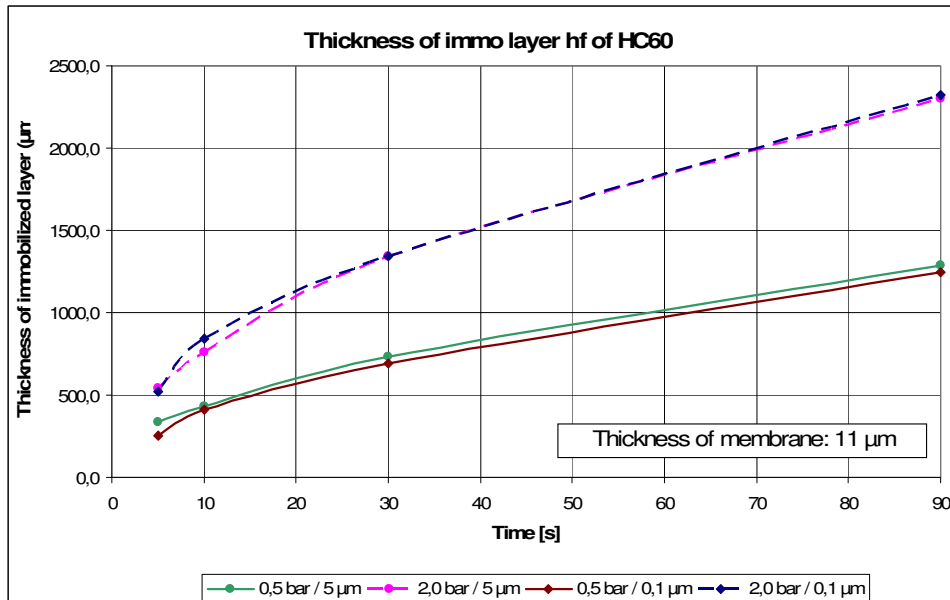
Pict. 10.3.16: Calculated thickness of immobilized layer (see equ. 7-3-1)

In the next step the Darcy coefficient of the immobilized layer can be calculated from:

$$Q = \frac{K * A * \Delta p}{\eta * L} \quad \rightarrow \quad K = \frac{dV * \eta * L}{dt * A * \Delta p}$$

In the Abo-GWR experiment the known parameters are:

- Filtrate volume dV/A (in g/m²)
- Time (sec)
- Pressure gradient (bar)

Viscosity of dewatered liquid (the liquid phase viscosity) has to be measured in a separate experiment (see later paragraph "measurement of liquid phase viscosity").

Thickness of immobilized layer (as a function of pressure, time and colour) is taken from the calculation in the previous step.
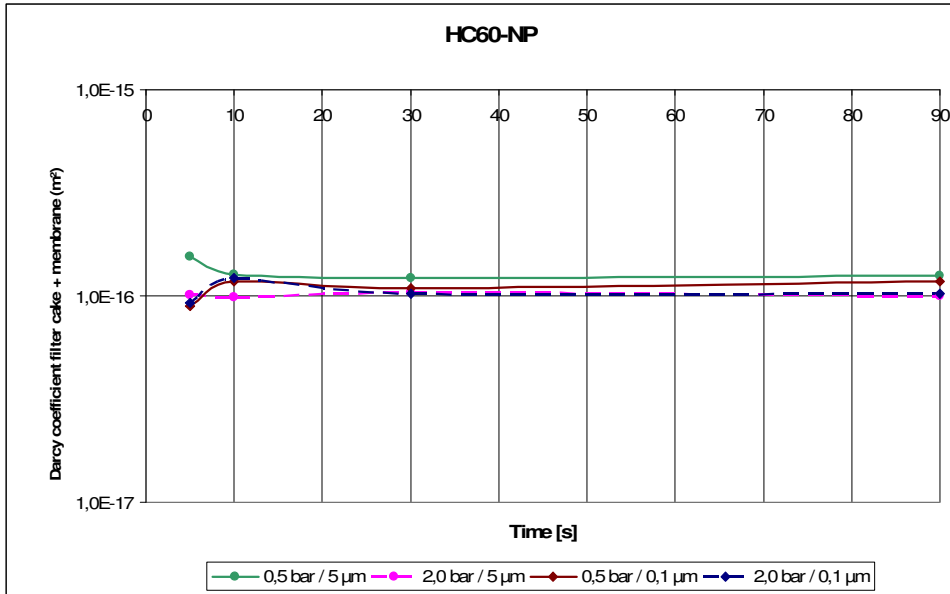
Pict. 10.3.17: Darcy coefficient of immobilized layer over pressure time

When penetration through an immobilized layer follows the Carman Kozeny equation the square of penetrated liquid volume must be a linear function of time according to:

Equ. 10-3-1: $V^2 = \dfrac{2 * \Delta p * A^2}{\eta * r * v} * t$.

This is valid for the tested HC60 slurry as shown in pict. 10.3.18:
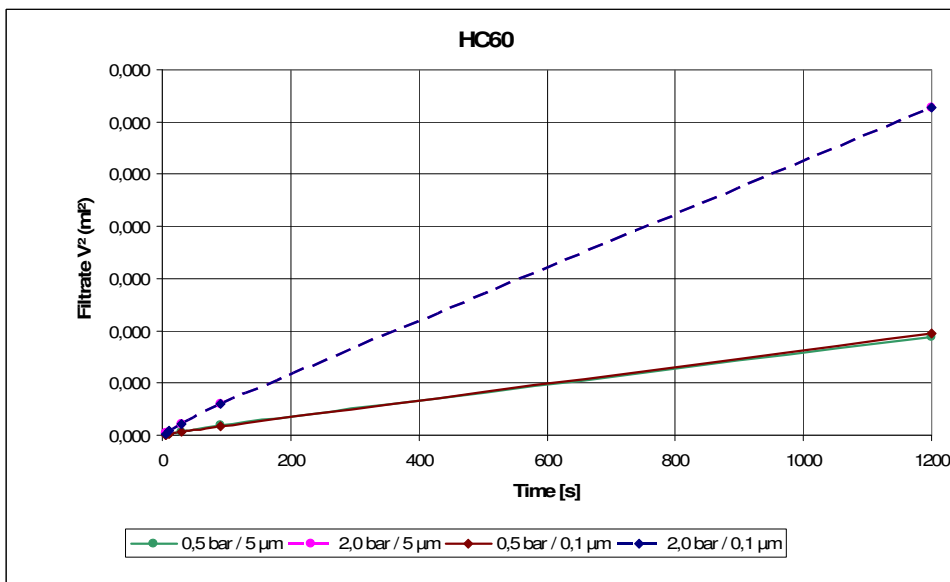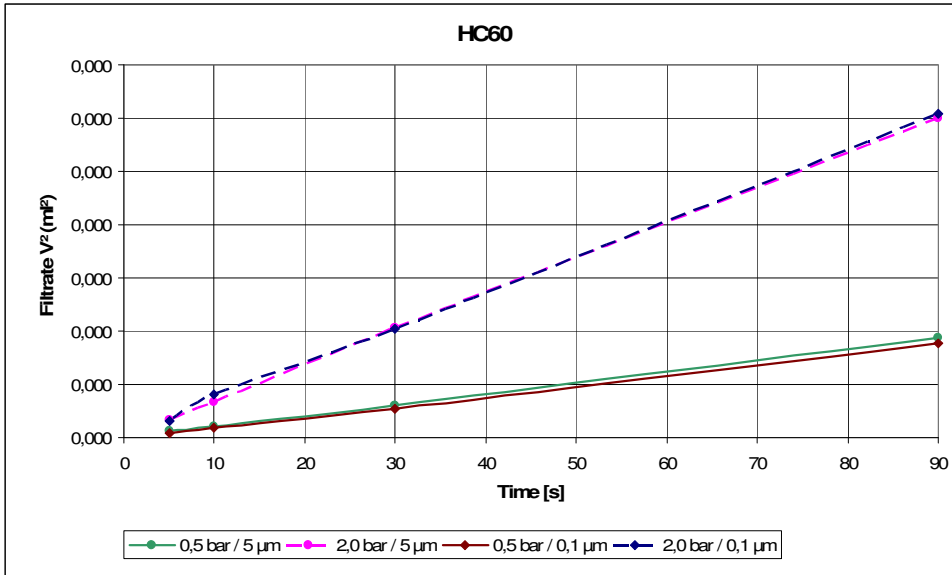
Pict. 10.3.18: Square of filtrate volume versus time

Carman's law can also be proved by plotting t/V versus V, according to:

Equ. 10-3-2: $\frac{t}{V} = \frac{\eta * r * v}{2 * \Delta p * A^2} * V + \frac{\eta * R}{\Delta p * A}$
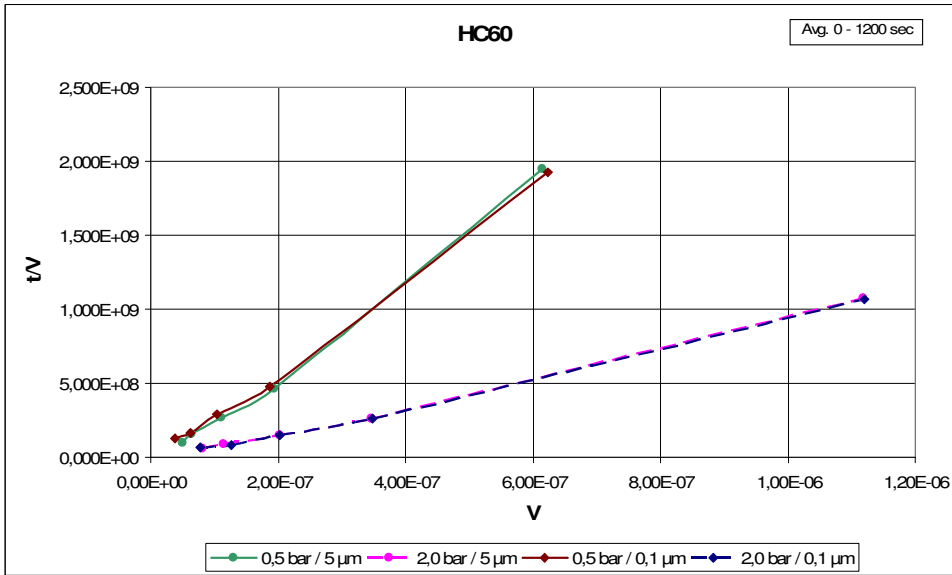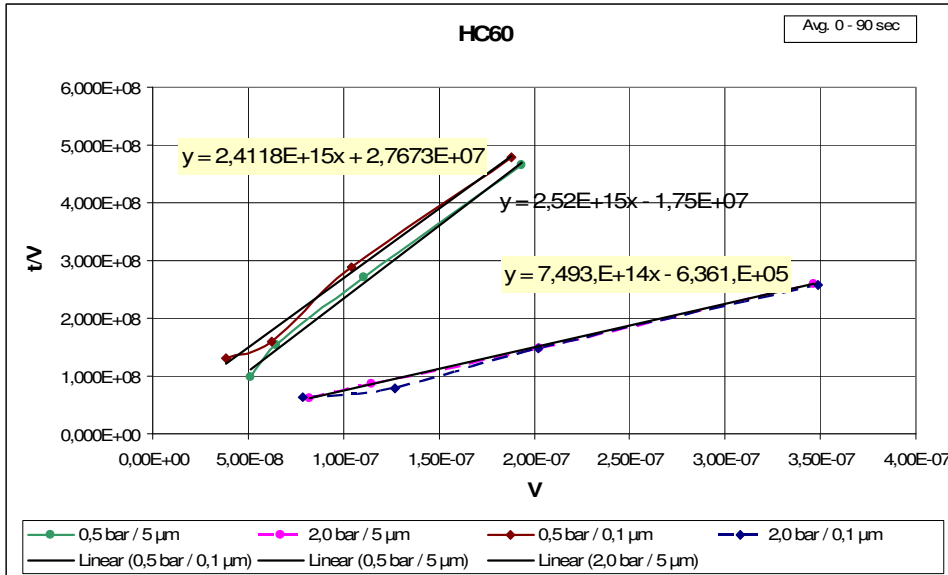
Pict. 10.3.20: t/V versus V of HC60 slurry

From the linear relationship between t/V and V the coefficient $b = \dfrac{\eta * r * v}{2 * P * A^2}$ and the

coefficient $\dfrac{\eta * R}{\Delta p * A}$ can be calculated (pict. 10.3.20).

The two coefficients are depending only on pressure gradient and thus on the immobilized layer; the type of membrane has no influence.

Knowing $b = \dfrac{\eta * r * v}{2 * P * A^2}$, the term $r * v$ can be calculated.

The volume of cake, deposited per volume of filtrate, named v, can be easily

calculated from: $L = \dfrac{v * V}{A}$ (m³/m³)

Knowing v, the penetration resistance r can be calculated from the known term $r * v$

Finally the porosity of the filter cake, ε can be determined by solving the Kozeny

equation $r = \dfrac{K * S_0{}^2 * (1 - \varepsilon)^2}{\varepsilon^3}$, assuming K = 5.

$\varepsilon^3 * r - K * S_0{}^2 * \varepsilon^2 + 2 * K * S_0{}^2 * \varepsilon - K * S_0{}^2 = 0$

$$A = K * S_0{}^2$$

$$r * \varepsilon^3 - A * \varepsilon^2 + 2 * A * \varepsilon - A = 0 \quad \text{and with a=r, b=-A, c=2A, d=-A}$$

$$a * \varepsilon^3 + b * \varepsilon^2 + c * \varepsilon + d = 0$$

Substituted by: $u = \varepsilon + \dfrac{b}{3a} = \varepsilon - \dfrac{A}{3 * r}$ leads to:

$$u^3 + p * u + q = 0$$

with $p = \dfrac{3 * a * c - b^2}{3 * a^2} = \dfrac{6 * r * A - A^2}{3 * r^2}$ and $q = \dfrac{2 * b^3}{27 * a^3} - \dfrac{b * c}{3 * a^2} + \dfrac{d}{a} = -\dfrac{2 * A^3}{27 * r^3} + \dfrac{2 * A^2}{3 * r^2} - \dfrac{A}{r}$

$$D_1 = \sqrt[3]{-\dfrac{q}{2} + \sqrt{\left(\dfrac{q}{2}\right)^2 + \left(\dfrac{p}{3}\right)^3}} \quad \text{and} \quad D_2 = \sqrt[3]{-\dfrac{q}{2} - \sqrt{\left(\dfrac{q}{2}\right)^2 + \left(\dfrac{p}{3}\right)^3}} \quad \text{and} \quad u_1 = D_1 + D_2$$

and ε from u.
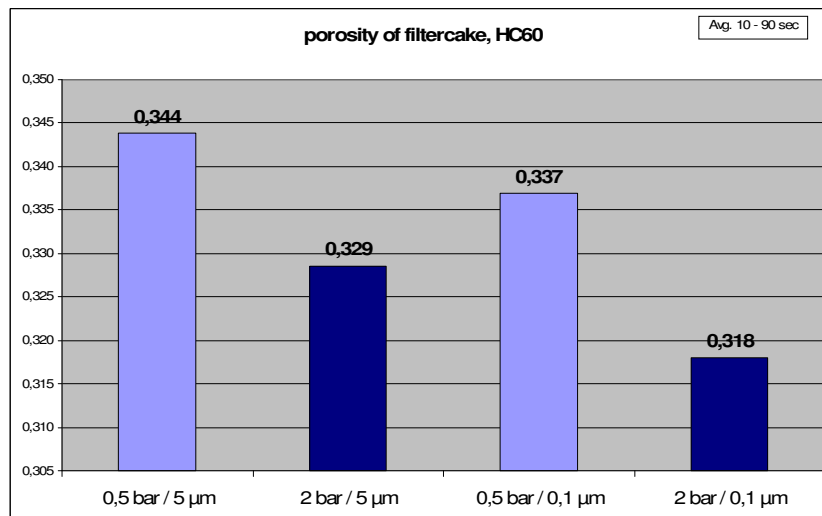
Pict. 10.3.21: Calculated porosity (%) of HC60 filter cake (x-axis: pressure / membrane pore diameter)

Pict. 10.3.21 shows that porosity of HC60 filter cake is mainly influenced by pressure level and particle size distribution in the filter cake. Pict. 10.3.22 shows the relatively broad particle size distribution (PSD) of HC60 which explains the drop of filter cake permeability by external pressure where fine particles are pressed into the path ways between coarse ones.
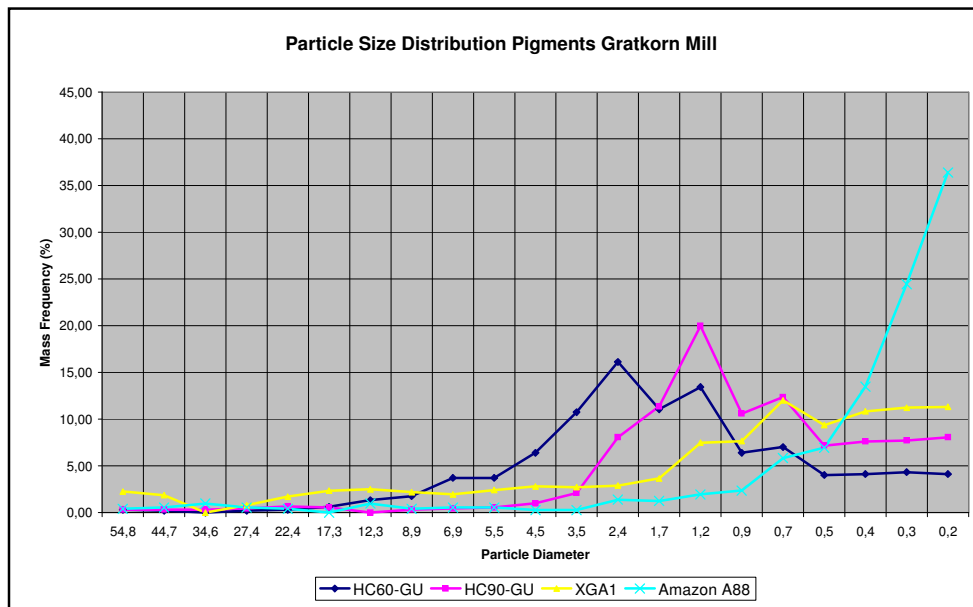
Pict. 10.3.22: Particle size distribution of different coating pigments (HC60: CaCO3 with 60% < 2 µm, HC90: CaCo3 with 90% < 2 µm, XGA1: CaCo3 with 99% < 2 µm, Amazon: Fine secondary clay)

Calculated porosity ε of filter cake from Hydrocarb 60 slurry is in the range of 30 – 40%, which is reasonable, compared to the porosity of a dry tablet of HC60, which is in the range of 20 – 30%.

The physical properties of the filter cake correspond to the coating / pigment slurry properties at the first critical concentration (FCC) where particles cannot be moved any more by outside mechanical forces.
When drying is continued after the FCC water is removed from immobilized coating and particles converge by high shrinkage forces due to evaporation of water until the second immobilization point (SCC) is reached, where no more movement of particles is possible.
The porosity at FCC must be somewhat higher than the dry tablet (data's see chapter "dense precoatings").

When coating colour is dewatered on a membrane a **filter cake** is formed on the membrane surface.

Darcy's law including the filter cake: $v = \dfrac{d(V/A)}{dt} = \dfrac{K_f * \Delta p_f}{\eta * h_f} = \dfrac{K_M * \Delta p_M}{\eta * h_M}$

K_f.....Darcy coefficient of filter cake

H_f.....thickness of filter cake at time t

K_M....Darcy coefficient of membrane (corresponds to Darcy coefficient of paper)

h_M.....thickness of membrane

Equ. 7-3-1: $v = \dfrac{d(V/A)}{dt} = \dfrac{\Delta p_f + \Delta p_M}{\eta * \left[\dfrac{h_f}{K_f} + \dfrac{h_M}{K_M}\right]}$

$\Delta p = \Delta p_f + \Delta p_M$

K_f can be calculated with:

$\left[\dfrac{h_f}{K_f} + \dfrac{h_M}{K_M}\right] = \dfrac{\Delta p}{\eta * \dfrac{d(V/A)}{dt}}$

$\dfrac{h_f}{K_f} = \dfrac{\Delta p}{\eta * \dfrac{d(V/A)}{dt}} - \dfrac{h_M}{K_M}$

$K_f = \dfrac{h_f}{\dfrac{\Delta p}{\eta * \dfrac{d(V/A)}{dt}} - \dfrac{h_M}{K_M}}$

At the Abo-GWR dewatering cell it's simple to measure:

- d(V/A) = volume of water in filtrate per m²
- dt = time difference between two readings
- Δp = applied pressure
- η = Viscosity of the drained water (has to be determined in a separate experiment)
- h_M = Thickness of membrane, measured in the lab
- K_M = Darcy coefficient of membrane, can be determined by air porosity

By applying Darcy's law, K_f can be easily calculated when h_f is known from mass balance.
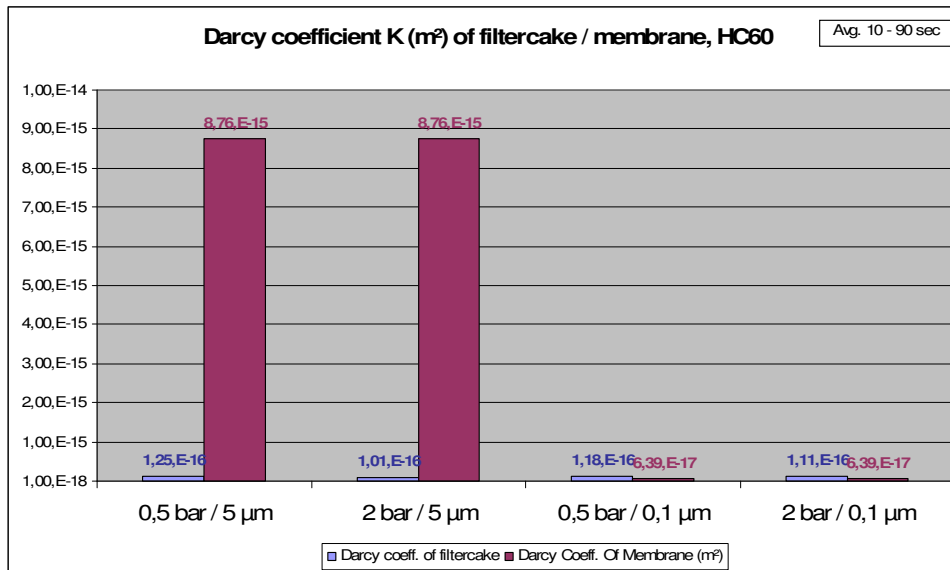
Pict. 10.3.23: Comparison of Darcy coefficients of HC60-filter cake for different membrane types (5 µm / 0,1 µm pore diameter)
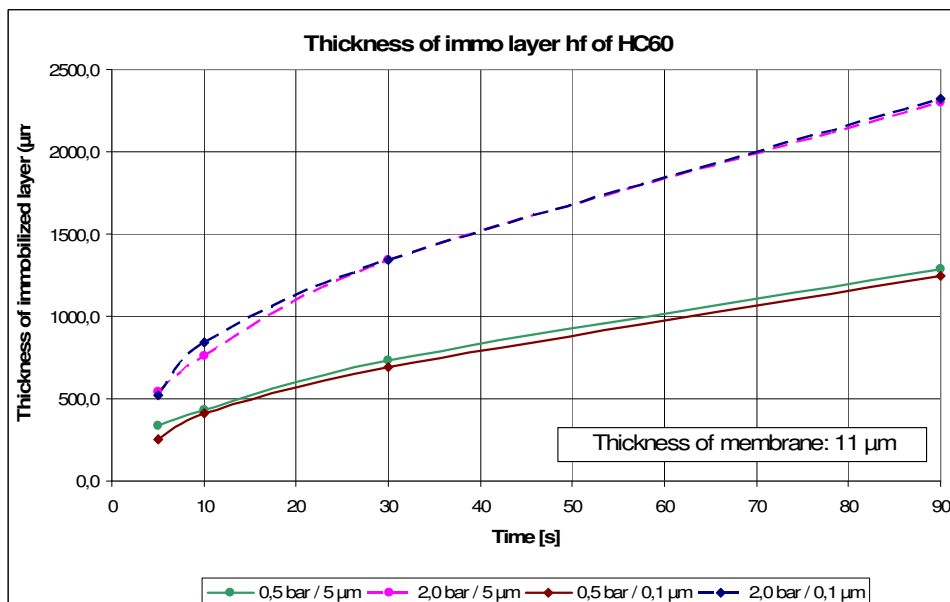
Pict. 10.3.24: Comparison of immobilized layer thickness with membrane thickness

As thickness of test membranes is one or two magnitudes lower than filter cake thickness, membranes are of minor importance for permeability experiments with Abo-GWR instrument. The factor h_m/K_m is much lower then h_f/K_f (pict. 10.3.23 – 25).

Page 521
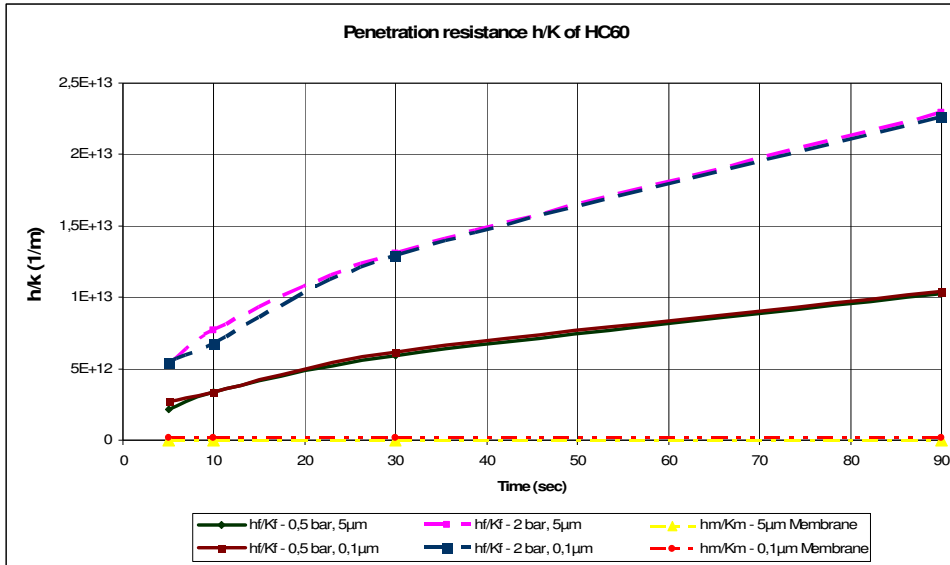
Pict. 10.3.25: Penetration resistance term h/K of HC60 slurry – comparison membrane (1,3 – 1,8 x 10-11) vs. filter cake

From Darcy's law the term **h/K** can be used to describe the overall **penetration resistance** of a filter cake (pict. 10.3.26).
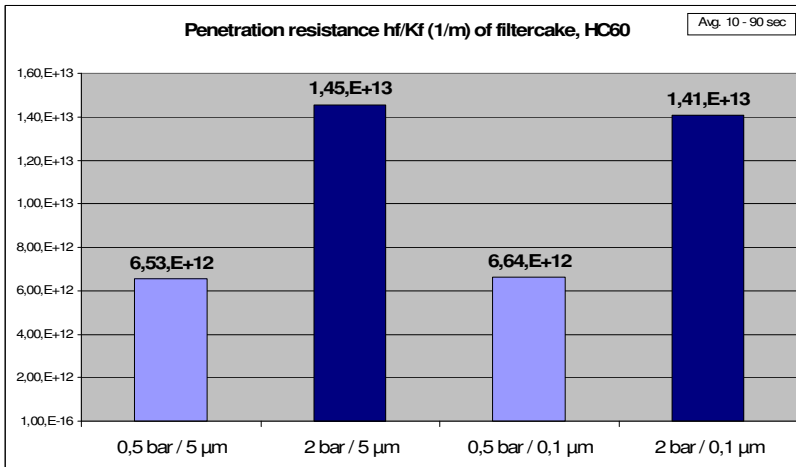
Pict. 10.3.26: Penetration resistance h_f/K_f of HC60 (x-axis: pressure / membrane pore diameter)

Darcy coefficient of filter cake K_f can be calculated from filter cake equation a shown in pict. 10.3.27.
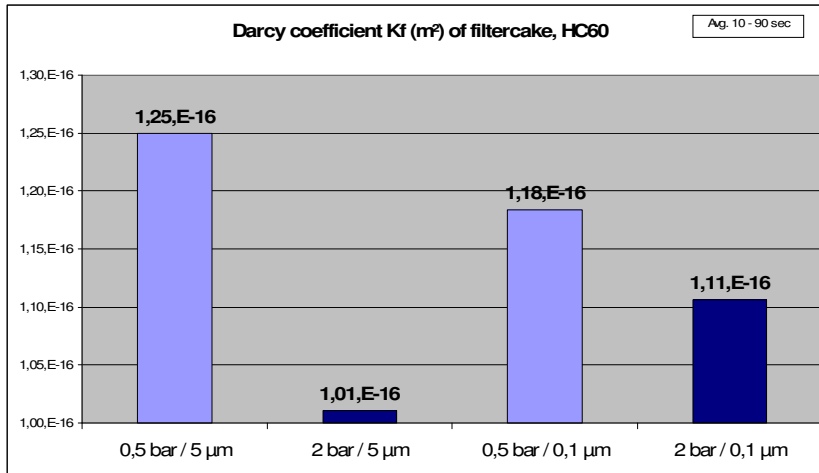
Pict. 10.3.27: Darcy coefficient of filter cake of HC60 slurry

Comparing the calculated Darcy coefficients leads the same result as achieved with calculated porosity of filter cake: Higher pressure leads to lower Darcy coefficients (denser filter cake) of HC60 slurry.

Pict. 10.3.25 shows that thickness of immobilized layer gets thicker with rising pressure.

Both terms h_f and K_f increase the penetration resistance term h_f/K_f at higher level of external pressure.

As the membrane type has a minor influence on filter cake forming the difference in penetration resistance h_f/K_f between the two membrane types is mainly caused by the different Darcy coefficient of immobilized layers.

As pores of coarse membrane (5 µm) are in the range of pigment particles (d = 0,1 – 10 µm), more coarse pigment particles get lost compared to 0,1 µm membrane which provides almost 100% holdout for pigment particles.

This can be detected also by pigment content in the filtrate as shown in pict. 10.3.28.
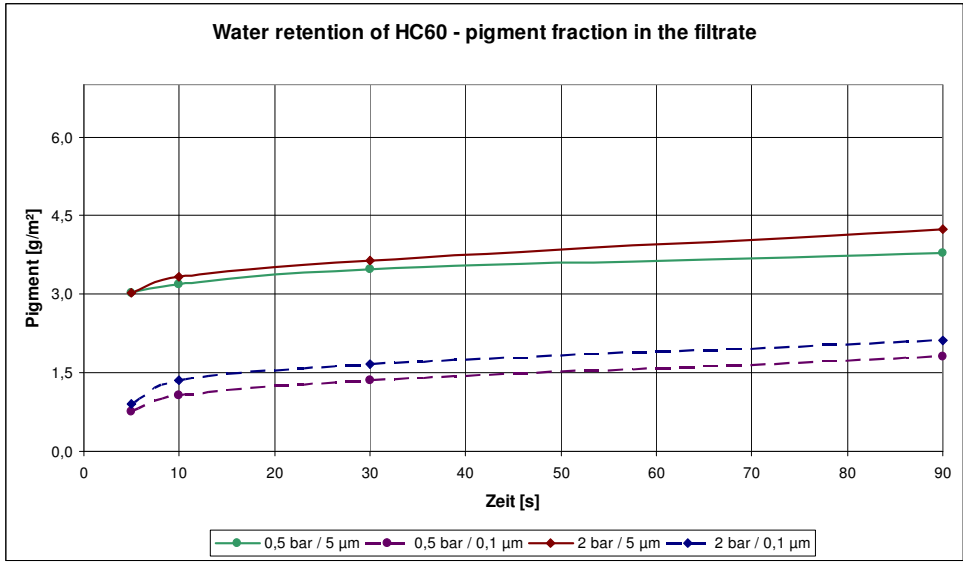
Pict. 10.3.28: Pigment fraction in the filtrate

Water retention experiments can be modelled by using the common filtration equation:

Equ. 10-3-3: $\dfrac{V}{A} = \sqrt{\dfrac{2 * \phi_1 * k(\phi) * \Delta p * \Delta t}{\eta}}$, with $k(\Phi)=(1-\Phi)^3/(K''*S^2*\Phi^2)$ and

$\Phi_1=(\Phi-\Phi_o)/\Phi_o$

Porosity at immobilization solids Φ and porosity of the original slurry Φ_0 must be know as well as specific surface area S and viscosity of liquid phase η.

When these data's were put into the filter cake equation 10-2-10 the experimental results with Abo-GWR unit could be confirmed as shown in pict. 10.3.29.
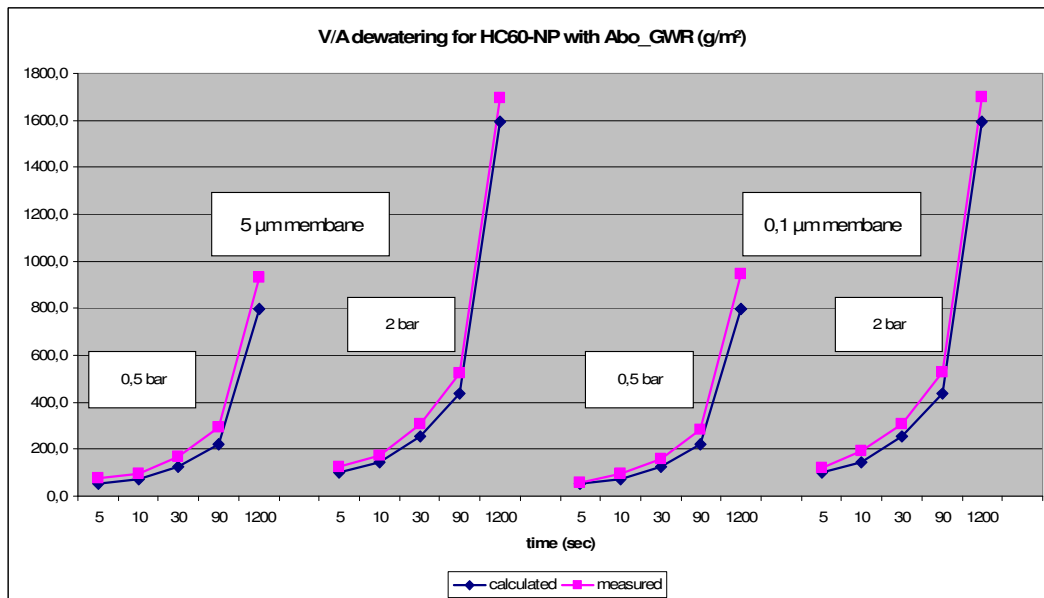
Pict. 10.3.29: Modelling the dewatering experiments with HC60 of Abo-GWR cell

All commercially used pigments in Gratkorn were compared in their water retention with the Abo-GWR method (pict. 10.3.30).

HC60 is a coarse GCC, HC90 a medium fine GCC, CC60 a GCC with steep PSD, HC95 and XGA1 are fine GCC's and Amazon is a fine secondary clay (pict. 10.3.22).
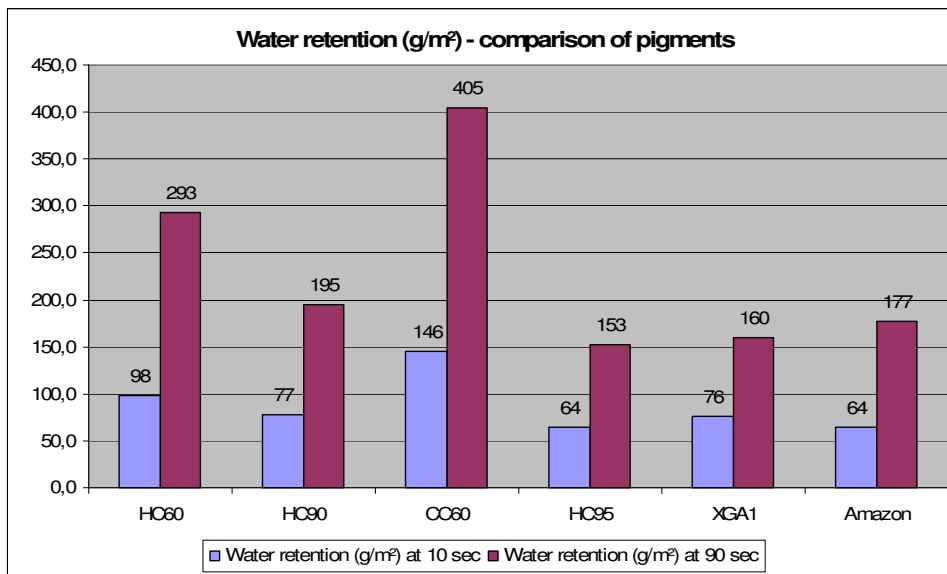
Pict. 10.3.30: Water retention of carbonates and clay

Water retention of pigment slurries improves with lower mean particle size and broader particle size distribution.

When immobilization solids are known from measurements using the BASF method and the Paar-Physica viscosimeter (pict. 10.3.31), the thickness of the immobilized layer can be calculated (pict. 10.3.32 – 10.3.33).
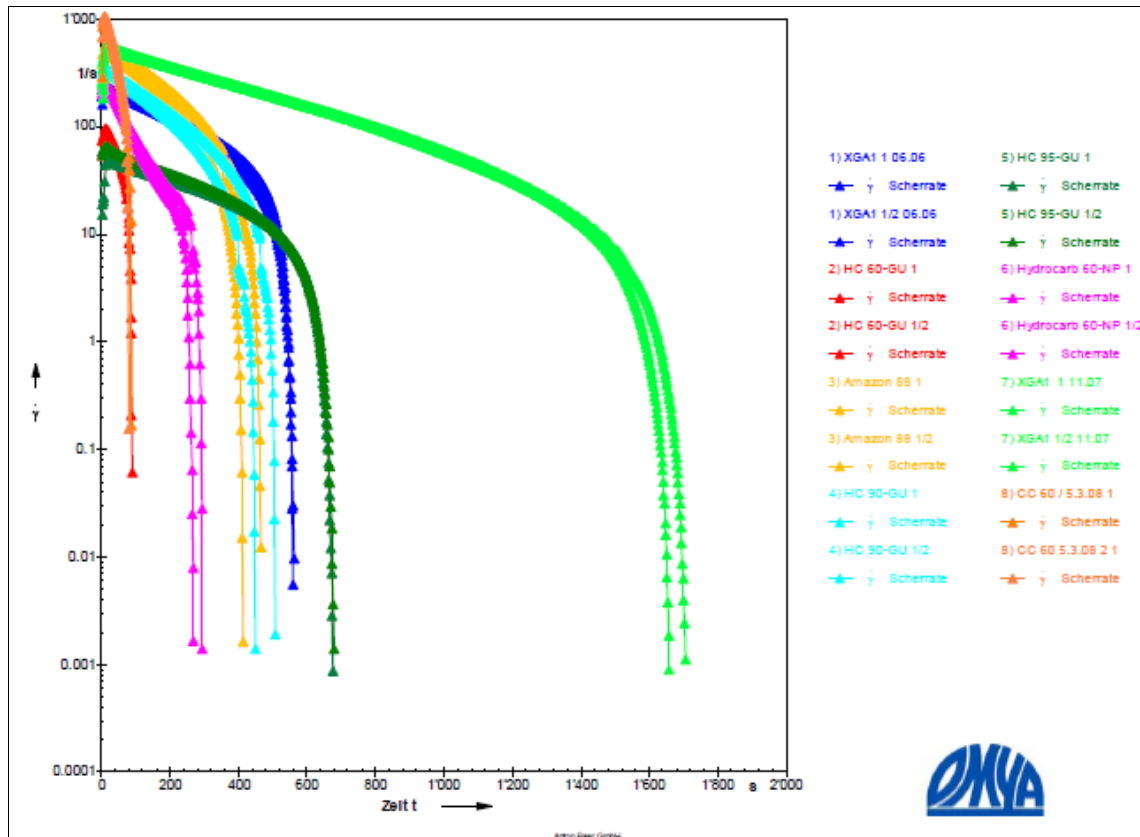
Farbmuster	FG / CC [%]	Immobilisierungszelle [Zeit / sek.]	Mittelwert sek.	FG nach I-Z [%]	Mittelwert %
1) XGA1/ 06.2006	71.9	560 / 564	562	80.5 / 80.4	80.4
2) HC 60-GU	77.5	95 / 95	95	85.3 / 85.4	85.3
3) Amazon 88	72.8	420 / 480	450	78.7 / 78.4	78.5
4) HC 90-GU	78.0	470 / 514	492	85.6 / 85.5	85.5
5) HC 95-GU	78.2	685 / 685	685	83.6 / 83.4	83.5
6) HC 60-NP	77.7	300 / 280	290	86.5 / 86.4	86.4
7) XGA1 /11.2007	72.4	1660 / 1720	1690	81.6 / 81.2	81.4
8) CC 60-GU / 3.08	71.3	90 / 94	92	82.1 / 82.3	82.2

Pict. 10.3.31: Immobilization time and solids for different carbonates
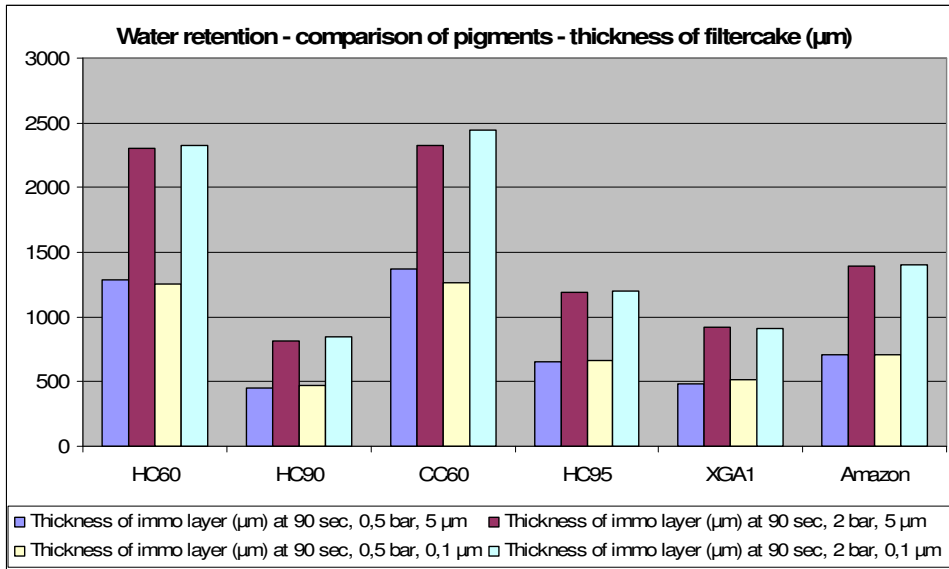
Pict. 10.3.32: Thickness of immobilized filter cake
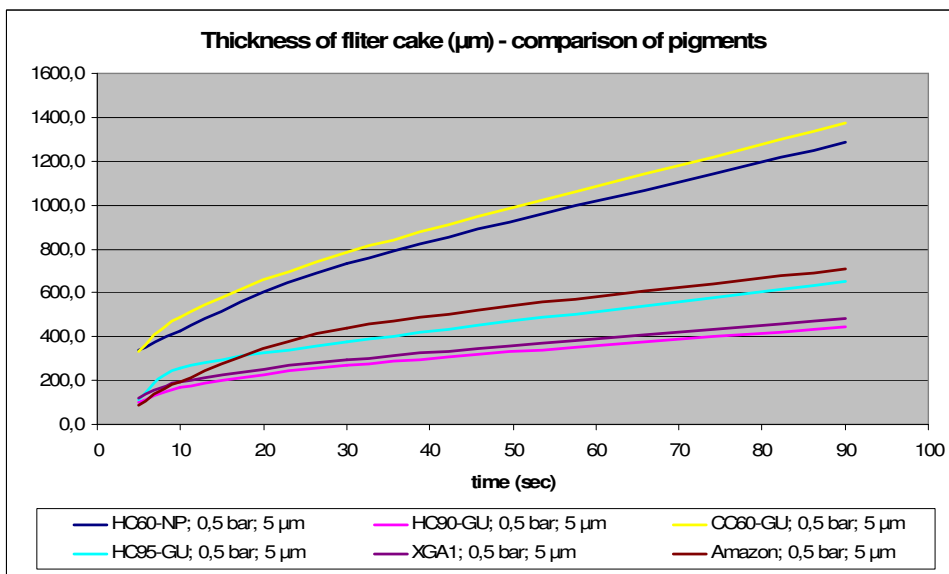
Pict. 10.3.33: Thickness of immobilized filter cake with 0,5 bar pressure and 5 µm membrane
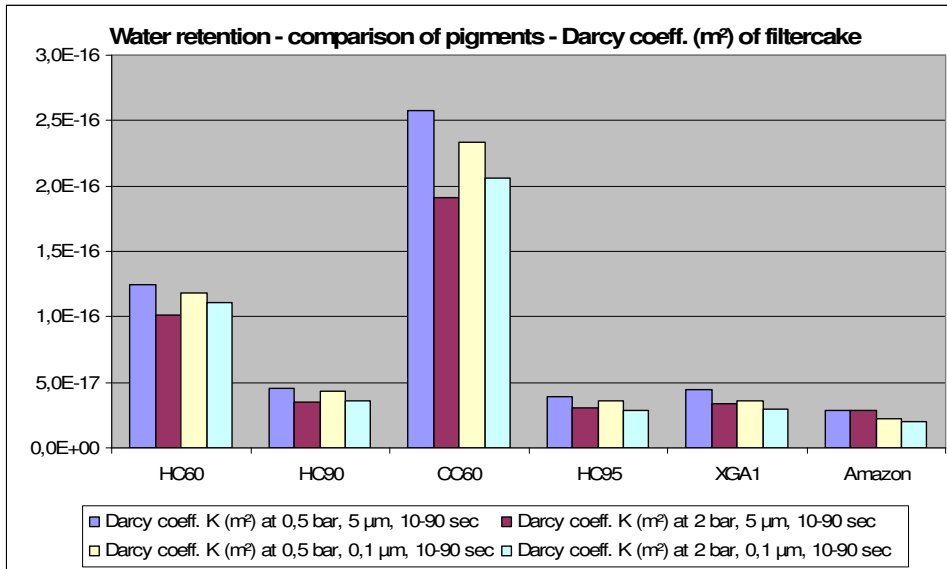
Pict. 10.3.34: Calculated Darcy coefficient of the filter cake
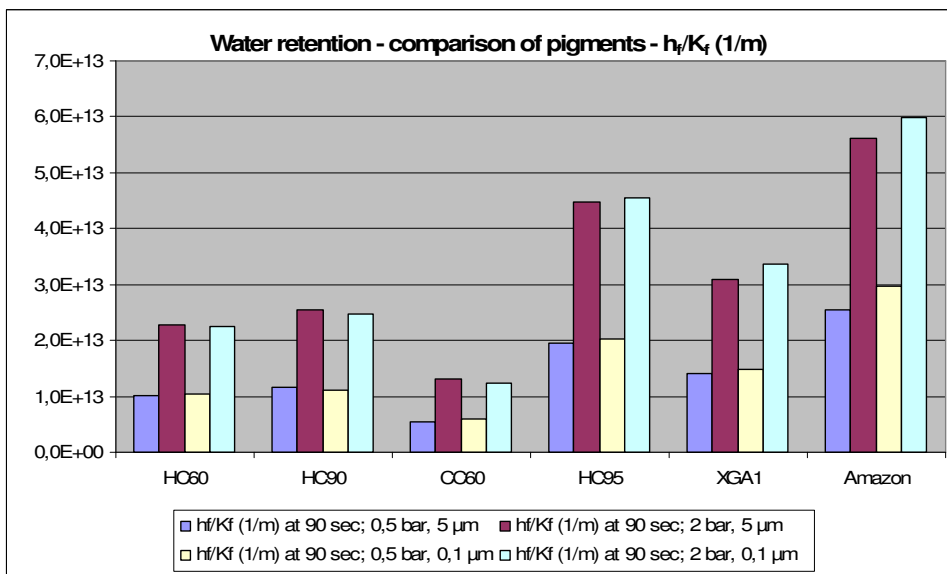
Pict. 10.3.35: Penetration resistance h_f/K_f

Pict. 10.3.34 and 10.3.35 show the calculated Darcy coefficient and the penetration resistance factor h_f/K_f. Fine pigments like the GCC's XGA1 and HC95 or Amazone clay are lower in immobilization solids as pigment packing gets more effectively with increasing solids. As gap between original solids and immobilization solids is lower, increase of immobilized layer thickness will be faster for these pigments.
Thickness of immobilized layer of coarse and steep carbonates HC60 and CC60 is high due to low water retention and fast dewatering.

Page 529

The steep particle size distribution of the Covercarb 60 (CC60) leads to the lowest packing density and highest permeability K_f of the immobilized layer. Therefore water retention of CC60 is worst.

Fine carbonates and ultrafine clays show the lowest Darcy coefficient of the filter cake.

As measured viscosity of liquid phase is almost same for all pigments (appr. 1,5 mPas) and thickness of membrane is almost zero, the penetration resistance can be described by h_f/K_f.

Darcy: $\dfrac{dV}{A} = \dfrac{K}{\eta * h_f} * \Delta p * dt$

Comparing the penetration resistance constant h_f/K_f, the superior water retention of the fine pigments is clearly visible.

For these fine pigments water retention improves with decreasing pore radius of the substrate: The finer the membrane the more fine pigments are retained in the immobilized layer and the lower the Darcy coefficient of the filter cake gets.

This is important for middle coatings: When applied on precoating with high pore radius and high permeability, fines of the middle coating get lost into the substrate and permeability of the middle coating layer increases – the "isolating" effect of the coating layer against base paper non-uniformities is less pronounced and mottling will be worse.

Therefore fine pigments in top coating colours can develop their gloss potential only when coated on dense pre-coated substrates.
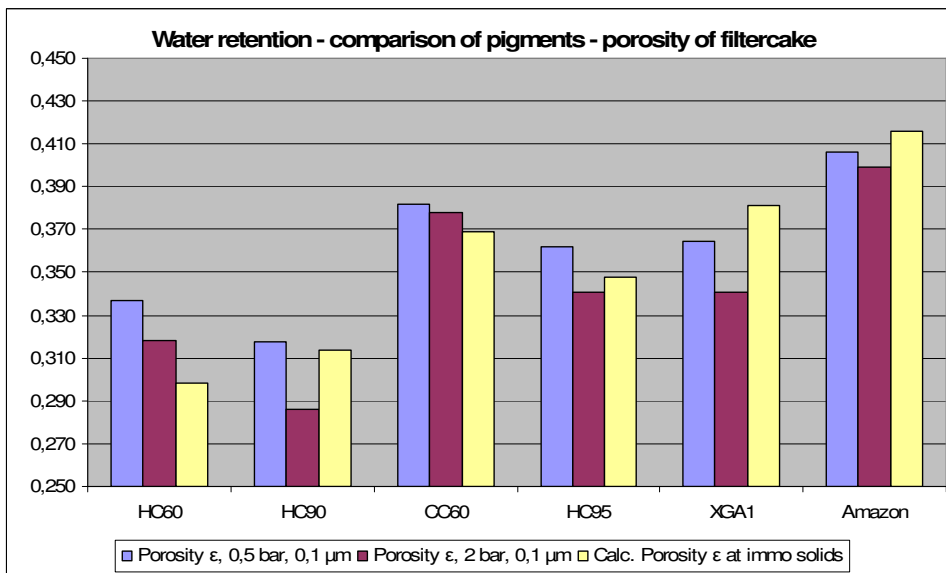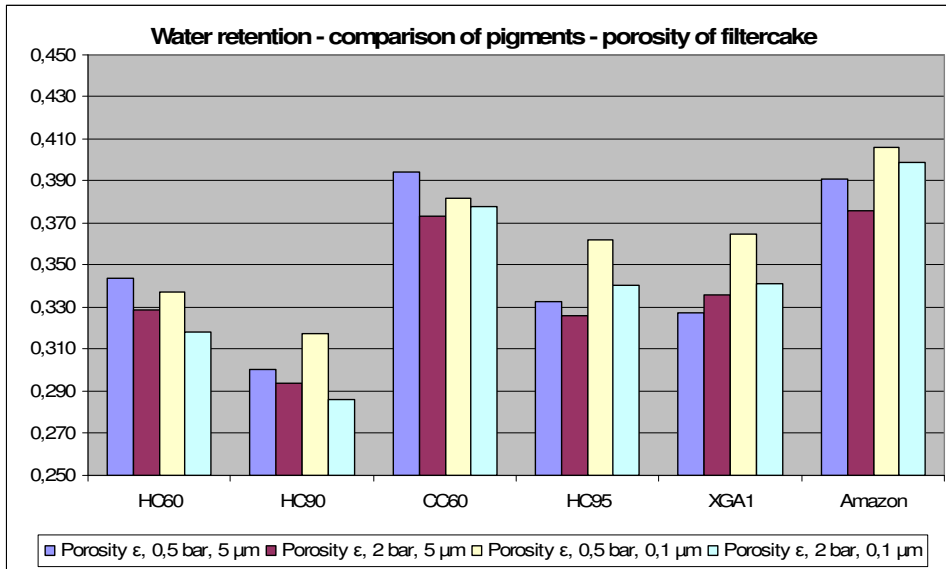
Pict. 10.3.36: Calculated porosity of filter cake

Calculating the porosity of filter cake with previous equations as shown in pict. 10.3.37 leads to results close to the theoretical porosity of the filter cake, which can be calculated from the immobilization solids.

$V_{total} = V_s + V_l$, with V_S the volume of solids and V_l the liquid volume in the slurry.

$$V_s = \frac{m_{total} * c_s}{\rho_s} \quad \text{and} \quad V_l = \frac{m_{total} * (1 - c_s)}{\rho_l}$$

$$\phi_s = \frac{V_s}{V_{total}} \quad \text{and} \quad \varepsilon = \phi_l = 1 - \phi_s$$

10.4 Water retention measurements of precoating formulations

In 2007 - 2008 a lab study with different precoating formulations was done by using the standard water retention method with the Abo-GWR instrument. Again the standard test procedure was expanded by lowering the time of penetration, using a finer membrane and a higher pressure level.

From filter cake theory, the following measures can be taken to improve mottling by improving the water retention of the first pre-coating (at PM11 applied by film press).

- Lower the porosity of filter cake (ε)
- Increase thickness of filter cake ($h_f = L$)
- Rise viscosity of liquid phase in filter cake (η)

10.4.1 Comparison 1: Denser filter cake with finer pigments:

The coarse precoating pigment Hydrocarb 60 was partly replaced by Hydrocarb 90 and Hydrocarb 95 which are lower in mean particle diameter (pict. 10.4.1).
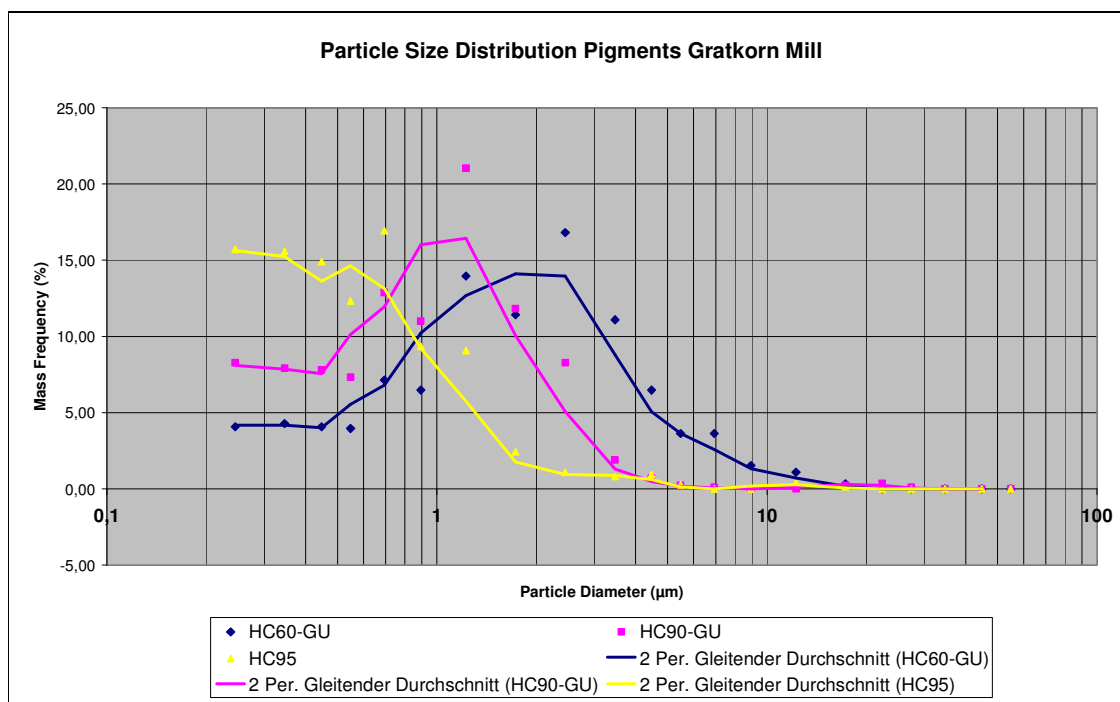
Pict. 10.4.1: Particle size distributions (PSD) of different carbonates.
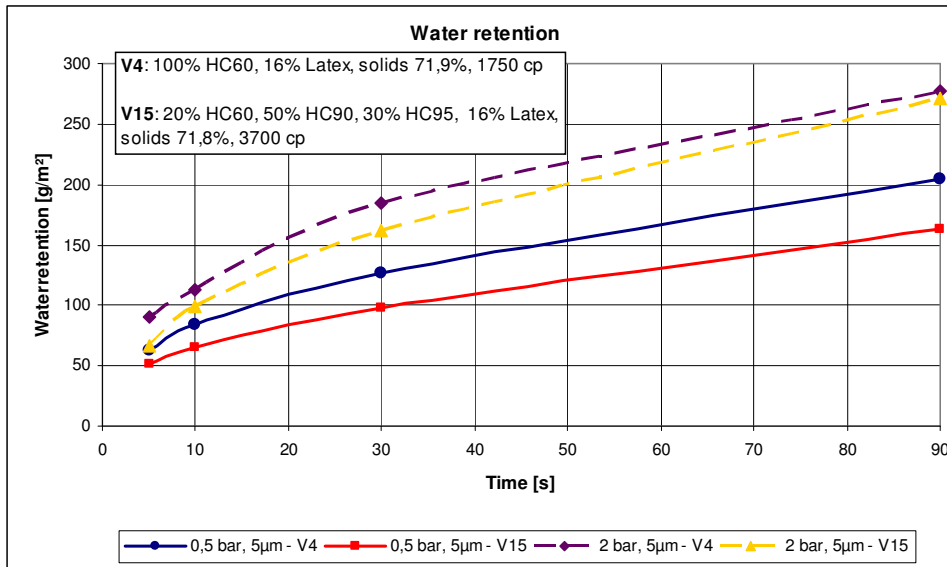
Pict. 10.4.2: Water retention of different Pigment mixtures

A clear advantage of fine pigment mixture against coarse HC60 can be seen in water retention (pict.10.4.2).
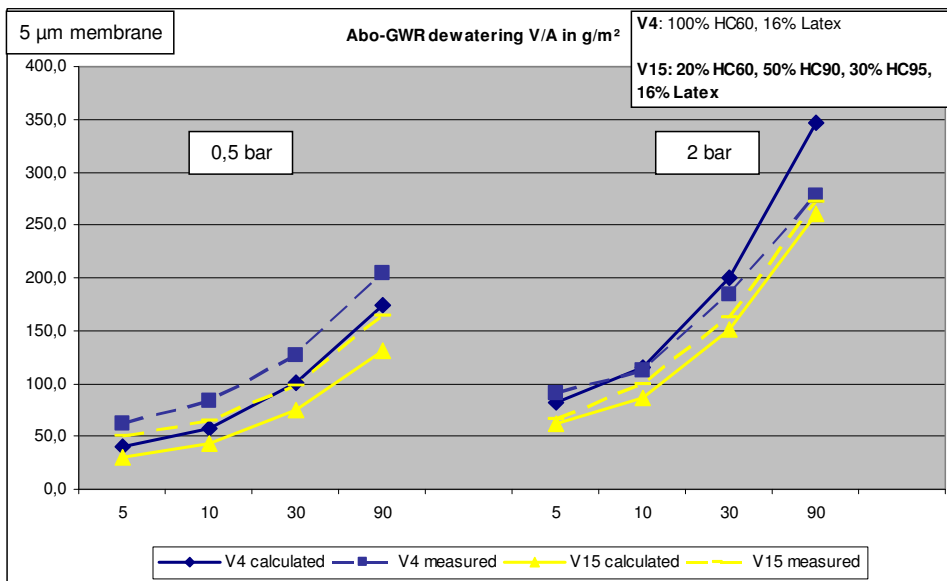
Pict. 10.4.3: Modelling the water retention experiment

Inserting the calculated thickness and permeability into the Darcy equation leads to a calculated amount of penetrated water at any time of the Abo-GWR experiment. Pict. 10.4.3 shows that this way of modelling the dewatering experiment fitted quite well to the measured data's with this instrument.
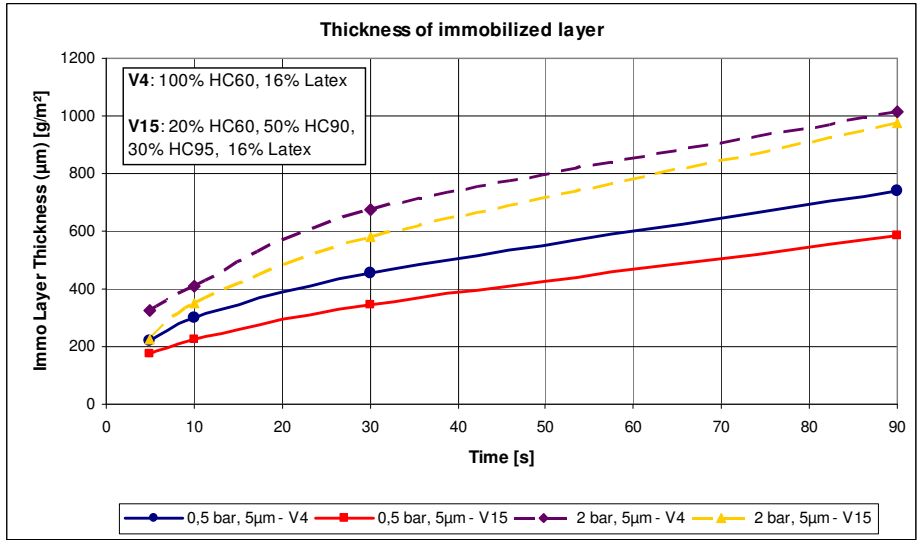
Pict. 10.4.4: Immobilized layer thickness - pigment comparison (immobilized solids 82% for both formulations)

Pict. 10.4.4 shows that a somewhat higher thickness of immobilized layer was calculated for the coating with coarse and fine carbonate mixture than for the coating based on pure coarse carbonate.
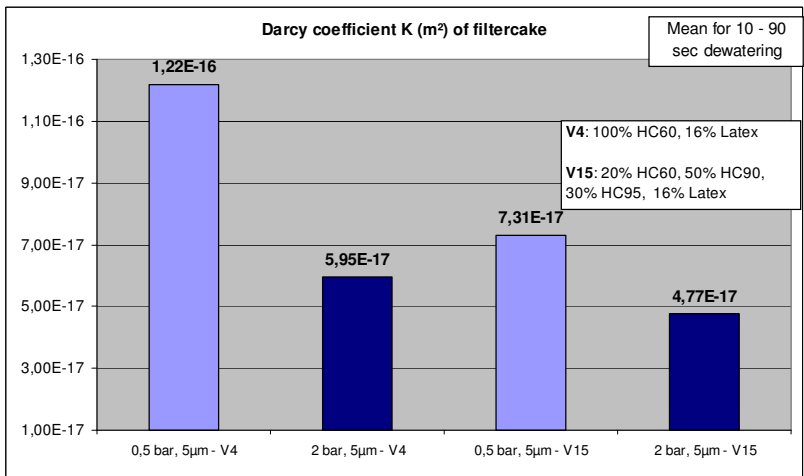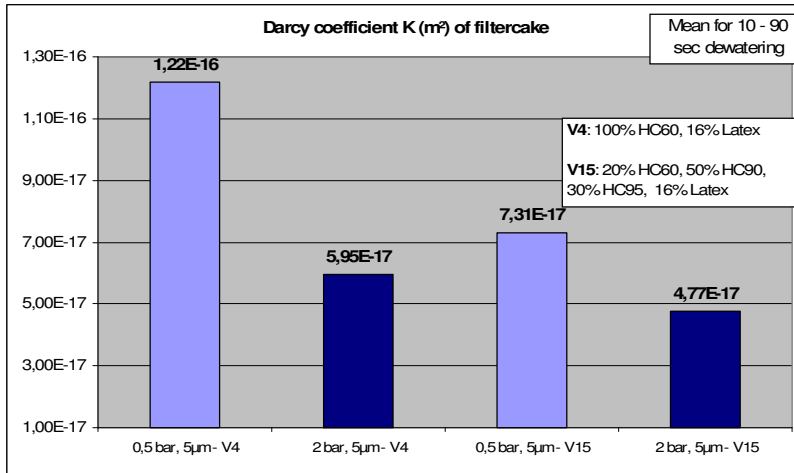
Pict. 10.4.5: Calculated Darcy coefficient - pigment comparison (viscosity of liquid phase: 3 mPas for both coatings)
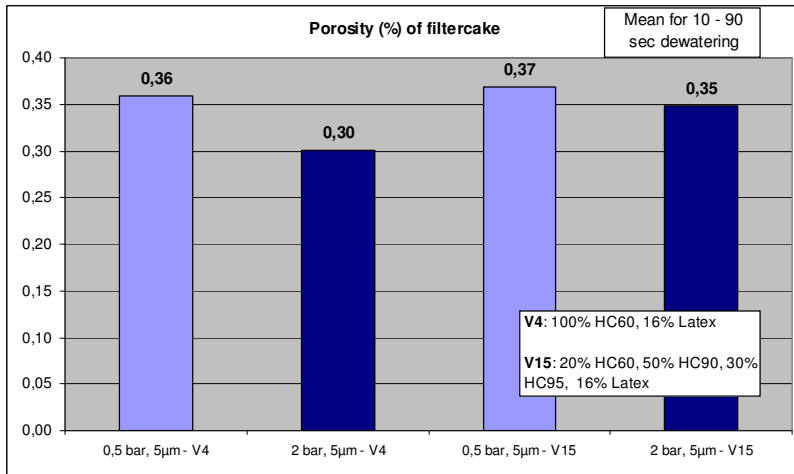
Pict. 10.4.6: Porosity of filter cake

Pict. 10.4.5 and 10.4.6 show that the improved water retention of formulation V15 containing finer pigments was caused by lower Darcy coefficient of its filter cake. The fine pigment particles from HC90 and HC95 block the path way of the liquid through the pores of the coarse HC60 matrix.
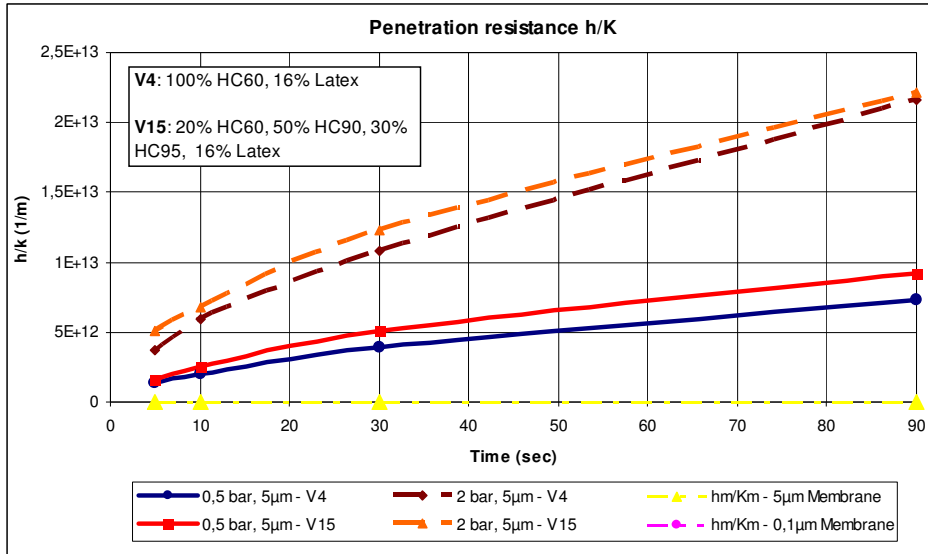
Pict. 10.4.7: Calculated penetration resistance h_f/K_f - pigment comparison
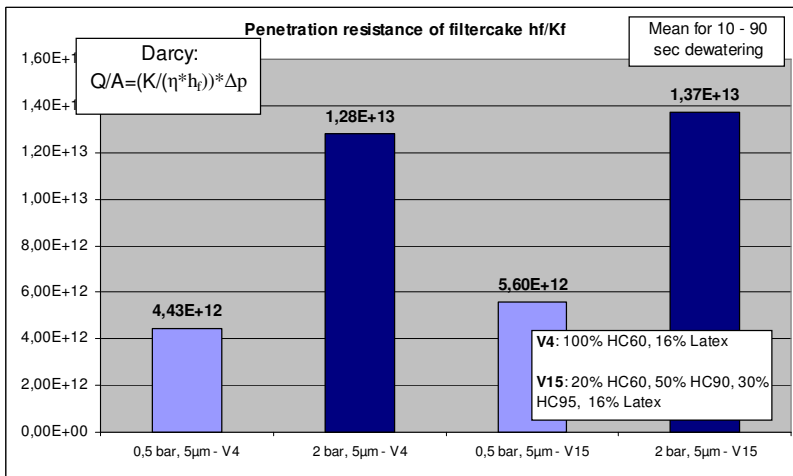
Pict. 10.4.8: Calculated penetration resistance h_f/K_f - pigment comparison

To predict penetration of water and soluble substances through immobilized filter cake of the corresponding coating colour a penetration resistance coefficient h_f/K_f can be set up.

The thicker the filter cake and the lower its Darcy coefficient, the higher the penetration resistance of the filter cake and the better the water retention of the coating colour is. Broad PSD of V15 with a high amount of fines leads to a low filter cake permeability as pigment particle packing is high and flow path of liquid is blocked by fines (pict. 10.4.7 -10.4.8).

Page 536

10.4.2 Comparison 2: Improving water retention by finer latex particles:

A special styrene / butadiene based varnish "Senolith" with broad PSD and a high amount of ultra fine particles (pict. 10.4.9) was taken instead of standard latex into the precoating formulation to lower porosity of filter cake and to achieve the same improvement in water retention as with fine pigments. Specific surface area was 40 m²/g for standard latex and 200 m²/g for fine varnish "Senolith".
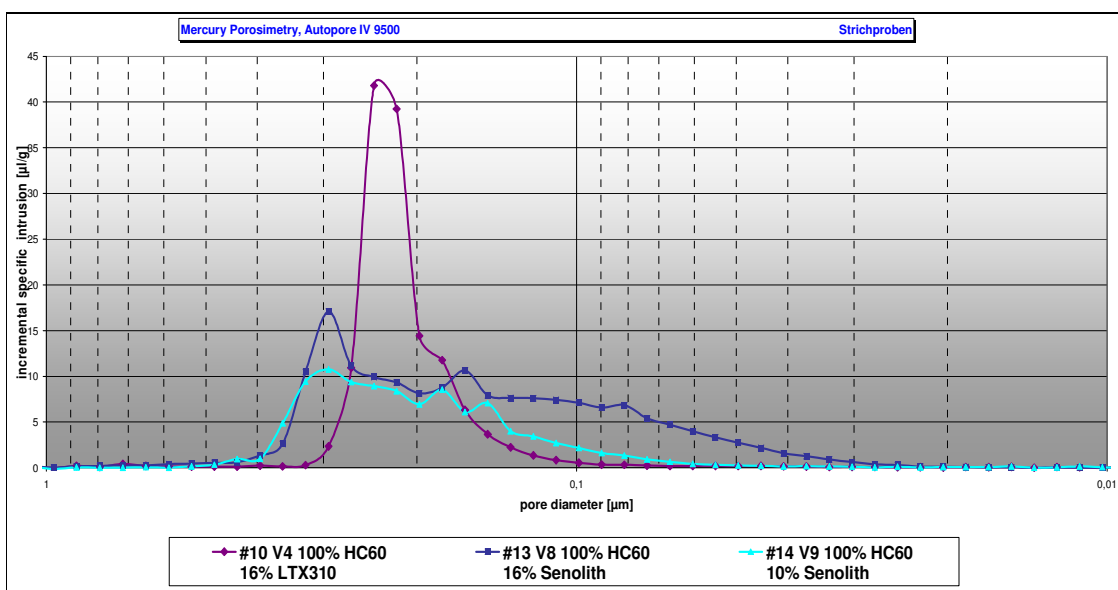
Pict. 10.4.9: Particle size distribution of precoating layer with varnish Senolith from Hg-porosity of coating tablets
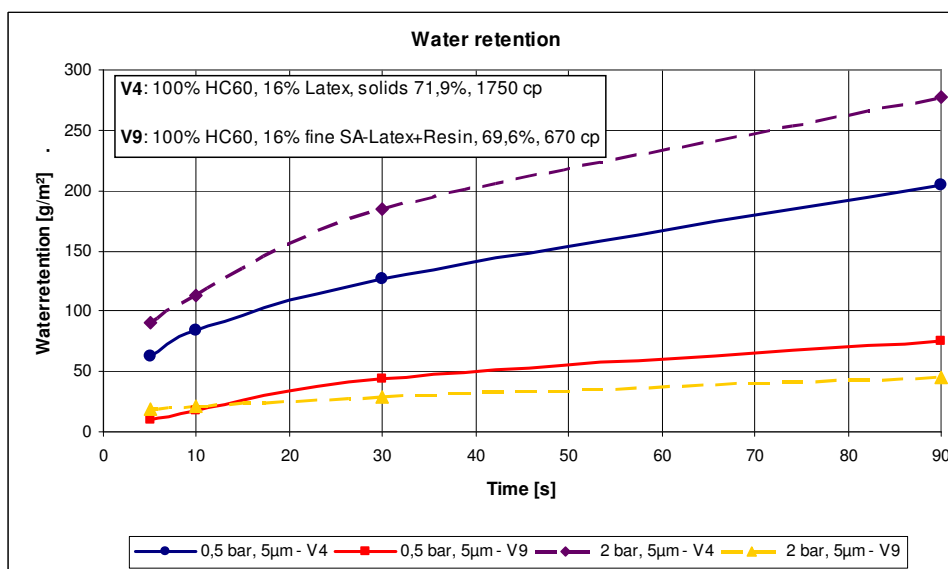
Pict. 10.4.10: Water retention comparison of fine Senolith with conventional latex

A big improvement of water retention was achieved with this special varnish when compared to the previous experiments with fine carbonates (pict. 10.4.10).
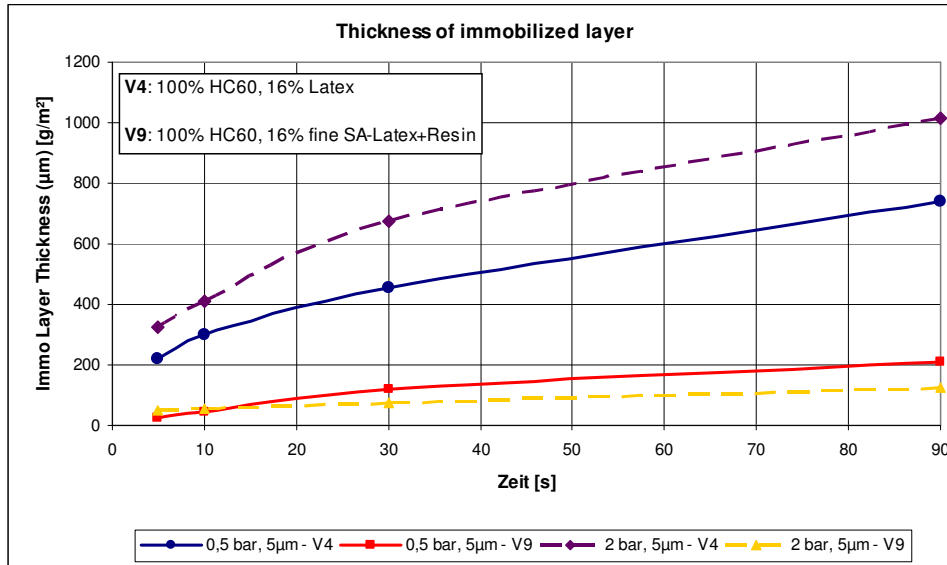
Pict. 10.4.11: Immobilized layer thickness (immobilized solids 80% for V4 and V9)
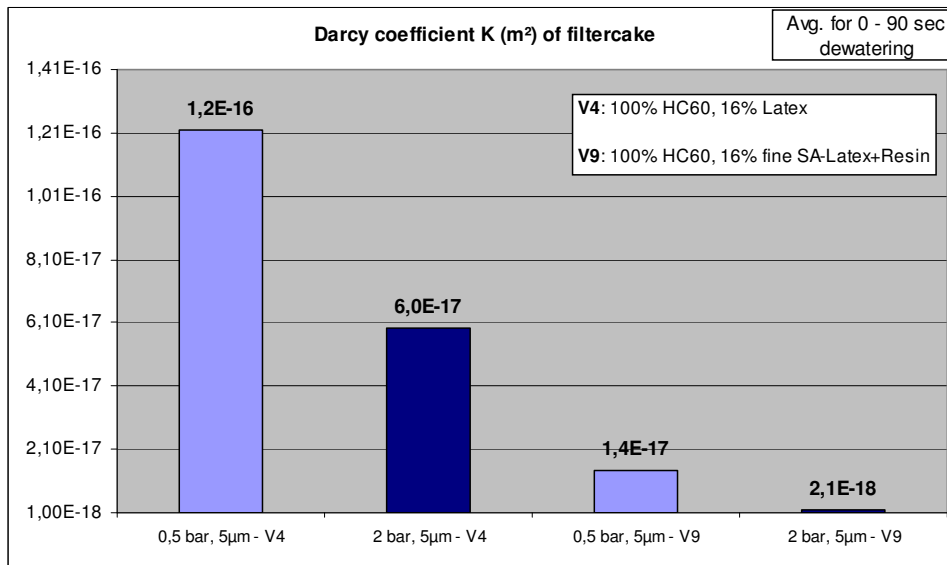
Pict. 10.4.12: Calculated Darcy coefficient (viscosity 3 mPas for V4 and 5 mPas for V9)

Thickness of immobilized layer increases much slower with fine Senolith as Darcy coefficient of this layer is much lower than for the standard latex (pict. 10.4.11 – 12).
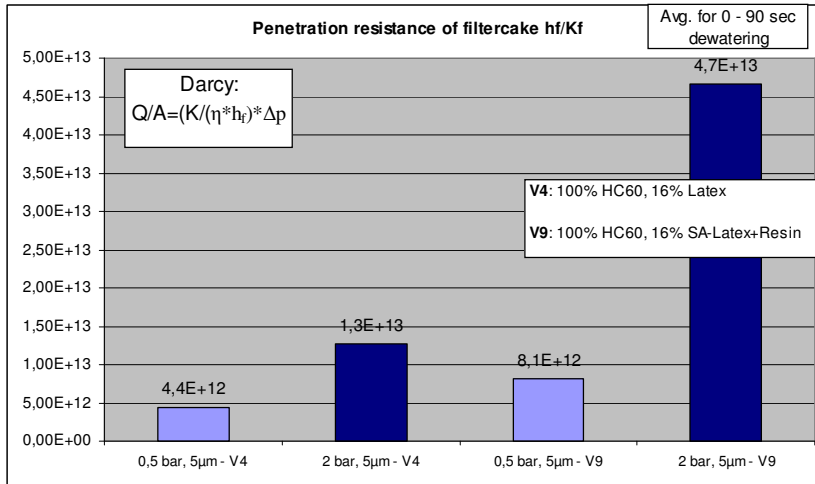
Pict. 10.4.13: Calculated penetration resistance h_f/K_f – latex comparison

Although filter cake thickness is much lower for fine latex based coating, penetration resistance h_f/K_f is higher especially at high pressure when compaction of filter cake is more pronounced and more fine particles are pressed through the pigment matrix (pict. 10.4.13).

These experiments show how important it is to measure water retention of coating colours under different pressure levels. At high speed coaters the pressure under the blade is in the range of 25 bar and therefore compaction of filter cake, which is built up between application and blade, is much higher than in lab water retention cells.

The membrane should be adapted to the investigated substrate – 5 µm corresponds to a typical base paper and 0,1 µm to a pre-coated paper (see pict. 9.2.7).

10.4.3 Comparison 3: Starch instead of latex – increasing viscosity of liquid phase

Starch is well known for improving coating colour water retention. It increases the water phase viscosity with its long molecules like associative thickeners. The higher the molecular weight of the starch solution the higher the liquid phase viscosity.
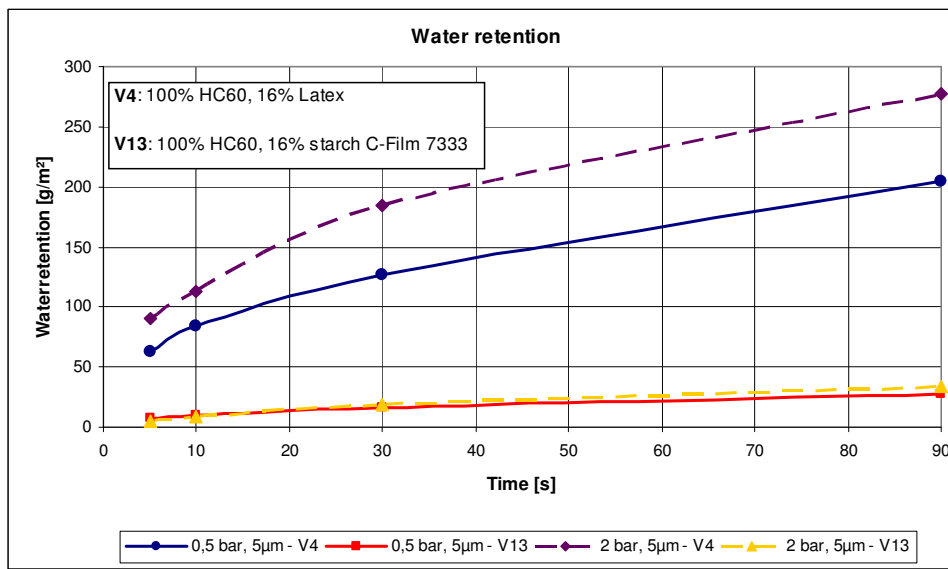
Pict. 10.4.14: Water retention – starch vs. latex
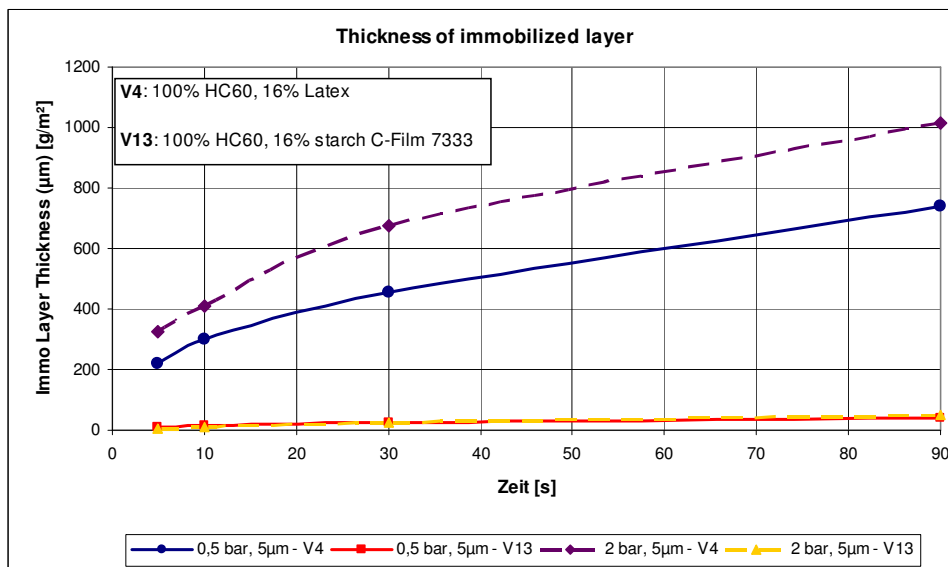
Pict. 10.4.15: Immobilized layer thickness (immobilized solids 80% for V13 and 82% for V4)
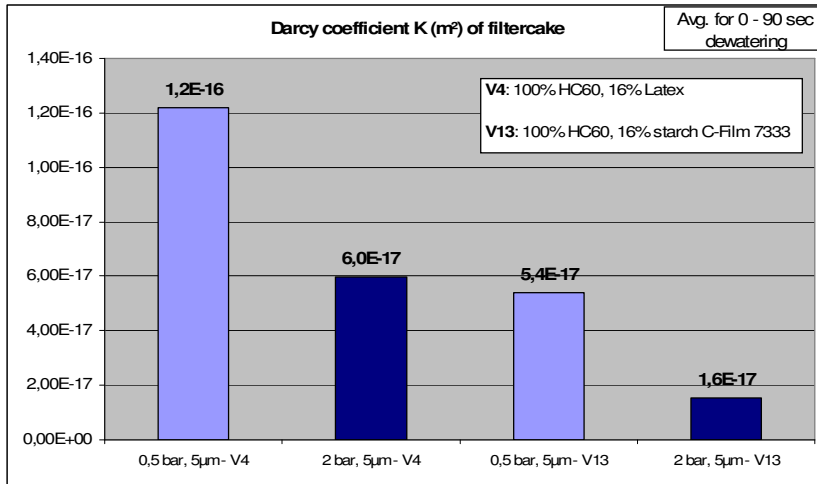
Pict. 10.4.16: Calculated Darcy coefficient (viscosity 3 mPas for V4 and 200 mPas for V13)
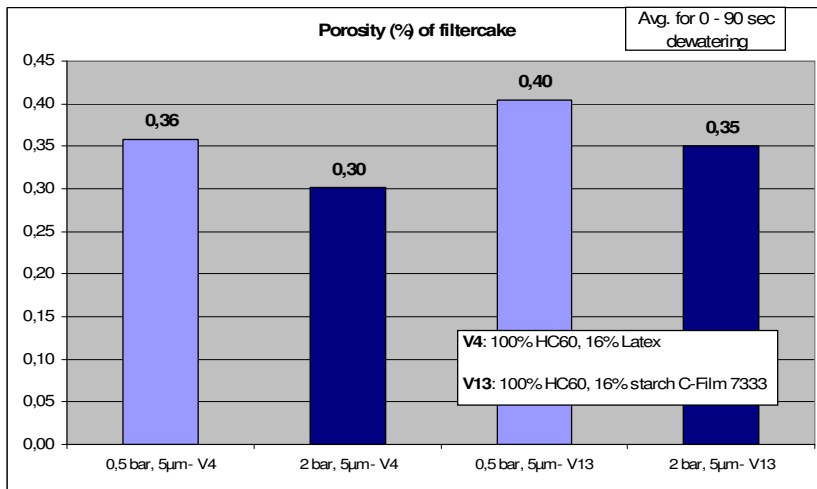
Pict. 10.4.17: Porosity of filter cake

Pict. 10.4. 14 shows the advantage of starch based precoating in water retention. Darcy coefficient of starch based coating colour is clearly lower (pict. 10.4.15 – 16) than that of the latex containing colour.

Porosity of starched based filter cakes is higher than that of latex based coatings due to higher viscosity of the coating colour and filter cake (pict. 10.4.17). Higher viscous filter cakes are most often more porous as the viscosity builds structure in coatings.

Caisa M. Andersson and Lars Järnström (L1.54) measured the penetration of starch and hydrophobic sizing agent in surface sizing into porous substrates.

Salt was used to flocculate a cationic starch and a cationic hydrophobic sizing agent. The holdout of this surface sizing liquid improved.

For anionic starches the effect was the opposite. Anionic starch and cationic hydrophobic sizing agent form flocs and this flocculation is inhibited by salt. Penetration increases.

With starch instead of latex a much thinner filter cake is formed during dewatering although the immobilization solids is 2% lower. But viscosity of liquid phase in this filter cake is much higher than for latex based coatings which slows down dewatering through the filter cake.
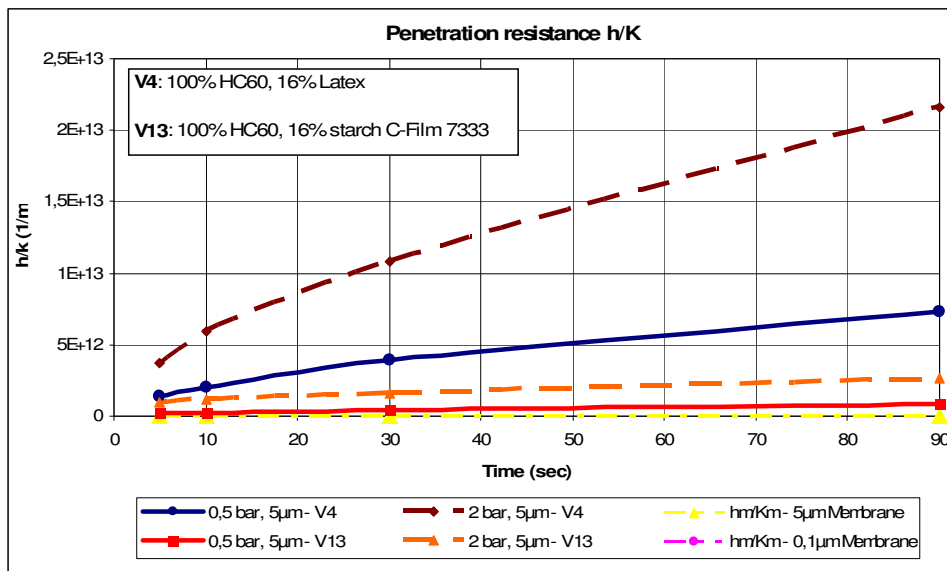
Pict. 10.4.18: Calculated penetration resistance h_f/K_f – starch vs. latex
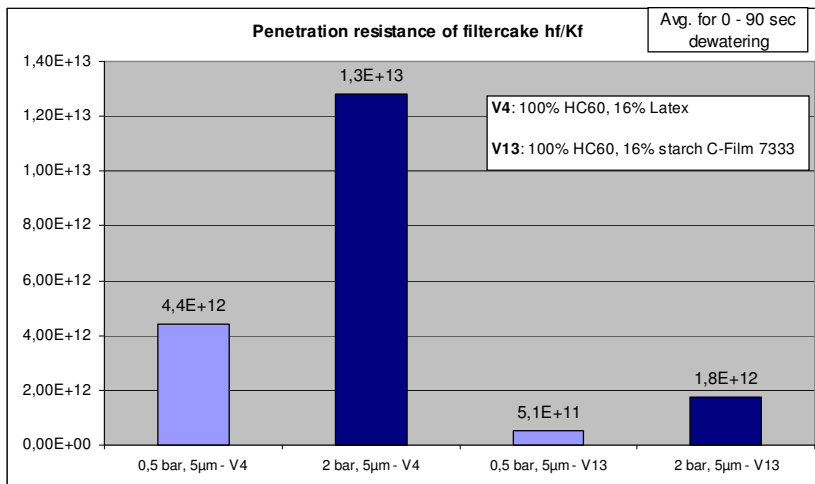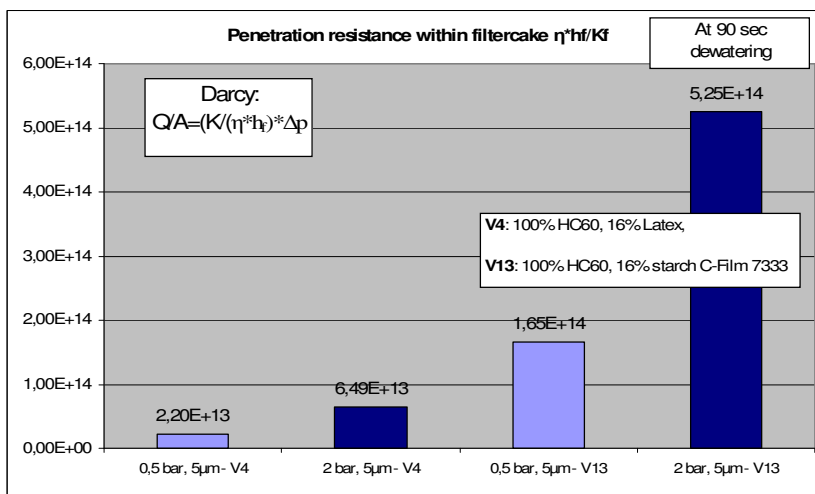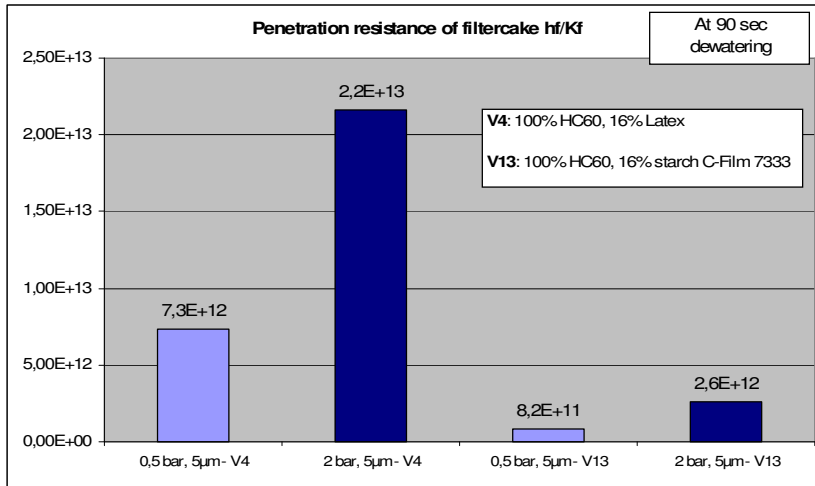
Pict. 10.4.19: Calculated penetration resistance h_f/K_f – starch vs. latex

Due to higher liquid phase viscosity the overall penetration resistance factor $\dfrac{K}{\eta * h_f}$ is

higher for the starch based coatings (pict. 10.4.18 – 10.4.19).

The advantage of starch in water retention can also be measured by the immobilization time of the BASF immobilization cell, where viscosity of the filter cake is measured during dewatering (pict. 10.4.20).
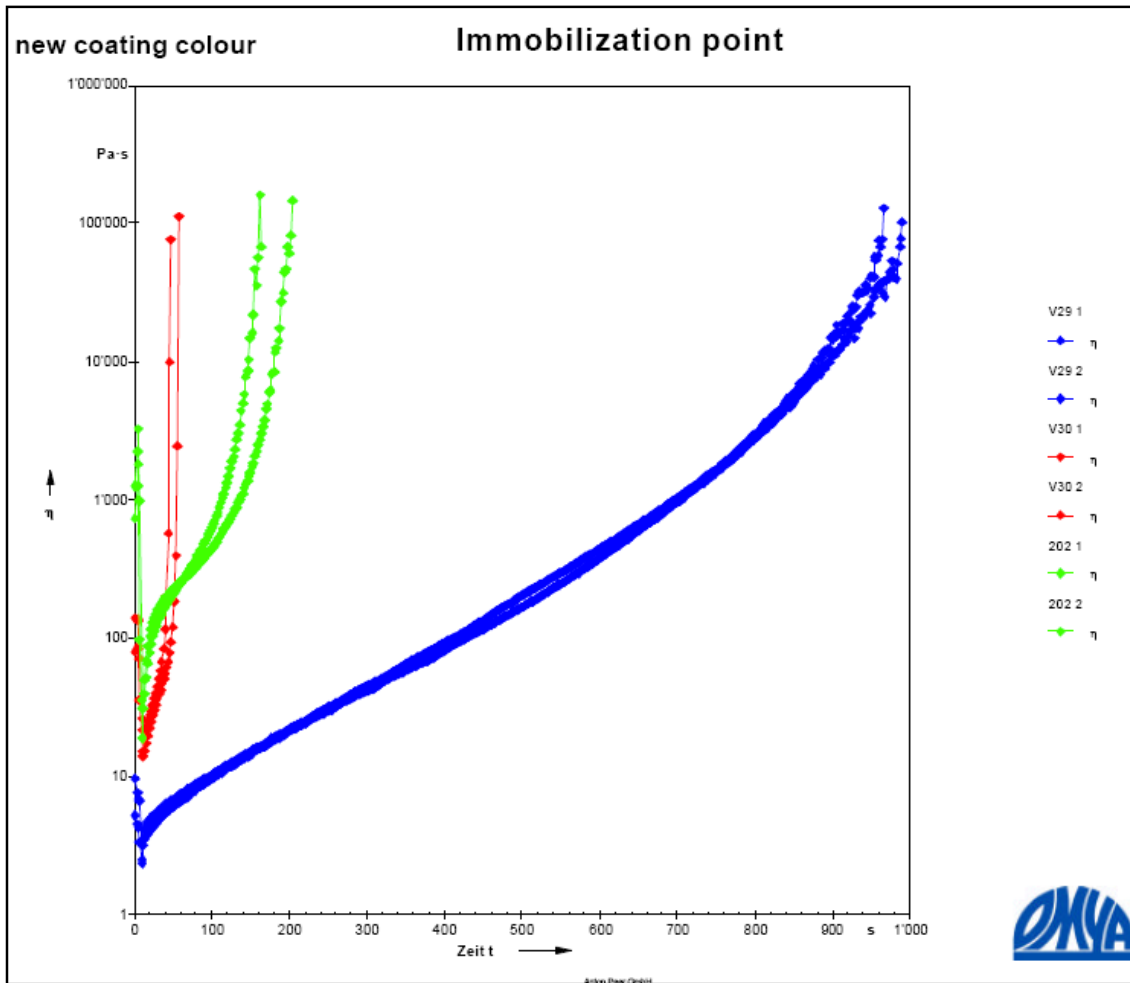
Pict. 10.4.20: BASF immobilisation cell – increase of viscosity during dewatering
(Rez. 202: Precoating with 68% solids based on coarse carbonate and 5% dextrin
starch, V30: starch free precoating, V29: Precoating with 6% high viscous dry starch
combined with plus 4% higher solid content of coating colour)

10.4.4 Comparison 4: Increase of liquid viscosity by CMC

Erikson and Rigdahl (L1.56) tested the dewatering behaviour of a clay based coatings under pressure with the Abo-GWR water retention instrument. They added thickeners CMC and starch to the coating colour, consisting of clay and SB latex.

They found, that CMC based coating colours dewatered much slower than starch based coatings at comparable viscosity of liquid phase in the filtrate. Starch based colours had higher immobilization layer porosity than CMC based coatings (pict. 10.4.21). The higher the level of thickener, the higher the porosity of the filter cake was as coatings got more structure by flocculation.
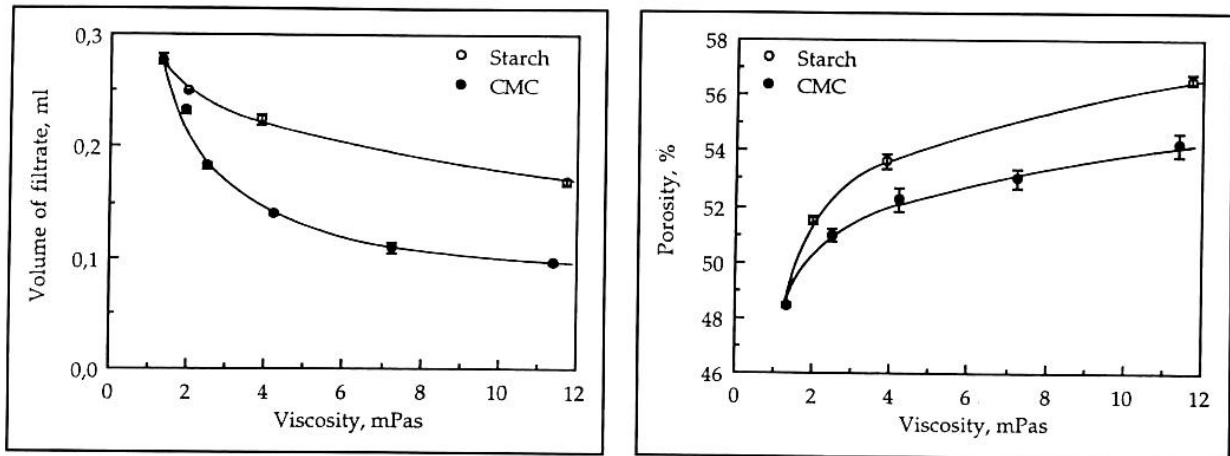
Pict. 10.4.21: Dewatering as a function of liquid phase viscosity (left) and filter cake porosity (right) (Erikson and Rigdahl)

According to Darcy and Carman-Kozeny the penetrated volume should be proportional to the square root of time and viscosity.

$$V = \sqrt{\frac{2 * A^2 * \Delta p * t}{r * V_f * \eta}}$$

V.....Volume of filtrate

A.....filtration area

r.....specific filtration resistance of filter cake

V_f....Volume of filter cake
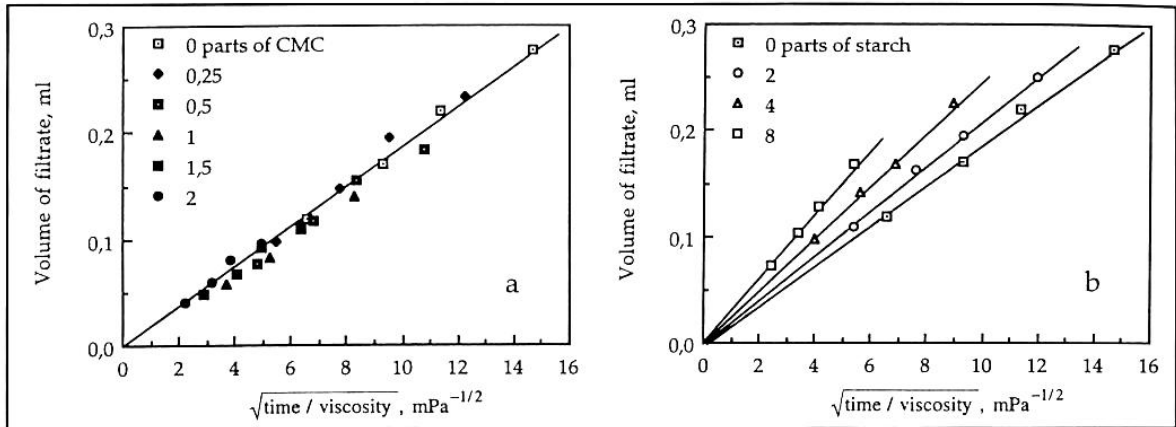
Pict. 10.4.22: Dewatering versus SQROOT of time/viscosity, experiments (Φ=0,33) (Erikson and Rigdahl)
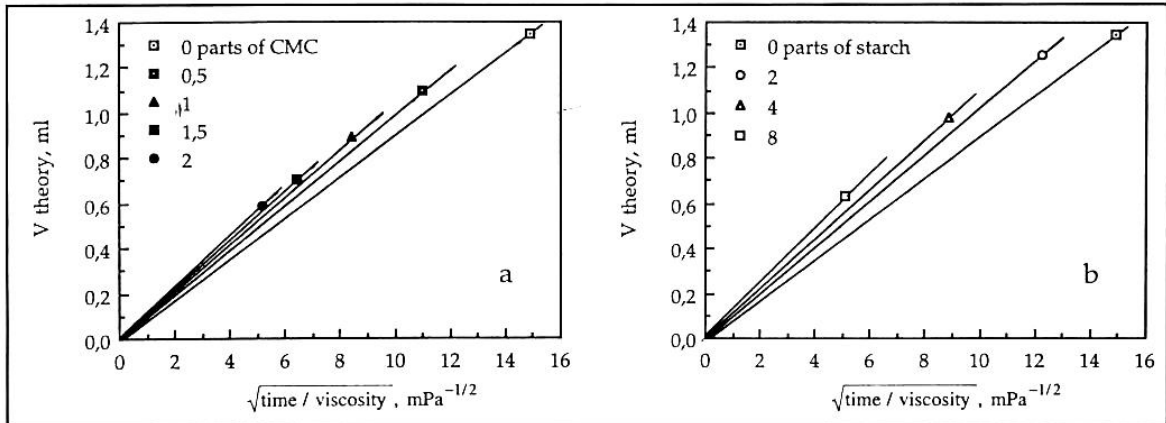
Pict. 10.4.23: Dewatering versus SQROOT of time/viscosity, calculated (Erikson and Rigdahl)

The results shown in pict. 10.4.22 and 10.4.23 proved the linear correlation between penetrated volume and square root of time and viscosity.

Ericson and Rigdahl showed, that calculating the porosity and the solid content of the immobilized layer from Abo-GWR lab dewatering experiments allows predictions of dewatering behaviour of coating colours under industrial conditions.

Similar results were obtained by Salminen and Roper, who tested different thickeners and by Erik and Stahl, who measured the filter cake permeability, depending on the zeta potential of pigment slurries.

At zero zeta potential the porosity of the filter cake is at its maximum and the highest Darcy coefficient is calculated.

Flocculation of coating colours and their filter is mainly achieved by adding water retention agents.

CMC is a substitute for starch as a natural thickener and is commonly used as a water retention additive in coating formulations.

Water retention

V4: 100% HC60, 16% Latex, solid 71,9%, 1750 cp

V17: 100% HC60, 16% Latex, 0,5% CMC, solid 71,4%, 7600 cp

Waterretention [g/l] vs Time [s]

— 0,5 bar, 5µm- V4   — 0,5 bar, 5µm- V17   — 2 bar, 5µm- V4   — 2 bar, 5µm- V17

Thickness of immobilized layer

V4: 100% HC60, 16% Latex

V17: 100% HC60, 16% Latex, 0,5% CMC

Immo Layer Thickness (µm) vs Zeit [s]

— 0,5 bar, 5µm- V4   — 0,5 bar, 5µm- V17   — 2 bar, 5µm- V4   — 2 bar, 5µm- V17
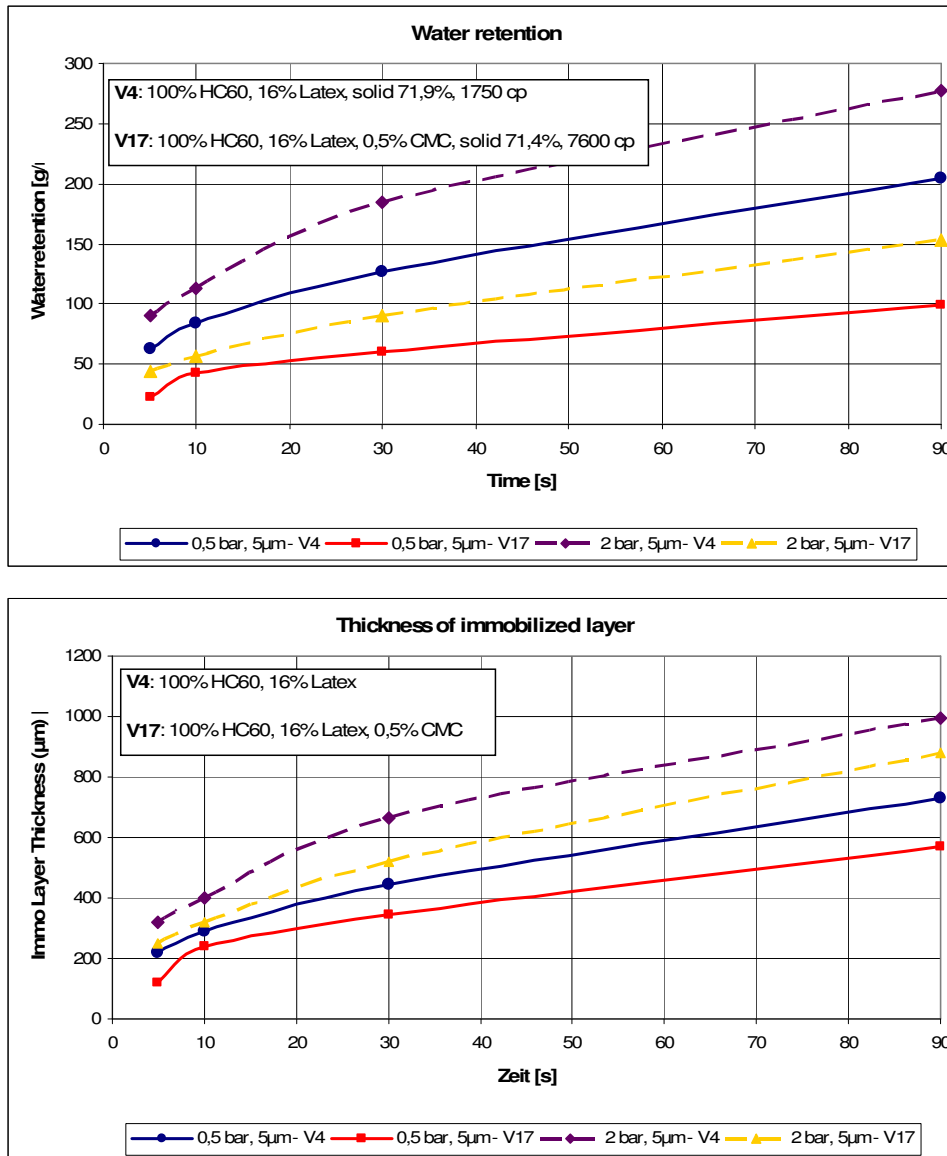
Pict. 10.4.24: Water retention and immobilized layer thickness (immobilized solids 78% for V17 and 82% for V4)
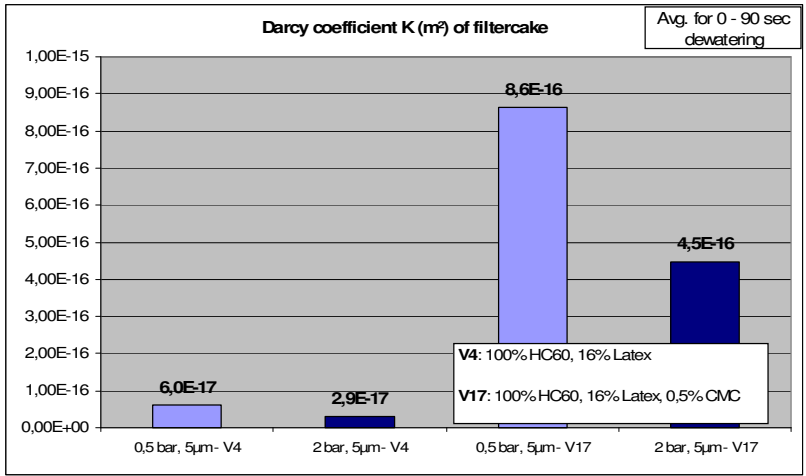
Pict. 10.4.25: Calculated Darcy coefficient (viscosity 1,5 mPas for V4 and 55 mPas for V13)
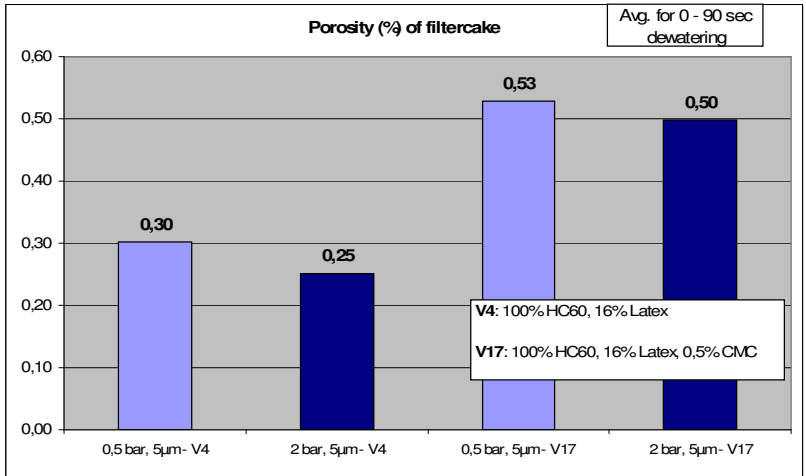
Pict. 10.4.26: Calculated porosity of filter cake
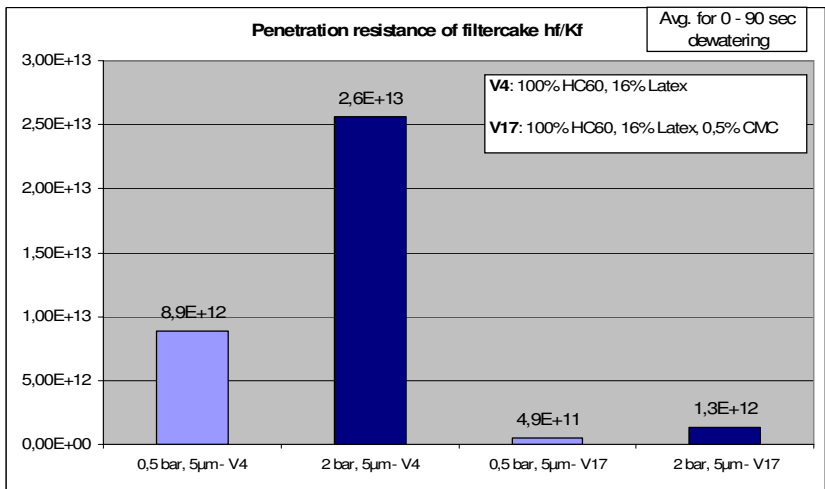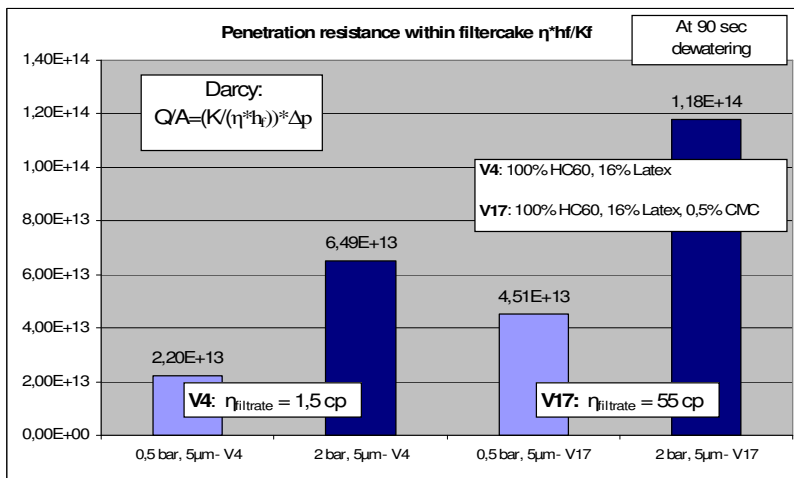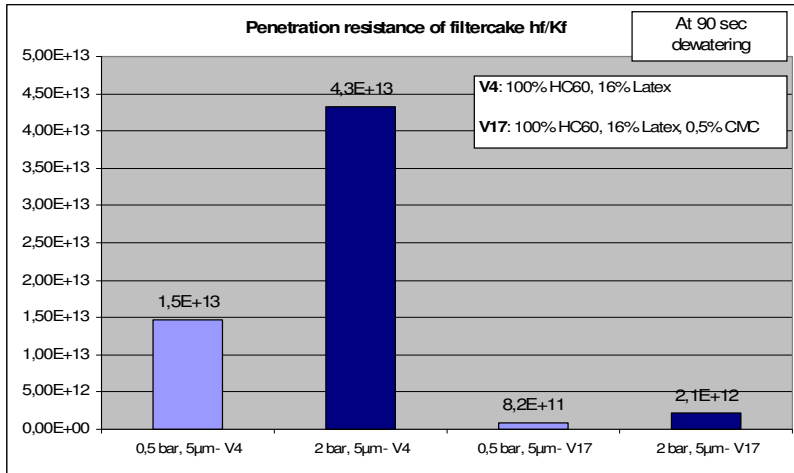
Pict. 10.4.27: Calculated penetration resistance h_f/K_f

Pict. 10.4.24 to 10.4.27 show that similar to starch based coatings porosity of filter cake is high for CMC containing coatings due to higher viscosity of coating colour. Thickness of immobilized filter cake falls with CMC but to a lower extend than for starch based coatings.

Overall penetration resistance factor $\eta*h_f/K_f$ is higher for CMC containing colour due to higher viscosity of liquid phase.

10.4.5 Comparison 5: Increase filter cake thickness by higher solid content

The solids content of a pre-coating formulation was increased by adding a dry pigment with the same PSD as the standard pigment in this formulation.
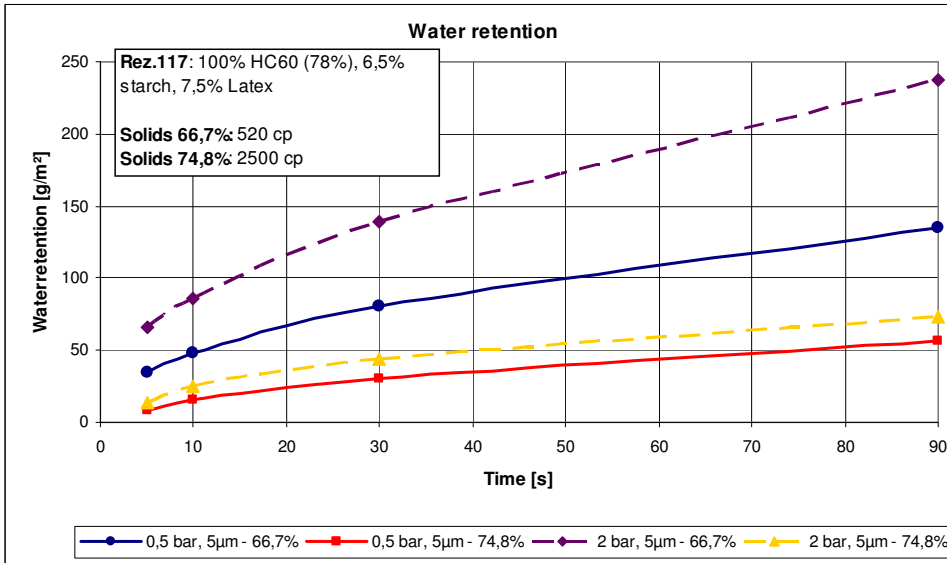
Pict. 10.4.28: Water retention improvement by increasing the solid content of a pre-coating
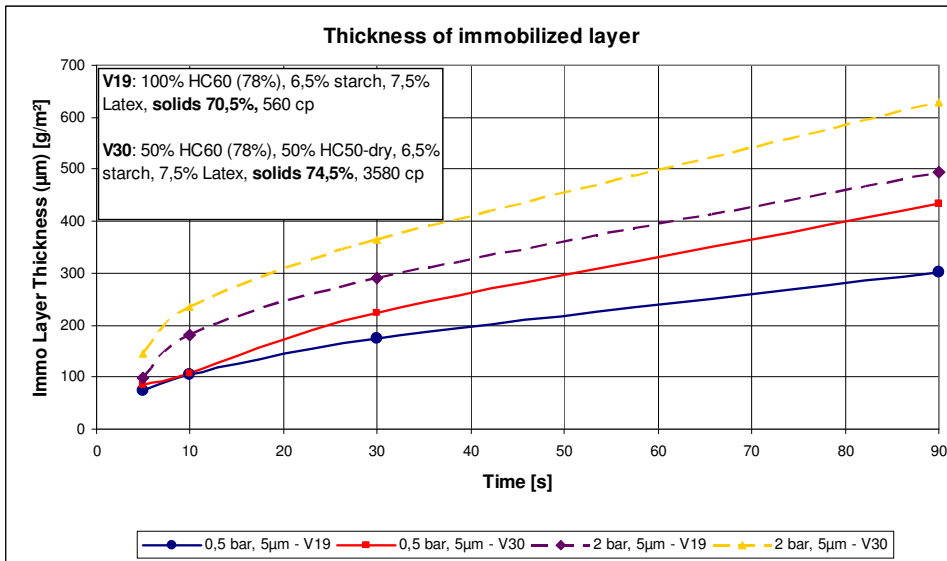
Pict. 10.4.29: Immobilized layer thickness (immobilized solids 81% for V19 and V30)
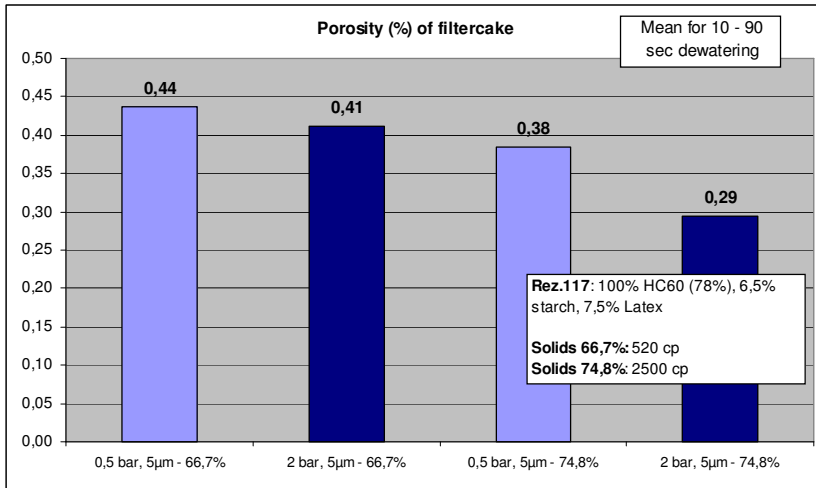
Pict. 10.4.31: Porosity of filter cake
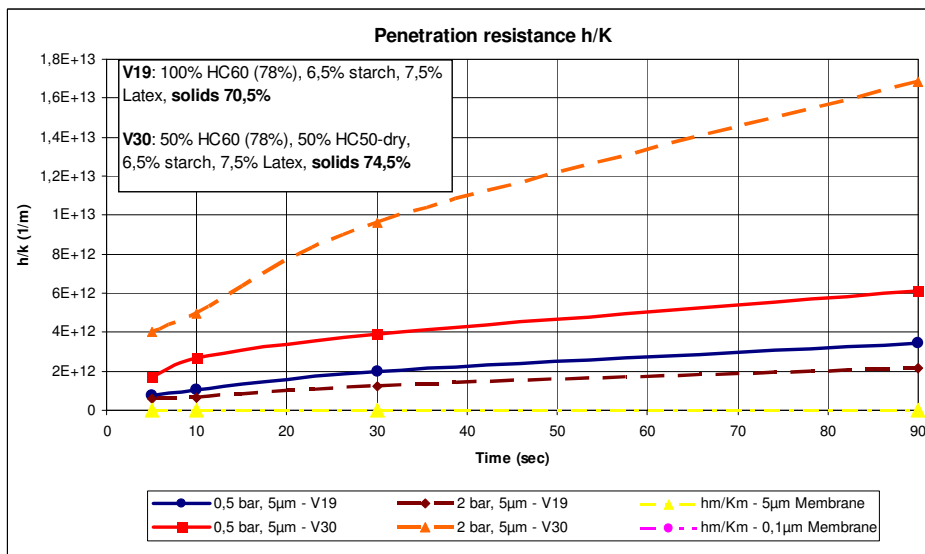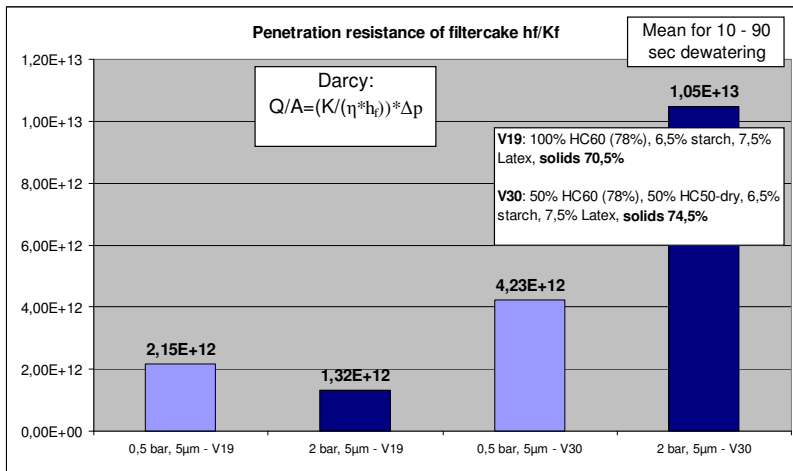
Pict. 10.4.32: Calculated penetration resistance h_f/K_f (viscosity is equal for both colours)

Page 551

Theoretically the immobilized layer thickness grows faster with higher solid content of a coating colour as the difference between the original coating colour solids and the immobilization solids gets lower. But the measurements and calculations of coatings with different solids as demonstrated in pict. 10.4.28 – 10.4.32 show the opposite especially at high pressure.

The higher the original coating solids the lower the gap to immobilization solids and the faster an immobilized layer is formed at the membrane. This layer slows down further dewatering of the coating colours and therefore water retention levels off.

In mill practice a higher solid content improves drastically the water and latex retention when coating colour is applied under high pressure because dewatering time is much shorter. When top coatings were switched from clay to carbonate, high solid coating had to be invented to reach the same level of mottling due to much worse water retention of carbonate based coatings at same level of solids.

The compaction of the immobilized layer can be seen in the lab data's at high pressure: Darcy coefficient and porosity is lower for the immobilized layer of the coating colour with the higher solid content leading to a higher overall penetration resistance coefficient.

10.4.6 Comparison of lab experiments to mill formulations of pre- and middle coaters at OMC9/11

With the same Abo-GWR pressure method different coating colours from OMC9 and OMC 11 were analysed.
Calculations were done in the same way as for pigments, described in the chapter before.

The standard middle coating colour 201 for OMC 11 was compared at 68 (VS 201-1) and 71,5 % solids (VS 201-2) in the following pictures 10.4.34 – 10.4.38.
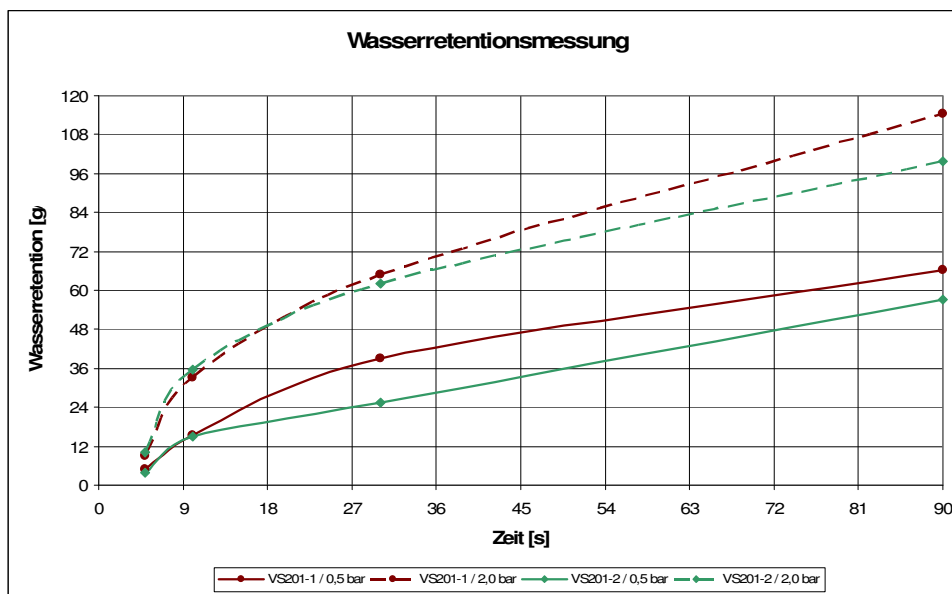
Pict. 10.4.34: Abo-GWR readings for Rez. 201 at 68,3% solids
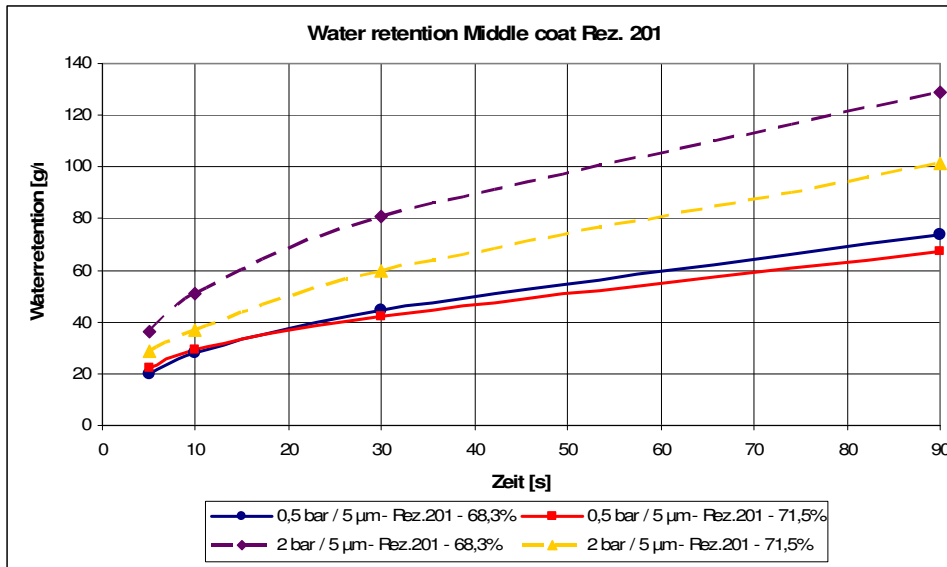
Pict. 10.4.35: Comparison of water retention curve of middle coat Rez. 201 with different solids
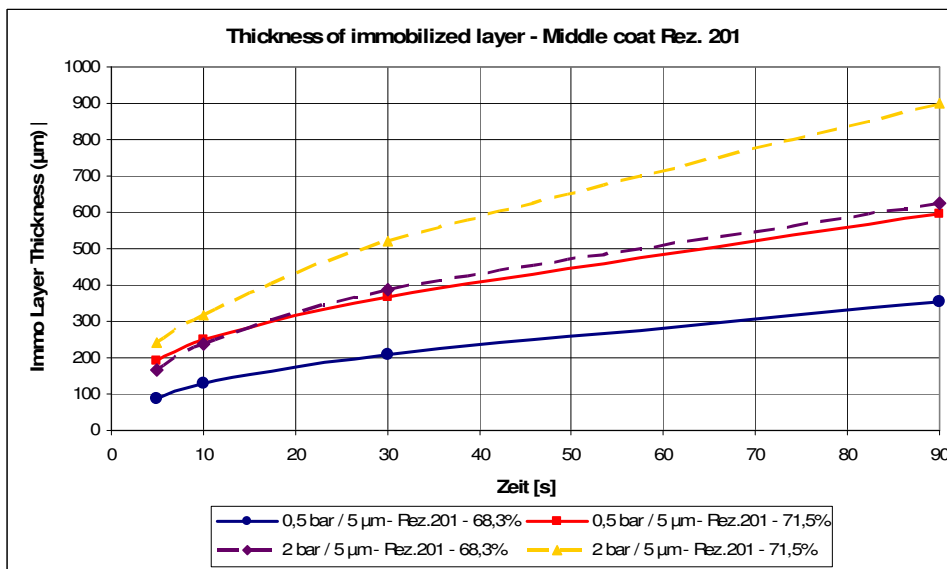
Pict. 10.4.36: Comparison of immobilized layer thickness of middle coat Rez. 201 with different solids
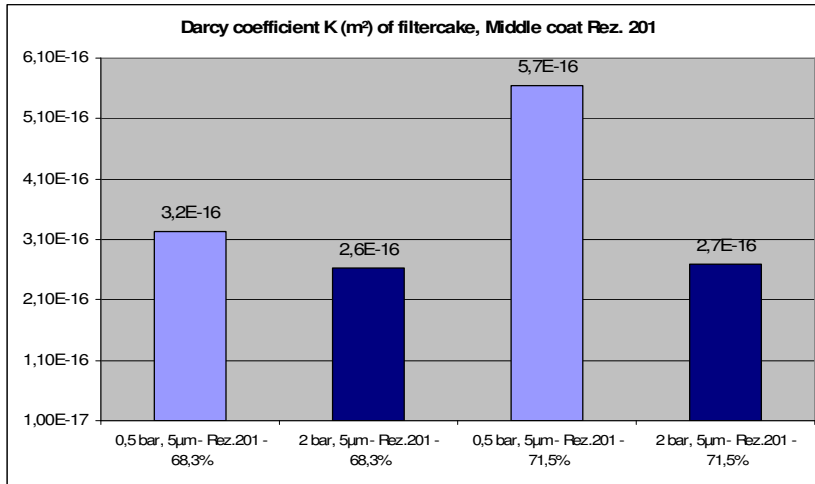
Pict. 10.4.37: Comparison of layer Darcy coefficient of immobilized middle coating layer (Rez. 201) with different solids
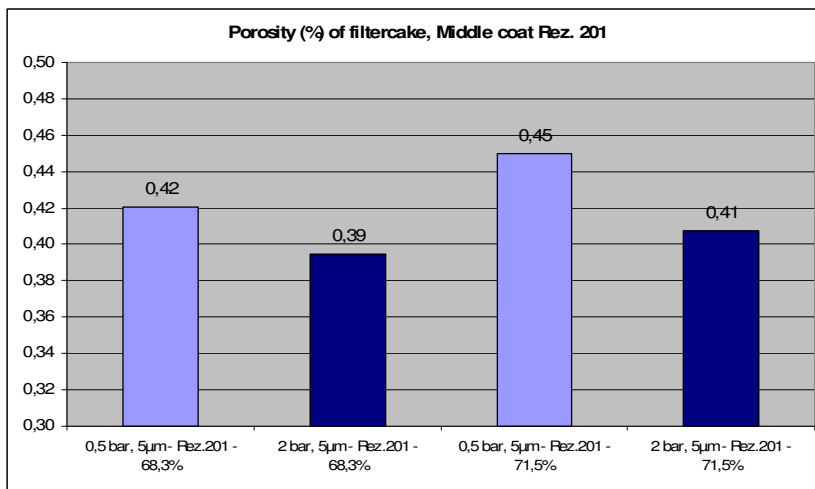
Pict. 10.4.38: Comparison of filter cake porosity of middle coat Rez. 201 with different solids

The coating colour with higher solid content showed a faster increase in immobilized layer thickness due to a smaller gap between original solids and immobilized solids. Porosity and permeability of the immobilized layer was similar as formulation remained unchanged.

For the penetration of coating colours under the blade penetration resistance of immobilized layer can be described by the term h_{Immo} / K_{Immo}. According to Darcy's law the amount of penetrated water is depending only on this term at a given pressure and time.
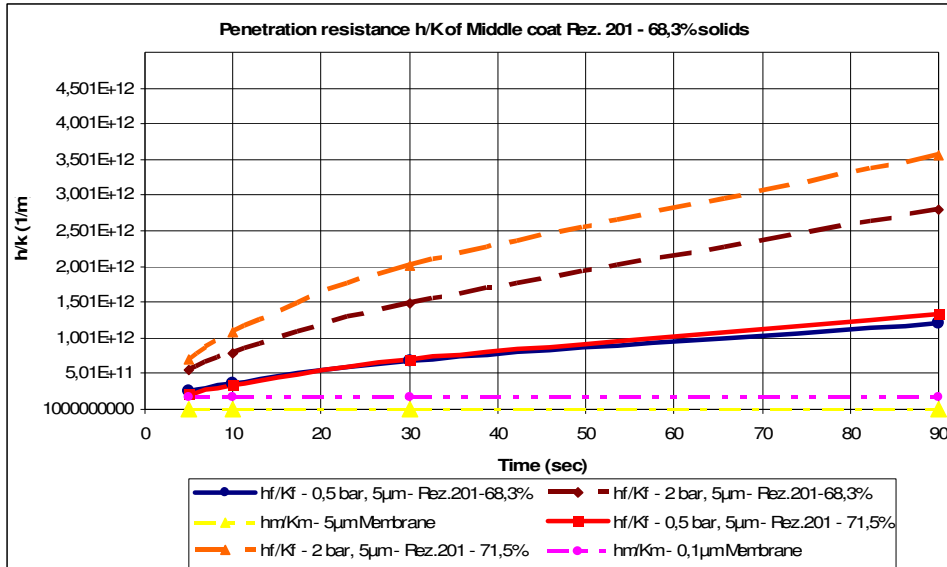
Pict. 10.4.39: Comparison of filtration resistance h_{Immo}/K_{Immo} of middle coat Rez. 201 different solids

When the filter cake is formed at low pressure, almost no difference in the penetration resistance $h_f/K_f = h_{Immo}/K_{Immo}$ can be seen in pict. 10.4.39 – the higher filter cake porosity and the higher Darcy coefficient at the higher solids are balancing each other.

When pressure is raised improved water retention with higher solids is caused by higher factor h_{Immo}/K_{Immo}

10.5 Comparison of static water retention of different precoating colours (1st part)

In the lab study of 2007 – 2008 different pre-coating formulations were prepared in the lab of PT4 and water retention was measured by Abo-GWR instrument (pict. 10.5.1 – 10.5.2).
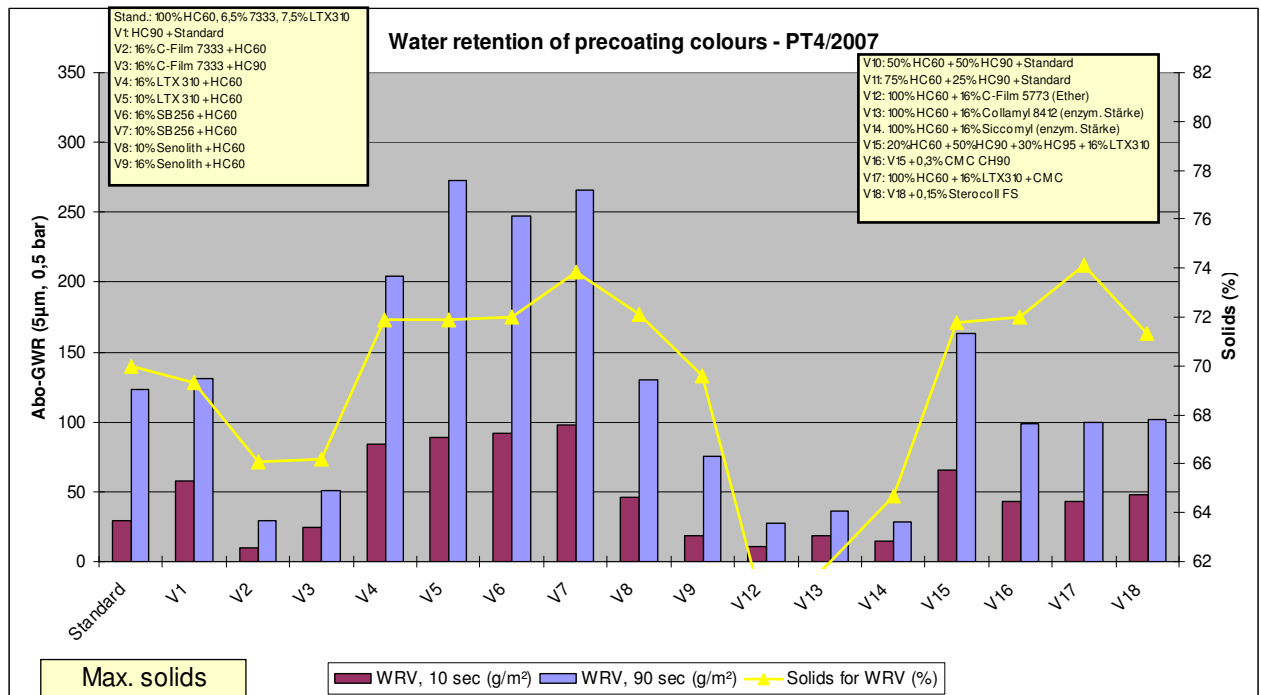
Pict. 10.5.1: Water retention vs. solid content of all tested pre-coatings

Water retention of precoating colours - PT4/2007

Stand.: 100%HC60, 6,5% 7333, 7,5%LTX310
V1: HC90 +Standard
V2: 16%C-Film 7333 +HC60
V3: 16%C-Film 7333 +HC90
V4: 16%LTX 310 +HC60
V5: 10%LTX 310 +HC60
V6: 16%SB256 +HC60
V7: 10%SB256 +HC60
V8: 10%Senolith +HC60
V9: 16%Senolith +HC60

V12: 100%HC60 +16%C-Film 5773 (Ether)
V13: 100%HC60 +16%Collamyl 8412 (enzym. Stärke)
V14: 100%HC60 +16%Siccomyl (enzym. Stärke)
V15: 20%HC60 +50%HC90 +30%HC95 +16%LTX310
V16: V15 +0,3%CMC CH90
V17: 100%HC60 +16%LTX310 +CMC
V18: V18 +0,15%Sterocoll FS

Max. solids

WRV, 10 sec (g/m²) · WRV, 90 sec (g/m²) · Visco 20 UpM

Pict. 10.5.2 : Water retention vs. viscosity of all tested pre-coating colours (right Y-axis: Water retention (g/m²), left Y-axis: BF20 viscosity (mPas))

From this comparison of static water retention measurements it can be concluded that <u>water retention can be improved by:</u>

- **Starch** instead of latex. Starch shows superior water retention although solid content of tested coatings was clearly lower due to the low solids of the cooked starches. Starch increases liquid phase viscosity and leads to faster immobilization.

- Increasing the **latex content**. When more fine particles are added to the coarse pigment matrix the density of the filter cake is raised.

- Latex types with broad particle size distribution, especially with high amount of **ultrafine particles** (denser filter cake). With the acrylic latex "Senolith" which is used in varnishes and which contains ultra fine particles, water retention improved to almost the same level as with starches.

- When **thickeners** are used in latex based coatings the liquid phase viscosity is increased and water retention is improved according to Darcy's law. Unfortunately the coating colour viscosity increases to a level which is much higher than for starch based coatings.

- **Finer pigments** lead to denser filter cakes in the same way as it is achieved with fine latices. Both measures don't change the rheology of the coating colour and are therefore easy to implement.

Comment to the suggested measures to improve water retention:
- **Finer pigments** are easy to implement but lead to higher costs.
- **Replacing latex by starch** is the best and cheapest choice to improve water retention and mottling, which was shown in several mill trials at PM11. The major risk is the worsening of cracking on the fold with rising amounts of brittle starch. Counter measures by increasing folding strength of base paper (eg. by NBSK) or starch additives in the coating have to be taken if cracking has to be kept on constant level.
- A **higher amount of latex** is also easy to implement but leads to significantly higher costs.
- Mixing different **types of latices** to achieve a bimodal PSD and a higher amount **of fine particles** is currently in development. Unfortunately these latices can be produced only from hard styrene and have therefore a high Tg of 25 °C. They worsen CaF like starches do and are much more expensive.
- Increasing the amount of **thickener** in coating colour leads to an increase in low and high shear viscosity and a lower immobilization solid. These formulations are more critical in runability at blade and film press coaters (see appendix).

The cheapest way would be to replace latex by new types of starch, which are less brittle by chemical modification.

The improvement in mottling was proven in mill trials BV2a and BV2f in 2007. The results are listed in the chapter "dense pre-coatings".

To improve mottling in a first step without extensive additional costs and without worsening CaF, the pigment mixture in all precoatings of PM11 was changed from 100% HC60 to 65% HC60 + 35% HC90.

10.6 Comparison of static water retention of different precoating colours (2nd part) – increasing solid content of coating colour

10.6 Comparison of static water retention of different precoating colours (2nd part) – increasing solid content of coating colour

In the second part of the water retention study in PT4 the main focus was **on increasing the solid content of the 1st pre-coating.**
This measure was chosen as one of the most promising actions against mottling as it combines quality improvement with lower costs.

Higher solids lead to lower drying costs especially when gas fired IR is used.

The major disadvantage is the risk of runability problems. Therefore extensive pilot and mill trials were made before this measure was implemented.

The previous studies showed that water retention improves with rising solids and starch or thickener content (pict. 10.6.1).

Pict. 10.6.1: Water retention vs. solid content of precoatings of PM11 /OMC11

Abo-GWR dewatering of Rez. 117 with increasing solids - 2 bar - 5 µm membane

Abo-GWR dewatering of Rez. 117 with increasing solids - 0,5 bar - 5 µm membane
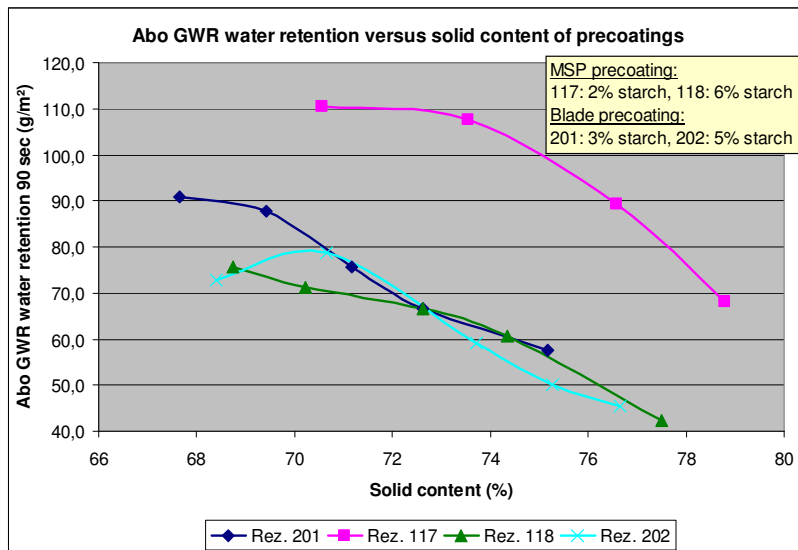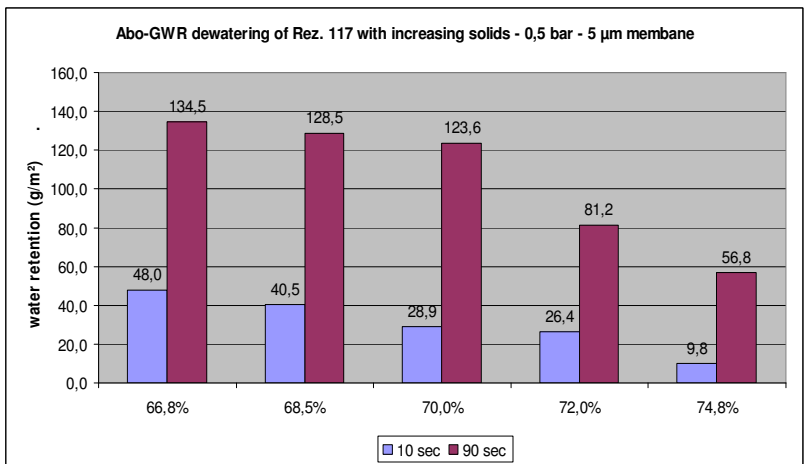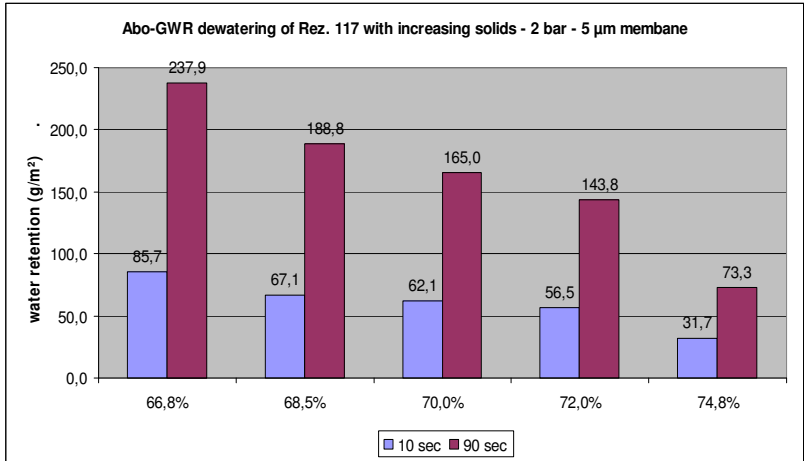
Pict. 10.6.2: Improvement in short term and long term water retention by solid content increase (film press pre-coating PM11 containing 2% starch and 10% latex)

Water retention improves with increasing solid content (pict. 10.6.2). The limit element is the exponential increase in low and high shear viscosity with raising solids which would lead to severe runability problems at mill coaters (pict. 10.6.3 – 10.6.4).
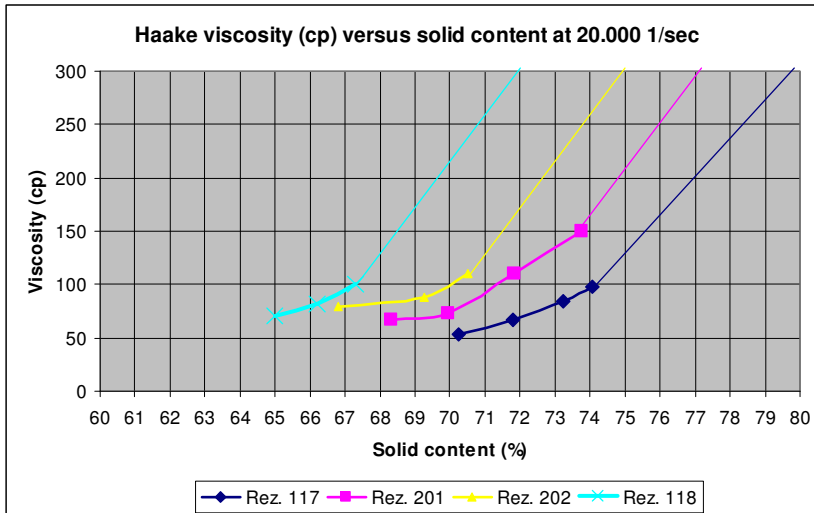
Pict. 10.6.3: Increase in high shear viscosity with increasing solid content
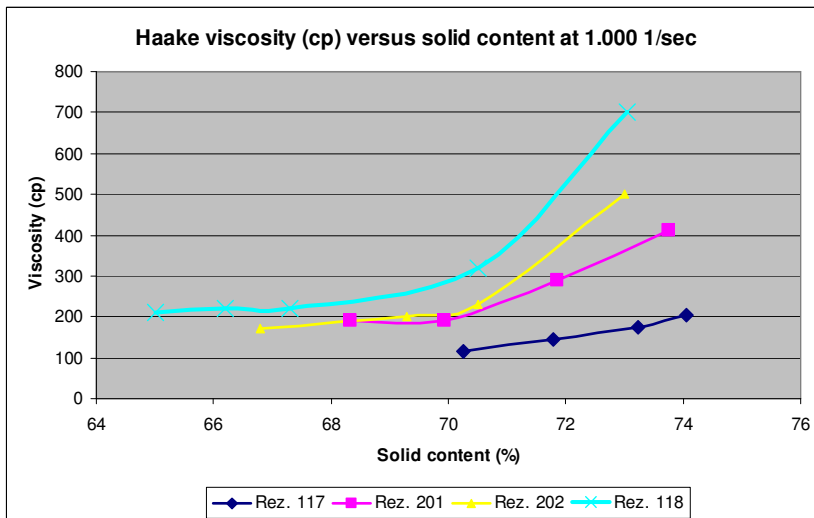
Pict. 10.6.4: Increase in low shear viscosity with increasing solid content

Precoatings with high amounts of starch (Rez. 118 for 1st pre-coat by MSP and Rez. 202 for 2nd middle coat by blade) show faster increase in viscosity with raising solids. Therefore runability problems will occur faster with high amounts of starch in coatings due to steep increase in high shear viscosity with rising solid content and in consequence lower immobilization solids.
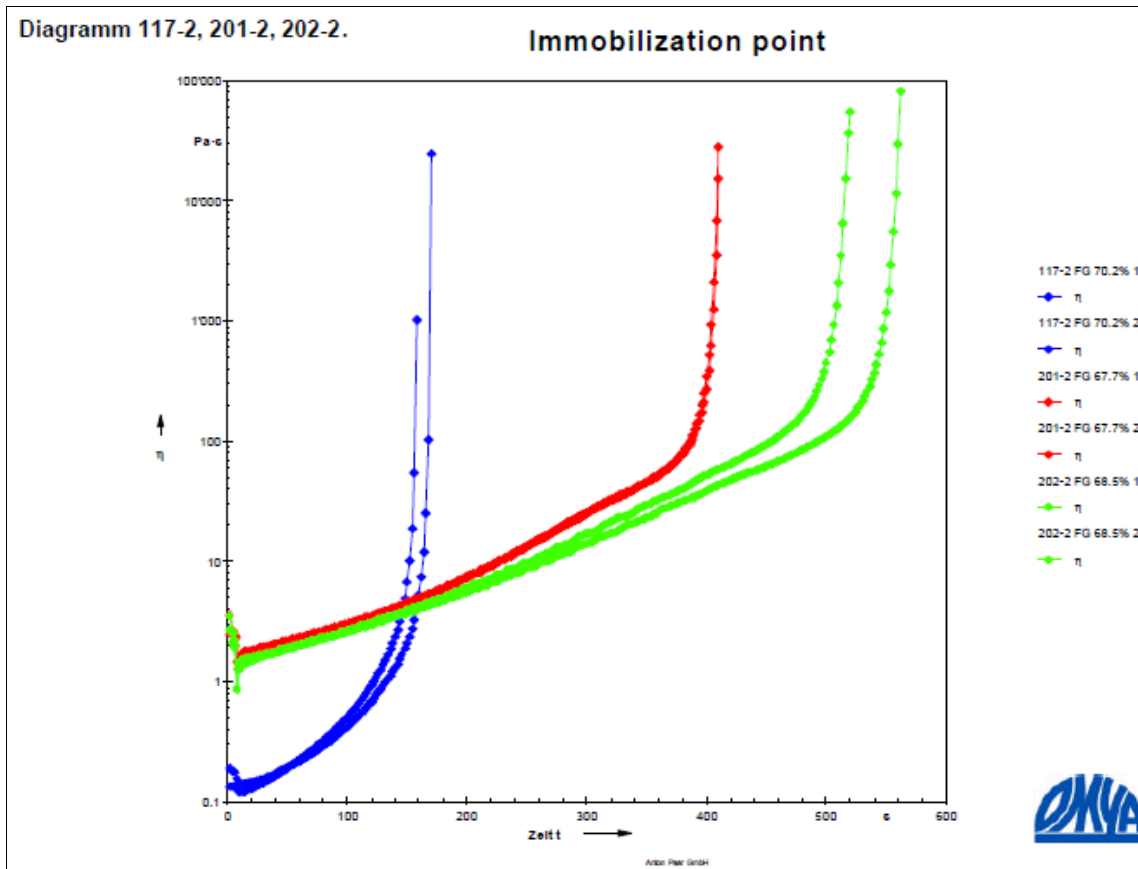
Pict. 10.6.5: Immobilization time of pre-coat 117 and middle coatings 201 and 202 with BASF/Paar immobilization cell (rotation viscosimeter)
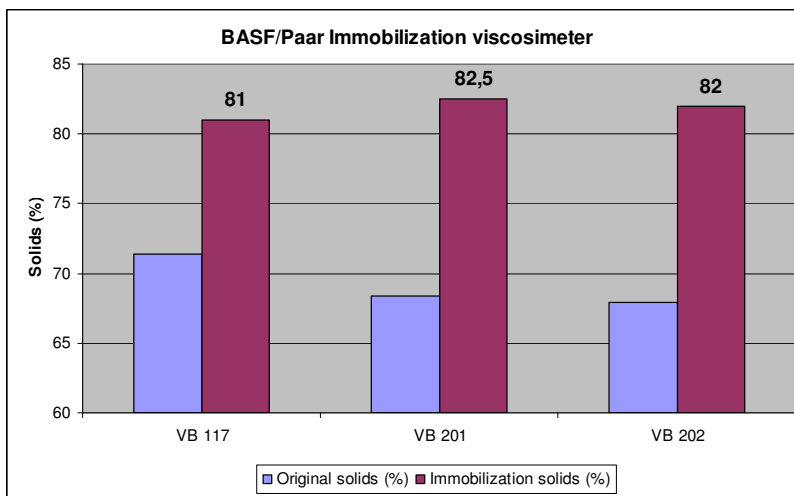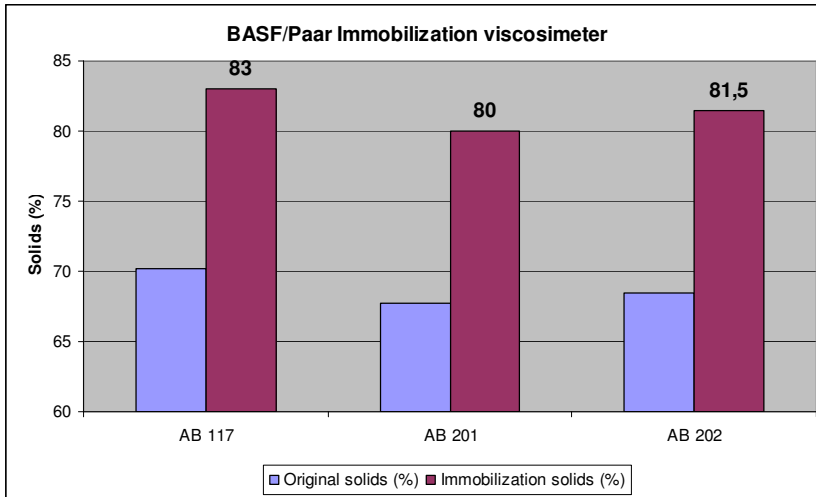
Pict. 10.6.6: Immobilization solids for pre-coating 117 and middle coatings 201 and 202 (VB = fresh coating colour in coating kitchen, AB = working tank at coater)
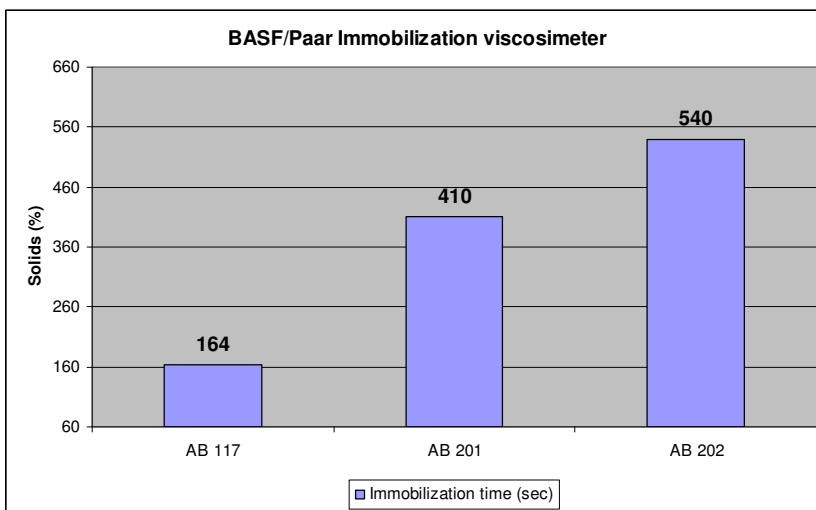
Pict. 10.6.7: Immobilization time for pre-coating 117 and middle coatings 201 and 202

Brookefield viscosity of 1st precoat with MSP at PM11 is relatively low with 500 cp at 20 RpM (solids 69%), compared with blade middle coating colours, which have typically 5000 cp at 20 RpM Brookefield and 69% solids.

The explanation can be found in the difference in associative thickeners: MSP coatings don't require synthetic thickeners, while blade middle coating colours contain approximately 0,5% CMC to get a baring free film after jet application.

As viscosity of film press coatings is lower than that of blade coatings, immobilization solids is higher and solids at the coater can be raised to a greater extend without risking runability problems (pict. 10.6.5 – 10.6.7).

Before year 2009 the solid content level at the MSP pre-coaters was 65 – 66 % for starch based formulations and 67 – 69 % for starch free formulations. The make up in the coating kitchen was 2% higher in solids. Film press coatings are often lower in working tank solids than in coating kitchen due to dilution by sealing water at the edge and rod bed lubrication water which compensate the minimal thickening of coating colour in the application nip.

To increase solid content of coating colour in the make down, the solid content of one or more components in the formulation has to be raised.

This can be done by smaller steps, e.g. increasing the latex solids from 50 to 54% or the solid content of the cooked starch from 30 to 35%.

A second way would be to use one product as a dry material. The three big components in the precoatings are carbonate, latex and starch. As latex is not available as a powder, the other two remain: Use dry pigment or use dry starch.

Dry carbonate was tested as HC60 / HC90 lab dried and as dry grinded HC50 powder from Gummern.
Cold soluble dry starch was supplied from Cerestar as iCoat.

Lab coating colours were prepared close to the maximum of Brookefield viscosity with 20 RpM of 5000 cp. Solid content of the coating colours was between 72 and 76%.

Two levels of starch (and therefore viscosity of film press formulation) were tested: 2% and 6,5%. The solids of the complete coating colour was kept at the maximum level, no additional free water was added to the coatings. Results of water retentions measurements with Abo-GWR method are shown in pict. 10.6.8 and 10.6.9.
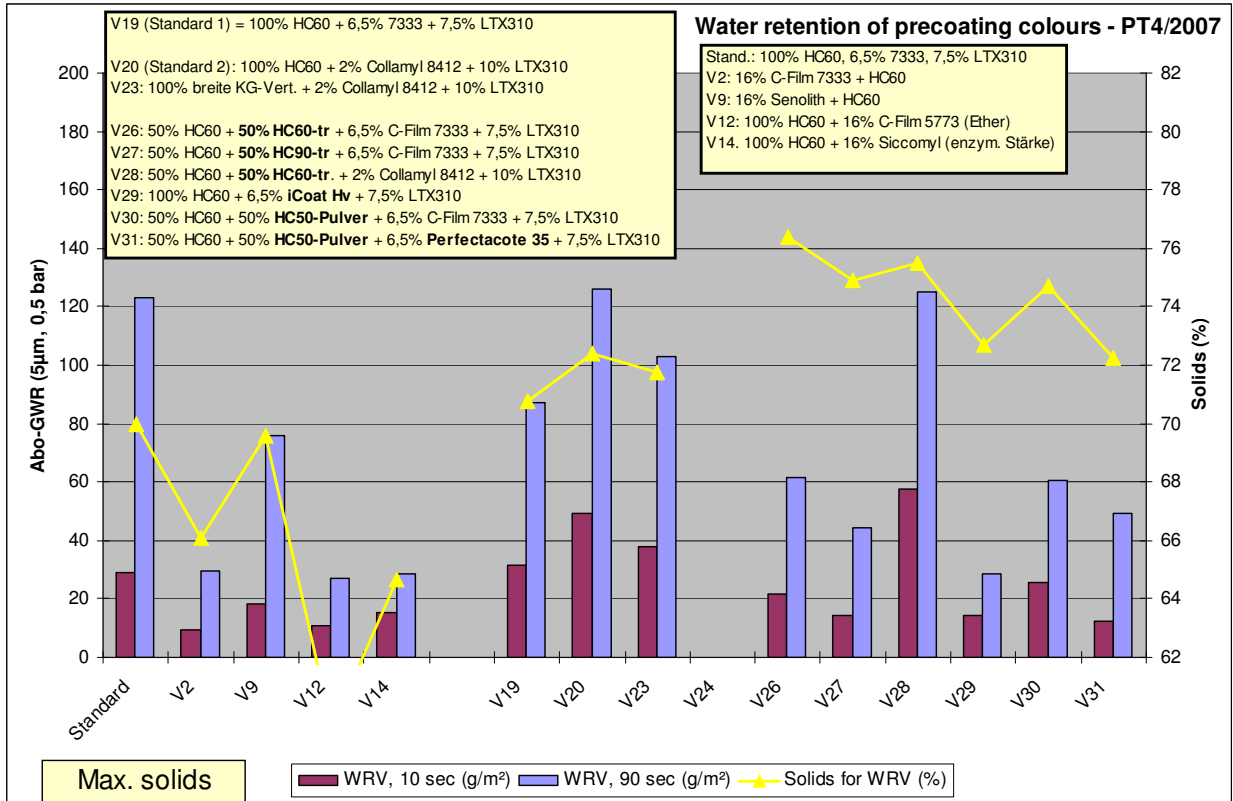
Pict. 10.6.8: Improving water retention by increased solids with different dry products
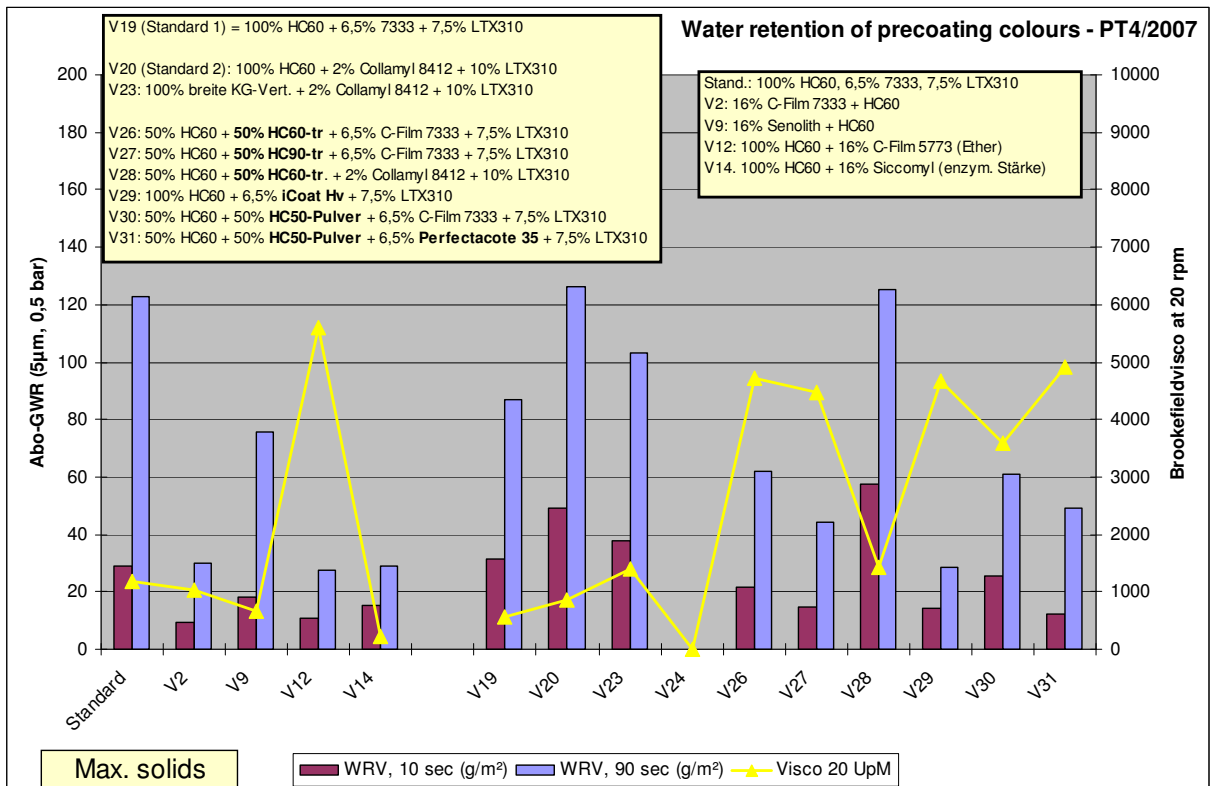
Pict. 10.6.9: Water retention vs. viscosity for pre-coatings with increased solids

Page 566

Results of the second lab study (pict. 10.6.8 – 10.6.9):

- At the higher starch level of 6,5% in the formulation the **water retention improved by 50%**, when the solid content of the coating colour was raised from 70% to 72 – 76%.

- When starch level in the formulation is with 2% low, the solids has to be raised to a bigger extend (>4%) to achieve improved water retention as delta solids of original coating colour to immobilization solids is higher than for 6,5% starch in the precoat.

- Dry starch iCoat-HV (high viscous starch) showed the far best water retention of all tested starch types. Water retention improved by 50% with an increase in solids from 70 to 72%. The viscosity of this starch was higher than the compared starch types (Dextrin 7333 and Perfectacote 35).

- Dry pigment plus cooked starch didn't reach the water retention level of iCoat but the improvement was on a level of 30% at a solid increase from 70 to 74 – 76%. It was chosen as the best compromise to improve water retention as the prices for dry starches were at least 30% higher than for cooked starches. Dry pigments are usually cheaper as slurries especially when transport costs are high.

Cost comparison:

The formulation with dry pigment is much cheaper as pigment price is lower than for standard pre-coating carbonates and less latex can be used to achieve same picking resistance due to latex better holdout (pict. 10.6.10).

	€/TA	Standard	iCoat	Dry pigment 1
HC60-slurry	95	100	100	85
HC40/50 dry	65			15
Polysalt	1516			0,1
Latex	1500	7,5	7,5	7
Dextrin starch	650	6,5		6,5
Dry starch	985		6,5	
		114	114	113,6
Price of formulation (€/TA):		**219,1**	**238,2**	**210,6**

Pict. 10.6.10: Cost comparison of dry products

As energy costs will go up in the next years, the main focus in reducing energy costs at coaters must therefore be on increasing coating solids. Using dry products can be a successful way to implement this strategy.

The positive result of this lab study was transferred in August 2008 by an investment in coating kitchen of PM11 (pict. 10.6.11). Dry carbonate is used since 2008 in all pre-coatings. A share of 10 - 15% in precoating formulation leads to a solid increase of 2 - 4%.
In pigment slurries coarser pigments than HC60 are not common due to problems with sedimentation during rail transport and storage.
Dosing dry carbonate directly into the coating mixer made the way free to use coarser pigments without these sedimentation problems.
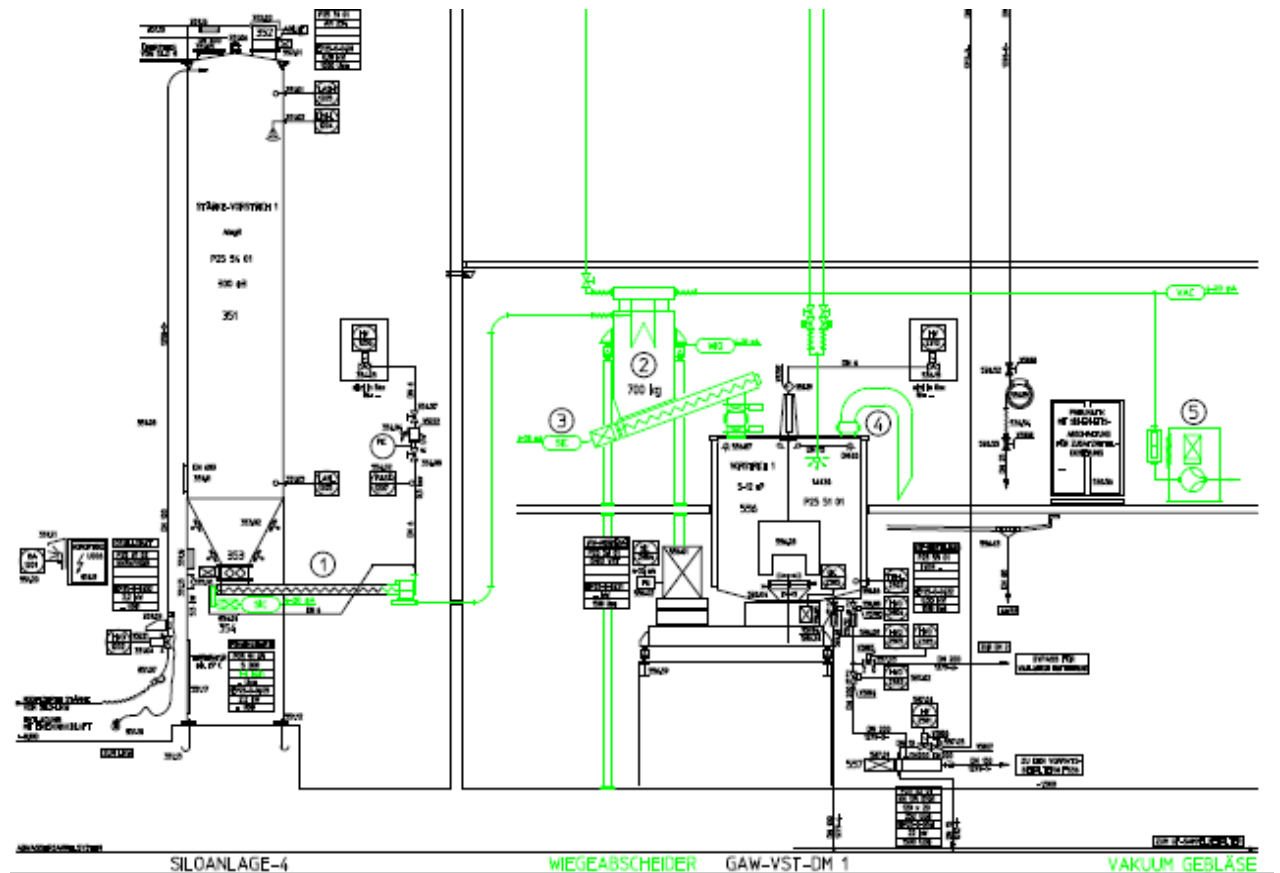
Pict. 10.6.11: Dosing equipment of dry pigment in coating kitchen PM11/OMC11

In coatings with low starch content the solid content could be raised up to 74% without runability problems. Mottling improved with increased solids and increased amount of starch in the precoating formulations which confirmed the findings of this chapter.

The limiting factor at film press coaters is rod pressure. It rises when solids and starch content are increased. During this optimization process the rod might have to be changed to a smaller diameter to keep the coat weight on the same level. At PM11 the rod stayed unchanged but coat weight was increased in all pre-coatings with raising solids as drying was no more the limiting factor. This led to an additional benefit in mottling as film press coaters are more uniform in in-plane coating layer permeability than blade coaters.

Increasing the solid content in film press coating reduced misting and drying costs.

10.7 Improving mottling by optimizing coating colour rheology - development of a new method to separate liquid phase from coating colour rheology and interaction between the components of coating colours.

10.7.1 Introduction

Base paper analysis showed the local pressure differences at flocs and voids (see chapter 3 – floc analysis, pict. 3.6.4). At flocs the liquid phase of the coating colour will penetrate deeper due to higher local pressure. Fine latex particles and soluble binders will follow the liquid phase (pict. 10.7.1.1). A lower local surface concentration of latex and soluble binders will be the consequence leading to a higher local permeability of the dry coating layer. Ink transfer into the coating layer will be locally higher at flocs and mottling is the consequence.
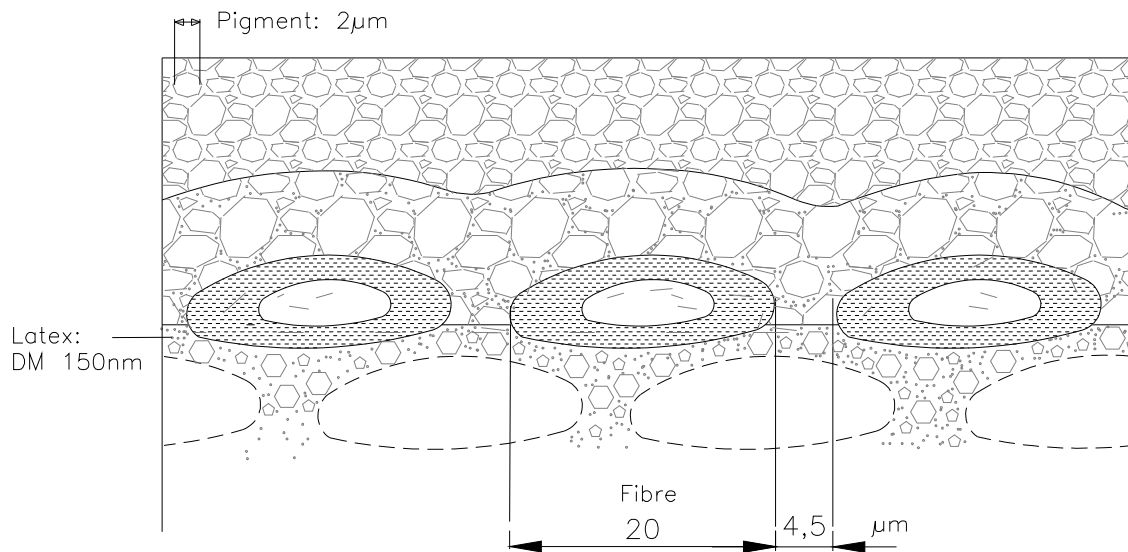
Pict. 10.7.1.1: Dimension or pores and particles in base paper and coatings – separation of coating colour into penetrating liquid phase and remaining solid phase at the surface of the substrate. Penetration of fine latex particles with liquid phase into substrate

Liquid penetration under external pressure is calculated by Darcy's law

$$v = \frac{d(V/A)}{dt} = \frac{\Delta p_f + \Delta p_s}{\eta * \left[\dfrac{h_f}{K_f} + \dfrac{h_s}{K_s} \right]}$$

With:

$$\Delta p = \Delta p_f + \Delta p_s$$

K_f…..Darcy coefficient of filter cake

h_f…..Thickness of filter cake at time t

K_s….Darcy coeff. of the penetrated substrate, here the penetrated pre-coating layer

h_s…..Thickness of the pre-coating layer

When top coatings are applied on a double precoated substrate, filter cake formation is inhibited by too low capillary sorption pressure of the substrate. Permeability of double precoated layer is so low, that penetration of water into the base by capillary sorption of fibre walls is prevented.
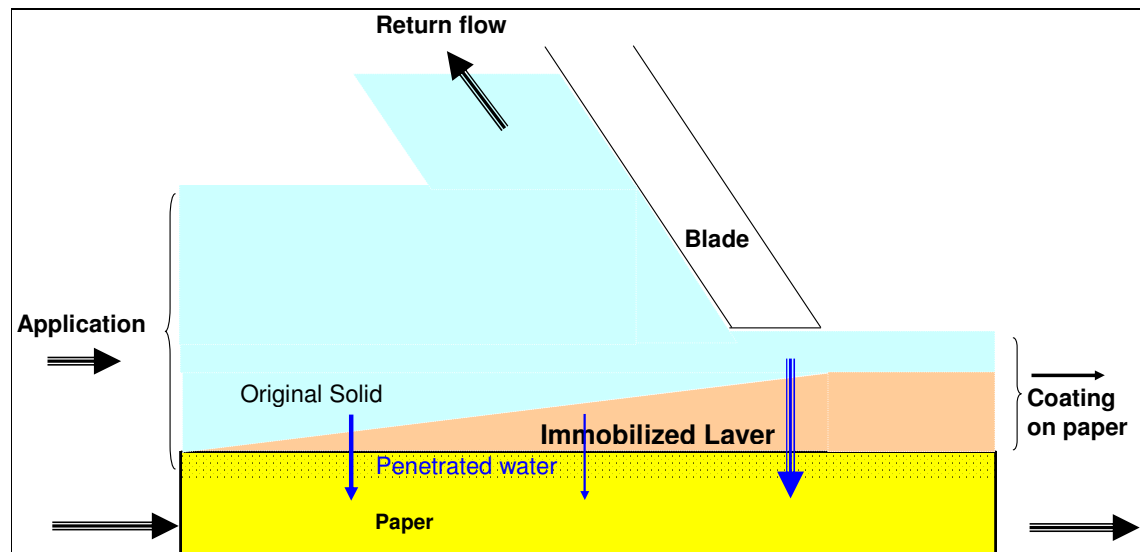
Fig. 10.7.1.2: Formation of immobilized layer before the blade by fibre capillary sorption

When the filter cake before the blade tip as shown in pict. 10.7.1.2 is missing under the blade, the term h_f/K_f gets negligible and penetration of liquid phase will be solely

depending on permeability of the substrate (its coating layer), pressure level, dwell time and liquid phase viscosity.

Comparison of levers for improvement of water/binder retention:

a) **Permeability of substrate:** A reduction of 10% was achieved in the trials shown in chapter "dense precoatings" when Darcy coefficient of precoating layer dropped by one magnitude.

b) **Blade pressure**: Can be reduced by higher blade angle and shorter facet length by a maximum of 30% (see chapter "blade coating")

c) **Penetration time**: Can be reduced by 10% by shorter facet length

d) **Liquid phase viscosity**: Differences of 50% where measured in the following study at constant high shear viscosity of coating colour

Therefore liquid phase viscosity seems to be the most promising measure to reduce pressure penetration under the blade and to improve mottling.

For the experiments in this chapter the shear rate for determining the liquid phase viscosity had to be fixed.

The VOF simulation from chapter 7 "blade coating" showed relatively moderate shear rate of 10^1 to 10^2 1/sec before the coating colour reaches the blade tip where 19 parts of 20 return into the working tank as coating colour travels with base paper.

At the incoming area before the blade the shear rate raises up to 10^5 while under the blade the shear rate is 10^6 1/sec (pict. 10.7.1.3 and 10.7.1.4). Dwell time under these high shear conditions is approximately 1 msec for coater speed of 1600 m/min. Such a short period of shear couldn't be simulated in the lab. Taking into account that liquid flow is laminar during penetration into the base under the blade Brookfield 100 RpM was chosen to describe the liquid phase viscosity before and under the blade (pict. 10.7.1.5 and 10.7.1.6).
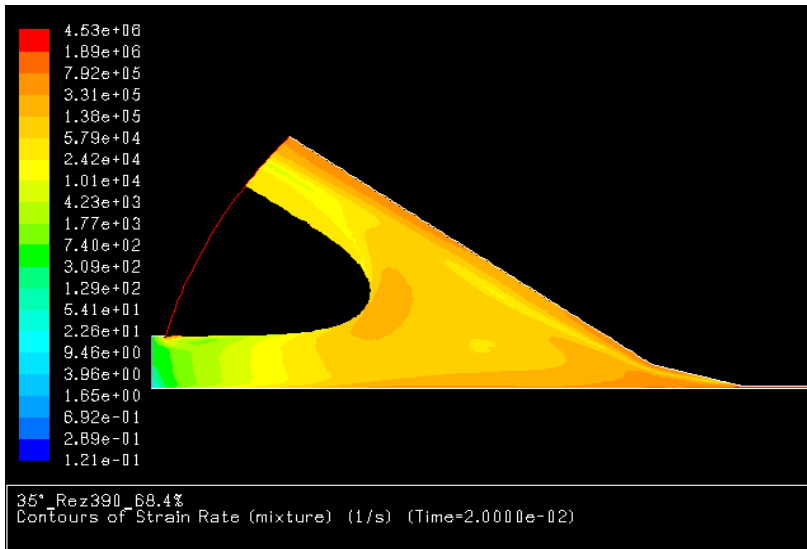
Pict. 10.7.1.3: Shear rate in converging nip before blade tip (OMC11, 1600 m/min, top coating)
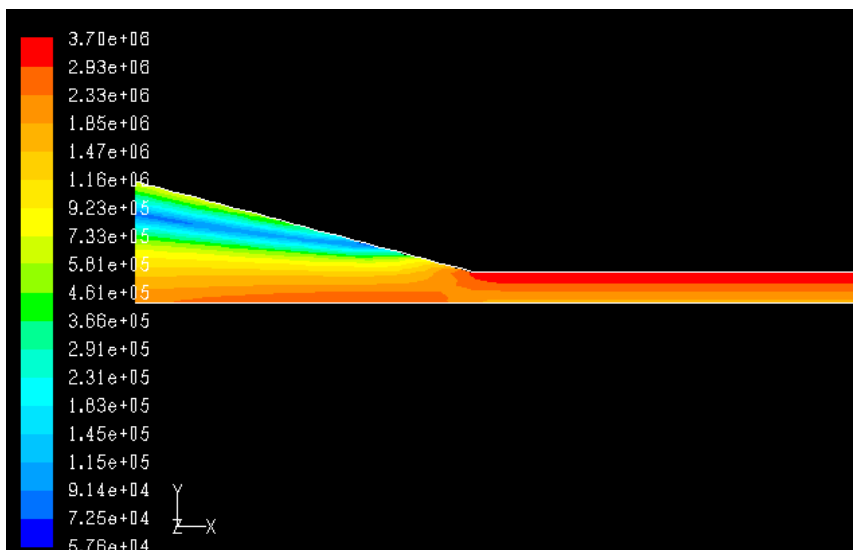
Pict. 10.7.1.4: Shear rate at blade tip and under blade
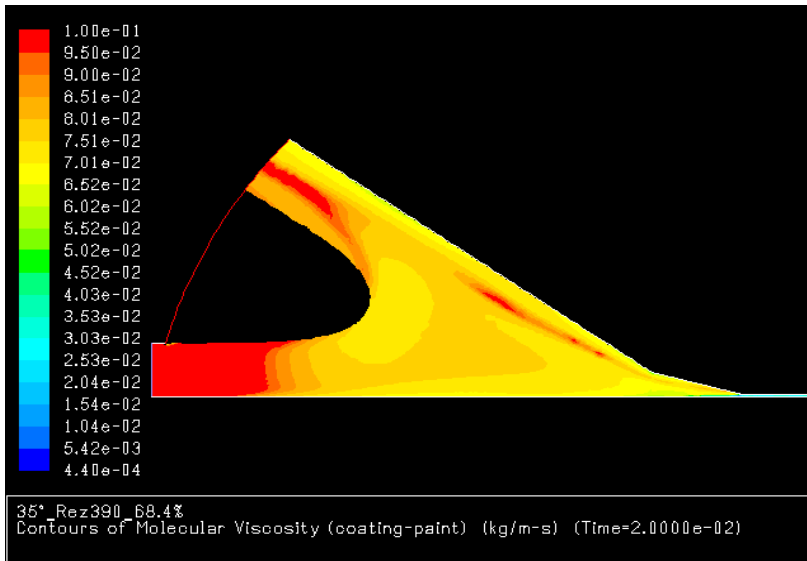
Pict. 10.7.1.5: Viscosity of coating colour in converging nip before blade tip (related from ACAV high shear measurement and shear rate from VOF)
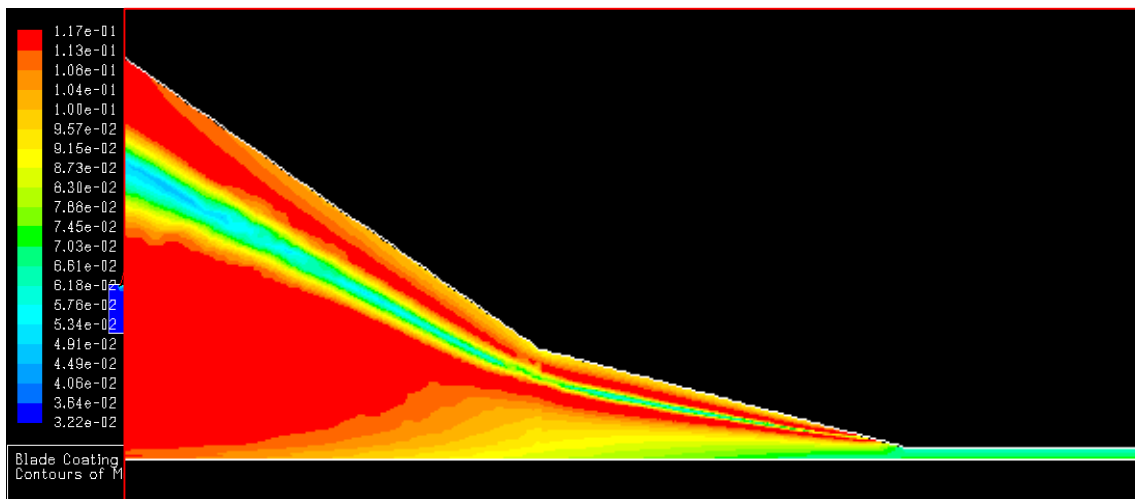
Pict. 10.7.1.6: Viscosity of coating colour at blade tip and under blade

10.7.2 Existing measuring methods to determine coating colour rheology

Viscosity is a key parameter to describe the deformation behaviour of a coating colour. Different kinds of viscosimeters were introduced to measure viscosity. In a plate – plate viscosimeter as shown in pict. 10.7.2.1 the tested material is deformed between a fixed and a moved plate.
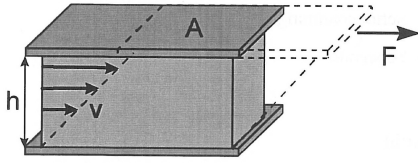
Pict. 10.7.2.1: Two-plate-model for deformation

Shear force from outside (movement of one plate) always leads to deformation of the tested material. If no re-deformation happens, ideal viscous Newtonian behaviour is measured. When whole impact of shear force is re-deformed the material shows ideal elastic behaviour described by Hooke's law. Materials between these two extremes show viscoelastic behaviour.

Shear stress τ is given by $\tau = F / A$ [Pa], with F the shear force and A the shear area.

Shear rate γ is $\gamma = v / h$ [s^{-1}] with v the speed and h the plate distance

Viscosity η is calculated with $\eta = \tau / \gamma$ [Pa.s]

Structure viscosity is the dependence of viscosity from shear rate for non Newtonian liquids (pict. 10.7.2.2).
$\eta_{ST} = \eta / \gamma$ [Pa * s^2]
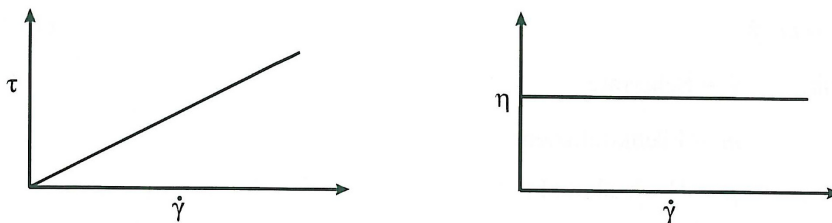
Pict. 10.7.2.2: Newtonian substance

Newtonian liquids show a minimum of interaction between molecules in the liquid.
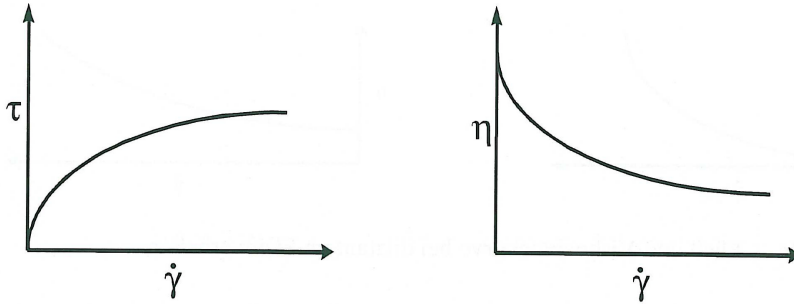
Pict. 10.7.2.3: Pseudo plastic substance with structure viscosity

When pseudo plastic or structure viscous substances are measured by rheometers, viscosity drops with increasing shear rate (pict. 10.7.2.3). The reason for this phenomenon can be a cross linking of macromolecules or a chemical interaction between components in the liquid, which is destroyed with increasing shear.

The mathematical description is given by Ostwald:
$\tau = m * \gamma^p$ with m the flow coefficient and p constant < 1.

When a liquid shows dilatant behaviour, viscosity increases with shear rate. One reason for that can be the breakdown of particles with shear and increase of specific surface area. More liquid is bound to this increasing surface. Particle motion gets more restricted. Another explanation is the expansion or rotation of particles at high concentrations, which is induced by the shear. A third possible mechanism is the enhanced collision of macro-molecules with increasing shear forcing them to form new structures.

Deformation γ describes the relation of deflection s to plate distance h and is dimensionless (pict. 10.7.2.4).
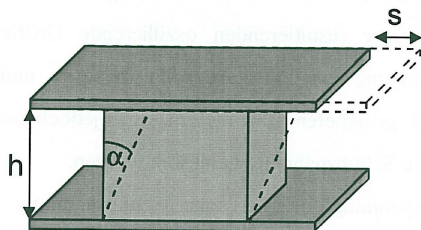
Pict. 10.7.2.4: Deformation of a substance

$\gamma = s / h = \tan \alpha \, [\,]$ with α the deformation angle.

Thixotropy describes the dependence of viscosity on time of shear. Viscosity of thixotropic liquids drops with shear time due to time dependent breakdown of internal macro molecular structures, similar to pseudo plastic behaviour. Once the shear is removed, viscosity increases again (pict. 10.7.2.5).
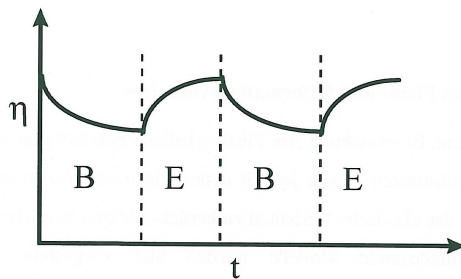
Pict. 10.7.2.5: Thixotrop substance with time dependent viscosity

In rheopex liquids viscosity increases with shear and drops again when shear is removed (pict. 10.7.2.6).
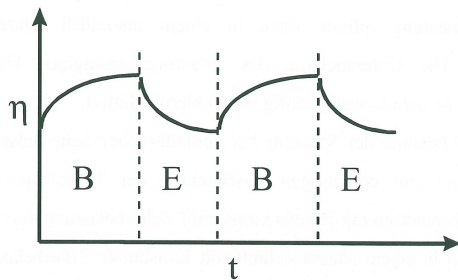
Pict. 10.7.2.6: Rheopex substance with time dependent viscosity

Thixotropy has to be determined in a separate experiment by measuring viscosity over a certain period of time at constant shear rate to avoid mix up with pseudo plastic measurements.

Models to describe viscoelastic behaviour are the Maxwell model for liquids and the Kelvin-Voigt-Model for solid materials.
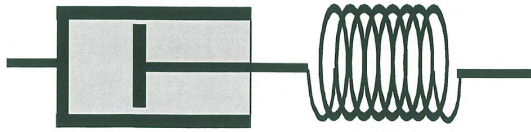
Pict. 10.7.2.7: Maxwell model

Liquids which behave according to the Maxwell model have an elastic component which acts like a spring according to Hooke's law and a viscous component which acts like a Newtonian shock absorber (pict. 10.7.2.7).

During shear both components are deformed. First the elastic part of stretch is taken to a certain level by the spring and afterwards the viscous part is taken. When stress is released, the elastic part springs back while the viscous component stays in its deformed status.
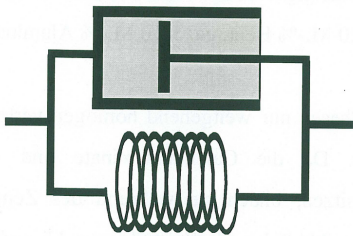
Pict. 10.7.2.8: Kevin-Voigt-model

In the Kevin-Voigt-model the viscous and elastic components are working parallel. Both components deform at the same time but the deformation of the elastic part is slowed down by the viscous component (pict. 10.7.2.8).

Oscillating experiments use plates which move into alternating directions with a certain frequency and amplitude (pict. 10.7.2.9).
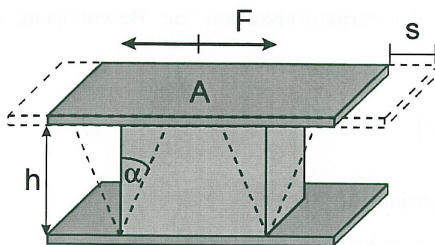
Pict. 10.7.2.9: Two-plate-model, oscillation experiment

Deformation is very small in oscillating experiments and microstructure of sample is not destroyed when amplitude is low.

In most cases a certain shear stress is used as a set point and the resulting deformation is measured. In some rheometers the deformation can be preset and the necessary shear stress can be measured.

The shear stress oscillates with $\tau(t) = \tau_0 * \sin(\omega * t)$.
τ_0 is the shear stress amplitude, ω is the circular frequency and t the time.

The deformation will have the same frequency as the shear stress but amplitude and phase can be different.
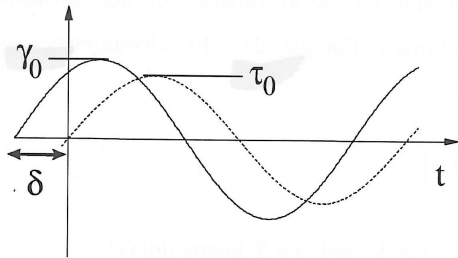
With γ_0 the deformation amplitude and δ the angle of phase shift.
$\gamma(t) = \gamma_0 * \sin(\omega * t + \delta)$

Only ideal elastic substances according to Hooke have the same phase in deformation as in the shear stress. All other liquids show an angle of phase shift δ.

The storage modulus G' describes the reversible stored deformation energy in the sample. It characterizes the elastic behaviour of a substance.

$G' = \tau_0 / \gamma_0 * \cos \delta$ [Pa]

The loss modulus G'' stays for the irreversible lost energy to environment and characterizes the viscous abilities of the sample.

$G'' = \tau_0 / \gamma_0 * \sin \delta$ [Pa]

The loss factor tan δ describes the relation between the viscous and elastic properties of the substrate.

tan δ = G'' / G' [ ]

In a rotational rheometer different shear geometries are used. For the experiments of this study a cylinder geometry was used in the Haake high shear rheometer, according to DIN 53019.
A laminar stratified flow is produced between the plates by rotating the inner cylinder against the fixed outer cylinder (Searle geometry). In Couette rheometers the outer cylinder rotates and the inner cylinder is kept in position (pict. 10.7.2.10).
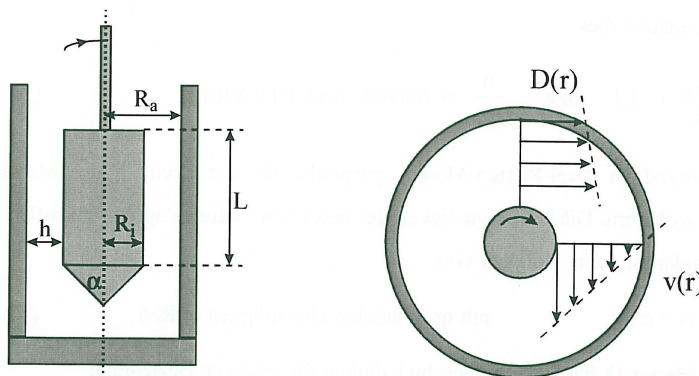
Pict. 10.7.2.10: Cylinder geometry, DIN 530199

Cylinder surface area A = 2 * π * r * L   with r the distance of the fluid from the axis

Driving force F = M / r   with M the applied external moment

Shear stress τ (r) = F / A = M / (2 * π * r^2 * L)

DIN 53019: R_a / R_i = 1,1   and h / R_a = 0,0909

Circumferential speed v(r) = ω * r   with ω in rad

Shear speed $D(r) = v / h = (1/r^2) * \omega * (2*R_i^2*R_a^2)/(R_a^2 - R_i^2)$

Viscosity $\eta = \tau / D = (R_a^2 - R_i^2) / (4 *\pi*L* R_i^2*R_a^2)*(M/\omega)$

Drawing the shear speed γ against the viscosity η in double logarithmic scale the important parameters of a viscoelastic coating colour can be described by the regression of Oswald (pict. 10.7.2.11).
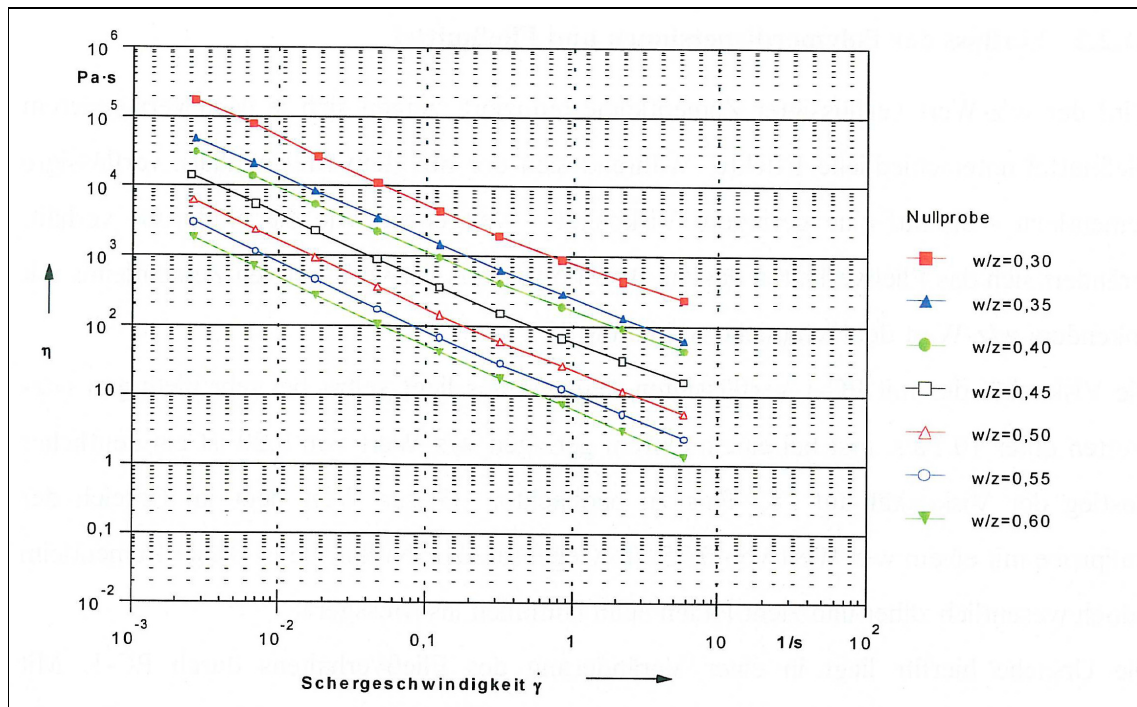
Pict. 10.7.2.11: Viscosity vs shear rate

Regression of Ostwald: $\ln(\eta) = a + b * \ln(\gamma)$ with a the viscosity [Pas] at $\gamma = 1$ sec^{-1} and b the gradient of the regression line [Pa*s^2], describing the structure viscosity. Low negative values of structure viscosity stand for low gradient of viscosity curve and typical structure viscous behaviour.

w/z-Wert	Viskosität [Pa·s]	Strukturviskosität [Pa·s^2]
0,30	825	-0,88
0,35	250	-0,88
0,40	169	-0,86
0,45	61,5	-0,89
0,50	23,1	-0,92
0,55	10,6	-0,93
0,60	6,18	-0,94

Different coating colours are currently most often compared as a single medium. The measured rheology parameters with the previously described methods are:

- Solids content
- pH
- Low and high shear viscosity
- Static water retention
- G' and G'' – elasticity and storage modulus

Thickeners are commonly used to increase coating colour viscosity. Unfortunately almost all current coating colour thickeners based on sustainable or synthetic chemistry raise in parallel high shear viscosity and in consequence blade pressure.

When mottle has to be improved the static water retention by Abo-GWR (see chapter "water retention" or the low shear viscosity of the coating colour is raised by increasing amount of thickener at a given limit of high shear viscosity.

An example of a "historical" lab study is shown in pict. 10.7.2.12 and 10.7.2.13.

Middle coat OMC11, Solids = 68 %

Middle coat OMC11, solids = 68 %
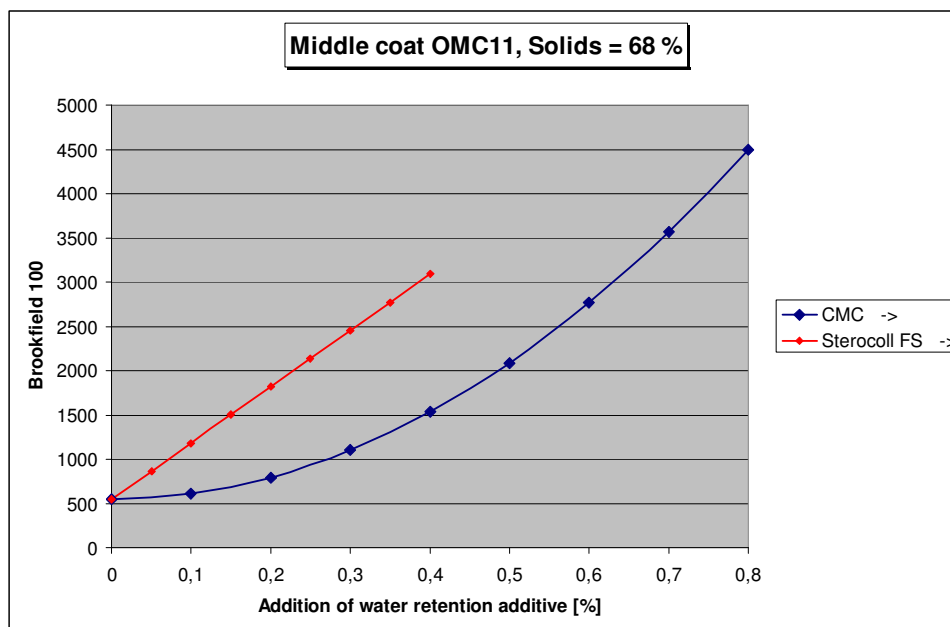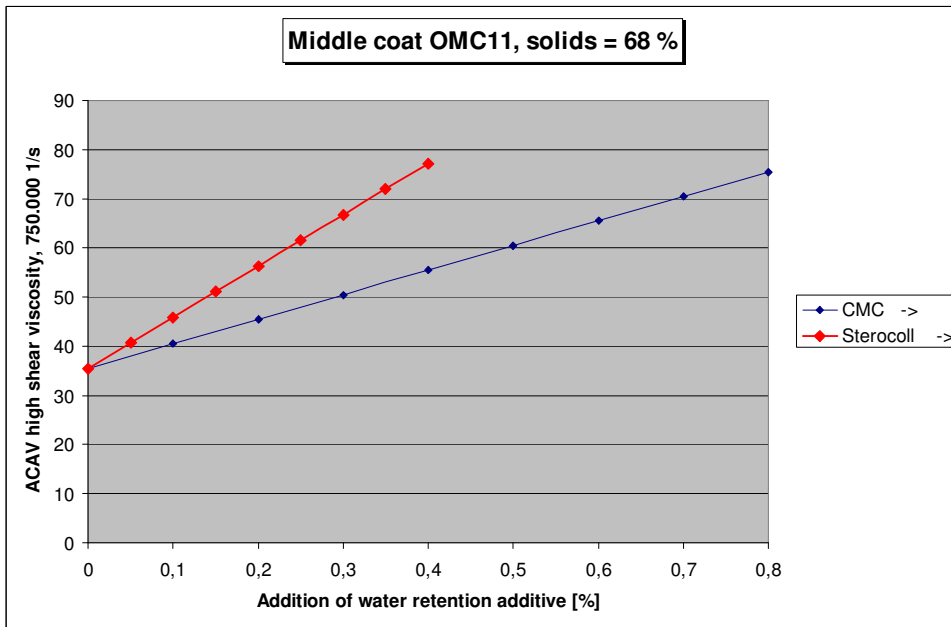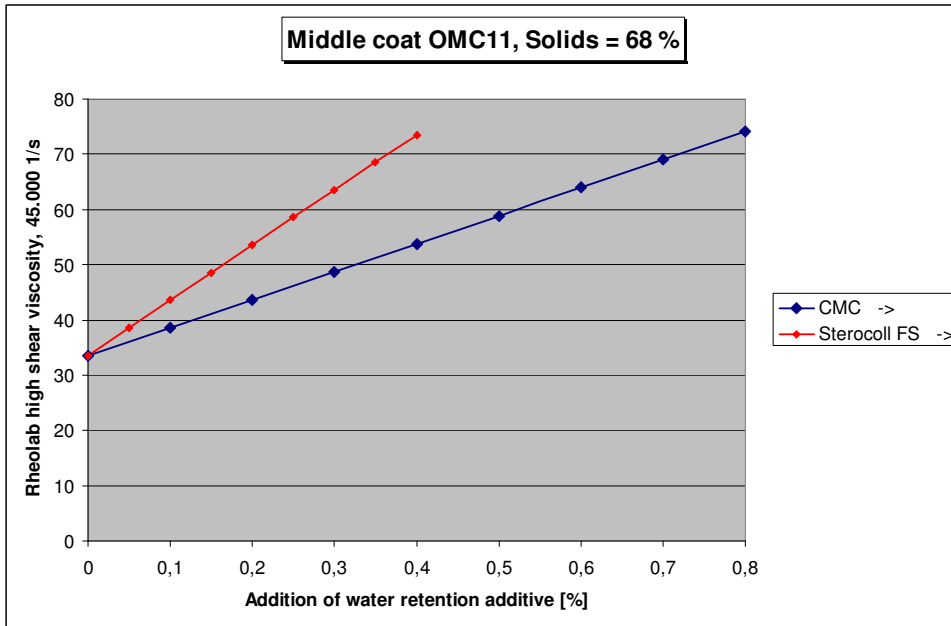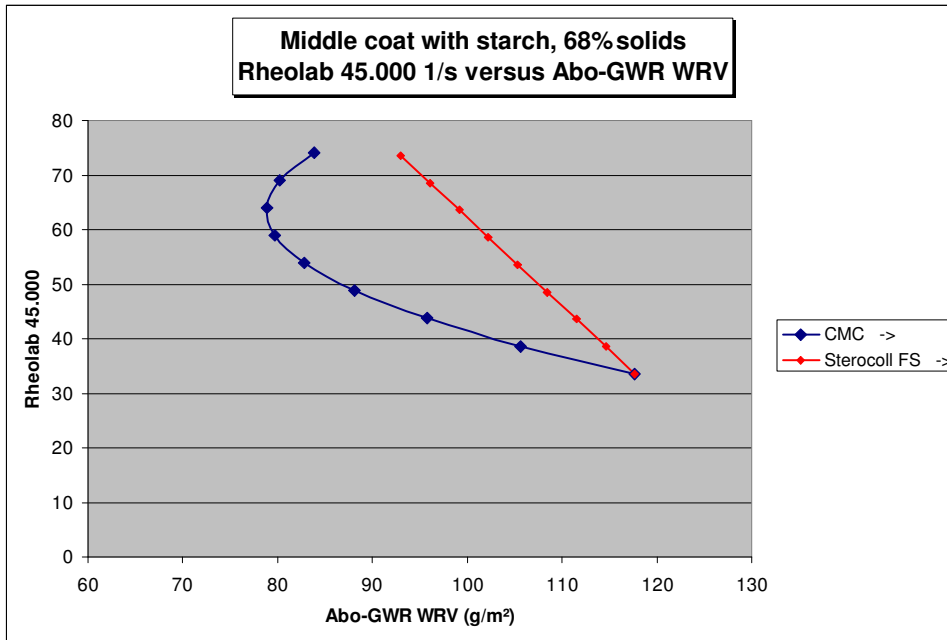
Pict. 10.7.2.12: Example of middle coat rheology study
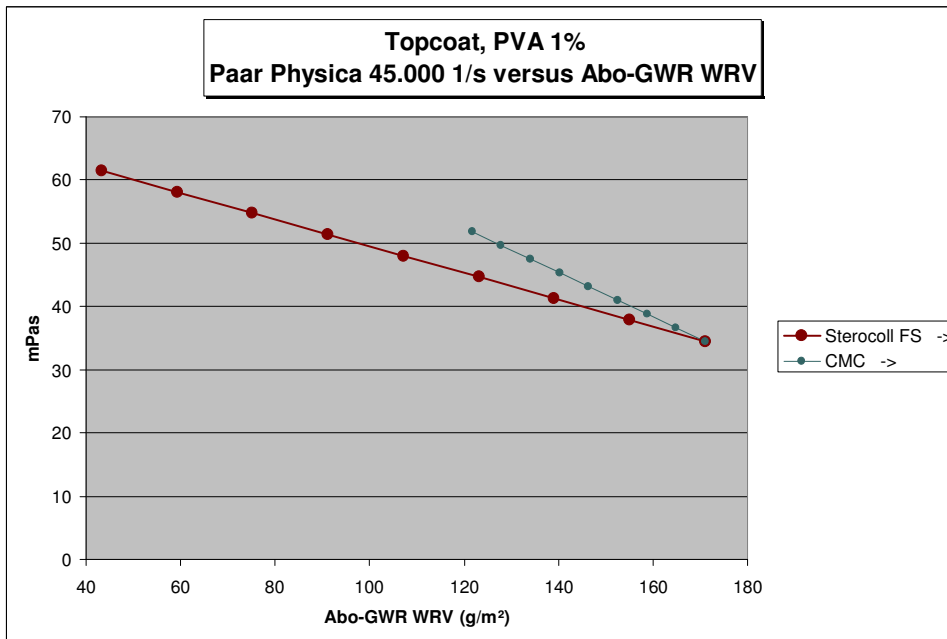
Pict. 10.7.2.13: Example of topcoat optimization – water retention versus high shear viscosity

In this lab study the synthetic water retention additive Sterocoll FS would be the better choice for the top coat as it has higher water retention at a given high shear viscosity against CMC.

In the middle coat the result is surprisingly the opposite.

The reason for these "unreasonable" results lays in the **interaction of the coating colour ingredients**.

Coating colour low shear viscosity is a function of liquid phase viscosity added by interaction of coating colour components (e.g. depletion flocculation of pigments by reaction with its hydration layer or interaction with latex particles).

Depletion flocculation which leads to raising blade pressure or drop in gloss is principally unwanted especially when the amount of thickener would be reduced for these reasons.

When cationic or anionic ions attack the hydration layer of the pigment and reduce its thickness depletion flocculation occurs. This kind of flocculation is reversible and sensitive against shear. Depletion flocculation of carbonate slurries was strong when highly ionic additives were used like caustic soda (fig. 11). Some latices[20] also contain a high amount of acidic ions in their liquid phase which cause depletion flocculation (fig. 12). They can be detected by nanofiltration, GC separation and conductivity measurement.

10.7.3 Depletion flocculation

Pigments are dispersed in water by adding dispersants like poly-acrylates which create a hydration layer at the pigment surface. The hydrophobic chain end is bound at the surface of the pigment and the opposite end of the polymer, which is hydrophilic, is oriented into the water phase around the pigment. Dispersants like poly-acrylates absorb high amounts of water at the hydrophilic chain ends. A thick hydration layer is formed around the pigment. According to OMYA this layer has a thickness of 20 nm. The hydration layer prevents collision of pigment particles in slurries with high pigment volume concentration.

Depletion flocculation can be produced by raising the level of dispersant over the threshold of minimum slurry viscosity (pict. 10.7.3.1, 10.7.3.2 and 10.7.3.4). The dispersant cannot be absorbed anymore on the pigment surface as it is already

totally covered with bounded dispersant. The excess of dispersant is moving into the liquid phase. Na-ions of free dispersant exchange the Na-ions of bounded dispersant on the pigment surface, thickness of hydration layer drops and viscosity of the pigment slurry increases.
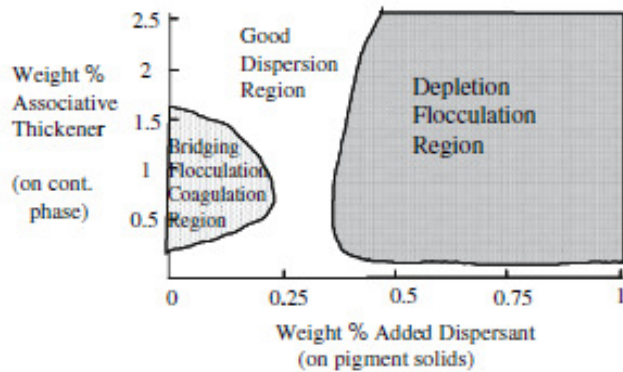
Pict. 10.7.3.1: Dispersion phase diagram (DPD) of pigment slurries
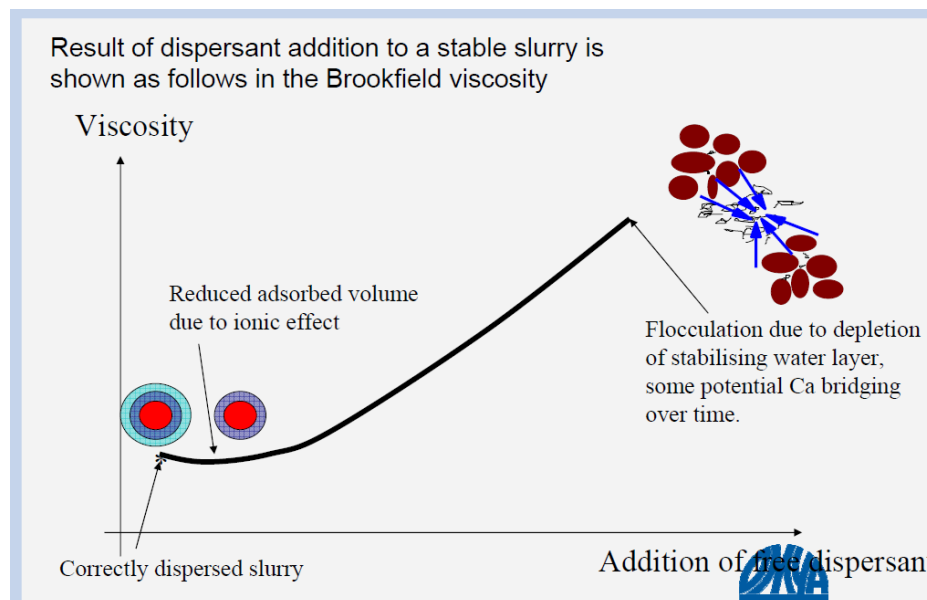
Pict. 10.7.3.2: Destruction of hydration layer of carbonate slurry by adding dispersant (source: OMYA)

The same destabilisation of pigment slurry takes place when pH drops (e.g. by biological contamination) and free cationic calcium ions from dissolved carbonate attack the hydration layer at the pigment (pict. 10.7.3.3). Ionic reaction between calcium ions and Na ions in the hydration layer reduces thickness of hydration layer and viscosity of pigment slurry increases.
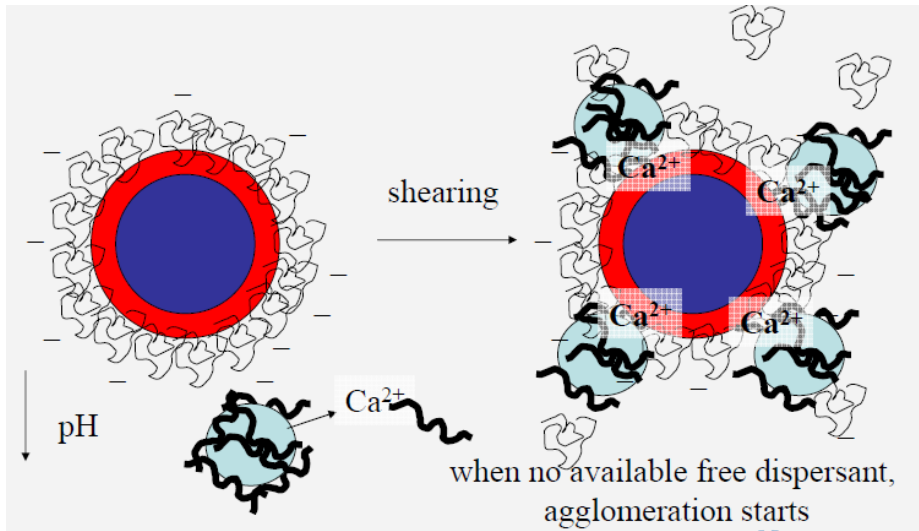
Pict. 10.7.3.3: Depletion flocculation by cationic ions (source: OMYA)
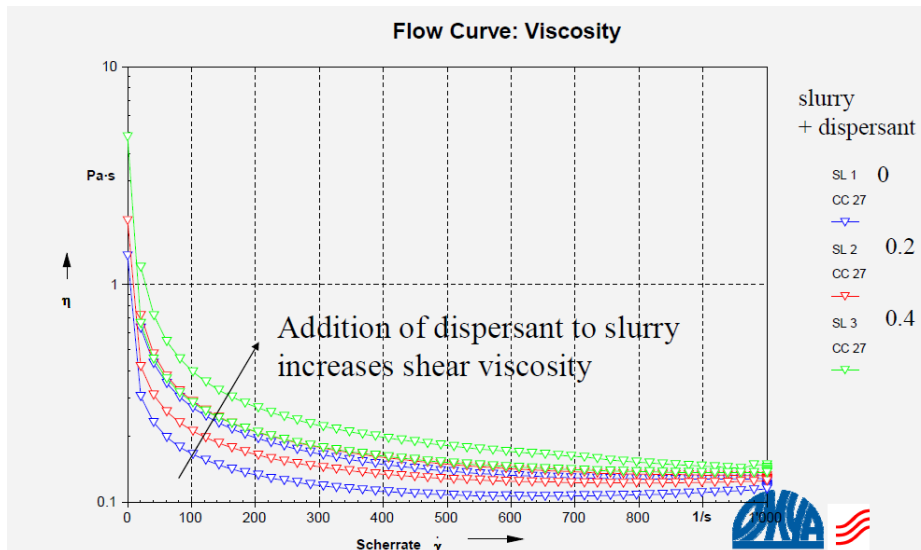
Pict. 10.7.3.4: Increase in viscosity by destroying the pigment dispersion (source: OMYA) – viscosity η (Pa s) versus shear rate γ (1/s)
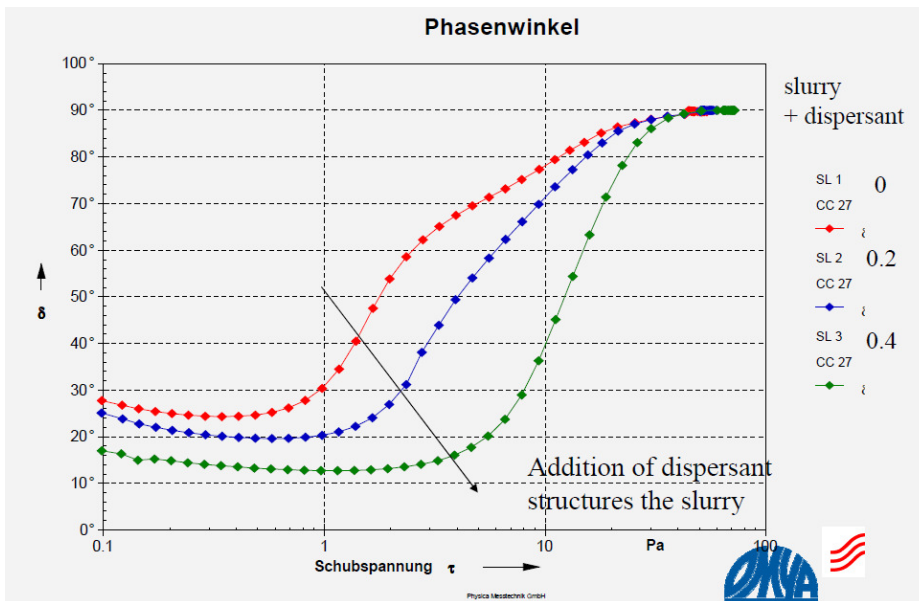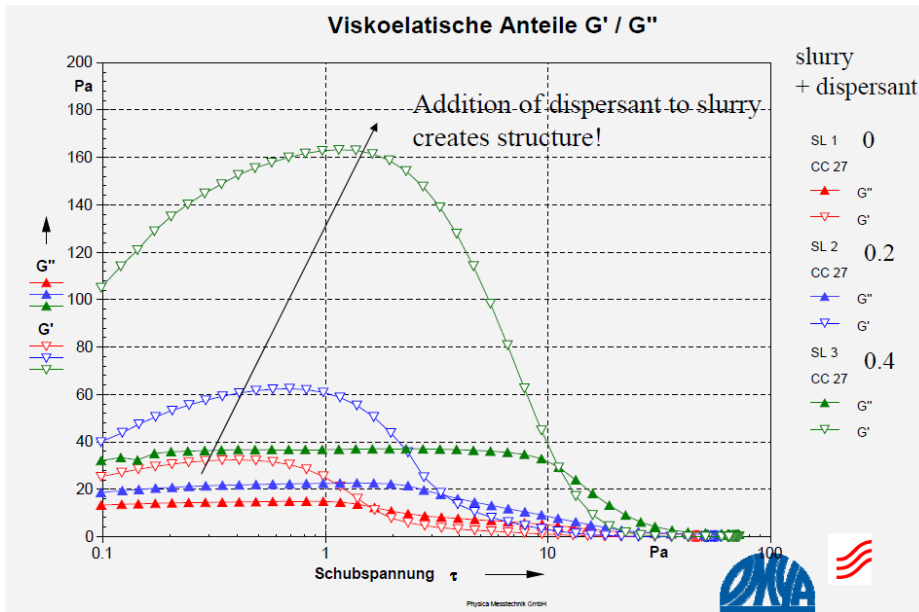
Pict. 10.7.3.5: Increase in elasticity by destroying the pigment dispersion (source: OMYA)

Depletion flocculation can be detected by G' and G'' measurements as it creates structure and G' raises while δ falls. Increasing the shear rate destroys this structure (pict. 10.7.3.5).

Depletion flocculation by caustic soda:

One of the best examples of severe interaction of coating colour components with pigment hydration layer is the reaction of concentrated caustic soda which is used to adjust the pH in coating colours.

The Na-ions of caustic soda exchange the Na-ions of poly-acrylate in the pigment hydration layer. Destroying the outer layers of the hydration envelope leads to reversible depletion flocculation. When extra dispersant is added, the viscosity drops and the original status is reached.

The pH of calcium carbonate dominated coating colours is kept over 8,5 to avoid formation of Ca-ions. Caustic soda is added to adjust the pH.

Sometimes coaters operate at pH of 9,5 – 11 to reduce bacterial contamination in the coating colour or to improve the performance of synthetic water retention additives. Rheology measurements were made for a calcium carbonate based precoating colour with increased amounts of caustic soda to show the effect of depletion flocculation.
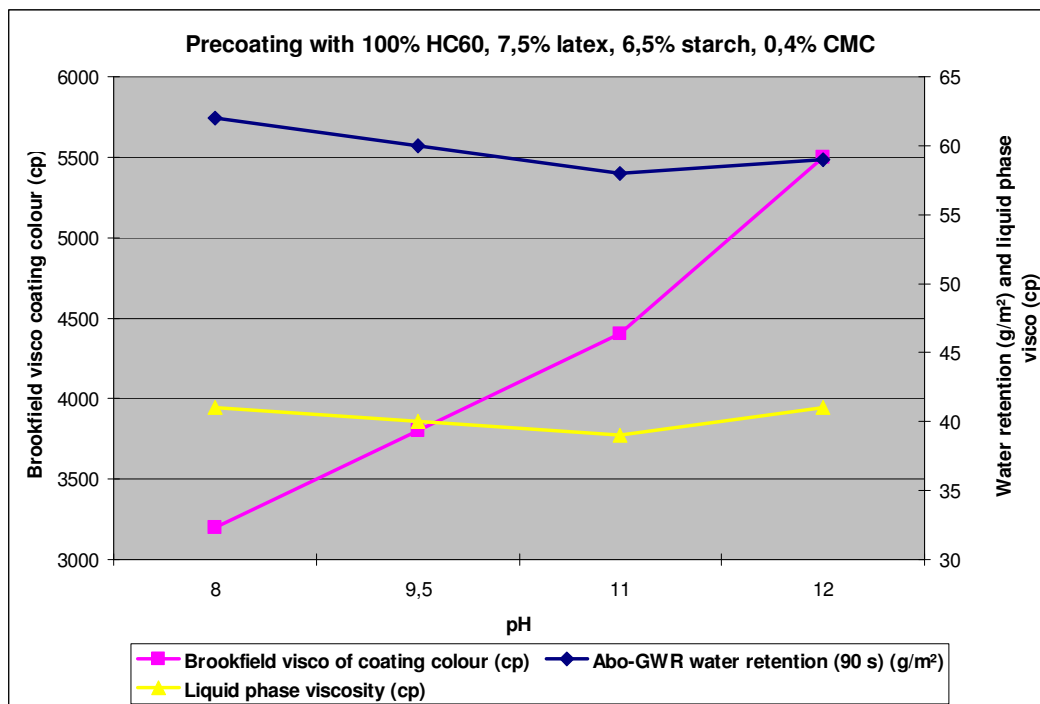
Pict. 10.7.3.6: Coating colour viscosity, liquid phase viscosity and water retention of a precoating colour with increasing amount of NaOH

Pict. 10.7.3.6 shows that caustic soda doesn't contribute to liquid phase viscosity but it increases coating colour viscosity by depletion flocculation of the pigment (Na exchange in hydration layer).

If caustic soda is added in a highly concentrated form with 20 - 50% solids as shown in pict. 10.7.3.7 (left), the hydration layer of almost all electro-statically stabilized pigment particles is immediately destroyed and pigment depletion flocculation is the consequence:

Pict. 10.7.3.7: Creation of pigment agglomerates by contact with too concentrated amount of caustic soda – residues on 45 µm screen (source: OMYA)

Haake high shear rheology of precoating with increasing pH

Legend:
- V40 - pH 8, solids 67,2%, visco 3200 cp
- V42 - pH 11,2, solids 67,3%, visco 4450 cp
- V43 - pH 12,1, solids 67,2%, visco 5560 cp
- V41 - pH 9,6, solids 67,2%, visco 3800 cp

Axes: Viscosity (Pa*s) vs Shear rate (1/s)
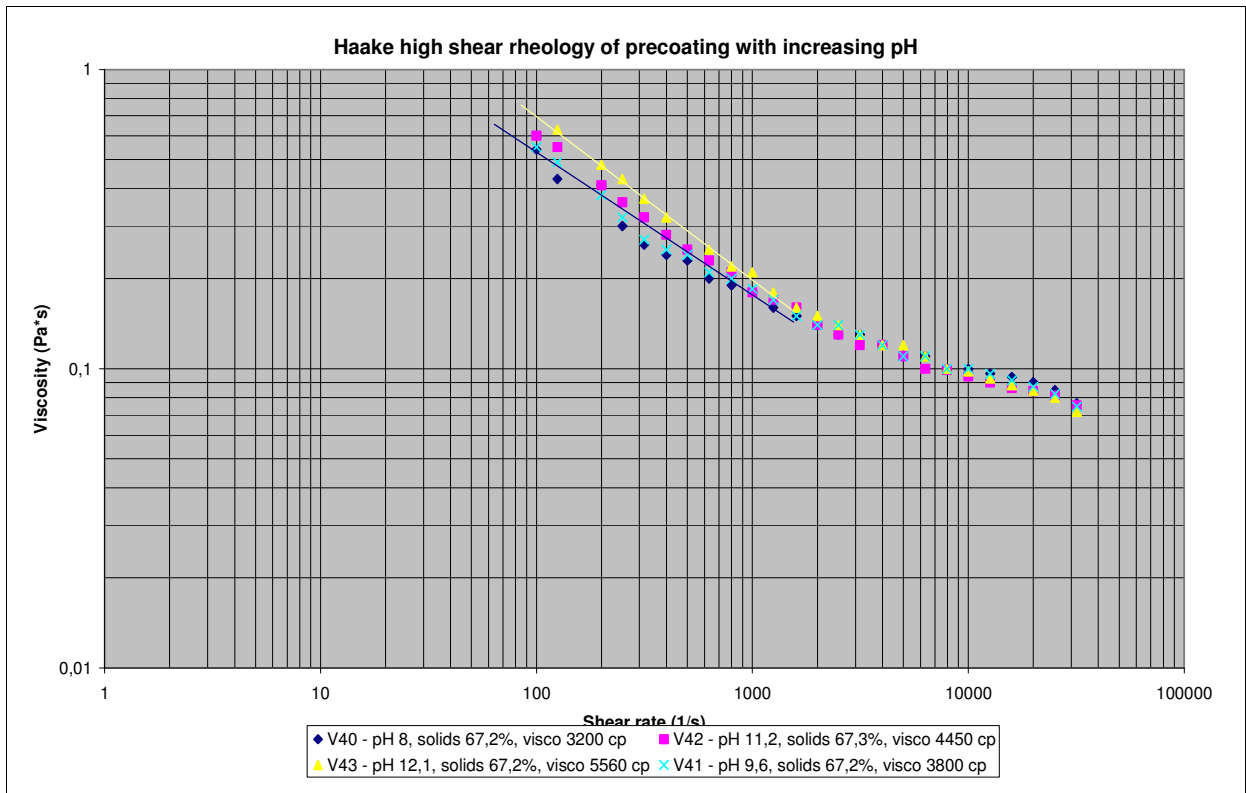
Pict. 10.7.3.8: Coating colour structure viscosity with increasing amount of amount of caustic soda

The replacement of Na-ions in the hydration layer of carbonate particles when caustic soda is added leads to a pigment floc structure, which is easily destroyed by shear forces. Structure viscosity (gradient in γ – η – diagram) increases.

Pict. 10.7.3.8 shows ACAV viscosity measurement with increasing shear. At low shear rate viscosity of flocculated coating colour with high pH is clearly higher but this structure is destroyed with increasing shear rate.
In contrast to this measurement a significant drop in blade load was observed at OMC11 when coating colour pH was reduced by lowering caustic soda as shown in pict. 10.7.3.9 and 10.7.3.10.

Pict. 10.7.3.9: Viscosity and blade load of middle coaters at OMC11 decreasing amount of caustic soda

Lowering the pH of the middle coat from 10-11 to 8-9 led to a drop in low- and high shear viscosity of 30% and in blade load of 20%!
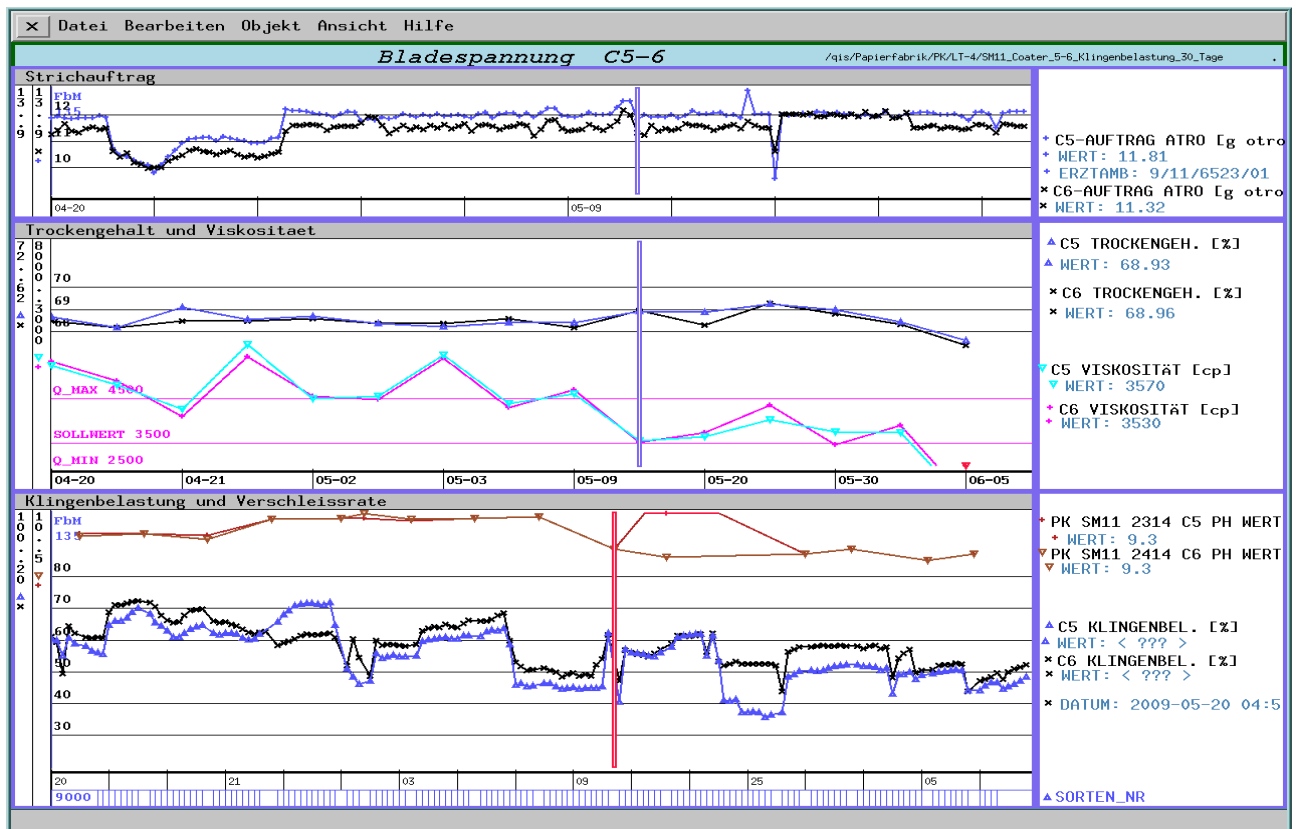
Pict. 10.7.3.10: Decrease in blade load by reducing the amount of caustic soda amount in top coaters OMC11

The fact that blade pressure at high speed coater dropped with lower amount of caustic soda and less depletion flocculation stays in contradiction to the fact that this depletion flocculation should be destroyed by the shear forces before the blade tip. The VOF simulations (see pict. 10.7.6.7) showed a shear rate of 10^5 1/s before the blade tip and the ACAV viscosity measurements demonstrated no difference in viscosity of top coating colour at this shear rate.

The reason for this conflict can be the thixotropic behaviour of the coating colour: Shear time before the blade is with 0,047 msec very short while rheology measurements by ACAV are made with much longer periods of shear. Therefore the flocculated structure of the coating colour might break down in mill coaters to a lower extend than in viscosimeters.

To reduce depletion flocculation of carbonate based coatings, caustic soda was replaced by an alternative anionic substance which was clearly lower in interaction with hydration layer of carbonates. Trials with the new anionic component were successfully performed in precoat of PM11 where solid content in the make down is high (up to 74%) and depletion flocculation was always an issue (pict. 10.7.3.11).

Strich:		VS 115	Versuch 199
FS	%	67,4	67,2
pH	1	9,5	9,9
T	°C	32	36,5
BF 100	mPa.s	810	662
BF 20	mPa.s	2280	1970
Spindel Nr.	1	4	4

Rez.115	pH	TRG.%	Brookfield low-shear cp			Haake high-shear (mPas)			WRV
			100U/min	50U/min	20U/min	10000[1/s]	20000[1/s]	40000[1/s]	
Standard	9,6	67,45	916	1356	2470	95	90	----	59,05
Trial **	9,85	67,15	702	1076	2020	84,5	77	55	81,75

Pict. 10.7.3.11: Trial with new product for increasing pH without depletion flocculation of $CaCO_3$

Depletion flocculation by latices:

Unfortunately almost all highly ionic coating colour components show interaction with the dispersant on the pigment surface and some also with each other.

Well described in literature is the reaction of acidic ions in the liquid phase of latices with dispersant in pigment hydration layer (similar to Ca^{++} interaction). After polymerisation a certain amount of acidic ions remains in the serum of all commercially available latices.

These acidic ions create depletion flocculation when a sufficient high amount of latex is mixed with pigment slurry. For experiments 20 vol% of latex were added to the pigment slurry which corresponds to 10% in mass.
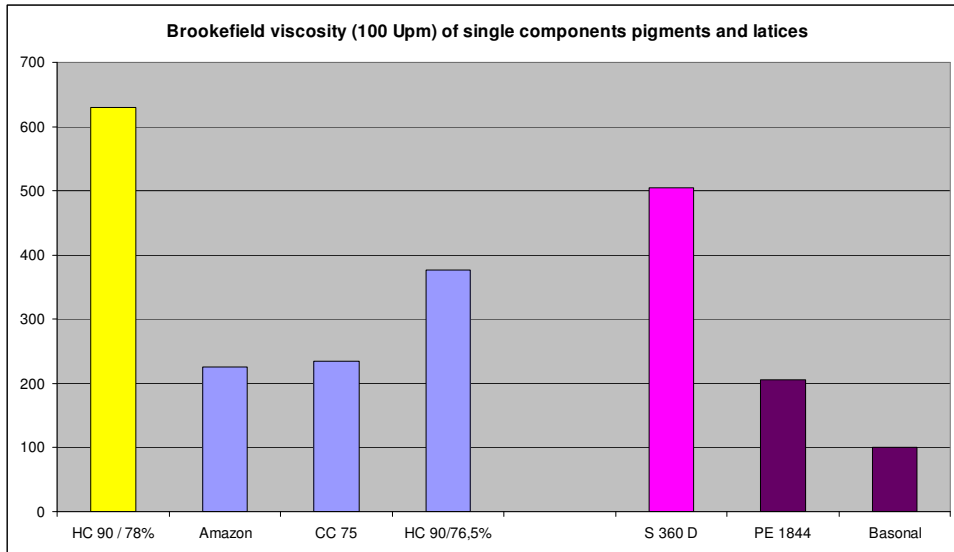
Pict. 10.7.3.12: Viscosity of pigment and latex alone
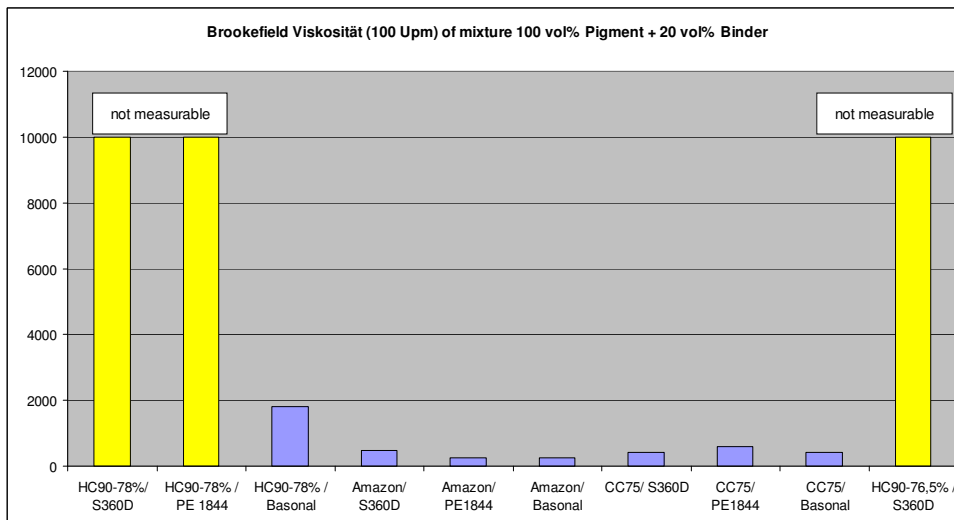
Pict. 10.7.3.13: Increase of pigment slurry viscosity by mixing binder with pigment

The results in pict. 10.7.3.12 and 10.7.3.13 show that latices with high amount of acidic ions in the serum like the SA-latex S360D and the SB-latex PE1844 strongly interact with pigment particles. The SB-latex Basonal 2296.01 with lower ion concentration in the serum (see conductivity measurements) was clearly lower in viscosity of the mixture latex + pigment.

In this lab study the interaction between latices and pigment is more severe for Hydrocarb 90 than for the other tested pigments due to a thinner hydration layer on the surface of HC90. The thicker the hydration layer, the more stable the pigment is against ion attack.

To measure ion concentration in the liquid phase of coating colour components, the liquid phase was removed by nano-filtration. With help of a GC the cationic and anionic ions were separated in the liquid phase. The ion concentration was measured by conductivity.
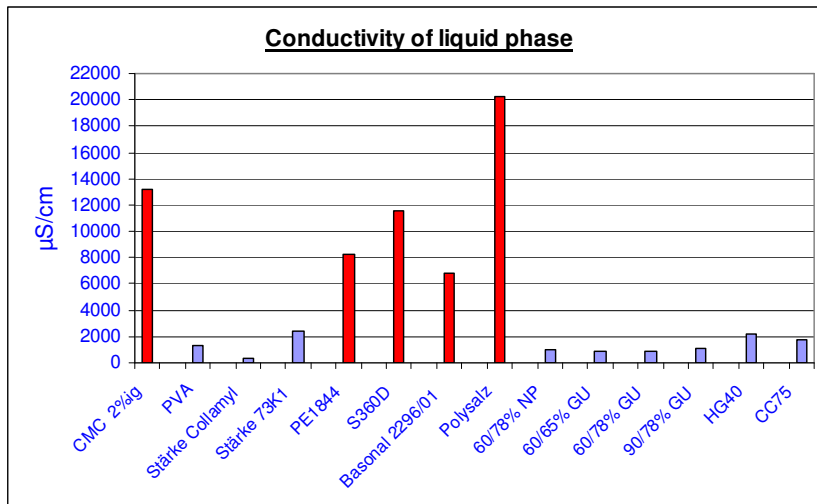
Pict. 10.7.3.14: Liquid phase conductivity of selected coating colour components
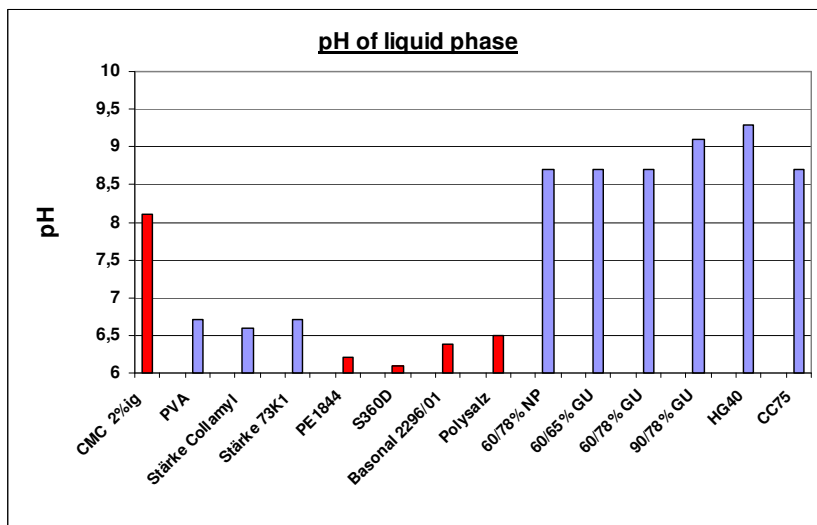
Pict. 10.3.7.15: Liquid phase pH of coating components

Pict. 10.3.5.14 and 15 show remarkable concentration of anions in synthetic thickeners, CMC and in dispersants (e.g. polyacrylate). All create depletion flocculation of carbonate slurries.

Low concentrations of Ca- ions were found some starches and in pigment slurries depending on history of biological contamination and process water used in their production.

It was observed that HC60-NP from OMYA-Neupirka was more stable against acidic ions than HC60-GU from Gummern due to a lower hardness of the process water in Neupirka.

In literature L1.68 J.C. Husband from Imerys investigated the interaction between ground calcium carbonate pigments and polymer latices (pict. 10.7.3.16).
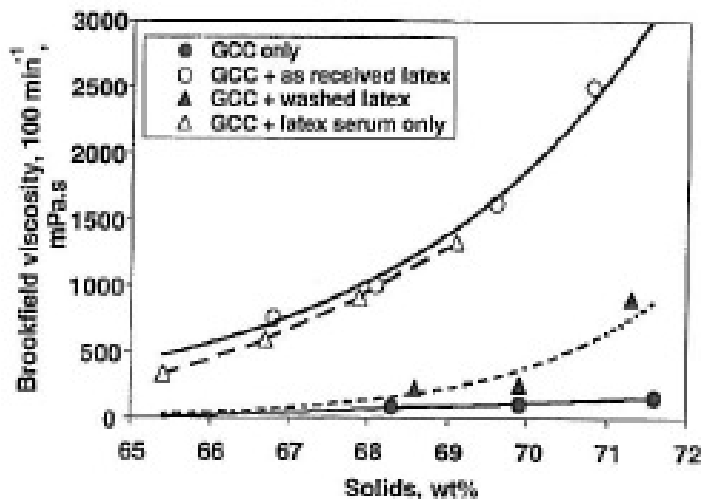
Pict. 10.7.3.16: Depletion flocculation by latex (J.C. Husband)
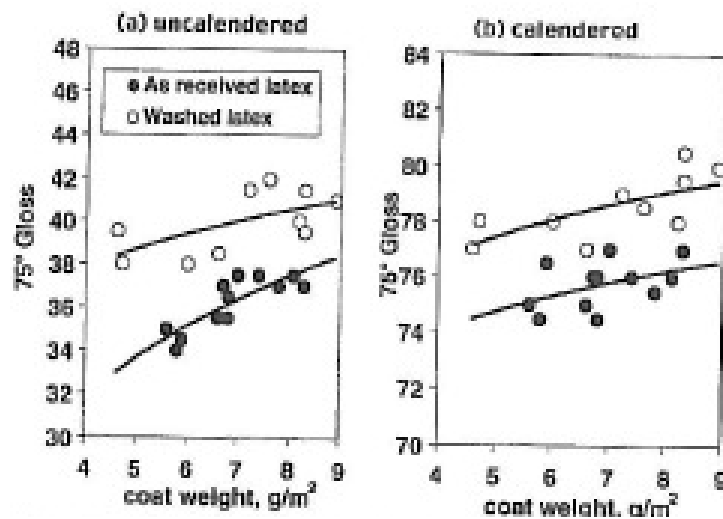
Pict. 10.7.3.17: Gloss of calendered paper (J.C. Husband)

Gloss dropped when latices with high concentration of acidic ions in liquid phase were used in a glossy top coating colour (pict. 10.7.3.17). When ions were removed from latex by nano-filtration and latex was diluted again with ion free water, calendered gloss of coatings based on this ion-free latex was much higher than for the coating with the original latex (pict. 10.7.3.18).
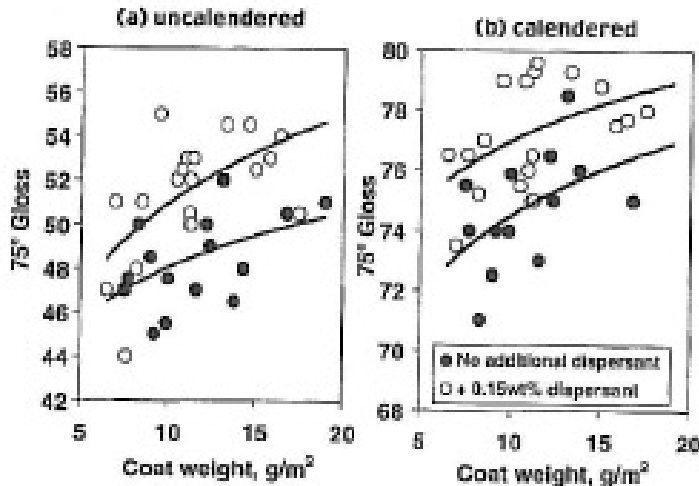
Pict. 10.7.3.18: Gloss after addition of dispersant (J.C. Husband)

As depletion flocculation is a reversible process the addition of poly-acrylate dispersant (Polysalt-S) to the coating colour with the original latex restored the hydration layer at the pigment and gloss was as high as for the coating based on the ion free latex.

The examples of depletion flocculation by caustic soda or latex show that it is not sufficient in lab studies to predict penetration of liquid phase by the low shear viscosity of the coating colour as **the low shear viscosity is an addition of liquid phase viscosity and interaction between all coating colour components.** These two mechanisms have to be separated, when lab studies for mottling improvement, e.g. by different thickeners are made.

10.7.4 Comparing the measured Brookfield low shear viscosity with the calculated viscosity from the Einstein / Hatschek equation

Viscosity of a two phase system is defined by the original Einstein's law.

$$\eta_{rel} = \frac{\eta_c}{\eta_l} = (1 + 2,5 * \varphi + 6,2 * \varphi^2),$$

where η_{rel} is the relative viscosity (dimensionless), η_c is the measured viscosity of the two phase system (coating colour), η_l is the liquid phase viscosity and φ is the volume phase of the solid particles.

If more types of solid components are added, e.g. pigment and latex, φ is the sum of it (e.g. $\varphi = \varphi_{pigm} + \varphi_{latex}$).

Hatschek measured the viscosity η_c of slurries at different volume concentrations and compared the results with Einstein's law $\eta_c = (1 + 2,5 * \varphi + 6,2 * \varphi^2) * \eta_l$. Different particles (sugar,..) were used and different liquid phase viscosities η_0 were tested. He found that measured viscosities of the two-phase slurries he used showed huge deviations to the equation $\eta_c = (1 + 2,5 * \varphi + 6,2 * \varphi^2) * \eta_l$ but the original law of Einstein

$\frac{\eta_c}{\eta_l} = \frac{1 + 0,5 * \varphi}{(1 - \varphi)^4}$ correlated well with the measured viscosities η_c.

The same result is found for carbonate slurries in this study.
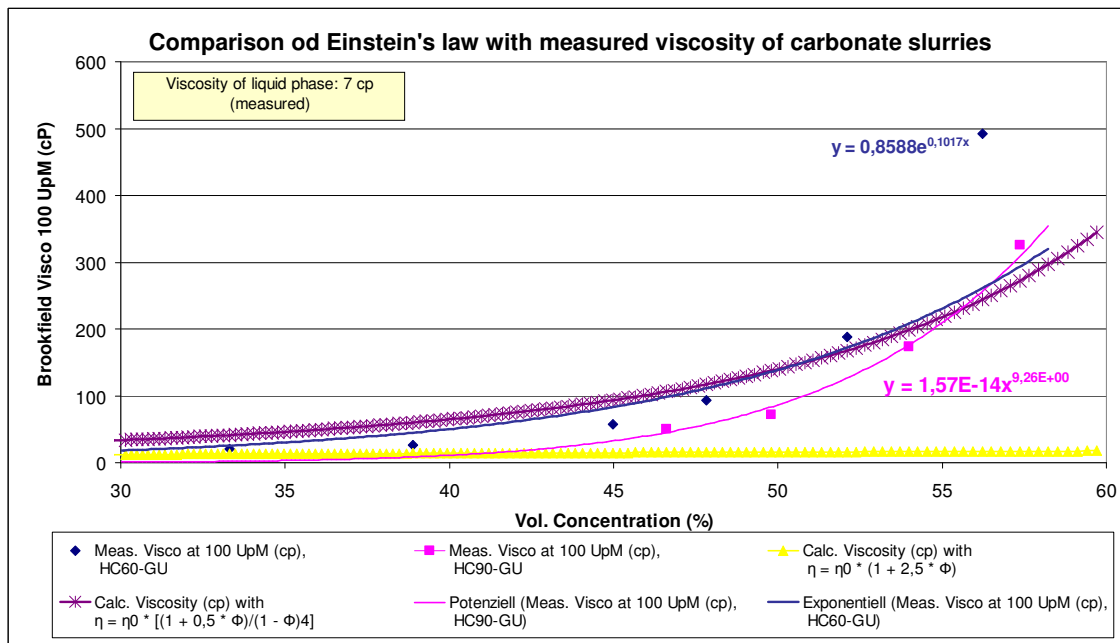
Pict. 10.7.4.1: Comparing Einstein's law to measured viscosity of pigment slurry HC60/HC90

Solid content was changed by diluting the pigment slurries. Measured Brookfield viscosity correlated well with calculated viscosity from the original Einstein equation as shown in pict. 10.7.4.1.

Comparison of Einstein's law with measured viscosity of slurries and colours

Measured viscosity of liquid phase in:
HC60-NP: 5 cp
Starch + water: 30 cp

Einstein's law:

$$\frac{\eta_c}{\eta_l} = \frac{1 + 0.5 * \varphi}{(1 - \varphi)^4}$$

HC60 + starch + NaOH

HC60 + starch

HC60

68% solids

Y-axis: Brookfield Visco 100 rpm (cp) of slurry/colour
X-axis: Vol. Concentration of pigment particles (%)

— Calc. Viscosity (cp) of HC60 with Einstein's law
— Meas. Visco at 100 UpM (cp), HC60-NP
— Calc. Viscosity (cp) of HC60 +10% starch with Einstein's law
— Meas. Visco at 100 UpM (cp), HC60 + 10% Dextrin 7333 starch
— Calc. Viscosity (cp) of HC60 +10% starch + NaOH for pH = 11,5 with Einstein's law
— Meas. Visco at 100 UpM (cp), HC60 + 10% Dextrin 7333 starch + NaOH for pH = 11,5

Pict. 10.7.4.2: Depletion flocculation by caustic soda

When cooked coating starch Dextrine 7333 was added to pre-dispersed dry pigment HC60, measured viscosity of coating was similar to calculated viscosity from Einstein's law as interaction between starch and pigment was again low (pict. 10.7.4.2).

Adding caustic soda to this coating led to viscosity measurements which were significantly higher than calculated viscosity from Einstein's law due to depletion flocculation.

10.7.5 Description of the new method to determine liquid phase viscosity

Part 1: Starch based colours

Liquid phase was prepared by adding to the calculated amount of free water in the coating colour to achieve 68% solids all soluble components. Dry HC60, which was wet ground at OMYA and pre-dispersed was used as pigment (pict. 10.7.5.1).

Liquid phase of starch based precoating colours consisted of:
- Free water to reach the target solids (pict. 10.7.5.2)
- Cooked Starch (regarded as soluble binder)
- Thickener
- PVA
- OBA

Viscosity of liquid phase was measured before the dry pigment was added.

Rohstoffname	FGH (%)	Dichte (g/cm³)	V70B Anteil (%)	g-atro	g-lutro	ml	V71B Anteil (%)	g-atro	g-lutro	ml	V72B Anteil (%)	g-atro	g-lutro	ml	V73B Anteil (%)	g-atro	g-lutro	ml
HC60-trocken	99	2,6	100	700	707	272	100	700	707	272	100	700	707	272	100	700	707	272
HC60-NP-Slurry	78	2	0	0	0	0	0	0	0	0	0	0	0	0	0	0	0	0
HC90-GU-Slurry	78	2	0	0	0	0	0	0	0	0	0	0	0	0	0	0	0	0
Dextrin 7333	36	1,15	10	70	194	169	0	0	0	0	0	0	0	0	0	0	0	0
Dextrin 73K1	38	1,17	0	0	0	0	10	70	184	157	0	0	0	0	0	0	0	0
Enzym. Starch	30	1,12	0	0	0	0	0	0	0	0	10	70	233	208	0	0	0	0
PVA, cooked	22	1,1	0	0	0	0	0	0	0	0	0	0	0	0	1,5	10,5	48	43
Water					230	230			240	240			190	190			290	290
Summe:					1132	671			1131	669			1130	670			1045	605
Calculated solid content:			68,1				68,1				68,1				68,0			

Pict. 10.7.5.1: Calculation of liquid phase and soluble binders

Rohstoffname	FGH (%)	Dichte (g/cm³)	V70 Anteil (%)	g-atro	g-lutro	ml	V71 Anteil (%)	g-atro	g-lutro	ml	V72 Anteil (%)	g-atro	g-lutro	ml	V73 Anteil (%)	g-atro	g-lutro	ml
HC60-trocken	99	2,6	0	0	0	0	0	0	0	0	0	0	0	0	0	0	0	0
HC60-NP-Slurry	78	2	100	700	897	449	100	700	897	449	100	700	897	449	100	700	897	449
HC90-GU-Slurry	78	2	0	0	0	0	0	0	0	0	0	0	0	0	0	0	0	0
Dextrin 7333	36	1,15	10	70	194	169	0	0	0	0	0	0	0	0	10	70	194	169
Dextrin 73K1	38	1,17	0	0	0	0	10	70	184	157	0	0	0	0	0	0	0	0
Enzym. Starch	30	1,12	0	0	0	0	0	0	0	0	10	70	233	208	0	0	0	0
PVA, cooked	22	1,1	0	0	0	0	0	0	0	0	0	0	0	0	1,5	10,5	48	43
Water					40	40			50	50			0	0			7	7
Summe:					1132	658			1132	656			1131	657			1147	668
Calculated solid content:			68,0				68,0				68,1				68,1			

Pict. 10.7.5.2: Calculation of complete coating colour

The rheology of the complete coating colour was determined by measuring Brookfield viscosity, Haake high shear viscosity, elasticity, pH and solid content. These parameters were compared to liquid phase viscosity (pict. 10.7.5.3).

Rohstoffname	FGH (%)	Dichte (g/cm³)	V70 Anteil (%)	g-atro	g-lutro	ml	V71 Anteil (%)	g-atro	g-lutro	ml	V72 Anteil (%)	g-atro	g-lutro	ml	V73 Anteil (%)	g-atro	g-lutro	ml
HC60-trocken	99	2,6	0	0	0	0	0	0	0	0	0	0	0	0	0	0	0	0
HC60-NP-Slurry	78	2	100	700	897	449	100	700	897	449	100	700	897	449	100	700	897	449
HC90-GU-Slurry	78	2	0	0	0	0	0	0	0	0	0	0	0	0	0	0	0	0
Dextrin 7333 = VS1-Stärke PM9	36	1,15	10	70	194	169	0	0	0	0	0	0	0	0	10	70	194	169
Dextrin 73K1 - Jetstärke	38	1,17	0	0	0	0	10	70	184	157	0	0	0	0	0	0	0	0
Collamyl 9100 (enzym. St.)	30	1,12	0	0	0	0	0	0	0	0	10	70	233	208	0	0	0	0
PVA, gekocht	22	1,1	0	0	0	0	0	0	0	0	0	0	0	0	1,5	10,5	48	43
Tinopal APB-E	26,5	1,17	0	0	0	0	0	0	0	0	0	0	0	0	0	0	0	0
Polysalz	45	1,3	0	0	0	0	0	0	0	0	0	0	0	0	0	0	0	0
Entschäumer	21	1,3	0	0			0	0			0	0			0	0		
Latexia PE1844	50	1,2	0	0	0	0	0	0	0	0	0	0	0	0	0	0	0	0
SB256	50	1,2	0	0	0	0	0	0	0	0	0	0	0	0	0	0	0	0
Acronal S360D	50	1,2	0	0	0	0	0	0	0	0	0	0	0	0	0	0	0	0
Styronal 809 PM9	50	1,2	0	0	0	0	0	0	0	0	0	0	0	0	0	0	0	0
Basonal 2296.01	50	1,2	0	0	0	0	0	0	0	0	0	0	0	0	0	0	0	0
NaOH	50	1,4	0	0	0	0	0	0	0	0	0	0	0	0	0	0	0	0
Wasser					40	40			50	50			0	0			7	7
Summe:					1132	658			1132	656			1131	657			1147	668
Errechneter Feststoffgehalt:			68,0				68,0				68,1				68,1			

	10% Dextrin 7333	10% Dextrin 73K1	10% enz. Starch	1,5% PVA

Gemessene Werte Flüssigphase : — Flüssigphase = Wasser + Stärke / Flüssigphase = Wasser + Stärke

		V70	V71	V72	V73
Feststoffgehalt	%	16,14	16,54	16,21	3
pH		7,2	7,1	6,9	7,3
Brookfield-Viskosität (20 UpM):	cp	20	<10	25	30
Brookfield viscosity liquid phase (1	cp	32	18	44	15
Haakevisco 10.000 1/sec	cp 0.000 1/se	11,8	5,19	24,5	1,5
Haakevisco liquid phase (20.000 1/sec)	cp 0.000 1/se	8,56	3	19,9	0,5
Haakevisco 31.800 1/sec	cp 1.800 1/se	3,76	0,9	13,3	0,1
Haakevisco 40.000 1/sec	cp 0.000 1/se	2	0,2	7,98	0,005

Gemessene Werte des Striches:

		V70	V71	V72	V73
Feststoffgehalt	%	67,87	67,94	68,00	68,51
pH		8,7	8,6	8,7	8,7
Brookfield-Viskosität (20 UpM):	cp	220	85	580	2240
Brookfield-Viskosität (100 UpM):	cp	180	95	480	930
Haakevisco 10.000 1/sec	cp	95,6	73,8	220	170
Haakevisco coating colour (20.000 1/sec	cp	87,7	67,7	180	160
Haakevisco 31.800 1/sec	cp	72,4	56,6	-	-
Abo GWR bei 0,5 bar, 90 sec., 5 μm	g/m²	57,532	107,494	27,252	36,336
Abo GWR of coating colour at 2 bar, 10 s	g/m²	12,112	54,504	12,112	10,598

Pict. 10.7.5.3: Liquid phase and coating colour measurements

Part 2 - Latex based colours

For latex based coatings the previous method of preparing the complete liquid phase before adding the dry components couldn't be used as latex cannot be separated into its liquid and solid phase (pict. 10.7.5.2).

Therefore experiments were made in the lab to get the liquid phase from different latices and pigments by nano-filtration and measure them with Brookfield viscosity. The results showed that viscosity of these liquid phases was close to water as no soluble thickener is added during production of pigments of latices.

When latex based coatings were prepared, HC60 was added in slurry form and latex in its original form as dispersion.

The water in the liquid phase was calculated by adding:
- Calculated free water to achieve 68% solids
- Calculated water in the pigment slurry (78% solids)
- Calculated water in the latex (50% solids)

Remark: The free water in the pigment slurry has to be calculated by subtracting the water in the hydration layer from the overall water in the slurry measured by the solid content. According to OMYA the water in the hydration layer can be calculated from the measured immobilization point of the slurry – it corresponds to the water which is left in the pigment when the immobilization point is reached (pict. 10.7.5.4).

Solids (%)	Density (kg/m³)	Bone dry (g)	Slurry (g)	Slurry (ml)	Water in Slurry (g)	Vol conc. (%)	%
78	1,964	1000	1282	653	282	56,8	100
84,5	1,964	1000	1183	603	183	69,6	**65,0**

Pict. 10.7.5.4: Calculation of free water in HC60-NP Pigment slurry (immobilization solids: 84,5%)

Example: For HC60-NP slurry with 78% solids, 65% of the whole water is located in the hydration layer.

The liquid phase was completed by adding the investigated type of thickener and for some coatings soluble substances like PVOH and OBA

When interaction of different thickeners with pigment slurry has to be investigated depletion flocculation from latex ions should be avoided. For this lab study latex Basonal 2296.01 from BASF with ultra low interaction due to low ion concentration in liquid phase (see conductivity measurements) was used.

For theoretical comparisons a model latex was created by BASF where the serum was removed by nano-filtration and the latex was afterwards diluted by ion free water. Difference in depletion flocculation to Basonal 2296.01 was so small that the experiments were continued with Basonal 2296.01.

10.7.6 Results of pre-study with different thickeners

Beside the interaction of coating colour components with hydration layer of the pigment which leads to depletion flocculation the chain length and chain structure of additives has a big impact upon low shear viscosity of coating colour and high shear viscosity of the coating colour.
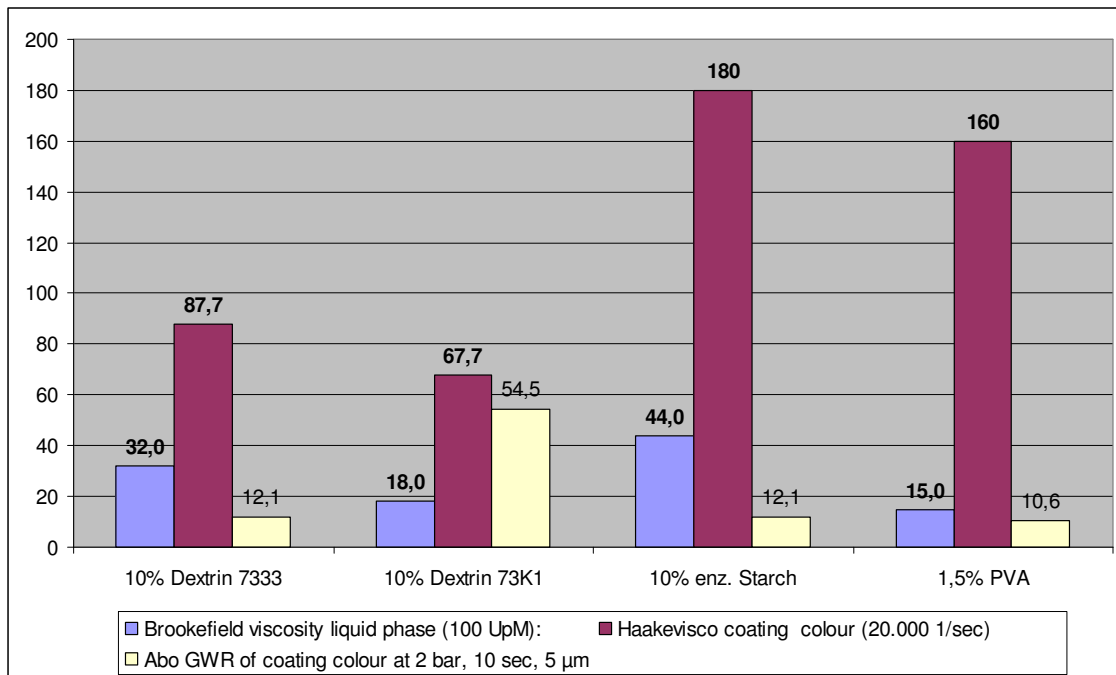
Pict. 10.7.6.1: Viscosity and water retention of HC60 based coatings with starch and extra PVOH (68% solids)
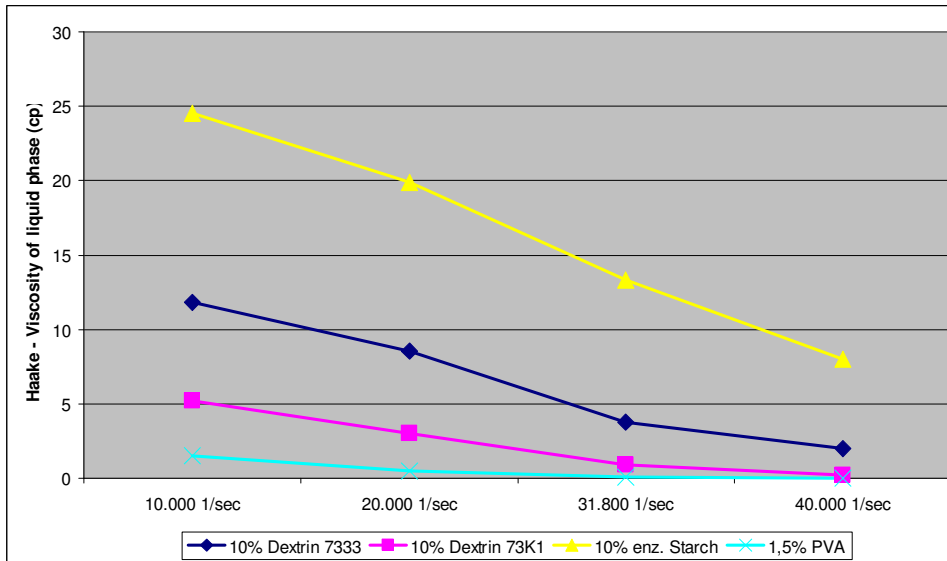
Pict. 10.7.6.2: Viscosity of liquid phase for coating colour with 68% solids (HC60 + 10% starch)

Pict. 10.7.6.1 and 10.7.6.2 show that replacing coating starch by PVOH increased high shear viscosity at comparable or lower liquid phase viscosity.

Polymer network structure of PVOH and its flocculation of pigment / latex particles breaks down slower under shear than that of purely starch based coatings. Structure viscosity (viscosity decreases with increasing shear) is less pronounced. Therefore high shear viscosity of PVOH based coating colour is much higher but liquid phase viscosity is lower.

The longer the molecular weight and the stronger the network structure of the thickener polymer molecules the higher the high shear viscosity of the coating colour will be.

A second pre-trial with starch based coatings (HC60 as pigment) was performed to compare liquid phase viscosity with coating colour rheology. Different thickeners were added to this precoating colour.
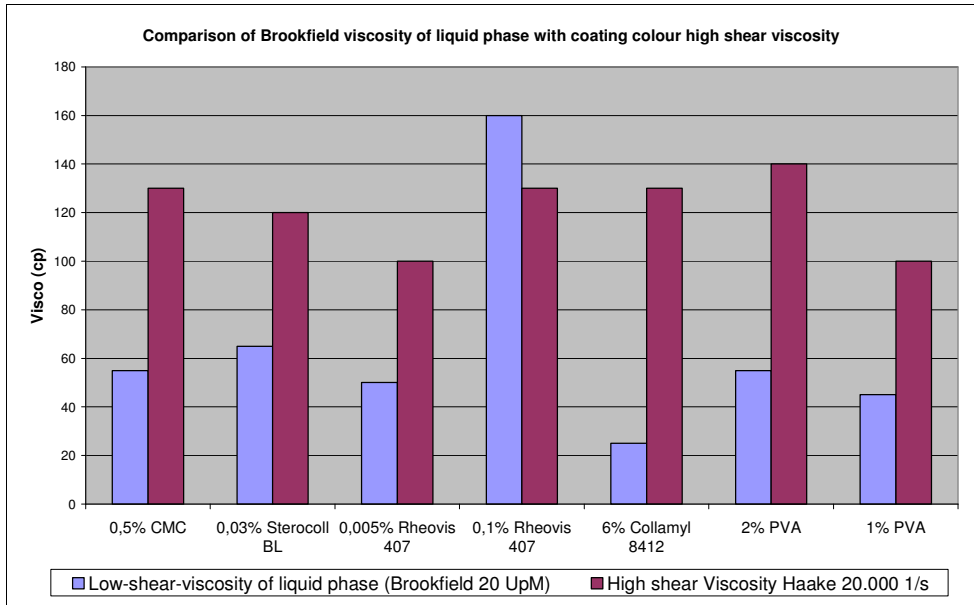
Pict. 10.7.6.3: Liquid phase viscosity (BF100) vs coating colour viscosity

HASE thickener Rheovis 407(pict. 10.7.7.6) gave the highest liquid phase viscosity at a given high shear viscosity (limited by blade pressure at high speed coater OMC11). Enzymatic starch Collamyl 8412 with high molecular weight and PVOH created the highest high shear viscosity in the coating colour at relatively low liquid phase viscosity (pict. 10.7.6.3).
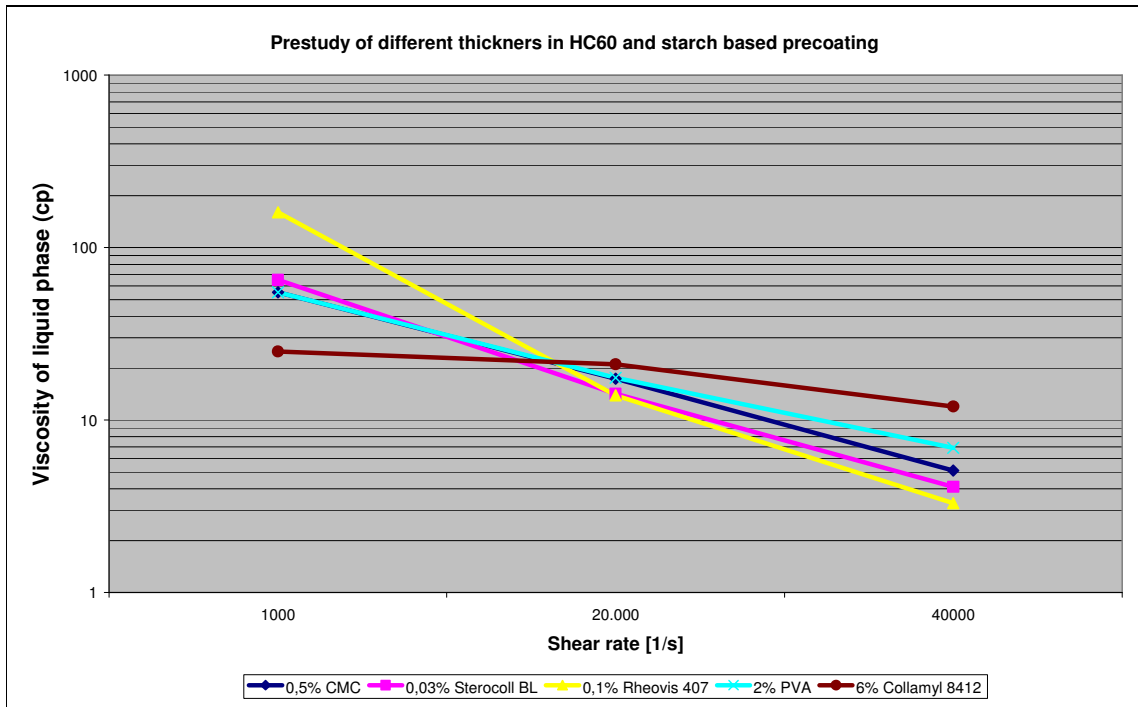
Pict. 10.7.6.4: Liquid phase viscosity (BF 100) as a function of shear rate
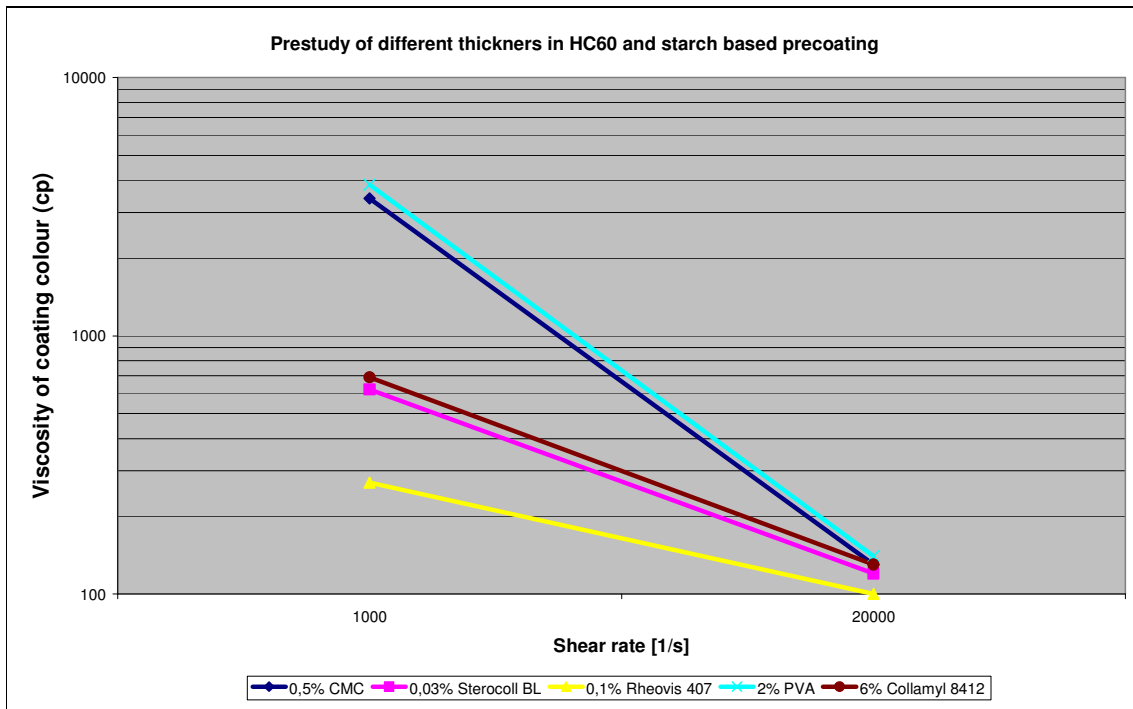
Pict. 10.7.6.5: Development of coating colour viscosity with increasing shear rate

All tested thickeners were highly structure viscous. Low shear viscosity in liquid phase (pict. 10.7.6.5) and coating colour (pict. 10.7.6.5) broke down fast under shear.

The ideal thickener is low in high shear viscosity of coating colour at high liquid phase viscosity. It shows either Newtonian behaviour – viscosity is independent from shear rate (no depletion flocculation of pigment) or highly pseudo plastic – structure from flocculation of pigment or latex particles breaks down fast under shear. Pict. 10.7.6.4 shows this behaviour for Rheovis 407.

To reduce ionic charge on the polymer surface which could interact with the hydration layer on the pigment new generations of HASE / HEUR thickeners are modified with hydrophobic molecules (see pict. 10.7.7.6 – 10).

If viscosity of coating colour is raised by flocculating pigment or latex particles the structure should break down as fast as possible under shear to reduce high shear viscosity and blade load. It has to be regained fast when shear is removed otherwise low shear viscosity in working tank would drop continuously with time.

Thickener	Chemistry	Solids (%)	Density (g/cm³)	pH	MW (Dalton)	Ions
PVOH Mowiol 4-98		20	1,07			
Encymatic corn starch Collamyl 8412		30	1,08			
Sterocoll BL	Water thickener in oil, linear	30	1		10^7	
BASF Sterocoll FS (F&E)	ASE (pH>8 in coating), linear,				10^6	acid
Clariant Cartacoat RM20	HASE	30	1,03			acid
CIBA Rheovis 401	HASE	39,3	1,1	**3,4**		acid
BASF Sterocoll PR8820 X	HASE, linear	26,5	1,05	**2,8**	10^7	acid
BASF Acrosol E20D	ASE with less carbon acid	50	1,08	**4**	$1,5 \times 10^5$	acid
BASF Collacral PU 75	HEUR (PU-Verdicker)	26	1,05	9,5	1×10^5	
CMC-Niclacell CH10 F	CMC, with low chain length	93,1		10	1×10^5	Na^+
CMC-Niclacell CH90 (SK11)	**Standard** CMC, mean chain length				$2,3 \times 10^5$	Na^+
CMC-Niclacell NC150C	CMC long chain length	92,3		10	$3,3 \times 10^5$	Na^+
CMC Lamberti Carbocel T300SC	CMC long chain length	92		8	$2,8 \times 10^5$	Na^+
Methycellulose		95,6				
Hydroxypropylmethylcellulose		97,5				
Hydroxyethylcellulose, high viscous		82,6				
ACAT Topbrane 200	**Shear Thinner**	34,4		**10,9**		
ACAT Flocstar 2248P	katioinsches PAM, 1,5 mol%, kurzkettig	verdünnt ansetzten, Lösung = 100% FGH			5×10^6	cat
ACAT Flocstar 2262 P	nichtioinsches PAM, 0 mol%, mittelkettig	verdünnt ansetzten, Lösung = 100% FGH			6×10^6	nonion
ACAT Flocstar 2281 P	anioinsches PAM, 5 mol%, mittelkettig	verdünnt ansetzten, Lösung = 100% FGH			8×10^6	anion
ACAT Flocstar 2293 P	anioinsches PAM, 5 mol%, kurzkettig	verdünnt ansetzten, Lösung = 100% FGH			3×10^6	anion
Alcogum L265	HASE, low chain length	30		4,7		
Coatex XP202	HEUR (PU-Thickener) high low-shear Visco	50	1,05	4 - 7		
Coatex XP1588	HEUR (PU-Thickener) higher low-shear Visco	50	1,06	6,5		
Coatex Rheocarb 100	Pigment dispersing agent, OBA carrier	25	1,04	6		
Coatex Rheocarb 120	Pigment dispersing agent, OBA carrier, low visco	26	1,05	6		
Agrana Amitrolit 8410	High viscous, structure viscous					
Agrana Amitrolit 8860	Corn 1200 - 1600 cp bei 5%, 5 mEqu/g	> 90%				
Agrana Amitrolit 8865	Corn 1200 - 1600 cp bei 5%	> 90%				
Agrana Amitrolit 8868	Potato 2500 - 5000 cp bei 5%, 5 mEqu/g	> 90%				
Agrana Amitrolit 8965	Wax maize, 6000 - 8000 cp bei 25%	> 87%				

Pict. 10.7.6.6: List of tested water retention additives ("thickeners")

The higher the molecular weight and the more cross-linked the network structure of the polymer, the higher the low shear viscosity of the liquid phase will be. Coating colour viscosity will increase to the same extend. The higher the charge of the thickener, the more pronounced pigment depletion flocculation will be (pict. 10.7.6.6).

Pict. 10.7.6.2 and 10.7.6.4 show, that liquid phase viscosity drops with shear. As the penetration of the liquid phase into the substrate proceeds under conditions of laminar flow, Brookfield viscosity of liquid phase would be sufficient for calculations using Darcy's law.
But VOF simulations in pict. 10.7.6.7 show that coating colour and in consequence the polymer in the liquid phase is sheared before and under the blade.
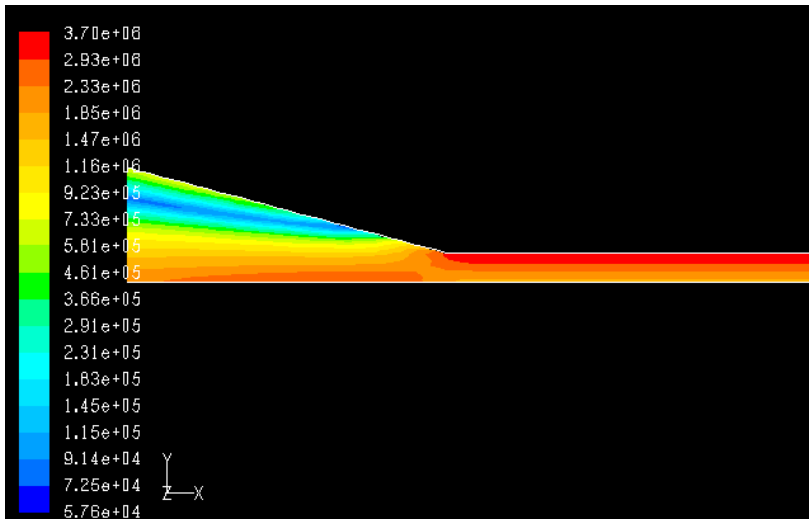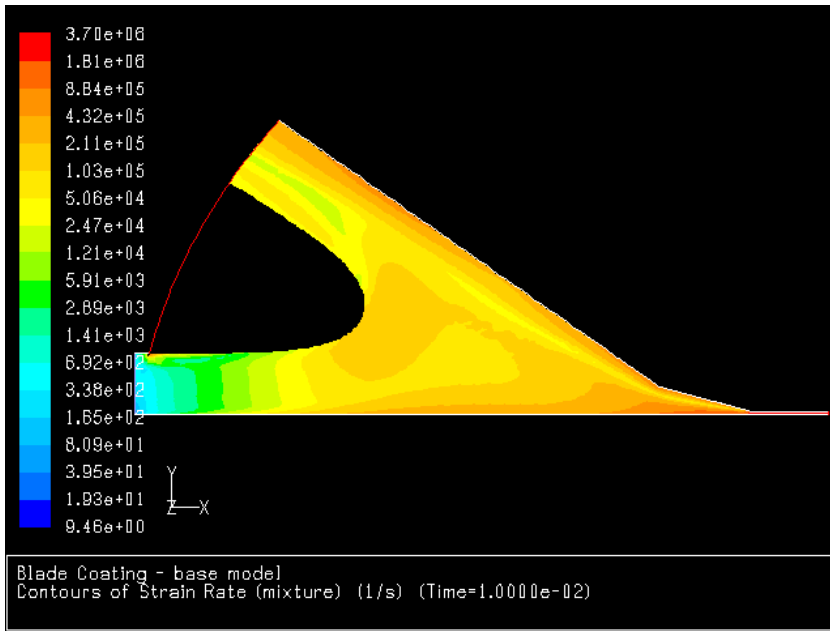
Pict. 10.7.6.7: Shear rate before and under blade from VOF (dwell time 0,047 sec before blade and 0,009 msec under blade)
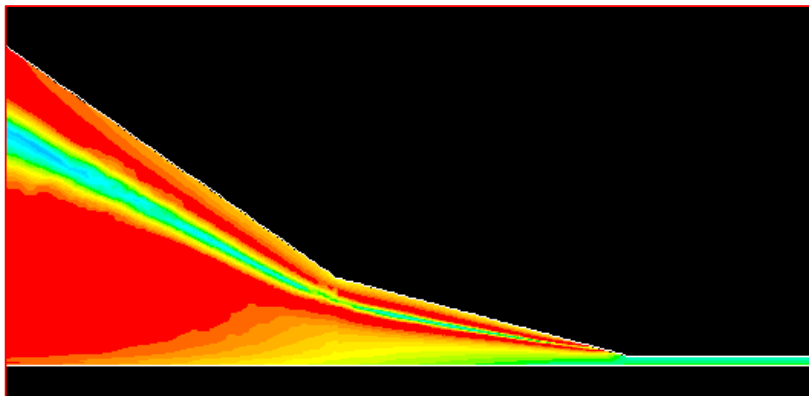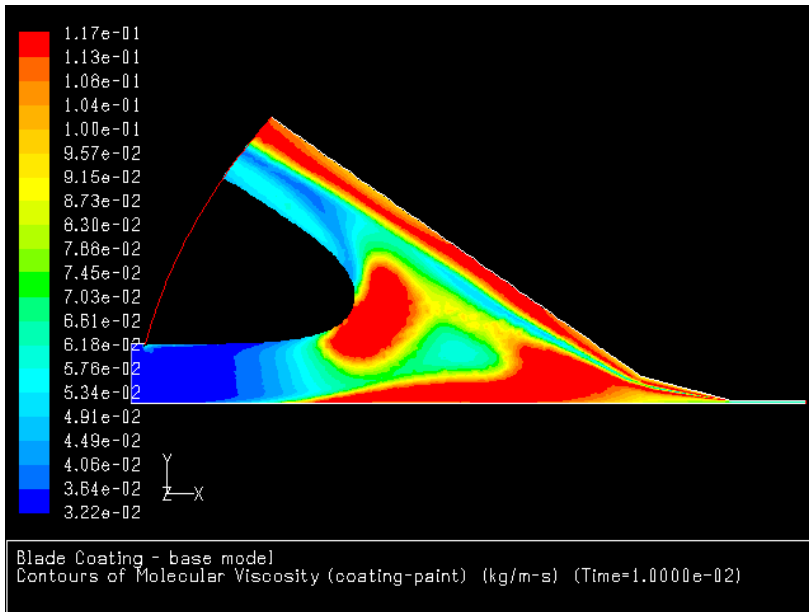
Pict. 10.7.6.8: Viscosity of Coating colour before and under blade
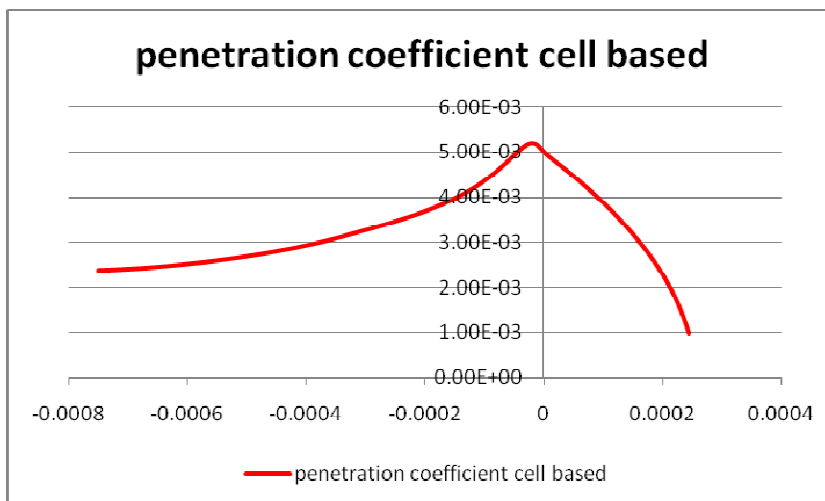
Pict. 10.7.6.9: Penetration coefficient $\sqrt{p} * \sqrt{t}$

When the shear rate before the blade tip from VOF simulation of OMC11 blade coaters is examined and the consequence on development of coating colour viscosity (pict. 10.7.6.8) one can see that most of the shear is applied under the blade at the boundary to the blade surface (10^7 1/s) and before the blade tip at the paper surface (10^6 1/s). Shear forces at the converging nip are with max. 10^5 1/s comparable low.

Taking into account that penetration of liquid phase is depending on $\sqrt{p} * \sqrt{t}$ and using the VOF simulation, the conclusion can be drawn that most of the liquid penetrated before the blade tip where pressure increases due to converging nip geometry (pict. 10.7.6.9). Shear rate is with $10^4 - 10^5$ 1/s relatively low at this area and therefore Brookfield RPM 100 viscosity of liquid phase can be taken for calculations using Darcy's law.

10.7.7 Comparison of thickeners in latex based coating colors

Thickener study latex based coating colours, part 1

Y-axis: High shear visco of coating colour at 31.800[1/sec] [cp]
X-axis: Brookfield Visco of liquid phase at 100 UpM [cp]

Legend:
- CMC CH90
- CMC T300SC
- ASE2-Rheovis 401
- HASE1-Sterocoll PR8820X
- HASE3-Cartacoat RM20
- Non ionic PAM-Flocstar P8892
- HASE2-Rheocarb 120
- HASE4-Alcogum L265
- HEUR1-Collarcral PU75
- HEUR2-XP202
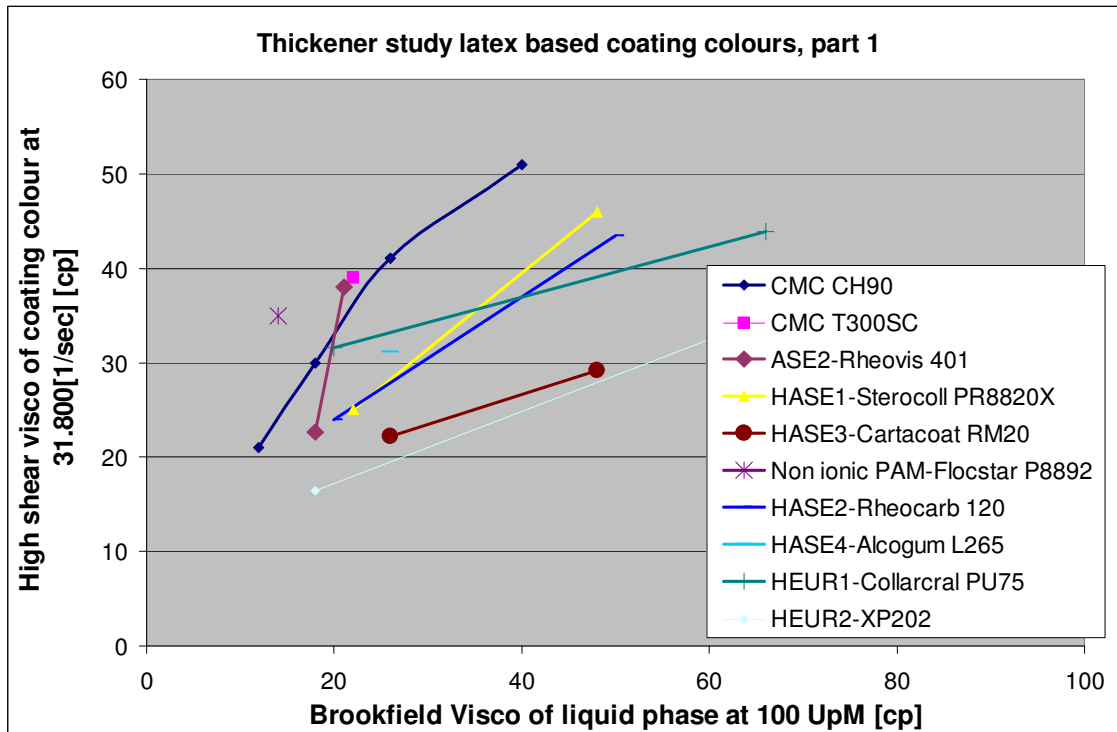
Pict. 10.7.7.1: Comparison of different thickeners for latex based coatings

At high speed blade coaters the ideal water retention additive should increase liquid phase viscosity (to reduce local differences in latex penetration) at the lowest possible high shear viscosity of the coating colour.
Pict. 10.7.7.1 shows an example of plotting these two parameters against each other to demonstrate the difference between different thickeners.

HASE thickeners Sterocoll PR8820X and Rheovis 401 had both lower high shear viscosity of coating colour at comparable liquid phase viscosity than CMC's and non-ionic PAM retention aid Flocstar 2262P.
In other words: **At a comparable high shear viscosity of the coating colour which is limited by the blade pressure the liquid phase viscosity can be increased by 100% when the thickener is changed for instance from CMC to a HASE type**. **Liquid phase seems to be the dominating parameter in Darcy equation which can be changed to the highest extend to improve mottling without influencing other parameters of coating colour, base paper or costs.**

The non-ionic retention polymer was thought to have the lowest interaction with the pigment dispersant but high shear viscosity was relatively high due to the elevated molecular weight and cross-linking of polymer chains leading to more pronounced network breakdown resistance against external shear force than for HASE thickeners. For future studies non ionic retention aids with much lower molecular weight must be used as water retention additives in coatings.
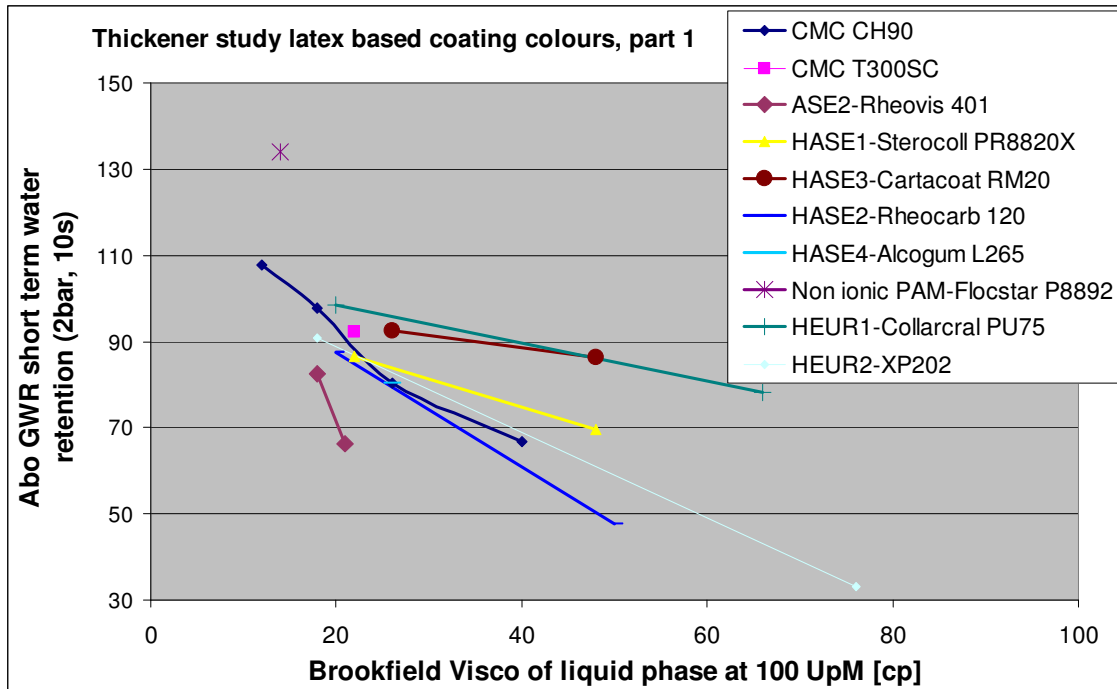
Pict. 10.7.7.2: Short term water retention by Abo-GWR vs. liquid phase viscosity

The assumption that penetration can be reduced by increasing liquid phase viscosity was proven by the correlation of Abo-GWR short term water retention and liquid phase viscosity shown in pict. 10.7.7.2 and 10.7.7.3.
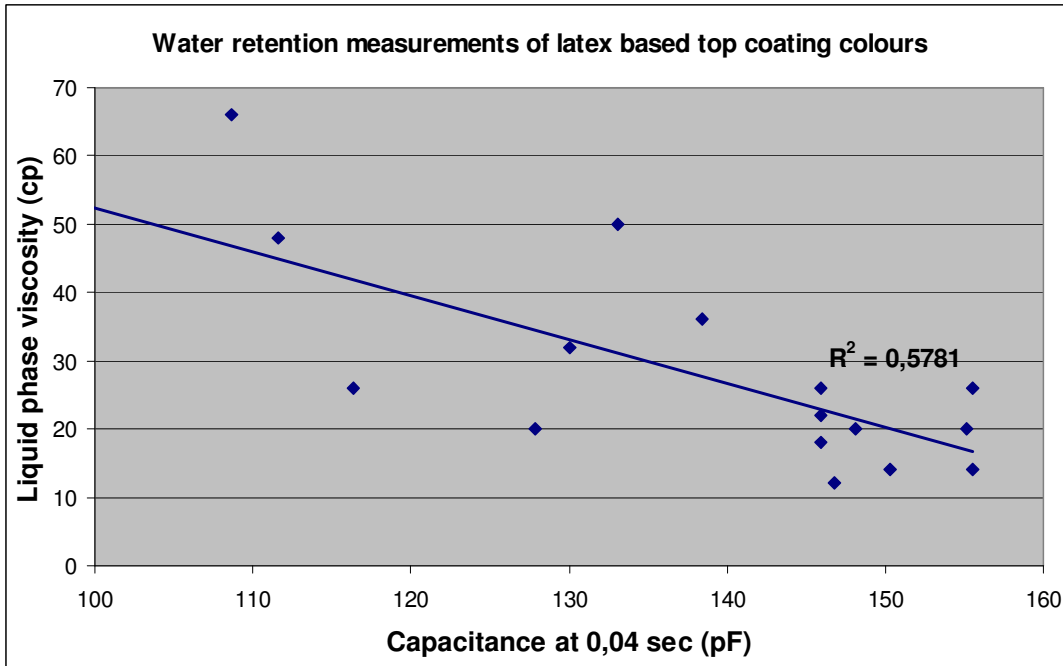
Pict. 10.7.7.3: Short term water retention by KCL-Clara vs. liquid phase viscosity

The same result was achieved when short term penetration was measured by KCL-Clara (see 10.7.13.10).
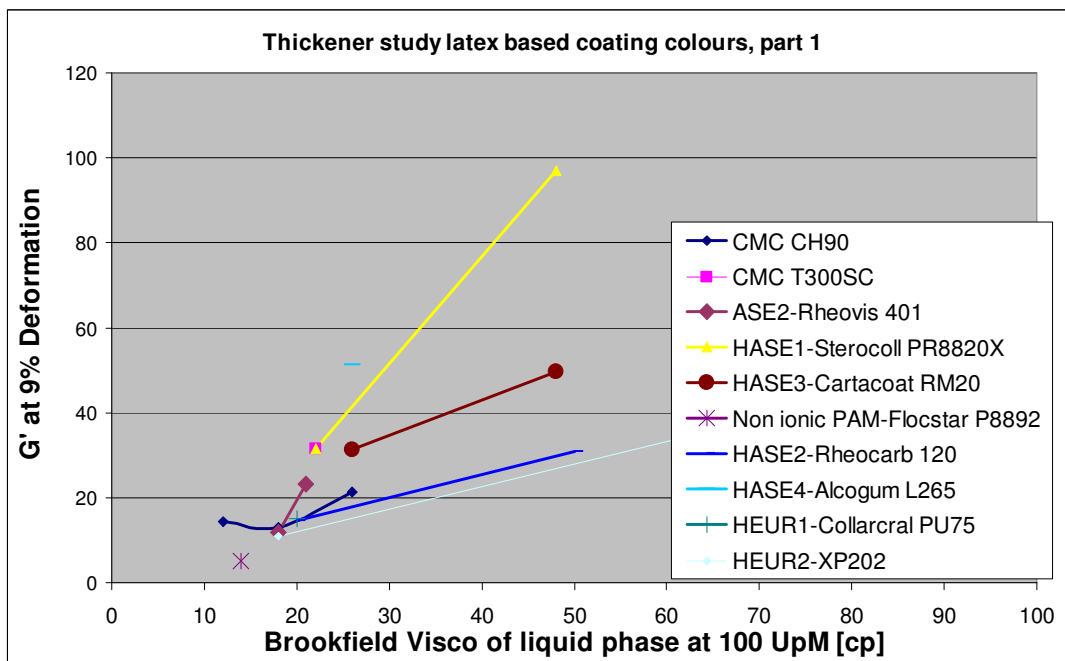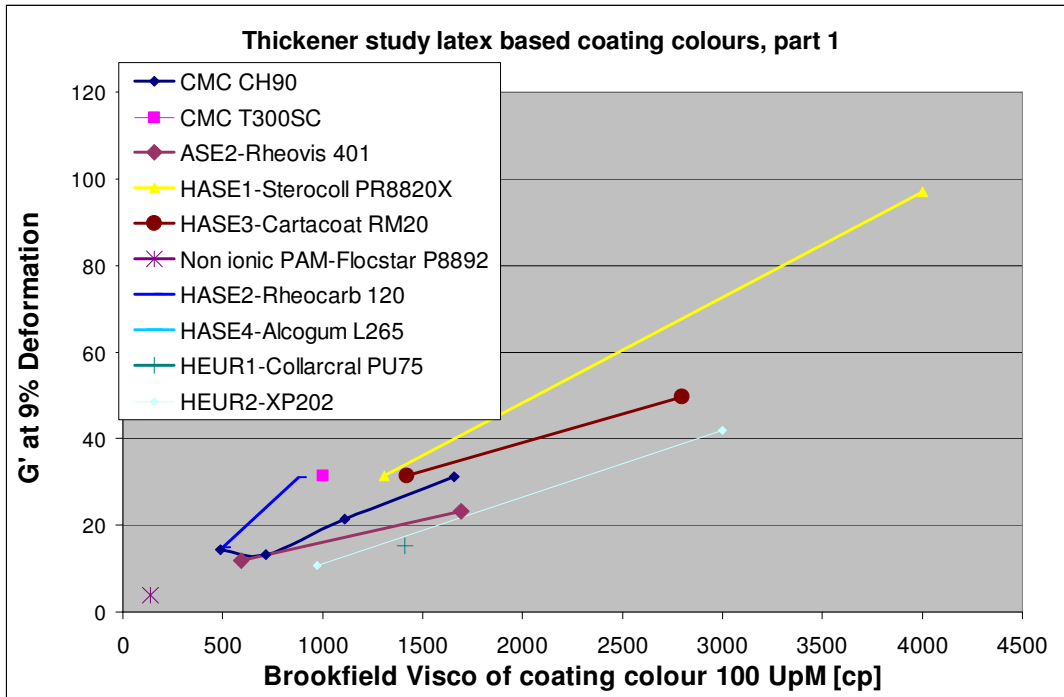
Pict. 10.7.7.4: Elasticity of latex based coatings
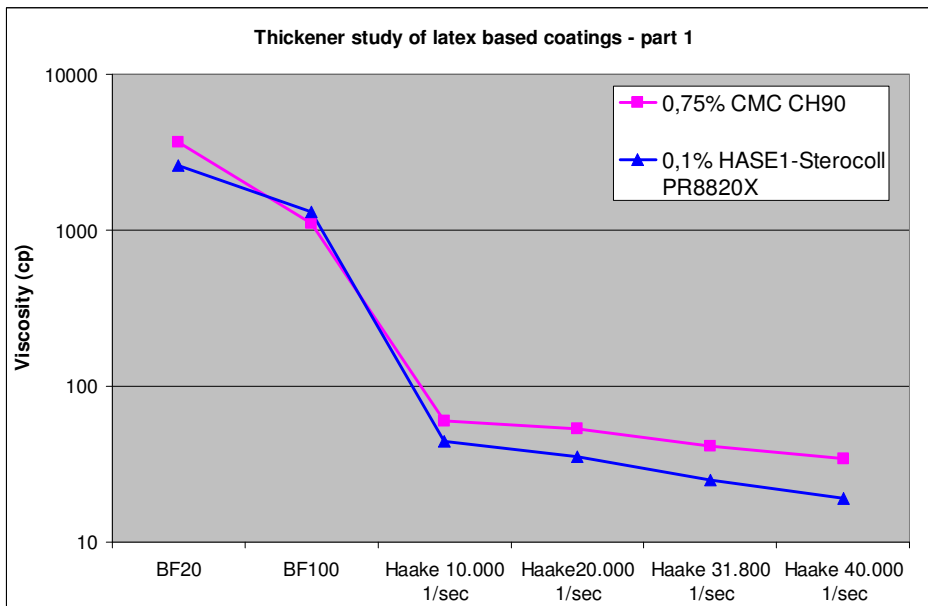
Pict. 10.7.7.5: Viscosity vs shear rate for CMC and HASE1 based coatings

Some of the HASE thickeners (HASE 1+3) increased the elasticity of the coating colour to a greater extend than HEUR and other HASE types due to stronger interaction with latex and pigment particles. As high shear viscosity of HASE based coating was relatively low, this structure broke down fast under shear (pict. 10.7.7.5).

HASE thickeners (pict. 10.7.7.6 and 10.7.7.7) are the new generation of thickeners for high speed blade coaters. They provide low interaction with pigment dispersant (pict. 10.7.7.8) due to hydrophobic modification of the acrylic chain, fast break down of polymer structure under shear and fast regain when shear is removed.

ASE-Thickeners (Alkali Soluble Emulsion):
- Thickening of the water phase
- Little interaction with particles
- Some carbonate dispersant exchange might occur

HASE-Thickeners (Hydrophobically modified Alkali Soluble Emulsion):
- Hydrophobic interactions with latex particles and in the water phase (pict. 10.7.7.9 and 10.7.7.10)
- High viscosity efficiency (low dosage)
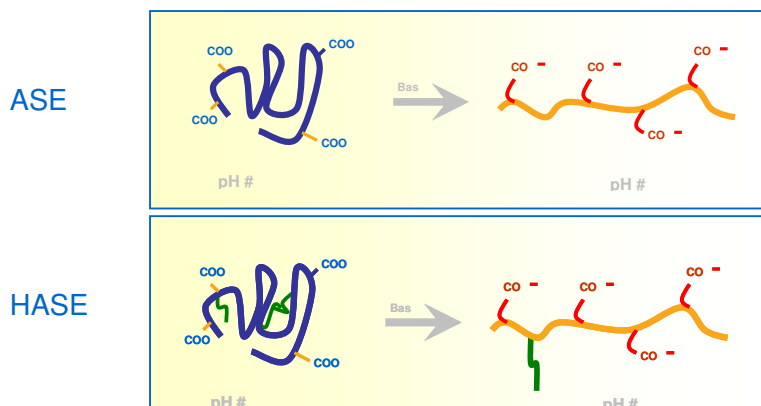
Pict. 10.7.7.6: Chemical structure of ASE/HASE thickeners (green: Hydrophobic end)
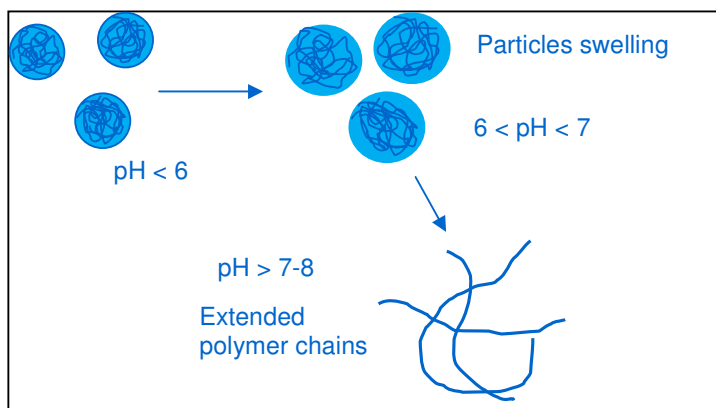
Pict. 10.7.7.7: Alkali swelling of ASE / HASE

ASE / HASE thickeners are delivered with pH of 2 – 5. The molecules are arranged in a ball structure. When pH is raised, eg. by adding caustic soda, the polymer chains are extended, the molecules are stretched and the interaction with the surface of pigment or latex particle surface starts.
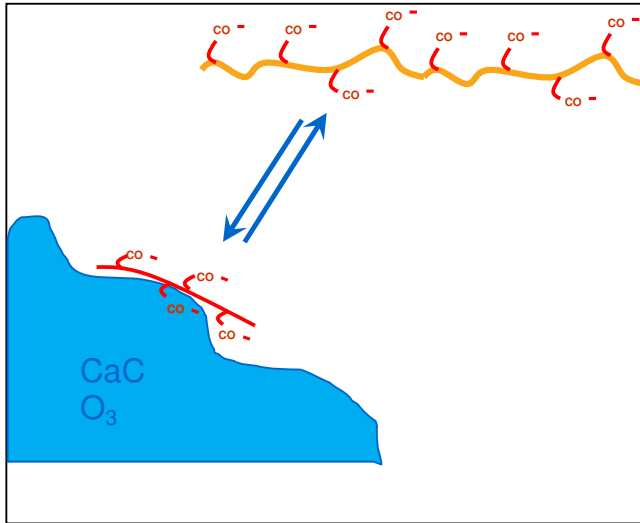
Pict. 10.7.7.8: Interaction of ASE / HASE carboxyl group with pigment surface
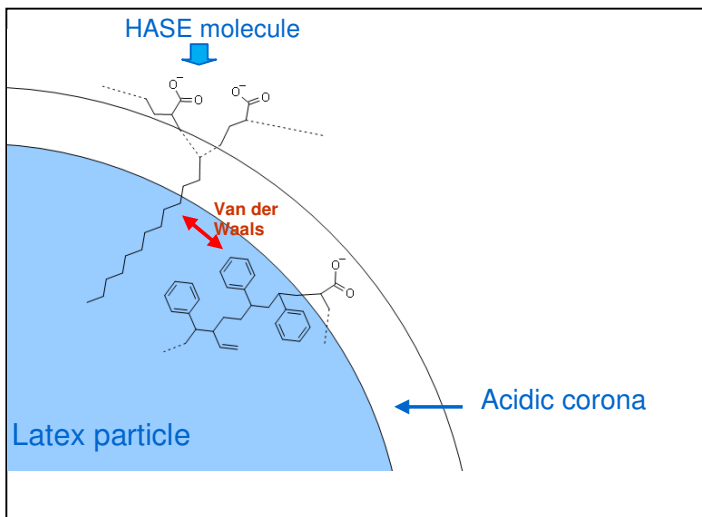
Pict. 10.7.7.9: Interaction of HASE molecule with latex
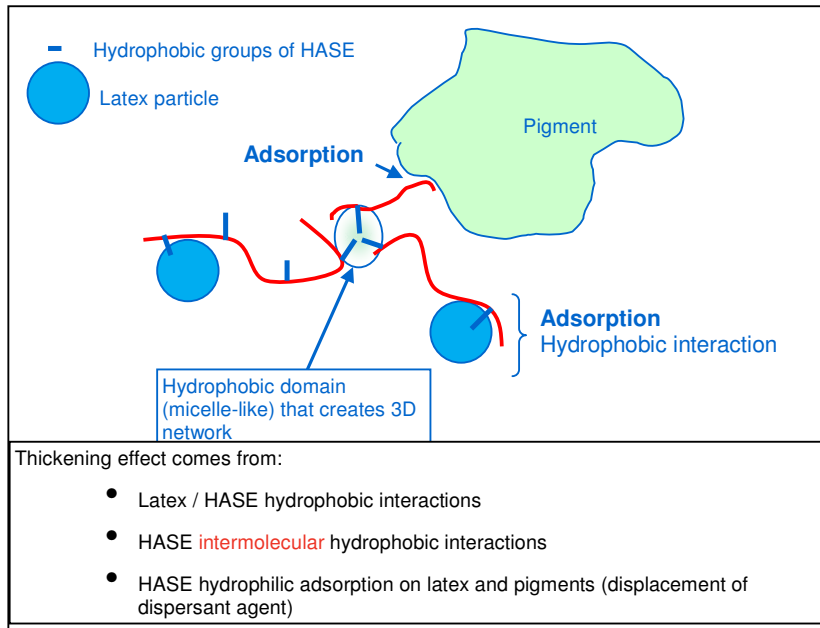
Pict. 10.7.7.10: Thickening effect of ASE / HASE

The disadvantage of ASE / HASE / PU thickeners against CMC is the missing carrier effect for OBA's. The consequence is a higher PVOH demand which again leads to an increase in high shear viscosity – the advantage of lower high shear viscosity of these thickeners gets lost when more PVOH has to be used (see pict. 10.7.6.3)

The best compromise is the acrylic thickener Rheocarb 120 which contains PE oxide and provides additional carrier effect for OBA's.

From paint industry polyurethane thickeners (HEUR) are well known for lowest interaction with pigment dispersants or latices. Low G' data's prove this theory.

HEUR thickeners (non-ionic hydrophobically modified ethylene oxide urethane block copolymers) are based on polyurethane and polyethylenglycol where the hydrophobic areas on the polymer react with each other and with latex particles. Some HEUR thickeners create Newtonian behaviour of coating colour where viscosity is independent on shear.
HEUR thickeners are expensive but the best choice as thickeners for coating colour used at high speed blade coaters. Similar to HASE thickeners low high shear viscosity was measured for PU based thickeners Collacral PU75 and Coatex XP202 at a given liquid phase viscosity (pict. 10.7.7.11).

The nnetwork of polyurethane based thickeners is therefore also very sensitive for shear.
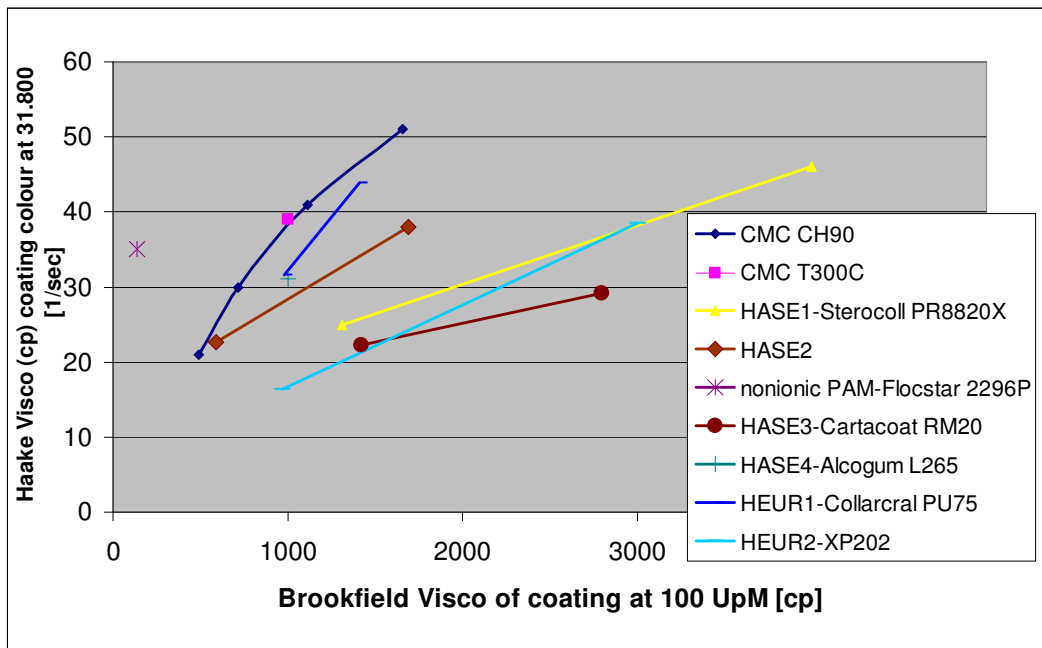
Pict. 10.7.7.11: BF viscosity vs high shear viscosity for latex based coatings, part 1

Brookfield viscosity correlated quite well with liquid phase viscosity when only results of part 1 where compared. HASE and HEUR thickeners were higher in BF viscosity of coating colour at a given level of high shear viscosity

Latex study part 2:

In the 2nd part of the study alternative water retention additives were studied, which are not common on the market.

The Flocstar products are polyacrylamides, which often used as retention aids in the wet end of paper machine. Anionic poly acryl amide (APAM) Flocstar 2281P and 2293P were compared to non-ionic PAM 2296P

The Amitrolit products were starch based thickeners, used in construction industry. Amitrolit 8410 is also used for tile adhesives.

Methylcellulose MEC and Hydroxyethylcellulose HEC are also used in construction industry.

In the 1st part (see pict. 10.7.7.3) a non-ionic poly acrylamide was compared to standard thickeners. The non-ionic PAM showed low interaction with pigment / latex and low G'. Low shear viscosity was not sufficient at comparable high shear viscosity.
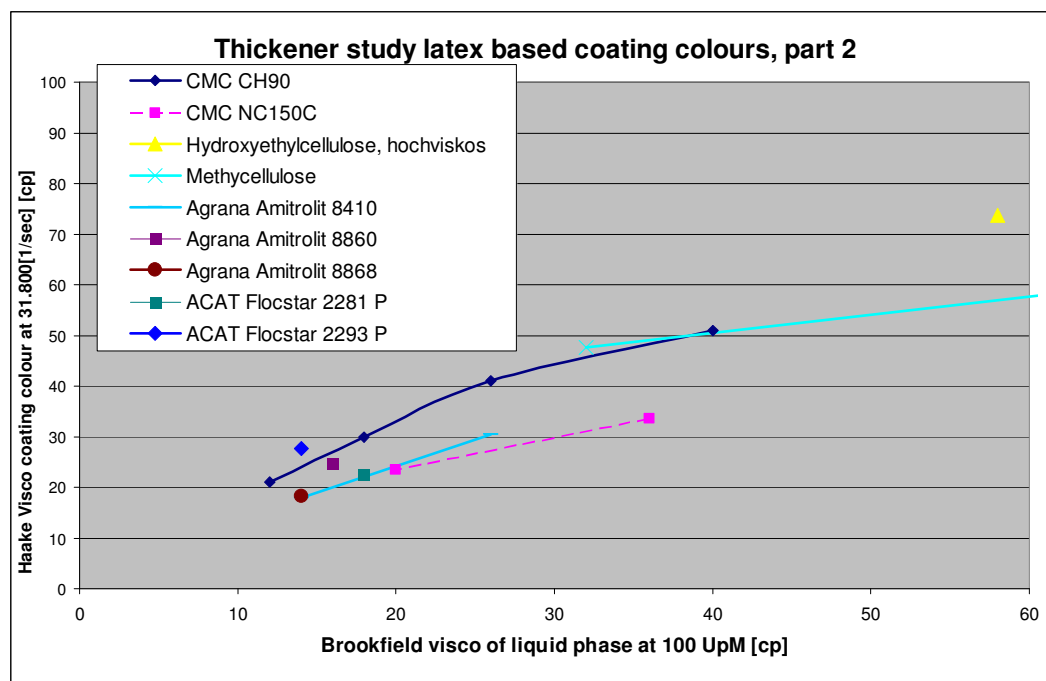
Pict. 10.7.7.12: Comparison of different thickeners in latex based coatings (part 2)

All tested alternative thickeners showed comparable performance (ratio liquid phase viscosity to coating colour high shear viscosity) to CMC (pict. 10.7.7.12) but are higher in costs.
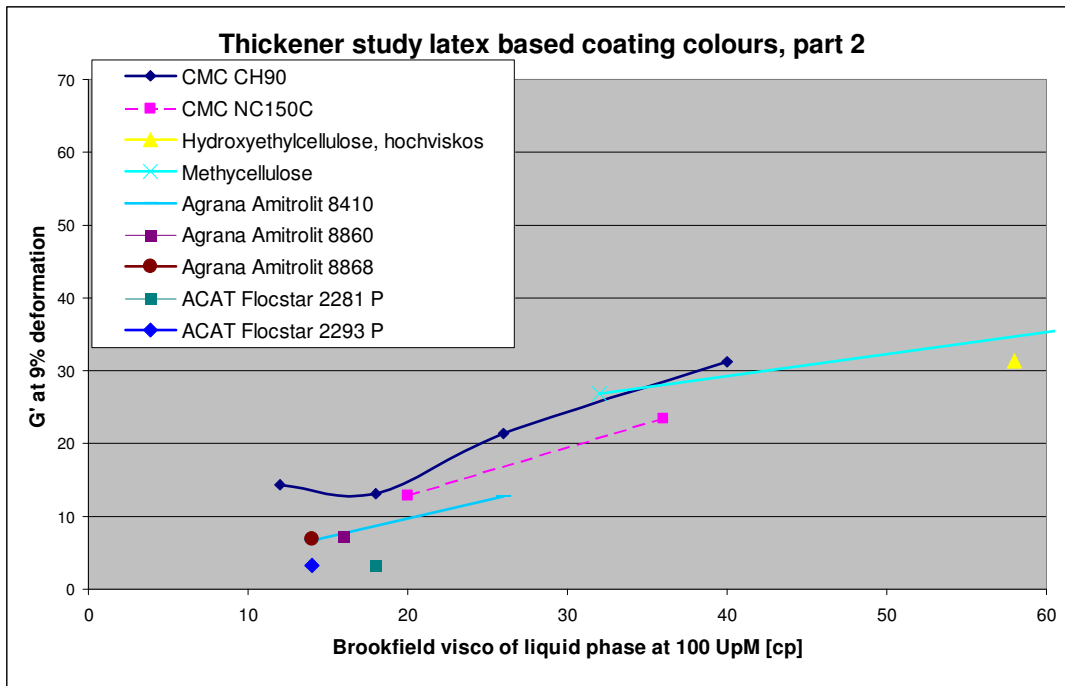
Pict. 10.7.7.13: G' of different thickeners in latex based coatings (part 2)

With increasing structure in the water phase (created by raising amount of thickeners) the elasticity of the coating colour G' increased as proven in the study part 1 (pict. 10.7.7.4 and 10.7.7.13).

10.7.8 Comparison of thickeners in starch based coating colors

The same thickeners of the previous chapter were tested in starch based coating colors. A pre-dispersed dry HC60 was used as pigment for this part of the lab study (see pict. 10.7.5.1). Starch was added and calculated as a soluble binder (with 30% dry content of soluble starch) and included in the liquid phase.
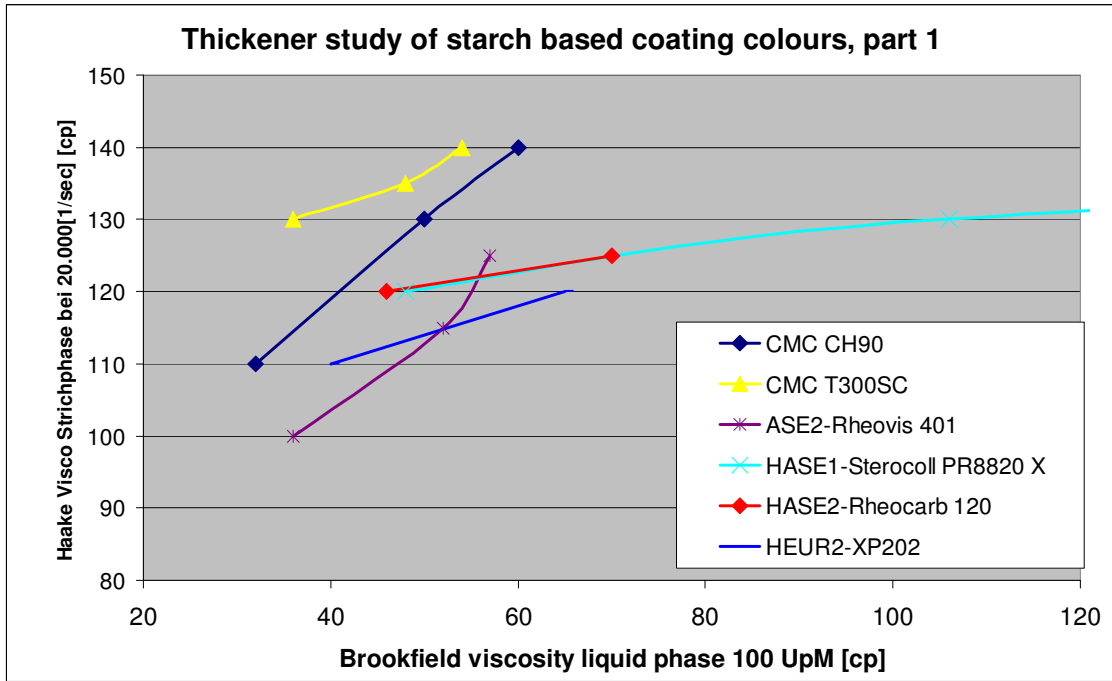
Pict. 10.7.8.1: Comparison of different thickeners for starch based coatings (part 1)
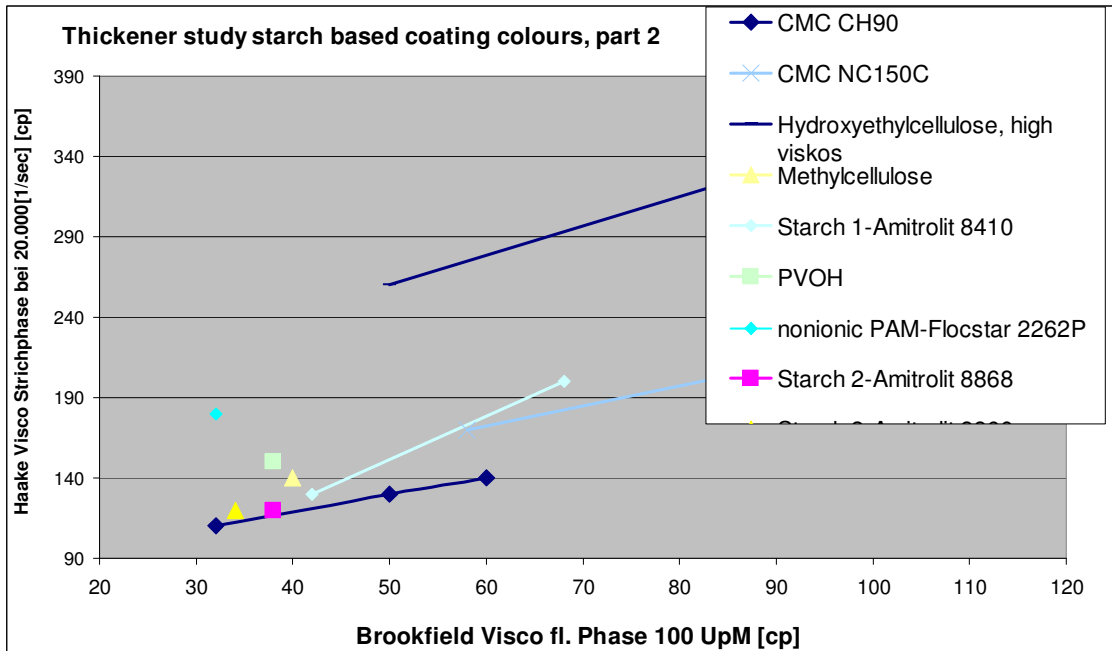
Pict. 10.7.8.2: Comparison of different thickeners for starch based coatings (part 2)

The results of starch based coating colours shown in pict. 10.7.8.1 and 10.7.8.2 fitted quite well to results from the study with latex based coatings: Again coatings based on HASE and HEUR thickeners showed lowest high shear viscosity of coating colour at comparable liquid phase viscosity.

10.7.9 Reducing coating colour high shear viscosity by rheology modifiers

In the next part the effect of a commercially available rheology modifier based on styrene (Topbrane 200 from Topchim Ltd.) is shown. Topbrane 200 is used to lower the blade pressure at high speed coaters. It reduces low and high shear viscosity of coating colours by improving the steric stabilization of pigment and binder particles.
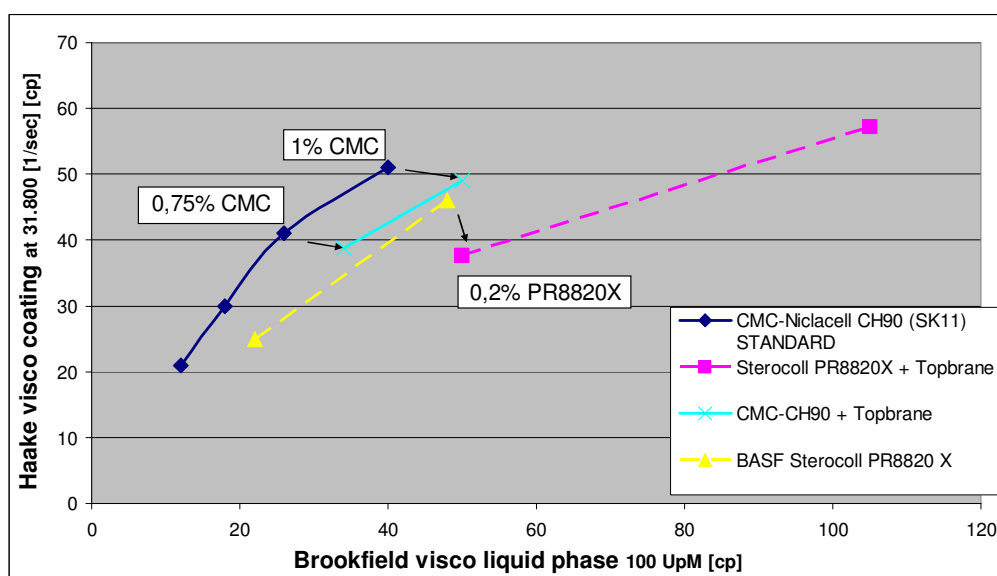
Pict. 10.7.9.1: Liquid phase viscosity vs high shear viscosity of coatings with Topbrane 200

At comparable liquid phase viscosity a somewhat lower high shear viscosity was measured when Topbrane was used in a carbonate and latex based precoating (pict. 10.7.9.1). To improve mottling the amount of water retention additive could be raised and liquid viscosity would be somewhat higher at comparable high shear viscosity. This impact on mottling improvement is relatively small as mill trials with Topbrane 200 showed. As costs increase by 2 – 3 €/to paper with Topbrane this measure was not implemented.

10.7.10 Comparison of new water retention additives in complete coatings

The new HASE water retention additives were tested in complete top coatings. All coating components were mixed stepwise and rheology measurements were made after each step.
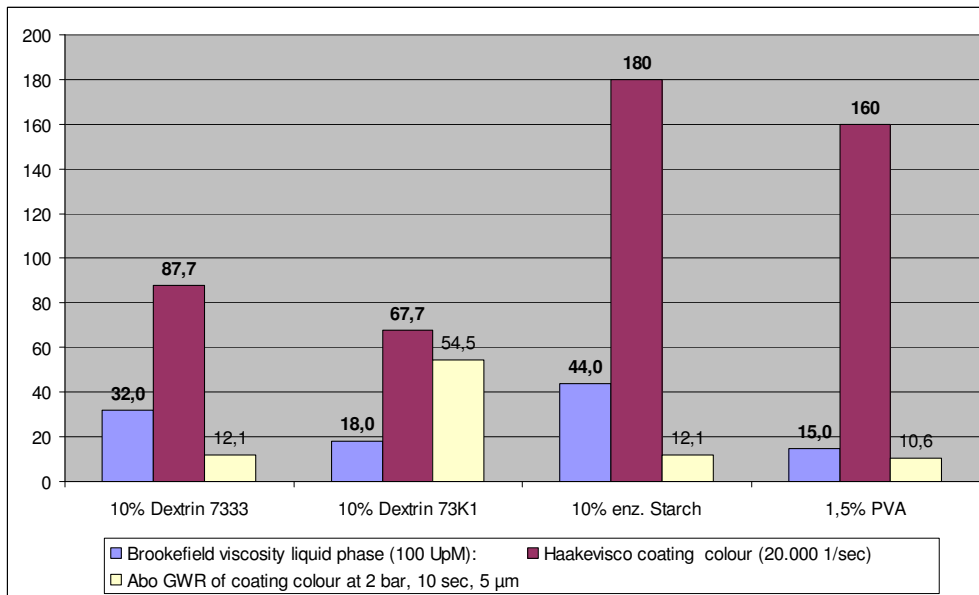
Pict. 10.7.10.1: Comparing liquid phase viscosity with high shear viscosity for starch based coatings (1,5% PVOH added in last column to 10% Dextrin 73K1)
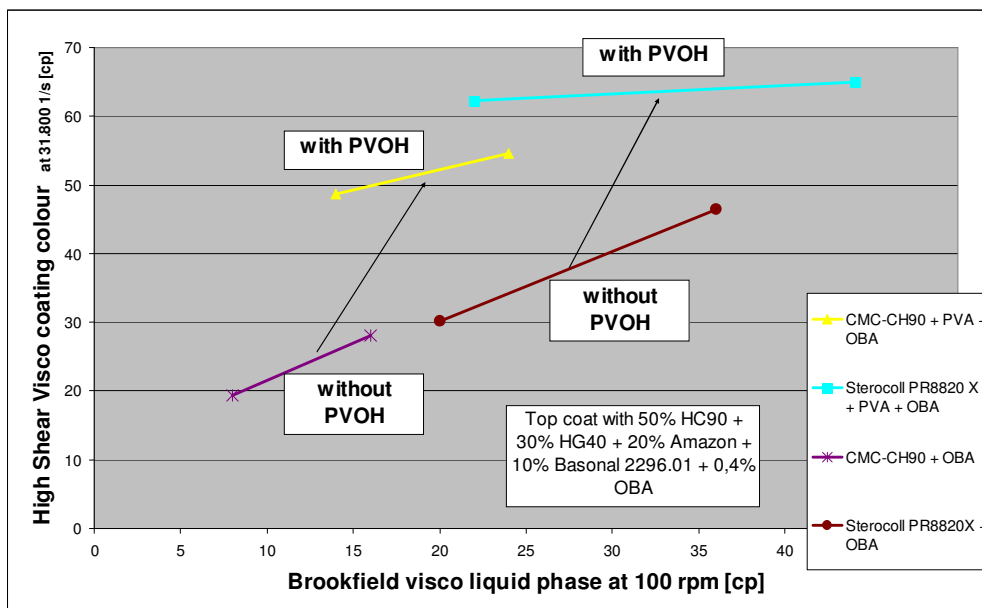
Pict. 10.7.10.2: Influence of PVOH on high shear viscosity and liquid phase viscosity of complete top coating
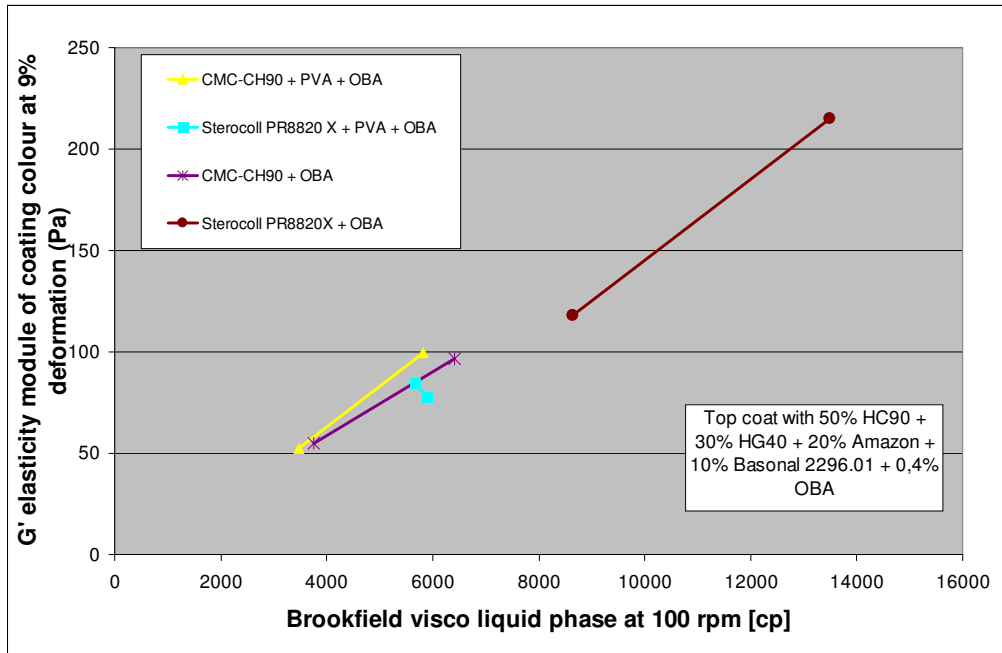
Pict. 10.7.10.3: Elasticity of top coating
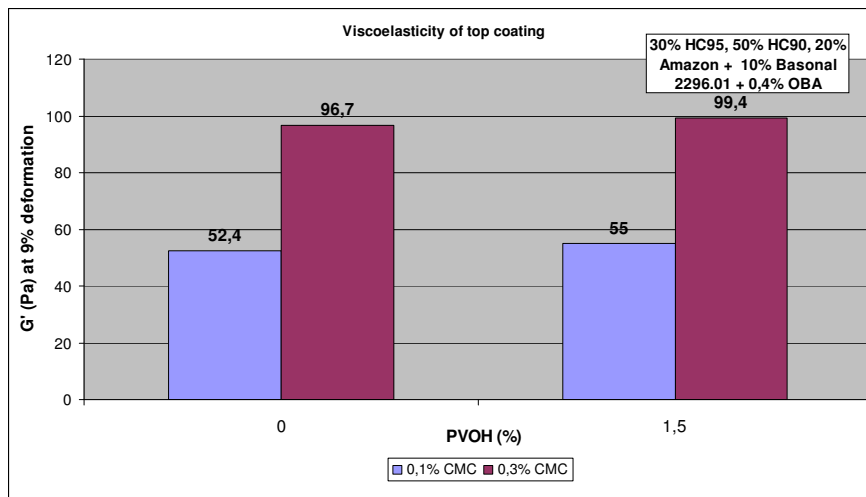
Pict. 10.7.10.4: Elasticity of top coating with different amounts of PVOH

PVOH had the biggest impact upon high shear viscosity without contributing much in liquid phase viscosity (pict. 10.7.10.1 and 10.7.10.2). The increase in coating colour viscosity was mainly caused by the polymer structure (chain length and cross-linking) of PVOH and less by depletion flocculation of the pigment as G' stays relative constant with increasing amount of PVOH (pict. 10.7.10.3 and 10.7.10.4).
Break down of polymer structure was relatively slow for PVOH and therefore high shear viscosity was highest of tested additives.

Mill trials showed that brightness drops when CMC was replaced by HASE thickeners. Pict. 10.7.10.2 shows that adding PVOH to compensate this drop in brightness would destroy the positive effect of HASE thickener on high shear viscosity.

10.7.11 Influence of latex type

Three different latices with different impact on depletion flocculation were investigated by the described method of separate measurement of liquid phase and coating colour viscosity.
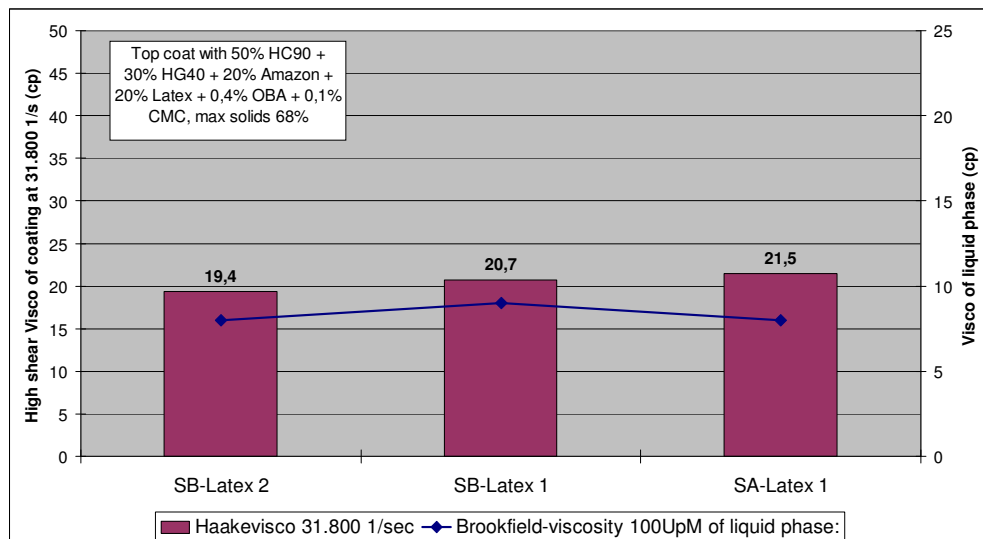
Pict. 10.7.11.1: Coating colour high shear viscosity of different latices vs. liquid phase viscosity
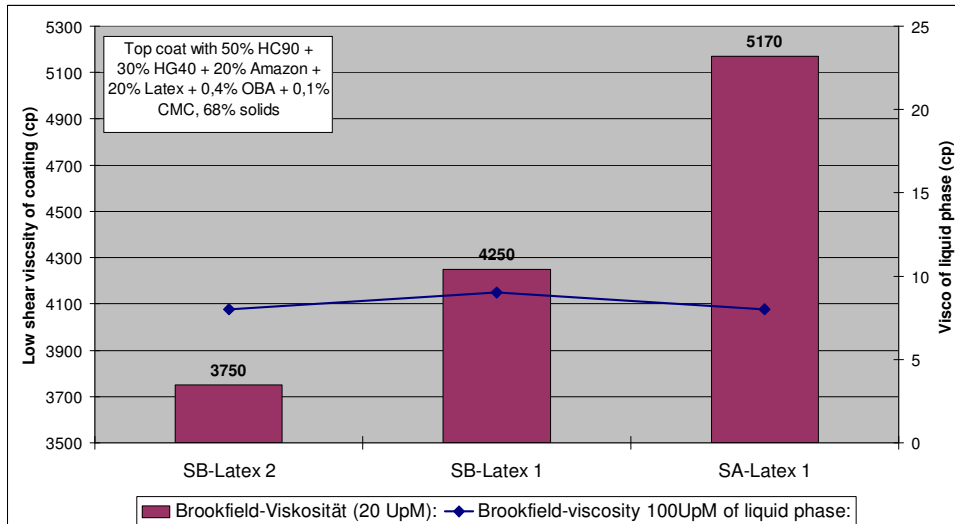
Pict. 10.7.11.2: Coating colour low shear viscosity of different latices vs. liquid phase viscosity
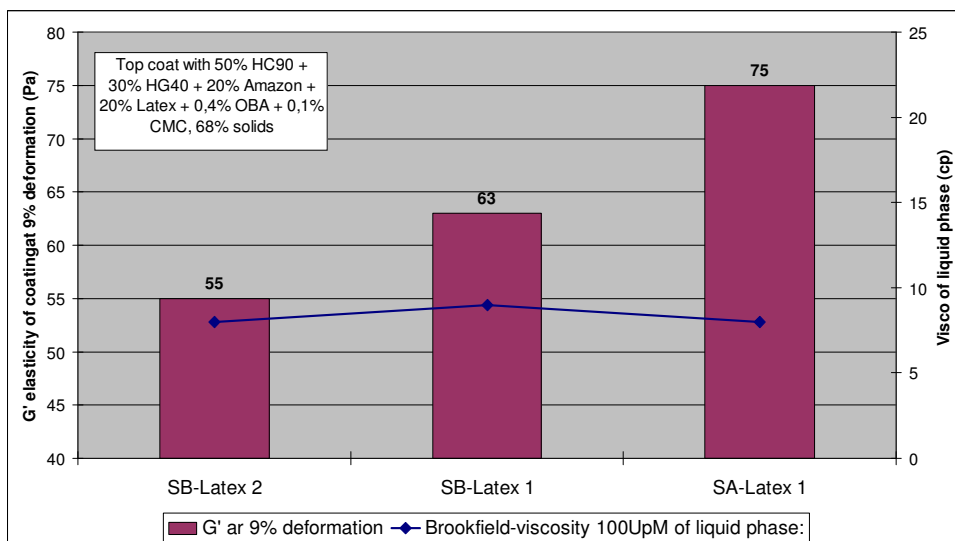
Pict. 10.7.11.3: Coating colour elasticity of different latices vs. liquid phase viscosity

No change in liquid phase viscosity was observed for all tested latices as they did not add structure to liquid phase like polymers (pict. 10.7.11.1).

SA-latex Acronal S360D, with highest concentration of acidic ions in liquid phase, showed strongest depletion flocculation. Low shear viscosity and elasticity of coating colour increased significantly when 20% of this latex was used in the coating colour (pict. 10.7.11.2 and 10.7.11.3).

10.7.12 Improving water retention by increasing the coating colour solids

Two contradictory ways to improve water retention of coatings were compared in the next part of the lab study:

a) Raise solid content at constant level of thickener (water retention will improve but high shear viscosity will raise in parallel)

b) Keep the solid content on constant level and raise amount of thickener (same consequences as for a))

Increasing solid content is a very common way to improve mottling. When solids is raised by reducing free water in coatings, the concentration of thickeners increases (as they are not changed in dosage) and therefore viscosity of liquid phase increases too. Unfortunately high shear viscosity rises exponentially with solids.

On the other hand when solid content would be lowered a higher amount of thickeners could be used at a certain limit of high shear viscosity.

These two strategies are compared in pict. 10.7.12.1.
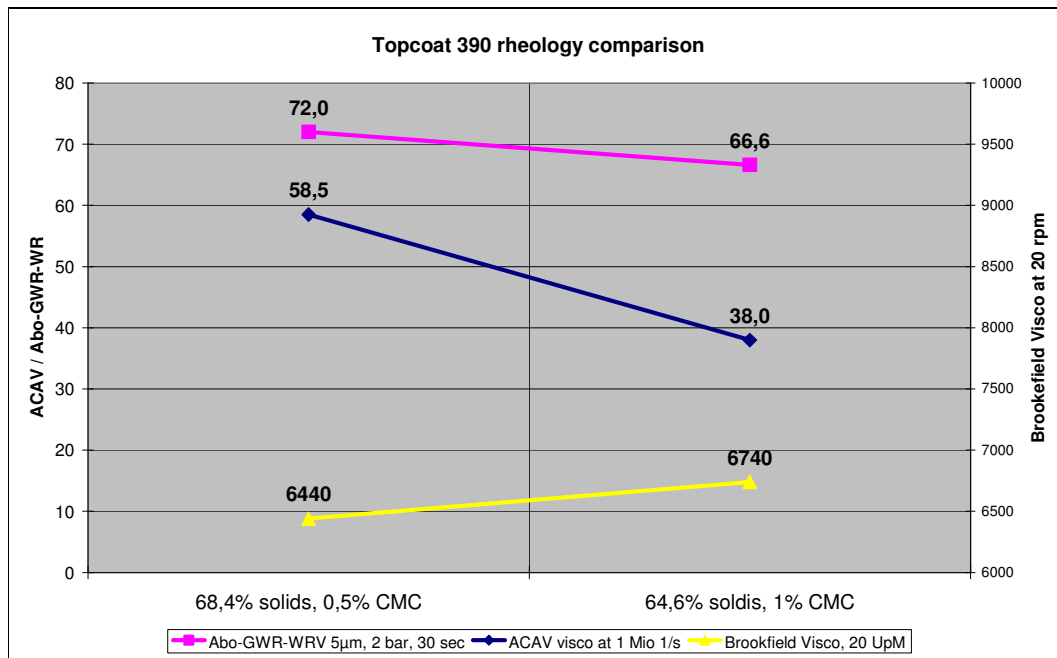
Pict. 10.7.12.1: Water retention versus high shear viscosity of two top coatings

For the investigated glossy top coating (20% clay, 80% fine carbonate, 1,2% PVOH, 7% SB-latex) a reduction in solids and increase in CMC content would be the better choice: Water retention is improved (lower g/m² in Abo-GWR = better) although high shear viscosity is lower than for the same coating with higher solid but lower CMC content.

The lab study was continued for starch and latex based precoatings with 100% HC60 as pigment phase. Solid content and thickener dosage were varied.
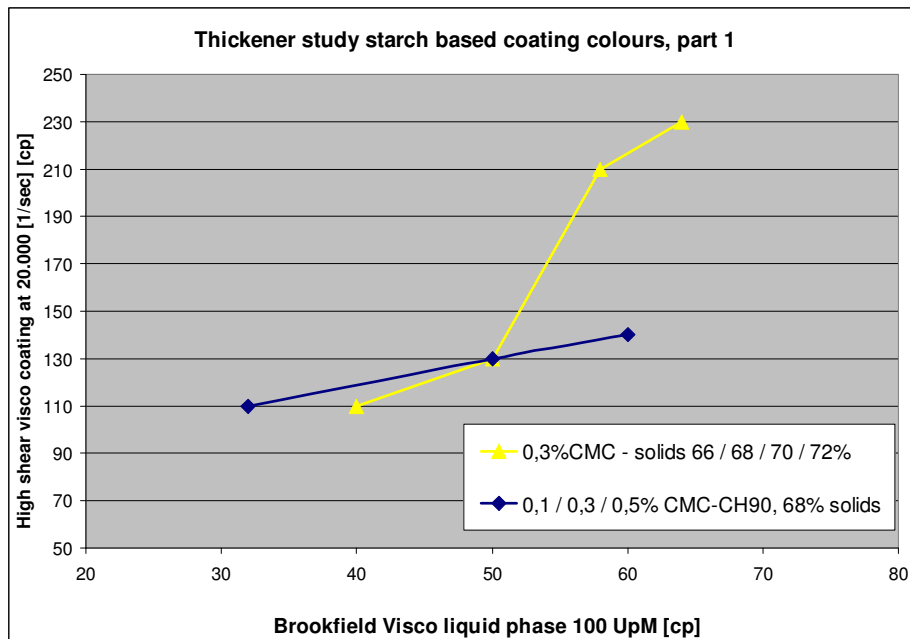
Pict. 10.7.12.2: Increasing liquid phase viscosity by rising the solid content vs. thickener content (starch based coating colour with 100% HC60)

Thickener study latex based coating colours, part 1

Legend:
- 0,3 / 0,5 / 0,75 / 1% CMC, 68% solids
- CMC 0,75%, solids 66 / 68 / 70 / 72%

Y-axis: Haake Visco coating colour at 31.800[1/sec] [cp]

X-axis: Brookfield Visco of liquid phase at 100 UpM [cp]
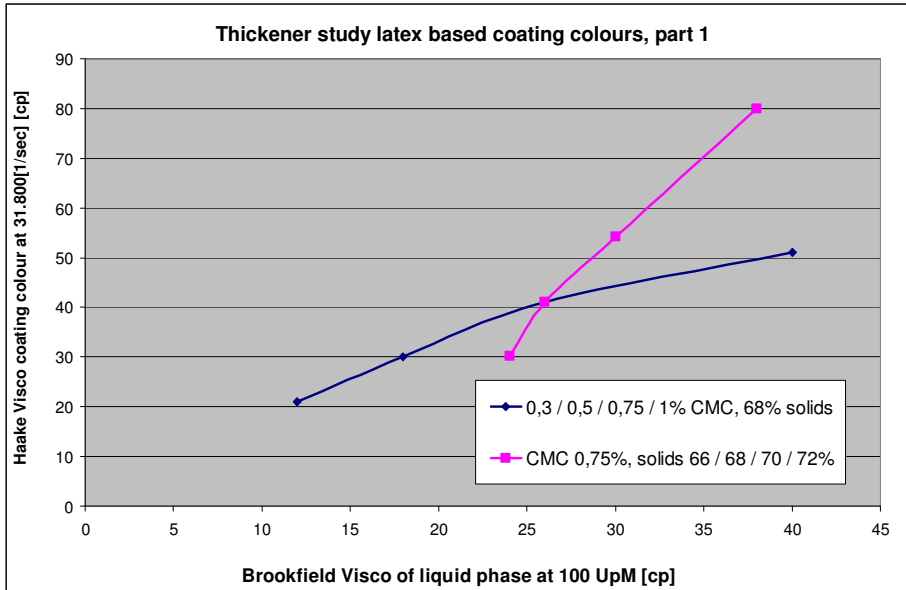
Pict. 10.7.12.3: Increasing liquid phase viscosity by rising the solid content vs. thickener content (latex based coating colour with 100% HC60)

Pict. 10.7.12.2+3 show that **above a threshold of 68% solids the better alternative to improve mottling would be to keep solids and increase the amount of CMC than to raise solid content and lower the amount of thickener**. Liquid phase viscosity is higher at given level of coating colour high shear viscosity for this strategy when solids over 68% are targeted.

When solid content is raised at high speed blade coaters the amount of thickener is most often reduced to keep blade load in the operating window. This procedure lowers liquid phase viscosity additionally. Mill trials have shown that lower solids of top coatings combined with high content of HASE thickeners led to improved mottling. The worst mottling was achieved when solid content was raised to maximum and thickener was completely taken out of the top coating formulation.

Unfortunately the measure to improve mottling by lowering solids and simultaneously increase the amount of thickener is an expensive way to improve mottling as thickeners are expensive substances.

10.7.13 Correlation of complete rheology measurements of coatings with liquid phase viscosity

Existing lab rheology studies lacked of liquid phase viscosity measurements. If BF viscosity of complete coating colour would correlate well with liquid phase viscosity the later could be left out from rheology studies. In the following graphs this assumption was checked.
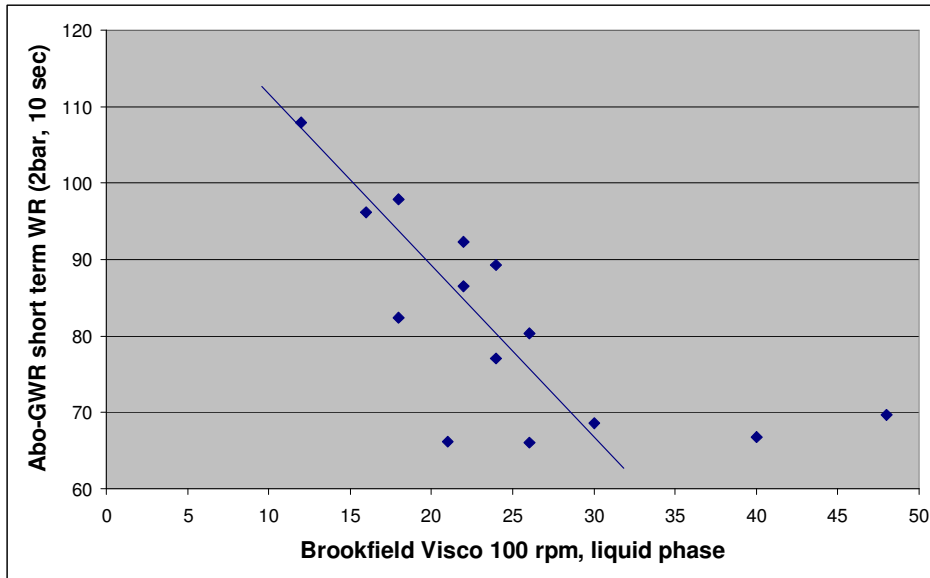
Pict. 10.7.13.1: Liquid phase viscosity vs. water retention for latex based coating colours – thickener study part 1
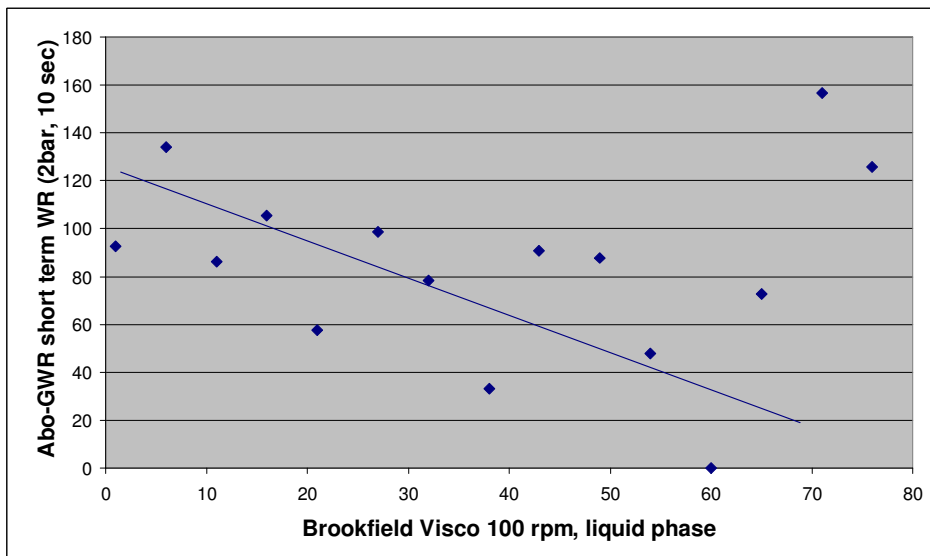
Pict. 10.7.13.2: Liquid phase viscosity vs. water retention for latex based coating colours – thickener study part 2
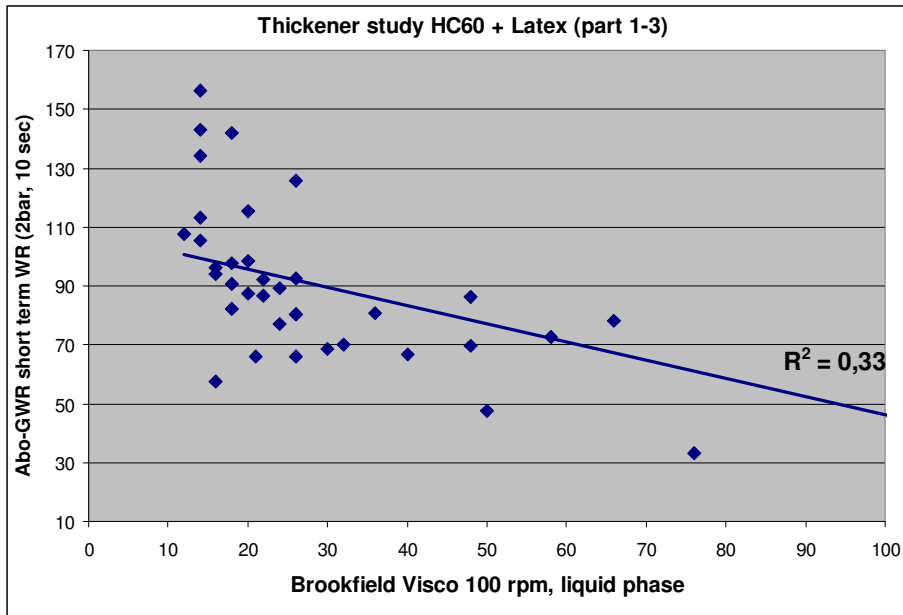
Pict. 10.7.13.3: Liquid phase viscosity vs. water retention for latex based coating colours – thickener study part 3

Abo short term water retention test correlated quiet well with liquid phase viscosity when small changes were made within one set of tests like e.g. increase the amount of thickener or change to similar type of thickener (pict. 10.7.13.1 and 10.7.13.2). When the whole series of tested coating colours was compared, the correlation was disappointing (pict. 10.7.13.3).
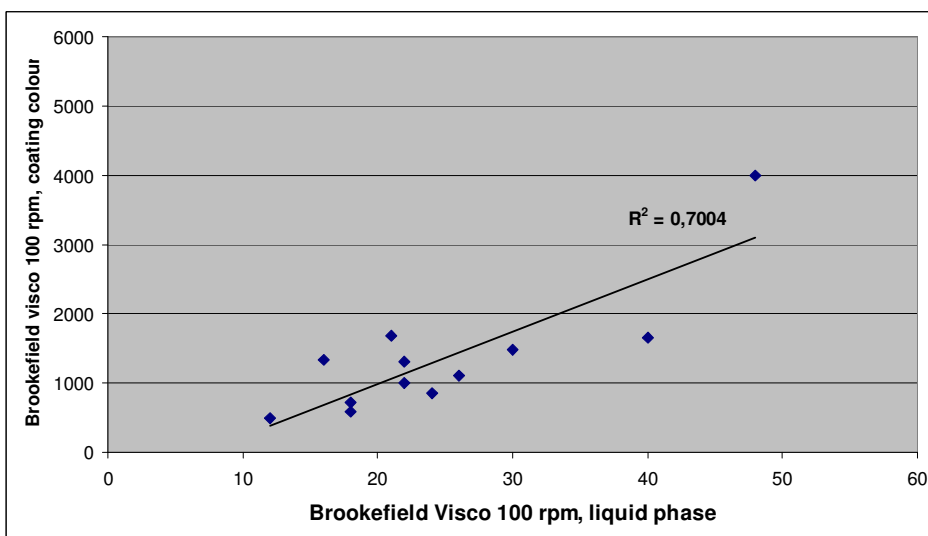
Pict. 10.7.13.4: Liquid phase viscosity vs. coating colour BF viscosity for latex based coating colours – thickener study part 1
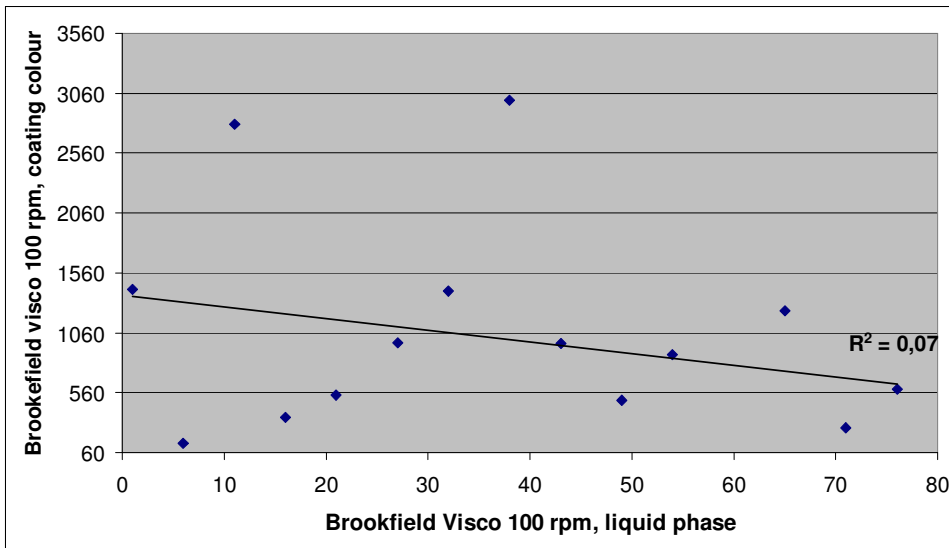
Pict. 10.7.13.5: Liquid phase viscosity vs. coating colour BF viscosity for latex based coating colours – thickener study part 2
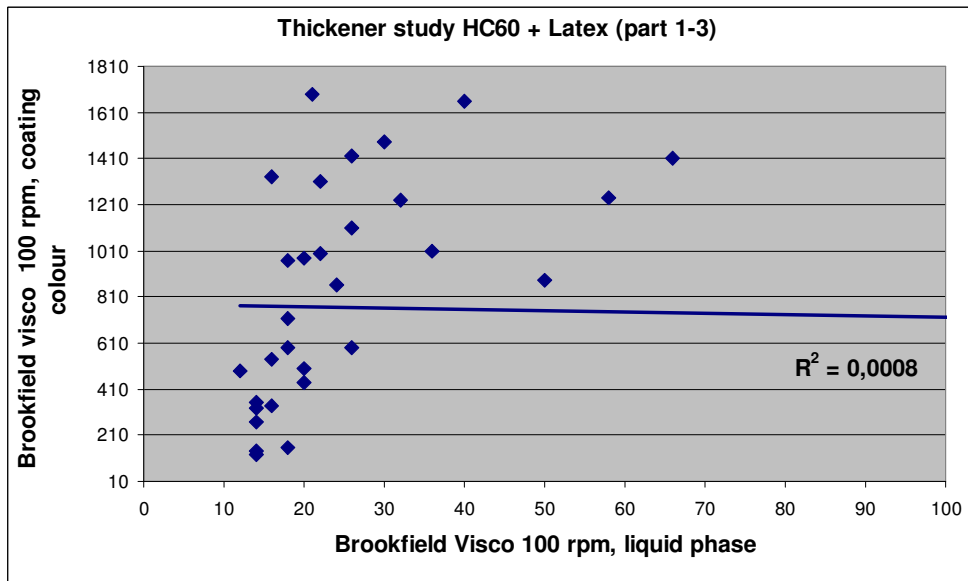
Pict. 10.7.13.6: Liquid phase viscosity vs. coating colour BF viscosity for latex based coating colours – thickener study part 3

When Brookfield viscosity of coating colour is compared with liquid phase viscosity the same experience was made. For one set of experiments correlation might be sufficient (pict. 10.7.13.4 and 10.7.13.5) but for the whole series of tested coatings it was totally insufficient (10.7.13.6).

Therefore liquid phase viscosity has to be measured separately when rheology studies with big variations in coating colour formulations are made to improve mottling.
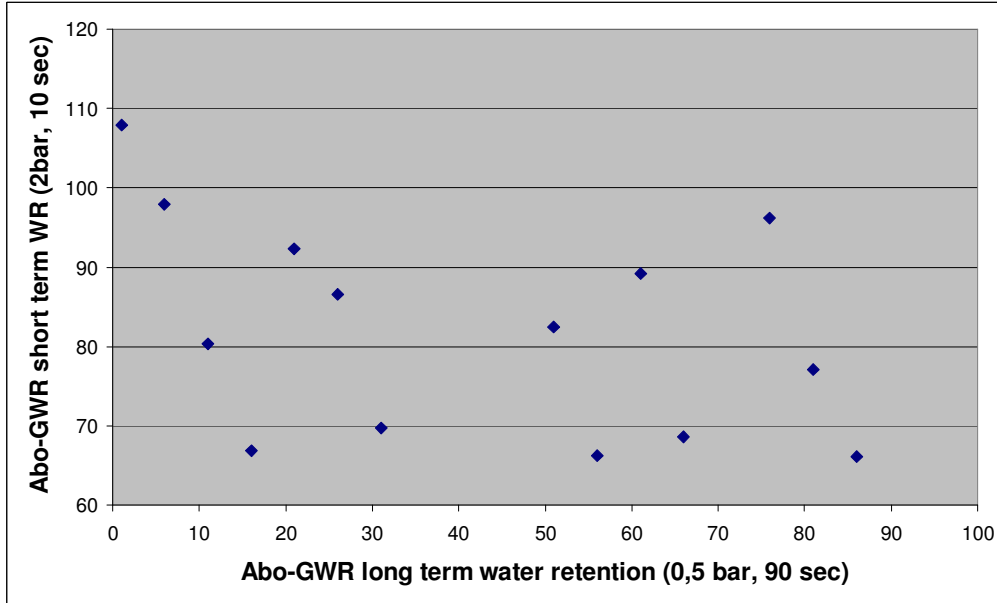
Pict. 10.7.13.7: Comparing water retention measurements by Abo-GWR for latex based coating colours – thickener study part 1
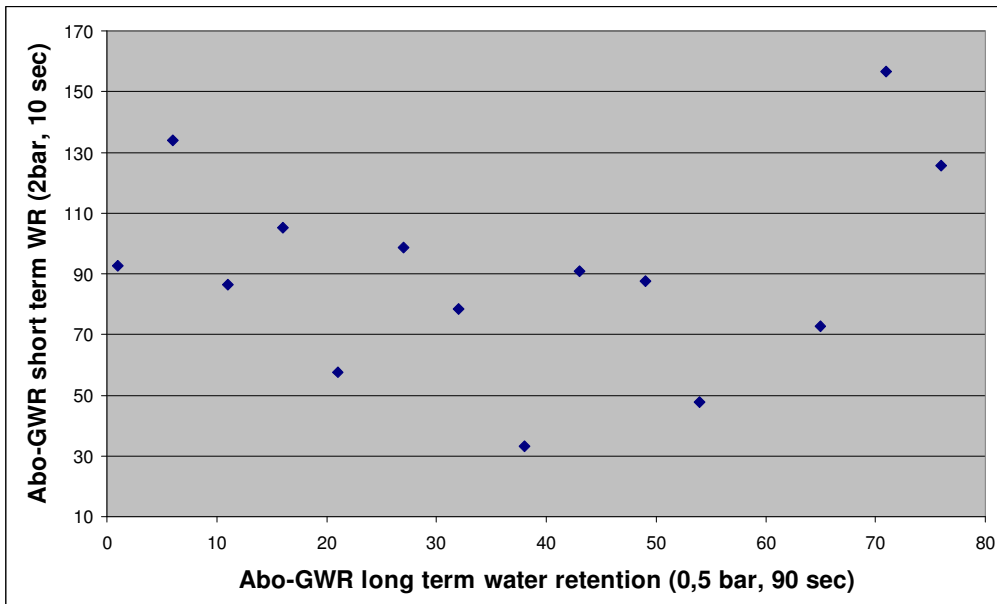
Pict. 10.7.13.8: Comparing water retention measurements by Abo-GWR for latex based coating colours – thickener study part 2
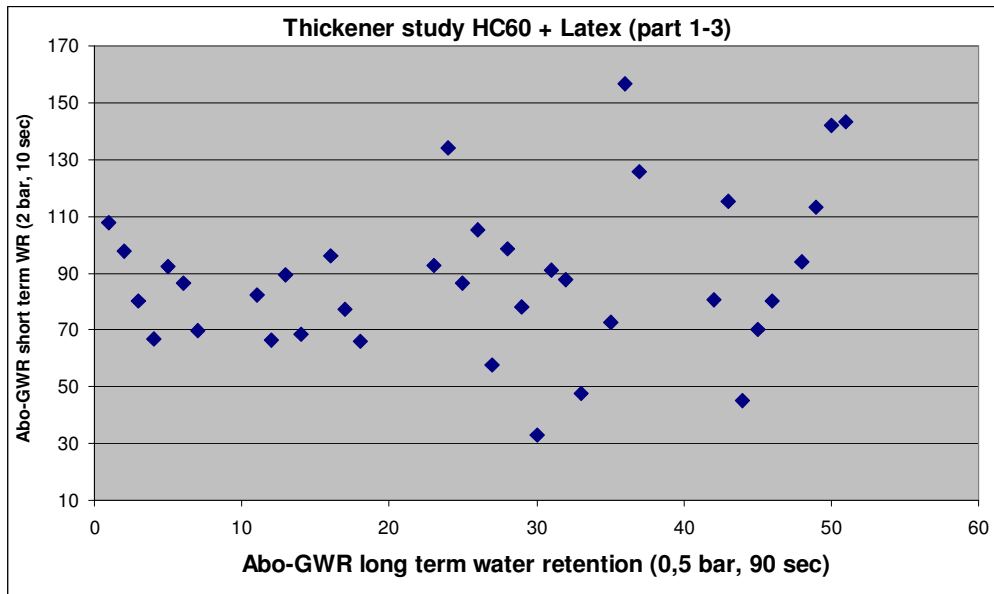
Pict. 10.7.13.9: Comparing water retention measurements by Abo-GWR for latex based coating colours – thickener study part 1 - 3

The standard water retention test for coatings is with the Abo-GWR instrument is done at 0,5 bar and 90 sec pressure time by using a 5 μm membrane. This test fits perfect to the capillary sorption of the base paper and the built up of a filter cake between the application and the blade. 5 μm is the pore size of base paper surfaces and 0,5 bar is a good average of fibre capillary sorption pressure.

Dewatering under blades where without filter cake built up before the blade (as proven for top coaters of OMC11) is not sufficiently covered with this test.
For these situations the pressure in the Abo-GWR was increased to 2 bars and the pressure time was reduced to 10 sec.

Pict. 10.7.13.7 – 10.7.13.9 show, that correlation between these two tests is rather bad. Therefore both tests have to be made if the two mechanisms of coating colour dewatering before and under the blade have to be investigated.

To confirm the Abo-GWR short term water retention measurements other methods were compared. Compared to the dewatering time under the blade which is lower than 0,1 msec, the shortest possible penetration time in the Abo-GWR instrument is with 10 sec relatively long.

The state-of-the-art short term water retention test where external pressure can be applied is the KCL Clara test as shown in pict. 10.7.13.10.
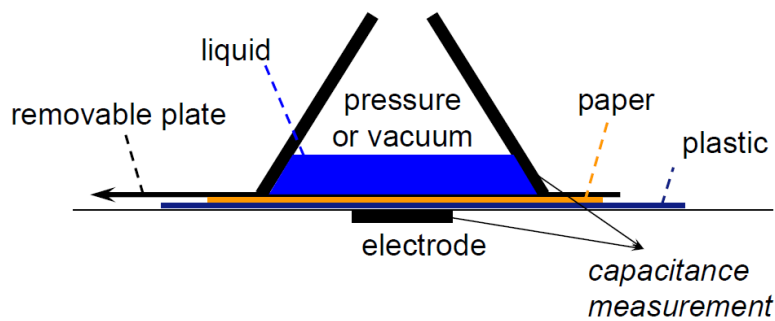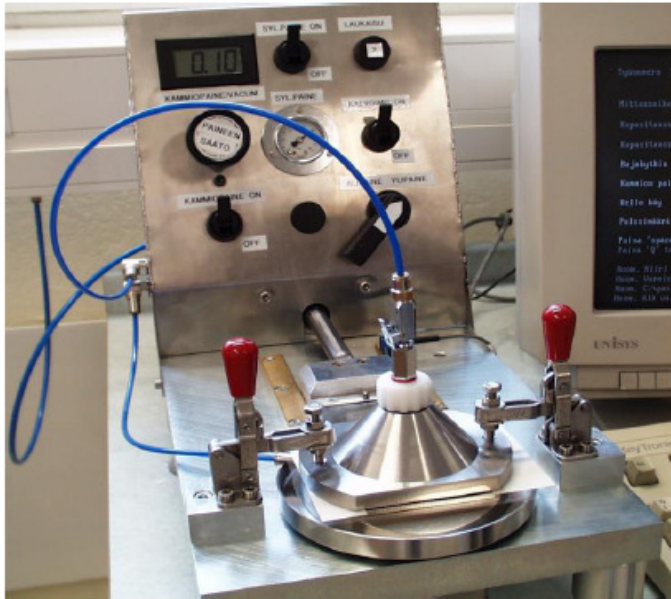
Pict. 10.7.13.10: KCL Clara test
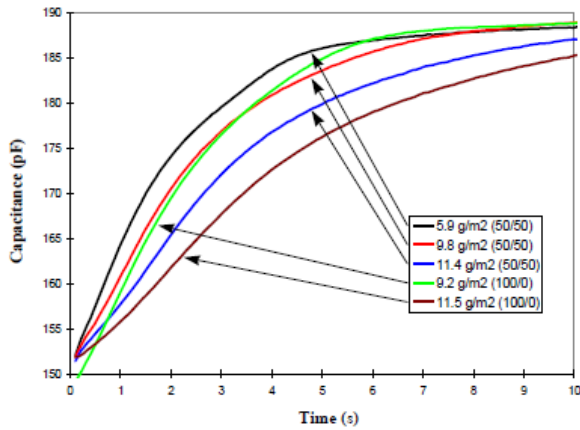
Pict. 10.7.13.11: Increase of capitance with time by capillary sorption of liquid phase from coating colour. In brackets: Kaolin / carbonate ratio in coating formulation

A high absorbent precoated paper based on CC60 was used as a substrate and selected coating colours from this study were dewatered with 5 bars and 40°C into this paper.

Liquid phase penetration was measured by conductivity (pict. 10.7.13.11 to 13).
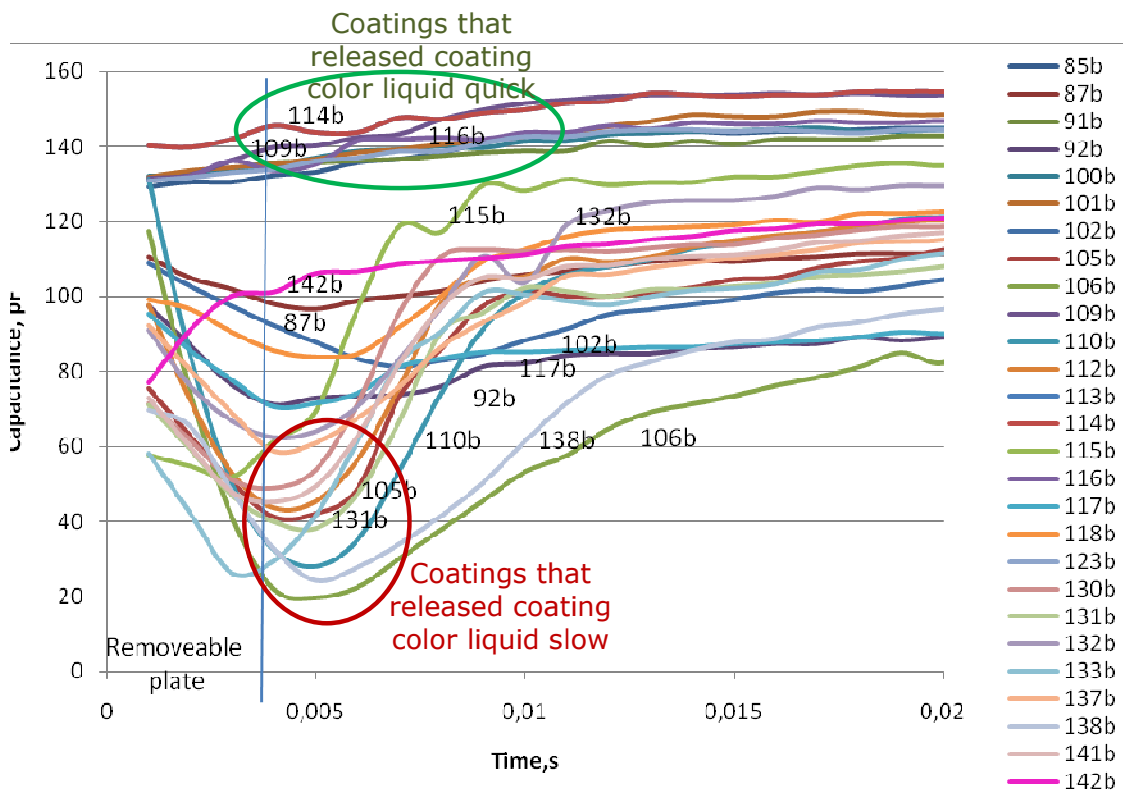
Pict. 10.7.13.12: Penetration data's from KCL Clara
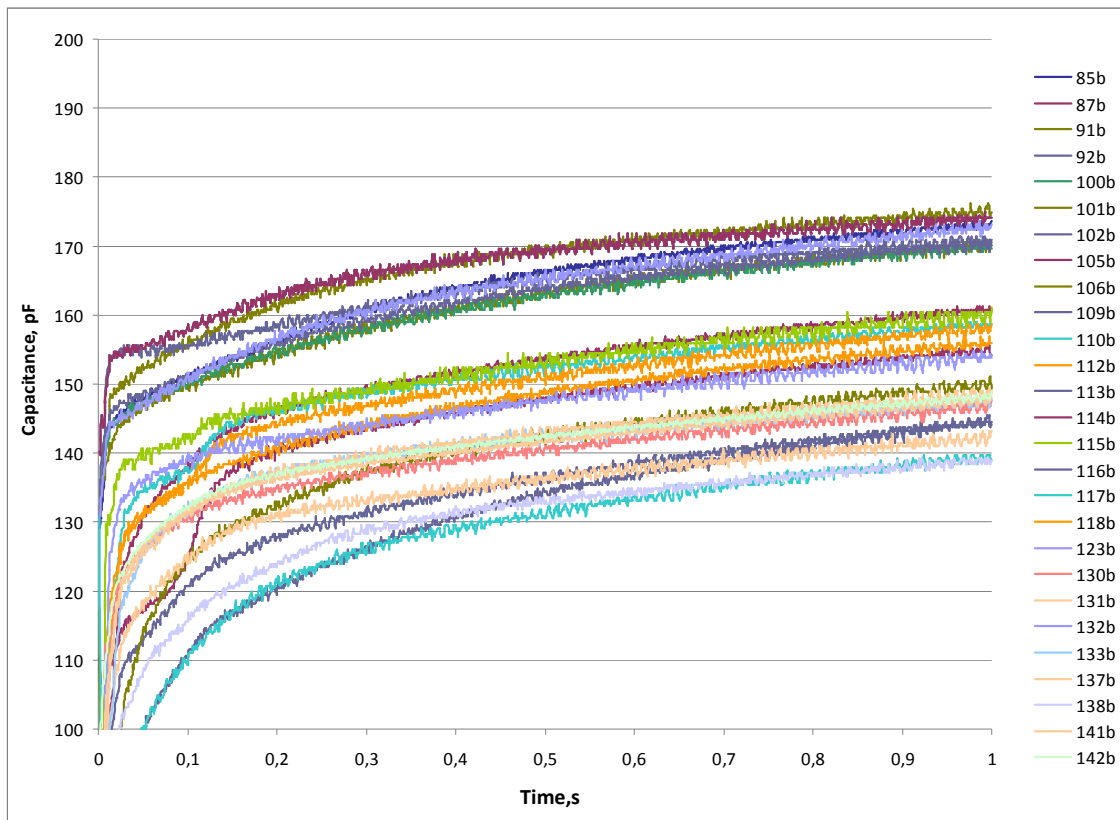
Pict. 10.7.13.13: KCL Clara pressure penetration test at 5 bar

Before KCL Clara test starts an isolating metal plate is removed between substrate and coating colour. When water retention of a coating colour is high, the liquid phase penetrates slowly into the substrate and conductivity is low over the whole time of measurement.

The data logging is very fast in the KCL Clara device (pict. 10.7.13.12 and 10.7.13.13); conductivity data's, which are measured in the first milli seconds, should correlate with the dewatering under the blade while conductivity data's after some seconds should correlate with dewatering of coating colour between application and blade.
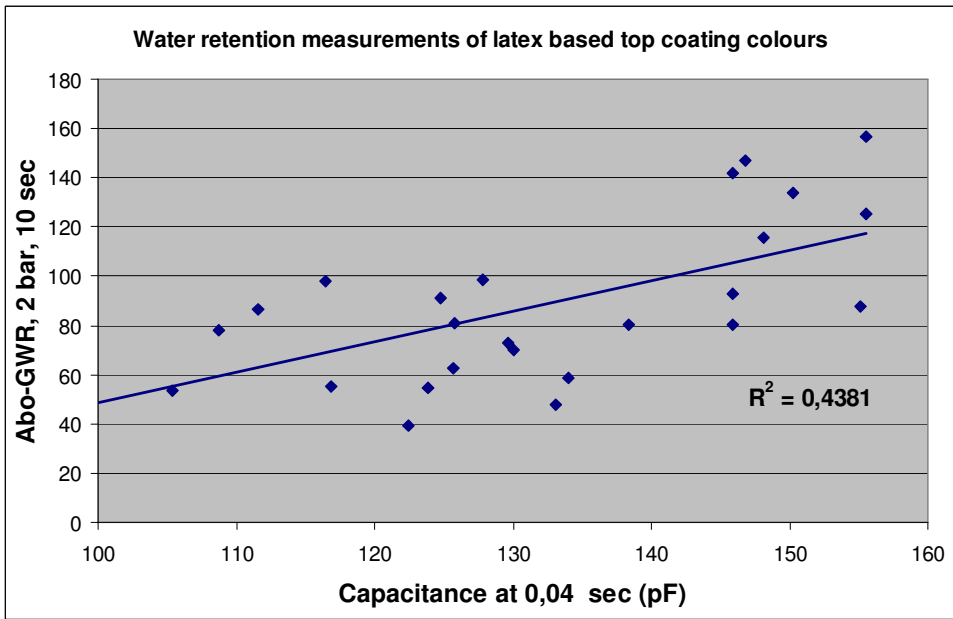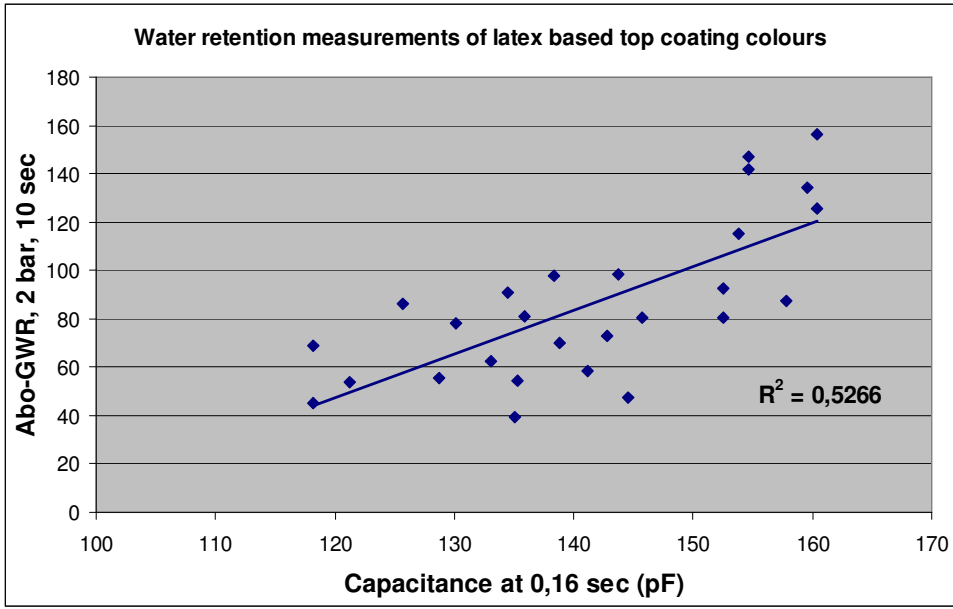
Pict. 10.7.13.14: Comparison of Abo-GWR short term water retention with KCL Clara
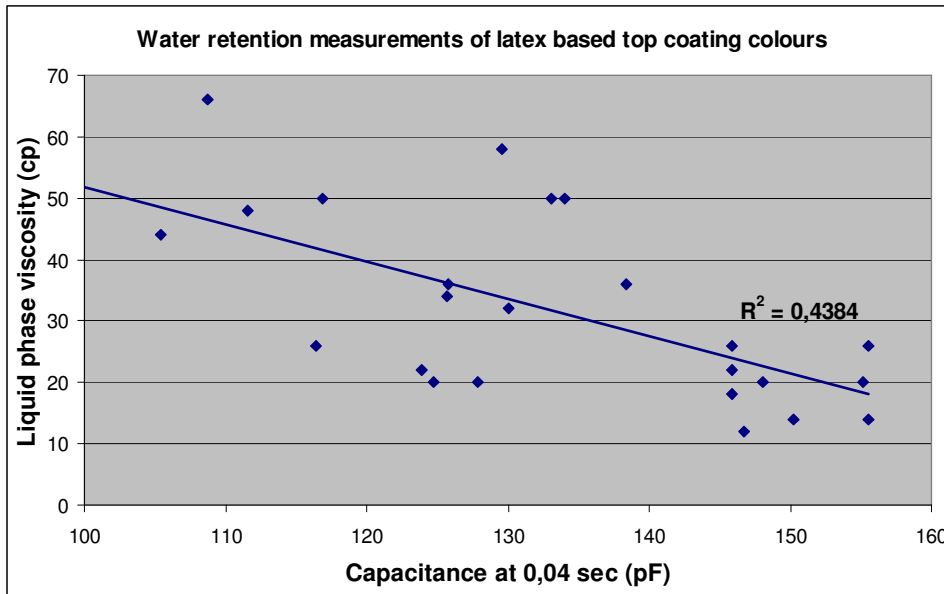
Pict. 10.7.13.15: Correlation of liquid phase viscosity and KCL Clara short term penetration

Pict. 10.7.13.13 – 10.7.13.15 show that correlation of Abo short term penetration and liquid phase viscosity, both measured in Gratkorn, with KCL Clara results from Finland was in the range of $r^2 = 0,5$ which is satisfying due to the fact that rheology of coatings might have changed during transport from Gratkorn to Finland especially when viscosity was high (> 5000 cp BF20).
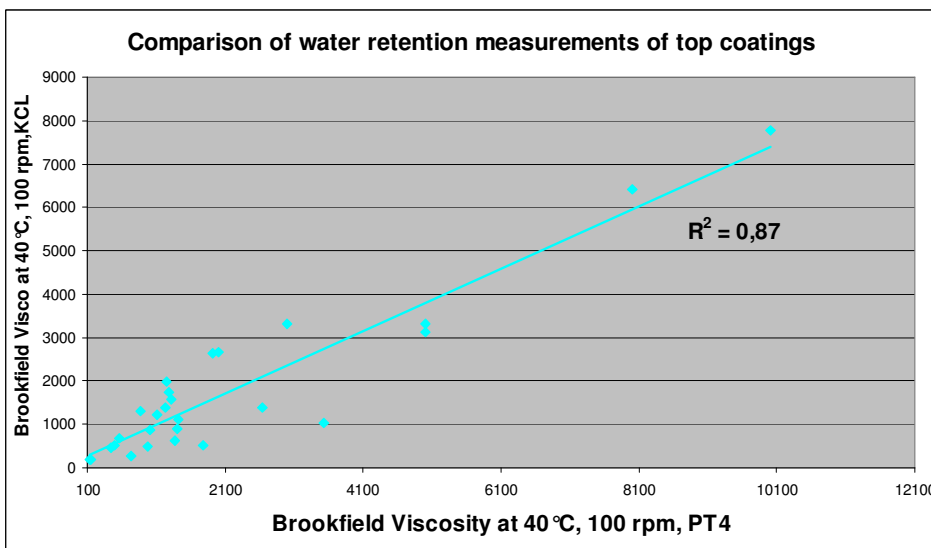
Pict. 10.7.13.16: Brookfield viscosity of coating colours measured in Gratkorn (PT4) and KCL

A similar method to determine the short term pressure and capillary penetration is the PDWR instrument as shown in pict. 10.7.13.17).

Pict. 10.7.13.17: ACA-PDWR water retention and base paper sorption instrument

A defined liquid is pressed under adjustable pressure into a substrate. When capillary penetration has to be studied the external pressure is set to zero. The time of penetration can be adjusted by a timer at the instrument. The amount of picked up water is measured after a certain time. The advantage to PDWR instrument against the Abo-GWR method is an adjustable and short penetration time which can be in the range of 1 – 5 sec. To compare water retention of different coating colours a precoated paper of PM11 was used as substrate for the PDWR measurements.
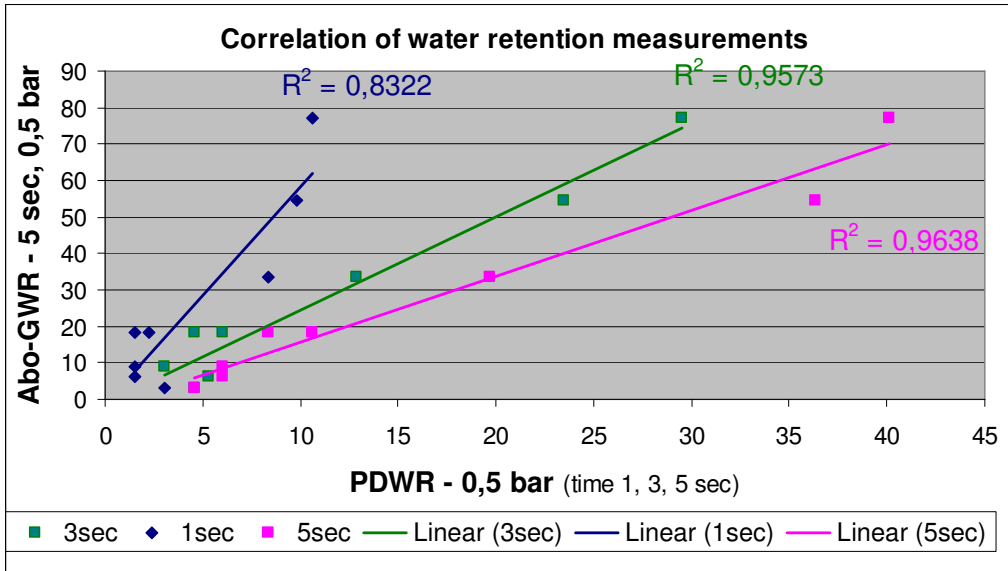
Pict. 10.7.13.18: Comparison of Abo-GWR short term water retention test with PDWR
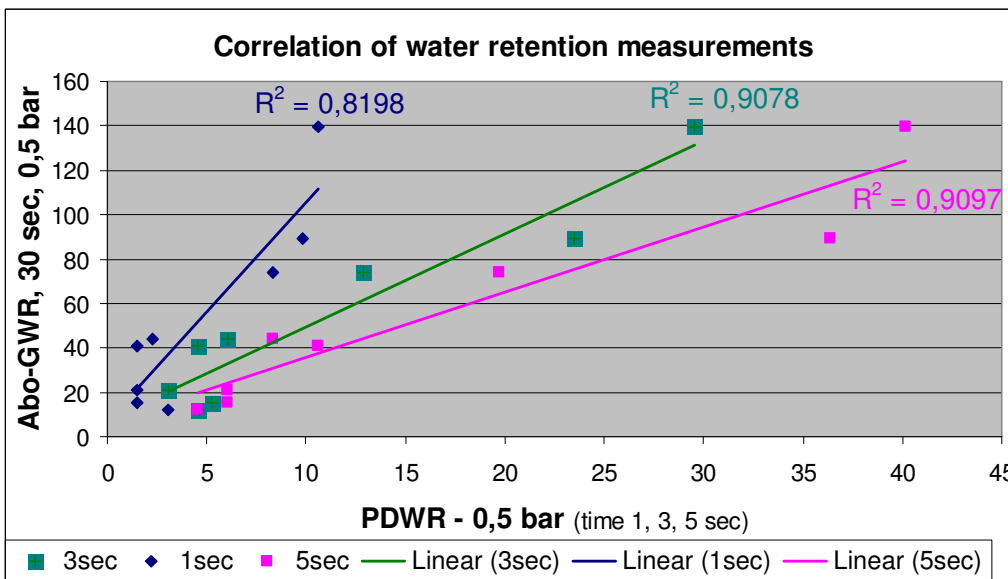
Pict. 10.7.13.19: Comparison of Abo-GWR short term water retention test with PDWR

For the wide range of tested latex based coating colours a good correlation between all short term pressure penetration tests was found (pict. 10.7.13.18 and 10.7.13.19).

Comparing the results and the time consumption for test procedure of all the investigated water retention tests, the Abo-GWR short term penetration test with 2 bars and 10 sec is the best compromise.

Elasticity of tested coatings was compared with their low shear viscosity to detect the impact of depletion flocculation.
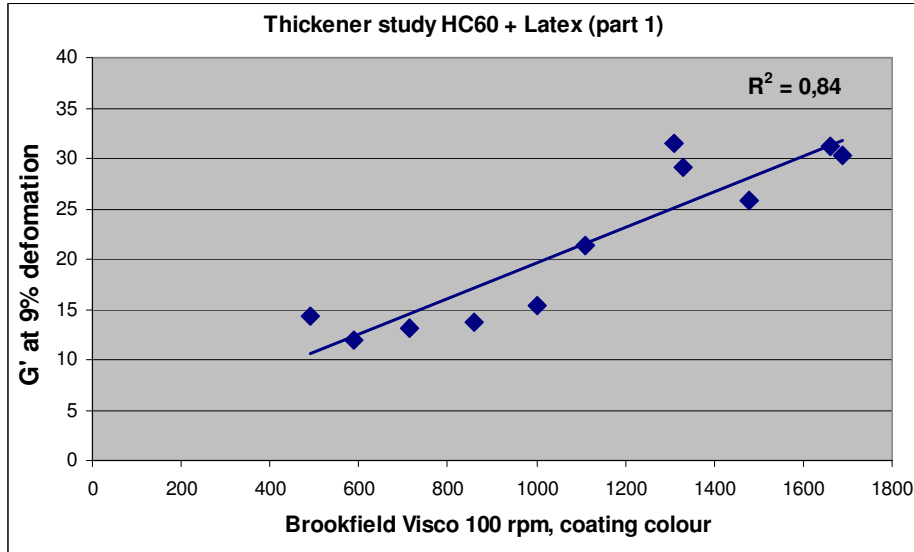
Pict. 10.7.13.20: G' versus low shear BF viscosity of coating colours in latex study part 1
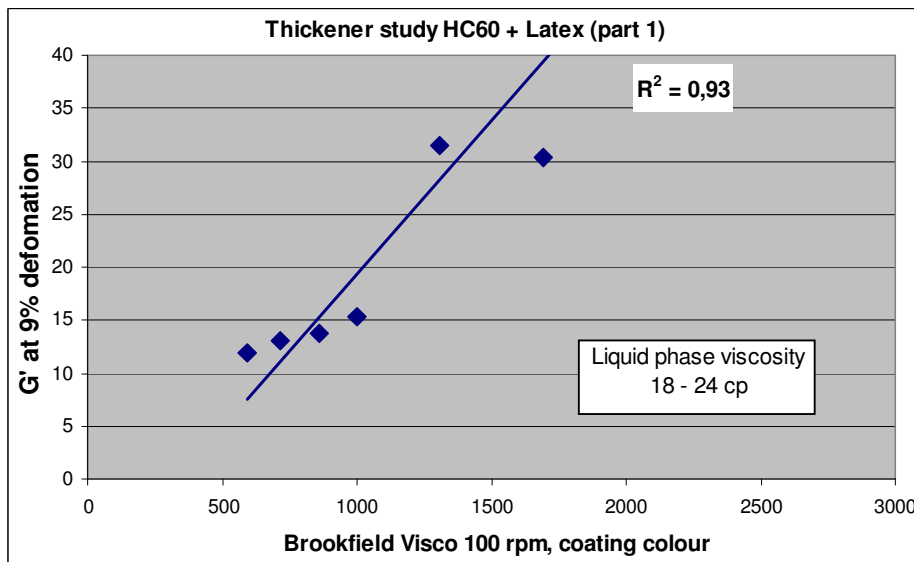
Pict. 10.7.13.21: G' versus low shear BF viscosity of latex based coating colours part 1 with selected range of liquid phase viscosity
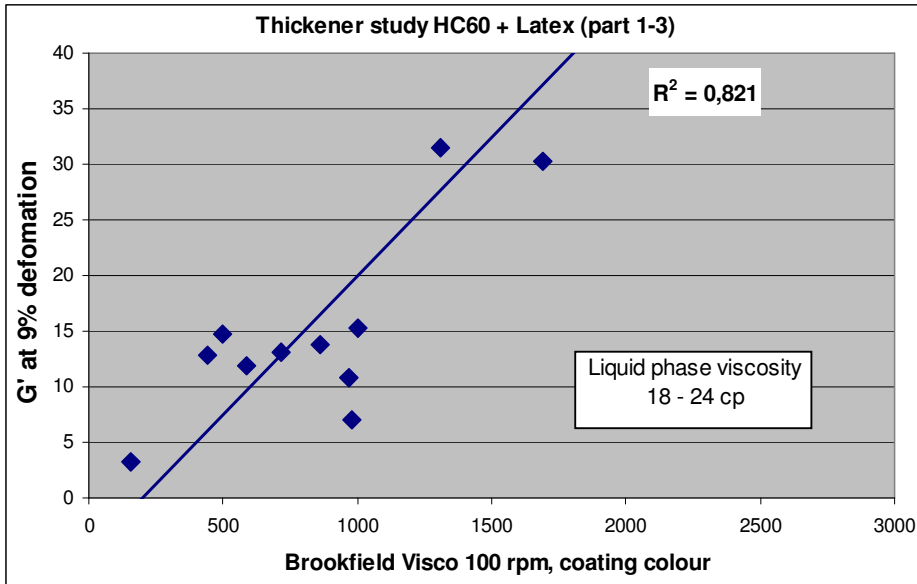
Pict. 10.7.13.22: G' versus low shear BF viscosity of all latex based coating colours with selected range of liquid phase viscosity
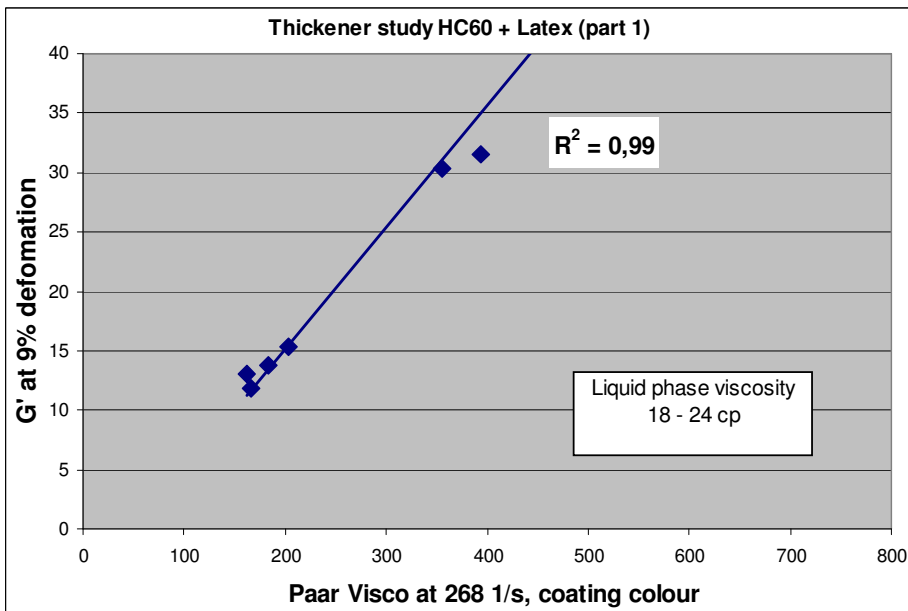
Pict. 10.7.13.23: G' versus low shear viscosity (Paar cone – plate - system) of latex based coating colours part 1 with selected range of liquid phase viscosity
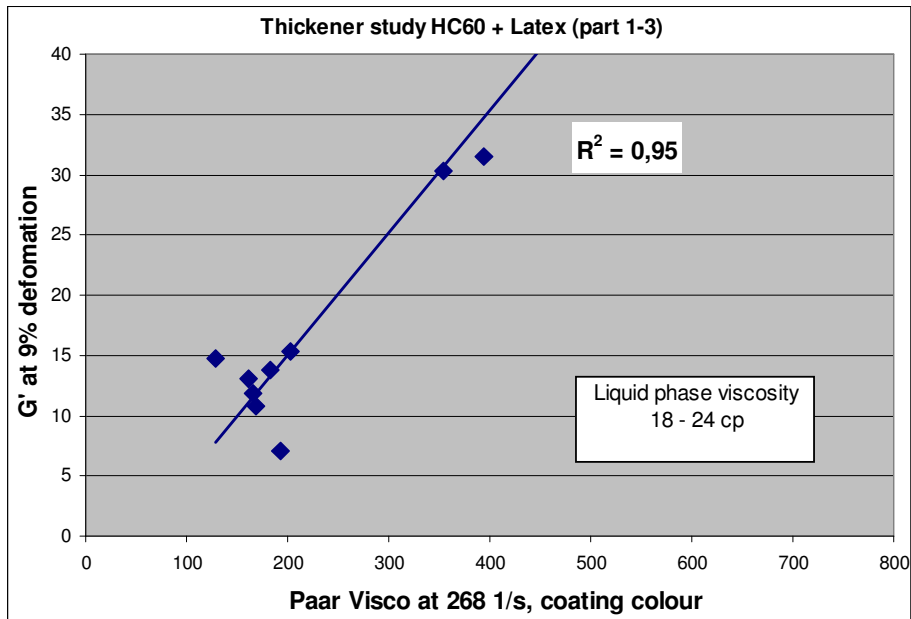
Pict. 10.7.13.24: G' versus low shear viscosity (Paar) of all latex based coating colours with selected range of liquid phase viscosity

Pict. 10.7.13.20 – 10.7.13.24 show that almost all tested water retention additives add elasticity to coatings by building bridges between pigment and/or latex particles. Low shear viscosity rose with G'.

10.7.14 Practical implementation of the results of this rheology lab study

At OMC11 mill trials were performed where CMC Niclacell CH90 was replaced in the top coatings by a new HASE thickener Cartacoat RM20 (formulation see pict. 10.7.14.1).

	Standard 0,45% CMC CH90 5161/MR1 - 6	Trial 0,2% HASE1 5161/MR7 - 13
Solid content in working tank C5 (%)	68,3	68,5
Solid content in working tank C6 (%)	68,5	68,7
Liquid phase viscosity BF20 (cp)	30	50
BF100 Vsicosity of coating colour (cp)	1820	1650
ACAV Viscosity at 300.000 1/s (cp)	102	88
Blade Load Top Coater 5 (%)	55	45
Blade Load Top Coater 6 (%)	58	43
Speed of OMC11 (m/min)	1650	1630
Coat Weight at C5 (g/m²)	12,2	12,1
Coat Weight at C6 (g/m²)	11,6	11,5
Tappi Gloss uncalandered TS (%)	32,2	33,4
Tappi Gloss uncalandered BS (%)	31,7	32,9
Backtrap mottling visual, TS (1-4)	2,25	2
Backtrap mottling visual, BS (1-4)	2,5	2

Pict. 10.7.14.1: Coating colour data's for HASE trial 1 at OMC11

Although CMC is not a bad choice as thickener, the change to a new HASE thickener in top coatings of OMC11 led to an increase in liquid phase viscosity at lower blade load (pict. 10.7.14.2 and 10.7.14.3). Back trap mottling improved in consequence (pict. 10.7.14.4).
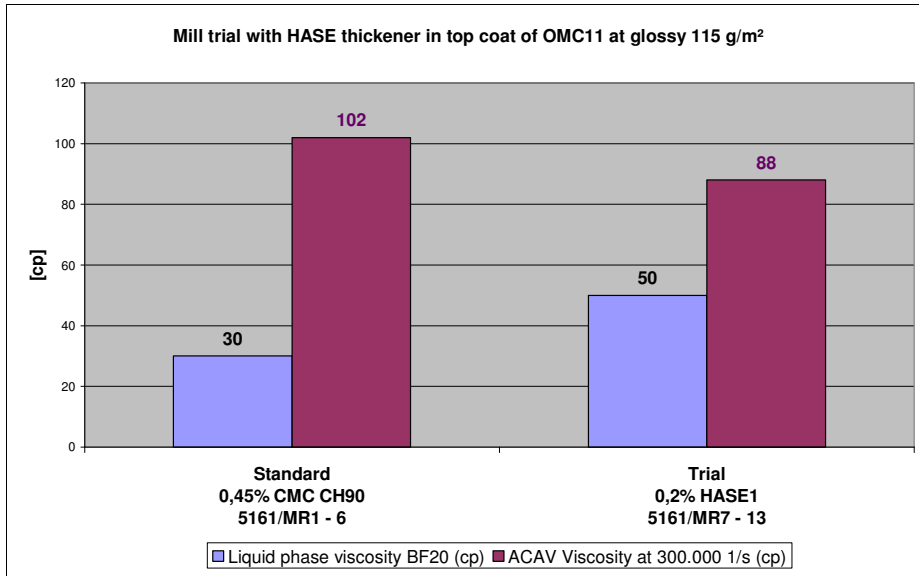
Fig. 10.7.14.2: Liquid phase viscosity vs. high shear viscosity of coating colour in working tank (solids 68 – 69% for standard and trial)
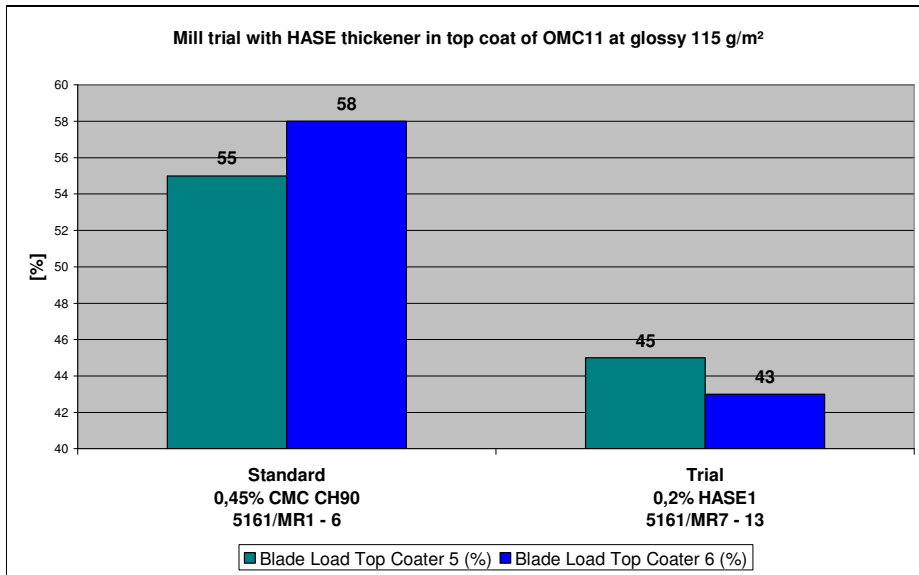
Fig. 10.7.14.3: Blade load of top coaters for standard (CMC) and trial (HASE)
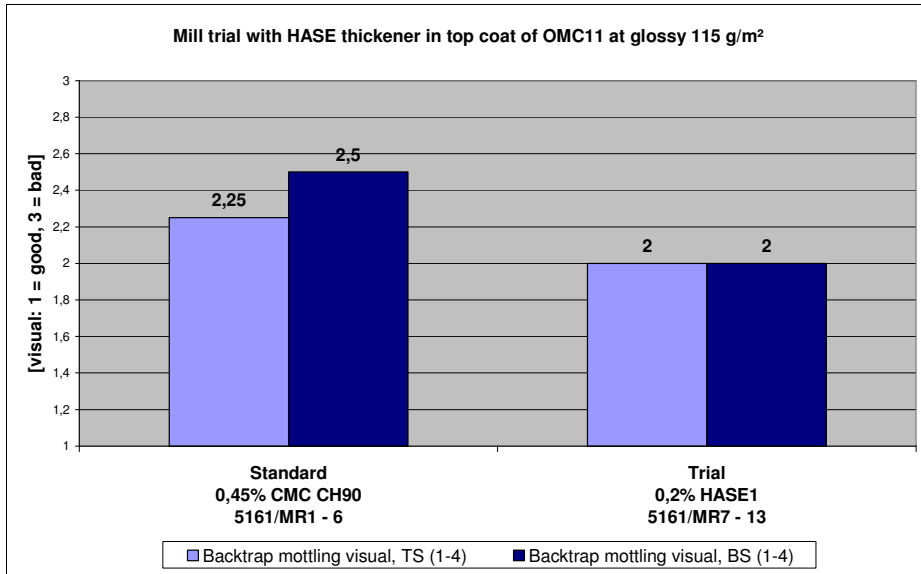
Fig. 10.7.14.4: Mottling comparison of trial with HASE to standard with CMC

But the HASE thickener Cartacoat RM20 showed **two disadvantages** which were common for all tested ASE/HASE/PU thickeners in SFPE paper mills:

a) They had **no carrier function** for the optical brightener, like CMC has. In consequence the PVOH had to be increased when these thickeners were used in top coatings and the advantage in lower high shear viscosity of the coating colour got lost. Expensive HASE versions like Rheocarb 120 or Acrosol E20D exist on the market with integrated carrier function to overcome this disadvantage.

b) They are **sensible for shear**. Brookfield viscosity dropped when shear was applied at the blade. It should regenerate in the working tank to the original level but the trials did not prove this assumption (pict. 10.7.14.5). Viscosity dropped with trial time. Brookfield viscosity must be kept over a certain minimum level at the jet application to avoid baring. To keep viscosity at this level a much higher amount of HASE thickener had to be used at high speed coaters than expected. The consequence was a much higher level of viscosity of the fresh coating colour in the coating kitchen than for CMC based coating colours which was critical in mixing and handling of the colour in the kitchen.

For blade precoatings the disadvantage of missing carrier function was no disadvantage and therefore HASE thickeners are successfully used already in many of these coatings.
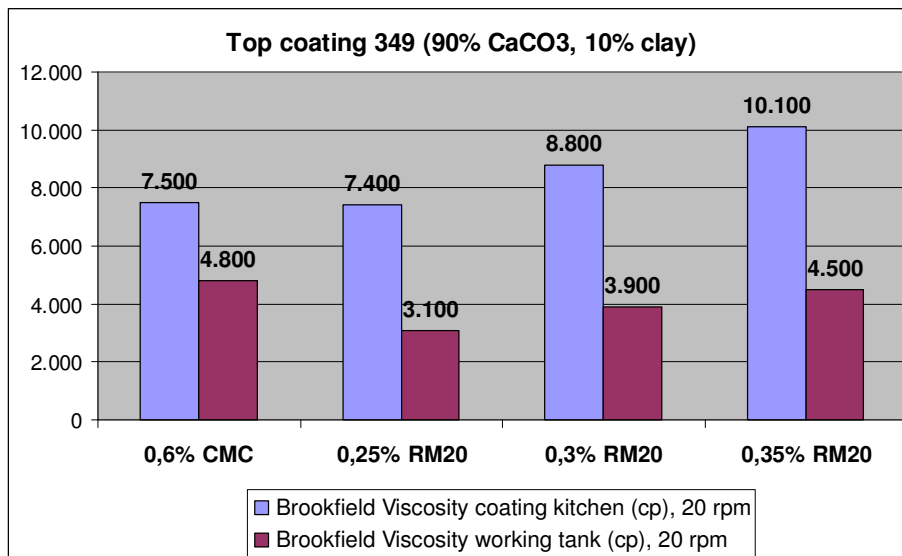
Pict. 10.7.14.5: Viscosity of Cartacoat RM20 versus CMC

An important step to improve mottling was the reduction of PVOH in top coatings by adapting the coating colour. To reduce PVOH and optical brightener and keep brightness on a constant level, clay can be replaced by carbonate or tetra-sulfo OBA's can be replaced by diulfo types. High shear viscosity dropped with falling amount of PVOH and more thickener could be used. Liquid phase viscosity was raised and mottling improved.

The trials at OMC11-Gratkorn and OMC6 in Maastricht showed an additional benefit in reduced scratches when PVOH lowered in top coatings.

Chapter 11: Latex film forming and drying induced mottling

11.1 Lab trials

11.1.1 Lab coatings on DOW roll coater

Influence of base paper on drying energy demand:

In a pre-study the possibility of testing the influence of base paper sorption and coating colour components on drying time of wet coatings was investigated in a lab coating study with the DOW roll coater of RD-Gratkorn.

The DOW roll coater in RD sappi Gratkorn is operated at a relatively low speed of 30 m/s.

The application unit is a trailing stiff blade where the coating colour is filled into a gap between the blade and the paper. It operates similar as a SDTA coater. Low shear viscosity of the coating colour, solid content and the adjustable blade pressure determines the coat weight. Blade pressure is much lower when compared to mill coaters, where hydrodynamic forces at the blade are much higher.

Drying conditions were kept constant. Two IR heaters and one airfoil were used for drying, similar to mill coaters.

Coat weight was varied by blade pressure. Moisture of base and of coated paper was measured in the lab. By knowing the solid content, the coat weight and the moisture, the applied and the evaporated amount of water as calculated and compared with each other. The more water has evaporated at a given application weight of water, the lower the drying energy demand.

To get separate information about drying speed in the 1st and 2nd drying stage a new developed surface moisture measuring instrument from Fibro AB in Sweden was used in all free draws of the lab coater to measure coating moisture.

<u>Influence of the base paper quality on drying energy demand:</u>

The substrate had the biggest impact on the drying energy speed. This was also proven by mill experience when precoaters of PM11 and middle coaters of OMC11 were compared in drying energy demand.

R&D-Vesuche

Trial 1-3: Substrates

$R^2 = 0,7188$

$R^2 = 0,5276$

$R^2 = 0,8793$

Evaporated amount of water (g/m²)

Applied water with coating (g/m²)

◆ Trial 1.7-12 on base paper (BS)
■ Trial 2.1-10 on precoated paper PM11
▲ Trial 3.1-6 on double precoated paper PM11
— Linear (Trial 3.1-6 on double precoated paper PM11)
— Linear (Trial 2.1-10 on precoated paper PM11)
— Linear (Trial 1.7-12 on base paper (BS))
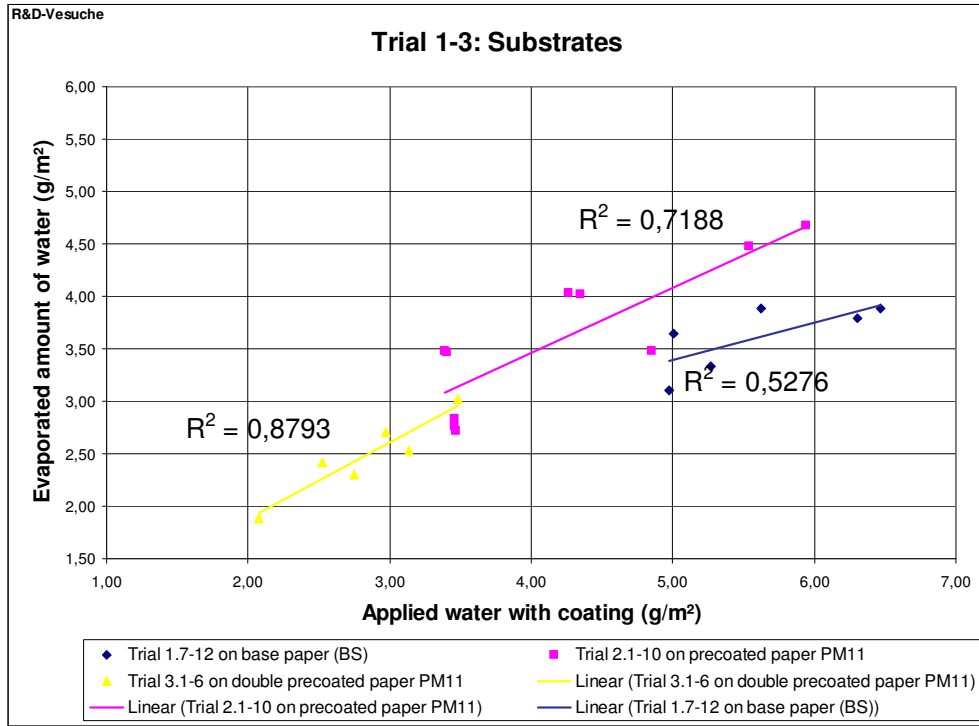
Pict. 11.1.1..1 : Comparison of drying rate on different base papers

The amount of evaporated water was much lower or in other words drying speed was much lower when the coating was applied on a base paper, compared with the precoated papers.

The reason is the more pronounced penetration of the water into the macro pores of the base paper and into the pores of the fibre walls. The deeper the penetration at the application, the longer is the distance to the surface and the higher the necessary evaporation energy will be. To evaporate water which has penetrated into the relatively small intra fibre wall pores (0,1 μm diameter), the capillary force of these small capillaries must be overcome and evaporation enthalpy is added by sorption enthalpy.

When more water is absorbed by the base paper the 2nd drying period is reached faster where drying speed is always lower than in the 1st period.

The same result was detected by Ph. Bernada and D. Bruneau (L3.12) who studied migration of starch as one of the binder components in coatings during drying. The movement to the surface by evaporation forces, the sorption into the base paper and the combination of both was investigated. Previous papers stated that motion of starch after the gel point is impossible while others proved the opposite.

At the first critical concentration (FCC), the so called "gel point" W_g, a bulky, three dimensional network is formed. The level of solid content at which this network structure is reached depends upon the colloidal interaction between the pigments and the binders.

As drying continues, capillary forces lead to shrinkage of the coating structure and the internal stress in the coating increases. When particles are no longer able to move, the second critical point (SCC) W_c is reached. It depends mainly upon chemical interaction between all coating components.
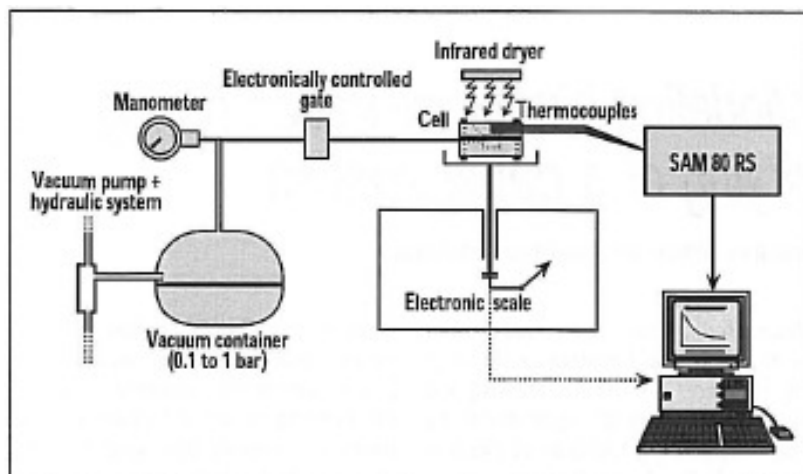
Pict. 11.1.1.2: Experiment configuration (D. Bruneau)
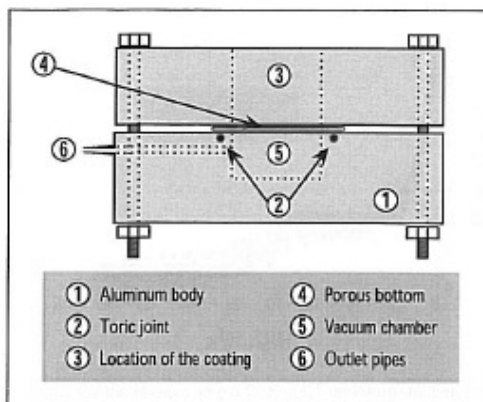
Pict. 11.1.1.3: Experimental cell for lab drying (D. Bruneau)

An infrared dryer with adjustable temperature (50 – 160 °C) was used on top of the sample for drying the wet coating colour.

At the bottom side of the wet coating colour a vacuum chamber was positioned to simulate base paper sorption pressure. Max pressure was - 0,9 bar.

The sandwich of vacuum chamber plus coating colour was put on a micro scale which determined the weight loss during drying and calculated the solid content of the coating layer.

The coating colour consisted of 50% $CaCO_3$, 50% clay, 16% latex, 6% starch and had a solid content of 65%.

To characterize liquid movement during drying and/or vacuum application the experiment was stopped at certain periods of time and the dry coating sample was cut vertically into 12 slices by moving the piston stepwise upwards and removing the vertical excess of coating colour by a blade. The moisture content of each slice was measured.
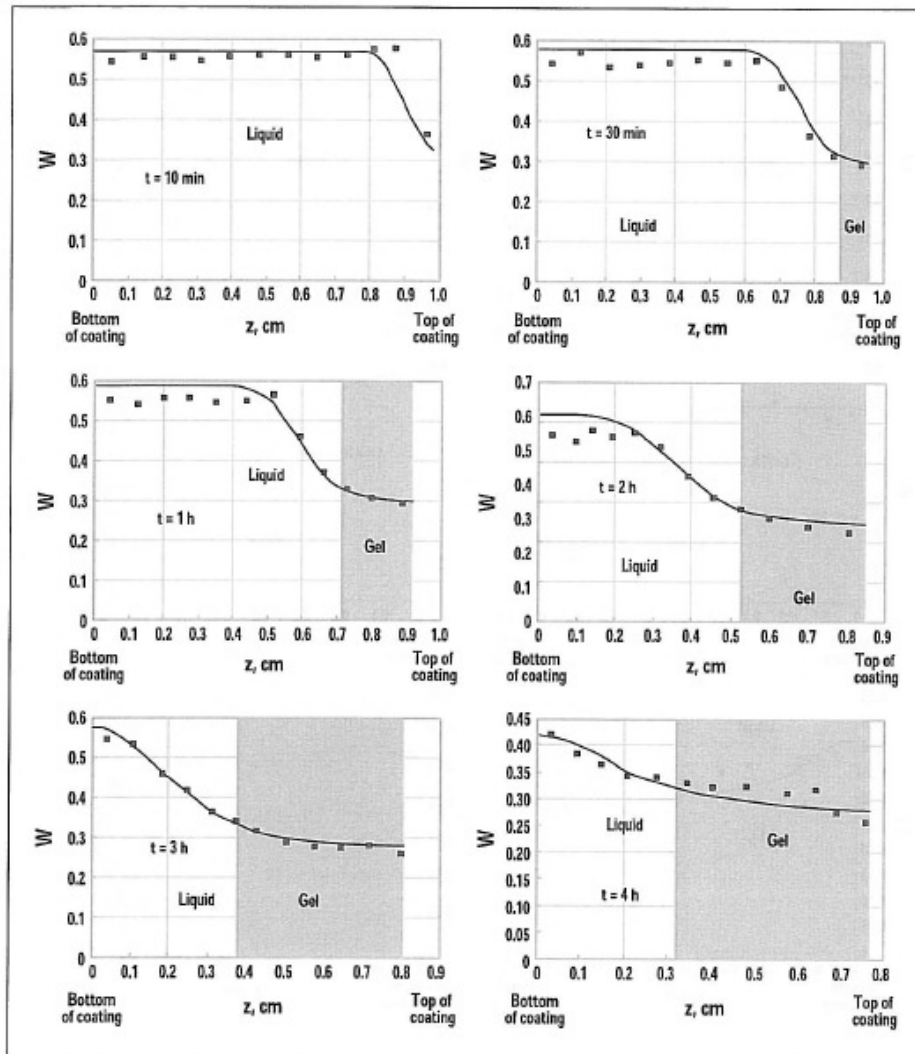
Pict. 11.1.1.4: IR drying with 60°C without dewatering to the base by vacuum; numerical calculation = continuous line and experiments = points (D. Bruneau)

Pict. 11.1.1.5: IR drying with <u>80°C</u> without dewatering to the base by vacuum; numerical calculation = continuous line and experiments = points (D. Bruneau)

Pict. 11.1.1.6: Starch concentration profiles for 60°C and 80° IR drying without dewatering (D. Bruneau)

Page 656

Pict. 11.1.1.7: IR drying with 60 °C with dewatering to the base by vacuum; numerical calculation = continuous line and experiments = points (D. Bruneau)

Pict. 11.1.1.8: IR drying with 80 °C <u>with dewatering</u> to the base by vacuum; numerical calculation = continuous line and experiments = points (D. Bruneau)

Pict. 11.1.1.9: Starch concentration profiles for: A = IR 60°C, no dewatering, B = IR 80°C no dewatering, C = IR 60°C, with dewatering, D = IR 80°C with dewatering (D. Bruneau)

Results: The movement of starch to the surface during drying was remarkably reduced, when vacuum was applied on bottom of the sample and base paper sorption was simulated. In the same way starch concentration at the bottom increased. The calculated gel point was $W_g = 0,32$ for all experiments.

T. Hattula and P.J. Aschan (L3.13): measured latex migration to base paper and surface for double coatings on 250 g/m² base board. Clay based coatings were used and speed of pilot coater was with 120 g/m² relatively low. They compared a soft and fast film forming styrene butadiene latex with a hard and non film forming polyvinyl acetate latex.

Latex concentration in Z-Direction of the double coating layer was measured by grinding of the dry coating colour and applying multiple internal reflectance infrared spectroscopy.
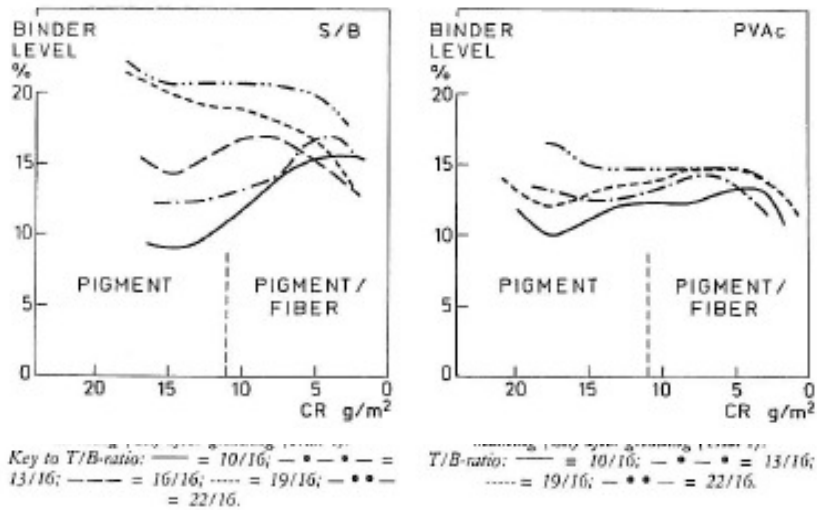
Pict. 11.1.1.10: Latex level vs. coating remaining after grinding (CR) for trial 1 (T. Hattula)

Polyvinyl acetate (PVAc) based coatings generally showed a bigger loss of latex into the base paper. When SB latex was used, 7% of this latex was lost from both coatings into the base paper by capillary and pressure penetration with the liquid phase. For PVAc latex this amount was doubled.

The higher the latex content in the top coating, the more latex was kept at the surface due to lower permeability of immobilized coating layer during drying.
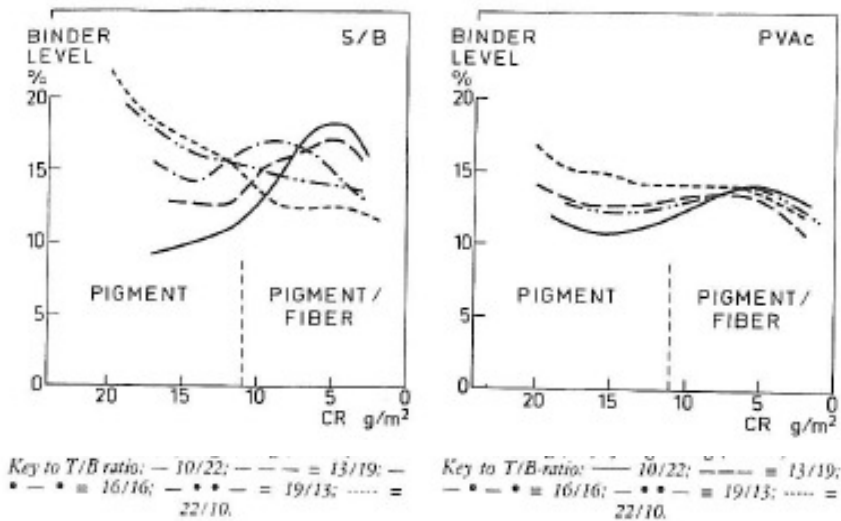
Pict. 11.1.1.11: Latex level vs. coating remaining after grinding (CR) for trial 2 (changing binder amount in top- and precoat from 10/22 to 22/10) / T. Hattula)

Page 660

Latex penetration from top coat into precoat increased, when latex level in precoating colour was low and thus the porosity of the dry precoat was high.

The higher the latex level in the precoat, the more latex of this coating was lost into the base paper as precoat filter cake permeability was increased.

PVAc latex again showed higher mobility than SB latex and bigger loss into the base paper.

In a separate experiment the authors proved that latex can penetrate through porous precoating layers into the base paper when mobility of latex is high enough.

With the IGT tester the surface strength was measured.
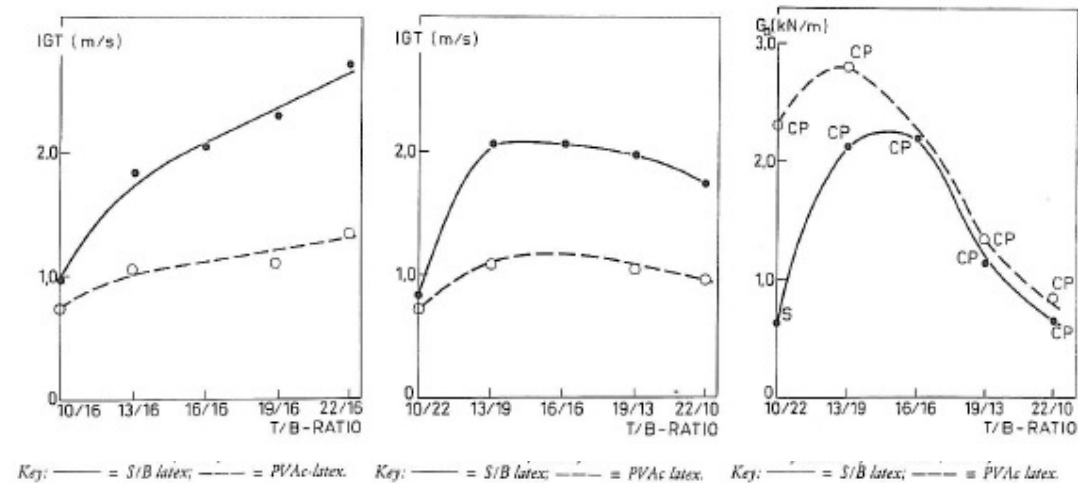
Pict. 11.1.1.12: IGT tests or trial series 2 (T. Hattula)

S/B coating showed higher IGT values than PVAc coatings as more latex was lost to the base paper with PVAc.

At low top coating latex content (10%) and high precoating latex content (22%) the lowest IGT values were found.

The higher the latex content in the top coating, the deeper the film split point at the IGT test was moved into the coating. When top coating latex content was above 16%, all samples were split at the boundary between base and precoating.

Lowering the latex content in the precoating led to a decrease of the IGT due to a lower binder concentration at the boundary to the base paper.

K. Kranich (L3.9) compared print mottling to different settings at a commercial off coater. Drying was done by airfoils and steam heated drying cylinders. High surface temperatures at the drying cylinders after the FCC led to severe print mottle. When air speed was reduced in the air caps mottling could be improved. Exchanging the airfoils by IR-dryers led to further improvement of mottling.

Kranich invented a nice lab method to compare the risk of mottling for different coating colours: A wet lab coated sheet was dried at a warm steel plate, which was perforated with drilled holes. At spots with holes less latex was detected at the coating surface due to lower evaporation rate. K&N absorption was higher at these spots due to higher coating layer porosity.

Kranich showed with his lab method that precoated papers showed less mottling sensitivity than base papers as coating holdout was far better on the precoated paper and the risk of drying induced mottling by uneven latex migration was lower. The higher the coat weight, the more mottling was observed. Using Kasein or PVA as thickener gave less mottling than CMC and starch. Low solids coatings based on satinwhite gave more mottling than kaolin, talc and carbonate based coatings.

One of the most important measurements for mottling optimization is the detection of coating colour moisture (or solid content). Unfortunately no standard instrument exists on the market. Together with company FIBRO-AB the instrument Fibro MCA1410 was developed for that purpose. It uses near infrared reflection to detect surface moisture.

Pict. 11.1.1.13: Fibro MCA IR surface moisture instrument

Lab trials at slow roll coater, pilot trials at fast pilot coaters and mill trials at OMC9/11 with different drying strategies were accompanied by Fibro MCA 1410 measurements.

Pict. 11.1.1.14: Measurement of surface moisture at OMC11

When the moisture is measured at both sides of the paper the penetration of water from coating colour by capillary sorption after the blade can be detected:
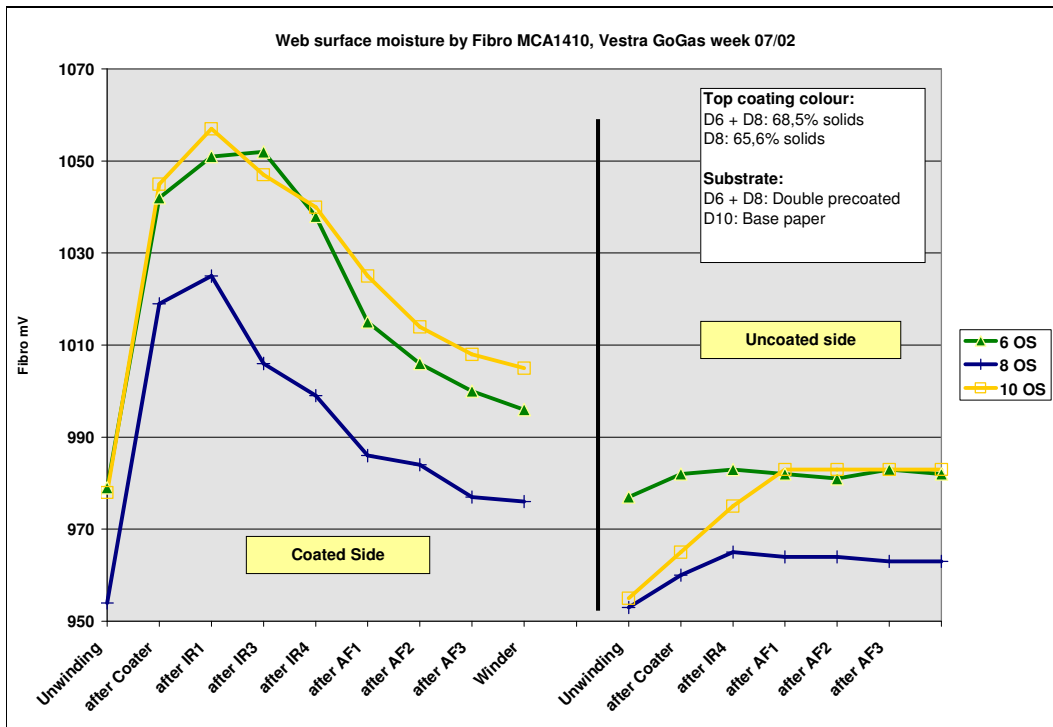
Pict. 11.1.1.15: Surface moisture measurement by Fibro MCA1410 (higher readings = higher moisture)

The example of Fibro MCA measurements at pilot trial Vestra 07/2002 shows the raise of back side moisture until the SCC was reached. Water from coating colour is absorbed by the base paper during the whole drying period up to the SCC.

On the coated side the surface moisture drops continuously during drying.

Comparing the drying energy demand of 1st and 2nd coating (= back side):
Mill experience from OMC11 and OMC9 showed a lower drying energy demand for back side coated papers. The 2nd side needed always less drying energy and showed better print mottle. The lab coater from DOW was used in RD-Gratkorn to verify this theory. Coating colours was applied single-sided by a blade coater. Drying was done by two electric IR's and one airfoil. 80 g/m² base paper from PM11 was used.

The drying energy demand was determined by comparing the amount of applied water with coating colour with the water which had been evaporated in the experiments where drying energy and drying conditions were kept constant. Solid content of fresh coating colour was also kept on constant level. When more water was evaporated at a given amount of applied water, drying energy demand was lower for this specific coating.
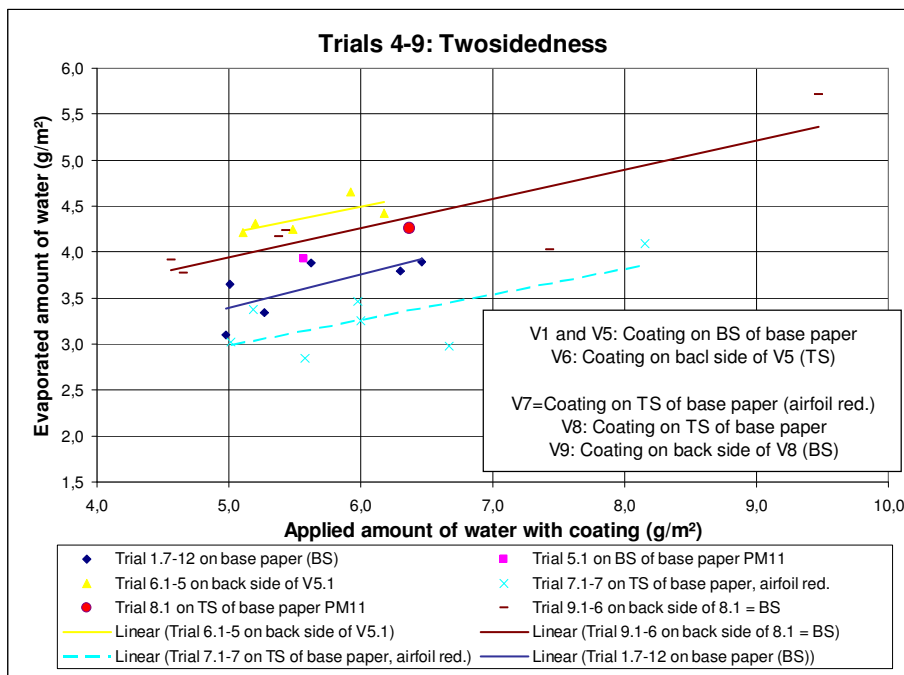
Pict. 11.1.1.16: Influence of back side coating upon drying speed

Airfoils operate with hot air from both sides. When the back side is uncoated its vapour permeability is much higher than when it's coated and therefore water which has penetrated the base can be removed more easily to an uncoated back side.
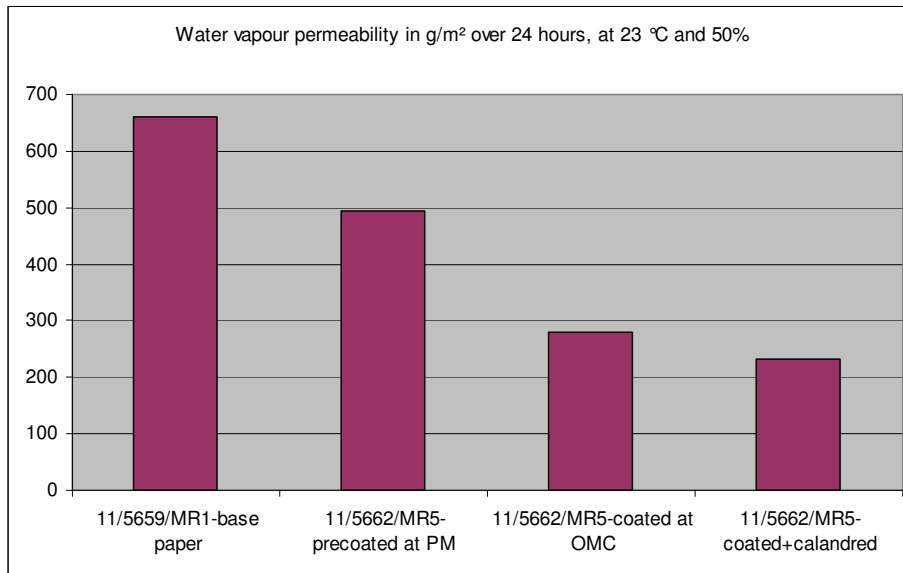
Pict. 11.1.1.17: Vapour permeability WddU of base paper, precoated, top coated and calendared paper

Results from lab and mill trials show the opposite result: Less drying energy was needed, when the back side was already coated.
Therefore the reason for the lower drying energy demand of back side coated papers is expected to be the lower penetration depth of the coating under the blade due to the air cushion in the base paper, which cannot be removed through the dense back side and reduces penetration depth of liquid phase under the blade.

This was proven by Chen and Scriven (L1.18), who calculated the influence of the air in the base paper pores on pressure penetration of the coating colour at the blade. The air volume of the base paper is compressed in an LDTA application nip to half and under the blade to 1/20 of its original volume.
Pressure penetration is reduced to one third when the trapped air is included in the calculation.
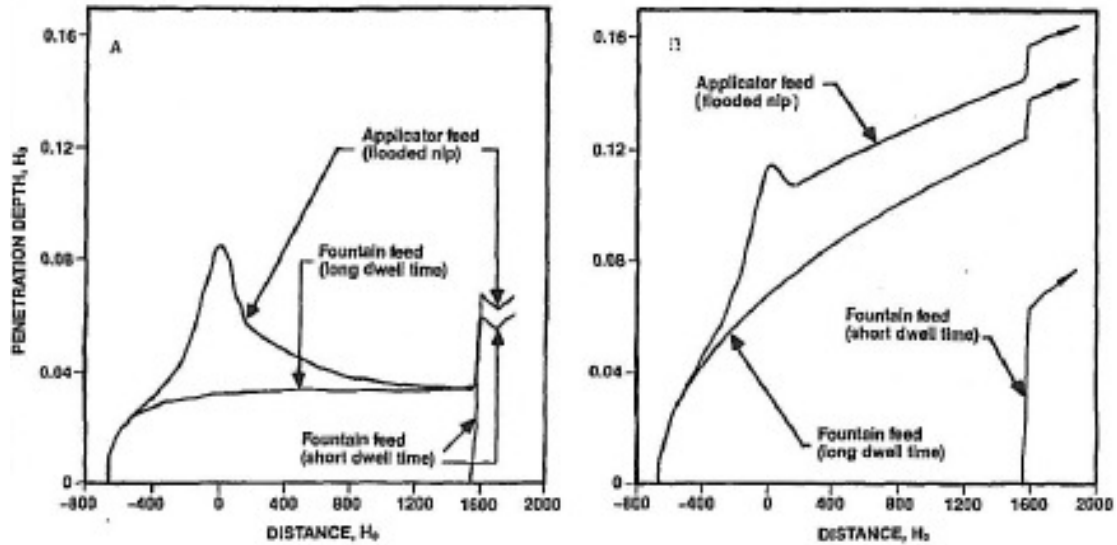
Pict. 11.1.1.18: Comparison of roll applicator (LDTA) with jet applicator (fountain) - left: complete air trapping, right: no air trapping (Chen and Scriven)

Influence of pigment type on drying energy demand

Coatings with 10% latex and 0,3% CMC were compared. Theoretically the drying energy demand should be lower for coatings with steep particle size pigments as water and vapour permeability is higher and drying rate in the 2nd drying period should improve.

Pict. 11.1.1.19: Influence of pigment on drying energy demand

Page 667
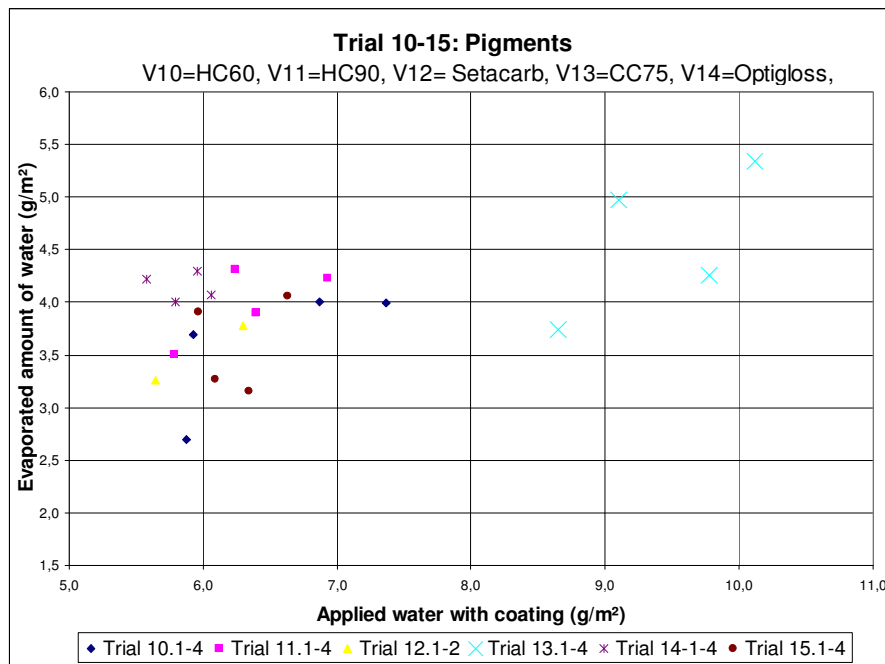
The lab coatings showed the opposite result: Steep PSD carbonate CC75 had the highest drying energy demand due to much lower water retention than the other pigments.

Pilot trials and mill trials gave lower drying energy demand for steep Covercarb only when applied in top coatings where water penetration is much lower than in precoatings (see chapter 11.2.1).

Influence of binder type:
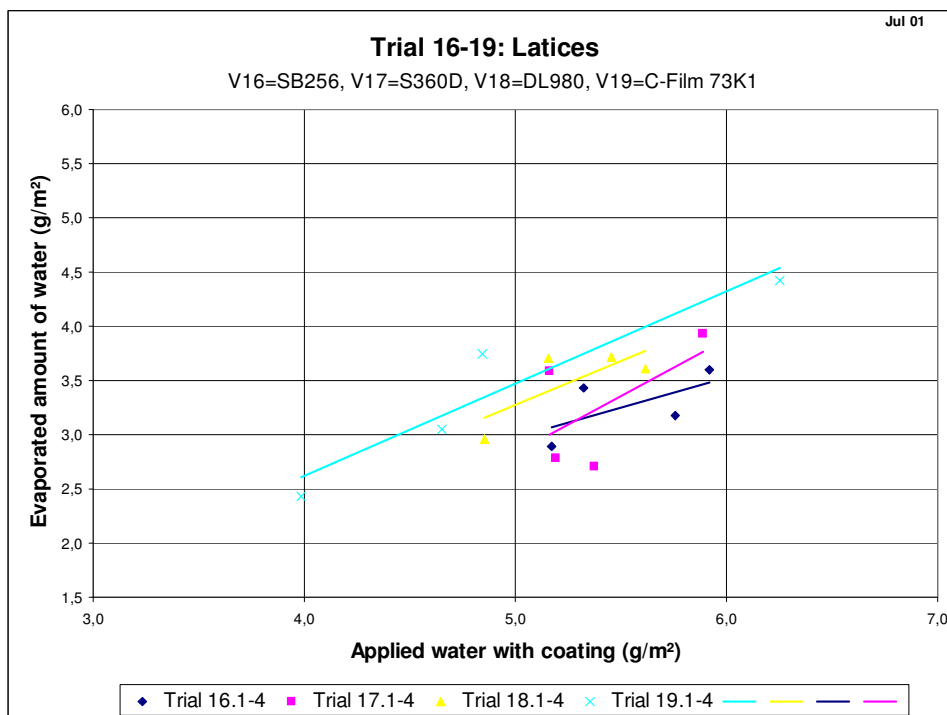
Pict. 11.1.1.20: Influence of binder type an drying energy demand

As base paper sorption was dominating the lab trials with DOW roll coater, starch C-Film had the lowest drying energy demand due to superior water retention. When starch containing coating colours are applied on less absorbent substrates, drying energy demand can be higher than for latex based coatings as short term vapour permeability and liquid permeability is lower for starch containing coatings after the FCC.
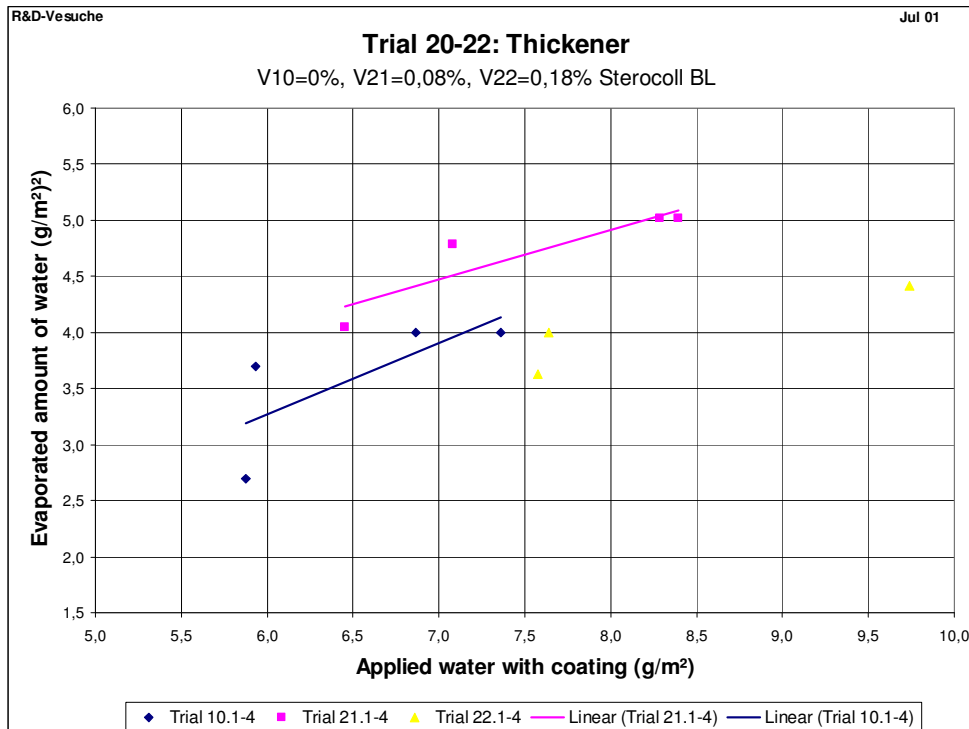
Pict. 11.1.1.21: Influence of thickener on drying speed

Increasing amount of thickener led to higher water retention and lower drying energy demand like for starch based coatings.

Fibro MCA surface moisture measurements:

For calculation of absolute paper moisture from the Fibro MCA measurements, a calibration was first done at the lab coater. The measured moisture after the blade was correlated with the measured Fibro readings.
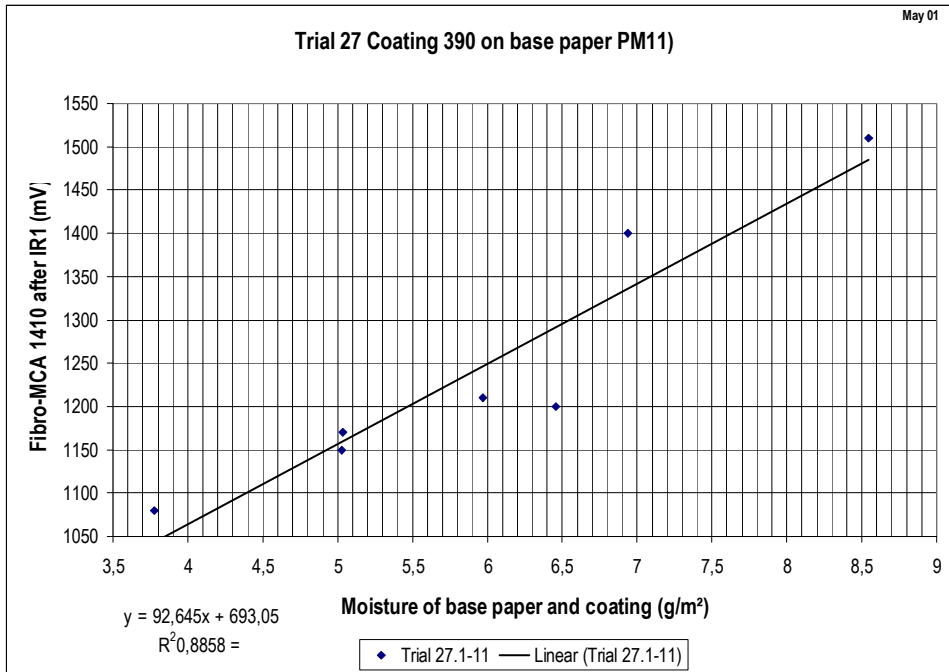
Pict. 11.1.1.22: Calibration of Fibro MCA
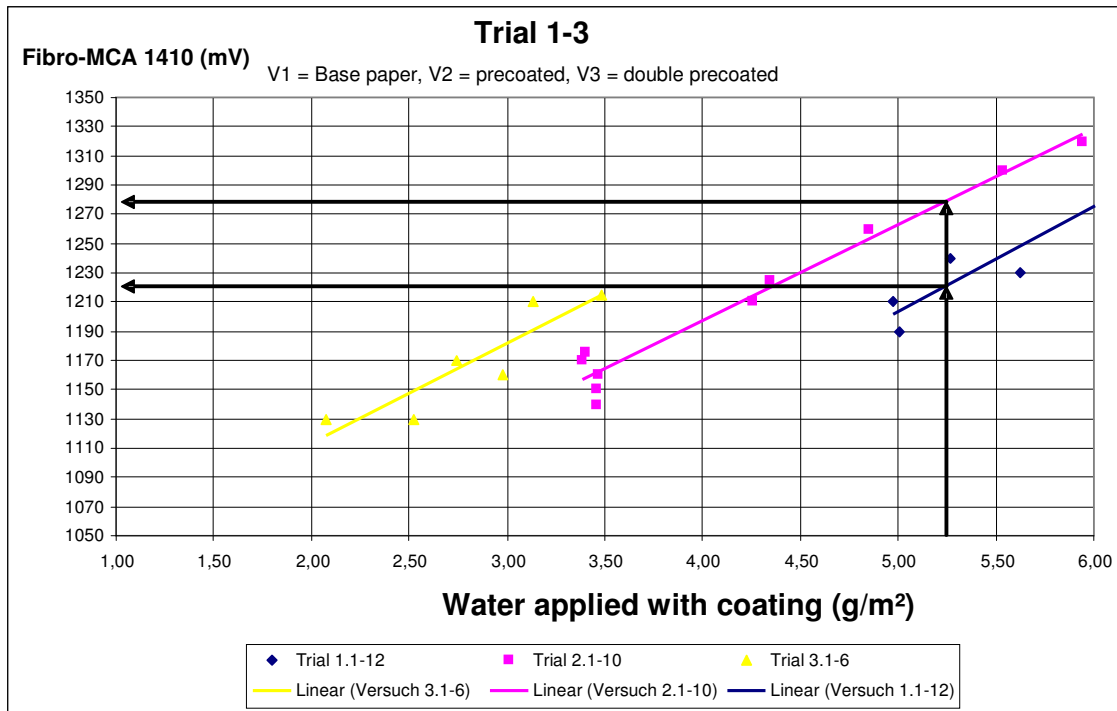
Pict. 11.1.1.23: Fibro MCA measurements after IR of different substrate

The trials on different substrates showed lower surface moisture when coating colour was applied on base paper compared to precoated papers, proving that more water was absorbed by the base paper and immobilization point was reached earlier on

highly absorbent substrates due to combined removal of water from coating by evaporation and base paper sorption.

11.1.2 Influence of binder type on drying and mottling – mill experience from OMC11

In lab coating + drying experiments 2003 and 2008 in PT4 the influence of latex type and drying conditions on mottling were studied in lab trials and transferred into mill practice by a series of pilot and mill trials at OMC11 which proved the importance of the right choice of latex and drying conditions in the top coatings of OMC11.

The trigger of the following lab studies was a severe worsening of drying induced back trap mottling when speed of OMC11 was increased 2002.

Precoating
bottom side
on **Coater 3**

Precoating
top side on
Coater 4

Top coating
bottom side
on **Coater 5**

Top coating
top side on
Coater 6
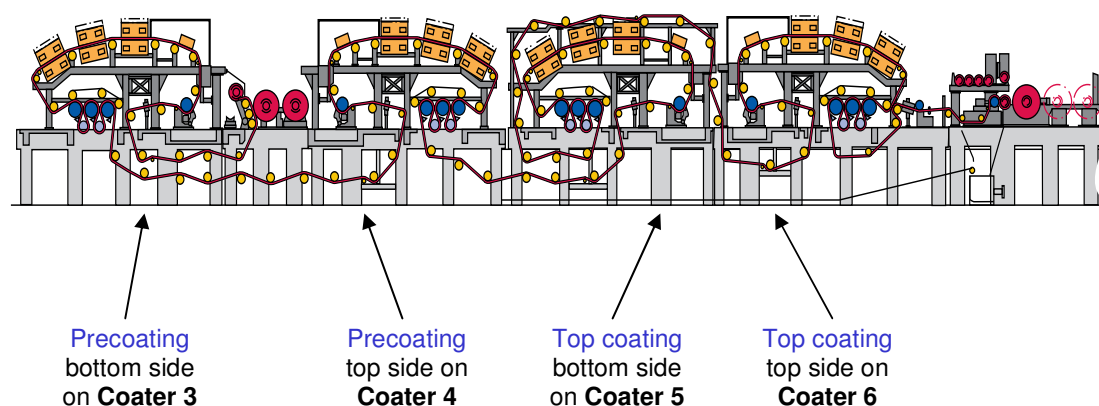
Pict. 11.1.2.1: Layout of OMC11

The influence of all important machine parameters on BTM was analysed by multiple regression using SIMCAT software.
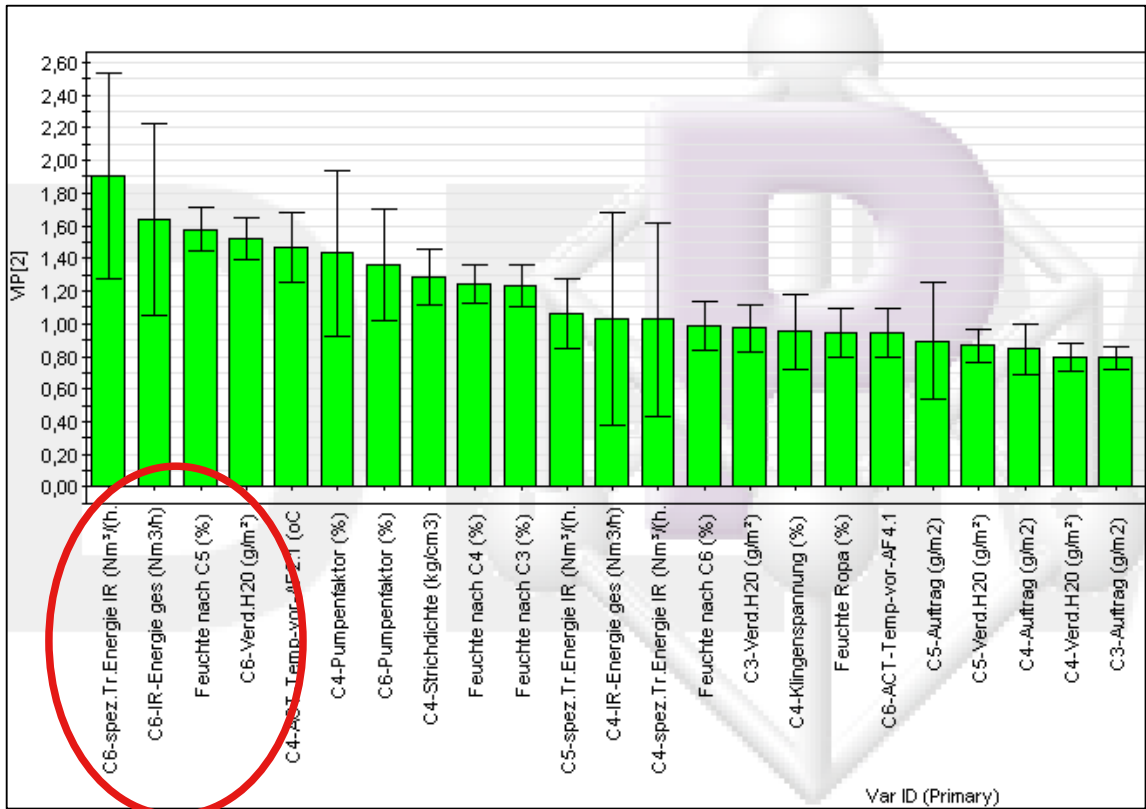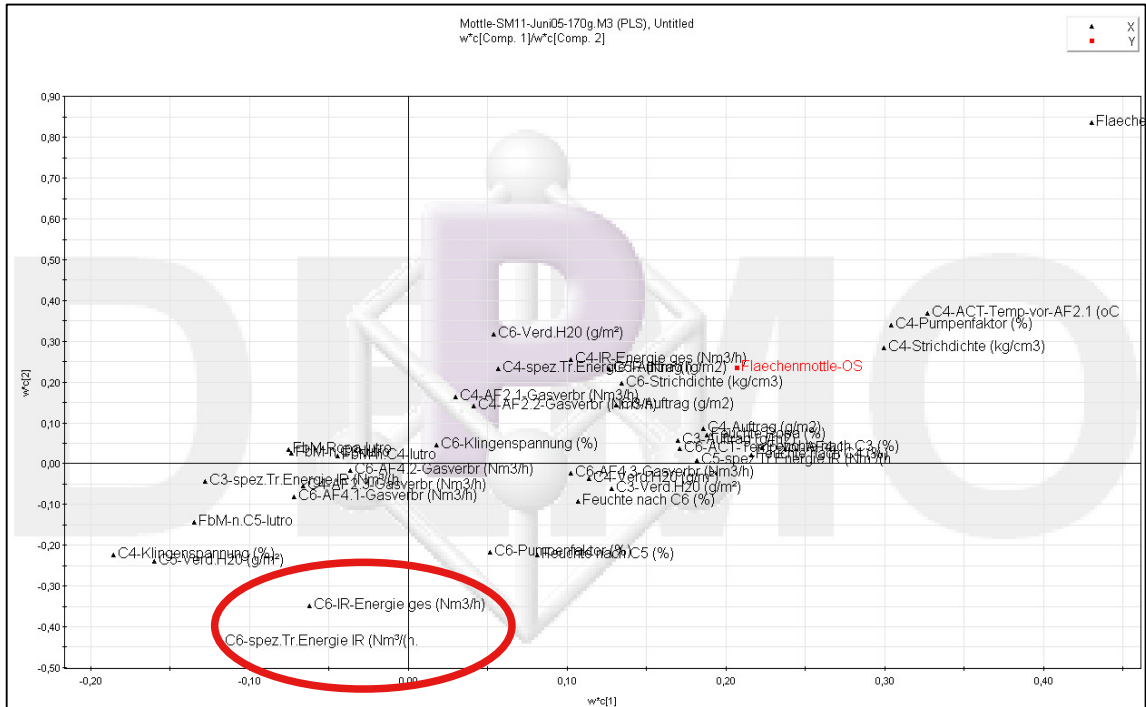
Pict. 11.1.2.2: Multiple regression of machine parameters of OMC11 with BTM on top side of Magnostar 170 g/m² by Simca software
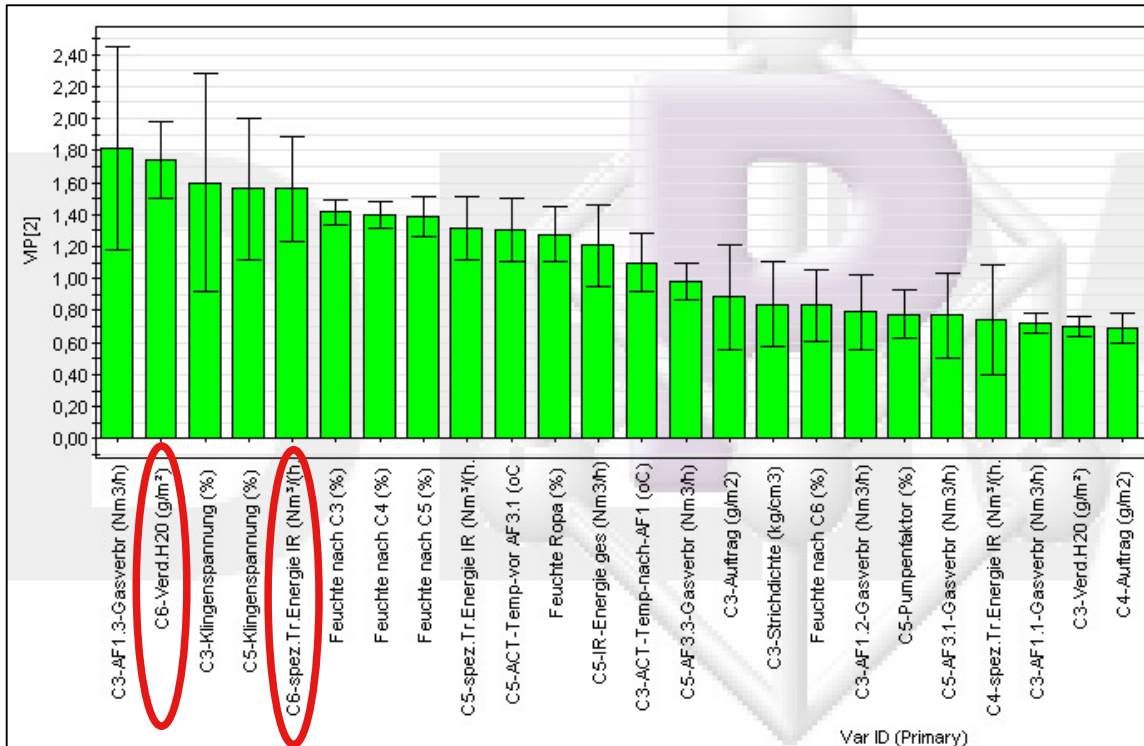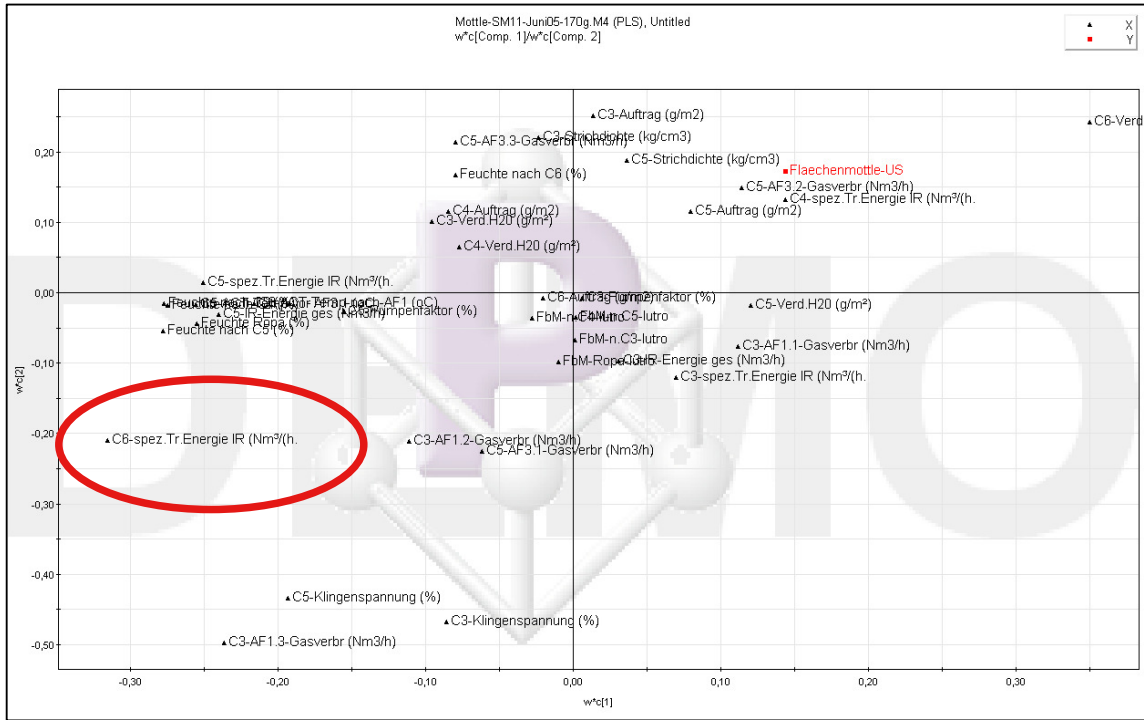
Pict. 11.1.2.3: Multiple regression of machine parameters of OMC11 with BTM on bottom side of Magnostar 170 g/m² by Simca

As speed was increased, the natural convection drying in the free draws was also raised, and less drying energy was generally needed. The reduction of energy was mainly implemented in the IR-section which is the 1st drying stage at OMC11.

At the top coaters the max web temperature after the IR rows dropped under 65°C. Latex film forming got generally worse and local differences in film forming increased.

When latex particles start to film form, porosity of the coating layer drops as latex particles change their shape from a sphere to a honeycomb form.
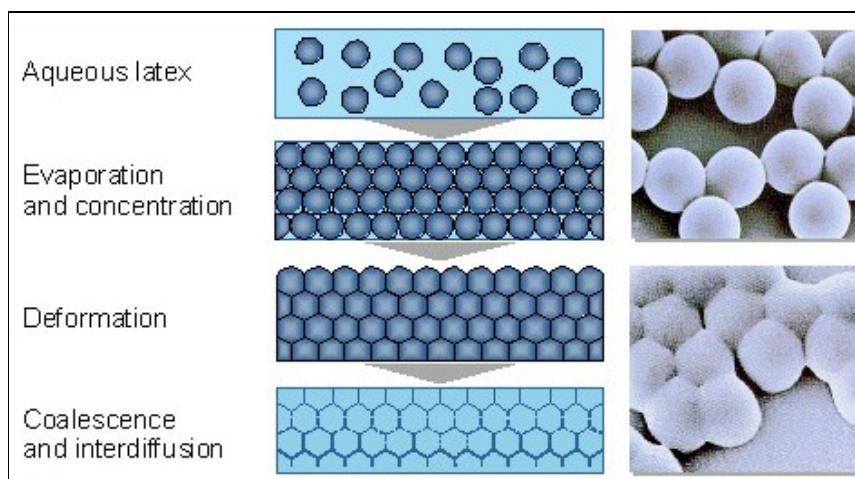
Pict. 11.1.2.4: Latex film forming (von BASF)

Assuming local porosity differences in the precoating layer on top of flocs and voids (see chapter "floc analysis"), the penetration depth of liquid phase from top coating colour will follow these porosity differences of the precoating layer. Local differences in solid content of the top coating colour after the blade will be the consequence. When capillary penetration of liquid phase from top coating into the precoating layer starts during drying, these local differences in solid content will be even more pronounced.

A necessary precondition for latex film forming is the removal of water between latex particles. Latex film forming will therefore start locally different, depending on local solid content. The earlier the SCC is reached, the faster latex film forming will start.

The time span for film forming is much shorter in a mill coater than in the lab and all commercially available latices are only partly film formed in mill coaters.

This can be demonstrated by comparing the picking resistance of a fresh mill coated paper with the same paper after treatment in lab oven where latex film forming is continued.
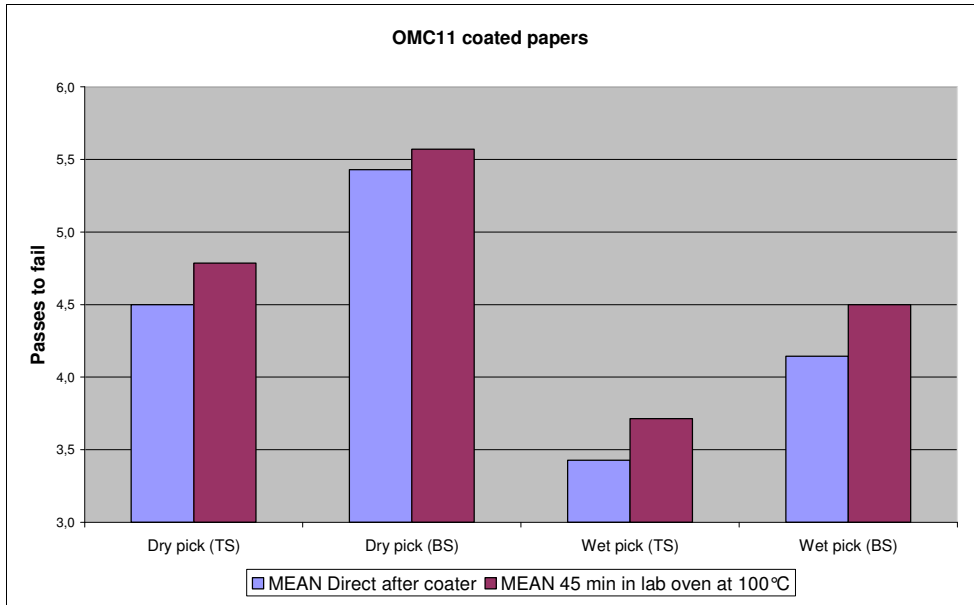
Pict. 11.1.2.5: Improvement of latex film forming by lab oven treatment after coater

Latex film forming is supported by increasing temperature after film forming has been started:
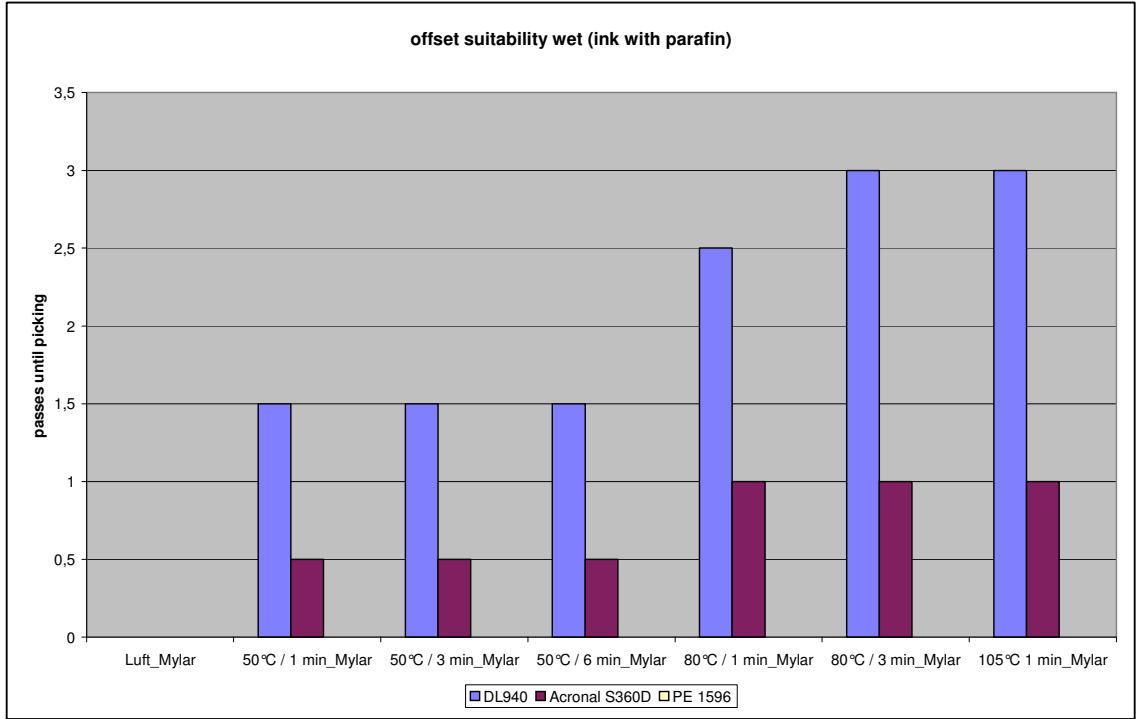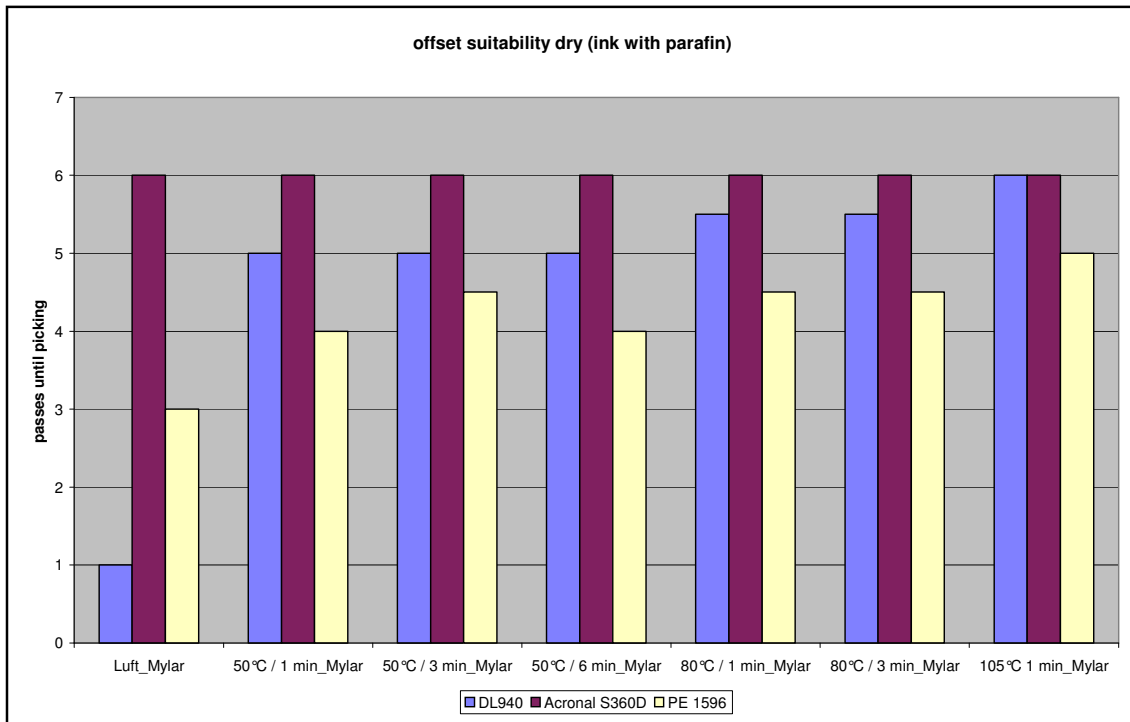
Pict. 11.1.2.6: Latex film forming by different temperature levels and dwell time
(DL940 = slow film forming SB-latex, Tg = 20°C, S360D = fast film forming SA-latex,
Tg = 0°C)

As web temperature after FCC/SCC dropped at OMC11 when speed was raised,
latex film forming generally got worse and local differences in film forming increased
too. When latex remains in its original sphere shape local differences in contact angle
and pore diameter are the consequence, which cause local differences in capillary
sorption of printing ink (after application nip) and severe back trap mottling.

At spots, where latex remains in its original sphere shape coating layer porosity and
permeability is higher. Ink penetration depth in the printing nip will be deeper. Due to
a high amount of fine pores (10 – 50 nm) between the latex spheres capillary sorption
of ink will be more pronounced at these spots and ink anchorage will improve
additionally. Less ink will be pulled off at these spots during back trapping in the
following printing nips.

Therefore local differences in solid content and in consequence back trap mottling from non-uniform latex film forming can have the pattern of the **base paper formation**.

A second root cause for back trap mottling is latex migration during drying of the coating layer. Literature shows that the deeper the latex penetrates into the substrate and the higher the drying energy after the first critical concentration (FCC) the worse **drying induced back mottling**. This kind of mottling is bigger in size of un-uniformities than the formation induced mottling (see chapter "floc analysis") as latex migrates in a random way to the surface.

Local differences in surface porosity after the FCC can lead to mottling caused by latex migration: When the drying energy is high after the FCC, the latex will follow the easiest path with the liquid or vapour phase to the surface – at spots with low vapour permeability (low evaporation resistance) more latex will travel with the liquid phase to the surface. When this latex is film formed by high drying energy after the FCC or by hot calendaring this spot will have low coating layer permeability and in consequence bad ink absorption.

Mill trials at OMC11 show that faster film forming latices and higher drying temperatures lead to lower differences in surface porosity, latex content and in consequence to less print mottle (see chapter 11.3).

11.1.3 Drying curves in the lab – part 1

The aim of the following study was to find latex types with low sensitivity for drying conditions. These latices should be fast in film forming and surface porosity should be independent from drying temperature or calendaring conditions. **To avoid differences in binder migration to the surface, vapour permeability of the coating layer after the FCC should be as high as possible** and water evaporation should not be hindered by a dense dry surface layer.

In the first study 2003 the principal differences in drying behaviour of practical w'fr. coating colours were evaluated.

The coatings were put between two glass fibre pads and dried in a microwave oven. Weight loss during drying was measured with a scale. The data's of the scale were transformed into:

X the moisture of the dried medium (kg/kg)

v the speed of drying (g/s)

t the time for drying

Drying is generally described by the following interrelations:

1) Diagram X – t (moisture of medium vs. time),

2) Diagram v – t (drying speed vs. time),

3) Diagram v – X and 1/v vs. X (drying speed vs. moisture).

Alternatively to microwave energy IR was used as drying energy source.

Drying curves from a scale with IR-dryer on top:
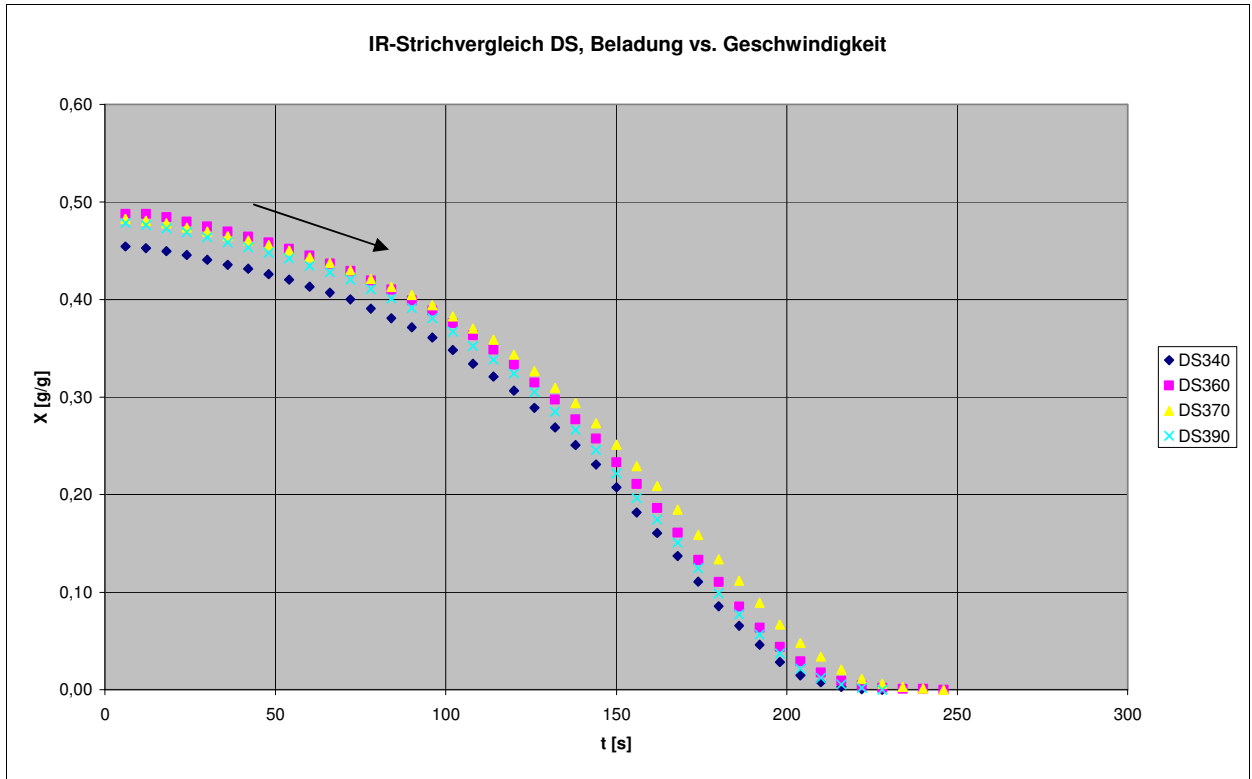
Pict. 11.1.3.1: X vs t – drying curve of similar top coatings of OMC11
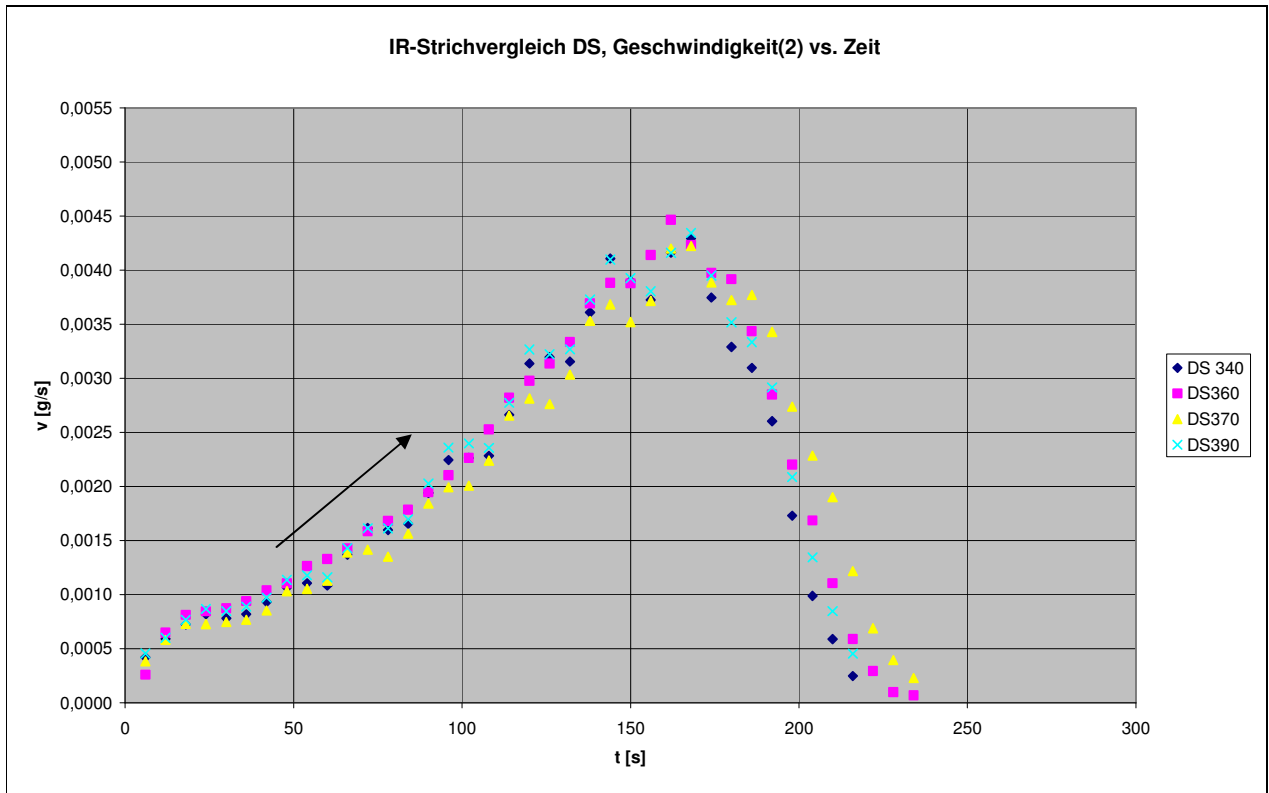
Pict. 11.1.3.2: v vs t – drying curve of similar top coatings of OMC11
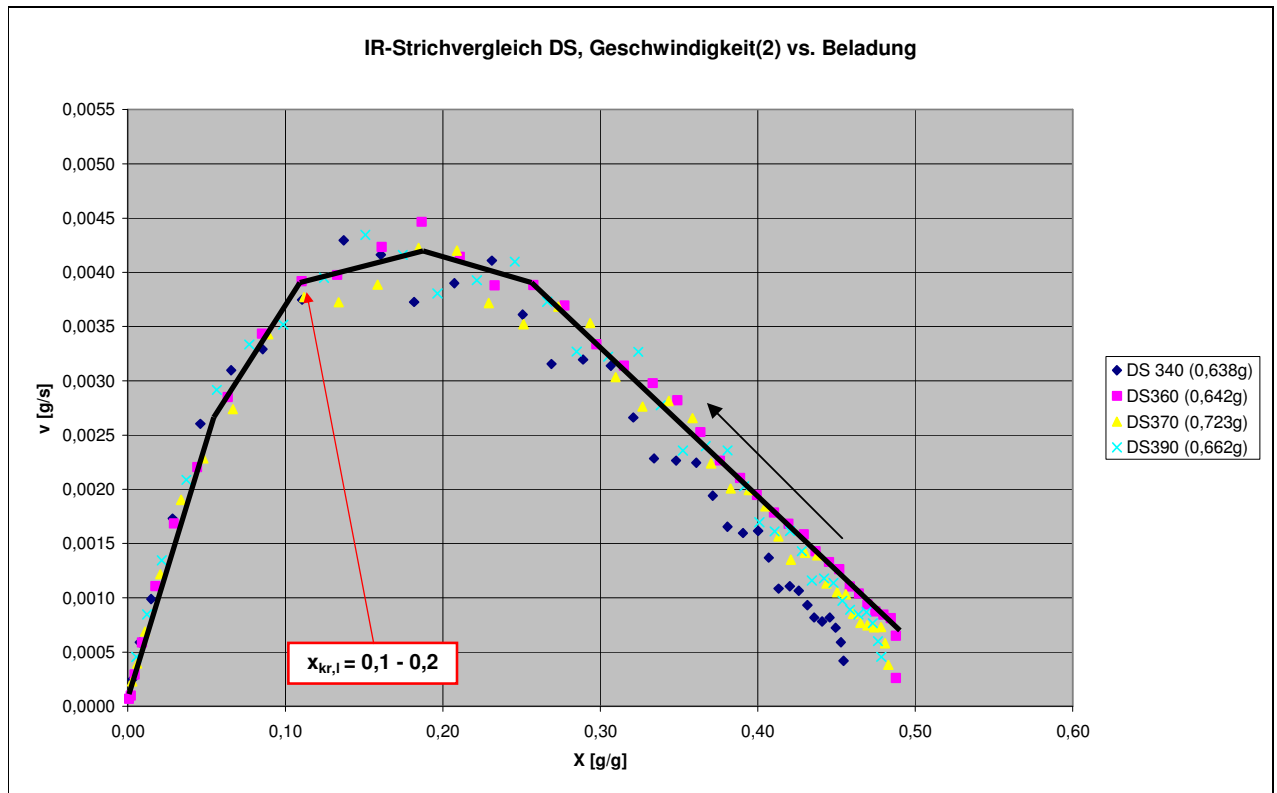
Pict. 11.1.3.3: X vs t – drying curve of top coatings (drying process runs from right to left)

The shape of the drying curves v –t and v – X show the typical three stages of drying: In the <u>first stage</u> evaporation is driven by the moisture gradient ΔX between the surface of the wet sample and air. There is always enough water on the surface for evaporation.

The temperature of the substrate rises due to energy transfer into the water molecules of the coating. Evaporation speed increases with raising sample temperature, lower moisture at the air boundary and is depending also on mass and heat transfer coefficient.

The first drying stage ends with a plateau phase where drying speed stays constant. When the first critical concentration, the FCC ($X_{cr,I}$) is reached the drying speed drops continuously. An immobilised layer is formed at the surface of the substrate. The <u>second drying stage</u> begins.

The sample temperature increases further but steeper. Water has to be transported from the bulk to the surface through the dense immobilized surface coating layer. The

web temperature increases as the capillary forces are no more able to transport the moisture from the inner part of the sample to the surface. The change from liquid to steam phase happens in the inner part of the sample. The transport of the vapour to the surface is hindered by the high diffusion resistance (μ) of the dry surface. The partial pressure of the steam rises together with the surface temperature. Heat transfer into the substrate is also hindered by lower heat conduction coefficient of the dry surface (due to air in the pores).

In the 2nd drying stage all free water in the pores of the coating and fibres is evaporated. The differences in moisture loss of different coatings in this stage were especially investigated in this study.

The 2nd period ends at the second critical moisture, the SCC (Xcr,II). The third drying stage starts. Chemically bound water has to be evaporated which leads to the highest demand in drying energy of all stages. Drying speed drops again and web temperature increases further until it reaches the surrounding air temperature.
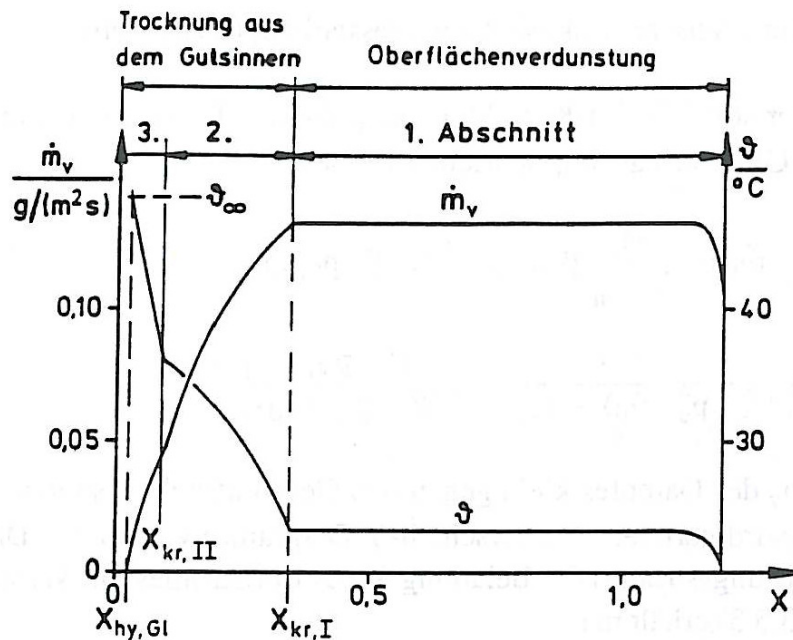
Pict. 11.1.3.4: Phases of drying

When the IR drying curves for different top coatings of OMC11 the following conclusions can be drawn:

Drying speed rises in the 1st drying period as external heat is continuously put into the substrate by the IR ramp. After a short plateau the 2nd drying stage starts. No 3rd stage could be observed in the time of the lab drying trials, the samples were dried to the hygroscopic equilibrium moisture X_{hy} of 0,045 – 0,055.

In the <u>first drying stage</u> drying velocity can be calculated according to V. Gnielinski with (see 11.3.1):

Equ. 11-1-1: $\dot{m}_{v,I} = \dfrac{P * M_v}{R * T_m} * \beta * \ln\left[\dfrac{P - p_{v,\infty}}{P - p_v(\vartheta_0)}\right]$ in kg/(m²/s), with

P the overall pressure in N/m², $p_{v,\infty}$ the partial pressure of the evaporating liquid in the air, M_v the mol weight of the evaporated liquid in g/mol, R the gas constant in J/(mol*K), T_m the mean temperature between surface and air in K and β the mass transfer coefficient in m/s.

The moisture X in the substrate is calculated with $X = \dfrac{kg_{water}}{kg_{dry}}$. The partial pressure of

wet air is determined by: $p_{v,\infty} = P * \dfrac{Y_\infty}{0,622 + Y_\infty}$ with Y_∞ the moisture in the air:

$Y_\infty = \dfrac{M_v}{M_g}$ or $Y_\infty = \dfrac{\tilde{M}_v}{\tilde{M}_g} * \dfrac{p_v}{P - p_v}$

Mass transfer coefficient β is calculated from Nusselt number: β = Nu * δ / L   (see 11.3.1).

$Nu = \sqrt{Nu_{lam}{}^2 + Nu_{turb}{}^2}$

$Nu_{lam} = 0,664 * Sc^{1/3} * \mathrm{Re}^{1/2}$

$Ni_{turb} = \dfrac{0,037 * \mathrm{Re}^{0,8} * Sc}{1 + (2,443 * \mathrm{Re} - 0,1 * (Sc^{2/3} - 1))}$

The material constants of Re, Pr and β are calculated wit the mean temperature T_m = $(T_0 + T_\infty)/2$ and $p_m = (p_v + p_{v\infty})/2$

The second series of lab experiments in 2003 were done with a microwave oven. The coating colour was applied on a highly absorbent glass fibre pad and dried on a scale under continuous drying by the microwave. The influence of binder type and amount was investigated.
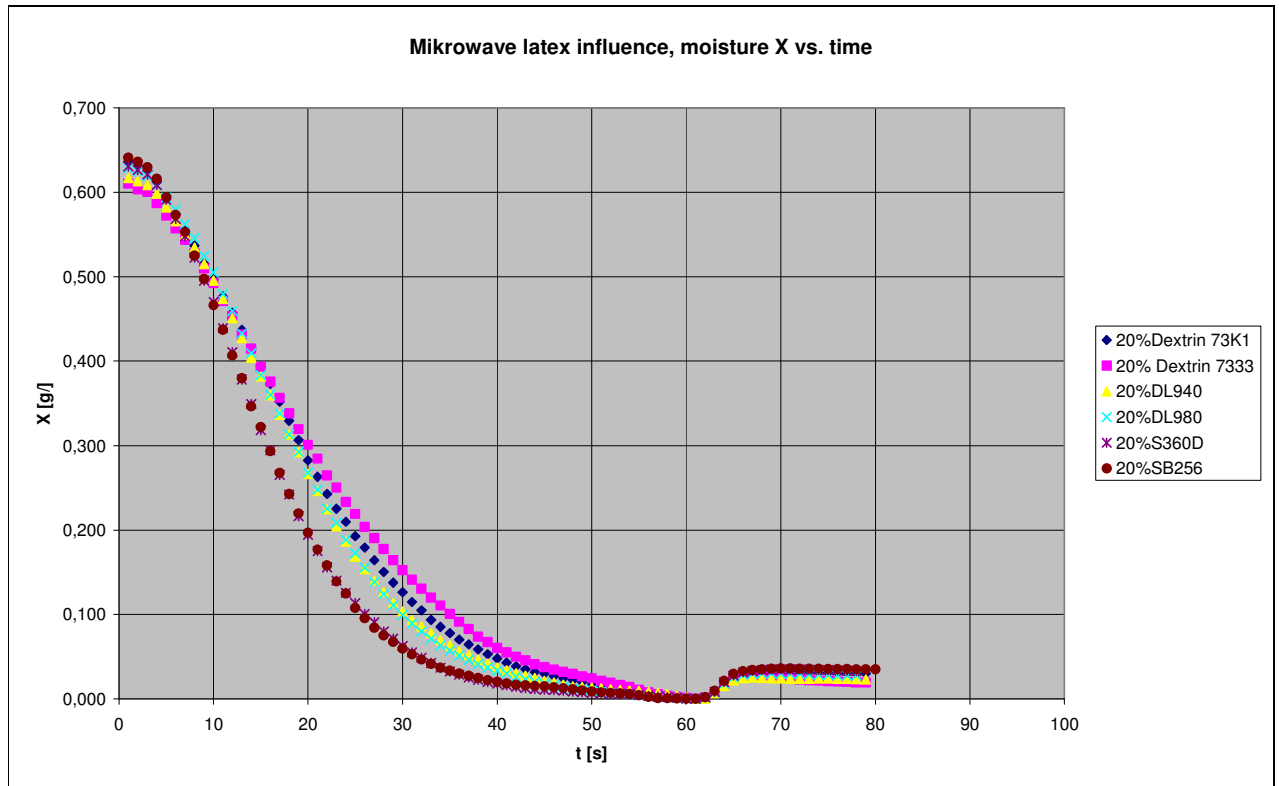
Pict. 11.1.3.5: X – t diagram (lab study PT4 in 2003)
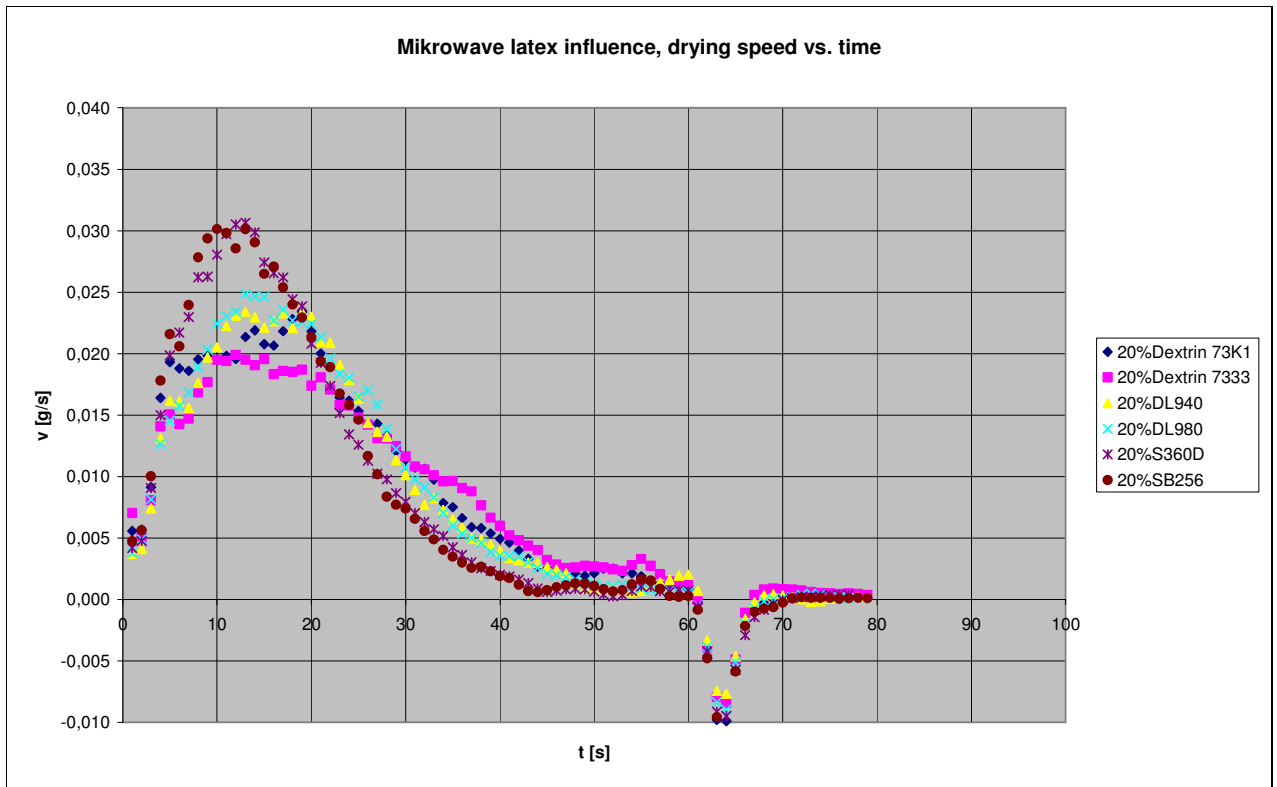
Pict. 11.1.3.6: v – t diagram (lab study PT4 in 2003)
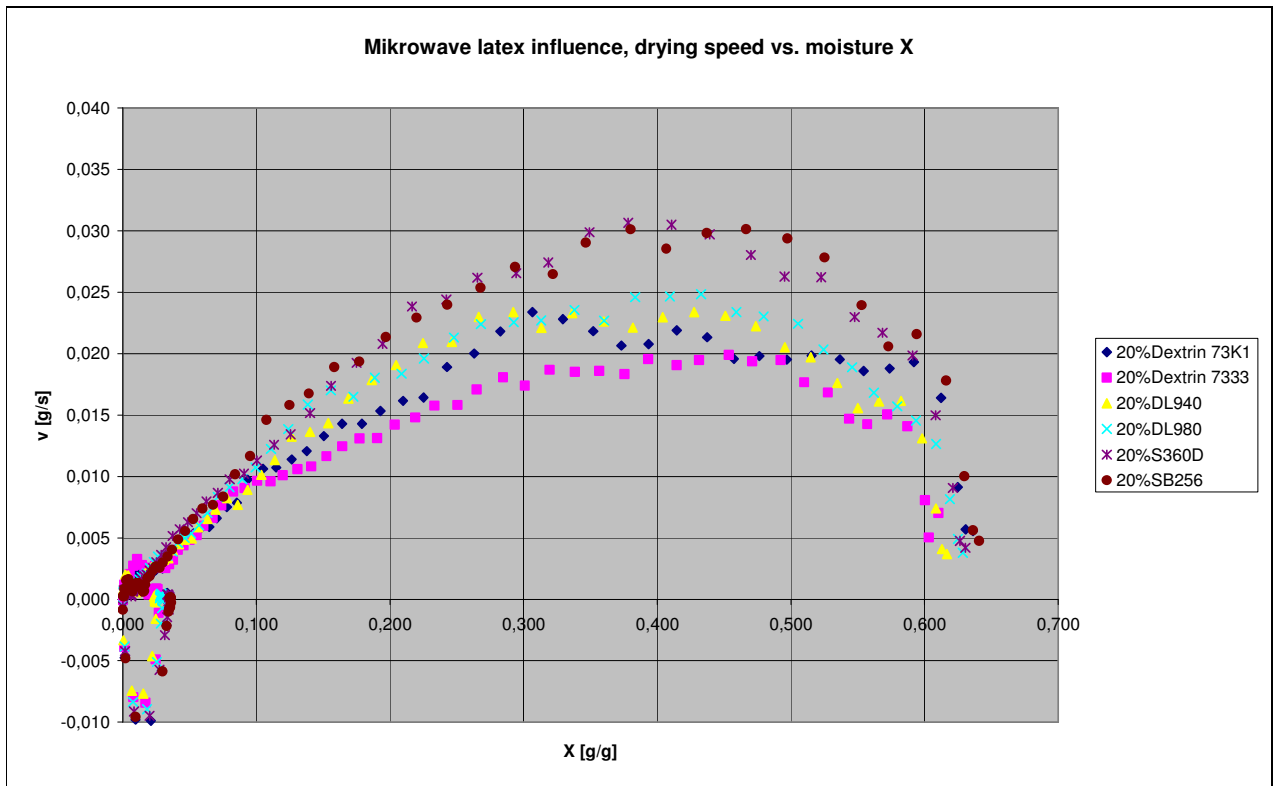
Pict. 11.1.3.7: v – x diagram (lab study PT4 in 2003)
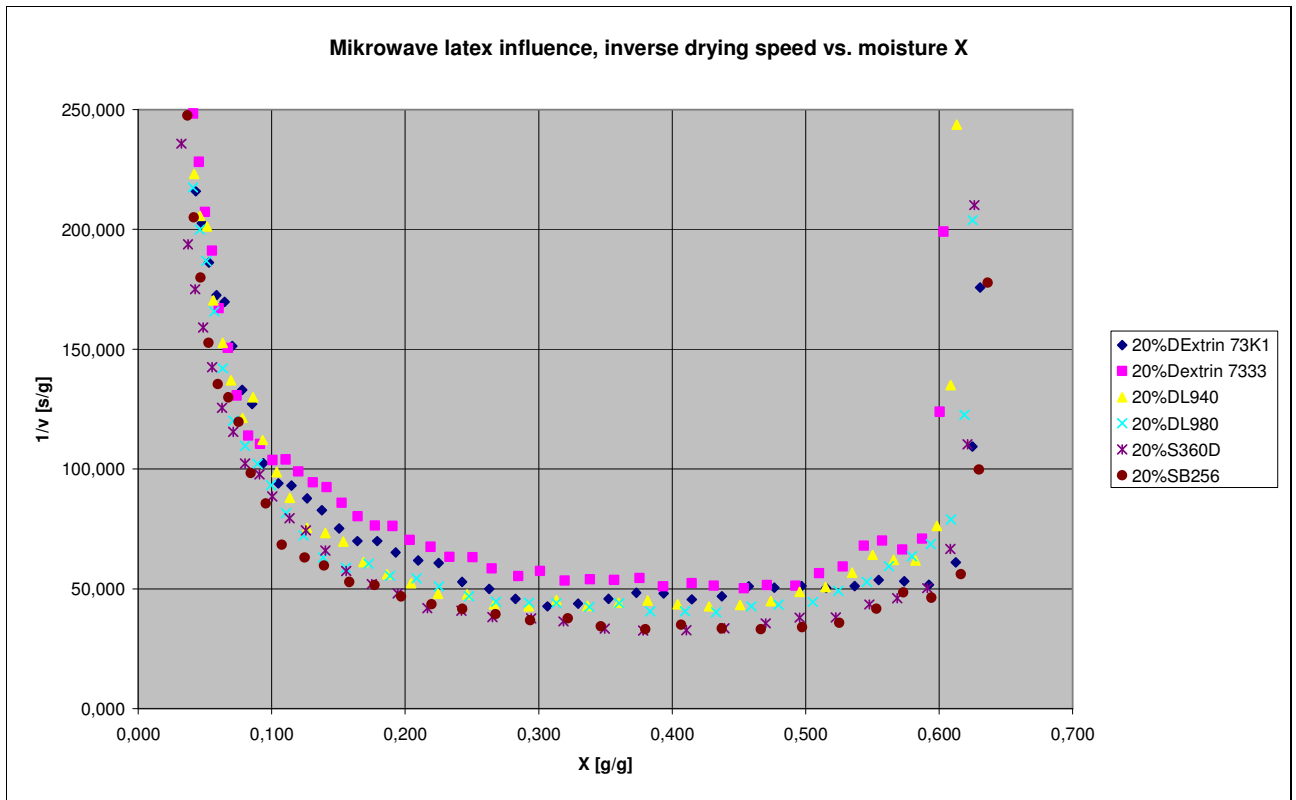
Pict. 11.1.3.8: 1/v – x diagram (lab study PT4 in 2003)

The drying time was calculated by using the equation

$$v_{drying} = \frac{m_{dry} * dX}{A * dt} = f(X)$$ leads to:

Equ. 11-1-15: $t_{drying} = \frac{m_{dry}}{A} * \int_{X_1}^{X_2} \frac{dX}{v}$

Drying time is the area under the curve 1/v – X (see diagram above).

Calculated drying time, coating with 100% HC90, 0,03<X<0,62
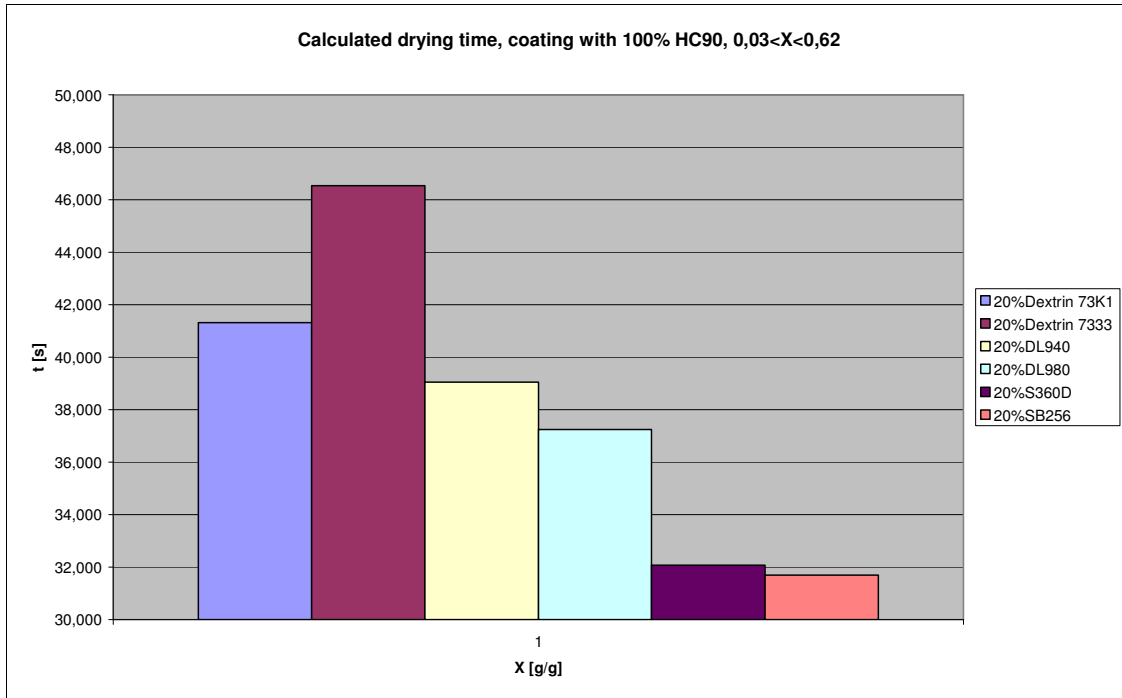
Pict. 11.1.3.9: Calculated drying time (lab study PT4 in 2003)

Hard SB-latex SB256 and soft SA-latex S360D showed fastest drying as vapour permeability of dry coating layer was higher (see measurements in next paragraph). The main difference between the coatings occurred in the second drying stage where vapour must be transported through the dense immobilized surface layer.

Starch based coatings were slowest in drying as their coating layer porosity was the lowest. This was proven by a pilot trial at Cerestar where coating layer permeability, determined by Bendtsen and Gurley was clearly higher for latex based coatings than when starch was used as coating binder.
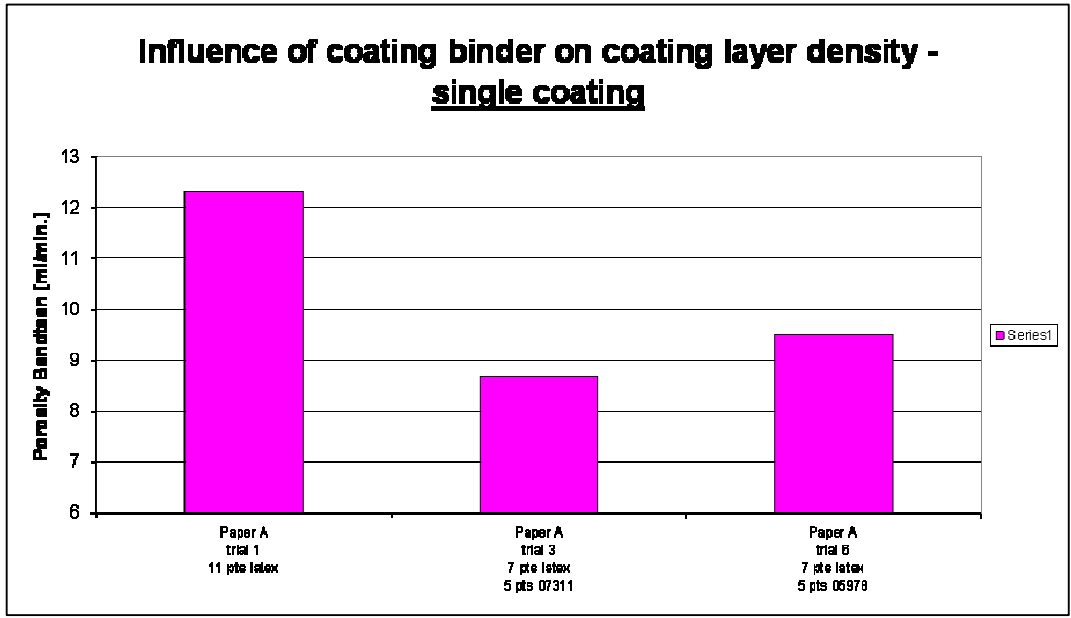
Pict. 11.1.3.10: Porosity of single coated paper with different ratio starch : latex

The drying speed can be described by the tangent in the graph v vs. X.

The 2nd drying period was taken for this comparison:
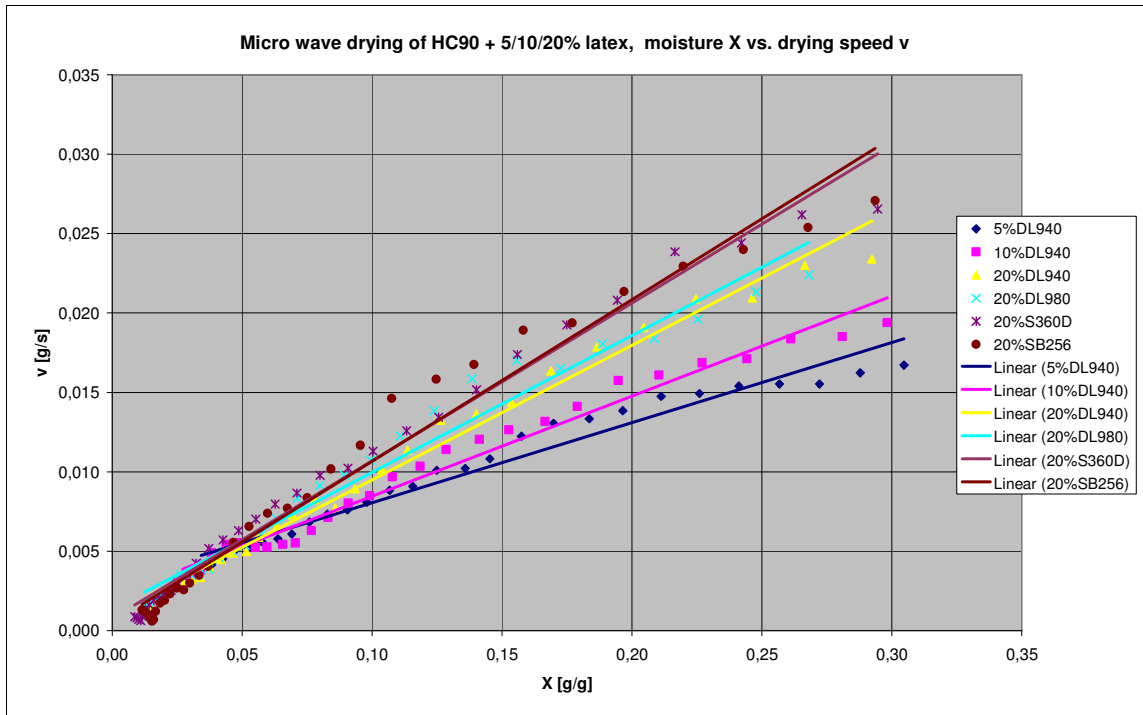
Pict. 11.1.3.11: v vs. X in the 2nd drying period

Page 687

The drying curve can be described by the function $y = f(X) = e^{(a+b*X^2)}$

The derivation with respect to time gives the drying speed:

Equ. 11-1-16: $y' = v = f'(X) = (2*b*X)*e^{(a+b*X^2)}$

Comparing the drying speed v of the tested coating colours with 5 / 10 / 20 % latex DL940 it can be concluded that **drying speed drops in the 2nd drying stage with increasing latex content** due to lower vapour permeability of the dry coating layer (see next paragraph).

Increasing latex particle diameter like done for Acronal S360D and SB256 (180 – 22 nm) **leads to higher drying speed** than for the fine latices DL940 and DL980 with 130 – 150 nm particle size.

Summary of the first lab study:

- Drying speed is highly depending upon capillary sorption of the substrate (either base paper fibres or glass fibre pad) as sorption force is working against evaporative energy
- The higher the binder amount, the more drying energy is needed as coating layer vapour permeability drops with latex content (PVC moves closer to CPVC).
- Starch lowers the coating layer liquid and vapour permeability and raises thereby drying energy demand. When water retention can be improved by starch drying energy demand drops the overall energy consumption can be balanced.
- Latices with higher particle diameter create coatings with higher permeability and need less drying energy therefore. They are used to improve blister resistance of web offset coated papers. Unfortunately they are lower in picking strength as specific surface drops with increasing particle diameter and less latex particles are available per unit of volume.

11.1.4 Drying curves in the lab – part 2

In the <u>second lab study</u> in 2008 different latices were again compared in drying behaviour but this time drying was done by IR which is closer to mill practice.
The latex films were tested alone (without pigment) and in combination with a mixture of 80% pigments and 20% binder.
Two different <u>substrates</u> were used: <u>Non absorbent Mylar foil</u> was compared with <u>highly absorbent base paper</u> of PM11.
Water retention was measured and found to be identical for all latices/coatings.
Therefore amount of penetrated water from coating colour by capillary sorption during drying was depending only on the substrate.

Moisture loss was measured by an integrated scale under the IR-dryer. From the weight readings moisture X was calculated in g water per g dry coating colour. A coating colour with 68% solids contains e.g. 680 g water in 1000 g wet coating and 320 g dry material. X would be 0,47 for this coating colour before starting the drying. Latex with 50% solids would have a moisture of X = 1,0.
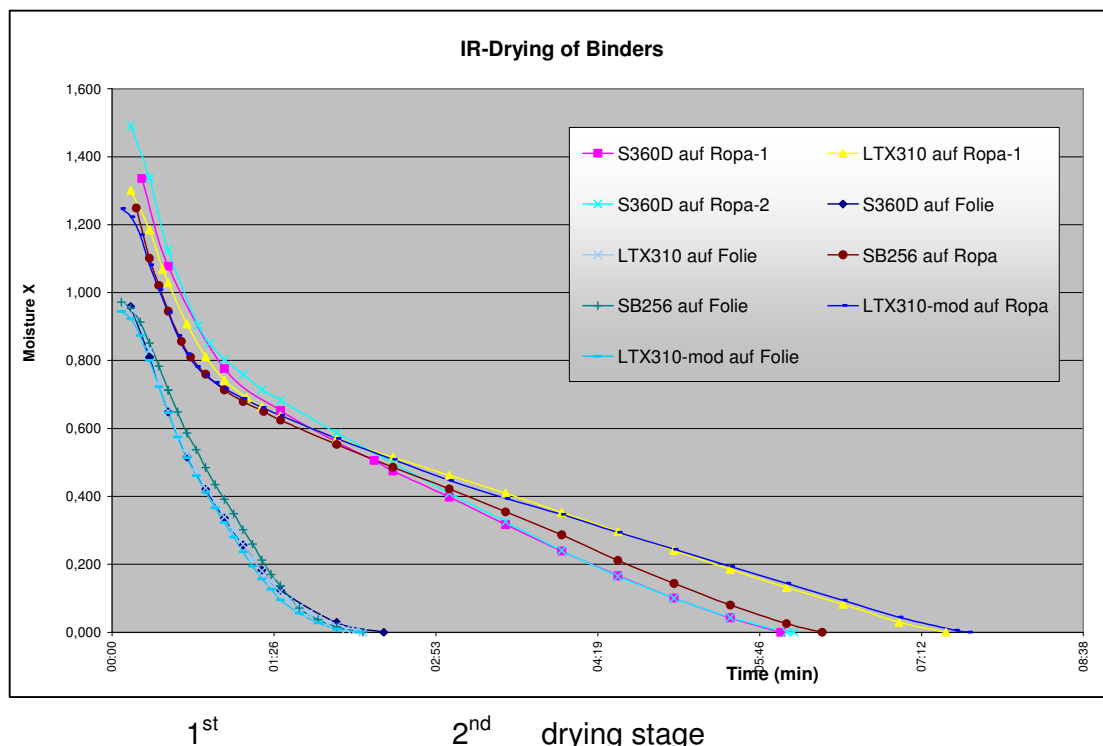
Pict. 11.1.4.1: X – t drying curve for different binders without pigment (lab study PT4 2008)

The drying curves for binders, applied on a dense Mylar film were totally different from application on a highly absorbent PM11-base paper.

Mylar films avoid capillary penetration of water from coating colour. Drying time for Mylar film applications was therefore dominated by the 1st drying stage. The 2nd drying stage started at a very low moisture of X = 0,1 g/g.

Comparing the different latices on the Mylar film no differences in drying speed were detected. Drying time was generally much shorter for applications on Mylar film.

Applying the same amount of latex dispersion (50% solids) on highly absorbent base paper of PM11 and led to totally different drying curves. Drying of pure latex dispersions started at X = 1,3 or a total moisture of 55 – 58% including base paper and latex with a solid content of appr. 50%.

The 2nd drying stage starts at X = 0,8 or a total moisture of appr. 45%. Drying velocity drops with a jump function due to latex film forming on the surface, resulting in a drop in vapour permeability of the surface layer.

Due to capillary sorption of the substrate the coating layers dries not only to the surface but also to the inside. The FCC at the surface is reached in half of the time compared to the same films applied at the Mylar foil.

Again the latices SB256 and S360D showed the lowest drying time at constant drying energy and comparable start and end solid content.

The standard SB latex types DL940 and DL980 were clearly higher in drying energy demand.

The differences between the latices arise in the 2nd drying stage when the porosity of the surface layer dominates the evaporation speed.

Latex properties:

SB256 is a hard web offset SB-latex. Monomers: SB (styrene + butadiene) Tg = 27°C, d50 = 175 nm, low cross-linking (gel content of appr. 30%).

S360D is a soft acrylate SA-latex. Tg = 0°C, d50 = 220 nm, low cross linking rate due to the linear acrylate molecules.

LTX310 is a soft sheet offset SB-latex. Tg = 0°C, d50 = 170 nm, high cross linking (gel content of appr. 80%). LTX310 is comparable latex to **DL980**

PE1831 is a sheet offset SB-latex, Tg = 15°C, d50 = 170 nm, high cross linking (gel content of appr. 80%). PE1831 is comparable to **DL940**.

VS2-Starch is a middle viscous **dextrine starch**. In contrast to the latex particles this type of binder has macromolecules which are dissolved in the water phase.
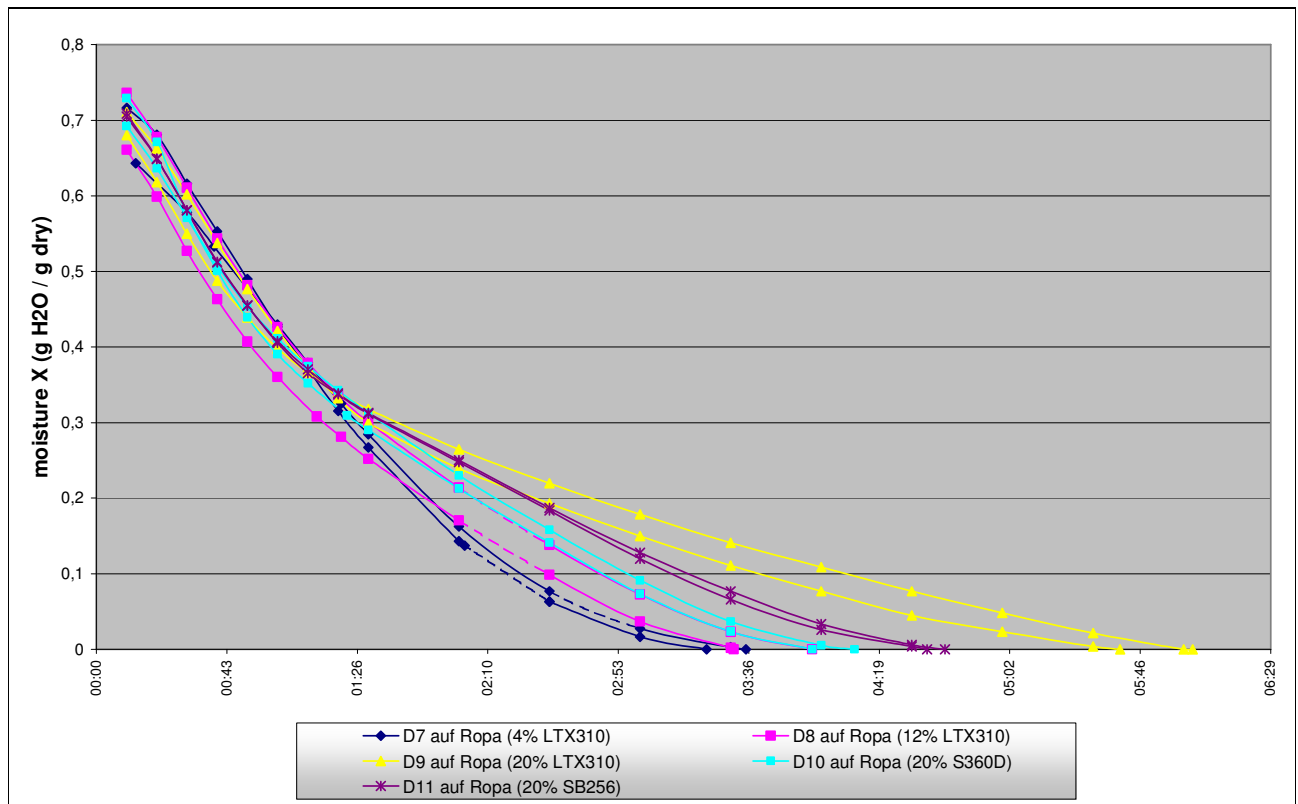
Pict. 11.1.4.2: X – t drying curve for different binders, mixed with carbonate HC90

Similar to results from lab study part 1, the drying energy could be reduced by lower binder content and raising latex particle diameter (SA S360D and SB256).

Mill trials (see end of this chapter) proved that drying mottle improved when these two latices were used. Acronal S360D was chosen as the best alternative as it improved mottling and ink drying.

Mixing only 10% latex with pigment leads to lower differences in evaporation speed between the different formulations:
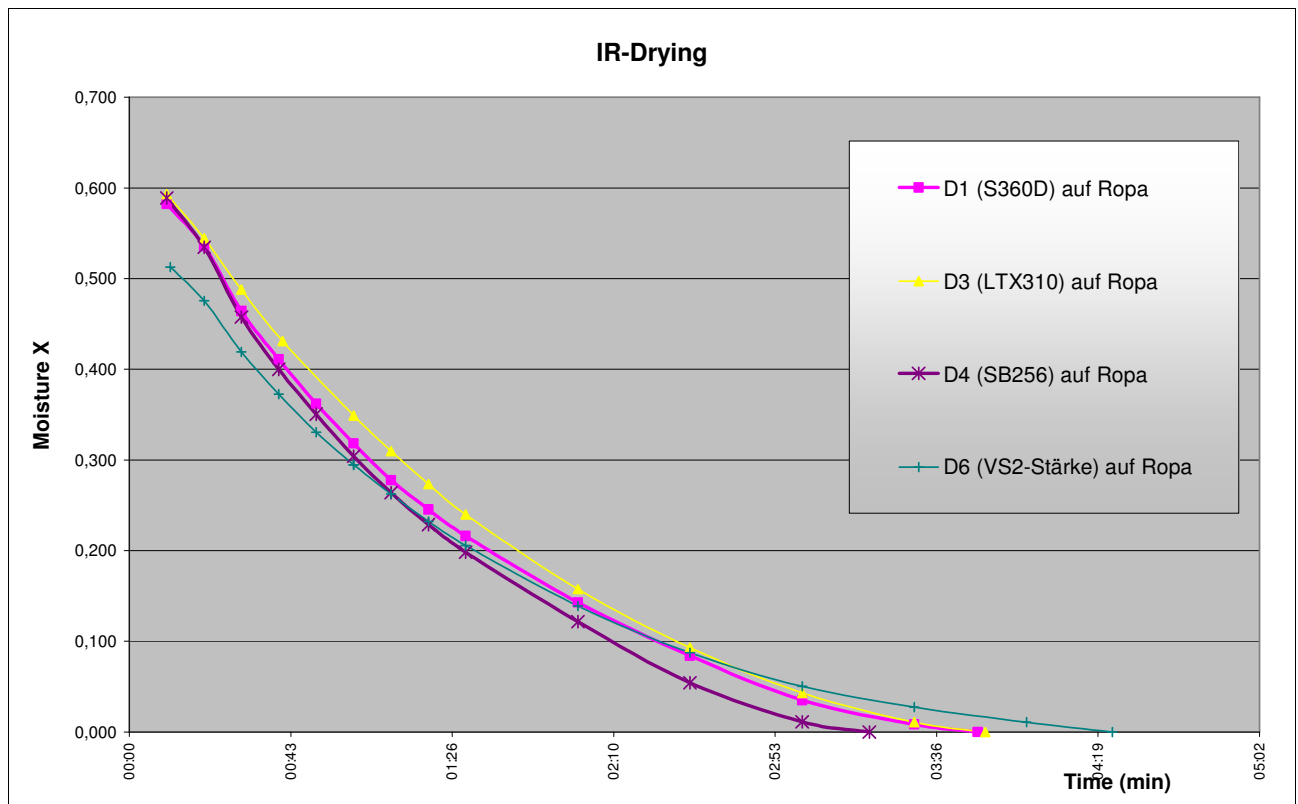
Pict. 11.1.4.3: X – t drying curve for different binders, 10 parts mixed with 100 parts pigment HC90 (lab study PT4 in 2008)

Using dextrine starch instead of latex, leads to a higher drying time at comparable drying energy. In the chapter "barrier layers" and "dense precoatings" the influence of starch on coating layer permeability was shown. Starch molecules form films with low permeability between the pigment particles.

Starch is relatively fast in film forming. No heat is needed to melt the molecules for film forming like it is necessary for latex particles. The only precondition for hydrogen bonding of the molecules and film forming is the removal of water between the molecules either by evaporation or by penetration into the substrate.

Combining the low permeability of starch films with its fast film forming properties, a surface layer is formed at the end of the 1st drying stage with low vapour permeability. As a consequence evaporation speed is lower in the 2nd drying stage than for most latex types. Therefore starch based coatings are very sensitive for drying induced back trap mottling.

In the 3rd drying stage the evaporation speed is also lower for starch based coatings due to the hydrophilic nature of the starch molecules. Starch builds hydrogen bridges

with the hydrophilic fibre surface and with the water molecules. Drying forces are increased when water is chemically bound on starch molecules.

The increase in shrinkage forces during drying was investigated by G. Laudone, G.P. Matthews and P.A.C. Gane from OMYA by a genius instrument.
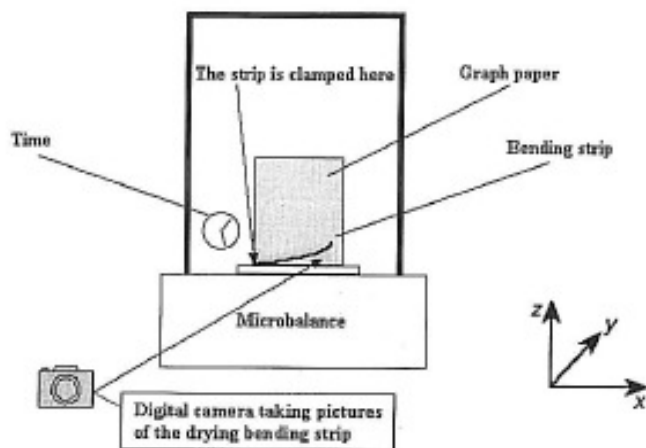
Pict. 11.1.4.4: OMYA-Apparatus for shrinkage of coating layers (G. Laudone)

Shrinkage of the wet coating layer during drying was observed with a camera. The coating was applied on a thin plastic Synteape film and put on a scale to determine the solid content over the evaporation period. A digital camera took pictures during drying to measure the curl. Drying was done by room temperature. The low-Tg latex (Tg = 5°C) and the starch was expected to film form while the high Tg-latex (Tg=22°C) got no chance to film form under these drying conditions. When water evaporates the volume of the coating shrinks and upwards curl is measured.
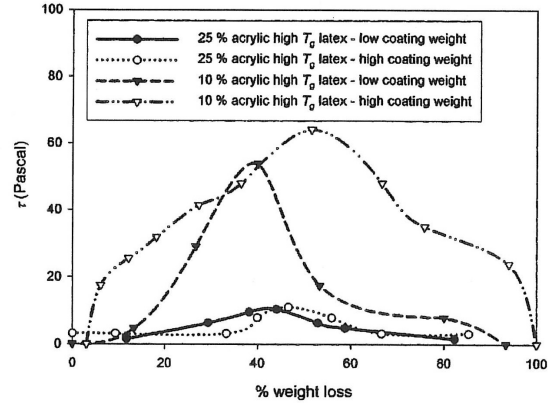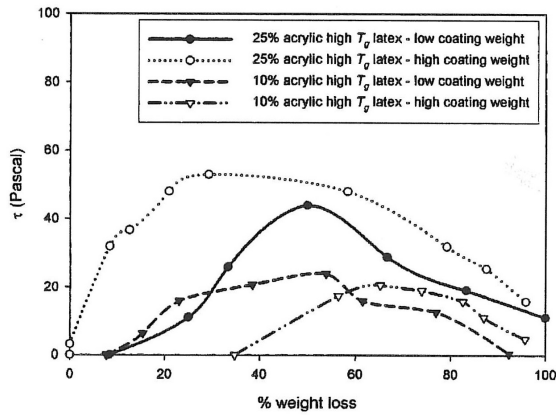
Pict. 11.1.4.5: Curl and stress in coating layer during drying for **high Tg acrylic latex** (left: HC60, right: HC90) (G. Laudone)
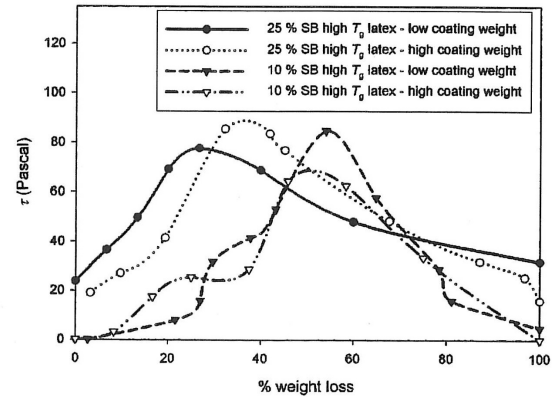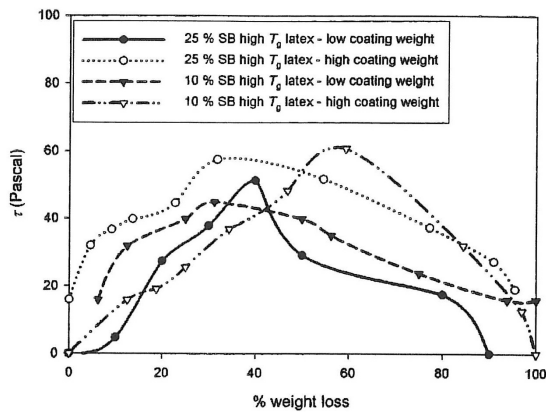
Pict. 11.1.4.6: Curl and stress in coating layer during drying for **high Tg SB latex** (left: HC60, right: HC90) (G. Laudone)
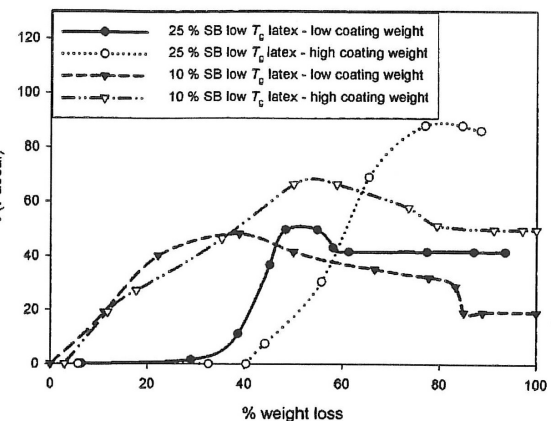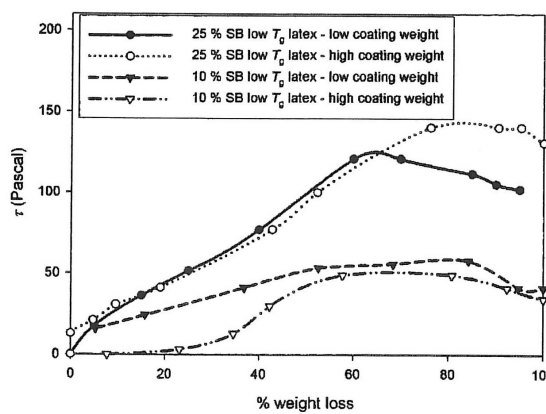
Pict. 11.1.4.7: Curl and stress in coating layer during drying for **low Tg SB latex** (left: HC60, right: HC90) (G. Laudone)

The remaining curl (corresponds to remaining stress τ) after drying was low for the high Tg-latices, medium for the low Tg-SB-latex and very high for starch as binder. Until the FCC was reached at approximately 81% solids, curl was comparable for all types of latices. It is driven by the reduction of pore volume in the pigment matrix when water is evaporated. Capillary forces try to move fine particles like latex into the pores by a stick–slip–moving–process. When particles have moved, stress in the coating layer is lowered. Latices with high Tg and low degree of film forming were longer able to move after the FCC has been reached and therefore the retained stress in the dry samples was lower than for low Tg-latices which film formed at FCC and hindered fine particles to move until the samples was dry.
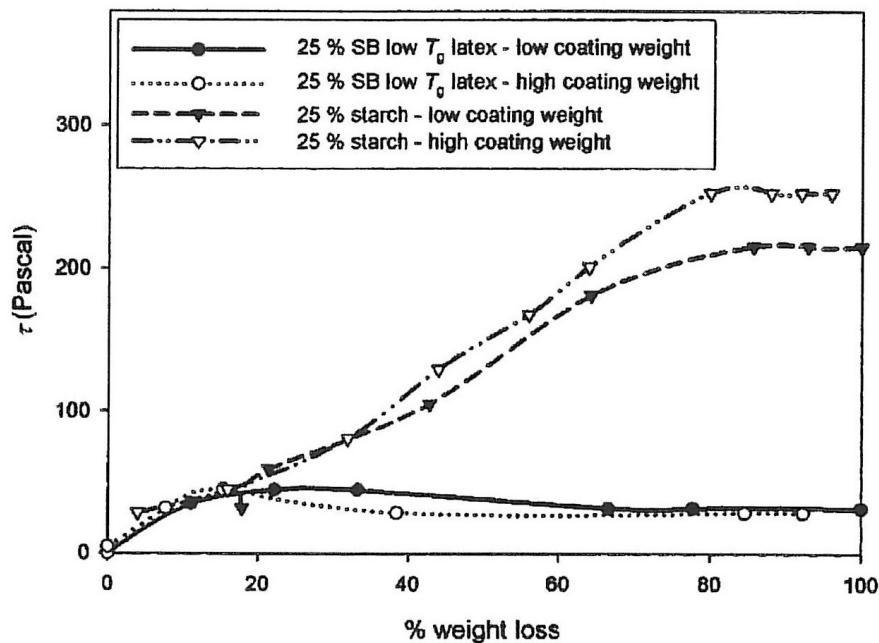
Pict. 11.1.4.8: DPP polystyrene pigment (G. Laudone)
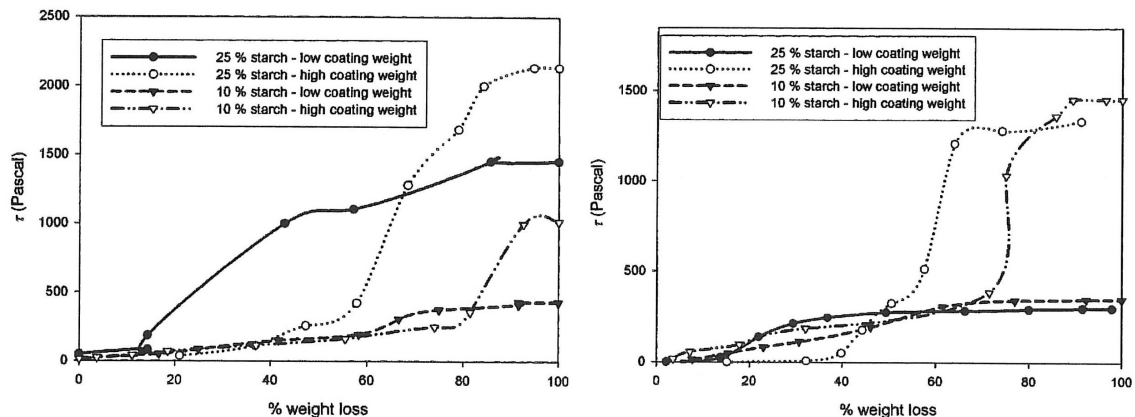
Pict. 11.1.4.9: Curl and stress in coating layer during drying for **starch** (left: HC60, right: HC90) (G. Laudone)

Starch showed a magnitude higher retained stress in the coating layer after drying. Mercury porosity of dry coating layer was lower than for latex based coatings. The change in dimension from loose to tight packing in starch based systems is large, leading to high retained stress after drying.

sample	high-T_g acrylic latex		high-T_g SB latex		low-T_g SB latex		starch	
	low	high	low	high	low	high	low	high
HC60 + 10% binder	26.1	24.8	30.8	25.8	21.8	18.7	17.4	15.7
HC60 + 25% binder	19.8	18.9	24.2	19.6	14.2	12.8	14.3	8.0
HC90 + 10% binder	38.4	24.5	39.9	32.2	28.5	24.9	26.5	22.5
HC90 + 25% binder	37.7	23.2	35.1	21.9	15.5	13.9	17.0	10.2
DPP + 25% binder					42.5	33.2	19.3	17.7

Pict. 11.1.4.10: Mercury porosity of dry coatings (G. Laudone)

S.X. Pan, H.T. Davis, L.E. Scriven from U Minnesota (L1.43) calculated binder migration to the surface during drying of coatings.
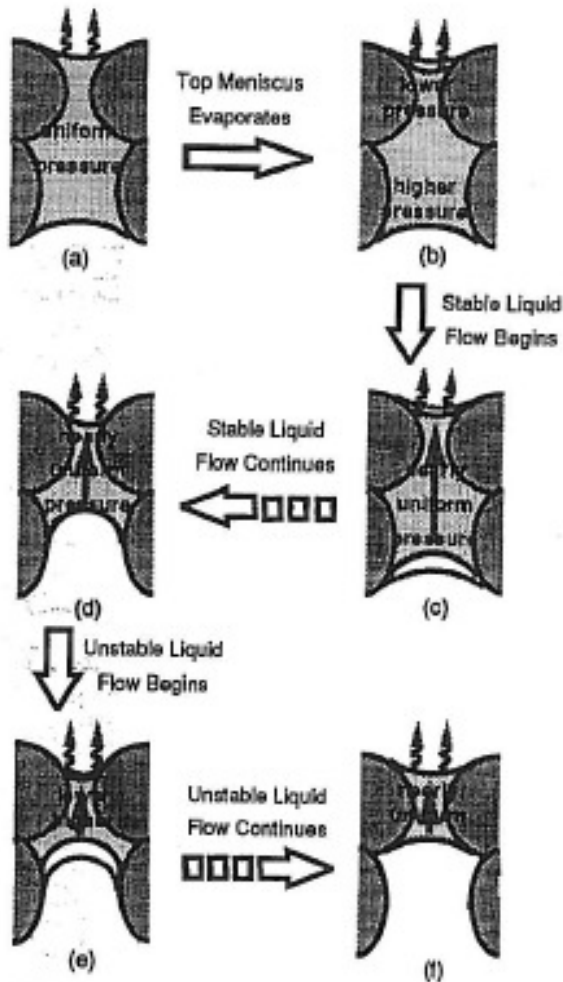
Pict. 11.1.4.11: Drying process (S.X. Pan)

During drying menisci are formed at the air liquid surface between pigment particles. These menisci create capillary force towards the surface. If this capillary force is higher than the capillary force towards the base paper, water and binder transport to the surface starts. Therefore drying of the surface should start as soon as possible after application.

Stable capillary transport of water within the coating colour and from the base paper continues (c) until the menisci reach their pore throat. The Haines jump starts (d). It ends, when all menisci are in converging pore sections (f).

Liquid flow in the drying process can be described by the capillary number

$Ca = \dfrac{\mu * W * L}{\sigma * \rho_1 * \Gamma_2 * (1 - \beta)}$ with μ the viscosity and β the size ratio of pore throats

where menisci lodge. The volumetric flow rate q_{ii} is proportional to the pressure difference and inversely to the viscosity according to Darcy's law.

Vapour transport was calculated with the Peclet number $Pe_v = \dfrac{W * L}{\rho_l * D_v}$.

For binder transport a similar Peclet Number Pe_b was used.

Binder concentration at the surface will be higher at thicker coating areas due to higher capillary forces at the surface.
At lower drying rates more latex will migrate from thin areas to thicker ones.
A lower diffusion coefficient of the binder achieved by interaction with pigment hydration layer led to less migration of latex towards the surface.
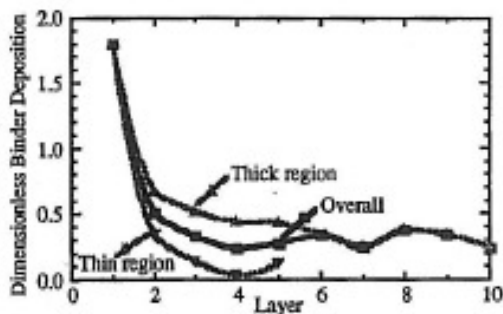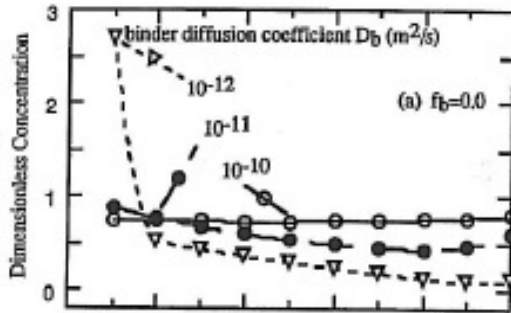
Pict. 11.1.4.12: Binder concentration at the surface (layer zero) as a function of binder diffusion coefficient and layer thickness (S.X. Pan)

M. Baumeister (L3.1) tried to reduce latex migration in low solids clay coatings by absorbing the latex particles on the clay surface. He modified the latex surface with functional polymers to increase adsorption affinity to clay surface. Small shear stable flocs were formed where the latex particles built the bridge between the pigment particles. M. Baumeister detected a remarkable drop in latex penetration into the base paper and less mottling in printing. Unfortunately these coatings couldn't be used for high speed coaters as low and high shear viscosity was on an unacceptable high level.

Do Ik Lee and M. Whalen-Shaw (L3.10) explained three fundamental filtration processes and their impact on latex penetration.
A) Medium filtration is a process, where the retained particles are larger than the holes of the filter medium.
B) Depth filtration occurs within the filter medium especially when this medium consists of various tortuous channels with unknown length and changing radius which cause high viscous flow resistance. Small particles of the filtrated suspension will be entrapped in these pores.
C) In cake filtration a bed of deposited solids is formed immediately after the filtration starts and the liquid has to flow through this filter cake.

When coating colour is applied, it will be filtered through the base paper, which behaves as a medium and depth filter (mechanism A + B) for larger particles in the coating colour.

When filtration time is long enough, which happens after the blade when drying is delayed, the coating colour forms a filter cake on the paper surface and cake filtration (mechanism C) is added.

Measurements of latex or starch concentration in Z-direction of wet coating layers showed an increase of latex/starch concentration at the boundary to the base paper due to these filtration mechanisms.

The authors showed that when more latex is moved to the surface during drying, ink absorption on this dry coating layer got worse.

They postulated that more stable colloidal systems of coating colours will have more pronounced mottling due to higher mobility of latex particles.

They suggested adding a controlled destabilization to the pigment particles by adding electrolytes or polymeric flocculants like proteins to floc the pigment slurry and reduce latex movement between the pigment particles.

When pigment affine latex types would be used in coating colours binder migration could be eliminated totally. Polyvinyl acetate latices e.g. form strong interactions with clay particles and migrate therefore less than styrene-butadiene latex.

The authors suggested the following strategies to reduce binder migration:
- Associate latex and clay like by hydrophobically modified cellulosic thickeners or soy proteins (disadvantage: viscosity increase)
- Destabilize the latex at the increasing temperatures in presence of isopylacrylamide
- Use temperature sensitive cross linkers like oligomeric aziridines
- Use multivalent salts, which get soluble at higher temperatures and destabilize the coating colour
- Use heat gelling thickeners (cellulosic ether or siloxanes).

A nice method to describe the uniformity of surface porosity was invented by Y. Xiang, D.W. Bousfield, J. Hassler, P. Coleman and A. Osgood (L3.11), who

developed an ink tack instrument at U. Maine to measure small spots of 2,2 mm diameter in ink absorption and ink split.
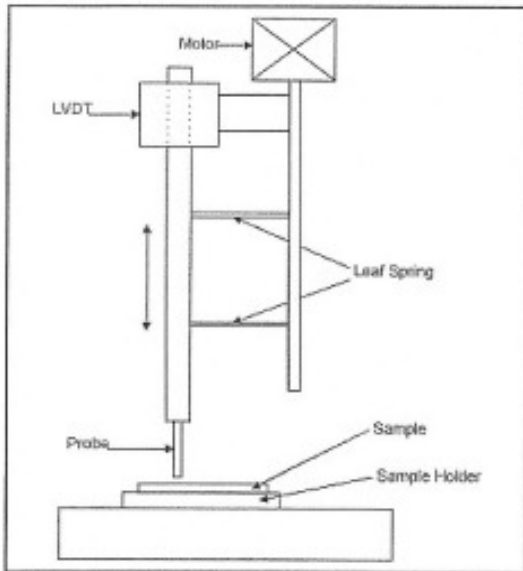
Pict. 11.1.4.13: Micro-Tackmeter of UMaine

16,5 g/m² ink was applied on a Mylar film with IGT AIC2-5. The printed film was attached on a smooth metal block with double sided tape.

The paper sample touched the inked Mylar film and around 8,2 g/m² of ink was transferred.

Once the contact force was established the motor moved the Mylar film upwards until the ink was separated. The minimum time to ink split was 5 seconds.

The authors found a quite good correlation between commercial print back trap mottling and standard deviation in ink split behaviour.
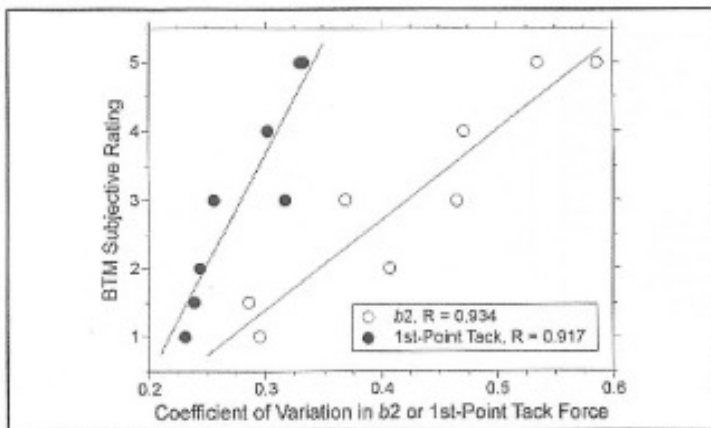
Pict. 11.1.4.14: Correlation between back trap mottle (BTM) and tack variation of spot measurements (1st point tack = 5 sec, spot diameter = 1,1 mm)

Together with latex supplier CIBA new types of SB-latices were developed, that aimed at Acronal S360D, the benchmark for high evaporation speed in the 2nd drying stage.

In principle this can be done either increasing the particle diameter or by lowering the cross linking of the polymer chains.

Latex type	Particle size (nm)	Tg (°C)
PE1844A	140	10
PE1844B	170	10
PE1844C	140	10
PE1844D	170	10
329	130	24
PE1919A	170	20
329 with plastizier		
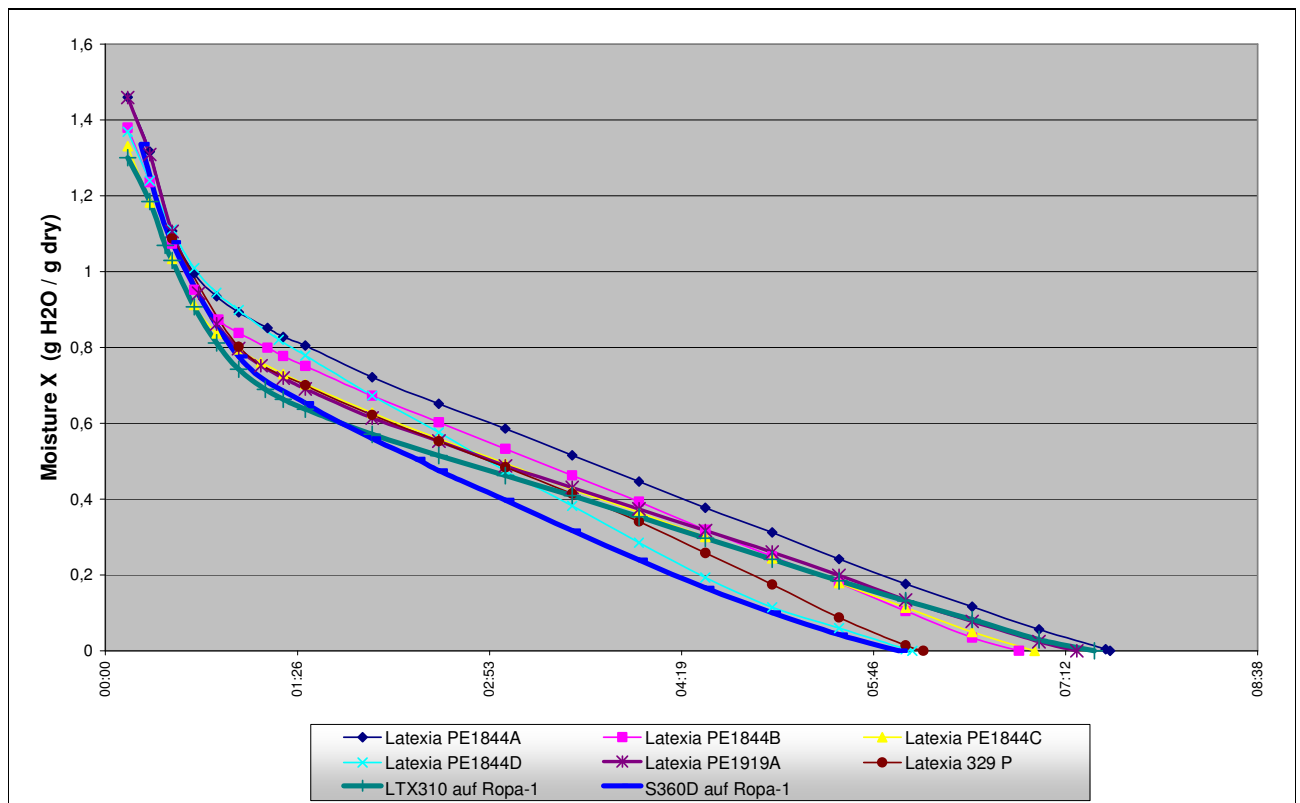
Pict. 11.1.4.15: X – t drying curve for different binders, 20 parts mixed with 100 parts pigment HC90 (lab study PT4 in 2008)

SB-latex PE1844D with increased particle diameter reached the same level of vapour permeability and drying speed than the benchmark Acronal S360D in.

Increasing latex particle diameter, like for PE1844D, leads unfortunately to a lower binding strength as specific surface area drops and less latex particles are available for binding pigment particles together. More latex PE1844D would be needed to achieve a comparable picking strength than for standard SB-latices. Vapour permeability would drop and costs would increase.

11.1.5 Vapour permeability measurements

The results of the lab drying curves were compared with vapour permeability (WddU) of the dry coatings on base paper at TUG.
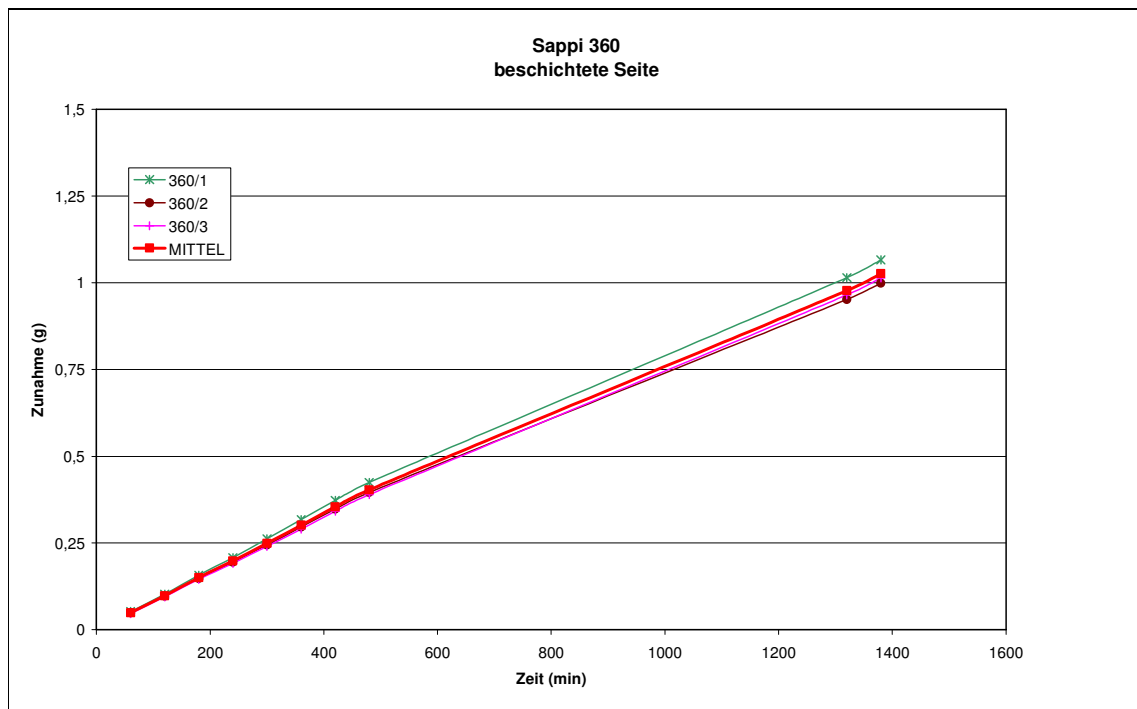
Pict. 11.1.5.1: Increase of moisture in the silica detected by weight over time at WddU test

Vapour permeability is measured by gluing a sample with wax on a pot filled with silica gel. This unit is now put into a climate of known conditions. Most often 50 or

85% relative humidity and 23 ℃ are taken for the WddU experiments. The water vapour transfer from the outside with high humidity through the tested paper (which acts like a membrane) to the inside with low humidity (due to silica gel) is measured over 24 hours.

To calibrate WddU measurements samples from all coating steps of a triple coated paper of PM11 were measured.

Water vapour permeability in g/m² over 24 hours, at 23 ℃ and 50%
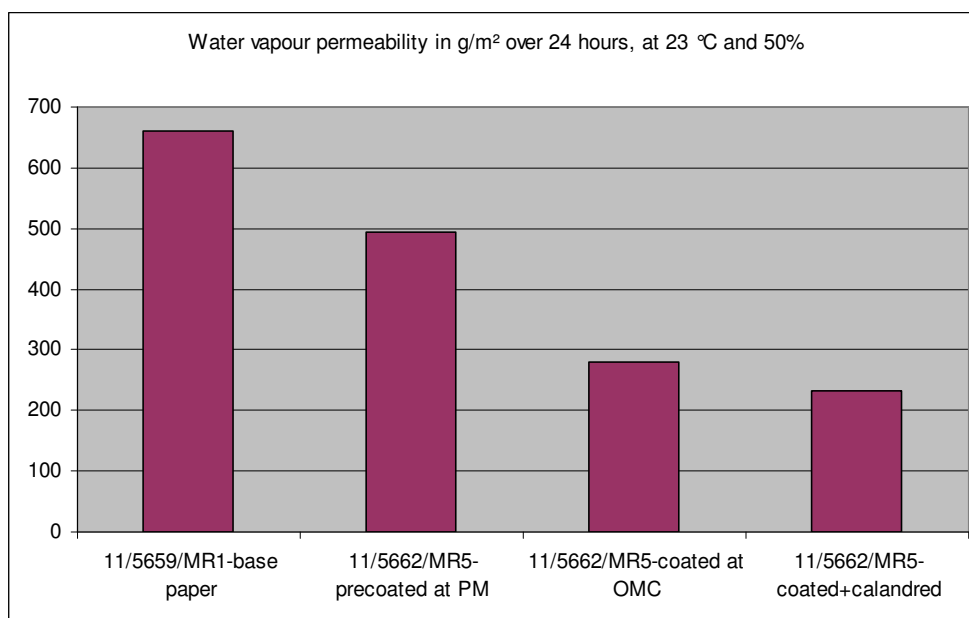
Pict. 11.1.5.2: WddU for different coating layers of triple coated paper PM11

With increasing number of coating layers vapour permeability drops due to better holdout of fine particles in coating.

Therefore higher coat weights increase the risk of drying induced mottling:
The higher the coat weight, the higher the lower the vapour permeability of dry coating layer and the more energy is needed to evaporate water through this dense surface layer. Vapour will search for the easiest way to the surface and latex will travel with vapour to the surface. Drying mottling is the consequence.

Applying pure binder instead of coating colours on precoated paper amplifies the differences in vapour permeability.
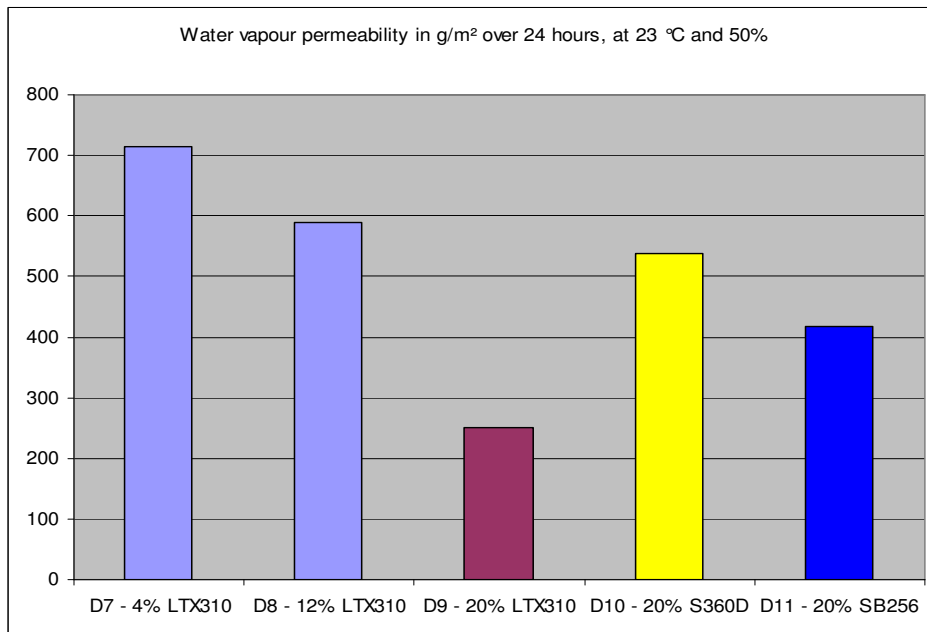
Pict. 11.1.5.3: WddU for different latex contents and latex types in single coating layer based on HC90 (applied with lab rod coater on base paper PM11, drying at 75°C over 20 sec)

With increasing latex content vapour permeability dropped due to fine particles blocking the path ways of vapour through the pigment matrix.

Soft SA-latex Acronal S360 D and hard SB-latex SB256 were higher in vapour permeability than soft SB-latex LTX310. Diffusion resistance coefficient μ increases with rising permeability and with D the drying speed in the 2nd drying stage is increasing.

$$g_{d,II} = \frac{1}{R_D * T} * \frac{1}{\frac{1}{\beta} + \frac{\mu * s'}{D}} * (p_D^{''} - P_{D,a})$$ [kg/m²h] (D diffusion coefficient of vapour in air,

β mass transfer coefficient and s' the distance of liquid front from surface)

The WddU measurements explain the higher evaporation speed in the 2nd drying stage of the coarse latices S360D and SB256 which were shown in the previous graphs.

Water vapour permeability in g/m² over 24 hours, at 23 ℃ and 50%
(single coated of binder on base paper, IR dried with 75℃ surfacetemperature)
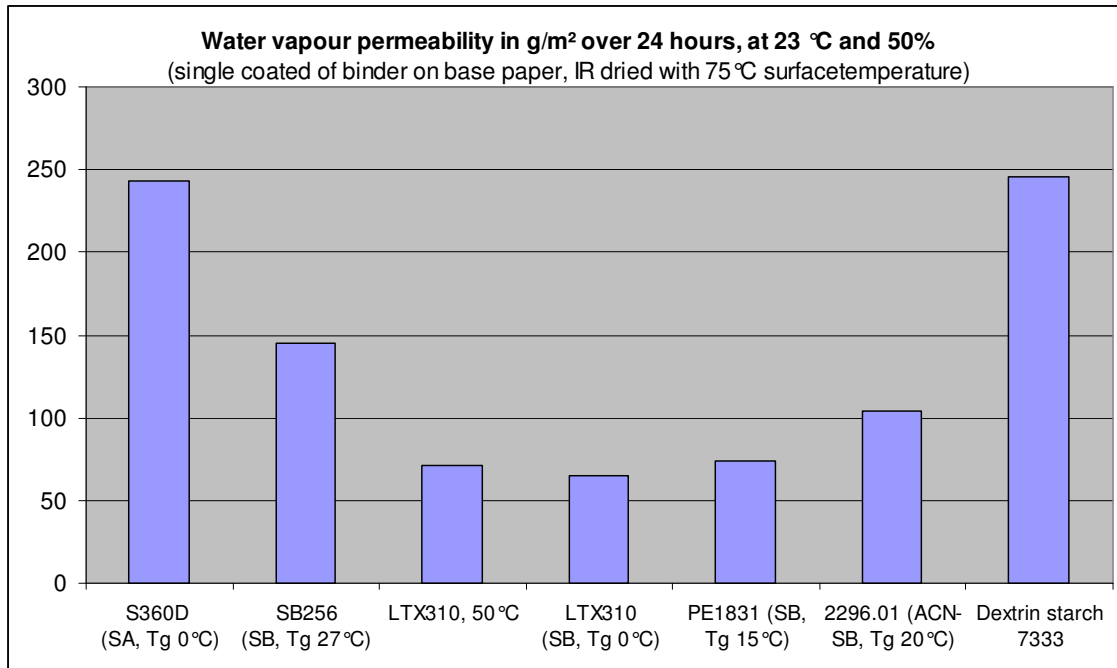
Pict. 11.1.5.4: WddU for different lattices in single coating by lab rod coater on base paper

Starch films were relatively high in vapour permeability which stays in contradiction to the lower evaporation speed of starch based coatings, detected in the previous lab trials. The reason is the hydrophilic nature of dry starch films, which leads to swelling during contact with water vapour. WddU measurements are done over a period of 24 hours where the vapour destroys the hydrophilic barrier of the starch film. In mill coaters the drying time in the 2nd and 3rd drying stage is much shorter and the vapour barrier properties of the starch film will not be destroyed. Short term vapour barrier of starch films will be therefore much higher than the WddU measurements.

During latex film forming the latex particles change their shape from sphere form to honeycomb structure. The bigger the latex particles the more difficult it gets to close the gap between the latex particles and to form a dense honeycomb structure. Permeability increases therefore with latex particle diameter. Theoretically a broad PSD of latex particles would give the lowest permeability but unfortunately latices have a relatively small PSD when compared with carbonate pigments. Mixing two latices with different mean particle diameter would result in a bimodal PSD and in lower permeability.

Tomi Kimpimäki (L3.16) showed the difference in vapour permeability of SA and SB latices with similar Tg. He studied latex coalescence and film forming of pure latex films in his PhD work at Tampere University of Technology.
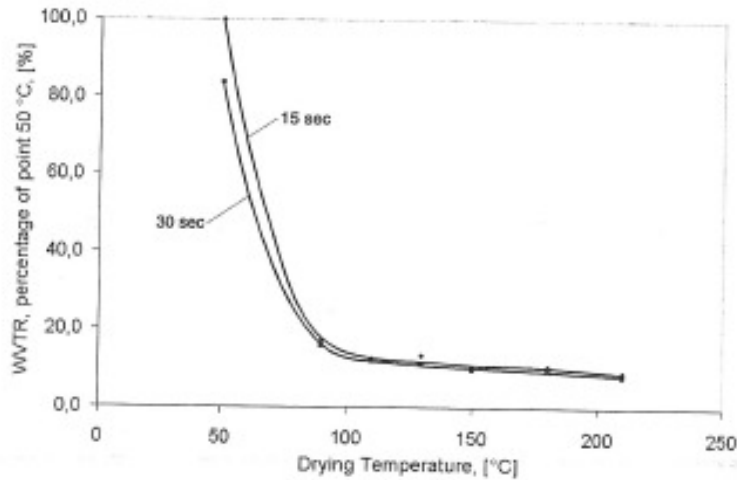
Pict. 11.1.5.5: Vapour transmission of SB dispersion (Tomi Kimpimäki)
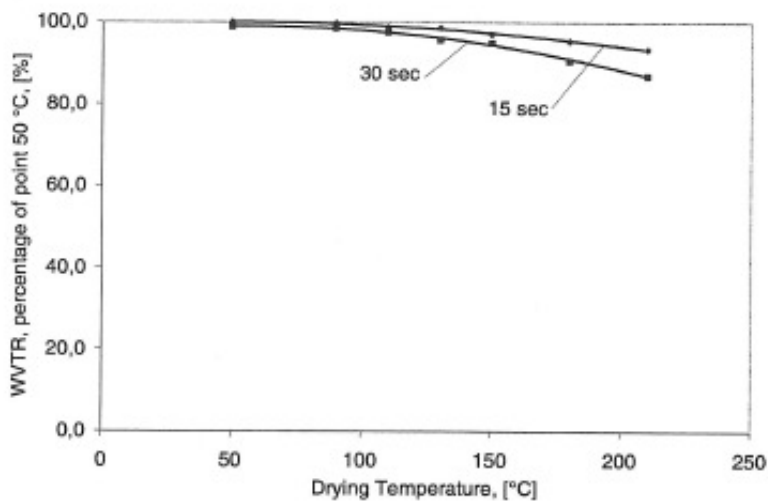
Pict. 11.1.5.6: Vapour transmission of acrylate dispersion (Tomi Kimpimäki)

Vapour permeability dropped when drying (and surface) temperature was increased. Surprisingly the SA-latex showed much higher vapour permeability than the SB-latex. This difference was detected for pigmented and pure latex films.
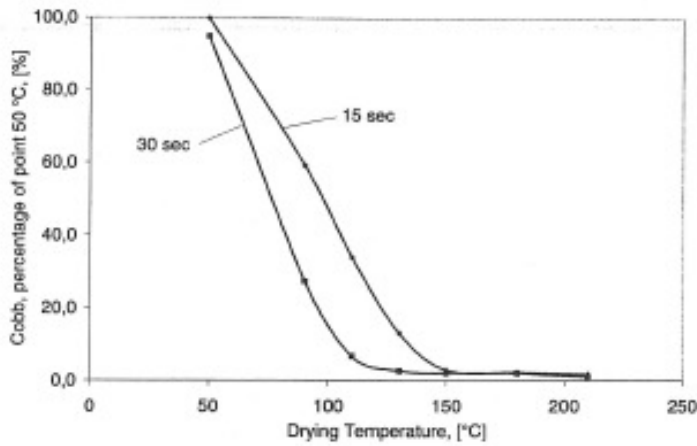
Pict. 11.1.5.7: Cobb of SB dispersion (Tomi Kimpimäki)
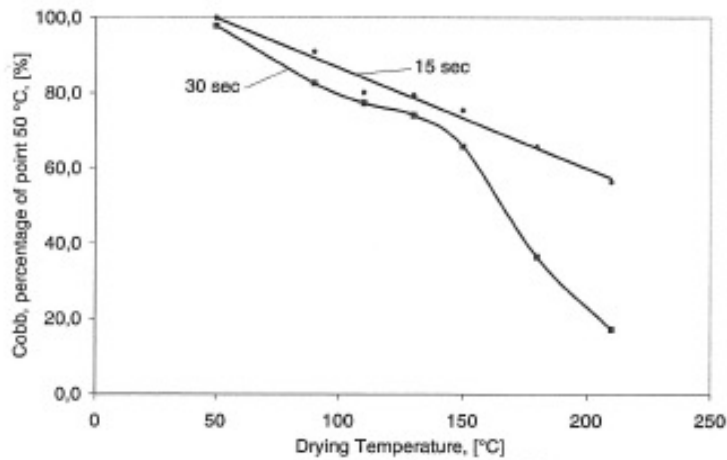
Pict. 11.1.5.8: Cobb of acrylate dispersion (Tomi Kimpimäki)

The difference in vapour permeability was also measured in water permeability of the coating layer by Cobb test.

Differential scanning calorimeter measurements (Perkin Elmer) were made to determine the drying energy, which was needed to dry the polymer film. DSC is used to characterize the glass transition point T_g of a polymer. The sample is heated from 20°C to 90°C, cooled to -60°C and heated again to 90°C with $\Delta T = 20$°C/min
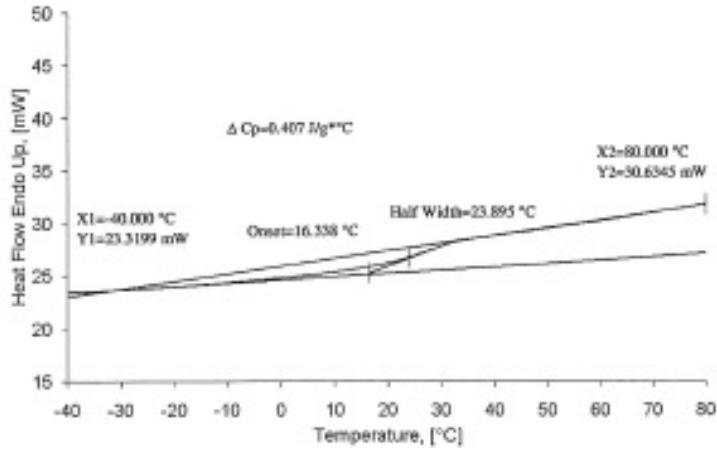
Pict. 11.1.5.9: DSC of SB dispersion (Tomi Kimpimäki)
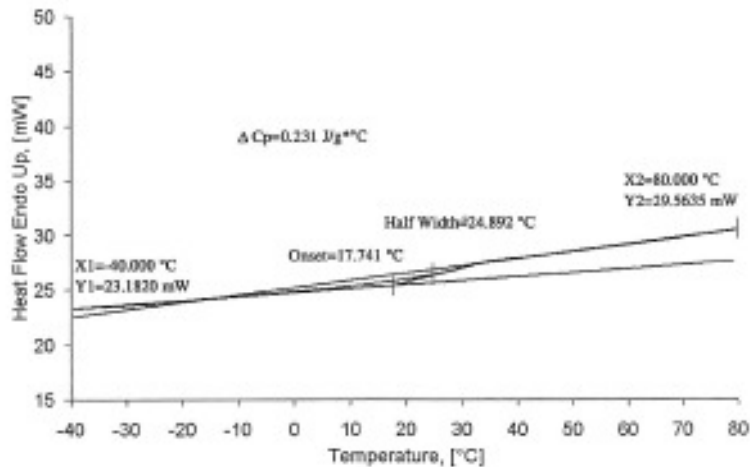
Pict. 11.1.5.10: DSC of acrylate dispersion (Tomi Kimpimäki)

Drying time was much shorter for the SA-dispersion as Δc_p was 1.8 times lower than for SB-dispersion.

To explain the higher vapour permeability Tomi Kimpimäki measured the coalescence angle during drying of the dispersion by AFM microscopy. When polymer particles get closer and film form in a honeycomb structure the coalescence angle drops.
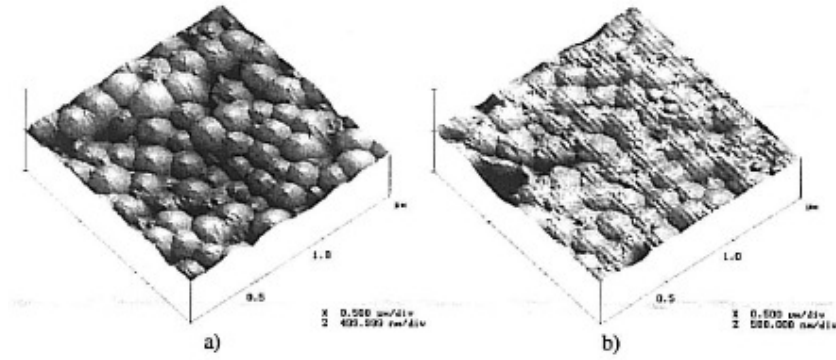
Pict. 11.1.5.11: Coalescence angle – change during drying (Tomi Kimpimäki)
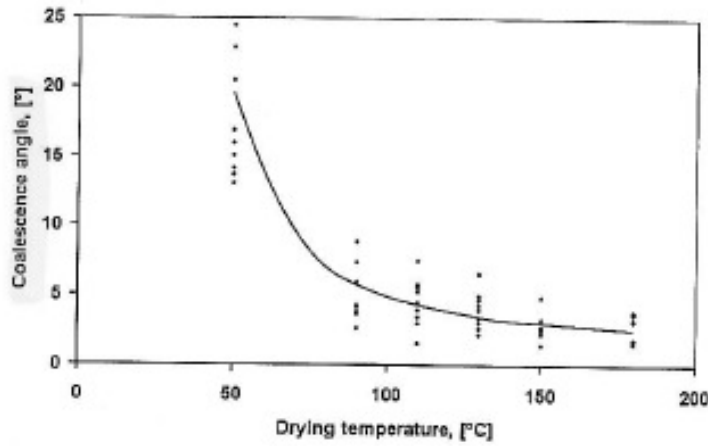
Pict. 11.1.5.12: Coalescence of SB dispersion, 15 sec. drying time (Tomi Kimpimäki)
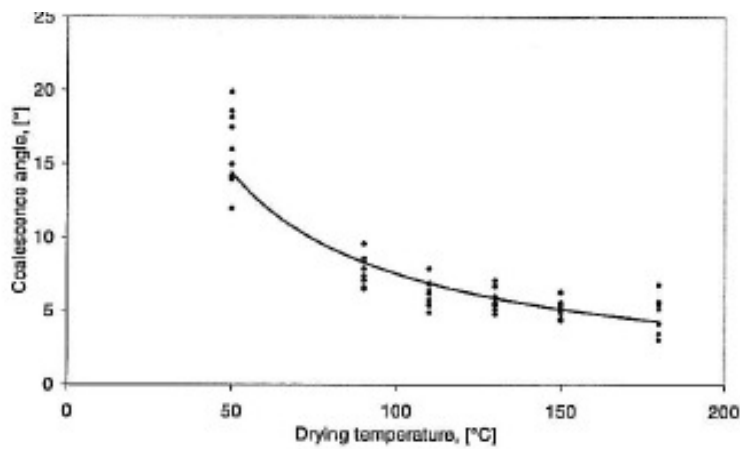
Pict. 11.1.5.13: Coalescence of SA dispersion, 15 sec. drying time (Tomi Kimpimäki)

The tested SA-latex starts at a comparatively low coalescence angle but with increased surface temperature during drying of the film the coalescence angle drops to a lower extend than for SB-latices. The sphere shape of the particles is still visible even at high drying temperatures leading to micro pores between the latex particles which increase the vapour permeability.

REM pictures with high resolution were made from previously described latex films on Mylar foil at TU-Graz to detect the honeycomb structure of latex particles after film forming:
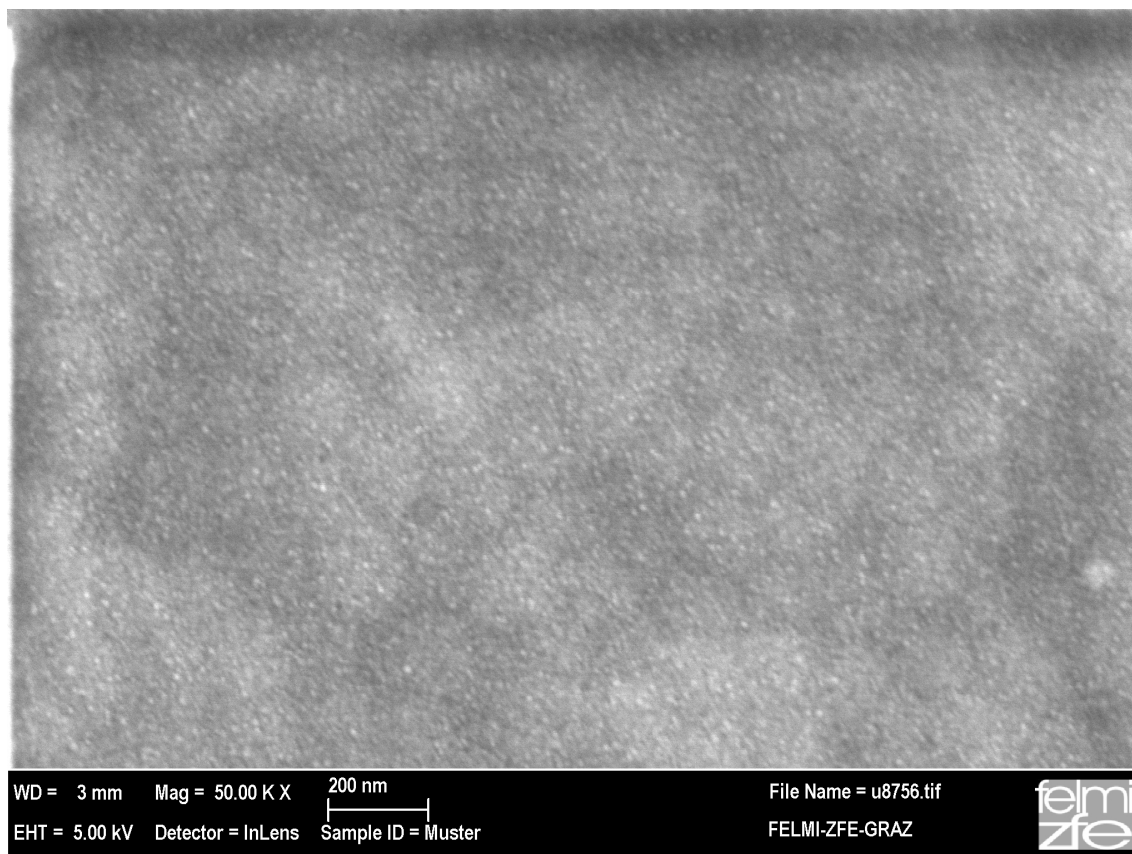
Pict. 11.1.5.14: Honeycomb structure of latex film (SB256)

The areas in the honeycomb structure where latex particles were melt together showed lower thickness of latex film in the REM pictures. At these spots vapour permeability will be lower than in the centre of the latex particle where film thickness is clearly higher.

When latex particle diameter is raised film forming gets more difficult as distance between the particles increases with diameter of the particles. Porosity of these latex films will be higher after film forming:
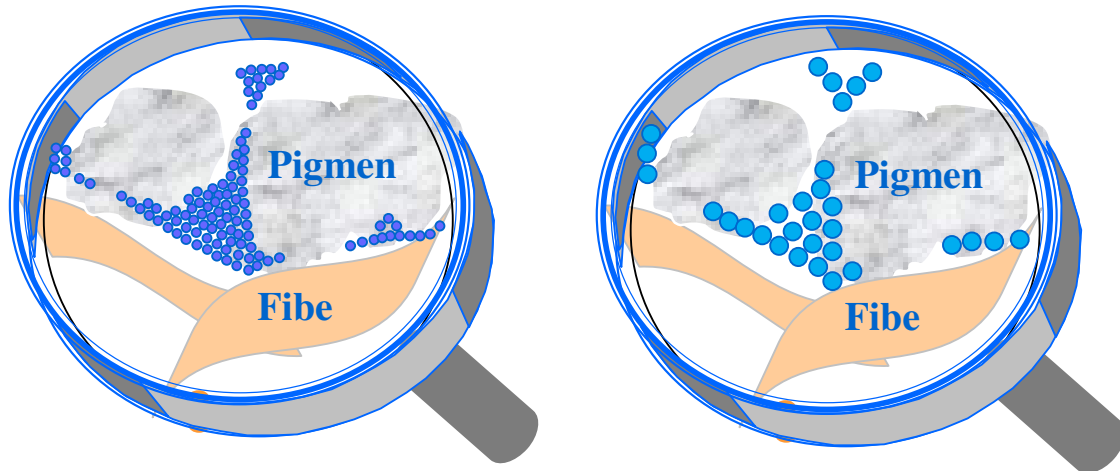
Pict. 11.1.5.15: Latex film porosity for different particle size – SB-latex with 150 µm PS mixed with carbonate Hydrocarb 60 (60% < 2 µm), mass ration 10 : 1 (BASF)

11.1.6 Influence of drying conditions on coating layer vapour permeability

Pure latex films were applied by a lab doctor blade on a base paper and dried in an IR-scale. The hold out of the latex layer was excellent as drying started immediately after application.

The drying time in the IR-dryer was:

- 5 sec to reach 50°C surface temperature

- 20 sec for 75°C

- 60 sec for 100°C

- 120 sec for 150°C.

Water vapour permeability in g/m² over 24 hours, at 23 °C and 50%
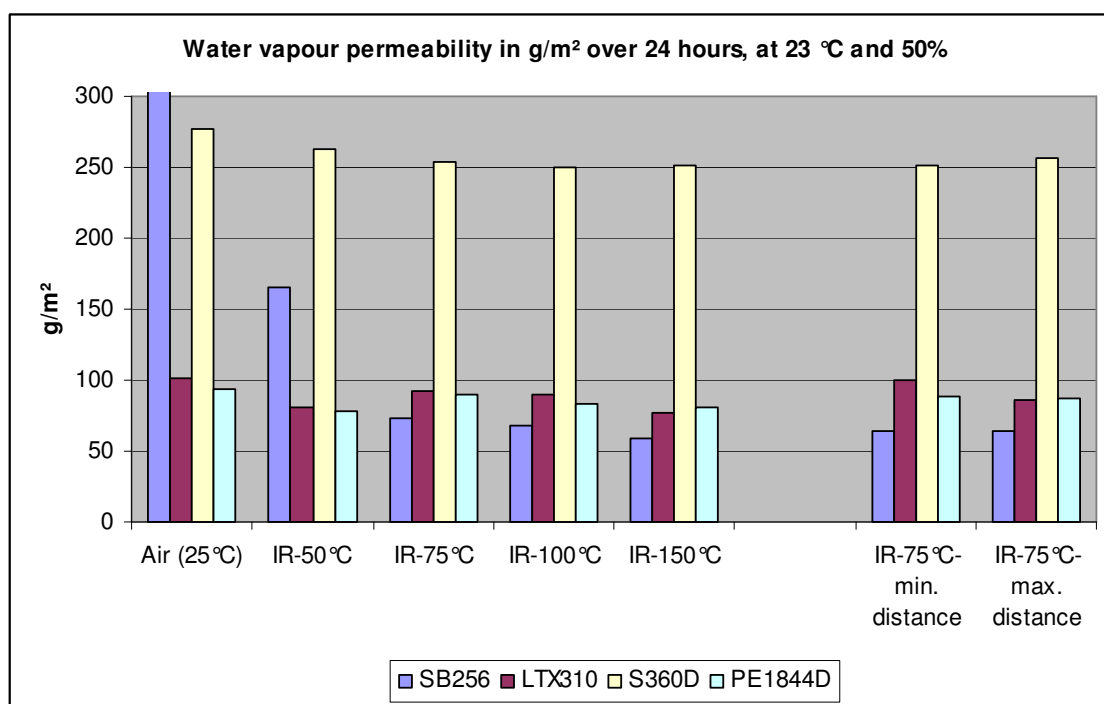
Pict. 11.1.6.1: WddU for four latices at different IR drying conditions.

The soft latices S360D (SA), LTX 310 (SB) and PE1844D (SB) were relatively independent from drying time and surface temperature as their mean film forming temperature (MFFT) was exceeded by all drying conditions. MFFT stays approximately 5° over the Tg for all tested latices.

Again <u>SA-latex S360 D</u> showed superior vapour permeability which is a clear advantage in lower drying energy demand, more uniform binder migration and less print mottle.

The <u>hard SB-latex SB256</u> with high Tg = 27°C showed again a strong dependence of vapour permeability on drying time and temperature. WddU dropped continuously when the surface temperature was raised from 25°C to 75°C as the MFFT of 32°C was exceeded and latex particles were melt together. When this hard latex is dried long enough at high web temperatures (high energy input) it looses its advantage of higher vapour permeability. This is important for web offset coatings based on this latex where WddU should be as high as possible.
Under mill drying conditions film forming of SB256 is never as perfect as in these lab trials as dwell time in drying is much shorter. Vapour permeability of hard SB-latices like SB256 is therefore most often higher than for soft SB-latices.

Both latices S360D and SB256 are commonly used as web offset latices where their advantage of higher vapour permeability is used for increasing the blister resistance of the coated paper.

The difference in dry coating layer porosity between soft SB LTX310 with low particle diameter (140 nm) and hard SB SB256 with coarse particles (175 nm) was also visible in Mercury porosity:
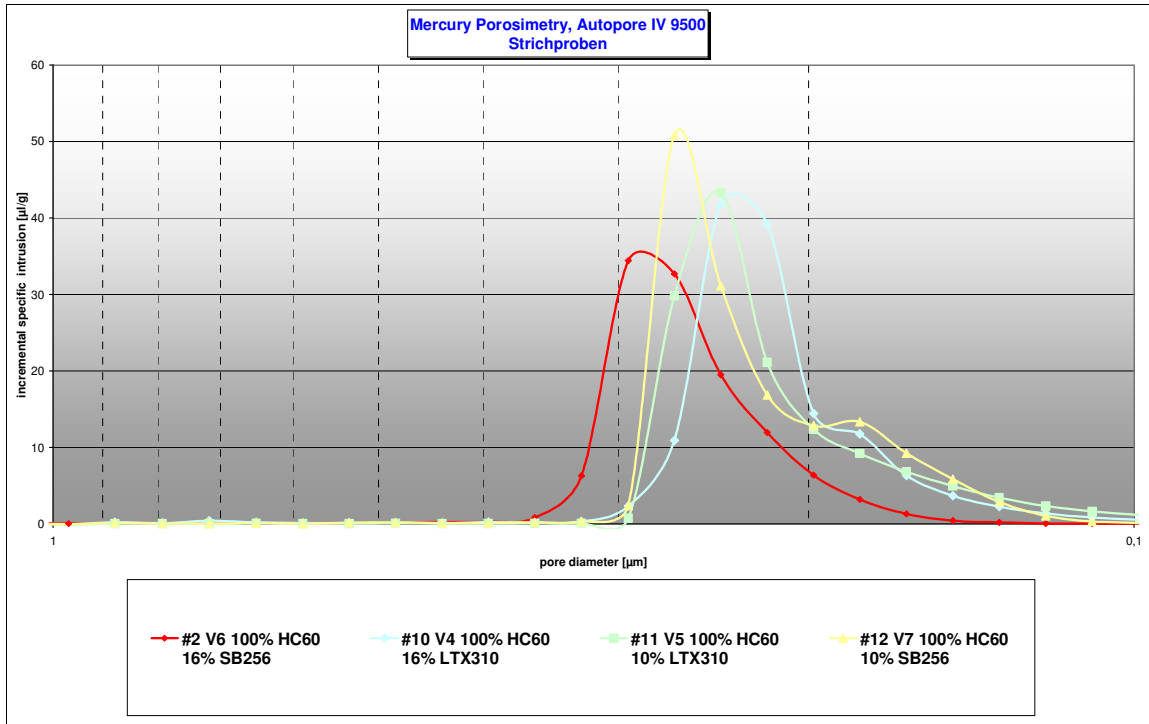
	100% HC60 10%LTX310	100% HC60 16%LTX310	100%HC60 10% SB256	100%HC60 16% SB256
Dmax [µm]	0,24	0,23	0,26	0,28
total pore volume [µl/g]	139	**105**	148	**118**

Pict. 11.1.6.2: Mercury porosity of coating tablets with fine SB-latex LTX310 and coarse SB-latex SB256

Tuulikki Hattula and P.J. Aschan (L3.6) came to the same conclusion by comparing styrene-butadiene and polyvinyl acetate latex with different Tg for double coated board. They varied latex content in pre and top coating and combined these two effects. PVAc-latex had a higher mobility than S/B-latex. Using a hard PVAc with high Tg led to a higher pore volume when compared with soft S/B (low Tg) as degree of film forming was lower. The pre coating latex penetrated into the base sheet and a high amount of latex was found in the boundary between precoat and base paper. Picking strength was lowest in the precoating layer on top of the boundary.
A higher degree of penetration of the top coat latex into the precoating layer was detected when latex content in precoating was low and porosity was high.

11.1.7 Influence of latex film forming on permeability and picking resistance of coating layer

In the next part of the lab coating studies different formulations with 20% binder content, based on carbonate HC90, were coated on a base paper by a lab rod coater. Coat weight was kept constant with 10 g/m². Drying was done in three different ways:

a) <u>Air drying</u> at room temperature of 23 °C

b) <u>Lab oven</u> using convective drying with 100 °C hot blow air and 1'30" min dwell time in the oven – sample surface temperature increased to 50 °C. Dwell time between coating and drying was relatively long with 12 sec.

c) <u>IR drying</u> with 20 sec dwell time under IR leading to a web temperature of 75 °C at end of drying. The dwell time between coating and drying was very low with 1 sec.

<u>Consequence of the three different drying conditions:</u>

• Air drying at room temperature simulated low energy input and high capillary sorption before FCC. As surface temperatures remained at 23°C only latices with MFFT below room temperature were able to film form.

• Convective drying in the lab oven simulated delayed drying with high penetration into the base paper before drying as dwell time was high between application and start of drying. Surface temperature exceeded MFFT of all tested latices.

• IR drying led to fast immobilization of coating layer and low amount of penetrated latex. Film forming was also sufficient as surface temperature of coating stood well above MFFT.

Permeability was measured both by air (Bendtsen ml/min) and by liquid with the new Prüfbau pressure penetration test.

As the base paper was kept constant the differences in permeability were caused solely by the coating layer.
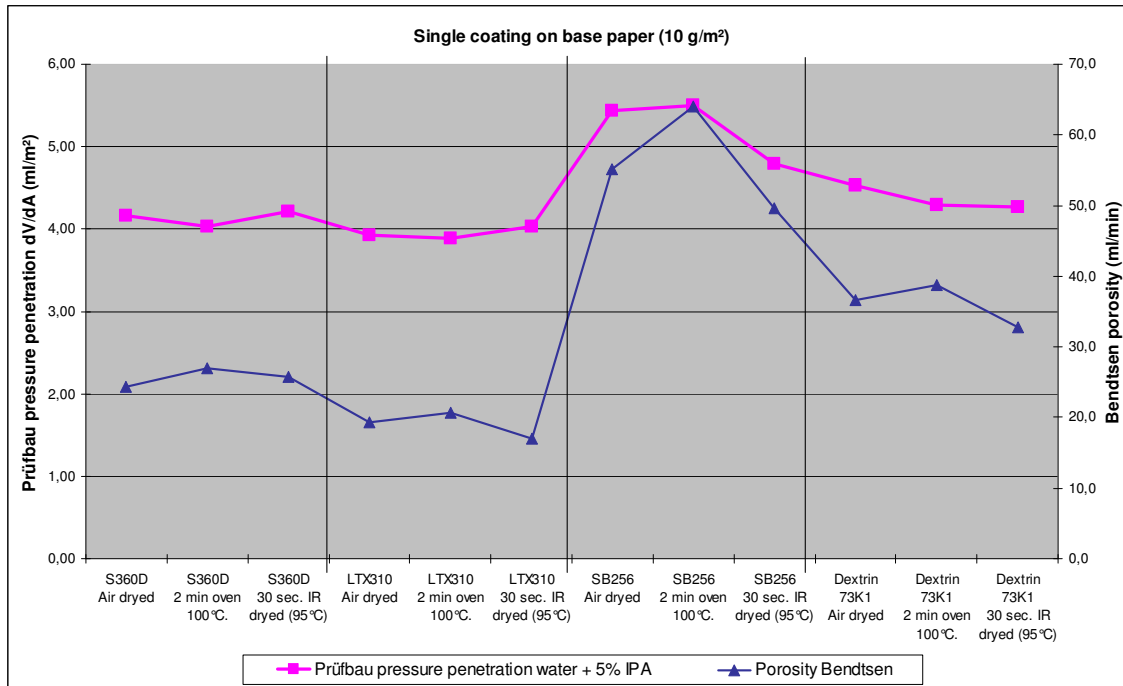
Pict. 11.1.7.1: Permeability of coated surface, measured with Bendtsen air porosity and Prüfbau droplet pressure penetration test (higher dV/dA corresponds to lower permeability)

With both air and water pressure penetration test the permeability of the coated layer was similar for soft acrylate latex Acronal S360D and soft SB latex Latexia LTX 310. Dependency of permeability on drying parameters was low, as both latex film formed at room temperature (Tg ≈ 0°C).
The soft acrylate latex S360D showed a somewhat higher porosity than the soft SB latex LTX310 at same Tg due to higher particle size and micro-cracks in the dry film.

Coarse and hard SB-latex SB256 showed high dependency of coating layer porosity on drying energy as Tg is much higher (Tg = 27°C). The higher the drying energy, the more latex is film formed and the lower the permeability was. In general water and air permeability of hard SB-latex SB256 was much higher than that of the soft SB and SA latices due to lower film forming and higher particle diameter. Time was too short in the IR dryer and web temperature was too low in the lab oven to get this latex totally film formed. In a mill coater drying time and web temperature is even lower than for these lab experiments resulting in lower permeability of SB256 based coatings compared to lab coatings.

Brittle starch Dextrine 73K1 showed higher coating layer permeability than soft latices due to micro cracks in the starch film, which were formed by shrinkage of the coating layer when dried to almost zero moisture (like in these experiments).

When starch based coatings are dried moderately, coating layer permeability is lower, as film forming is fast, and shrinkage of the coating is more pronounced, than for latex based coatings.
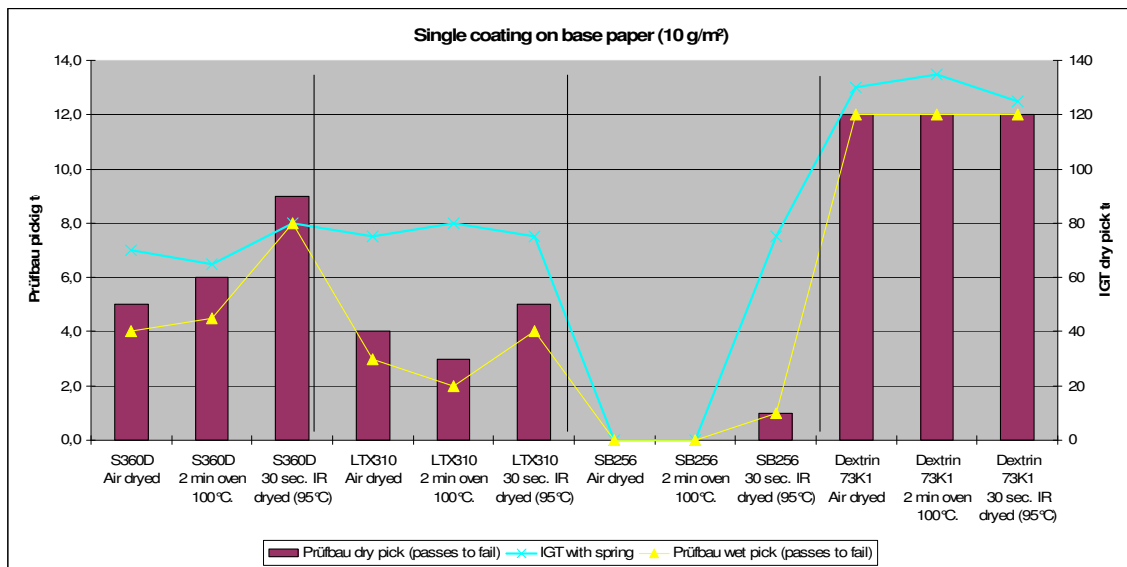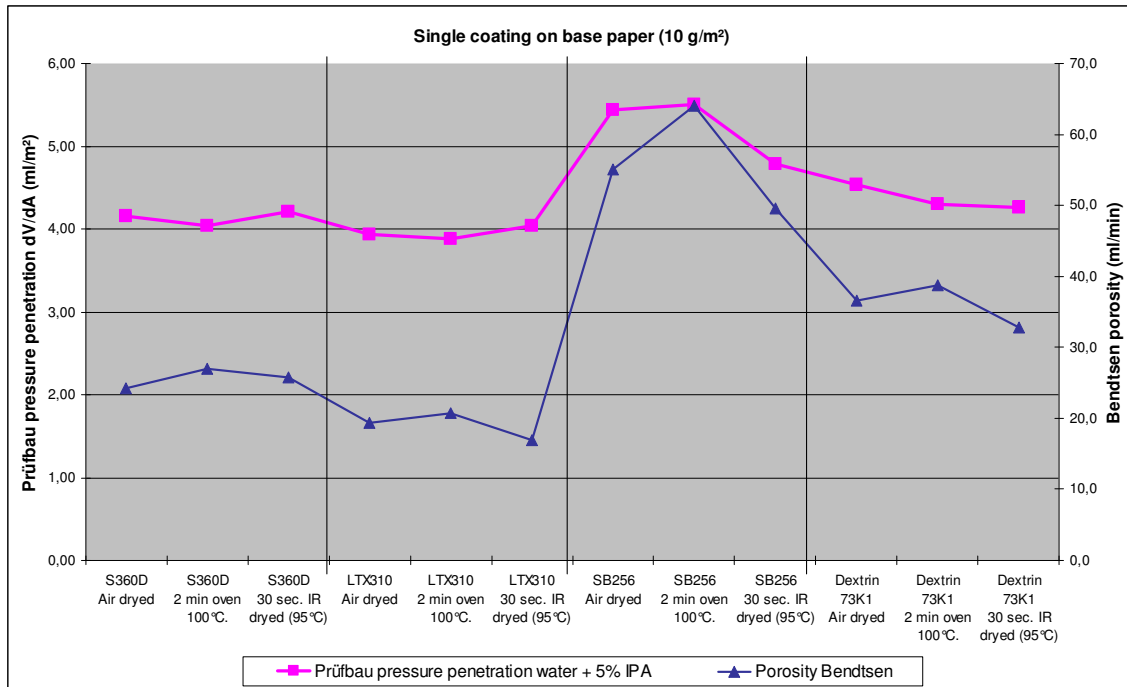
Pict. 11.1.7.2: Comparison of Prüfbau permeability (higher dV/dA corresponds to lower permeability) with picking resistance of drying tests

The picking tests fit well to the porosity data's: The less latex penetrates into the base paper and the higher the degree of film forming, the higher the picking resistance.

Lab oven and IR dried samples of S360D based coatings were higher in picking resistance than the corresponding air dried samples which shows the positive effect of latex holdout in the dwell time between application and SCC.
All three tested latices showed a denser coating layer with higher picking resistance when IR was used as the drying energy source compared to oven dried samples as immobilization started faster, less latex penetrates into the base and surface temperature (film forming temperature) was higher than for lab oven dried samples.

Picking resistance of starch based coatings was much higher than that of latex based coatings due to a high amount of hydrogen bonding points between starch molecules and pigment surface. Therefore a switch from latex to starch as a precoating binder leads most often to an increase of picking resistance of the whole coating layer (see chapter "dense precoatings"). The exchange rate can be 1:1 in precoatings.

Picking resistance of starch based coatings was relatively independent on drying energy as hydrogen bonds are immediately formed when water is removed from the coatings during drying. This is an advantage in some applications where drying energy for precoatings is limited, e.g. after rebuilds with limited space for new dryers, and low surface temperatures would lead to insufficient latex film forming.

Finally a comparison of the conventional Prüfbau droplet test and the new Prüfbau pressure penetration test was made for this part of the lab coating study.
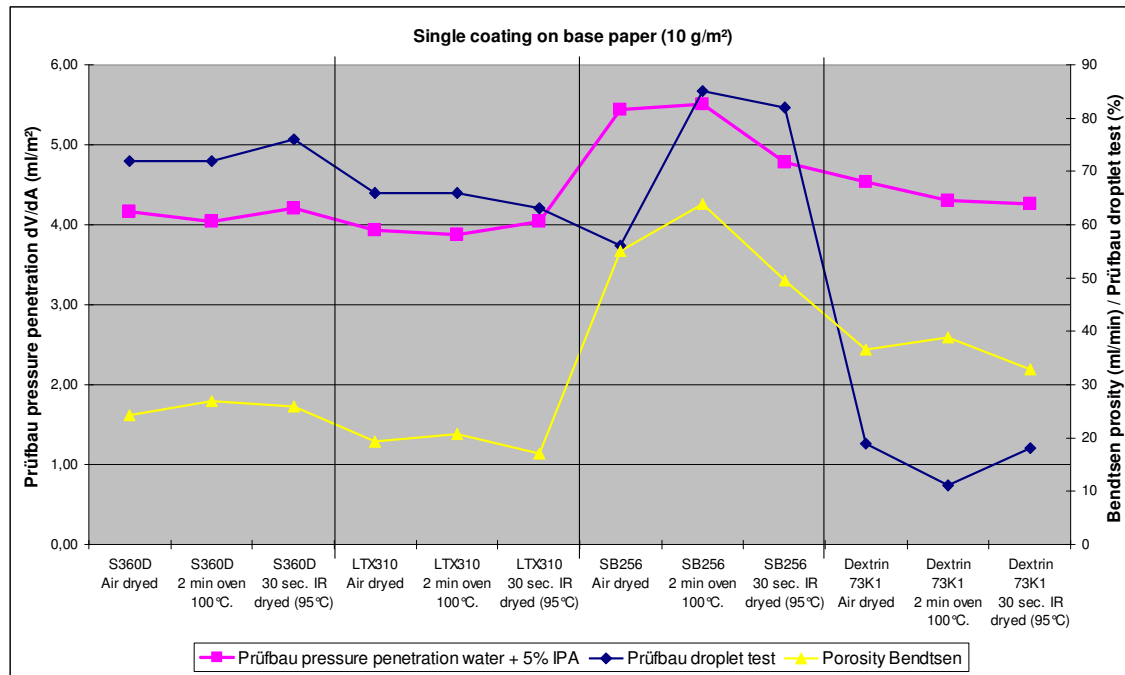
Pict. 11.1.7.3: Permeability of coated surface (higher dV/dA corresponds to lower permeability), including Prüfbau standard droplet test

Comparing the standard Prüfbau droplet test with the new pressure penetration test no correlation was found between the two tests.

The reason is the difference in dependence on contact angle and surface energy of the two tests: The pressure penetration test is independent of contact angle as the earlier comparison between oil and water of same viscosity in this test showed – the water droplet is pressed into the surface within milliseconds. The standard droplet test is dependent on contact angle – first a drop of water is applied on the paper surface, it spreads and after some seconds this droplet is rolled out on the paper surface by a roll covered with ink. The tested samples showed big differences in droplet diameter at the application point – proving the dependency of this test on contact angle.

11.1.8 Influence of binder holdout on permeability

In the last lab study 05/2009 (16-02-2009) the four binders LTX310 (soft SB), SB256 (hard SB), S360D (soft SA) and dextrine starch 7333 were again compared on two different substrates: A highly porous base paper with big pores (4,5 µm) and a dense precoated paper with low pore diameter (0,25 µm).

The results fit quite well into the previous studies.
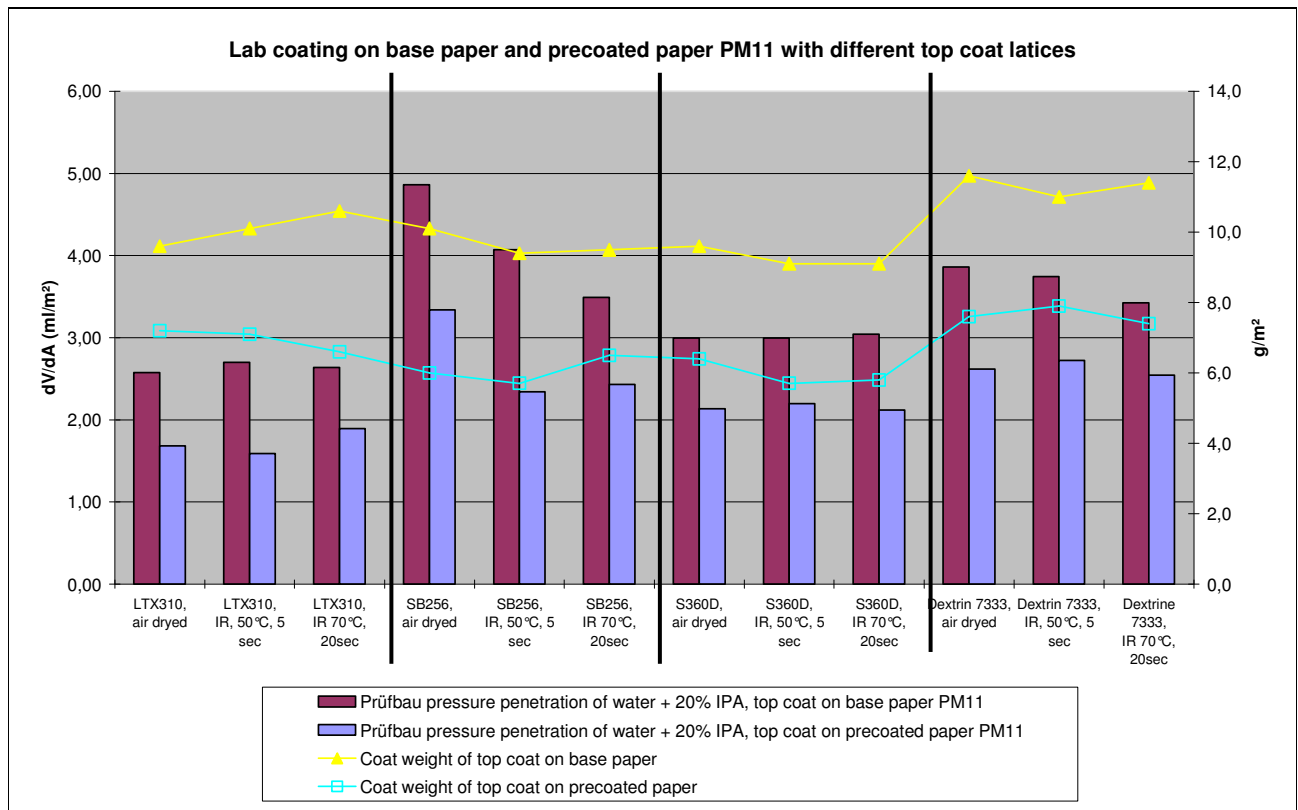
Pict. 11.1.8.1: Prüfbau pressure penetration test with water + IPA (higher dV/dA corresponds to lower permeability)
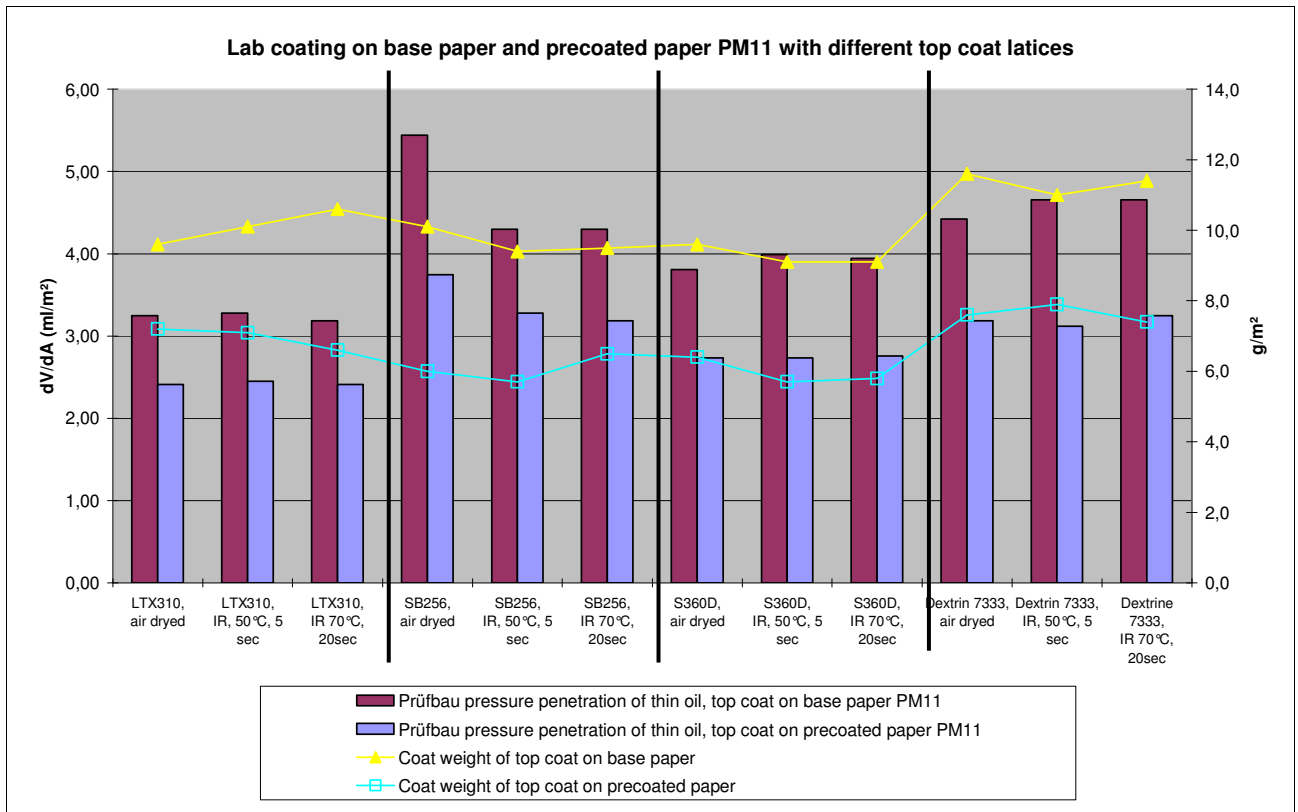
Pict. 11.1.8.2: Prüfbau pressure penetration test with thin oil (higher dV/dA corresponds to lower permeability)
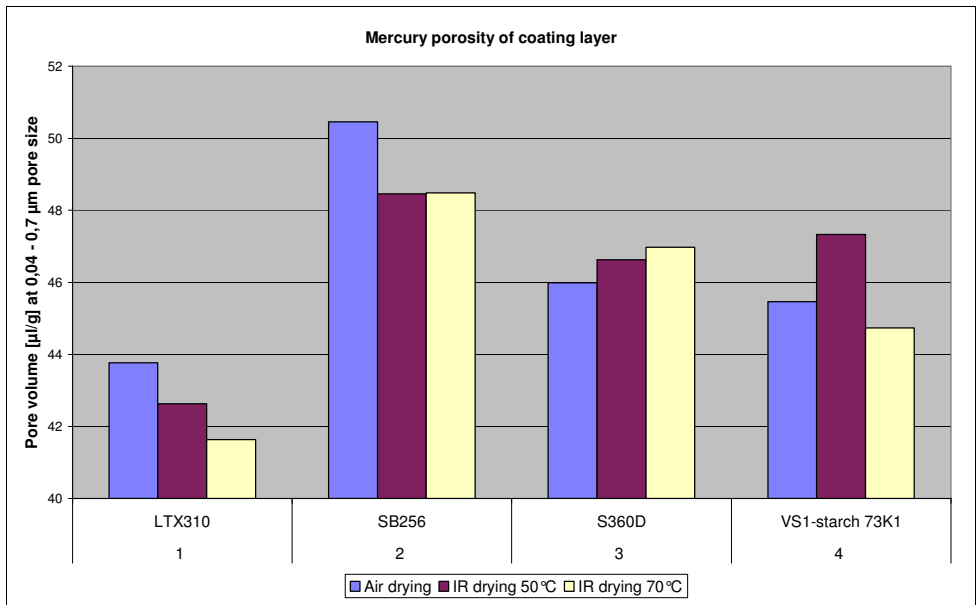
Pict. 11.1.8.3: Mercury porosity of coating layer for different binders under different drying conditions

Comparing the two SB-latices soft LTX310 (Tg=0°C) and hard SB256 (Tg=27°C) one can see, that liquid pressure penetration of a fountain solution or print oil is higher, when latex is not film formed during drying of the coating layer as the latex remains in its original sphere shape. Permeability of this coating layer is higher.

Comparing the two soft latices LTX310 (SB) and S360D (SA) shows that coating layer permeability of SA based coatings is higher. This is caused by higher mean particle diameter of S360D.

Starch and acrylic latex S360D with linear polymer configuration were relatively insensitive against drying conditions. Their coating layer porosity was independent from applied drying energy.

Permeability of all coating layers was lower for applications on the dense precoated paper compared to films applied on the porous base paper due to raising latex holdout.
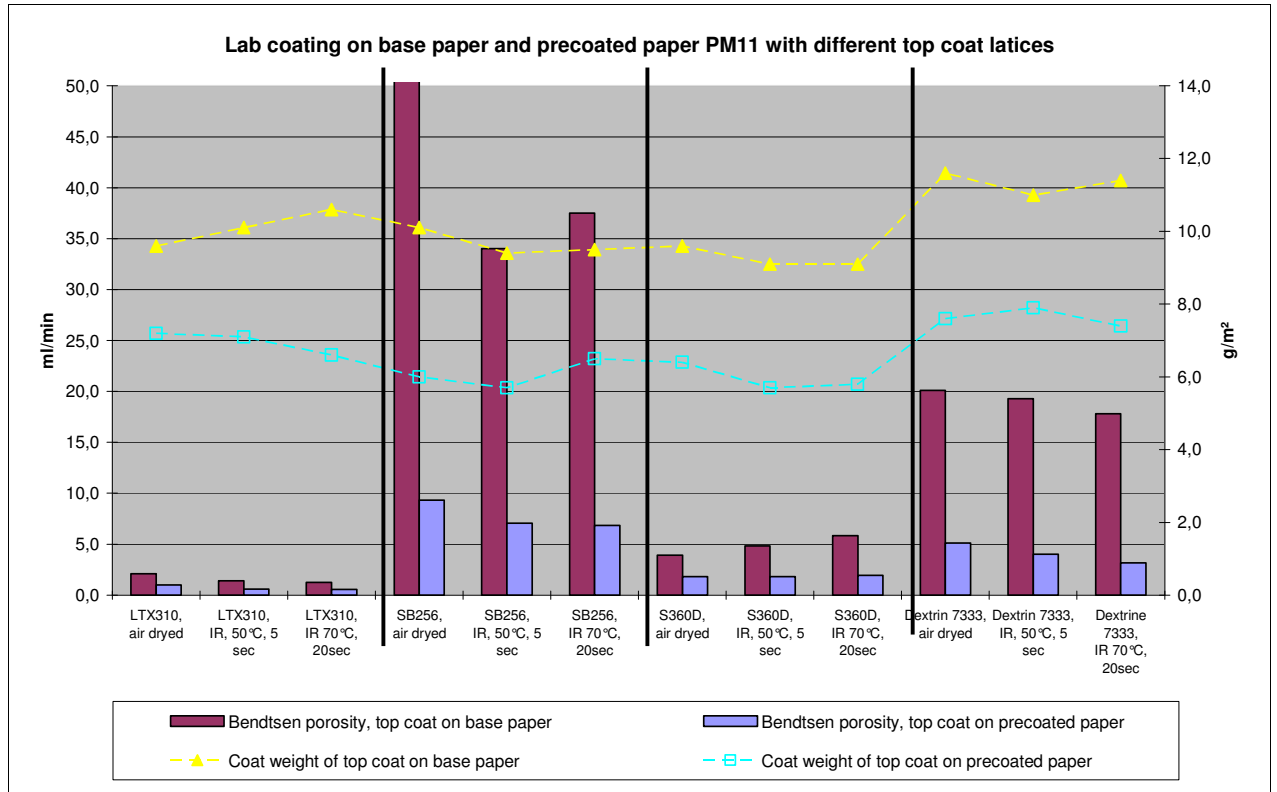
Pict. 11.1.8.4: Bendtsen porosity – comparison of coating on base paper and on double precoated paper

The differences in air permeability were similar to the permeability results from Prüfbau pressure penetration tests. Coarse and hard SB256 was highest in coating layer permeability.
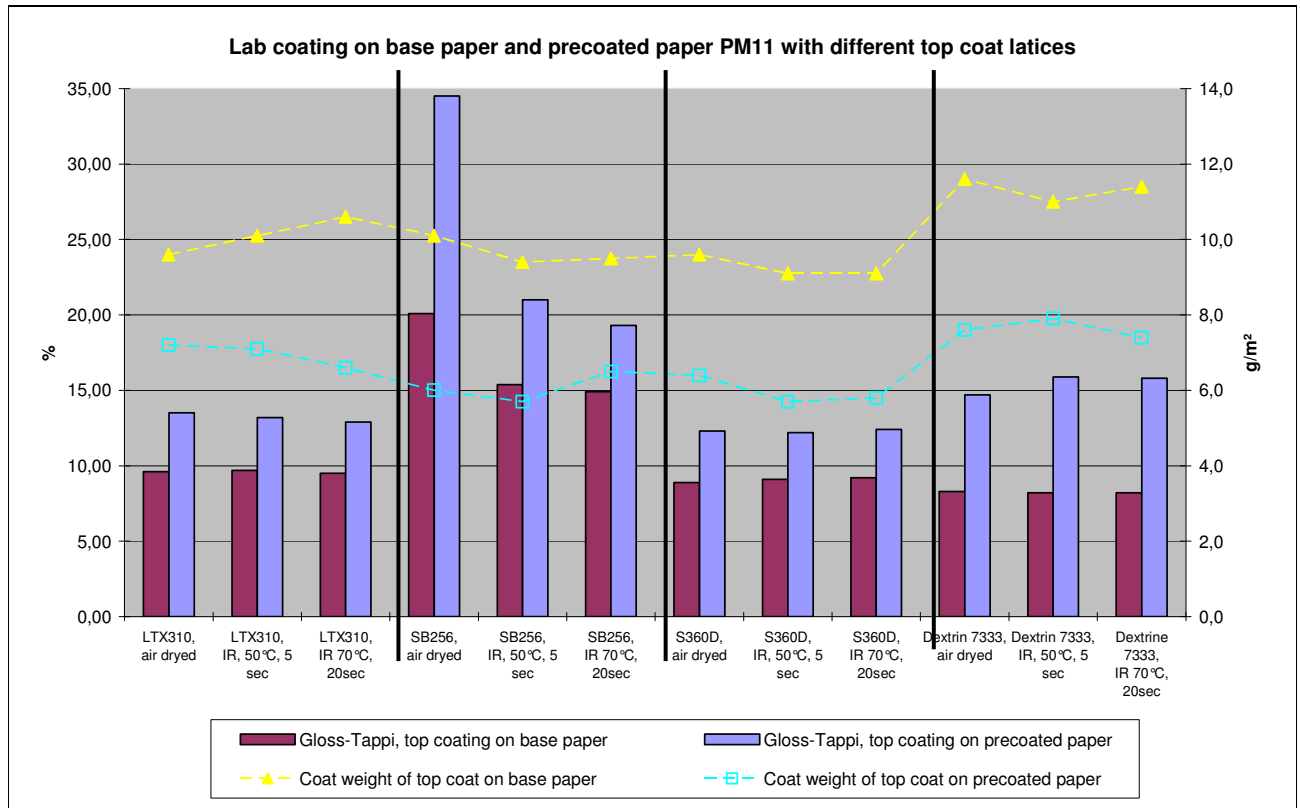
Pict. 11.1.8.5: Gloss Tappi 75°

The uncalendered gloss was higher, when film formation of the latex was poor and shrinkage of coating layer was low during dying. Pigment particles weren't re-orientated and moved to form a rougher surface structure due to shrinkage forces.
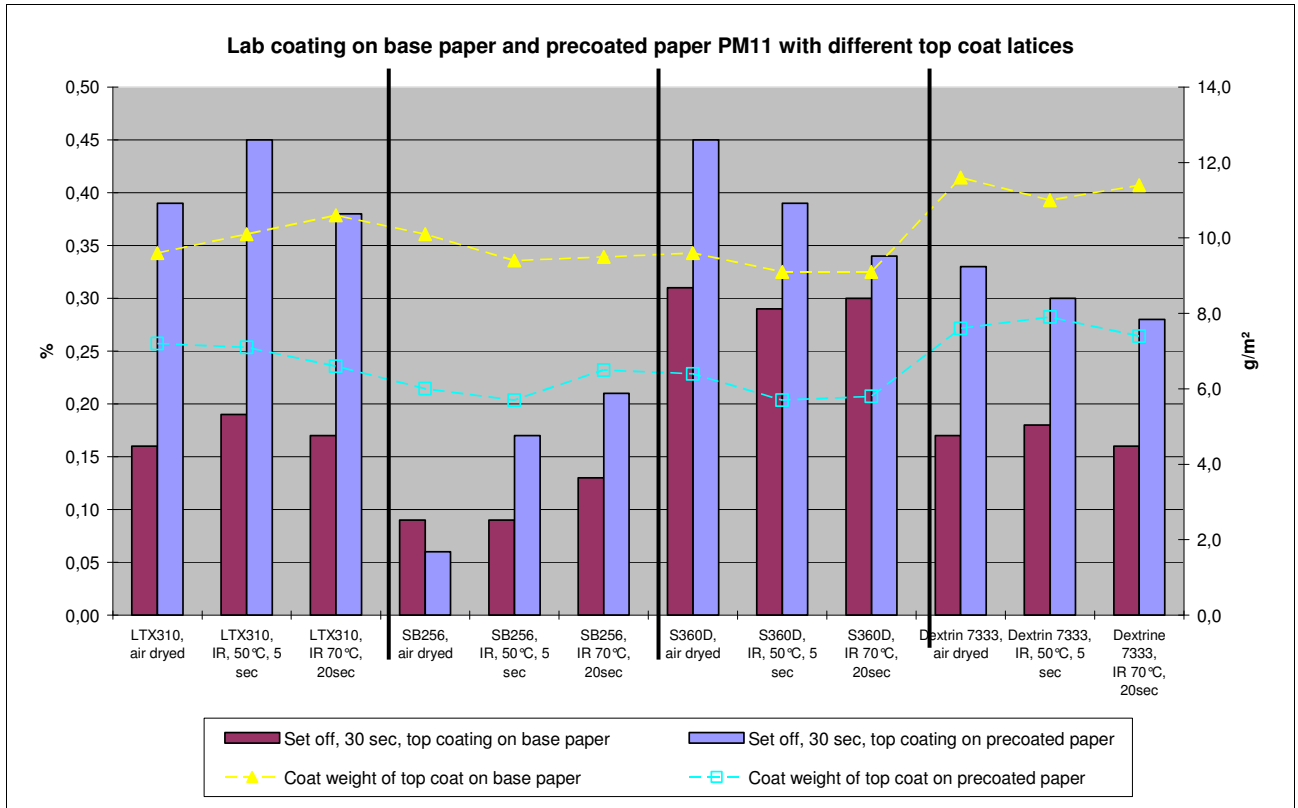
Pict. 11.1.8.6: Set off test

Ink set off improved with lower permeability of the coating layer and lower pore radius. The highly porous SB256 coating was fastest in set off.

Set off got generally slower when the coatings were applied on the dense precoated paper as latex holdout improved.

Conclusions of film forming lab studies for precoatings:

When formation induced mottling must be improved by a dense precoating layer, a SB-latex with high MFFT and Tg (>20°C) cannot be recommended. A much higher drying energy would be needed to get the same degree of film forming and to reach the same coating layer permeability of soft SB-latices.

Coarse latices with mean particle diameter of > 175 nm can also not be recommended as permeability increases with latex diameter. Most of the acrylic latices are higher in particle diameter than latices based on styrene-butadiene and can therefore not be recommended to reduce permeability of precoatings.

Starch is the ideal binder for precoatings with high binder retention, fast film forming, low permeability and high picking resistance.
Drying of starch based coatings has to be moderate in the 2nd and 3rd drying stage as starch molecules can easily migrate with vapour to the surface and starch forms a relatively dense film with low vapour and liquid permeability.
The high stiffness and brittleness of starch is sometimes limiting its use in precoatings. Cracking on the fold gets critical with high amounts of starch in precoatings. To increase the elasticity of starch based coatings the moisture after drying should be as high as possible and humidifiers can be added.

When starch cannot be used in precoatings, SB-latices with low MFFT (Tg = 0°C) and low particle diameter (< 140 nm) should be used. Permeabiltiy can be further reduces when a bimodal latex PSD is achieved by adding additional latex with particle diameter of < 100 nm. Water retention of these latex based precoatings should be maximized by adding water retention additives to reduce latex penetration into the base paper.
Drying should start as fast as possible to avoid capillary transport of water and latex into the substrate.

Conclusions for top coatings:

When coating speed is high, top coat latices should be <u>fast in film forming</u> and <u>high in vapour permeability</u> to avoid local differences in latex migration to the surface in the 2nd drying stage.

Soft SA-latices with Tg = 0°C and starches fulfil the first requirement of fast film forming. SA-latices are generally faster in film forming than SB-latices of same Tg. They consist mainly of linear polymer chains which are easier to film form than the cross-linked macro-molecules of SB-latices.

Film forming of SB/SA-latices improves with falling MFFT. Therefore hard latices with high MFFT/Tg need high initial drying energy to get fast film forming which is generally difficult to achieve at fast coaters.

Latices with high mean particle diameter are high in vapour permeability of dry coating layer but low in picking resistance as specific surface is also lower.

Mill trials at OMC11 show, that when latex film forming is not properly done in the coater, the risk of back trap mottle due to local differences in capillary sorption of ink increases.

Hot calendaring can enhance back trap mottle as latex is softened by web temperature up to 90°C and local pressure differences (due to local thickness / compressibility differences in the coated paper) are transferred into local coating layer porosity differences. At flocs the higher local pressure will lead to more pronounced compaction of the coating layer and to lower permeability of the coating layer.

Once the FCC is reached drying energy should be reduced to avoid non-uniform latex migration to the surface. Especially in convective dryers the surface gets immediately dry and a dense surface layer hinders the water from base paper to evaporate. Water, latex and soluble binders will search for the easiest way to the surface and concentrate locally at these spots. Such surface spots of lower local surface layer permeability will be characterized by low degree of latex film forming.

Mill trials at OMC9 and OMC11 showed that SA-latices like Acronal S360D are less sensitive in drying induced back trap mottle against SB-latices with a comparable MFFT as film forming is much faster.

At flocs, where more water penetrates into the base paper due to higher local pressure, film forming will start earlier as the solid content is higher compared to coatings on top of voids. SA-latices will level out these local differences in solid content due lower temperature sensitivity of film forming.

11.2 Pilot trials to improve drying induced mottling

11.2.1 Pilot trial with OMYA to increasing vapour permeability by replacing GCC with broad PSD by GCC with steep PSD

George Alderfer, Esko Aarni from SMI and Pasi Rajala, John Anderson from Metso (L6-19) compared drying energy demand of PCC based coatings with GCC based coatings at a pilot coater.

	CTC with IR	CTC without IR	CIC with IR	CIC without IR
☐ Fine Broad PSD GCC	2.9	3.4	3.2	2.7
☐ Fine Aragonite PCC	2.7	2.7	2.8	2.0
☐ Fine Prismatic PCC	2.7	2.6	2.7	2.0

* See text about the low energy values.
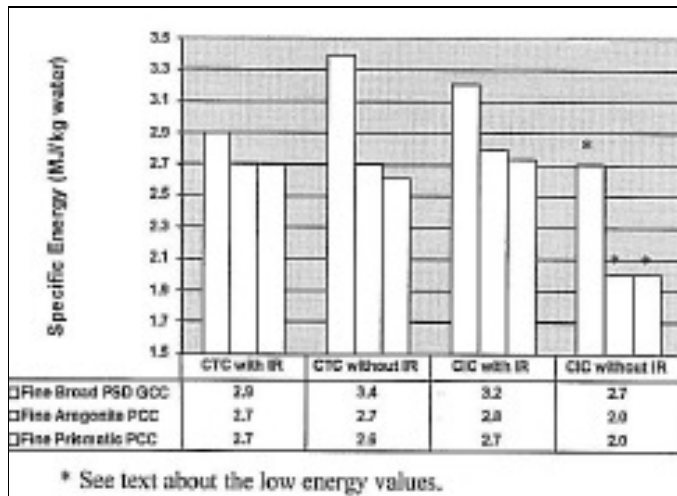
Pict. 11.2.1.1: Drying energy demand for PCC and GCC coatings (trial 1 + 2) (G. Alderfer)

The results indicated a lower drying energy demand for the steep PSD PCC. The difference got bigger, when IR was left out and drying was delayed.

	Fine Broad PSD GCC	Fine Aragonite PCC
☐ 100% Large Broad PSD GCC	4.32	3.16
■ 50% Large Aragonite PCC: 50% Large Broad PSD GCC	3.45	2.99
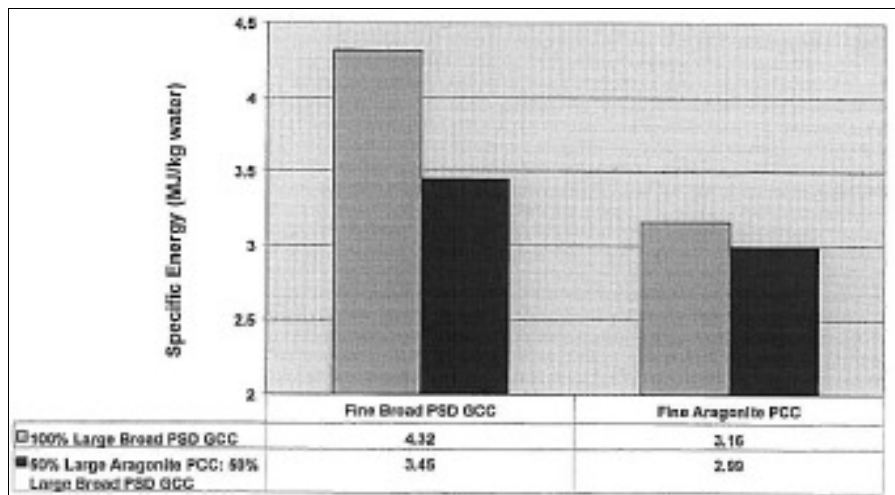
Pict. 11.2.1.2: Specific drying energy for trial 3 + 4 (G. Alderfer)

In the second series of trials drying energy of precoat was 4,38 MJ/kg of water for broad PSD and 3,16 MJ/kg for steep PSD.

According to G. Alderfer coatings based on steep PSD pigments should lower the drying energy demand by 30%.

In the next paragraph the results from a pilot coating trial with OMYA at Vestra pilot coater are shown. The goal was to evaluate the influence of steep PSD Covercarb on drying energy demand and mottling. Covercarb was used in these days in blade top coatings which were applied on single precoated paper from PM11. Due to its steep PSD and high coating layer porosity it was expected to lower the drying energy demand as WddU was expected to be also lower than that of broad PSD carbonates with lower coating layer porosity.

Mottling was evaluated by practical print test in a commercial printing machine. Drying energy demand was calculated for each trial point by comparing the theoretical energy which was necessary for evaporating the removed water with the applied drying energy. The ratio between these two parameters defines the efficiency of applied drying energy.

The amount of evaporated water (m³/s) is the difference between paper moisture at unwinding station and moisture at winding station added by the amount of water applied with coating colour.

Equ. 11-2-1: $X = \dfrac{v * B * BW * x}{100 - x}$

X......Water in paper (kg/s)

v.......Speed of coater (m/s)

B......Width of coater (m)

BW...Basis weight of paper (kg/m²)

x......Moisture of paper (%)

Equ. 11-2-2: $X_{evap} = X_{rewinder} + X_{coating} - X_{winder}$

Equ. 11-2-3: $X_{coating} = \dfrac{v * B * CW * (100 - c_{coating})}{c_{coating}}$

CW…Coat weight bone dry (kg/m²)

$C_{coating}$…Solid content of coating colour

Moisture of the online Measurex sensors at winder and unwinder was controlled in the lab for each trial point and Measurex reading were corrected by these lab measurements.

			0,5		Correction of Measurex::					**0**					
Moisture unwinder (%)	Basis weight unwinder (g/m²)	Moisture unwinder (%)	Moisture unwinder (%)	Moisture winder (%)	Basis weight winder (g/m²)	Moisture winder (%)	Moisture winder (%)	Coat weight Mx, calculated (g/m²)	Coat weight (g/m²)	Moisture winder (%)	Basis weight winder (g/m²)	Moisture unwinder (%)	Basis weight unwinder (g/m²)	Coat weigth (g/m²)
Measurex	Measurex	Lab	Diff. Lab minus Mx	Measurex	Measurex	Lab	Diff. Lab minus Mx	From BW + moisture	Diff. Lab minus Mx	Measurex corrected	Measurex corrected	Measurex corrected	Measurex corrected	Measurex corrected
3,5	99,7	4,03	0,5	4,4	109,0			8,0	-12,1	4,4	109,0	4,0	99,7	8,5
4,0	115,0			4,8	121,5	4,97	0,2	5,3	-11,7	4,8	121,5	4,5	115,0	5,9

Pict. 11.2.1.3: Correction of Measurex online basis weight and moisture measurements by lab

Theoretical drying energy (kJ/s) is the product of removed water and evaporation enthalpy of water (2250 kJ/kg).

$G_{evap} = X_{evap} * h_{water}$

The applied drying energy in the pilot plant was calculated by adding the applied energy in IR-section to applied energy in airfoil section. Gas consumption (m³/s) was measured at each IR-block and at every airfoil. By multiplying it with the spec. energy content in methane gas (35828 kJ/Nm³) and adding the electrical energy for ventilation at IR's and airfoils the total energy consumption was determined.

Vestra 4 - KW18_02

Energieinhalt Gas (kJ/Nm³): 35828
Corrected $p_{norm} * Q_{norm} = p_{meas} * Q_{meas} \to Q_{norm}$ [Nm³]: 4,19 with p_{meas} = 4,2 ba

Vestra Trial Nr.	IR1-4 %	IR 5-12 %	IR13-20 %	IR21-28 %	AF1 Temp - air speed	AF2 Temp - Air speed	AF3 Temp - Air speed	Gas consumption IR-Block 2 (m³/s)	Gas consumption IR-Block 1,3,4 (m³/s)	Gas consumption Airfoil 1 (m³/s)	Gas consumption Airfoil 2 (m³/s)	Gas consumption Airfoil 3 (m³/s)	Sum gas consumption IR (m³/s)	Sum gas consumption AF (m³/s)	Sum gas consumption IR+AF (m³/s)	Energy in gas of IR + AF (kW) based on m³/s gas	Energy in gas of IR + AF (kW) based on Nm³/s gas
1 OS	4/90	8/90	7/90	0	130/8	130/8	130/8	0,0095	0,0141	0,0016	0,0003	0,0018	0,0236	0,0037	0,0273	978,1	233,4
1 US	4/90	8/90	7/90	0	130/8	140/8	135/8	0,0094	0,0141	0,0014	0,002	0,0018	0,0235	0,0052	0,0287	1028,3	245,4

Pict. 11.2.1.4: Energy input from IR and airfoils

spezifische Wärme von Wasser: 4,19   kJ/kg K

T_{min}	T_{max}	ΔT	Energy for heat up (kJ/s)	Geschw. m/min	Water in paper at unwinder (kg/h)	Water in coating (kg/h)	Water in paper at winder (kg/h)	Evaporated water (kg/h)	Net evaporation energy (kW=kJ/s)	Net heating energy (kJ/s)	Net heating + evaporation energy (kJ/s)	Real energy IR+AF (kW)	Energy efficiency of IR+AF incl. heating (%)	Energy efficiency of IR+AF excl. heating (%)
20	79	59	0,0	1200	164,5	177,1	198,7	143,0	89,4	23,5	112,8	233	48,3%	38,3%
31	77	46	0,0	1200	214,6	124,5	240,5	98,6	61,7	18,2	79,8	245	32,5%	25,1%

Pict. 11.2.1.5: Calculation of energy efficiency in IR and airfoil drying section by comparing the consumed energy in gas with theoretical energy demand for evaporation

Trial Nr.	Pigment	Main binder	Minor binder	Solids	Drying curve	Screen Mottle	Backtrap Mottle solid area	Total efficiency of evaporation (%)	Evaporated water (kg/h)	Total energy input by IR+AF (kW)
D1	Setacarb	Hard SB	Acrylate	66	B	2,38	2,25	31,7%	120,8	1003
D5	Setacarb	Hard SB	Acrylate	68,5	B	2,50	2,38	30,2%	84,9	734
D9	CC75+Set	Acrylate	Soft SB	66	B	2,13	1,50	25,3%	96,5	998
D10	HG40	Hard SB	Acrylate	66	B	2,13	1,88	31,6%	104,6	867
D14	CC75	Acrylate	Hard SB	66	B	2,25	1,75	31,1%	98,4	826

Pict. 11.2.1.6: Vestra – OMYA pilot trial: Pigment comparison

Drying energy demand didn't drop when fine Setacarb or HG40 was replaced by steep Covercarb 75 as efficiency of used drying energy didn't improve. Obviously the positive effect of increasing the coating layer vapour permeability and the negative effect of lower coating water retention are balancing each other when Covercarb coatings are applied on single precoated paper.

Back trap mottling was significantly improved by steep carbonate due to lower immobilization solids for steep carbonates (see chapter "water retention") which leads to faster built up of a filter cake layer at the boundary between wet coating and base hindering latex from coating colour to penetrate with liquid phase.

Mill trials at OMC9 and OMC11 where Covercarb was used instead of broad GCC in pre- and middle coatings proved the result from the Vestra pilot trial: Energy demand of Covercarb based coatings was similar to standard GCC based coatings when solids of coatings were comparable. Most often the solid content of Covercarb based

coatings is lower as steep pigments are lower in slurry solids. In this case higher energy demand was found for CC coatings.

The difference of results from mill and pilot trials to the findings of G. Alderfer can be explained by the difference in end moisture: George Alderfer dried the paper to moisture lower than 3%. Therefore a high amount of water had to be evaporated through the dense dry coating layer in the 2nd drying period where PCC/CC based coatings are higher in vapour permeability.

Mean for TS/BS:	Screen Mottle	Backtrap Mottle solid area	Total efficiency of evaporation (%)	Evaporated water (kg/h)	Total energy input by IR+AF (kW)
D1-74% Setacarb, 2,5% Acrylat, 7% hard SB, 3 IR, 3 AF with 130°, 66%	2,38	2,25	31,7%	120,8	1003
D2-74% Setacarb, 2,5% acrylate, 7% hard SB, 4 IR, without AF, 66% so	2,00	2,13	32,5%	117,2	940
D3-74% Setacarb, 2,5% acrylate, 7% hard SB, 2 IR, 3 AF with 250°, 66%	2,75	2,63	23,9%	83,8	919
D10-74% XG90, 2,5% acrylate, 7,5% hard SB, 3 IR, 3 AF with 130°, 66%	2,13	1,88	31,6%	104,6	867
D11-74% XG90, 2,5% acrylate, 7,5% hard SB, 4 IR, without AF, 66% so	1,88	1,50	37,1%	126,5	899
D12-74% XG90, 2,5% acrylate, 7% hard SB, 2 IR, 3 AF with 250°, 66%	2,50	2,13	27,1%	90,4	872

Pict. 11.2.1.7: Vestra – OMYA pilot trial: Comparison of drying curves

Drying efficiency improved when drying started as fast as possible with high amount of IR-energy right from the start and airfoils were opened (drying curve A). Delaying the evaporation from IR-section to airfoils led to a significant drop in drying efficiency – more energy was needed to evaporate the water which had penetrated the base through the dense dry coating layer at the surface. Drying strategy A was implemented later at OMC9 and OMC11.

Trial Nr.	Pigment	Main binder	Minor binder	Solids	Drying curve	Screen Mottle	Backtrap Mottle solid area	Total efficiency of evaporation (%)	Evaporated water (kg/h)	Total energy input by IR+AF (kW)
D1	Setacarb	Hard SB	Acrylate	66	B	2,38	2,25	31,7%	120,8	1003
D5	Setacarb	Hard SB	Acrylate	68,5	B	2,50	2,38	30,2%	84,9	734
D7	Setacarb	Acrylate	Soft SB	66,0	B	2,38	2,00	29,1%	109,0	966
D8	Setacarb	Soft SB	Acrylate	66,0	B	2,25	2,25	23,2%	78,5	876

Pict. 11.2.1.8: Vestra – OMYA pilot trial: Comparison of latices

When different latices were compared in the top coatings the advantage of acrylic latex Acronal S360D in mottling was clearly visible. Drying energy demand increased (efficiency dropped) when a soft SB-latex was used instead of SA-latex or hard SB-latex. The later two latices were higher in particle diameter and therefore vapour permeability was lower.

Page 732

11.2.2 BASF pilot trial – influence of latex types and drying parameters

In this pilot trial four different latices were compared under different drying conditions.
Top coatings were applied on double precoated paper of PM11/OMC11.
Soft SB and hard SB latex were compared to soft SA and hard SA-latex.
Nine different drying strategies were applied at each latex type among them low
energy input and high energy input caused by different moisture of the double
precoated base.
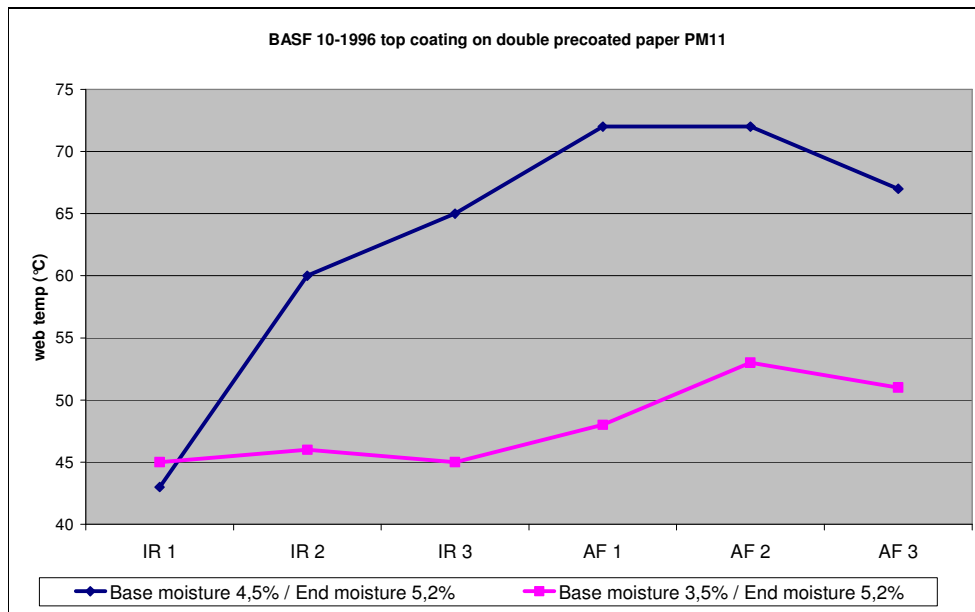
Pict. 11.2.2.1: Drying curves for low and high incoming moisture and constant end
moisture
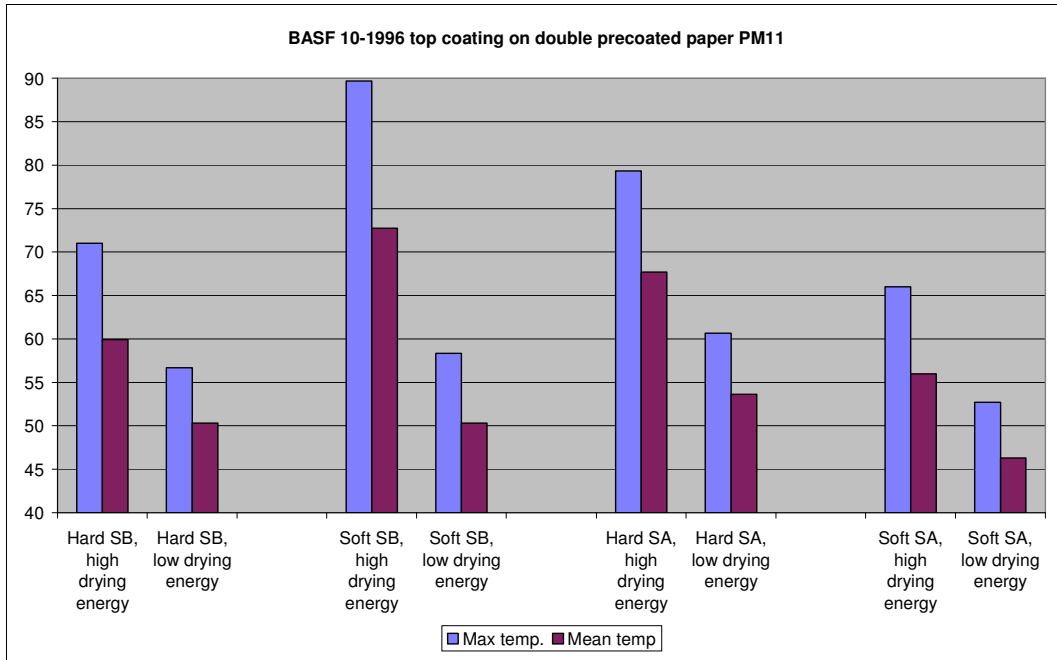
Pict. 11.2.2.2: Max temperature (°C) and average temperature (°C) in drying section

With the lower incoming moisture of 3,5% the level of web temperature in drying section stood well below 60°C for all tested latices. This temperature level was chosen to simulate the described BTM problems at OMC11.
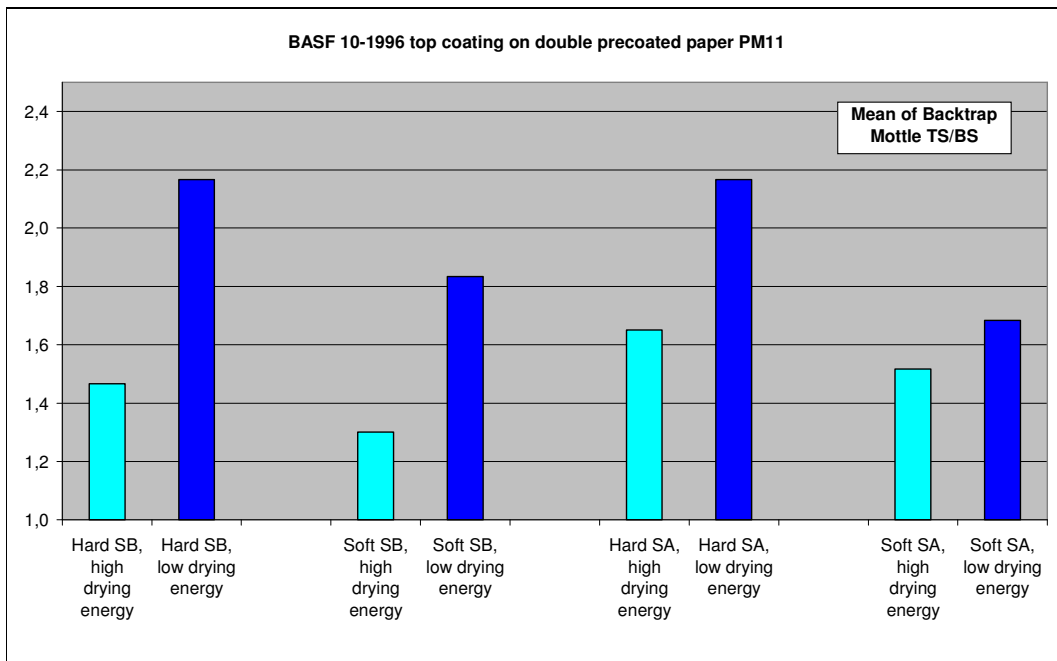
Pict. 11.2.2.3: Back trap mottling of calendared paper (visual: 1 = good, 3 = bad)

The same negative effect of insufficient latex film forming and in consequence back trap mottling was detected in this pilot trial when coatings were dried at low web temperature and soft/hard SB-latex or hard SA-latex was used where film forming is highly dependent on web temperature and time after FCC.

Soft SA-latex (similar to Acronal S360D) was relative insensitive against changing drying conditions as film forming was fastest for all tested latices due to linear polymer chains and low Tg (0°C).

Correlation of BTM with max temperature was more distinctive for the hard latices with high Tg than for the soft latices:
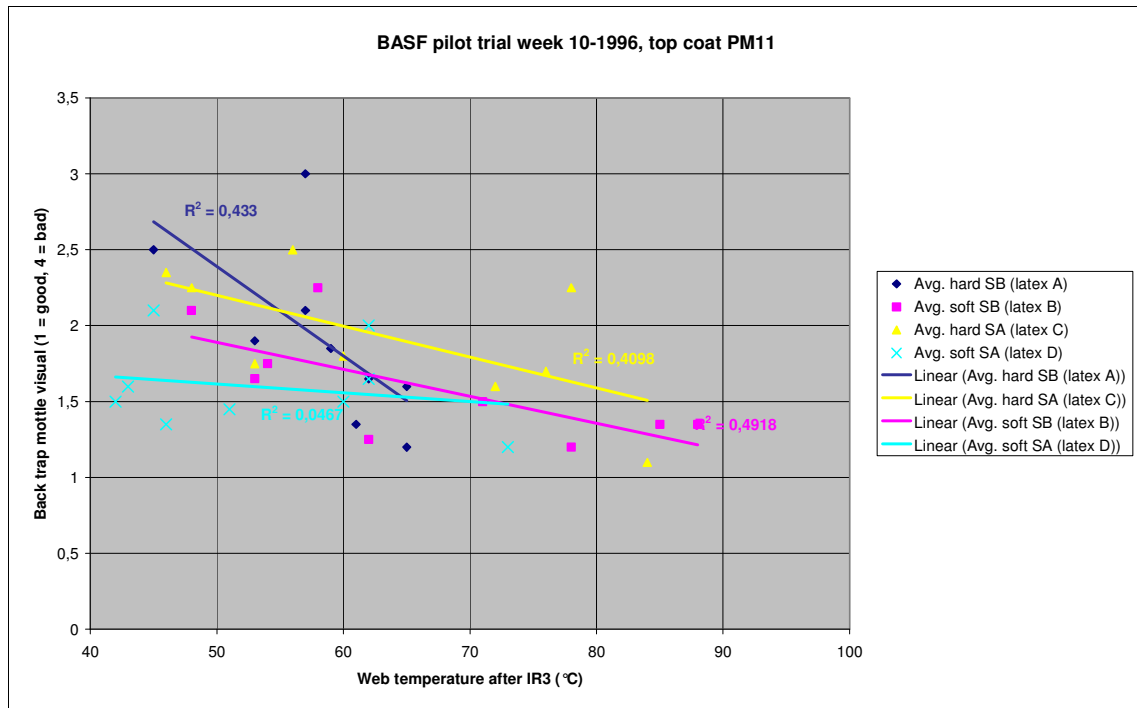
Pict. 11.2.2.4: Correlation of max temperature after IR section with BTM
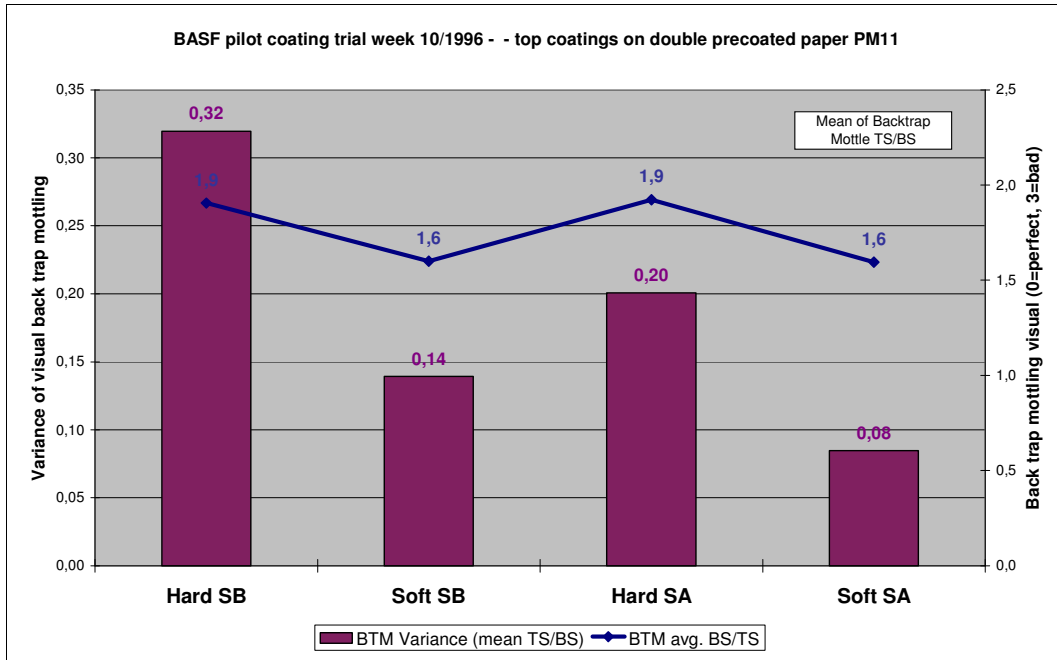
Pict. 11.2.2.5: Back trap mottling and variance of mottling of calendared paper

The dependency of mottling on drying conditions can be also seen in the variance of mottling. The four different latices were separated into classes and variance of mottling was evaluated for each class. The soft latices showed a generally lower mean level of mottling and lower variance of mottling indicating lower dependency of mottling on drying conditions as film forming was less dependent on web temperature variations from the different drying strategies.

Simca software was used to model back trap mottling from drying and quality parameters:
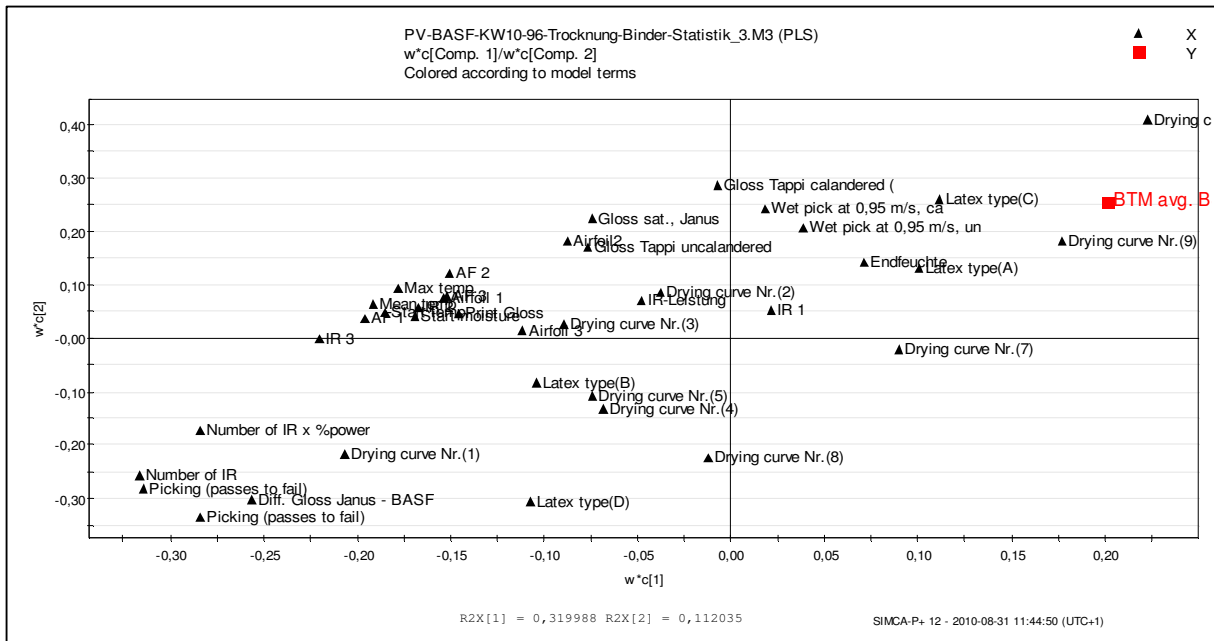
Pict. 11.2.2.6: Variable influence plot on BTM (left + below quarter: Higher = better; right + above quarter: Lower = better)
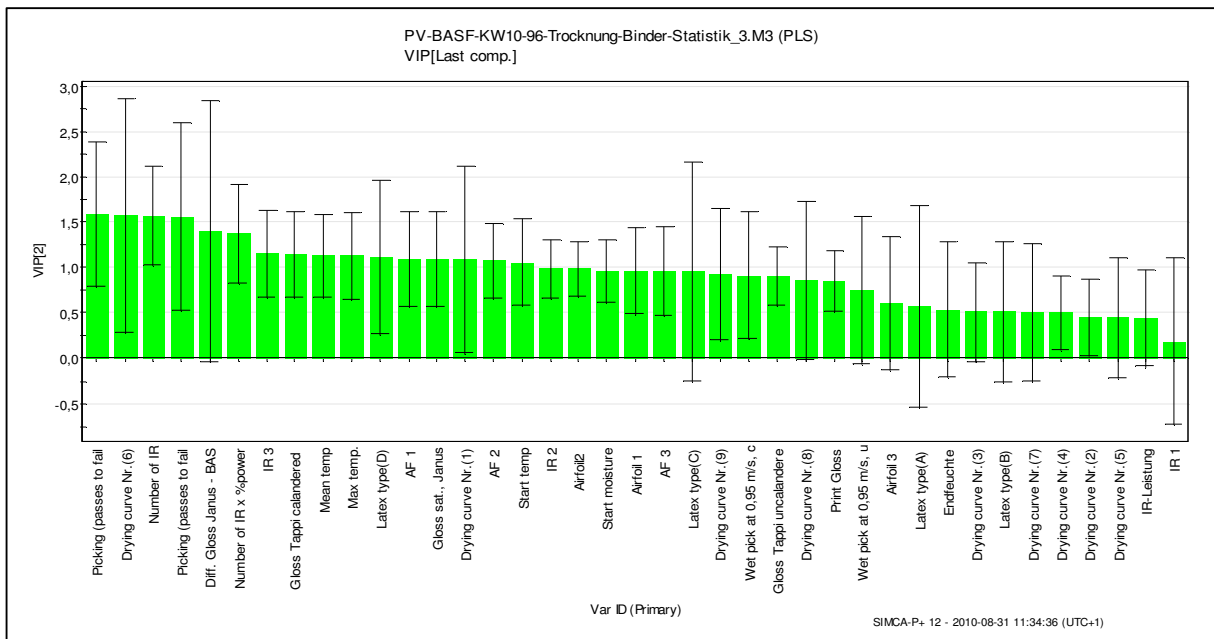
Pict. 11.2.2.7: Variable importance plot of drying parameters and quality measurements on BTM (mean for TS/BS)

Elevated drying temperature in the 1st stage by higher IR energy led to improved mottling. With this drying strategy picking resistance was improved as it correlated well with print mottle (the higher the picking resistance, the better the mottling was).

Page 737

Improved latex film forming led to lower calendared gloss as more time was needed to soften the latex in the calander and allow pigment particles to move.
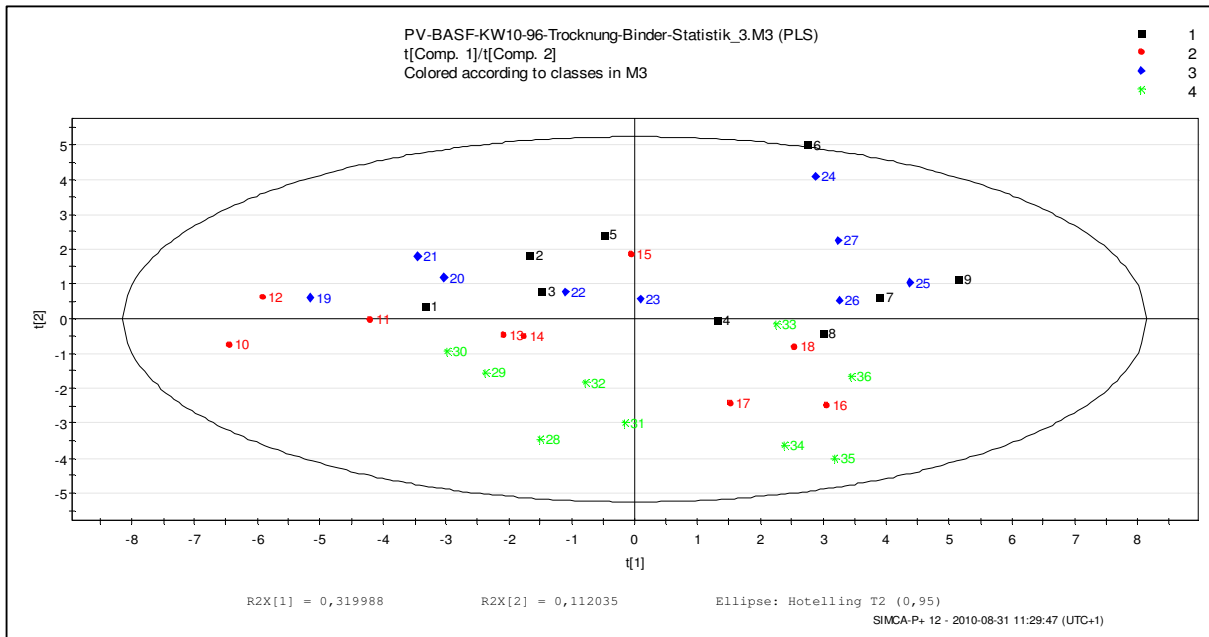
Pict. 11.2.2.8: Properties of 4 latex types (1 = hard SA, 2 = soft SA, 3 = hard SB, 4 = soft SB)

Simca software model can be also used to correlate drying parameters with back trap mottle for separated classes of latex types:
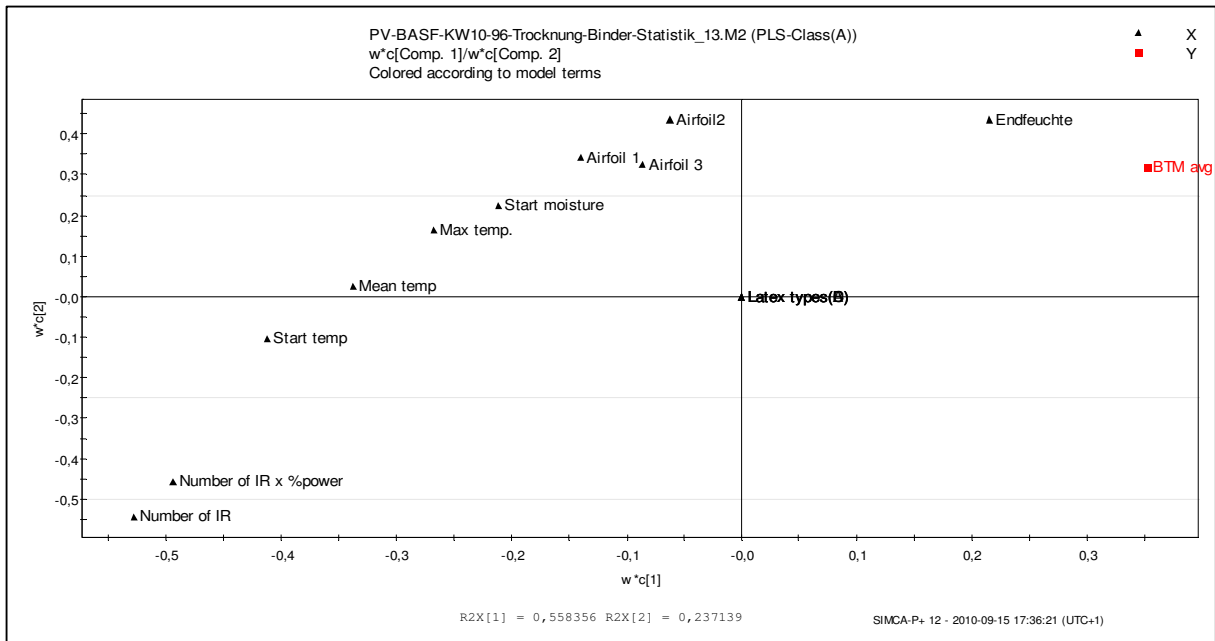
Pict. 11.2.2.9: BTM vs. drying parameters for class of latex A (hard SB)
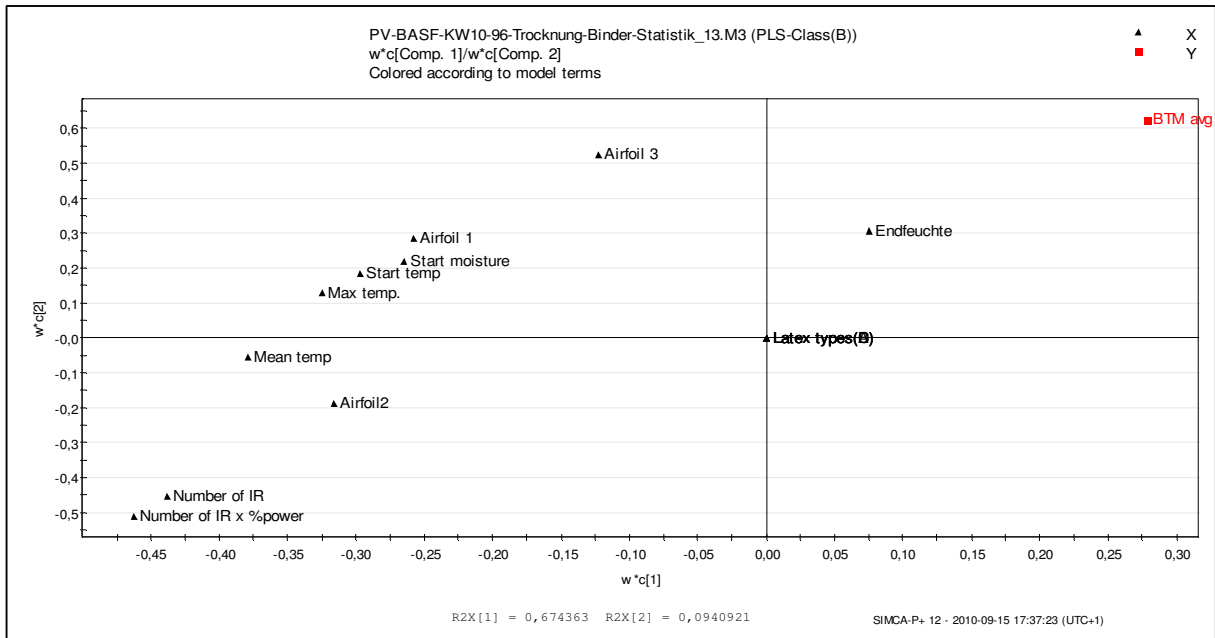
Pict. 11.2.2.10: BTM vs. drying parameters for class of latex B (soft SB)
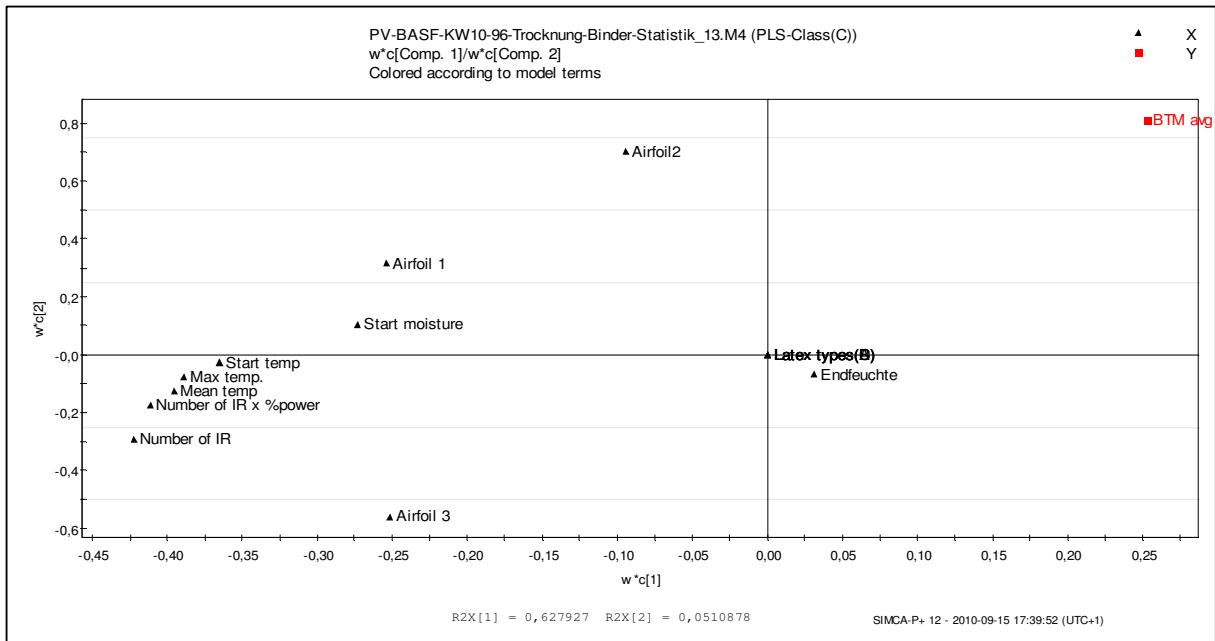
Pict. 11.2.2.11: BTM vs. drying parameters for class of latex C (hard SA)
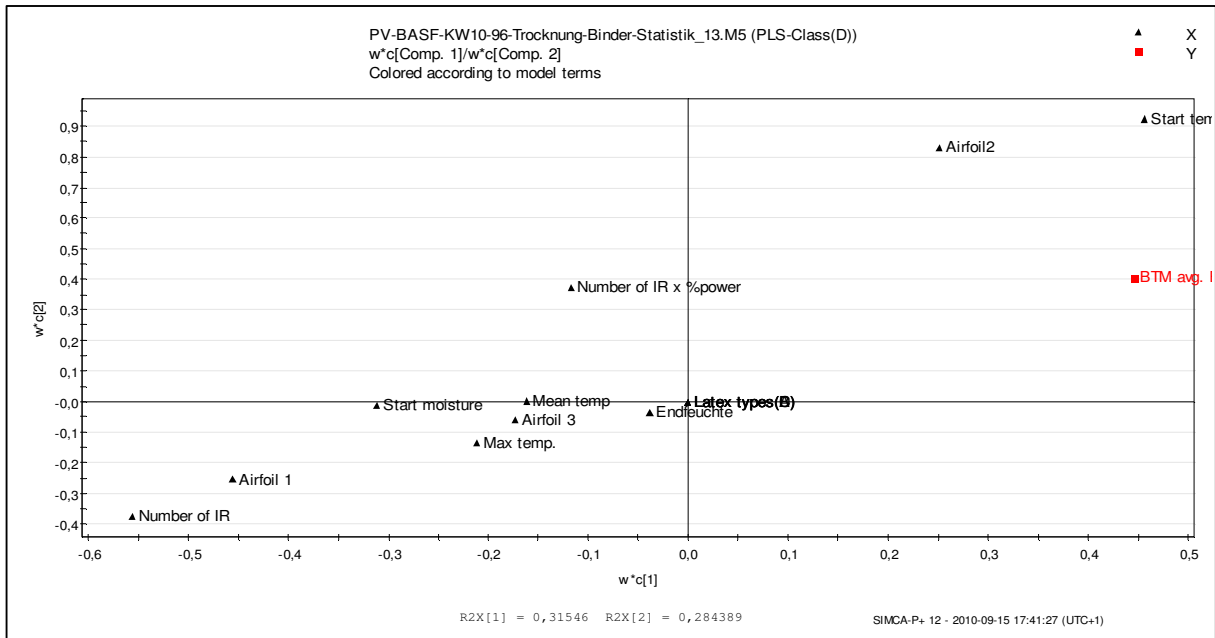
Pict. 11.2.2.12: BTM vs. drying parameters for class of latex D (soft SA)

Back trap mottling of soft SA-latex was relatively independent on drying conditions, which were defined by start/end moisture, number of IR units multiplied with IR-power and airfoil temperature.

Back trap mottling of this latex was also depending to a lower extend on max web temperature in the drying section as film forming was less dependent on web temperature.

No major difference of dependence of mottling on drying parameters was found between soft and hard SB-latex. Mottling was highly dependent on drying parameters for these latices and improved with increasing max temperature and fast initial drying by high IR energy. The same finding was evaluated for hard SA-latex with high MFFT.

The later the latex is film formed, the higher it's mobility in the critical period between FCC and SCC. Latex particles which are film formed are glued together and will no more be able to move with liquid phase to the base or surface. The pilot trial at BASF in week 10-1996 showed that delaying drying by low energy input in the primary IR-section leads to low web temperature at the FCC and high risk of latex migration between FCC and SCC.

The effect of latex film forming on gloss after calendaring in the BASF supercalander was detected in the next part.
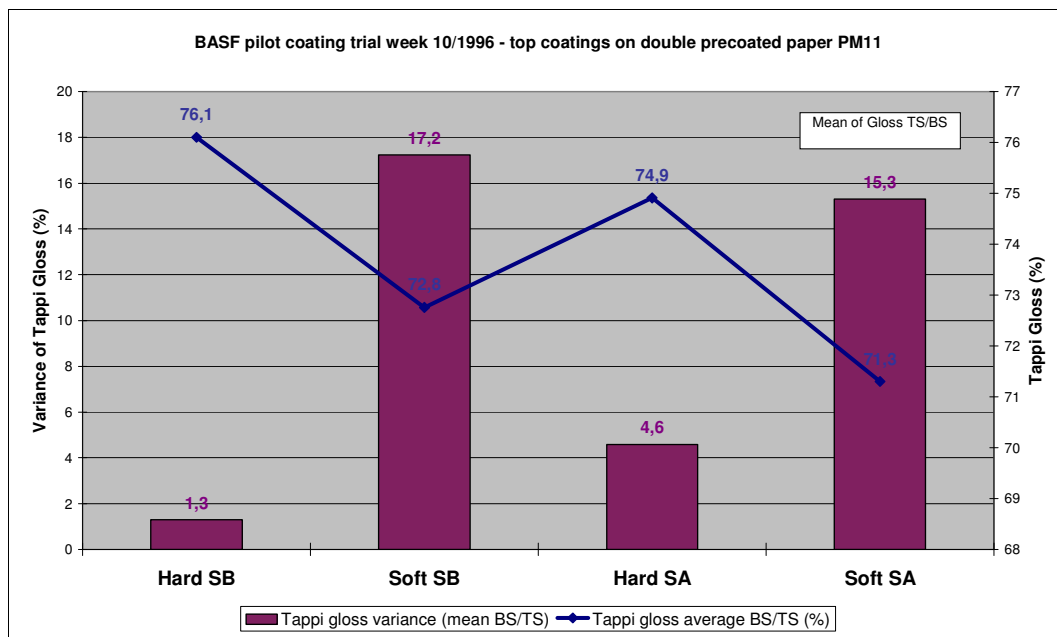
Pict. 11.2.2.13: Tappi gloss and variance of gloss of calendared paper

The calendared Tappi gloss was generally higher for the hard latices as film forming was not complete after the coater and latex softening started earlier in the calander as it needed less heating energy.

Standard deviation of calendared gloss was much higher for the soft latices indicating that gloss was highly depending for these latices on drying conditions and latex film forming at the coater.
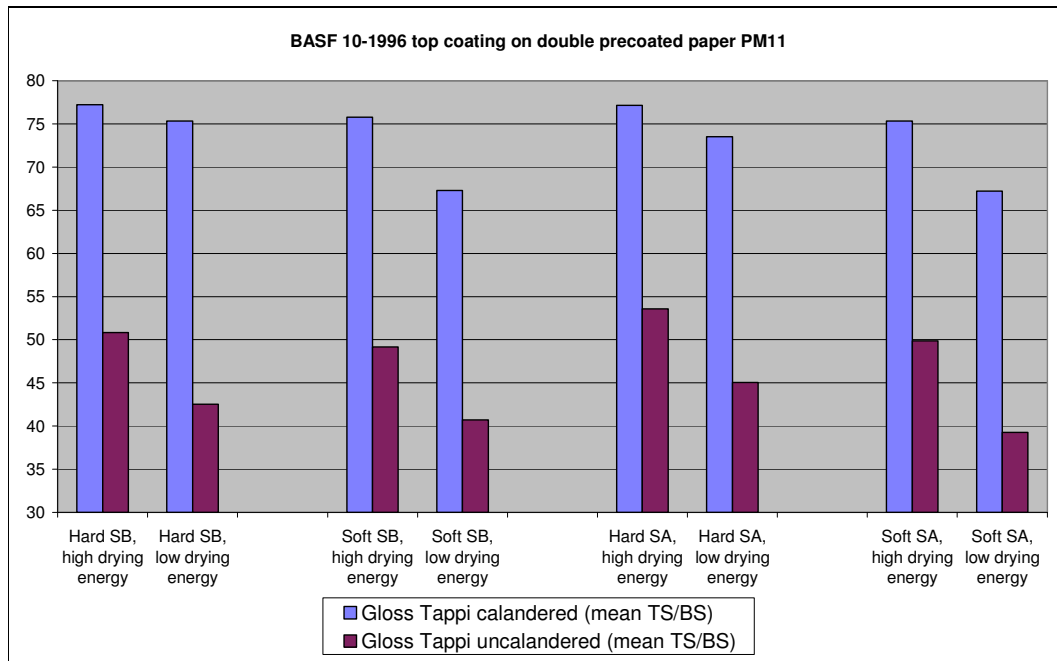
Pict. 11.2.2.14: Tappi gloss 75° (%) of calendared and uncalendered paper

Uncalendered and calendared gloss dropped with falling web temperatures during drying. This was the opposite of what was expected: When latex film forming is insufficient, pigment particles can be easier moved together under heat and external calander pressure.

Low web temperature was linked to low drying rates and in consequence to high capillary sorption of the precoated base. As drying was delayed with lower energy input, more fine pigment (and latex) particles travelled with the liquid front into the precoated base until the FCC was reached. Gloss might have dropped due to lack of fine pigment particles at the surface.
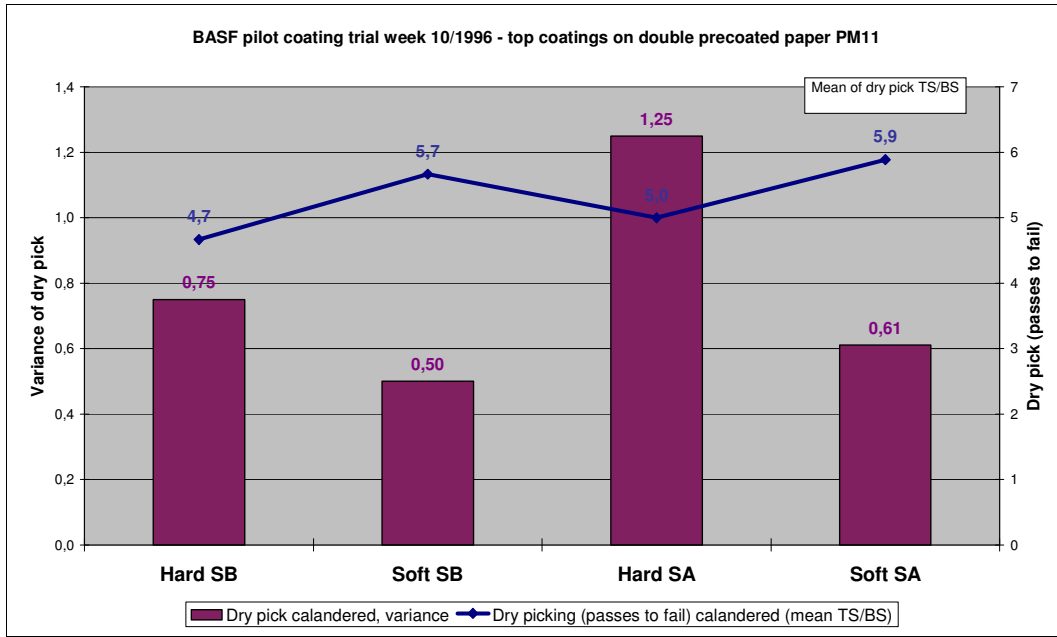
Pict. 11.2.2.15: Dry pick resistance and variance of picking of calendared paper
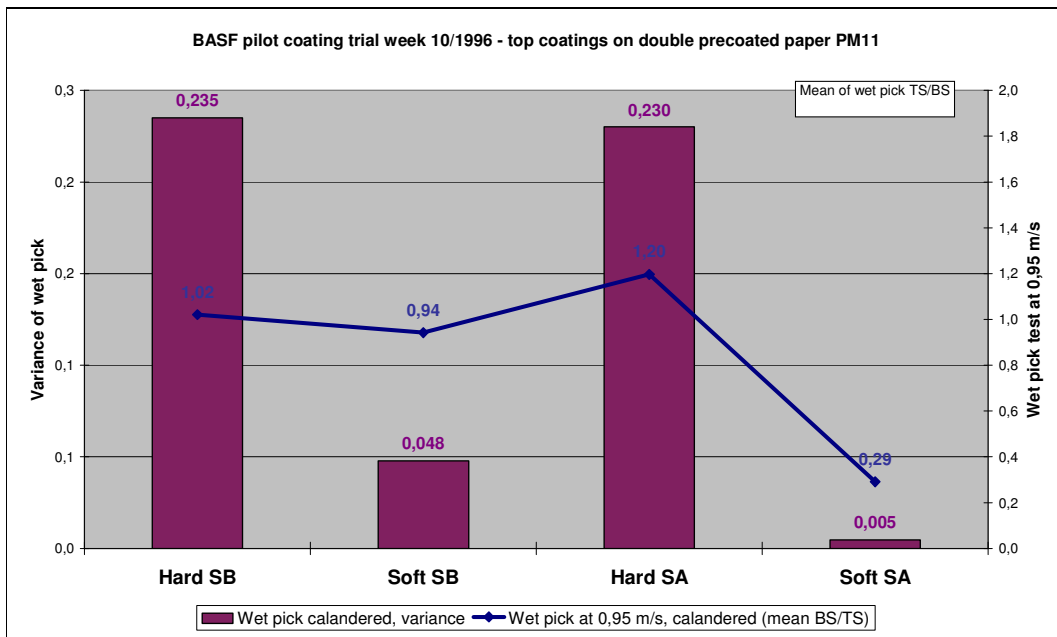
Pict. 11.2.2.16: Wet pick resistance and variance of picking of calendared paper

Dry and wet pick resistance of uncalendered and calendared papers was generally higher for the soft latices as film forming was achieved to a higher extend in the coater. Variance of picking was lower for these latices as their film forming was depending less on drying conditions in the coater.
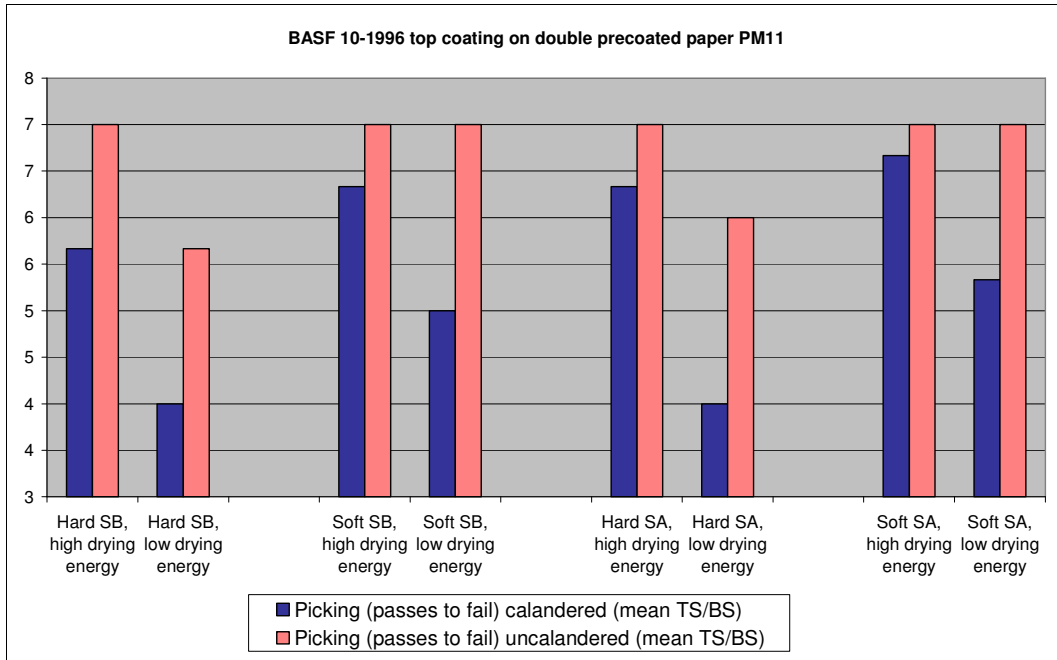
Pict. 11.2.2.17: Dry Picking resistance of calendared and uncalendered paper
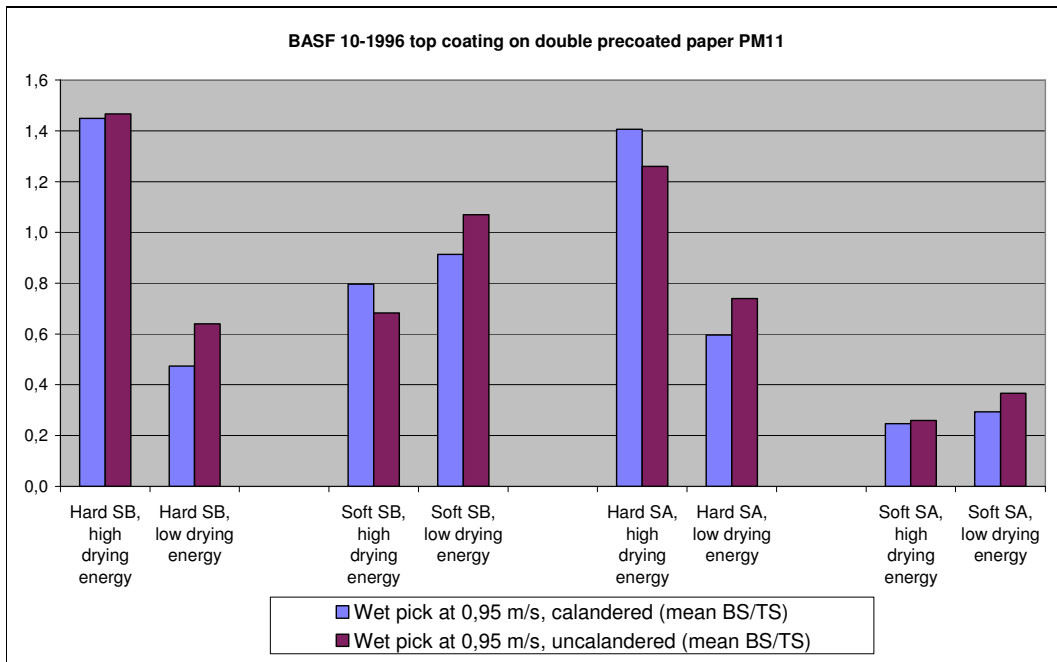
Pict. 11.2.2.18: Wet pick test of calendared and uncalendered paper

Picking resistance was significantly lower for the hard latices when drying energy was low and latex film forming was on low level.

Picking of soft latices was less sensitive against drying conditions as film forming was also less depending on these parameters.

Simca software was used to correlate the major quality parameters of gloss and picking with back trap mottling for separated classes of latex types:
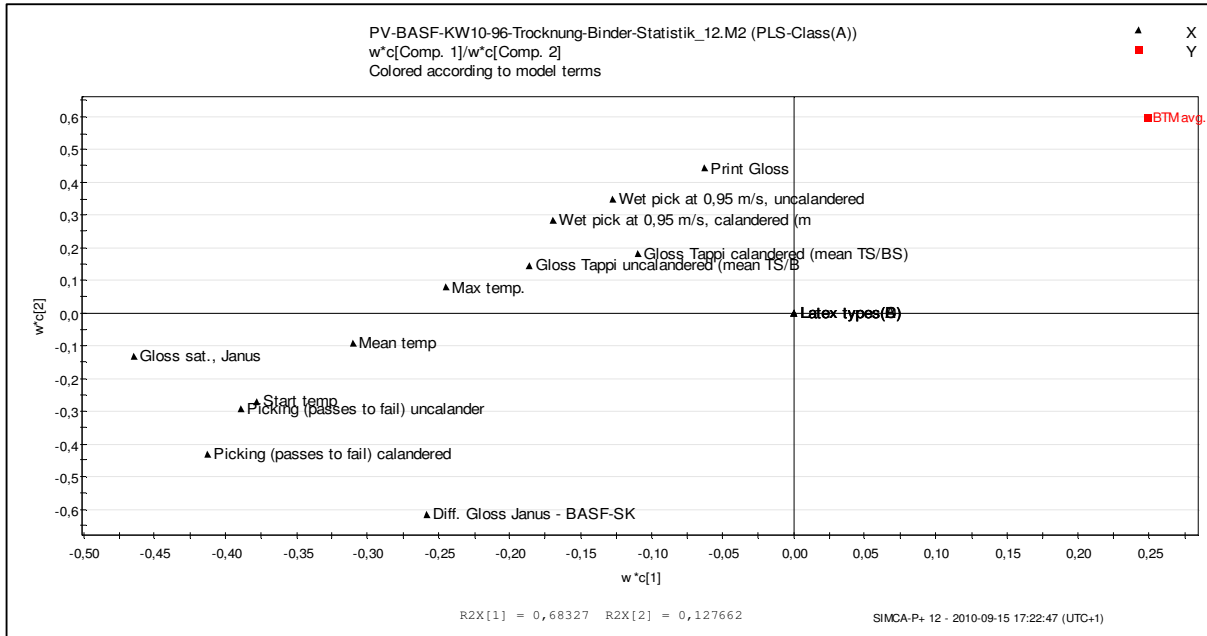
Pict. 11.2.2.19: BTM vs. quality parameters for class of latex A (hard SB)
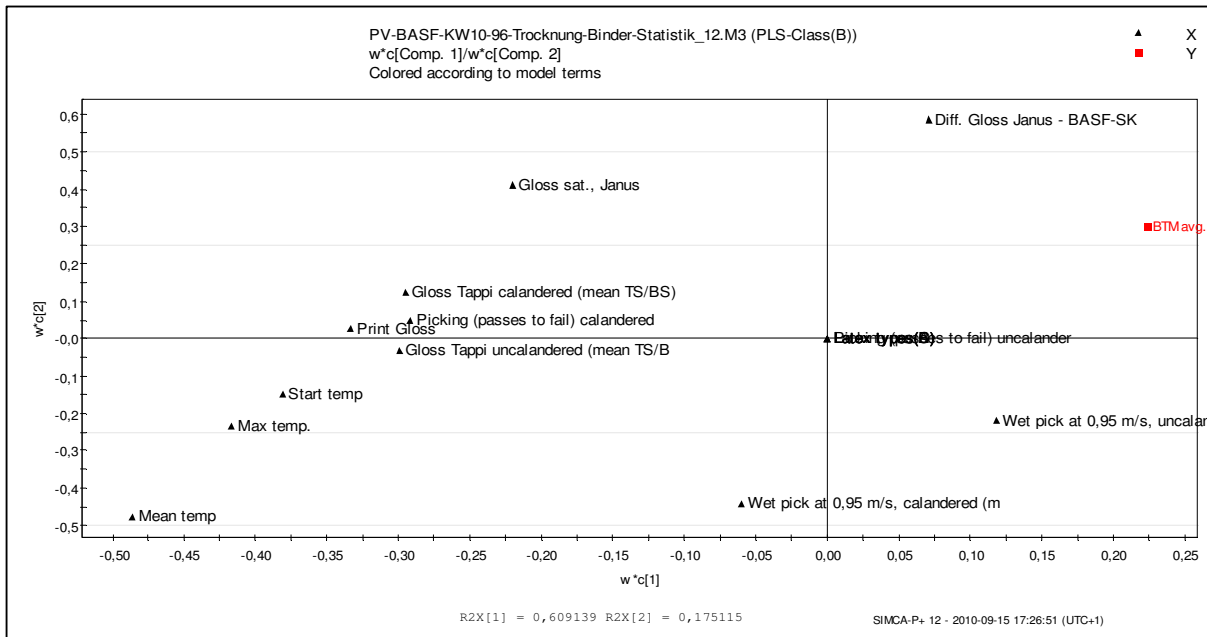
Pict. 11.2.2.20: BTM vs. quality parameters for class of latex B (soft SB)
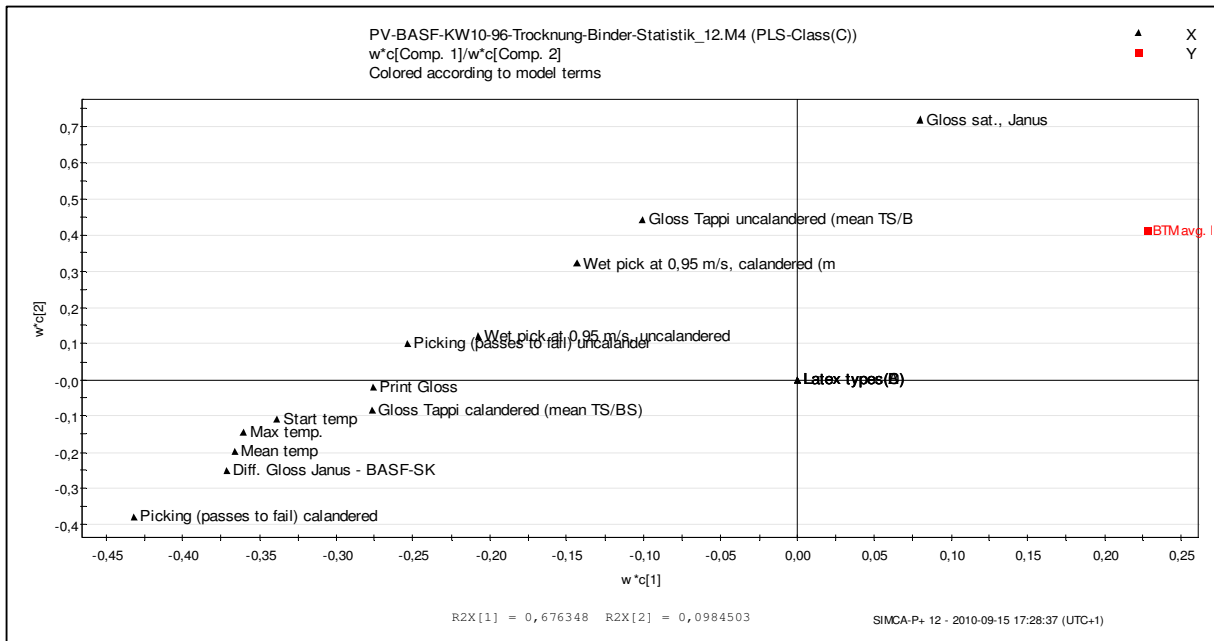
Pict. 11.2.2.21: BTM vs. quality parameters for class of latex C (hard SA)
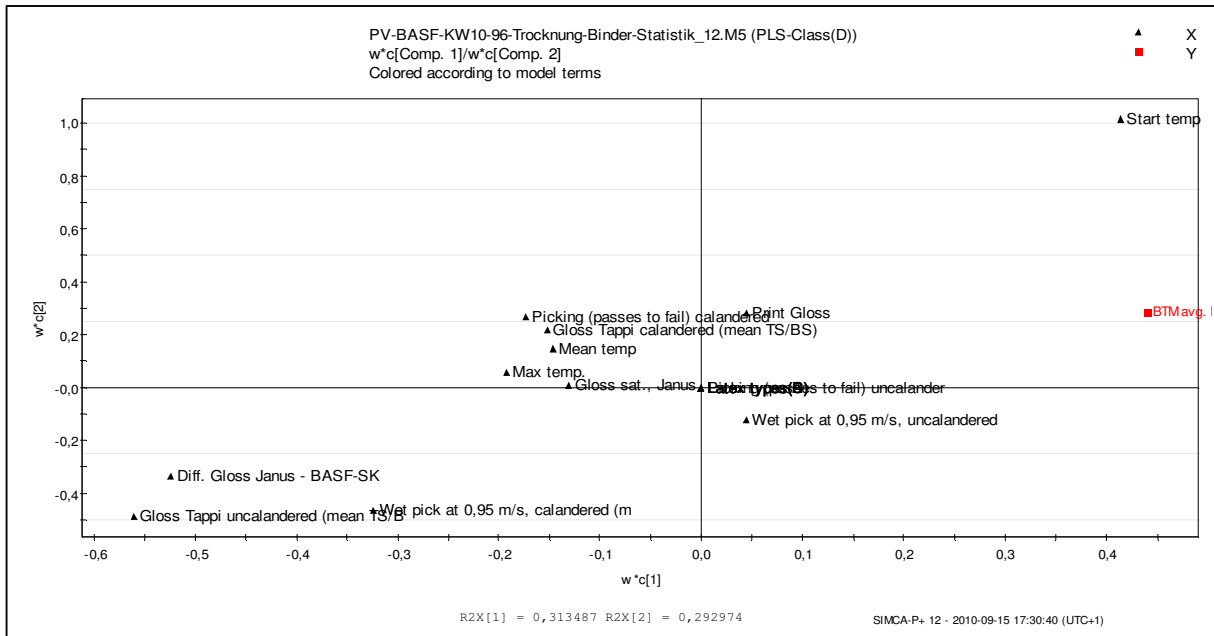
Pict. 11.2.2.22: BTM vs. quality parameters for class of latex D (soft SA)

For the hard latices with high MFFT gloss and picking resistance was depending to a higher extend on back trap mottling than for the soft latices where film forming is much faster.

Influence of drying conditions on pore volume (ml/g)
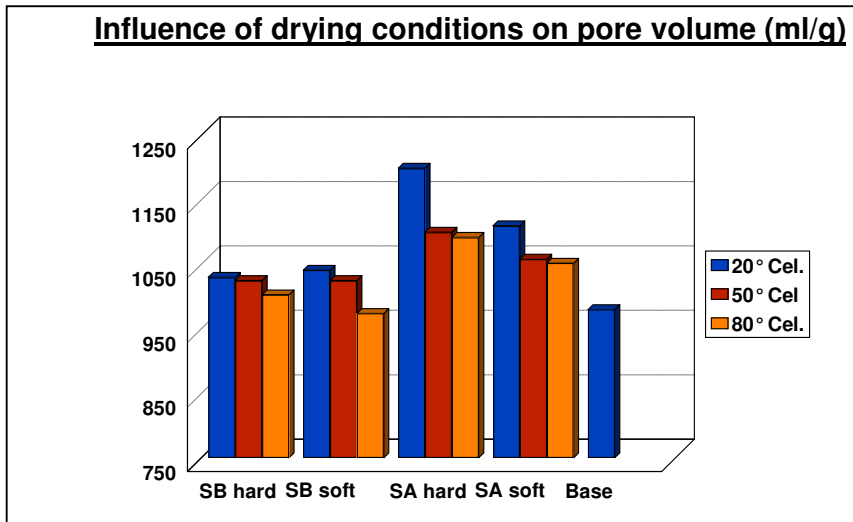
Pict. 11.2.2.23: Mercury porosity of coating (BASF)

Influence of drying conditions on pore radius (nm)
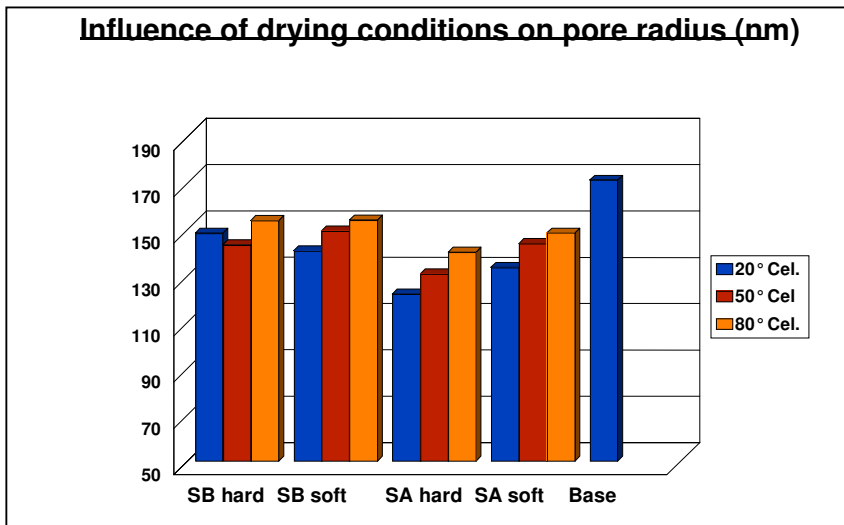
Pict. 11.2.2.24: Pore radius from Mercury porosity of coating (BASF)

Mercury porosity measurements of the coating layer showed that the coarser particles of SA-latices caused higher coating layer porosity. Mean pore radius was lower due to many small pores between latex particles.
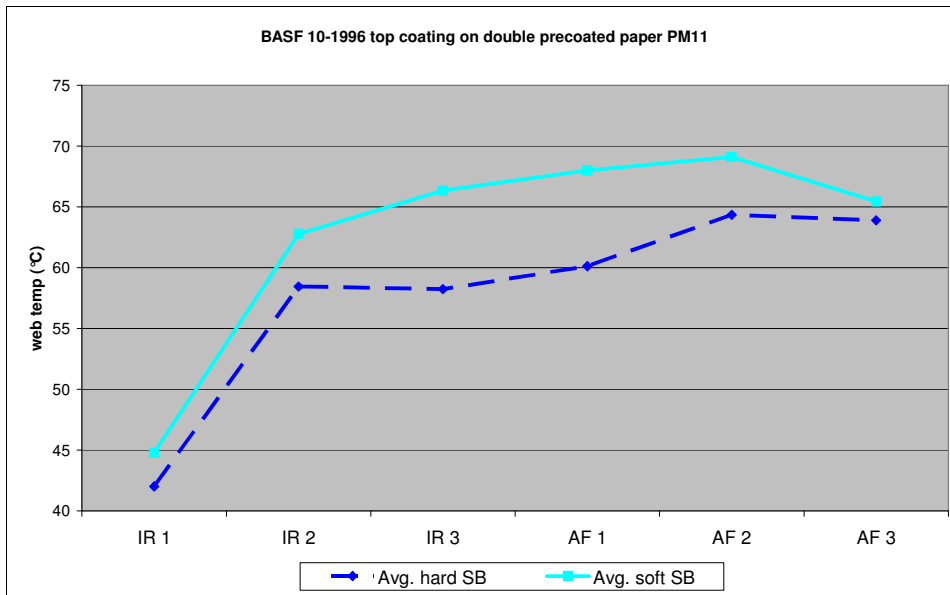
Pict. 11.2.2.25: Web temperature for hard and soft SB (average from 9 different drying strategies)

The pilot trial at BASF confirmed the results of the lab trials in the previous paragraphs: Using a hard SB-latex with bigger particle size and slower film forming properties led to lower drying energy demand and in consequence to lower web temperature during drying than when a fast film forming soft SB –latex was used.

The soft SA-latex demonstrated its insensitiveness against drying conditions in this pilot trial. Therefore it was mainly used for later mottling improvement in all top coatings of OMC11.

11.3 Mill trials with different drying curves at OMC11 to improve back trap mottling

11.3.1 Improving latex film forming by raising drying energy in 1st drying stage

C. Guyton (L6.4) used Raman – Microscopy to detect differences in latex content at the coating surface under spots with local differences in print density (mottling). Raman-Microscopy uses visible light from a laser which is partly reflected, partly absorbed by the tested medium. The reflected light has usually the same frequency of the light as the light source ($v_d = v_0$) according to Rayleigh.
But Raman recognized that a small part is reflected with a different frequency ($v_d \neq v_0$). This part was called the Raman reflection.
In a microscope the laser can be focused on the sample. The measuring spot hat a diameter of 1 μm. Calcium carbonate and styrene have Raman reflection, clay has no peaks.
C. Guyot found a lower latex content at spots with high printing density or in other words deep penetration of ink into the coating layer. Lower latex content leads to higher permeability and lower contact angle. Therefore more ink penetrates at the application print nip by pressure penetration and also by capillary sorption after the application nip.

J. Wayne Dappen (L6.2) studied the separation of starch from clay based coating colours during drying. He recognized that when the coatings were air dried less starch was detected at the coating surface than when oven drying was applied. Starch is relatively small in molecular size compared to latex particles and penetrates therefore faster together with the water phase into the base paper by capillary sorption of fibres. The same finding was detected at OMC11. Middle coaters C3/4 operating with starch containing coatings show always much more pronounced mottling than starch free top coaters. When fine pigments with high amount of free dispersant in the water phase were used, mottling got worse as these low molecular weight substances migrate easily with vapour to the surface during drying.

The findings of this study to improve drying induced mottling were implemented at OMC11 to improve mottling which had significantly suffered in 2002 when speed was increased.

A new faster film forming latex type was chosen and drying energy at top coaters of OMC11 was raised by increasing the incoming moisture before the top coaters. Web temperature in the IR drying section of the top coater had to be increased to a minimum threshold of 75°C to remove drying induced back trap mottling.
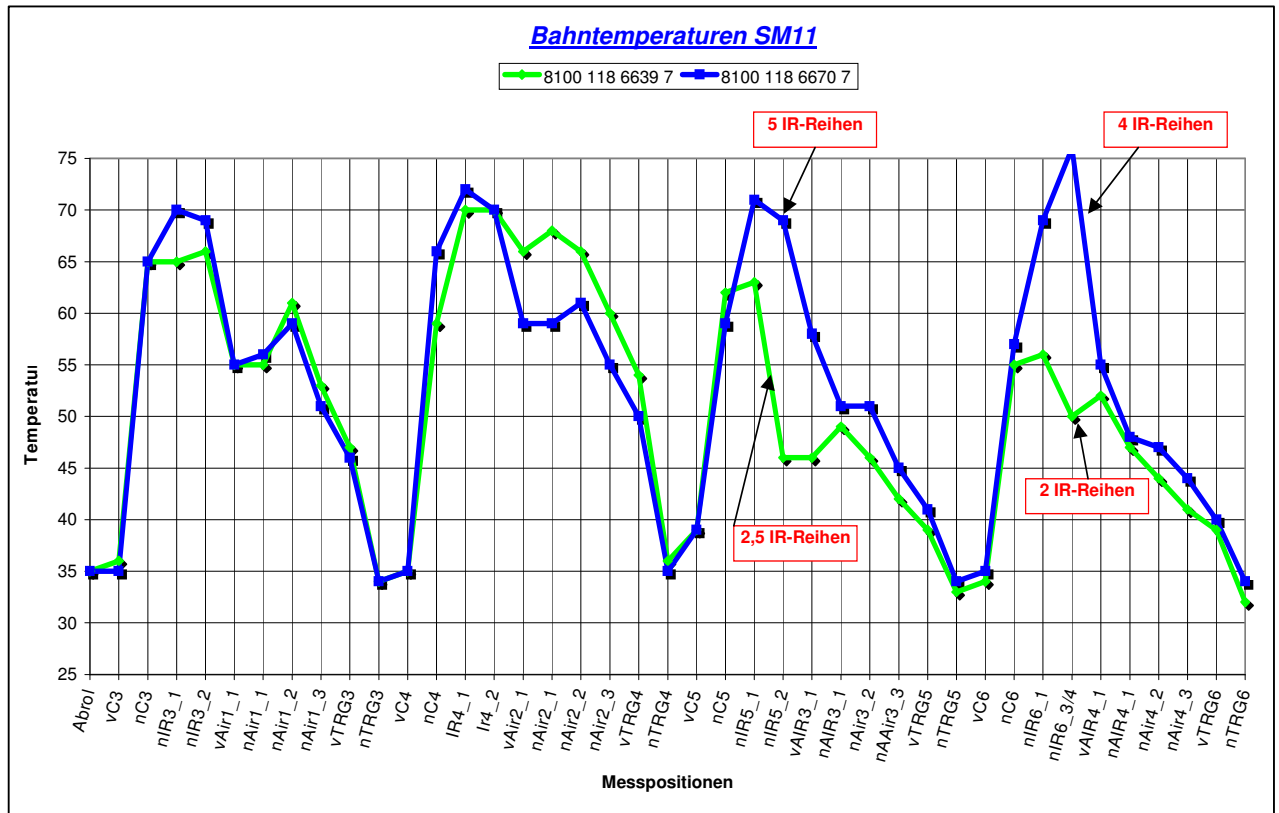
Pict. 11.3.1.1: Web temperature before and after optimization of mottling (115 g/m²)
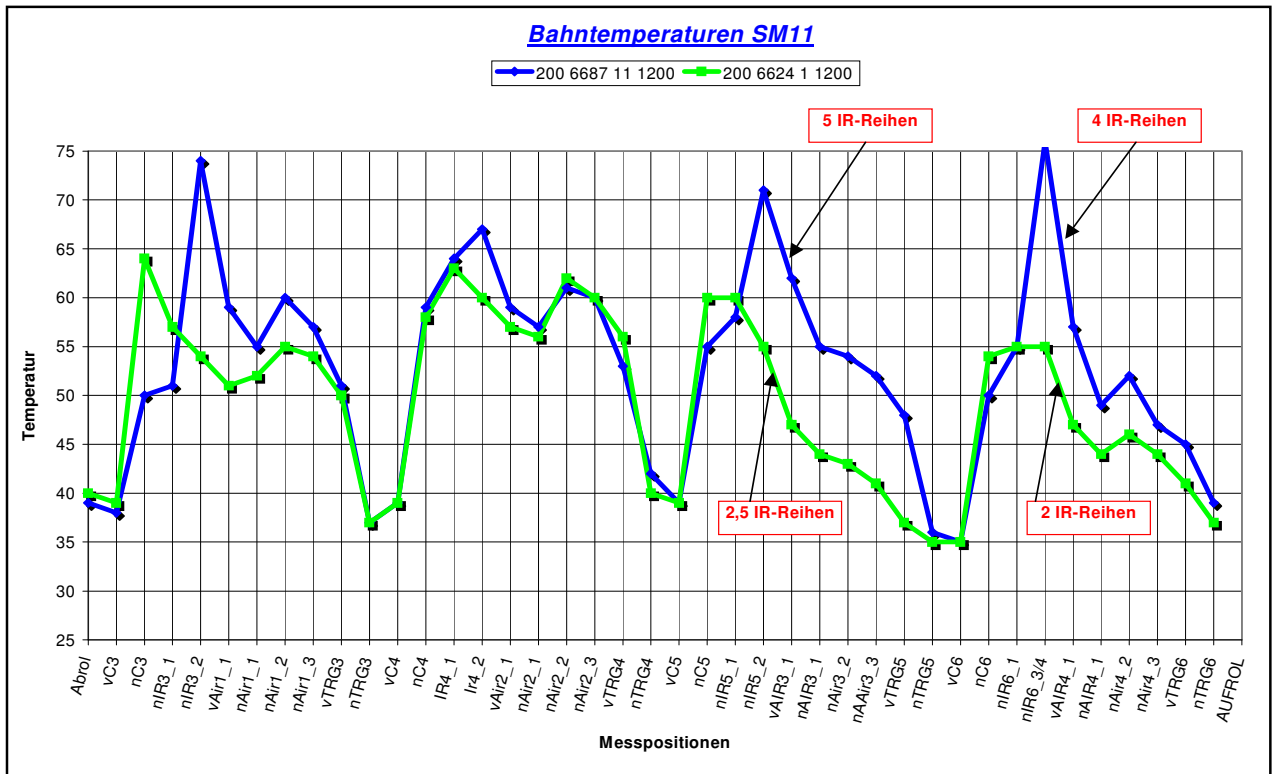
Pict. 11.3.1.2: Web temperature before and after optimization of mottling (200 g/m²)

The relatively flat drying curves with constant web temperature over the whole drying section was changed to a drying curve with fast increase in web temperature by high IR-energy input followed by a period with open airfoils and no external heating.

Many authors in literature came to the same conclusion that this kind of drying curve is the optimal way of drying coatings (see chapter "blade coating"). As surface porosity drops at FCC, drying rate has to be reduced in the same way to avoid local differences in binder migration with vapour to the surface. Especially for coatings with low porosity this is a very important strategy. High amounts of starch in middle coaters of OMC11 were very sensitive for drying mottling and evaporation had to be reduced after the IR section.
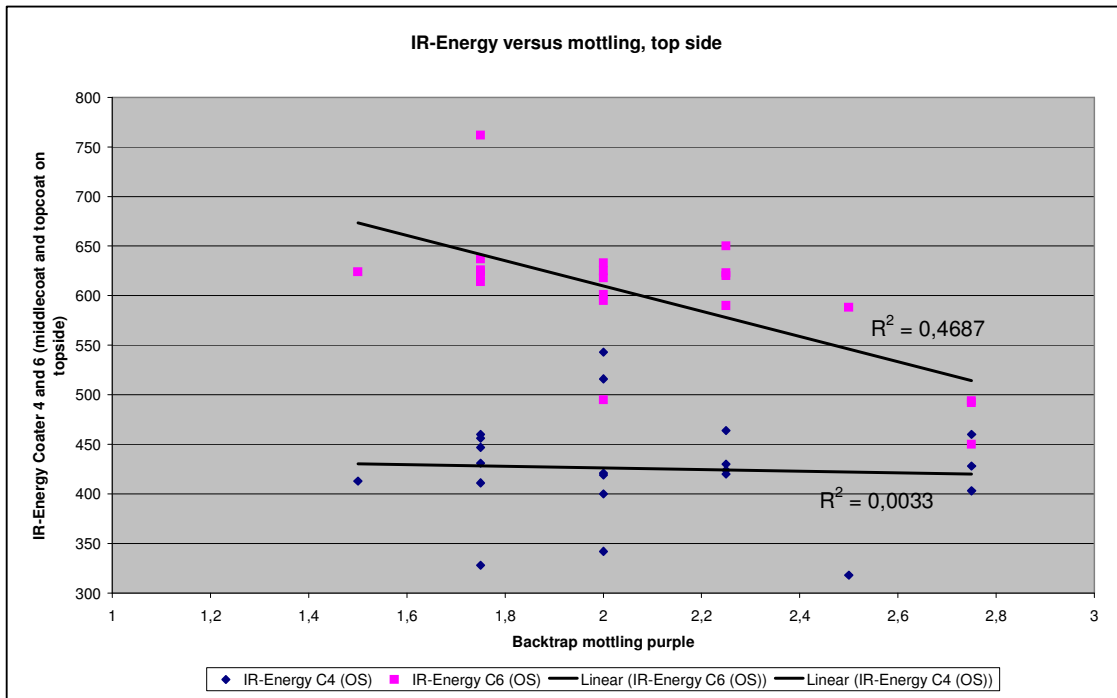
Pict. 11.3.1.3: Reducing BTM by raising IR energy (1st drying stage) at top coated C6. Comparison: middle coater C4

Calculation of drying speed by forced convection at infrared and airfoil dryers in the 1st drying stage:

During the **1st drying period** the surface is covered with water. When water is evaporated at the surface it is replaced by water from inside the paper. As long as transport of water to the surface is as fast or faster than evaporation rate at the surface the surface remains wet and the 1st drying stage is continued.

When not enough water can be supplied from inside the paper, the 1st critical moisture $X_{cr,I}$, in coating practice called the first critical moisture (FCC), is reached. Until that point drying is depending only on air properties (temperature, moisture, velocity) and on surface temperature of coating. The properties of the coating layer are irrelevant.

Drying speed (Equ. 11-1-1) in the 1st stage can be simplified by the equation:

$$m = \beta * \rho * (X_p - X_a)$$

m….specific drying speed [kg/(m² s)]

β….mass transfer coefficient [m/s]

Page 752

ρ....density of wet air at t [kg/m³]

X_p...water at surface of paper [kg/kg]

X_a...water vapour in air boundary [kg/kg]

In the mass transfer coefficient β the flow conditions in the boundary layer are integrated. It can be calculated from dimensionless characteristic numbers.

$X_p – X_a$ stands for the driving force of the drying process in the 1st stage.

X_p is the result of the equilibrium vapour pressure $p_{d,p}$ of the water at the surface of the coating:

$X_p = M_{H20}/M_{air} * (p_{d,p}/(P – p_{d,p}))$

X_a is taken from Mollier diagram for a given air temperature and air moisture.

At the boundary of the coated surface to the air convective drying will take place. The boundary will change its thickness δ with the coordinate x (length L in MD). Two kinds of boundary layers are defined: In the flow boundary the velocity is reduced to zero until the wall surface is reached (unstable flow velocity). In the thermal boundary the local temperature increases or drops until the temperature of the wall is reached.
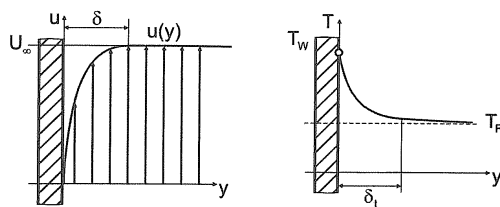
Pict. 11.3.1.4: Boundary layer of flow and temperature
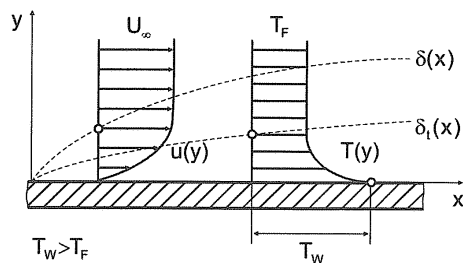
Pict. 11.3.1.5: Development of flow and heat exchange boundary layer with length

In air-dryers and infrared-dryers **forced convection** is taking place as ventilators blow hot air on the paper surface.

In the open draws between the drying elements evaporation of water occurs by **free convection** with no external energy source.

Heat flux:

Equ. 11-3-1-1: $\dot{q} = \dfrac{d\dot{Q}}{dA} = -\lambda * \dfrac{dT}{dh}$

q….Density of heat flux through area A

λ….Specific heat conductivity of material

h….Thickness of material where heat is transferred

Heat transfer by radiation – Stefan Boltzmann law:

Equ. 11-3-1-2: $\dot{E} = \varepsilon * \sigma * T^4$

ε….Coefficient describing the emission of the material (black radiators with ε = 1 have T_s of 5777 K)

σ….Stefan Boltzmann constant 5,67 * 10^{-8} W m^{-2} K^{-4}

Heat transfer general:

$\dot{Q} = \alpha * A * \Delta T$ with α the heat transfer coefficient and A the area of heat transfer

Combining with $\dot{q} = \dfrac{d\dot{Q}}{dA} = -\lambda * \dfrac{dT}{dh}$ leads to:

$\dfrac{\alpha * L}{\lambda} = -\dfrac{(dT / dh)_{contact\_area}}{\Delta T / L}$ with L an arbitrary length

$Nu = \dfrac{\alpha * L}{\lambda}$ …Nusselt number stands for the heat transfer coefficient α multiplied with λ/L which defines the heat transfer through the medium.

λ/α defines the thermal boundary layer thickness. Both coefficients are depending on temperature:

For laminar flow at an even plate where incompressible water is evaporating from a medium the following equations can be used:

Equ. 11-3-1-3: Continuity equ.: $\dfrac{\partial u}{\partial x} + \dfrac{\partial v}{\partial y} = 0$

Equ. 11-3-1-4: Impulse equation in x-direction: $u*\dfrac{\partial u}{\partial x}+v*\dfrac{\partial v}{\partial y}=v*\dfrac{\partial^2 u}{\partial y^2}$

Equ. 11-3-1-5: Thermal energy equation: $u*\dfrac{\partial T}{\partial x}+v*\dfrac{\partial T}{\partial y}=a*\dfrac{\partial^2 T}{\partial y^2}$

Equ. 11-3-1-6: Blasius defined the flow field with: $\dfrac{u}{U_\infty}=f'(\eta)$

With dimensionless temperature diff. $\tilde{\theta}=\dfrac{T-T_W}{T_\infty-T_W}$, the analogy $\eta=\dfrac{y}{\delta}=y*\sqrt{\dfrac{U_\infty}{v*x}}$

and transformed u and v: $u=U_\infty*f'$ and $v=-\dfrac{1}{2}*\sqrt{\dfrac{U_\infty}{x}}*(f-\eta*f')$,

the energy equ. can be put into: $\dfrac{d^2\tilde{\theta}}{d\eta^2}+\dfrac{\text{Pr}}{2}*f*\dfrac{d\tilde{\theta}}{d\eta}=0$ (Pr = v / a and a = λ / (ρ*c_p))

f is the connection of the thermal properties to the flow field.

This equation can be solved numerically for the boundary conditions

$\tilde{\theta}(0)=0;\tilde{\theta}(\infty)=1$ when Pr-number is defined.

For Pr = 0,6: $\dfrac{d\tilde{\theta}}{d\eta}=0{,}332*\text{Pr}^{1/3}$ at η=0

This dimensionless temperature gradient corresponds to the Nusselt number:

$Nu=\dfrac{\alpha*L}{\lambda}=-\dfrac{\partial\tilde{\theta}}{\partial\tilde{y}}$ at $\tilde{y}=0$

with $\tilde{y}=\dfrac{y}{L}$, the Blasius equations $\eta=\dfrac{y}{\delta}$ and $\bar{\delta}=\sqrt{\dfrac{v*x}{U_\infty}}$: $L*\tilde{y}=\eta*\sqrt{\dfrac{v*x}{U_\infty}}$

for L → x: $\tilde{y}=\eta*\sqrt{\dfrac{v}{x*U_\infty}}$

$Nu=\dfrac{\alpha*x}{\lambda}=\dfrac{d\tilde{\theta}}{\sqrt{\dfrac{v}{U_\infty*x}}d\eta}=\sqrt{\dfrac{U_\infty*x}{v}}*\dfrac{d\tilde{\theta}}{d\iota}$ at η = 0

Equ. 11-3-1-7: $Nu_x=\dfrac{\alpha*x}{\lambda}=0{,}664*\text{Re}^{1/2}*\text{Pr}^{1/3}$ for laminar flow

Thickness of turbulent boundary layer is higher ($\delta\approx x^{4/5}$) than that of laminar boundary ($\delta\approx x^{1/2}$). In turbulent flow fields thickness of thermal boundary layer is independent on Prandtl-number.

Prandtl number for calculation of Nusselt number: $\Pr = \dfrac{v}{a}$.

v….kinematic viscosity of wet air in boundary layer [m²/s]

a….thermal conductivity of wet air in boundary layer [m²/s]

Equ. 11-3-1-8: $a = \dfrac{\lambda}{\rho * c_p}$ (thermal conductivity [m²/s])

Equ. 11-3-1-9: $\mathrm{Re} = \dfrac{w * L * \rho_m}{\eta_m}$ with w the air speed at the surface and L the

contacted length (the calculation length of the element) and ρ_m / η_m the properties of wet air in the boundary.

Thermal boundary layer thickness corresponds to boundary thickness of flow field δ_t = δ.

Re, Pr, α and β are calculated with mean temperature $T_m = (T_0+T_\infty)/2$ and $p_m = (p_v+p_{v\infty})/2$

Equ. 11-3-1-10: $p_{v,\infty} = P * \dfrac{Y_\infty}{0{,}622 + Y_\infty}$ with Y∞ the moisture in the air $Y_\infty = \dfrac{M_v}{M_g}$ or

Equ. 11-3-1-11: $Y_\infty = \dfrac{\tilde{M}_v}{\tilde{M}_g} * \dfrac{p_v}{P - p_v} = 0{,}622 * \dfrac{p_v}{P - p_v}$

According to VDI V. Gnielinski the Nusselt number is calculated for turbulent flow field (0,6 < Pr < 60) by:

Equ. 11-3-1-12: $Nu_{turb} = \dfrac{0{,}037 * \mathrm{Re}^{0{,}8} * \Pr}{1 + (2{,}443 * \mathrm{Re}^{-0{,}1} * (\Pr^{2/3} - 1))}$

Heat transfer coefficient α is calculated from Nusselt number by:

Equ. 11-3-1-13: $\alpha_{turb} = \dfrac{Nu_{turb} * \lambda}{L}$ and $\alpha_{lam} = \dfrac{Nu_{lam} * \lambda}{L}$

Mass transfer coefficient β is calculated from <u>heat – mass – exchange analogy:</u>

Equ. 11-3-1-14: $\dfrac{\alpha}{\beta} = \rho * c_p * Le^{(1-n)}$ with $Le = \dfrac{\lambda}{\rho * c_p * \delta} \approx 1$ for water-air and n = 1/3 for

laminar and n = 0,4 for turbulent flow γ = 1,3.

Diffusion coefficient according to Schirmer: $\delta = 22,6 * 10^{-6} * \left[\dfrac{1}{P}\right] * \left[\dfrac{T_m}{273,15}\right]$

Equ. 11-3-1-15: $\beta_{turb} = \dfrac{\alpha_{turb}}{\rho_m * c_{p,m}}$ and $\beta_{lam} = \dfrac{\alpha_{lam}}{\rho_m * c_{p,m}}$

Single sided mass transfer coefficients:

Equ. 11-3-1-16: $\beta_{h,turb} = \dfrac{\beta_{turb}}{1 - \dfrac{P_{d,0}}{P}}$ and $\beta_{h,lam} = \dfrac{\beta_{lam}}{1 - \dfrac{P_{d,0}}{P}}$

with $P_{d,0}$ the saturation pressure of vapour and P_{dl} the partial pressure of vapour in boundary.

Finally the evaporated amount of water is calculated for forced convective drying by:

Equ. 11-3-1-17: $g_{d,turb} = \beta_{h,turb} * \dfrac{R_d * T_m}{P_d - P_{dl}}$ and $g_{d,lam} = \beta_{h,lam} * \dfrac{R_d * T_m}{P_d - P_{dl}}$

Free convection due to <u>density difference</u> between fresh air and saturated air at boundary to coating surface is the driving force for drying in free draws.

$$\dot{q} = \alpha * (T_{coat} - T_{air}) \text{ or } \alpha = \frac{\dot{q}}{\Delta t}$$

$t_m = \dfrac{t_{coat} + t_{air}}{2}$ with t_{coat} the surface temperature of the coating and $t_{air} = t_\infty$

Equ. 11-3-1-18: Viscosity of air $\eta_m = \dfrac{((P - P_{vm}) * \eta_g * \sqrt{\tilde{M}_g}) + (p_{vm} * \eta_v * \sqrt{\tilde{M}_v})}{((P - p_v m) * \sqrt{\tilde{M}_g}) + (p_{vm} * \sqrt{\tilde{M}_v})}$

Equ. 11-3-1-19: Density of wet air $\rho_m = \dfrac{P}{R * T_m} * \dfrac{(P - p_{vm}) * \tilde{M}_g + p_{vm} * \tilde{M}_v}{P}$

This density difference is integrated in the Grashof-number Gr and the Rayleigh-number

Equ. 11-3-1-20: Ra = Gr * Pr

Nusselt number can be calculated according to VDI with Nu = 0,7 * Ra$^{1/4}$ at laminar flow and with Nu = 0,155 * Ra$^{1/3}$ for turbulent flow.

Grashof number: $Gr = \dfrac{g * l^3 * \gamma * (T_{coat} - T_{air})}{v^2}$

g….9,81 m/s²

v….kinematic viscosity of air in boundary layer

γ….heat extension coefficient of water; γ = 1/T$_{air}$

$\gamma \equiv -\dfrac{1}{\rho} * (\dfrac{\partial \rho}{\partial T})$ for ideal gases: $\gamma = \dfrac{1}{T_\infty} = \dfrac{1}{T_{air}}$

For even surfaces with length L the Nusselt-number for free convection drying can be calculated according to VDI-Fa (H. Klan):

Equ. 11-3-1-21: $Nu_{free} = 0,15 * (Ra * f(\text{Pr}))^{1/3}$

Equ. 11-3-1-22: $f(\text{Pr}) = \left[1 + (\dfrac{0,322}{\text{Pr}})^{11/20} \right]^{-20/11}$

Typically: Pr = 0,7 and f(Pr) = 2,7 * 10^8

For turbulent flow Ra * f(Pr) must be > 7 * 10^4

Finally: $\alpha = \dfrac{Nu * \lambda}{L}$ and β and g$_d$ with same calculation as for forced convection (Equ. 11-3-1-14 to 11-3-1-16).

Convective drying in the 2nd drying stage:

In the 2nd drying period the surface gets dry and evaporated water must be transported through this dense surface layer. The heat conductivity of the dry surface starts to get more important than the flow conditions in the boundary air layer. As the evaporated water has to be replaced by fresh water from inside the coating or base paper, the diffusion coefficients through dense coating layers start to play also an important role. In contrast to the 1st drying period evaporation speed is no more depending on air conditions but mainly on coating properties.

Diffusion and heat transfer coefficients will be influenced by the pore structure of the coating which is in fact a mixture of three components: Water, air and solid material. Common mass data's of each component do not provide sufficient information for further calculations.

For non-hygroscopic materials the driving force for evaporation is always positive and X$_0$ is always higher than X$_{air}$. Drying speed drops in the 2nd drying stage but the material is getting dry on its own under any air condition.

For hygroscopic materials the sorption forces of water have to be overcome and evaporation enthalpy is increased by sorption enthalpy. Measurements of paper sorption isotherms led to $\Delta h_{Sorp} = 1364 * e^{\left(-\frac{19,45*x}{1+x}\right)}$ [kJ/kg].
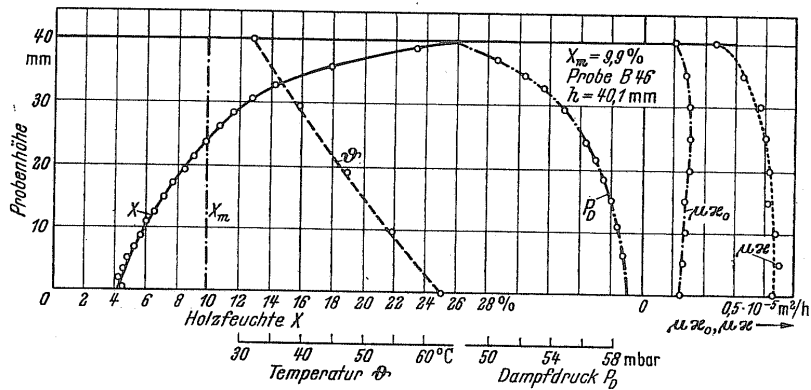
Pict. 11.3.1.6: Paper sorption isotherm from lab

Vapour pressure is reduced depending on pore size and hygroscopic forces. X_0 is dropping. When it's equal to X_{air}, drying speed is 0. The 2nd critical moisture $W_{cr,II}$ is reached.

For the 2nd drying period a dimensionless drying speed is defined by $\dot{v} = \dfrac{\dot{m}}{\dot{m}_I}$ with m depending on moisture of the material and m_I a constant drying speed from 1st drying stage.

A dimensionless material moisture ξ is defined with $\xi = \dfrac{X - X_{hy}}{X_{cr,I} - X_{hy}}$ and a

dimensionless drying time τ is defined with $\tau = \dfrac{m_I * A}{G_t * (W_{cr,I} - W_{hy})} * t$ (A = exchange area, G_t = mass of dry material (kg) and t = real drying time).

Drying time can be calculated from $\dfrac{d\xi}{d\tau} + \dot{v}(\xi) = 0$ and integrated: $-\int\limits_0^\tau d\tau = \int\limits_\xi^{\xi_0} \dfrac{d\xi}{\dot{v}(\xi)}$ or

$\tau = \int\limits_\xi^{\xi_0} \dfrac{d\xi}{\dot{v}(\xi)}$.

While in the 1st drying stage drying speed is defined with: $g_{d,I} = \dfrac{\beta}{R_D * T} * (p_D{}'' - P_{D,a})$

with R_D the gas constant of the vapour, β the mass transfer coefficient and $p_D{}''$ / $p_{D,a}$

the partial vapour pressure at the coating surface and in the air, in the 2nd drying stage this equation is expanded to:

Equ. 11-3-1-23: $g_{d,II} = \dfrac{1}{R_D * T} * \dfrac{1}{\dfrac{1}{\beta} + \dfrac{\mu * s'}{D}} * (p_D{}'' - P_{D,a})$ [kg/m²h] with D the diffusion

coefficient of vapour in air, μ the diffusion resistance coefficient (how much slower water vapour travels through the dense surface of the material compared to air diffusion) and s' the distance of the moisture level from the surface of the material. S' is changing with time as the moisture is removed from the surface during the 2nd drying period.

Comment to the calculation of drying curves from OMC11:

At OMC11 the following parameters were measured for Magnostar 200 g/m²:

- Basis weight and moisture of paper before coater and after complete drying by traversing Measurex online measurement (calibrated by lab)
- Dry coat weight by differential calculation of dry basis weight before and after coater
- Coating colour solids after blade by scrapping off the wet coating colour directly after the blade
- Web temperature before and after each drying element by IR measurement offline
- Air speed, temperature and moisture of boundary layer by anemometer and hygrometer offline
- Gas demand by gas flow meters at each drying element

The length of the drying elements and the distance between the drying elements (free draws) were taken from original Voith-CAD-drawings.

Drying at IR-dryers and airfoils was done with forced convection equations and drying in free draws by free convection equations. The calculation is valid only for the 1st drying stage, until the FCC ($X_{cr,I}$) is reached.

Two different data sets from top coater 5 (back side of base paper) were compared for the same grade before and after mottling optimization.

The calculation includes capillary sorption of the double precoated paper. Sorption speed was taken from Fibro-DAT measurements of 1,1% CMC solution on this substrate (see chapter "capillary sorption").

The drying curve before mottling optimization was characterized by low IR-drying energy, low web temperature, low degree of latex film forming, low drying rates in the 1st drying stage and high amount of capillary water penetration (including fine latex particles). All 3 airfoils were in operation.

Optimized drying was characterized by maximum amount of IR-energy in the 1st drying stage, high web temperature and elevated latex film forming. All airfoils were opened to shift drying rate to the IR-dryers in the 1st stage.
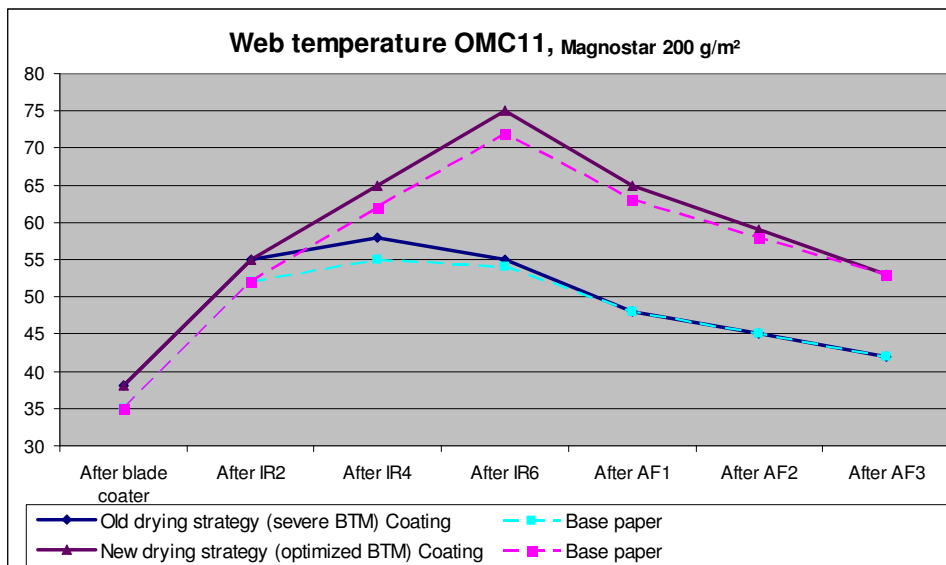
Pict. 11.3.1.7: Web temperature before and after mottling optimization (Coater 5)

Drying element: **IR1**

Working width	b	8,5	m	
Length of calc. Element (IR)	L	0,948	m	
Air circulation	U	25.000	m³/h	
-- " --	U	6,944	m³/s	U/3600
Gap heigth between IR and paper	h	0,1	m	
Air circulation speed	u	8,170	m/s	u = U/(b*h)
Air speed	w	23,333	m/s	For IR,FD: w = v; for AF: w = u
Web speed	v	1400	m/min	
-- " --	v	23,33	m/s	v/60
Overall pressure	P	100000	Pa	
Gas pressure	p_g	2,34	bar	
Density of gas	ρ_g	1,666	kg/m³	at p_g
-- " --	ρ_g	0,71		at P
Antoine-constants for water	A	7,19621		
-- " --	B	1730,63		
-- " --	C	233,426		
Temperature of air at boundary	t_U	115	°C	Measured at OMC11
-- " --	t_U	388,15	K	
Rel. moisture of air at boundary	Φ	0,020		Measured at OMC11
Spec. Vapour content in air	x	0,018	kg$_W$/kg$_{dry\ air}$	Φ=x/(x+0,622)*P/P$^S_{dl}$
				x=0,622/(P/(P^S*Φ)-1)
Temperature coating, in	**t$_{C,in}$**	**38**	**°C**	Measured at OMC11
-- " --	$T_{C,in}$	311,15	K	
Temperature paper, in	**t$_{p,in}$**	**35**	**°C**	Measured at OMC11
-- " --	$T_{p,in}$	308,15	K	
Basis weight paper, in (wet)	$P_{w,in}$	190,172	g/m²	online meas. OMC11 (HMx): Base + wet coating
Moisture paper, in	**X$_{P,w,in}$**	**0,044**	**kg$_W$/kg$_{P,wet}$**	online meas. OMC11 (HMx): Moisture before co
	$X_{P,d,in}$	0,0706	kg$_W$/kg$_{P,dry}$	$X_{P,dry} = W_P/P_{dry}$
Water in paper, in	$W_{P,in}$	12,54	g$_w$/m²	$W_P = P_w*X_{P,w}$
-- " --	$W_{P,in}$	1053,4	kg$_w$/mh	$W_P = W_P/1000*v$
Basis weight paper, in (dry)	$P_{d,in}$	177,6	g/m²	$P_d = P_w - W_P$
-- " --	$P_{d,in}$	14921,1	kg$_d$/mh	$P_d = P_d/1000*v$
Coat weigth, dry	**C$_d$**	**11**	**g/m²**	online measurement OMC11 (HMx)
-- " --	C_d	924	kg$_d$/mh	$C_d = C_d/1000*v$
Solid content coating, in	**c$_{coat,in}$**	**72,5**	**%**	Measured by lab at OMC11
Moisture in coating, in	$X_{c,w,in}$	0,275	kg$_W$/kg$_{c,wet}$	$X_{c,w} =(100-c_{coat})/100$
-- " --	$X_{c,d,in}$	0,379	kg$_W$/kg$_{c,dry}$	$X_{c,d} =W_c / C_d$
Coat weigth, wet, in	$C_{w,in}$	15,172	g/m²	$C_w =C_d*100/c_{coat}$
Water in coating, in	**W$_{c,in}$**	**4,172**	**g/m²**	$W_c = C_w*X_{c,w}$
-- " --		1274,483	kg$_W$/mh	$C_w =C_w/1000*v$
Gas consumption per IR-row	g	5,70	m³/h	
-- " --		2,43	Nm³/h	
Dwell time in calc. Element	t	0,0406286	s	t = L/v
Spec. heat capacity of water **at t$_{c,m}$**	$c_{p,w}$	4,211	kJ/kgK	Calc. formula from VDI Db2
Spec. heat capacity of dry paper	$c_{p,P,d}$	1,2	kJ/kgK	
Spec. heat capacity of dry coating	$c_{p,c,d}$	1,7	kJ/kgK	
Spec. heat capacity of wet paper	$c_{p,P,w}$	1,332	kJ/kgK	
Spec. heat capacity of wwet coating	$c_{p,c,w}$	2,390	kJ/kgK	
Temperature of coating after IR, out	**t$_{c,out}$**	**46,5**	**°C**	Measured at OMC11
-- " --	$T_{c,out}$	319,7	K	
Mean temp. of coating under IR	$t_{c,m}$	42,3	°C	$t_{c,m} = (t_{c,out} + t_{c,in})/2$
-- " --	$T_{c,m}$	315,4	K	
Temperature of paper after IR, out	**t$_{P,out}$**	**43,5**	**°C**	Measured at OMC11
-- " --	$T_{P,out}$	316,7	K	
Mean temp. of paper under IR	$t_{p,m}$	39,3	°C	$t_{p,m} = (t_{P,out} + t_{p,in})/2$
-- " --	$T_{P,m}$	312,4	K	
Mean boundary temperature	t_m	78,63	°C	$t_m = (t_U+t_{c,m})/2$
-- " --	T_m	351,8	K	

Page 763

General gas constant	R	8,31451	kJ/kmol K	
Individual gas constant for water	R_d	0,4615	kJ/kmol K	$R_d = R / MW_W$ (18,015)
Individual gas constant for dry air	R_a	0,28710	kJ/kmol K	$R_a = R / MW_a$ (28,96)
Individual gas constant for wet air	R_w	0,2903	kJ/kmol K	$R_w = (R_a + x \cdot R_d)/(1+x)$
Vapour saturation pressure in boundary air	P^S_{dl}	169517,90	Pa	$P^S_{dl} = 1000 \cdot 10^{**}(A-B/(C+t_U))$
Saturation pressure of vapour	P_{dO}	10321,78	Pa	$P_{dO} = 1000 \cdot 10^{**}(A-B/(C+t_{c,out}))$
Partial pressure of vapour in boundary air	P_{dl}	3390,36	Pa	$P_{dl} = \Phi \cdot P^S_{dl}$
-- " --	P_{dl}	2870,0	Pa	Control: $P_{dl} = x \cdot P/(R_a/R_d+x)$
Densisty of dry air	ρ_a	866,93	g/m³	$\rho_a = (P-P_{dl})/(R_a \cdot T_a)$ with $T_a = T_U$
Density of vapour	ρ_d	18,93	g/m³	$\rho_d = P_{dl}/(R_d \cdot T_U)$
Density of wet air	ρ	885,85	g/m³	$\rho = \rho_a + \rho_d$
Spec. heat capacity of dry air at t_m	c_{pa}	1,0071	kJ/kg K	Calc. formula from VDI Db16
Spec. heat capacity of vapour at t_m	c_{pd}	2,1402	kJ/kg K	Calc. formula from VDI Db5
Spec. heat capacity of wet air at t_m	c_p	1,03135	kJ/kg K	$c_p = (\rho_a \cdot c_{pa}+\rho_d \cdot c_{pd})/\rho$
Heat conductivity for dry air at t_m	λ_a	0,03036	J/msK	Calc. formula from VDI Db16
Heat conductivity for vapour at t_m	λ_d	0,02318	J/msK	Calc. formula from VDI Db8
Heat conductivity for wet air at t_m	λ	0,030203	J/msK	$\lambda = (\rho_a \cdot \lambda_a+\rho_d \cdot \lambda_d)/\rho$
Kinematic viscosity of dry air at t_m	v_a	2,06E-05	m²/s	Calc. formula from VDI Db16
Kinematic viscosity of vapour at t_m	v_d	1,74E-06	m²/s	Calc. formula from VDI Db10
Kinematic viscosity of wet air at t_m	v	2,02E-05	m²/s	$v = (\rho_a \cdot v_a+\rho_d \cdot v_d)/\rho$
Temp. conductivity of wet air	a	3,31E-05	m²/s	$a = \lambda/(\rho \cdot c_p)$
Diffusion coefficient vapour in air	D	3,648E-05	m²/s	$D=0,083/3600 \cdot (10^{**}(5/P)) \cdot ((T_m/273,15)^{**}1,81)$
Heat transfer turbulent	α_{turb}	58,8957	J/m²sK	$\alpha_{turb} = Nu_{turb} \cdot \lambda/L$ from $Nu = \alpha \cdot L/\lambda$
Heat transfer laminar	α_{lam}	18,8153	J/m²sK	$\alpha_{lam} = Nu_{lam} \cdot \lambda/L$ from $Nu = \alpha \cdot L/\lambda$
Mass transfer turbulent	β_{turb}	0,06446	m/s	$\beta_{turb} = \alpha_{turb}/(\rho \cdot c_p)$ from $\alpha/\beta=\rho \cdot c_p$
Mass transfer laminar	β_{lam}	0,0205941	m/s	$\beta_{lam} = \alpha_{lam}/(\rho \cdot c_p)$ from $\alpha/\beta=\rho \cdot c_p$
Mass transfer turbulent (single sided)	$\beta_{h,turb}$	0,071883	m/s	$\beta_{h,turb} = \beta_{turb}/(1-P_{d0}/P)$
Mass transfer laminar (single sided)	$\beta_{h,lam}$	0,022964	m/s	$\beta_{h,lam} = \beta_{lam}/(1-P_{d0}/P)$
Dimensionless numbers:				
Reynolds number	Re	1094721		$Re=w \cdot L/v$
Nusselt number, turbulent	Nu_{turb}	1848,6		$Nu_{turb}=0,037 \cdot Re^{**}0,8 \cdot Pr/(1+2,443 \cdot Re^{**}(-0,1) \cdot Pr^{**}(2/3)-1))$
Nusselt number, laminar	Nu_{lam}	590,6		$Nu_{lam} = 0,664 \cdot Re^{**}0,5 \cdot Pr^{**}0,33$
Prandtl number	Pr	0,6112		$Pr = v/a$
Schmidt number	Sc	0,5538		$Sc = v/D$
Lewis number	Le	0,9061		$Le = Sc / Pr = a/D$
Sherwood number, turbulent	Sh_{turb}	1867,78		$Sh_{turb} = \beta_{h,turb} \cdot L/D$
Sherwood number, laminar	Sh_{lam}	596,70		$Sh_{lam} = \beta_{h,lam} \cdot L/D$
Vapour flow density, turbulent	$g_{d,turb}$	3,069	g/m² s	$g_{d,turb} = \beta_{h,turb}/(R_d \cdot T_m) \cdot (P_{do}-P_{dl})$
Vapour flow density, laminar	$g_{d,lam}$	0,980	g/m² s	$g_{d,lam} = \beta_{h,lam}/(R_d \cdot T_m) \cdot (P_{do}-P_{dl})$
Evap. water into the boundary air, turbulent	**$W_{a,turb}$**	**0,125**	**g/m²**	$W_{a,turb} = g_{d,turb} \cdot t$
Evap. water into the boundary air, laminar	**$W_{a,lam}$**	**0,040**	**g/m²**	$W_{a,lam} = g_{d,lam} \cdot t$
Calculation of paper and coating moisture excluding capillry sorption:				
Coat weigth, wet, out	$C_{w,out}$	15,048	g/m²	$C_w = C_d \cdot 100/c_{coat}$
Solid content coating, out	$c_{coat,out}$	73,10	%	$c_{coat} = c_d \cdot 100/c_w$ (**Immo solids=FCC: 81%**)
Moisture in coating out	$X_{c,w,out}$	0,269	$kg_w/kg_{c,wet}$	$X_{c,w} = (100-c_{coat})/100$
Water in coating, out	**$W_{c,out}$**	**4,048**	**g/m²**	$W_c = C_w \cdot X_{c,w}$
-- " --	$W_{c,out}$	1264,0	kg_w/mh	$C_w = C_w/1000 \cdot v$
Moisture in coating out	$X_{c,d,out}$	0,368	$kg_w/kg_{c,dry}$	$X_{c,d} = W_c / C_d$
Water in paper, out	$W_{P,out}$	12,415	$g_w/m²$	$W_{P,out} = W_{p,in} - (W_{c,out} - W_{c,in})$
-- " --	$W_{P,out}$	1042,9	kg_w/mh	$W_P = W_P/1000 \cdot v$
Basis weight paper, out (wet)	$P_{w,out}$	190,05	g/m²	$P_{w,out} = P_{d,in} + W_{p,out}$
Moisture paper, out	**$X_{P,w,out}$**	**0,0653**	**$kg_w/kg_{P,wet}$**	$X_{p,w} = W_P/P_w$
	$X_{P,d,out}$	0,0699	$kg_w/kg_{P,dry}$	$X_{P,dry} = W_P/P_{dry}$
Calculation of paper and coating moisture including capillry sorption:				
Capillary sorption of liquid phase dV/dt	dV/dt_{sorp}	0,0032	µl/s	From Fibro-DAT with 1,1% CMC solution on double precoated paper OMC11
Area of droplet penetration	A_{drop}	3,35	mm²	
Capillary sorption speed of double precoated	$v_{sorp,MC}$	9,64E-07	m/s	
Cap. Sorption in time t of double precoated p	**V_{sorp}/A**	**0,04**	**g/m² = ml/m²**	
Coat weigth, wet, out	$C_{w,out}$	15,009	g/m²	$C_w = C_d \cdot 100/c_{coat}$
Solid content coating, out	$c_{coat,out}$	73,29	%	$c_{coat} = c_d \cdot 100/c_w$ (**Immo solids=FCC: 81%**)
Moisture in coating out	$X_{c,w,out}$	0,267	$kg_w/kg_{c,wet}$	$X_{c,w} = (100-c_{coat})/100$
Water in coating, out	**$W_{c,out}$**	**4,009**	**g/m²**	$W_c = C_w \cdot X_{c,w}$
-- " --	$W_{c,out}$	1260,7	kg_w/mh	$C_w = C_w/1000 \cdot v$
Moisture in coating out	$X_{c,d,out}$	0,364	$kg_w/kg_{c,dry}$	$X_{c,d} = W_c / C_d$
Water in paper, out	$W_{P,out}$	12,376	$g_w/m²$	$W_{P,out} = W_{p,in} - (W_{c,out} - W_{c,in})$
-- " --	$W_{P,out}$	1039,6	kg_w/mh	$W_P = W_P/1000 \cdot v$
Basis weight paper, out (wet)	$P_{w,out}$	190,01	g/m²	$P_{w,out} = P_{d,in} + W_{p,out}$
Moisture paper, out	**$X_{P,w,out}$**	**0,0651**	**$kg_w/kg_{P,wet}$**	$X_{p,w} = W_p/P_w$
	$X_{P,d,out}$	0,0697	$kg_w/kg_{P,dry}$	$X_{P,dry} = W_P/P_{dry}$

Pict. 11.3.1.8: Calculation of forced convection

Page 764

Drying element: **FD1**

Working width	b	8,5	m	
Length of calc. Element (free draw)	L_{FD}	2,284	m	
Characteristic length	l_{FD}	0,900	m	I = L*b/(2*(L+b))
Air circulation	U	0	m³/h	
-- " --	U	0,000	m³/s	U/3600
Gap heigth between FD and paper	h	0,1	m	
Air speed	w	23,333	m/s	For IR,FD: w = v; for AF: w = u

Web speed	v	1400	m/min	
-- " --	v	23,33	m/s	v/60

Overall pressure	P	100000	Pa	

Antoine-constants for water	A	7,19621		
-- " --	B	1730,63		
-- " --	C	233,426		

Air temperature in coater hall	$t_{x,0}$	35	°C	$t_u = t_{x,0}$
Moisture of air in hall	$\Phi_{x,0}$	0,32	[-]	
Spec. Vapour content in air	x	0,528	kg$_w$/kg$_{dry\ air}$	$\Phi=x/(x+0,622)*P/P^S_{dl}$
				$x=0,622/(P/(P^S*\Phi)-1)$
Gravity	g	9,81	m/s²	

Temperature of air at boundary	t_m	45,0	°C	
-- " --	t_m	318,15	K	

Temperature coating, in	$t_{C,in}$	55	°C	t_{out} of previous calcculation element
-- " --	$T_{C,in}$	328,15	K	
Temperature paper, in	$t_{p,in}$	52	°C	t_{out} of previous calcculation element
-- " --	$T_{p,in}$	325,15	K	

Basis weight paper, in (wet)	$P_{w,in}$	189,84	g/m²	P_{out} of previous calcculation element
Moisture paper, in	$X_{P,w,in}$	0,0643	kg$_w$/kg$_{P,wet}$	$x_{p,out}$ of previous calcculation element
	$X_{P,d,in}$	0,069	kg$_w$/kg$_{p,dry}$	$X_{P,dry} = W_P/P_{dry}$
Water in paper, in	$W_{P,in}$	12,21	g$_w$/m²	$W_P = P_w*X_{P,w}$
-- " --	$W_{P,in}$	1025,3	kg$_w$/mh	$W_P = W_P/1000*v$
Basis weight paper, in (dry)	$P_{d,in}$	177,63	g/m²	$P_d = P_w - W_P$
-- " --	$P_{d,in}$	14921,12	kg$_d$/mh	$P_d = P_d/1000*v$

Coat weigth, dry	C_d	11	g/m²	
-- " --	C_d	924	kg$_d$/mh	$C_d = C_d/1000*v$
Solid content coating	$c_{coat,in}$	74,13	%	
Moisture in coating	$X_{c,w,in}$	0,26	kg$_w$/kg$_{c,wet}$	$X_{c,w} =(100-c_{coat})/100$
-- " --	$X_{c,d,in}$	0,35	kg$_w$/kg$_{c,dry}$	$X_{c,d} =W_c / C_d$
Coat weigth, wet, in	$C_{w,in}$	14,84	g/m²	$C_w =C_d*100/c_{coat}$
Water in coating	$W_{c,in}$	3,84	g/m²	$W_c = C_w*X_{c,w}$
-- " --		1246,465	kg$_w$/mh	$C_w =C_w/1000*v$

Dwell time in calc. Element	t	0,09789	s	t = L/v
Spec. heat capacity of water at 20°C	$c_{p,W}$	4,149	kJ/kgK	Calc. from VDI Db2
Spec. heat capacity of dry paper	$c_{p,P,d}$	1,2	kJ/kgK	
Spec. heat capacity of dry coating	$c_{p,c,d}$	1,7	kJ/kgK	
Spec. heat capacity of wet paper	$c_{p,P,w}$	1,390	kJ/kgK	
Spec. heat capacity of wwet coating	$c_{p,c,w}$	2,334	kJ/kgK	

Temperature of coating after FD, out	$t_{c,out}$	52,3	°C	Measured at OMC11
-- " --	$T_{c,out}$	325,4	K	
Mean temp. of coating under FD	$t_{c,m}$	53,6	°C	$t_{c,m} = (t_{c,out} + t_{c,in})/2$
-- " --	$T_{c,m}$	326,7796	K	

Temperature of paper after FD, out	$t_{P,out}$	49,3	°C	Measured at OMC11
-- " --	$T_{P,out}$	322,4	K	
Mean temp. of paper under FD	$t_{p,m}$	50,6	°C	$t_{p,m} = (t_{P,out} + t_{p,in})/2$
-- " --	$T_{P,m}$	323,7796	K	

Mean boundary temperature	t_m	45,0	°C	$t_m = (t_U+t_{c,m})/2$
-- " --	T_m	318,2	K	

Page 765

General gas constant	R	8,31451	kJ/kmol K	
Individual gas constant for water	R_d	0,4615	kJ/kmol K	R_d = R / MW_W (18,015)
Individual gas constant for dry air	R_a	0,287103246	kJ/kmol K	R_a = R / MW_a (28,96)
Individual gas constant for wet air	R_w	0,3474	kJ/kmol K	R_w= (R_a + x*R_d)/(1+x)
Vapour saturation pressure in boundary air	P^S_{dl}	5608,98	Pa	P^S_{dl}=1000*10**(A-B/(C+t_U))
Saturation pressure of vapour	P_{dO}	13752,71	Pa	P_{dO}=1000*10**(A-B/(C+$t_{c,out}$))
Partial pressure of vapour in boundary air	P_{dl}	1794,87	Pa	P_{dl}=Φ_{hall} * P^S_{dl}
Densisty of dry air	ρ_a	1110,03	g/m³	ρ_a=(P-P_{dl})/(R_a*T_a) with T_a = $T_{x,0}$
Density of vapour	ρ_d	12,62	g/m³	ρ_d=P_{dl}/(R_d*$T_{x,0}$)
Density of wet air	ρ	1122,65	g/m³	ρ = ρ_a + ρ_d
Spec. heat capacity of dry air at tm	$c_{p,a}$	1,0053	kJ/kg K	Calc. from VDI Db16
Spec. heat capacity of vapour at t_m	$c_{p,d}$	1,8212	kJ/kg K	Calc. from VDI Db5
Spec. heat capacity of wet air at tm	c_p	1,0145	kJ/kg K	c_p=(ρ_a*c_{pa}+ρ_d*c_{pd})/ρ
Heat conductivity for dry air at tm	λ_a	0,02800	J/msK	Calc. from VDI Db16
Heat conductivity for vapour at t_m	λ_d	0,01969	J/msK	Calc. from VDI Db8
Heat conductivity for wet air at tm	λ	0,027910	J/msK	λ=(ρ_a*λ_a+ρ_d*λ_d)/ρ
Kinematic viscosity of dry air at tm	v_a	2,10E-05	m²/s	Calc. from VDI Db16
Kinematic viscosity of vapour at t_m	v_d	4,76E-07	m²/s	Calc. from VDI Db10
Kinematic viscosity of wet air at tm	v	2,08E-05	m²/s	v=(ρ_a*v_a+ρ_d*v_d)/ρ
Temp. conductivity of wet air	a	2,45E-05	m²/s	a = λ/(ρ*c_p)
Diffusion coefficient vapour in air	D	3,042E-05	m²/s	D=0,083/3600*(10**(5/P))*((T_m/273,15)**1,81)
Heat extension coefficient	γ	0,00325	1/K	γ = 1/$T_{x,0}$

Dimensionless numbers:

Reynolds number	Re	2563187		Re=w*L/v
Prandtl number	Pr	0,8485		Pr = v/a
Function (Pr)	f(Pr)	0,4319		f(Pr)=[1+(0,322/Pr)$^{11/20}$]$^{-20/11}$
Grashof number	Gr	1,07E+09		Gr = (g*l³*γ*(t_{coat} - $t_{x,0}$))/v²
Raleigh number	Ra	9,11E+08		Ra = Gr * Pr
Criterion for turbulent or laminar	K	3,94E+08		K = Ra * f(Pr)) > 7 * 10^4 for turbulent heat transfer
Nusselt number, turbulent	Nu_{turb}	109,929		Nu_{turb} = 0,15 * [Ra*f(Pr)]$^{1/3}$
Heat transfer turbulent	α_{turb}	3,4085	J/m²sK	α_{turb} = Nu_{turb}*λ/l from Nu = α*L/λ
Mass transfer turbulent	β_{turb}	0,00299	m/s	β_{turb} = α_{turb}/(ρ*c_p) from α/β=ρ*c_p
Mass transfer turbulent (single sided)	$\beta_{h,turb}$	0,003470	m/s	$\beta_{h,turb}$ = β_{turb}/(1-P_{d0}/P)
Vapour flow density, turbulent	$g_{d,turb}$	0,283	g/m² s	$g_{d,turb}$ = $\beta_{h,turb}$/(R_d*T_m)*(P_{do}-P_{dl})
Evap. water into the boundary air, turbulent	$W_{a,turb}$	**0,028**	g/m²	$W_{a,turb}$ = $g_{d,turb}$ * t
-- " --		19,749	kg/h	
Coat weigth, wet, out	$C_{w,out}$	14,811	g/m²	C_w=C_d*100/c_{coat}
Solid content coating, out	$c_{coat,out}$	**74,27**	%	c_{coat} = c_d*100/c_w **(Immo solids=FCC: 81%)**
Moisture in coating out	$X_{c,w,out}$	0,257	kg$_W$/kg$_{c,wet}$	$X_{c,w}$=(100-c_{coat})/100
Water in coating, out	$W_{c,out}$	**3,811**	g/m²	W_c = C_w*$X_{c,w}$
-- " --	$W_{c,out}$	0,0	kg$_W$/mh	C_w=C_w/1000*v
Moisture in coating out	$X_{c,d,out}$	0,346	kg$_W$/kg$_{c,dry}$	$X_{c,d}$=W_c / C_d
Water in paper, out	$W_{P,out}$	12,179	g$_w$/m²	$W_{P,out}$ = $W_{p,in}$ - ($W_{c,out}$ - $W_{c,in}$)
-- " --	$W_{P,out}$	0,0	kg$_w$/mh	W_P = W_P/1000*v
Basis weight paper, out (wet)	$P_{w,out}$	189,81	g/m²	$P_{w,out}$ = $P_{d,in}$ + $W_{p,out}$
Moisture paper, out	$X_{P,w,out}$	**0,0642**	kg$_W$/kg$_{P,wet}$	$X_{p,w}$=W_P/P_w
	$X_{P,d,out}$	0,0686	kg$_W$/kg$_{P,dry}$	$X_{P,dry}$ = W_P/P_{dry}
Capillary sorption of liquid phase dV/dt	dV/dtsorp	0,0032	µl/s	From Fibro-DAT with 1,1% CMC solution on double precoated paper OMC11
Area of droplet penetration	A_{drop}	3,35	mm²	
Capillary sorption speed of double precoated	$v_{sorp,MC}$	9,64E-07	m/s	
Cap. Sorption in time t of double precoated p	V_{sorp}/A	**0,09**	g/m² = ml/m²	
Coat weigth, wet, out	$C_{w,out}$	14,639	g/m²	C_w=C_d*100/c_{coat}
Solid content coating, out	$c_{coat,out}$	**75,14**	%	c_{coat} = c_d*100/c_w **(Immo solids=FCC: 81%)**
Moisture in coating out	$X_{c,w,out}$	0,249	kg$_W$/kg$_{c,wet}$	$X_{c,w}$=(100-c_{coat})/100
Water in coating, out	$W_{c,out}$	**3,639**	g/m²	W_c = C_w*$X_{c,w}$
-- " --	$W_{c,out}$	1229,6	kg$_W$/mh	C_w=C_w/1000*v
Moisture in coating out	$X_{c,d,out}$	0,331	kg$_W$/kg$_{c,dry}$	$X_{c,d}$=W_c / C_d
Water in paper, out	$W_{P,out}$	12,006	g$_w$/m²	$W_{P,out}$ = $W_{p,in}$ - ($W_{c,out}$ - $W_{c,in}$)
-- " --	$W_{P,out}$	1008,5	kg$_w$/mh	W_P = W_P/1000*v
Basis weight paper, out (wet)	$P_{w,out}$	189,64	g/m²	$P_{w,out}$ = $P_{d,in}$ + $W_{p,out}$
Moisture paper, out	$X_{P,w,out}$	**0,0633**	kg$_W$/kg$_{P,wet}$	$X_{p,w}$=W_p/P_w
	$X_{P,d,out}$	0,0676	kg$_W$/kg$_{P,dry}$	$X_{P,dry}$ = W_P/P_{dry}

Pict. 11.3.1.9: Calculation of free convection

Page 766
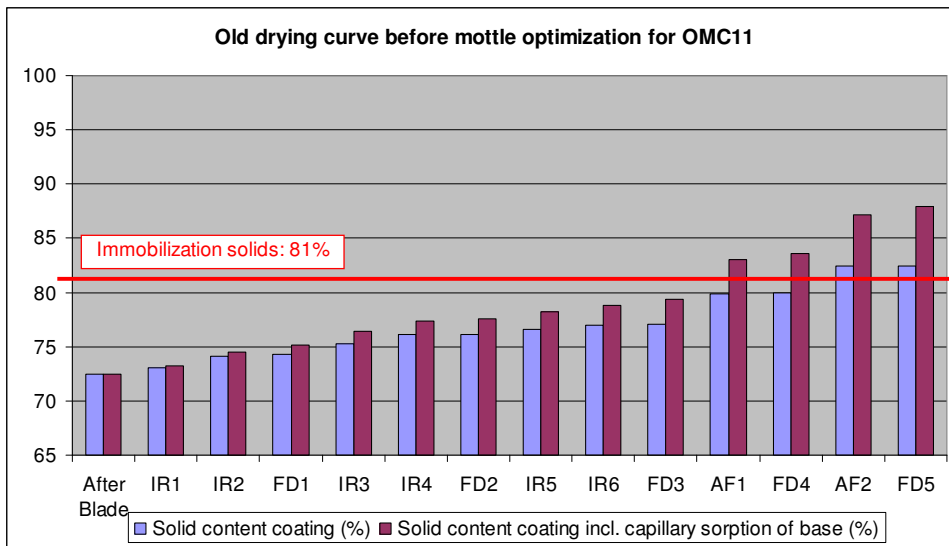
Pict. 11.3.1.10: Calculated solid content in coating – old drying curve with bad mottling (2 airfoils in operation)
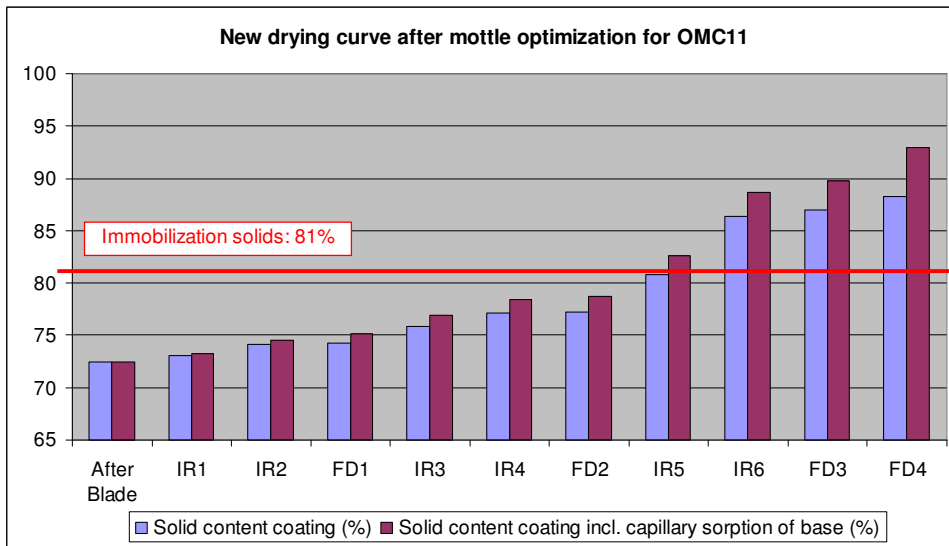
Pict. 11.3.1.11: Calculated solid content in coating – new drying curve with optimized mottling (airfoils open = free draw)

The solid content in the coating (plus partially in the boundary to the base paper) was controlled by Fibro MCA1410 infrared surface moisture measuring instrument. These measurements showed together with the web temperature (see pict. 11.3.1.7) clearly the difference between the new and the old drying strategy:
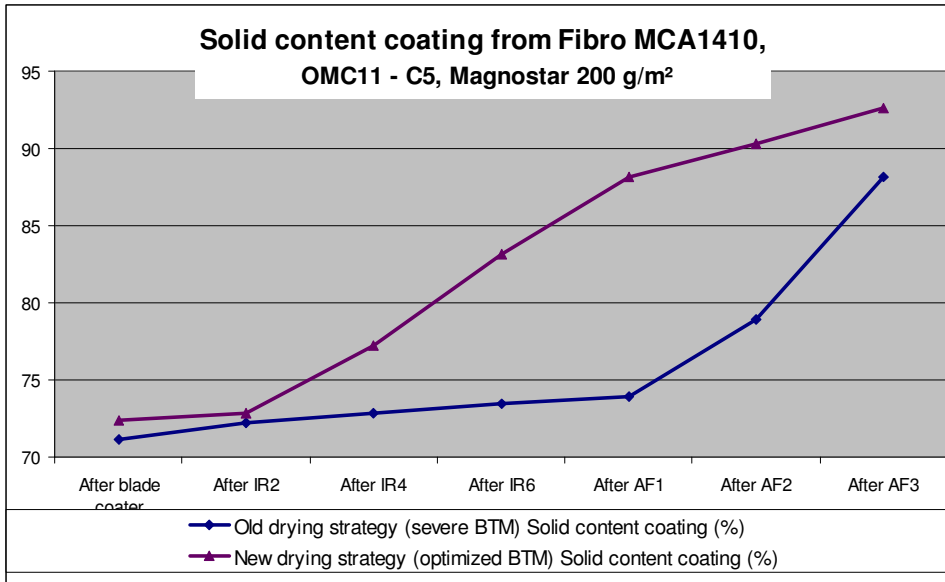
Pict. 11.3.1.12: Coating solid content calculated from Fibro MCA 1410
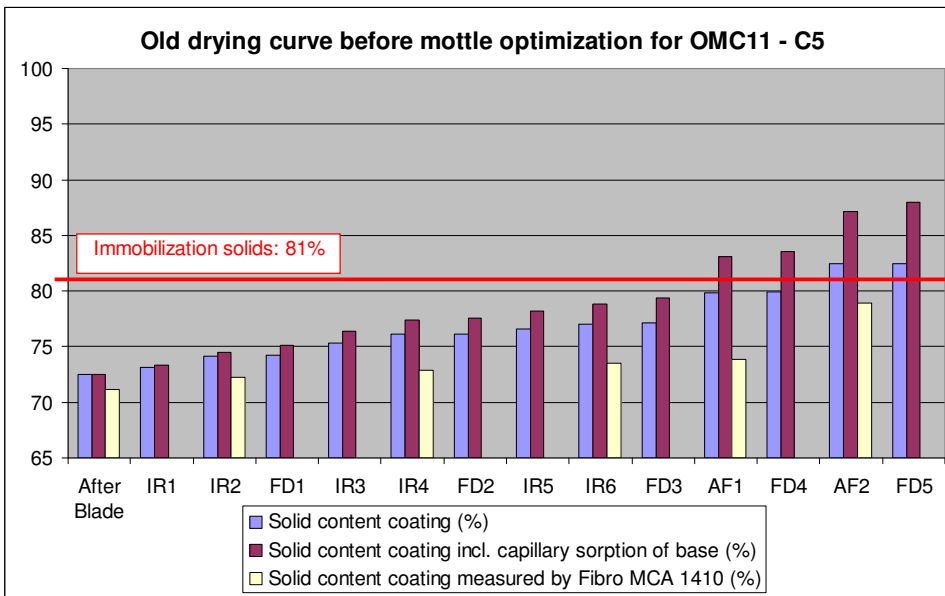
Pict. 11.3.1.13: Coating solid content including Fibro MCA 1410 – old drying strategy
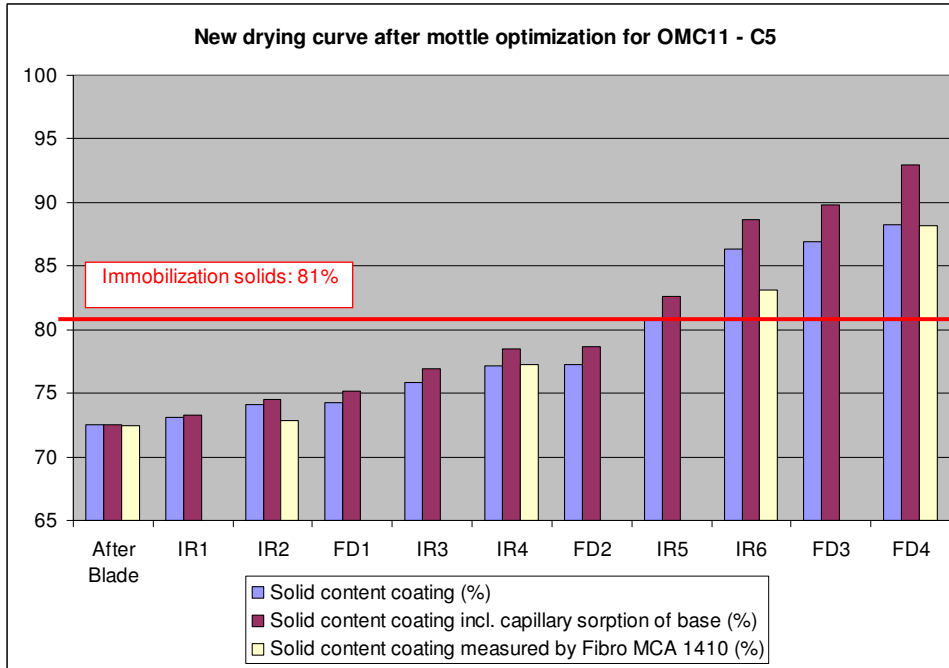
Pict. 11.3.1.14: Coating solid content including Fibro MCA 1410 – new drying strategy
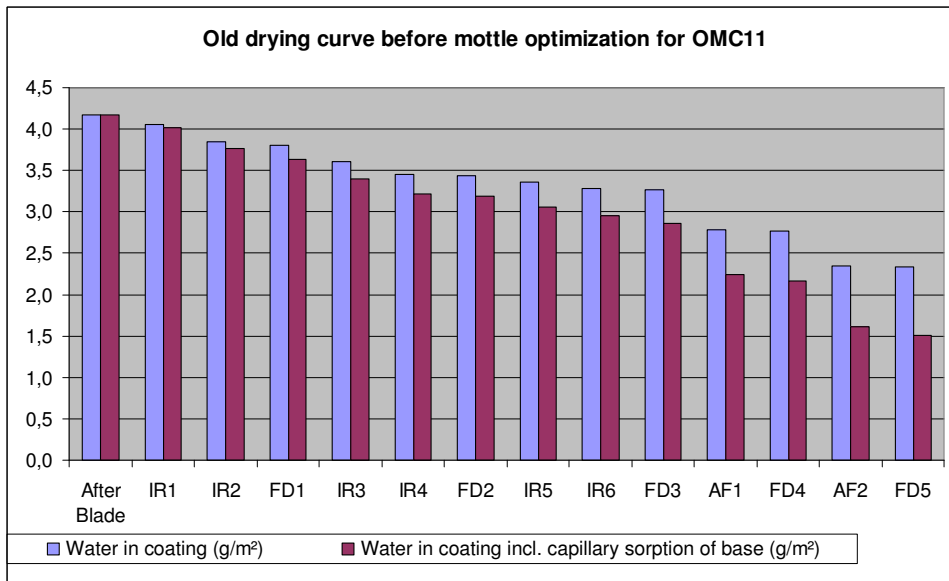
Pict. 11.3.1.15: Calculated moisture in coating – old drying curve with bad mottling
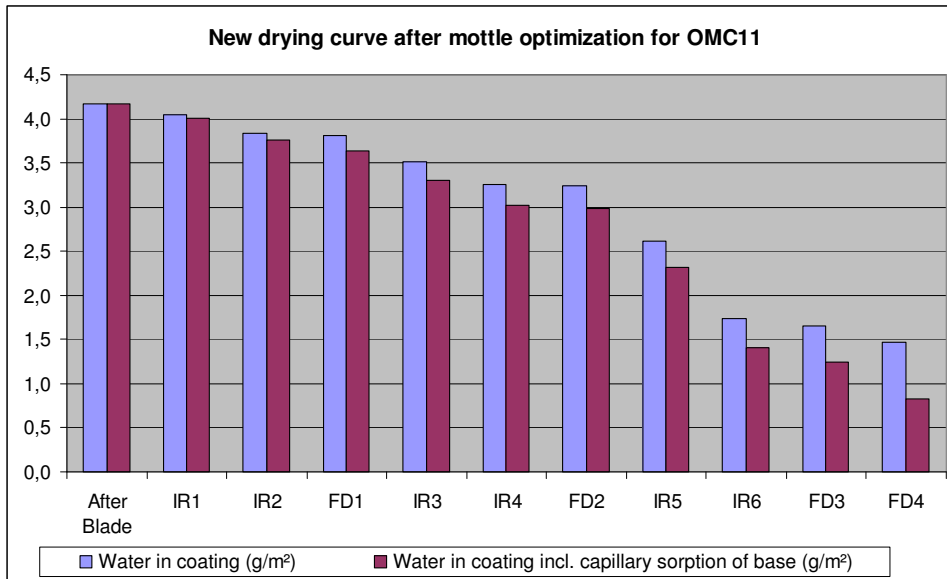
Pict. 11.3.1.16: Calculated moisture in coating – new drying curve with optimized mottling
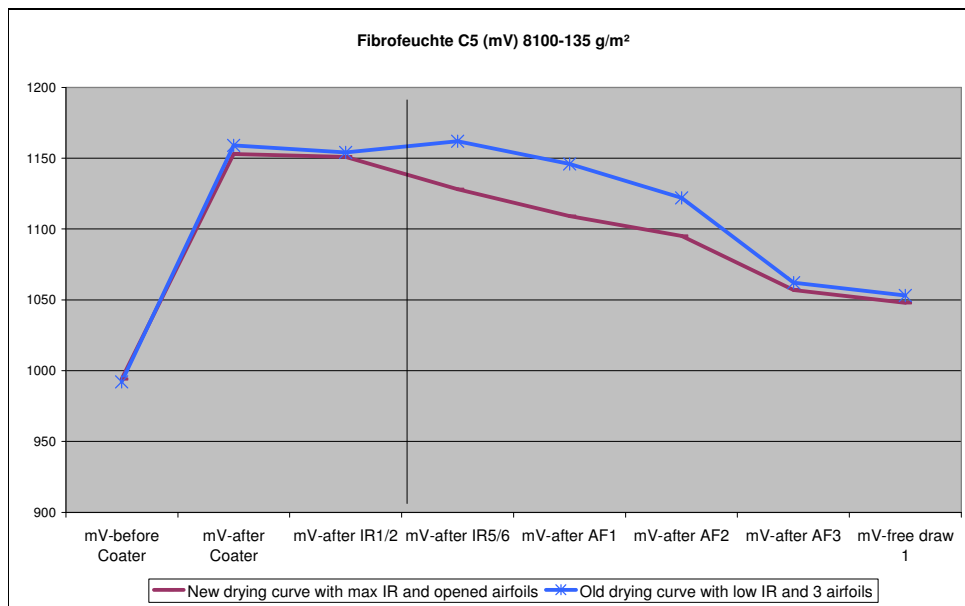
Pict. 11.3.1.17: Moisture in coating – comparing old and new drying strategy with Fibro-MCA IR measurement of surface moisture
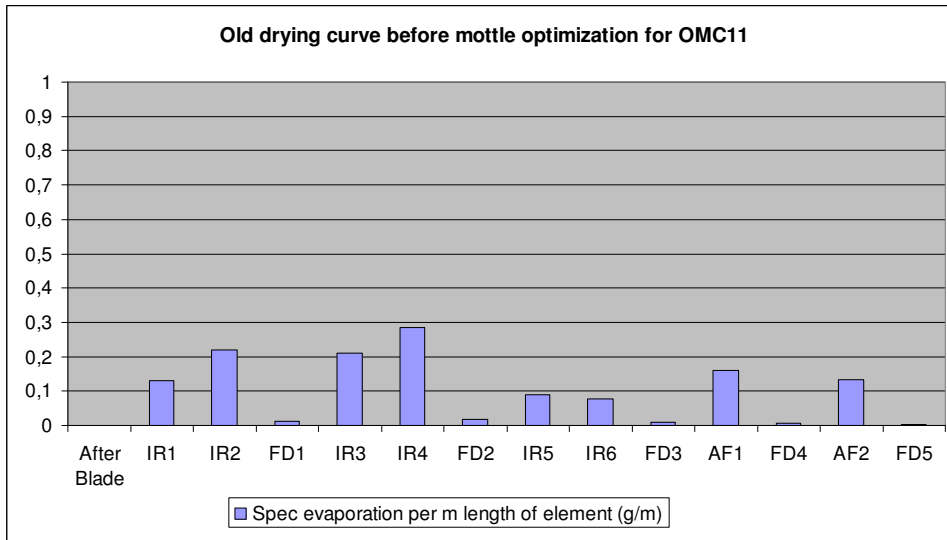
Pict. 11.3.1.18: Evaporation rate at each drying element – old drying curve with bad mottling
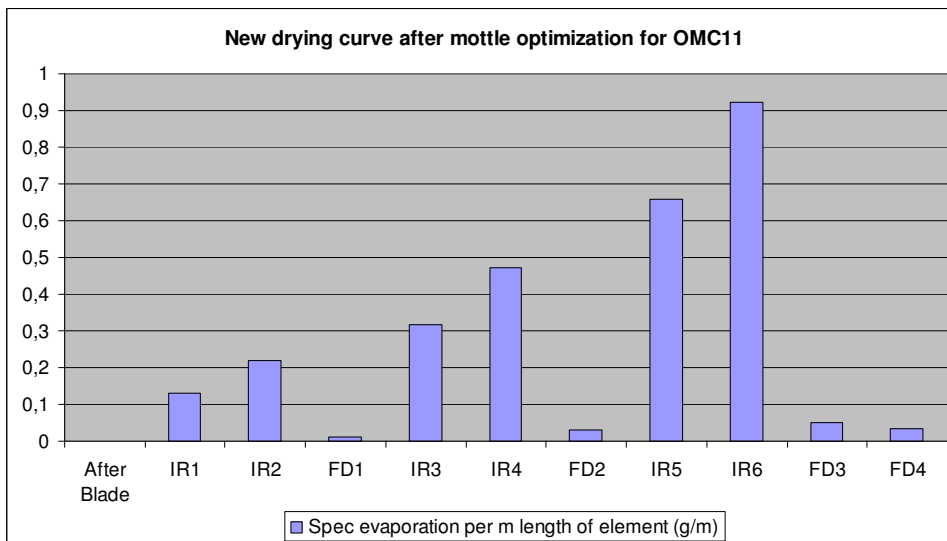
Pict. 11.3.1.19: Evaporation rate at each drying element – new drying curve with optimized mottling

The comparison of the two drying curves shows that drying rate in the 1st drying stage and web temperature was significantly lower for the old drying strategy. Immobilization solids was reached later and penetration of water into base was more pronounced. As web temperature was low at the FCC, latex film forming was poor and latex mobility was high in the period between FCC and SCC. Uneven latex migration to the surface after the FCC was provoked by delayed drying at the old drying strategy.

11.3.2 BASF pilot coating trial – influence of drying conditions

In pilot trial BASF 08/05 the successful change of drying strategy at OMC11 from low drying energy input to high drying energy in the initial stage was simulated for top coatings.

Additionally delayed start of evaporation in the 1st drying stage was compared to fast start of drying.

The BASF coater was equipped with 3 groups of IR which contained in sum 21 IR rows, followed by 3 airfoils.

End moisture was kept constant and evaporation was shifted between the different drying groups.

The glossy top coating was applied on a double precoated paper from PM11/OMC11.

trial point	web temperature after IR 2	web temperature after IR 3,4	web temperature after IR 5,6,7	air circulation IR	air foil 1	air foil 2	air foil 3	coating colour
top coating trials								
DS1	70 - 75°C	70 - 75°C	70 - 75°C	MAX.	open	open	80 - 100°C	Standard TC 390
DS2	50°C	50 - 55°C	55°C	MAX.	80 - 130°C	80 - 130°C	80 - 130°C	Standard TC 390
DS3	50°C	50 - 55°C	70 - 75°C	MAX.	open	open	80 - 100°C	Standard TC 390
DS4	70 - 75°C	70 - 75°C	50 - 55°C	MAX.	open	open	80 - 100°C	Standard TC 390
DS5	70 - 75°C	70 - 75°C	70 - 75°C	MIN.	open	open	80 - 100°C	Standard TC 390
DS6	50°C	50 - 55°C	70 - 75°C	MIN.	open	open	80 - 100°C	Standard TC 390
DS7	70 - 75°C	70 - 75°C	50 - 55°C	MIN.	open	open	80 - 100°C	Standard TC 390
DS8	70 - 75°C	70 - 75°C	70 - 75°C	MAX.	open	open	80 - 100°C	TC with Lupamin

Pict. 11.3.2.1: Drying strategies of BASF pilot week 08-2005

The drying curve "DS2" corresponds to the old strategy of OMC11 after speed increase where IR energy was low. "DS7" simulated the new drying strategy where IR energy was high and airfoils were opened after IR section to let the web evaporate under moderate drying conditions by natural convection.
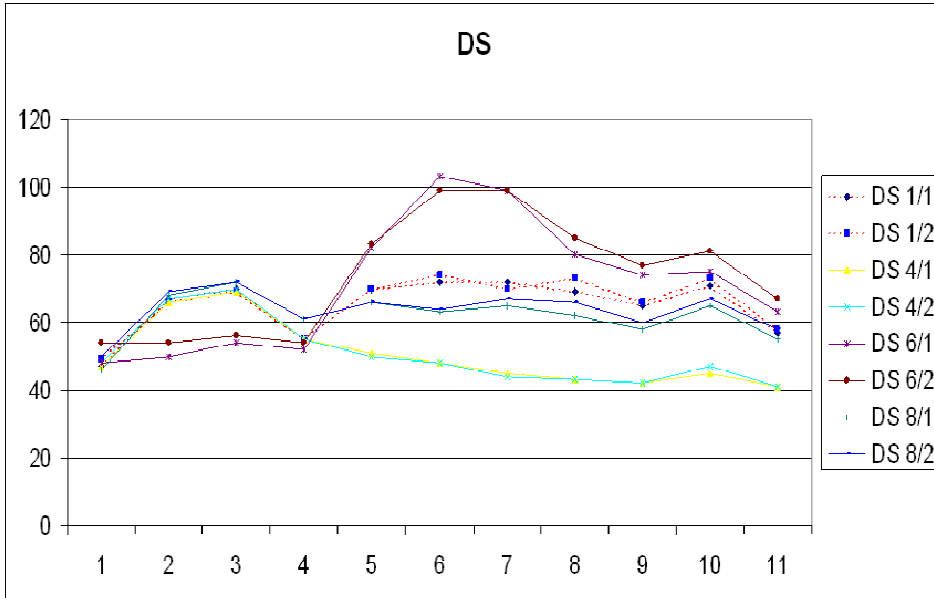
Pict. 11.3.2.2: Web temperatures in drying section – selected trial points - DS2,6:
Low IR-energy at start, DS1,4,8: High IR-energy at start
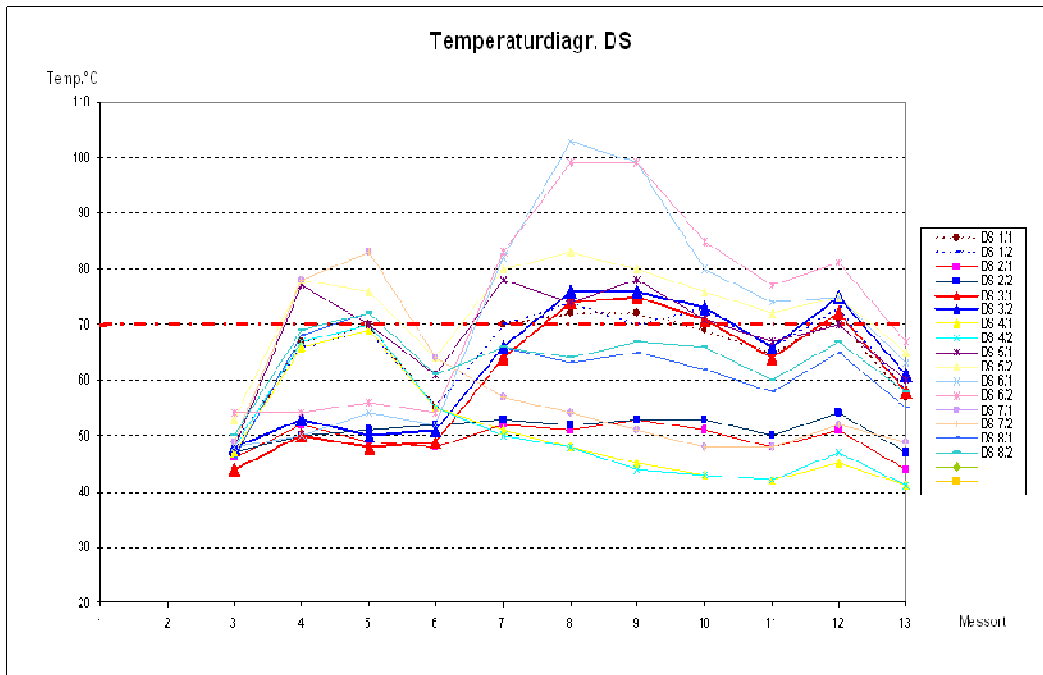
Pict. 11.3.2.3: Web temperatures in drying section – all trial points
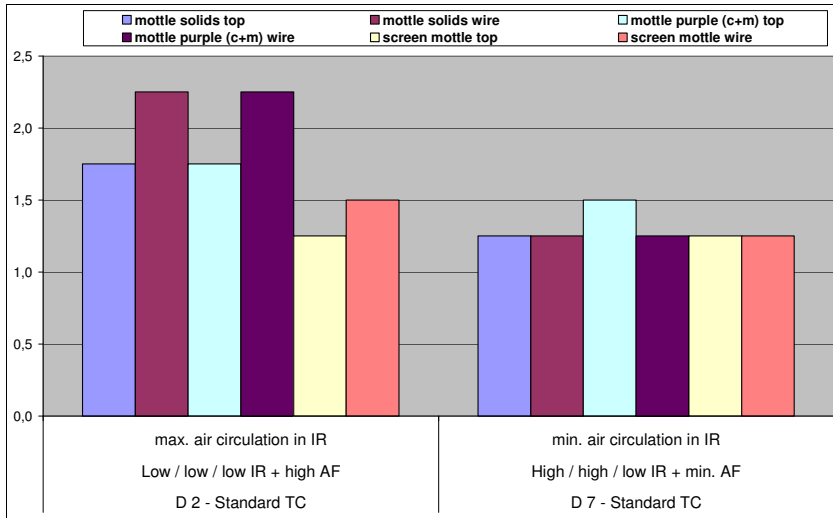
Pict. 11.3.2.4: Mottle of top coated, uncalendered papers: D2 = old drying curve of OMC11, D7 = new drying curve of OMC11
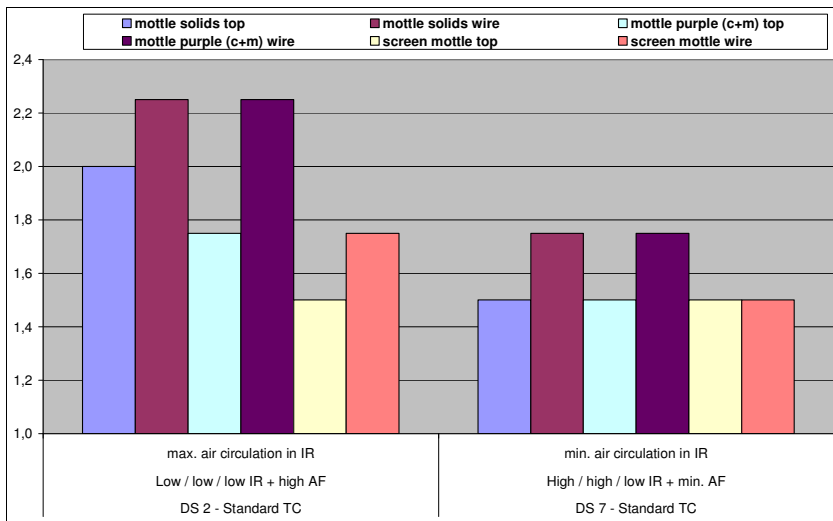
Pict. 11.3.2.5: Mottle of calendared paper: D2 = old drying curve of OMC11, D7 = new drying curve of OMC11

The pilot trial showed that both uncalendered and calendared mottle improved significantly when the new drying strategy was applied where drying started immediately after coating by high IR energy and evaporation rate was reduced in the 2nd drying stage.

The limit of this strategy is the rising amount of craters in the coating surface due to fast evaporation of water in the 1st drying stage. They can be detected under the microscope.
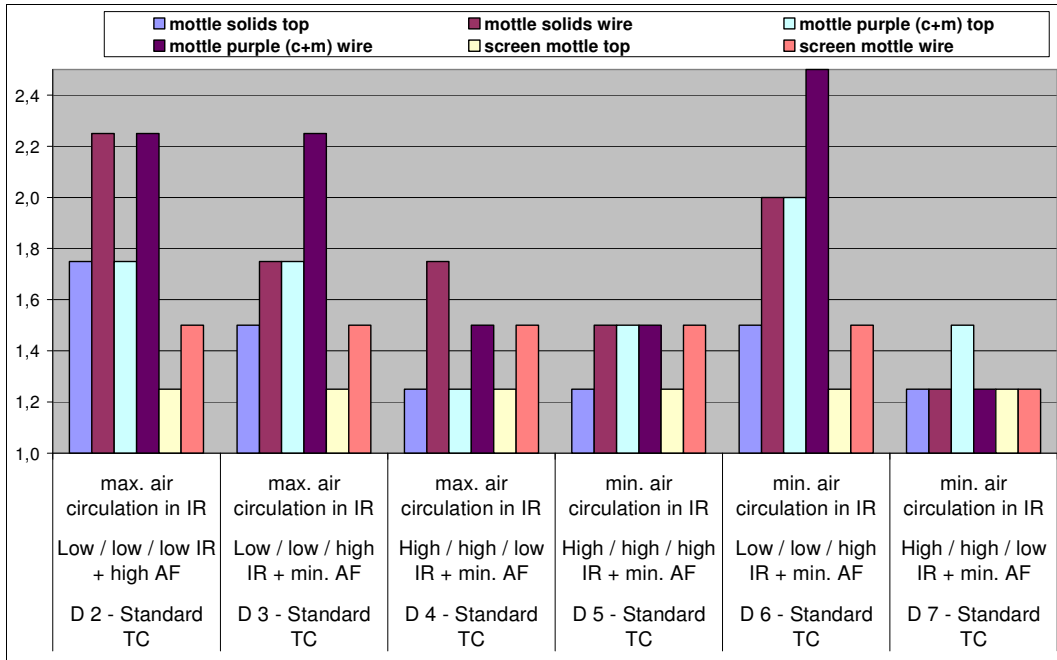
Pict. 11.3.2.6: Mottle of top coated, uncalendered papers
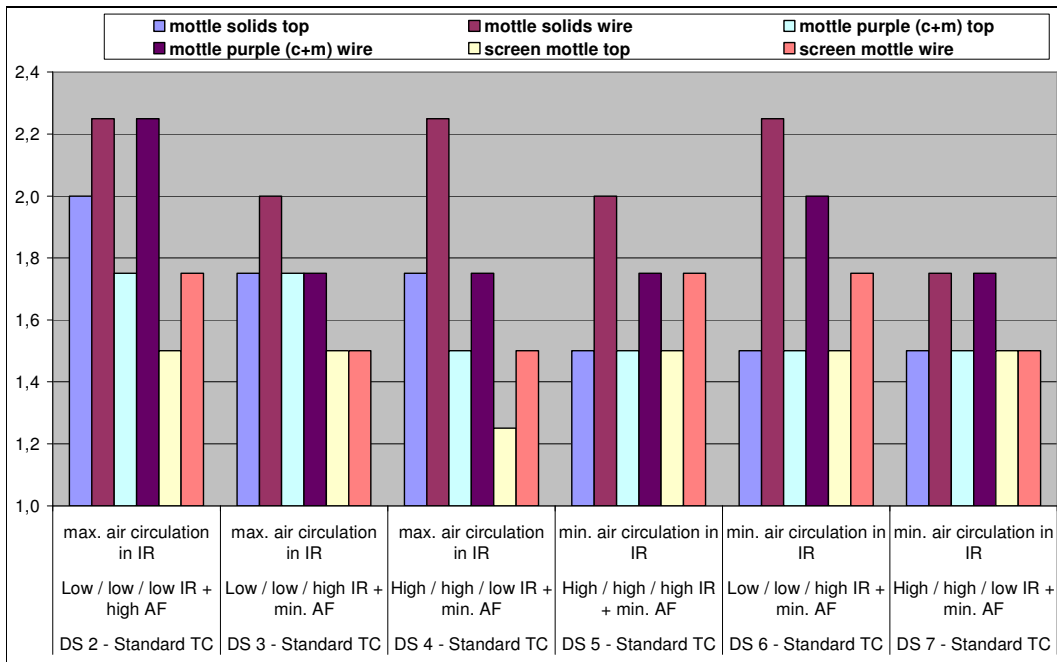
Pict. 11.3.2.7: Mottle of calendered papers

Comparing all applied drying strategies at the BASF pilot trial the conclusion can be drawn that drying has to be started as soon as possible by high energy input in the 1st drying stage. Mottling got worse with delayed drying and high web temperatures in the airfoil section.

The worst mottle was achieved when web temperature low over the whole drying section and latex film forming was not sufficient.

11.3.3 Mill trials with new binder concept in top coatings of OMC11 to improve mottling

The lab trials with new latex types were transferred into the mill by two steps:
In a first step the top coating SB-latex was changed to a type which was faster in film forming by lower gel content in the latex (lower cross linking)
In a second step this latex was partly replaced by SA-latex Acronal S360D and by starch. Both are fast in film forming.

Combining the faster film forming latices with increased web temperature in top coating drying section mottle was significantly improved:
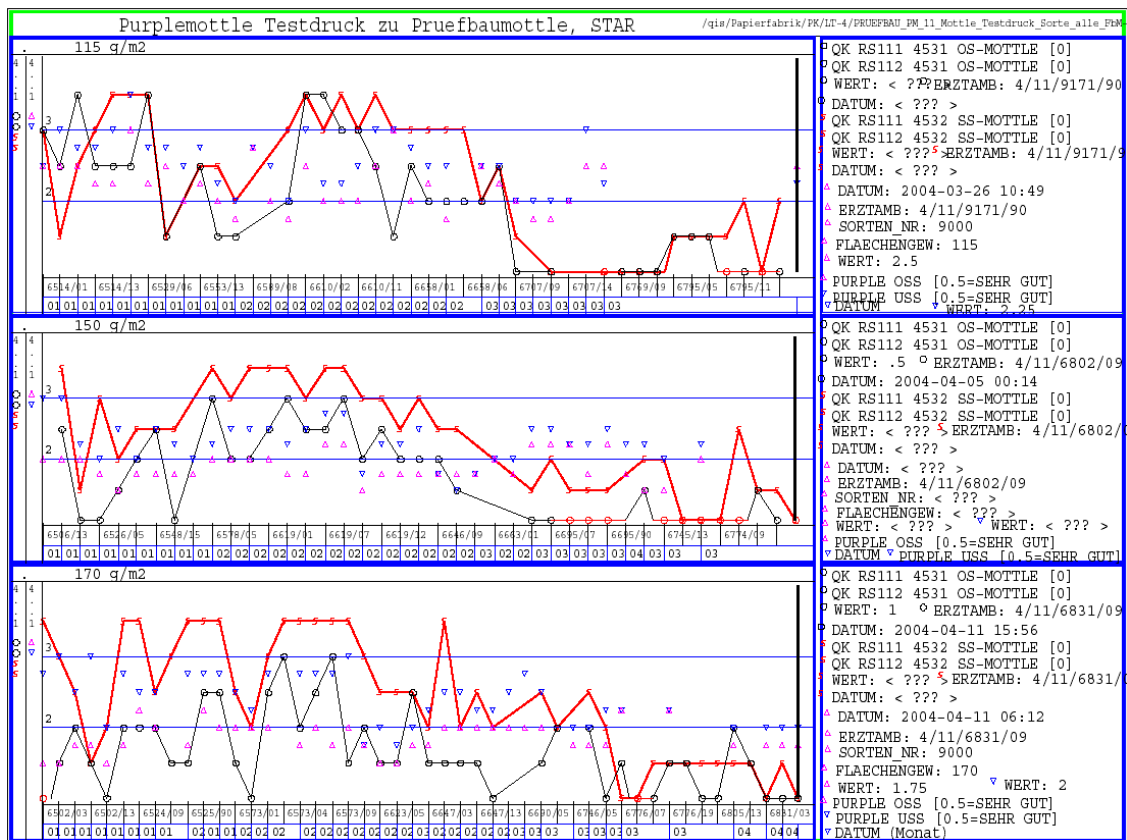
Pict. 11.3.3.1: Trend in mottling after implementation of countermeasures against BTM
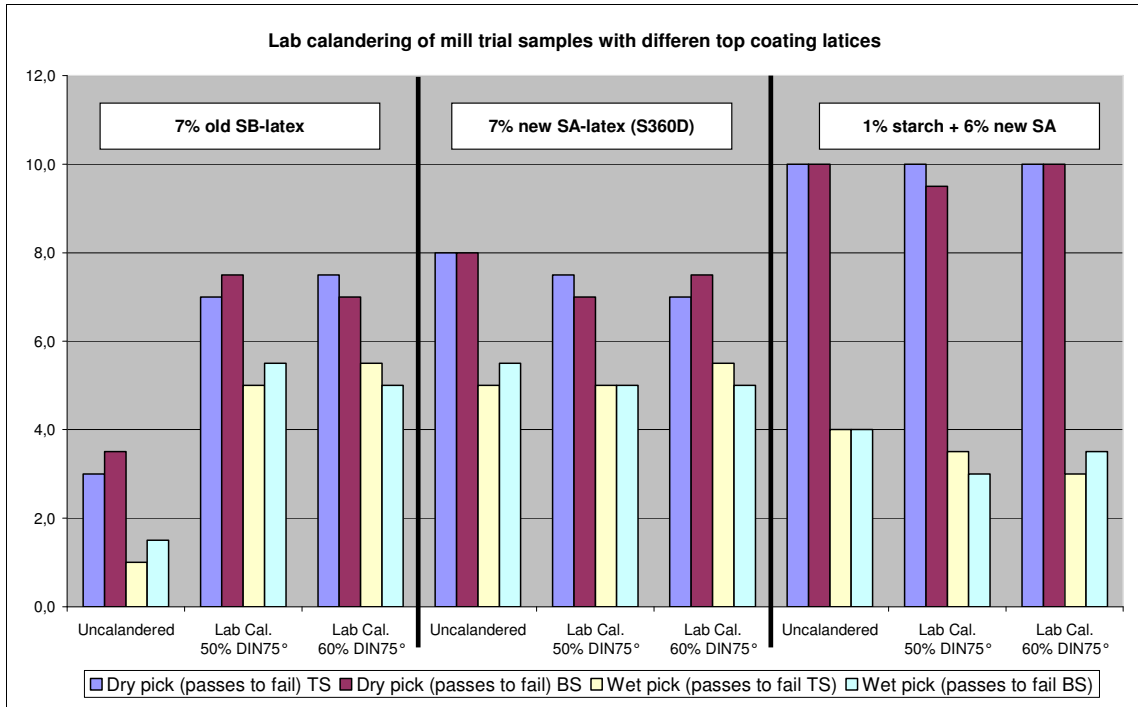
Pict. 11.3.3.2: Picking resistance of new binder concept in top coatings of OMC11

The improvement in film forming of the new SA-latex can be also seen in higher picking strength for fresh coated samples which were tested directly after they were produced at OMC11.

Adding small amounts of starch to top coatings improved film forming further in the same way as it was previously shown by lab results.

Hot lab calendaring is adding film forming and picking strength to the old SB-latex while the new binder strategy was already completely film formed at the coater.
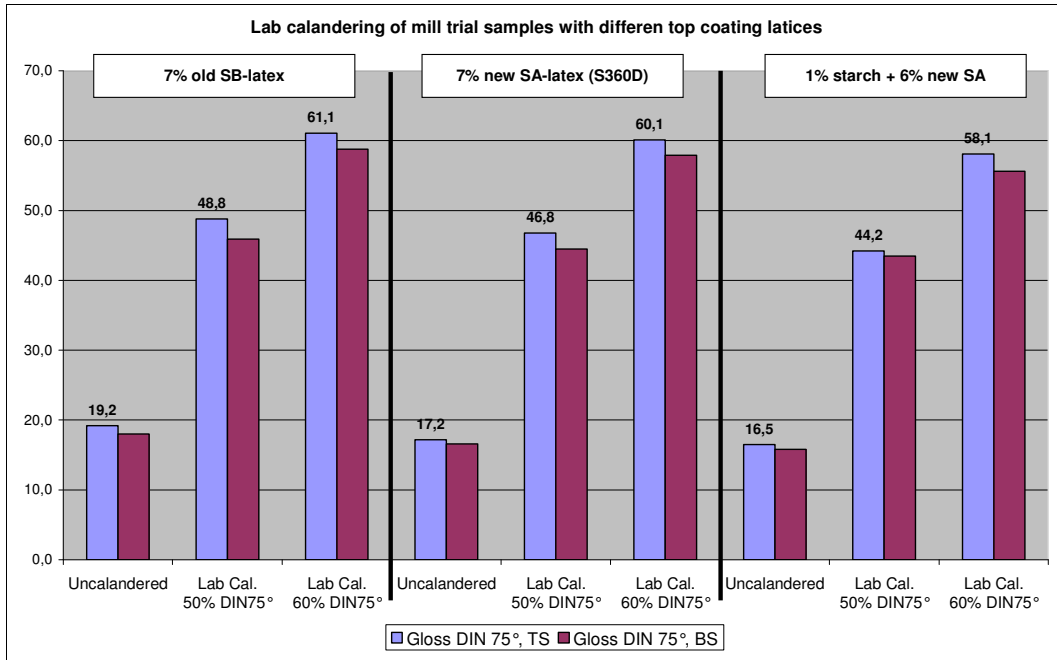
Pict. 11.3.3.3: Gloss of new binder concept in top coatings of OMC11

The higher the degree of film forming in the coating machine, the lower the gloss after the calander was. Therefore mottle improvement at OMC11 was accompanied by a small drop in gloss after calander.
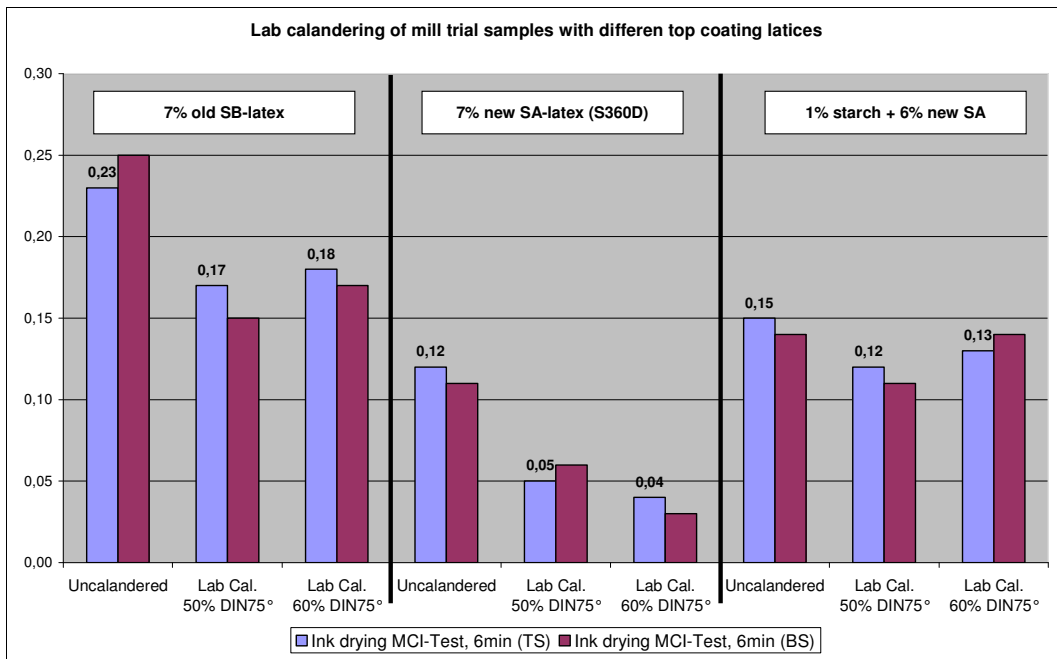
Pict. 11.3.3.4: Ink drying by capillary forces of coating layer for new binder concept in top coatings of OMC11 (lower = faster absorption)

Lab calandering of mill trial samples with differen top coating latices

	7% old SB-latex	7% new SA-latex (S360D)	1% starch + 6% new SA

(Chart values)
- 7% old SB-latex: Uncalandered 46, Lab Cal. 50% DIN75° 47, Lab Cal. 60% DIN75° 50
- 7% new SA-latex (S360D): Uncalandered 6, Lab Cal. 50% DIN75° 10, Lab Cal. 60% DIN75° 9
- 1% starch + 6% new SA: Uncalandered 25, Lab Cal. 50% DIN75° 31, Lab Cal. 60% DIN75° 28

Legend: ☐ Droplet Test, TS ☐ Droplet Test, BS
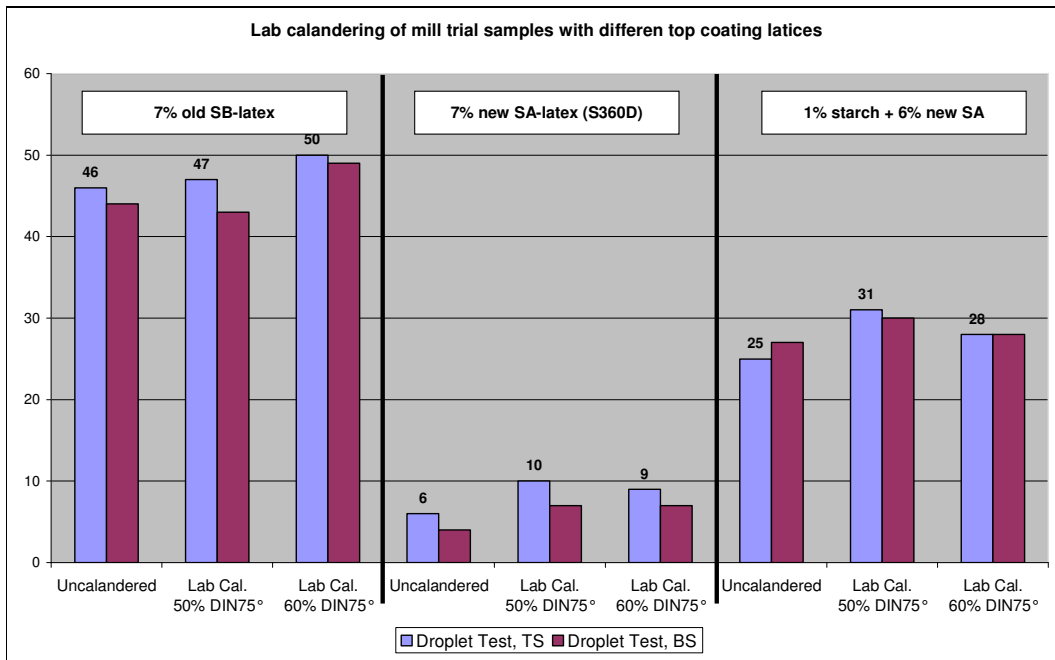
Pict. 11.3.3.5: Water absorption by capillary forces of coating layer for new binder concept in top coatings of OMC11 (lower = faster absorption)

Capillary sorption of both ink and water improved when top coat latex was switched to acrylic latex Acronal S360D as micro-porosity is higher for coarse SA-latices than for fine standard SB-latex (see lab trials and pilot trials).

This higher micro-porosity facilitated the vapour removal in top coating layer after FCC and reduced the risk of back trap mottling by uneven in-plane latex migration.

Acronal S360D improved ink anchorage by higher capillary sorption of the top coating layer and reduced the risk of ink pull off in the following printing nips by back trapping.

In earlier times the higher polarity of SA based top coatings and in consequence the higher affinity to fountain water was used as an explanation for improved mottling. But contact angle measurements with polar and un-polar liquids on SA and SB based coatings show that in fact dry acrylate films are less polar than SB-latex based films.

In a mill trial which aimed at mottling improvement the top coat latex was changed from a mixture of SA/SB to 100% SA-Latex.

sappi GK/PQ	TITEL		
INT.U-NR.		Standard: 70% S360D + 30% SB	Trial: 100% Acronal S360D in top coat 399
PM 11 57/2009 BV 16d KW 51 2009	Sorte-g/m²	Star 150 g/m²	Star 150 g/m²
	Erz. / MR	Mittelw.	Mittelw.
Basis weight	g/m²	149,2	148,3
Thickness	mm	0,107	0,106
Bulk	cm³/g	0,72	0,72
Ash	%	50,0	50,0
GLOSS (Tappi)	%	OS	68,9	67,1
	%	SS	72,9	72,0
GLOSSS (DIN75°)	%	OS	55,0	53,7
	%	SS	56,0	55,6
Cobb (60)	g/m2	OS	44	43
	g/m²	SS	49	48
Set off, 30 sec		OS	0,36	0,43
		SS	0,34	0,39
Mottlingtest		OS	3,00	2,25
		SS	3,00	2,58
Droplet Test	%	OS	44	51
	%	SS	44	52
Passes to fail with prafin (dry)		OS	5,0	5,3
		SS	5,0	5,3
Passes to fail with prafin (wet)		OS	3,8	4,5
		SS	4,0	4,5
MCI-Test(GK/PQ)	2 min.	OS	0,67	0,70
		SS	0,49	0,50
	6 min.	OS	0,07	0,08
		SS	0,05	0,05
	10 min.	OS	0,02	0,02
		SS	0,02	0,02
TD / Mottling sreen		OS	1,50	1,50
		SS	1,50	1,50
TD / Mottling backtrap		OS	1,50	1,25
		SS	1,63	1,50
TD / Mottling purple		OS	2,25	1,88
		SS	2,38	2,00

Pict. 11.3.3.6: Mill trial at OMC11 with 100% SA-latex Acronal S360D in top coat

Polarity of the top coated and calendared surface was checked by the Fibro-DAT system. Droplets of polar distilled water (surface tension 72,8 mN/m) and un-polar DMSO (Dimethylsulfoxid) (surface tension 44,1 mN/m) are applied on the surface and contact angle is measured. From both measurements the polar and the dispersive (unpolar) surface energy is calculated.

According to Owens and Wendt the dispersive and the polar part of surface energy is calculated with:

Equ. 11-3-3-1: $\sigma_l * (1 + \cos\theta) = 2 * (\sqrt{(\sigma_l^{\,d} * \sigma_s^{\,d})} + \sqrt{(\sigma_l^{\,p} * \sigma_s^{\,p})})$

σ^d.....dispersive part of surface tension

σ^p.....polar part of surface tension

σ_l......liquid surface tension

θ......contact angle
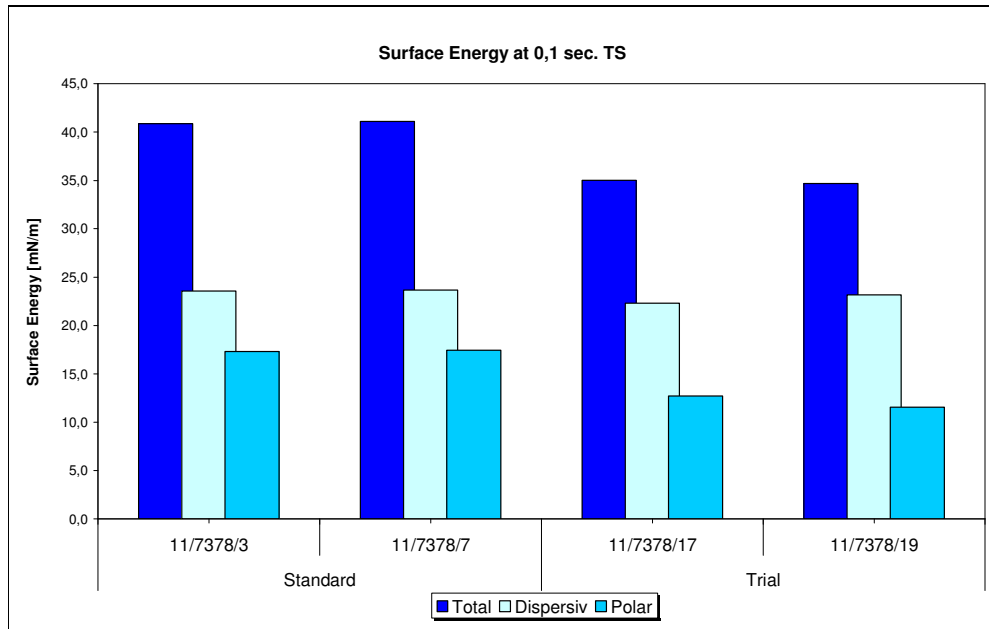
Pict. 11.3.3.7: Polarity of surface, top side
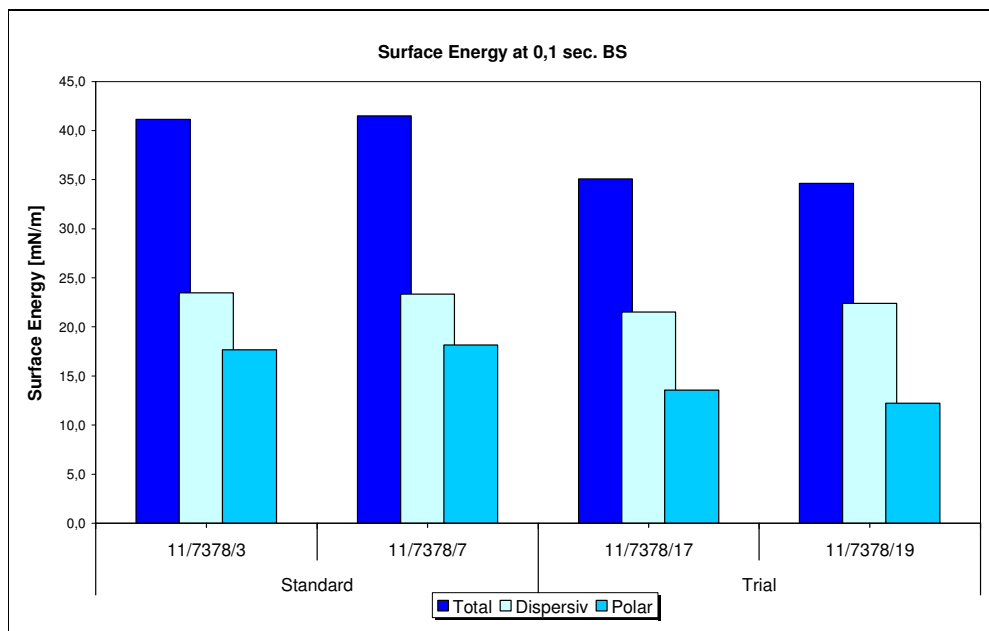
Pict. 11.3.3.8: Polarity of surface, bottom side

11.3.4 Influence of calendaring on latex film forming

In the next part the influence of the calander on latex film forming and mottling was studied.

Hot calendaring will add film forming as paper web temperature is in the range of 80 – 90 °C, which is clearly above the surface temperature in the drying part of the coating machine and clearly above the MFFT of all commercial latices.
As this temperature is also above the Tg of the latices they will get soft and the coating layer can be compacted under pressure.
The lower the degree of film forming in the coating machine the easier the coating film can be compacted in the calander. Local differences in latex film forming will therefore lead to local differences in coating layer porosity and in consequence to ink transfer in the printing press.
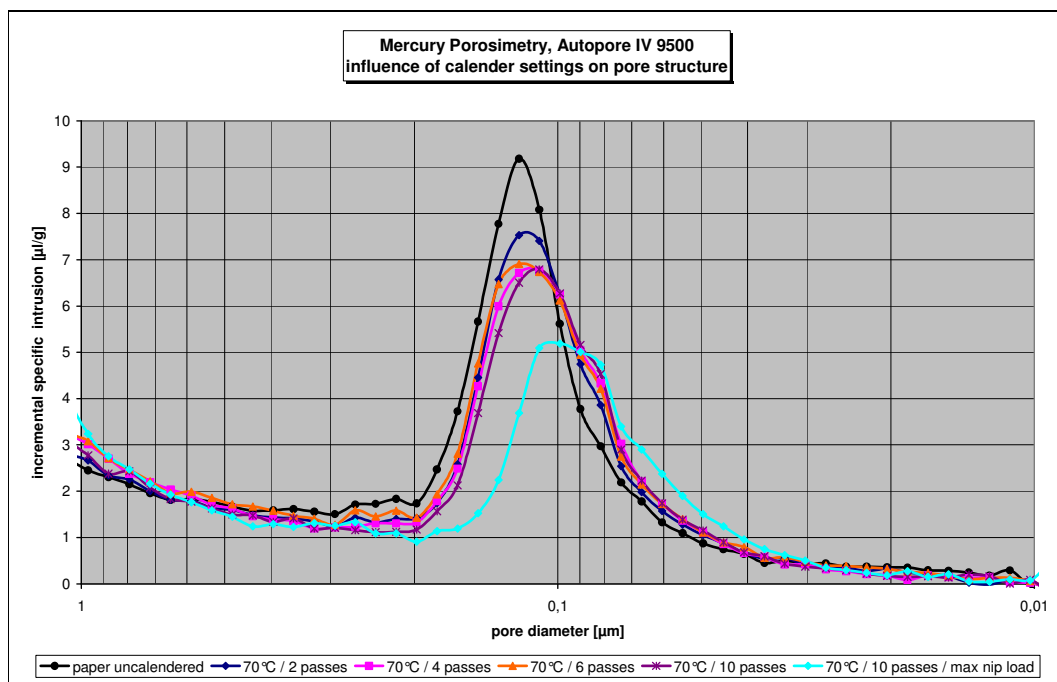
Pict. 11.3.4.1: Hot lab calendaring – influence of nip load and nip passes on Mercury porosity of coating layer (source: P. Resch)
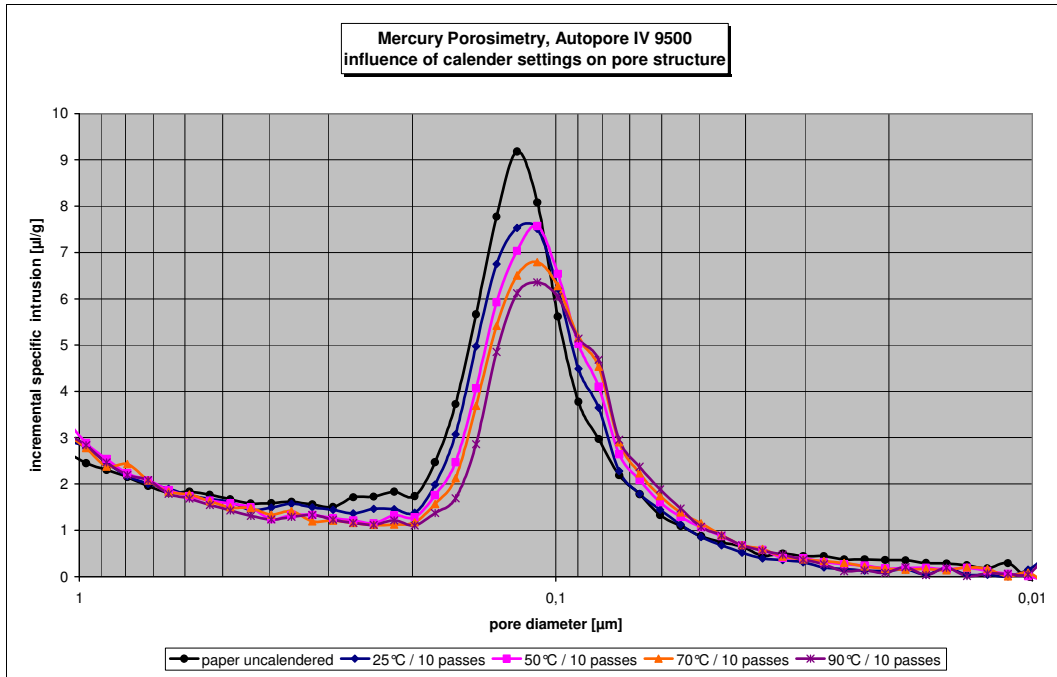
Pict. 11.3.4.2: Hot lab calendaring – influence of nip temperature on Mercury porosity of coating layer (source: P. Resch)
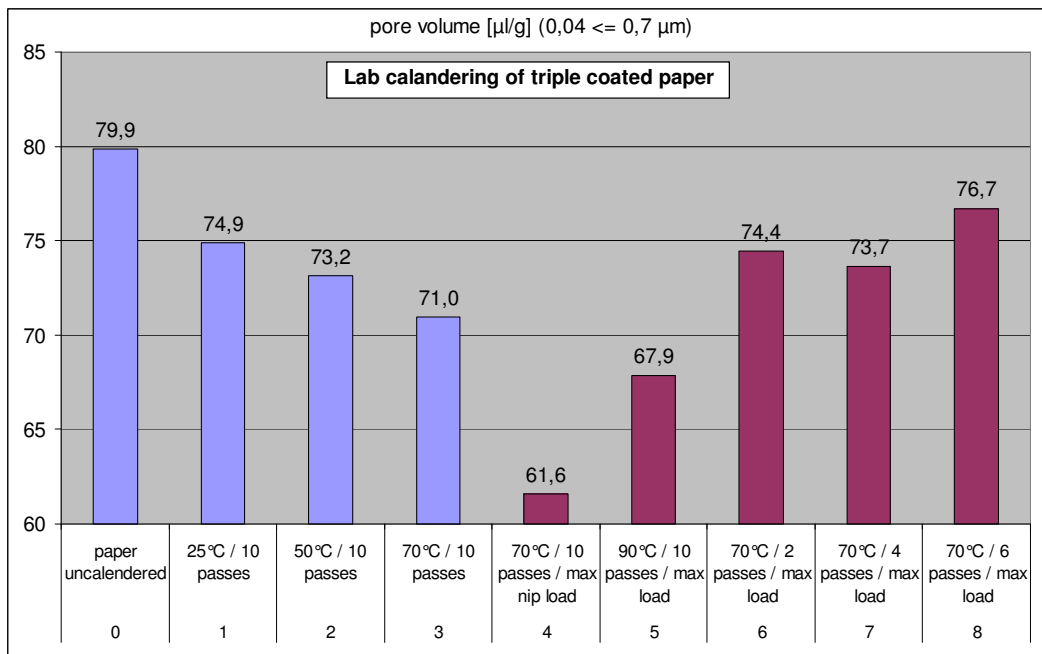
Pict. 11.3.4.3: Loss in coating layer porosity by hot calendaring for different latices

As the local pressure in the calander is higher at flocs, coating layer compaction is more severe at flocs. Coating layer porosity will be lower at flocs than at voids.

Page 784

Therefore it is a common fact, that coated papers are more critical in back trap mottling when calendared to high gloss.
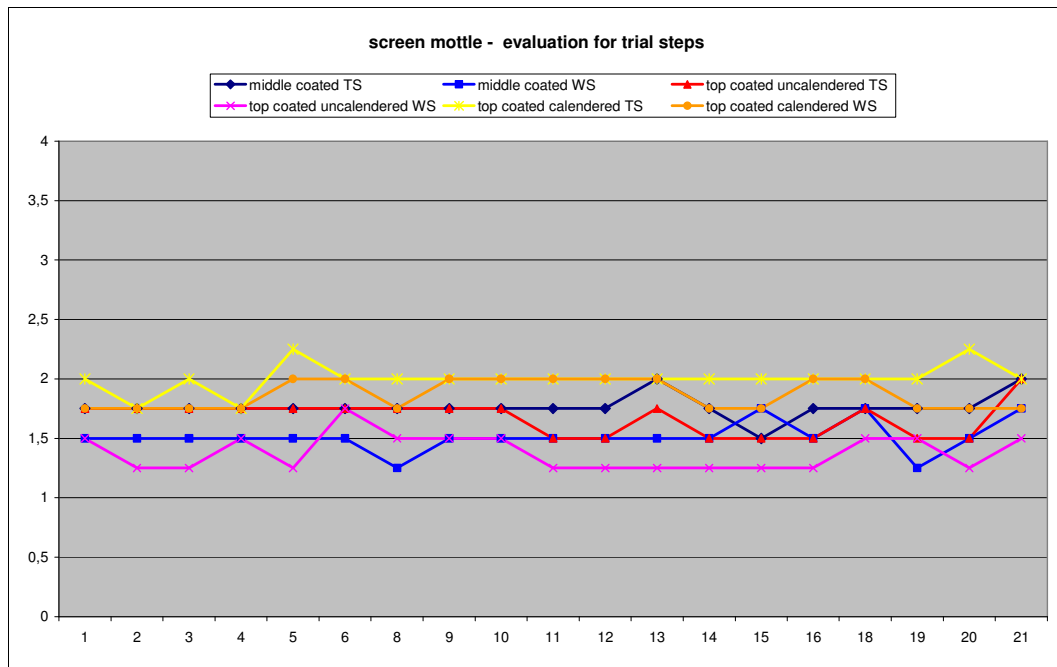
Pict. 11.3.4.4: Screen mottling for different coating steps and after calendaring

Local differences in coating layer porosity will increase when the latex gets soft during heating in the calander.

When the top coating latex isn't properly film formed in the coating machine the coating layer can be compacted more easily in the calander. When latex is fully film formed in the coating machine it reaches its maximum in stiffness. This stiffness gets lost during hot calendaring as the latex is softened when the Tg is exceeded (which happens for almost all commercial latices in modern hot calanders with polymer rolls where web temperature is in the range of 70 – 90 °C in the bottom nips).

Therefore low web temperatures in the coating machine can create severe back trap mottling after hot calendaring. The only advantage of a low film forming in the coating machine is a higher gloss after calendaring as the pigment matrix can be compacted more easily.
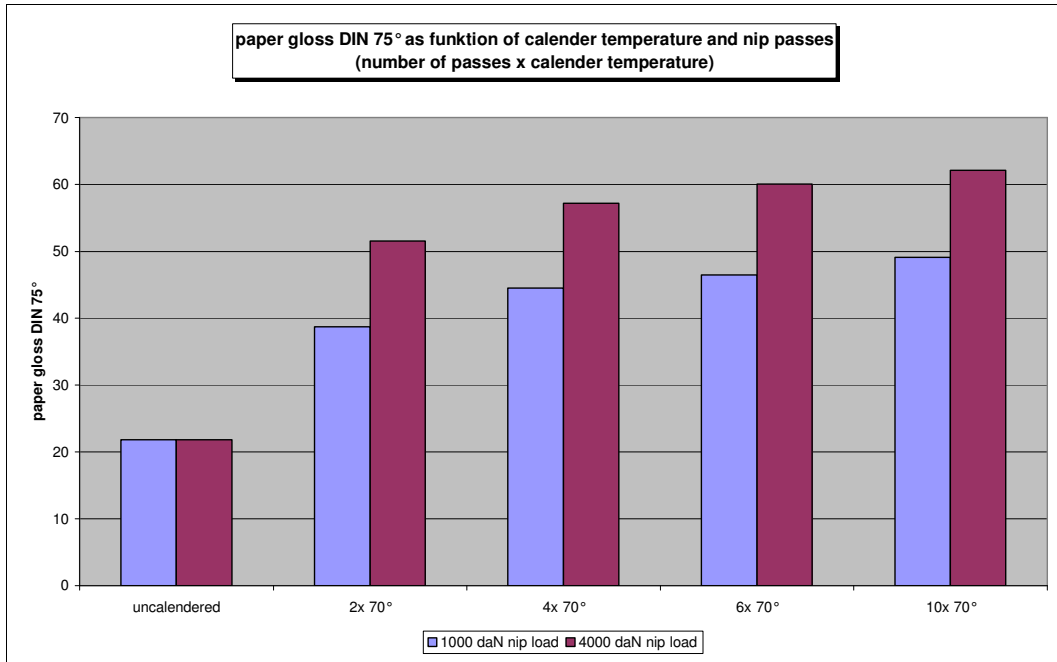
Pict. 11.3.4.5: Gloss increase with nip load in lab calander (source: P. Resch)
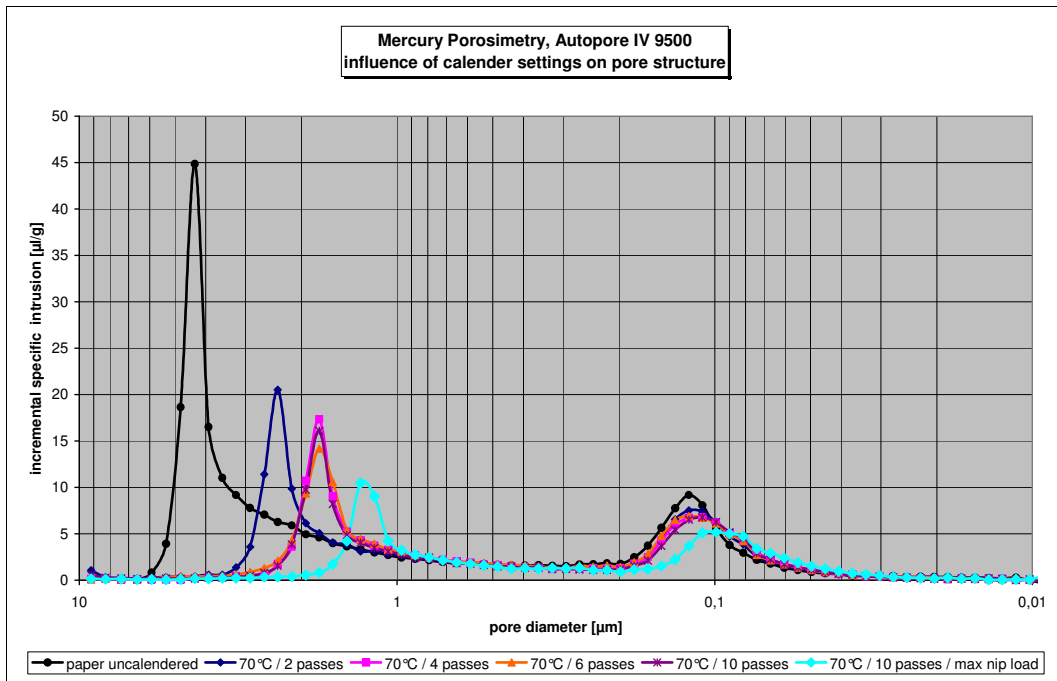
Pict. 11.3.4.6: Loss in pore volume of base paper and coating with nip load in lab calander (source: P. Resch)

The Mercury porosity readings show the loss in pore volume of base paper by coating layer compaction with increasing number of passes in the lab calander.

When mottling is optimized by comparing different types of latices the difference in coating layer porosity before and after calendaring should be independent on drying conditions at the coater.

The four latices (soft SA-latex S360D, soft SB-latex LTX310, hard SB-latex SB256 and dextrine starch C-Film 7333) which were compared in the previous lab drying studies were compared in their calendaring properties.
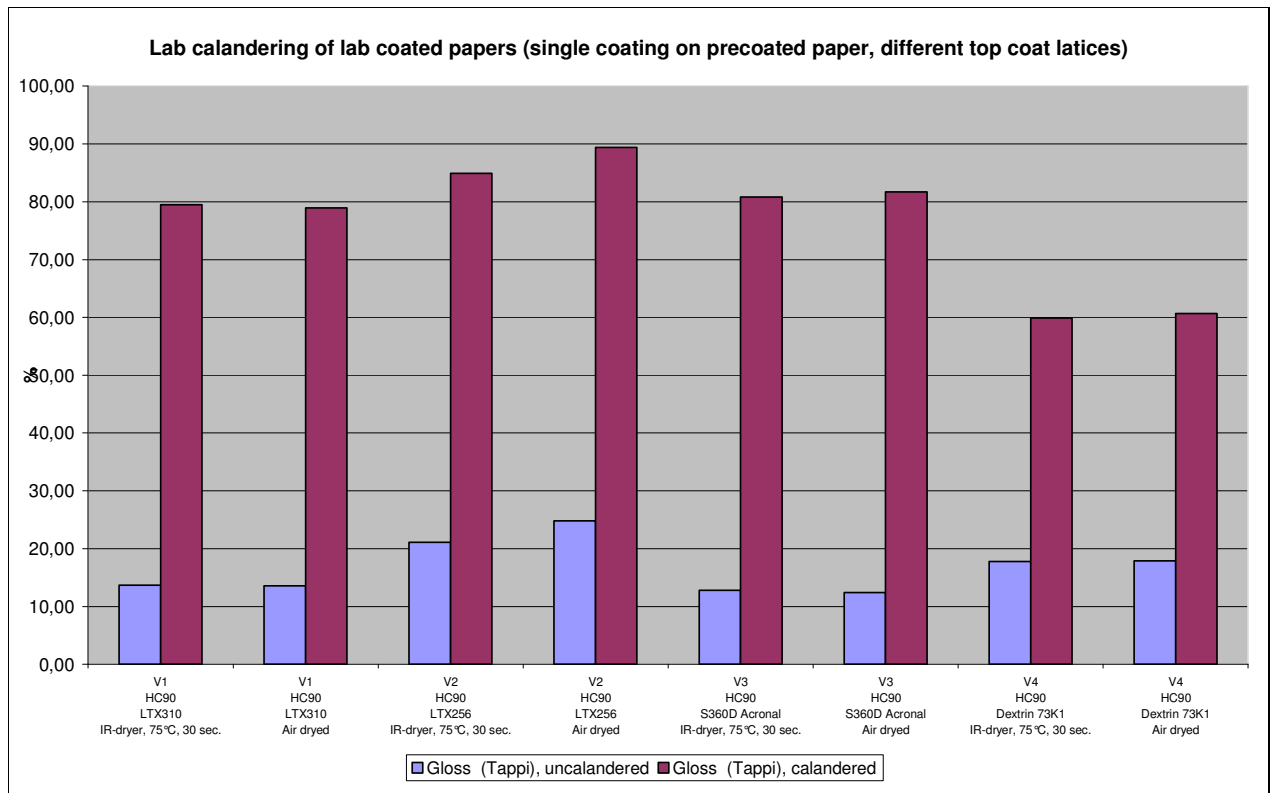
Pict. 11.3.4.7: Tappi gloss of lab coated and lab calendared papers
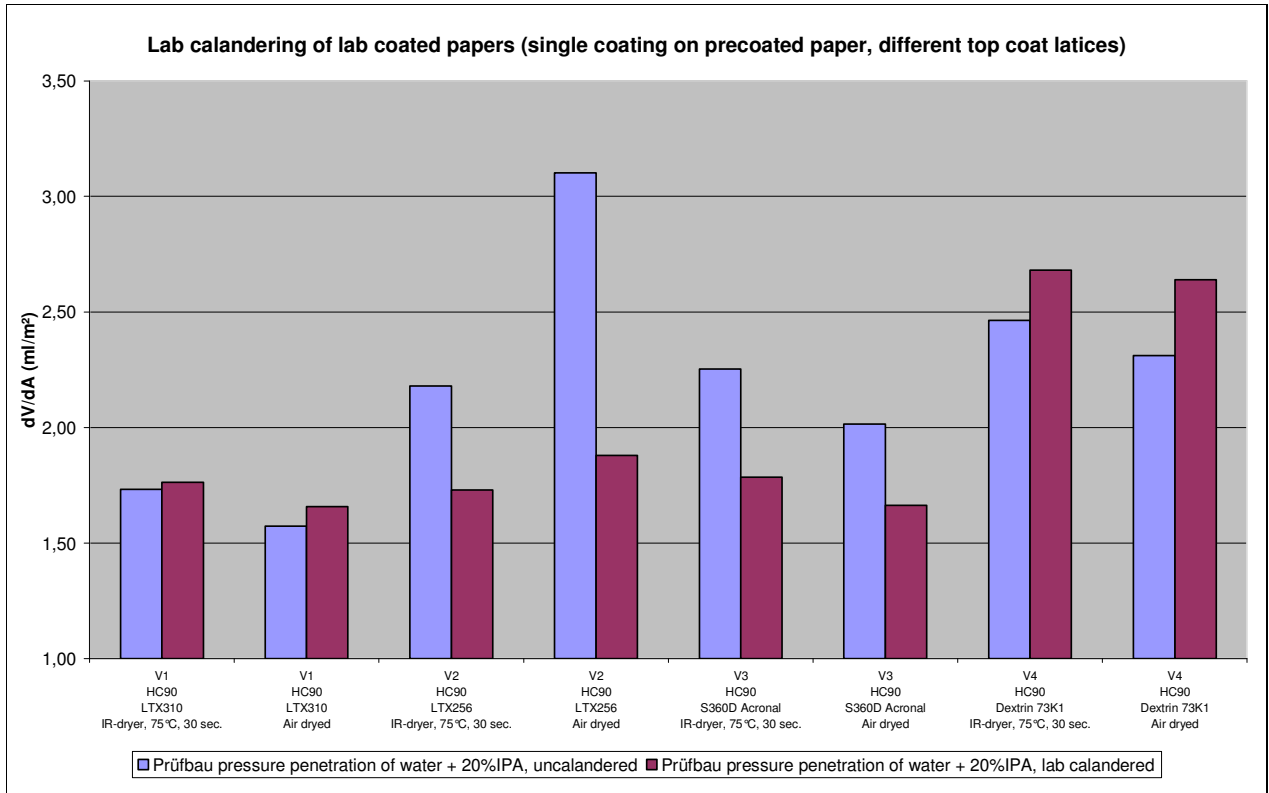
Pict. 11.3.4.8: Pressure penetration test of lab coated and lab calendared papers
(lower dV/dA = lower Darcy coefficient = denser coating)
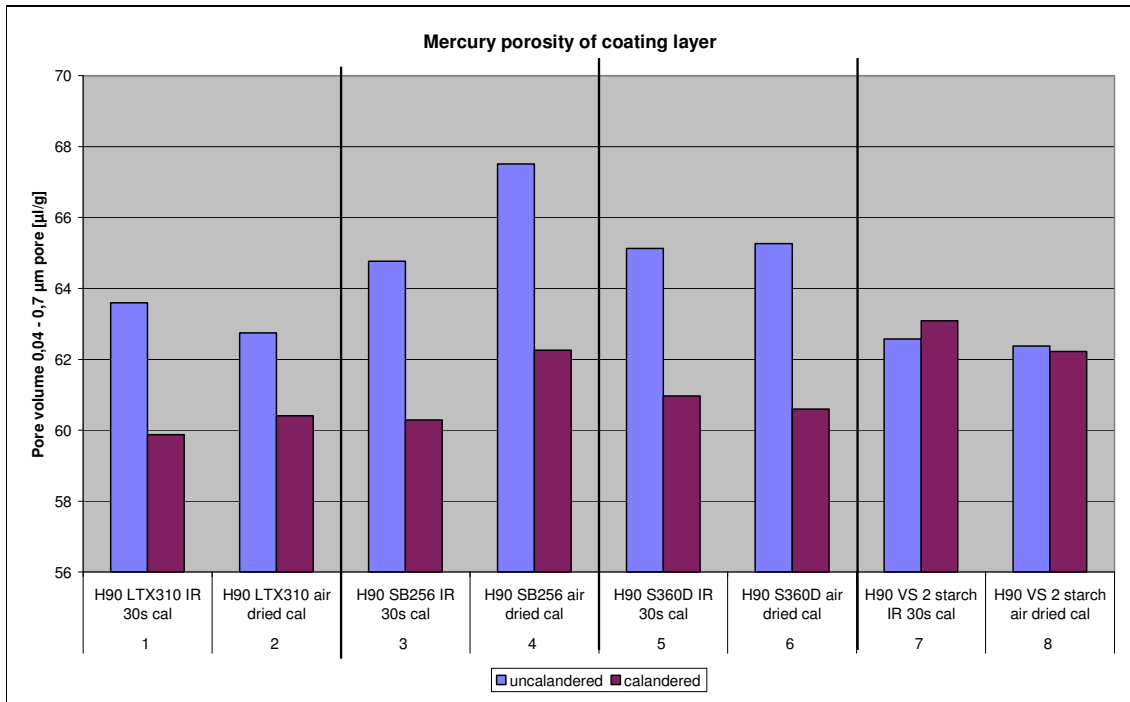
Pict. 11.3.4.9: Mercury porosity of coating layers

Results in coating layer permeability for uncalendered samples:
- The highest permeability was again measured for coarse and hard SB-latex SB256=LTX256. Increasing the web temperature during drying above MFFT lowered permeability of coatings based on this latex.
- The other latices and starch were insensitive against variations in drying conditions as their MFFT is lower than room temperature. Fast drying by IR leads to much higher shrinkage forces than for air drying under room temperature. Permeability of SA-latex S360D increased with raising shrinkage forces during drying as micro-cracks in the latex film are formed in the 2nd drying stage.

Results in coating layer permeability for calendared samples:
- The biggest drop in coating layer permeability by calendaring happened for the hard SB-latex SB256 as film forming was not complete after coating. Therefore coatings based on this latex are extremely sensitive in calander mottle on drying conditions and latex film forming at the coater.
- SB256 coatings showed the highest gloss after calendaring due to low film forming during drying of the coating. Less energy was needed to orientate and compact the pigment matrix at the surface.
- **Starch** is the total opposite: As film forming is complete after removing the water in the coating machine and stiffness of starch based coatings stays high during heating in the calander (softening is less pronounced than for latices) **porosity and permeability stay almost unchanged during calendaring** which is advantageous to avoid permeability differences in the coating layer by calendaring but disadvantageous to get a high gloss - a much higher energy is needed in the calander to re-orientate the pigment particles.
- Permeability of SA-latex Acronal S360D dropped by calendaring to a higher extends than that of soft SB-latex LTX310 and starch as a binder.

Lab calandering of lab coated papers (single coating on precoated paper, different top coat latices)

Legend: Opacity uncalandered ■ Opacity calandered
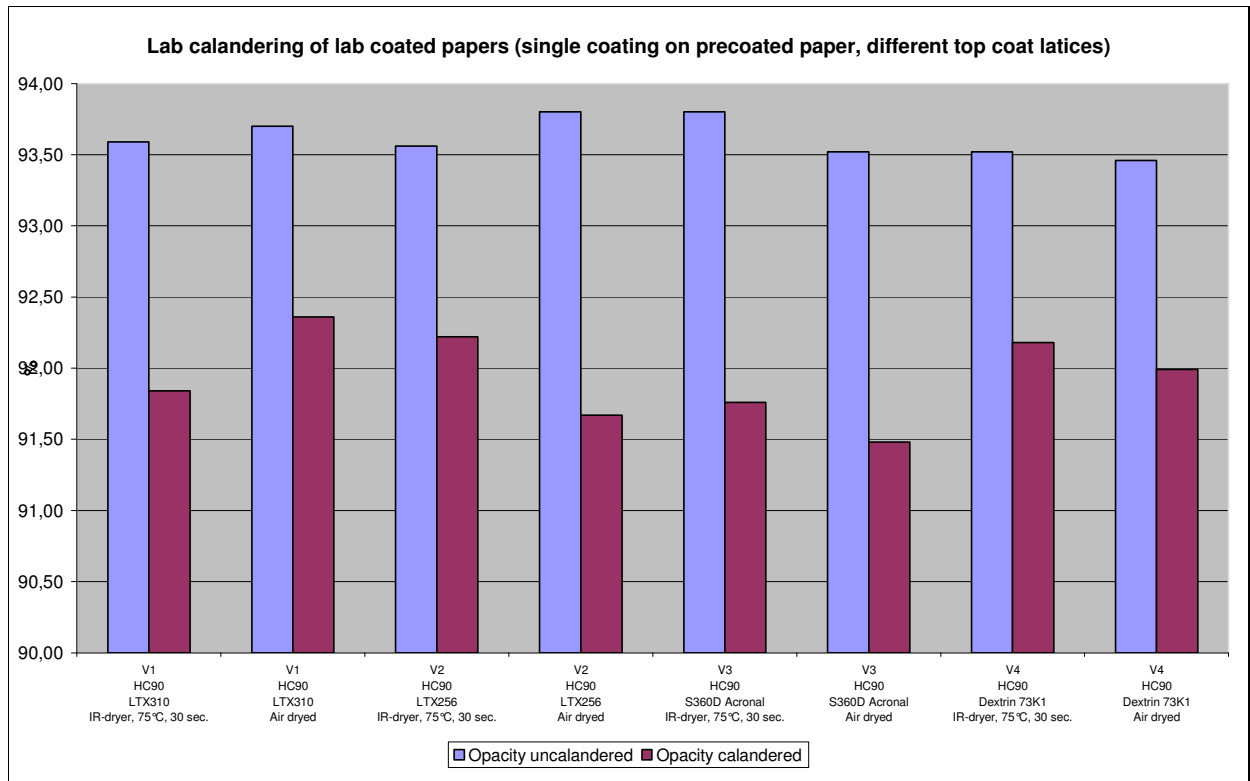
Pict. 11.3.4.10: Opacity of lab coated and lab calendared papers

A similar effect can be seen in the opacity: When film formation is poor, the coating layer can be more easily compacted in the calander and opacity drops with lower pore volume of the coating layer to a higher extend than for fully film formed latices. This can be seen for the air dried latex SB256.

When the film formation is perfect, the loss in opacity by calendaring is much lower – visible for the Dextrine starch.

On the other hand a higher calander pressure is needed for these binders to achieve a certain gloss.

Summary calander study:

To reduce the negative impact of hot calendaring on back trap mottling binders should be chosen for top coatings, which provide the lowest possible drop in coating layer porosity and permeability by calendaring.

When nip pressure is applied mainly at flocs, coating layer porosity and permeability would stay in the same level as at voids next to them. In-plane ink sorption by capillary forces would be kept on a comparable level and BTM would improve.

From this study starches can be recommended for that purpose.

Mill trials with 1 – 2% starch in glossy top coatings instead of latex proved that mottling can improve when starch is used in top coatings. Preconditions to achieve this result are constant high solids (use high solids starches) and moderate drying conditions after the FCC.

Conclusion and mill implementation:

At fast coaters the risk of insufficient latex film forming is relatively high. Lab investigations showed a huge difference in vapour permeability and ink absorption between non-film-formed and totally film-formed latex in coatings. These local differences are responsible for back trap mottling which is highly dependent on capillary forces.

At OMC 11 latex film forming was generally improved in top coatings by **higher web temperature** and by switching to **latex types which are easier to film form**. **Starches** and **soft acrylic latices** provide this property. Meanwhile also SB-latices with film forming additives are available.

When **latex particle size** is increased vapour permeability of coating layer increases and the risk of drying mottling after FCC by uneven latex migration to the surface is reduced. Drying energy demand drops with these latices.

As starch forms a binder film with low vapour permeability the risk of drying mottling is highest for all tested binders. Migration with vapour to the surface is easier due to lower size of molecules when compared to latex particles.

Adding 1 – 2% starch to top coatings improved back trap mottling at glossy grades as differences in compaction of coating layer in calander were reduced.

Chapter 12: Executive summary and outlook

The trigger of this PhD work was the deterioration of formation mottling when speed of PM11 was increased from 1000 to 1500 m/min. This speed increase was accompanied by a decline in formation, harder and stronger flocs, higher blade pressure and more elevated penetration of liquid phase into the base paper.

Additionally the share of natural convective drying increased and IR-energy was reduced which provoked drying induced mottling.

The countermeasures to bring both kinds of mottling back to the original level of PM11 after startup are described in this PhD work.

The experience from many years of mottling comparison of PM9 (hybrid former) and PM11 (gap former) proved that **formation** is the most critical parameter for mottling. Gapformers produce base papers with worse Ambertec formation leading to worse screen and backtrap mottling.

Replacing the onsite produced long fibre sulfit pulp by Eucalyptus sulphate would improve formation in general but also the **compressibility differences** between flocs and voids as the compression studies showed. Correlating formation induced mottling with base paper parameters showed that mottling is not described completely by the Ambertec formation. The 2D compression matrix of the base paper or in other words the compressibility difference between flocs and voids is of high importance as it determines the difference of water phase penetration from coating applied on top of flocs and voids.
Flocs with high density of fibres and fines are much less compressible than corresponding voids with low density. Wet pressing increases these local compressibility differences.

The main goal of formation improvement trials at PM11 in the last years was to form "softer" flocs – exactly spoken to reduce the gradient of basis weight between flocs and voids.

This was achieved by reducing the length of the sheets in the headbox which leads to bigger but softer flocs; contrast between flocs and voids is lower than for "hard" flocs. Formation induced mottling improved in comparison to hard and small flocs from long sheets.

Additionally the retention system was switched to a three component system with low demand of high molecular weight CPAM. Lab studies simulating headbox feed flow showed that CPAM's produce stable and dense flocs.

Filmpress trials of J. Grön showed already that coating holdout and mottling improved with increasing base ash content at the surface of the base paper.

PM11 gapformer produces an extremely two-sided base paper due to 45° configuration with high ash content at the surface of the top side and low ash on the bottom side. The ideal gap former would have a vertical design with symmetrical dewatering and high capacity of dewatering in the primary dewatering area. Pilot trials will be performed in the future to prepare a proper former design for a potential rebuilt of gapformer PM11.

A small improvement in two-sidedness of PM11 was achieved in the last years by increasing the FSP index of the bottom wire and changing the base filler to a coarser carbonate.

The increase in speed of PM11 increased the ratio of primary dewatering as centrifugal forces increased. Therefore formation got worse as the consistency in the bar-section increased and less fibres were re-orientated in this section.

The development of denser wires reduced the retention aid demand, delayed dewatering in the D-bar section and shifted the water line to the same point in the D-bar-section as before speed increase. A former dewatering model was established to calculate the water line and to observe the trials with different wires.

The development of wire types and retention systems can be regarded as terminated.

The disadvantage in formation of PM11 is partly compensated by the **filmpress precoaters** which apply the coating colour with much lower pressure than blade

coaters. Lowering the application pressure reduces penetration differences of liquid phase into flocs and voids. Mill trials showed the advantage of the filmpress precoater against a blade precoater for double coated grades of PM11.

The ideal precoater would be a curtain coater. Recent pilot trials have proven this theory.

To reduce the blade pressure at middle and top coaters of OMC11 a hew generation of TC-blades was developed with much shorter facet length.

The most successful step in mottling improvement of PM11 was done by reducing the Darcy coefficient (**permeability**) of the **precoatings**.
Parts of the standard coarse carbonate Hydrocarb 60 were substituted by fine carbonate Hydrocarb 90 to achieve the densest possible structure of the pigment matrix.
In addition to this measure latex was replaced by starch which reduced costs and improved simultaneously quality.
As coating starch demand increased the quality was changed from dextrine to enzymatic converted type. Conversion is done onsite and costs of this starch are one-quarter of the latex price (comparison based on bone dry material).

The main disadvantage of rising starch content in the precoatings was the worsening of cracking-on-the-fold.
A material was found which acts as a starch softener. Pilot trials proved that almost latex free precoatings can be applied which combines the improvement in mottling with cracking advancement and cost reduction.

Another method which reduces costs and simultaneously improves mottling is to reduce the permeability of the precoatings by keeping the binder (latex or starch) in the coating layer or in other words reducing the loss of binder into the base paper during pressure application of the coating colour. The corresponding measure is to increase the water retention of the coating colour as the small latex particles and soluble binders / co-binders like starch, PVOH or CMC travel with water into the base paper.

A new pressure penetration test was developed at the Prüfbau lab printing instrument to describe the penetration of liquids into different base papers or precoating layers.

One of the most effective ways to **improve water retention** is to **increase the solid content** of the coating colour. The gap between coating and immobilization solid content is reduced and the formation of an immobilized layer in the filmpress nip is accelerated. This immobilized layer acts like a barrier layer against penetration of latex particles into the base paper.

Solid content in working tanks of blade coaters rises continuously with operating time due to capillary sorption of the base paper between application and blade. Filmpress coaters show no increase of solid content in the working tank as recirculation rate is much lower and penetration time is much shorter. The contrary happens as water from rod lubrication and side sealings is diluting the coating colour in the working tank.

To increase the solid content of PM11 precoatings a dosing unit for dry pigment or starch was built. Solids up to 74% are now reality at the filmpress precoaters of PM11.

One of the most effective ways to improve mottling would be the pressure-less application of a barrier layer between the coating layers. A soft starch could be used as barrier liquid. Curtain coating is the only possibility for successful application. If the liquid is applied under pressure mottling would deteriorate as barrier liquids are relatively low in viscosity and differences in penetration depth of barrier liquid cause differences of water phase penetration from coating colour of the subsequent coater.

At blade coaters local penetration differences of water phase from coating colour (together with latex particles and soluble cobinders) can be reduced by increasing the thickness of the immobilized coating layer before the blade. Unfortunately this layer doesn't exist in top coatings of triple coated papers where capillary sorption pressure of the dense double precoated paper is much lower than that of the uncoated base paper.

At blade coaters with highly absorbent base paper and coating colours with low water retention a thick immobilized layer is formed between application and blade. When

the solid content of the coating colour under the blade reaches the immobilization solid content wet bleeding occurs.

Increasing the solid content of the coating colour in the working tank of blade coaters and increasing thereby the thickness of the immobilized layer before the blade by reducing the amount of water retention additives in the coating colour doesn't necessarily lead to improvement of mottling as these agents are important to avoid latex penetration with water phase into the substrate.

If water retention additives are reduced in coatings more binder particles and soluble cobinders are lost into the base paper and permeability of the immobilized layer and the dry coating layer increases which is detrimental for mottling. Therefore only high solids combined with high water retention of the coating colour offers the possibility to improve mottling.

Mills trials where the water retention agent was taken out almost completely from top coatings to allow an increase of the solid content to a maximum level of 72 – 76% showed worsening of print mottle as water phase viscosity was lowered by this measure.

A new lab method was set up to measure separately water phase viscosity and coating colour rheology parameters. Coating colour viscosity is a sum of liquid phase viscosity and particle – particle or particle- liquid phase – interaction. All three mechanisms can be described now separately with this new lab method. The results show severe depletion flocculation of the dispersed carbonate particles by almost all currently used coating colour components including serum from latices, caustic soda, PVOH or thickeners. This kind of interaction is unwanted for the coating process as it increases blade load and reduces paper gloss.

As a result of the lab study a **new generation of synthetic thickeners** was developed to reduce latex penetration with liquid phase into the base paper. These HASE (hydrophobically modified alkali swellable emulsified) thickeners provide high liquid phase viscosity at comparable low coating colour high shear viscosity.

Mill trials proved the results from the lab study and pointed out that water phase viscosity is one of the most important parameters to control mottling.

The new type of thickener is now used in almost all sappi mills.

Research work will continue in the next years to increase liquid phase viscosity without influencing coating colour high shear viscosity.

When the speed of OMC11 was raised the share of the natural convective drying increased. IR rows were switched of thereby. The first critical concentration (FCC) was shifted from the IR section to the airfoil section. Severe **drying mottling** occurred which can be distinguished from formation mottling by a much coarser pattern different in size than the typical base paper floc structure.
Especially when water retention of top coating colour was low and latex particles had to travel a long way from base paper to the surface during drying drying mottling was highly pronounced.
The same happened when latex types were used which produced a dense dry coating film with low water vapour permeability (WddU).

When the change in drying curves was described by an evaporation calculation the drying strategy was changed. Top coatings are currently dried solely by IR. Immobilization point has to be reached as fast as possible to avoid uneven latex penetration into the base by capillary sorption.

An acrylic latex was developed in the lab which provides fast film forming and high water vapour permeability. It is currently the preferred latex when drying induced mottling has to be solved.

Increasing the solid content of the coating colour reduces the risk of drying mottling as FCC is reached earlier and less latex will penetrate with liquid phase into the base paper. Drying strategy has to be adapted – IR energy is needed to immobilize as fast as possible and airfoils have to be avoided to reduce the risk of uneven binder migration between FCC and SCC (second critical concentration).

Future work at paper coaters will concentrate on reducing drying energy which is currently mainly based on methane gas. Increasing the solid content without lowering

liquid phase viscosity or reducing coating colour water retention and risk mottling will be the goal for the next research generation.

Erich Zeyringer, March 2011

Equations:

Crowding number:

Eq. 3-1-1: $N = \frac{2}{3} * c_V * \left(\frac{L}{D}\right)^2$ .... [ ]

Eq. 3-1-2: $N = \frac{2}{3} * \frac{c_m}{\rho_f} * \frac{L^2 * \rho_f * \pi}{\omega * 4} \approx \frac{1}{2} * \frac{c_m * L^2}{\omega} \approx \frac{5 * c_m * L^2}{\omega}$

Hooke's law:

Eq. 3-5-1: $F = -D * \Delta L$, with D the spring constant (N/m=kg/s²)

Eq. 3-5-2: $D = \frac{E * A}{L_0}$, with E the E-modulus.

Darcy's law:

Eq. 3-12-1: $\frac{dV}{dt} = Q = \frac{K * A * \Delta p}{\eta * L}$ [m³/s]

Eq. 3-12-2: $K_1 = \frac{\varepsilon^3}{K * S_0^2 * (1 - \varepsilon)^2}$, Kozeny constant

Equ. 7-1-2: $V = \sqrt{C} * \sqrt{A} * \sqrt{\Delta p} * \sqrt{t}$ ... Darcy integrated

Young equation

Eq. 5-1-1: $0 = \gamma_{SV} - \gamma_{SL} - \gamma * \cos\theta_C$

Lucas Washburn

Eq. 5-2-1: $\Delta P_c = \frac{2 * \gamma * \cos\theta}{r}$

Equ. 5-4-3: $x^2 = \frac{r * t * \gamma * \cos\theta}{2 * \eta}$

Equ. 7-1-1: $\frac{dl}{dt} = \frac{r * \gamma * \cos\theta}{4\eta * l}$

Hagen Poiseuille for cylindrical pores:

Eq. 5-3-1: $\frac{dl}{dt} = \frac{r^2 * \Delta p}{8\mu * l}$

Bosanquet:

Eq. 5-4-1: $x^2 = \dfrac{2 * \gamma * \cos\theta * t^2}{r * \rho}$

Eq. 5-4-1: $x^2 = \dfrac{2 * \gamma * \cos\theta * t^2}{r * \rho}$

Carman Kozeny equation:

Equ. 6-9-1: $K = \dfrac{(1-\Phi)^3}{k_0 * T^2 * \Phi^2 * A_s{}^2}$

Darcy extended to filter cake equation:

Equ. 7-3-1: $v = \dfrac{d(V/A)}{dt} = \dfrac{\Delta p_f + \Delta p_s}{\eta * \left[\dfrac{h_f}{K_f} + \dfrac{h_s}{K_s}\right]}$

Continuity equation:

Equ. 7-4-1: $\dfrac{\partial}{\partial t}(\alpha_q) + \dfrac{\partial}{\partial x_i}(u_j * \alpha_q) = \dfrac{S_{\alpha q}}{\rho_q} + \dfrac{\sum\limits_{p=1}^{n}(\dot{m}_{pq} - \dot{m}_{qp})}{\rho_q}$

Navier Stokes equation:

Equ. 7-4-2: $\dfrac{\partial}{\partial t}(\rho * \vec{v}) + \nabla * (\rho * \vec{v} * \vec{v}) = -\nabla p + \nabla\left[\mu * (\nabla\vec{v} + \nabla\vec{v}^T)\right] + \rho * g + \vec{F}$

Hertz equation:

Equ. 7-1-1: $b = 2 * \sqrt{\dfrac{8 * q * r}{\Pi * E^*}}$

Equ. 7-1-2: $r = \dfrac{R_1 * R_2}{R_1 + R_2}$

Equ. 7-1-3: $E^* = \dfrac{2 * E_1 * E_2}{\left[(1 - \mu^2{}_1) * E_2 + (1 - \mu^2{}_2) * E_1\right]}$

Equ. 7-1-4: $s_m = \dfrac{q}{b}$

Equ. 7-1-5: $s_{max} = \dfrac{4 * q}{\Pi * b}$

Navier-Stokes-Equation:

Equ. 10-2-1: $\rho * \dfrac{\partial v}{\partial t} + \rho * (v * \nabla) * v = -\nabla p + \eta * \Delta v + (\lambda + \eta)\nabla(\nabla * v) + f$

Navier-Stokes-Equation for liquid flow in porous media <u>with uni-dimensional flow</u> in z-direction, incompressible media and no volume forces:

Equ. 10-2-2: $\dfrac{\partial}{\partial t} * \rho * v = -\dfrac{\partial}{\partial z} * \rho * v^2 + \eta * \dfrac{\partial^2 v}{\partial z} - \dfrac{\partial p}{\partial z}$

Equ. 10-2-3: $\dfrac{\partial}{\partial t} * \rho * v = -\dfrac{\partial}{\partial z} * \rho * v^2 - \dfrac{1}{K} * \eta * v - \dfrac{\partial p}{\partial z}$

With equation of continuity $div\,\vec{v} = 0$ and stationary flow with $\dfrac{\partial v}{\partial t} = 0$ → <u>Darcy's law</u>:

Equ. 10-2-4: $v = -\dfrac{K}{\eta} * \dfrac{\partial p}{\partial z}$ or $Q = \dfrac{K * A * \Delta p}{\eta * L}$

Darcy + Kozeny:

Equ. 10-2-5: $\dfrac{dV}{dt} = \dfrac{A * \Delta p}{r * \eta * L}$ with $r = \dfrac{K * S_0^2 * (1 - \varepsilon)^2}{\varepsilon^3}$

Equ. 10-2-6: $K = \dfrac{\varepsilon^3 * d^2_{eff}}{35 * (1 - \varepsilon)^2 * \kappa} = \dfrac{(1 - \phi)^3}{k_0 * \tau^2 * \phi^2 * A^2_s}$

Equ. 10-2-7: $v = \dfrac{1}{A} * \dfrac{dV}{dt} = \dfrac{(\Delta p)_t}{L * a_m + a_w}$ (pressure penetration in wire sections)

Equ. 10-3-1: $V^2 = \dfrac{2 * \Delta p * A^2}{\eta * r * v} * t$.

Equ. 10-3-2:   : $\dfrac{t}{V} = \dfrac{\eta * r * v}{2 * \Delta p * A^2} * V + \dfrac{\eta * R}{\Delta p * A}$

Equ. 10-3-3: $\dfrac{V}{A} = \sqrt{\dfrac{2 * \phi_1 * k(\phi) * \Delta p * \Delta t}{\eta}}$,   with $k(\Phi) = (1-\Phi)^3/(K''*S^2*\Phi^2)$ and $\Phi_1 = (\Phi -$

$\Phi_o)/\Phi_o$ (filter cake equation)

<u>Drying speed in 1st drying stage:</u>

Equ. 11-1-1: $\dot{m}_{v,I} = \dfrac{P * M_v}{R * T_m} * \beta * \ln\left[\dfrac{P - p_{v,\infty}}{P - p_v(\vartheta_0)}\right]$ [kg/(m²/s)]

Equ. 11-2-1: $X = \dfrac{v * B * BW * x}{100 - x}$

Equ. 11-2-2: $X_{evap} = X_{rewinder} + X_{coating} - X_{winder}$

Equ. 11-2-3: $X_{coating} = \dfrac{v * B * CW * (100 - c_{coating})}{c_{coating}}$

Equ. 11-3-1-1: $\dot{q} = \dfrac{d\dot{Q}}{dA} = -\lambda * \dfrac{dT}{dh}$, heat transfer

Equ. 11-3-1-2: $\dot{E} = \varepsilon * \sigma * T^4$, Stefan Boltzmann

Equ. 11-3-1-3: Continuity equ.: $\dfrac{\partial u}{\partial x} + \dfrac{\partial v}{\partial y} = 0$

Equ. 11-3-1-4: Impulse equation in x-direction: $u * \dfrac{\partial u}{\partial x} + v * \dfrac{\partial v}{\partial y} = v * \dfrac{\partial^2 u}{\partial y^2}$

Equ. 11-3-1-5: Thermal energy equ.: $u * \dfrac{\partial T}{\partial x} + v * \dfrac{\partial T}{\partial y} = a * \dfrac{\partial^2 T}{\partial y^2}$

Equ. 11-3-1-6: Blasius defined the flow field with: $\dfrac{u}{U_\infty} = f'(\eta)$

Equ. 11-3-1-7: $Nu_x = \dfrac{\alpha * x}{\lambda} = 0{,}664 * \mathrm{Re}^{1/2} * \mathrm{Pr}^{1/3}$ for laminar flow

Equ. 11-3-1-8: $a = \dfrac{\lambda}{\rho * c_p}$ (thermal conductivity [m²/s])

Equ. 11-3-1-9: $\mathrm{Re} = \dfrac{w * L * \rho_m}{\eta_m}$

Equ. 11-3-1-10: $p_{v,\infty} = P * \dfrac{Y_\infty}{0{,}622 + Y_\infty}$

Equ. 11-3-1-11: $Y_\infty = \dfrac{\tilde{M}_v}{\tilde{M}_g} * \dfrac{p_v}{P - p_v} = 0{,}622 * \dfrac{p_v}{P - p_v}$

Equ. 11-3-1-12: $Nu_{turb} = \dfrac{0{,}037 * \mathrm{Re}^{0,8} * \mathrm{Pr}}{1 + (2{,}443 * \mathrm{Re}^{-0,1} * (\mathrm{Pr}^{2/3} - 1))}$

Equ. 11-3-1-13: $\alpha_{turb} = \dfrac{Nu_{turb} * \lambda}{L}$ and $\alpha_{lam} = \dfrac{Nu_{lam} * \lambda}{L}$

Equ. 11-3-1-14: $\dfrac{\alpha}{\beta} = \rho * c_p * Le^{(1-n)}$ with $Le = \dfrac{\lambda}{\rho * c_p * \delta} \approx 1$

Equ. 11-3-1-15: $\beta_{turb} = \dfrac{\alpha_{turb}}{\rho_m * c_{p,m}}$ and $\beta_{lam} = \dfrac{\alpha_{lam}}{\rho_m * c_{p,m}}$

Equ. 11-3-1-16: $\beta_{h,turb} = \dfrac{\beta_{turb}}{1 - \dfrac{P_{d,0}}{P}}$ and $\beta_{h,lam} = \dfrac{\beta_{lam}}{1 - \dfrac{P_{d,0}}{P}}$

Equ. 11-3-1-17: $g_{d,turb} = \beta_{h,turb} * \dfrac{R_d * T_m}{P_d - P_{dl}}$ and $g_{d,lam} = \beta_{h,lam} * \dfrac{R_d * T_m}{P_d - P_{dl}}$

Equ. 11-3-1-18: Viscosity of air $\eta_m = \dfrac{((P - P_{vm}) * \eta_g * \sqrt{\tilde{M}_g}) + (p_{vm} * \eta_v * \sqrt{\tilde{M}_v})}{((P - p_v m) * \sqrt{\tilde{M}_g}) + (p_{vm} * \sqrt{\tilde{M}_v})}$

Equ. 11-3-1-19: Density of wet air $\rho_m = \dfrac{P}{R * T_m} * \dfrac{(P - p_{vm}) * \tilde{M}_g + p_{vm} * \tilde{M}_v}{P}$

Equ. 11-3-1-20: Ra = Gr * Pr

Equ. 11-3-1-21: $Nu_{free} = 0{,}15 * (Ra * f(\mathrm{Pr}))^{1/3}$

Equ. 11-3-1-22: $f(\mathrm{Pr}) = \left[1 + (\dfrac{0{,}322}{\mathrm{Pr}})^{11/20} \right]^{-20/11}$

Drying speed in 2nd drying stage:

Equ. 11-3-1-23: $g_{d,II} = \dfrac{1}{R_D * T} * \dfrac{1}{\dfrac{1}{\beta} + \dfrac{\mu * s'}{D}} * (p_D^{"} - P_{D,a})$ [kg/m²h]

Equ. 11-3-3-1: $\sigma_l * (1 + \cos\theta) = 2 * (\sqrt{(\sigma_l^d * \sigma_s^d)} + \sqrt{(\sigma_l^p * \sigma_s^p)})$

Figures:

Chapter 2: Mottling in offset printing

Pict. 2.1.1: Subtractive mixing of colours cyan, magenta and yellow

Pict. 2.1.2: Four colour offset printing – combining cyan, magenta, yellow and black to achieve any possible colour

Pict. 2.1.3: Ink dots of cyan, magenta and yellow in screen area

Pict. 2.1.4: Five colour sheet offset printing machine

Pict. 2.1.5: Offset printing station

Pict. 2.1.6: Plate making process (a: Using a positive image, b: Negative image) (Heidelberger)

Pict. 2.1.7: Dots of on aluminium plate after removal of photo sensitive film at unprinted areas (dots: Oleophilic coating has remained on plate)

Pict. 2.1.8: Transfer of ink and fountain water to plate

Pict. 2.1.9: Transfer of ink to the substrate

Pict. 2.2.1: Bad back trap mottle (cloudy structure of PM11 formation)

Pict. 2.2.2: Good back trap mottle

Pict. 2.2.3: Difference of ink absorption without pre-wetting on porous / dense coating surface (screen mottling and back trap mottling)

Pict. 2.2.4: Difference of ink absorption with pre-wetting on porous / dense coating surface

Pict. 2.3.1: Prüfbau pressure penetration test with water + oil

Pict. 2.3.2: Prüfbau pressure penetration test with water + oil for different papers

Pict. 2.3.3: Prüfbau water + oil penetration test at base papers

Pict. 2.3.4: Liquids for penetration tests

Pict. 2.4.1: Capillary sorption in pores of coating

Chapter 3: Floc analysis

Pict. 3.1.1: STFI flocculation circuit – floc size versus fibre length

Pict. 3.1.2: Rotational turbulence in the tube bank

Pict. 3.1.3: Boundary swirls

Pict. 3.4.1: Aligning, rotating and cutting the images for match analysis

Pict. 3.4.2: Fit sizes and filtering of images for software analysis

Pict. 3.4.3: Principle of match analysis

Pict. 3.4.4: Match analysis of Ambertec basis weight and UBM topography of lab sheet

Pict. 3.4.5: Match analysis of Ambertec and UBM topography of PM11 base paper

Pict. 3.5.1: Zwick thickness vs. load (upper black curve: load, lower curve: relief)

Pict. 3.5.2: Definition of compressibility according to Brecht and Schädler (1961):

Pict. 3.5.3: Deformation of base paper – components of compression

Pict. 3.5.4: Definition of elasticity modulus E according to Kluge (1996)

Pict. 3.5.5: Hooke's law: Spring stretches by vertical force $F = m*g$

Pict. 3.5.6: Deformation $\varepsilon = \Delta L$ vs load σ (corresponds to vertical force F) for base paper PM11 ($d_r – d_k$ = elastic deformation, $d_a - d_r$ = plastic deformation)

Pict. 3.5.7: Burgers model for deformation of paper: Spring for elastic part and attenuator for plastic compression (Jokio 1998)

Pict. 3.5.8: Thickness vs. External pressure at Zwick

Pict. 3.5.9: Work under load (integration of thickness vs. pressure) for base paper

Pict. 3.5.10: Spring constant D and E-modulus under compression for base paper PM11

Pict. 3.5.11: Comparison of spring constants for base paper and precoated paper

Pict. 3.6.1: LCSA at STFI for compression measurements

Pict. 3.6.2: Pressure image map at 10 MPa of a) uncoated base, b) blade coated, c) film-coated d) curtain coated

Pict. 3.6.3: Lab press with pressure sensitive film

Pict. 3.6.4: Fuji pressure sensitive film image of base paper with Ambertec = 0,5 (left) and base paper with Ambertec = 0,3 (right) – deeper red = higher pressure

Pict. 3.6.5: Comparison of Ambertec image (left) with Fuji film scan ("Abdruck") of same area of base paper PM11 (dark = high pressure)

Pict. 3.6.6: Match analysis of Ambertec basis weight and Fuji film colour ("Abdruck")

Pict. 3.6.7: Match analysis of Transmission light formation ("TR") and Fuji film colour ("Abdruck")

Pict. 3.6.8: Thickness of PM11 precoated papers at different press time and pressure

Pict. 3.7.1: Thickness variations in base paper

Pict. 3.7.2: REM picture of triple coated paper (paper thickness = 85 µm) – length of cutting = 160 µm

Pict. 3.7.3: Coating layer thickness on top side and bottom side upon flocs (F1,2) and valleys (T1,2) of MSP precoated paper PM11 (90 g/m² with 12 g/m² precoat per side)

Pict. 3.7.4: Mean coating layer thickness on top side and bottom side of flocs and valleys

Pict. 3.7.5: REM analysis of 8 mm long microtome cutting at PTS in 2003 (PM11 MSP precoating)

Pict. 3.7.6: Calculated coat weight at flocs and valleys (film coating)

Pict. 3.8.1: 3D-diagramm of base paper basis weight

Pict. 3.8.2: 3D-diagramm of calculated coat weight

Pict. 3.8.3: Match analysis for base paper basis weight and coat weight

Pict. 3.8.4: Match factors for Heliocoater samples (mean of six areas)

Pict. 3.9.1: Gamma radiogram of coated paper

Pict. 3.10.1: Pressure distribution before and under the blade for different facet geometries

Pict. 3.10.2: Calculated normal pressure with Bernoulli and capillary shear measurements

Pict. 3.10.3: Base paper thickness difference between flocs and valleys as a function of local pressure difference

Pict. 3.11.1: Beta formation of PM11 base paper vs. screen mottling of coated paper

Pict. 3.11.2: Floc size distribution by wave let analysis of different base papers from PM9 / 11 measured with Ambertec (measured area: 45x45 mm)

Pict. 3.11.3: Screen mottling (visual) of different base papers, coated and calandered

Pict. 3.11.4: Screen mottling (visual) vs. Ambertec mottle viewer formation index

Pict. 3.11.5: Formation vs. screen mottling

Pict. 3.11.6: Comparison of Ambertec of base paper and coated sheet

Pict. 3.11.7: Thickness change of base paper by 5-nip-lab calandering

Chapter 4: Solution 1 for formation mottle: Improve base paper structure

Pict. 4.2.23: Comparison of compression deformation of base papers and coated papers at 500 kPa.

Chapter 5: Penetration by capillary pressure

Pict. 5.1.1: Definition of contact angle

Pict. 5.1.2: Contact angle of different liquids on different substrates

Pict.. 5.2.1: Principle of Fibro-DAT capillary sorption measurement

Pict. 5.2.2: Fibro-DAT measurement with water on base paper PM11-3408-MR3

Pict. 5.2.3: Fibro DAT volume of drop vs. time for base paper (liquid: water)

Pict. 5.2.4: Fibro DAT contact angle vs. time for base paper (liquid: water)

Pict. 5.2.5: Fibro DAT volume of drop vs. time for base, pre- and middle coated paper (liquid: water)

Pict. 5.2.6: Surface tension and viscosity of test liquids for Fibro DAT experiments

Pict. 5.2.7: Contact angle of different liquids on different paper samples from Fibro-DAT

Pict. 5.3.1: Mean pore radius of base paper from Mercury porosity of base papers, pre-, middle- and topcoated papers from PM11

Pict. 5.3.2: Mean pore radius of coating layer from Mercury porosity of base papers, pre-, middle- and topcoated papers from PM11

Pict. 5.3.3: Calculation of capillary pressure of base papers

Pict. 5.4.1: Water transfer unit invented by Dan Eklund / Abo Akademi

Pict. 5.4.2: Absorbed water vs. square root of time for different application pressure levels (D. Eklund)

Pict. 5.4.3: Water penetration vs square root of time for different pressure levels (P. Salminen)

Pict. 5.4.4: Influence on water viscosity on penetration: Left: 0 kPa, right: 50 kPa application pressure (P. Salminen)

Pict. 5.4.5: Influence of rosin sizing on capillary penetration (left) and pressure penetration with 50 kPa (right) for water as test liquid (P. Salminen)

Pict. 5.4.6: Experimental results for liquid packaging board with varying structure and sizing level (S. Ramaswamy)

Pict. 5.4.7: Kinetics of penetration: a) drop in the capillary, b) drop out of the capillary (D. Danino)

Pict. 5.4.8: Penetration of surfactant drops (upper line) and isopropanol (bellow) (G. Strom)

Pict. 5.4.9: Fibro DAT of different stages of paper production at PM11 / OMC11 – penetrated volume vs. SQROOT of time for water + 20% IPA (A = constant)

Pict. 5.4.10: Fibro DAT of different stages of paper production at PM11 / OMC11 – penetrated volume vs time for water + 20% IPA (A = constant)

Pict. 5.5.1: J.E. Elftonson, G. Strom (L1.42) : Penetration of aqueous solutions into models for coating layers - V/A vs. SQROOT of time for surfactants

Pict. 5.5.2: Contact angle comparison of CMC solution with water

Pict. 5.5.3: Fibro-DAT of different liquids, top side of precoated paper PM11; 0,01 – 10 s; volume vs. log t

Pict. 5.5.4: Fibro-DAT of different liquids, top side of precoated paper PM11; 0,01 – 3s; volume vs. log t

Pict. 5.5.5: Fibro-DAT 1 – 10 sec, top side of precoated paper PM11

Pict. 5.5.6: Fibro-DAT 1 – 10 sec, bottom side of precoated paper PM11

Pict. 5.5.7: Fibro-DAT V/A vs. square root of time for top side + bottom side, 0 – 10 s

Pict. 5.5.8: Fibro-DAT V/A vs square root of time for TS and BS, 0,2 – 10 sec

Pict. 5.5.9: Fibro-DAT V/A vs. square root of time for top side + bottom side, 0,2 – 10 sec, 1,1% CMC solution

Pict. 5.5.10: Comparison of capillary penetration pressure of top and bottom side of precoated paper PM11

Pict. 5.5.11: Base ash two-sidedness PM11

Pict. 5.5.12: Calculation of base paper sorption pressure from Fibro-DAT with Darcy equation for hydrophilic liquids with different viscosity

Pict. 5.6.1: Calculating the theoretical thickness of coated paper

Pict. 5.7.1: Calculation of pore volume of base paper

Pict. 5.7.2: Base paper pore volume vs. absorbed water at middle coaters OMC11

Pict. 5.7.3: Comparison of pore volumes and penetrated liquid volume at coater

Chapter 6: Pressure penetration

Pict. 6.4.3: Sample on the sample holder

Pict. 6.4.4: Ink in the pipette

Pict. 6.4.5: Ink on the aluminium roll

Pict. 6.4.6: Starting the printing process

Pict. 6.4.7: Ink rolled into the paper surface

Pict. 6.4.8: Measuring the size of the penetrated area

Pict. 6.4.9: Calculating the Darcy coefficient from Prüfbau pressure penetration test

Pict. 6.4.10: Prüfbau water penetration test – comparison base paper (10 µl) to pre-coated paper (only 5 µl)

Pict. 6.4.11: Prüfbau water penetration test – comparison base paper (10 µl) to top coated paper (5 µl)

Pict. 6.4.12: Prüfbau water penetration test for all stages of coating of PM11 papers

Pict. 6.4.13: Prüfbau water penetration test for precoated samples PM11 (film press precoating)

Pict. 6.4.14: Prüfbau water penetration test for middle coated samples PM11 (MSP + blade)

Pict. 6.4.15: J. Grön: Coating holdout in MSP as a function of base ash

Pict. 6.4.16: J. Grön: Latex holdout as a function of base ash

Pict. 6.4.17: Prüfbau water penetration test for top coated samples PM11 (MSP+blade+blade)

Pict. 6.5.1: Calc. Darcy coefficient from Prüfbau pressure penetration test at base paper (water as test liquid)

Pict. 6.5.2: Calc. Darcy coeff. from Prüfbau pressure penetration test at double precoated paper (water as test liquid)

Pict. 6.6.1: Physical properties of test liquids

Pict. 6.6.2: Prüfbau water + oil penetration test: C1/2 = precoated, C3/4 = middle coated, C5/6 = top coated

Pict. 6.6.3: Correlation of Prüfbau pressure penetration test on different substrates for oil and water with same viscosity

Pict. 6.6.4: Prüfbau pressure penetration test with different liquids on different substrates (Ropa = base paper, PM = precoated, SM = topcoated, RS = calandered)

Pict. 6.7.1: Prüfbau pressure penetration test with different conditions of application

Pict. 6.8.1: Prüfbau pressure penetration test versus Bendtsen air porosity for base different papers PM11

Pict. 6.9.1: Pressure cell for calculation of Darcy coefficient at OMYA
Pict. 6.9.2: Darcy coefficient with OMYA pressure cell of precoat (Rez. 117) and middle coat (Rez. 201)
Pict. 6.9.3: Coating layer thickness from REM
Pict. 6.9.4: Darcy coefficient of different coating layers PM11
Pict. 6.9.5: Loss in volume as a function of coating holdout
Pict. 6.9.6: Comparison of measured mercury porosity with measured permeability (OMYA pressure penetration cell)
Pict. 6.9.7: Correlation of calculated permeability (from mercury porosity) with measured permeability

Pict. 6.10.1: Gloss two sidedness PM11 double and triple coated papers, increasing with basis weight
Pict. 6.10.2: Smoothness two sidedness of base paper PM11 due to 4th press felt on bottom side
Pict. 6.10.3: Base ash two-sidedness at heavy basis weight of PM11 (100 gm² base)

Pict. 6.10.4: Base ash two-sidedness at low basis weight of PM11 (60 gm² base)
Pict. 6.10.5: Prüfbau water penetration test for precoated samples PM11 (MSP coater)
Pict. 6.10.6: Gap former layout of PM11
Pict. 6.10.7: Mass balance of wire section PM11for a 100 g/m² base
Pict. 6.10.8: Calculated two sidedness of dewatering in primary dewatering section of PM11
Pict. 6.10.9: Primary and secondary dewatering section of PM11
Pict. 6.10.10: Comparison of primary and secondary dewatering two-sidedness PM11
Pict. 6.10.11: Two-sidedness in back trap mottle PM11
Pict. 6.10.12: Mottle two-sidedness PM11: Standard = Bottom side coated first in OMC11; Trial = Top side coated first

Chapter 7: Blade and film press coating

Pict. 7.1.1: Areas of coating colour penetration at a blade coater

Pict. 7.1.2: Pressure and time of penetration in the blade coating process

Pict. 7.1.3: Pressure development from application to blade

Pict. 7.1.4: Penetrated liquid in blade coating phases

Pict. 7.2.1: LDTA and jet applicators

Pict. 7.3.1: Mechanism of capillary sorption

Pict. 7.3.2: Dewatering at LDTA application (Ph. Letzelter)

Pict. 7.3.3: Dewatering with SDTA application (Ph. Letzelter)

Pict. 7.3.4: Difference in penetration under the blade for LDTA vs. SDTA application (Ph. Letzelter)

Pict. 7.3.5: Dewatering between application and blade for different paper sorption pressure levels (Ph. Letzelter)

Pict. 7.3.6: Dewatering before the blade for roll application as a function of application solids (Ph. Letzelter)

Pict. 7.3.7: Roll applicator

Pict. 7.3.8: Jet applicator

Pict. 7.3.9: OptiCoat Duo – jet with long dwell time application

Pict. 7.3.10: Comparing the dewatering of different application systems

Pict. 7.3.11: Pilot coater study of different pre- and topcoat application systems on a 220 g/m² three ply base board with MG cylinder and hard nip calander for base

Pict. 7.3.12: Topography of different double coated samples (higher variance = rougher surface)

Pict. 7.3.13: Density increase of coating colour in the working tank of Coater 4 over 6 hours after coater start up

Pict. 7.3.14: Density vs. solid content of precoating colour

Pict. 7.3.15: Density increase of coating colour in the working tank of Coater 3 over 6 hours after coater start up

Pict. 7.3.16: Solid increase in working tank at startup of of coater 1 at OMC9

Fig. 7.3.17: Solid content of fresh coating colour, in working tank and after blade C3/4

Fig. 7.3.18: Solid content of fresh coating colour, in working tank and after blade C5/6

Pict. 7.4.40: Dewatering process under the blade

Pict. 7.4.41: SLIT rheometer (Natalia Egorova)

Pict. 7.4.42: Pressure distribution before and in the capillary (non-Newtonian fluid), with $p_{ent} = p_{kin} + p_{Nent} + P_{elast}$ (Natalia Egorova)

Pict. 7.4.43: Typical Bagley plot for $CaCO_3$ based coating colour (Natalia Egorova)

Pict. 7.4.44: Pressure contours from VOF model at the blade tip (A. Roshanzamir)

Pict. 7.4.45: Pressure contour lines from VOF model at the blade tip, blade 2: Max pressure = 40 kPa (A. Roshanzamir)

Pict. 7.4.46: Doctoring pressure as a function of blade geometry (A. Roshanzamir)

Pict. 7.4.47: Pressure pulses in the middle of the gap (A. Roshanzamir)

Pict. 7.4.48: Detailed blade geometry for 35/25° TC blade with pre-angle at tip

Pict. 7.4.49: Hybride grid of calculation (hexahedron & tetrahedron) with17904 elements of 5 x 2 µm size for OMC11 blade VOF.

Pict. 7.4.50: Modelling of two phase systems by volume fraction α (blue = liquid, white = air)

Pict. 7.4.51: Blade geometry data's for 35/25° TC blade with pre-angle at tip

Pict. 7.4.52: Parameters of OMC11 for 2D VOF simulation process parameters (speed 1600 m/min, coat weight 12 g/m², solids 68%, excess factor 1:20)

Pict. 7.4.53: ACAV high shear viscosity of top coating formulation No. 340

Pict. 7.4.54: Normal vector of flow

Pict. 7.4.55: Velocity profile in flow of coating colour to the blade plus return flow and exit under the blade

Pict. 7.4.56: Velocity profile of flow before the blade tip

Pict. 7.4.57: Velocity profile of flow at the blade tip (35/25° blade with pre-angle only)

Pict. 7.4.58: Velocity profile of flow at the blade tip

Pict. 7.4.59: Dwelling time of coating colour before blade

Pict. 7.4.60: Dwelling time of coating colour at the blade tip (35/25° blade only)

Pict. 7.4.61: Strain rate (1/s) in the coating colour flow to the blade

Pict. 7.4.62: Strain rate (1/s) in the coating colour flow at the tip and under the blade (35/25° blade only)

Pict. 7.4.63: Absolute pressure in the coating flow to the blade

Pict. 7.4.64: Absolute pressure at the blade tip

Pict. 7.4.65: Comparison of pressure on paper in Z-direction before and under the blade

Chapter 8: Solution 4 for formation and drying mottle: Thin barrier layer

Pict. 8.7.6: Cracking on the fold of triple coated papers with starch or Styrofan barrier on precoat and middle coat

Pict. 8.8.1: Fibro-DAT capillary water sorption of flocs/valleys of base paper PM11
Pict. 8.8.2: Cost comparison of barrier coating concept with conventional concept

Chapter 9: Solution 5 for formation and drying mottle: Reduce permeability of precoatings

Pict. 9.2.1: Lab rod coater PT4
Pict. 9.2.2: Influence of latex type and amount on air permeability of dry coating layer
Pict. 9.2.3: Mercury porosity of coating tablets with different latex types
Pict. 9.2.4: Mercury porosity of standard latex LTX310 compared to Senolith varnish
Pict. 9.2.5: Mercury porosity of Senolith inline primer varnish based coatings
Pict. 9.2.6: Pore size distribution – effect of pre-calandering
Pict. 9.2.7: Pore size distribution of base papers and coated papers
Pict. 9.2.8: Pore size distribution of coating layers
Pict. 9.2.9: Comparison of permeability of latex based coatings with starch based coatings
Pict. 9.2.10: Hg-porosity of starch and latex based precoatings
Pict. 9.2.11: Mercury porosity of starch based coatings
Pict. 9.2.12: Comparing different carbonates in precoating permeability
Pict. 9.2.13: Mercury porosity of precoating colours with coarse HC60 and fine HC90
Pict. 9.2.14: Porosity of coating tablets (no loss of fines and solubles into base paper) – comparison of different precoating formulations

Pict. 9.3.1: Tested lab coatings
Pict. 9.3.2: Mercury porosity of the coating layer
Pict. 9.3.3: Calculated Darcy coefficient of coating layer from Prüfbau pressure penetration test
Pict. 9.3.4: Increase in precoating layer permeability by shift from HC60 to Covercarb 75
Pict. 9.3.5: Mono sphere vs. multi sphere particle packing (OMYA)

Chapter 10: Solution 6 for formation and drying mottle: Improve water retention of coating colour

Pict. 10.4.22: Dewatering versus SQROOT of time/viscosity, experiments (Φ=0,33) (Erikson and Rigdahl)

Pict. 10.4.23: Dewatering versus SQROOT of time/viscosity, calculated (Erikson and Rigdahl)

Pict. 10.4.24: Immobilized layer thickness Pict. 10.4.25: Calculated Darcy coefficient

Pict. 10.4.26: Calculated porosity of filter cake

Pict. 10.4.27: Calculated penetration resistance h_f/K_f

Pict. 10.4.28: Water retention improvement by increasing the solid content of a pre-coating

Pict. 10.4.29: Immobilized layer thickness (immobilized solids 81% for V19 and V30)

Pict. 10.4.31: Porosity of filter cake

Pict. 10.4.32: Calculated penetration resistance h_f/K_f

Pict. 10.4.34: Abo-GWR readings for Rez. 201 at 68,3% solids

Pict. 10.4.35: Comparison of water retention curve of middle coat Rez. 201 with different solids

Pict. 10.4.36: Comparison of immobilized layer thickness of middle coat Rez. 201 with different solids

Pict. 10.4.37: Comparison of immobilized layer Darcy coefficient of middle coat Rez. 201 with different solids

Pict. 10.4.38: Comparison of filter cake porosity of middle coat Rez. 201 with different solids

Pict. 10.4.39: Comparison of filtration resistance h_{Immo}/K_{Immo} of middle coat Rez. 201 different solids

Pict. 10.5.1: Water retention of all tested pre-coatings

Pict. 10.6.1: Water retention vs. solid content of precoatings of PM11 /OMC11

Pict. 10.6.3: Increase in high shear viscosity with increasing solid content

Pict. 10.6.4: Increase in low shear viscosity with increasing solid content

Pict. 10.6.5: Immobilization time of pre-coat 117 and middle coatings 201 and 202 with BASF/Paar immobilization cell (rotation viscosimeter)

Pict. 10.6.6: Immobilization solids for pre-coating 117 and middle coatings 201 and 202

Pict. 10.6.7: Immobilization time for pre-coating 117 and middle coatings 201 and 202

Chapter 11: Latex film forming and drying induced mottling

Pict. 11.1.1.5: IR drying with <u>80°C</u> without dewatering to the base by vacuum; numerical calculation = continuous line and experiments = points (D. Bruneau)

Pict. 11.1.1.6: Starch concentration profiles for 60°C and 80° IR drying without dewatering (D. Bruneau)

Pict. 11.1.1.7: IR drying with 60°C <u>with dewatering</u> to the base by vacuum; numerical calculation = continuous line and experiments = points (D. Bruneau)

Pict. 11.1.1.8: IR drying with 80°C <u>with dewatering</u> to the base by vacuum; numerical calculation = continuous line and experiments = points (D. Bruneau)

Pict. 11.1.1.9: Starch concentration profiles for: A = IR 60°C, no dewatering, B = IR 80°C no dewatering, C = IR 60°C, with dewatering, D = IR 80°C with dewatering (D. Bruneau)

Pict. 11.1.1.10: Latex level vs. coating remaining after grinding (CR) for trial 1 (T. Hattula)

Pict. 11.1.1.11: Latex level vs. coating remaining after grinding (CR) for trial 2 (changing binder amount in top- and precoat from 10/22 to 22/10) / T. Hattula)

Pict. 11.1.1.12: IGT tests or trial series 2 (T. Hattula)

Pict. 11.1.1.13: Fibro MCA IR surface moisture instrument

Pict. 11.1.1.14: Measurement of surface moisture at coated side during drying at OMC11

Pict. 11.1.1.15: Surface moisture measurement by Fibro MCA1410 (higher readings = higher moisture)

Pict. 11.1.1.16: Influence of back side coating upon drying speed

Pict. 11.1.1.17: Vapour permeability WDDu of base paper, precoated, top coated and calandered paper

Pict. 11.1.1.18: Comparison of roll applicator (LDTA) with jet applicator (fountain) - left: complete air trapping, right: no air trapping (Chen and Scriven)

Pict. 11.1.1.19: Influence of pigment on drying energy demand

Pict. 11.1.1.20: Influence of binder type an drying energy demand

Pict. 11.1.1.21: Influence of thickener on drying speed

Pict. 11.1.1.22: Calibration of Fibro MCA

Pict. 11.1.1.23: Fibro MCA measurements after IR of different substrate

Pict. 11.1.2.1: Layout of OMC11

Page 839

Pict. 11.1.7.2: Comparison of Prüfbau permeability (higher dV/dA corresponds to lower permeability) with picking resistance of drying tests
Pict. 11.1.7.3: Permeability of coated surface (higher dV/dA corresponds to lower permeability), including Prüfbau standard droplet test

Pict. 11.1.8.1: Prüfbau pressure penetration test with water + IPA (higher dV/dA corresponds to lower permeability)
Pict. 11.1.8.2: Prüfbau pressure penetration test with thin oil (higher dV/dA corresponds to lower permeability)
Pict. 11.1.8.3: Mercury porosity of coating layer for different binders under different drying conditions
Pict. 11.1.8.4: Bendtsen porosity – comparison of coating on base paper and on double precoated paper
Pict. 11.1.8.5: Gloss Tappi 75°
Pict. 11.1.8.6: Set off test

Pict. 11.2.1.1: Drying energy demand for PCC and GCC coatings (trial 1 + 2) (G. Alderfer)
Pict. 11.2.1.2: Specific drying energy for trial 3 + 4 (G. Alderfer)
Pict. 11.2.1.3: Correction of Measurex online basis weight and moisture measurements by lab
Pict. 11.2.1.4: Energy input from IR and airfoils
Pict. 11.2.1.5: Calculateion of energy efficiency in IR and airfoil drying section by comparing the consumed energy in gas with theoretical energy demand for evaporation
Pict. 11.2.1.6: Vestra 2002 – Pigment comparison
Pict. 11.2.1.7: Vestra 2002 – Comparison of drying curves
Pict. 11.2.1.8: Vestra 2002 – comparison of lattices

Pict. 11.2.2.1: Drying curves for low and high incoming moisture and constant end moisture
Pict. 11.2.2.2: Max temperature and average temperature in drying section
Pict. 11.2.2.3: Backtrap mottling of calandered paper
Pict. 11.2.2.4: Correlation of max temperature after IR section with BTM

Page 841

Pict. 11.3.3.4: Ink drying by capillary forces of coating layer for new binder concept in top coatings of OMC11 (lower = faster absorption)

Pict. 11.3.3.5: Water absorption by capillary forces of coating layer for new binder concept in top coatings of OMC11 (lower = faster absorption)

Pict. 11.3.3.6: Mill trial at OMC11 with 100% SA-latex Acronal S360D in top coat

Pict. 11.3.3.7: Polarity of surface, top side

Pict. 11.3.3.8: Polarity of surface, bottom side

Pict. 11.3.4.1: Hot lab calandering – influence of nip load and nip passes on Mercury porosity of coating layer (source: P. Resch)

Pict. 11.3.4.2: Hot lab calandering – influence of nip temperature on Mercury porosity of coating layer (source: P. Resch)

Pict. 11.3.4.3: Loss in coating layer porosity by hot calandering for different latices

Pict. 11.3.4.4: Screen mottling for different coating Stepps and after calandering

Pict. 11.3.4.5: Gloss increase with nip load in lab calander (source: P. Resch)

Pict. 11.3.4.6: Loss in pore volume of base paper and coating with nip load in lab calander (source: P. Resch)

Pict. 11.3.4.7: Tappi gloss of lab coated and lab calandered papers

Pict. 11.3.4.8: Pressure penetration test of lab coated and lab calandered papers (lower dV/dA = lower Darcy coefficient = denser coating)

Pict. 11.3.4.9: Mercury porosity of coating layers

Pict. 11.3.4.10: Opacity of lab coated and lab calandered papers

Literature

Lit. 1: Penetration, WRV

L1.1 W. Windle, K.M. Beazley: Part 1+2 Liquid migration from coating colours – Tappi Vol. 52, No.11, Nov. 1969 + Tappi Vol. 53, No. 12, 1970

L1.2 J. Anthony Bristow: Liquid absorption into Paper during short time intervals – Svensk Papperstiding No. 19 – Okt. 1967

L1.3 W. Windle, K.M. Beazley: Liquid migration in blade coatings – Tappi, Vol. 52, No.11, Nov. 1969

L1.4 K.M. Beazley: Liquid migration from coating colours – Tappi Vol.53, No. 12, Dec. 1970

L1.5 Milton H. Voelker: Role of base sheet properties in the development of coated and supercalanders sheet properties – Tappi Vol. 55, No.2, Febr. 1972

L1.6 Einat Bohemer, Jan Lute: Adhesive migration and water retention with reference to blade coating – Svensk Papperstiding, No. 18, Sept. 1966

L1.7 R.C. Hamlen, L.E. Scriven: Permeabilites to fluid flow vary with sheet compression – Tappi coating conference 1991, p. 355

L1.8 Doeung Choi, Shri Ramaswarmy: In-plane liquid flow characteristics in paperboard- Forest products No. 324, Vol. 96

L1.9 Pal Lokendra, Margaret Joyce, Paul Fleming: A simple method for calculation of the permeability coefficient of porous media – Tappi Vol. 5, No.9, Sept. 2006

L1.10 Dan Eklund: Water transport in the blade coating process – Tappi coating conference 1986, p.1

L1.11 Pekka Salminen: Water transport in base paper – effect of some liquid and paper variables – Tappi coating conference 1988, p.209

L1.12 Seongnam Ahn, Douglas W. Bousfield (Maine): Coating consolidation rate: A new test method and model – Tappi coating conference 2002

L1.13 L. Nilsson, S. Stenström: A study of the permeability of pulp and paper – Int. J. Multiphase Flow, Vol. 23, No. 1, p. 131 – 153, 1997

L1.14 Markku Leskelä, Sami Simula: Transport phenomena

L1.15 Teng Shau Young, D. Pivonka, L. Weyer, Bob Ching: A study of coating water loss and immobilization under dynamic conditions – Tappi J., Vol. 76, No. 10, Oct. 1993

L1.16 P.A.C: Gane, J. Schoelkopf: Observing fluid transport into porous coating structures – Tappi J., Vol. 53, No. 12, Dez. 1970

L1.17 Sanna M. Rousu, P.A.C. Gane, Dan Eklund: Influence of coating pigment chemistry and morphology on the chromatographic separation of offset ink constituents

L1.18 K.S.A. Chen, L.E. Scriven: Liquid penetration into a deformable porous substrate – Tappi Jan. 1990

L1.19 Mark A. Paradis, J. Genco, D. Bousfield, J. Hassler: Determination of drainage resistance coefficients under known shear rate – Tappi J., Vol. 1, No. 6, Aug. 2002

L1.20 D. Bousfield (Maine): Prediction of velocity and coat weight limits, based on filter-cake formation – Tappi Journal, Vol. 77, No. 7, July 1994

L1.21 S. Ramaswamy, B.V Ramaro, A. Goel: Theoretical and experimental investigation on liquid penetration in porous media

L1.22 A. Marmur, R.C. Cohen: Characterization of porous media by the kinetics of liquid penetration – the vertical capillaries model – Journal of colloid and interface science – 189 – 1997

L1.23 L. Abrahams, C. Favorite, P. Caprano, R. Johnson: Using mercury porosimetry to characterize coating pore structure and it's relation to coating optical performance – Tappi Coating Conference 1996, p. 185

L1.24 Dganit Danino, A. Marmur: Radial Capillary penetration into Paper: Limited and unlimited reservoirs – Journal of Colloid and Interface Science, 166, 245-250 (1994)

L1.25 Henk W. Louman: Mottling and wetability

L1.26 J. Skowronski, P. Lepoutre: Water paper interaction during paper coating, changes in paper structure – Tappi Nov. 1985

L1.27 J.A. van den Akker, W.A. Wink: Mechanisms of liquid phase movement of water through paper – Tappi Vol 52, No. 12, Dec. 1969

L1.28 U.P. Rüegger: Die Bestimmung von Flüssigkeitspenetration mit einem neuen Penetrationstester – WBl. 1976

L1.29 G. Engström, V. Morin, Song Lin Bi: Analysis of porosity distribution in coating layers – Tappi Vol. 80, No.5, 1997

L1.30+31 J. Schelkopf, P.A.C. Gane: Imbition behaviour of offset inks, Part 1+2 – Tappi Vol. 2, No.6, 2003, Tappi Vol. 2, No.7, 2003

L1.32+33 D. Vidal, X. Zou: Modelling coating structure development using Monte Carlo deposition method, Part 1+2 – Tappi Vol. 2, No. 4, 2003, Tappi Vol. 2, No. 5, 2003

L1.34 L. Larrando, C. Monaterios: The porous structure of paper coatings – a comparison of mercury porosimetry and stain imbition methods of measurement – Tappi coating conference 1995, p.79

L1.35 P.A.C. Gane, J. Schoelkopf: Fluid transport into porous coating structures, part 2

L1.36 U. Forsström, J. Grön: Interactions between paper and coating colour with double coated paper – Wochenblatt für Papierfabrikation 18-2002, p. 1208

L1.37 Ph. Letzelter, D. Eklund (Abo): Coating colour dewatering in blade coaters – Tappi coating conference 1993, p.247

L1.38 V. Wildfong, J.M. Genco: An examination of two hybrid top wire former configurations for producing newsprint – Tappi Vol. 2, No. 10, Oct. 2003

L1.39 S. Malkov, V. Kuzmin: Modelling the process of water penetration into softwood chips –Journal of pulp and paper science, Vol. 29, No.4, Apr. 2003

L1.40 M.C. Asensio: Determination of the capillary pressure function for paper using centrifuge data – Tappi engineering conference 1994, p. 981

L1.41 J. Schwartz: The importance of low dynamic surface tensions in water borne coatings – Polymers and coatings conference 1990

L1.42 J.E. Elftonson, G. Strom: Penetration of aqueous solutions into models for coating layers - Tappi coating fundamental symposium 1995

L1.43 S.X. Pan, H.T. Davis, L.E. Scriven (Minnesota): Substrate effects on binder migration in drying porous coatings – Tappi coating conference 1996, p.115

L1.44 P.A.C. Gane: Pulse dewatering and the mechanisms of blade defects in high speed coating – Tappi coating conference 1994, p. 311

L1.45 M. Toivakka: Numerical investigation of droplet impact spreading in spray coating of paper – Tappi advanced coating fundamentals symposium 2003

L1.46 H. Koyamoto: Effect of surface properties of base paper on print quality – Nippon paper industry internal paper

L1.47 N. Triantafillopoulos, N. Altug: A comparative study of forces in blade coating – Forest products symposium 1991, p.141

L1.48 U. Höke, E. Daub: Absorptionsverhalten von Wellpappenpapieren - Wochenblatt für Papierfabrikation, 1986, 10A, p.76 and 7, p.320

L1.49 Ericson, Rigdahl: Clay and CMC as water retention agents – Journal of pulp and paper science No. 11

L 1.50 Pekka Salminen: Determining the Dynamic water retention contribution of various cobinders and thickeners- Tappi coating conference 1995

L 1.51 J. Malik, J. Kline: Water retention of water soluble polymers - Tappi coating conference 1992

L1.52 R. Knappich: Wet and dry coating structure of calcium carbonate with narrow particle size distribution – Tappi Journal, vol. 83, No. 2, Febr. 2000

L1.53 F. Aloi: Understanding the link between film formation and paper surface properties - Pira conference Prag, 2001

L1.54 C. Andersson and Lars Järnström: Control of penetration of starch and hydrophobic sizing agent in surface sizing of porous materials - Appita, Vol. 59, No.3

L1.55 B. Reinhart: Possibilities of surface sizing of silicone base papers - WBl. 6/1992

L1.56 U. Ericson, M. Rigdahl: Dewatering of Coating Colours, Containing CMC or Starch – Journal of P&P science 1994, No.11

L1.57 Pekka Salminen, John Roper, Mark Pollock and Yohannes Chonde: The dynamic water retention – Tappi coating conference 1995

L1.58 Lohendra Pal, M. Joyce, P. Flemming : A simple method for calculation of the permeability coefficient of porous media – Tappi Journal, Vol. 5, No.9, Sept. 2006

L1.59 Cathy Ridgeway and P.A.C. Gane: Effect of latex and pigment volume concentration on suspension and consolidation packing – OMYA internal publication

L1.60 Alexandra Wallström and Lars Järnström: The influence of thickeners on coating surface structure: Pair distribution analysis and correlations to structure and porosity – Tappi Journal, Vol. 6, No. 10, Oct. 2007

L1.61 Mika Väha-Nissi, Antti Savolainen, martti Talja, Raja Mörö: Dispersion barrier coating of high-density base papers – Tappi Journal, Vol. 81, No. 11, Nov. 1998

L1.62 J. Schoelkopf, P.A.C. Gane, C.J. Ridgeway: A comparison of the various liquid interaction radii derived from experiment and network modelling of porous pigmented structures – Colloids and surfaces A; Physiochem. Eng. Aspects 251 (2004), 149 – 159

L1.63 P.A.C: Gane: Pulse dewatering and the mechanics of blade defects in high speed coating – Tappi Coating Conference 1994, pp. 311-312

L1.64 J. Schoelkopf, P.A.C. Gane, C.J. Ridgeway: Pigment coating permeability, measurement and correlation with wetting front penetration – OMYA internal publication

L1.65 S. Moser, Physikalische Eigenschaften einer Silikonrohpapier-Oberfläche und deren Einfluß auf die Silikonisierung – WBl. No.16/April 1986

L1.66 Y. Jiang and T. Amari, Ink penetration into paper near a percolation threshold – Printing Inks 1993(4)

L1.67 C. Ridgeway, P.A.C. Gane: Bulk density measurement and coating porosity calculation for coated paper samples – Nordic Pulp and Paper Research Journal Vol. 18 no. 1/2003

L1.68 J.C. Husband: Interactions between ground calcium carbonate pigments and polymer latices – Nordic Pulp and Paper Research Journal Vol. 15, No. 5/2000

L1.69 J. Skowronski, P. Lepoutre: Water-paper interaction during paper coating, changes in paper structure – Tappi Journal Nov. 1985, Vol. 68, No. 11

L1.70 P.A. Bodurtha, G.P. Matthews, J.P. kettle: The influence of structural anisotropy on fluid permeation in porous media – U Plymouth internal paper

L1.71 S. Lohmander, M. Martinez, L. Lason, M. Rigdahl : Dewatering of coating dispersions – model experiments and analysis – Swedish Research Council for Engineering Science (TFR)

L1.72 Cathy Ridgeway, P.A.C. Gane, Effect of latex and pigment volume concentration on suspension and consolidated particle packing and coating strength – OMYA internal publication

L1.73 G.M. Laudon, G.P. Matthews, P.A.C. Gane: Modelling the shrinkage in pigmented coatings during drying: A stick-slip mechanism – Journal of Colloid and Interface Science

L1.74 P.A.C. Gane, N. Gerteiser, C.J. Ridgeway: Curtain Coating – Die Porenstruktur - OMYA internal publication

L1.75 G.M. Laudone, G.P. Matthews, P.A.C. Gane: Effect of Latex volumetric concentration on void structure, particle packing and effective size distribution in a pigmented paper coating layer – Ing. Eng. Chem. Res. 2006, 45, 1918 - 1923

L1.76 C.J. Ridgeway, P.A.C. Gane: Bulk density measurement and porosity calculation for coated paper samples – OMYA internal publication

L1.77 D. Vidal, C. Ridgeway: Effect of particle size distribution and packing compression on fluid permeability – Computers and Chem. Engineering 2008

L1.78 Peter Resch and Wolfgang Bauer: Porenstruktur von gestrichenen Papieren Autoren - Österreichische Papierfachtagung Graz, 10.05.2005

Lit. 2: Filtration

L2.1 A. Erk, W. Stahl: Rheology of fine particulate suspensions and effects at solid liquid separation – U. Karlsruhe internal publication

L2.2 Carina Maria Alles, Harald Anlauf: Fine Particles in compressible filter cakes – ECCE 2001

L2.3 G. Metreveli, J. Heuser: Grenzflächeneffekte bei der Trennung und Aufbereitung feinstpartikulärer Fest-Flüssig Systeme mit Hilfe filtrierender Verfahren

L2.4 Carina Maria, Harald Anlauf: Process strategies for cake filtration with fine particles - U. Karlsruhe internal publication

L2.5 Ali Akar, Mehmet Polat: Challenges and opportunities in mineral processing - U. Karlsruhe internal publication

L2.6 M. Beiser: Influence of additives on the sedimentation behaviour of fine grained solids in the centrifugal field –Filtration, 4(3), 2004

L2.7 B.K. Parekh, R. Hogg, A. Fonseca: Evaluation of hyperbaric filtration for fine coal dewatering - U. Karlsruhe internal publication

L2.8 Carman – Fundamental principles of industrial filtration – Inst. Of chem. Eng., 1938, No.16, p.168-188

L2.9 Ali Akar, Ü. Ipekoglu, I. Cöcen, M. Polat: Challenges and opportunities in mineral processing – Mining Development Foundation of Turkey- 2004

L2.10 Carina Maria Alles, Harald Anlauf: Fine Particles in compressible filter cakes – AFS 1999:

Lit. 3: Mottling – Latex migration

L3.1 M. Baumeister: Quality optimisation by control of coating structure – Tappi coating conference 1980

L3.2 P.A.C. Gane: Mottle and the influence of coating and binder migration

L3.4 D. Ma, D. Carter, R. Hardy, Ching-Yih Chen (Huber): Print mottle reduction through clay engineering and pore structuring in paper coating

L3.5 M.F.J. Bohan: A model for Ink impression in printing contacts – Journal of pulp and paper science, Vol. 26, No. 11, Nov. 2000

L3.6 Tuulikki Hattula, P.J. Aschan: A comparison of double coatings of board based upon styrene-butadiene and polyvinyl acetate latex – Paeri ja Puu – No.5, 1981

L3.7 G. Engström: Binder distribution and mass distribution of the coating layer, cause and consequence - Tappi Journal, May 1991, pp. 171 - 179

L3.8 C. Guyot: Mottling determined by Raman microscopy - WBl. 14/15, 1995

L3.9 K. Kranich: Migrationserscheinungen Praxis – Labor (Wbl. 6/1988)

L3.10 Do Ik Lee, M. Whalen-Shaw: Fundamentals and Strategies

L3.11 Y. Xiang, D.W: Bousfield, J. Hassler, P. Coleman and A. Osgood: Measurement of Local Variation of Ink Dynamics – Journal of Pulp and Paper Science, Vol. 25, No.9, Sept. 1999

L3.12 Ph. Bernada, D. Bruneau: Modeling binder migration during drying of paper coating – Tappi Journal September 1996, Vol. 79, No. 9

L3.13 T. Hattula, P.J. Aschan: A comparison of double coatings of board based upon styrene butadiene and polyvinylacetate latex – Paperi ja Puu, No. 5, 1981

L3.14 Charles S. Kan, L.H. Kim, Do I. Lee, R. v. Gildern: Viscoelastic properties of paper coatings: Relationship between coating structure, viscoelasticity and end-use performance – Tappi Journal Vol. 80, No. 5, May 1997

L3.15 R. Groves, A. Lanham: Some influence of latex on coating structure – Paper Technology January 1991

L3.16 Tomi Kimpimäki: Effect of drying temperature on the coalescence of polymer particles and on the properties of dispersion coated paperboard (PhD work Tampere University of technology 1997)

L3.17 J.S. Bergh, D.J. Lundberg and E. Glass: Rheology of associative thickener pigment and pigmented commercial latex dispersions – Progress in Organic Coatings, 17 (1989), p.155 – 173

L3.18 D.M. Mahli, J.M. Wegner and J.H.E.Glass: Waterborne latex coatings of color I. Component influences on viscosity decreases – JCT Research, Vol. 2, No. 8, Oct. 2005

L3.19 E. Kostansek: Controlling particle dispersion in latex paints containing associative thickeners – JCT, Res. 4 (4), 2007, p. 375 – 388

L3.20 E.A. Johnson: Interaction between rheology modifiers and dispersants in pigments – Farbe & Lack, 9/1994, p. 759 – 764

L3.21 D.J. Lundberg and E. Glass: Pigment stabilization through mixed associative thickener interactions – JCT, Vol. 64, No. 807, April 2002, p. 53 – 61

L3.22 E. Kostansek: Controlled coagulation of emulsion polymers – JCT Research, Vol. 1, No. 1, Jan. 2004, p. 41 - 44

L3.23 E. Kostansek: Associative polymer/particle dispersion phase diagrams III: Pigments – JCT Research, Vol. 3, No. 3, July 2006, p. 165 - 171

Lit. 4: Blade coating

L4.1 Hideku Fujiwara: The effect of water penetration on offset mottling –Tappi coating conference 1991

L4.2 Dissertation of Natalia Egorova: Using slit rheometry in characterising coating colour flow in the blade coating process

L4.3 M. Johnson: An investigation of the exit flow from a bevelled blade coater with implications for weeping – Tappi coating conference 2000, p. 185

L4.4 A. Roshanzamir, C. Gooch: Hydrodynamic pressure generated by doctoring in blade gap formers – Tappi Vol. 84, No.7, 2001

L4.5 F.R. Pranckh, L.E. Scriven: The physics of blade coating of a deformable substrate – Tappi, Jan.1990

L4.6 D. Eklund, J. Kahila: Blade coating, Part 1: Theory – PTS symposium 1977

L4.7 J. Weigl, H. Grossmann: Factors impeding high speed runability of blade coaters – Tappi Vol. 80, No. 11, Nov. 1997

L4.8 St. Kuni, M. Laves: jet coating technology for high quality board – Tappi coating conference 2002

L4.9 G. Engström: Formation and consolidation of coating layer and the effect on offset print result - Tappi Journal, Aug. 1994

L4.10 Nick Triantafillopoulos, N. Altug: A comparative study of forces in blade coating – Tappi Forest Products Symposium 1991

L 4.11 G. Engström, V. Morin: Analysis of the processes of forming and consolidation in blade coating - Tappi Journal, Vol. 79, No. 9, Sept. 1996, p. 120 – 128

L4.12 D. Eklund, S.J. Kahila, D. Obetko: Die Vorgänge unter dem Schaber beim Glättschaberstreichen – II. Praktische Versuche – WBl. 18-1978

L 4.13 Ilkka Kartovaara: Lateral force under the blade tip in bevelled blade coater – Tappi coating conference 1991, p. 385 – 399

L4.14 P. Isakson. M. Rigdahl, P. Flink, S. Forsberg: Aspects of the elongational flow behaviour of coating colours – Journal of pulp & paper science, Vol. 24, No. 7, July 1998

L4.15 P.A.C. Gane, L. Coggon: Coating blade geometry: Its effect on coating color dynamics and coated sheet properties – Tappi Journal Dez. 1987, p.87 – 96

L4.16 P.A.C. Gane, Ph. McGenity, Ph. Watters: Factors influencing the runability of coating colors at high speed – Tappi Journal, May 1992

L4.17 D. Eklund, T.O. Granvist, R. Salahetetdin (Abo): Influence of viscosity and water retention on the blade forces – PTS Streicherei Symposium 2003, p. 21-1

L4.18 W.J. Follette, R.W. Fowells: Operating variables of a blade coater – Tappi Journal Vol. 43, No. 11, Nov. 1960

L4.19 P. Isaksson, M. Rigdahl, P. Flink, S. Forberg: Aspect of elongational flow behaviour of coating colours - Journal of pulp and paper science 1998, 24(7), pp. 204-209.

Lit. 5: Film press coater (MSP)

L5.1 U. Forsström, Johann Grön: MSP coating holdout – PTS-Symposium 1999 – Art. 25-10:

L5.2 Ph. Letzelter, Dan Eklund: Die Entwässerung von Streichfarben in der Filmpresse – WBl. 11/12, 1987

L5.3 X Zou, D. Vidal: Film press for pigment coating – Tappi MSP conference 2002

L5.4 U. Forsström: The role of base paper porosity in MSP coating – Paperia Piu, Vol. 85, No. 8, 2003

Lit. 6: Drying induced mottling

L6.1 Helmut Graab: Trocknung gestrichener Papiere – WBl 17-1983

L6.2 J. Wayne Dappen: Distribution of starch in clay coatings – Tappi Vol. 34, No.7, July 1951

L6.3 R. Aust: Rechnerische Simulation des Trocknungsverlaufes in Streichanlagen- PTS Streicherei Symposium 2001

L6.4 C. Guyot: Mottling von gestrichenen Papieren, Untersuchungen mit Raman Mikroskopie – WBl. 14/15, 1995

L6.5 R. Aust: IR-Trocknung mit hoher Energieausbeute - PTS-Symposium 1997

L6.6 Ph. Norddahl: Effect of drying conditions on LWC quality – Tappi Journal, May 1991

L6.7 P. Rajala: Statistical investigation of drying effect on offset paper quality – Tappi Journal, July 2004, No.4

L6.8 J. Paaso: Kontrolle der Bedruckbarkeit während dem Strichprozess – PTS-Symposium 2005

L6.9 K.G. Hagen: IR for coating drying – Tappi Journal may 1989

L6.10 K.G. Hagen: A fundamental assessment of the effect of drying on coating quality – Tappi Journal 49 (1) – 1986

L6.11 K. Yamazaki: Print mottle effect of binder migration and latex film formation during coating consolidation – Tappi Journal 1992, Vol. 76, No. 5

L6.12 E.J. Heisser, D.W. Cullen: Effects of drying on adhesive redistribution and coated paper – Tappi Journal 48 (8) – 1965

L6.13 L. Kim, M. Pollock: Reduction of back trap mottling through optimization of the drying process – Tappi coating conference 1997

L 6.14 V. Traudt: Vorgänge bei der Strichtrocknung mit IR und Airfoil – PTS-Symposium 1989

L6.15 Matti Toivakka, Dan Eklund, Douglas W. Bousfield: Pigment motion during drying – Forest Products Symposium 1991

L6.16 G.M. Laudone, G.P. Matthews and P.A.C. Gane: Coating shrinkage during evaporation: Observation, measurement and modelling within a network structure – Tappi Spring Advanced Coating Fundamentals Symposium 2003

L6.17 G. M. Laudone, G.P. Matthews, P.A.C. Gane: Observation of Shrinkage during Evaporative Drying of Water-Based Paper Coatings – Ing. Eng. Chem. Res. 2004, 43, pp712 – 719

L6.18 G.M. Laudone, G.P. Matthews, P.A.C. Gane: Modelling the shrinkage in pigment coatings during drying: A stick-slip mechanism – Journal of Colloid Interface Science 304 (2006), 180 – 190

L6-19 George Alderfer, Esko Aarni, SMI and Pasi Rajala, John Anderson: Evaproate Energy demands of coatings formulated with calcium carbonate pigment - Tappi coating conference 2002

L6.20 G. Laudone, G.P. Matthews and P.A.C. Gane: Oberservation of shrinkage during evaporative drying of water-based paper coatings – Ing. Eng. Chem. Res. 2004, 43, p.712 – 719

L6.21 G. Bluvol, M. Kässberger, F. Reichart: Maximizing solids content in blade coating – PTS coating symposium Sept. 2009

7. Fibre sorption and flocculation

L7.1 M.C. Asensio, J. Seyed-Yagoobi and C.C. Tijerina: Determination of the capillary pressure function for paper using centrifuge data – Tappi Engineering Conference 1994

L7.2 Danny G. Eagleton and Jorge A. Marcondes: Moisture-sorption isotherms for paper-based components of transport packaging for fresh produce – Tappi Journal, Vol. 77, No. 7, July 1994

L7.3 Okubayashi, Griesser: Water accessibilities of man-made cellulosic fiber - Springer, Vol. 12, No.4, 2005

L7.4 Erik Baggrud and Stig Stenström: Modelling of moisture gradients for convective drying of industrial pulp sheets – Paper No. 30 – 2000

L7.5 E.K.O. Hellén, J.A. Ketoja, K.J. Niskannen and M.J. Alava: diffusion through fibre networks – Journal of pulp and paper science, Vo. 28, No.2, Febr. 2002

L7.6 G.V. Laivins, A.M. Scallan (P&P RD Quebec): Removal of water from pulps by pressing, part I: Inter- and intra-wall water – Tappi Engineering Conference 1993

L7.7 T. Bither, J. Waterhous: Strenght development through refining and wet pressing – Tappi International Paper Physics Conference 1991

L7.8 L. Paavilainen (RD Jakko Pöyry): Influence of fibre morphology and processing on the paper making potential of softwood sulfate pulp fibres – Tappi Pulping Conference 1994

L7.9 T. Karppinen, I. Kassamakov, E. Haeggström: Measuring paper wetting processes with laser transmission

L7.10 Huawei Yan and Bo Norman: A flow loop system for study of fibre suspension Flocculation - Nordic Pulp and Paper Research Journal Vol 21 no. 1/2006

L7.11 Markus Lechthaler: Erfassung von Oberflächen unbedruckter und bedruckter Papiere im Nanometerbereich, Österreichissch Papier Fachtagung 10.5.2005

L7.12 Martin Tietz and Isabel Endres: Erfassung von Oberflächen unbedruckter und bedruckter Papiere im Nanometerbereich – Tappi Journal Nov. 2007